



SUPPLEMENTAL PROCEEDINGS



TMS

 Springer

The Minerals, Metals & Materials Series

The Minerals, Metals & Materials Society
Editor

TMS 2021 150th Annual Meeting & Exhibition Supplemental Proceedings

TMS

 Springer

Editor
The Minerals, Metals & Materials Society
Pittsburgh, PA, USA

ISSN 2367-1181 ISSN 2367-1696 (electronic)
The Minerals, Metals & Materials Series
ISBN 978-3-030-65260-9 ISBN 978-3-030-65261-6 (eBook)
<https://doi.org/10.1007/978-3-030-65261-6>

© The Minerals, Metals & Materials Society 2021

This work is subject to copyright. All rights are solely and exclusively licensed by the Publisher, whether the whole or part of the material is concerned, specifically the rights of translation, reprinting, reuse of illustrations, recitation, broadcasting, reproduction on microfilms or in any other physical way, and transmission or information storage and retrieval, electronic adaptation, computer software, or by similar or dissimilar methodology now known or hereafter developed.

The use of general descriptive names, registered names, trademarks, service marks, etc. in this publication does not imply, even in the absence of a specific statement, that such names are exempt from the relevant protective laws and regulations and therefore free for general use.

The publisher, the authors and the editors are safe to assume that the advice and information in this book are believed to be true and accurate at the date of publication. Neither the publisher nor the authors or the editors give a warranty, expressed or implied, with respect to the material contained herein or for any errors or omissions that may have been made. The publisher remains neutral with regard to jurisdictional claims in published maps and institutional affiliations.

This Springer imprint is published by the registered company Springer Nature Switzerland AG
The registered company address is: Gewerbestrasse 11, 6330 Cham, Switzerland

This volume is a collection of papers from the TMS 2021 Virtual Annual Meeting & Exhibition. The contributions represent 40 symposia from the meeting. This volume and the other 10 volumes published for the meeting—complemented by contributions to TMS archival journals—represent the available written record of the 86 symposia held at TMS2021 Virtual.

Contents

Part I 2D Materials—Preparation, Properties and Applications	
Cesium Lead Bromides—Structural, Electronic and Optical Properties	3
Aneer Lamichhane and N. M. Ravindra	
Structure and Electrochemical Property of Coal-Based Activated Carbon Modified by Nitric Acid	15
Mengyao Ma, Wencui Chai, and Yijun Cao	
Thermal Laser-Assisted Manufacturing of Two-Dimensional Atomic Layer Heterostructures	25
Yingtao Wang and Xian Zhang	
Part II Additive Manufacturing: Beyond the Beam II	
3D Printing Architecture	37
Virginia San Fratello	
Effect of HS Binder on Reducing the Amount of Bentonite in Oxidized Pellets	50
Qianqian Duan, Yongbin Yang, Rui Xu, Yingrui Dong, and Zhichen Yuan	
Linear Friction Welding: A Solid-State Welding Process for the Manufacturing of Aerospace Titanium Parts	60
N. Piolle	

Part III Additive Manufacturing Fatigue and Fracture V: Processing-Structure-Property Investigations and Application to Qualification	
Defect-Based Fatigue Modeling for AlSi10Mg Produced by Laser Powder Bed Fusion Process	75
Avinesh Ojha, Wei-Jen Lai, Ziang Li, Carlos Engler-Pinto, and Xuming Su	
Effect of Laser Remelting on Microstructure, Residual Stress, and Mechanical Property of Selective Laser Melting-Processed Ti-6Al-4V Alloy	92
Yiwa Luo, Yu Jiang, Jun Zhu, Jiguo Tu, and Shuqiang Jiao	
Notch Sensitivity of AlSi10Mg Aluminum Alloy Produced by Laser Powder Bed Fusion Process	100
Avinesh Ojha, Wei-Jen Lai, Carlos Engler-Pinto Jr., and Xuming Su	
Progressive Amplitude Fatigue Performance of Additively Manufactured Stainless Steel Superalloy	110
Sanna F. Siddiqui, Krystal Rivera, Isha Ruiz-Candelario, and Ali P. Gordon	
Part IV Additive Manufacturing for Energy Applications III	
Detection of Defects in Additively Manufactured Metals Using Thermal Tomography	121
Alexander Heifetz, Dmitry Shribak, Zoe L. Fisher, and William Cleary	
Part V Additive Manufacturing of Metals: Applications of Solidification Fundamentals	
Influence of Pore Formation and Its Role on the Tensile Properties of 17-4 PH Stainless Steel Fabricated by Laser Powder Bed Fusion	131
Dyuti Sarker, Usman Ali, Farid Ahmed, Reza Esmaeilizadeh, Ali Keshavarzkermani, Ehsan Marzbanrad, and Ehsan Toyserkani	
Melt Pool Evolution in High-Power Selective Laser Melting of Nickel-Based Alloy	142
Borisov Evgenii, Starikov Kirill, Popovich Anatoly, and Popovich Vera	
On Mesoscopic Surface Formation in Metal Laser Powder-Bed Fusion Process	149
Shanshan Zhang, Subin Shrestha, and Kevin Chou	

Part VI Additive Manufacturing: Solid-State Phase Transformations and Microstructural Evolution

Evolution of Microstructure and Dispersoids in Al-Mg 5xxx Alloys Under Wire + Arc Additive Manufacturing and Permanent Mold Casting 165
 K. Liu, A. Algendy, J. Gu, and X. -G. Chen

Main Microstructural Characteristics of Ti-6Al-4V Components Produced via Electron Beam Additive Manufacturing (EBAM) 176
 Silvia Lopez-Castaño, Philippe Emile, Claude Archambeau, Florence Pettinari-Sturmel, and Joël Douin

Microstructural Characterization of Maraging 300 Steel Fabricated by Select Laser Melting 189
 J. Rodriguez, E. Hoyos, F. Conde, A. L. Jardini, J. P. Oliveira, and J. Avila

Tailoring Microstructure of Selective Laser Melted TiAl-Alloy with In-Situ Heat Treatment via Multiple Laser Exposure 197
 Igor Polozov, Artem Kantyukov, Anatoly Popovich, and Vera Popovich

Part VII Advanced Characterization Techniques for Quantifying and Modeling Deformation

Analysis of Slip Transfer in Ti-5Al-2.5Sn (Wt%) at Two Temperatures in Comparison with Pure Aluminum 207
 Chelsea Edge and Thomas R. Bieler

Part VIII Advanced Functional and Structural Thin Films and Coatings

Atomic Layer Deposition and Atomic Layer Etching—An Overview of Selective Processes 219
 Samiha Hossain, Oktay H. Gokce, and N. M. Ravindra

Investigations on the Process Stability of Dry Deep Drawing with Volatile Lubricants Injected Through Laser-Drilled Microholes 230
 Gerd Reichardt, Manuel Henn, Paul Reichle, Daniel Hemming, Georg Umlauf, Kim Riedmüller, Rudolf Weber, Jakob Barz, Mathias Liewald, Thomas Graf, and Günter E. M. Tovar

Nanoengineered Coating; Lotus Effect, Morphology, Contact Angles and Wettability 247
 N. B. Singh, Lisa Kelly, Narasimha Prasad, Brett Setera, Stacey Sova, David Sachs, Bradley Arnold, Fow-Sen Choa, and Christopher Cooper

Temperature Dependence of Energy Gap in Semiconductors—Influence on Solar Cell Performance	259
Rayan Daroowalla, Ritvik R. Rangaraju, Leqi Lin, and Nuggehalli M. Ravindra	
Part IX Advanced High Strength Steels V	
Correlation of Rolling Schedules, Mechanical Properties, and SCC Susceptibility of API X70 Steel	271
A. Roccisano, S. Nafisi, D. Stalheim, and R. Ghomashchi	
Part X Advanced Magnetic Materials for Energy and Power Conversion Applications	
Magnetic Augmented Rotation System (MARS)—An Update	285
Tyler Brunstein-Ellenbogen, B. S. Mani, Tien See Chow, and Nuggehalli M. Ravindra	
Oxide Thin-Film Electronics for the Front-End Conditioning of Flexible Magnetic Field Sensors	294
Niko Münzenrieder, Giuseppe Cantarella, Luisa Petti, and Júlio Costa	
Part XI Advanced Materials for Energy Conversion and Storage VII	
Aluminum-Ion Battery Made of AlCl_3-Trimethylamine Hydrochloride Ionic Liquid With Superior Performance	305
Kok Long Ng, Tony Dong, John Anawati, and Gisele Azimi	
Investigation of Cost-Effective AlCl_3-Urea Ionic Liquid Analog for Al-Ion Batteries	316
Monu Malik, Kok Long Ng, and Gisele Azimi	
Part XII Advanced Real Time Imaging	
In-Situ Quantitative Study of Heat Transfer Performance of Mold Flux by Using Double Hot Thermocouple Technology	331
Zhe Wang, Guanghua Wen, Wenbo Jiang, Ping Tang, and Shuheng Huang	
Synchronized High-Speed Microscopy and Thermoanalytical Measurement for Sub-mm/sub-ms-scale Cathodic Behavior in Molten Salt Electrolysis	338
Shungo Natsui, Ryota Shibuya, Hiroshi Nogami, Tatsuya Kikuchi, and Ryosuke O. Suzuki	
X-ray Radiography Study on Defect Analysis of Electron Beam Welded Plain C-Steel and Fe-7% Al Alloy Joints	346
Soumitra Kumar Dinda, Prakash Srirangam, and Gour Gopal Roy	

Part XIII Advances in Powder and Ceramic Materials Science

Biodegradability and Bioactivity of Porous Hydroxyapatite–Hardystonite–PCL for Using in Bone Tissue Engineering Application 359
 Fariborz Tavangarian, Sorour Sadeghzade, and Rahmattollah Emadi

Effect on Mechanical Properties of Porous Titanium by Adding Ferrovandium Powder 365
 Xu Wang, Guibao Qiu, Yilong Liao, Yuanhui Li, and Zhen Ma

Layered Ceramic Structures $In_{1+x}(Ti_{1/2}Zn_{1/2})_{1-x}O_3(ZnO)_m$ ($m = 2, 4$ and 6 ; $x = 0.5$): Synthesis, Phase Stability and Dielectric Properties 375
 Victor Emmanuel Alvarez Montaña, Subhash Sharma, Francisco Brown, and Alejandro Durán

Microwave Drying Behavior of Zinc Leaching Residue 383
 Chengyu Sun, Xuemei Zheng, Yongguang Luo, Aiyuan Ma, and Song Li

Synthesis of Willemite Bio-Ceramic by Mechanochemical Procedure 392
 Sorour Sadeghzade, Rahmattollah Emadi, and Fariborz Tavangarian

Thermal Shock Resistance of Silica-Free Alumina–Spinel Castables 398
 Yang Liu, Min Chen, Xianglan Yang, and Shan Wang

Thermodynamic Analysis of Fe-FeAl₂O₄ Composite Material Prepared by Molten Salt Deoxidation 409
 Yanke Xu, Hongyan Yan, Chao Luo, Hui Li, and Jinglong Liang

Part XIV Advances in Surface Engineering III

Evaluation of the Surface Integrity of Titanium Nitride Coating Deposited on the Ni–Ti Substrate Through the Near-Dry Electrical Discharge Surface Coating Process 421
 Ramver Singh, Akshay Dvivedi, and Pradeep Kumar

Part XV Advances in Titanium Technology

Investigation to Hole Surface Microstructure Evolution in Drilling of Aerospace Alloys: Ti-5553 433
 David P. Yan

Part XVI AI/Data Informatics: Applications and Uncertainty Quantification at Atomistics and Mesoscales

Solving Stochastic Inverse Problems for Structure-Property Linkages Using Data-Consistent Inversion 447
Anh Tran and Tim Wildey

Part XVII AI/Data Informatics: Design of Structural Materials

Incorporating Historical Data and Past Analyses for Improved Tensile Property Prediction of 9% Cr Steel 461
Madison Wenzlick, Osman Mamun, Ram Devanathan, Kelly Rose, and Jeffrey Hawk

Prediction of the Mechanical Properties of Aluminum Alloy Using Bayesian Learning for Neural Networks 473
Shimpei Takemoto, Kenji Nagata, Takeshi Kaneshita, Yoshishige Okuno, Katsuki Okuno, Masamichi Kitano, Junya Inoue, and Manabu Enoki

Solving Inverse Problems for Process-Structure Linkages Using Asynchronous Parallel Bayesian Optimization 481
Anh Tran and Tim Wildey

Part XVIII Algorithm Development in Materials Science and Engineering

2D Microstructure Reconstruction for SEM via Non-local Patch-Based Image Inpainting 495
Anh Tran and Hoang Tran

Dislocation Dipole Study on Material Hardening/Softening 507
Abu Bakar Siddique, Tariq Khraishi, and Hojun Lim

Model and Improved Dynamic Programming Algorithm for Optimization of Unplanned Slab Allocation in the Steel Plant 514
Yongzhou Wang, Zhong Zheng, Cheng Wang, and Xiaoqiang Gao

Part XIX Alloys and Compounds for Thermoelectric and Solar Cell Applications IX

Order Parameter from the Seebeck Coefficient in Thermoelectric Kesterite Cu_2ZnSnS_4 527
Eleonora Isotta, Binayak Mukherjee, Carlo Fanciulli, Nicola M. Pugno, and Paolo Scardi

Part XX Biological Materials Science

Effect of Cobalt Metal on the Microstructure of Titanium Foam 543
 Hanghang Zhou, Guibao Qiu, Ding Yang, and Tengfei Lu

**Part XXI Characterization of Nuclear Materials and Fuels
 with Advanced X-ray and Neutron Techniques**

**Non-destructive Correlative 3D Characterization of Nuclear
 Graphite: From the Micro-scale to the Nano-scale** 553
 Stephen Kelly, Robin White, William Harris, Tobias Volkenandt,
 Benjamin Tordoff, Giuliano Laudone, Katie Jones, and Ben Veater

**Part XXII Computational Techniques for Multi-scale
 Modeling in Advanced Manufacturing**

**A Parametric Study of Grain Size and Its Volume Fraction
 Effect on Heterogeneous Materials Mechanical Properties** 565
 Khaled Adam and Tarek Belgasam

**Computational Multi-scale Modeling of Segregation
 and Microstructure Evolution During the Solidification of A356
 Ingots Processed via a 2-Zone Induction Melting Furnace** 571
 Aqi Dong and Laurentiu Nastac

**Effect of Nozzle Injection Mode on Initial Transfer Behavior
 of Round Bloom** 579
 Pu Wang, Liang Li, Da-tong Zhao, Wei-dong Liu, Song-wei Wang,
 Hai-yan Tang, and Jia-quan Zhang

**Study on the In-mold Flow Behavior Driven by a Subsurface
 Electromagnetic Stirring for IF Steel Slab Casting** 590
 Hong Xiao, Shao-xiang Li, Pu Wang, Hai-yan Tang, and Jia-quan Zhang

**Part XXIII Corrosion in Heavy Liquid Metals for Energy
 Systems**

**Corrosion Investigations of Materials in Antimony–Tin
 and Antimony–Bismuth Alloys for Liquid Metal Batteries** 605
 Tianru Zhang, Annette Heinzl, Adrian Jianu, Alfons Weisenburger,
 and Georg Müller

**Engineering Model of the Kinetics of the Steel Oxide Layer
 in a Flow of a Heavy Liquid Metal Coolant Under Various
 Oxygen Conditions** 615
 A. V. Avdeenkov, A. I. Orlov, and Nafees Kabir

Exposure Tests of Different Materials in Liquid Lead for LFRs: Effect of the Dissolved Oxygen on Corrosion 626
 S. Bassini, C. Sartorio, A. Antonelli, S. Cataldo, A. Fiore, M. Angiolini, D. Martelli, M. R. Ickes, P. Ferroni, I. Di Piazza, and M. Tarantino

Fundamental Interactions of Steels and Nickel-based Alloys with Lead-based Liquid Alloys or Liquid Tin 642
 Carsten Schroer

Numerical and Analytical Research of the Formation and Accumulation of Deposits on the Circuit with HLM Coolant Within the Consistent Model for Physical and Chemical Processes 657
 A. V. Avdeenkov, O. I. Achakovsky, and A. I. Orlov

Part XXIV Deformation Induced Microstructural Modification

Analysis of Al 6061 and Mild Steel Joints from Rotary Friction Welding 669
 Nikhil Gotawala and Amber Shrivastava

Investigation of Mechanical Properties and Microstructural Valuation Under Different Heat Treatment Parameters of AA6060 Alloy Used in Crash Boxes 679
 Murat Konar, Salim Aslanlar, Erdiñç Ilhan, Cagatay Bölükbaşı, Melih Kekik, Mehmet Buğra Güner, and Görkem Ozcelik

Part XXV Electronic Packaging and Interconnections 2021

On Interface Formation in Zr-Based BMG/6061 Al Interconnects Joined by μ FSSW 691
 David Yan and Logan Vahlstrom

Reliability Evaluation of Ag Sinter-Joining Die Attach Under a Harsh Thermal Cycling Test 701
 Zheng Zhang, Chuantong Chen, Aiji Suetake, Ming-Chun Hsieh, Aya Iwaki, and Katsuaki Suganuma

Part XXVI Environmentally Assisted Cracking: Theory and Practice

A Multiphysics Model of Synergistic Environmental Exposure-Assisted Damage of Composite Using Homogenization-Based Degradation Variables 711
 Zhiye Li and Michael Lepech

Assessing the Susceptibility of Existing Pipelines to Hydrogen Embrittlement 722
 Tim Boot, Ton Rienslag, Elise Reinton, Ping Liu, Carey L. Walters, and Vera Popovich

Combined Ab Initio and Experimental Study of Hydrogen Sorption in Dual-Phase Steels 730
 Saurabh Sagar, Vera Popovich, Pascal Kömmelt, and Poulumi Dey

Stress Corrosion Cracking of TRIP Fe₃₉Mn₂₀Co₂₀Cr₁₅Si₅Al₁ (at.%) High Entropy Alloy 742
 P. Varshney, R. S. Mishra, and N. Kumar

Part XXVII Fatigue in Materials: Fundamentals, Multiscale Characterizations and Computational Modeling

Microstructure and Fatigue Damage Evolution in Additive-Manufactured Metals Using Enhanced Measurement Techniques and Modeling Approaches 753
 M. Awd, F. Walther, S. Siddique, and A. Fatemi

Part XXVIII Frontiers in Solidification Science VIII

Research on Solidification and Heat Transfer Characteristics of Molten Converter Slag in Air Quenching Granulation Process 765
 Wen-Feng Gu, Jiang Diao, Jing Lei, Liang Liu, and Bing Xie

Part XXIX Functional Nanomaterials: Functional Low-Dimensional Materials (0D, 1D, 2D) Driving Innovations in Electronics, Energy, Sensors, and Environmental Engineering and Science 2021

Silicon Carbide Biotechnology: Carbon-Based Neural Interfaces 777
 Chenyin Feng, Mohamad Beygi, Christopher L. Frewin, Md Rubayat-E Tanjil, Ashok Kumar, Michael Cai Wang, and Stephen E. Sadow

Part XXX Heterostructured and Gradient Materials (HGM IV): Tailoring Heterogeneity for Superior Properties

Gradients, Singularities and Interatomic Potentials 793
 K. Parisi and E. C. Aifantis

Part XXXI High Temperature Electrochemistry IV

- Investigation on Preparation of Fe–Al Alloys by Direct Reduction of Fe₂O₃–Al₂O₃ Powder in CaCl₂–NaCl Molten Salt System** 803
Jinrui Liu, Hui Li, and Jinglong Liang

- Liquid Bipolar Electrode for Extraction of Aluminium and PGM Concentrate from Spent Catalysts** 812
Andrey Yasinskiy, Peter Polyakov, Dmitriy Varyukhin, and Sai Krishna Padamata

Part XXXII Materials for High Temperature Applications: Next Generation Superalloys and Beyond

- Open Die Forging Simulation of Superalloy NIMONIC 115 Using DEFORM 3D Software** 829
Swarup Jana, Jyoti Mukhopadhyay, Rajashekar Rao, and Venkatesh Meka

Part XXXIII Mechanical Behavior of Nuclear Reactor Components

- In-situ Scanning Electron Microscopic Observation of Creep and Creep-Fatigue of Alloy 709** 839
Amrita Lall, Rengen Ding, Paul Bowen, and Afsaneh Rabiei
- Simulation of Intergranular Void Growth Under the Combined Effects of Surface Diffusion, Grain Boundary Diffusion, and Bulk Creep** 853
John W. Sanders, Negar Jamshidi, Niloofar Jamshidi, Mohsen Dadfarnia, Sankara Subramanian, and James Stubbins

Part XXXIV Mechanical Response of Materials Investigated Through Novel In-Situ Experiments and Modeling

- In Situ Characterization of the Damage Initiation and Evolution in Sustainable Cellulose-Based Cottonid** 867
R. Scholz, A. Delp, and F. Walther
- Non-destructive Inspection of Contaminated Epoxy Plates Using Propagating Acoustic Waves** 879
I. M. McBrayer and F. Barsoum

Part XXXV Phase Transformations and Microstructural Evolution

Application of High-Throughput Experimental Techniques in Metal Materials Research 891

Hui-cheng Li, You Xie, Jing Yuan, and Xiang-yang Deng

Dilatometric Analysis of Tempering Kinetics in a Cr–Mo–V Medium-Carbon Steel 902

E. F. Barrera-Villatoro, O. Vázquez-Gómez, A. I. Gallegos-Pérez, H. J. Vergara-Hernández, E. López-Martínez, and P. Garnica-González

Thermal and Mechanical Characterization of Non-isothermal Tempering of an Experimental Medium-Carbon Steel 909

P. G. Díaz-Villaseñor, O. Vázquez-Gómez, H. J. Vergara-Hernández, A. I. Gallegos-Pérez, E. López-Martínez, and B. Campillo

Part XXXVI Phonons, Electrons and Dislons: Exploring the Relationships Between Plastic Deformation and Heat

Unified Analysis of Temperature Fields Arising from Large Strain Deformation and Friction in Manufacturing Processes 921

Harish Singh Dhami, Priti Ranjan Panda, Debapriya Pinaki Mohanty, Anirudh Udupa, James B. Mann, Koushik Viswanathan, and Srinivasan Chandrasekar

Part XXXVII Powder Materials for Energy Applications

Thermodynamic Behavior Analysis of Fe-FeAl₂O₄ Cermet Prepared by Zinc Kiln Slag 935

Chao Luo, Jun Peng, Hongyan Yan, Hui Li, and Jinglong Liang

Tunable Morphology Synthesis of Lithium Iron Phosphate as Cathode Materials for Lithium-Ion Batteries 943

Yin Li, Keyu Zhang, Li Wang, Meimei Yuan, and Yaochun Yao

Part XXXVIII Recent Advances in Functional Materials and 2D/3D Processing for Sensors, Energy Storage, and Electronic Applications

3D Printed Passive Sensors—An Overview 955

Vishal R. Mehta and Nuggehalli M. Ravindra

Modeling of Rheological Properties of Metal Nanoparticle Conductive Inks for Printed Electronics 964

Patrick Dzisah and Nuggehalli M. Ravindra

Performance of Chromium Doped Zinc Selenide Nanocrystals: Morphological and Fluorescence Characteristics	980
N. B. Singh, Ching Hua Su, Bradley Arnold, Fow-Sen Choa, Brett Setera, David Sachs, Christopher E. Cooper, Lisa Kelly, and K. D. Mandal	
Part XXXIX Recycling and Sustainability for Emerging Technologies and Strategic Materials	
Characterisation and Techno-Economics of a Process to Recover Value from E-waste Materials	995
Md Khairul Islam, Nawshad Haque, and Michael A. Somerville	
Computational Modeling of Current Density Distribution and Secondary Resistances for Aluminum Electrorefining in Ionic Liquids	1007
M. K. Nahian, Y. Peng, L. Nastac, and R. G. Reddy	
Conductivity of AlCl₃-BMIC Ionic Liquid Mixtures Containing TiCl₄ at Different Temperatures and Molar Ratios	1017
M. K. Nahian, A. N. Ahmed, P. S. Shinde, and R. G. Reddy	
Determination of Physico-Chemical and Hardness Properties of Mullite Rich Tailings from Density Separated Copper Smelter Dust for Ceramic Application	1026
D. O. Okanigbe, A. P. I. Popoola, and T. N. Makua	
Electrochemical Separation of Aluminum from Mixed Scrap Using Ionic Liquids	1036
Aninda Nafis Ahmed and Ramana Reddy	
Iron Recovery from Nickel Slag by Aluminum Dross: A Static Model from Industrial Practice View	1045
Guangzong Zhang, Nan Wang, Min Chen, Xiaobao Li, Hui Li, Ying Wang, and Yanqing Cheng	
Resource Recovery of Cerium from Spent Catalytic Converter Using Aqueous Metallurgy	1055
Sadia Ilyas, Hyunjung Kim, and Rajiv Ranjan Srivastava	
Transient Vortex Flow Characteristics in Three-Strand Bloom Tundish at the End of Casting	1063
Mingtao Xuan, Min Chen, Kaizhu Zhang, and Xiaojie Hua	

Part XL Thermal Property Characterization, Modeling, and Theory in Extreme Environments

Energy Balance Investigation of Close-Coupled Optimized-Pressure Gas Atomization Pour-Tube Design Geometry to Prevent Melt Freeze-Off 1075
 F. Hernandez, E. Deaton, T. Prost, and I. E. Anderson

Author Index 1085

Subject Index 1091

Part I
2D Materials—Preparation, Properties
and Applications

Cesium Lead Bromides—Structural, Electronic and Optical Properties



Aneer Lamichhane and N. M. Ravindra

Abstract In recent years, it has been found that lowering the dimensionality of halide perovskites leads to enhanced photoluminescence and stability than their three-dimensional counterparts. Further, the change in the dimensionality of an inorganic halide perovskite can evoke surprising ramifications to its intrinsic behavior. The dimensionality in perovskites is governed by its octahedral cages. In zero-dimensional perovskites, the octahedral cages are discrete, whereas in two-dimensional perovskites, they are connected with one another resulting in the formation of a layer. Likewise, in three-dimensional perovskites, the octahedral cages share the corner atoms with each other. This study describes the two-dimensional counterpart of cesium lead bromide perovskites. The structural, electronic and optical properties, in conjunction with their three-dimensional structure, are presented. The emergence of new physical phenomena with respect to the decreasing dimensionality of cesium lead bromide perovskites is analyzed.

Keywords $CsPbBr_3$, $CsPbBr_4$, $CsPb_2Br_5$ · Structural properties · Electronic properties · Optical properties

Introduction

Perovskite solar cells have gained notoriety in the last few years as their light-harvesting capacity has been augmented from 3.8% in 2009 to over 24.2% in 2019 [1]. Despite the demonstration of increasing efficiency of perovskite solar cells in a short time, there are several issues such as fabrication processes, stability, degradation, predictability in behavior, durability, toxicity that have hindered their use in the commercial realm [2–4]. Methylammonium lead halide has been extensively studied

A. Lamichhane (✉) · N. M. Ravindra (✉)
Interdisciplinary Program in Materials Science & Engineering, New Jersey Institute of
Technology, Newark, NJ 07102, USA
e-mail: al593@njit.edu

N. M. Ravindra
e-mail: nmravindra@gmail.com

© The Minerals, Metals & Materials Society 2021
TMS 2021 150th Annual Meeting & Exhibition Supplemental Proceedings,
The Minerals, Metals & Materials Series,
https://doi.org/10.1007/978-3-030-65261-6_1

from the very beginning due to its potential as a perovskite solar cell material [5, 6]. However, this material deteriorates rapidly when exposed to light, heat, air or moisture [7, 8]. As an alternative to methylammonium lead halide, it has been found that lead-based and tin-based inorganic halide perovskites show better stability under external conditions and qualify as suitable materials for solar cells and other optoelectronic devices [9–12]. From the environmental perspective, tin-based perovskites are considered as a better choice than lead-based perovskites [13]. Nevertheless, the efficiency and stability of tin-based perovskites are inferior. Furthermore, it has been found that lead-based perovskite solar cells pose a minor environmental hazard [14–17]. Among several inorganic halide perovskites, cesium lead bromide, $CsPbBr_3$, shows promise as a candidate for the fabrication of solar cells and optoelectronic devices due to its stability, inherent direct band gap, broad absorption spectrum and good transport properties [18–20].

In recent years, it has been found that lowering the dimensionality of halide perovskites leads to enhanced photoluminescence and stability than their three-dimensional counterparts [21–24]. Further, the change in the dimensionality of an inorganic halide perovskite can evoke surprising ramifications to its intrinsic behavior. The dimensionality in perovskites is governed by their octahedral cages. In zero-dimensional perovskites, the octahedral cages are discrete, whereas they are connected with one another forming a layer in two-dimensional perovskites. Likewise, in three-dimensional perovskites, the octahedral cages share the corner atoms with each other. Generally, 2D perovskites are synthesized by inserting some suitable chemical that sits in the intercalated region and acts as a spacer between the layered structures. This technique is profound in 2D organic–inorganic hybrid perovskites. Moreover, the variation of such a spacer not only produces the desired stability to the structure but also yields different functionalities of significant interest to the required 2D system. This is illustrated in Fig. 1.

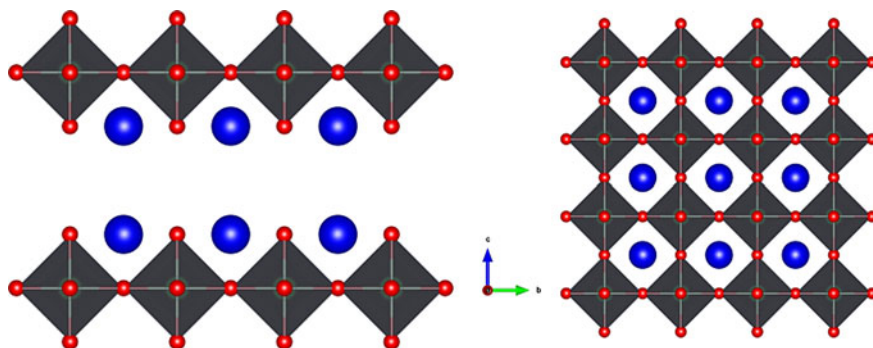


Fig. 1 Illustration showing the role of intercalated atoms as a spacer between the layer of octahedral cages in 2D (left) perovskites whereas the corner atoms link octahedral cages in all directions in 3D (right) perovskites. (Color figure online)

This paper describes the two-dimensional (2D) counterpart of $CsPbBr_3$. One plausible model for 2D- $CsPbBr_3$ would be Ruddlesden–Popper (RP) phase [25]— Cs_2PbBr_4 . Unfortunately, the RP phase is not so frequent in halide perovskites in contrast to oxide perovskites [26]. Nevertheless, it is of interest to proceed with the theoretical study of RP phase of $CsPbBr_3$. On the other hand, the most likely second model for 2D counterpart of $CsPbBr_3$ would be ternary halogen-plumbate $CsPb_2Br_5$. In contrast to Cs_2PbBr_4 , $CsPb_2Br_5$ can be synthesized at room temperature, different from $CsPbBr_3$ which requires a higher temperature. The first report on the synthesis of $CsPb_2Br_5$ was probably mentioned by Yu et al. [27] describing its efficient photoluminescence in the visible region (512 nm) with a quantum yield of 87%. In the paper of Sun et al. [28], the authors have reported that $CsPb_2Br_5$ results as a byproduct during the synthesis of $CsPbBr_3$, yielding higher photoluminescence by transitioning to $CsPb_2Br_5$. However, the work of Jiang et al. [29] has some contradiction by reporting $CsPb_2Br_5$ as an indirect band gap material with inactive photoluminescence. Further, Zhang et al. [30], in their paper, have clarified from the luminescence mechanism that $CsPb_2Br_5$ exhibits a band edge emission in the ultraviolet region and photoluminescence is associated with $CsPbBr_3$ byproduct in $CsPb_2Br_5$.

The need for a theoretical study of Cs-Pb-Br variants is significant due to the complexity in the synthesis and characterization of these materials. The aim of this paper is to study the structural, electronic and optical properties of 3D- $CsPbBr_3$ in conjunction with its 2D counterparts both RP phase Cs_2PbBr_4 and $CsPb_2Br_5$, utilizing the framework of density functional theory (DFT). The emergence of new physical phenomena with respect to the decreasing dimensionality of $CsPbBr_3$ is analyzed. It is anticipated that this work will be beneficial in the design and fabrication of solar cells and other potential optoelectronic devices.

Computational Details

This work utilizes first principles calculations based on DFT in which projector augmented wave (PAW) method was implemented using the Vienna Ab initio Simulation Package (VASP) [31, 32]. All the calculations were performed within the generalized gradient approximation (GGA) using Perdew, Burke and Ernzerhof (PBE) as exchange-correlation functional [33, 34]. The plane wave basis functions with large cut off energy—400 eV (greater than 1.3 times the maximum cut off energy) were used in all the three variants of Cs-Pb-Br along with a sufficiently large Monkhorst K-mesh for Brillouin zone integration. The lattice optimizations were performed with total energy convergence criteria of 10^{-6} eV and final force acting on each atom smaller than 0.02 eV/Å. The resultant optimized structures, along with the lattice parameters, are summarized in Table 1. For post processing, simulation tools such as Vesta [35], Vaspkit [36], Phonopy [37] and Sumo [38] are used in this study.

Table 1 Calculated structure of unit cell geometry with lattice parameters (a, b, c) along with their corresponding literature values in Angstrom

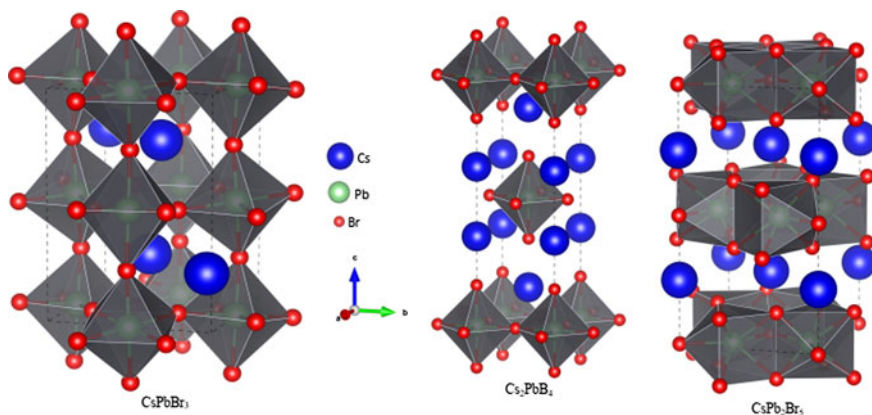
Material	Crystal system	Space group	Unit cell dimensions	Others work Experimental (Theoretical)
$CsPbBr_3$	Orthorhombic	Pnma (62)	$a = 8.34, b = 8.40$ $c = 11.97$	$a = 8.21, b = 8.25$ $c = 11.76$ [39]
Cs_2PbBr_4	Tetragonal	I4/mmm (139)	$a = b = 5.97$ $c = 18.33$	$(a = b = 5.95, c = 18.19)$ [40]
$CsPb_2Br_5$	Tetragonal	I4/mcm (140)	$a = b = 8.61$ $c = 15.47$	$a = b = 8.49$ $c = 15.19$ [41]

Results and Discussion

Structure and Stability

The computed structure of $CsPbBr_3$ crystallizes in the orthogonal space group of Pnma (62) and its 2D counterpart Cs_2PbBr_4 and $CsPb_2Br_5$ in the tetragonal space group of I4/mmm (139) and I4/mcm (140), respectively. Their structures are shown in Fig. 2.

$CsPbBr_3$ has interconnected or corner-sharing octahedron cage $[BX_6]^{-1}$ and Cs^{+1} residing at the center formed by eight such octahedral cages, whereas they are disjoint in Cs_2PbBr_4 . Similarly, the structure of $CsPb_2Br_5$ reveals that Cs^{+} resides in the intercalated region of $[Pb_2Br_5]^{-}$ layers. Further, the stability of these molecules can be verified by calculating their cohesive energy. The cohesive energy per atom (ΔE_c) for any molecule, say $A_aB_bX_x$, is quantified through the relation,

**Fig. 2** Structure of 3D and 2D variants of Cs-Pb-Br. (Color figure online)

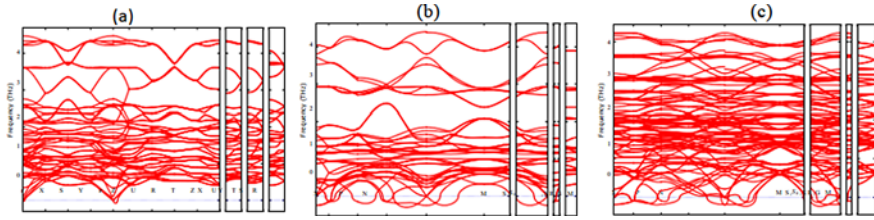


Fig. 3 Phonon dispersion diagram-**a** $CsPbBr_3$, **b** Cs_2PbBr_4 and **c** $CsPb_2Br_5$ under harmonic approximation. (Color figure online)

$$\Delta E_c(A_a B_b X_x) = \frac{aE(A) + bE(B) + xE(X) - E(A_a B_b X_x)}{a + b + x} \quad (1)$$

where $E(i)$, $i = A, B, X$ is the energy of an isolated atom i and $E(A_a B_b X_x)$ represents the total energy of $A_a B_b X_x$. The calculated values of cohesive energy per atom in eV for $CsPbBr_3$, Cs_2PbBr_4 and $CsPb_2Br_5$ are 2.89, 2.87 and 2.88, respectively. Therefore, it appears easy to dissociate Cs_2PbBr_4 among the three compounds of Cs - Pb - Br . Moreover, the orthorhombic phase is possibly the ground-state structures of $CsPbBr_3$, and tetragonal phases of their 2D counterparts are unstable at 0 K temperature. This can be seen by the presence of soft modes in their phonon dispersion diagram, as illustrated in Fig. 3. It has been reported that the stability can be affected by temperature as well as with the number of layers, in the case of 2D [42, 43]. Henceforth, one has enough room to suspect that these tetragonal structures might be stable at room temperature or higher, unless they have low phase transition temperature.

Electronic Properties

For simulating their electronic properties, we have computed the band structures, the total density of states (DOS) and partial density of states (PDOS); these are shown in Figs. 4(i) and (ii). One can notice that except $CsPb_2Br_5$, the other variants show direct band gap. Due to heavy atom Pb, the spin-orbit coupling (SOC) is included in all our calculations. In all three variants of Cs - Pb - Br , there is no significant change in the topography of the valence band with the inclusion of SOC. However, to demonstrate the conduction band degeneracy or split due to SOC, an illustration has been shown for $CsPb_2Br_5$. The calculated values of the band gap with SOC and without SOC, along with their literature values, are shown in Table 2.

It is well known that DFT calculations, using standard functional, severely underestimate the band gap, and due to the intrinsic error cancellation between SOC and neglect of quasi-particle corrections, the band gap computed without SOC has higher proximity to the correct value. Further, the orbital contribution of the valence band maximum (VBM) and the conduction band minimum (CBM) can be analyzed from

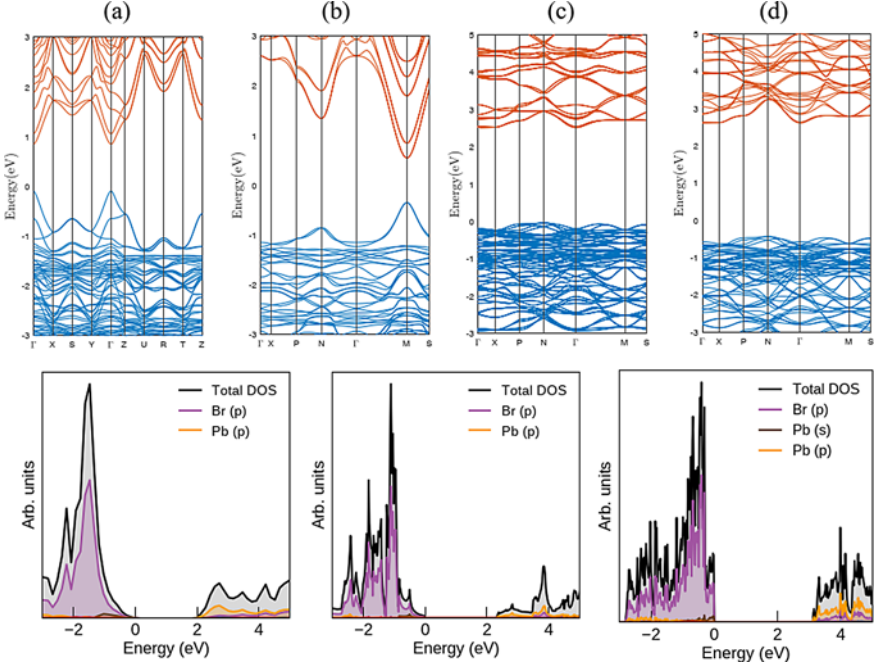


Fig. 4 (i). Top—Calculated band structure diagrams with SOC—**a** $CsPbBr_3$, **b** Cs_2PbBr_4 . **c** and **d** represent $CsPb_2Br_5$ with SOC and WSOC (without SOC), respectively. (ii). Bottom—Their corresponding DOS and PDOS are shown. (Color figure online)

Table 2 Calculated values of band gap (E_g) with SOC and WSOC along with their corresponding literature values in electron volts

Material	E_g SOC; WSOC	Experimental; Theoretical
$CsPbBr_3$	0.95; 2.0	2.25 [44]; 2.16 [45]
Cs_2PbBr_4	0.98; 2.26	—; 2.29 [46]
$CsPb_2Br_5$	2.55; 3.04	3.87 [47]; 3.08 [45]

their DOS and PDOS. In all three variants, the VBM is dominated by Br p state and the CBM mainly constitute Pb p state. It is interesting to note that Cs has no direct contribution to the band edge state.

The absorption of photons in halide perovskite solar cells leads to the generation of electrons and holes. These charge carriers are coupled with each other via Coulomb interaction to form quasiparticles in the form of excitons. The effective mass (m^*) is estimated by the parabolic fitting of energy (E) with momentum (k),

$$m^* = h^2 \left[\frac{\partial^2 E}{\partial k^2} \right]^{-1} \quad (2)$$

and the exciton binding energy (E_b) is calculated by utilizing the Wannier exciton model [48],

$$E_b = \frac{2\mu e^4}{(h8\pi\epsilon(\infty))^2} \quad (3)$$

where μ and \hbar are the reduced effective mass and Planck constant, respectively, e is the electronic charge and $\epsilon(\infty)$ is the permittivity at high wavelength limit (low frequency—static). In the case of $CsPbBr_3$, the computed values of m_e^* and m_h^* , under the effect of SOC, are $0.157 m_e$ and $0.124 m_e$, respectively, and E_b is $51.72 meV$. The literature values of m_e^*/m_h^* are slightly greater/less than $0.2 m_e$, indicating $m_h^* < m_e^*$ [49]. The calculated values of exciton binding energy for $CsPbBr_3$ are in the range of $27\text{--}63 meV$ [50]. Likewise, the values of m_e^* , m_h^* and E_b for Cs_2PbBr_4 are $0.17 m_e$, $0.19 m_e$ and $102.5 meV$, respectively. The values of m_e and m_h for Cs_2PbBr_4 are $0.194 m_e$ and $0.316 m_e$, respectively [51]. Similarly, for $CsPb_2Br_5$, the values of m_e^* , m_h^* and E_b are $0.52 m_e$, $2.41 m_e$ and $292.30 meV$, respectively. It should be noted that the high value of m_h^* can be justified by the flat valence band, as shown in Fig. 4c and d. The relative permittivity values, used in the calculations for $CsPbBr_3$, Cs_2PbBr_4 and $CsPb_2Br_5$, are 4.29, 3.45 and 4.47, respectively. These values are the geometric mean of their respective anisotropic values.

Optical Properties

For investigating the optical properties, the absorption coefficient spectra have been studied for all the three variants of $Cs\text{-}Pb\text{-}Br$. The absorption spectra of materials are of paramount significance as the first and foremost criterion for solar cells should exhibit very high values of the absorption coefficient in the visible range of the solar spectra. Secondly, they play a major role in determining the thickness of cells and therefore in influencing the aspects of cell design. For instance, materials having a higher absorption coefficient are not only suitable for solar cells, but also comparatively thin cells can be designed. The absorption coefficients of materials depend on the frequency of incident photons. The absorption spectral characteristics of $CsPbBr_3$, Cs_2PbBr_4 and $CsPb_2Br_5$ are shown in Fig. 5. The absorption coefficients were calculated from frequency (ω) dependent dielectric functions, $\epsilon(\omega) = \epsilon_1(\omega) + i\epsilon_2(\omega)$ according to the relation [52],

$$\alpha(\omega) = \frac{2\omega}{c} \left[\frac{(\epsilon_1^2(\omega) + \epsilon_2^2(\omega))^{\frac{1}{2}} - \epsilon_1(\omega)}{2} \right]^{\frac{1}{2}}, \quad (4)$$

The absorption edge values found in the literature for $CsPbBr_3$ and $CsPb_2Br_5$ are $2.4 eV$ [53] and $3.26 eV$ [54], respectively, which indeed agree well with our

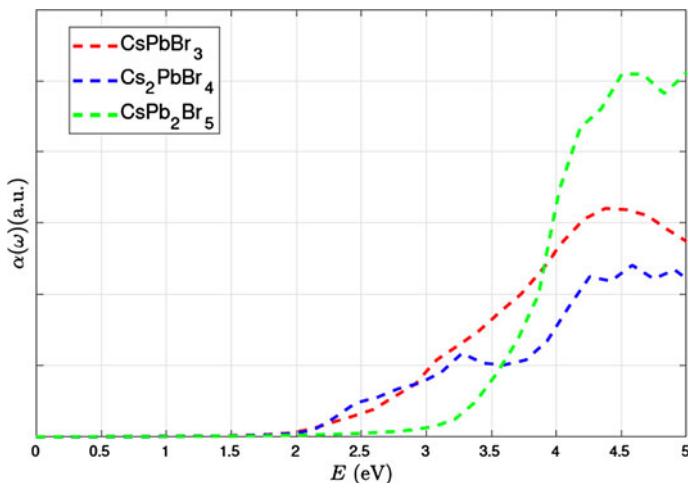


Fig. 5 Calculated absorption coefficients of *Cs-Pb-Br* variants in 100 directions. *CsPbBr₃* is anisotropic in all directions, whereas its counterparts *Cs₂PbBr₄* and *CsPb₂Br₅* are isotropic in 100 and 010 directions. (Color figure online)

computed values. It can be seen that there is no absorption below the band edge of these materials. *CsPbBr₃* and *Cs₂PbBr₄* show broad absorption ranging from the visible to UV region, whereas *CsPb₂Br₅* shows absorption prominent in the UV region. Therefore, *CsPbBr₃* and *Cs₂PbBr₄* are more suitable for photovoltaic applications.

Conclusions

In summary, we have studied the structural, electronic and optical properties of *CsPbBr₃* along with its 2D variants-*Cs₂PbBr₄*, *CsPb₂Br₅*. There is no significant difference in the cohesive energy of these compounds. All of them show anisotropy, and their band structures show noticeable variation in the conduction band region, due to spin-orbit coupling. Except *CsPb₂Br₅*, the other two variants possess intrinsic direct band gap. The optical properties reveal that *CsPbBr₃* and *Cs₂PbBr₄* have absorption edge in the wavelength range of visible to low UV, while *CsPb₂Br₅* shows dominant absorption in the UV region. The calculations show that the excitons are loosely bound in *CsPbBr₃* than its 2D counterparts.

Acknowledgements The authors acknowledge with thanks the support of the Academic & Research Computing Systems, NJIT, especially Dr. Glenn (Gedaliah) Wolosh and Dr. Kevin Walsh.

References

1. Selvakumar Pitchaiya, Muthukumarasamy Eswaremoorthy, Nandhakumarand Natarajan, Agilan Santhanam, Vijayshankar Asokan, Venkatraman Madurai Ramakrishnan, Balasundara-prabhu Rangasamy, Senthilarasu Sundaram, Punniamoorthy Ravirajan, and Dhayalan Velauthapillai (2020) Perovskite solar cells: A porous graphitic carbon based hole transporter/counter electrode material extracted from an invasive plant species *eichhornia crassipes*. *Scientific Reports*, 10(1):6835
2. Djurišić AB, Liu FZ, Tam HW, Wong MK, Ng A, Surya C, Chen W, and He ZB (2017) Perovskite solar cells—an overview of critical issues. *Progress in Quantum Electronics*, 53:1–37
3. Meng Lei, You Jingbi, Yang Yang (2018) Addressing the stability issue of perovskite solar cells for commercial applications. *Nature Communications* 9(1):5265
4. Yaoguang Rong, Yue Hu, Anyi Mei, Hairen Tan, Maksud I. Saidaminov, Sang Il Seok, Michael D. McGehee, Edward H. Sargent, and Hongwei Han (2018) Challenges for commercializing perovskite solar cells. *Science*, 361(6408)
5. Kojima Akihiro, Teshima Kenjiro, Shirai Yasuo, Miyasaka Tsutomu (2009) Organometal halide perovskites as visible-light sensitizers for photovoltaic cells. *J Am Chem Soc* 131(17):6050–6051
6. Quarti Claudio, Mosconi Edoardo, De Angelis Filippo (2014) Interplay of orientational order and electronic structure in methylammonium lead iodide: Implications for solar cell operation. *Chem Mater* 26(22):6557–6569
7. Jun Hong Noh, Im Sang Hyuk, Heo Jin Hyuck, Mandal Tarak N., and Seok Sang Il (2013) Chemical management for colorful, efficient, and stable inorganic–organic hybrid nanostructured solar cells. *Nano Letters*, 13(4):1764–1769
8. Tanzila Ava, Abdullah Mamun, Sylvain Marsillac, and Gon Namkoong (2019) A review: Thermal stability of methylammonium lead halide based perovskite solar cells. *Applied Sciences*, 9:188
9. Azat F. Akbulatov, Lyubov A. Frolova, Nadezhda N. Dremova, Ivan Zhidkov, Vyacheslav M. Martynenko, Sergey A. Tsarev, Sergey Yu. Luchkin, Ernst Z. Kurmaev, Keith J. Aldoshin, Sergey M. and Stevenson, and Pavel A. Troshin (2020) Light or heat: What is killing lead halide perovskites under solar cell operation conditions? *The Journal of Physical Chemistry Letters*, 11(1):333–339
10. Zou Shibing, Li Feng (2020) Efficient all-inorganic CsPbBr₃ perovskite solar cells by using CdS/CdSe/CdS quantum dots as intermediate layers. *Journal of Nanomaterials* 2020:7946853
11. Konstantakou Maria, Stergiopoulos Thomas (2017) A critical review on tin halide perovskite solar cells. *J. Mater. Chem. A* 5:11518–11549
12. Pablo Boix, Shweta Agarwala, Teck Ming Koh, Nripan Mathews, and Subodh Mhaisalkar (2015) Perovskite solar cells: Beyond methylammonium lead iodide. *The Journal of Physical Chemistry Letters*, 6:898–907(150213091342008)
13. Shi Zejiao, Guo Jia, Chen Yonghua, Li Qi, Pan Yufeng, Zhang Haijuan, Xia Yingdong, Huang Wei (2017) Lead-free organic–inorganic hybrid perovskites for photovoltaic applications: Recent advances and perspectives. *Adv Mater* 29(16):1605005
14. Lucía Serrano-Luján, Nieves Espinosa, Thue Trofod, Jose Abad, Antonio Urbina, and Fredrik Krebs (2015) Tin- and lead-based perovskite solar cells under scrutiny: An environmental perspective. *Advanced Energy Materials*
15. Gao Fengqiang, Li Chunhai, Qin Liang, Zhu Lijie, Huang Xin, Liu Huan, Liang Liming, Hou Yanbing, Lou Zhidong, Yufeng Hu, Teng Feng (2018) Enhanced performance of tin halide perovskite solar cell by addition of lead thiocyanate. *RSC Adv.* 8:14025–14030
16. Billen Pieter, Leccisi Enrica, Dastidar Subham, Li Siming, Lobaton Liliana, Spatari Sabrina, Fafarman Aaron T, Fthenakis Vasilis M, Baxter Jason B (2019) Comparative evaluation of lead emissions and toxicity potential in the life cycle of lead halide perovskite photovoltaics. *Energy* 166:1089–1096

17. Syed Azkar Ul Hasan, David S. Lee, Sang Hyuk Im, and Ki-Ha Hong (2020) Present status and research prospects of tin-based perovskite solar cells. *Solar RRL*, 4(2):1900310
18. Xin Li, Yao Tan, Hui Lai, Shuiping Li, Ying Chen, Suwei Li, Peng Xu, and Junyou Yang (2019) All-inorganic CsPbBr₃ perovskite solar cells with 10.45% efficiency by evaporation-assisted deposition and setting intermediate energy levels. *ACS Applied Materials & Interfaces*, 11(33):29746–29752
19. Juan Li, Rongrong Gao, Fei Gao, Jie Lei, Haoxu Wang, Xin Wu, Jianbo Li, Hao Liu, Xiaodong Hua, and Shengzhong (Frank) Liu (2020) Fabrication of efficient CsPbBr₃ perovskite solar cells by single-source thermal evaporation. *Journal of Alloys and Compounds*, 818:152903
20. Zeng Junpeng, Zhou Hai, Liu Ronghuan, Wang Hao (2019) Combination of solution-phase process and halide exchange for all-inorganic, highly stable CsPbBr₃ perovskite nanowire photodetector. *Science China Materials* 62(1):65–73
21. Niu Tingting, Ren Hui, Bo Wu, Xia Yingdong, Xie Xiaoji, Yang Yingguo, Gao Xingyu, Chen Yonghua, Huang Wei (2019) Reduced-dimensional perovskite enabled by organic diamine for efficient photovoltaics. *The Journal of Physical Chemistry Letters* 10(10):2349–2356
22. Yulia Lekina and Ze Xiang Shen (2019) Excitonic states and structural stability in two-dimensional hybrid organic-inorganic perovskites. *Journal of Science: Advanced Materials and Devices* 4(2):189–200
23. Daniela Marongiu, Michele Saba, Francesco Quochi, Andrea Mura, and Giovanni Bongiovanni (2019) The role of excitons in 3d and 2d lead halide perovskites. *J. Mater. Chem. C*, 7:12006–12018
24. Wancai Li, Jiaqi Ma, Xue Cheng, and Dehui Li (2020) Giant enhancement of photoluminescence quantum yield in 2d perovskite thin microplates by graphene encapsulation. *Nano Research*, Jul 2020
25. Ruddlesden SN, Popper P (1957) New compounds of the K₂NiF₄ type. *Acta Crystallogr A* 10(8):538–539
26. Yi Yu, Zhang Dandan, Yang Peidong (2017) Ruddlesden–popper phase in two-dimensional inorganic halide perovskites: A plausible model and the supporting observations. *Nano Lett* 17(9):5489–5494
27. Wang Kun-Hua, Liang Wu, Li Lei, Yao Hong-Bin, Qian Hai-Sheng, Shu-Hong Yu (2016) Large-scale synthesis of highly luminescent perovskite-related CsPb₂Br₅ nanoplatelets and their fast anion exchange. *Angew Chem Int Ed* 55(29):8328–8332
28. Xiaoli Zhang, Bing Xu, Jinbao Zhang, Yuan Gao, Yuanjin Zheng, Kai Wang, and Xiao Wei Sun (2016) All-inorganic perovskite nanocrystals for high-efficiency light emitting diodes: Dual-phase CsPbBr₃-CsPb₂Br₅ composites. *Advanced Functional Materials*, 26(25):4595–4600
29. Li Guopeng, Wang Hui, Zhu Zhifeng, Chang Yajing, Zhang Ting, Song Zihang, Jiang Yang (2016) Shape and phase evolution from CsPbBr₃ perovskite nanocubes to tetragonal CsPb₂Br₅ nanosheets with an indirect bandgap. *Chem Commun* 52:11296–11299
30. Li Jing, Zhang Huijie, Wang Song, Long Debing, Li Mingkai, Guo Yizhong, Zhong Zhicheng, Kaifeng Wu, Wang Duofa, Zhang Tianjin (2017) Synthesis of all-inorganic CsPb₂Br₅ perovskite and determination of its luminescence mechanism. *RSC Adv.* 7:54002–54007
31. Kresse G, Hafner J (1993) Ab initio molecular dynamics for liquid metals. *Phys. Rev. B* 47:558–561
32. G. Kresse and J. Furthmüller (1996) Efficient iterative schemes for ab initio total-energy calculations using a plane-wave basis set. *Phys. Rev. B*, 54:11169–11186
33. Perdew John P, Burke Kieron, Ernzerhof Matthias (1996) Generalized gradient approximation made simple. *Phys Rev Lett* 77:3865–3868
34. Perdew John P, Burke Kieron, Wang Yue (1996) Generalized gradient approximation for the exchange-correlation hole of a many-electron system. *Phys. Rev. B* 54:16533–16539
35. Momma Koichi, Izumi Fujio (2011) VESTA3 for three-dimensional visualization of crystal, volumetric and morphology data. *J Appl Crystallogr* 44(6):1272–1276
36. Wang Vei, Nan Xu (2019) Jin Cheng Liu, Gang Tang, and Wen-Tong Geng. A user-friendly interface facilitating high-throughput computing and analysis using VASP code, Vaspkit

37. Togo A, Tanaka I (2015) First principles phonon calculations in materials science. *Scr. Mater.* 108:1–5
38. Alex Ganose, Adam Jackson, and David Scanlon (2018) sumo: Command-line tools for plotting and analysis of periodic ab initio calculations. *Journal of Open Source Software*, 3:717
39. Rodová M, Brožek J, Knížek K, and Nitsch K (2003) Phase transitions in ternary caesium lead bromide. *Journal of Thermal Analysis and Calorimetry*, 71(2):667–673
40. Li Jiangwei, Qin Yu, He Yihui, Stoumpos Constantinos C, Niu Guangda, Trimarchi Giancarlo G, Guo Hang, Dong Guifang, Wang Dong, Wang Liduo, Kanatzidis Mercouri G (2018) $Cs_2PbI_2Cl_2$, all-inorganic two-dimensional ruddlesden–popper mixed halide perovskite with optoelectronic response. *J Am Chem Soc* 140(35):11085–11090
41. Dursun Ibrahim, DeBastiani Michele, Turedi Bekir, Alamer Badriah, Shkurenko Aleksander, Yin Jun, El-Zohry Ahmed M, Gereige Issam, AlSaggaf Ahmed, Mohammed Omar F, Eddaoudi Mohamed, Bakr Osman M (2017) $CsPb_2Br_5$ single crystals: Synthesis and characterization. *Chemosuschem* 10(19):3746–3749
42. Qi Meng, Yichuan Chen, Yue Yue Xiao, Junjie Sun, Xiaobo Zhang, Chang Bao Han, Hongli Gao, Yongzhe Zhang, and Hui Yan (2020) Effect of temperature on the performance of perovskite solar cells. *Journal of Materials Science: Materials in Electronics*, Feb 2020
43. Chan Myae Myae Soe, G. P. Nagabhushana, Radha Shivaramaiah, Hsinhan Tsai, Wanyi Nie, Jean-Christophe Blancon, Ferdinand Melkonyan, Duyen H. Cao, Boubacar Traore´, Laurent Pedesseau, Mikae’l Kepenekian, Claudine Katan, Jacky Even, Tobin J. Marks, Alexandra Navrotsky, Aditya D. Mohite, Constantinos C. Stoumpos, and Mercouri G. Kanatzidis (2019) Structural and thermodynamic limits of layer thickness in 2d halide perovskites. *Proceedings of the National Academy of Sciences*, 116(1):58–66
44. Constantinos C. Stoumpos, Christos D. Malliakas, John A. Peters, Zhifu Liu, Maria Sebastian, Jino Im, Thomas C. Chasapis, Arief C. Wibowo, Duck Young Chung, Arthur J. Freeman, Bruce W. Wessels, and Mercouri G. Kanatzidis (2013) Crystal growth of the perovskite semiconductor $CsPbBr_3$: A new material for high-energy radiation detection. *Crystal Growth & Design*, 13(7):2722–2727
45. Huang ZhiPeng, Ma Bo, Wang Hao, Li Na, Liu Rui-Tong, Zhang Ze-Qi, Zhang Xiao-Dong, Zhao Ji-Hua, Zheng Pei-Zhu, Wang Qiang, Zhang Hao-Li (2020) In situ growth of 3d/2d ($CsPbBr_3/CsPb_2Br_5$) perovskite heterojunctions toward optoelectronic devices. *The Journal of Physical Chemistry Letters* 11(15):6007–6015
46. Yang Ji-Hui, Yuan Qinghong, Yakobson Boris I (2016) Chemical trends of electronic properties of two-dimensional halide perovskites and their potential applications for electronics and optoelectronics. *The Journal of Physical Chemistry C* 120(43):24682–24687
47. Zhang Zhaojun, Zhu Yanming, Wang Weiliang, Zheng Wei, Lin Richeng, Huang Feng (2018) Growth, characterization and optoelectronic applications of pure-phase large-area $CsPb_2Br_5$ flake single crystals. *J. Mater. Chem. C* 6:446–451
48. Stefano Sanguinetti, Mario Guzzi, and Massimo Gurioli. 6—accessing structural and electronic properties of semiconductor nanostructures via photoluminescence. In Carlo Lamberti, editor, *Characterization of Semiconductor Heterostructures and Nanostructures*, pages 175 – 208. Elsevier, Amsterdam, 2008
49. Negar Ashari-Astani, Simone Meloni, Amir Hesam Salavati, Giulia Palermo, Michael Grätzel, and Ursula Rothlisberger (2017) Computational characterization of the dependence of halide perovskite effective masses on chemical composition and structure. *The Journal of Physical Chemistry C*, 121(43):23886–23895
50. Hamid M. Ghaithan, Zeyad A. Alahmed, Saif M. H. Qaid, Mahmoud Hezam, and Abdullah S. Aldwayyan (2020) Density functional study of cubic, tetragonal, and orthorhombic $CsPbBr_3$ perovskite. *ACS Omega*, 5(13):7468–7480
51. Yang Ji-Hui, Yuan Qinghong, Yakobson Boris I (2016) Chemical trends of electronic properties of two-dimensional halide perovskites and their potential applications for electronics and optoelectronics. *The Journal of Physical Chemistry C* 120(43):24682–24687
52. Yong Hua Duan and Yong Sun (2013) First-principles calculations of optical properties of Mg_2Pb . *Science China Physics, Mechanics and Astronomy*, 57:233–238

53. Hamid M. Ghaitan, Zeyad A. Alahmed, Saif M. H. Qaid, Mahmoud Hezam, and Abdullah S. Aldwayyan (2020) Density functional study of cubic, tetragonal, and orthorhombic $CsPbBr_3$ perovskite. *ACS Omega*, 5(13):7468–7480
54. Jin Mingge, Li Zhibing, Huang Feng, Wang Weiliang (2019) Electronic and optical properties of $CsPb_2Br_5$: A first-principles study. *Mod Phys Lett B* 33(22):1950266

Structure and Electrochemical Property of Coal-Based Activated Carbon Modified by Nitric Acid



Mengyao Ma, Wencui Chai, and Yijun Cao

Abstract Coal gasification fine slag (CGFS) is a kind of industrial waste with more than 30% of carbon, a large surface area, and a broad pore size distribution, which provides favorable conditions for the preparation of activated carbon. In this paper, activated carbon was prepared from residual carbon of CGFS processed by flotation and modified by nitric acid. The effects of nitric acid on the pore structure, surface properties and electrochemical performance of activated carbon were investigated. The results showed that after treated with nitric acid, the content of mesoporous and surface functional groups of coal-based activated carbon increased, leading to the significant improvement of electrochemical properties and electro-adsorption performance.

Keywords Coal-based activated carbon · Electrode materials · Pore structure · Electrochemical performance

Introduction

Coal gasification fine slag (CGFS) is a kind of industrial waste, and China's annual emissions are tens of millions of tons, with more than 30% of carbon. At present, the utilization of coal gasification slag mainly focuses on the separation of residual carbon and application as the admixture of building materials [1]. The residual carbon in coal gasification fine slag can be the precursor to prepare activated carbon with certain specific surface area and pore structure.

W. Chai (✉) · Y. Cao

Henan Province Industrial Technology Research Institution of Resources and Materials,
Zhengzhou University, 450001 Zhengzhou, People's Republic of China
e-mail: cwczu@126.com

Y. Cao

e-mail: yijuncao@126.com

M. Ma · Y. Cao

School of Chemical Engineering and Energy, Zhengzhou University, 450001 Zhengzhou, People's Republic of China

Activated carbon is divided into coal-based activated carbon, wood activated carbon, and nutshell activated carbon according to the raw materials. Coal-based activated carbon has the characteristics of wide raw materials and low price. The preparation of traditional coal-based activated carbon generally divided into two steps: (1) carbonization to remove organic matter and volatiles; (2) activation to obtain a rich pore structure [2]. Activated carbon could be directly obtained by activating the carbon of CGFS, which has low organic matter and volatiles content, and certain pore structure, making the preparation process more simplified. Therefore, the preparation of activated carbon from the residual carbon of CGFS could be an effective way to recycle solid waste.

Electrosorption, a desalination technology developed in recent years, has the characteristics of economy, energy saving and no secondary pollution [3]. Compared with other carbon-based electrode materials, activated carbon is cheap and easy to obtain, widely used in electrosorption desalination. However, due to the low specific capacitance of conventional activated carbon, it often needs to load metal oxides [4, 5] or modify by acid [6] or alkali treatment [7]. Huang et al. [7] found that after modification with nitric acid, the oxygen-containing functional groups and capacitance of activated carbon increase, and the resistance decreases, thereby improving the desalination performance. Moreover, nitric acid can also remove impurities in the gasification slag and improve the pore utilization rate.

In this work, coal-based activated carbon (CAC) was prepared from the residual carbon of CGFS processed by flotation and then was modified by HNO_3 to improve its electrochemical performance. The effects of HNO_3 on the pore structure and electrochemical performance of activated carbon were studied using advanced analytical techniques. The electrosorption performance of CAC for nitrate was investigated through electrosorption tests.

Materials and Methods

Materials

CGFS was obtained from a gasification slag plant in Henan province of China. The residual carbon of CGFS was prepared in our lab. Nitric acid (HNO_3) and sodium nitrate (NaNO_3) were purchased from Sinopharm Chemical Reagent Co., Ltd. N-methylpyrrolidone (NMP) from Macklin, Polyvinylidene fluoride (PVDF) from Arkema, conductive carbon black (Hunan Durban Activated Carbon Manufacturing Co., Ltd.) and foam nickel from Shenzhen Feixin Filter Equipment Co., Ltd. The reagents used in this work are of analytical grade. Deionized water ($18.2 \text{ M}\Omega$) was used for all experiments and acquired from Millipore.

Characterizations

The specific surface area of the samples was determined by using a Macchicker Bayer analyzer (MaxII) based on the BET method. Fourier transform infrared spectrometer (Nicolet Is5) was used to identify the chemical structure and the functional groups presented on the samples. The electrochemical properties of CAC and N-CAC electrodes were obtained by using an electrochemical comprehensive analysis system (Princeton PARSTAT4000A). Scanning electron microscope (Zeiss/auriga-bu, Germany) was used to detect the surface morphology of the samples.

Synthesis and Modification of CAC

The residual carbon of CGFS was firstly grinded to below 75 μm using a universal pulverizer. The residual carbon was activated at 800 $^{\circ}\text{C}$ for 1.5 h in a quartz tube furnace with N_2 atmosphere and heating rate of 10 $^{\circ}\text{C}/\text{min}$ and then cooled to room temperature to obtain the coal-based activated carbon (CAC). The CAC was modified with a range of different concentrations of HNO_3 according to the following step: CAC and HNO_3 solution were mixed in a conical flask and conditioned in a thermostatic oscillator at room temperature to react for 12 h. After reaction, the modified activated carbons were separated by centrifugation, washed with deionized water until the filtrate is neutral and finally placed in a 60 $^{\circ}\text{C}$ vacuum drying oven for 12 h. The modified coal-based activated carbon with HNO_3 was named as 1-N-CAC, 2- N-CAC, 4- N-CAC, 6- N-CAC, 8- N-CAC, respectively.

Electrosorption Experiments

The fabrication of carbon electrode was referenced in the reported literature [3]. Take 100 mg/L NaNO_3 solution and circulate it in electro-adsorption cell at a flow rate of 25 mL/min through a peristaltic pump. Use a DC stabilized power supply to apply a 1.4 V potential at both ends of the electrode. Use a conductivity meter to record every 5 min until the conductivity value no longer drops, and then, the opposite voltage is applied to regenerate the electrode.

Results and Discussion

Electrochemical Performance Analysis

In this study, the electrochemical performance test conducted through CV, EIS and GCD on the electrochemical comprehensive analysis system produced by AMETEK Advanced Measurement Technology. In the test, platinum was used as the counter electrode, Ag/AgCl as the reference electrode, and the electrolyte was 0.5 mol/L KCl solution. The scan rate is 5 ~ 50 mV/s, and the voltage range is $-0.4 \sim -0.8$ V.

The cyclic voltammety curve is usually a center-symmetric curve, and the capacitance and reversibility can be judged according to the shape. According to formula (1), the specific capacitance can be calculated

$$C = \frac{A}{2mk\Delta V} \quad (1)$$

where C —specific capacitance, F/g ; A —cyclic voltammety integral area, $V \cdot A$; m —mass of active material, g ; k —scanning speed, V/s ; ΔV —pressure difference, V (Fig. 1).

At low scanning speeds, the CV curves of CAC and N-CAC are both rectangular, but as the scanning speed increases, the polarization becomes more serious, and the CV curves appear leaf-like. There is no obvious redox peak in the CV curve, which proves that activated carbon is used for ion storage through electric double layer, and the desalination process is mainly electrostatic. Calculating the specific capacitance, cyclic voltammety (CV) studies revealed that 8 mol/L HNO₃ treated

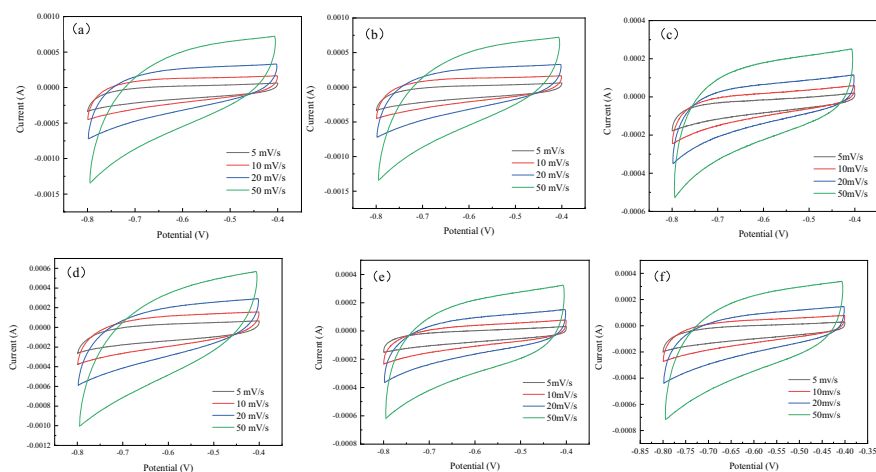


Fig. 1 CV of different concentrations of nitric acid modified activated carbon: **a** 1-N-CAC, **b** 2-N-CAC, **c** 4-N-CAC, **d** 6-N-CAC, **e** 8-N-AC, **f** CAC. (Color figure online)

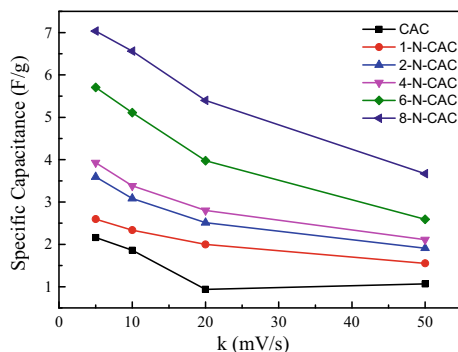


Fig. 2 Specific capacitance of different concentrations of nitric acid modified activated carbon. (Color figure online)

carbon had the highest specific capacitance of 7.07 F/g, lastly un-treated carbon having the capacitance of 2.16 F/g (Fig. 2), and the specific capacitance increases with the increase of the concentration of nitric acid [8].

In order to investigate the difficulty of electronic transmission, EIS test was performed within the frequency range of 10^{-2} ~ 10^5 . The approximately vertical straight line in the low frequency region indicates the capacitance characteristics of the sample; the semicircular arc in the high frequency region is the impedance of the interface between the carbon particles in the activated carbon electrode. In Fig. 3, semicircular arc of the high frequency region is hardly small, indicating that the internal impedance of the electrode material is low and the electron transfer in the hole is relatively easy [9]. The inclined line in the impedance spectrum of modified activated carbon is closer to 45° , indicating that the diffusion resistance of ions in the electrolyte is lower. It may attribute to the surface of 8-N-CAC has more surface functional groups, stronger hydrophilicity, and the pore diameter is also improved, which reduces the resistance of ions in the electrolyte and the pores of the electrode material.

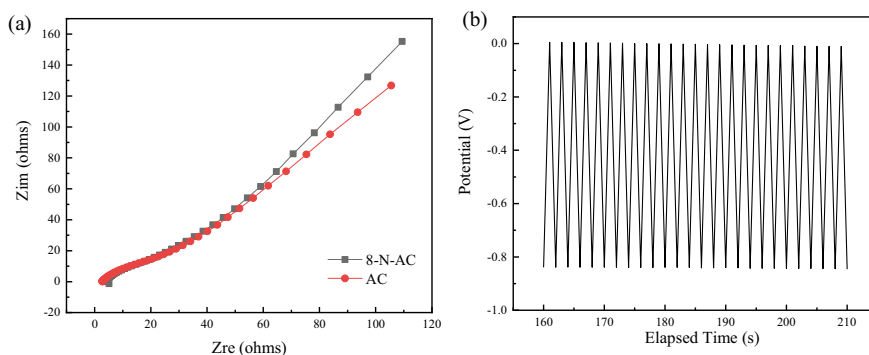


Fig. 3 **a** EIS spectrum of CAC and 8-N-CAC, and **b** GCD of 8-N-CAC. (Color figure online)

As shown in Fig. 3, the charging and discharging curve of 8-N-CAC are of isosceles triangle shape with good reversibility and typical double-layer capacitance characteristics. After 200 cycles, there is no obvious attenuation trend, and 8-N-CAC has good cycling performance.

Morphological Characterizations

The SEM image shows the surface morphology of CAC and 8-N-CAC. As shown in Fig. 4a, c, CAC has certain pore structure, distributes unevenly, and the surface and pores contain a lot of impurities, resulting in poor performance. Figure 4b, d is CAC modified with 8 mol/L HNO_3 (8-N-CAC). It can be seen that after modified, the surface pore structure of activated carbon changed obviously, the pore size increased, and impurities in the pores decreased. Therefore, nitric acid can not only enhance the pore structure of activated carbon, but also reduce the impurity content.

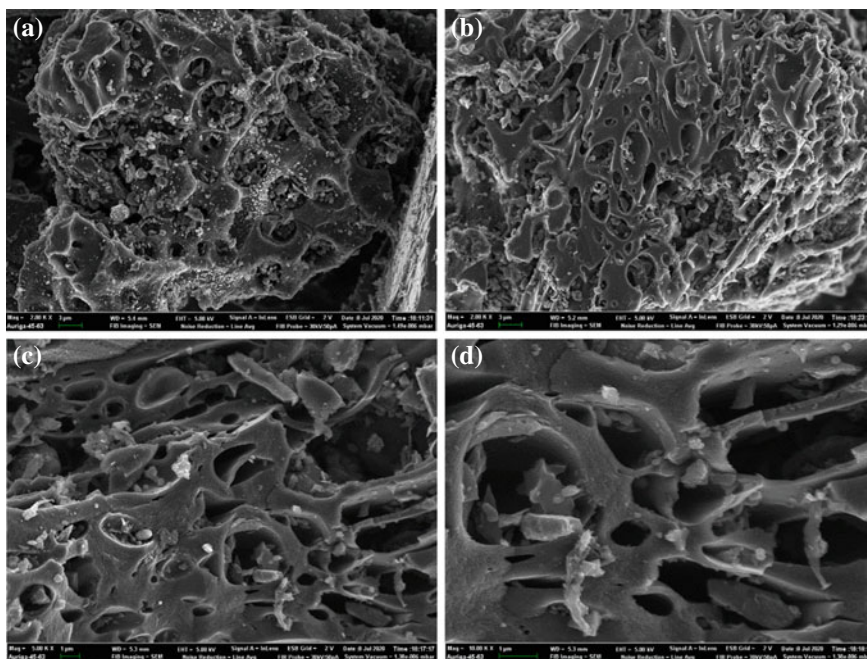
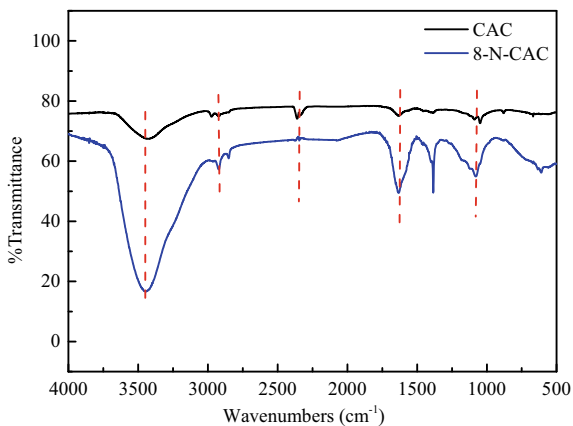


Fig. 4 SEM images of **a** and **c**: CAC, **b** and **d**: 8-N-CAC. (Color figure online)

Fig. 5 FTIR spectra of CAC and 8-N-CAC. (Color figure online)



FTIR Analysis

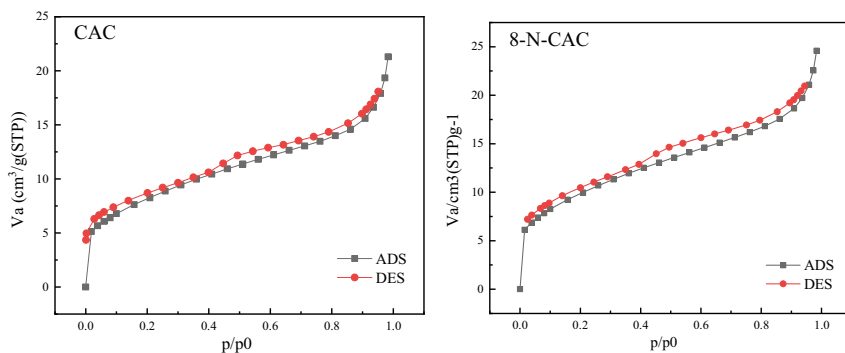
Fourier transform infrared (FTIR) spectroscopy is shown in Fig. 5. The characteristic peak of -OH at 3500 cm^{-1} represents the phenolic and alcoholic hydroxyl groups on the surface of activated carbon, and the intensity of this peak increases significantly after modification. The characteristic peaks for the physical adsorption peak of CO_2 on the surface of activated carbon disappear after modification. The characteristic peaks for -C=O and -COO- around 1400 and 1600 cm^{-1} present in both composites. The absorption peak at 1100 cm^{-1} is attributed to the antisymmetric stretching peak of the carboxylate exist in both CAC and 8-N-CAC. The FTIR test shows that N-CAC surface retains most of the oxygen-containing functional groups in the CAC and enhances partly [10]. These oxygen-containing functional groups can improve the wettability of the surface of the activated carbon electrode material to improve the electrosorption performance

N₂ Adsorption/Desorption Isotherms and Pore Structure

In Fig. 3, the adsorption isotherms of CAC and 8-N-CAC belong to the type II according to the International Union of Pure and Applied Chemistry (IUPAC) adsorption isotherm classification. When the relative pressure (P/P_0) is greater than 0.45, there is a hysteresis loop in the isotherm, which usually related to the capillary condensation in the mesoporous structure. Under low pressure, the adsorption and desorption isotherms overlap, indicating a large number of micropores in the samples. The HK model and BJH model are used to calculate the pore size distribution of CAC and 8-N-CAC. As shown in Table 1, the specific surface area dropped from $35.306\text{ m}^2/\text{g}$ to $29.356\text{ m}^2/\text{g}$ after modification, and total pore volume is

Table 1 Pore structure test results

	$a_{s,BET}/m^2 \cdot g^{-1}$	Volume/cm ³ · g ⁻¹	Average diameter/nm
CAC	35.306	0.038	4.31
8-N-CAC	29.356	0.033	4.48

**Fig. 6** N₂ adsorption/desorption isotherms of CAC and 8-N-CAC. (Color figure online)

slightly reduced. However, the average pore size increased because of the increase in mesoporous content. Nitric acid plays a role in regulating the pore structure (Fig. 6).

Electrosorption Performance

The electro-adsorption performance of CAC and 8-N-CAC was investigated. The adsorption capacity and removal efficiency of activated carbon electrode after modification get better, and electro-adsorption time gets shorter. This is because the content of mesopores in CAC is less, and there are more impurities in the pores. After HNO₃ modified, oxygen-containing functional groups on CAC surface increased, the ratio of mesopores increased, the impurities in the pores reduced, thereby improving the pore utilization rate. Therefore, the electro-adsorption capacity of 8-N-CAC is significantly higher than CAC, salt removal gets more thoroughly, and the concentration of NaNO₃ decreased from 100 mg/L to less than 10 mg/L (Fig. 7).

Conclusions

In this paper, coal-based activated carbon was prepared from fine carbon of coal gasification fine slag flotation. The surface properties and pore structure of HNO₃ modified activated carbon were regulated. It was found that not only the microstructural characteristics of activated carbon could be changed, but also the surface

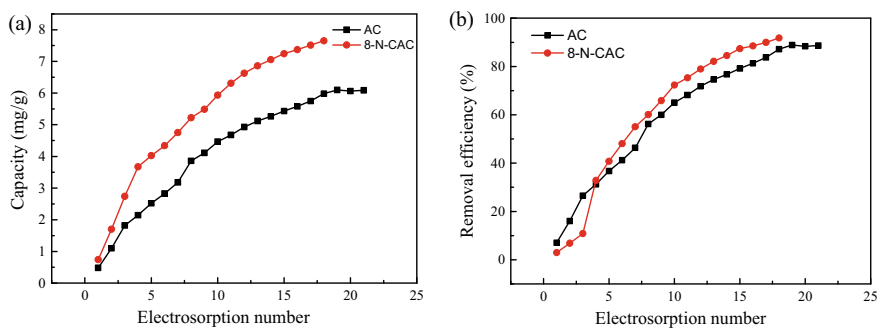


Fig. 7 **a** Electrosorption capacity and **b** removal efficiency of CAC and 8-N-CAC for NaNO₃. (Color figure online)

physical and chemical properties of activated carbon were significantly affected. The optimal concentration of nitric acid modified activated carbon was 8 mol/L, the 8-N-CAC has highest specific capacitance of 7.07 F/g, compared to the CAC, the specific capacitance is increased by 227%. In addition, after modified by nitric acid, the pore structure of activated carbon was developed, the mesoporous content increased, the impurities in the pore reduced, the surface oxygen-containing functional groups increased, so the electro-adsorption performance of activated carbon greatly improved, the concentration of NaNO₃ could be reduced from 100 mg/L to below 10 mg/L.

Acknowledgements The authors acknowledge the financial support of the Key scientific research projects of colleges and universities in Henan Province (No. 21A610011) and High-level Talent Introduction and Training Project of Zhengzhou University (No. 22180012).

References

1. Guo F et al (2019) Fractal analysis and pore structure of gasification fine slag and its flotation residual carbon. *Colloids Surf A* 585:124148
2. Yue X et al (2017) Preparation of coal-based activated carbon electrodes by two steps of physical-chemical activation. *Zhongguo Kuangye Daxue Xuebao/J China Univ Min Technol* 46(4):888–894
3. Tang W et al (2015) Fluoride and nitrate removal from brackish groundwaters by batch-mode capacitive deionization. *Water Res* 84(NOV.1):342–349
4. Xia et al (2016) Electrosorption of fluoride on TiO₂-loaded activated carbon in water. *Colloids Surf A Physicochemical Eng Aspects*
5. A XM et al (2019) Enhanced desalination performance via mixed capacitive-Faradaic ion storage using RuO₂-activated carbon composite electrodes. *Electrochimica Acta* 295:769–777
6. Villar I et al (2010) Capacitive deionization of NaCl solutions with modified activated carbon electrodes. *Energy Fuels* 24(MAY-JUN.):3329–3333
7. Huang W et al (2014) Desalination by capacitive deionization process using nitric acid-modified activated carbon as the electrodes. *Desalination* 340:67–72
8. Chuan-Xiang Z et al (2009) Influence of pore structure of coal-based activated carbons on electric double layer capacitance. *J China Univ Min Technol*

9. B OSA et al (2020) Enhanced electrosorption capacity of activated carbon electrodes for deionized water production through capacitive deionization. *Sep Purif Technol* 247
10. Xue-Yan T, Zhen-Qian C (2018) Change of physico-chemical properties of activated carbons modified with acid-base. *Build Energy Environ*

Thermal Laser-Assisted Manufacturing of Two-Dimensional Atomic Layer Heterostructures



Yingtao Wang and Xian Zhang

Abstract A unique and novel concept about laser printing technology by incorporating a preformed cartridge was proposed to fabricate two-dimensional (2D) heterostructure photoelectric devices. COMSOL multiphysics software was used to perform a simulation to study the factors influencing laser printing performance by constructing a 3D physical model, including material thickness, laser power and spot size. The thinner material thickness can ensure the same temperature distribution on the upper and lower surfaces of PPC, which is conducive to the consistent melting performance. The laser power mainly affects the temperature intensity. The laser power needs to be finely adjusted because even if the laser power differs by 0.5 mW, the temperature can differ by close to 5 °C. The laser spot size has a great influence on the temperature resolution, with the resolution of 100 and 200 nm differing by about 1 time. Under optimal conditions, a resolution of 48 nm can be obtained, which is only nearly 50% of the laser spot size. It is also feasible to obtain 2D materials of other sizes by modifying the parameters to achieve a flexible and controllable preparation scheme. In addition, it is achievable to accomplish a multi-layer printing process of 2D materials that do not affect each other, thereby realizing the free combination of heterostructures. The simulation results provide a foundation for technology optimization of subsequent process realization.

Keywords Two-dimensional materials · Heterostructures · Printing · Simulation

Introduction

Since graphene was synthesized for the first time by stripping using tapes in 2004 [1], the 2D materials family expands increasingly rapidly due to their unique chemical and physical property [2–4] and has applied to a wide range of fields, including

Y. Wang · X. Zhang (✉)

Department of Mechanical Engineering, Stevens Institute of Technology, Hoboken, NJ 07030, USA

e-mail: xzhang4@stevens.edu

energy conversion and storage [5–7], catalysis [8, 9], adsorption [10, 11], electron device [12, 13], photoelectric device [14, 15], medical treatment [16, 17], etc. Numerous materials belong to the category of 2D materials, including transition metal dichalcogenides (TMDs) [18], hexagonal boron nitride (h-BN) [19], graphitic carbon nitride (g-C₃N₄) [20], some metal-organic frameworks (MOFs) [21], covalent-organic frameworks (COFs) [22], transition metal carbides and/or nitrides (MXenes) [23], etc.

Chemical vapor deposition (CVD) and mechanical exfoliation are usually applied to prepare 2D materials [24, 25]. Among them, CVD method can directly deposit the material on the substrate. Materials prepared by mechanical exfoliation are mostly stored in the dispersion agent [26]. The transfer of the materials obtained by these two methods and the subsequent assembly of the devices are complicated that the material is easily contaminated and damaged [27]. Therefore, the subsequent transfer and assembly process of 2D materials have become a research focus [27, 28]. In addition, the heterostructure of two 2D semiconductor materials can offer the material with better optical and electrical properties, which also has attracted large numbers of research interests in many fields [29, 30].

In this paper, a unique laser printing concept incorporating a preformed ‘cartridge’, similar in principle to the method used in laser printing, will be proposed as a new method for fabricating 2D heterostructure photoelectric devices. First, polypropylene carbonate (PPC) and 2D materials will be prepared to form a double-layer structure. Under the heating action of the laser, PPC will obtain viscosity above 50 ~ 52°C and adhere the underlying 2D layer together. If the PPC is removed, the 2D layer under the sticky PPC will be removed together, leaving the 2D layer elsewhere. Alternatively, PPC will melt as the temperature rises to above 90 ~ 95°C. Once the solid PPC is removed, the 2D layer under the melt PPC will remain, while other 2D material will be removed. Laser heating can achieve instantaneous high-temperature heating, and the resolution can reach a level similar to the size of the laser.

COMSOL multiphysics is a large-scale advanced numerical simulation software, widely used in scientific research and engineering calculations in various fields [31–34]. It contains lots of modules, providing a powerful simulation research platform for many fields such as acoustics, thermology, chemical reactions, biological sciences, electromagnetics, optics and fluid mechanics. In order to study the influence of various factors, such as material thickness, laser intensity, spot size and other factors on the printing performance, and to obtain the best printing conditions and offer theoretical support for future printing preparation experiments, the solid heat transfer module was constructed to simulate the printing system.

Experimental

To facilitate research and improve the accuracy of simulation, only the heat generation and heat transfer process of laser in PPC, excluding other components, were studied. Two-dimensional material is much thinner than PPC. The minimum thickness of

the PPC used is $1\ \mu\text{m}$, while that of the 2D layer may be only a few nanometers [35]. The thermal conductivity of the 2D material is comparatively large [36], so it has almost no effect on the heat distribution. Secondly, it is only needed to study the temperature distribution on the bottom surface of PPC and the changes of its physical characteristics. No other components are necessary for modeling. With the purpose of better simulating the interaction between laser irradiation and PPC, such as heat generation, absorption and conduction processes, it is beneficial to use general form of partial differential equations (PDE) to simulate Beer–Lambert law.

Figure 1 shows the constructed 3D thermal model. Constructing a quarter cylinder can better observe the temperature changes around the laser irradiation area. After several simulations and comparisons, it is determined that the radius of the sector is $0.5\ \text{mm}$, because the simulation results of smaller radius are inconsistent with that of larger sizes, which are more accurate. Choosing $0.5\ \text{mm}$ can ensure that the simulation is closer to the real heat transfer situation. A smaller cylinder is built by subtraction method in the middle area of the cylinder. It is the area where the laser is incident and studied by the general form PDE. A Dirichlet boundary is constructed on the upper surface, giving the surface heat flux. The inner side face of the model is set to be thermally insulated, and the outer side and bottom surface are set to radiate heat to the environment. The ambient temperature is room temperature $25\ ^\circ\text{C}$, which is also the initial temperature of the model. The mesh is customized to have a minimum cell size of $100\ \text{nm}$ and a maximum cell size of $10\ \mu\text{m}$. Transient calculation was conducted using the laser heating time $1\ \text{ms}$.

In the COMSOL simulation, the parameters used are as follows: The density of PPC is $1.26\ \text{g}/\text{cm}^3$, the specific heat capacity is $1800\ \text{J}/(\text{kg}\cdot\text{K})$, the thermal conductivity used in the simulation of $90\ ^\circ\text{C}$ is $0.4\ \text{W}/(\text{m}\cdot\text{K})$, and the thermal conductivity for $50\ ^\circ\text{C}$ simulation is $0.22\ \text{W}/(\text{m}\cdot\text{K})$. The laser distribution mode is Gaussian distribution. The expression of laser intensity is

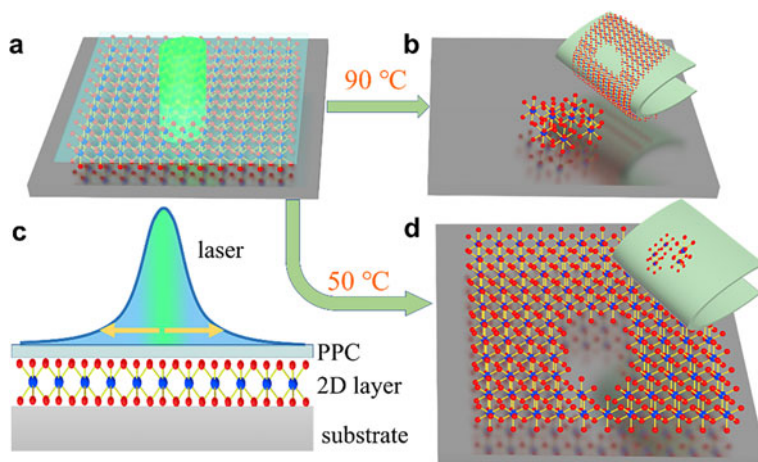


Fig. 1 Schematic diagram of printing technology of laser heating PPC to obtain 2D materials. (Color figure online)

$$0.95 \times P[\text{W/m}^2] \times \exp\left(-\frac{x^2 + y^2}{r^2}\right)$$

where P is the laser intensity after correction, and r is the laser spot radius. 0.95 is the corrected value taking into account the laser loss. For example, for a 15-mW laser, the result value of the double integration of the function $P[\text{W/m}^2] \times \exp\left(-\frac{x^2+y^2}{r^2}\right)$ in a circle with a radius of 100 nm is 15 mW. Through calculation, P is $7.56 \times 10^{11} \text{ W/m}^2$. The absorption coefficient of PPC is 2000 1/m. The source term is $I_z - 2000[1/m] \times I \text{ W/m}^3$. Where I is the laser intensity (W/m^2), and I_z is the partial derivative of I in the z - direction.

Results and Discussion

To study the influence of different thicknesses on the temperature distribution, four conditions were set, i.e. 1, 5, 10 and 100 μm . The simulation was conducted using a 15-mW laser, whose spot size is a circle with a radius of 100 nm. The previous experiments have proved that PPC will melt above 90 ~ 95 $^\circ\text{C}$. Therefore, the expected temperature is set to 90 $^\circ\text{C}$. Figure 2 shows the simulation results. It is found that different thicknesses have almost no effect on the maximum temperature. The highest temperature in the simulation results of the four thickness conditions is about 92 $^\circ\text{C}$. The reason might be that the thermal properties of PPC, such as thermal conductivity

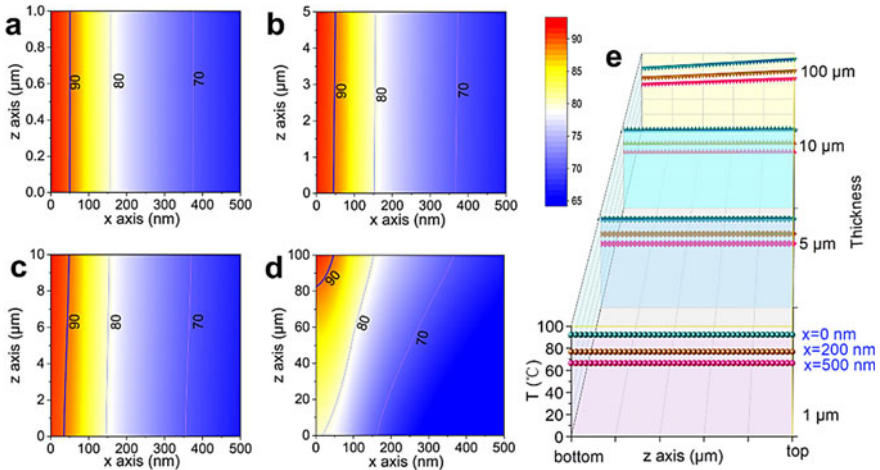


Fig. 2 Temperature distribution of x - z cross section under different thickness conditions of **a** 1, **b** 5, **c** 10, **d** 100 μm . **e** The temperature shifts in the z -axis direction when the x -axis distance is 0, 200 and 500 nm under different thickness conditions. (Color figure online)

and specific heat capacity, have small limit to heat transfer and will not concentrate heat in a specific area to hinder heat transfer.

The thickness affects the uniformity of temperature distribution most. The isotherms of smaller thicknesses such as 1, 5 and 10 μm are much straighter than that of 100 μm . The temperature distribution on the upper and lower surfaces of the material with a thickness of 100 μm is comparatively different and uneven (as shown in Fig. 2d and e). This leads to uncertainty in the melt performance of PPC. Also, the different temperature distribution in the vertical direction means that the melting of PPC at specified location is incomplete, leading to uncertainty about how much 2D material will remain on the substrate. Obviously, this phenomenon is not favorable for the printing performance. Therefore, neat vertical isotherms, like smaller thicknesses shown, are more advantageous to stable viscosity and melt performance. In the following simulation, a thickness of 1 μm will be used.

Another factor that affects the printing performance of 2D materials is the laser power. When the laser power is increased, PPC gains more energy and the temperature rises more. However, an appropriate temperature is beneficial to the resolution of the printed material. Therefore, it is necessary to explore the suitable power to obtain the expected temperature. In order to discuss the temperature distribution of PPC materials under different laser power conditions, four power conditions are set: 10, 12, 15 and 20 mW. The laser spot is a circle with a radius of 100 nm.

Figure 3 shows that the laser power mainly affects temperature intensity. When the power is 10 mW, the highest temperature in the system is only 69.4 $^{\circ}\text{C}$. As the power increases, the maximum temperature gradually increases to 78.4, 92.3 and 114 $^{\circ}\text{C}$.

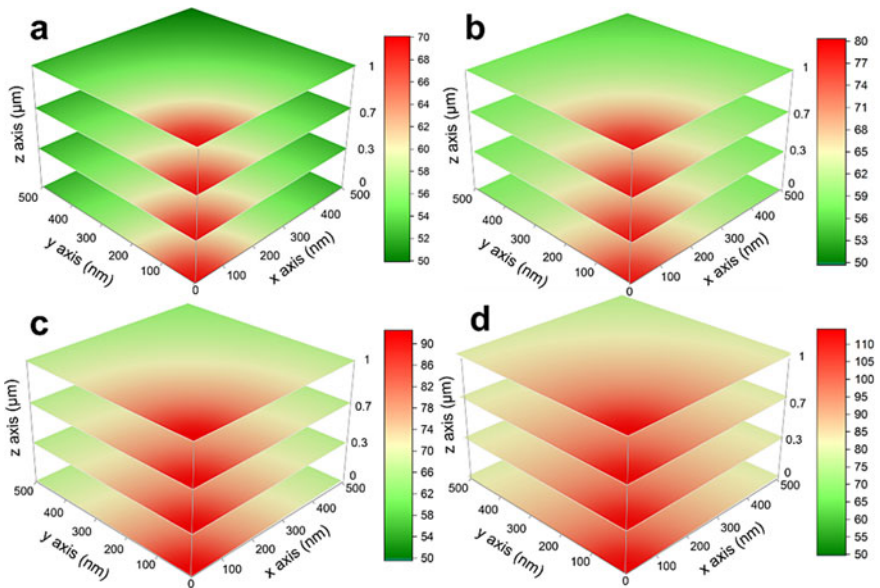


Fig. 3 Temperature simulation results under different power conditions. **a** 10, **b** 12, **c** 15, **d** 20 mW. (Color figure online)

This indicates that the optimal power condition is around 15 mW. To obtain a suitable temperature and a higher-temperature resolution (with a smaller temperature above 90 °C), the power needs to be fine-tuned.

Different laser spot sizes also have an impact on printing performance. With the same laser power, when the spot size is increased, because the laser energy distribution presents a Gaussian distribution, the laser energy distribution will be more dispersed. The energy cannot be concentrated to effectively heat a specific area but disperses in a larger area. This will result in ineffective heating and will not be able to raise the temperature of a specific area to the expected temperature but increase the temperature of other areas.

To explore this effect in detail, four size conditions were set: 100, 200, 400 and 500 nm. A 15-mW laser was used for simulation experiments. As shown in Fig. 4, the temperature distribution varies greatly under different conditions. First of all, it can be shown from the maximum temperature in the system. The maximum temperature of the bottom surface under the four sizes is 92.2, 84.0, 75.9 and 73.3 °C, respectively.

In addition, laser spot sizes also have a great influence on temperature resolution. As shown in Table 1, setting the temperature range of 5 °C, it is found that the temperature resolution is 79, 159, 322 and 404 nm, respectively. As the spot size increases, the maximum temperature gradually decreases, and the temperature resolution deteriorates. The reason, mentioned above, is that the unfocused laser energy brought by larger spot sizes, not only causes lower temperature and energy waste, but also leads to poor temperature resolution.

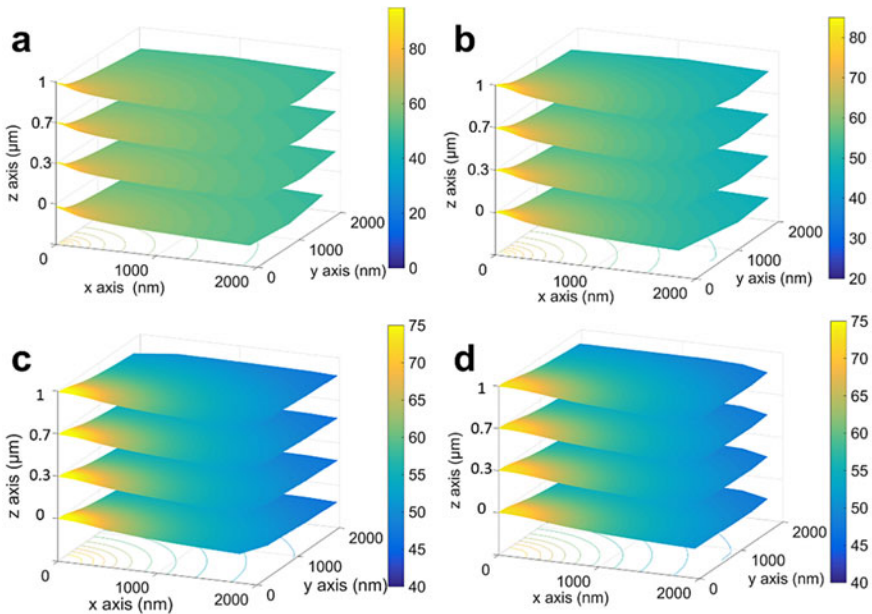


Fig. 4 Simulated temperature results under different laser spot sizes of **a** 100, **b** 200, **c** 400, **d** 500 nm. (Color figure online)

Table 1 Comparison of simulated results under different laser spot sizes

Spot size (nm)	5 °C resolution range	Resolution (radius: nm)
100	87.2 ~ 92.2	79
200	79.0 ~ 84.0	159
400	70.9 ~ 75.9	322
500	68.3 ~ 73.3	404

Table 2 Comparison of simulated results of 90 °C by fine-tuning laser power

Laser power (mW)	Temperature range (> 90 °C)	Resolution (radius: nm)
14.5	89.9	None
15	90 ~ 92.2	48
15.5	90 ~ 94.3	72
16	90 ~ 94.5	77

Through the above discussion, the best printing parameters are that the thickness of the PPC is 1 μm and the spot size is 100 nm. The power needs to be further fine-tuned to obtain the best laser power condition. As shown in Table 2, four power conditions were set: 14.5, 15, 15.5 and 16 mW. After comparison, it is found that 15 mW is the optimal power condition. 14.5 mW is not enough to heat PPC materials above 90 °C. 15.5 and 16 mW obtain similar simulation results. The maximum temperature is 94.3 and 94.5 °C, and the resolution is 72 and 77 nm, respectively.

The desired temperature range obtained by 15 mW is 90 ~ 92.2 °C, and the resolution is 48 nm. Considering that 15 mW satisfies the 90 °C temperature condition and obtains the highest resolution, it is selected as the optimal power condition. Figure 5a–b shows the simulated temperature distribution results under optimal conditions.

The experimental results prove that PPC begins to have viscosity at temperatures above 50 ~ 52 °C. Removal of PPC at 50 °C can bring about the opposite printing effect, i.e. removing the 2D material in the laser-heated area. Therefore, it is vital to simulate and discuss the conditions required to heat PPC to 50 ~ 52 °C. This simulation follows some of the results discussed above, using a laser size of 100 nm and a PPC thickness of 1 μm. Only by fine-tuning the laser power, the optimal power condition of 50 °C is obtained.

Three power conditions were set to get the optimal power condition, i.e. 3, 3.5, 4 mW. As shown in Table 3, 3.5 mW can obtain the expected temperature range, which is 50 ~ 52.5 °C, and the resolution is 85 nm, which is the optimal power condition. 3 mW only heats the PPC material to 47.9 °C, which does not satisfy the expected temperature. The 4-mW laser can heat the PPC material to 55.6 °C, which is higher than the expected temperature, and its resolution is 150 nm, which is much lower than the 3.5-mW’s resolution. Figure 5c–d shows the 3D temperature distribution map under the optimal condition.

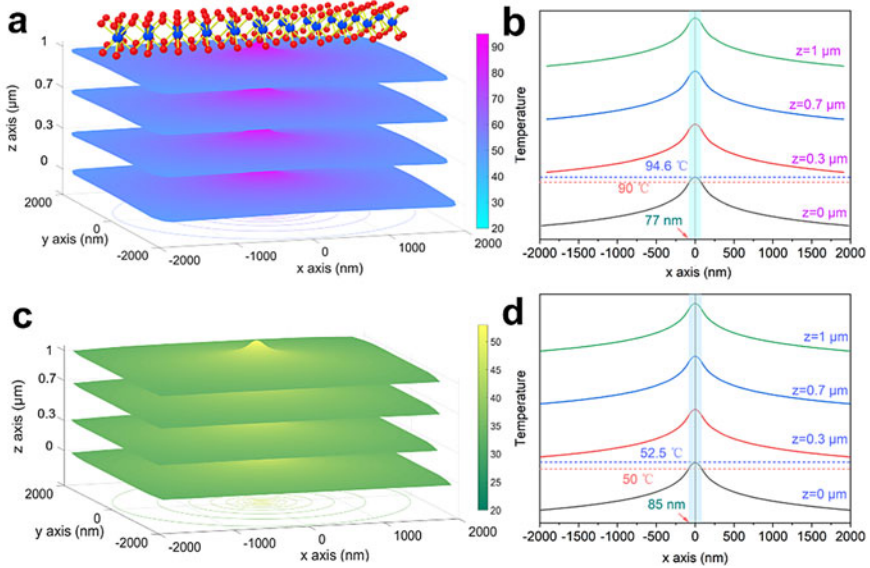


Fig. 5 Simulated temperature distribution results under optimal conditions for temperature of **a–b** 90 °C, **c–d** 50 °C. (Color figure online)

Table 3 Comparison of simulated results of 50 °C by fine-tuning laser power

Laser power (mW)	Temperature range (> 50 °C)	Resolution (radius: nm)
3	47.9	None
3.5	50 ~ 52.5	85
4	50 ~ 55.6	150

The printing of dual 2D material atomic layers is independent to each other. Therefore, all the contents discussed above are equally applicable to the printing of the first and second layer of 2D materials. The printing of the second layer is not affected by the printing of the first one. The same conditions as those of the first layer of material can be used, or other conditions can be selected, and the thickness and width of the second layer of material can be controlled.

Conclusion

In conclusion, in order to study the laser heating of the PPC material to 90 °C to melt it and lose its viscosity to leave a layer of 2D material, a COMSOL thermal conduction simulation was carried out to discuss several factors affecting the laser heating performance, such as the thickness of PPC, the laser power and the laser

spot size. The thinner thickness can ensure the same temperature distribution on the upper and lower surfaces, which is helpful to the consistent melting performance. The laser power mainly affects the temperature intensity. In order to obtain a suitable temperature, the laser power needs to be finely adjusted. For example, the simulation results show that even if the laser power differs by 0.5 mW, the temperature can differ by close to 5 °C. The laser spot size has a great influence on the temperature resolution. For example, the resolution of 100 nm and 200 nm changes by about 1 time. The optimal resolution is 48 nm, whose temperature range obtained by 15 mW is 90 ~ 92.2 °C. Removal of PPC at 50 °C can remove the 2D material in the laser-heated area, with the resolution under optimal condition being 85 nm.

References

1. Novoselov KS, Geim AK, Morozov SV (2004) Electric field effect in atomically thin carbon films. *Science* 306(5696):666–669
2. Long M, Wang P, Fang H (2018) Progress, challenges, and opportunities for 2D material based photodetectors. *Adv Funct Mater* 29(19):1803807
3. Xia F, Wang H, Xiao D (2014) 2D material nanophotonics. *Nat Photonics* 8(12):899–907
4. Butler SZ, Hollen SM, Cao L (2013) Progress, challenges, and opportunities in 2D materials beyond graphene. *ACS Nano* 7(4):2898–2926
5. Chaudhari NK, Jin H, Kim B (2018) Mxene: an emerging 2D material for future energy conversion and storage applications. *J Mater Chem A* 5(47):24564–24579
6. Guan Y, Li N, Li Y (2020) Two dimension ZIF-derived ultra-thin Cu-N/C nanosheets as high performance oxygen reduction electrocatalysts for high-performance Zn-air batteries. *Nanoscale* 12:14259–14266
7. Mei J, Liao T, Kou L (2017) Two-dimensional metal oxide nanomaterials for next-generation rechargeable batteries. *Adv Mater* 29(48). <https://doi.org/10.1002/adma.201700176>
8. Deng D, Novoselov KS, Fu Q (2016) Catalysis with 2D materials and their heterostructures. *Nat Nanotechnol* 11(3):218–230
9. Wang Y, Mao J, Meng X (2019) Catalysis with 2D materials confining single atoms: concept, design, and applications. *Chem Rev* 119(3):1806–1854
10. Lin X, Lu JC, Shao Y (2017) Intrinsically patterned 2D materials for selective adsorption of molecules and nanoclusters. *Nat Mater* 16(7):717–721
11. Guo X, Zhang X, Zhao S (2016) High adsorption capacity of heavy metals on 2D MXenes: an ab initio study with molecular dynamics simulation. *Phys Chem Chem Phys* 18(1):228–233
12. Gong C, Zhang X (2019) 2D magnetic crystals and emergent heterostructure devices. *Science* 363(6428). <https://doi.org/10.1126/science.aav4450>
13. Chhowalla M, Jena D, Zhang H (2016) 2D semiconductors for transistors. *Nat Rev Mater* 1(11):16052
14. Wu Z, Tai G, Wang X (2018) Large-area synthesis and photoelectric properties of few-layer MoSe₂ on molybdenum foils. *Nanotechnology* 29(12):125605
15. Zhou N, Gan L, Yang RS (2019) Nonlayered 2D defective semiconductor γ -Ga₂S₃ toward broadband photodetection. *ACS Nano* 13(6):6297–6307
16. Tao W, Ji X, Zhu X (2018) Two-dimensional antimonene-based photonic nanomedicine for cancer theranostics. *Adv Mater* 30(38). <https://doi.org/10.1002/adma.201802061>
17. Yang B, Chen Y, Shi J (2018) Material chemistry of 2D inorganic nanosheets in cancer theranostics. *Chem* 4(6):1284–1313
18. Manzeli S, Ovchinnikov D, Pasquier D (2017) 2D transition metal dichalcogenides. *Nat Rev Mater* 2:17033

19. Meng JH, Wang DG, Cheng LK (2019) Recent progress in synthesis, properties, and applications of hexagonal boron nitride-based heterostructures. *Nanotechnology* 30(7):074003
20. Liao G, Gong Y, Zhang L (2019) Semiconductor polymeric graphitic carbon nitride photocatalysts: The “holy grail” for the photocatalytic hydrogen evolution reaction under visible light. *Energy Environ Sci* 12(7):2080–2147
21. Zhu H, Liu D (2019) The synthetic strategies of metal–organic framework membranes, films and 2D MOFs and their applications in devices. *J Mater Chem A* 7(37):21004–21035
22. Wang J, Li N, Xu Y (2020) Two-dimensional MOF and COF nanosheets: synthesis and applications in electrochemistry. *Chem Euro J* 26(29):6402–6422
23. Jun B, Kim S, Heo J (2019) Review of MXenes as new nanomaterials for energy storage/delivery and selected environmental applications. *Nano Res* 12(3):471–487
24. Zhang Y, Yao YY, Sendeku MG (2019) Recent progress in CVD growth of 2D transition metal dichalcogenides and related heterostructures. *Adv Mater* 31(41):1901694
25. Huang Y, Pan YH, Yang R (2020) Universal mechanical exfoliation of large-area 2D crystals. *Nat Commun* 11. <https://doi.org/10.1038/s41467-020-16733-4>
26. Samorì P, Palermo V, Feng X (2016) Chemical approaches to 2D materials. *Adv Mater* 28(29):6027–6029
27. Cai X, Luo Y, Liu B (2018) Preparation of 2D material dispersions and their applications. *Chem Soc Rev* 47(16):6224–6266
28. Tao H, Zhang Y, Gao Y (2017) Scalable exfoliation and dispersion of 2D materials—an update. *Phys Chem Chem Phys* 19(2):921–960
29. Liao W, Huang Y, Wang H (2019) Van der waals heterostructures for optoelectronics: progress and prospects. *Appl Mater Today* 16:435–455
30. Shifa TA, Wang F, Liu Y (2019) Heterostructures based on 2D materials: a versatile platform for efficient catalysis. *Adv Mater* 31(45):1804828
31. Turgay MB, Yazicioglu AG (2018) Numerical simulation of fluid flow and heat transfer in a trapezoidal microchannel with comsol multiphysics: a case study. *Numer Heat Transfer Part A-Appl* 73(5):332–346
32. Obraztsov NV, Subbotin DI, Popov VE (2018) Modelling of heating of plasma-chemical reactor in comsol multiphysics. *J Phys Conf* 1038:012137
33. Zhou S, Rabczuk T, Zhuang X (2018) Phase field modeling of quasi-static and dynamic crack propagation: comsol implementation and case studies. *Adv Eng Softw* 122:31–49
34. Wei Z, Weavers LK (2016) Combining COMSOL modeling with acoustic pressure maps to design sono-reactors. *Ultrason Sonochem* 31:490–498
35. Zhang X, Sun D, Li Y (2015) Measurement of lateral and interfacial thermal conductivity of single- and bi-layer MoS₂ and MoSe₂ using refined optothermal raman technique. *ACS Appl Mater Interfaces* 7(46):25923–25929
36. Yalo E, Aslan OB, Smithe KK (2017) Temperature-dependent thermal boundary conductance of monolayer MoS₂ by Raman thermometry. *ACS Appl Mater Interfaces* 9(49):43013–43020

Part II
Additive Manufacturing:
Beyond the Beam II

3D Printing Architecture



Virginia San Fratello

Abstract This paper will focus on the research and collective work of Emerging Objects, a MAKE tank, that is transforming materials into sustainable buildings for the future using additive manufacturing. Humble and traditional building materials, such as salt and soil, can be transformed into sophisticated building materials through additive manufacturing. Waste materials such as sawdust and chardonnay grape skins and seeds are converted for use in 3D printing and turned into bricks, blocks, and tiles for construction assemblies. The use of additive manufacturing technologies and radical, alternative materials, will allow architects and engineers to impact the way buildings and cities will be constructed in the future.

Keywords Additive manufacturing · 3D printing · Paste extrusion · Powder materials · Architecture · Sustainability

Introduction

What if the world's waste materials could be transformed into sustainable building materials for the future? Can humble and traditional building materials, such as salt and mud, become sophisticated building materials for the twenty-first century? How can technologies such as additive manufacturing impact the way we attempt to solve social problems such as housing? These are all contemporary concerns that architecture must address if it is to stay relevant. The case studies discussed in this paper attempt to answer some of these questions through material experimentation and innovation and by prototyping new structures. Chardonnay grape skins are an agricultural waste product that is left to rot in the field, in the *Cabin of 3D Printed Curiosities* it is used as a local building material. Many proprietary powders and

V. S. Fratello (✉)
San Jose State University, One Washington Square, San Jose, CA 95192, USA
e-mail: virginia.sanfratello@sjsu.edu

resins used in 3D printing are very expensive, the materials used for 3D printing described in this paper including soil and salt are either free or very low cost which makes 3D printing more accessible. The *Saltygloo* is printed using local salt from the San Francisco Bay and the *MUD Frontiers* project uses locally harvested wild soil and clay from the jobsite, eliminating the need to purchase and ship materials around the world.

Each of the three case studies described in the paper is easy to assemble with unskilled labor. Blocks, tiles, and puddled coils, printed with inexpensive equipment, are connected using simple fasteners such as Velcro, screws, or simply gravity, to hold parts into place making the 3D printing building components easily handled and aggregable to create larger structures. Developing one's own materials and using simple assembly methods for 3D printed parts open the door for new material compositions within geometrically complex forms, and it also reduces cost and allows for new color variations and textures. The use of local, indigenous, and recycled materials in additive manufacturing not only addresses issues around the future of sustainability and economics but it also creates new, contemporary craft, and architectural traditions.

The Case Studies

Salt

The *Saltygloo* (Fig. 1) is an experiment in 3D printing using locally harvested salt from the San Francisco Bay to produce a large-scale, lightweight, additively manufactured structure. In the landscape of the San Francisco Bay Area, employing only the sun and wind, 137,000 tonnes of sea salt are produced each year, making salt

Fig. 1 *Saltygloo*. (Color figure online)



a locally available building material. The salt is harvested from 110-year-old salt crystallization beds in Newark, California, where salt water from the bay is brought into a series of large evaporation beds. Over the course of three years, the brine evaporates, leaving 13–16 cm of solid crystallized salt that is then harvested for food and industrial use. From this landscape, a new kind of salt-based architecture created through the lens of 3D printing and computer-aided design is realized, inspired by traditional cultures that employ the building material found directly beneath their feet, such as the Inuit Igloo. It is named *Saltygloo*, because it is made of salt y glue; it is made of a combination of salt harvested from the San Francisco Bay and glue derived from recycled plant-based resins that come from by or waste products and do not displace food-based agriculture, which makes for an ideal 3D printing material and strengthening infiltrate, called Super Sap by entropy resins [1], one that is not only strong and waterproof but also lightweight, translucent, and inexpensive.

The form of the *Saltygloo* is drawn from the forms found in the Inuit Igloos (Fig. 2), but also the shapes and forms of tools and equipment found in the ancient process of boiling brine. Additionally, each tile is based upon the microscopic forms of crystallized salt. The 330—3D printed salt tiles (Fig. 3) that make up the surface of the *Saltygloo* are connected with removable binder clips to form a rigid shell that is further strengthened by connecting the closed clips to lightweight aluminum rods flexed in tension, making the structure extremely lightweight and able to be easily transported and assembled in only a few hours—in many ways it is a salt tent.

The inherent optical properties of the salt make it translucent (Fig. 4) and shimmer and allow for light to permeate the enclosure and highlight its structure. The grainy crystals of the salt tiles are tactile, they feel gritty, grainy, and abrasive, and they communicate the use of one of humankind's most essential materials not only through vision but also through touch.

Printing with local salt in an inkjet printer greatly lowers ecological lifecycle impacts when compared to other materials and 3D printers. In tests conducted by Jeremy Faludi at the University of California Berkeley using the ReCiPe method [2], when the Zcorp inkjet is printing four salt parts together, which it did for the construction of the *Saltygloo*, it has 1/5th the ReCiPe endpoint-score per job as the next-best technology, PLA printed by small desktop FDM. The inkjet has roughly

Fig. 2 Community of igloos

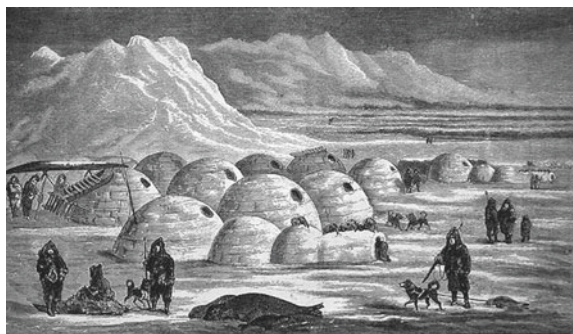


Fig. 3 Close up of crystal tile form. (Color figure online)



Fig. 4 Saltygloo interior. (Color figure online)



1/38th to 1/40th the impact score per job as a polyjet printer, regardless of whether both are printing one part at a time or four parts at a time. ReCiPe is the most recent indicator approach available in life cycle impact assessment and the primary objective of the ReCiPe method, is to transform the long list of life cycle inventory results, into a limited number of useful indicator scores. The chart of Fig. 6 shows how 3D printing with salt on an inkjet printer compares to 3D printing with PLA, PET, and ABS on desktop FDM printer, printing with photopolymer resins on a polyjet printer, and resin in a SLA printer [3] (Fig. 5).

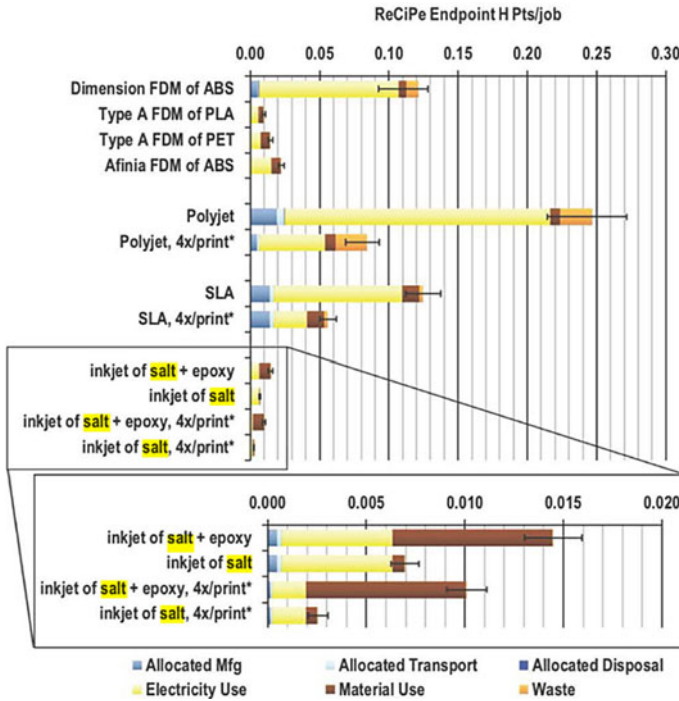


Fig. 5 Ecological impacts per job at maximum utilization scenarios. Scenarios denoted by (*) are four parts being printed simultaneously. Reprinted from [3], with permission. (Color figure online)

Soil

The use of ubiquitous, free, and sustainable materials such as local soils for 3D printing enables a more accessible, portable, and ecological approach to additive manufacturing at the architectural scale. The MUD Frontier project is addressing the challenge of creating accessible robotics for construction through the development of a mobile and lightweight, 3D printing setup that can easily be transported to the field or jobsite. The construction industry is the largest global consumer of raw materials and accounts for 25 to 40% of the world’s total carbon emissions [4]. A return to mud as a building material attempts to correct the errors of a wasteful, polluting, and consumptive industry. Ecological and sustainable issues are at the forefront of conversations surrounding the future of construction and soil-based construction materials are the most “earth friendly” materials that exist [5]. Earth is a ubiquitous material and buildings made of local soils can be found in almost every region of the world. A large number of earthen building codes, guidelines, and standards have appeared around the world over the past two decades, based upon a considerable

Fig. 6 Robotic setup at the rubin center. (Color figure online)



amount of research and field observations regarding the seismic, thermal, and moisture durability performance of earthen structures opening the door for the nascent revival of building with earth.

The Scara robotic 3D printer (Fig. 6) that was developed for this endeavor is combined with a continuous flow hopper that can print wall sections and enclosures up to 2200 mm diameter circle and 2500 mm tall, structures considerably larger than the printer itself. The setup can be carried by 1–2 people and relocated in order to continue printing.

The printer is able to 3D print local soils directly from the print site in order to demonstrate the possibilities of sustainable and ecological construction in a two-phase project that explores traditional material craft at the scale of both architecture and pottery. The clays harvested for the projects are free, as they can be dug directly from the ground or surrounding region where the walls, enclosures, and pottery are being printed.

Phase I of the MUD Frontier project took place along the USA—Mexico border in El Paso, Texas and Ciudad Juarez, Chihuahua, where earthen architecture and clay pottery of the Mogollon culture (A.D. 200—1450) define the archeological history of the region. Excavated pit houses and above ground adobe structures defined the historic architecture of the region.

A large 3D printed adobe structure was also manufactured using largely the same material as the pots, but with the introduction of sand. The vessels reveal the nature of the local geology and the creativity of local ceramic artisans from the contemporary Jornada Mogollon region. The fired earthenware exposes a range of clay complexions: greens, browns, purples, wheat, pink, and red colors that speak to the nature of mono-, bi-, and polychrome traditions that developed over time. The structure and vessels were produced with the intent of connecting the forefront of digital manufacturing with the traditional coiled pottery techniques, and subterranean and adobe architecture of the borderland regions between Texas and New Mexico in the USA and the state of Chihuahua in Mexico.

During Phase I the robotic setup for printing the large structure was installed at the Rubin Center Gallery in El Paso, Texas, which sits very close to the border wall. The gallery was maintained at a constant temperature of approximately 20 °C. A mixture of five parts locally sourced sand and three parts clay was mixed with chopped straw and water and pumped through the printer. The layer height of each mud coil is 30 mm and each coil is between 40 and 60 mm wide. The overall structure is 213 cm tall and 180 cm wide and took seven days to print at approximately 300 mm per day (Fig. 7).

Phase II of the MUD Frontier project took place in the high alpine desert of the San Luis Valley which spans southern Colorado and northern New Mexico in the USA (Fig. 8). The second phase of the research reflects the earthen construction of the Indo-Hispano settlers of the valley and the local Rio-Grande pueblo culture. The

Fig. 7 MUD frontier large-scale structure and vessels at the rubin center gallery as part of the new cities, future ruins exhibit. (Color figure online)





Fig. 8 Fabrication setup. (Color figure online)

temperature of the valley floor fluctuated from a high of 30 °C during the day to 6 °C at night. The desert environment was sunny, windy with some rain over the sixty days of printing. It was observed that printing was most successful when the weather conditions were dry, sunny, and most importantly, windy. The mud mixture used was wild, dug directly from the ground, sieved to a particle size of less than 6.35 mm, and mixed with chopped straw and water. The clay/sand/loam mixture in this region has historically been used to make mud bricks and mud plaster for local buildings and there is a tacit understanding among the community about where to dig for the mud and how moist it should be. The mixture proved to be very well suited for 3D printing coiled mud structures (Quentin Wilson, an adobe expert living and building in this region of southern Colorado and northern New Mexico, recommends using the jar test to identify a mixture that is less than 30% clay [6]). The layer height of each mud coil is on average 30 mm and each coil is between 40 and 60 mm wide. Four structures were printed of varying dimensions; however, it was observed that under ideal weather conditions an average of 400 mm in height could be printed per every 24-hour period.

The research during phase II was conceptualized under four themes: The Hearth, Beacon, Lookout, and Kiln. The Hearth explores the decorative aspects of structure (Fig. 9). The structural reinforcement of double-layer earthen walls creates a simple interior environment and an exterior that has structural expressiveness. The thin mud wall construction is reinforced using local, rot-resistant juniper wood, to hold the interior and exterior coiled walls together. The wood sticks extend beyond the walls

Fig. 9 3D printed hearth.
(Color figure online)



of the structure on the outside and are flush on the inside, referencing the cultural differences between the architectural traditions of pueblo and indo-hispano buildings. It also recalls traditional African architecture such as the Mosque in Djenne, where the wood sticks protruding from the building are not only decorative but also used as scaffolding. The interior holds a 3D printed mud bench, surrounding a fireplace that burns the aromatic juniper (Fig. 10).

The beacon is a study in lightness, both illumination and weight. It explores how texture and the undulation of the 3D printed coil of mud can produce the thinnest possible structural solution for enclosure. These coils are then illuminated at night contrasting the difference between the concave and convex curves that create the mud walls. The lookout is an exploration in structure and is a 3D printed staircase that is made entirely of mud. A dense network of undulating mud coils is laid out to create a structure that can be walked on. This also demonstrates how wide, yet airy, walls

Fig. 10 Fireplace and mud bench.
(Color figure online)



can create interior enclosures that represent possibilities for insulation, especially in the harsh climate of the San Luis Valley which can drop below $-29\text{ }^{\circ}\text{C}$ in the winter. The Kiln explores several of the techniques discussed, including undulating /interlocking mud deposition to create structural and insulative walls. The Kiln is also used to enclose an area that draws in oxygen and keeps in heat to fire locally sourced clay fired with juniper wood, which burns hot.

The *MUD Frontier* project reexamines and conceptually unearths ancient building traditions and materials using twenty-first-century technology and craft coupled with local skills to explore new possibilities for ecological and local construction techniques. Based on the research so far, the robotic printing of local soils shows promise for the rapid creation of robotically crafted, geometrically complex, buildings that are durable and structural, using wild clays that have historically proven successful in building construction. Upon their 40th anniversary, the Smithsonian Magazine announced the 40 most important things they believed one should know about the next 40 years. Number one on their list was that “Sophisticated Buildings will be made of mud” [7]. *MUD Frontiers* aims to see this prediction become a reality.

Chardonnay

The 3D printed tiles made of chardonnay grape skins on the façade of the *Cabin of 3D printed Curiosities* have been described as a box of exquisite chocolates—the façade is composed of 3D printed *Planter Tiles* that create a living wall of succulents (Fig. 11a). The chardonnay grape skins are a deep, warm brown that evokes the buttery bitterness of chocolate. They have an herbaceous scent that is complemented by the succulents in the tiles. The reuse of local waste materials that has been shaped through digital processes engenders a new aesthetic, one that is part of a new vernacular that



Fig. 11 Planter tile façade on the cabin of 3D printed curiosities. (Color figure online)

takes advantage of materials in local waste streams and nascent global technologies such as 3D printers (Fig. 11b).

The San Francisco Bay Area is experiencing a housing crisis; never before has the cost of real estate, new construction, and rent been so high. Because of this emergency situation, cities around the Bay Area have relaxed their zoning laws, design review process, and permitting requirements in order to allow home-owners to build secondary structures on their lots. These relaxed laws opened the door to for the *Cabin of 3D Printed Curiosities* to be built. The cabin takes advantage of these relaxed codes and laws and brings many of material, software, and hardware experiments together to demonstrate the architectural potential of additive manufacturing on a weather tight, structurally sound building. All of the cabin's componentry are produced in a microfactory, the print farm, which is located nearby the site of the cabin.

The roof gable and east and west facades are clad in 3D printed ceramic tiles that serve as a rain screen (Figs. 12a, b). The clay for the tiles comes from California. Designed for easy assembly, these tiles are made to be hung on a building facade or interior. The surface of each ceramic tile visually emulates a knitting technique called the seed stitch. G-code is used to control each line of clay as it is 3D printed to create a loopy texture that looks like seeds scattered across the surface. While all ceramic tiles are printed from the same file, each tile is intentionally unique as a product of



Fig. 12 3D printed ceramic tiles on façade. (Color figure online)

fabrication, during which the tiles wave back and forth, causing the printer to pull at the line of clay and creating longer and shorter loops toward the end of each tile, producing a distinct machine-made texture that is different every time.

The *Cabin of 3D Printed Curiosities* represents the first steps to a future that we can embrace for both its functionality and beauty. It solves problems around architectural issues that we face every day, it brings value to the occupant's lives and it has a strong connection to its locale technologically, geologically, and agriculturally through the use of materials and additive manufacturing.

Conclusion

The *Cabin of 3D Printed Curiosities*, the mud pavilions, and *Saltygloo* all speak to the possibility of a future that is just emerging, a future that takes advantage of powders that come from dust, waste, and traditional materials, on their journey to becoming part of a twenty-first-century architectural terroir that influences the meaningful crafting of objects and buildings. As pointed out by Gareth Williams, "In order to retain relevance in the modern world, craft must engage with contemporary concerns. One of the most pressing issues today is the impact of production, consumption and disposal of goods upon the earth's resources and ecological balance" [8]. 3D printing also raises questions about its role in craft and how it might make bespoke architecture more accessible, as the objects and buildings produced are not necessarily handmade but are customized, however the close connections between design, iteration, technique, material behavior, and analysis, and manufacturing suggest that 3D printing, especially when coupled with modes of production that employ materials from sustainable resources and waste streams, is a contemporary form of manufacturing with increasing relevance.

References

1. <https://entropyesins.com>, accessed 23-04-20
2. <https://www.pre-sustainability.com/recipe>, accessed 23-04-20
3. Faludi J, Hu Z, Alrashed S, Braunholz C, Kaul S, Kassaye L (2015) Does material choice drive sustainability of 3D printing. *World Acad Sci Eng Technol Int J Mech Mechatron Eng* 9(2):216–223
4. Renz A, Solas MZ (2016) Shaping the future of construction. a breakthrough in mindset and technology. Technical report, World Economic Forum
5. Rael R (2009) *Earth architecture*, Princeton Architectural Press
6. <http://www.greenhomebuilding.com/QandA/adobe/mixes.htm>, accessed 27-04-20

7. Smithsonian Magazine. [Online] <http://microsite.smithsonianmag.com/content/40th-Anniversary/>, accessed 27-04-20
8. Williams G (2003) Creating lasting values. In: Greenhalgh P (ed) *The persistence of craft: the applied arts today*, Piscataway, NJ, Rutgers University Press, p 61

Effect of HS Binder on Reducing the Amount of Bentonite in Oxidized Pellets



Qianqian Duan, Yongbin Yang, Rui Xu, Yingrui Dong, and Zhichen Yuan

Abstract In order to decrease the amount of bentonite in the production of oxidized pellets, the addition of HS binder is carried out in response to the problems of wasting of resources, high costing and serious pollution in the production and application of bentonite in China. In this study, the effect of the organic binder in iron ore pellets was characterized by using pelletizing, preheating and roasting experiments; the optimal ratio of HS binder to bentonite was determined. The results showed that combination of bentonite and HS binder can significantly reduce the amount of bentonite. When the ratio of bentonite of HS binder was HS binder dosage 0.2% and bentonite dosage 0.7%, the drop strength of green pellets reached 3.2 times/(0.5 m) and the amount of bentonite reduced the mass of 1.6% compared with that of without HS binder. Under the best preheated roasted conditions, the strength of the preheated ball was 436.9 N/P and the roasted ball strength achieved 2794.3 N/P, which could meet the demands.

Keywords Oxidized pellets · Bentonite · Organic binder · Preheating roasting

Introduction

Bentonite is widely used as binder in domestic oxidation pellet factories. Although the bentonite has good bonding performance, the content of Al_2O_3 and SiO_2 is high, which leads to the increase of coke ratio and the decrease of pellet grade. According to the data, the coke ratio will be reduced by 2.0–2.5% and the output will increase by about 3% for every 1% increase in the iron grade [1, 2]. Therefore, it is of great significance to increase the iron grade of pellets to reduce the iron consumption and increase the production of blast furnace. However, in China's pellet production, due to the constraints of bentonite resources and other aspects, the use of poor performance of natural calcium bentonite is very common, resulting in the actual production of bentonite dosage which is too high (about 2 ~ 3.5%) [3]. Researchers in China have

Q. Duan · Y. Yang (✉) · R. Xu · Y. Dong · Z. Yuan
School of Minerals Processing and Bioengineering, Central South University, Hunan, China
e-mail: ybyangcsu@126.com

been developing new adhesives to partially or even completely replace bentonite. When organic binders (such as peredo, carboxymethyl cellulose and organic binders GPS) [4–6] are used alone, the cost of pellets increases, and the raw pellets are liable to burst, and the preheating strength difference is difficult to meet the production requirements of soccer balls [7]. Cao [8] used composite binder to replace some bentonite, which reduced the bentonite content from 2.56% to 1.46% and improved the iron grade of pellets by 0.77%. Zhu [9] studied that adding organic compound bentonite could significantly improve the performance of raw pellets and the iron grade of pellets. When the ratio of organic compound bentonite was 1.2%, the raw pellet strength could reach 2.2% when the bentonite content was added. In this study, HS binder was used to partially replace bentonite, so as to reduce the consumption of bentonite, improve the grade of iron in finished pellets and control the cost of production of football league.

Experimental

Properties of Raw Materials

The iron-bearing raw materials used in the experiment were four kinds of iron concentrates (expressed as concentrates A, B, C and D) from the production site of A factory in Shandong Province. The four kinds of iron concentrates A, B, C and D were made into pellets according to the mixture ratio (30, 30, 30 and 10%, mass fraction). The chemical composition, static pelletizing properties and particle size composition of iron concentrate are shown in Tables 1, 2 and 3.

The data in Tables 2 and 3 show that the mixed ore has good pelletization. The chemical composition and basic physical properties of bentonite are shown in Tables 4 and 5.

HS binder is a kind of high molecular compound containing a large number of hydroxyl and carboxyl groups. The polar groups contained in it act on the surface of magnetite in the form of chemisorption. The hydrophilic group has strong hydrophilicity and acts on the surface of iron concentrate. The structure of organic chain frame is cohesive, which can improve the performance of magnetite pellets.

Table 1 Chemical composition of iron concentrate w/%

Chemical composition	TFe	FeO	CaO	MgO	SiO ₂	Al ₂ O ₃
A	65.96	27.02	0.20	0.38	8.38	0.10
B	65.69	26.40	0.92	0.44	6.58	0.45
C	66.07	25.47	0.54	0.30	6.40	0.45
D	67.87	30.12	0.45	0.30	6.06	0.10
Mixed ingredients	66.10	26.68	0.54	0.37	7.01	0.31

Table 2 Static pelletizing performance of iron concentrate

Sample	Maximum molecular water/%	Maximum capillary water/%	Capillary water migration speed /mm · (min) ⁻¹	Balling performance index	Spheroidity
A	4.81	12.59	4.68	0.62	Good
B	5.43	12.89	4.37	0.73	Good
C	3.91	13.87	4.40	0.39	Medium
D	6.55	12.97	4.55	1.02	Excellent
Mixed ingredients	4.12	12.56	4.89	0.49	Medium

Table 3 Size distribution of iron

Particle size composition		Specific surface area /m ² ·g ⁻¹
Mineral species	<0.074 mm (%)	
A	92.23	0.589
B	65.27	0.864
C	67.50	1.294
D	74.95	1.106
Mixed ingredients	75.83	0.633

Table 4 Composition analysis of bentonite w/%

SiO ₂	Al ₂ O ₃	CaO	Fe	Na ₂ O	MgO	LOL
51.19	12.98	8.28	4.31	2.58	2.89	11.61

Table 5 Physical properties of bentonite

Colloid index (% 3 g)	Swelling capacity (%)	Water absorption ratio (%)	Blue absorption (g/100 g)	Montmorillonite content (%)	Particle size composition <0.074 mm (%)
71.5	13.5	263.1	33.8	76.47	97.065

After preheating and roasting, the products are CO₂ and water vapor, with less residue and less pollution compared with bentonite [10]

Experimental Method

Pelletizing

Weigh 5 kg of iron-containing mixture in proportion, add a certain proportion of bentonite and HS binder, mix on the rubber cloth, and then add pre-wetting moisture to make the moisture of the mixture lower than 1% of the suitable moisture of the raw ball -2%, and then mix for the second time. The preparation of green balls is carried out on a disc pelletizer with a diameter of 1000 mm, a side height of 150 mm, a rotation speed of 25r/min (adjustable) and an inclination of 47°.

Determination of Burst Temperature of Green Ball

The decrepitation temperature of pellet was measured in a vertical tube furnace (650*1000 mm). The ball dropped repeatedly from 0.5 m height to 10 mm thick steel plate, until the ball was broken. The number of tests was n, the ball drop strength was n-1. Ten balls were measured each time, and the average value was taken as the falling intensity of the balls (unit: times/0.5 m).

Preheating Roasting Experiment

The preheating roasting small-scale test was carried out in a horizontal tubular electric furnace. The electric furnace consists of an iron chromium aluminum wire resistance furnace with a furnace diameter of 50 mm and a silicon carbon tube resistance furnace. The former is used for preheating and the latter is used for roasting. Raw balls with a diameter of 10–15 mm are first dried in a drying box at a temperature of 120 °C. The raw balls are loaded into a porcelain boat during the test. Carry out preheating and roasting according to the pre-established operation system.

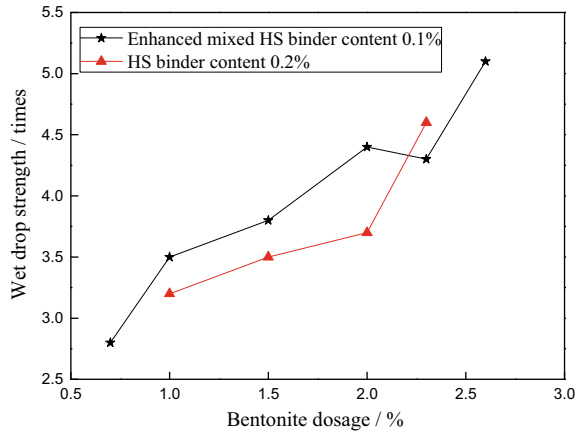
Results and Discussion

Study on the Preparation of Pellets with Added HS Binder

Effect of Strengthening Mixing HS-Type Binder

Figure 1 is the test results of the amount of bentonite used when the amount of HS binder is 0.2% when it is not strengthened and the amount of HS binder is 0.1% when it is strengthened and mixed. It can be seen from the figure that the addition of 0.2% HS-type binder has a significant improvement in the performance of green balls.

Fig. 1 Effect of enhancing mixed HS binder on bentonite dosage. (Color figure online)

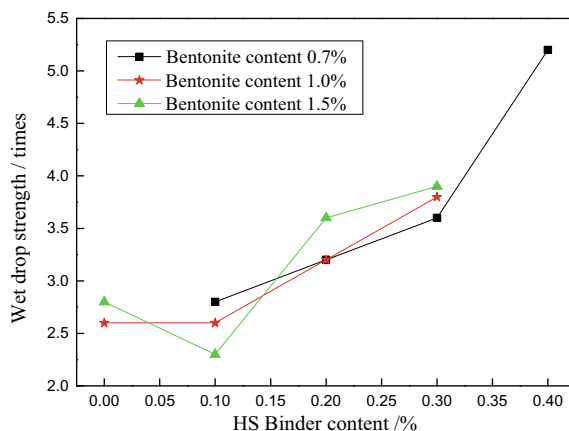


The amount of bentonite 1.0% can reach the drop strength level when using bentonite alone 2.3%. When adding 0.2% HS-type binder on the basis of adding 2.3% bentonite, the drop strength of green ball is increased from 3.2 times/0.5 m to 4.6 times/0.5 m. Therefore, from the perspective of pelletizing effect, the HS binder has a significant effect on reducing the amount of bentonite. For the small amount of organic binder (1000 grade), it is generally difficult to fully mix into the mixture, so there is a high requirement for mixing operation, and strengthening mixing will be conducive to better play the role of organic bonding effect. In this experiment, the dosage of HS binder was reduced to 0.1% by strengthening the mixing operation, and the effect was further improved. Although the amount of HS binder decreased from 0.2% to 0.1%, the falling intensity of green pellets increased from 3.2 times/0.5 m to 3.5 times/0.5 m when the amount of bentonite was 1.0%, and it increased from 3.7 times/0.5 m to 4.4 times/0.5 m when the amount of bentonite reached 2.0%. Therefore, by strengthening the mixing operation, the effect of HS binder has been better highlighted.

Influence of HS Binder Dosage

Figure 2 shows the influence of the dosage of HS binder on the falling strength of green pellets when the dosage of bentonite is 1.5%, 1.0% and 0.7%, respectively. As can be seen from the figure, the amount of bentonite is 1.5%. With the increase of the amount of HS binder, the falling intensity of the spore shows an upward trend (0.1% of the point is abnormal fluctuation). When the dosage of HS binder is 0.2% and the dosage of bentonite is 1.5%, the requirements of raw pellet strength can be satisfied. When the amount of bentonite was 1.0%, the falling strength of the spheroidal material increased with the increase of the amount of HS binder. When 1.0% bentonite was used and 0.2% HS binder was used, the falling intensity of green pellets was 3.2 times/0.5 m, which was equivalent to 2.3% when bentonite was

Fig. 2 Effect of HS binder dosage on the performance of green balls. (Color figure online)



used alone. In order to further understand the effect of HS binder, the experiment in this group examined the condition that the dosage of HS was 0.7%, and the falling intensity of the ball at this time was up to 8.0 times/0.5 m, which further verified the efficient effect of HS binder.

As can be seen from Fig. 2, if the bentonite dosage is reduced to 0.7%, the intensity of falling balls can still reach 3.2 times/0.5 m with the addition of 0.2% HS binder, and the effect is equivalent to the use of 2.3% bentonite alone. When addition of 0.2% HS binder, the amount of bentonite decreased from 2.3% to 0.7%. HS-type binder is a kind of high efficiency binder, which has a good application prospect in pelletizing iron concentrate.

Preheating and Roasting of HS Binder Pellets

Although the binder is used for the purpose of pelletizing, it will inevitably change or interact with iron concentrate under high temperature conditions, so it is very important to study its influence on the preheating and roasting performance of pellets. The reaction between bentonite and iron ore will promote the interfacial action and the formation of appropriate liquid phase, which can promote the consolidation of pellets in the process of preheating and roasting. The addition of organic binder will affect the preheating and roasting performance of pellets. On the one hand, its decomposition and volatilization at high temperature may produce a certain reducing atmosphere, which may affect the oxidation and consolidation of pellets. In addition, the decrease of bentonite content weakens the promoting effect of pellets on the consolidation. Therefore, the use of organic binder must be combined with the preheating effect of a comprehensive test.

For this reason, the pellets with HS binder were preheated and roasted, and the application effect and prospect were comprehensively examined. Figure 3 shows pellets prepared with HS binder 0.2% + 0.7% bentonite after intensified mixing. The

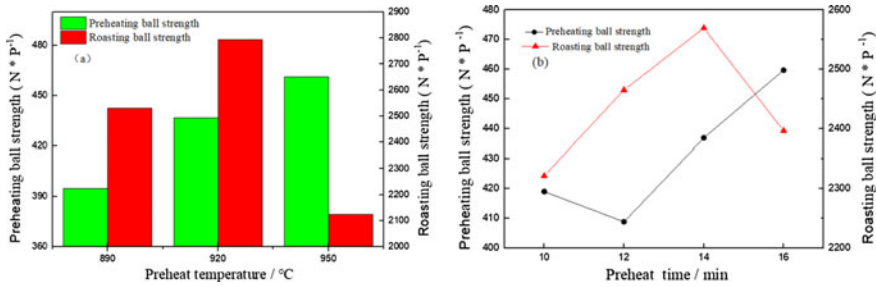


Fig. 3 Effect of preheating conditions on preheating and roasting of pellets. (Color figure online)

corresponding strength index can be obtained by changing the preheating and roasting conditions. Figure 3a shows the result of preheated pellets roasting at preheating temperature, and clearly shows that temperature had significant effect on the strength of preheated ball, strength is greater than 400 N/P. With the extension of preheating temperature continue, the ball strength still can continue to improve, fixed roasting conditions, when the preheating temperature of 920 °C, the roasting strength is exceed than 2500 N/P. Figure 3b is the test result of preheating time on pellets preheating and roasting.

The effect of preheating time on improving the strength of pellets is weak, because the crystallization rate and consolidation degree of Fe₂O₃ grains in the preheating stage are mainly affected by the preheating temperature. Except for the abnormal fluctuation at the time of preheating for 12 min, the rest are above 2500 N/P, which can meet the strength requirements of pellet products. In combination with the field practice, the preheating temperature is 920 °C and the preheating time is 14 min. The FeO in the pellet is fully oxidized, and more Fe₂O₃ microcrystals are generated. Therefore, the pellet that meets the industrial needs can be obtained.

Figure 4 is the experimental result of the effect of roasting conditions on the roasting strength of pellets. It can be seen from the figure that in the high-temperature roasting process of the composite pellets of 0.2% HS binder and 0.7% bentonite,

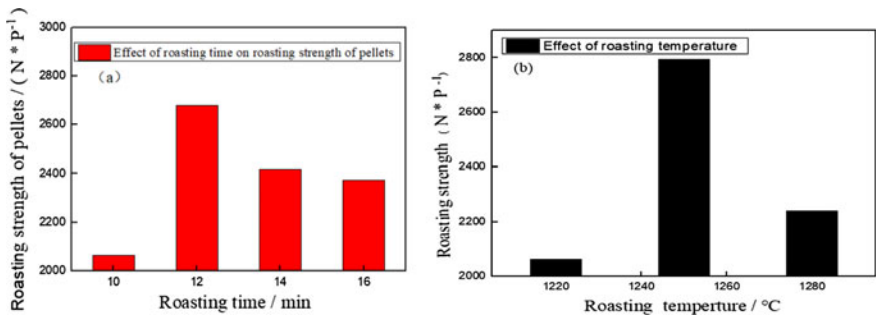


Fig. 4 Effect of roasting conditions on roasting strength of pellets. (Color figure online)

when the roasting temperature increases, the physical and chemical reactions inside the pellets will be accelerated, the particle diffusion will be accelerated, the pores in the pellets will be reduced, and the Fe_2O_3 microcrystals inside the pellets will be recrystallized and polycrystalline, making the pellets more dense and stronger. The best calcination temperature is $1250\text{ }^\circ\text{C}$, in which the pellet is oxidized completely. If the calcination temperature is too high, silicate liquid phase will appear in the inner lattice of the pellet. The decrease of Fe_3O_4 content and porosity in the pellet will significantly reduce the strength of the pellet. However, at high temperature, part of Fe_2O_3 is decomposed into Fe_3O_4 and FeO . Fe_3O_4 will react with SiO_2 in the pellets in a liquid phase, forming a liquid phase bond and reducing the pellet strength. Therefore, the optimal roasting time in this experiment is 12 min.

Comparison of the Properties of HS Binder and Bentonite Pellets

The above research shows that under the optimized test conditions, the HS binder from a factory in Shandong is mixed with bentonite to achieve the purpose of reducing the amount of bentonite. In this study, the properties of the oxidized pellets obtained by the four binders were comprehensively compared, as shown in Table 6. Four kinds of pellets were obtained under the same preheating and roasting system: The preheating temperature was $920\text{ }^\circ\text{C}$, the preheating time was 14 min, the roasting temperature was $1250\text{ }^\circ\text{C}$, and the roasting time was 12 min.

- (1) As the amount of bentonite increases, the green ball drop strength gradually increases. When the amount of bentonite is 0.7–2.3%, the green ball drop strength increases from 2.1 times/0.5 m to 3.2 times/0.5 m. When the amount of bentonite continues to increase above 2.3%, the green ball drop strength will be greatly improved. When the amount of bentonite reaches more than 2.3%, the green ball falling strength meets the qualified index.
- (2) When adding 0.4% HS-type binder, without adding bentonite, the strength of the preheated ball (284 N/P) is lower than the strength requirement of the preheated ball, and roasted ball is only slightly below the furnace to the strength of the

Table 6 Comparison of quality of pellets with four binders

HS content %	Bentonite content %	The green ball falls [times/0.5 m]	Compressive strength/N	Preheating compressive strength/N	Roasting compressive strength/N
	0.7	2.1	10.3	403.1	2906.3
	2.3	3.2	26.2	586.9	3704.4
0.4	/	4.0	12.5	284.0	2412.0
0.2	0.7	3.2	12.2	436.9	2794.3

pellets. Therefore, HS binder cannot be used alone or can completely replace bentonite.

- (3) Under the condition of intensified mixing, after reducing the amount of bentonite to 0.7%, adding 0.2% HS-type binder can still achieve the green ball drop strength of 3.2 times/0.5 m. The pellet strength is about 2500 N/P. The main reason for the decrease in preheating roasting performance is the decrease in the amount of bentonite which weakens the promotion of pellet consolidation. Therefore, the pellet strength of this combination is close to the critical level required by the index. We thought the main reason of strength changing was brought by low dosage of bentonite, which weaken the promoting function of the pellets roasting consolidation.

Conclusions

- (1) In order to meet the requirements of pelletizing, the amount of bentonite shall be more than 2.3% when bentonite is used alone as binder in the structure of the raw material. HS binder can meet the requirements of pelletizing and obtain good pelletizing performance when used alone.
- (2) The combination of HS type binder and bentonite can significantly reduce the amount of bentonite. Adding type binder 0.2% can reduce the amount from 2.3% to 1.5%. Combined with the intensified mixing measures, the amount of bentonite can be further significantly reduced to a maximum of 0.7%, the pellet performance and the preheating and roasting performance can meet the production requirements, and the amount of bentonite can be reduced as much as 1.6% compared with the amount of bentonite without addition.
- (3) For the structure of raw materials in this experiment, the binder combination of 0.2%HS + 0.7% bentonite can just meet the requirements of pelletizing performance and preheating and roasting performance, but the spare space is very small, which is close to the critical state.

The results showed that the combination of 0.2% HS binder and no less than 0.7% bentonite could meet the needs of pelletizing and pellet preheating and roasting and was feasible in industry and could effectively reduce the amount of bentonite

References

1. Xie X, DT, Zheng F et al (2018) Study of magnetite oxidized pellet prepared by modified composite binder. *Metal Mine* (01):79–83
2. Manman ZYOXL et al (2018) Application effect of humic acid modified bentonite binder in iron ore pellet. *Sintering Pelletizing* 43(04):27–32
3. Yang YB, Huang GX, Jiang T (2007) Application of organic binder as substitutes for bentonite in pellet preparation. *J Cent South Univ (Science and Technology)* 05:850–856

4. Kawatra SK, Ripke SJ (2001) Developing and understanding the bentonite fiber bonding mechanism. Elsevier Ltd 14(6)
5. Zhang YB, Zhou YL, Jiang T (2012) Applications of MHA binder in oxidized pellets preparation from vanadium, titanium-bearing magnetite concentrates. *J Central South Univ (Science and Technology)* 43(07):2459–2466
6. Hongxi L, W D, Hu Y et al (2001) Mechanism of sodium carboxymethyl starch to increase pellet strength. *J Cent South Univ (Science and Technology)* (04):351–354
7. Jiang Tao LH, Zhucheng Huang (1998) Preliminary study on molecular structure design of iron ore pellet binder. *Sintering Pelletizing* 01:30–35
8. Cao L, WH, Wang J et al (2007) Application of composite binder (QNP) in baotou steel pellet. *Sintering Pelletizing* (02):49–52
9. Zhu D, LH-m, Yu W et al (2009) An organic activated bentonite mechanism for improving pelletization. *J Chong Qing University* 32(05):582–588
10. Guixiang H (2007) Study on preparation of Oxidized Pellet by New-style Organic Binder Center South University

Linear Friction Welding: A Solid-State Welding Process for the Manufacturing of Aerospace Titanium Parts



N. Piolle

Abstract Linear friction welding (LFW) is a solid-state joining process offering new opportunities of cost reduction and quality improvement for aerospace titanium part manufacturing. The process produces in a few seconds high integrity joints with fine grain, hot-forged microstructure and narrow heat-affected zone. The LFW process reached a high enough level of maturity, robustness, and reliability to be ready for mass production of blisks (“bladed disks”) for aircraft engines. It is now being developed for aircraft structural parts in titanium and aluminum alloys. This process allows not only to manufacture a given part at a lower cost, it also opens new part design possibilities that were not available with traditional manufacturing processes. The LFW process is explained through physical aspects, process parameters, mechanical characterization of the joint, and microstructural data. Several LFW aerospace applications are introduced and evaluated through feasibility, weight reduction, post-weld operations, and overall cost savings.

Keywords Linear friction welding · Solid-state welding · Friction welding · Titanium welding · Ti-6Al-4V · Blisk · Aerostructure · Buy-to-Fly · LFW

Introduction to Linear Friction Welding Process

Linear Friction Welding (LFW) is a solid-state joining process as it does not cause melting of the parent material. It produces forge quality, high integrity joints, with narrow heat-affected zone. Materials are forged using frictional heat through the controlled, reciprocal linear oscillation movement of two components under high contact load. As the faying surfaces rub together, the material at the interface is heated to a plastic state, while axial load is maintained. The layer of soften material is expelled out of the interface under the combined action of the contact pressure and the oscillation motion pushing out a small amount of material at each oscillation. The oscillation motion is stopped after a desired parameter has been reached: axial

N. Piolle (✉)
ACB, 27 rue du Ranzay, 44319 Nantes, France
e-mail: nicolas.piolle@acb-ps.com

© The Minerals, Metals & Materials Society 2021
TMS 2021 150th Annual Meeting & Exhibition Supplemental Proceedings,
The Minerals, Metals & Materials Series,
https://doi.org/10.1007/978-3-030-65261-6_6

shortening, absolute position, time, or a combination of these three. The two components are then aligned, and the axial load is maintained or increased to consolidate the joint during the cooling down. The overall weld process is very fast as the oscillation phase generally takes 2–5 s, and the cooling down 5–10 s.

The process is controlled by a small number of input parameters: the oscillation amplitude, the oscillation frequency, the axial pressure, and the end criterion for the oscillation motion. The main outputs, or process resulting parameters, are the in-plane friction force, the temperature increase at the interface, and the material flow resulting in upset displacement and flash. The process gives remarkably good results on titanium alloys thanks to their low thermal conductivity and consequently an ability to plasticize closely to the faying surface. In the late 1990's, LFW was investigated by Vairis and Frost [1, 2] and they made a description of the process in four steps: the initial phase, the transition phase, the equilibrium phase, and the deceleration phase. Their investigations were the starting point of many works and influenced the way research and industrial people investigated LFW and developed numerical modeling approaches. Temperature profile in LFW of Ti-6Al-4V was rapidly well understood and many observations showed that welding temperature is just beyond beta transus temperature. We had to wait for Turner et al. [3] works using FEM analysis to have a better idea of strain rates. The works of Wanjara and Jahazi [4] shall be mentioned for understanding the impact of process parameters for alpha-beta Ti-6Al-4V welding. They demonstrated that LFW process window resulting in sound welds is very wide. Additional conclusions regarding process parameters optimization were given by Romero et al. [5], and they demonstrated that residual stress would be advantageously mitigated using high pressure in LFW.

LFW of Ti-6Al-4V is now well understood by scientific community and process parameters providing sound welds seem to be well defined. Particularly, process conditions consisting of amplitude between 2 mm and 2.5 mm, a frequency between 35 Hz and 50 Hz and a minimum upset distance of 2 mm are making consensus. Impact of weld pressure is not as evident because no affection was found on elongation or mechanical resistance using whether 50 MPa or 90 MPa. However, this parameter was found to have a significant impact on residual stress and literature suggests that high pressures should be preferred as it reduces the heat input: indeed, a higher pressure causes the material to flow at a lower temperature, and the faster upset speed leads to shorter heating time. Except the small impact on elongation at low amplitude or frequency, authors agree that there is a very wide process window, within which welds properties match or are close to base material properties.

From the machine control, the process can be broken down in four steps (Fig. 1):

- Contact. The two parts are put in contact.
- Conditioning. The axial force is applied, and the oscillation motion starts. The irregularities of faying surfaces are rubbed and the temperature at the interface increases under the effect of the friction.
- Burn-off. The pressure and motion are still applied, and the hot, softened material is expelled.

- Forge. Oscillations are stopped and pressure is maintained or increased during the cooling down.

The evolution of a typical LFW cycle is shown on Fig. 2.

The total width of weld zone (WZ) and thermo-mechanically affected zone (TMAZ) can be from 0.3 mm to 1 mm in total, depending on process parameters [5]. In the nugget zone (welding joint), there is a Widmanstätten microstructure with very fine grains, close to hot-forged microstructure [4, 5]. Maintaining the axial

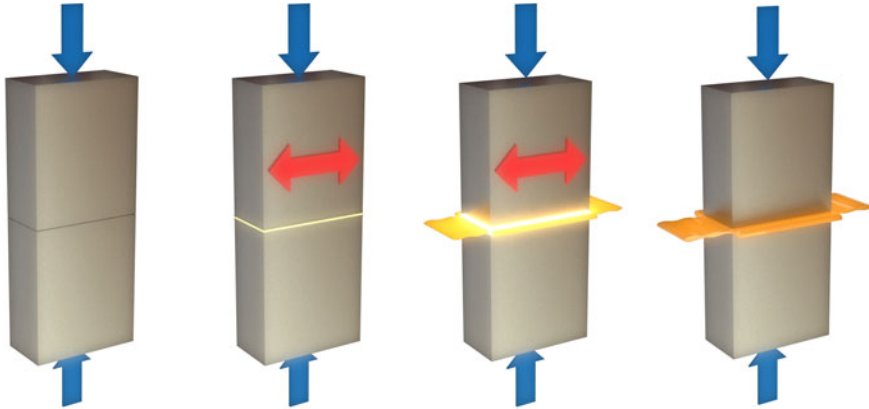


Fig. 1 LFW process steps, from left to right: contact, conditioning, burn-off, and forge. (Color figure online)

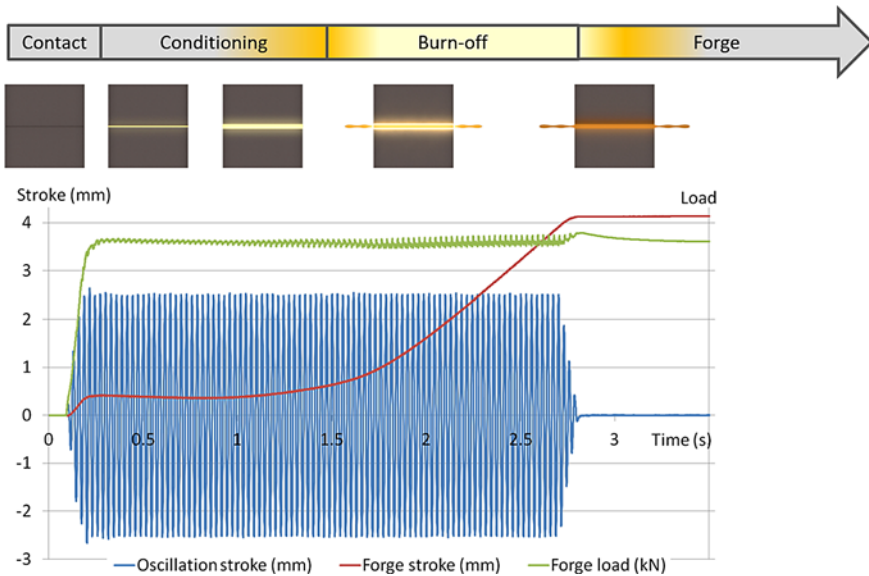


Fig. 2 LFW typical cycle, recorded on the LFW machine MDS30. (Color figure online)

pressure during the entire process cycle and in particular during the cooling down prevents grains from growing in the weld zone, which explains the presence of very fine, hot-forged microstructure in the weld line (Figs. 3 and 4).

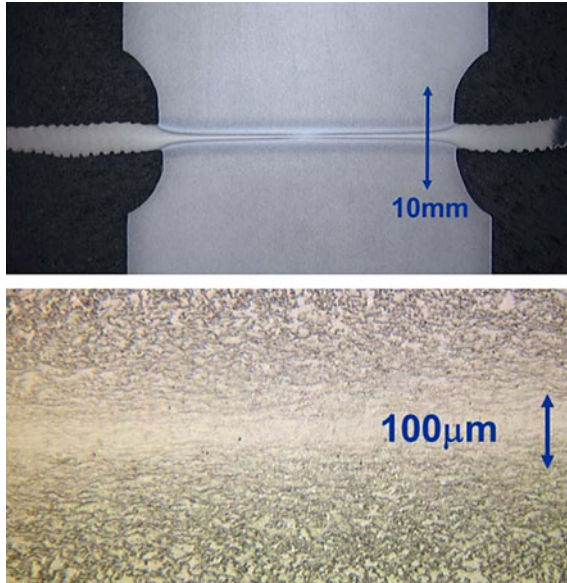


Fig. 3 LFW Ti-6Al-4V micrography. (Color figure online)

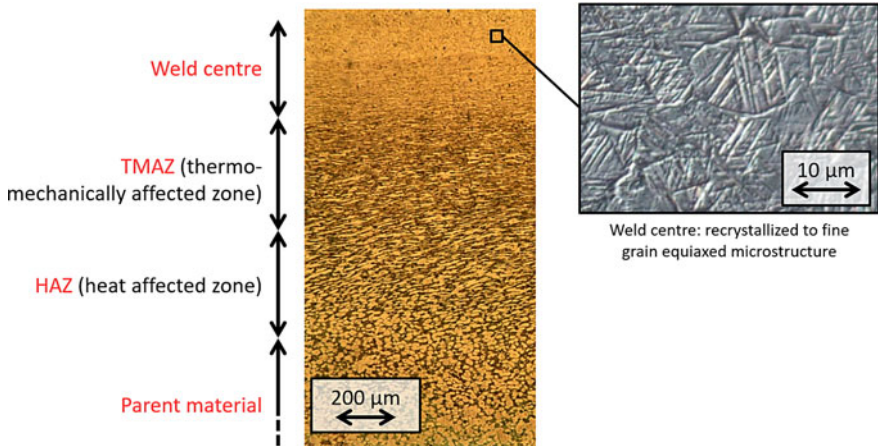


Fig. 4 LFW Ti-6Al-4V micrography. (Color figure online)

Main Advantages of LFW Process

Excellent Mechanical Properties

LFW is a low temperature welding, solid-state joining process. For Ti-6Al-4V the temperature reached at the welding interface is about 1000–1200 °C, so below the melting point. As there is no melting of the parent material, common problems associated with fusion welding such as solidification cracking, porosity, and segregation are avoided. In addition, LFW cycle time is very short: only two or three seconds of friction, and five-to-ten seconds of cooling down are necessary. The combination of low temperature and short-cycle time results in low heat input, so small heat affected zone (HAZ). Regarding the static and dynamic behaviors (tensile and fatigue tests), LFW welds have properties very close to those of the parent material: for Ti-6Al-4V, Wanjara and Jahazi observed ultimate strength, tensile strength, and elongation slightly higher than those of parent material [4].

Self-cleaning Process

Besides, LFW is a self-cleaning process as all the impurities or oxides that could be present at the interface are expelled with the flash outside the interface. Thus, the preparation of the welding joint is minimal and LFW can be done in open air, no gas shield is required.

A Machine Based Process Quality Assurance

The execution of LFW process involves a fairly low number of input parameters, mainly loads and displacements, to the extent that it can be fully automated. All the energy input is produced by mechanical sources and can be controlled by displacements and loads. With the development of the technology on servo-hydraulic actuators, sensors and high-speed acquisition systems, modern hydraulic LFW machines are able to achieve very accurate and repeatable process control, provided the machine mechanical structure is stiff enough and with the use of rapid and smart motion control algorithms. The high level of automation and the fact that the energy input is controlled by repeatable mechanical actions makes this process very consistent and robust from the quality control point of view.

Comparison with the Rotary Friction Welding

The principle of LFW is very close to the better-known Rotary Friction Welding (RFW) process, in which the reciprocal motion is a rotation rather than a linear oscillation. This makes an important difference on the heat input: in LFW the frictional heat is produced uniformly across the contact surface, contrary to RFW where the friction velocity in a given point of the interface is proportional to the distance with the rotation axis; so at the center of a rotary friction weld, the heat is supplied only by conduction. Also the LFW allows to weld non-axisymmetric parts and complex geometry, whereas the RFW is suitable mainly for revolution parts.

From the equipment technology point of view, however, the LFW process requires more complex and expensive machines and toolings, and the state-of-the-art currently limits the LFW forge forces to about 1,000 kN, while rotary friction welders can provide up to 20,000 kN for the largest inertia welding machines. As a consequence of the significant gap between LFW and RFW machine cost and maximum forge force, usually the LFW is preferred to RFW only when the part geometry demands it or for very difficult to weld alloy combinations.

LFW Applications in Aerospace Industry

Applications in Aircraft Engines

The three ways to manufacture bladed disks are:

- Mechanical dovetail or fir-tree assembly
- Machining from solid
- Linear Friction Welding by welding the blades to the disk (Fig. 5).

The use of blisks (bladed disks) as single parts instead of the assembly of a disk and individual, removable blades, started in the mid-1980's initially for military jet engines and was implemented more recently on civil turbofans like CFM Leap-X, PowerJet SaM146, and General Electric Passport and GEnx. The blisk design can be used for small military or business jet engine fans as well as for compressor stages of larger civil engines. The blisk design provides a better efficiency, lower weight, and better fatigue behavior than the conventional design. However, for a blisks machined from solid the material usage and machining time is much higher than for a conventional bladed disk.

For the blisk manufacturing, using LFW rather than machining from solid results in raw material savings from 20% to 30% and a significant reduction of machining costs. Besides it opens to possibility to weld dissimilar materials or hollow blades.

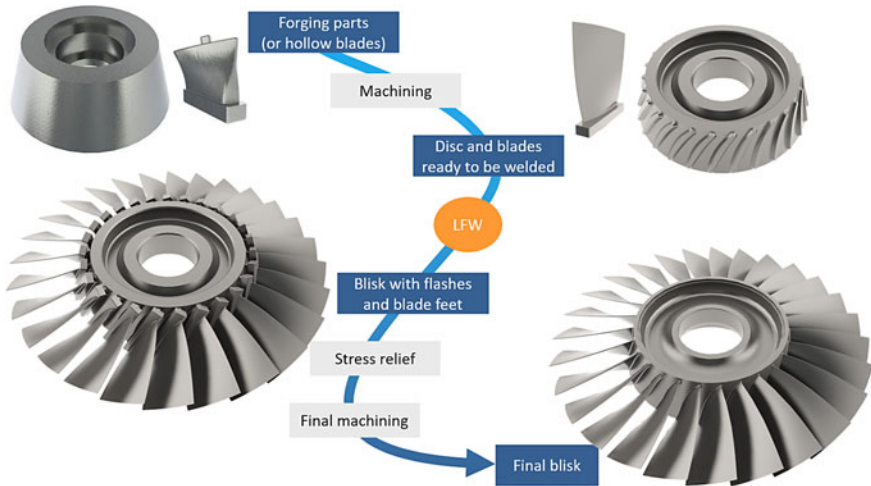


Fig. 5 Overview of the LFW blisk manufacturing process. (Color figure online)

Applications in Aircraft Structures

Introduction

The air traffic growth predicted for the next decades, in conjunction with the development of carbon composite parts in the aircraft that requires more titanium, will lead to an increase of titanium use in aerospace. Considering that titanium is extremely expensive in terms of purchase cost ($> \$70 \text{ kg}^{-1}$), energy consumption ($> 500 \text{ MJ.kg}^{-1}$) and CO_2 emissions ($> 40 \text{ kg.kg}^{-1}$), there is a pressing need in the aerospace industry for the development of processes which could replace the current manufacturing methods, and reduce the Buy-To-Fly ratio of titanium structural parts [6].

With LFW, a lot of aircraft titanium parts currently machined from solid could be produced at a lower cost and with less raw material, without downgrading the metallurgical properties and mechanical performances of the parts. Besides, a lot of weld configurations were proved to be feasible to produce LFW near-net-shape blanks (Fig. 6).

From the economic point of view, on the one hand using LFW can save material and machining cost; on the other hand, it requires some specific post-weld operations in addition to the welding itself: flash cutting, and in some cases, non-destructive weld inspection and heat-treatment. Some titanium structure parts will show no economic advantage in being manufactured using LFW, and for others the overall saving can reach 50%. Each case requires a study involving feasibility, pre-weld part design, tooling design, selection of most appropriate LFW production machine and post-weld process routes.

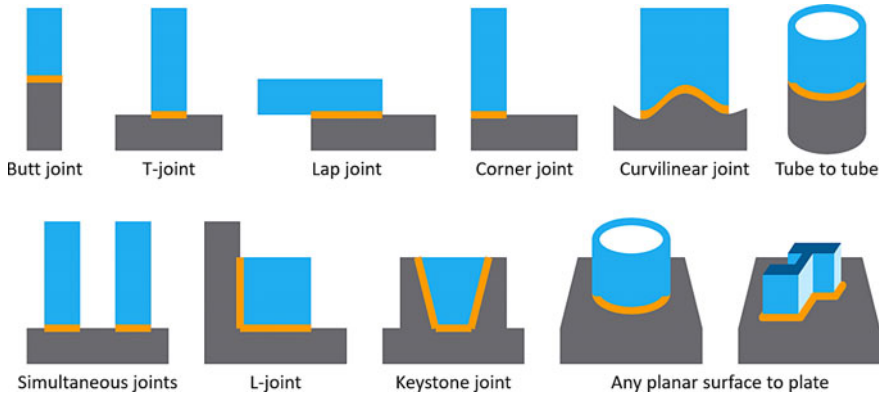


Fig. 6 LFW weld configurations. (Color figure online)

Over the past five years, several case studies were made by the authors, in cooperation with major aircraft manufacturers.

Example of LFW Application

The Figs. 7 and 8 show an actual Ti-6Al-4V aircraft structure part, produced using LFW instead of machining from solid. The pre-weld part design uses standard thickness plates in order to optimize the overall manufacturing costs. Pre-weld parts were

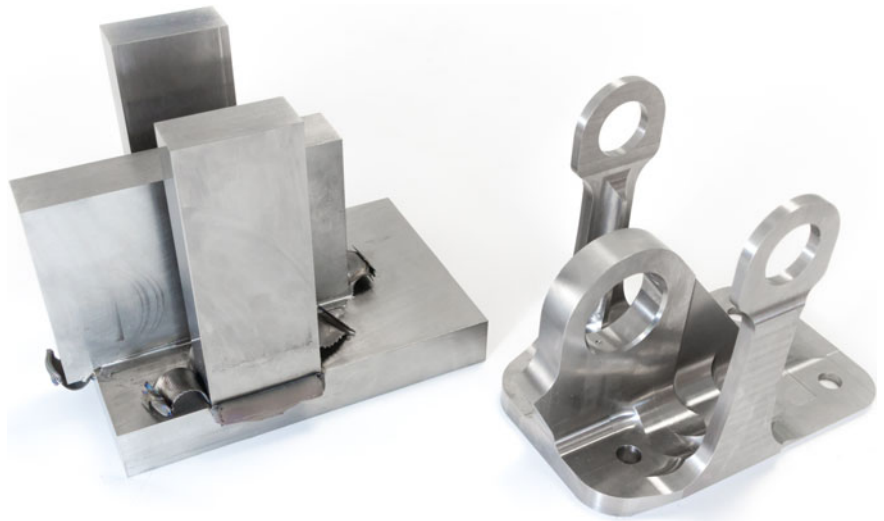
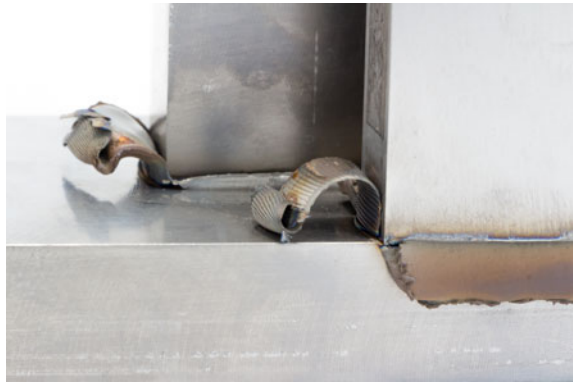


Fig. 7 Near-net-shape blank after LFW (left) and final part after machining (right). (Color figure online)

Fig. 8 Detail of the flashes.
(Color figure online)



water jet cut before welding, and the only pre-weld surface preparation was a cleaning manually with cloth and diestone. The welds were performed on the LFW machine MDS30 (Fig. 9), which has a maximum forge force of 300 kN. The central plate was welded first (“T-joint configuration”), then the flash was removed so that the flashes produced by the next weld operations can flow freely. Then the two-side plates were welded in one operation (“simultaneous corner joints” configuration). Then the entire part was heat-treated, inspected by ultrasonic inspection, and machined to final geometry.

Using LFW rather than conventional machining from solid leads to the following overall savings:

- Raw material savings: 6.05 kg
- Waste reduction: 73%
- Buy-to-Fly improvement: 3.7:1 instead of 10.7:1
- Overall production cost savings (with production costs assumptions): 31% (Fig. 10).

Combination of LFW with Other Processes

Further optimization can be achieved by combining other processes to LFW in order to produce more complex blanks. The following combinations were tested and show good results in terms of joint integrity, joint strength, and process repeatability:

- “L-joint” welds on an “L” extruded profile for a hinge application (Fig. 11).
- “T-joint” welds on an “H” extruded profile for a seat track application (Fig. 12).
- “Keystone” welds in a “U” extruded profile, formed by Hot Stretch Forming before welding, for a door frame application. The overall dimensions of this part are over 4.2 m long and 1 m width. For this part, the Buy-to-Fly ratio decreased from 54:1 to 13:1 (Fig. 13).
- “L-joint” weld in a “L” part, formed by Hot Forming before welding, for a bracket application (Fig. 14).

Fig. 9 Linear friction welder MDS30. (Color figure online)



Fig. 10 Estimation of overall production costs (note: water jet cutting cost is included in raw material cost). (Color figure online)

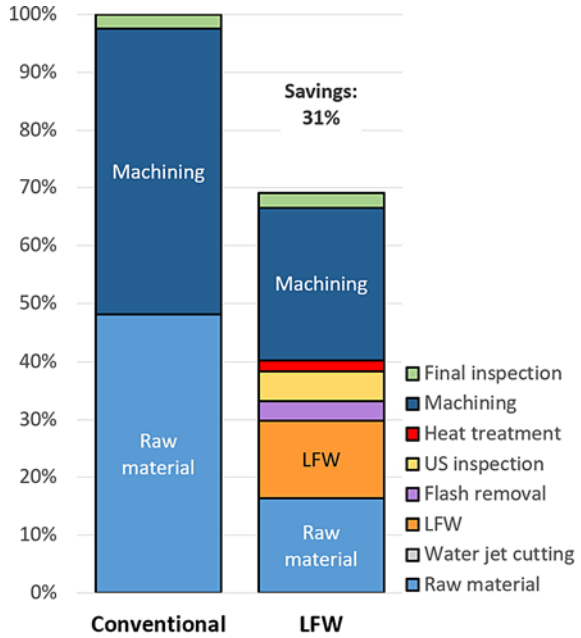




Fig. 11 Combination of extrusion (“L” profile) and LFW for a hinge demonstrator. (Color figure online)

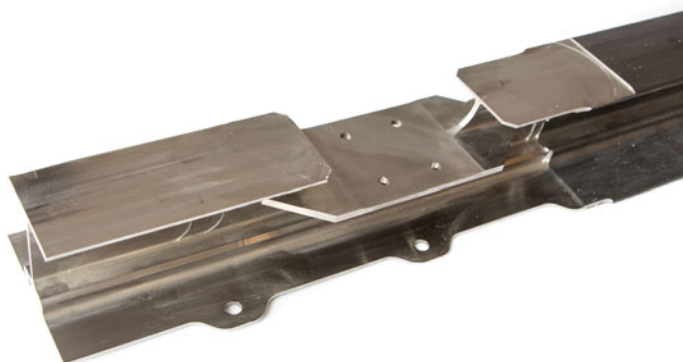


Fig. 12 Combination of extrusion (“H” profile) and LFW for a seat track demonstrator. (Color figure online)



Fig. 13 Combination of extrusion (“U” profile), Hot Stretch Forming and LFW for a door frame demonstrator. (Color figure online)

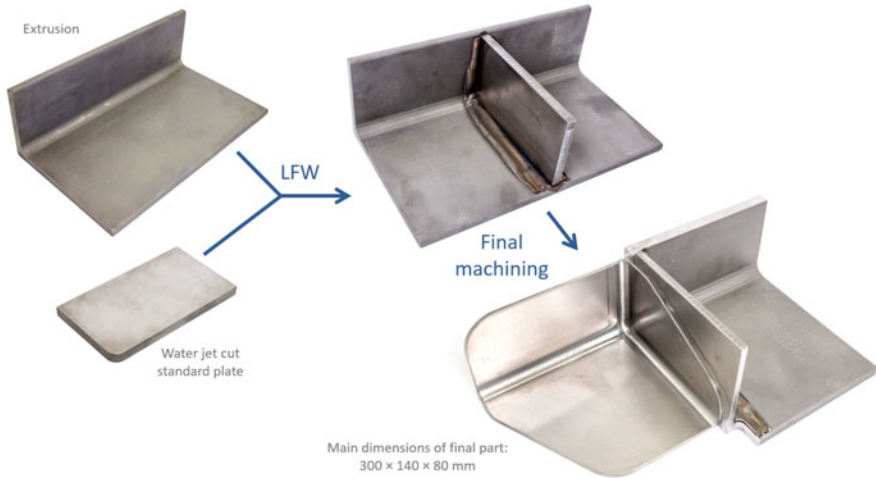


Fig. 14 Combination of Hot Forming and LFW for a bracket application. (Color figure online)

- Weld of hollow blades formed by superplastic forming and diffusion bonding, for a blisk application.

Applications on Aluminum Parts

Aluminum alloys are more difficult to weld by LFW because of their higher thermal conductivity, and the greater tendency of alloy elements to precipitate and form brittle intermetallic compounds. However some encouraging results were obtained on several aluminum alloys, including Al 2024 with an ultimate tensile strength of the weld over 90% of the strength of parent material [7].

Since the aluminum alloys are less expensive and easier to machine than titanium, the benefit of using LFW is less obvious on small parts. However, some applications on large parts like wing ribs are promising as the LFW could allow considerable raw material savings.

Conclusions

The linear friction welding (LFW) process was proven to produce high-quality welds with hot-forged microstructure, thanks to a low process temperature, short heat input time, self-cleaning of the weld interface, and a high pressure during the process and cooling down. As all the heat input is provided by machine-controlled mechanical sources, the process is very repeatable, easy to automate, and the quality assurance can be automatically achieved by monitoring and analyzing the data recorded by the machine sensors.

After introducing this process on titanium alloys for the manufacturing of “blisks” (bladed disks) for jet engine applications, the aerospace industry now investigates the opportunity to use LFW to reduce the cost of titanium and aluminum aircraft structure parts through linear friction welded near-net-shape blanks.

Several weld configurations and process combinations were successfully studied and applied to actual part designs, and the LFW has shown a significant potential for raw material savings and overall manufacturing costs.

References

1. Vairis A, Frost M (2000) Modelling the linear friction welding of titanium blocks. *Mater Sci Eng*, pp 8–17
2. Vairis A, Frost M (1999) On the extrusion stage of linear friction welding of Ti-6Al-4 V. *Mater Sci Eng*, pp 477–484
3. Turner R et al (2011) Linear friction welding of Ti-6Al-4 V: modelling and validation. *Acta Materialia* 59:3792–3803
4. Wanjara P, Jahazi M (2005) Linear friction welding of Ti-6Al-4 V: processing, microstructure, and mechanical-property inter-relationships. *Metall Mater Trans*
5. Romero J et al (2009) Effect of the forging pressure on the microstructure and residual stress development in Ti-6Al-4 V linear friction welds. *Acta Materialia* 57:5582–5592
6. Martina F (2014) Control of geometry, microstructure and mechanical properties in titanium large scale wire + arc additive manufacturing. Ph.D. Thesis. Cranfield University
7. Rotundo F, Morri A, Ceschini L (2012) Linear friction welding of a 2024 al alloy: microstructural, tensile and fatigue properties. *Light Metals*

Part III
Additive Manufacturing
Fatigue and Fracture V:
Processing-Structure-Property
Investigations and Application
to Qualification

Defect-Based Fatigue Modeling for AlSi10Mg Produced by Laser Powder Bed Fusion Process



Avinesh Ojha, Wei-Jen Lai, Ziang Li, Carlos Engler-Pinto, and Xuming Su

Abstract Defects are inevitable in metal parts manufactured by any process; the size, shape and location of such defects play a critical role in determining the material's fatigue strength. Due to the random nature of the defects' distribution in the part, a statistical method must be employed for fatigue strength estimation. The laser powder bed fusion (L-PBF) process introduces two main types of porosity defects: keyhole pores and lack-of-fusion pores. A defect-based statistical fatigue strength model has been developed and validated for the L-PBF AlSi10Mg aluminum alloy containing keyhole defects with different size distributions. Artificial defects were also introduced for model validation. The approach is based on the modified Murakami's formulation to address the material dependence and followed the Romano's approach to consider the statistical behavior of the fatigue strength. The proposed model successfully predicts the fatigue strength of different keyhole porosity distributions but is unable to predict the fatigue strength of materials containing lack-of-fusion porosity, possibly due to the higher stress concentration induced by its morphology.

Keywords Fatigue · Defects · AlSi10Mg · Laser powder bed fusion

Introduction

Additive manufacturing (AM) has gained considerable interest in recent years as it offers the possibilities of fabricating near net shape parts with complex geometries that are difficult to build using traditional manufacturing processes. The laser powder bed fusion (L-PBF) process has the advantage over other metal AM processes because of its high-dimensional accuracy and low defect volume. AlSi10Mg is one of the first few aluminum alloys utilized for L-PBF process. It finds a number of applications in the automotive industry, particularly for powertrain components. Since durability is a major concern for such components, understanding the fatigue behavior of L-PBF materials becomes extremely important for successful product design.

A. Ojha · W.-J. Lai (✉) · Z. Li · C. Engler-Pinto · X. Su
Ford Motor Company, 1 America Rd., Dearborn, MI, USA 48121
e-mail: wlai11@ford.com

© The Minerals, Metals & Materials Society 2021
TMS 2021 150th Annual Meeting & Exhibition Supplemental Proceedings,
The Minerals, Metals & Materials Series,
https://doi.org/10.1007/978-3-030-65261-6_7

There are several important factors that govern the fatigue properties of AM parts, such as surface roughness [1–10], heat treatment [11–13], residual stresses [14–17], and notch effect [18]. Defects such as porosity or inclusions are key factors affecting the fatigue strength of metal AM parts [2, 9, 19–24]. The defect size distribution and morphology depend on powder properties and morphology, processing parameters (such as laser power, scan speed, etc.), and environment (such as gas flow rate). These defects act as microscopic stress raisers, which result in local plastic deformation and can act as crack initiation sites under fatigue loading.

Another important factor that governs the fatigue properties of AM materials is the surface roughness. Surface roughness can be seen as defects with sharp notches and can trigger premature failure under cyclic loading. It has been reported in the literatures that surface roughness decreases the fatigue strength of AM materials by more than 40–50% as compared to the polished surfaces [1–3]. Several models have been proposed to correlate roughness to the fatigue strength reduction, such as the popular empirical model in FKM guideline [25] and the one proposed by Arola [8, 26] based on fatigue notch sensitivity approach, which is able to predict the fatigue strength reduction due to surface roughness

The well-established Kitagawa-Takahashi (KT) diagram [27] and El-Haddad formulations [28] can successfully correlate fatigue strength to defect parameters. One of the widely used models, and perhaps the simplest one, that quantifies the influence of defects and inhomogeneities on the fatigue strength was proposed by Murakami and Endo [29, 30], who found that the fatigue strength corresponds to a threshold stress at which the small cracks do not propagate. The Murakami's approach is based on the Kitagawa-Takahashi diagram, where the threshold stress intensity factor is affected only by the Vickers hardness and the area of the defect projected along the loading direction. The Murakami's equation can be written as

$$\sigma_f = \frac{1.43(120 + HV)}{(\sqrt{\text{area}})^{1/6}} \quad (1)$$

where σ_f is the fatigue strength, HV is the Vickers hardness, and *area* is the area of the defect projected along the loading direction. Note that the Murakami's fatigue strength prediction depends only on two variables: the area of the defect and the hardness value. It is worth noting that Murakami calibrated the model constants (1.43 and 120 in Eq. 1) using fatigue data from many steels and only one wrought aluminum alloy (2017-T4) [31]. The model overestimated the experimental values by approximately 10% for the aluminum alloy [31]. These results indicate that the constants may be material dependent. Another issue is that the model is calibrated using rotating bending fatigue data. Since the fatigue strength measured by rotating bending is always higher than the one measured by uniaxial fatigue testing, the model can significantly overestimate the uniaxial fatigue strength. There are several other studies [32, 33] where new sets of material constants were used to develop and validate Murakami's approach for aluminum alloys. However, none of these models have yet been validated for L-PBF materials. The equations used by Ueno et al. [32] and by Tajirja et al. [33] are shown in Eqs. 2 and 3, respectively.

$$\sigma_f = \frac{1.43(45 + HV)}{(\sqrt{\text{area}})^{1/6}} \quad (2)$$

$$\sigma_f = \frac{1.43(75 + HV)}{(\sqrt{\text{area}})^{1/6}} \quad (3)$$

The current work aims to investigate some preliminary fatigue results and to understand the effect of defects and other material parameters on the fatigue strength of the AlSi10Mg alloy manufactured by L-PBF. This study is critical, as L-PBF alloys have totally different microstructures compared to conventional alloys due to the extremely rapid cooling rate. In addition, the applicability of the defect-based fatigue strength model for L-PBF AlSi10Mg with different defect morphologies (keyhole and lack-of-fusion, LoF) has been investigated. Artificial defects of predetermined sizes were also introduced to generate additional validation points to the proposed modeling approach.

Experimental Procedures

Materials and Sample Preparation

The AlSi10Mg aluminum alloy has been selected for this study. The alloy composition is listed in Table 1. Total four groups of samples (A-D) were produced in this study. Group A and Group B samples were built using the SLM-125 machine by SLM Solutions with the tensile axis in the Z-direction (vertical direction) using optimum process parameters (referred to as “standard” parameters thereafter). An inside-out laser scan strategy was adopted, which melts the center portion first, followed by a contour scan and border scan on the outer part to improve the dimensional accuracy and reduce the surface roughness.

Group A fatigue samples were machined from as-built 15-mm diameter cylindrical rods and then mechanically polished along the axial direction to remove machining marks; these samples are denoted as “MP” (machined and polished).

Two sets of samples were prepared from Group B: one set was machined and polished (MP) and the other set was produced to shape using the L-PBF process (no machining needed) and then mechanically polished to remove the roughness; these samples are denoted as “P” (polished only). The samples were then heat treated at 500°C for 1 hour (solutionizing). Table 2 summarizes the process parameters and heat treatments for these samples.

Groups C and D consist of MP samples built in the horizontal and vertical directions using the SLM-500 machine. These samples were stress relieved at 300°C for 2 hours. Group C uses the standard laser parameters and Group D uses a lower volumetric energy density (VED), which was intentionally optimized to introduce a large amount of LoF defects with the goal to understand the effect of defect morphology on

Table 1 Chemical composition of AISi10Mg aluminum alloy

	Si(%)	Fe(%)	Cu(%)	Mg(%)	Cr(%)	Ni(%)	Ti(%)	Ca(%)	Ga(%)	Sr(ppm)	V(%)	Al(%)
AISI10Mg	10.48	0.125	0.0057	0.291	0.012	0.0108	0.129	0.0059	0.0123	142	0.0146	88.8

Table 2 Summary of process parameters for different groups of fatigue specimens

	Machine	Region	Power (W)	Speed (mm/s)	Hatch spacing (mm)	Layer thickness (mm)	Built plate temperature (°C)	Post heat treatment
Group A (Standard)	SLM 125	Border & Contour	200	730	0.2	0.03	150	N/A
		Hatch	350	1650	0.13			
Group B (Standard)	SLM 125	Border & Contour	330	730	0.2	0.03	150	500°C/1 h
		Hatch	350	1650	0.13			
Group C (Standard)	SLM 500	Border & Contour	300	730	0.17	0.03	200	300°C/2 h
		Hatch	370	1975	0.17			
Group D (Lack of fusion)	SLM 500	Border & Contour	300	730	0.17	0.03	200	300°C/2 h
		Hatch	370	1975	0.17			

the fatigue strength. The laser process parameters were optimized to produce a very small amount of keyhole defects in Group A, B, and C specimens. The LoF defects in Group D specimens are highly irregular with sharp notches along the borders of the defects.

In addition to the naturally occurring defects, drilled holes of different sizes which are larger than the intrinsic defects were introduced in Group A (MP) and Group B (P) specimens. The purpose was to validate the current modeling approach with additional data points. Note that these “artificial defects” resemble keyhole defects in terms of their morphology.

Tensile Test and Hardness Measurement

Tensile tests were carried out in an MTS 100 kN servohydraulic frame for Group A, C, and D samples. The specimen geometry is shown in Fig. 1a, which conforms to ASTM E8 [34]. The displacement rate is 0.19 mm/min up to 1 mm and then 1 mm/min until fracture occurs.

Metallographic samples were cold-mounted to avoid additional heating. Samples were polished; the porosity was measured in the XY-plane; Vickers hardness values were also measured on the same samples using a 300-g force with a dwell time of 13 seconds (5 indentations per specimen).

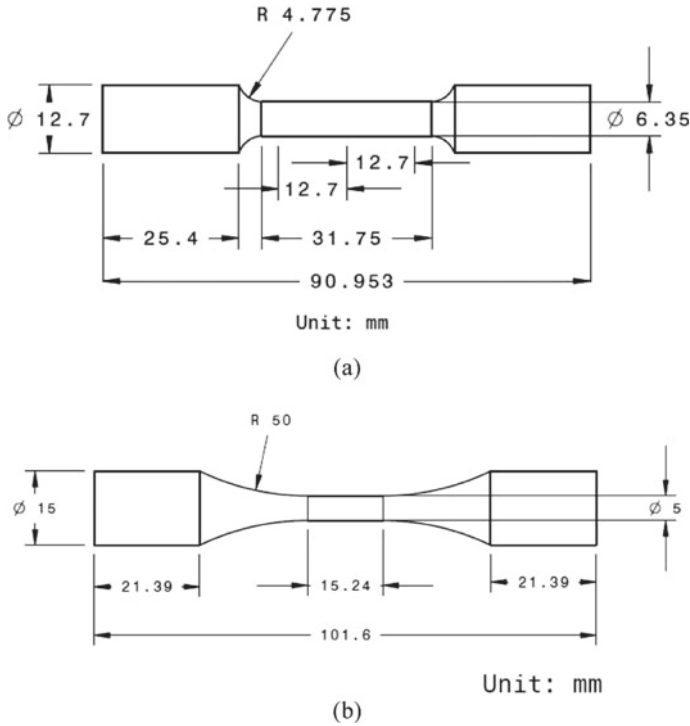


Fig. 1 a Tensile and b fatigue specimen geometries

High Cycle Fatigue (HCF) Test

Fatigue tests were conducted using 100 kN sevohydraulic frames. The specimen geometry follows ASTM E466 [35] and is shown in Fig. 1b. The tests were conducted at a frequency of 70 Hz. The temperature on the specimen surface was monitored during the test using an infrared thermometer. The temperature increase on the specimen surface was limited to $\leq 5^{\circ}\text{C}$ during the test.

Tensile Test and Hardness Measurement

The tensile engineering stress/strain curves are shown in Fig. 2. The average ultimate tensile strength (UTS), yield strength (YS), elastic modulus, elongation to fracture, and Vickers hardness values are provided in Table 3. Mechanical properties of Group A to D specimens. The results are an average of at least three tests for which standard deviations are reported. Table 2. Group A has the highest UTS and YS since it is not post heat treated. The vertical and horizontal samples do not show significant

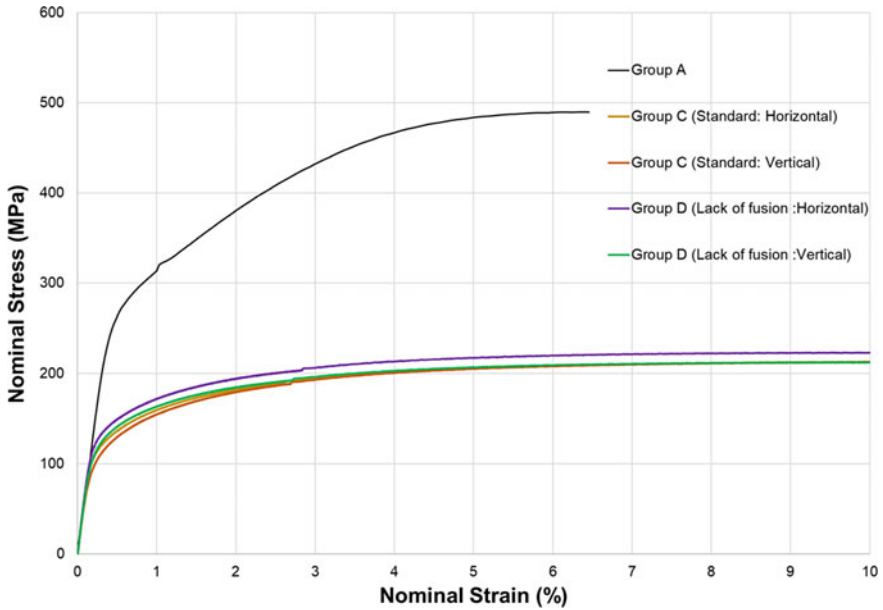


Fig. 2 Average stress/strain curves of Group A-D specimens. Strains up to 10% are shown. (Color figure online)

Table 3 Mechanical properties of Group A to D specimens

	Yield strength (0.2%, MPa)	Elastic modulus (GPa)	Ultimate tensile strength (MPa)	Elongation at fracture (%)	Hardness (HV)
Group A	280.2 ± 1.3	67.1 ± 4.0	491.3 ± 1.8	6.4 ± 0.4	136.6 ± 2.2
Group B	–	–	–	–	67.3 ± 0.7
Group C (Horizontal)	127.5	67.5	212.5	24.8	74.7
Group C (Vertical)	121.3	65.9	210.3	24.2	74.1
Group D (Horizontal)	139.0	70.2	221.4	24.8	78
Group D (Vertical)	135.7 ± 4.4	67.2 ± 1.8	220.5 ± 6.6	20.1 ± 1.9	80 ± 1.3

The results are an average of at least three tests for which standard deviations are reported

difference in Group C and Group D after stress relieving. However, the samples from Group D have slightly higher tensile mechanical properties than the ones in Group C. This might be due to the faster cooling rate associated with the lower VED in Group D.

HCF

Figure 3a, b shows the S-N curves obtained for all groups of specimens (Groups A-D; solid symbols indicate failures and hollow symbols indicate runouts at 10^7 cycles). The method used for fatigue strength calculation needs to consider fatigue behavior of the material tested. Many models have been proposed to fit the fatigue S-N curves; however, these models cannot capture S-N curves near the high-cycle fatigue regime. In the current work, the fatigue strength was calculated using the random fatigue limit (RFL) model [36], which fits the S-N curve using the equation below.

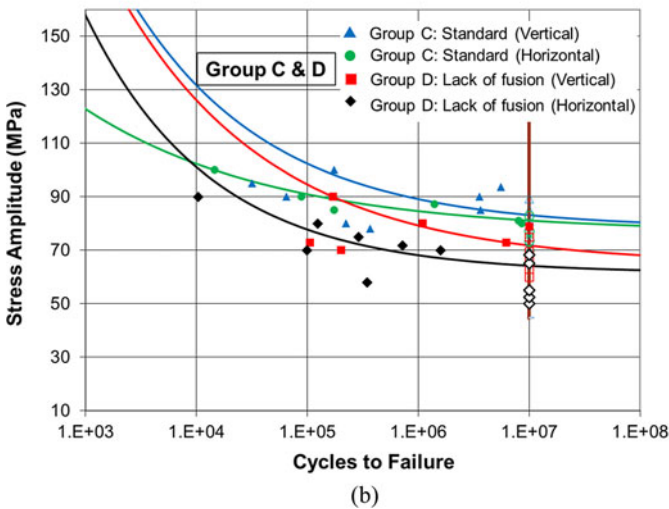
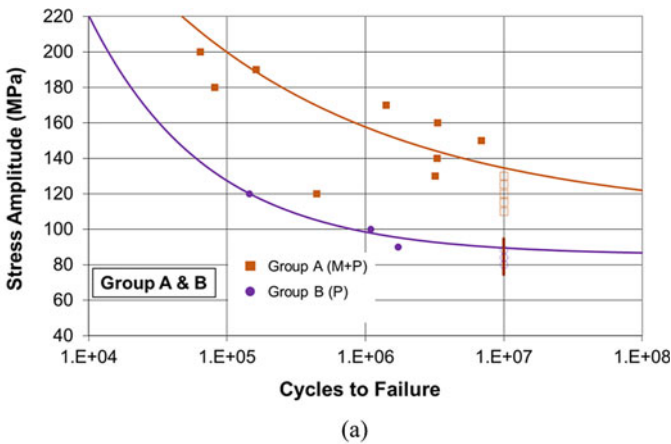


Fig. 3 S-N curves of **a** Group A and B specimens, and **b** Group C and D specimens fitted using RFL method. (Color figure online)

Table 4 Fatigue strengths at 10^7 cycles (and associated standard deviations) obtained from the RFL model

	Fatigue strength (MPa) at 10^7 cycles					
	Group A	Group B	Group C		Group D	
	Vertical	Vertical	Vertical	Horizontal	Vertical	Horizontal
Polished (P)	–	89 ± 2.0	–	–	–	–
Machined & Polished (MP)	133 ± 15.0	–	83.1 ± 10.5	81.1 ± 2.3	71.9 ± 9.3	64.3 ± 6.5

$$S_a - S_L = C(2N_f)^b \quad (4)$$

where S_a is the stress amplitude, S_L is the infinite-life fatigue limit of the material (a random variable following the Weibull distribution), N_f is the number of cycles to fracture, and C and b are empirical constants. In this study, the fatigue S-N curves were fitted using an RFL model with the aid of the maximum likelihood method [37] to account for the runout data points. The model can properly capture the changing slope of the fatigue S-N curves. The fatigue strength distribution is then calculated at 10^7 cycles. The fatigue strength for each group of specimens is provided in Table 4 together with the standard deviation.

Note that the fatigue strength values provided in Table 4 are derived from S-N curves in Fig. 3 which use multiple specimens. Each individual specimen has a different defect distribution and a different fatigue strength; therefore, the fatigue strength reported in Table 4 is the average fatigue strength of all samples tested. Fitting the Murakami's model, on the other hand, requires the fatigue strength to be determined for a single specimen for which the defect area is known. In order to find the fatigue strength of a single specimen, the approach proposed by Maxwell and Nicholas [38] has been followed. According to this approach, a specimen is cycled first at a low stress level (σ_i) until it reaches a pre-determined number of cycles ($N_i = 10^7$ cycles). The specimen is then checked for any microcracks and, if no cracks are detected, the stress level is increased by 5% to σ_{i+1} . This process is continued until the specimen fails at N_{i+1} cycles. The fatigue strength (σ_w) are then estimated using the equation below:

$$\sigma_w = \sigma_i + (\sigma_{i+1} - \sigma_i) \left(\frac{N_{i+1}}{N_i} \right) \quad (5)$$

The major assumption of this method is that there is no significant damage incurred in the specimen at stress levels below the fatigue strength of the material. Therefore, the lives obtained at a higher stress level would not be influenced by the cyclic loading history at the previous lower stress levels. This assumption has been verified and reported in the literature [38].

Figure 4a–c shows the representative micrographs of the fractured surfaces and defect morphologies for Group A–D specimens. The defect from which the fatigue

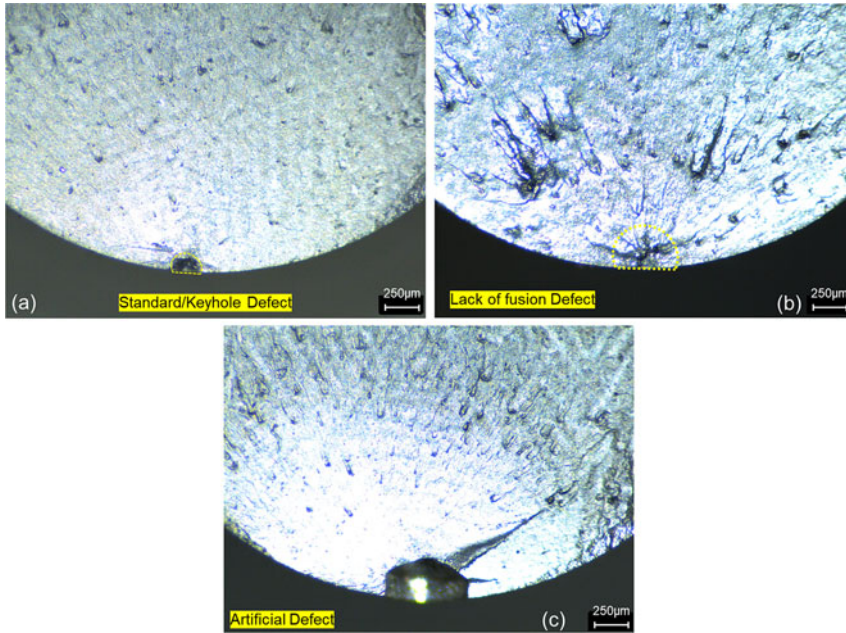


Fig. 4 Optical micrographs showing **a** keyhole defect in Group A (MP) specimen **b** LoF defect in Group D (vertical built) specimen, and **c** artificially introduced defect in Group A (P) specimen. (Color figure online)

crack initiates can be easily identified from the micrographs. The measured areas of the defects are provided in Table 5 with the corresponding fatigue strengths for several tested specimens. The areas were calculated following guidelines described by Murakami [19, 31].

Figure 5 shows the fatigue strength as a function of $\sqrt{\text{area}}$, where $\sqrt{\text{area}}$ is the square root of the measured area of the defect that causes fatigue crack initiation projected in the section perpendicular to the loading direction. The curves in the figure are the Murakami's model predictions for different hardness values. The value of $\sqrt{\text{area}}$ is between 30 and 300 μm for all the specimens considered in the study. To generate additional data for validation, we artificially introduced defects in the specimens by drilling holes in Group A (MP) and Group B (P) specimens. The $\sqrt{\text{area}}$ for these artificial defects is between 400 and 700 μm . These artificially introduced defects are much larger than the naturally occurring ones and fatigue failure originated from these defects is shown in Fig. 4c. The areas of these artificial defects along with their fatigue strengths for all specimens considered in the present study are listed in Table 5. As seen from Fig. 5, Murakami's model prediction using Eq. 3 with modified material constants proposed by Tajiria et al. [33] shows good agreement with the experimental results for different hardness values and areas of the defects for keyhole defects present in Group A to C specimens. However, the model overestimates the fatigue strengths by more than 30% for LoF defect in Group D horizontally built specimens. This is possibly due to higher stress concentration

Table 5 Summary of defect area and experimentally determined fatigue strength for different groups of specimens

	Specimen ID	Build direction	Machining condition	Defect $\sqrt{\text{area}}$ (μm)	Experimental fatigue strength (MPa)
Group A	A1	Vertical	MP	104	147
	A2		MP	57	146
	A3		MP	101	148
	A4		MP	93	140
	A5		MP	114	144
	A6		MP	124	154
	A7		MP	33	111
	A8*		MP	519	106
	A9*		MP	420	119
	A10*		MP	449	109
	A11*		MP	602	100
Group B	B1	Vertical	P	129	81
	B2		P	109	85
	B3*		P	284	73
	B4		MP	33	111
Group C	C1	Vertical	MP	82	92
	C2	Vertical	MP	118	83
	C3	Horizontal	MP	241	80
	C4	Horizontal	MP	163	84
Group D	D1	Vertical	MP	289	72
	D2	Vertical	MP	276	79
	D3	Horizontal	MP	156	69
	D4	Horizontal	MP	261	55

Data with * represents artificially introduced defects

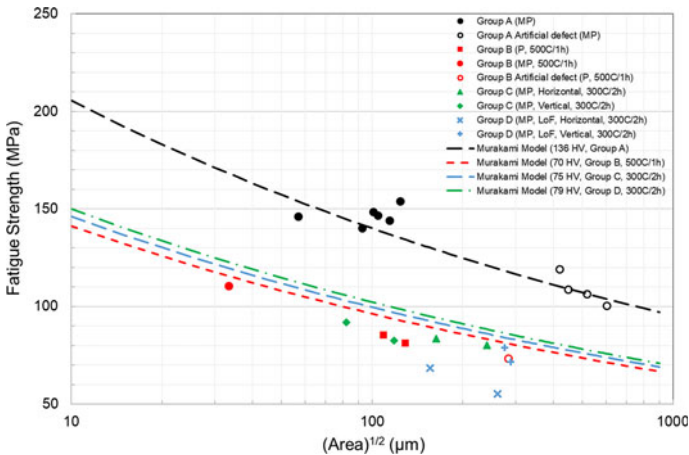


Fig. 5 Fatigue strength as a function of area parameter for different groups of specimens considered in the present study. Dashed lines show Murakami model predictions for different hardness values. (Color figure online)

existing at the irregular LoF defect boundaries. It is worth noting that the measured area of LoF defect on the fracture surface is larger compared to the one of keyhole defect in the specimens. This is in agreement with previous findings in the literature [2].

Probabilistic Approach to Fatigue Strength Prediction

Figure 6a–b shows the micrographs of specimens with keyhole and LoF defects, respectively. The percentage of porosity area is 0.96% and 1.7% for keyhole and LoF specimens, respectively. Note that LoF defects have sharp edges along the borders, which contributes to a higher stress concentration (and lower fatigue strength) than predicted by the current modeling approach. It is well known that defect morphologies can be correlated with the VED [39–42]. The optimal VED for minimizing porosity in AlSi10Mg is between 50–70 J/mm³ based on data reported in the literature [39–42]. VEDs lower than this value will result in lack of fusion defects, and hence lower fatigue strength.

A probabilistic approach is adopted following Beretta and Romano’s work [2, 9, 20, 21] to predict fatigue properties from the measured pore size distribution. This approach assumes that the fatigue crack will initiate from the largest defect near the surface when a given volume of material is subjected to the same cyclic stress. Therefore, the estimation of fatigue strength is based on the probability of finding the largest defect in a given volume of the material. Figure 7a shows the pore size distribution for Group B (P) specimen. The porosity (% area) is 0.85% and the hardness value is 70 HV. Figure 7b shows the corresponding three-parameter Weibull fitting for pores larger than 30 μm (equivalent diameter). The three-parameter Weibull distribution is expressed as

$$f(d) = \frac{\beta}{\eta} \left(\frac{d - \gamma}{\eta} \right)^{\beta-1} e^{-\left(\frac{d - \gamma}{\eta} \right)^\beta} \quad (6)$$

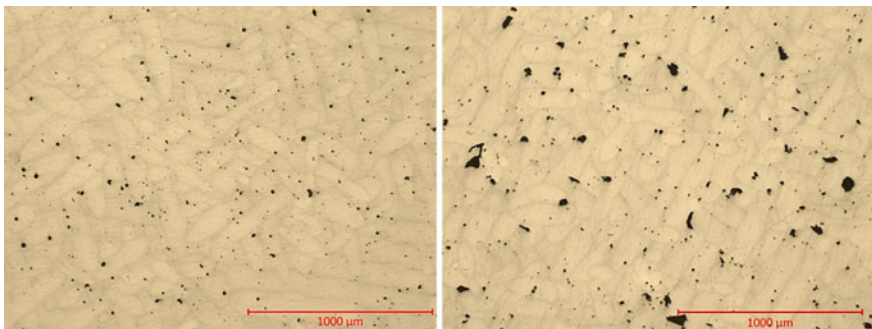


Fig. 6 Defect distribution in specimen with **a** keyhole defects **b** lack of fusion defects. (Color figure online)

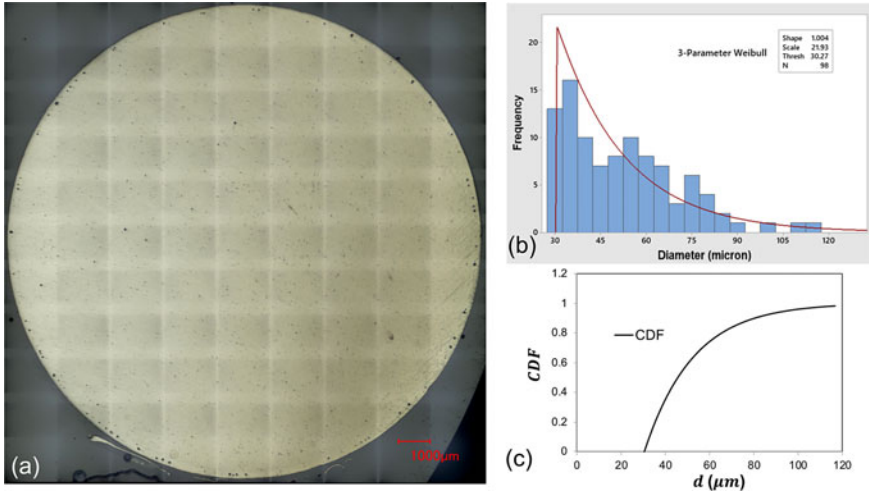


Fig. 7 a A micrograph showing the pore distribution of a Group B (P) specimen. b Probability density function (PDF) and c cumulative distribution function (CDF) of a Group B (P) specimen based on three-parameter Weibull distribution. (Color figure online)

where β, η, γ are the shape, scale, and location parameters, respectively, and d is the equivalent diameter of the pore. The corresponding cumulative distribution function (CDF) is expressed as

$$F(d) = 1 - e^{-(d/\eta)^\beta} \tag{7}$$

Defects smaller than 30 μm in diameter are ignored in the current analysis as that they do not contribute to fatigue failure in most cases. This is also based on the current observation that all fatigue failures initiate from defects which are much larger than 30 μm, as listed in Table 5. Most of the fatigue failures initiate from surface and near-surface pores. Hence only defects within 0.5 mm from the surface are considered and the number density of pores can be estimated by counting the number of pores from the micrograph. Assuming that the pore size distribution is the same in the specimen, the total number of pores in the surface layer of the sample gauge volume is known. Then, the pore size for a given probability $P(\leq d)$ is calculated. The CDF gives the probability of finding a defect smaller than or equal to a certain d and allows us to estimate the fatigue strength of the specimen based on Murakami’s equation. The equations of fatigue strength estimation combining the probabilistic approach and Murakami’s model are shown in Eqs. 8 and 9. Note that the Murakami’s model constants used here are based on the ones used by Tajiria et al. [33]. As shown in Table 6, the predicted fatigue strength of Group B (P) is 88 MPa with the probability $P(\leq d) = 0.5$. This means there is a 50% chance that the fatigue strength of the specimen is above 88 MPa. This value is close to the experimental value of 83 MPa.

Table 6 Summary of fatigue strength predicted using statistical approach

Specimen	Vickers hardness (HV)	Predicted fatigue strength (MPa)	Experimental fatigue strength (MPa)
Group A (MP)	135	120	130
Group B (P)	70	88	83

Similarly, the predicted fatigue strength for Group A (MP) specimen is 120 MPa, which is within 10% of the experimentally obtained value of 130 MPa.

$$\sigma(P(\leq d)) = \frac{1.43(75 + HV)}{\sqrt{\pi \left(\frac{d}{2}\right)^2}}^{1/6} \quad (8)$$

$$d = \eta[-\ln(1 - P(\leq d))]^{(1/\beta)} + \gamma \quad (9)$$

Discussion

One of the important observations in this study is that Murakami's fatigue strength model predicts the fatigue strength quite well for keyhole defects which are rather spherical. However, the fatigue strength prediction for LoF defects has a large deviation from the experimental value. The micrograph shown in Fig. 6b clearly shows that LoF defects are irregular with very sharp notches along the boundaries. However, Murakami [31] reported that fatigue strength is insensitive to defect morphology (based on his experimental observations). Murakami tested samples with drilled holes and cracks with the same defect area in medium carbon steels and the results show very similar fatigue strength. Note that these tests were conducted on conventional alloys which have different microstructure and grain size compared to L-PBF alloys.

Murakami has proposed an effective area concept [19] to calculate the fatigue strength for irregular shaped defect (such the LoF defects observed in L-PBF materials). The effective area is calculated based on defect orientation, distance from the surface, and proximity of one defect to another. The current study used similar guidelines to calculate the effective defect area. However, the model cannot successfully predict the fatigue strength solely based on $\sqrt{\text{area}}$ parameter for materials containing LoF defects. The current results show that defect morphology must also be considered for L-PBF alloys as they are more notch sensitive than conventional cast alloys. This is possibly due to the fine grain structure present in L-PBF alloys [43, 44]. It has been reported that for ultrafine grain alloys, the notch sensitivity factor is even higher than 1 [43]. For this reason, the shape of the defects plays a critical role in dictating the fatigue strength in L-PBF alloys. The modeling of LoF will be considered in a future publication and is beyond the scope of the current work.

In the current study, residual stresses are removed using post heat treatments for Group B, C, and D. The residual stress is removed in Group A during the machining process. The post heat treatment, in addition, also allowed us to investigate the applicability of Murakami's approach by changing the hardness values. It is noted that an increase in hardness value by 10 HV roughly increased the fatigue strength by approximately 7 MPa for the same area of the defect.

Beretta and Romano [2, 9, 20, 21, 24, 45] published a series of papers using El-Haddad's formulation with extreme value statistics to predict the fatigue strength of L-PBF AlSi10Mg. The results show that the fatigue strength is a strong function of the defect size. The use of X-ray CT scan to capture the defect size distribution and defect morphology to correlate mechanical properties is well established. Several authors have discussed this technique, and used the concept of extreme value statistics for a probabilistic approach for fatigue strength prediction [2, 21]. Although the X-ray CT scan provides an accurate information on the defect size distribution, the current study utilizes defect size distribution on a given cross section of the specimen. The assumption is that the process should not affect the defect size distribution from one layer to another and a cross section from any location should be representative of the entire specimen. The current probabilistic approach relies on the concept that only the largest defect at or near the surface of the specimens is considered to cause fatigue failure. The probabilistic approach can successfully predict the fatigue strength within 15% of the experimental value for keyhole defects. This further confirms the applicability of the current modeling approach.

Conclusions

The following conclusions are drawn from the current study.

- (i) The static and fatigue properties of L-PBF AlSi10Mg are obtained for different build orientations and post heat treatments in the current study. The average fatigue strength of specimens containing primarily keyhole defects is slightly higher than the ones containing primarily LoF defects.
- (ii) Fatigue results show that the predicted fatigue strengths based on the Murakami's model are in good agreement with the experimental results for keyhole defects. However, the model cannot be applied to LoF defects.
- (iii) A statistical defect-based model is proposed based on the Murakami's fatigue strength model with modified material constants. The defect-based model can predict the fatigue strength with known defect size distribution of the specimen. The predicted fatigue strengths of L-PBF AlSi10Mg specimen containing keyhole defects are within 15% of the experimental measurement.

References

1. Mower TM, Long MJ (2016) Mechanical behavior of additive manufactured, powder-bed laser-fused materials. *Mater Sci Eng, A* 651:198–213
2. Romano S et al (2017) Qualification of AM parts: extreme value statistics applied to tomographic measurements. *Mater Des* 131:32–48
3. Yadollahi A et al (2018) Fatigue life prediction of additively manufactured material: Effects of surface roughness, defect size, and shape. *Fatigue Fract Eng Mater Struct* 41(7):1602–1614
4. Molaei R, Fatemi A (2019) Crack paths in additive manufactured metallic materials subjected to multiaxial cyclic loads including surface roughness, HIP, and notch effects. *Int J Fatigue* 124:558–570
5. Suraratchai M et al (2008) Modelling the influence of machined surface roughness on the fatigue life of aluminium alloy. *Int J Fatigue* 30(12):2119–2126
6. Mardaras J, Emile P, Santgerma A (2017) Airbus approach for F&DT stress justification of additive manufacturing parts. *Procedia Struct Integrity* 7:109–115
7. Greitemeier D et al (2016) Effect of surface roughness on fatigue performance of additive manufactured Ti–6Al–4 V. *Mater Sci Technol* 32(7):629–634
8. Arola D, Williams C (2002) Estimating the fatigue stress concentration factor of machined surfaces. *Int J Fatigue* 24(9):923–930
9. Beretta S, Romano S (2017) A comparison of fatigue strength sensitivity to defects for materials manufactured by AM or traditional processes. *Int J Fatigue* 94:178–191
10. Pegues J et al (2018) Surface roughness effects on the fatigue strength of additively manufactured Ti–6Al–4 V. *Int J Fatigue* 116:543–552
11. Brandl E et al (2012) Additive manufactured AlSi10Mg samples using selective laser Melting (SLM): Microstructure, high cycle fatigue, and fracture behavior. *Mater Des* 34:159–169
12. Aboulkhair NT et al (2016) Improving the fatigue behaviour of a selectively laser melted aluminium alloy: influence of heat treatment and surface quality. *Mater Des* 104:174–182
13. Zhang C et al (2018) Effect of heat treatments on fatigue property of selective laser melting AlSi10Mg. *Int J Fatigue* 116:513–522
14. Mercelis P, Kruth JP (2006) Residual stresses in selective laser sintering and selective laser melting. *Rapid Prototyping J*
15. Uzan NE et al (2018) On the effect of shot-peening on fatigue resistance of AlSi10Mg specimens fabricated by additive manufacturing using selective laser melting (AM-SLM). *Add Manuf* 21:458–464
16. Leuders S et al (2013) On the mechanical behaviour of titanium alloy TiAl6V4 manufactured by selective laser melting: fatigue resistance and crack growth performance. *Int J Fatigue* 48:300–307
17. Edwards P, Ramulu M (2014) Fatigue performance evaluation of selective laser melted Ti–6Al–4V. *Mater Sci Eng, A* 598:327–337
18. Kahlin M, Ansell H, Moverare J (2017) Fatigue behaviour of notched additive manufactured Ti6Al4V with as-built surfaces. *Int J Fatigue* 101:51–60
19. Masuo H et al (2018) Influence of defects, surface roughness and HIP on the fatigue strength of Ti–6Al–4V manufactured by additive manufacturing. *Int J Fatigue* 117:163–179
20. Romano S et al (2018) Fatigue properties of AlSi10Mg obtained by additive manufacturing: defect-based modelling and prediction of fatigue strength. *Eng Fract Mech* 187:165–189
21. Romano S, Miccoli S, Beretta S (2019) A new FE post-processor for probabilistic fatigue assessment in the presence of defects and its application to AM parts. *Int J Fatigue* 125:324–341
22. Pellizzari M et al (2020) Effects of building direction and defect sensitivity on the fatigue behavior of additively manufactured H13 tool steel. *Theoret Appl Fract Mech* 108:102634
23. Molaei R, Fatemi A (2018) Fatigue design with additive manufactured metals: issues to consider and perspective for future research. *Procedia Eng* 213:5–16
24. Murakami Y, Beretta S (1999) Small defects and inhomogeneities in fatigue strength: experiments, models and statistical implications. *Extremes* 2(2):123–147

25. Forschungskuratorium Maschinenbau e.V. Analytical strength assessment of components in mechanical engineering, FKM guideline (Frankfurt am Main: VDMA, 2003)
26. Arola D, Ramulu M (1999) An examination of the effects from surface texture on the strength of fiber reinforced plastics. *J Compos Mater* 33(2):102–123
27. Kitagawa H (1976) Applicability of fracture mechanics to very small cracks or the cracks in the early stage. *Proc of 2nd ICM, Cleveland*. 1976:627–631
28. El Haddad M, Topper T, Smith K (1979) Prediction of non propagating cracks. *Eng Fract Mech* 11(3):573–584
29. Murakami Y, Endo M (1994) Effects of defects, inclusions and inhomogeneities on fatigue strength. *Int J Fatigue* 16(3):163–182
30. Murakami Y, Endo T (1980) Effects of small defects on fatigue strength of metals. *Int J Fatigue* 2(1):23–30
31. Murakami Y (2019) *Metal fatigue: effects of small defects and nonmetallic inclusions*. Elsevier
32. Ueno A et al (2014) Fatigue limit estimation of aluminum die-casting alloy by means of \sqrt{a} area method. *J Soc Mater Sci, Japan* 63(12):844–849
33. Tajiri A et al (2014) Fatigue limit prediction of large scale cast aluminum alloy A356. *Procedia Mater Sci* 3:924–929
34. ASTM E8 (2001) Standard test methods for tension testing of metallic materials. Annual book of ASTM standards. ASTM
35. ASTM E466 (2003) Standard practice for conducting force controlled constant amplitude axial fatigue tests of metallic materials. Annual Book of ASTM. American Society for Testing and Materials
36. Siebel E, Gaier M (1956) Untersuchungen über den Einfluss der Oberflächenbeschaffenheit auf die Dauerschwingfestigkeit metallischer Bauteile. *VDI-Z* 98(30):1715–1723
37. Engler-Pinto Jr C et al (2005) Statistical approaches applied to fatigue test data analysis. *SAE Trans*, pp 422–431
38. Maxwell DC, Nicholas T (1999) A rapid method for generation of a Haigh diagram for high cycle fatigue. In *Fatigue and Fracture Mechanics: 29th Volume*. ASTM International
39. Read N et al (2015) Selective laser melting of AlSi10Mg alloy: process optimisation and mechanical properties development. *Mater Des (1980–2015)*. 65:417–424
40. Palumbo B et al (2017) Tensile properties characterization of AlSi10Mg parts produced by direct metal laser sintering via nested effects modeling. *Materials* 10(2):144
41. Thijs L et al (2013) Fine-structured aluminium products with controllable texture by selective laser melting of pre-alloyed AlSi10Mg powder. *Acta Mater* 61(5):1809–1819
42. Kempen K et al (2012) Mechanical properties of AlSi10Mg produced by selective laser melting. *Phys Procedia*. 39:439–446
43. Karry R, Dolan T (1953) Influence of grain size on fatigue notch-sensitivity. Illinois Univ at Urbana Engineering Experiment Station
44. Lorenzino P, Navarro A (2015) Grain size effects on notch sensitivity. *Int J Fatigue* 70:205–215
45. Beretta S, Murakami Y (1998) Statistical analysis of defects for fatigue strength prediction and quality control of materials. *Fatigue Fract Eng Mater Struct* 21(9):1049–1065

Effect of Laser Remelting on Microstructure, Residual Stress, and Mechanical Property of Selective Laser Melting-Processed Ti-6Al-4V Alloy



Yiwa Luo, Yu Jiang, Jun Zhu, Jiguo Tu, and Shuqiang Jiao

Abstract Laser remelting is often used during selective laser melting (SLM) processes to restrain the residual stress and improve the mechanical strength of the products. However, researches regarding its effects on porous metals with trabecular or thin-walled structure are still quite lacking. Hereby, remelting treatments have been employed during the SLM processes of a porous Ti-6Al-4V alloy in this study and their influences on dimensional accuracy, microstructure, mechanical property, and residual stress were researched. The results indicate that remelting treatments can provide a stronger bonding condition for the cellular structure, and improve the yield strength and elastic modulus of the alloy. Rescanning with 75% energy density results in 33.5–38.0% reduction of residual stress. In terms of pore structure and morphology, the porosities of remelted specimens are 2–4% lower than that of single-scanned specimens. This inconsistency increases with the increase of sheet thickness. It is suggested that the rescan laser power should be turned down during the preparation of porous titanium with thick cell walls to ensure dimensional accuracy.

Keywords Ti-6Al-4V · Selective laser melting · Residual stress · Mechanical property

Y. Luo · J. Tu · S. Jiao (✉)

State Key Laboratory of Advanced Metallurgy, University of Science and Technology Beijing, Beijing 100083, People's Republic of China
e-mail: sjiao@ustb.edu.cn

Y. Jiang

The Department of Orthopedics, Peking University Third Hospital, Beijing 100191, People's Republic of China
e-mail: medicojoe@126.com

J. Zhu

Ningxia Deyun Titanium Co Ltd., Shizuishan, Ningxia 735000, People's Republic of China

Introduction

Selective laser melting (SLM) technique integrates advanced laser technology, CAD design, and powder metallurgy technology, which has great advantages in the preparation of porous materials with precise size and complex structure. Comparing with traditional methods, SLM technique can provide micro-porous structures with global morphological properties that are highly controlled through computer. However, metals processed by laser as heat source generally have great residual stress due to rapid heating and cooling [1]. Residual stress will lead to deformation and distortions, and in some extreme cases, can cause cracking [2]. The conventional stress relief annealing method can eliminate the residual stress of the implants, but if the material has been deformed or cracked, it can not be recovered by subsequent heat treatment. This problem can be solved by remelting treatment which reduce the residual stress of the material in situ SLM. Remelting could reduce the temperature gradient and avoid rapid melting/cooling of the alloy. Most of the related research focus on solid alloys; the research on porous parts was rare [3, 4].

The aim of the current study is to reduce the residual stress and improve the mechanical strength of alloys with porous structures during SLM, reducing production procedures, and ameliorate the rapid prototyping products. In this work, one of popular porous material, namely Ti-6Al-4V alloy, was chosen as the experimental material for SLM. The effect of remelting treatments is studied by characterizing on the samples' microstructure, mechanical properties, and residual stress.

Experimental

Materials

Table 1 shows the composition of Ti-6Al-4V-ELI powder with a particle size of 10–53 μm , used within this investigation. The oxygen content was 0.15 wt%, which is below the minimum requirement of the biomedical materials (0.20 wt%) [5].

Table 1 Chemical composition of Ti-6Al-4V powders wt%

Element	Ti	Al	V	Fe	O	N	C	H
Content	Bal	5.5–6.5	3.5–4.5	0.1	<0.15	<0.01	<0.03	<0.01

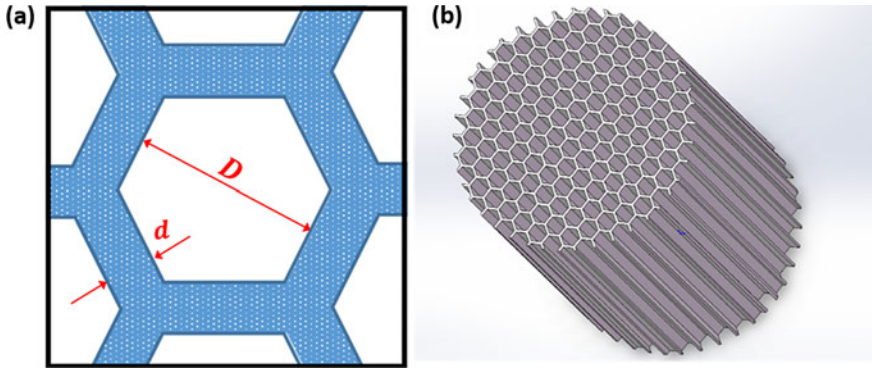


Fig. 1 Porous Ti-6Al-4V structure. **a** a unit cell, **b** the CAD model of the test sample. (Color figure online)

Fabrication of Porous Ti-6Al-4V by SLM 3D Printing

The unit cell used as the microarchitecture of the porous Ti alloy was honeycomb structure, which the porosity and pore size could be controlled by adjusting the CAD model parameter D and d (Fig. 1a). Porous structures with the same pore size ($D = 600 \mu\text{m}$) and different thickness ($d = 100, 200, 300, 400,$ and $500 \mu\text{m}$) were designed and manufactured through SLM (EOS, M300, German). Cylindrical specimens with dimensions of $\varphi 10 \times 15 \text{ mm}^3$ and cubic specimens with the dimensions of $10 \times 10 \times 10 \text{ mm}^3$ were produced with their longitudinal axis perpendicular to the build plate (Fig. 1b).

The processing parameters used in this experiment were as follows: Power 240 W, scanning speed 0.8 m s^{-1} , layer thickness $30 \mu\text{m}$, and scanning interval $50 \mu\text{m}$. The specimens prepared via the above-mentioned process parameters were referred to *C-AM*. The other series of specimens were scanned again by double laser system immediately after each layer had experienced laser melting. The laser power and the scanning speed of the second scan in this experiment were set as 180 W and 0.5 m s^{-1} , respectively, which provided 75% of the energy density of the first scan.

Material Characterization

The cell wall and fracture morphology of the porous Ti-6Al-4V alloy were characterized employing a metalloscopy (Leica, Leica-DM4M, German) and field emission SEM (Carl Zeiss, Zeiss-EVO18, German). The metallographic photos of the specimens were analyzed via Image-Pro Plus software to measure the pore size.

Static uniaxial compression was carried out using a universal testing machine (XinSanSi, CMT4305, China) at room temperature following the standard of ASTM

E9-09. Average values are derived from the mean of five specimens for each Ti-6Al-4V alloy with a particular sheet thickness. Cylindrical specimens with a diameter of 10 mm and height of 15 mm were used for axial compression test, which the load was applied to the top of the cylinder. The cubic specimens with the dimensions of $10 \times 10 \times 10 \text{ mm}^3$ were used for radial compression test, which the load was applied to the cell walls.

A nano-indenter (MNT, N2100, America) was employed to measure the residual stress of titanium alloy with different sheet thickness. The specimens were polished and measured with a fixed load (1 mN). The measurement range of each sample was 3×3 lattice with the spacing of $10 \mu\text{m}$ between each indentation. Then calculated the residual stress of each sample by Suresh model [6].

Results and Discussion

Physical Structures of the Porous Ti-6Al-4V Alloys

Figure 2 show the porosities of the porous Ti-6Al-4V structures produced by SLM the actual pore sizes of SLM-manufactural specimens are generally smaller than that of CAD models (Fig. 2a). Moreover, the inconsistency increases with the increasing cell thickness. The deviation is $32 \mu\text{m}$ when the cell thickness is $100 \mu\text{m}$ and $102 \mu\text{m}$ when the cell thickness is $500 \mu\text{m}$. The porosity of the specimens is in the range of 40.4–78.6% (Fig. 2b). As discussed above, the actual porosities of specimens C-AM and D-AM are smaller than that of CAD models, and the error of specimens D-AM is 2–4% larger.

Microstructures of cell walls from C-AM and D-AM is investigated and shown in Fig. 3. The microstructure of Ti-6Al-4V alloy is mainly α acicular martensite because of the rapid cooling. The grain boundaries are clearly visible in the case of no double

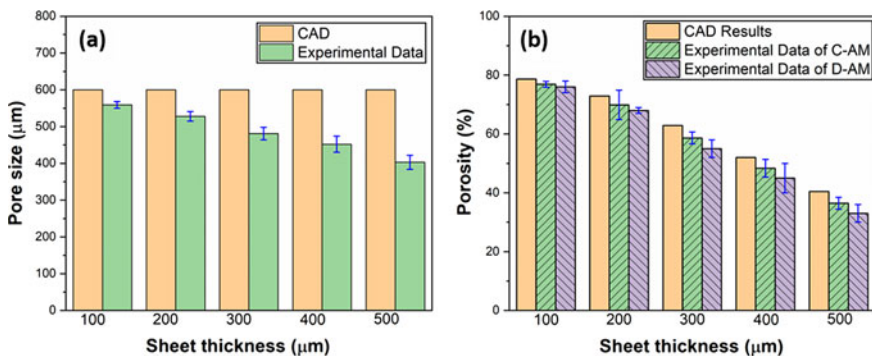


Fig. 2 a Comparison of the pore size of the SLM specimens and CAD models. b Porosities of the CAD models, C-AM and D-AM. (Color figure online)

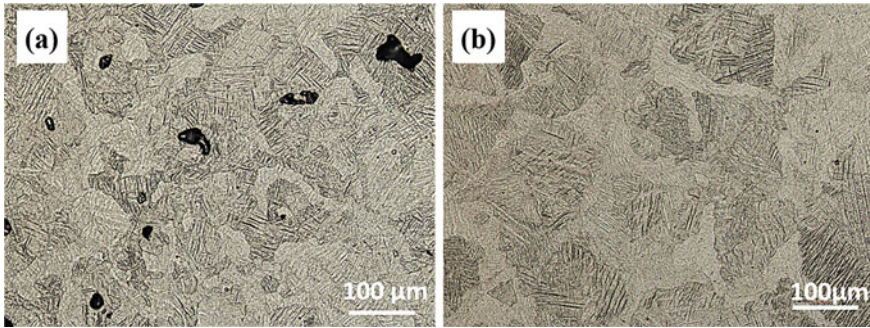


Fig. 3 SEM microtopography of the specimens fabricated by different processes. **a** C-AM200, **b** D-AM200. (Color figure online)

scanning. In contrast, the grain boundaries are unobvious due to the redistribution of chemical substances at high temperature after rescanning. The grains melt again when the laser rescans the powder layer, which leads to the epitaxial growth of the strengthened grains and martensite. The growth of martensite helps to improve the strength of Ti-6Al-4V alloy. However, martensite reduces the toughness of the alloy. Hence, the laser power of the second scan should be turned down suitably in order to avoid the brittleness of Ti-6Al-4V. The main defect of Ti-6Al-4V alloy melted by conventional technology is the irregular pores caused by unfused powder, and the defects are obviously reduced after rescanning.

Mechanical Properties and Deformation Mechanisms

The porosity of porous Ti-6Al-4V has a significant influence on its mechanical and biological properties. With the increase of the porosity, the strength decreases correspondingly. Uniaxial compression tests based on radial direction (RD) and axial direction (AD) have been conducted on the porous Ti-6Al-4V structures. Table 2

Table 2 Comparison of mechanical properties of the different types of porous Ti-6Al-4V

Sheet thickness	Yield strength (MPa)		Elastic modulus (GPa)		RD compressive strength (MPa)		AD compressive strength (MPa)	
	C-AM	D-AM	C-AM	D-AM	C-AM	D-AM	C-AM	D-AM
100	33.58	43.19	2.05	4.59	24.85	51.73	171.81	259.69
200	40.06	60.65	3.54	6.05	85.36	143.47	193.29	289.61
300	97.03	111.49	6.22	10.34	169.48	316.43	202.31	350.28
400	147.84	184.57	9.14	16.68	211.54	384.26	263.16	405.65
500	206.41	275.38	11.33	23.96	304.39	447.58	335.97	490.12

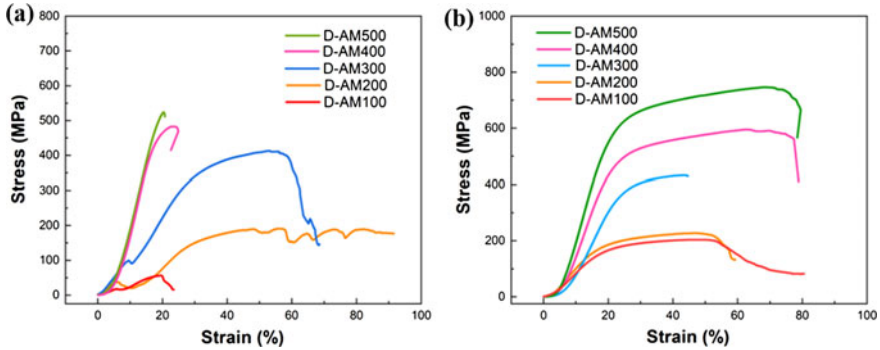


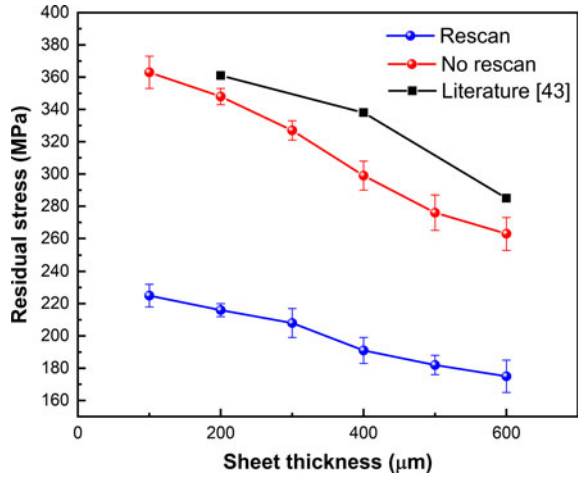
Fig. 4 Compressive stress/strain curves for the porous Ti-6Al-4V specimens. **a** radial direction, **b** axial direction. (Color figure online)

illustrates the details of the mechanical performance values of the single- and double-scanned samples. On account of the existence of pores, the yield strength and elastic modulus of porous Ti-6Al-4V are not as good as those of bulk alloy and decrease with the increase of porosity. The double-scanned structures reveal higher elastic modulus and better mechanical strength than the conventional porous structure. This is mainly attributed to the fact that remelting treatment could achieve a more uniform temperature and retain more solute segregation in the cell walls. The elastic modulus of porous Ti-6Al-4V prepared by new process in this work is in the range of 4.59 GPa–23.96 GPa.

Figure 4 depicted the RD and AD quasi-static stress/strain relationships of specimens D-AM during compression. The compressive stress/strain curve of porous titanium is usually consisted of three stages: linear elastic stage, platform stage, and densification stage [7]. From Fig. 4, the following characteristics can be concluded:

- In the first stage of the stress/strain curve, the deformation of porous Ti-6Al-4V with different porosity presents linear elastic behavior in both radial and axial directions. The elastic modulus decreases with the decrease of sheet thickness.
- The transition from the first stage to the second stage is smooth, and no obvious yield point can be observed on the stress/strain curve. It is suggested that the stress increases in a nonlinear way with the increase of compression stress.
- In the second stage, the porous Ti-6Al-4V shows an obvious unsteady plateau stress in the radial direction, while in the axial direction, the plateau stress is more stationary. Moreover, specimens D-AM400 and D-AM500 are fractured directly under radial stress after yielding without plastic deformation, which is attributed to the reduction in plasticity based on the thickening of the cell walls.
- In the third stage, the specimens with low porosities (D-AM300/D-AM400/D-AM500) are fractured when the compressive stress reaches the peak value. On contrast, porous Ti-6Al-4V with high porosities (D-AM100/D-AM200) enter the densification stage without obvious fracture.

Fig. 5 Effect of rescanning on the residual stress of porous Ti-6Al-4V. (Color figure online)



In consequence, porous titanium with different sheet thickness has the same elastic deformation stage, but different plastic deformation stage.

Residual Stress

Figure 5 shows a relation between residual stress and sheet thickness. The residual stresses of the double-scanned specimens are 33.5–38.0% lower than that of the single-scanned specimens. A decrease in residual stress with increasing sheet thickness is consistent with the findings of Wang et al. [8] Ali et al. [9] reported that rescanning with 150% energy density resulted in 33.6% reduction in residual stress. However, the mechanical properties of the samples were reduced and failed prematurely. In the present study, the yield strength and elastic modulus of porous Ti-6Al-4V were improved through double scanning process with low power and slow speed.

Conclusions

In this work, 3D-printed porous Ti-6Al-4V with different cell wall thickness were produced through remelting treatment with 75% energy density. The porosities of remelted specimens are 2–4% lower than that of single-scanned specimens. The remelted structures reveal higher elastic modulus and better mechanical strength than the conventional porous structure. It is suggested that remelting treatment achieves a more uniform temperature and retains more solute segregation in the cell walls. The elastic modulus of porous Ti-6Al-4V prepared by remelting process in this

work is in the range of 4.59–23.96 GPa, and the density indexes are larger, which means the bonding conditions are stronger than those of single-scanned specimens. Rescanning with 75% energy density resulted in 33.5–38.0% reduction of residual stress. Moreover, the residual stress of porous Ti-6Al-4V decreases with increasing sheet thickness. This method could prove useful for decreasing residual stress in situ laser additive manufacturing while ensuring the dimensional accuracy of the thin-walled structure.

Acknowledgements This work was financially supported by the National Natural Science Foundation of China (Grant No. 51804012 and No. 51725401). The helpful comments, suggestions, and encouragement from editors and anonymous reviewers are gratefully acknowledged.

References

1. Strantz M, Ganeriwala RK, Clausen B, Phan TQ, Levine LE, Pagan D, King WE, Hodge NE, Brown DW (2018) *Mater Lett* 231:221
2. Roehling JD, Smith WL, Roehling TT, Vrancken B, Guss GM, McKeown JT, Hill MR, Matthews MJ (2019) *Addit Manuf* 28:228
3. Yu W, Sing SL, Chua CK, Tian X (2019) *J Alloys Compd* 792:574
4. Wei K, Lv M, Zeng X, Xiao Z, Huang G, Liu M, Deng J (2019) *Mater Charact* 150:67
5. Yan XC, Li Q, Yin S, Chen ZY, Jenkins R, Chen CY, Wang J, Ma WY, Bolot R, Lupoi R, Ren ZM, Liao HL, Liu M (2019) *J Alloys Compd* 782:209
6. Suresh S, Giannakopoulos AE (1998) *Acta Mater* 46:5755
7. Bobbert FSL, Lietaert K, Eftekhari AA, Pouran B, Ahmadi SM, Weinans H, Zadpoor AA (2017) *Acta Biomater* 53:572
8. Wang JF, Yuan JT, Wang ZH, Zhang B, Liu JX (2019) *Laser Tech* 43:411
9. Ali H, Ghadbeigi H, Mumtaz K (2018) *Mater Sci Eng, A* 712:175

Notch Sensitivity of AlSi10Mg Aluminum Alloy Produced by Laser Powder Bed Fusion Process



Avinesh Ojha, Wei-Jen Lai, Carlos Engler-Pinto Jr., and Xuming Su

Abstract Stress gradient influence factors and fatigue notch factors were measured for the AlSi10Mg aluminum alloy produced by laser powder bed fusion (L-PBF) processing with respect to different stress gradients (notch geometries). Modeling the stress gradient is critical for accurate fatigue life estimations for parts containing notches or fillets. Uniaxial fatigue tests were performed to obtain the fatigue strengths at $R = -1$ for notched and unnotched specimens. The fatigue results were then used to calibrate the stress gradient influence factor model for fatigue life estimation. Due to the small grain size produced by the L-PBF process, the stress gradient influence factor is much lower compared to the cast A319-T7 alloy (at 120 °C) at the same stress gradient.

Keywords Notch effect · Fatigue · AlSi10Mg · Laser powder bed fusion

Introduction

Materials produced by the laser powder bed fusion (L-PBF) process are known for its distinct microstructure. The small grain size produced by this process gives rise to superior mechanical properties but can also change the notch sensitivity [1–3]. Potential high notch sensitivity was observed in fatigue test samples where failures tend to occur at the end of the straight gauge section. Slight stress concentration (approximately 3%) is commonly seen at the end of the straight gauge section, where the cross-sectional area starts to increase. However, it is usually not an issue when conventionally manufactured materials are tested, i.e. failure usually occurs within the gauge. A higher number of fatigue failure observed at the stress concentration location for the alloys produced by L-PBF suggests potential high notch sensitivity induced by this process. The study is to confirm this hypothesis and obtain notch sensitivity data for fatigue strength estimation of L-PBF AlSi10Mg parts.

A. Ojha · W.-J. Lai (✉) · C. Engler-Pinto Jr. · X. Su
Ford Motor Company, Detroit, MI, USA
e-mail: william721225@hotmail.com

Experimental Procedure

Sample Preparation

The AlSi10Mg aluminum alloy is selected for this study. The composition of the alloy is shown in Table 1. The fatigue samples were manufactured using the SLM-125 machine, by SLM Solutions Group AG. All the samples were built in the form of cylindrical rods with the tensile axis in the vertical direction. The dimension of the rod stock is 12.7 mm in diameter and 100 mm in length. The laser process parameters are summarized in Table 2. A three-step inside-out scan strategy was adopted: The laser hatches the center portion first, followed by a contour scan and lastly a border scan on the outer diameter.

The rod stock was stress relieved at 300 °C for two hours to remove residual stresses. Four types of samples were machined from the rod stock, as shown in Fig. 1.

The hourglass sample, shown in Fig. 1a, was used to obtain the fatigue strength without stress gradient. Figures 1b–d shows the notched fatigue samples with different notch geometries: 1.5-mm U-notched, 0.47-mm U-notched, and 0.25-mm V-notched samples, respectively. The notch geometries were designed to provide different stress gradients at the notch roots. The hourglass samples were mechanically polished in the longitudinal direction to remove the surface roughness due to machining. The notched fatigue samples were not polished. The reason for using an hourglass sample (instead of a straight gauge sample) is to maintain a similar volume of material under loading.

Fatigue Test

Uniaxial fatigue tests were performed at stress ratio $R = -1$ according to the ASTM E466 standard [4]. Tests were conducted at room temperature at frequencies ranging from 60 to 70 Hz. Samples were tested until full separation or until 10^7 cycles (runouts).

The fatigue strength was calculated using the random fatigue limit (RFL) model [5], which fits the S-N curve using the equation below.

$$S_a - S_L = C(2N_f)^b \quad (1)$$

where S_a is the stress amplitude, S_L is the infinite-life fatigue limit of the material (a random variable), N_f is the number of cycles to failure, and C and b are empirical constants. In this study, the fatigue S-N curves were fitted using an RFL model with the aid of the maximum likelihood method, as described by Engler-Pinto [6], to

Table 1 Chemical composition of AISi10Mg aluminum alloy

	Si (%)	Fe (%)	Cu (%)	Mg (%)	Cr (%)	Ni (%)	Ti (%)	Ca (%)	Ga (%)	Sr (ppm)	V (%)	Al (%)
AISI10Mg	10.48	0.125	0.0057	0.291	0.012	0.0108	0.129	0.0059	0.0123	142	0.0146	88.8

Table 2 Summary of laser parameters of AlSi10Mg samples

Region	Power (W)	Speed (mm/s)	Hatch Spacing (mm)	Layer Thickness (mm)
Border & Contour	200	730	0.2	0.03
Hatch	350	1,650	0.13	

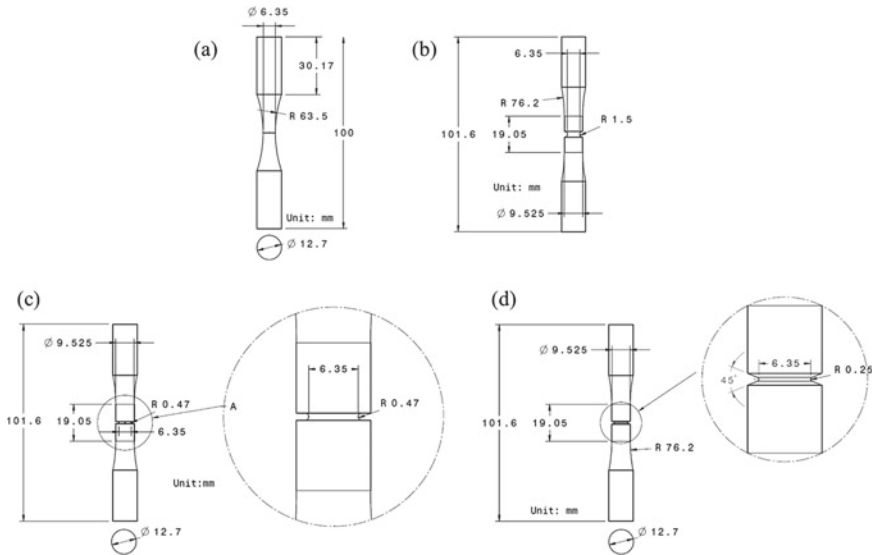


Fig. 1 Dimensions of **a** hourglass, **b** 1.5-mm U-notched, **c** 0.47-mm U-notched, and **d** 0.25-mm V-notched samples

account for the runout data points. The fatigue strength distribution is then estimated at 10^7 cycles.

Finite Element Stress Analysis

The finite element methodology (FEM) was used to obtain the maximum stress and the relative stress gradient at the notch. Quadratic axial symmetrical elements CAX8R were used in ABAQUS [7]. Elastic and elastoplastic analyses were performed. The elastoplastic analysis uses the experimental tensile stress–strain curve as input, as shown in Fig. 2. Note that, for this exercise, the nominal stress applied at the smallest cross section in the elastoplastic model is the fatigue strength of each specimen geometry ($\sigma_{f,-1}$), as listed in Table 3. Relative stress gradients were calculated based on the stresses at the notch root node and the node next to it,

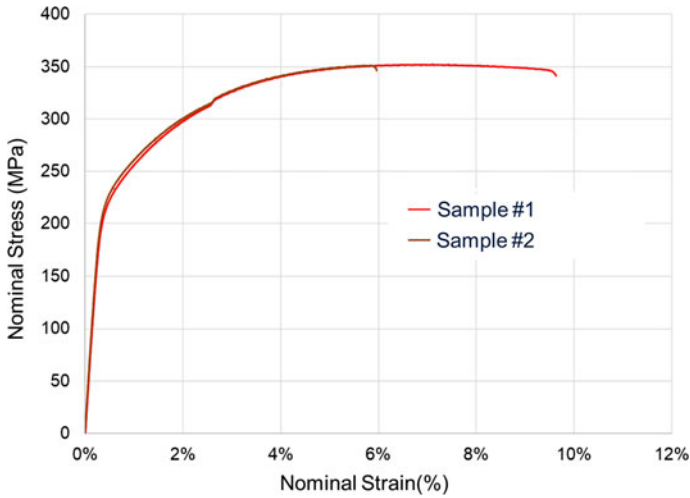


Fig. 2 Nominal tensile stress–strain curve of L-PBF AlSi10Mg stress relieved at 300 °C for 2 h. (Color figure online)

Table 3 Summary of key values used for fatigue influence factor calculation

	1.5-mm U-notch	0.47-mm U-notch	0.25-mm V-notch
$(\sigma_{e,i}$ (MPa), d_i (mm))	(36.94, 3.175)	(57.35, 3.175)	(74.66, 3.175)
$(\sigma_{e,i-1}$ (MPa), d_{i-1} (mm))	(35.95, 3.160)	(49.54, 3.147)	(63.71, 3.159)
χ'	1.748	4.819	8.895
$\sigma_{f,-1}$ (MPa)	63.0	41.8	33.5
K_t (FEM)	1.811	2.859	3.746
K_t (Formula) [5]	1.83	2.81	3.49
$\sigma_{A,tsc}$ ($= \sigma_{f,-1} \cdot K_t$) (MPa)	114.1	119.5	125.5
$f_{GR,af}$ (test)	1.329	1.391	1.462
K_f	1.36	2.05	2.56
q	0.433	0.580	0.626

The values are calculated based on the nominal stress of 22.5 MPa at the smallest cross section for specimens shown in Fig. 1

along the direction where the stress gradient is to be evaluated. The relative stress gradient (χ') is defined as

$$\chi' = \frac{\chi}{\sigma_e} \quad (2)$$

where σ_e is the Mises stress and χ is the stress gradient. The stress gradient (χ) is defined as

$$\chi = \frac{d\sigma_e}{dx} \tag{3}$$

In this study, the relative stress gradient is calculated at the surface node, as illustrated in Fig. 3.

The maximum stress from FEM was used to calculate the stress concentration factor (K_t) which is defined as

$$K_t = \frac{\sigma_{\max}}{\sigma_{\text{nominal}}} \tag{4}$$

where σ_{\max} and σ_{nominal} are the maximum stress and the nominal stress at the notch root from the FEM analysis in the loading direction, respectively. The nominal stress (σ_{nominal}) is defined as the applied load (P) divided by the cross-sectional area at the notch root (A) (the smallest cross section).

Similarly, the fatigue notch factor K_f is defined as:

$$K_f = \frac{\sigma_{f,\text{smooth}}}{\sigma_{f,\text{notched}}} \tag{5}$$

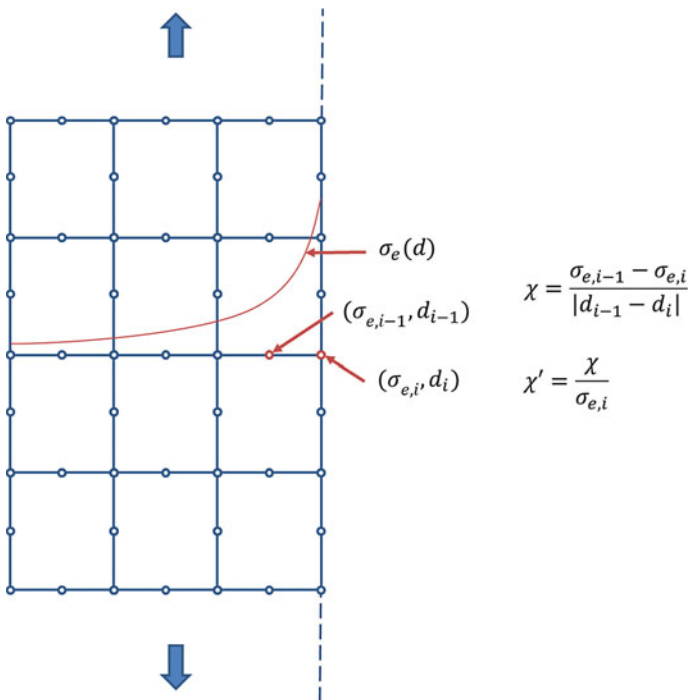


Fig. 3 A schematic showing how the relative stress gradient is calculated at the node in this study. (Color figure online)

where $\sigma_{f,\text{smooth}}$ and $\sigma_{f,\text{notched}}$ are the fatigue strengths at $R = -1$ of smooth and notched specimens, respectively. K_f is equal or larger than 1 and always less than or equal to K_t . Note that the fatigue strengths here are the nominal stress without considering stress concentration. The notch sensitivity parameter (q) can then be defined as:

$$q = \frac{K_f - 1}{K_t - 1} \quad (6)$$

The value of q typically ranges from 0 to 1. A value of 0 indicates that the material has no notch effect and a value of 1 indicates that the material has full theoretical notch effect.

Results and Discussion

The FEM models are shown in Fig. 4. The stress concentration factors and stress gradients are summarized in Table 3, together with the stresses at the surface nodes used for the calculation. The analytical solutions of stress concentration factors from Pilkey [8] are also listed for reference. One thing worth noting is that the elasto-plastic analysis results in all three models with notches show no plastic deformation anywhere in the models when the nominal stress at the smallest cross section equals the fatigue strength of each notched specimen. This means no plastic deformation occurs at the notch root when the specimen is tested at the stress level equal to the fatigue strength. Hence, the stresses are the same as the ones obtained from the elastic analyses. It is noted that the stress concentration factors for the 1.5-mm U-notch and 0.47-mm U-notch obtained from the FEM analyses are close to the analytical solutions, while the stress concentration factor for the 0.25-mm V-notch from the FEM analysis is higher than the analytical solution.

The fatigue S-N curves are shown in Fig. 5. The S-N curves were fitted using the RFL method described earlier. The fatigue strengths ($\sigma_{f,-1}$) were estimated at 10^7 cycles and summarized in Table 3. Note that the fatigue strength in Table 3 is the nominal fatigue strength. The true fatigue strength ($\sigma_{A,tsc}$) is the nominal fatigue strength multiplied by the stress concentration factor.

The stress gradient influence factor ($f_{GR,af}$) [9] used to characterize the effect of the stress gradient on the fatigue strength when the stress gradient is present is expressed as

$$f_{GR,af} = 1 + \frac{\frac{\sigma_{A,b}}{\sigma_{A,tsc}} - 1}{\left(\frac{z}{t}\right)^v} \cdot \chi^{\nu} \quad (7)$$

where $\sigma_{A,b}$ is the fatigue strength for bending, $\sigma_{A,tsc}$ is the fatigue strength for tension–compression, t is the thickness or diameter of the bending fatigue sample,

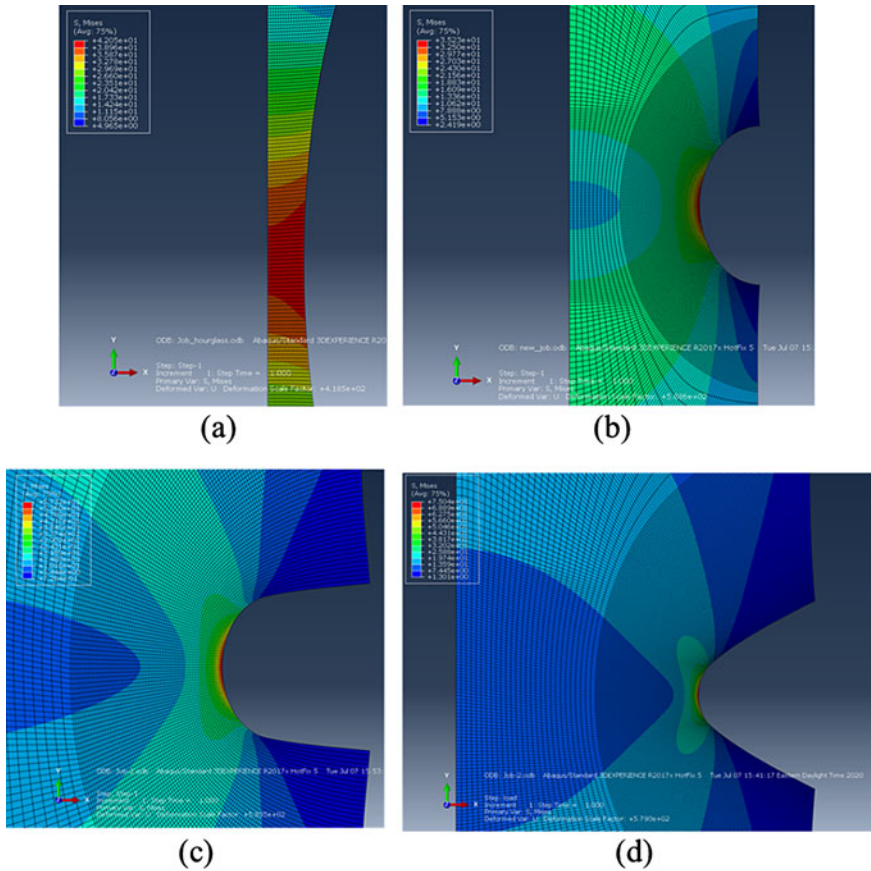


Fig. 4 FEM models of **a** hourglass, **b** 1.5-mm U-notched, **c** 0.47-mm U-notched, and **d** 0.25-mm V-notched samples. (Color figure online)

and ν is the material parameter. Thus, the fatigue strength with the stress gradient is expressed as

$$\sigma_{af,C} = \sigma_{A,tsc} \cdot f_{GR,af} \tag{8}$$

where $\sigma_{af,C}$ and $\sigma_{A,tsc}$ are the fatigue strengths with and without stress gradient at $R = -1$, respectively. Note that $\sigma_{af,C}$ is the true stress at the notch instead of the nominal stress used for $\sigma_{f,notched}$ in Eq. 5. In this study, the fatigue strength of the hourglass sample is used for $\sigma_{A,tsc}$. Thus, the parameters needed to be fitted are $\sigma_{A,b}$, t , and ν in Eq. 7. The stress gradient influence factors of different samples are shown in Fig. 6. The values are also listed in Table 3. The parameters ($\sigma_{A,b}$, t , and ν) were fitted using Excel solver. The fitted parameters are listed in Table 4.

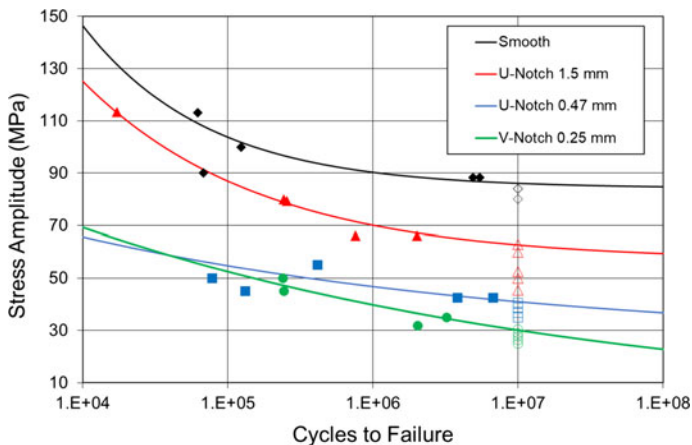


Fig. 5 S-N curves of hourglass, 1.5-mm U-notched, 0.47-mm U-notched, and 0.25-mm V-notched samples at $R = -1$. (Color figure online)

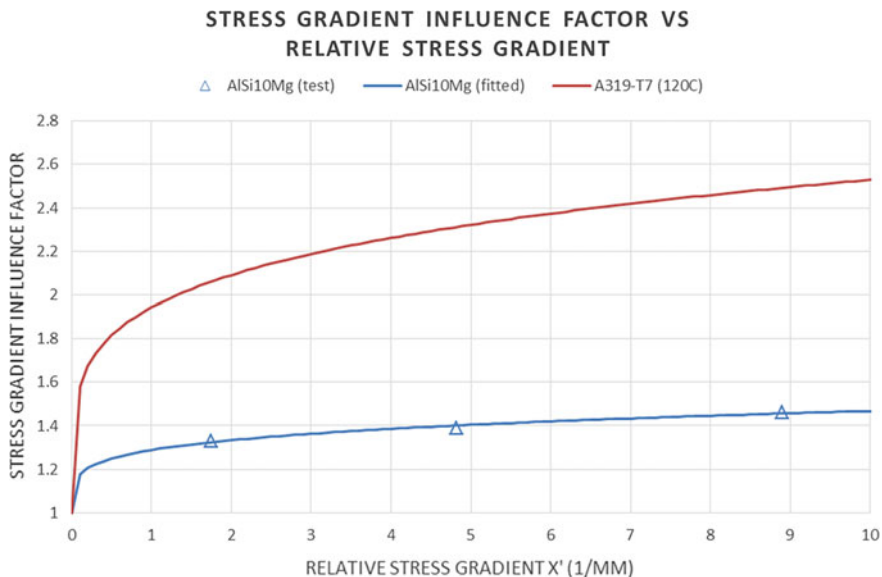


Fig. 6 Stress gradient influence factor versus relative stress gradient for L-PBF AlSi10Mg and A319-T7 (120°C). (Color figure online)

Table 4 Summary of parameters in Eq. 5 for L-PBF AlSi10Mg and A319-T7 (120 °C)

	$\sigma_{A,tsc}$ (MPa)	$\sigma_{A,b}$ (MPa)	t (mm)	ν
L-PBF AlSi10Mg (stress relieved)	85.88	108.3	3.20	0.209
Cast A319-T7 (120°C) [10]	45.5	72.2	5.56	0.464

Bold values are fitted parameters

The fitted curve is compared with the cast A319-T7 tested at 120 °C [10]. As seen in the figure, L-PBF AlSi10Mg shows much lower values than A319-T7. This is consistent with the experimental observation that the notch sensitivity increases with the decreasing grain size [1]. The high notch sensitivity of L-PBF AlSi10Mg is possibly the main reason which causes failures at the end of the straight gauge section of samples during fatigue testing.

Conclusion

Stress gradient influence factors were measured for L-PBF AlSi10Mg aluminum alloy with respect to different stress gradients using notched fatigue samples. L-PBF AlSi10Mg shows much lower stress gradient influence factors at the same relative stress gradients compared to cast aluminum A319-T7 (at 120 °C). Also, the high notch sensitivity factors (q) for L-PBF AlSi10Mg (shown in Table 3) suggest that the material is very notch sensitive, which could be resulted from the small grain size. The fitted stress influence factor curve should be used for fatigue strength estimation to obtain the most accurate prediction.

References

1. Karry RW, Dolan TJ (1953) Influence of grain size on fatigue notch-sensitivity. *Am Soc Test Mater Proc* 53:789–804
2. Kanemaru T, Kawagoishi N, Kondo E, Wang QY, Ohzono Y (2008) Influence of grain size on notch sensitivities in fatigue of carbon steel. *Key Eng Mater* 385–387:197–200. <https://doi.org/10.4028/www.scientific.net/kem.385-387.197>
3. Lorenzino P, Navarro A (2015) Grain size effects on notch sensitivity. *Int J Fatigue* 70:205–215. <https://doi.org/10.1016/j.ijfatigue.2014.09.012>
4. ASTM E466-07 Standard practice for conducting force controlled constant amplitude axial fatigue tests for metallic materials (ASTM International, West Conshohocken, 2007). <https://doi.org/10.1520/e0466-07>
5. Pascual FG, Meeker WQ (1999) Estimating fatigue curves with the random fatigue-limit model. *Technometrics* 41:277–290
6. Engler-Pinto C, Lasecki J, Frisch R, DeJack M, Allison J (2005) Statistical approaches applied to fatigue test data analysis. SAE Technical Paper 2005-01-0802. <https://doi.org/10.4271/2005-01-0802>
7. Abaqus Analysis User's Guide (2018)
8. Pilkey WD (1997) Peterson's stress concentration factors, 2nd edn. Wiley, New York
9. Eichlseder W (1989) Rechnerische Lebensdaueranalyse von Nutzfahrzeugkomponenten mit der FE-Methode, Dissertation, TU Graz
10. Shea A, DeJack M, Lasecki J, Su X, Allison J (2002) Applying fatigue and stress analysis of a notched W319 cast al alloy to the FEMFAT software program, Research Conference on Statistics in Industry and Technology, May, 20–22, Ann Arbor, MI

Progressive Amplitude Fatigue Performance of Additively Manufactured Stainless Steel Superalloy



Sanna F. Siddiqui, Krystal Rivera, Isha Ruiz-Candelario, and Ali P. Gordon

Abstract Advances in aerospace component manufacturing design are being achieved through the additive manufacturing (AM) technology. Variations in cyclic loads (i.e. variable amplitude fatigue) is a common phenomenon experienced by aerospace components during in-service use, hence the need for AM components to withstand fatigue failure under these conditions. This study has performed progressive strain amplitude fatigue tests at increasing strain ranges with the intent to capture the fatigue failure life, hardening/softening response, and fracture response of as-built direct metal laser sintered (DMLS) Stainless Steel GP1. Preliminary results indicate fatigue failure in specimens prior to reaching strain ranges where plasticity effects become more pronounced. Also, evident is variation in cyclic softening/hardening response to stabilization at elastic versus plastic strain ranges. Scanning electron microscopy was used to identify the precursors for fatigue crack initiation and propagation under progressive amplitude fatigue loading.

Keywords Variable amplitude fatigue · Additive manufacturing · Stainless steel GP1

Introduction

Additive manufacturing (AM) has shown to be advantageous for the aerospace industry because it allows for rapid prototyping and design flexibility, facilitating the manufacturing of complex geometries [1]. To date, studies have primarily investigated the axial, torsional, and rotating bending fatigue performance of AM stainless steel alloys [2–6]. It was determined that one of the major factors affecting fatigue life are defects directly related to the manufacturing process, such as voids and surface

S. F. Siddiqui (✉) · K. Rivera · I. Ruiz-Candelario
Department of Mechanical Engineering, Florida Polytechnic University, Lakeland, FL, USA
e-mail: ssiddiqui@floridapoly.edu

A. P. Gordon
Department of Mechanical and Aerospace Engineering, University of Central Florida, Orlando, FL, USA

roughness [1–3, 7–12], resulting in fatigue life for AM specimens to be significantly less than for their wrought counterparts [2, 9–13]. These defects have been shown to be reduced by post-processing, positively impacting fatigue life [1, 2, 10–12].

During in-service operation, aerospace components are also subjected to variable amplitude (VA) fatigue loading conditions, necessitating the design of AM components to withstand these loading conditions [7, 14–16]. Unlike constant amplitude fatigue, where all load cycles are identical, in VA fatigue, load amplitudes and/or mean stresses may change at regular intervals, impacting both fatigue crack growth and cyclic plasticity [17, 18]. Tensile mean stress overloads in VA have been shown to contribute to fracture [17]. Variable amplitude fatigue performance has been reported for additively manufactured Ti-6Al-4V and stainless steel 15-5PH [7, 14]. An investigation into the variable amplitude fatigue performance of laser sintered versus electron beam melted (EBM) as-built Ti-6Al-4V has revealed that the rough surface contributed to a lower fatigue strength for this material [7]. It was further shown that the cumulative damage approach produced similar findings between the predicted and experimental VA life of this alloy [7]. A comparison between the predicted fatigue cycles under the cumulative damage approach versus experimental testing has been reported for laser-based powder bed fusion produced 15-5 PH stainless steel parts, under both zero and tensile mean stresses [14]. Multiple crack initiation sites were reported for VA under tensile mean stress as opposed to zero mean stress, for which a distinct crack initiation site was observed [14].

The proposed study is unique in that it provides preliminary findings into the progressive amplitude fatigue performance of additively manufactured stainless steel (SS) GP1, which has a chemical composition similar to stainless steel 17-4PH [19], but varies in mechanical performance as reported in other studies [20–22]. Progressive strain amplitude fatigue tests are performed at increasing strain ranges for as-built direct metal laser sintered (DMLS) SS GP1, in order determine its fatigue failure life, hardening/softening response, and identify the role of AM induced defects on the resulting fatigue fracture response.

Experimental Design

To assess the progressive amplitude fatigue performance of as-built additively manufactured stainless steel (SS) GP1, specimens of horizontal build orientation (X, Y, and XY45) were manufactured using the EOS M280 direct metal laser sintering (DMLS) system in a nitrogen environment with a layer thickness of 20 μm . EOS-optimized processing parameters were used to manufacture the specimen design shown in Fig. 1, which were not subject to heat-treatment. The as-built specimens boxed support structure were removed with conventional hand tools, and the gripping sections of the specimens were machined from the manufactured diameter of 0.625 in to 0.5 in prior to progressive amplitude fatigue testing. Further details regarding specimen preparation prior to fatigue testing can be found in [6].

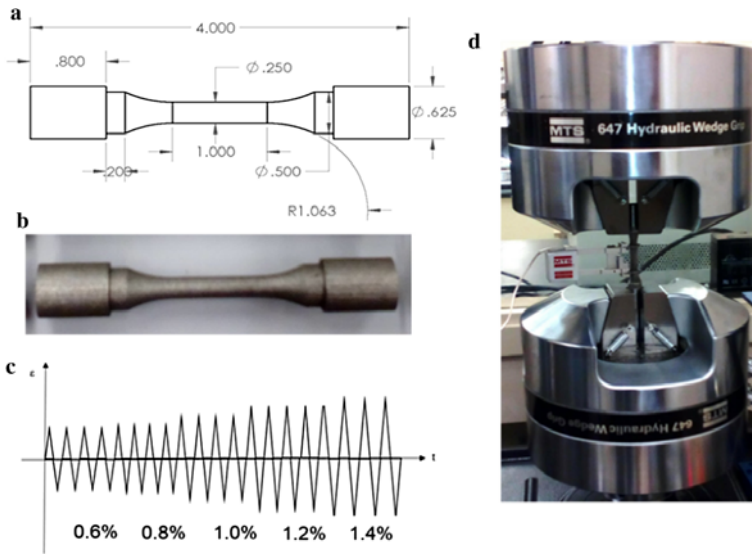


Fig. 1 **a** Sample geometry (dimensions in inches), **b** as-built DMLS Stainless Steel GP1 prior to machining gripping section, **c** proportional amplitude fatigue test sequence, **d** experimental setup [6, 20]. (Color figure online)

Progressive strain amplitude fatigue testing was performed to assess the increase in strain range (elasticity, equivalent amounts of elasticity and plasticity, and plasticity) on crack initiation/propagation in as-built AM test specimens [6]. Strain-control progressive amplitude fatigue tests ($R_\epsilon = -1$) were performed using the MTS LandMark 793 servohydraulic system at room temperature with a strain rate of 10^{-3} (mm/mm/s) and sampling rate of 25 Hz [6]. In an effort to identify the cyclic stress–strain response of DMLS SS GP1, testing was performed at strain ranges of $\Delta\epsilon = 0.6\%$, $\Delta\epsilon = 0.8\%$, $\Delta\epsilon = 1.0\%$, $\Delta\epsilon = 1.2\%$, and $\Delta\epsilon = 1.4\%$, as shown in Fig. 1. Testing was performed for a set number of cycles (~ 100) at each strain range, which was identified from preliminary testing to approximately achieve stabilization of hysteresis loops at each strain range. In addition to determining the total fatigue failure life, hardening/softening response at each strain range, hysteresis deformation response, and fracture mechanics under progressive amplitude fatigue conditions were explored. The Hitachi SU 3500 scanning electron microscope (SEM) was used to characterize the fracture surfaces (i.e. crack initiation and propagation) of DMLS SS GP1 samples due to progressive amplitude fatigue loading conditions, including defects at the microstructural level contributing to observed fracture response. The sample was mounted onto a 51 mm specimen stub, using double-sided conductive adhesive tape [23], and imaged using secondary electron (SE) mode at varying magnifications. The resulting fracture surfaces and associated key features observed are presented and discussed in the results and discussion section.

Results and Discussion

Progressive amplitude fatigue cycling of DMLS stainless steel GP1 specimens resulted in the following stress–life plot shown in Fig. 2. Given that the specimens were manufactured in the horizontal build orientation (X, Y or XY45), the progressive amplitude fatigue response at each strain range is similar. Hence, suggesting that manufacturing at build orientations in the horizontal plane plays a limited role in impacting progressive amplitude fatigue performance. Also, evident from Fig. 2 is the presence of hardening and softening within each strain range. At a highly elastic strain range of $\Delta\varepsilon = 0.6\%$, softening is evident to stabilization. However, at strain ranges where plasticity is more pronounced or equivalent amounts of elasticity and plasticity are present (i.e. $\Delta\varepsilon = 1.0\%$ and $\Delta\varepsilon = 1.2\%$), cyclic hardening is observed to stabilization. The rate of cyclic hardening appears to increase with strain range. This may suggest that at strain ranges where plasticity effects become more pronounced, the hardening behavior may be attributed to a strain-induced austenite to martensite phase transformation, as suggested in other studies on additively manufactured stainless steel 17-4PH [2, 6]. Future work through x-ray diffraction techniques will be used to capture phase transformations to confirm this finding.

An assessment of fatigue life under progressive amplitude fatigue loading is also captured in Fig. 2. Here, it is evident that all specimens regardless of build orientation in the xy plane fractured at a strain range of $\Delta\varepsilon = 1.4\%$. On average, specimens fractured after approximately 416 cycles, after cycling for 100 cycles at strain ranges of $\Delta\varepsilon = 0.6\%$, $\Delta\varepsilon = 0.8\%$, $\Delta\varepsilon = 1.0\%$, and $\Delta\varepsilon = 1.2\%$. The increase in strain range, in which plasticity effects became more pronounced, is suggested to accelerate fatigue crack growth resulting in specimen failure upon reaching a strain range of $\Delta\varepsilon = 1.4\%$. It is suggested that defects at the microstructural level, such as the as-built surface roughness, contributed to fatigue crack initiation and accelerated crack propagation. This is further explored through SEM micrographic imaging.

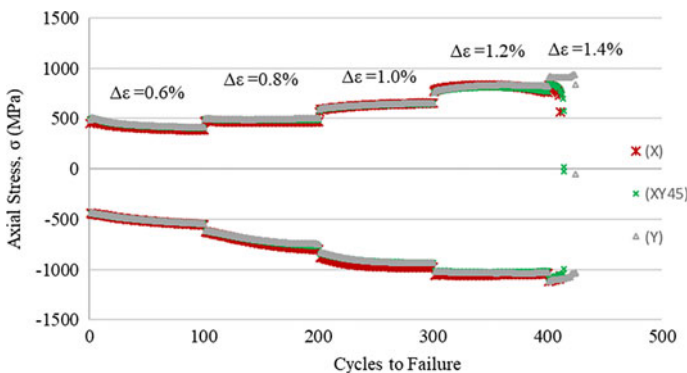


Fig. 2 Stress–life of as-built DMLS SS GP1, of varying build orientation, under progressive amplitude fatigue testing from $\Delta\varepsilon = 0.6\%$ to $\Delta\varepsilon = 1.4\%$. (Color figure online)

Nevertheless, it would appear that progressive amplitude fatigue testing is detrimental to the life of as-built DMLS SS GP1 manufactured in the horizontal build plane [6]; however, as these results are based upon a small sample size, future work will be done to confirm these findings.

An analysis of the fracture surface of DMLS SS GP1 through scanning electron microscopy (SEM) is presented in Fig. 3. The overall fracture surface reveals multiple crack initiation sites near the surface and evidence of striation patterns indicating fatigue crack propagation. Internal defects, such as regions of powder particles and lack of fusion, can also be observed from the SEM micrograph images. This has been shown in recent studies on additively manufactured Ti-6Al-4V and SS 15-5PH subject to variable amplitude fatigue loading as well [7, 14]. Overall, fatigue cracks under progressive amplitude fatigue loading have been found to initiate at un-melted powder particles near the as-built rough surface.

To further evaluate the cyclic deformation response of DMLS SS GP1 under progressive amplitude fatigue loading, the first and stabilized cycles at each strain range are presented in Fig. 4. Since findings across build orientation in the xy plane were similar, as discussed earlier, the hysteresis curves presented are only for the (Y) build orientation. As stabilization occurred after cycling at ~ 100 cycles for each strain range, the last cycle prior to increase in strain range has been considered as the stabilized cycle within these plots. Given that all specimens failed under cycling at a

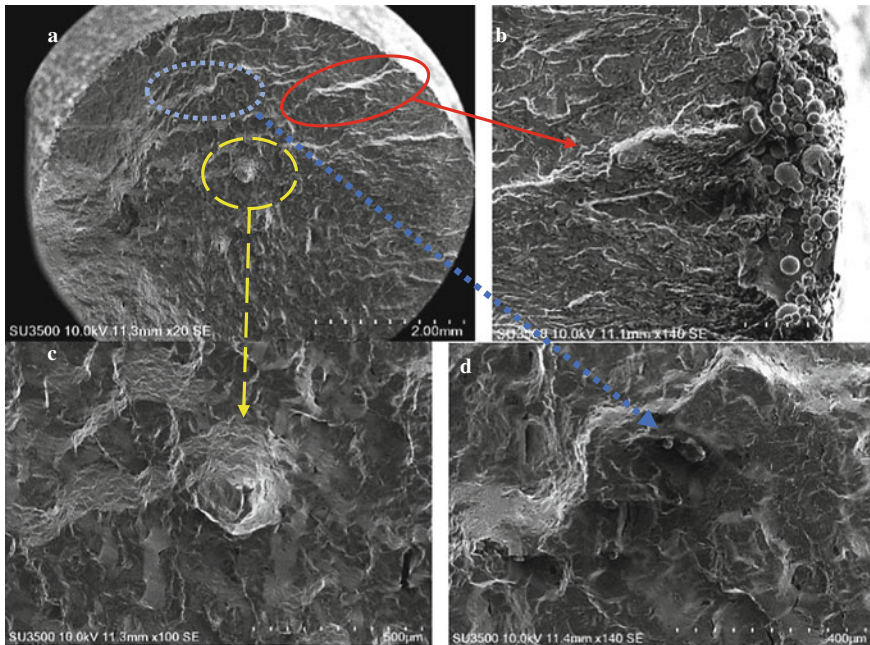


Fig. 3 a Complete fracture surface, b crack initiation site at un-melted powder particles near surface, c and d presence of un-melted powder particles and regions of lack of fusion. (Color figure online)

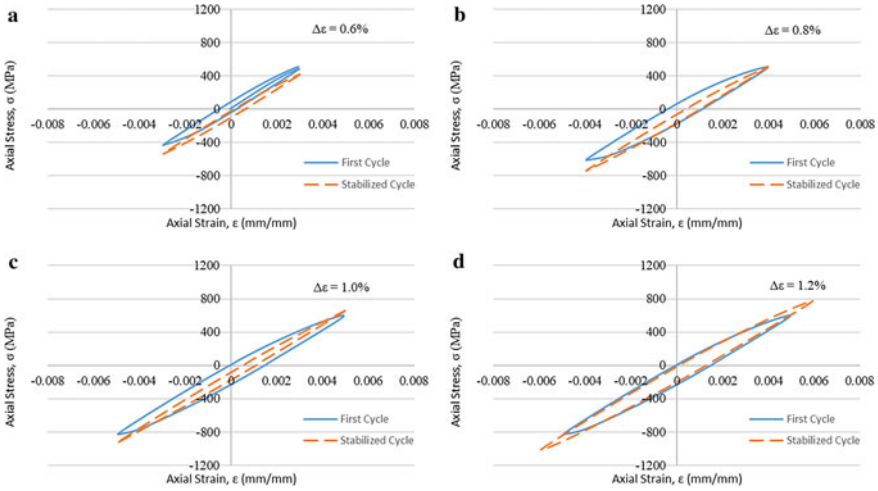


Fig. 4 Hysteresis deformation response (first cycle and stabilized cycle) at each strain range, **a** $\Delta\varepsilon = 0.6\%$, **b** $\Delta\varepsilon = 0.8\%$, **c** $\Delta\varepsilon = 1.0\%$, and **d** $\Delta\varepsilon = 1.2\%$. (Color figure online)

strain range of $\Delta\varepsilon = 1.4\%$, the hysteresis curves for the first and stabilized cycles are plotted up to a strain range of $\Delta\varepsilon = 1.2\%$. An analysis of the hysteresis curves reveals minimum plastic strain range as compared with elastic strain range. A compressive mean stress is also evident from the plots. Evident from both the stress–life plots and analysis of hysteresis curves is cyclic softening at $\Delta\varepsilon = 0.6\%$ and slight cyclic hardening at $\Delta\varepsilon = 0.8\%$, following by considerable cyclic hardening at $\Delta\varepsilon = 1.0$ and 1.2% .

Conclusions and Future Work

This study has investigated the role of progressive strain amplitude fatigue on the life, softening/hardening response, and fracture response of DMLS SS GP1. Specimens were subject to cycling at strain ranges of $\Delta\varepsilon = 0.6\%$ to $\Delta\varepsilon = 1.4\%$, under completed reversed ($R_\varepsilon = -1$) conditions, from which the following conclusions were drawn:

- At strain ranges where plasticity is more pronounced or equivalent amounts of elasticity and plasticity are present (i.e. $\Delta\varepsilon = 1.0\%$ and $\Delta\varepsilon = 1.2\%$), cyclic hardening is observed to stabilization. The rate of cyclic hardening appears to increase with strain range. Cyclic softening is observed at a strain range of $\Delta\varepsilon = 0.6\%$.
- When subject to progressive strain amplitude fatigue loading, from $\Delta\varepsilon = 0.6\%$ to $\Delta\varepsilon = 1.4\%$, for 100 cycles at each strain range, DMLS SS GP1 manufactured in the horizontal build plane is found to fracture during cycling at a strain range of $\Delta\varepsilon = 1.4\%$.

- Specimens manufactured in the horizontal build plane (X, Y and XY45 build orientations) yielded similar performance under progressive amplitude fatigue testing.
- SEM micrographic images reveal multiple fatigue cracks initiating at regions of un-melted powder particles near the as-built rough surface.

Future work will explore the role of build orientation on the progressive amplitude fatigue performance of DMLS SS GP1, providing insight into the variation in cyclic stress–strain curve with build orientation.

Acknowledgements The authors would like to thank Dr. Abiodun A. Fasoro for additively manufacturing the Stainless Steel GP1 specimens used in this study. DMLS manufacturing of specimens was carried out using the EOS M280 system in the Manufacturing Engineering Department at Central State University.

References

1. Frazier WE (2014) Metal additive manufacturing: a review. *J Mater Eng Perform* 23:1917–1928. <https://doi.org/10.1007/s11665-014-0958-z>
2. Yahollahi A, Shansaei N, Thompson S, Elwany A, Bian L (2017) Effects of building orientation and heat treatment on fatigue behavior of selective laser melted 17-4 PH stainless steel. *Int J Fatigue* 94:218–235. <https://doi.org/10.1016/j.ijfatigue.2016.03.014>
3. Yu C, Zhang P, Zhang Z, Liu W (2020) Microstructure and fatigue behavior of laser-powder bed fusion austenitic stainless steel. *J Mater Sci Technol* 46:191–200. <https://doi.org/10.1016/j.jmst.2019.08.047>
4. Ochi Y, Matsumura T, Masaki K, Yoshida S (2002) High-cycle rotating bending fatigue property in very long-life regime of high-strength steels. *Fatigue Fract Eng Mater Struct* 25:823–830. <https://doi.org/10.1046/j.1460-2695.2002.00575.x>
5. Siddiqui SF, Irmak F, Fasoro AA, Gordon AP (2020) Torsional fatigue failure of additively manufactured stainless steel of reduced specimen size. *JOM* 72:440–447. <https://doi.org/10.1007/s11837-019-03842-9>
6. Siddiqui SF (2018) Characterization of anisotropic mechanical performance of as-built additively manufactured metals, Ph.D. Dissertation, University of Central Florida
7. Kahlin M, Ansell H, Moverare J (2017) Fatigue behavior of additive manufactured Ti6Al4V, with as-built surfaces, exposed to variable amplitude loading. *Int J Fatigue* 103:353–362. <https://doi.org/10.1016/j.ijfatigue.2017.06.023>
8. Yadollahi A, Shamsaei N (2017) Additive manufacturing of fatigue resistant materials: challenges and opportunities. *Int J Fatigue* 98:14–31. <https://doi.org/10.1016/j.ijfatigue.2017.01.001>
9. Yadollahi A, Shamsaei N, Thompson SM, Elwany A, Bian L, Mahmoudi M (2015) Fatigue behavior of selective laser melted 17–4 PH Stainless Steel
10. Bajaj P, Hariharan A, Kini A, Kürnsteiner P, Raabe D, Jagle EA (2019) Steels in additive manufacturing: a review of their microstructure and properties. *Mater Sci Eng* 772. <https://doi.org/10.1016/j.msea.2019.138633>
11. Yusuf SM, Cutler S, Gao N (2019) Review: the impact of metal additive manufacturing on the aerospace industry. *Metals* 9. <https://doi.org/10.3390/met9121286>
12. Carneiro L, Jalalahmadi B, Ashtekar A, Jiang Y (2019) Cyclic deformation and fatigue behavior of additively manufactured 17–4 PH stainless steel. *Int J Fatigue* 123:22–30. <https://doi.org/10.1016/j.ijfatigue.2019.02.006>

13. Rack HJ, Kalish D (1974) The strength, fracture toughness, and low cycle fatigue behavior of 17-4 PH stainless steel. *Metall Mater Trans* 5:1595–1605. <https://doi.org/10.1007/BF02646331>
14. Sarkar S, Kumar CS, Nath AK (2018) Investigation on the mode of failures and fatigue life of laser-based powder bed fusion produced stainless steel parts under variable amplitude loading conditions. *Add Manuf*. <https://doi.org/10.1016/j.addma.2018.10.044>
15. Schijve Jaap (2009) *Fatigue under variable-amplitude loading. Fatigue of structures and materials*. Springer, Dordrecht, pp 296–297
16. Kardomateas GA, Geubelle PH (2010) Fatigue and fracture mechanics in aerospace structures. *Encycl Aerosp Eng* 3. <https://doi.org/10.1002/9780470686652.eae142>
17. Marquis GB (2011) Fatigue assessment methods for variable amplitude loading of welded structures. In: *Fracture and fatigue of welded joints and structures*. pp 208–238. <https://doi.org/10.1533/9780857092502.2.208>
18. Pommier S (2003) Cyclic plasticity and variable amplitude fatigue. *Int J Fatigue* 25:983–997. [https://doi.org/10.1016/S0142-1123\(03\)00137-3](https://doi.org/10.1016/S0142-1123(03)00137-3)
19. EOS GmbH-Electro Optical Systems. Material Data Sheet: EOS Stainless Steel GP1 for EOSINT M 270. 1–5
20. Siddiqui SF, Fasoro AA, Cole C, Gordon AP (2019) Mechanical characterization and modeling of direct metal laser sintered stainless steel GP1, *J Eng Mater Technol* 141(3)
21. Facchini L, Vicente N, Lonardelli I, Magalini E, Robotti P, Molinari A (2010) Metastable austenite in 17-4 precipitation-hardening stainless steel produced by selective laser melting. *Adv Eng Mater* 12(3):184–188
22. Luecke WE, Slotwinski JA (2014) Mechanical properties of austenitic stainless steel made by additive manufacturing. *J Res Natl Inst Stand Technol* 119:398–418
23. Hitachi High-Technologies Corporations (2014) Model SU3500 Scanning Electron Microscope: Easy operation guide, Japan

Part IV
Additive Manufacturing for Energy
Applications III

Detection of Defects in Additively Manufactured Metals Using Thermal Tomography



Alexander Heifetz, Dmitry Shribak, Zoe L. Fisher, and William Cleary

Abstract Quality control of additively manufactured (AM) metallic structures is essential prior to deployment of these structures in a nuclear reactor. We investigate the limits of detection of sub-surface porosity defects in AM stainless steel 316L using thermal tomography nondestructive evaluation method. Thermal tomography reconstructs spatial thermal effusivity of the structure from time-dependent surface temperature measurements of flash thermography. Our studies are based on computer simulations of heat transfer through solids using COMSOL software suit. Using the model of layered media, in which defect in a solid is represented with a layer of un-sintered metallic powder with appropriate thermophysical parameters, we obtain depth profile of thermal effusivity for the structure. Computer simulations indicate that at 1 mm depth, layers of 50 μm thickness are detectable in SS316L.

Keywords Additive manufacturing · Nondestructive evaluation · Thermal tomography

Introduction

Additive manufacturing (AM) is an emerging method for cost-efficient production of low-volume custom and unique parts with minimal supply-chain dependence. In particular, AM potentially provides a cost-saving option for replacing aging nuclear reactor parts and reducing costs for new construction of advanced reactors [1]. Metals of interest for passive structures in nuclear applications typically include

A. Heifetz (✉) · D. Shribak · Z. L. Fisher
Nuclear Science and Engineering Division, Argonne National Laboratory, Argonne, IL, USA
e-mail: aheifetz@anl.gov

Z. L. Fisher
Nuclear Science and Engineering Department, Massachusetts Institute of Technology, Cambridge, MA, USA

W. Cleary
Fuel Fabrication Facility, Westinghouse Electric Company, Columbia, SC, USA

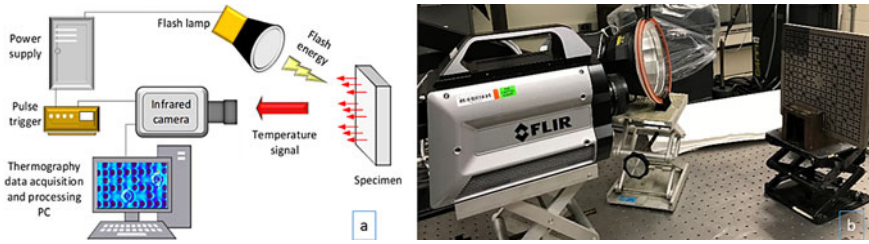


Fig. 1 **a** Schematics of pulsed thermal tomography system. **b** Laboratory setup. (Color figure online)

high-strength corrosion-resistant stainless steel and nickel super alloys. Because of high strength, shape forming of these metals into complex geometry structures is not trivial. AM of such metals is currently based on laser powder-bed fusion (LPBF). Because of the intrinsic features of LPBF, material defects such as porosity and anisotropy can appear in the metallic structure [2, 3]. A pore is potentially a seed for crack formation in the structure due to thermal and mechanical stresses in nuclear reactor. Quality control (QC) in AM involves detection of material flaws in real time during manufacturing, and nondestructive evaluation (NDE) of the structure after manufacturing. Currently, there exist limited options for nondestructive examination (NDE) of AM structures either during or post-manufacturing. Deployment of high-resolution NDE systems, such as X-ray tomography, is limited by spatial constraints of the metal 3D printer, large size, and complex shapes with lack of rotational symmetry of the AM parts. Contact NDE techniques, such as ultrasound, face challenges because AM structures have rough surfaces which affect probe coupling. In addition, NDE methods such as ultrasound require time-consuming point-by-point raster scanning of specimens.

As a solution to NDE of AM structures, we are developing pulsed thermal tomography (PTT) algorithms for 3D imaging and material flaw detection [4, 5]. The method is non-contact and scalable to arbitrary structure size. A schematic depiction of the PTT setup is shown in Fig. 1. The method consists of illuminating material with white light flash lamp, which rapidly deposits heat on the material surface. Heat transfer then takes place from the heated surface to the interior of the sample, resulting in a continuous decrease of the surface temperature. A megapixel fast frame infrared (IR) camera records thermograms, time-resolved images of surface temperature distribution $T(x, y, t)$. Thermal tomography obtains reconstruction of 3D spatial effusivity $e(x, y, z)$ from the data stack of thermography images.

Thermal Tomography Principles

The reconstruction algorithm of thermal tomography obtains apparent spatial effusivity $e(x, y, z)$ from time-dependent surface temperature $T(x, y, t)$ measurements of flash thermography. The reconstruction model assumes that heat propagation is

one-dimensional along the z -coordinate. This assumption is strictly valid for uniform planar structures. However, approximate solutions can be obtained for locally planar structures. Detailed study of non-planar structures is outside the scope of this paper. For 1D heat diffusion,

$$\frac{\partial T}{\partial t} = \alpha \frac{\partial^2 T}{\partial z^2}, \tag{1}$$

where z is the depth coordinate, x and y are coordinates in the transverse plane, and α is thermal diffusivity defined as

$$\alpha = k/\rho c. \tag{2}$$

Here, k is thermal conductivity, ρ is density, and c is specific heat. The reconstructed $e(z)$ at the location (x, y) in the plane is obtained only from the surface temperature transient $T(t)$ measured at the location (x, y) . The algorithm starts with the assumption that the medium can be treated as semi-infinite. The analytic solution for semi-infinite slabs is given as [2–4]

$$T(z, t) = \frac{Q}{\sqrt{\rho c k \pi t}} \exp\left(-\frac{z^2}{4\alpha t}\right), \quad 0 \leq z \leq \infty, \tag{3}$$

where Q is the instantaneously deposited surface thermal energy density (J/m^2). Thermal effusivity, which is a measure of how the material exchanges thermal energy with its surroundings, is defined as

$$e = \sqrt{\rho c k}. \tag{4}$$

Using Eqs. (3) and (4), one can express observed or apparent time-dependent effusivity of the medium as

$$e(t) = \frac{Q}{T(z = 0, t)\sqrt{\pi t}}. \tag{5}$$

Using the characteristic relationship between time and depth [5–7]

$$z = \sqrt{\pi \alpha t}. \tag{6}$$

And relating temporal effusivities $e(z)$ and $e(t)$ are related through a convolution integral, where $1/z$ is the transfer function [5–7]

$$e(t) = \int_0^z z^{-1} e(\zeta) d\zeta. \tag{7}$$

We obtain the final equation for apparent effusivity as

$$e(z) = z \frac{2Q}{\pi \sqrt{\alpha}} \frac{d}{dt} \left(\frac{1}{T(t)} \right) \Big|_{t=z^2/\pi\alpha} \quad (8)$$

This shows that spatial reconstruction of apparent effusivity $e(z)$ is given as a product of depth function z and time derivative of the inverse of surface temperature evaluated at time t corresponding to depth z according to Eq. (6). Information obtained from thermal tomography is relative because Q is usually not known. In principle, relative information can be converted to absolute scale through calibration. However, for estimation of geometrical parameters and detecting material flaws, relative effusivity reconstruction in non-dimensional units is sufficient.

Parametric Studies of Apparent Effusivity Reconstruction with COMSOL Computer Simulations of Heat Transfer

To obtain estimates of thermal tomography sensitivity to defects in LPBF, we reconstruct apparent effusivity from data generated with COMSOL computer simulations of heat transfer in a layered metallic structure. The structure modeled in COMSOL is a stainless steel disc with $R = 30$ cm radius and $L = 5$ mm thickness. Diffusion of heat in a plate with such geometry (transverse dimensions are much larger than the thickness) closely resembles the case of an infinite plate of finite thickness. For the solid media in the structure, we used stainless steel 316L thermophysical parameters $\rho = 7954$ kg/m³, $k = 13.96$ W/m*K, $c = 499.07$ J/kg [8]. For modeling the amplitude of defect layer, we linearly scaled the thermophysical parameters as $\eta\rho$, ηc and ηk , where ρ , c and k are those of the solid metal, and the scaling parameter values are in the range $\eta = 0.7$ – 0.9 . The range of scaling parameter values was chosen to correspond to that of the filling factor of un-sintered metallic powder. According to random close packing (RCP) model, packing density of mono-dispersed spheres is 0.65 [9], but size distribution and non-spherical shapes of powders may result in higher packing density [10]. Working in normalized units, we set $\rho = c = k = 1$ for solid medium, so that $e_{\text{solid}} = 1$. While density and heat capacity typically scale linearly with powder filling factor, scaling of thermal conductivity is potentially nonlinear. Therefore, this study provides information about parametric dependence of effusivity reconstruction, where a hypothetical defect does not exactly correspond to a physical powder model.

The defect was introduced into the structure as a layer of metallic material with lower thermophysical parameters than those of the host solid plate. In LPBF, heat diffusion is likely to result in smooth transitions from solid metal to defect. The defect was introduced into COMSOL grid as a subtracted Gaussian with the mean of μ and standard deviation σ . Thus, in normalized units, the defect actual effusivity is modeled as

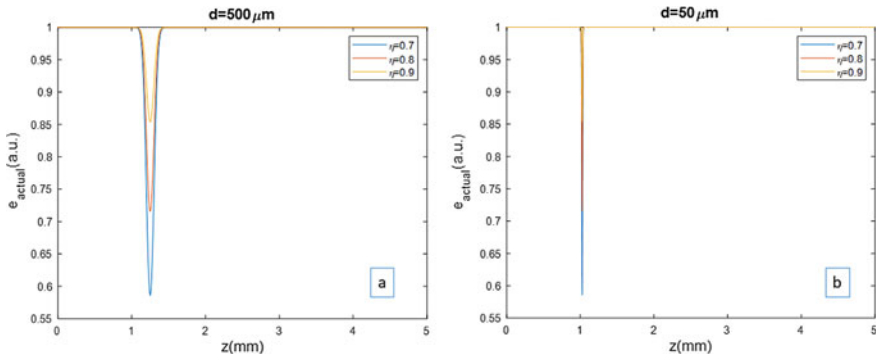


Fig. 2 Actual effusivities in normalized units for $L = 5$ mm plate with a defect layer with equivalent thickness of **a** $d = 500 \mu\text{m}$ and **b** $d = 50 \mu\text{m}$. (Color figure online)

$$e_{actual}(z) = \left(1 - (1 - \eta)e^{-(z-\mu)^2/2\sigma^2}\right)^{3/2} \tag{9}$$

Defects with equivalent width of $d = 500 \mu\text{m}$ and $d = 50 \mu\text{m}$ were considered in COMSOL computer simulations of the layered model. The defects were modeled as subtracted Gaussians with $\mu = 1.25$ mm and $\sigma = 50 \mu\text{m}$, and $\mu = 1.025$ mm and $\sigma = 5 \mu\text{m}$, respectively. Actual effusivities for the two defects are plotted in Figs. 2a and b. The scaling parameter η in both figures is in the range from 0.7 to 0.9.

In COMSOL computer simulations, the plate is initially at room temperature, and the incident heat source is a Gaussian pulse with variance of 0.5 ms. Although the reconstruction model in thermal tomography assumes that heat was deposited instantaneously on the material surface, real flash heat sources have a finite duration time. High intensity flash is usually generated by discharging a capacitor through a white light lamp, with typical capacitor time constant on the order of a few milliseconds (see Fig. 1). Thermal insulating boundary conditions were selected for all plate surfaces. Temperature transients were calculated with 0.1 ms time step for 20 s total problem runtime. Temperature data was exported from COMSOL to perform apparent effusivity reconstruction with algorithm implemented in MATLAB. We observed in COMSOL simulations that the surface temperature of the plate is maximum at the time when the incident Gaussian heat pulse reaches the maximum value. While heat is still applied by the pulse, surface plate temperature begins to decay due to diffusion of heat into the bulk of the plate. This affects the decay rate of the surface temperature. Therefore, when performing effusivity reconstruction, the origin of the surface temperature transient should be chosen such that the heat source has no effect on surface temperature decay. The starting time for the temperature transient used for effusivity reconstruction is 8 ms after the surface temperature reaches the maximum value.

Figure 3a–c shows apparent effusivity reconstructions for scaling parameter $\eta = 0.7, 0.8,$ and $0.9,$ respectively. In each figure, reconstructions are shown for a structure containing a defect with $d = 500 \mu\text{m}$ layer and another structure containing

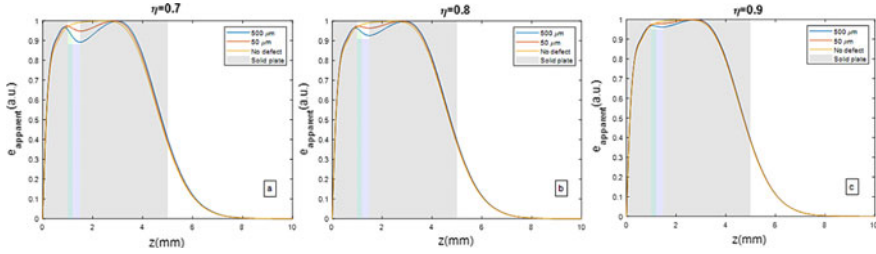


Fig. 3 Apparent effusivity $e(z)$ reconstructions for variable defect thermophysical properties from surface temperature transients produced with COMSOL computer simulations data of heat transfer. The structure has $L = 5$ mm total thickness with Gaussian defect. Thermophysical parameters of the defect layer are scaled as $\eta\rho$, ηc and ηk , where ρ , c and k are those of the SS316L solid metal, and the scaling parameter values are in the range **a** $\eta = 0.7$ **b** $\eta = 0.8$ **c** $\eta = 0.9$. (Color figure online)

$d = 50 \mu\text{m}$ layer. Apparent effusivity reconstruction $e(z)$ is plotted as a normalized variable. In the sketch of the layered structure shown in Fig. 3, the front and back planes are at $z = 0$ and at $z = 5$, respectively. Detection of defect is interpreted as deviation from the effusivity reconstruction for a defect-free solid plate. The defect layer is indicated as $500 \mu\text{m}$ and $50 \mu\text{m}$ -thick stripes overlaid on the solid plate structure colored in gray. The strip is slightly larger than 2σ width of the Gaussian model of the defect. One can observe from Fig. 3 that the reconstruction for a solid plate with no defect (yellow curve) agrees well at the front edge of the plate. However, reconstruction is blurred at the back edge of the plate. As the scaling factor η is decreased, apparent effusivity depth profile curve shows a dip in the spatial region corresponding to the defect. As expected, the dip decreases with increasing value of η .

Quantitative analysis of the data in Fig. 3 is shown in Table 1. Reconstructed effusivity of the defect is obtained by measuring the minimum value at the dip of the effusivity curve. Based on computer simulations for defects located below 1 mm depth, reconstruction of the defect with $500 \mu\text{m}$ thickness offers approximately 10–5% contrast, while reconstruction of the defect with $50 \mu\text{m}$ thickness offers approximately 5–2% contrast relative to solid plate effusivity.

Table 1 Apparent effusivity of defect layer obtained from COMSOL computer simulations

η	Defect apparent effusivity (normalized units)	
	500 μm	50 μm
0.7	0.89	0.95
0.8	0.93	0.96
0.9	0.96	0.98

Conclusion

Our results based on computer simulations of heat transfer in a layered media indicate that detection of defects as small as 50 μm located at 1 mm depth in SS316L can be possible, in principle. Because results are obtained from simulated data with no experimental noise, results based on computer simulations are likely to give the upper bound for detection of material defects with thermal tomography reconstructions of experimental data. In addition, sensitivity threshold of IR camera in detecting temperature differences has to be taken into consideration. Future work will be aimed performing experimental validations of thermal tomography sensitivity with imprinted calibrated defects.

Acknowledgements This project is sponsored by NEET Advanced Methods in Manufacturing (AMM) program. Other contributors include Brian Saboriendo, Thomas Elmer, and Sasan Bakhtiari from Argonne National Laboratory, Boris Khaykovich from MIT Nuclear Laboratory, Gregory Banyay and Leo Carrilho from Westinghouse Electric Company.

References

1. Lou X, Gandy D (2019) Advanced manufacturing for nuclear energy. *JOM* 71:2834–2836
2. Lewandowski JJ, Seifi M (2016) Metal additive manufacturing: a review of mechanical properties. *Ann Rev Mater Res* 46:151–186
3. King WE, Anderson AT, Ferencz RM, Hodge NE, Kamath C, Khairallah SA, Rubenchik AM (2015) Laser powder bed fusion additive manufacturing of metals: physics, computational and materials challenges. *Appl Phys Rev* 2:041304
4. Heifetz A, Shribak D, Liu T, Elmer TW, Kozak P, Bakhtiari S, Khaykovich B, Cleary W (2019) Pulsed thermal tomography nondestructive evaluation of additively manufactured reactor structural materials. *Trans Am Nucl Society* 121(1):589–591
5. Heifetz A, Elmer TW, Sun JG, Liu T, Shribak D, Saboriendo B, Bakhtiari S, Zhang X, Saniie J (2019) “First annual report on pulsed thermal tomography nondestructive evaluation of additively manufactured reactor materials and components,” ANL-19/43
6. Sun JG (2016) Quantitative three-dimensional imaging of heterogeneous materials by thermal tomography. *J Heat Transf* 138:112004
7. Sun JG (2014) Pulsed thermal imaging measurement of thermal properties for thermal barrier coatings based on a multilayer heat transfer model. *J Heat Transfer* 136:081601
8. Kim CS (1975) “Thermophysical properties of stainless steels,” ANL-75-55
9. Jaeger HM, Nagel SR (1992) Physics of granular states. *Science* 255(5051):1523–1531
10. Donev A, Cisse I, Sachs D, Variano EA, Stillinger FH, Connelly R, Torquato S, Chaikin PM (2004) Improving the density of jammed disordered packings using ellipsoids. *Science* 303(5660):990–993

Part V
Additive Manufacturing of Metals:
Applications of Solidification
Fundamentals

Influence of Pore Formation and Its Role on the Tensile Properties of 17-4 PH Stainless Steel Fabricated by Laser Powder Bed Fusion



Dyuti Sarker, Usman Ali, Farid Ahmed, Reza Esmaeilizadeh, Ali Keshavarzkermani, Ehsan Marzbanrad, and Ehsan Toyserkani

Abstract Additive manufacturing (AM) is a promising technique due to the scope of producing complex objects from a digital model, where materials are deposited in the successive layers as distinct from the conventional manufacturing approaches. In this study, laser powder bed fusion (LPBF), a class of additive manufacturing (AM), is used to make testing samples with gas atomized 17-4 PH stainless steel (SS) powder at different process parameters in argon (Ar) environment. A thorough study on powder characteristics, such as particle size distribution, powder morphology, phase formation at different atmospheres, as well as the microstructure and tensile properties of the printed parts at various energy densities were carried out. The microstructural analysis discovered the presence of columnar dendrites with complete martensite phases regardless of the process parameters. A detailed X-ray computed tomography (CT) scan analysis on printed samples explored the correlation between the pores and energy density. The sample printed with adequate energy density obtained lower porosity (volume of pores: 2×10^4 to $9 \times 10^4 \mu\text{m}^3$, compared to 2×10^4 to $130 \times 10^4 \mu\text{m}^3$) resulting in maximum tensile strength and elongation of 770 MPa and 38%, respectively. Therefore, it is obvious that the quantity, size and shape of pores in the printed parts significantly affect the fracture mode.

Keywords 17-4 PH stainless steel · Laser powder bed fusion · Additive manufacturing · Martensite · Energy density

Introduction

Laser powder bed fusion (LPBF) also known as selective laser melting (SLM) is an AM technique where powder particles are selectively melted or fused with a point heat source to build parts using a layer by layer fabrication approach [1, 2]. Regardless

D. Sarker (✉) · U. Ali · F. Ahmed · R. Esmaeilizadeh · A. Keshavarzkermani · E. Marzbanrad · E. Toyserkani

Multi-Scale Additive Manufacturing Lab, Department of Mechanical and Mechatronics Engineering, University of Waterloo, 200 University Ave W, Waterloo, ON N2L 3G1, Canada
e-mail: dsarker@ryerson.ca

of the advantages of LPBF in the production of complex shapes [3], there still remain difficulties that restrict its extensive implementation in commercial applications. For example, there exists a lack of knowledge on the process–property correlation that assists the manufacturer to envisage the mechanical performance of the fabricated parts with adequate assurance. The inadequate understanding is ascribed by the rapid solidification which significantly influences the microstructure development and phase formation. The metallurgy in AM is manipulated by the characteristics of powder particles (powder composition, size distribution and morphology) as well as the cyclic thermal loading during the process. Other factors that affect the structural development are laser power, laser beam shape/intensity, laser scan pattern, chamber atmosphere as well as machine features [4–8] which govern the solidification kinetics. For the entire process, the heating and cooling rates dominate further precipitation kinetics, phase transformation and grain growth [9]. Mechanical properties of LPBF processed parts are stimulated by their microstructure and crystallographic phases, which are actually influenced by thermal characteristics such as cooling/solidification rates and thermal gradients [10].

Several researchers have worked on the microstructure, phase transformation, porosity level, and mechanical property of LPBF processed 17-4 PH SS. Among them, Pasebani et al. [11] studied the effects of powder atomizing media (water atomization vs. gas atomization) on phase transformation and mechanical properties of laser melted 17-4 PH SS parts. Gas atomized powder formed martensitic phases, whereas water atomized powder revealed dual phases of martensite and austenite. The microstructural study by Cheruvathur et al. [12] reported the dendritic structure with martensite and 50% retained austenite, where niobium carbide is aligned along the interdendritic boundaries. More microstructural study of LPBF processed 17-4 PH SS have been presented by Sun et al. [7, 13] and LeBrun et al. [14]. In a study by Facchini et al. [15], the microstructure development of 17-4 PH SS in the LPBF technique was presented, where the gas atomization and printing atmospheres were Ar. From their work, mostly austenitic phases were reported which transformed into martensite during tensile deformation. On the other hand, Murr et al. [16] have investigated the Ar and N₂ atmospheric effect in the LPBF technique on the martensite and austenite phase formation, respectively. The presence of both martensite and retained austenite in the LPBF processed parts in the N₂ build atmosphere implies that N₂ can influence the stability of the austenite. Rafi et al. [17] also worked on the mechanical and microstructural development of 17-4 PH SS, in the LPBF technique using both Ar and N₂ atmosphere. Their results focused on the formation of martensite and austenite phases, which are influenced by powder chemistry, fabrication atmosphere and grain morphology. However, Starr et al. [18] showed austenite phases and their transformation to martensite during LPBF of 17-4 PH SS powders. From their work, it is emphasized that, based on the powder chemistry, LPBF process parameters, post-process conditions, the resulted microstructure and the phase compositions could be much different than those manufactured using conventional techniques.

Therefore, the laser input energy density can also affect the build part microstructure. The presence of porosity in the microstructure experienced due to the different energy densities. With appropriate energy input, pores and un-melted conditions can

be alleviated to some extent in LPBF. Our recent study on 17-4PH SS shows that initial state of the powder is controlling the mechanical properties of the printed parts [19]. However, to the authors' best knowledge, there was no comprehensive study on the correction between energy density and tensile property of the 17-4 PH SS. It is also not clear how the energy density influences the morphologies like size and shape of the porosity which affects the mechanical properties of the printed parts. In this work, the effect of energy densities on LPBF processed 17-4 PH SS is explored based on the details of microstructural features such as phases, defects specifically the porosity, etc. and made a correlation with mechanical properties leading to the fracture mechanisms.

Materials and Experiments

The sample fabrication was carried using EOS M290 (EOS GmbH, Krailling, Germany), LPBF system and 17-4 PH SS powder. The ranges of particle size of the powder were between 16 μm and 63 μm . Samples were printed using recycled powder in an Ar atmosphere with a layer thickness of 40 μm , hatch spacing 90 μm . Details of the printing strategy with build plate dimension are presented in previous works [19, 20]. The specimens in all prints were built using different laser powers, scanning speeds and with a constant hatch distance. Among the all printed conditions, three samples at different input parameters are considered for detail study, i.e. sample I (170 W, 1000 mm/s: 47 J/mm³), sample II (170 W, 800 mm/s: 59 J/mm³), sample III (195 W, 800 mm/s: 68 J/mm³). To explore the effect of process parameters on mechanical property, tensile samples were built using three different energy densities.

Powder and printed samples microstructure were examined using scanning electron microscope (SEM) and electron backscatter diffraction (EBSD). The printed samples were prepared following standard metallographic techniques and etching with a mixture of 2.5 ml ethanol, 2.5 g picric acid, and 5 ml hydrochloric acid. EBSD was conducted using JEOL7000F SEM, with operational Oxford EBSD detector. The tensile tests were conducted at a crosshead speed of 0.45 mm/min in accordance with ASTM E8 standard, using Instron 8872 equipped with a 25 KN load cell. To obtain the distribution of the porosity, X-ray computed tomography (CT) was performed using scan (Zeiss Xradia 520 Versa, Oberkochen, Germany). For an applied voltage of 140 kV, 801 2D slices of specimens were subjected to 10 W X-ray radiation for 1 s.

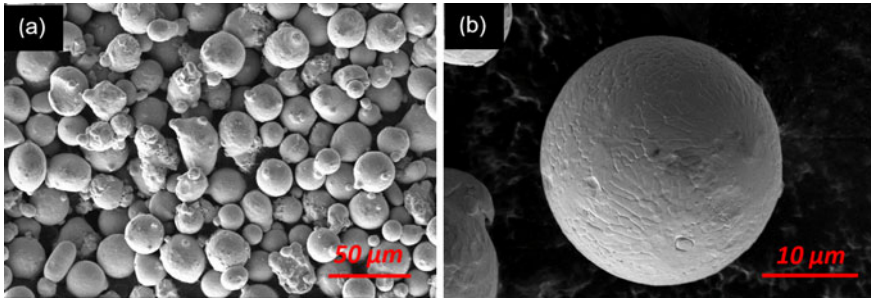


Fig. 1 SEM micrograph shows powder morphology of used powders: **a** multiple particles at low magnification, **b** surface morphology of the single particle at high magnification. (Color figure online)

Results

Powder Morphology

Powders, as feedstock materials, must be carefully chosen in terms of quality and cost in connection with the AM process used in the part fabrication. The powder morphology, both agglomerated and the cross-section of the powders, was studied using SEM, as presented in Fig. 1. From the micrograph, most of the particles of powders are spherical in shape, as shown in Fig. 1a. The magnified single spherical particle in Fig. 1b exhibits various orientation of dendritic structure on its outer surface.

Microstructure

The SEM micrograph shows similar structural features in LPBF processed 17-4 PH SS in three different samples, where samples I, II, and III show typical columnar grains, as obvious in Figs. 2a–c, respectively. The columnar grains are formed in the solidified parts and their cross-sections along the building direction shows martensitic laths inside the grains. The martensitic laths are clearly visible in magnified image of sample III, presented in Fig. 2d. The solidified parts are characterized by columnar grains oriented in various directions. The martensitic laths of various orientations are also seen within the grains. The structural feature implies that the direction of dendritic progression is parallel to the heat flow and develops a higher orientation tendency in the solidified parts [17]. On the martensitic laths, in Fig. 2d, white sparking precipitates are visible. This type of precipitates was also reported by Wang et al. [21], in LPBF processed 17-4 PH SS.

The IPF orientation of the printed sample I obtained using EBSD is shown in Fig. 3. The EBSD images fall within the longitudinal cutting plane, where columnar

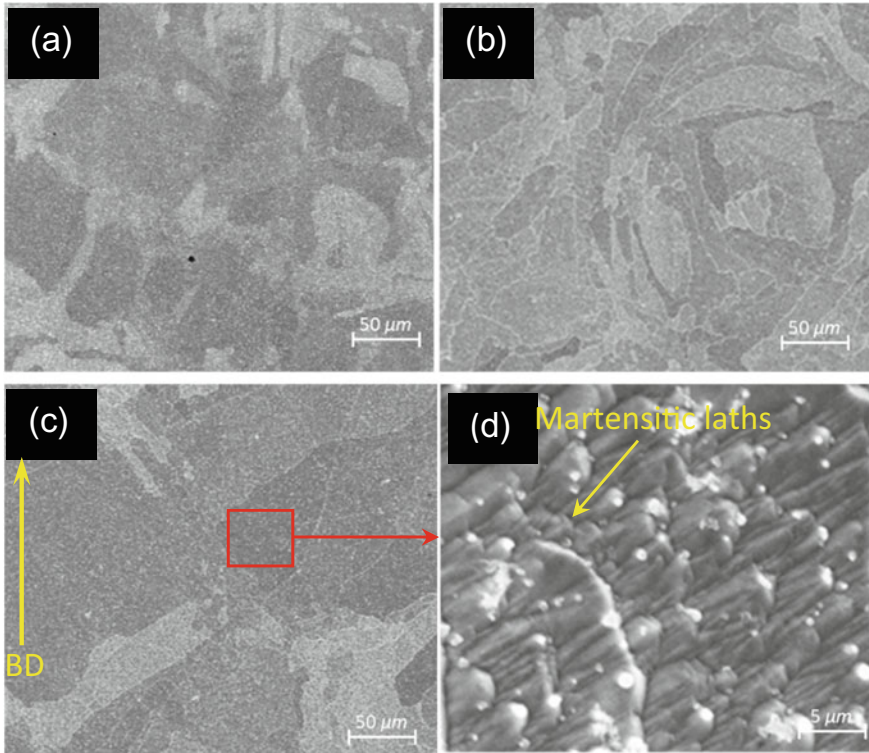


Fig. 2 SEM micrograph showing similar structural features in 17-4 PH printed parts at different parameters, **a** sample I, **b** sample II, **c** sample III, and **d** magnified view of sample III (along the building direction (BD)). (Color figure online)

grains are perpendicular (Fig. 3a) and parallel (Fig. 3b) to the build direction. This emphasizes that columnar grains form in multiple direction and grow parallel to the heat flow. The columnar grains along the build directions appears like globular shapes, whereas, from normal direction, elongated shapes are evident. The inverse pole figures presented in the bottom of the images (Fig. 3a and b) are identical and confirm the presence of random texture in the solidified parts.

The EBSD image mapping in Fig. 3c (along the build direction like 3a) is showing the distribution of low-angle grain boundaries (LAGB) and high-angle grain boundaries (HAGB), which correspond to red and black colors, respectively. The intersecting angle between grains below 15 ° is considered as LAGB, whereas greater than 15 ° is the HAGB. The grain boundary mapping shows about 65% percentage of HAGB, while only 35% grain boundaries are LAGB that indicates the remelting layers during printing. Similar type results were reported by Wang et al. [21].

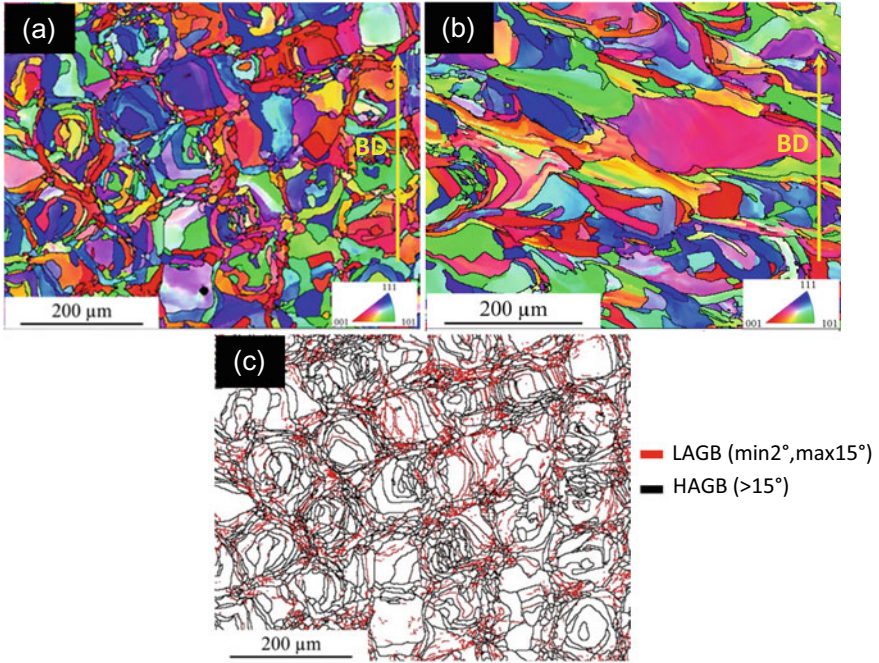


Fig. 3 EBSD image mapping of LPB processed 17-4 PH steel, **a** along the build direction, **b** normal to the build, **c** image mapping showing LAGB and HAGB. (Color figure online)

Porosity Distribution

CT scan results of Samples I, II, and III are presented in Fig. 4. The three samples printed in different energy densities show significant variations in pore distribution.

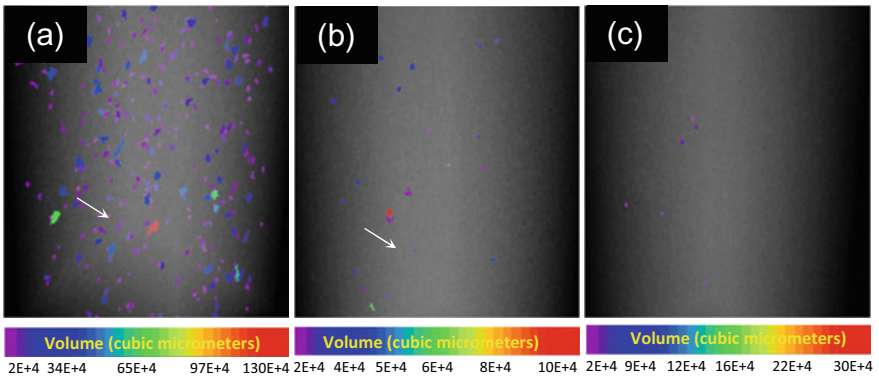


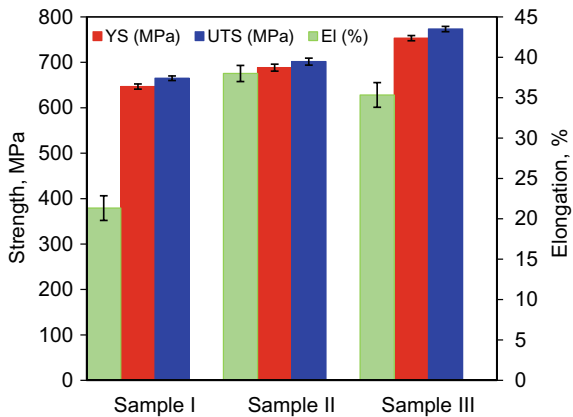
Fig. 4 Porosity distribution in LPBF processed samples at various energy density, **a** Sample I, **b** Sample II, and (III), **c** Sample III. (Color figure online)

The variation of the volumes of pores detected in the printed samples is presented in the legends. The scale bar corresponds to each color indicates pore volume in cubic micrometer. It is evident that the quantity and quality of the pores are linked with the energy density of the input parameters. At lower energy density, Sample I (47 J/mm) shows higher porosity than the Sample II (59 J/mm) and III (67 J/mm), respectively. In Sample I, the elongated and irregular pores are greater in number, as well as with larger volume sizes, which ranges from 2×10^4 to $130 \times 10^4 \mu\text{m}^3$. Sample II possesses smaller quantity of pores, and volume size ranges from 2×10^4 to $10 \times 10^4 \mu\text{m}^3$. In Sample III, very few quantities of spherical pores are observed, and from the scale bar, it is evident that volume size of these pores ranges from 2×10^4 to $9 \times 10^4 \mu\text{m}^3$.

Tensile Property

Figure 5 shows the tensile properties includes yield strength (YS), ultimate tensile strength (UTS), and elongation (EI) for different energy density. The three different energy densities exhibited significant changes in the tensile properties. In general, sample (Sample I) fabricated with lower energy density (47 J/mm) exhibit poor tensile property. In contrast, Samples II and III with increasing energy density (59 and 68 J/mm, respectively) show greater tensile properties. The ultimate tensile strength (UTS) is lower in Sample I (665 MPa), compared to Sample II (701 MPa) and Sample III (773 MPa). The ductility also improves from Sample I (23%) to Sample II (38%) and Sample III (35%). A small increase in elongation is observed in Sample II than Sample III, exhibiting better ductility with minor amount of pore formation. In Sample III, higher YS (753 MPa) is observed than Sample II (688 MPa) and Sample I (646 MPa).

Fig. 5 Engineering stress–strain curves, values of yield strength (YS), ultimate tensile strength (UTS), and elongation (EI) of LPBF processed 17-4 PH SS, at three different energy densities. (Color figure online)



Discussion

In current study, the phase formed in the LPBF processed 17-4 PH SS shows only martensitic structure for both powder and the printed samples. Moreover, it is reported that the LPBF processed 17-4 PH SS samples possess austenitic phase, depending on the process environment [11, 16, 17, 21, 22]. The presence of both martensite and retained austenite can be explained by the experimental atmosphere during powder atomization followed by LPBF of 17-4 PH SS. However, the samples in the present study were printed in Ar atmosphere. So, identical microstructural features are obvious at different energy densities (Fig. 2). The structure of elongated columnar grains and martensitic lath formation is due to the heat dissipation along the build direction. Similar columnar grains are presented in the LPBF processed 17-4 PH SS samples, where the result indicates that dendritic growth approaches parallel to the heat flow showing higher orientation tendency in the melt zone [17]. Moreover, the EBSD results emphasize the grain morphology and the orientation of the grains together with the grain boundary angles. The crystallographic orientation of columnar dendrites was color coded in the EBSD map (Fig. 3a and b), where different color corresponds to different orientations. In directional solidification, the primary dendrites propagate in the opposing direction of the thermal gradient, which also perpendicular to the mushy zone are categorized by various growth directions.

Porosity is one of the common defects in AM parts, which can adversely affect the mechanical properties. The source of the porosities could be various, i.e., powder made, process made or a product of solidification [23]. Generally, the spherical pores are generated from the entrapped gas because of the vapor pressure of the entrapped gas, stimulated by manufacturing process of both powder and the printed parts [24]. The irregular shaped pores are the result of some factors, such as cracks caused by thermal stress, partial melting of powders, balling phenomena, which occurs when melt pools are unable to defeat surface tension and results partial coverage for the following layers [25]. Because of the irregularity in the shape, these pores are bigger in size compared to the spherical pores [26]. The elongated pores are generated from the inadequate melting of powder within layer into layer initiating cracking and elongated voids [27]. Therefore, the presence of irregular and elongated pores in Sample I are associated with the inadequate energy density through the LPBF process, leading to incomplete melting of powders. Process made porosity can impact other factors, such as powder consolidation, which may influence to an inaccurately packed powder bed to completely dense parts [28]. The distributed powder on the powder bed may contain particles bigger in diameter than the layer thickness and through melting consolidated into a layer of proper height. The samples printed in different energy densities show a significant change in tensile properties. The better tensile strength and ductility can be attributed with the size and shape of the pores formed in the printed samples. The bigger size of irregular and elongated pores in Sample I caused premature failure results poor tensile property. In contrast, the smaller size of irregular pores in Sample II promotes a combination of brittle and ductile failure.

The negligible smallest size of pores in Sample III can resolve much load during tensile testing and resulting ductile failure with better tensile property.

Conclusions

This study explains how the energy density influences the size and shape of the porosity which affects the tensile properties of the printed parts. Samples of 17-4 PH SS were printed using LPBF in Ar atmosphere at three different energy densities using recycled gas atomized powders. Through the experimental results, microstructure and tensile properties are affected by energy densities. From the above discussion, it can be summarized as follows:

- (a) Unlike other research works, the samples printed in Ar atmosphere shown complete martensitic transformation. The columnar dendrites and martensite phases are observed in all three printed samples (Samples I, II, and III).
- (b) The sample printed with lower energy density (47 J/mm^3) formed greater number of pores with larger volume sizes. With higher energy density (59 J/mm^3 and 67 J/mm^3), the pore content reduces as well as the volume of the individual pores.
- (c) As the Sample I, exhibits significant volume of pores, they did not pass through the necking, which indicates premature failure. On the other hand, the lower pore density in Samples II and III show necking with higher tensile property. Therefore, both the pore quantity and shapes influence the tensile property, which is evident in Sample III through higher tensile strength of 770 MPa and elongation of 38%.

Acknowledgements This work was supported by funding from the Natural Sciences and Engineering Research Council of Canada (NSERC), the Federal Economic Development Agency for Southern Ontario (FedDev Ontario) and Siemens Canada Limited. The authors would like to acknowledge the support from Jerry Ratthapakdee and Karl Rautenberg for helping with design and printing of LPBF parts. In addition, the authors would like to acknowledge the encouragement and support from the members of Multi-Scale Additive Manufacturing group (MSAM), Fatigue and Stress Analysis Lab (FATSLAB) at the University of Waterloo and Canadian Center of Electron Microscopy members (CEEM).

References

1. Gibson I, Rosen DW, Stucker B (2010) Additive manufacturing technologies: rapid prototyping to direct digital manufacturing
2. Kruth JP, Levy G, Klocke F, Childs THC (2007) Consolidation phenomena in laser and powder-bed based layered manufacturing. CIRP Ann Manuf Technol. <https://doi.org/10.1016/j.cirp.2007.10.004>

3. Waller JM, Parker BH, Hodges KL, Burke ER, Walker JL (2014) Nondestructive evaluation of additive manufacturing state-of-the-discipline report, NASA/TM-2014-218560, <https://doi.org/10.13140/rg.2.1.1227.9844>
4. Cherry JA, Davies HM, Mehmood S, Lavery NP, Brown SGR, Sienz J (2015) Investigation into the effect of process parameters on microstructural and physical properties of 316L stainless steel parts by selective laser melting. *Int J Adv Manuf Technol* 76(5–8):869–879. <https://doi.org/10.1007/s00170-014-6297-2>
5. Yusuf SM, Gao N (2017) Influence of energy density on metallurgy and properties in metal additive manufacturing Influence of energy density on metallurgy and properties in metal additive manufacturing. *Mater Sci Technol* 33(11):1269–1289. <https://doi.org/10.1080/02670836.2017.1289444>
6. Rashid R, Masood SH, Ruan D, Palanisamy S, Rahman Rashid RA, Brandt M (2017) Effect of scan strategy on density and metallurgical properties of 17-4PH parts printed by selective laser melting (SLM), *J Mater Process Technol* 249:502–511, <https://doi.org/10.1016/j.jmatprotec.2017.06.023>
7. Sun Y, Hebert RJ, Aindow M (2018) Effect of heat treatments on microstructural evolution of additively manufactured and wrought 17-4PH stainless steel. *Mater Des* 156:429–440. <https://doi.org/10.1016/j.matdes.2018.07.015>
8. Keshavarzkermani A et al (2019) An investigation into the effect of process parameters on melt pool geometry, cell spacing, and grain refinement during laser powder bed fusion, *Opt Laser Technol*, <https://doi.org/10.1016/j.optlastec.2019.03.012>
9. Cantor B, Kim WT, Bewlay BP, Gillen AG (1991) Microstructure - cooling rate correlations in melt-spun alloys. *J Mater Sci* 26(5):1266–1276. <https://doi.org/10.1007/BF00544465>
10. Selcuk C (2011) Laser metal deposition for powder metallurgy parts, *Powder Metall*, <https://doi.org/10.1179/174329011x12977874589924>
11. Pasebani S, Ghayoor M, Badwe S, Irrinki H, Atre SV (2018) Effects of atomizing media and post processing on mechanical properties of 17-4 PH stainless steel manufactured via selective laser melting, *Addit Manuf*, <https://doi.org/10.1016/j.addma.2018.05.011>
12. Cheruvathur S, Lass EA, Campbell CE (2016) Additive manufacturing of 17-4 PH stainless steel: post-processing heat treatment to achieve uniform reproducible microstructure, *JOM*, <https://doi.org/10.1007/s11837-015-1754-4>
13. Sun Y, Hebert RJ, Aindow M (2018) Non-metallic inclusions in 17-4 PH stainless steel parts produced by selective laser melting, *Mater Des*, <https://doi.org/10.1016/j.matdes.2017.11.063>
14. LeBrun T, Nakamoto T, Horikawa K, Kobayashi H (2015) Effect of retained austenite on subsequent thermal processing and resultant mechanical properties of selective laser melted 17-4 PH stainless steel. *Mater Des* 81:44–53. <https://doi.org/10.1016/j.matdes.2015.05.026>
15. Facchini L, Vicente N, Lonardelli I, Magalini E, Robotti P, Alberto M (2010) Metastable austenite in 17-4 precipitation-hardening stainless steel produced by selective laser melting. *Adv Eng Mater* 12(3):184–188. <https://doi.org/10.1002/adem.200900259>
16. Murr LE et al (2012) Microstructures and properties of 17-4 PH stainless steel fabricated by selective laser melting. *J Mater Res Technol* 1(3):167–177. [https://doi.org/10.1016/S2238-7854\(12\)70029-7](https://doi.org/10.1016/S2238-7854(12)70029-7)
17. Rafi HK, Pal D, Patil N, Starr TL, Stucker BE (2014) Microstructure and mechanical behavior of 17-4 precipitation hardenable steel processed by selective laser melting, *J Mater Eng Perform*, <https://doi.org/10.1007/s11665-014-1226-y>
18. Starr TL, Rafi K, Stucker B, Scherzer CM (2012) Controlling phase composition in selective laser melted stainless steels
19. Ali U et al (2019) Identification and characterization of spatter particles and their effect on surface roughness, density and mechanical response of 17-4 PH stainless steel laser powder-bed fusion parts, *Mater Sci Eng A*, <https://doi.org/10.1016/j.msea.2019.04.026>
20. Ahmed F, Ali U, Sarker D, Marzbanrad E, Choi K, Mahmoodkhani Y (2019) Study of powder recycling and its effect on printed parts during laser powder-bed fusion of 17-4 PH stainless steel, *J Mater Process Tech*, November, p 116522, <https://doi.org/10.1016/j.jmatprotec.2019.116522>

21. Wang D et al (2019) The effects of fabrication atmosphere condition on the microstructural and mechanical properties of laser direct manufactured stainless steel 17-4 PH. *J Mater Sci Technol*. <https://doi.org/10.1016/j.jmst.2019.03.009>
22. Gu H, Gong H, Pal D, Rafi K, Starr T, Stucker B (2013) Influences of energy density on porosity and microstructure of selective laser melted 17– 4PH stainless steel, <https://doi.org/10.1007/s13398-014-0173-7.2>
23. Kruth JP, Wang X, Laoui T, Froyen L (2003) Lasers and materials in selective laser sintering, *Assem Autom*. <https://doi.org/10.1108/01445150310698652>
24. Zhao X, Chen J, Lin X, Huang W (2008) Study on microstructure and mechanical properties of laser rapid forming Inconel 718, *Mater Sci Eng A*, <https://doi.org/10.1016/j.msea.2007.05.079>
25. Gu DD, Meiners W, Wissenbach K, Poprawe R (2012) Laser additive manufacturing of metallic components: materials, processes and mechanisms. *Int Mater Rev* 57(3):133–164. <https://doi.org/10.1179/1743280411Y.0000000014>
26. Sames WJ, List FA, Pannala S, Dehoff RR, Babu SS (2016) The metallurgy and processing science of metal additive manufacturing. *Int Mater Rev* 61(5):315–360. <https://doi.org/10.1080/09506608.2015.1116649>
27. King WE et al (2014) Observation of keyhole-mode laser melting in laser powder-bed fusion additive manufacturing. *J Mater Process Technol* 214(12):2915–2925. <https://doi.org/10.1016/j.jmatprotec.2014.06.005>
28. Körner C, Bauereiß A, Attar E (2013) Fundamental consolidation mechanisms during selective beam melting of powders, *Model Simul Mater Sci Eng*, <https://doi.org/10.1088/0965-0393/21/8/085011>

Melt Pool Evolution in High-Power Selective Laser Melting of Nickel-Based Alloy



Borisov Evgenii, Starikov Kirill, Popovich Anatoly, and Popovich Vera

Abstract The paper studies melt pool evolution in nickel-based alloy as a function of the high-energy selective laser melting parameters. The influence of the geometric melt pool characteristics on the development of microstructure as well as on the formation of defects is investigated. Several laser processing parameters varying in volumetric and linear energy density were chosen. The shrinkage porosity was also studied, and its dependence on the process parameters, resulting density and microstructure were determined.

Keywords Single crystal alloy · Nickel-based alloy · Selective laser melting · High laser power · Additive manufacturing

Introduction

Search for the new materials suitable for additive manufacturing (AM) of complex and high-demanding components is currently driving the future developments. There are many scientific papers devoted to the application of new materials in the additive industry [1–5]. Currently, nickel heat-resistant single-crystal alloys are the most popular in the production of blades for gas turbine engines. Direct crystallization technology of such blades is associated with the inability to fully utilize the potential of the alloy. Such a limitation is caused by the segregation of alloying elements within dendritic cells, structural heterogeneity and formation of shrinkage micropores [6]. Modern methods of additive manufacturing make it possible to control

B. Evgenii · S. Kirill · P. Anatoly · P. Vera (✉)
Peter the Great St. Petersburg Polytechnic University, St. Petersburg, Russian Federation
e-mail: vpopovich@tudelft.nl

B. Evgenii
e-mail: evgenii.borisov@icloud.com

P. Vera
Faculty of Mechanical, Maritime, and Materials Engineering,
Delft University of Technology (TU Delft), Mekelweg 2, 2628 CD Delft, The Netherlands

the microstructure of the manufactured product more precisely, which in turn can provide a higher relative density of nickel heat-resistant single-crystal alloy products [7–9]. However, the use of the selective laser melting (SLM) technique is associated with several technological problems. One of these issues is related to the specimens cracking during the growing process [10–15].

Thus, the aim of this work is to determine the dependence of the specimen's relative density and cracking on the melt pool depth formed by using various parameters of the selective laser melting process.

Materials and Methods

The Aconity3D MIDI selective laser melting system was used for the experiment. The machine is equipped with variable focal spot diameter laser source with Gauss power distribution and a maximum power 1000 Watts. Moreover, machine is equipped with a module to enable operation with platform preheating up to 1200 °C. The parameters of the selective laser melting process were selected in such a way that different depths of the melt pools were provided during the samples production. The platform was heated to 1000 °C. This influence was realized by varying the volume and linear energy densities given to the material in the SLM process. As a result, seven scanning modes with different values of laser power, scanning speed, and hatch distance were selected. A constant layer thickness of 50 μm and laser spot diameter 400 μm was used.

The samples were made from nickel heat-resistant single-crystal alloy. The chemical composition of the powder is shown in Table 1. The powder particle size distribution was measured using Fritsch analysette 22 NanoTec plus by laser diffraction techniques.

Seven cubic samples with dimensions of 10 × 10 × 25 mm and different SLM parameters were produced. The samples were built without supports on a steel platform.

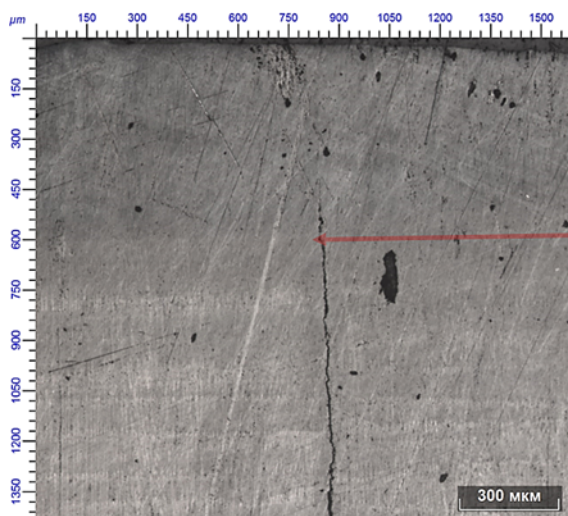
The presence of shrinkage defects was estimated based on the relative density and cross-sectional microscopy. The relative density was obtained by hydrostatic weighing (Archimedes method) of the samples.

The samples were cut along the growing direction along the line of the laser passage in the upper layer. The resulting metallographic samples were etched in a solution of HCl-20 ml, H₂SO₄-1 ml, and CuSO₄-4 g until the visible boundaries of the melt pool appeared. The depth of the melt pool was determined graphically using the Leica DMI 5000 light optical microscope as the maximum distance (due to the

Table 1 Chemical composition of nickel alloy powder (wt. %)

Ni	Cr	Al	Mo	W	Co	Re	Ta	Nb	C	B
60.45	4.9	5.9	1.1	8.4	9.0	4.42	4.1	1.6	0.12	0.01

Fig. 1 Boundaries of the melt pool of sample 2. (Color figure online)



rounded shape of the boundary of the melt pool) from the upper edge of the sample to the boundary of the melt bath of the last laser pass. An example of determining the depth of a melt bath using an optical microscope is shown in Fig. 1.

Based on the data obtained, the dependence of the sample density on the depth of the melt pool provided by the scanning parameters during the production of this sample was determined.

Results and Discussion

The powder particle size distribution measured by laser diffraction showed the following: $D_{10} = 28.6 \mu\text{m}$, $D_{50} = 55.8 \mu\text{m}$, $D_{90} = 92.3 \mu\text{m}$ (Fig. 2).

Secondary electron (SE) and back-scattered electron (BSE) analysis of the powder was performed by scanning electron microscope. According to the results of the BSE analysis, it is possible to draw conclusions about the chemical uniformity of the alloy and the absence of numerous particles with surface oxide layers (Fig. 3a). Based on the results of SE analysis, it can be concluded that there are a small number of satellites and irregularly shaped particles which will not affect the fluidity of the powder during the process (Fig. 3b).

As shown in Table 2, there is no clear correlation between the values of linear energy densities and the depth of the melt pool. This can be explained by the fact that the depth of the melt pool is affected by many characteristics, and together they can give an effect that is not reflected by the linear energy density value. In addition, in this paper we used a significant heating of the working platform and the modes with large values of linear energy density. This led to the fact that the size of the melt pool in the samples is larger. Thus, it turns out that the lifetime of the melt

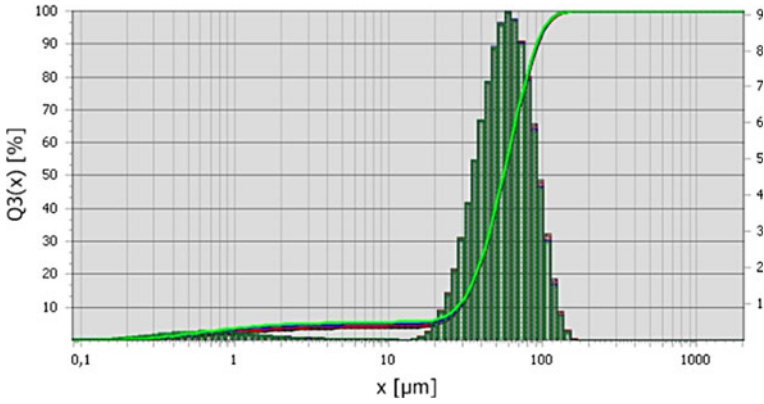


Fig. 2 Particle size distribution by volume fraction. (Color figure online)

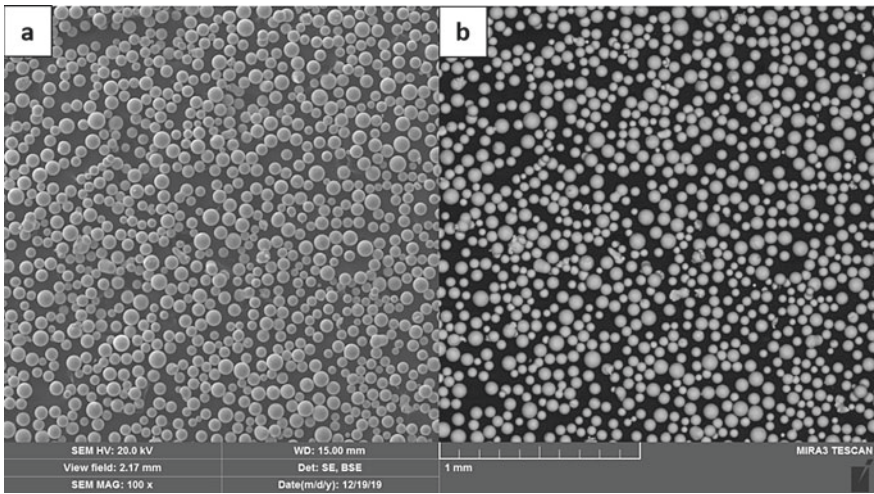


Fig. 3 Nickel heat-resistant single-crystal alloy BSE a, SE b

Table 2 Overview of the samples, showing relative density, depth of the melt pool and linear energy density

Sample №	1	2	3	4	5	6	7
Relative density, (g/mm ³)	8.77	8.76	8.76	8.75	8.72	8.69	8.66
Depth of the melt pool, (μm)	690	600	510	450	360	340	320
Linear energy density, (J/mm)	0.89	0.6	0.8	0.8	0.97	0.97	0.84

pool is significantly higher than in the traditional SLM process. Apparently, these facts are the reason why there is no obvious connection between the values of the linear energy density and the depth of the melt pool. As the depth of the melt pool increases, the relative density of the samples also rises (Table 2), which indicates a decrease in the number of shrinkage defects in the samples. This effect is due to the fact that the scanning parameters that provide a greater depth of the melt pool increase the crystallization time of the upper layers of the sample which leads to a significant increase in the size of the γ —phase cells and a reduction in the boundary zones.

The microstructure of the obtained samples consists of elongated cells located mainly along the growing direction of the samples γ —solid solution with scattered particles γ' —phase formed on the basis of the intermetallic compound Ni₃Al (Fig. 4a) which in turn consist of cuboid microparticles with an average size of ~ 200 nm (Fig. 4b).

Nb and Mo carbides are isolated along the boundaries of the γ —phase cells. The presence of carbides of alloying elements improves the properties of heat-resistant alloys at temperatures above the solubility limit of the intermetallic γ' —phase (Fig. 5). However, at the same time, their presence leads to the formation of micropores of shrinkage origin.

When the melt is crystallized in boundary zones limited on the one hand by the boundaries of growing dendrites, on the other by carbides released in the melt, the melt volumes are isolated from the total volume. Then, as a result of thermal shrinkage at the crystallization front, micropores and other defects of shrinkage

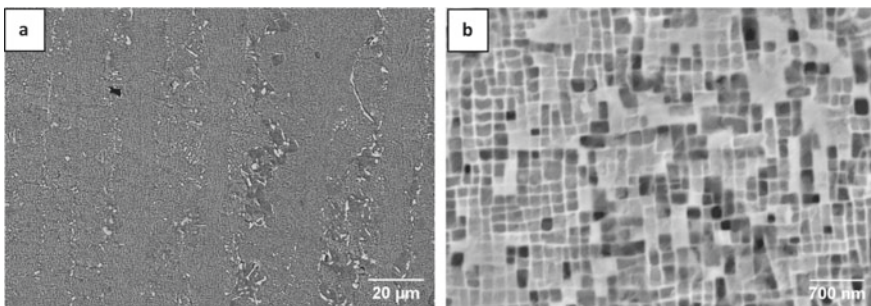


Fig. 4 Microstructure of specimen obtained by selective laser melting

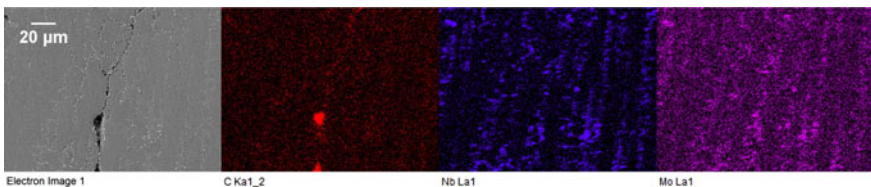


Fig. 5 EDS of the selective laser melted specimen. (Color figure online)

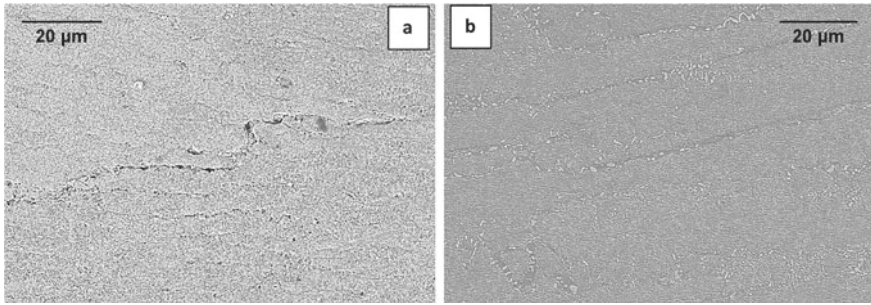


Fig. 6 Microstructure of the specimen 7—**a** and specimen 1—**b**

origin are formed in areas isolated from the total volume of the melt due to the lack of the liquid phase. The presence of such defects in the alloy significantly reduces its performance at operating temperatures.

High crystallization rates are characterized by a smaller γ —PDAS (primary dendritic arm space) size and a larger overall boundary length which in turn increases the probability of shrinkage defects formation in the sample. The volume fraction of defects can be reduced by increasing the crystallization time which will ensure the growth of γ/γ' —phase cells of greater width and a reduction in the total length of the boundaries (Fig. 6).

Conclusions

This paper presents the research results of the geometric characteristics, namely the depth of the melt pool formed during the selective laser melting of products, and its effect on the amount of shrinkage defects. The number of defects in the obtained samples was determined by the relative density, which in turn was measured by hydrostatic weighing. As a result, it was determined that as the depth of the melt pool increases, the relative density of the samples also increases. This effect is explained by a decrease in the rate of crystallization in the SLM production of samples according to the parameters that provide a greater depth of the melt pool. Slowing down the crystallization rate in the printing process provides a greater growth of γ —phase cells and, as a result, a decrease in the volume fraction of γ' —phase in which the formation of shrinkage defects occurs.

Funding This research was supported by Russian Science Foundation grant (project No 19-79-30002).

References

1. Chauvet E, Tassin C, Blandin JJ, Dendievel R, Martin G (2018) Producing Ni-base superalloys single crystal by selective electron beam melting. *Scripta Mater* 152:15–19
2. Polozov I, Sufiiarov V, Popovich A, Masaylo D, Grigoriev A (2018) Synthesis of Ti-5Al, Ti-6Al-7Nb, and Ti-22Al-25Nb alloys from elemental powders using powder-bed fusion additive manufacturing. *J Alloy Compound* 763:436–445
3. Goncharov IS, Razumov NG, Silin AO, Ozerskoi NE, Shamshurin AI, Kim A, Popovich AA et al (2019) Synthesis of Nb-based powder alloy by mechanical alloying and plasma spheroidization processes for additive manufacturing. *Mater Lett* 245:188–191
4. Razumov NG, Popovich AA, Grigor'ev AV, Silin AO, Goncharov IS (2019) Morphology of high-strength heat-resistant steel powder for machines for additive production from shavings. *Met Sci Heat Treat* 60(11–12):710–714
5. Xu J, Lin X, Guo P, Dong H, Wen X, Li Q, Huang W et al (2018) The initiation and propagation mechanism of the overlapping zone cracking during laser solid forming of IN-738LC superalloy. *J Alloy Compd* 749:859–870
6. Zavodov AV, Petrushin NV, Zaitsev DV (2017) Microstructure and phase composition of ZHS32 superalloy after selective laser melting, vacuum heat treatment and hot isostatic pressing. *Lett. Mater.* 7(2):111–116
7. Popovich VA, Borisov EV, Sufiyarov VS et al (2019) Tailoring the properties in functionally graded alloy inconel 718 using additive technologies. *Met Sci Heat Treat* 60:701–709
8. Sufiiarov VS, Popovich AA, Borisov EV, Polozov I (2015) Selective laser melting of titanium alloy and manufacturing of gas-turbine engine part blanks. *Tsvetnye Metally* 8:76–80
9. Sh Sufiyarov V, Borisov EV, Polozov IA, Masaylo DV (2018) Control of structure formation in selective laser melting process. *Tsvetnye Metally* 7:68–74
10. Kou S (2015) A criterion for cracking during solidification. *Acta Mater* 88:366–374
11. Qiu C, Chen H, Liu Q, Yue S, Wang H (2019) On the solidification behaviour and cracking origin of a nickel-based superalloy during selective laser melting. *Mater Charact* 148:330–344
12. Yang J, Li F, Wang Z, Zeng X (2015) Cracking behavior and control of Rene 104 superalloy produced by direct laser fabrication. *J Mater Process Technol* 225:229–239
13. Han Q, Mertens R, Montero-Sistiaga ML, Yang S, Setchi R, Vanmeensel K, Fan H et al (2018) Laser powder bed fusion of Hastelloy X: effects of hot isostatic pressing and the hot cracking mechanism. *Mater Sci Engi: A* 732:228–239
14. Liu Z, Qi H, Jiang L (2016) Control of crystal orientation and continuous growth through inclination of coaxial nozzle in laser powder deposition of single-crystal superalloy. *J Mater Process Technol* 230:177–186
15. Borisov EV et al (2020) Selective laser melting of Inconel 718 under high laser power. *Mater Today: Proc*

On Mesoscopic Surface Formation in Metal Laser Powder-Bed Fusion Process



Shanshan Zhang, Subin Shrestha, and Kevin Chou

Abstract During Laser Powder-Bed Fusion (LPBF), the surface formation of the selected-melted powder-bed region is subject to a melting-solidification process along the line-scans and sensitive to the process conditions. This study focuses on the surface formation of mesoscopic line-scans in LPBF and aims to investigate the effect of different process parameters, such as laser power and layer thickness, on the track morphology and surface roughness. For this purpose, single-track scans were produced by an LPBF system and then were characterized under a white-light interferometer. A discrete element method and 3D thermo-fluid modeling were applied to simulate powder spreading and laser scanning. The results show that the line-scan surface morphology and the surface roughness of the quasi-steady regions on the line scans are significantly dependent on the process conditions both longitudinally and transversely. As a result of continuous melting in the line scans, increasing laser power and decreasing layer thickness lead to smoother surface finish, respectively.

Keywords Laser Powder-Bed Fusion · Mesoscopic surface formation · Surface roughness · Thermo-fluid modeling

Introduction

Metal laser powder-bed fusion (LPBF), additive manufacturing (AM) process utilizes a laser source to selectively fuse modeled regions on the metal powder bed, and continuously repeats the layer-wise deposition to generate 3D parts [1]. Due to the

S. Zhang (✉) · K. Chou

Department of Industrial Engineering, University of Louisville, Louisville, KY 40292, USA
e-mail: shanshan.zhang@utrgv.edu

S. Shrestha

Department of Mechanical Engineering, University of Louisville, Louisville, KY 40292, USA

S. Zhang

Rapid Response Manufacturing Center, University of Texas Rio Grande Valley, Edinburg, TX 78539, USA

flexibility to fabricate complex geometries directly from the CAD model, LPBF has been growing popularity with high-demanded potentials among numerous AM technologies. Particularly, LPBF exhibits extraordinary advantages in surface quality compared with other powder-bed processes, i.e., electron beam melting (EBM). However, surface quality is a key assessment criterion in many AM applications [2, 3]. Although the surface quality can be improved largely by post-treatment or even during the build processing through re-melting [4, 5] and pulse shaping [6], the as-built surface quality is still a limit in the AM field.

Since the formation of 3D parts in LPBF is made up by the metallurgical bonding among adjacent raster line scans in successive layers, the individual line scans are considered as the fundamental component to examine the stability and quality of the fabricated parts [7]. Due to a complex thermal fluid dynamics interacting the heat source and metallic powder, the melt pool for the line scans goes through a continuous rapid melting-solidifying process. The applied fabrication process parameters and involved powder-bed status can significantly influence the quality of line-scan formation [8, 9]. Additionally, for a single line scan while traveling a long path, the melt pool may reach a thermodynamic balance status assuming the scan direction is not changed. However, as the laser practically experiences acceleration and deceleration while laser on and off or reaches at 180° turn points, the melt pool will lose the balance and reveal significantly different from the quasi-static region [10].

Recent years, many studies have investigated the LPBF fused metallic melt pool of single tracks. Experimentally, Gong et al. characterized the surface topology of single line scans using Ti-6Al-4V (Ti64) in LPBF, and exhibited the dissimilarity at different energy density situations [11]. Caprio et al. estimated the penetration depth of melt pool based on the detection of melt pool surface oscillations using a novel monitoring technique [12]. On the other hand, from the simulation perspective, Ahn et al. developed an analytical equation to predict the surface roughness for different inclination angles using measurement data from experiment and interpolation method [13]. Additionally, Dai and Gu applied a 3D volume of fluid (VOF) model using finite volume approach to predict the surface morphology based on the thermo-capillary effect and pressure boundary condition at the interface [14]. Powder-scale models were utilized to predict the free surface formation some studies by Khairallah et al. [15] and Xia et al. [16]. Shrestha et al. utilized a VOF model to predict the heat transfer, fluid flow, and resultant track morphology of the single-track formation [17].

The objective of this study is to investigate the mesoscopic surface formation with respect to different process conditions in LPBF, and to have reliable understanding on the quasi-static profile roughness of the mesoscopic surfaces. In this study, the single-track scanned specimens were fabricated in an LPBF system with Ti64 powder, and then examined using a white-light interferometer (WLI) to investigate the surface morphology and profile roughness. In addition, a discrete element method and 3D thermos-fluid modeling were applied to simulate the powder spreading and laser scanning process.

Experimental Methods

The experimental specimen consists of a semi-circular solid substrate and line scans exposed on the top surface of the substrate as shown in Fig. 1a. The distances between the neighboring tracks were far enough to avoid the influence of heat dissipation caused by overlapped melt pools. In addition to examine the effect of layer thickness on the single-track formation and to fabricate the tracks under the consistent build environment, a 20 μm stair in the semi-circular was designed as shown in Fig. 1b. As such, the single tracks could be deposited on the two sides of the semi-circular specimen with different layer thicknesses, 20 μm and 40 μm , respectively.

In this study, an EOS M270 LPBF system was utilized to fabricate the specimens. Pre-alloyed Ti64 powder supplied by LPW technology was used. All of the semi-circular substrates were manufactured using the EOS default parameter set to form full dense solids and consistent surface status. Then, the tracks were fabricated on the substrate surfaces with different conditions, as exhibited in Table 1. Specimens P1 to P3 were formed with different laser power at the layer thickness of 30 μm . Also, to fabricate the tracks at layer thicknesses of 20 and 40 μm , the build was performed at the 20 μm powder layer. After the substrate surface was finished, the 20 μm stair was exposed at the one half side of the surface, and at this layer, no tracks were exposed. Then, the next 20 μm powder layer was spread over. At the current layer, the thickness of the powder bed was 20 μm on the right side and 40 μm on the left, and thus, the track scans were produced at different powder layer thicknesses.

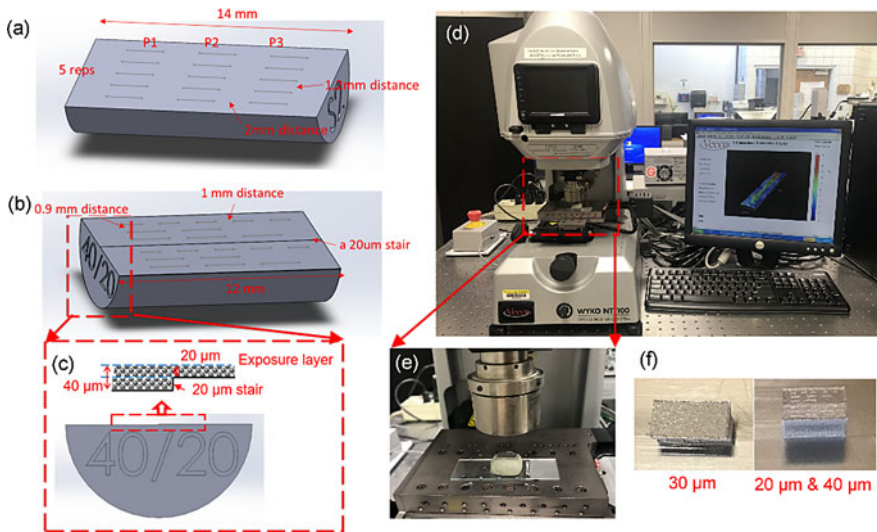


Fig. 1 CAD models for single-track formed specimens with layer thicknesses of **a** 30 μm , and **b** 20 and 40 μm ; **c** Illustration for powder packing; **d** White-light interferometer; **e** Specimen setup on the stage; **f** As-built specimens. (Color figure online)

Table 1 Design of experimental parameters for single-track scans

Specimen #	Layer thickness, μm	Laser power, W
P1	30	120
P2	30	150
P3	30	180
P4	20	150
P5	40	150

In addition, all the tracks were produced with a fixed scan speed of 1000 mm/s with skywriting setting turned on.

Moreover, to examine the surface morphology, a non-contact WYKO NT1100 white-light interferometer was utilized, shown in Fig. 1d. The flat surface with single lines fabricated is face-up placed on the sample stage (Fig. 1e). The vertical scanning interferometry (VSI) measurement mode is applied to evaluate the rough surfaces. In this study, $0.5\times$ magnification field-of-view (FOV) lens and $50\times$ objective lens was built-in. The scan region and scan length were set based on the length and height of the deposited single line scans.

Results and Discussion

Track Surface Morphology

The as-built specimens were cut off from the build substrate after fabricated from EOS M270 system. The semi-circular specimens were placed with the flat surfaces upwards to observe the tracks under WLI. The surface morphology observation and roughness measurement of the mesoscopic surface formation are elaborated in this section.

Track Repeatability

Figure 2 shows the 5 replicates of 2 mm single tracks produced using a laser power of 150 W and a scan speed of 1000 mm/s at a layer thickness of 30 μm , respectively. The track profiles can be identified from the isometric view with various colors, indicating of vertically elevated region in red and lowered region in blue. The scanning direction of these tracks were exposed from right-hand side to left in the view of Fig. 2. It is noticed that the 5 replicates of single tracks are consistently repeatable in general although unique morphology appears for every single-track scan.

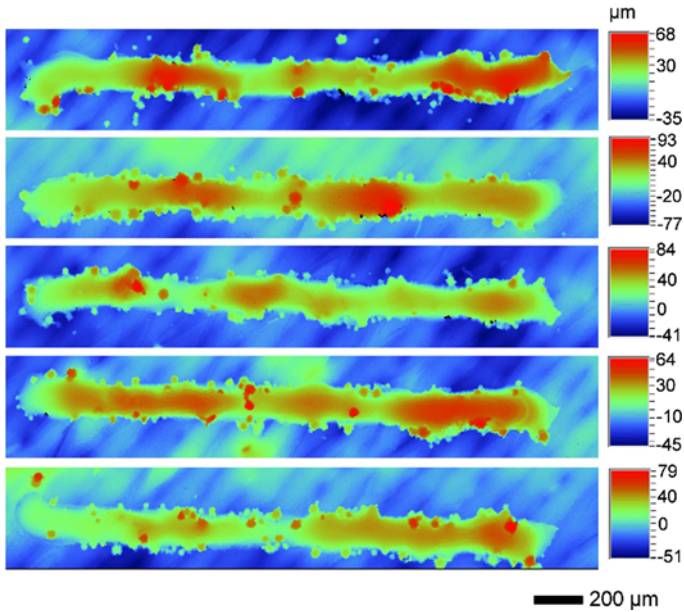


Fig. 2 Consistency of 2 mm single-track scans fabricated using 150 W laser power and 1000 mm/s scan speed at 30 μm layer thickness. (Color figure online)

Laser Power Effect on Single-Track Formation

3-dimensional displays of representative single-track scans produced using various laser powers are shown in Fig. 3, with the scan direction from back to front. It can be identified that the track produced with 120 W laser power shows a wavy profile and occasional discontinuous valleys in the longitudinal direction (Fig. 3a), whereas the laser powers of 150 and 180 W made continuous tracks (Fig. 3b, c); among the latter two tracks, the one using 180 W apparently shows an increase in height than 150 W due to more energy input contributed to deposit more powder. In addition, the bead width is observed to fluctuate along the tracks, and is generally ascending with an increase of laser energy input. It is also observed that the tails of tracks using laser

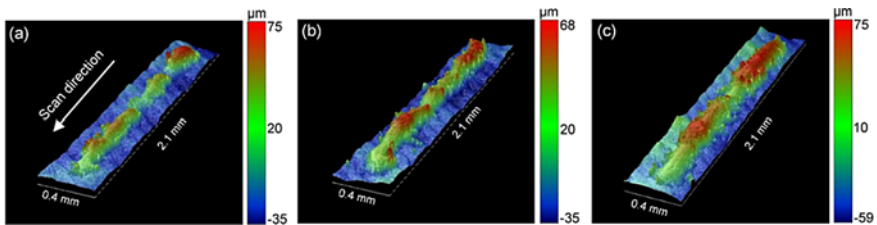


Fig. 3 3D displays of single-track scans fabricated via different laser powers of **a** 120 W; **b** 150 W and **c** 180 W. (Color figure online)

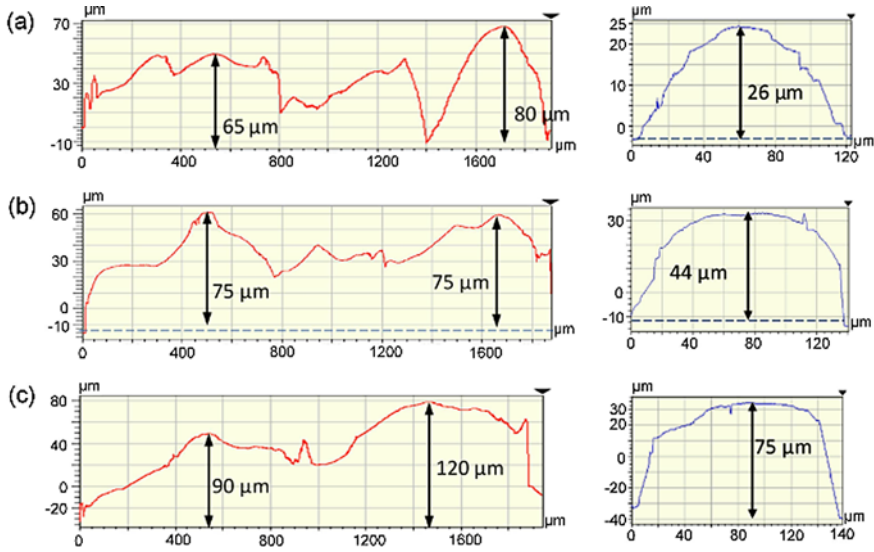


Fig. 4 2D profiles of the single tracks fabricated via laser power of **a** 120 W; **b** 150 W and **c** 180 W in longitudinal (*Left*) and transverse (*Right*) directions. (Color figure online)

powers of 120 and 150 W show irregularly distortion. The transient thermal dynamic behavior is considered that when the laser is off, the melt flow is slowed down while the boiling and evaporation of the melt powder create recoil pressure that leads to distortion of the single tracks [18]. Besides, the tracks formed by higher laser power applied present more powder particles attached on the track surface due to spatter generation caused by higher heat input [19].

Figure 4 shows the 2D profiles of the tracks in Fig. 3 in longitudinal and transverse directions. Both directional profiles present the surface fluctuation status of the middle cutoff of the tracks. Among these tracks, the one using 120 W laser power exhibits disconnection near the beginning of the scan and low profile at the center, leading to the instable profile, shown as Fig. 4a at the left. Although no discontinuity is observed in the other two tracks, occasional small peaks due to attached particles being noticed. Quantitatively, at the beginning region of tracks, the height of peaks exhibits dependent on the energy input, showing an increase (from 120 μm to 80 μm) with ascending laser power because higher energy deposition creates higher thermal gradient and assists melting more surrounding powder. Another peak region near the track tails is measured as well, and similar tendency with respect to the laser power is noticed. In addition, it can be seen that the ending region presents inclined that is considered caused by recoil force to the melted metal surface [20]. On the other hand, the profiles of the three track cutoffs in the transverse directions generally exhibit semi-circular morphologies, although fluctuation and spattering powder during solidification may cause distorted profiles. It is indicated that the height of the middle cross-sectional cutoffs shows increasing with a rising laser power. Due to

the semi-circular shape, the peaks are basically around the center line of the profile, and thus, the track height can be analyzed with an overall view at the longitudinal profiles.

Layer Effect on Single-Track Formation

Additionally, the single tracks deposited via the same process parameters at different layer thickness powder bed were scanned under WLI, as shown in Fig. 5. As expected, it is observed that the track height displays dependent upon the layer thickness: The track built at 20 μm powder layer generally presents lower height than those built at 30 and 40 μm . Specifically, a shallow tail end of the 20 μm layer track is significantly shown in Fig. 5a. This can be because of insufficient flow of melt pool at the end of track scans after the laser is stopped, whereas the accumulated heat cannot dissipate immediately, and the melted surface is pushed down by recoil force [21]. Moreover, in terms of track continuity, three representative tracks do not exhibit disconnection due to sufficient energy input, which also does not lead to significant difference on the track width visually. Besides, the inclusions due to incomplete melting can be seen on the surfaces of the tracks and surrounding regions, with an increasing amount with the thickened powder layers during fabrication.

The 2D surface profiles in both longitudinal and transverse directions are investigated in Fig. 6. Similar to the observation in the 3D views, the profile height of these tracks displays dependent on the layer thickness, increasing to a peak value of 85 μm at the powder layer thickness of 40 μm . In addition, the continuity of the tracks without breakage reveals that the linear energy density created by the process parameter combination of 150 W laser power, and 1000 mm/s scan speed is sufficient in fabrication at the studied range of powder layer thickness. Specifically, it is noticed that the profile of the track built on 20 μm powder layer (Fig. 6a) exhibits a smoother surface finish along the track formation. In contrast, the other two tracks present obvious bumps on their profiles, showing ascending height values with an increase of layer thickness due to more powder melted during fabrication. On the other hand, the transverse cross-sectional profiles are shown in Fig. 6. It is noted that the transverse cutoffs exhibit semi-circular shape. Besides, the width of the track

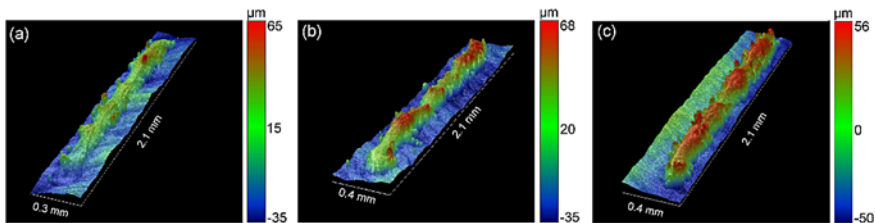


Fig. 5 3D displays of single tracks fabricated at different layer thicknesses of **a** 20 μm ; **b** 30 μm and **c** 40 μm . (Color figure online)

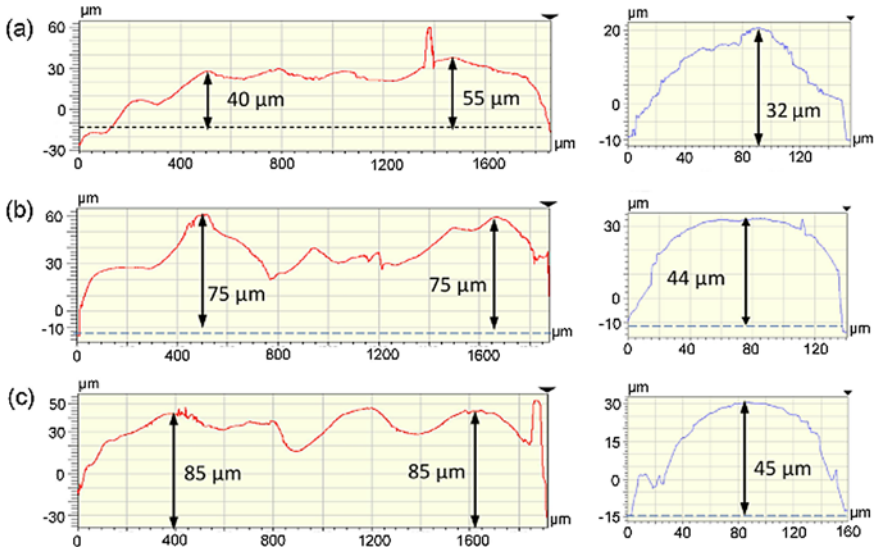


Fig. 6 2D profiles of the single tracks fabricated at layer thicknesses of **a** 20 μm , **b** 30 μm , and **c** 40 μm in longitudinal (*Left*) and transverse (*Right*) directions. (Color figure online)

with 40 μm layer thickness (Fig. 6c) exhibits greater due to more powder fed during laser deposition.

Specifically, the shallow tail end of the track at 20 μm layer thickness has been noticed with a bimodal profile in the depressed zone and inclination on both sides in the transverse view of cutoff, shown in Fig. 7. Such a phenomenon can be contributed by Marangoni effect caused by temperature gradient, and thus, the fluid flows from low surface tension region to high surface tension region, exhibiting an outward flow from center to the edge of the melt pool [22].

Quasi-static Surface Roughness

As the experimental 2 mm single tracks were experienced transient regions at both ends along the laser traveling direction, the surface roughness in this study would be measured for the dynamic-balanced region excluding the transient regions. The quasi-static length in the longitudinal direction was estimated in a range of 1062 μm to 1100 μm with an ascending tendency with decreasing laser power applied at 30 μm layer thickness. Therefore, to keep the Ra measurement consistent, a 1000 μm measure length in the middle portion of the tracks was applied to examine the quasi-static roughness.

The profile roughness measurement with respect of exposed laser power is shown in Fig. 8. The longitudinal roughness reveals that the lowest laser power (120 W)

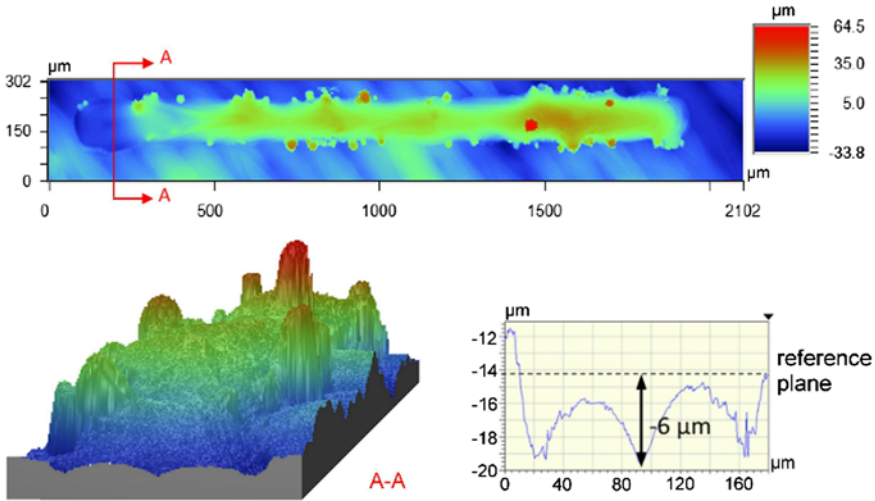
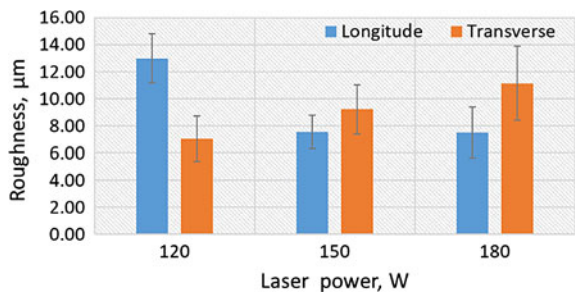


Fig. 7 Depressed tail of single track (Fig. 5a) made at 20 μm layer thickness. (Color figure online)

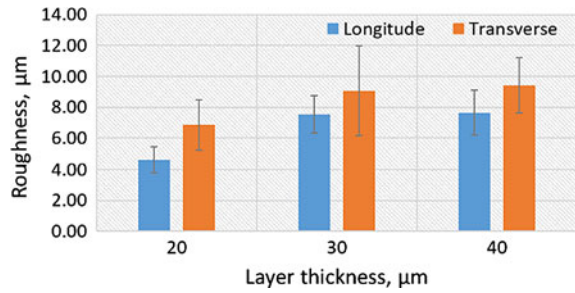
Fig. 8 Profile roughness of single tracks at 30 μm layer thickness in longitudinal and transverse directions. (Color figure online)



gives the highest roughness of $13 \mu\text{m} \pm 1.8 \mu\text{m}$ compared to other two laser power levels, while not much difference of the roughness values (approximately $7.5 \mu\text{m}$) is observed between 150 W and 180 W. In the transverse direction, the middle slice of the track was measured. It can be noticed that the transverse roughness increases with the increasing laser power.

In addition, single-track scans exposed at different layer thicknesses using 150 W laser power and 1000 mm/s scan speed were analyzed about the profile roughness. As shown in Fig. 9, the longitudinal roughness exhibits an increasing tendency with an increase of layer thickness; therein, the roughness of tracks deposited at 40 μm powder layer reveals almost twice value of that at 20 μm powder layer, which can be a reason that thicker layer may cause a higher bead height but wavier profile due to less energy density. On the other hand, the roughness in the transverse direction is observed that higher profile roughness occurs at thicker powder layer.

Fig. 9 Profile roughness of single tracks at different layer thickness in longitudinal and transverse directions. (Color figure online)



Numerical Study

A 3D thermo-fluid model was developed using FLOW-3D software. The powder over the base platform was imported from the LIGGGHTS simulation result. The domain was represented based on the fluid fraction. Powder and solid had a fluid fraction of 1 and the rest has 0 fluid fraction. Since the VOF model was used to predict the surface formation, a hexahedral mesh of $5\ \mu\text{m}$ was applied. In addition, all the walls of the domain were assigned with adiabatic boundary conditions. During the simulation, the laser was turned on at 0.2 in positive X (along laser movement) and Y (transverse) directions and the total scan length used was 1 mm. After the laser traveled 1 mm, it was turned off and the melt pool was let to solidify. The process parameters used in the simulation were 150 W laser power and 1000 mm/s scan speed as consistent in the experiment.

Figure 10a shows the temperature distribution and the melt pool when the laser is in motion. The upper limit of the temperature distribution is limited to the melting temperature. Hence, the red area represents the melt pool. Besides, a depression is formed at the laser application area due to the recoil pressure. The single track formed after the solidification is shown in Fig. 10b.

Single-track scans at various layer thicknesses of 20, 30, and 40 μm were simulated. The 2D melt pool profiles of these tracks were obtained from the center of the domain, shown in Fig. 11. Generally, the longitudinal profiles show a decreasing melt pool penetration depth along the laser traveling direction. The depth of the track appears maximum at the beginning, and depression is observed at the end of

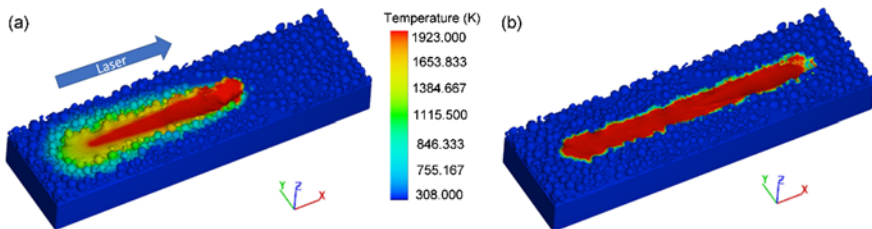


Fig. 10 **a** Temperature distribution during laser melting process, and **b** single-track solidification. (Color figure online)

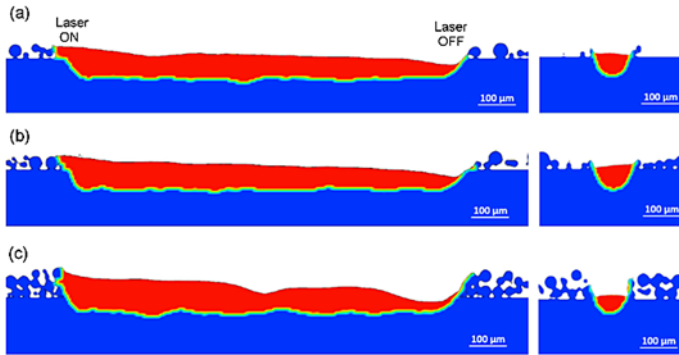


Fig. 11 Longitudinal (*Left*) and transverse (*Right*) melt pool profiles with layer thicknesses of **a** 20 μm , **b** 30 μm , and **c** 40 μm . (Color figure online)

track. The formation of such a profile occurs due to the backward melt flow driven by the thermo-capillary effect. The longitudinal profiles of the three tracks show little variation in the melt pool depth, while difference exists on the surface profiles that the 40 μm layer-thickness track (Fig. 11c) presents more fluctuation, which was observed in the experimental results as well. On the other hand, the transverse profiles of the three tracks are resulted semi-circular shape. Therein, the melt pool depth with 40 μm layer-thickness exhibits relative lower compared to those with 20 and 30 μm layer-thicknesses, while their transverse surface profiles do not vary with much variation. However, the counterparts from experiments were observed more fluctuation due to the presence of incomplete melted powder particles attached and denudation.

Conclusions

In this study, the mesoscopic formation of single-track scans was fabricated in a LPBF process, and examined the surface morphology under WLI. Using a consistent measure length of 1000 μm , the quasi-static regions of the single-track scans were examined in the longitudinal and transverse directions. Additionally, the discrete element method and 3D thermos-fluid modeling were utilized to simulate the powder spreading and laser scanning process.

The achieved findings are summarized: (1) The surface formation of single-track scans is significantly dependent on the fabrication parameters. At the powder laser thickness of 30 μm , higher laser power results in smoother surface finish, along with an increase in track width and bead height. (2) At a constant laser power and scan speed, the single-track scan formation is affected by the layer thickness. The increase in layer thickness leads to increasing track height. (3) When the layer thickness is 20 μm , a depression at the tail end of the track is observed. (4) In the longitudinal

direction, the roughness of single-track scans exhibits an increase with a decreasing of laser power at a certain scan speed and layer thickness, and with an ascending layer thickness at a constant laser processing parameters, including laser power and scan speed. (5) In the transverse direction, the quasi-steady roughness of single tracks presents an increase with an increasing laser power at a certain scan speed and layer thickness, and with an increasing laser thickness at a constant laser processing.

Acknowledgements This study is supported by Navy STTR Program (Contract No. N68936-20-C-0023). The authors acknowledge the technical support from Additive Manufacturing Institute of Science and Technology (AMIST) at University of Louisville.

References

1. ISO/ASTM52911-1-19, Additive manufacturing—Design—Part 1: Laser-based powder bed fusion of metals (2019). ASTM International, West Conshohocken, PA
2. Li P, Warner D, Fatemi A, Phan N (2016) Critical assessment of the fatigue performance of additively manufactured Ti–6Al–4V and perspective for future research. *Int J Fatigue* 85:130–143
3. Greitemeier D, Palm F, Syassen F, Melz T (2017) Fatigue performance of additive manufactured TiAl6V4 using electron and laser beam melting. *Int J Fatigue* 94:211–217
4. Kruth J-P, Deckers J, Yasa E (2008) Experimental investigation of laser surface remelting for the improvement of selective laser melting process. Paper presented at the 2008 international solid freeform fabrication symposium
5. Temmler A, Willenborg E, Wissenbach K (2011) Design surfaces by laser remelting. *Phys Procedia* 12:419–430
6. Mumtaz K, Hopkinson N (2010) Selective laser melting of thin wall parts using pulse shaping. *J Mater Process Technol* 210(2):279–287
7. Yadroitsev I, Smurov I (2010) Selective laser melting technology: from the single laser melted track stability to 3D parts of complex shape. *Phys Procedia* 5:551–560
8. Bidare P, Bitharas I, Ward R, Attallah M, Moore AJ (2018) Fluid and particle dynamics in laser powder bed fusion. *Acta Mater* 142:107–120
9. Qiu C, Panwisawas C, Ward M, Basoalto HC, Brooks JW, Attallah MM (2015) On the role of melt flow into the surface structure and porosity development during selective laser melting. *Acta Mater* 96:72–79
10. Martin AA, Calta NP, Khairallah SA, Wang J, Depond PJ, Fong AY, Thampy V, Guss GM, Kiss AM, Stone KH (2019) Dynamics of pore formation during laser powder bed fusion additive manufacturing. *Nat Commun* 10(1):1987
11. Gong H, Gu H, Zeng K, Dilip J, Pal D, Stucker B, Christiansen D, Beuth J, Lewandowski JJ (2014) Melt pool characterization for selective laser melting of Ti-6Al-4V pre-alloyed powder. Paper presented at the solid freeform fabrication symposium
12. Caprio L, Demir AG, Previtali B (2020) Observing molten pool surface oscillations during keyhole processing in laser powder bed fusion as a novel method to estimate the penetration depth. *Addit Manuf* 36: 101470
13. Ahn D, Kim H, Lee S (2009) Surface roughness prediction using measured data and interpolation in layered manufacturing. *J Mater Process Technol* 209(2):664–671
14. Dai D, Gu D (2015) Tailoring surface quality through mass and momentum transfer modeling using a volume of fluid method in selective laser melting of TiC/AlSi10Mg powder. *Int J Mach Tools Manuf* 88:95–107

15. Khairallah SA, Anderson A (2014) Mesoscopic simulation model of selective laser melting of stainless steel powder. *J Mater Process Technol* 214(11):2627–2636
16. Xia M, Gu D, Yu G, Dai D, Chen H, Shi Q (2016) Influence of hatch spacing on heat and mass transfer, thermodynamics and laser processability during additive manufacturing of Inconel 718 alloy. *Int J Mach Tools Manuf* 109:147–157
17. Shrestha S, Rauniyar S, Chou K (2019) Thermo-fluid modeling of selective laser melting: single-track formation incorporating metallic powder. *J Mater Eng Perform* 28(2):611–619
18. Yadroitsev I, Gusarov A, Yadroitsava I, Smurov I (2010) Single track formation in selective laser melting of metal powders. *J Mater Process Technol* 210(12):1624–1631
19. Mumtaz K, Hopkinson N (2010) Selective laser melting of Inconel 625 using pulse shaping. *Rapid Prototyp J*
20. Cheng B, Li X, Tuffile C, Ilin A, Willeck H, Hartel U (2018) Multi-physics modeling of single track scanning in selective laser melting: powder compaction effect. Paper presented at the 29th annual international solid freeform fabrication symposium—an additive manufacturing conference
21. Xiang Y, Zhang S, Wei Z, Li J, Wei P, Chen Z, Yang L, Jiang L (2018) Forming and defect analysis for single track scanning in selective laser melting of Ti6Al4V. *Appl Phys A* 124(10):685
22. Gu H, Wei C, Li L, Han Q, Setchi R, Ryan M, Li Q (2020) Multi-physics modelling of molten pool development and track formation in multi-track, multi-layer and multi-material selective laser melting. *Int J Heat Mass Transf* 151:119458

Part VI
Additive Manufacturing: Solid-State Phase
Transformations and Microstructural
Evolution

Evolution of Microstructure and Dispersoids in Al-Mg 5xxx Alloys Under Wire + Arc Additive Manufacturing and Permanent Mold Casting



K. Liu, A. Algendy, J. Gu, and X. -G. Chen

Abstract The microstructure and the formation of dispersoids in Al-Mg 5xxx alloys under wire + arc additive manufacturing (WAAM) and permanent mold casting (PM) were investigated with the aid of optical microscopy and scanning/transmission electron microscopies. In the as-deposited/as-cast condition, the grains and intermetallics in WAAM sample are finer, and its related microhardness is higher than PM sample. However, during the heat treatment at 425 °C, the formation of dispersoids in WAAM sample is slower with bigger size and lower volume, leading to its lower microhardness than PM sample. In addition, the area fraction of the dispersoid zone in WAAM sample is much lower than PM sample. Two types of dispersoids are observed in both WAAM and PM samples. The formation and distribution of dispersoids during heat treatment have been characterized aiming to discover the influence of fabrication processes (WAAM and PM) on the precipitation behavior of dispersoids.

Keywords Wire + arc additive manufacturing · Permanent mold casting · Al-Mg 5xxx alloys · Microstructure · Dispersoids

Introduction

The application of additive manufacturing (AM) process in aluminum alloys has gained continuously growing interests due to their less restrictions compared with the traditional fabrication process, especially on the parts with complex geometries. The wire + arc additivity manufacturing (WAAM) is one of the AM processes used dominantly for large scale aluminum structural parts with modern complexity due to its own advantages, i.e., lower equipment cost, higher deposition rate, and more design flexibility [1]. Up to date, a number of works have been carried out with

K. Liu (✉) · A. Algendy · X. -G. Chen
Department of Applied Science, University of Quebec at Chicoutimi, Chicoutimi, QC, Canada
e-mail: kun.liu@uqac.ca

J. Gu
Department of Materials Science and Engineering, Yanshan University, Hebei, China

WAAM on aluminum alloys, such as Al-Cu [2, 3], Al-Zn-Mg-Cu [4] and Al-Mg alloys [5, 6]. Among these alloys, Al-Mg-Mn 5xxx alloys attract particular interests due to their wide applications in aerospace, automobile, and marine industries because of their high strength and corrosion resistance [7]. Meanwhile, the WAAM process has been further optimized to improve the as-deposited mechanical properties of Al-Mg-Mn alloys [6, 8, 9]. For instance, the ultimate tensile strength of Al-Mg-Mn alloy has been improved from 273 MPa under gas tungsten arc welding (GTAW) [10] to 344 MPa when applying the inter-layer rolling to cold metal transfer (CMT) WAAM process [6].

Nowadays, the elevated-temperature properties of aluminum alloys are one of the hot interests due to the urgent demand from the automotive industry on improving the fuel efficiency and reducing the emission of greenhouse gas. The introduction of thermal-stable fine dispersoids through the proper heat treatment is approved to be one of most effective approaches to improve the elevated-temperature properties of aluminum alloys, such as in 3xxx and 6xxx wrought alloys [11–13]. In our previous work, the yield strength at 300 °C of Al-Mn-Mg 3004 alloys has been significantly enhanced from 55 MPa under industrial heat treatment (600 °C/4 h) to 97 MPa under newly developed two-step heat treatments (250 °C/24 h + 375 °C/48 h) with optimized alloy compositions [12]. In Al-Mg-Mn 5xxx alloys, the research of dispersoids is principally focusing on their role during the hot deformation [14–16], while limited study has been performed on the optimization of characteristics of dispersoids (distribution, size and volume fraction) at relatively low heat treatment temperature, such as 350–450 °C [11]. On the other hand, the after-deposition heat treatment is seldom applied after WAAM process in Al-Mg-Mn alloys due to their weak contribution from the precipitation strengthening, and there are much little researches on discovering the flexibility of WAAM Al-Mg-Mn alloy on the elevated-temperature applications. Therefore, it is of interest to investigate the evolution of dispersoids in WAAM 5xxx alloys.

In the present work, a comparison on the microstructure and the formation of dispersoids in Al-Mg-Mn 5183 alloys under WAAM and traditional permanent mold casting (PM) was performed. The formation and evolution of intermetallic compounds (IMCs) under the as-deposited/as-cast conditions and after heat treatment have been studied and quantified. Meanwhile, the formation behavior of dispersoids during the heat treatment has been preliminarily studied regarding to the two different manufacturing processes.

Experimental

The Al-5%Mg-0.7%Mn alloys were prepared under WAAM and PM methods and their chemical compositions analyzed using an optical emission spectrometer (OES) are shown in Table 1.

For WAAM samples, it was provided by Yanshan University (China) and fabricated by WAAM using the commercial 5183 wire with a diameter of 1.2 mm.

Table 1 Chemical composition of experimental alloys

Alloy code	Elements, wt%						
	Mg	Mn	Si	Fe	Cr	Ti	Al
WAAM	5.1	0.67	0.05	0.1	0.08	0.1	Bal.
PM	5.2	0.72	0.26	0.31	0.18	0.1	Bal.

The WAAM deposition system was mainly comprised of a self-developed variable polarity gas tungsten arc welding (VP-GTAW) power supply, a moving working table, wire feeder system, and torch. A 12 mm thick 5083 aluminum alloy plate was used as the substrate, which was cleaned by using the alkaline water, mechanical brushing, and acetone in sequence before usage. A single-track straight wall was built layer by layer. A variable pulse of 130 A positive current and 150 A negative current with a duration time ratio of 4:1 was adopted in manufacturing. Meanwhile, the wire feeding speed (2.4 m/min), travel speed (300 mm/min), contact tip to work-piece distance (15 mm), shielding gas flow rate of pure Ar (15 L/min), and the diameter of the tungsten electrode (3.2 mm) were set as constant during deposition. One WAAM wall with a dimension of 380 × 110 × 6.3 mm was deposited. More details can be found in [17].

For PM samples, it was prepared with commercially pure Al (99.7%) and pure Mg (99.9%), Al-25%Fe, Al-50%Si, Al-25%Mn, Al-10%Cr, and Al-5%Ti-1%B master alloys. Approximately, 3 kg of material was prepared in a clay-graphite crucible using an electric resistance furnace. The temperature of the melt was maintained at ~750 °C for 30 min. The melt was degassed for 15 min and then poured into a permanent mold preheated at 250 °C. The dimension of cast ingots was 30 × 40 × 80 mm.

After decomposition/solidification, a heat treatment at 425 °C up to 24 h followed by the water quench to room temperature was applied on two experimental alloys to study the formation and evolution of dispersoids during the heat treatment. The selection of the heat treatment temperature is based on the precipitation behavior of dispersoids in 5xxx Al-Mg alloys [11, 18].

The microstructural features, including the grain structures, intermetallics, and dispersoids under different conditions, were observed by optical and electron microscopes. To reveal the dispersoids clearly, the polished samples were etched in 0.5% HF for 30 s. The grain structure was characterized by polarized-light optical microscopy after electron-etching. A scanning electron microscope (SEM) equipped with an energy dispersive x-ray spectrometer (EDS) and electron backscatter diffraction (EBSD) was used to identify the various intermetallics while the dispersoids were principally characterized by a transmission electron microscope (TEM).

In addition, the evolution of dispersoids was also evaluated by the electrical conductivity (EC) and microhardness, which were measured at room temperature. The EC was taken as the average value of 5 measurements, while microhardness was the average of 20 measurements with a load of 25 g and a dwell time of 20 s. It should

be mentioned that the polishing surface of all WAAM samples as well as the TEM sample were taken from transvers section of the “intra layer” rather than the “inter layer” of last 2–3 layers to have a better uniform distribution of microstructure [3].

Results and Discussion

Microstructure Under As-Deposited/As-Cast and Heat-Treated Conditions

Figure 1 shows the grain structures of WAAM and PM samples under as-deposited/as-cast conditions and after heat treatment at 425 °C/24 h. As shown in Fig. 1a, b, the grains in both WAAM and PM samples are equiaxed and the grain size of WAAM sample is slightly smaller than the PM sample, which is 52 μm of WAAM sample (similar to the grain size reported in [19]) compared with 64 μm of PM sample. After 425 °C/24 h, the grains in both samples grew moderately, in which the grain size increases to 54 μm for WAAM sample and to 78 μm for PM sample (Fig. 1c, d), which is also reported in the literature [20]. The minor difference on the grain

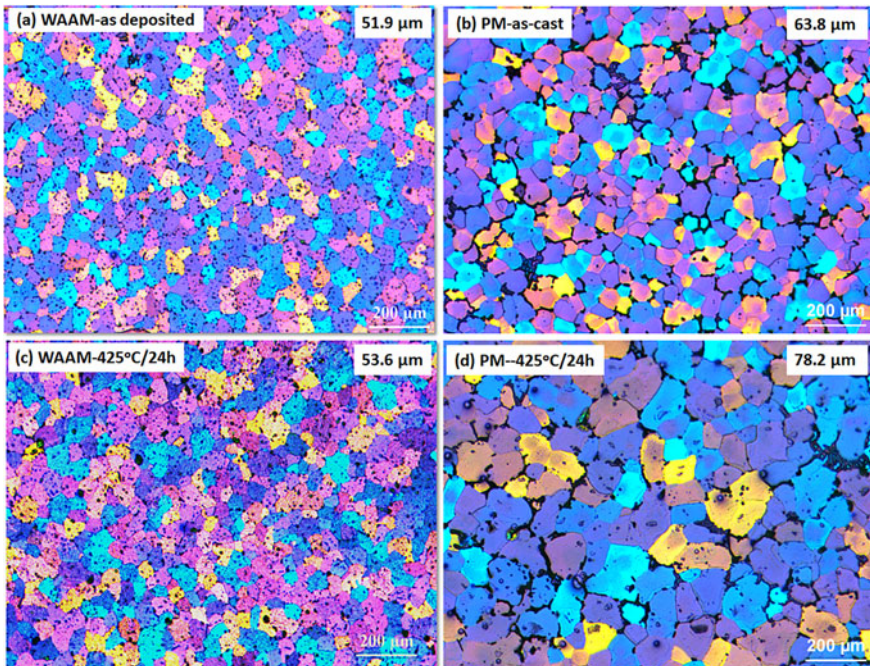


Fig. 1 Grain structures and sizes of WAAM and PM samples at as-deposited/as-cast (a, b) and after 425 °C/24 h (c, d). (Color figure online)

structures between WAAM and PM is likely attributed to the different manufacturing processes that the cooling rate and the temperature gradient of WAAM is higher than that in PM [1, 6].

In addition, as shown in Fig. 1, the size and volume of IMCs (black particles at the grain boundaries) are finer and lower in WAAM than that in PM. Detailed distribution of IMCs is shown in Fig. 2 and Table 2. As shown in Fig. 2a, the IMCs are much finer under as-deposited condition of WAAM sample compared with the coarse IMCs in as-cast PM sample (Fig. 2c). Meanwhile, the volume of IMCs is greatly different between WAAM and PM. As shown in Table 2, the total area fraction of IMCs is 3 times higher in PM than WAAM, which is 3.72% in PM vs. 1.26% in WAAM.

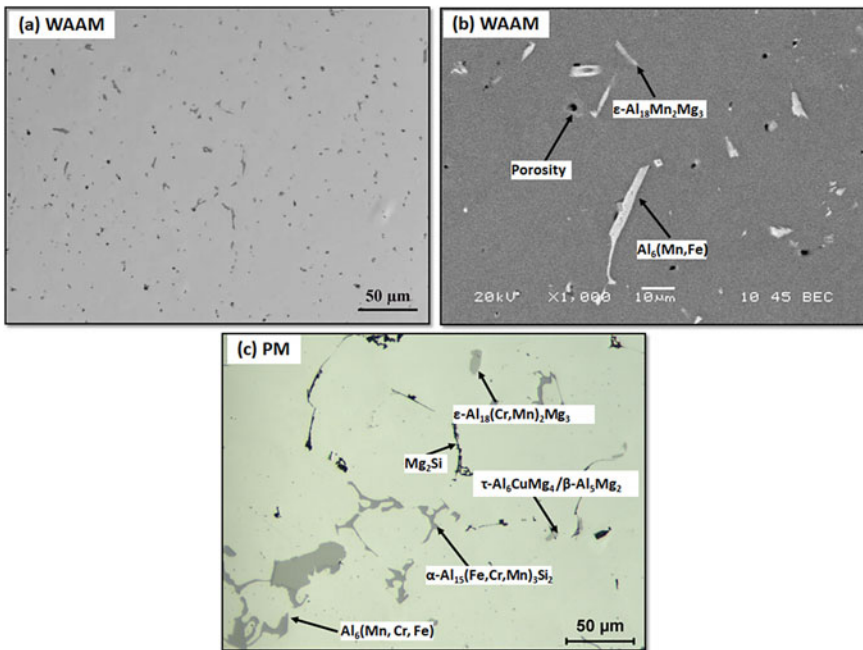


Fig. 2 IMCs in as-deposited WAAM (a, b) and as-cast PM (c) sample. (Color figure online)

Table 2 Area fractions of IMCs of WAAM and PM samples

IMCs	Conditions			
	WAAM		PM	
	as-deposited	425 °C/24 h	as-cast	425 °C/24 h
Fe-rich IMCs	1.13 ± 0.4	1.12 ± 0.3	2.78 ± 0.6	2.46 ± 1.2
Mg ₂ Si	0.11 ± 0.05	0.09 ± 0.03	0.82 ± 0.3	0.65 ± 0.4
Others	0.02 ± 0.01	0.02 ± 0.01	0.12 ± 0.04	0.05 ± 0.02
Total	1.26	1.23	3.72	3.16

Among all IMCS, the Fe-rich IMCs is dominant in both WAAM and PM samples, and the significant difference on their volume can be related to the higher Fe in PM (0.31 wt%) than that in WAAM (0.13 wt%). In addition, the type and the morphology of IMCs is also different between WAAM and PM. As shown in Fig. 2b, only platelet $\text{Al}_6(\text{Mn, Fe})$ and block-like $\epsilon\text{-Al-Mn-Mg}$ phase are detected in as-deposited WAAM sample [6], while more types of IMCs are observed in as-cast PM sample (Fig. 2c), which include the Chinese script $\alpha\text{-Al}_{15}(\text{Fe, Cr, Mn})_3\text{Si}_2$, Mg_2Si , block $\tau\text{-Al-Cu-Mg}$ and $\beta\text{-Al}_5\text{Mg}_2$ in addition to the Chinese script $\text{Al}_6(\text{Mn, Cr, Fe})$ and block-like $\epsilon\text{-Al-Mn-Mg}$. The difference is likely due to the higher Si as well as the lower cooling rate in PM sample, especially for the $\alpha\text{-Al}_{15}(\text{Fe, Cr, Mn})_3\text{Si}_2$ as well as the $\tau\text{-Al-Cu-Mg}$ and $\beta\text{-Al}_5\text{Mg}_2$, which are generally reported in traditional permanent mold casting [18]. Meanwhile, the morphology in Chinese script Fe-rich IMCs, such as, $\alpha\text{-Al}_{15}(\text{Fe, Cr, Mn})_3\text{Si}_2$ and $\text{Al}_6(\text{Mn, Cr, Fe})$, is well developed in PM sample with branches in different directions, while $\text{Al}_6(\text{Mn, Fe})$ are still in the platelet without any branches in WAAM sample. The presence of Fe-rich IMCs in both WAAM and PM samples are further confirmed by SEM-EBSD with lower mean angular value (MAD) than 0.7 [21]. One example of $\text{Al}_6(\text{Mn, Fe})$ phase in WAAM sample is shown in Fig. 3, confirmed by the EBSD pattern with the MAD of 0.245.

Figure 4 shows the distribution of IMCs in two experiment alloys after $425^\circ\text{C}/24\text{h}$. There is only a small change of Fe-rich IMCs observed in both WAAM and PM

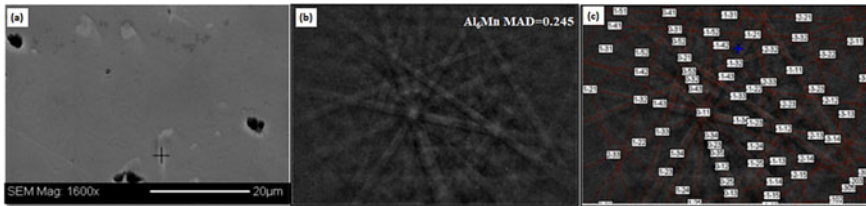


Fig. 3 EBSD identification of Al_6Mn in WAAM sample: (a) phase under SEM; (b) EBSD pattern and (c) simulated results. (Color figure online)

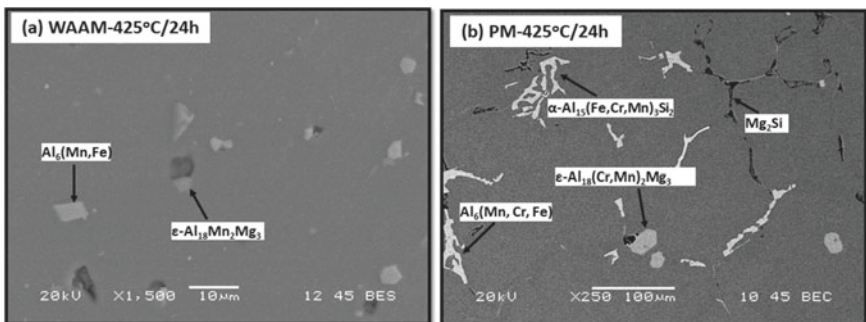


Fig. 4 IMCs in WAAM (a) and PM (b) samples after $425^\circ\text{C}/24\text{h}$

samples, while some low-melting-point phases, such as τ -Al-Cu-Mg, β -Al₅Mg₂ and Mg₂Si, are partially dissolved into the aluminum matrix in PM sample. This is further confirmed by the evolution of IMCs in Table 2, in which the total area fraction of IMCs is stable at 1.23–1.26% in WAAM sample, while it decreases from 3.72% under as-cast to 3.16% after 425 °C/24 h.

Formation of Dispersoids During Heat Treatment

Figure 5 shows the evolution of EC and microhardness of both experimental alloys when treated at 425 °C. The time of “0” indicates the as-deposited/as-cast condition. As shown in Fig. 5, the EC of WAAM is higher than PM (21.2 versus 19.1%IACS in Fig. 5a) but the microhardness is also still higher (103 versus 98 HV in Fig. 5b) at as-deposited/as-cast condition. It is widely accepted the evolution of EC can be an indicator of the solution level of atoms in the aluminum matrix, especially the Mn element [11]. However, the higher EC in WAAM is not expected, which indicates the less Mn in the matrix after solidification. As shown in Table 2, much lower volume Fe-rich IMCs formed during the solidification of WAAM, which should consume less Mn than PM sample. Moreover, a higher cooling rate of WAAM is favorable to increase the supersaturate solid solution level of Mn in the matrix. More investigation will be performed to discover the reason. On the other hand, though the higher EC of WAAM sample indicated a lower level of solid solution and hence a less contribution on the microhardness, the microhardness of as-deposited WAAM sample is still higher than PM sample (103 HV versus 98 HV). The reason is not fully understood, but it is possibly due to the residual strain and relative higher dislocation density during the WAAM process than PM [6, 22]. It is reported that the microhardness of as-deposited Al-Mg-Mn 5083 alloy improved from 75 to 107 after applying the inter-layer rolling between the each deposited layer [6].

During heat treatment, it can be found that the EC values of both WAAM and PM samples increase with the time. However, the increase rates are different between

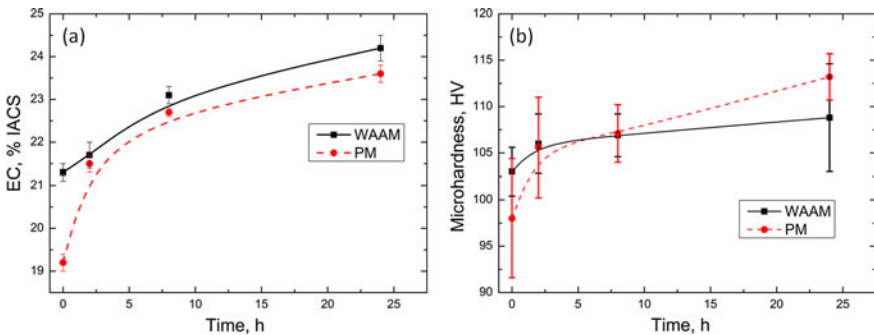


Fig. 5 Evolution of EC (a) and microhardness (b) during heat treatment at 425 °C. (Color figure online)

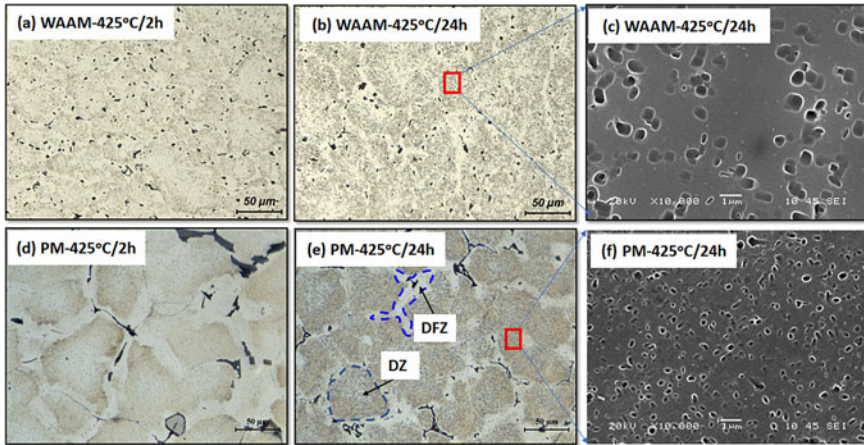


Fig. 6 Distribution of dispersoids during heat treatment in WAAM and PM samples. (Color figure online)

two samples, especially at the first 2–8 h when the increase of EC in WAAM sample is considerably slower than that in PM sample (Fig. 5a). The similar tendency exists for the increase of microhardness (Fig. 5b). As shown in Fig. 5b, the HV of WAAM increases from 103 HV at as-deposited condition slightly to 106 HV after 425 °C/2 h and 108 HV after 425 °C/24 h, while it gradually increases from 98 HV to 106 HV and further to 113 HV for PM sample. The increase in EC with time is principally attributed to the decomposition of supersaturated solid solution of Mn and to the formation of the dispersoids. Consequently, the hardness increase with time is due to the increasing presence of dispersoids and their strengthening effect on the matrix [11, 12]. Therefore, the evolution of EC and microhardness in Fig. 5 indicates the distinct precipitation behavior of dispersoids between WAAM and PM samples.

Figure 6 displays the distribution of dispersoids after 2 and 24 h during heat treatment. It can be found that the precipitation of dispersoids in WAAM sample (Fig. 6a–c) is not as obvious as that in PM sample (Fig. 6d–f). For instance, the dispersoids are already observable after 2 h in PM sample (Fig. 6d), while it is very weaker in WAAM sample (Fig. 6a), explaining the faster increase in EC and microhardness of PM samples than that in WAAM samples (Fig. 5). Even after 24 h, the dispersoids are still sparsely distributed in the matrix of WAAM sample (Fig. 6b) while the dispersoids zone (DZ) and dispersoids free zone (DFZ) [11] are obvious in PM sample (Fig. 6e). Under the SEM observation in the DZ (Fig. 6c, f), it can be found that the dispersoids in WAAM are considerably less dense and their size is bigger (Fig. 6c) than that in the PM sample (Fig. 6f). The number density in WAAM is around $0.8/\mu\text{m}^2$, while it is $6.8/\mu\text{m}^2$ in PM sample after 425 °C/24 h, explaining the lower microhardness of WAAM than PM (108 HV versus 113 HV in Fig. 5b). The likely reason for the bigger but lower volume of dispersoids in WAAM sample can be principally attributed to the lower Mn supersaturated solid solute level indicated by the higher EC at as-deposited condition (Fig. 5a). Another possible reason can be the

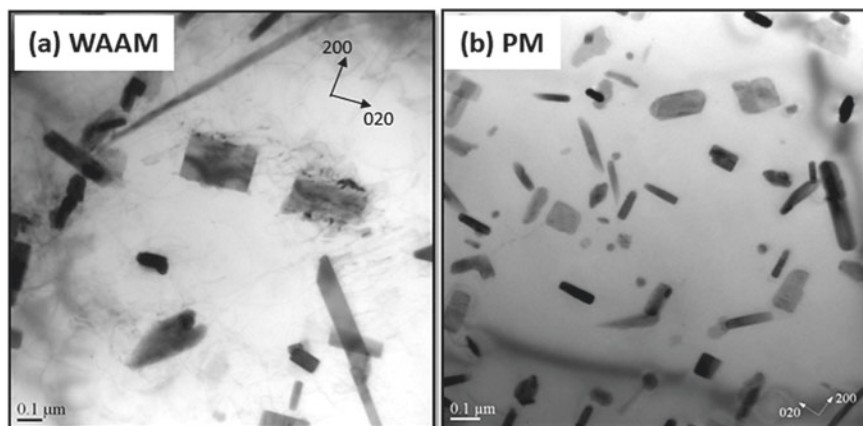


Fig. 7 Dispersoids in WAAM (a) and PM, (b) samples after 425 °C/24 h

lower Si level in WAAM sample, which reduces the formation of intermediate Mg_2Si phase during the heating process of heat treatment, which favors the nucleation of dispersoids [12].

TEM study was further performed to obtain the detailed information of dispersoids and the distribution of dispersoids after 425 °C/24 h are shown in Fig. 7. The characteristics of dispersoids are similar with finding from the SEM results in Fig. 6, namely the number density of dispersoids is lower and the size is bigger in WAAM sample than that in PM sample. As shown in Fig. 7a, only few and large dispersoids can be observed in WAAM sample, while many fine dispersoids are present in PM sample (Fig. 7b). Therefore, it can be concluded that the precipitation of dispersoids in WAAM sample is slower than that in PM sample during the heat treatment at 425 °C.

As shown in Fig. 7, there are generally two types of dispersoids classified from their morphology: cubic/block-like and rod-like in both WAAM and PM samples. From the morphology and TEM-EDS results as well the information from literature [15, 16], the cubic/block-like dispersoids are likely to be Al_4Mn , while the rod-like ones are likely belonged to Al_6Mn . As shown in Fig. 7, it seems that the fraction of cubic/block dispersoids in WAAM is higher than that in PM sample and more systematically work will be performed to identify and quantify the different dispersoids. In the present work, due to the limited materials, only the preliminary comparison on the microstructure between WAAM and PM samples were performed, and the detailed evolution of dispersoids and their effect on elevated-temperature mechanical properties in WAAM and PM samples will be investigated in the future.

Summary

In the present work, the evolution of microstructure and dispersoids under the as-deposited/as-cast conditions and during heat treatment for two different manufacturing processes (WAAM and PM) was preliminary investigated and the main conclusions can be drawn:

1. In the as-deposited/as-cast condition, the grains in both WAAM and PM samples are equiaxed and the grain size of WAAM sample is slightly smaller than the PM sample, while the IMCs in WAAM sample are much finer and its related microhardness is higher than sample. On the other hand, more types of IMCs were observed in PM sample, such as the α -Al₁₅(Fe, Cr, Mn)₃Si₂, τ -Al-Cu-Mg and β -Al₅Mg₂ in addition to the Al₆(Mn, Fe) and block ϵ -Al-Mn-Mg present in both WAAM and PM samples.
2. During the heat treatment at 425 °C, the precipitation of dispersoids in WAAM sample is slower and dispersoids have bigger size and lower volume. Due to this fact, the microhardness in WAAM sample after heat treatment is lower than that in PM sample.
3. Two types of dispersoids (cubic/block-like Al₄Mn and rod-like Al₆Mn) are observed after the heat treatment in both WAAM and PM samples. Future work is dedicated on the detailed evolution of dispersoids and their effect on elevated-temperature properties.

Acknowledgements The authors would like to acknowledge the financial support of the Natural Sciences and Engineering Research Council of Canada (NSERC) under the Grant No. CRDPJ 514651-17 through the Research Chair in the Metallurgy of Aluminum Transformation at University of Quebec in Chicoutimi.

References

1. Wu B, Pan Z, Ding D, Cuiuri D, Li H, Xu J, Norrish J (2018) A review of the wire arc additive manufacturing of metals: properties, defects and quality improvement. *J Manuf Process* 35:127–139
2. Fang X, Zhang L, Li H, Li C, Huang K, Lu B (2018) Microstructure evolution and mechanical behavior of 2219 aluminum alloys additively fabricated by the cold metal transfer process. *Materials* 11(5):812
3. Gu J, Bai J, Ding J, Williams S, Wang L, Liu K (2018) Design and cracking susceptibility of additively manufactured Al-Cu-Mg alloys with tandem wires and pulsed arc. *J Mater Process Technol* 262:210–220
4. Xie C, Yang S, Liu H, Zhang Q, Wang Y, Zou Y (2018) Microstructure and mechanical properties of robot cold metal transfer Al5.5Zn2.5Mg2.2Cu aluminium alloy joints. *J Mater Process Technol* 255:507–515
5. Horgar A, Fostervoll H, Nyhus B, Ren X, Eriksson M, Akselsen OM (2018) Additive manufacturing using WAAM with AA5183 wire. *J Mater Process Technol* 259:68–74

6. Gu J, Wang X, Bai J, Ding J, Williams S, Zhai Y, Liu K (2018) Deformation microstructures and strengthening mechanisms for the wire + arc additively manufactured Al-Mg4.5Mn alloy with inter-layer rolling. *Mater Sci Eng A* 712:292–301
7. Thapliyal S (2019) Challenges associated with the wire arc additive manufacturing (WAAM) of aluminum alloys. *Mater Res Express* 6(11):112006
8. Colegrove PA, Coules HE, Fairman J, Martina F, Kashoob T, Mamash H, Cozzolino LD (2013) Microstructure and residual stress improvement in wire and arc additively manufactured parts through high-pressure rolling. *J Mater Process Technol* 213(10):1782–1791
9. Xie Y, Zhang H, Zhou F (2016) Improvement in geometrical accuracy and mechanical property for arc-based additive manufacturing using metamorphic rolling mechanism. *J Manuf Sci Eng* 138(11)
10. Geng H, Li J, Xiong J, Lin X, Zhang F (2017) Geometric limitation and tensile properties of wire and arc additive manufacturing 5A06 aluminum alloy parts. *J Mater Eng Perform* 26(2):621–629
11. Liu K, Chen XG (2015) Development of Al–Mn–Mg 3004 alloy for applications at elevated temperature via dispersoid strengthening. *Mater Des* 84:340–350
12. Liu K, Ma H, Chen XG (2018) Improving the elevated-temperature properties by two-step heat treatments in Al–Mn–Mg 3004 alloys. *Metall Mater Trans B* 49(4):1588–1596
13. Li C, Liu K, Chen XG (2020) Improvement of elevated-temperature strength and recrystallization resistance via Mn-containing dispersoid strengthening in Al–Mg–Si 6082 alloys. *J Mater Sci Technol* 39:135–143
14. Kannan K, Vetrano JS, Hamilton CH (1996) Effects of alloy modification and thermo-mechanical processing on recrystallization of Al–Mg–Mn alloys. *Metall Mater Trans A* 27(10):2947–2957
15. Li YJ, Zhang WZ, Marthinsen K (2012) Precipitation crystallography of plate-shaped Al₆(Mn, Fe) dispersoids in AA5182 alloy. *Acta Mater* 60(17):5963–5974
16. Lee S-L, Wu S-T (1987) Identification of dispersoids in Al–Mg alloys containing Mn. *Metall Trans A* 18(8):1353–1357
17. Sun R, Li L, Zhu Y, Guo W, Peng P, Cong B, Sun J, Che Z, Li B, Guo C, Liu L (2018) Microstructure, residual stress and tensile properties control of wire-arc additive manufactured 2319 aluminum alloy with laser shock peening. *J Alloys Compd* 747:255–265
18. Engler O, Miller-Jupp S (2016) Control of second-phase particles in the Al–Mg–Mn alloy AA 5083. *J Alloys Compd* 689:998–1010
19. Su C, Chen X, Gao C, Wang Y (2019) Effect of heat input on microstructure and mechanical properties of Al–Mg alloys fabricated by WAAM. *Appl Surf Sci* 486:431–440
20. Yang Q, Xia C, Deng Y, Li X, Wang H (2019) Microstructure and mechanical properties of AlSi7Mg0.6 aluminum alloy fabricated by wire and arc additive manufacturing based on cold metal transfer (WAAM-CMT). *Materials* 12(16):2525
21. Liu K, Cao X, Chen XG (2013) Formation and phase selection of iron-rich intermetallics in Al–4.6Cu–0.5Fe cast alloys. *Metall Mater Trans A* 44(2):682–695
22. Hönnige JR, Colegrove PA, Ganguly S, Eimer E, Kabra S, Williams S (2018) Control of residual stress and distortion in aluminium wire + arc additive manufacture with rolling. *Addit Manuf* 22:775–783

Main Microstructural Characteristics of Ti-6Al-4V Components Produced via Electron Beam Additive Manufacturing (EBAM)



Silvia Lopez-Castaño, Philippe Emile, Claude Archambeau, Florence Pettinari-Sturmel, and Joël Douin

Abstract Electron Beam Additive Manufacturing (EBAM) is a Wire Directed Energy Deposition (W-DED) process that is receiving much more attention than other Additive Manufacturing (AM) techniques, especially in the aeronautical sector for the serial production of metallic parts. However, this technique leads to singular microstructures due to the rapid heating and cooling cycles generated during the deposition of the pieces. In this work, a first identification of the main microstructural features of Ti-6Al-4V parts manufactured by EBAM technology is performed to better understand the general characteristics of this type of parts for further improvement of this technology. The characterization is carried out by means of Optical Microscopy (OM), Scanning Electron Microscopy (SEM) observations, and Energy Dispersive X-Ray Spectrometry (EDS) analysis. The most remarkable aspects found are the formation of long columnar prior beta grains throughout several layers in the built material and the presence of many parallel thermal bands perpendicular to the thermal gradient. Quantitative measurements such as the average width of the α lamellae, the volume fraction of β phase, and the chemical composition at different positions are also accomplished. A heterogeneous microstructure is reported, which mainly derives from the complex and diverse thermal histories at the different positions of the deposited material. In addition, Al vaporisation is noticed. However, no significant change along the deposit material is observed for a same configuration. Next, experiments will focus on the influence of different key processing parameters on the microstructure and mechanical properties.

Keywords Additive manufacturing · Directed energy deposition (DED) · Titanium alloys · Heterogeneity · Microstructure

S. Lopez-Castaño (✉) · P. Emile · C. Archambeau
Airbus Operations S.A.S, 316 Route de Bayonne, 31060 Toulouse, France
e-mail: silvia.lopez-castano@airbus.com

S. Lopez-Castaño · F. Pettinari-Sturmel · J. Douin
CEMES-CNRS, Université de Toulouse, 29 Rue Jeanne Marvig, 31055 Toulouse, France

Introduction

Additive Manufacturing (AM), also known as three-dimensional (3D) printing, includes the set of processes that allow the production of components layer-by-layer from a virtual geometry or 3D computer-aided design (CAD) model of the sliced part [1]. These techniques have been developed over the last 30 years and they present today an interesting alternative to conventional manufacturing technologies, especially in the aerospace industry, as they are able to meet both technical and economic needs such as cost and environmental impact reduction [2, 3]. There are multiple AM processes that can be classified according to different criteria, for example, energy source (e.g. laser, electron beam or plasma/arc), or initial feedstock (e.g. powder or wire) [4]. Among all of them, Wire Directed Energy Deposition (W-DED) technologies are today very interesting in several sectors where the serial production of large metal workpieces is important. This is due to its high deposition rates and its big build envelopes [5]. Nowadays, there are several W-DED systems that are under development including Wire and Laser Additive Manufacturing (WLAM) [6], Wire Arc Additive Manufacturing (WAAM) [7], and Electron Beam Additive Manufacturing (EBAM) [8]. In particular, EBAM technology has been the first one to be commercialized and it is the one studied in this paper.

AM processes are already applied in different engineering metallic materials including, for example, aluminum alloys, titanium alloys, nickel-based superalloys and steels [9]. Titanium alloys are particularly of interest for AM because of their frequent use in aeronautical applications where the buy-to-fly ratio is very high when using conventional manufacturing methods. This ratio could be significantly reduced thanks to AM, from the range of 10–20 to nearly 1, thus reducing considerably the manufacturing cost, material waste, and at the same time giving the possibility to produce light-weight structures [10]. The alloy studied in the present paper is Ti-6Al-4V alloy, the most widely used titanium alloys in the aerospace sector due to its remarkable combination of low density, high strength resistance, and high corrosion resistance in multiple chemical media at low to moderate temperatures [11]. Ti-6Al-4V is a typical $\alpha + \beta$ dual phase alloy whose microstructure is very sensitive to thermal history from which a wide range of microstructures, and therefore mechanical properties, can be obtained at room temperature [12].

On the other hand, one of the main drawbacks of AM technologies is their complex periodic heat treatments, which are not yet accurately controlled, that produce singular, heterogeneous, and anisotropic microstructures throughout the built part compared to traditional technologies. These complex thermal cycles are generated when depositing different layers, and they are dependent on the processing parameters of the AM technology [13]. In the case of the EBAM process, a huge amount of processing parameters are available, what makes its understanding even more complicated. Another challenge of AM technology includes the thermal residual stresses that are created due to the severe temperature gradients developed during the deposition process. Reducing residual stresses is crucial as they can decrease the mechanical properties and hence degrade the performance of the components in

service. In order to tackle this and be able to use EBAM technology for the production of aeronautical parts, stress relief treatments are usually applied to near-net shape parts.

Therefore, to ensure that AM is a viable manufacturing process, the microstructure must be well understood and controlled in order to produce components with reliable and repeatable mechanical properties. Some studies have already been performed on the microstructural evolution of AM-ed Ti-6Al-4V parts for different processes [14, 15]. From them, it is well known that there is a similarity in some of the features, although every process has its own specificities.

Limited work has been done on Ti-6Al-4V components produced with electron beam deposition with wire. The purpose of this research is to make a first identification of the main microstructural characteristics of the as-received Ti-6Al-4V parts manufactured by EBAM technology. This will provide a general idea of the predominant microstructure features that have to be taken into account when searching for the best configuration in terms of processing parameters, in order to achieve the desired mechanical properties.

Materials and Methods

The present study was performed on a single-bead component that was deposited on a thick rolled Ti-6Al-4V substrate. The starting feedstock material was a 3.2 mm diameter wire of Ti-6Al-4V, and the deposition was performed by an EBAM machine. The EBAM technology consists in an electron beam that melts the wire, depositing it layer-upon-layer until the part is built as desired. This system operates in a high-performance vacuum environment with a work envelope of $1.778 \times 1.194 \times 1.6$ m and a pressure of 10^{-4} mbar. This vacuum conditions prevents the oxidation in the melted pool, making EBAM technology a good choice for refractory alloys such as Ti-6Al-4V. The chosen coordinate system is shown schematically in Fig. 1a along with the rest of components of the EBAM system.

The single-bead wall was deposited with a length of 235 mm, a width of 15 mm and a height of 60 mm using nominal parameters. The deposition pattern used was simple, as seen in Fig. 1b. Once deposited, it underwent a stress relieved heat treatment at 650 °C for 3 h.

For microstructural characterizations, samples of 3 mm of thickness were cut by wire electrical discharge machining along the YZ plane including the substrate. The samples were grounded with papers up to 4000 grit, as well as chemical-mechanical polished using OPS solution following the standard metallographic techniques. Finally, they were chemically attacked using Kroll's etchant in order to reveal the microstructure.

Optical microscopy (OM) and Scanning Electron Microscopy (SEM) observations were conducted on OLYMPUS DSX100 and FIB Helios Nanolab 600i microscopes, respectively. Prior β grain widths were measured using the intercept method described in the technical standard ASTM E112-13. Moreover, chemical analyses were also

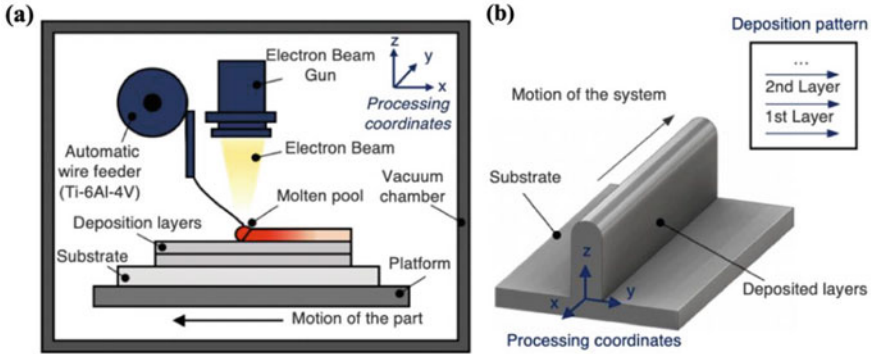


Fig. 1 Schematic drawing of the characteristics of **a** the EBAM technology and **b** the studied single-bead deposit. (Color figure online)

performed using FEI Quanta FEG 250 scanning electron microscope equipped with Energy Dispersive Spectrometer device (EDS). In addition to the qualitative investigations, quantitative measurements such as the average width of α lamellae, the volume fraction of β phase, and the chemical composition throughout the part height are also carried out. In order to perform the quantification of the first two features, two SEM images for each position with a $\times 2000$ magnification were analysed in an image processing program developed using MATLAB software following the stereological procedure outlined by [16].

Results and Discussion

Macrostructure Features

A macrograph of a Ti-6Al-4V part fabricated by EBAM technique is shown in Fig. 2a. A very dense structure with no porosities can be distinguished. In addition, three different regions are identified:

- Zone 1** corresponds to the area where the substrate is present. In this region, the substrate is affected by the heat generated due to the deposition of the first layers. As shown in Fig. 2b, this creates at the same time three distinct areas. The base material (BM) region is not affected by the generated heat, and therefore, its microstructure is the same as the as-received material (e.g. globular primary grains elongated in the rolling direction). Then, the heat affected zone (HAZ) is distinguished, whose peak temperature is sufficiently high but below the β transus temperature (T_β , which is around 995 °C) that creates a equiaxed grain structure. These equiaxed grains become bigger from the bottom to the top of this area. Finally, the fusion zone (FZ) is identified, with a local temperature higher than T_β

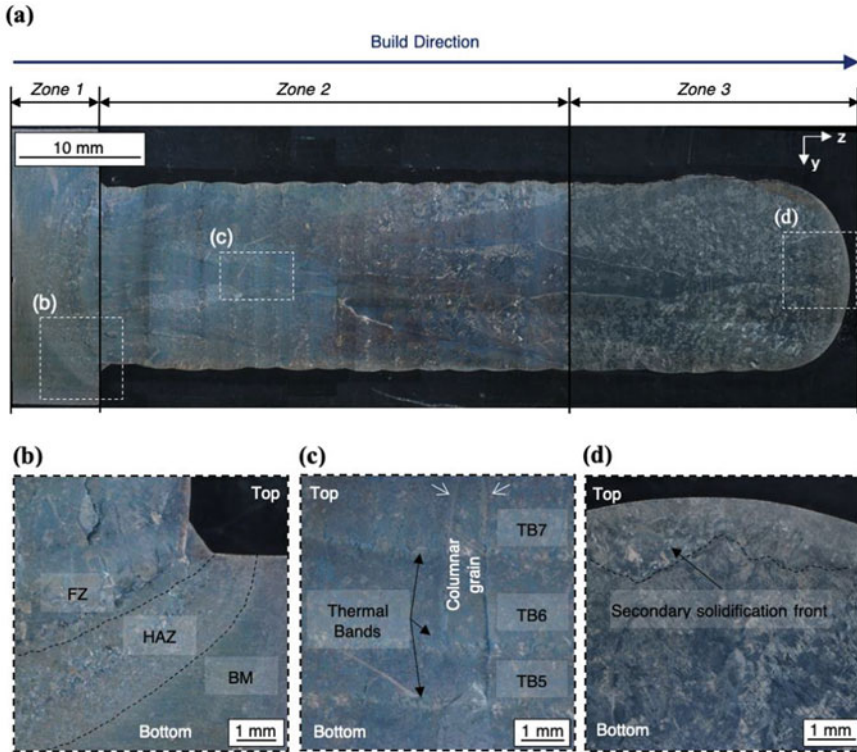


Fig. 2 **a** Macroscopic cross section (YZ plane) of the Ti-6Al-4V EBAM component and in detail, **b** the different areas inside the substrate in Zone 1, **c** the presence of thermal bands and elongated columnar grain in Zone 2 and **d** the absence of thermal marks and the presence of a secondary solidification front in Zone 3. (Color figure online)

when the first layer is deposited. In this area, large columnar prior β grains start to grow perpendicularly to the substrate along multiple layers up to almost the top of the deposit in Zone 3, indicating an epitaxial growth towards the heat flux. The mean prior β grain width in the entire part increases with the increase build height being 0.6 mm, 1.78 mm, and 2.49 mm, respectively, in the bottom, middle and top of the deposit. Finally, note that such elongated prior β grains is a typical feature of metal AM, and it has been linked to anisotropy in the mechanical properties [13].

- **Zone 2** is the area of the deposit wall that is reheated below T_{β} when depositing the last layer. As seen in Fig. 2c, it is characterized by the presence of parallel bands, which can be distinguished from the rest of the microstructure under OM observations because of their characteristic color. In this specific case, they seem to be almost regularly distributed as few variations in the processing parameters were done during the deposition. These bands are another characteristic commonly observed in metal AM, which are created due to thermal cycling effects. For this

reason, in the present work, these bands will be named “thermal bands” from now on. Similar thermal bands are reported in other DED techniques such as in LMD [17], SMD [18] and WAAM [19]. Their structure is addressed in detail in the microstructure analysis further down.

- **Zone 3** includes the area where no parallel bands are visible as it has been entirely heated above the T_{β} when the last layer was deposited (Fig. 2d). In the present case, this region measures 23.5 mm, which means that the area melted and re-melted was very deep as it went through several layers. Therefore, important heat input and melt pool in the last layer is applied. Moreover, the presence of a secondary solidification front is seen at the top of this zone where equiaxed grains are present.

Quantitative compositional analysis using EDS technique were also performed all along the build as shown in Fig. 3. In previous studies, aluminum vaporization was observed in AM-ed Ti-6Al-4V parts, especially in processes that operate under vacuum such as in EBM [20] and EBAM [21] techniques. In addition, it was shown that the loss in aluminum content depends on the processing parameters applied (e.g., power, wire feed speed and transverse speed) and it results in a decreased of the mechanical properties. In Fig. 3, it can be seen that, for a same configuration, a decreased in Al content starts at the FZ and then it remains almost constant throughout the rest of the deposit wall. This is because at the FZ, as well-known in welding processes, the base material, and filler material are mixed, and therefore, the resulting chemical composition results in a combination of both. Moreover, it is evident that Al content is decreased when the metal is melted. In this case, the difference between the material melted and not melted is around 1%, which may be non-negligible in

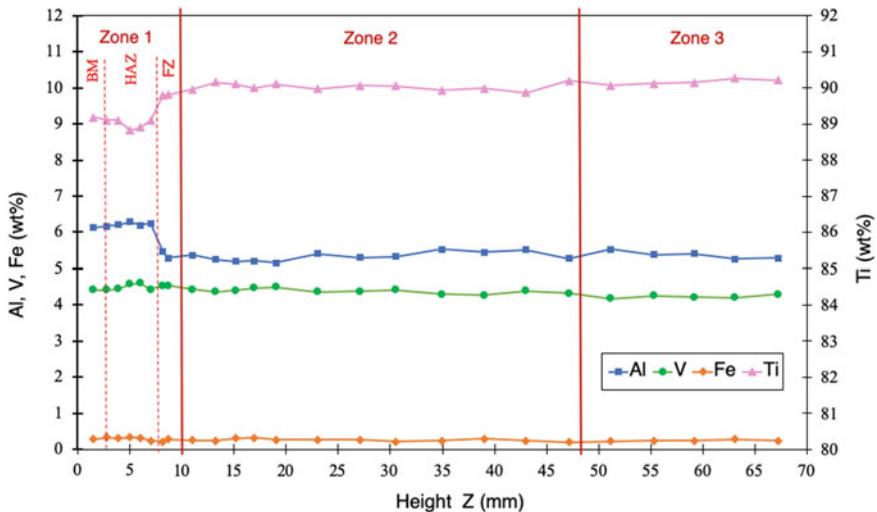


Fig. 3 Chemical composition profile, as evaluated from EDS analysis, of the deposit as a function of its height (Z). (Color figure online)

terms of mechanical properties. Therefore, a special attention has to be taken when choosing the input processing parameters. At the same time, vanadium and iron contents appear to be constant along the whole deposit, as expected.

Observed Microstructure and Its Evolution

Global Microstructure Evolution

Figure 4 shows the microstructure in three different regions (bottom, middle and top) of the deposit wall. For the first two positions, SEM micrographs were taken between thermal bands in order to avoid any effect that does not represent the general microstructure. A heterogeneity in the microstructure along the deposit is observed. In the bottom and middle regions, basketweave structure is present as seen in Fig. 4a–b. However, the microstructure is finer in the bottom compared to the center of the deposit. This is because the substrate acts as a thermal sink causing higher cooling rates in the first layers and therefore, thinner α lamellae thickness. Moreover, this difference in lamellae size is also due to a heat accumulation produced during continuous deposition as the heat input is maintained constant in all the deposition process. At the top of the deposit layer, a very fine microstructure is observed (Fig. 4c).

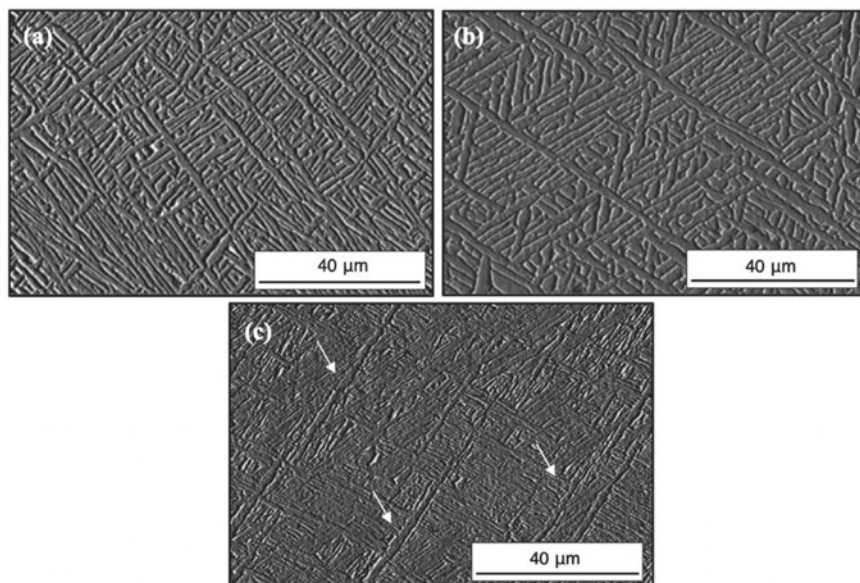


Fig. 4 SEM-BSE micrographs showing the microstructure in the **a** bottom, **b** middle and **c** top regions of the deposited wall. The bottom corresponds to the interface between Zone 1 and Zone 2 whereas the top region represents the middle of Zone 3

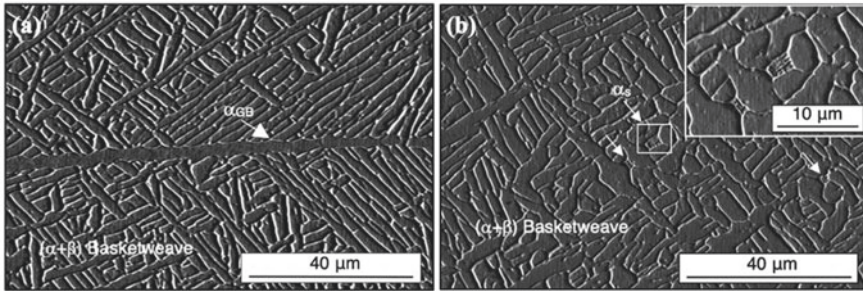


Fig. 5 SEM-BSE images showing the presence of **a** grain boundary alpha (α_{GB}) and **b** secondary alpha (α_s)

The morphology in this region has not been identified with certainty although there appears to be a bit of α' martensite, as indicated by the arrows in Fig. 4c. The presence of totally or partially martensite structure near the top surface was reported in very few studies such as in [22–24]. The existence of martensite in the top region would indicate that when depositing the last layer, high cooling rates occurred, and no fully decomposition neither coarsening of the microstructure happen as this region is not reheated. In order to clarify this last point, X-Ray Diffraction Analysis (XRD) are scheduled for further investigation.

Apart from the nominal microstructure, other phases are formed in the wall deposit. This is the case of grain boundary alpha (α_{GB}) which is observed continuously inside the prior β grains in the reheated region (Fig. 5a), meaning that the cooling rates were sufficiently slow to be formed and grow. Their presence cannot be neglected when determining mechanical properties as its presence can have an important effect in the ductility of the material [25]. Moreover, secondary alpha phase (α_s) is also noticed inside the basketweave structure, as shown in Fig. 5b. This phase precipitates due to the heating experienced in the $\alpha + \beta$ field during subsequent layers. In addition, it is observed that their volume increases when going towards the middle of the deposit. This is another consequence of heat accumulation in the deposit.

Local Evolution in the Vicinity of the Thermal Bands

As explained above, several parallel thermal bands (TB) were discerned along the deposit. These bands are observed to be areas of microstructure transition as shown in Fig. 6a, which creates the distinguishing color when observing the specimen in the OM. Indeed, it is systematically observed in SEM micrographs that there is a colony microstructure above the thermal bands, whereas a coarse basketweave microstructure is present below (Fig. 6b–c). In addition, as seen in Fig. 6d, a fine basketweave microstructure is noticed between two thermal bands, which suggests that the lamellae size continuously increases between two subsequent thermal bands

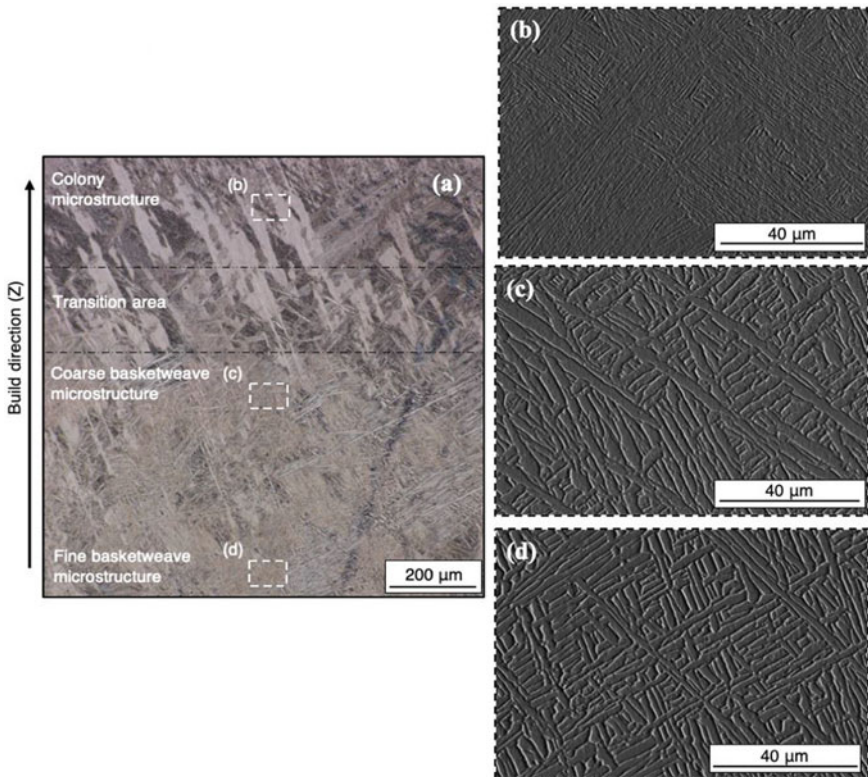


Fig. 6 a OM image in the surroundings of a thermal layer and in detail the main microstructures of deposit wall such as b colony microstructure, c coarse basketweave microstructure and d fine basketweave microstructure. (Color figure online)

and thereby inside each pair of them a gradient microstructure is formed. These microstructural characteristics are repeated for each thermal band. Finally, note that the local microstructure evolution in the vicinity of thermal bands results from different thermal histories due to the deposition of subsequent layers. A detail explanation of the formation of these thermal bands has been proposed in [17].

Quantitative measurements of α lath thickness were performed all along Zone 2 in the build direction, where the thermal bands are present, as this size is the main factor influencing the mechanical properties. A mean average lamellae thickness of $1.05 \pm 0.10 \mu\text{m}$ was reported above the thermal bands where the colony microstructure is found. This corresponds well with the results obtained by Kelly [17] for the LMD technique. On the contrary, Ho et al. [19] found it to be around $0.65 \mu\text{m}$ for WAAM technique. However, special attention has to be taken when comparing technologies as different processing parameters have a significant influence on the formed microstructure. From Fig. 7a, it is observed that colony alpha lath size is

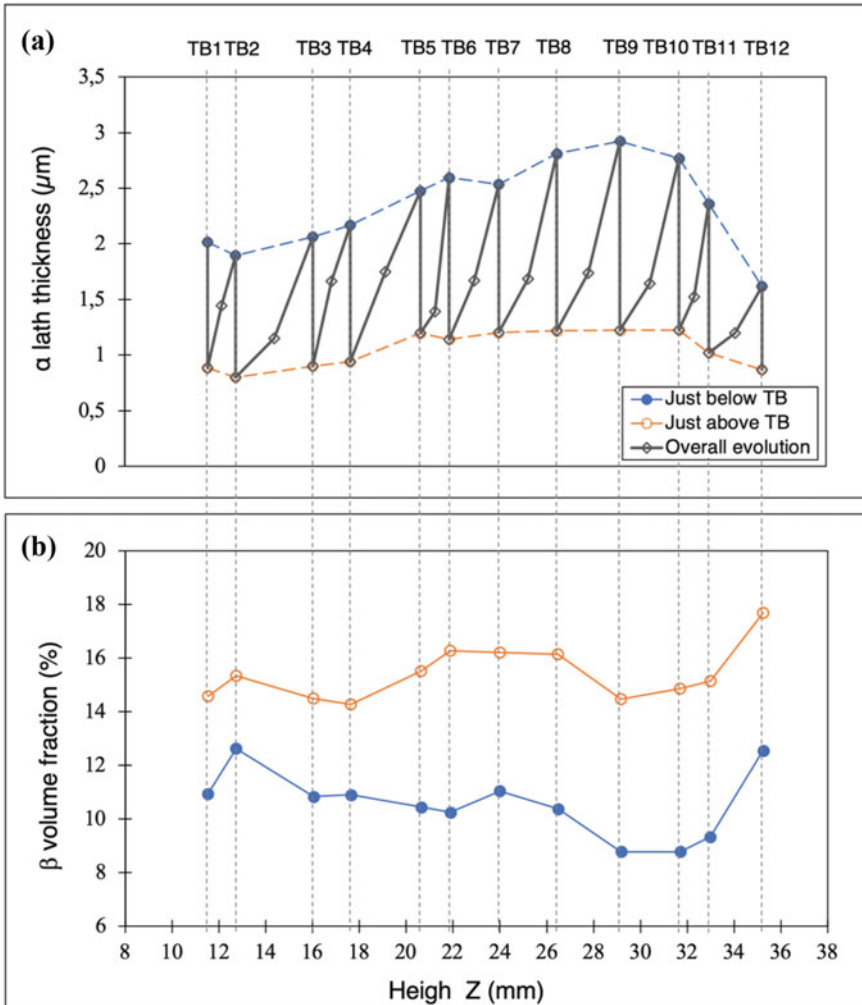


Fig. 7 a Evolution of α lamellae thickness along the deposit height (Z). Dashed vertical lines represent thermal bands (TB) and longer dashed lines represent the envelope of the overall curve illustrating the evolution of α lamellae thickness just above and below thermal bands, along with **b** the average β volume fraction at these last positions as a function of the deposit height (Z)

quite constant at the different thermal bands. Nevertheless, the alpha lamellae thickness below the thermal bands, where coarse nominal basketweave microstructure is present, increases significantly from $2.02 \pm 0.45 \mu\text{m}$ up to $2.92 \pm 0.8 \mu\text{m}$ from the 1st to the 9th horizontal thermal band, respectively (Fig. 7a). From this parallel band the α lamellae size decreases considerably up to the last layers bands. This is because in the middle of the deposit (9th layer) the heat accumulated is maximum, what means that the microstructure coarsens more as it passes longer time at high temperatures. From

the middle region the size starts to decrease as we are closer to the top surface. When comparing the sizes of the coarse basketweave lamellae with the above mentioned studies, it can be seen that there is a considerable difference. This may suggest that EBAM technology is a far hotter process with lower rates of heat extraction due to vacuum environment as compared with other W-DED processes. Finally, it was found that the average lamellae size of the fine basketweave microstructure between thermal bands is almost the mean of the other two microstructures mentioned above, being $1.54 \pm 0.20 \mu\text{m}$.

Moreover, in order to complete the microstructural characterization of the thermal bands, volume fraction analysis was also done as shown in Fig. 7b, where the average β volume fraction is presented as a function of the deposit height inside Zone 2. In this region, the average β volume fraction varies from 8.78% to 17.7%, which are coherent values as compared with literature. The results presented in Fig. 7b indicates that there is a considerable difference in β volume fraction between the two different microstructures present on each side of the thermal band. Indeed, it can be shown that the trend of the β volume fraction is proportionally inverse to the α lath thickness, which means that the β volume fraction is lower when the microstructure is coarser and vice versa. This difference was expected as these two microstructures result from different cooling rates, peak temperatures and times at this peak temperature.

Conclusions

The main objective of this work was to characterize the microstructure of as-received Ti-6Al-4V parts produced with EBAM technology. Based on these experiments, the following conclusions can be addressed:

- The main macrostructural features in EBAM parts are the presence of elongated prior β grains and thermal bands. These bands are found to be the result of a morphology and alpha lath thickness change. The microstructure mainly consists in basketweave microstructure, although colony microstructure is also found in a narrow region at thermal bands.
- A graded microstructure is also reported along the build. This is due to the heat accumulation produced as going towards the center of the deposit. This may be explained by the fact that EBAM technology is a very hot process with low rates of heat extraction due to the vacuum environment.
- Al vaporization is reported in the EBAM deposits. However, no significant variation of Al concentration along the deposited material is found for a given configuration, meaning that the loss of Al content is homogeneous throughout the deposit. Nevertheless, this loss may change along the length of the deposit if other processing parameters are used.

The size and volume fraction of the different phases observed in this study are very dependent on the processing parameters. Therefore, next steps will involve the study of the influence of different processing parameters on the microstructure and

the mechanical properties in order to design a guideline that will help to achieve components with the desired mechanical properties.

References

1. Brandl E, Palm F, Michailov V, Viehweger B, Leyens C (2011) Mechanical properties of additive manufactured titanium (Ti-6Al-4V) blocks deposited by a solid-state laser and wire. *Mater Des* 32:4665–4675. <https://doi.org/10.1016/j.matdes.2011.06.062>
2. Duda T, Raghavan LV (2016) 3D metal printing technology. *IFAC-PapersOnLine* 49(29):103–110. <https://doi.org/10.1016/j.ifacol.2016.11.111>
3. Gebler M, Schoot Uiterkamp AJM, Visser C (2014) A global sustainability perspective on 3D printing technologies. *Energy Policy* 74:158–167. <https://doi.org/10.1016/j.enpol.2014.08.033>
4. Frazier WE (2014) Metal additive manufacturing: a review. *J Mater Eng Perform* 23:1917–1928. <https://doi.org/10.1007/s11665-014-0958-z>
5. Ding R, Guo ZX, Wilson A (2002) Microstructural evolution of a Ti-6Al-4V alloy during thermomechanical processing. *Mater Sci Eng A* 327:233–245. [https://doi.org/10.1016/S0921-5093\(01\)01531-3](https://doi.org/10.1016/S0921-5093(01)01531-3)
6. Heralić A (2012) Monitoring and control of robotized laser metal-wire deposition. Ph.D thesis, Chalmers University of Technology
7. Williams SW, Martina F, Addison AC, Ding J, Pardal G, Colegrove P (2016) Wire + Arc Additive Manufacturing. *Mater Sci Technol* 32:641–647. <https://doi.org/10.1179/1743284715Y.0000000073>
8. Watson JK, Tamingier KM, Hafley RA, Petersen DD (2002) Development of a prototype low-voltage electron beam freeform fabrication system. Paper presented at the Proceedings of 13th SFF Symposium, 2002
9. Herzog D, Seyda V, Wycisk E, Emmelmann C (2016) Additive manufacturing of metals. *Acta Mater* 117:371–392. <https://doi.org/10.1016/j.actamat.2016.07.019>
10. Flower HM (1995) High performance materials in aerospace. Springer, London
11. Peters M, Kumpfert J, Ward CH, Leyens C (2003) Titanium alloys for aerospace applications. *Adv Eng Mater* 5:419–427. <https://doi.org/10.1002/adem.200310095>
12. Donachie MJ (1988) Titanium: a technical guide. ASM International, Materials Park, Ohio
13. Kok Y, Tan XP, Wang P, Nai MLS, Loh NH, Liu E, Tor SB (2018) Anisotropy and heterogeneity of microstructure and mechanical properties in metal additive manufacturing: a critical review. *Mater Des* 139:565–586. <https://doi.org/10.1016/j.matdes.2017.11.021>
14. Al-Bermani SS, Blackmore ML, Zhang W, Todd I (2010) The origin of microstructural diversity, texture, and mechanical properties in electron beam melted Ti-6Al-4V. *Metall Mater Trans A Phys Metall Mater Sci* 41:3422–3434. <https://doi.org/10.1007/s11661-010-0397-x>
15. Saboori A, Gallo D, Biamino S, Fino P, Lombardi M (2017) An overview of additive manufacturing of titanium components by directed energy deposition: microstructure and mechanical properties. *Appl Sci* 7(9):883. <https://doi.org/10.3390/app7090883>
16. Tiley J, Searles T, Lee E, Kar S, Banerjee R, Russ JC, Fraser HL (2004) Quantification of microstructural features in α/β titanium alloys. *Mater Sci Eng A* 372:191–198. <https://doi.org/10.1016/j.msea.2003.12.008>
17. Kelly SM, Kampe SL (2004) Microstructural evolution in laser-deposited multilayer Ti-6Al-4V builds: part I. Microstructural characterization. *Metall Mater Trans A Phys Metall Mater Sci* 35A:1869–1879. <https://doi.org/10.1007/s11661-004-0094-8>
18. Baufeld B, Brandl E, Van Der Biest O (2011) Wire based additive layer manufacturing: comparison of microstructure and mechanical properties of Ti-6Al-4V components fabricated by laser-beam deposition and shaped metal deposition. *J Mater Process Technol* 211:1446–1458. <https://doi.org/10.1016/j.jmatprotec.2011.01.018>

19. Ho A, Zhao H, Fellowes JW, Martina F, Davis AE, Prangnell PB (2019) On the origin of microstructural banding in Ti-6Al4V wire-arc based high deposition rate additive manufacturing. *Acta Mater* 166:306–323. <https://doi.org/10.1016/j.actamat.2018.12.038>
20. Gaytan SM, Murr LE, Medina F, Martinez E, Lopez MI, Wicker RB (2009) Advanced metal powder based manufacturing of complex components by electron beam melting. *Mat Tech* 24:180–190. <https://doi.org/10.1179/106678509X12475882446133>
21. Brice CA, Rosenberger BT, Sankaran SN, Taminger KM, Woods B, Nasserrafi R (2009) Chemistry control in electron beam deposited titanium alloys. *Mat Sci Forum* 618–619:155–158
22. Alphons Anandaraj A (2012) Microstructure, texture and mechanical property evolution during additive manufacturing of Ti6Al4V alloy for aerospace applications. Ph.D, University of Manchester
23. Qian L, Mei J, Liang J, Wu X (2005) Influence of position and laser power on thermal history and microstructure of direct laser fabricated Ti-6Al-4V samples. *Mater Sci Technol* 21:597–605. <https://doi.org/10.1179/174328405X21003>
24. Martina F, Colegrove PA, Williams SW, Meyer J (2015) Microstructure of interpass rolled wire + arc additive manufacturing Ti-6Al-4V components. *Metall Mater Trans A* 46:6103–6118. <https://doi.org/10.1007/s11661-015-3172-1>
25. Sauer C, Lütjering G (2001) Influence of α layers at β grain boundaries on mechanical properties of Ti-alloys. *Mater Sci Eng A* 319–321:393–397. [https://doi.org/10.1016/S0921-5093\(01\)01018-8](https://doi.org/10.1016/S0921-5093(01)01018-8)

Microstructural Characterization of Maraging 300 Steel Fabricated by Select Laser Melting



J. Rodriguez, E. Hoyos, F. Conde, A. L. Jardini, J. P. Oliveira, and J. Avila

Abstract 3D printing of components using a layer-based deposition of materials is referred to as additive manufacturing (AM). The ability to build complex geometry components, reduce waste and avoid assembly are the main advantages of this process. AM has been used in different industries like aerospace, medical, goods and automotive. In the aerospace, materials with high performance are needed to fulfill the requirements of the industry. Maraging steels are among the materials widely used for several applications in the aerospace industry due to its high strength and toughness. These steels are hardened by the precipitation of intermetallics in a martensitic matrix. In this work, a maraging 300 steel powder was used to produce components by selective laser melting (SLM). Two heat treatments were applied to study the martensite-to-austenite reversion, HT1: 480 °C/3 h and HT2: 980 °C/1 h + 2 × 690 °C/5 min + 480 °C/6 h. The microstructural characterization was assessed by optical microscopy (OM), scanning electron microscopy (SEM) and electron backscatter diffraction (EBSD). As-built condition revealed a cellular and dendritic morphology with segregation of Ti, Ni and Mo to the grain boundaries. Direct aging treatment does not erase the typical AM morphology, but a solubilization at 980 °C/1 h

J. Rodriguez (✉) · E. Hoyos

EIA University, Km 2 + 200 Vía al Aeropuerto José María Córdova, Envigado 055428, Antioquia, Colombia
e-mail: johnnatan.rodriguez@eia.edu.co

F. Conde

Department of Materials Engineering São Carlos School of Engineering (EESC), University of São Paulo (USP), Av. Joao Dagnone, 1100 Jd. Sta Angelina, Sao Carlos 13563-120, Brazil

A. L. Jardini

BIOFABRIS—National Institute of Science and Technology in Biomanufacturing, Faculty of Chemical Engineering, University of Campinas, Campinas, SP 13081-970, Brazil

J. P. Oliveira

UNIDEMI, Departamento de Engenharia Mecânica e Industrial, Faculdade de Ciências e Tecnologia, Universidade Nova de Lisboa, Caparica, Portugal

J. Avila

São Paulo State University (UNESP), Campus of São João Da Boa Vista, Av. Profa. Isette Corrêa Fontão, 505, Jardim Das Flores, São João Da Boa Vista, SP 13876-750, Brazil

© The Minerals, Metals & Materials Society 2021

TMS 2021 150th Annual Meeting & Exhibition Supplemental Proceedings,

The Minerals, Metals & Materials Series,

https://doi.org/10.1007/978-3-030-65261-6_17

was capable of fully recrystallize the microstructure. The EBSD analysis showed the increase of reverted austenite for the HT2 and this was attributed to the cycling reversion.

Keywords Additive manufacturing · Maraging steel · Microstructural characterization · SLM

Introduction

The manufacturing of components from 3D computational modeling by the deposition of material in successive layers is called additive manufacturing (AM). Due to the possibility of manufacturing parts with complex and tailor-made geometries, AM has gained strength in different industrial sectors. Understanding the influence of the process parameters in the “as-built” microstructure in the formation of discontinuities and the mechanical properties of products is of great importance for the development of the process and aids the dissemination of the technique.

Microstructural evolution and mechanical properties of the samples produced by AM have been extensively studied in titanium alloys for applications in the aerospace and medical industry. However, there is still a need for further studies for materials in specific applications of mechanical properties of the components produced by AM and of the phase transformations that occur during the processing of the materials [1]. Such is the case for maraging steels, low carbon martensitic steels, recognized for their high strength. Unlike traditional steels, these are not hardened by carbon but by the precipitation of intermetallic compounds. Carbon is considered an impurity in this type of steels and its content is limited to the lowest commercially feasible [2]. The term maraging refers to the hardening mechanism, which consists of a martensitic transformation followed by hardening due to precipitation or aging [3]. Precipitation hardening causes the formation of precipitates in the martensitic matrix. Nanometric precipitates hinder the movement of dislocations, thus, contributing to their superior properties [4].

There are several types of maraging steels with different compositions, alloys and heat treatments. For the traditional maraging steel, the nomenclature characterizes them by degrees that in turn indicate the ultimate resistance in ksi—[5]. Maraging 300 steel provides good mechanical properties and can be heat treated to obtain a good combination of mechanical strength and toughness [6].

Although maraging steels has been traditionally produced by conventional manufacturing, AM has become a major focus of current research [7]. The minimal presence of interstitial alloy elements leads to good weldability, which makes them suitable for AM processes, particularly, for direct energy deposition and selective laser melting (SLM) [8]. This work shows the resulting microstructure of an AM produced maraging 300-grade steel, and the effect of subsequent heat treatment upon the as-built morphology.

Experimental Methods

Samples used in this project were supplied by the *Biofabris* Laboratory of the University of Campinas using an EOSINT M-280 3D selective laser melting printer. The power used varied between 180 and 200 W, layer thickness was set at 50 μm , laser beam diameter stayed between 100 and 200 μm and argon was used as a purge gas. The chemical composition of the metal powder is shown in Table 1.

Figure 1 depicts the location and nomenclature of the samples obtained based on the printing order; subsequently, thermal cycling is a factor of interest for this manufacturing process.

Two heat treatments (HT) were performed, the first a conventional aging heat treatment where the samples were treated at 480 $^{\circ}\text{C}$ for 3 h. For the second heat treatment, three stages of treatment were applied: the first, homogenization to solubilize any prior precipitate and also to erase AM morphology, followed by a cycling heating treatment for martensite-to-austenite reversion, and finally aging, as summarized in Table 2. For each HT, three repetitions were made.

Table 1 Chemical composition of the powder used

Element	Ni	Co	Mo	Ti	Al	Mn, Si	P, S	C
%wt	17–19	8.5–9.5	4.5–5.2	0.6–0.8	0.05–0.15	≤ 0.1	≤ 0.01	≤ 0.03

Fig. 1 Sample location: T: top, M: middle and I: Initial layers. (Color figure online)

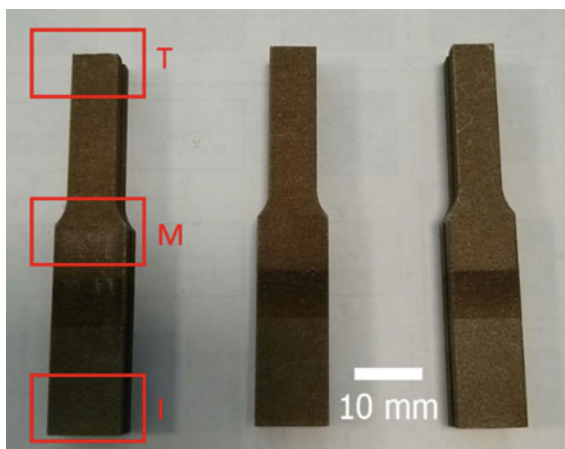


Table 2 Heat treatment summary

Sample	Homogenization	Supercritical	Aging
HT1	–	–	480 $^{\circ}\text{C}$ /3 h
HT2	980 $^{\circ}\text{C}$ /1 h + air cooling	2 \times 690 $^{\circ}\text{C}$ /5 min + water quenching.	480 $^{\circ}\text{C}$ /6 h

Basic characterization was carried out using the optical microscope (OM) of Universidad EIA (Nikon Eclipse LV100) and for advanced features; the scanning electron microscope (SEM—JEOL JSM5910LV) of Universidad Nacional de Colombia was employed. Additionally, the backscattered electron diffraction technique (EBSD—SEM Quanta 650 FEG) was performed at the Brazilian Nanotechnology National Laboratory (LNNano). Sample preparation was performed using the standard procedure of sanding with SiC abrasive paper of 80–1200 grain and polishing with 1 μm diamond paste. Subsequently, the chemical etching was carried out using Nital 10% and Vilella to reveal the microstructures.

Results and Discussion

Figure 2 shows the as-built microstructures of the maraging 300 steel fabricated by SLM for the middle and top of the samples. A similar microstructure morphology for the bottom of the samples was observed. However, the optical images are not shown here. The boundaries of the deposition of the material are observed, similar to welding beads. In addition, martensitic microstructure with grains crossing the solidification boundaries was noticed.

A deep analysis of the microstructures of the as-built and heat-treated samples is shown in Fig. 3. For the as-built samples, the cellular morphology was observed for the three locations: top, middle and bottom (Fig. 3a–f). The cellular domains of the grains extend beyond the weld tracks and different cellular orientations are observed. The morphology observed was also reported by other researches [9]. Moreover, the segregation of Ti, Ni and Mo elements to the cell boundaries was reported as a result of AM in the maraging steel [10]. No significant difference among the microstructure of the three locations examined was noticed.

With the heat treatments, changes in the morphology of the microstructure were observed. A reduction of solidification cracks and residual stresses, and variations in the dendritic and cellular morphology of the martensite were noticed. In the maraging steels with moderate and low quenching, martensite microstructure is noticed, as observed in this work. Figure 3g–h depicts the heat-treated microstructure caused by the direct aging at 480 $^{\circ}\text{C}/3$ h, causing a reduction of the cellular array. For the HT2, the combination of homogenization step, cycling tempering and prolonged aging

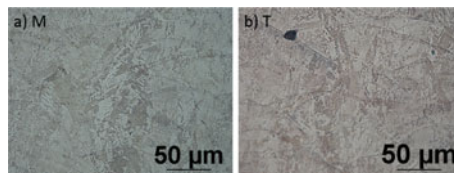
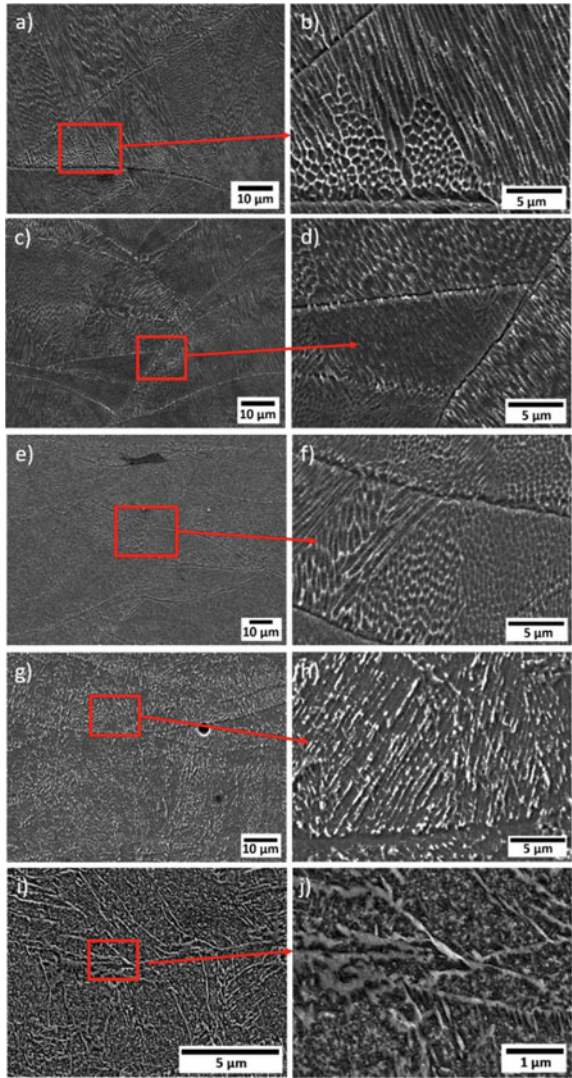


Fig. 2 Optical images of the as-built microstructures of the maraging 300 steel. **a** Middle and **b** top of the samples. (Color figure online)

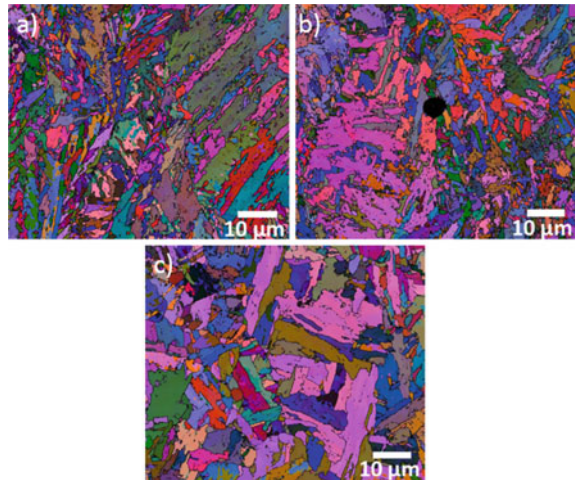
Fig. 3 SEM analysis of the morphology of the samples as-built, **a–b** top, **c–d** middle, **e–f** initial layers, heat treated **g–h** HT1 and **i–j** HT2. (Color figure online)



caused the coalescence of the prior AM microstructure, martensite laths, as shown in Fig. 3i–j.

Figure 4 displays the Euler-orientation map carried out in the as-built and heat-treated samples. As mentioned before and observed in Euler-orientation map, the as-built sample showed an acicular microstructure and a random grain orientation. With the HT1, the acicular microstructure persists because the temperature was not enough to cause the recrystallization of the grains. Only solubilization of some precipitates could have happened. However, the HT2 showed a homogenous recrystallized grain microstructure, completely free from the AM fine acicular morphology.

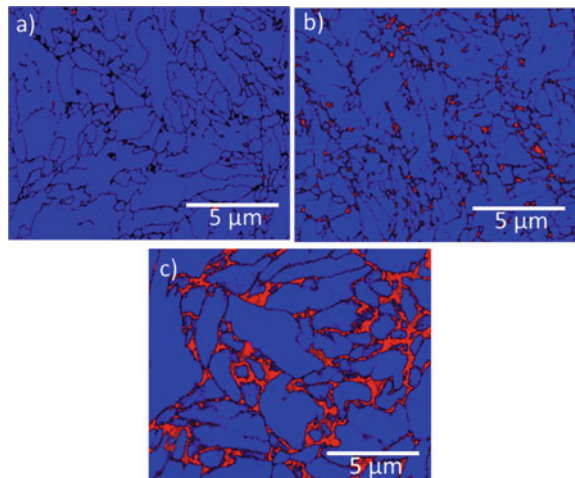
Fig. 4 EBSD
Euler-orientation map
analysis of the samples
a as-built, **b** HT1 and **c** HT2.
(Color figure online)



The combination of homogenization and thermal cycles experienced during the HT2 erased the AM microstructure.

The contrast phase maps of the as-built and heat-treated samples are shown in Fig. 5. The microstructure of the samples is composed mainly of martensite (blue phase) and in less amount by austenite (red phase). For the as-built, the retained austenite percentage was 1.2%. HT1 presented austenite volume percentage of 4.8% and the HT2 the austenite increased to 22.8%. The direct aging treatment provides lower temperature, therefore, lower diffusional capacity, not providing

Fig. 5 EBSD contrast phase
map of the samples
a as-built, **b** HT1 and **c** HT2.
(Color figure online)



higher martensite-to-austenite reversion. Longer aging periods allow the martensite-austenite reversion and the stabilization depends on the diffusion [11, 12]. For HT2, the cycling treatment at higher temperature caused austenite-stabilizer element partitioning, causing enhanced martensite-to-austenite reversion [13].

Conclusions

- The results of the microstructural evaluation indicate that there are no significant differences in the microstructure with the variation of the position in the samples as manufactured. The samples were characterized in the initial, middle and top or last areas to be deposited.
- For all samples, a martensitic structure, characteristic of maraging steels, with some precipitates and the formation of reverse austenite for the heat-treated samples was observed.
- HT1 did not produce significant changes in the microstructure because the treatment temperature was not high enough to recrystallize the microstructure. HT2 erased the original microstructure of the AM process and the recrystallization of martensite grains was observed.
- The formation of reverse austenite increased with temperature and heat treatment cycles, from 1.2% to 22.8%.

Acknowledgements The authors would like to thank the EIA University and FAPESP (2017/17697-5) for providing enough funding to execute this work, Brazilian Nanotechnology National Laboratory for the use of the SEM/EBSD. Fabio Conde acknowledge the financial support of Coordenação de Aperfeiçoamento de Pessoal de Nível Superior—Brasil (CAPES)—Finance Code 001. Andre Jardini acknowledge the financial support of FAPESP (2008/57860-3) and CNPQ (573661/2008-1).

References

1. AM Sub-Platform (2014) AM SRA final document 2014 additive manufacturing: strategic research agenda
2. Sha W, Guo Z (2009) Maraging steels: modelling of microstructure, properties and applications. Woodhead Publishing limited, Cambridge
3. International Molybdenum Association (2008) Maraging Steels
4. Raabe D, Ponge D, Dmitrieva O et al (2009) Designing ultrahigh strength steels with good ductility by combining transformation induced plasticity and martensite aging. *Adv Eng Mater* 11:547–555
5. Hall AM, Slunder CJ (1968) The metallurgy, behavior, and application of the 18-percent nickel maraging steels. *Natl Aeronaut Sp Adm* 141
6. SSA Corporation (2018) Data sheet of high strength maraging steel 0–2

7. Jäggle EA, Choi P, Humbeeck J Van, et al (2014) Precipitation and austenite reversion behavior of a maraging steel produced by selective laser melting. *J Mater Res* [Internet] 29:2072. Available from <http://journals.cambridge.org>
8. Jäggle EA, Sheng Z, Kürnsteiner P et al (2017) Comparison of maraging steel micro- and nanostructure produced conventionally and by laser additive manufacturing. *Materials* (Basel) 10:8
9. Prashanth KG, Eckert J (2017) Formation of metastable cellular microstructures in selective laser melted alloys. *J Alloys Compd* [Internet] 707:27–34. Available from <http://dx.doi.org/10.1016/j.jallcom.2016.12.209>
10. Bai Y, Yang Y, Xiao Z, et al (2017) Selective laser melting of maraging steel : mechanical properties development and its application in mold. *Rapid Prototyp J*
11. Raabe D, Ponge D, Dmitrieva O, et al (2009) Nanoprecipitate-hardened 1.5 GPa steels with unexpected high ductility. *Scr Mater* [Internet] 60:1141–1144. Available from <http://dx.doi.org/10.1016/j.scriptamat.2009.02.062>
12. Wang MM, Tasan CC, Ponge D, et al (2014) Smaller is less stable: size effects on twinning vs. transformation of reverted austenite in TRIP-maraging steels. *Acta Mater* [Internet] 79:268–281. Available from <http://dx.doi.org/10.1016/j.actamat.2014.07.020>
13. Conde FF, Escobar JD, Oliveira JP, et al (2019) Austenite reversion kinetics and stability during tempering of an additively manufactured maraging 300 steel. *Addit Manuf* [Internet] 29:100804. Available from <https://doi.org/10.1016/j.addma.2019.100804>

Tailoring Microstructure of Selective Laser Melted TiAl-Alloy with In-Situ Heat Treatment via Multiple Laser Exposure



Igor Polozov, Artem Kantyukov, Anatoly Popovich, and Vera Popovich

Abstract Intermetallic titanium aluminide (TiAl) alloys are considered attractive materials for high-temperature applications in aerospace, automotive, and energy industries. Additive manufacturing is a promising way of producing complex TiAl-alloy parts; however, it remains challenging due to brittleness of this alloy. While high-temperature preheating can mitigate cracking during selective laser melting, the microstructure of TiAl-alloys still needs to be optimized to achieve better mechanical performance. In this work, multiple laser exposures were used during selective laser melting of TiAl-based alloy to tailor its microstructure. Applying additional laser exposure of up to 20 times per layer induced an in situ heat treatment, which allowed to modify volume fraction and size of different phases. Microstructure, phase and chemical composition, and hardness of TiAl-alloys were investigated with regards to several laser exposures during the selective laser melting process.

Keywords TiAl alloy · Intermetallic · Selective laser melting · Additive manufacturing · In situ heat treatment

Introduction

Gamma TiAl-based intermetallic alloys are promising materials for manufacturing lightweight components of aerospace and automotive engines due to their high strength at elevated temperatures, low density, good oxidation, and creep resistance [1, 2]. These properties make them promising candidates for replacing nickel-based superalloys currently used in gas turbine engines [3, 4]. TiAl-based alloys possess very low room temperature ductility and poor hot deformability and are prone to cracking during conventional processing methods. This makes manufacturing parts

I. Polozov (✉) · A. Kantyukov · A. Popovich
Peter the Great St. Petersburg Polytechnic University, St. Petersburg, Russian Federation
e-mail: polozov_ia@spbstu.ru

V. Popovich
Department of Materials Science and Engineering, Delft University of Technology, Delft, The Netherlands

from TiAl-based alloys very expensive and time consuming. Existing conventional methods, for example, extrusion or casting and isothermal forging, have extremely high costs and results in heterogeneous microstructure. On the other hand, additive manufacturing (AM) processes offer a possibility to produce net-shaped parts with a complex geometry. AM technologies, such as selective laser melting (SLM) and electron beam melting (EBM), allow the fabrication of complex-shaped components with high mechanical properties from powder feedstock [5].

High cooling rates typical for powder bed AM techniques lead to high residual stresses which make it difficult to produce crack-free intermetallic parts [6]. Utilizing a high-temperature powder bed preheating allows to fabricate crack-free titanium aluminide alloy samples [7]. Microstructure and mechanical properties of TiAl-based alloys strongly depend on processing temperature and cooling rates. TiAl-alloys fabricated by AM techniques might require postprocessing by means of heat treatment to obtain an optimal microstructure depending on the application requirements. Depending on annealing temperature, a wide range of microstructures can be obtained, for example, nearly lamellar, fully lamellar, duplex, and near gamma [8].

Using a specific set of processing parameters during AM, heat input, and cooling rates can be adjusted to achieve a required microstructure. For example, Xu, W, et al. showed [9] that by adjusting SLM process parameters, Ti-6Al-4V martensite can be decomposed into ($\alpha + \beta$)-phases. In [10], in situ heat treatment was realized for 420 steel alloy during the SLM process by adjusting laser energy input. Multiple scan strategy was used in [11] to tailor the microstructure of TiAl-based alloy during the EBM process. Addition multiple scanning with low energy electron beam resulted in aluminum loss and formation of new phases with optimized properties.

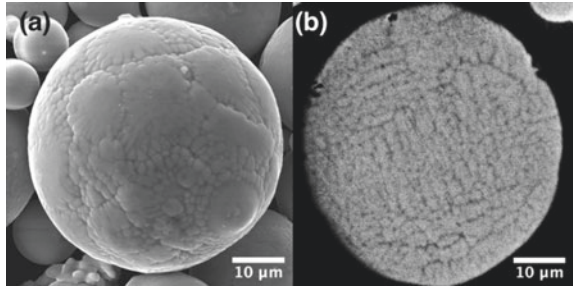
In this work, Ti-48Al-2Cr-2Nb alloy was fabricated by SLM process using high-temperature platform preheating. Additional multiple laser scans were used to realize in situ heat treatment and tailor the microstructure of the TiAl-based alloy. The microstructures, phase composition, and microhardness of the fabricated samples were investigated.

Materials and Methods

Gas-atomized powder of Ti-48Al-2Cr-2Nb (at. %) alloy (AMC Powders, China) was used in the SLM process to produce the specimens. The particle size distribution of the powder can be characterized as following: $d_{10} = 17.4 \mu\text{m}$, $d_{50} = 33.8 \mu\text{m}$, $d_{90} = 60.5 \mu\text{m}$. As shown in Fig. 1, the powder particles have spherical shape and dendritic microstructure typical for the gas atomization process.

AconityMIDI SLM system was used to fabricate bulk samples. The system is equipped with 1000 W fiber laser with 1060 nm wavelength. An inductive heating element was utilized to preheat a titanium base plate to 900 °C. During the SLM process, the process chamber was purged with Argon gas. The values for laser power, layer thickness and hatching distance used to fabricate the sample are shown in Table 1. The process parameters values were chosen based on the preliminary

Fig. 1 BSE-SEM images of the Ti-48Al-2Cr-2Nb alloy powder showing **a** surface morphology and **b** cross-section of a particle



experiments using titanium aluminide alloy [12, 13]. Chessboard scanning strategy with 5×5 mm field size was used. X1 sample was produced using only one laser scanning per layer, while samples X5, X10, and X20 were additionally scanned with a defocused laser beam after the first scan with 5, 10, and 20 additional scans per layer, respectively.

Cylindrical samples with 10 mm height and 10 mm diameter were produced for further investigation.

The as-fabricated samples were cut and polished along the build direction (BD) for the microstructural characterization using a standard metallographic technique. TESCAN Mira 3 LMU scanning electron microscope (SEM) with backscattered electrons (BSE) mode was utilized for the microstructural characterization. Energy dispersive spectroscopy (EDS) was used for the chemical analysis of the samples. The phase composition was analyzed with a Bruker D8 advance X-ray diffraction (XRD) meter using $\text{Cu-K}\alpha$ ($\lambda = 1,5418 \text{ \AA}$) irradiation. The microhardness of the samples was measured using a Buehler VH1150 testing machine with 300 g load and 10 s dwell time.

Results and Discussion

Figure 2 shows microstructural images of the TiAl-alloy samples fabricated using no additional laser exposure and 5, 10, 20 additional laser scans during the SLM process. When no additional laser scan was used, the microstructure consists of the fine lamellar α_2/γ colonies as can be seen in Fig. 2a. The XRD results (Fig. 3) confirm that the alloy consists mainly of γ phase (TiAl) and α_2 (Ti_3Al) phase. Applying additional laser scanning resulted in microstructural modifications depending on the number of laser scans. In case of five additional laser scans, the volume fraction of lamellar α_2/γ colonies reduced and equiaxed γ phase grains formed as a result of additional laser exposure. Lamellar α_2/γ colonies are located mostly around the γ -grains. Increasing the number of additional laser scans to 10 times led to an increased volume fraction of equiaxed γ -grains (Fig. 2c). At the same time, the lamellar spacing of α_2/γ colonies also increased indicating that the sample was heated to a higher temperature when a higher number of laser scans was used. Further increasing the number of laser scans

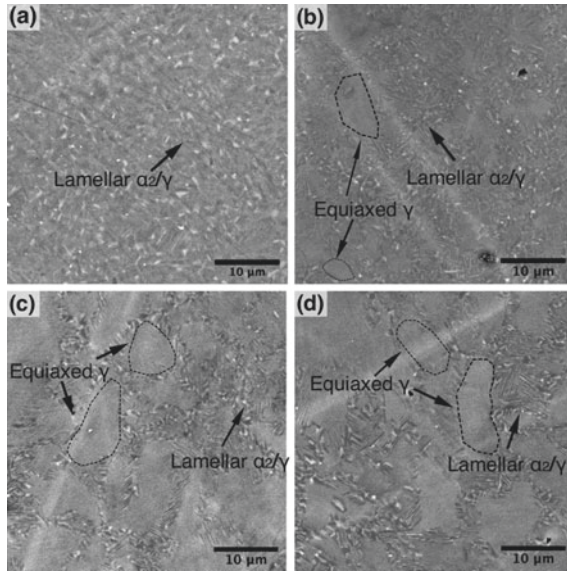


Fig. 2 BSE-SEM images of the fabricated TiAl-alloy samples: **a** X1, **b** X5, **c** X10, **d** X20

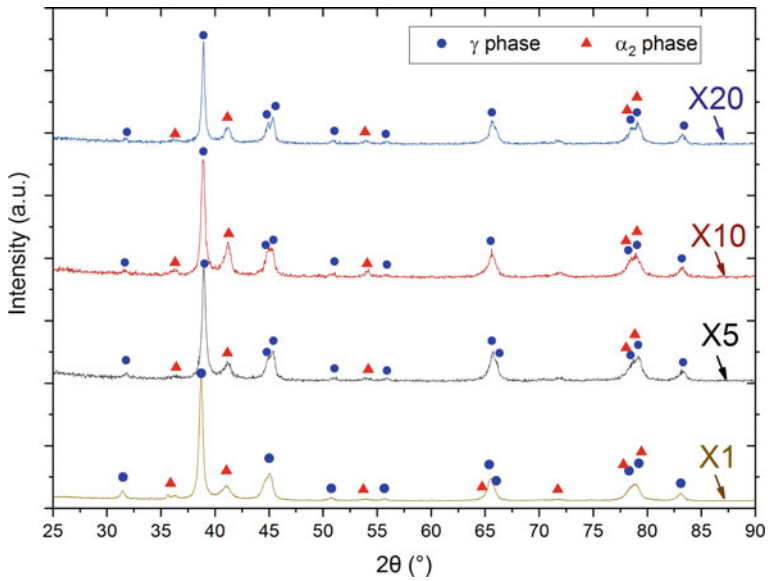


Fig. 3 XRD patterns of the fabricated TiAl-alloy samples. (Color figure online)

Table 2 Aluminum content in the fabricated samples (in at. %) measured by EDS

Sample			
X1	X5	X10	X20
45.2 ± 0.3	43.0 ± 0.2	42.5 ± 0.2	42.7 ± 0.3

to 20 times in case of X20 sample did not lead to any significant changes in the microstructure compared to X10 sample.

In general, SLM process involves cyclic heating and cooling of the material. When additional laser scans are used, the solidified material is heated to a certain temperature resulting in an in situ heat treatment during the SLM process. Microstructure of TiAl-based alloys can be significantly modified depending on the heat treatment temperature [14]. In case of SLM-ed TiAl-alloy, additional laser scanning resulted in a duplex microstructure indicating that after the solidification, the samples were subsequently heated in the $\alpha + \gamma$ phase region. As shown in [15], heat treatment in the $\alpha + \gamma$ region results in the duplex microstructure containing equiaxed γ -TiAl grains, which is in agreement with the obtained results.

Table 2 shows the aluminum content in the produced samples measured by EDS. There is a slight loss of aluminum compared to the feedstock powder indicating that aluminum evaporation occurred during the SLM process. Applying five additional laser scans resulted in a loss of around 2% at. aluminum; however, further increasing the number of laser scans did not change the aluminum content significantly.

As shown in Fig. 3, there are no significant changes in the XRD patterns depending of the number of additional laser exposures. The phase composition of the samples corresponds to γ and α_2 phases.

As shown in Fig. 4, applying multiple laser exposure during the SLM of TiAl-alloy resulted in microhardness change. When the volume fraction of equiaxed γ -grains increased with an increase of number of scans, microhardness of the alloy decreased. This is in agreement with the results of [16] where it was shown that α_2 phase has higher hardness compared to γ phase. A decreased microhardness can also be attributed to an increased lamellar spacing of α_2/γ colonies.

Conclusions

In this study, TiAl-based alloy samples were fabricated using SLM with the high-temperature platform preheating and a scanning strategy with multiple laser exposure. Applying additional laser scanning with a defocused laser beam immediately after the main laser exposure and solidification resulted in an in situ heat treatment and microstructural changes of the TiAl-based alloy.

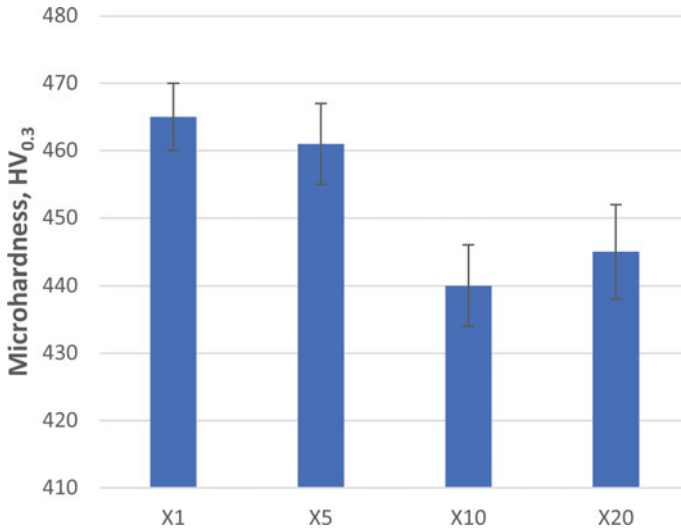


Fig. 4 Microhardness of TiAl samples produced by SLM with different number of additional laser exposures. (Color figure online)

Multiple laser scans allowed to transform the microstructure from lamellar α_2/γ to duplex microstructure with equiaxed γ -grains surrounded with lamellar colonies of α_2/γ . The change in microstructure resulted in a decreased microhardness of the alloy. A further investigation of mechanical properties will be further carried out to evaluate the effect of multiple laser exposure.

Acknowledgements This research was supported by Russian Science Foundation grant (project No 19-79-30002).

References

1. Murr LE, Gaytan SM, Ceylan A, Martinez E, Martinez JL, Hernandez DH, Machado BI, Ramirez DA, Medina F, Collins S (2010) Characterization of titanium aluminide alloy components fabricated by additive manufacturing using electron beam melting. *Acta Mater* 58:1887–1894. <https://doi.org/10.1016/j.actamat.2009.11.032>
2. Bystrzanowski S, Bartels A, Clemens H, Gerling R, Schimansky FP, Dehm G, Kestler H (2005) Creep behaviour and related high temperature microstructural stability of Ti–46Al–9Nb sheet material. *Intermetallics* 13:515–524. <https://doi.org/10.1016/j.intermet.2004.09.001>
3. Bartolotta P, Barrett J, Kelly T, Smashey R (1997) The use of cast Ti–48Al–2Cr–2Nb in jet engines. *JOM* 49:48–50. <https://doi.org/10.1007/BF02914685>
4. Popovich VA, Borisov EV, Sufiyarov VS, Popovich AA (2019) Tailoring the properties in functionally graded alloy inconel 718 using additive technologies. *Met Sci Heat Treat* 60:701–709

5. Baudana G, Biamino S, Klöden B, Kirchner A, Weißgärber T, Kieback B, Pavese M, Ugues D, Fino P, Badini C (2016) Electron beam melting of Ti-48Al-2Nb-0.7Cr-0.3Si: feasibility investigation. *Intermetallics* 73:43–49. <https://doi.org/10.1016/j.intermet.2016.03.001>
6. Doubenskaia M, Domashenkov A, Smurov I, Petrovskiy P (2018) Study of selective laser melting of intermetallic TiAl powder using integral analysis. *Int J Mach Tools Manuf* 129:1–14. <https://doi.org/10.1016/j.ijmactools.2018.02.003>
7. Gussone J, Hagedorn Y-C, Gherekhloo H, Kasperovich G, Merzouk T, Hausmann J (2015) Microstructure of γ -titanium aluminide processed by selected laser melting at elevated temperatures. *Intermetallics* 66:133–140. <https://doi.org/10.1016/j.intermet.2015.07.005>
8. Kim Y-K, Hong JK, Lee K-A (2020) Enhancing the creep resistance of electron beam melted gamma Ti-48Al-2Cr-2Nb alloy by using two-step heat treatment. *Intermetallics* 121:106771. <https://doi.org/10.1016/j.intermet.2020.106771>
9. Xu W, Brandt M, Sun S, Elambasseril J, Liu Q, Latham K, Xia K, Qian M (2015) Additive manufacturing of strong and ductile Ti-6Al-4V by selective laser melting via in situ martensite decomposition. *Acta Mater* 85:74–84. <https://doi.org/10.1016/j.actamat.2014.11.028>
10. Krakhmalev P, Yadroitsava I, Fredriksson G, Yadroitsev I (2015) In situ heat treatment in selective laser melted martensitic AISI 420 stainless steels. *Mater Des* 87:380–385. <https://doi.org/10.1016/j.matdes.2015.08.045>
11. Zhou J, Li H, Yu Y, Li Y, Qian Y, Firouzian K, Lin F (2020) Fabrication of functionally graded materials from a single material by selective evaporation in electron beam powder bed fusion. *Mater Sci Eng A* 793:139827. <https://doi.org/10.1016/j.msea.2020.139827>
12. Polozov I, Popovich V, Razumov N, Makhmutov T, Popovich A (2020) Gamma-titanium intermetallic alloy produced by selective laser melting using mechanically alloyed and plasma spheroidized powders. In: TMS 2020 149th annual meeting & exhibition supplemental proceedings. The minerals, metals & materials series. Springer, berlin, pp 375–383
13. Polozov I, Sufiurov V, Kantuykov A, Razumov N, Goncharov I, Makhmutov T, Silin A, Kim A, Starikov K, Shamshurin A, Popovich A (2020) Microstructure, densification, and mechanical properties of titanium intermetallic alloy manufactured by laser powder bed fusion additive manufacturing with high-temperature preheating using gas atomized and mechanically alloyed plasma spheroidized powder. *Addit Manuf* 34:101374. <https://doi.org/10.1016/j.addma.2020.101374>
14. Kościelna A, Szkliniarz W (2009) Effect of cyclic heat treatment parameters on the grain refinement of Ti-48Al-2Cr-2Nb alloy. *Mater Charact* 60:1158–1162. <https://doi.org/10.1016/j.matchar.2009.03.008>
15. Hoosain SE, Pityana SL, Tlotleng M, Legopeng T (2017) A comparative study on laser processing of commercially available titanium aluminide (Ti-48Al-2Cr-2Nb) and in-situ alloying of titanium aluminide. In: 18th annual international rapid product development association of South Africa (RAPDASA), 7–10 November 2017, Durban ICC, South Africa
16. Schloffer M, Iqbal F, Gabrisch H, Schwaighofer E, Schimansky F-P, Mayer S, Stark A, Lippmann T, Göken M, Pyczak F, Clemens H (2012) Microstructure development and hardness of a powder metallurgical multi phase γ -TiAl based alloy. *Intermetallics* 22:231–240. <https://doi.org/10.1016/j.intermet.2011.11.015>

Part VII
Advanced Characterization
Techniques for Quantifying and Modeling
Deformation

Analysis of Slip Transfer in Ti-5Al-2.5Sn (Wt%) at Two Temperatures in Comparison with Pure Aluminum



Chelsea Edge and Thomas R. Bieler

Abstract Understanding the deformation mechanisms present near grain boundaries in polycrystalline hexagonal alloys will aid in improving modeling methods. Ti-5Al-2.5Sn samples were tensile tested at 296 and 728 K, and slip behavior was assessed near grain boundaries. From the EBSD measurements of grain orientations, various metrics related to the slip systems, traces, residual Burgers vectors, and grain boundary misorientation were computed for boundaries showing evidence of slip transfer and boundaries showing no evidence of slip transfer. This work is compared to a similar study of an aluminum oligo-crystal to aid in understanding the differences in slip behavior near grain boundaries in HCP and FCC crystal structures.

Keywords Titanium · Aluminum · Slip transfer

Introduction

The overarching goal of the research is to further understand the deformation mechanisms in titanium alloys, specifically Ti-5Al-2.5Sn (Ti525). Knowledge of the deformation mechanisms can aid in improving the modeling methods such as crystal plasticity finite element (CPFE) modeling, to enable more predictive ability to model heterogeneous strain near grain boundaries.

The slip transfer that will be discussed is where perfect slip transfer does not occur across the grain boundary, resulting in some residual Burgers vector (Δb) left in the grain boundary. The residual Burgers vector, Δb , is estimated by the dislocation reaction equation: $\Delta b = \vec{b}_1 - \vec{b}_2$. The geometric compatibility factor, m' , is used as a criterion to determine if slip transfer is likely to occur. An m' value closer to 1 would imply that slip transfer is more likely to occur on the specified slip systems, as they would be nearly collinear, as opposed to a slip system pair that has lower m' values. The Schmid factor is used as a metric to determine the most likely slip

C. Edge (✉) · T. R. Bieler
Michigan State University, East Lansing, MI, USA
e-mail: edgechel@msu.edu

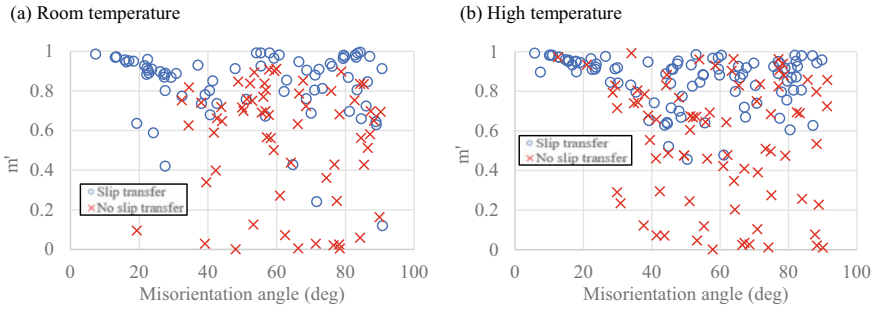


Fig. 1 m' versus misorientation angle for **a** the room temperature (296 K) sample and **b** the high temperature (728 K) sample. There is a decreasing trend for misorientation angles below 20° in both samples. (Color figure online)

systems that are activated in the two neighboring grains when there is unidirectional stress.

The Ti-5-Al-2.5Sn (Ti525) alloy was provided by Pratt & Whitney, Rocketdyne. It was forged in the upper half of the $\alpha + \beta$ phase field. The material was then annealed at 1127 K for 1 h for recrystallization, followed directly by air cooling, followed by a vacuum annealing process at 1033 K for 4 h to reduce the hydrogen content. The samples examined were in situ tensile tested within the Tescan Mira3 SEM, with a displacement rate of 0.004 mm/s (approximate strain rate of 10^{-3} s^{-1}). One sample was tested at 296 K and another at 728 K.

If there were correlated slip traces in one grain and a neighboring grain, a set of criteria were considered to determine if slip transfer accounted for the correlated slip traces. These criteria are: (1) Determination of probable slip systems would be consistent with observed slip traces. (2) A m' value associated with the observed correlated slip systems is generally larger than 0.7. (3) The residual burgers vector (Δb) associated with the observed correlated slip systems is generally smaller than $0.5b$. (4) The Schmid factor of each slip system is generally larger than 0.25. (5) The topography at the grain boundary is small indicating that the boundary does not lead to heterogenous strain on both sides. (6) The observed slip traces on each side have a topographical directional sense that implies that the slip planes are approximately parallel.

Results

Misorientation Angle Versus m'

Figure 1 shows the trend of the “slip transfer” and “no slip transfer” data for misorientation versus the geometric compatibility factor (m'). Below 20° misorientation

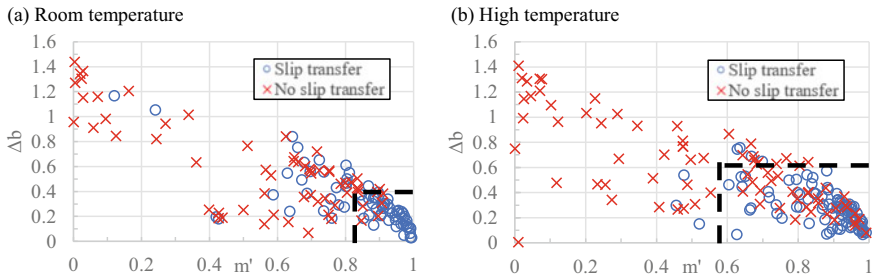


Fig. 2 m' versus the residual Burgers vector for **a** the room temperature (296 K) and **b** the high temperature (728 K) sample. The cluster of “slip transfer” points, denoted with dotted lines, have high m' parameters and low residual Burgers vectors. (Color figure online)

angle in both the room temperature and high temperature sample, there is a trend of high m' values that slopes downward as the misorientation angle increases.

m' Versus Residual Burgers Vector (Δb)

The Luster-Morris parameter (m') versus the residual Burgers vector (Δb) is plotted in Fig. 2. The black dotted lines are plotted such that the maximum number of “slip transfer” points are inside the box, and the maximum number of “no slip transfer” points are outside the box. 64 and 91% of the “slip transfer” points are located inside the black dashed, and 94 and 68% of the “no slip transfer” points are outside the dashed box for the room and high temperature samples, respectively. The high temperature data shows a much larger black dotted box compared to the room temperature data, and the relative percentages of the two populations inside and outside the box are reversed. The “slip transfer” data are clustered in the lower right-hand corner of the graph, i.e., at high m' and low residual Burgers vector values. The “no slip transfer” points are spread out, and there are many points within the lower right box for the high temperature data. This indicates that slip transfer happens more frequently with lower m' and higher residual Burger vectors in the high temperature sample.

Misorientation Angle Versus the Sum of the Schmid Factors

($m'(SF_{LG} + SF_{RG})$) is plotted against the misorientation angle in Fig. 3. The “no slip transfer” data have a larger spread of $m'(SF_{LG} + SF_{RG})$, while the “slip transfer” data have a $m'(SF_{LG} + SF_{RG})$ closer to 1 for both data sets. In the high temperature data set, there is a cluster of “slip transfer” points between 35° and 50° misorientation

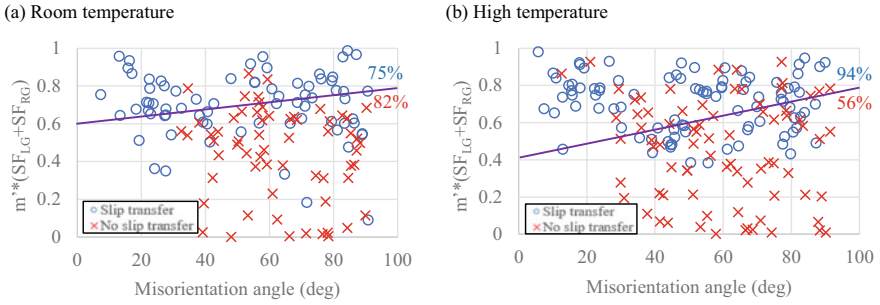


Fig. 3 $m'(SF_{LG}+SF_{RG})$ parameter versus misorientation angle for **a** the room temperature (296 K) and **b** the high temperature (728 K) sample. There is a decreasing trend in “slip transfer” data below 30° misorientation angle. The “no slip transfer” data are mostly present above 30° misorientation angle. (Color figure online)

that has a $m'(SF_{LG}+SF_{RG})$ value below 0.6. This cluster is not present in the room temperature data.

Misorientation Angle Versus $m'/\Delta b$

Figure 4 shows the relationship between misorientation angle and $m'/\Delta b$. The purple lines are constructed to have maximum “slip transfer” points above, and maximum “no slip transfer” points below it. There is a decreasing $m'/\Delta b$ trend for “slip transfer” data below the 30° misorientation angle for both samples. The high temperature data set is observed to have a stronger trend in this region, as the data is more closely packed. Above 30° misorientation angle, both “no slip transfer” and “slip transfer” data have a larger spread but there appears to be a threshold for the “slip transfer”

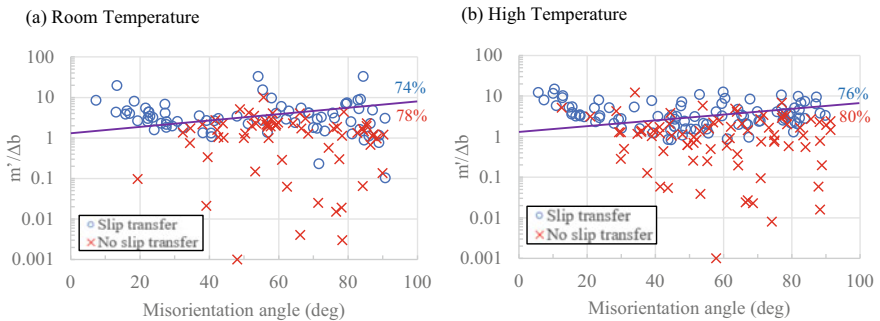


Fig. 4 $m'/\Delta b$ versus misorientation angle for **a** the room temperature (296 K) and **b** the high temperature (728 K) sample. In both samples, a strong decreasing $m'/\Delta b$ trend for ‘slip transfer’ data below 30° misorientation. (Color figure online)

data (above $m'/\Delta b = 1$), while the “no slip transfer” data are scattered over a wider range. Both the “no slip transfer” and “slip transfer” data for the room temperature sample has a larger spread compared to the high temperature data.

Discussion

This chapter will compare the results of the high temperature tensile-tested sample, to the room temperature tensile-tested sample. In addition, the results obtained in the Ti525 samples are compared to the results of “A criterion for slip transfer at grain boundaries in Al” by R. Alizadeh. Alizadeh performed an investigation in an aluminum oligo-crystal tensile sample tested at room temperature.

m' Versus Residual Burgers Vector (Δb)

Figure 5 compares the m' versus residual Burgers vector (Δb). The green box identifies the cluster boundary determined by Alizadeh. Alizadeh maximized the percentage of “slip transfer” points within the box and percentage of “no slip transfer” points outside the box. A comparison of Al maximized boundaries and titanium maximized boundaries are given in Table 1. The aluminum sample has a boundary of lower Δb and higher m' values compared to the high temperature tensile-tested sample. In comparing the room temperature Ti525 sample and the room temperature aluminum sample, the boundaries are very similar. This shows the temperature

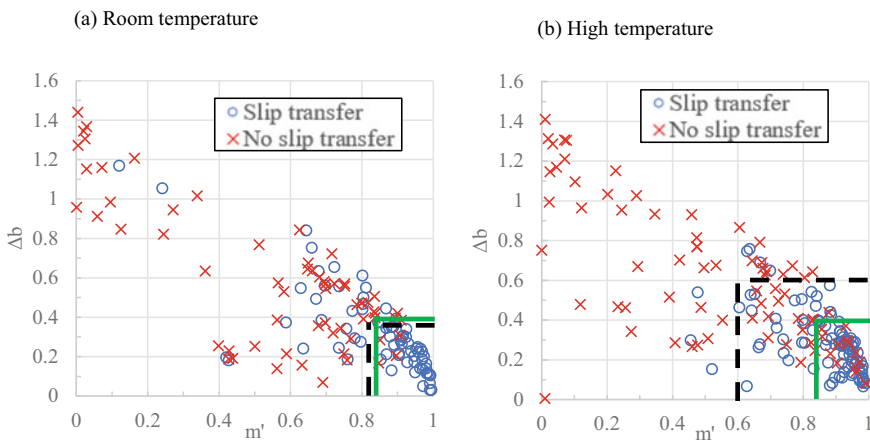


Fig. 5 m' versus Δb data for the **a** room temperature (296 K) and **b** the high temperature (728 K) tensile-tested Ti525 sample. Green boxes indicate comparable Al oligo-crystal tensile results at room temperature. (Color figure online)

Table 1 Percentages of “slip transfer” and “no slip transfer” inside and outside of boundaries, respectively. RT and HT Ti525 relationships are flipped with high percentage of “no slip transfer” outside of the box in RT and high percentage of “slip transfer” inside the box for HT

	Slip transfer (Inside) (%)	No slip transfer (Outside) (%)
RT Ti525	64	94
HT Ti525	91	68
RT Al	93	86

Table 2 Temperature comparison for Al and Ti525. RT Al and HT Ti525 have similar homologous temperatures

	Homologous temperature (T_m)	Melting temperature (Kelvin)	Test temperature (Kelvin)
RT Ti525	0.16	1863	296
RT Al	0.32	933	296
HT Ti525	0.39	1863	728

dependence of the m' versus Δb factors. Higher Δb values and lower m' values enable slip transfer when the temperature in the material is hotter. In comparing the titanium room temperature sample to the titanium high temperature sample, more points with lower m' values are observed.

Dislocation climb in titanium alloys is facilitated by higher temperatures. If dislocations can climb near the boundary to align themselves with a lower m' geometry partner, then slip transfer is enabled under less favorable conditions. Higher diffusion rates enable recovery processes to take place near and within grain boundaries, so that residual Burgers vector debris is more easily absorbed.

The homologous temperatures of the two materials are given in Table 2. The RT Al and HT Ti525 homologous temperatures are similar to each other.

Given that the slip transfer behavior in aluminum and Ti525 are more similar to each other at room temperature, the effect of alloying elements and/or the much lower CRSS in pure aluminum may lead to less stress-assisted climb forces for a similarly high homologous temperature, such that the higher stresses in Ti525 facilitated climb more effectively than in Al. The stiffness normalized strength in Ti525 was 0.006 for the room temperature sample and 0.003 for the high temperature sample while it was 0.00036 in pure Al. The aluminum compensated strength is significantly lower than the Titanium alloy, due to the effects of alloying.

Misorientation Angle Versus m'

Figure 6 shows the misorientation angle versus m' for both the titanium oligo-crystal and the aluminum alloy samples. The room temperature (296 K) Ti525 tensile sample

(a) and the high temperature (728 K) Ti525 tensile sample (b) are overlaid with the shaded areas representing the locus of most of the points in the aluminum polycrystal. Since aluminum has a cubic structure with maximum disorientations of 63° , there is a much larger range of misorientation as well as m' values for Ti525 slip transfer points. Alizadeh identified a threshold of about 20° that best separated the “slip transfer” and “no slip transfer” categories, which occurred in the middle of the “slip transfer” region (blue region). The titanium alloy shows similar behavior, but the threshold is not as distinct, as most observations are at misorientations larger than 20° . This disparity could arise from the fewer easy slip systems in hexagonal crystal structures that lead to more heterogeneous stress states in titanium. Another possibility is that the aluminum oligo-crystal grains have mostly free surfaces while the Ti525 sample is a polycrystal, where only one side of the grain has a free surface, which makes the stress state more complex.

Unlike the titanium alloy, the aluminum oligo-crystal has a strong texture, so that most grains had a more similar stress state and strain response. With fewer easy slip systems available in the Ti525, slip may be required on slip systems that do not facilitate slip easily, leading to a wider variation in the local stress state, which would lead to more spread in the data. Furthermore, the “no slip transfer” points are not present in the room temperature titanium sample below $\sim 30^\circ$ misorientation, while in the aluminum and high temperature Ti525 data sets, they are present at misorientations as low as $\sim 10^\circ$ in Al and the high temperature Ti525 data. These differences imply that differences in crystal structure and geometrical limitations need to be considered.

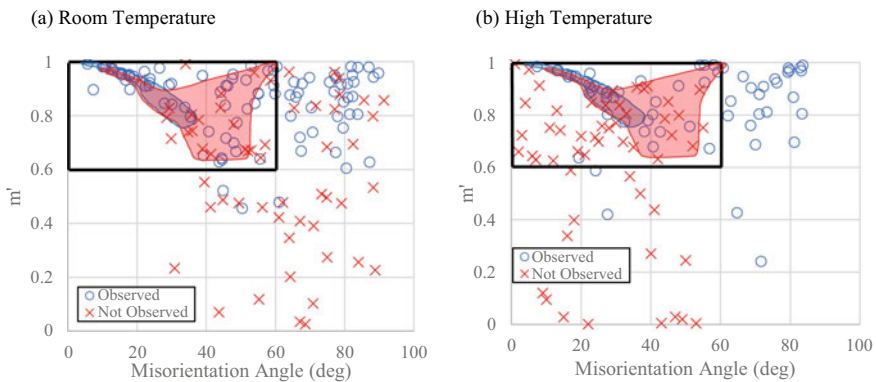


Fig. 6 Aluminum oligo-crystal “slip transfer” (blue shaded area) and “no slip transfer” (red shaded area) compared to data of the titanium polycrystal data for **a** the room temperature (296 K) and **b** the high temperature (728 K) sample. Titanium “slip transfer” and “no slip transfer” points do not follow as strict of a trend compared to the aluminum data. (Color figure online)

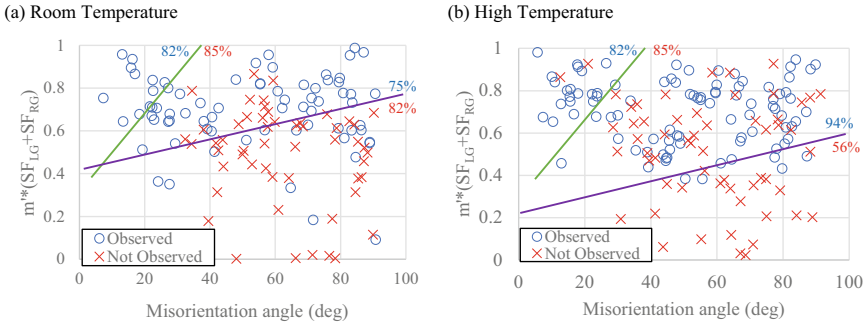


Fig. 7 Misorientation angle versus $m'(SF_{LG} + SF_{RG})$ for the **a** room temperature Ti525 and **b** the high temperature Ti525 sample. The aluminum boundaries represented by the green line show the difference between the aluminum data set which has a steep slope and the titanium data set which slope is flatter. (Color figure online)

Misorientation Angle Versus the Sum of Schmid Factors

Figure 7 shows comparison between the misorientation angle versus $m'(SF_{LG} + SF_{RG})$ for the (a) room temperature and (b) high temperature Ti525 alloy. The green solid line represents the thresholds for aluminum, where “slip transfer” points was prevalent above the green line. The same process was done with the titanium data. The trends between the boundaries of the aluminum and titanium “slip transfer” data are significantly different, in that a shallow positive slope best separates prevalent “slip transfer” and “no slip transfer” populations, and the threshold is much lower threshold than that for Al. The boundaries for the high temperature and room temperature samples in the titanium alloy are very similar, but lower for high temperature data. This also indicates that a threshold for $m'(SF_{LG} + SF_{RG})$ versus misorientation angle is heavily dependent on material and crystal structure. Clearly, the geometrical constraints for slip transfer are much smaller in the hexagonal crystal structure than in Al.

Misorientation Angle Versus $m'/\Delta b$

Figure 8 presents the misorientation angle versus $m'/\Delta b$ for (a) the room temperature and (b) the high temperature Ti525 sample. The shaded areas are approximate representations for misorientation angle versus $m'/\Delta b$ for the aluminum oligo-crystal. The blue shaded region for the aluminum oligo-crystal “slip transfer” data and the blue cluster of data from the titanium alloy below 30° misorientation angle line up well, indicating a strong correlation between the two data sets in this range. The red shaded area representing the aluminum “no slip transfer” data expands greatly below $m'/\Delta b = 1$, as do the titanium “no slip transfer” data. The black rectangle

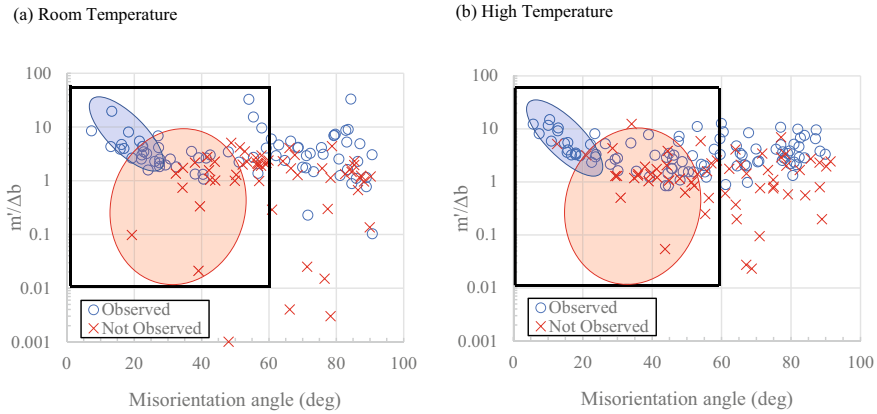


Fig. 8 Misorientation versus $m'/\Delta b$ for **a** the room temperature (296 K) and **b** the high temperature (728 K) sample. The red shaded area represents the aluminum oligo-crystal “no slip transfer” data. The blue shaded area represents the aluminum oligo-crystal “slip transfer” data and line up with the slip transfer points in the Ti525 data. (Color figure online)

represents the data bounds for the FCC aluminum data set. Figure 8 also shows that there are less geometrical constraints for slip transfer in the hexagonal Ti alloy than the aluminum FCC material. In comparing the 296–728 K Ti525 data, the boundary lines separating maximum “slip transfer” and “no slip transfer” are nearly the same, but the higher temperature has a slightly smaller slope indicating that temperature does not have a great effect on $m'/\Delta b$ versus the misorientation angle.

Summary and Conclusions

This paper describes the method and results of a study of Ti-5Al-2.5Sn deformation behavior focusing on slip transfer across grain boundaries at two different temperatures (296 and 728 K). The study investigates “slip transfer” conditions across grain boundaries. The results are compared to a similar study that was done with pure aluminum by R. Alizadeh. In comparing the titanium results to an aluminum sample, some trends are similar, such as favorable slip transfer of the same slip system family at low misorientations. Details associated with geometrical constraints of more slip systems in the hexagonal crystal structure, but few facile ones, versus face-centered cubic crystal structure in aluminum. These results show that slip transfer is much more commonly accomplished in the Ti-5Al-2.5Sn deformation in and room and to a greater extent at high temperatures, which provides a basis for installing slip transfer criteria into CPFEE modeling of the alloy.

Conclusions

1. “Slip transfer” data is more prevalent than “no slip transfer” data at misorientation angles $<30^\circ$. At these low misorientation angles, slip traces are categorized as “slip transfer” more than being categorized as “no slip transfer” at both 296 and 728 K.
2. There is a decreasing trend of m' “slip transfer” traces with increasing misorientation below 20° for both Al and Ti525. Many “slip transfer” cases occur at high misorientations in titanium.
3. Literature suggests that high m' and low Δb enable slip transfer. This hypothesis was found true in Ti525. Room temperature Ti525 and room temperature aluminum show a similar behavior in m' versus Δb .
4. Considering both the Schmid factor versus m' , and m' versus Δb , geometrical constraints for “slip transfer” in hexagonal crystal structure are smaller than FCC.

Part VIII
Advanced Functional and Structural Thin
Films and Coatings

Atomic Layer Deposition and Atomic Layer Etching—An Overview of Selective Processes



Samiha Hossain, Oktay H. Gokce, and N. M. Ravindra

Abstract The continued evolution in nanoelectronics and nanophotonics has been made possible by the recent developments in Atomic Layer Deposition and Atomic Layer Etching. While uniform deposition of conformal films with controllable thickness is a key feature of Atomic Layer Deposition, Atomic Layer Etching offers the advantages of controlled removal of chemically modified areas. Various case studies of the applications of these technologies in dielectrics, metals and diffusion barriers will be discussed.

Keywords Atomic layer deposition · Atomic layer etching · Metallization · Dielectrics · Diffusion barriers · Microelectronics

Introduction

Subtractive processing technologies for planar microelectronic structures have been employed for about six decades. Selective technologies bring a new way of processing of structures that are starting from the bottom and built up. The adsorption of the precursors on the non-growth areas should be controlled and minimized in order to control the selectivity. The coverage of the non-growth area can be both on the existing nucleation sites and the new developing nucleation sites generated during the process on the growing nuclei. Suppression of chemical activity on non-growth surfaces can be achieved with surface treatment methods prior to deposition. The periodic cleaning by selective etching of adsorbed precursor on these areas contributes to

S. Hossain · O. H. Gokce (✉) · N. M. Ravindra
Interdisciplinary Program in Materials Science & Engineering,
New Jersey Institute of Technology, Newark, NJ 07102, USA
e-mail: gokce@njit.edu

S. Hossain
e-mail: samihahossain87@gmail.com

N. M. Ravindra
e-mail: nmravindra@gmail.com

the sustainability of the overall process. Both the selective deposition and etching processes need to be considered as parts of a completely selective manufacturing scheme. In this respect, the Atomic Layer Deposition (ALD) and Atomic Layer Etching (ALE) work together in a complementary way to yield the desired structures. The type of a selective process can be in the form of deposition or etching. Such processes can be employed at various stages of device manufacturing. Deposition processes can be studied as area- and material-selective deposition processes as well as topology-selective deposition processes. The latter depends on the shape that needs to be coated. Both deposition and etch processes can be in isotropic and anisotropic variations. This paper is a condensed review of deposition processes for metals and dielectrics using selective processes in submicron device manufacturing technology.

Area-Selective ALD

Area selective deposition (AS-ALD) is a topic of significant relevance to many potential applications in electronic devices, biological and chemical sensors, microfluidics, optoelectronic devices, and heterogeneous catalysts [1–5]. It is a bottom-up patterning process that retains many of the characteristics that make ALD such a compelling procedure. It guarantees uniformity, exceptional conformality and thickness control. Patterns are created on a substrate via selective deposition by modifying the chemical properties of the surface which determines how ALD precursors are adsorbed [1]. Even though ALD and ALE are widely established processes, the overall development of material-selective processes is still insufficient. Several studies have been performed in the literature on increasing the efficiency of these processes [6].

AS-ALD is a selective bottom-up chemical patterning process in which the selectivity of ASD is dependent on the energy difference between the growth and non-growth areas. Surfaces with suitable nucleation and growth energies favor immediate film deposition while the remaining areas have an energy barrier that prevents the formation of nuclei [6]. The deposition selectivity gradually decreases as the quantity of the precursor deposits increase on the surface. This can be combated by various methods such as: pretreating the surface to prolong incubation time [6–10], non-growth area deactivation by self-assembled monolayers (SAM) [6, 11–18], ASD by surface activation [6, 19, 20], ALD super-cycles with an inhibitor step [6, 9], and super-cycles consisting of an etching step to restore an incubation time on the non-growth area [6, 21–25].

Selective deposition in ALE can be achieved by various mechanisms. The bond energy of etching materials is lowered when they chemically bind with the reactants thus providing a processing window to achieve selective ALE [6]. Silicon-to-SiO₂ etching selectivity is obtained using this method. Chlorinated SiO₂ has a higher energy threshold than chlorinated Si which allows for selective removal of modified Si layers via low energy Ar⁺ bombardment [6]. Metzger et al. developed a fluorocarbon (FC)-based ALE process that cyclically deposited a thin FC layer on a SiO₂ surface;

then, the fluorinated layer is removed by low energy Ar^+ bombardment [6]. FC-based processes are much more efficient than chlorine-based ones because of the much higher FC consumption rate of SiO_2 compared to Si [6]. However, this process causes some material loss due to a buildup of a passivation layer on the non-etching surface, but this can be mitigated by optimizing process parameters which facilitate a simultaneous etch step and buildup of the passivation layer [6]. Huard et al. addressed this problem by varying the deposition thickness and etching-step length in SiO_2 and Si_3N_4 and pretreating the surface. Under ideal conditions, a steady amount of SiO_2 can be removed while a passivation layer is formed quickly on Si_3N_4 [26]. These approaches, however, are not as compatible with high-dielectric constant materials such as HfO_2 . The requirement of higher levels of ion energy [27–29] or a higher substrate temperature [30, 31] for the removal of etching by-products causes extra Si loss, thus reducing the etching selectivity of HfO_2 to Si [6].

Self-assembled monolayers can be used to deactivate non-growth areas as shown by Hashemi et al. [15] (Fig. 1) in which octadecylphosphonic acid self-assembled monolayers (ODPA SAMs) were used to deposit a blocking layer on a copper surface, including CuO , Cu_2O , and Cu . The SAMs did not bind to SiO_2 which enabled the deposition of a dielectric film in a pattern. An etchant is then used to selectively remove the SAMs and any surplus dielectric film that adhered to the Cu surface without disrupting the film on SiO_2 [6].

AS-ALD can also be achieved by using super-cycles combined with a selective etching step (Fig. 2). Vallat et al. used a super-cycle of $\text{NF}_3/\text{O}_2/\text{Ar}$ etching step in a Ta_2O_5 ALD process to remove the unwanted layers in Si non-growth areas to enable selective deposition [24]. Inhibitors can also be used to deactivate non-growth areas which lengthen incubation times and potentially maximize deposition selectivity [6]. After AS-ALD is used to cover the non-etching area with a passivation layer, ALE can be initiated to etch a pattern into the designated area. Lin et al. introduced an approach that combined AS-ALD along with etching where they studied the deposition behavior of mixtures of methane (CH_4) with trifluoromethane (CHF_3) and mixtures of methane with octafluorocyclobutane (C_4F_8) on HfO_2 and Si surfaces [6]. It was found that a $\text{CH}_4/\text{C}_4\text{F}_8$ mixture produces a fluorocarbon (FC) layer on both

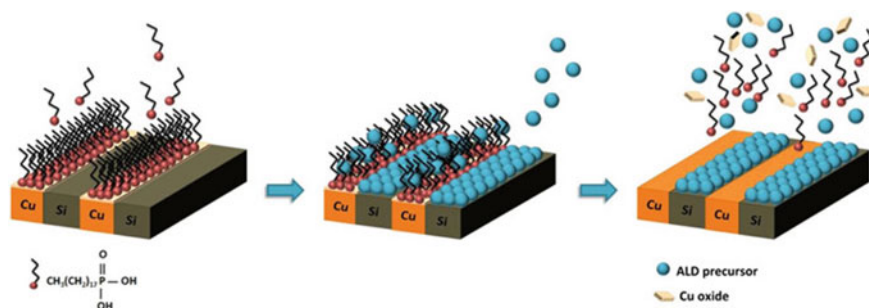
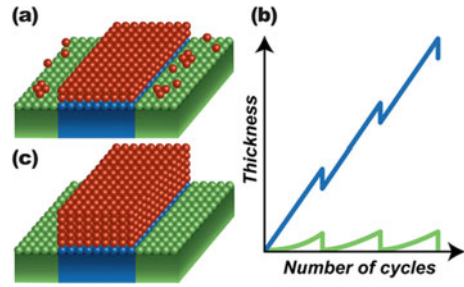


Fig. 1 Schematic showing ODPA SAMs deactivating Cu oxide layer while enabling a dielectric film deposition on SiO_2 [15] [With Permission from the American Chemical Society]. (Color figure online)

Fig. 2 Selectivity of AS-ALD is improved by introducing super-cycles of a selective etching step [32] [With Permission from the American Chemical Society]. (Color figure online)



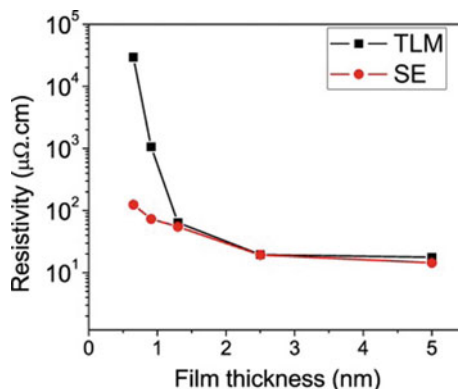
Si and HfO_2 but CH_4/CHF_3 mixture formed a FC film only on the Si surface which allowed selective removal of HfO_2 over Si [6]. The advantage of this method is that it enhances selective deposition by restoring the surface conditions of the non-growth areas [6].

Metallization Schemes

ALD is a critical technique used for the deposition of insulating, semiconducting, and conducting materials in the semiconducting and microelectronics industry as it enables enhanced control over the thickness and composition of thin film device layers [33]. Current trends in the industry call for 7 nm or less for the thickness of the films which is consistently achievable via ALD techniques. Copper has been used in the past as the wiring material but when its dimensions are shortened, the linear relationship between resistivity and dimensions falls apart which causes issues in its performance and reliability [34]. Several alternatives have been suggested to counter this issue. One measure is to replace metal liners with cobalt (Co) or ruthenium (Ru) because of their increased wettability and lower resistivity [34]. Cu connects can also be replaced with Co, tungsten (W), or Ru [34].

Tungsten (W) is an extremely hard transition metal which is quite inert to chemical degradation due to moisture but is also easily etched in fluorine plasma [35]. Tungsten films can be deposited with very high conformality and can be used as gate filling metal for nodes at 22 nm and beyond. They can also be used to protect silicon layers underneath. Yang et al. used hot-wire assisted ALD to deposit high purity α phase tungsten films on SiO_2 at 275 °C. A W seed layer was required for the formation of these films which had a uniform and conformal coverage of high-aspect-ratio structures. TLM structures and the Drude-Lorentz SE model reveal a low resistivity of 15 $\mu\Omega$ cm for the Hot-wire Atomic Layer Deposition (HWALD) W [36] (Fig. 3). An inverse relationship was noted between the thickness of the film and the resistivity of W. Bobb-Semple et al. deposited W on Si substrates using AS-ALD techniques and octadecylphosphonic acid (ODPA) self-assembled monolayers (SAMs) as the deactivating agent. W-ODPAs showed good results for blocking ZnO and Al_2O_3 ALD at 32 and 8 nm features, respectively [34]. Kalanyan et al. showed that modifying

Fig. 3 A comparison of the resistivity of tungsten films on SiO_2 substrate obtained by optical (SE, red circles) (275 °C) and electrical (TLM, black squares) (Room temperature) methods [36] [With Permission from Elsevier] (Color figure online).

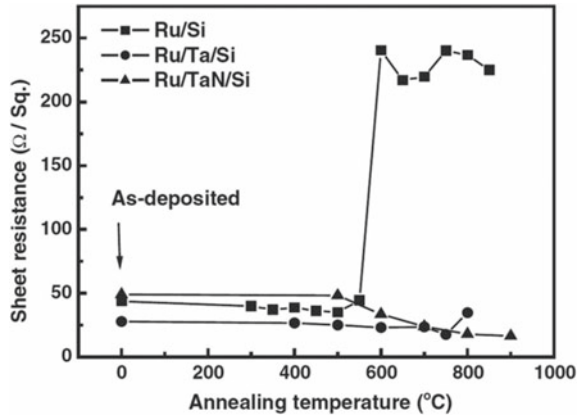


the W ALD process chemistry by adding H_2 during WF_6 dose step passivates SiO_2 against W nucleation without affecting the growth on Si, thereby expanding the ALD “selectivity window” [37].

Cobalt (Co) is a ferromagnetic transition metal that has been popular in interconnect technology to reduce RC delay in state-of-the-art devices [23, 38]. Kerrigan et al. used ALD techniques to deposit cobalt films on Si (with native oxide), thermal SiO_2 , and other metal substrates with bis(1,4-di-tert-butyl-1,3-diazadienyl)cobalt and tert-butylamine or diethylamine as precursors. At 200 °C, there was no growth on SiO_2 , Si with native oxide or hydrogen-terminated silicon after 500 cycles [41]. Silicide films are also a viable alternative for contact material to address narrow line-width effect issues [42–44]. Materials that have low contact resistance and good compatibility with silicon are imperative in the device scaling process, and several materials have been identified such as WSi_2 [42, 45, 46], TaSi_2 [42, 47, 48], and MoSi_2 [42, 49, 50]. These films are somewhat difficult to grow by direct reaction with silicon [42]; however, cobalt has proven to be an attractive candidate as it has a wider silicidation window and superior thermal and chemical stability [51–54]. CoSi_2 also has a comparable crystal structure to Si substrate which makes it an even better candidate for use as a contact material [55]. Various precursors and co-reactants have been used to create cobalt films with bis(cyclopentadienyl)cobalt(II) (cobaltocene, CoCp_2) precursor producing low resistivity and high purity films while being cost-effective. Lee et al. and Yoon et al. investigated the growth of Co films using NH_3 and H_2/N_2 plasma, respectively, and found that high quality films are formed [38–40]. This was further confirmed by Vos et al. in 2019 [23].

Ruthenium is a good candidate for diffusion barrier layers. It has lower resistivity than tantalum and titanium-based barriers which makes it a viable contender for their replacement. Ruthenium has good thermal stability, low resistivity and good adherence, and copper filling can be directly applied to Ru film without the need for a seed layer [56]. The thickness and the heat exposure time play a fundamental role in the diffusion limiting efficiency of pure Ru layers. Crystallinity also strongly affects its interdiffusion resistance. If grain boundaries are present, then there is strong Cu interdiffusion within the Ru layer [56]. Arunagiri et al. [57] deposited 5 nm layers

Fig. 4 Sheet resistance variation for Ru, Ru/Ta and Ru/TaN layers as a function of annealing temperature [56] [With Permission from The Electrochemical Society]

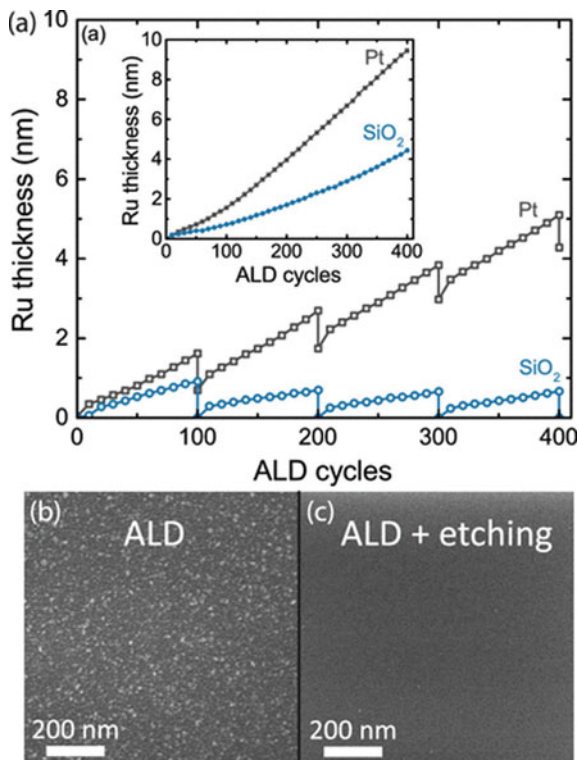


which were amorphous to combat this issue. Interdiffusion resistance can also be improved by introducing another substance, such as P or C, to form Ru alloys as they induce amorphization [56]. Ru layers, within the range of 10–30 nm, fail to form on Si as shown by Damayanti et al. [58]. This is due to the formation of Ru_2Si_3 which has a higher resistivity than pure Ru and thus causes a decline in conductivity as well as other barrier properties. Silicide formation can be detected by measuring the sheet resistance as shown in Fig. 4. This can be mitigated by placing a Ta film between the Si and the Ru films which has superior stability. Choi et al. and Xie et al. prepared Ru barrier layers on TaN by using plasma enhanced ALD [56, 59, 60] which were able to withstand temperatures higher than 400 °C. Wen et al. and Kwon et al. deposited Ru films on TiN via ALD with good thermal resistance of the final structure [56]. Vos et al. used a combination of AS-ALD and O_2 plasma etching to deposit Ru films on SiO_2/Si substrates (Fig. 5) [23].

Dielectrics

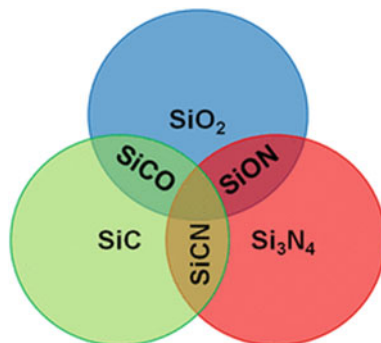
Despite the need for highly conformal Si-based dielectric films on high-aspect-ratio nanostructures in the microelectronics and semiconductor industries, it has been challenging to create these films at a low substrate temperature at different stages of integration into manufacturing [61]. Silicon dioxide (SiO_2) is one of the most widely used dielectric materials in the industry and has found applications in many silicon-based electronics as interconnects, gate spacers, diffusion barriers, etc. [63]. SiN_x films have been achieved by ALD processes but creating SiO_2 films at low temperatures with high conformity has been a challenge. For SiN_x films, the biggest issue has been identifying N precursors reactive enough to enable SiN_x film growth at substrate temperatures <400 °C [61]; this was overcome by employing N_2 plasma

Fig. 5 **a** Inset: Thickness as a function of ALD cycles for deposition on SiO_2 and Pt without etch cycles. Main figure: Ru film thickness as a function of ALD cycles for growth on SiO_2 and Pt with an intermittent etch cycle after every 100 ALD cycles. **b, c** Top-view SEM images after 400 ALD cycles on SiO_2 , **b** without etch cycles, or **c** with an etch cycle after every 100 ALD cycles [23] [With Permission from the American Chemical Society]. (Color figure online)



assisted ALD instead of thermal ALD. This method produced films that etch isotropically and have a low H content with conformity of typically <80% in HAR nanostructures [61, 62]. A chlorosilane precursor and NH_3 at high temperatures are used to create SiN_x films for industrial applications. A diagram showing the three most technologically relevant Si-based dielectrics and their ternary blends is shown in Fig. 6.

Fig. 6 Diagram showing the three most technologically relevant Si-based dielectrics and their ternary blends [61] [With Permission from the American Institute of Physics]



Shin et al. deposited SiO_2 films on Si(100) substrates at 50, 100, and 200 °C using ALD with di-isopropylaminosilane as a silicon source and oxygen as plasma. They varied the plasma time to optimize saturated growth-per-cycle (GPC) and found that films created at 50 °C had high GPC and refractive index values that were typical of thermal ALD SiO_2 [63]. Lee et al. also deposited SiO_2 films at temperatures between 100 and 200 °C using di-isopropylaminosilane ($\text{SiH}_3\text{N}(\text{C}_3\text{H}_7)_2$, DIPAS) as the Si precursor and ozone as the reactant, and achieved refractive index, density, and roughness that were comparable to conventionally deposited SiO_2 films [64].

Hafnium oxide (HfO_2) is a wide bandgap, chemically inert, and optically transparent dielectric [65] with a high-dielectric constant which has many applications in the semiconductor industry. Ultrathin interfacial HfO_2 layers were first used to passivate the surfaces of dye sensitized solar cells which reduced the density of interface states at the mesoporous TiO_2 /dye/electrolyte interface [65, 66]. Since then, only moderate levels of surface passivation have been reported. Excellent surface conformation has only been observed for wafers passivated with a $\text{HfO}_2/\text{Al}_2\text{O}_3$ stack [65] but this was predominantly due to the presence of Al_2O_3 . In 2017, Cui et al. investigated the deposition of hafnium oxide 15 nm thin films by ALD on n- and p-type crystalline silicon solar cells. There was a positive correlation between surface recombination and crystallinity of the HfO_2 which was, in turn, dependent on the film thickness and annealing temperature [65]. Oudot et al. demonstrated that HfO_2 layers deposited on a chemical silicon oxide substrate exhibited decrease in the density of interface traps at the Si/ SiO_2 interface [67]. The layers also presented an additional field effect passivation due to being negatively charged [67].

Future Directions

The growing multi-patterning process requirements compel the industry to use self-aligned structures for manufacturing new devices. Selective technologies are inherently self-aligned and are desirable for bottom-up processes. The development of new processes and materials are needed for such additive manufacturing. For most of the device structures, the use of metals and dielectrics are in the following forms. For the front end, lowest level, the conducting metal is either tungsten or cobalt. Some form of SiO_2 is the interlayer dielectric. Sidewall spacers are Si_3N_4 -type materials, such as carbon-doped silicon nitride to reduce the dielectric constant. For the back end, where there are 10–12 layers, the current choice for the metal and low-k dielectric materials are copper and C-doped SiO_2 . For the new manufacturing technologies, Co and Ru are the potential materials to eliminate the use of liners required for copper. As the reliability of AS-ALD technology develops, their applications in high volume productions becomes more relevant. It already plays a significant role in the nanoelectronics industry, but it is also important in catalysis where it can be used to fabricate model catalysts [32]. These applications are only the beginning of AS-ALD as it has the capacity to be used in various new avenues.

References

1. Khan R et al (2018) Area-selective atomic layer deposition using Si precursors as inhibitors. *Chem Mater* 30(21):7603–7610
2. Fang M, Ho JC (2015) Area-selective atomic layer deposition: conformal coating, subnanometer thickness control, and smart positioning. *ACS Nano* 9:8651–8654. <https://doi.org/10.1021/acs.nano.5b05249>
3. Kim H, Lee H-B-R, Maeng W-J (2009) Applications of atomic layer deposition to nanofabrication and emerging nanodevices. *Thin Solid Films* 517:2563–2580. <https://doi.org/10.1016/j.tsf.2008.09.007>
4. Mackus AJM, Bol AA, Kessels WMM (2014) The use of atomic layer deposition in advanced nanopatterning. *Nanoscale* 6:10941–10946. <https://doi.org/10.1039/C4NR01954G>
5. Singh JA, Yang N, Bent SF (2017) Nanoengineering heterogeneous catalysts by atomic layer deposition. *Annu Rev Chem Biomol Eng* 8:41–62. <https://doi.org/10.1146/annurev-chembioeng-060816-101547>
6. Lin K-Y et al (2020) Selective atomic layer etching of HfO₂ over silicon by precursor and substrate-dependent selective deposition. *J Vac Sci Technol, A* 38(3):032601
7. Haider A et al (2016) Area-selective atomic layer deposition using an inductively coupled plasma polymerized fluorocarbon layer: a case study for metal oxides. *J Phys Chem C* 120(46):26393–26401
8. Lemaire PC et al (2016) Understanding inherent substrate selectivity during atomic layer deposition: effect of surface preparation, hydroxyl density, and metal oxide composition on nucleation mechanisms during tungsten ALD. *J Chem Phys* 146(5):052811
9. Mameli A et al (2017) Area-selective atomic layer deposition of SiO₂ using acetylacetone as a chemoselective inhibitor in an ABC-type cycle. *ACS Nano* 11(9):9303–9311
10. Stevens E et al (2018) Area-selective atomic layer deposition of TiN, TiO₂, and HfO₂ on silicon nitride with inhibition on amorphous carbon. *Chem Mater* 30(10):3223–3232
11. Leskelä M, Ritala M (2003) Atomic layer deposition chemistry: recent developments and future challenges. *Angew Chem Int Ed* 42(45):5548–5554
12. Chen R et al (2005) Achieving area-selective atomic layer deposition on patterned substrates by selective surface modification. *Appl Phys Lett* 86(19):191910
13. Färm E et al (2006) Self-assembled octadecyltrimethoxysilane monolayers enabling selective-area atomic layer deposition of iridium. *Chem Vap Deposition* 12(7):415–417
14. Ras RHA et al (2008) Blocking the lateral film growth at the nanoscale in area-selective atomic layer deposition. *J Am Chem Soc* 130(34):11252–11253
15. Minaye Hashemi FS et al (2015) Self-correcting process for high quality patterning by atomic layer deposition. *ACS Nano* 9(9):8710–8717
16. Minaye Hashemi FS et al (2016) Selective deposition of dielectrics: limits and advantages of alkanethiol blocking agents on metal-dielectric patterns. *ACS Appl Mater Interfaces* 8(48):33264–33272
17. Hashemi FSM, Bent SF (2016) Sequential regeneration of self-assembled monolayers for highly selective atomic layer deposition. *Adv Mater Interfaces* 3(21):1600464
18. Closser RG et al (2017) Correcting defects in area selective molecular layer deposition. *J Vac Sci Technol, A* 35(3):031509
19. Heyne MH et al (2016) Two-dimensional WS₂ nanoribbon deposition by conversion of pre-patterned amorphous silicon. *Nanotechnology* 28(4):04LT01
20. Delabie A et al (2015) Low temperature deposition of 2D WS₂ layers from WF₆ and H₂S precursors: impact of reducing agents. *Chem Commun* 51(86):15692–15695
21. Mackus AJM (2018) Approaches and opportunities for area-selective atomic layer deposition. 2018 Int Symp VLSI Technol Syst Appl (VLSI-TSA)
22. Mameli A et al (2017) (Invited) Area-selective atomic layer deposition: role of surface chemistry. *ECS Trans* 80(3):39–48
23. Vos MFJ et al (2019) Area-selective deposition of ruthenium by combining atomic layer deposition and selective etching. *Chem Mater* 31(11):3878–3882

24. Vallat R et al (2019) Area selective deposition of TiO₂ by intercalation of plasma etching cycles in PEALD process: a bottom up approach for the simplification of 3D integration scheme. *J Vac Sci Technol, A* 37(2):020918
25. Song SK et al (2019) Integrated isothermal atomic layer deposition/atomic layer etching supercycles for area-selective deposition of TiO₂. *Chem Mater* 31(13):4793–4804
26. Huard CM et al (2018) Transient behavior in quasi-atomic layer etching of silicon dioxide and silicon nitride in fluorocarbon plasmas. *J Vac Sci Technol, A* 36(6):06B101
27. Martin RM, Chang JP (2009) Plasma etching of Hf-based high-k thin films. Part I. Effect of complex ions and radicals on the surface reactions. *J Vac Sci Technol, A* 27(2):209–216
28. Martin RM et al (2009) Plasma etching of Hf-based high-k thin films. Part II. Ion-enhanced surface reaction mechanisms. *J Vac Sci Technol, A* 27(2):217–223
29. Marchack N, Chang JP (2012) Chemical processing of materials on silicon: more functionality, smaller features, and larger wafers. *Ann Rev Chemical Biomol Eng* 3(1):235–262
30. Hélot M et al (2005) Plasma etching of HfO₂ at elevated temperatures in chlorine-based chemistry. *J Vac Sci Technol, A* 24(1):30–40
31. Bodart P et al (2012) SiCl₄/Cl₂ plasmas: a new chemistry to etch high-k materials selectively to Si-based materials. *J Vac Sci Technol, A* 30(2):020602
32. Mackus AJM et al (2019) From the bottom-up: toward area-selective atomic layer deposition with high selectivity. *Chem Mater* 31(1):2–12
33. King MJ et al (2018) Ab initio analysis of nucleation reactions during tungsten atomic layer deposition on Si(100) and W(110) substrates. *J Vac Sci Technol, A* 36(6):061507
34. Bobb-Semple D et al (2019) Area-selective atomic layer deposition assisted by self-assembled monolayers: a comparison of Cu, Co, W, and Ru. *Chem Mater* 31(5):1635–1645
35. Dobkin D (2020) Tungsten and tungsten silicide chemical vapor deposition from https://www.enigmatic-consulting.com/semiconductor_processing/CVD_Fundamentals/films/W_WSi.html#:~:text=Tungsten%20is%20used%20because%20of,W%20to%20the%20silicon%20dioxide
36. Yang M et al (2018) Low-resistivity α -phase tungsten films grown by hot-wire assisted atomic layer deposition in high-aspect-ratio structures. *Thin Solid Films* 646:199–208
37. Kalanyan B et al (2016) Using hydrogen to expand the inherent substrate selectivity window during tungsten atomic layer deposition. *Chem Mater* 28(1):117–126
38. Tökei Z et al (2016) On-chip interconnect trends, challenges and solutions: how to keep RC and reliability under control. In: 2016 IEEE Symposium VLSI Technology
39. Yoon J et al (2011) Atomic layer deposition of Co using N₂/H₂ plasma as a reactant. *J Electrochem Soc* 158(11):H1179
40. Lee H-B-R, Kim H (2006) High-quality cobalt thin films by plasma-enhanced atomic layer deposition. *Electrochem Solid-State Lett* 9(11):G323
41. Kerrigan MM et al (2017) Low temperature, selective atomic layer deposition of cobalt metal films using Bis(1,4-di-tert-butyl-1,3-diazadienyl)cobalt and alkylamine precursors. *Chem Mater* 29(17):7458–7466
42. Bernal-Ramos K et al (2015) Atomic layer deposition of cobalt silicide thin films studied by in situ infrared spectroscopy. *Chem Mater* 27(14):4943–4949
43. Lee H et al (2009) Cobalt and nickel atomic layer depositions for contact applications. In: 2009 IEEE international interconnect technology conference
44. Colgan EG et al (1996) Formation and stability of silicides on polycrystalline silicon. *Mater Sci Eng: R: Rep* 16(2):43–96
45. Telford SG et al (1993) Chemically vapor deposited tungsten silicide films using dichlorosilane in a single-wafer reactor: growth, properties, and thermal stability. *J Electrochem Soc* 140(12):3689–3701
46. Saito T et al (2007) Kinetic modeling of tungsten silicide chemical vapor deposition from WF₆ and Si₂H₆: determination of the reaction scheme and the gas-phase reaction rates. *Chem Eng Sci* 62(22):6403–6411
47. Widmer AE, Fehlmann R (1986) The growth and physical properties of low pressure chemically vapour-deposited films of tantalum silicide on n⁺-type polycrystalline silicon. *Thin Solid Films* 138(1):131–140

48. Chang KY, Pancholy RK (1981) Tantalum silicide interconnect characterization by surface analytical techniques. *Appl Surface Sci* 9(1):377–387
49. Inoue S et al (1983) Properties of molybdenum silicide film deposited by chemical vapor deposition. *J Electrochem Soc* 130(7):1603–1607
50. Yao Z et al (1999) Molybdenum silicide based materials and their properties. *J Mater Eng Perform* 8(3):291–304
51. Bocelli S et al (1995) Experimental identification of the optical phonon of CoSi_2 in the infrared. *Appl Surf Sci* 91(1):30–33
52. Hsia SL et al (1992) Resistance and structural stabilities of epitaxial CoSi_2 films on (001) Si substrates. *J Appl Phys* 72(5):1864–1873
53. Takahashi F et al (2001) Growth and characterization of CoSi_2 films on Si (100) substrates. *Appl Surf Sci* 169–170:315–319
54. Wölfel M et al (1990) Optical constants of thin CoSi_2 films on silicon. *Appl Phys A* 50(2):177–181
55. Starke U et al (1998) Structure of epitaxial CoSi_2 films on Si(111) studied with low-energy electron diffraction (LEED). *Surf Rev Lett* 05(01):139–144
56. Bernasconi R, Magagnin L (2018) Review—ruthenium as diffusion barrier layer in electronic interconnects: current literature with a focus on electrochemical deposition methods. *J Electrochem Soc* 166(1):D3219–D3225
57. Arunagiri TN et al (2005) 5nm ruthenium thin film as a directly plateable copper diffusion barrier. *Appl Phys Lett* 86(8):083104
58. Damayanti M et al (2006) Effects of dissolved nitrogen in improving barrier properties of ruthenium. *Appl Phys Lett* 88(4):044101
59. Choi BH et al (2010) Preparation of Ru thin film layer on Si and TaN/Si as diffusion barrier by plasma enhanced atomic layer deposition. *Microelectron Eng* 87(5):1391–1395
60. Xie Q et al (2009) Ru thin film grown on TaN by plasma enhanced atomic layer deposition. *Thin Solid Films* 517(16):4689–4693
61. Ovanesyan RA et al (2019) Atomic layer deposition of silicon-based dielectrics for semiconductor manufacturing: current status and future outlook. *J Vac Sci Technol, A* 37(6):060904
62. Park J-M et al (2016) Plasma-enhanced atomic layer deposition of silicon nitride using a novel silylamine precursor. *ACS Appl Mater Interfaces* 8(32):20865–20871
63. Shin D et al (2018) Plasma-enhanced atomic layer deposition of low temperature silicon dioxide films using di-isopropylaminosilane as a precursor. *Thin Solid Films* 660:572–577
64. Lee Y-S et al (2017) Low temperature atomic layer deposition of SiO_2 thin films using di-isopropylaminosilane and ozone. *Ceram Int* 43(2):2095–2099
65. Cui J et al (2017) Highly effective electronic passivation of silicon surfaces by atomic layer deposited hafnium oxide. *Appl Phys Lett* 110(2):021602
66. Bills B et al (2011) Effects of atomic layer deposited HfO_2 compact layer on the performance of dye-sensitized solar cells. *Thin Solid Films* 519(22):7803–7808
67. Oudot E et al (2017) Hydrogen passivation of silicon/silicon oxide interface by atomic layer deposited hafnium oxide and impact of silicon oxide underlayer. *J Vac Sci Technol, A* 36(1):01A116

Investigations on the Process Stability of Dry Deep Drawing with Volatile Lubricants Injected Through Laser-Drilled Microholes



Gerd Reichardt, Manuel Henn, Paul Reichle, Daniel Hemming, Georg Umlauf, Kim Riedmüller, Rudolf Weber, Jakob Barz, Mathias Liewald, Thomas Graf, and Günter E. M. Tovar

Abstract To prevent damage to components and tools during deep-drawing processes, the use of lubricants is recommended. Depending on the demands of given processes and materials, different types of lubricants such as mineral oils, synthetic oils, emulsions or waxes are generally used. However, these lubricants often contain substances that are harmful to human health and environment. Additionally, they must be applied before forming operations and washed off afterwards to enable subsequent processes. A novel tribological system using volatile lubricants such as CO₂ or N₂ has been developed and tested to counteract these disadvantages. The operating principle of this tribological system is based on the injection of volatile media into the friction zone under high pressure to ensure the separation of tool and sheet metal surface. This contribution presents the latest findings on the laser drilling of microholes and on process stability of the dry deep-drawing process under endurance conditions.

Keywords Dry forming · Deep drawing · Friction investigations · Ultrashort pulsed · Laser drilling

G. Reichardt (✉) · K. Riedmüller · M. Liewald
Institute for Metal Forming Technology, University of Stuttgart, Holzgartenstrasse 17, 70174 Stuttgart, Germany
e-mail: gerd.reichardt@ifu.uni-stuttgart.de

M. Henn · R. Weber · T. Graf
Institut für Strahlwerkzeuge, University of Stuttgart, Pfaffenwaldring 43, 70569 Stuttgart, Germany

P. Reichle · D. Hemming · G. E. M. Tovar
Institute of Interfacial Process Engineering and Plasma Technology, University of Stuttgart, Nobelstraße 12, 70569 Stuttgart, Germany

G. Umlauf · J. Barz
Fraunhofer Institute for Interfacial Engineering and Biotechnology, Nobelstraße 12, 70569 Stuttgart, Germany

Introduction

Deep drawing is generally used in sheet metal forming industries as a manufacturing process for a large number of components. Thus, in addition to applications in the car body sector, deep drawing is also used to manufacture smaller products, e.g., in the electrochemical industry (battery sleeves) as well as in medical industries (aspirator housings, medication containers), where requirements in terms of technical cleanliness are of great importance.

Deep-drawing processes are significantly dependent on the prevailing friction effects, which are particularly influenced by the relative movement and the contact pressures occurring between the tool and component surfaces during the process. The control of this tribological system is of central importance, as otherwise negative effects such as component surface damage, tool wear and component failure due to tears caused by excessive friction forces can arise. Therefore, lubricants are used in conventional deep-drawing processes to reduce such frictional effects and thus ensure high component quality and low tool wear. However, these lubricants can consist of mineral oils, synthetic oils, emulsions or waxes, which have to be applied prior to forming and then laboriously removed again [1]. In addition, such conventional lubricants often contain additives such as chlorinated paraffins or heavy metals that are harmful to the environment and health, aimed at improving their lubricating properties [2].

Within the research initiative SPP1676 “Dry Forming” funded by the German Research Foundation from 2014 until 2020, a novel tribological system for deep drawing was investigated at the University of Stuttgart. In this process, volatile lubricants are introduced under high pressure directly into the frictional contact interfaces between tool and sheet metal component via tightly spaced, laser-drilled microholes. As shown in Fig. 1, gaseous nitrogen (N_2) or liquid carbon dioxide (CO_2) from gas cylinders is used as a volatile lubricant. The advantages of this tribological system include, on the one hand, a reduction in the process chain with regard to the application of lubricants and the cleaning of components, and, on the other hand, a significant improvement in process reliability due to the very good separating effect of volatile lubricants [3]. In addition, these volatile lubricants evaporate without any residue directly after the forming which results in a high level of technical cleanliness on the surfaces of formed components.

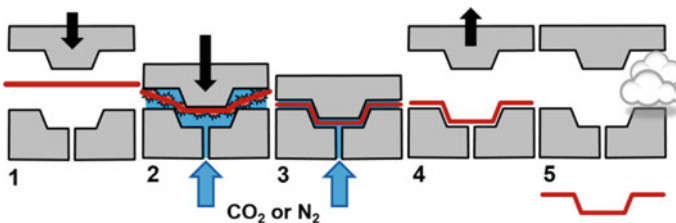
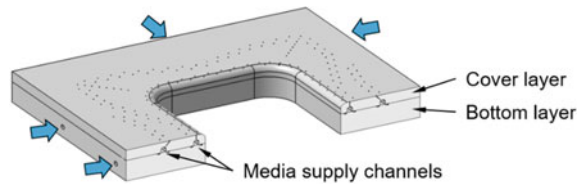


Fig. 1 Deep drawing with novel tribological system using volatile lubricants [4]. (Color figure online)

Fig. 2 Setup of deep-drawing die/tool inserts with integrated media supply channels. (Color figure online)



To characterize this novel tribological system, numerous model tests were carried out by means of strip drawing tests on the flat track and stretch bending tests. The main objective of these experimental investigations was the determination of the friction coefficients as a function of contact normal pressure, drawing speed, lubricant, number and distribution of the microholes, and the geometry of the microholes themselves. The results obtained showed that for CO_2 as well as for N_2 , a diffuser geometry with a gas inlet diameter of $200\ \mu\text{m}$ ($2 \cdot r_1$) and a gas outlet diameter of $600\ \mu\text{m}$ ($2 \cdot r_2$) achieves the lowest friction coefficients and therefore is best suited for the tribological system [5]. Based on the results of the model tests, the tribological system was implemented in the tool inserts of a deep-drawing tool for a rectangular cup geometry. Thereby, besides the development of the tool with the laser-drilled microholes, the media supply was also designed, as shown in Fig. 2.

Especially, the maximum achievable drilling depth by laser-drilling and the necessary operational stability of the tool inserts with gas supply, consisting of blank holder and die, pose some challenges. During forming, the tool inserts are loaded perpendicular to the contact surface by the blank holder force, tangential to the contact surface by the tensile and frictional forces and from the inner side of the tool by the media pressure. When designing the tool inserts, it is therefore important to ensure that the cover layers of die and blank holder are sufficiently dimensioned, and that the media feed is designed in favor to reduce notch stress. A material thickness of at least 5 mm has proven to be appropriate for applied media pressures between 60 and 100 bars (6–10 MPa) in combination with the chosen tool steel 1.2379. The necessary microholes (see Fig. 6), having a depth of 5 mm (orthogonal hole axis) and approx. 6.7 mm (inclined hole axis), were manufactured using a laser-drilling process, that enables conical hole geometries.

Laser Drilling of the Microholes

Percussion drilling of particularly deep microholes has already been investigated in previous works [6, 7]. Equations for the calculation of the necessary pulse energy needed to achieve the desired drilling depth as well as the desired microhole diameter were described. A high pulse energy of 5 mJ was used to achieve the desired drilling depth of 5 mm. Meeting the required microhole diameter of $2 \cdot r_2 = 600\ \mu\text{m}$ was accomplished by changing the position of the sample surface relative to the focus position, since the ablation radius is a function of the distance in the direction of the

beam propagation. To some extent, this technique enabled for longitudinal shaping of the microholes, since the ablation diameter and the drilling depth are linked and result in a conical hole shape [8].

The resulting shape of the produced microholes was close to the requirements for initial testing. However, there was potential for improvement of the quality in terms of roundness at the microhole outlet (r_2) as well as a preferably larger inlet radius (r_1). In order to improve both features, a new drilling concept using a galvanometer-scanning optic has been investigated, in which the laser beam is moved transverse to the beam propagation along a circle-or spiral-path during the drilling process.

Laser Drilling with Scanning Optics

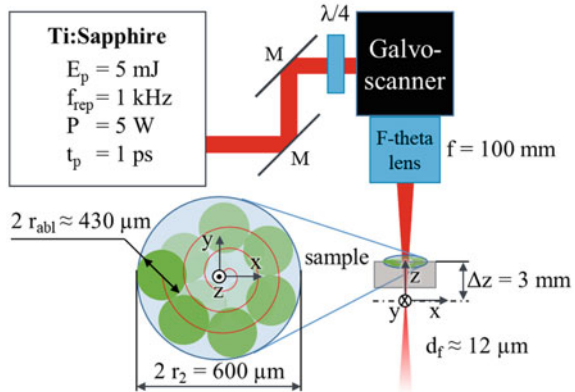
The same ultrashort pulsed Ti:Sapphire laser as shown in previous work [8], was used for the experiments. The technical specifications of the laser beam source are listed in Table 1. In this setup, a galvanometer-scanner was used to enable transversal beam movement during the drilling process. The experimental setup is shown in Fig. 3. The linearly polarized raw laser beam was circularly polarized passing through a $\lambda/4$ wave plate, before entering the scanning head, and focused with a telecentric f-theta lens with a focal length of 100 mm onto the samples, which were mounted on xyz-translation stages. The combination of a raw beam diameter of $D_r = 10$ mm with the short focal length of 100 mm lead to a focus diameter of $d_f \approx 12 \mu\text{m}$ and a very short Rayleigh-length of only $z_R \approx 122 \mu\text{m}$. With the help of the z-axis, it was possible to move the samples in beam propagation. This allowed the spot size and effectively the ablation diameter on the sample surface to be adjusted.

The radius of the microhole on the side of the laser impact is determined by the ablation radius. According to [6] the ablation radius can be calculated analytically to

Table 1 Process parameters of the used laser system

Laser system: spectra physics spitfire H	
Wavelength (λ)	800 nm
Beam quality (M^2)	<1.2
Max. pulse energy (E_p)	7 mJ
Pulse repetition rate (f_{rep})	1 kHz
Max. average power (P)	7 W
Pulse duration (τ_p)	1 ps
Raw beam diameter (D_r)	10 mm
Focal length (f_L)	100 mm
Rayleigh-length (z_R)	$\approx 122 \mu\text{m}$

Fig. 3 Experimental setup and scanning strategy (bottom left, not to scale). (Color figure online)



$$r_{abl}(z, E_p) = r_{beam}(z) \cdot \sqrt{\frac{1}{2} \ln \left(\frac{2 \cdot E_p}{\pi \cdot r_{beam}(z)^2 \cdot \phi_{th}} \right)}, \quad (1)$$

where ϕ_{th} is the local fluence threshold, at which ablation of the material occurs. The ablation radius is mainly dependent on the pulse energy E_p and the beam radius $r_{beam}(z)$, which in turn is a function of the position along the laser beam propagation in z direction and given by

$$r_{beam}(z) = w_0 \cdot \sqrt{1 + z^2 \cdot \left(\frac{M^2 \cdot \lambda}{\pi \cdot w_0^2} \right)^2}, \quad (2)$$

where w_0 is the beam radius in focus ($z = 0$), M^2 the beam quality and λ the wavelength of the laser beam. When working with high pulse energies in combination with ultrashort pulse durations τ_p , an air-breakdown can occur in the focal region ($z \approx 0$), where the irradiance increases far beyond 10^{13} W/cm². Avoiding this effect proved to be particularly important in order to produce microholes with precise entrance dimensions, as shown in [8]. The irradiance is given by

$$I(z) = \frac{2 \cdot E_p}{\pi \cdot r_{beam}(z)^2 \cdot \tau_p} \quad (3)$$

and can be limited by increasing the spot size on the sample surface.

In the following example also shown in Fig. 3, the sample surface was moved 3 mm closer to the focusing lens, resulting in a beam radius on the surface of approximately 150 μ m. For a chosen pulse energy of $E_p = 5$ mJ and a pulse duration of $\tau_p = 1$ ps, the irradiance at this position amounts to approximately $I \approx 1.4 \cdot 10^{13}$ W/cm². With a threshold fluence of $\phi_{th} = 0.09$ J/cm² for steel, the resulting ablation radius was approximately $r_{abl} \approx 214$ μ m.

With the use of the galvanometer-scanner, a scanning strategy with a spiral path was chosen. To meet the required microhole radius, the scanning radius r_{scan} , which describes the outermost point of a spiral, can be derived to

$$r_{scan,max} = r_{hole} - r_{abl} \tag{4}$$

In the case of the previously calculated ablation radius and the desired microhole entrance radius $r_2 = 300 \mu\text{m}$, the resulting scanning radius is approximately $86 \mu\text{m}$.

The scanning speed was set to $v_{scan} \approx 430 \text{ mm/s}$, which resulted in a circumferential pulse overlap of 0% at a given pulse repetition rate of 1 kHz. A schematic of the scanning strategy is also shown on the left of Fig. 3. For this experiment, samples made from stainless steel (1.4301) with a thickness of 5 mm were used.

Results and Discussion of Laser-Drilling

For the production of the microholes into the radius inserts (see Section “Tribological Investigations”), the setup described in the previous section was used.

Figure 4 shows a comparison between microhole shapes produced with stationary and moving beam. The cross-section of a microhole drilled with a stationary beam is shown in Fig. 4a, the corresponding inlet and outlet-radii (r_1 and r_2) are shown in (b) and (c), respectively. The dotted circles represent equivalent cross-sectional areas.

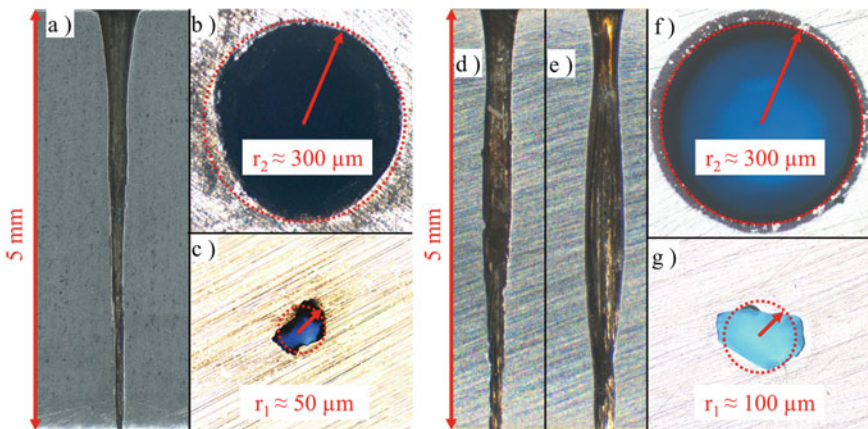


Fig. 4 Comparison of microhole shapes between percussion drilling with stationary and moving beam. **a** Cross-section of a microhole drilled with a stationary beam with corresponding outlet and inlet-radii shown in **(b)** and **(c)**, respectively. **d** Cross-section of a microhole drilled with a moving beam along a spiral path. The corresponding outlet and inlet-radii are shown in **(f)** and **(g)**, respectively. **e** Cross-section of a microhole drilled with the same parameters as in **(d)**, but with a higher number of pulses, showing pronounced bulging at approximately half of the drilling depth. The dotted circles represent equivalent cross-sectional areas. (Color figure online)

The general shape of this microhole is mostly conical and therefore similar to the ideal shape. The shape of the microhole on the important gas outlet side (r_2) shows some minor but still noticeable deviations in roundness. On the side of the gas inlet (r_1), a rather rectangular outline can be seen, where the marked equivalent radius r_1 is approximately 50 μm . About 2.1×10^5 pulses were necessary for the production of this microhole.

Cross-sections of microholes drilled with a moving beam, described in the previous chapter, are shown in Fig. 4d and e. Images of the gas-outlet and inlet sides corresponding to the cross-section of (d) are shown in (f) and (g), respectively. Apart from a slight transverse bulge stretching over the midsection, the general shape of the microhole is mostly conical. When compared to the cross-section in (a), the overall ablated volume increased significantly. Also, the inlet-radius increased by a factor of two, resulting in an equivalent radius r_1 of approximately 100 μm . However, the shape of the gas inlet is still rather rectangular. An almost perfect circle can be observed at the gas outlet where the laser beam impacts. This is due to the movement of the beam during drilling. The grey ring around the microhole is merely a slight discoloration of the surface. Roughly 3×10^5 pulses were necessary for the drilling of this microhole.

Figure 4e shows a cross-section of a microhole drilled with the same parameters as in (d). However, the number of pulses necessary to drill through was around 4.2×10^5 . A long and pronounced bulging in the midsection can be observed. In addition, the ablated volume as well as the inlet diameter have been further increased. The transverse growth could be due to a particle-ignited plasma inside the microhole. This effect can be caused by particles remaining in the microhole which were ablated in previous pulses and which have not yet exited the microhole or been deposited again. It is assumed that the very short Rayleigh-length of the setup used here can favor the formation of such particle-induced plasmas. The position of the laser focus was 3 mm below the sample surface, at this point very high irradiances can still occur.

Basic Characterization of Used CO_2 as Lubricant Substitutes

In literature, carbon dioxide is frequently associated with a reduction of the coefficient of friction [9, 10]. Another point is its inertness, the non-toxicity, and its relative cheap price. Because of the same benefits, another possible volatile lubricant is nitrogen. That is why this research focusses on these two lubrication media.

The expansion of the lubricant inside the microhole and the working zone between tool and sheet metal leads to a cool down (see Fig. 8). This effect is called the Joule-Thompson effect. In case of CO_2 and an expansion from 60 bar to ambient conditions, it effects an averaged cooling of 1.1 K bar^{-1} [12]. The special feature of using CO_2 is that it is in a liquid state at room temperature (293 K) and pressures above $6 \times 10^6 \text{ Pa}$ (see Fig. 5). Therefore, if the fluid is extracted from a gas cylinder by a riser pipe in its liquid state, another effect occurs. The carbon dioxide evaporates partially. To overcome the intermolecular reactions, the enthalpy of vaporization is

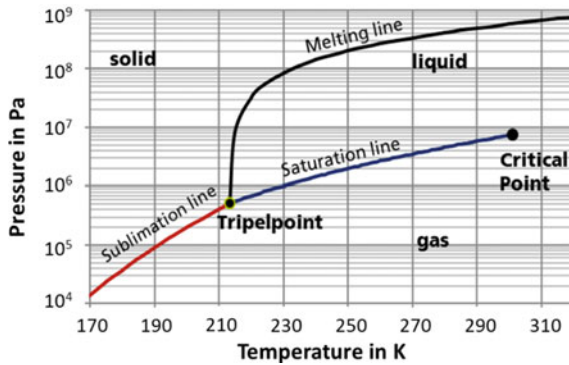


Fig. 5 Phase diagram of CO₂ including the three states. Adapted from [11]. (Color figure online)

needed—the temperature drops again. In case of small droplets, this cooling effect leads to temperatures around $-78\text{ }^{\circ}\text{C}$ and can surmount the heat of crystallization causing CO₂ to shift to its solid state. The forming of dry ice is the reason why previous investigations showed a lower coefficient of friction by using liquid in contradiction to gaseous carbon dioxide [13]. In contrast to carbon dioxide, the nitrogen stays constantly gaseous at the given process parameters. Hence, to examine the lubrication effects of different phases of the lubrication media the following investigations focuses on the usage of CO₂.

Numerical Investigation of the Fluid Behavior Inside the Microholes

Background and Boundary Conditions

As mentioned (see Fig. 6), the manufactured microholes gradually widen their cross section in flow direction of the lubrication media like a diffusor in subsonic velocities. At supersonic velocities, this means a rising velocity of the fluid. To investigate how the shape of the microholes can influence the velocity, pressure and temperature conditions of the lubricant, CFD simulations, especially for CO₂, were carried out. As shown in Figs. 2 and 6, the lubricant supply for the microholes is implemented by a bigger supply channel inside the tool. For a proper lubrication, it is necessary to locate microholes in different highly loaded areas of the tool. Because of the position of the supply channels, it is not generally possible to keep the depth of the microholes constant at 5 mm. In some areas, a microhole with a depth of 6.7 mm is required. Caused by production, this leads to a halving of the lubricant-entrance radius (r_1) at the supply channel from 100 to 50 μm . Previous studies [13, 14] examined the fluid

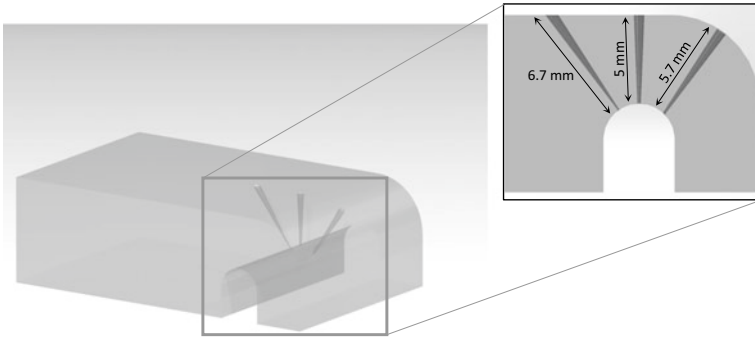


Fig. 6 Cross-section of a 3D tool model with three possible types of microholes (vertical: regular hole, inclined: longer holes with reduced entrance radius r_1)

flow behavior inside the 5 mm microholes. To compare the flow conditions of the two different microhole types pursuing CFD simulations were carried out.

The simulations of the fluid flow were carried out with the open source program OpenFOAM. The software includes special solver for calculating fluid dynamics. To describe the dynamics, the $k-\varepsilon$ turbulence model was used. Previous investigations showed for this model a sufficient accuracy compared to the moderate computing time. The fringes of the model were defined in a simplified way—the wall roughness was neglected and a constantly widening diameter in flow direction was modeled. As temperature of the surrounding material, room temperature was implemented. However, different measurements (IR-camera, pyrometer and thermocouple) showed only a low decrease of the tool temperature. The specific heat capacity of the lubricant was set constant to $1450 \text{ kJ (kg K)}^{-1}$. As the carbon dioxide is extracted directly from the gas cylinder, an inlet pressure of 60 bar was determined. The start pressure inside the microhole was set to atmospheric pressure (1 bar). The viscosity was calculated using the Sutherland's law in dependence of the fluid temperature. Because of the proximity to the critical point, the compressibility factor of the carbon dioxide was defined in advance by Peng-Robinson equation and set constant to 0.74.

As mentioned, a number of simplifications were made to design the model as a 2D axis-symmetric radius selection (see Fig. 8). In a following step, the radius section can be rotated along the central axis to create a 3D model as shown in Fig. 7. To implement the supply line to the microhole as well as the inflow behavior, a kind of storage vessel was implemented before the microhole entrance.

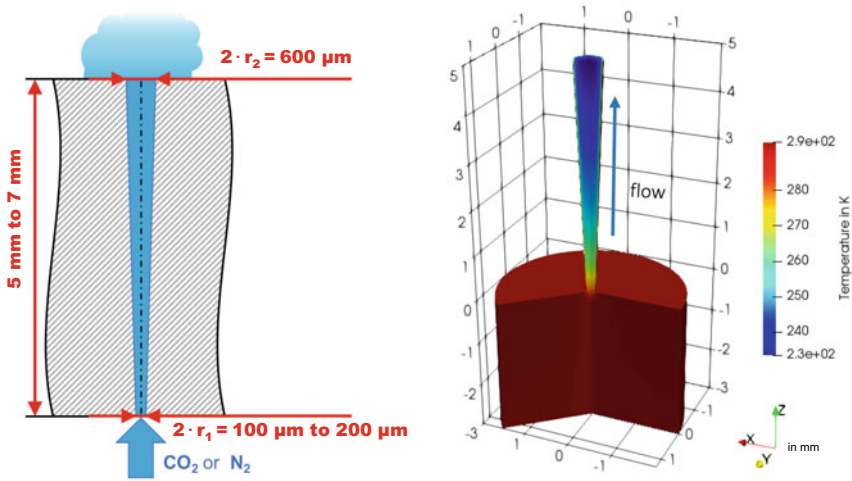


Fig. 7 Left: Drawing of a cross section trough a simplified microhole. Right: 3D fluid flow simulation of the lubricant temperature inside of a microhole created from a symmetric rotated 2D radius section. (Color figure online)

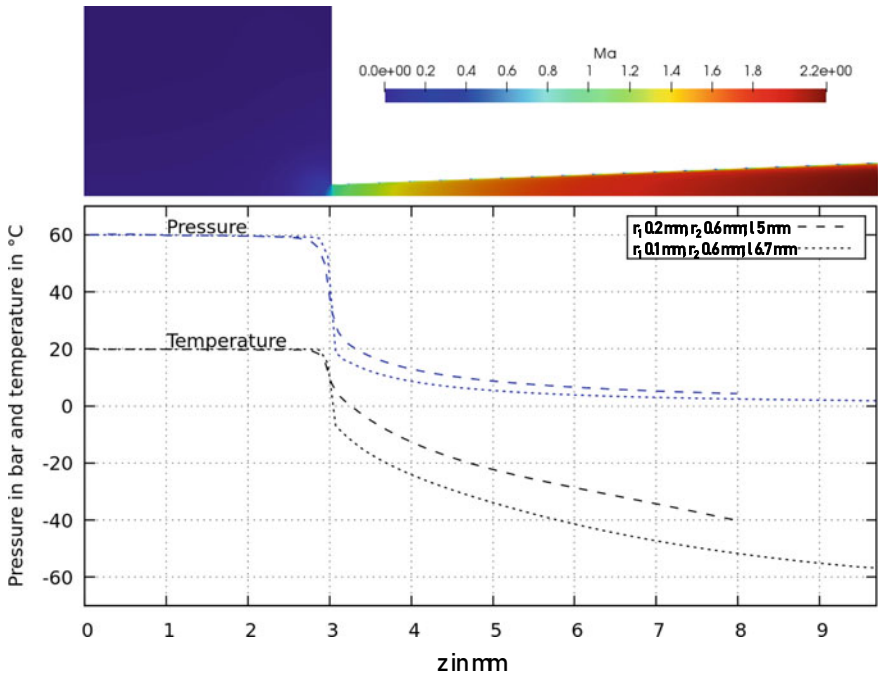


Fig. 8 Comparison of the simulation results (pressure and temperature) of the CO₂ fluid flow inside of the two different microhole geometries (bottom). To illustrate the microhole geometry along the z-axis, a symmetric radius section of the fluid velocity (in Mach) inside the 6.7 mm microhole is shown (top). (Color figure online)

Table 2 Parameters of SBTs

Sheet metal material	DC05 + ZE
Tool material	1.2379 fully hardened to HRC60, polished
Tool radius insert	R5, R7.5, R10, R12.5
Lubricant	CO ₂ (l.) and ZO3368
Media pressure	60 bar = 6 MPa
Microholes	11 microholes single-line, diffuser
Injection angle	45°
Drawing velocity	100 mm/s
Retention force Fr	3.4; 4; 5 and 6.1 kN

Results and Discussion of Fluid Behavior

To check the outlet temperatures of the simulation (Fig. 8), several tests with laser-drilled microholes of different geometries were carried out. The measured temperatures ranged from -35 to -63 °C. For reasons of the measuring method via thermocouple and heat transfer effects, partially lower temperatures are possible. Therefore, the results of the simulation can be assumed as realistic.

As expected, the results from the CDF simulation show, that an increase in depth of the microhole leads to a decrease of the outlet pressure and a higher velocity at the outlet. Compared to the relatively small pressure difference, a strong temperature difference of nearly 20 °C can be obtained. Such low temperatures arise mainly due to the smaller inlet diameter for reasons of a higher expansion and acceleration. The lower temperatures as well as the longer residence time inside the microhole can lead to an escalation of dry ice formation. Hence, the friction reduction caused by the decrease of surface pressure due to the applied lubricant pressure, acting in the interstice between tool and sheet metal, seems to be lower. Nevertheless, the effect of the lubrication due to dry ice is expected to be higher by using the deeper microholes.

Tribological Investigations

Stretch Bending Testing Rig

Tool radii of forming tools are the areas most exposed to friction during deep drawing. For a meaningful evaluation of tribosystems, a friction characterization is therefore necessary, especially at such highly loaded tool radii. In the investigations reported about in this paper, the friction coefficients at tool radii were therefore determined using a Stretch Bending Test (SBT). Varied parameter of this investigation (see Table 2) were radius size, retention force and lubricant (liquid CO₂ and conventional drawing oil ZO3368). The setup of the testing rig is depicted in Fig. 9. For each

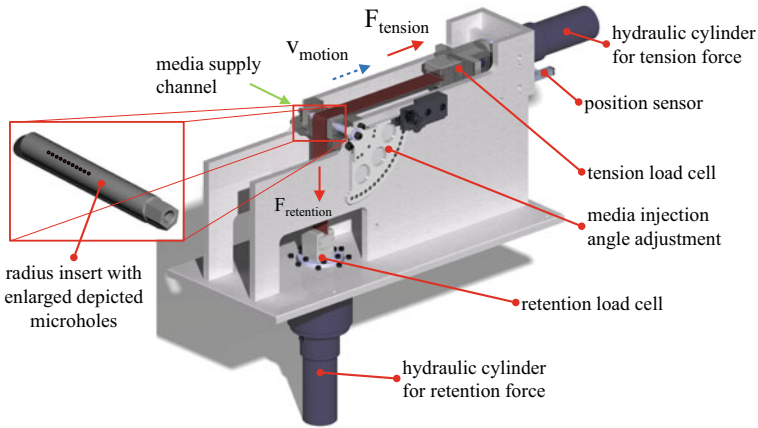


Fig. 9 Experimental setup for stretch-bending-test (SBT) using volatile lubricants [15]. (Color figure online)

experiment, a 60 mm wide sheet metal strip was drawn over a radius at constant speed and constant retention force. The lubricating media was supplied via an axial borehole in the radii, which was connected with laser-drilled microholes on the contact surface. Finally, the coefficient of friction μ could be calculated indirectly from the tensile and retention forces F_t and F_r measured during the experiments using the rope friction equation according to Euler/Eytelwein.

$$\text{Rope friction according to Euler/Eytelwein: } \mu = \frac{1}{\theta} \cdot \ln\left(\frac{F_t}{F_r}\right) \quad F_t > F_r; \theta = \frac{\pi}{2} \tag{4}$$

In this investigation, the bending force for the calculation of the coefficient of friction was neglected due to the low material strength (DC05) and the low sheet thickness (0.7 mm). The SBT results presented in the following focus on CO₂ as volatile lubricant and an injection angle of 45° [15, 16]. Here, advantage of liquid CO₂ is the phase change occurring during the friction effects (see See section “Basic characterization of used CO₂ as lubricant substitutes”).

Normal Contact Pressure of Radii Using FE-Methods

Experimentally investigated coefficient of friction are strongly influenced by radius size and retention force of SBT. For this reason, the experimentally obtained coefficients of friction using different parameter set-ups cannot be compared directly with each other. In order to enable a comparative study of the coefficients of friction, the

maximum occurring normal contact pressure along the radii was chosen. To calculate the maximum normal contact pressure, the distribution of normal contact pressure along different radius sizes and applied retention forces were determined by numerical investigations using LS-Dyna FE-Code. The numerical method was conducted, because normal contact pressure distributions cannot be determined experimentally during SBTs. To validate the simulations, the tension and retention forces, measured during the experiments carried out, were used. The FE-Model used for determining normal contact pressure distributions along radii is presented in Fig. 10 and Table 3.

The results of the numerical investigated maximum normal contact pressure are depicted in Fig. 11 for all varied retention forces and radius sizes. As expected, the value of maximum normal contact pressure increases with decreasing radius size. Furthermore, Fig. 11 shows that an increasing retention force also results in an

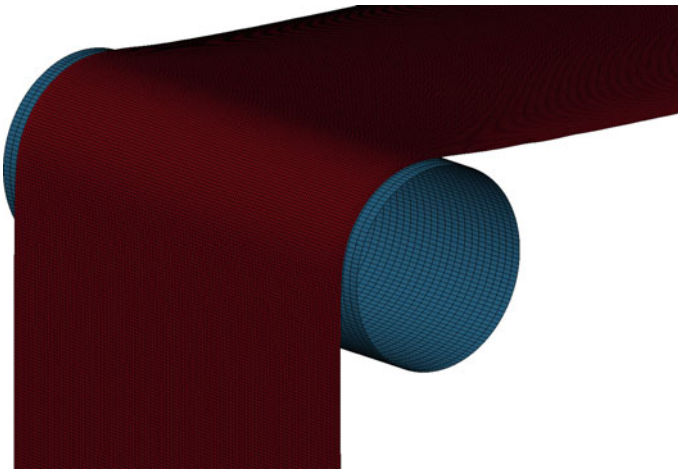


Fig. 10 Numerical model of SBT in LS-Dyna. (Color figure online)

Table 3 Parameters of FE-simulations

Sheet material	Mat36—3 Parameter Barlat, DC05 + ZE
Element type sheet material	ET16—fully integrated shell element
Integration points	9 through shell thickness
Tool material	Mat20—rigid
Mesh size	Edge length 0.4—0.5 mm
Radius sizes	R5, R7.5, R10, R12.5
Retention force F_r	3.4; 4; 5, 6.1 and 7 kN
Contact model	Automatic surface to surface mortar

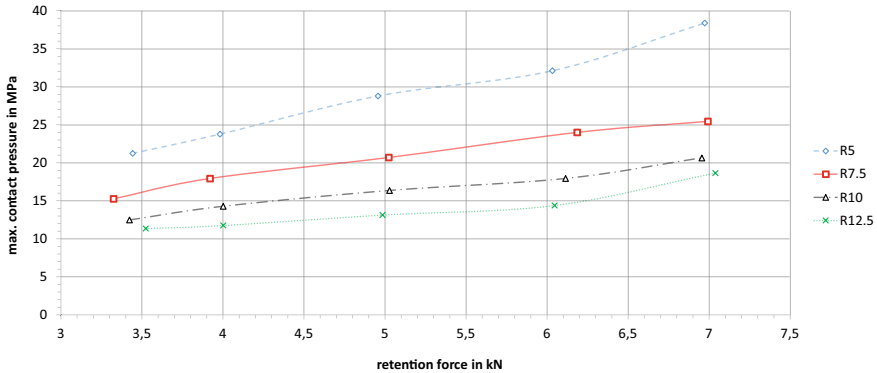


Fig. 11 Estimated maximum normal contact pressures of SBTs with varied retention forces and radius sizes by FE-simulations. (Color figure online)

increasing maximum normal contact pressure. The results of the numerical investigation are used in the following chapter for the comparative study of the coefficients of friction.

Comparative Study of Coefficients of Friction Measured by SBTs Using Normal Contact Pressure

Using the numerical results of Section “Normal Contact Pressure of Radii Using FE-Methods”, a comparison of all experimentally determined coefficients of friction by means of SBTs is feasible. For each of the SBTs performed with different experimental parameters and thus for each coefficient of friction measured, the corresponding maximum value of the numerically calculated normal contact pressure distribution could be assigned. This allows a direct comparison of all friction values as a function of maximum contact pressure, as depicted Fig. 12. Principally, almost all measured coefficients of friction show the same tendency when using both CO₂ and conventional drawing oil ZO3368 as lubricant and when radius size remains the same. However, the most remarkable fact is that all coefficients of friction of volatile CO₂-lubrication (continuous lines in Fig. 12) are below the friction values of the conventional mineral oil-based lubricant ZO3368 (dashed lines in Fig. 12). Reduced coefficients of friction cause reduced tensile stress in sheet metal components and thus reduce the risk of necking and splits. This indicates the high potential of CO₂ as volatile lubricant.

The decrease of the friction values with increasing surface pressure, which occurs in all conventionally lubricated tests (dashed lines) as well as with R5 and R7.5 with CO₂ as lubricant, corresponds to the behavior known from literature [17, 18]. When using conventional lubricants, the hydrostatic and hydrodynamic lubrication effects caused by higher surface pressures are responsible for this behavior. With volatile

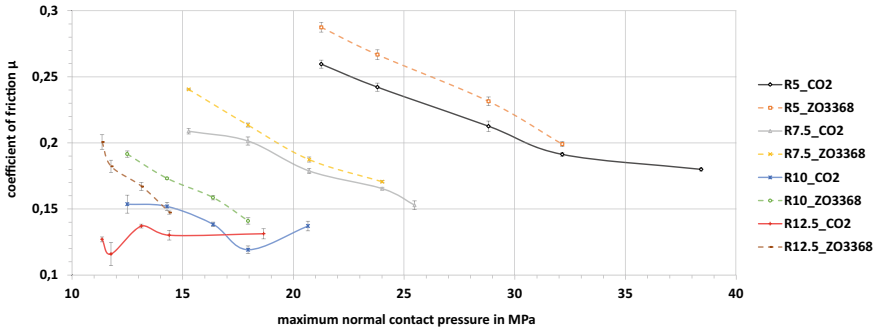


Fig. 12 Experimental results for coefficient of friction of SBT plotted over maximum normal contact stress at radii. The data points are connected by lines to guide the eye. (Color figure online)

lubricants, this friction reducing effect occurs due to a sealing effect of the contact interface caused by higher surface pressure. Due to this sealing effect, the gap between the tool and the sheet material is reduced and the media pressure increases until a state of equilibrium is reached. The higher media pressure increases the load-bearing capacity and thus the separating effect of the friction partners. Friction contact is still a mixed friction of metal on metal and gas friction, as is the case with conventional lubricants.

The curves of the radii R10 and R12.5 with CO₂ as lubricant deviate from the descending behavior. R10 with CO₂ initially shows a decreasing curve with increasing surface pressure. With increasing sealing effect (increasing surface pressure), a uniform load-bearing behavior is shown, ranging between a friction value of 0.12–0.14. In the case of radius R12.5, with CO₂, this uniform load-bearing behavior, and thus, the constant coefficient of friction is evident apart from small fluctuations. It can be seen that a radius of approx. 10–12 mm causes no further reduction of the coefficient of friction, which indicates a minimum. A further increase of the tool radii would not lead to a further reduction of friction and thus to an improvement of the load-bearing capacity of the tribological system with volatile lubricants. For lower normal contact pressures in combination with R10 and R12.5 using CO₂ as lubricant the error bars are slightly higher than for all other SBT results. This is due to an occurring stick slip effect for low normal contact pressures when using volatile lubricants. Here, the already mentioned sealing effect of the gap between tool (radius) and sheet metal strip shows an unstable behavior. For a small gap, less CO₂ can flow out of the gap, which leads to an increasing pressure of CO₂ in the gap. Due to the low surface pressure, which is not sufficient to compensate the media pressure, the sheet metal specimen lifts. This in turn leads to an increased outflow of the gas and thus to a reduction of the gap, causing the pressure to rise again and the stick slip effect to be repeated. Due to this oscillation behavior, the friction coefficients fluctuate slightly more.

Conclusion and Outlook

The presented research results contribute to the topic of dry forming for the characterization of friction at tool radii during deep drawing using volatile lubricants including numerical fluid flow simulations inside the microholes. Furthermore, this article addresses a laser-drilling strategy to improve the finish quality of microholes with a depth of 5 mm, using a galvanometer-scanning optic allowing for transversal beam movement along a spiral path during the drilling process. The calculation of the scanning radius was described to achieve the desired ablation radius on the gas outlet side of the microhole. An improvement of the quality in terms of roundness at the gas outlet as well as a larger gas inlet radius could be achieved. The CFD simulation of the CO₂ lubricant flow insight the different microholes showed a pressure and temperature reduction at the outlet of the longer holes. This leads to a reduced lifting effect of the sheet metal caused by the lubricant pressure. On the other hand, the friction can be reduced because of a higher dry ice formation inside the microhole. With the numerical modeling of the SBT, the normal contact pressure at tool radii could be determined for all parameter combinations of radius size and retention force. The normal contact pressure was assigned to the experimentally determined friction values so that a comparative evaluation of all determined friction values with liquid CO₂ and a drawing oil (ZO3368) could be carried out independently of the retention force. The results show that CO₂ causes lower coefficients of friction than the conventional drawing oil across all experiments. Furthermore, a limit for the radius size using CO₂ lubrication could be defined, above which a further increase of radius size does not cause any further friction reduction. Supplementary research will investigate laser-drilling with galvanometer-scanning optics in combination with longer Rayleigh-lengths as well as a transfer to laser sources with higher average power to increase productivity. Furthermore, future investigations will include the friction characterization of the volatile lubricant N₂ in order to assign the normal contact pressure in dependence of the test parameters. The aim is to achieve an evaluation of the friction independent of the retention force. For this research, simulation can be a possible component to get a better understanding of the lubrication effects. In addition, the tribosystem using volatile media will be transferred to other sheet metal materials.

Acknowledgements The scientific investigations of this paper were funded by the German Research Foundation (DFG) within the priority program SPP 1676 Dry Metal Forming—Sustainable Production by Dry Processing in Metal Forming. We thank the German Research Foundation (DFG) for the funding of this research project.

References

1. Bay N, Nakamura T, Schmid S (2010) Green lubricants for metal forming. *Proc 4th Int Conf Tribol Manuf Process* 1:4–33
2. Ceron E, Bay N (2013) A methodology for off-line evaluation of new environmentally friendly tribo-systems for sheet metal forming. *CIRP Ann Manuf Technol* 62(1):231–234
3. Wörz C, Reichardt G, Liewald M, Zahedi E, Weber R (2018) Dry deep drawing of a rectangular cup assisted by volatile media injected from laser-drilled microholes. *Dry Met Form OAJ FMT* 4 4:1–8
4. Singer M, Liewald M, Feuer A (2015) Development of a new ecological lubrication system for sheet metal forming based on CO₂ in liquid. *Key Eng Mater* 651–653:480–485
5. Wörz C, Zahedi E, Umlauf G, Liewald M, Weber R, Tovar GEM (2017) Tiefziehen eines U-Profiles mit flüchtigen Medien als Schmierstoffersatz. *Dry Met Form OAJ FMT* 3 3
6. Henn M, Reichardt G, Weber R, Graf T, Liewald M (2020) Dry metal forming using volatile lubricants injected into the forming tool through flow-optimized, laser-drilled microholes. *JOM*
7. Förster DJ, Weber R, Holder D, Graf T (2018) Estimation of the depth limit for percussion drilling with picosecond laser pulses. *Opt Express* 26(9):11546–11552
8. Henn M, Reichardt G, Weber R, Graf T, Liewald M (2020) Advances in dry metal forming using volatile lubricants injected through laser-drilled microholes. In: *TMS 2020—supplemental proceedings*, pp 1979–1991
9. Velkavrh I, Ausserer F, Kliken S, Brenner J, Forêt P, Diem A (2014) The effect of gaseous atmospheres on friction and wear of steel–steel contacts. *Tribol Int* 79:99–110
10. Wu X, Cong P, Nanao H, Minami I, Mori S (2004) Tribological behaviors of 52100 steel in carbon dioxide atmosphere. *Tribol Lett* 17(4):925–930
11. ChemicalLogicCorporation, Carbon Dioxide Phase Diagram. <https://www.chemicallogic.com/Pages/DownloadPhaseDiagrams.html>, 14.09.2020
12. Atkins PW, de Paula J, Keeler J (2018) *Atkins' physical chemistry*, eleventh ed. Oxford University Press, Oxford and New York
13. Liewald M, Tovar GEM, Woerz C, Umlauf G (2019) Tribological conditions using CO₂ as volatile lubricant in dry metal forming. *Int J Precis Eng Manuf Technol* 11(3):361
14. Reichardt G, Wörz C, Singer M, Liewald M, Henn M, Förster DJ, Zahedi E, Boley S, Feuer A, Onuseit V, Weber R, Graf T, Umlauf G, Reichle P, Barz J, Tovar GEM, Hirth T (2020) Tribological system for cold sheet metal forming based on volatile lubricants and laser structured surfaces. *Dry Met Form OAJ* 128–165
15. Reichardt G, Liewald M (2019) Investigation on friction behaviour of deep drawing radii using volatile media as lubricant substitutes. In: *Procedia Manufacturing, SheMet 2019*, vol 29, pp 193–200
16. Reichardt G, Liewald M (2019) Friction conditions on deep-drawing tool radii when using volatile media as lubrication substitute. In: *TMS 2019—supplemental proceedings*, pp 1603–1613
17. Filzek J (2004) Kombinierte Prüfmethode für das Reib-, Verschleiß- und Abriebverhalten beim Tief- und Streckziehen. Technische Universität Darmstadt
18. Papaioanu A (2016) Einsatz eines neuartigen Verfahrens zum kombinierten Recken und Tiefziehen von Außenhauptbeplankungen aus Feinblech. University of Stuttgart

Nanoengineered Coating; Lotus Effect, Morphology, Contact Angles and Wettability



N. B. Singh, Lisa Kelly, Narasimha Prasad, Brett Setera, Stacey Sova, David Sachs, Bradley Arnold, Fow-Sen Choa, and Christopher Cooper

Abstract The understanding of the surface behavior, interaction, wettability, and topographies of surfaces with fluids is very important to remove impurities from the devices and components and to develop washing fluids to clean large area surfaces. We synthesized nano particle filled composites by wet and semi-wet techniques to achieve hydrophobicity and hence the lotus effect. Nanocomposites with different composition of polymers doped with titania nanoparticles were studied to evaluate effects on wettability. Light scattering methods were used to study the absorptions and particle size. The contact angle and hydrophobic characteristics were very composition dependent in thin film composites. At certain compositions, we observed that material showed very high anisotropy in droplet shapes which diminished with loadings of nanoparticles. These composites did not show any change in hydrophobic characteristics when exposed with ultraviolet radiation.

Keyword Hydrophobicity · Nanocomposites · Lotus effect · Contact angle · Morphology

Background

Since the publication of classic papers of Sundquist and Oriani [1, 2], Hillig and McCarroll [3], and Cahn et al. [4–6] on nucleation and thermodynamics, a large number of papers have been published on experimental aspects of miscibility, contact angle, and wetting. In past few years, organic and polymeric transparent materials have been used [7–12] for direct observations. The contact angle dynamics between two phase composites and solid surfaces is very important and researchers are continuously developing models for nucleation, contact angle, and wetting because of

N. B. Singh (✉) · L. Kelly · B. Setera · S. Sova · D. Sachs · B. Arnold · F.-S. Choa · C. Cooper
University of Maryland Baltimore County, 1000 Hilltop Circle, Baltimore, MD 21240, USA
e-mail: singna@umbc.edu

N. Prasad
NASA Langley Research Center, Hampton, VA 23681, USA

great industrial applications. Some of these papers describe flow of nutrients on the surfaces. The surfaces with different shapes polishing, decoration, and geometries exhibit unusual wetting and nucleation characteristics. It is well known that the surface of even a moderately hydrophobic material can become highly nutrient repellent of contamination when altered with a pattern of microscopic morphologies such as pillars, facets or micro, and nano structures. This effect of the water repellent properties is known as the lotus effect. The lotus effect is known from centuries for self-cleaning properties in nature for leaves of the lotus plant. This effect can also be utilized for cleaning of ground and space born vehicles surfaces exposed to wetting liquid. In the present paper, we report the effect of surface topographies of substrates with nanoengineered titanium oxides nanoparticles embodied in polystyrene and studied the effect of the composites to create different wetting characteristics. The surface, morphology, and contact angle of composites prepared by wet and semi-wet techniques were determined to understand interactions of nutrients on the glass substrates. These results showed an increasing ripple amplitude on the substrate increased or decreased pull-off forces, as well as provide information on the extent of contact and probability of pressure-sensitive adhesion with substrates.

Experimental Method

Synthesis of Composites

We prepared a polymer mixture of the composition 70/30 weight % mixture of polystyrene (PS) and polymethylmethacrylate (PMMA) by dissolving 4.2738 g of PS and 2.2360 g of PMMA in 70 mL tetrahydrofuran. It was heated to the temperature range of 50 °C and stirred continuously for two hours until all polymer had dissolved into the solution. The mixture was cooled to room temperature.

Synthesis and Characterization of Titanium Oxide Nanoparticles

Titanium nanoparticles were synthesized using a sol-gel technique. We reacted 100% ethanol with TiCl_4 . Approximately, 4.0 mL of TiCl_4 was added to 10.00 mL of 100% ethanol under nitrogen flow and on ice surface. This resulted in a yellow gel. We added 45.00 mL of 15.0 M acetic acid dropwise and stirred this mixture continuously. This solution was refluxed at 65 °C for two hours until the solution became opaque. Synthesis at pH = 1 yielded an opaque white solution in aqueous media. The aqueous nanoparticles were characterized by UV-Vis and infrared spectroscopy. The infrared spectrum of the solution showed peaks at 1640 cm^{-1} attributed to O-H stretching, peaks appearing at 1075 cm^{-1} are attributed to Ti-O-C stretching, and

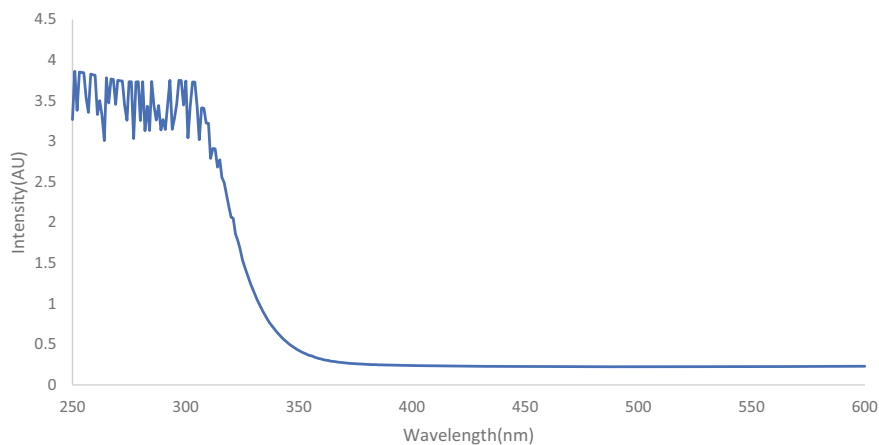


Fig. 1 Absorption spectra of TiO₂ nanoparticles. There was no significant absorption in the studied range. (Color figure online)

peaks below 700 cm^{-1} were attributed to Ti–O–Ti stretching according to literature. The absorbance of the aqueous nanoparticles had a peak absorbance at 380 nm and the absorbance reached the detectors maximum below 355 nm. Since the polymers were dissolved in THF, the nanoparticle solution was dried down and dissolved in THF. The resulting solution was orange in color and had a broad absorption from 350 to 600 nm with a peak maximum at 425 nm and retained the sharp maximum at 380 nm as the aqueous solution. When the nanoparticle solution was mixed with the polymer solution, the orange color persisted. This orange color showed the aggregation of aqueous nanoparticles in organic solvent. We measured the absorption characteristics of particles prepared by semi-wet technique using a Beckman D640 spectrometer in the ultraviolet and near infrared wavelength region. As shown in Fig. 1, the UV absorption spectra showed no significant absorption peak. The size distribution was determined by dynamic light scattering (DLS) method. The DLS showed an average particle size of 40 nm with a range of roughly 10–100 nm. Figure 2 shows the results of size and distributions of particles.

Morphological Studies of Nanoparticles

TiO₂ nanoparticles were isolated by drying using a rotary evaporator, yielding a white powder. The morphology of crystals was determined by scanning electron microscope (SEM) model NOVA NANOSEM 450. The data were taken for the energy range of 10KeV. Figure 3 shows images of the isolated powder obtained after drying. The morphology showed spherical particles and some places clusters of 1 micron. The remaining TiO₂ powder was suspended in tetrahydrofuran (THF) for use as an impurity in the polymer matrix.

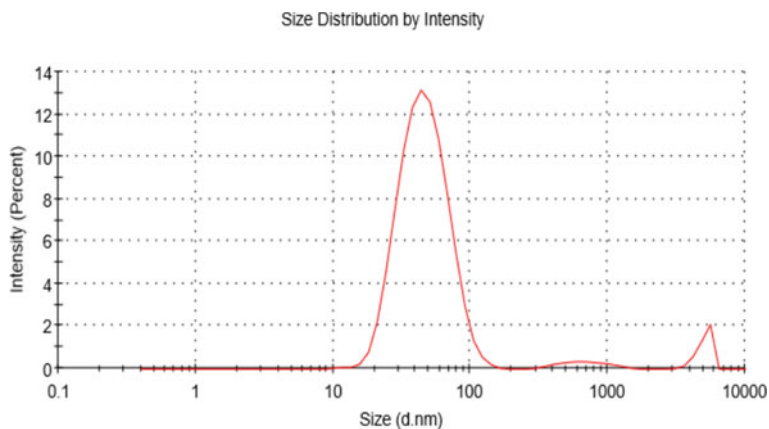


Fig. 2 Light scattering data showing distribution of particles sizes. (Color figure online)

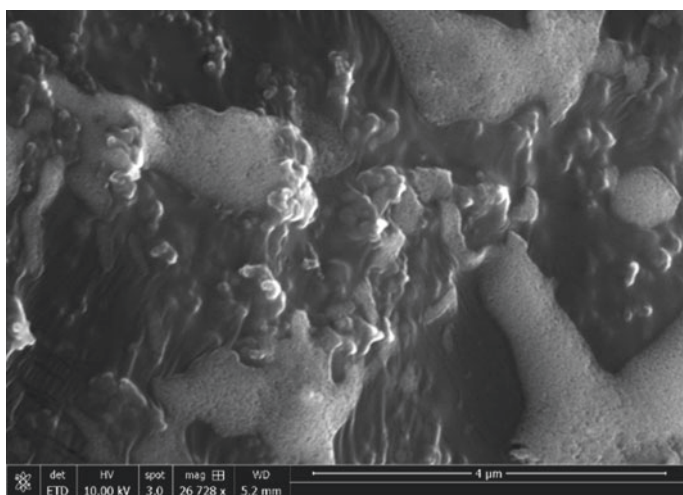


Fig. 3 SEM morphologies of isolated and clusters of TiO_2 particles

Spin Casting on the Glass and Silicon Surface

The polymer mixture was spin cast onto glass slides and silicon wafers using a CHEMAT spin-coater KW-4A. To properly fit glass slides for spin casting, a simple glass slide holder was designed and 3D printed to fit the spin-coater. The polymer was applied to the glass slide substrate while spinning at 400 rpm for 18 s. Once applied, the slide was spun at 2000 rpm for 90 s. At the first stage, only the polymer solution was spin cast onto the slides. Then, 10.00 mL of polymer solution was mixed with 4.0 mL nanoparticle solution and spin cast onto glass slides.

Results and Discussion

The surface morphology and adherence were studied by determining shape flow, hydrophilic and hydrophobic characteristics of the polymer and nanoparticle filled composites.

Effect of Composition

The composition, characteristics of polymer, and nanoparticles have significant effect on the adherence on the substrates. The substrate glass slides were cleaned by a dilute mixture of $\text{HNO}_3 + \text{HF} + \text{H}_2\text{O}$, followed by very dilute nitric acid and repeated distilled water. The slides were dried in vacuum at $120\text{ }^\circ\text{C}$ for a period of several hours. We used three different compositions of the polymers for the present study. For a test, we spin casted a sample of 20.0 mL of the 66/34 weight percent solution of polystyrene-polymethylmethacrylate containing 4.0 mL of the TiO_2 nanoparticle. To study effect of nanoparticle loading and washing with solvent, we studied the sample of (1) polymer mixture, (2) polymer mixture with nanoparticles suspended, (3) polymer mixture subjected to a cyclohexane wash, and (4) polymer mixture with nanoparticles suspended subjected to a cyclohexane wash. In an independent experiment, glass slides were washed with $65\text{ }^\circ\text{C}$ cyclohexane to remove the polystyrene from the matrix to increase surface roughness. This process was repeated to vary the compositions as 34/66, 50/50, and 66/34 weight percent of PS/PMMA in the solution. For the glass substrates, during casting, we observed different instabilities at interfaces in identical rotation of the spin cast. There was no large difference on the morphological breakdown of growth interfaces.

Spectral and Morphological Characteristics of Polystyrene and Polymethylmethacrylate (PS/PMMA) Film

A mixture of polystyrene and polymethylmethacrylate and/or titania nanoparticles was dissolved in THF and spin cast onto a glass slide. The films were washed with cyclohexane and dried at $100\text{ }^\circ\text{C}$ for 20 min. The thin films composition on a glass slide was determined by the FTIR spectra. We observed peaks at 2800, 2900, 3030, and 3060 cm^{-1} which indicated that both PMMA and PS were still present in the film after washing. Some of the literatures have reported [10] that synthesizing super hydrophobic polymers in this manner removed all PS from their films after washing with cyclohexane at $70\text{ }^\circ\text{C}$. We washed samples at room temperature and then dried for 20 min which may be responsible for the discrepancy in polymer composition.

The composite containing titania nanoparticles in THF had an orange color but when the sample was washed and dried, the color faded and changed to a white

film. Since transmission is very important for coating and washing, we measured the transmission of the typical hydrophilic material loaded with titania nanoparticles. The result is shown in Fig. 4. The data showed complete transparency in the studied wavelength region of 300 to 1200 nm.

The SEM morphologies of composites of the films are shown in Fig. 5. The PMMA/PS films formed an anisotropic smooth surface with distinct grain boundaries. The grain size and shape varied from 1.0 to 2 μm in diameter. The surface of this film was slightly rough, which plays an important role in wettability. Ti nanoparticles layered on the PMMA/PS substrate had isotropic properties with uneven coating of the polymer. The uneven layering could be due to the non-uniform distribution of grains. Individual nanoparticles cannot be seen in the SEM image, but the spherical

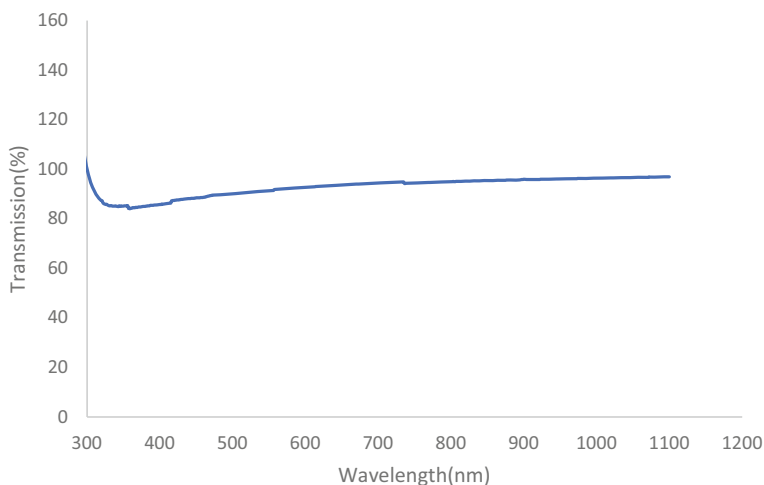


Fig. 4 Transmission of hydrophobic thin film (50% PS, 50% PMMA, TiO₂ nanoparticles). (Color figure online)

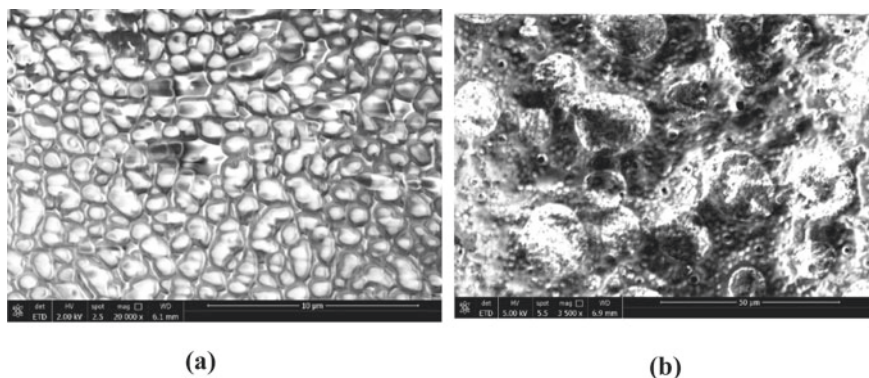


Fig. 5 SEM image on glass substrate **a** PMMA/PS, **b** PMMA/PS/Titania nanoparticles mixed film

outlines are visible. When the titania nanoparticles were mixed with PMMA/PS solution and then spin cast onto the substrate, they showed the formation of an isotropic surface. The nanoparticles aggregated into larger spheres from the organic solvent. Nanoparticles were tens of nanometers to micron in size, but the aggregate which formed a sphere was $40\ \mu$ in diameter. Although for all the samples, there was no distinct roughness within the film, the further loading of titania nanoparticles into the film changed the surface from anisotropic to isotropic by repulsion of hydrophobic and hydrophilic counterparts.

Effect of Ultraviolet Radiation

Pant et al. [11] have shown that ultraviolet radiation elicits significant response from samples containing titania nanoparticles. We exposed our samples containing titania nanoparticles to a mercury vapor-lamp for 3 h, and the hydrophobicity was tested. SEM morphology of exposed film is shown in Fig. 6. The film did not show change in appearance, structure or in color, similar to results reported in references 11 and 12. However, the film with a layer of nanoparticles irradiated for 3 h showed individual nanoparticles, whereas the unirradiated sample did not show this type of particle characteristics. The nanoparticle sizes ranged from tens of nanometers to micron in the size. This may be due to the further drying of sample and removal of trapped solvents. The structure of the irradiated mixed nanoparticle film remained unchanged, with large aggregates of nanoparticles and aggregates of polymer. The absorbance spectrum of irradiated nanoparticles in solution did not show change in the absorbance at 380 nm, but absorbance in the UV range increased slightly.

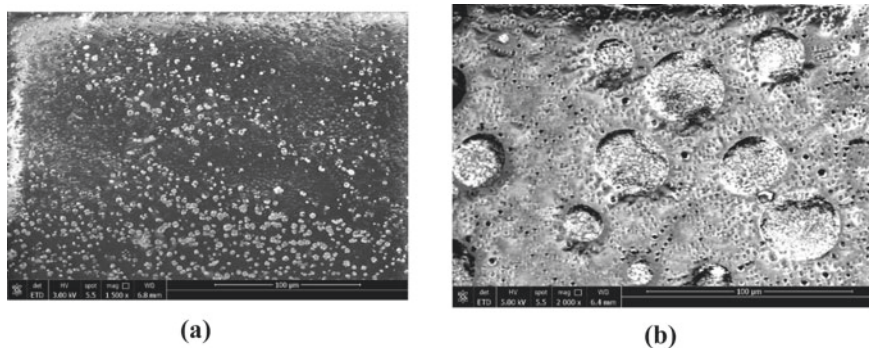


Fig. 6 SEM image of **a** PMMA/PS composite thin film on glass substrates and **b** PMMA/PS/Titania nanoparticle mixed composite film on glass substrate

Contact Angle Measurements

Experiments performed by Glicksman et al. [13–15] by maintaining temperature in range of few milli kelvin for pure and doped organic materials showed that the interface energy, contact angle, and grain groove formation are very sensitive to composition and temperature. In the present study, we evaluated interface characteristics by using water droplet on the coated surfaces with nanocomposites all at room temperature. All surfaces were hydrophobic in nature with water sliding off the films, except for the film where very large particles adhered to the surface. Contact angle determinations were made using the software ImageJ with a plugin called “Dropsnake” provided as an open source from National Institute of Health (NIH). Dropsnake was found to be suitable due to the ability to manually map the points for the fit.

We used two different methods for setting up the camera to capture the droplet shapes. In the first case, we used a tripod-based camera [16] and in the second case we developed a process where a microscope was mounted on a 3D printed housing. Figure 7 shows examples of the droplets using first approach. As shown in Fig. 7, the contact angle measurements utilizing Dropsnake provides left and right angles as well as ability to add as many points as necessary to properly map the curve. Further, the droplet-coating substrate interaction is difficult to differentiate from the droplet, but mapping of the curve was possible using this software.

In the second approach, a custom contact angle goniometer was created using a Carson zPix MM-640 digital microscope backlit with LED lighting mounted in a 3D printed housing. Contact angles were measured by dropping a 50 μL droplet of deionized water from a height of 25 mm onto the substrate surface and analyzing the angles using the same DropSnake program. Contact angles were measured on the left side and the right side of the droplet and averaged, as shown in Fig. 8. As shown in this Fig. 8, composition of the polymer had significant effect on the contact angle.

Thin films without a cyclohexane wash initially showed that all samples were slightly hydrophobic, exhibiting a contact angle of greater than 90° , as shown in Table 1. Further, the effect of annealing on samples greatly increased the contact

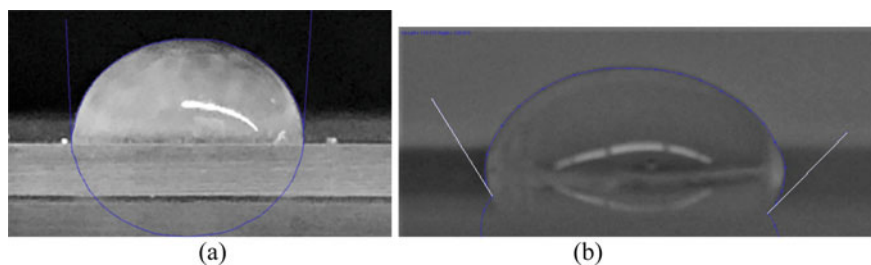


Fig. 7 Contact angle modeling of water on **a** spin cast polymer slides utilizing the Dropsnake plugin and **b** tangent lines between the surface and droplet were highlighted in white to increase visibility. (Color figure online)

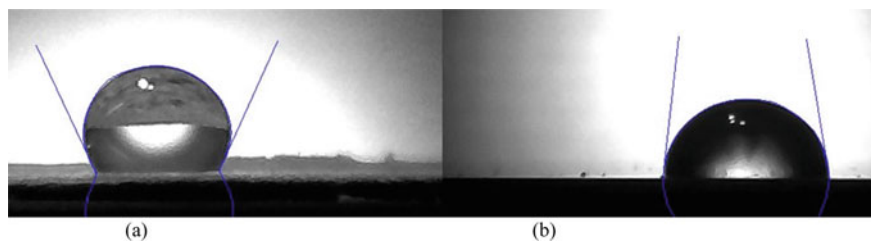


Fig. 8 Representative images of ImageJ software used to determine contact angles of 50 μL droplets on substrates. **a** 20:80% PS:PMMA demonstrating a hydrophobic surface, contact angle $>90^\circ$. **b** 33:66% PS:PMMA demonstrating a hydrophilic surface, contact angle $<90^\circ$. Contact angles for each sample were averaged to determine overall contact angle. (Color figure online)

Table 1 Contact angle of water on PS/PMMA thin film mixtures with no cyclohexane wash

Composition (% by weight)	Contact angle, raw	Contact angle, annealed	Contact angle, TiO_2
66/33 PS/PMMA	91.4	119.7	119.3
50/50 PS/PMMA	98.1	127.8	129.2
33/66 PS/PMMA	97.8	112.1	123.2

angle by as much as 18° in some cases. Thin films treated with a cyclohexane wash showed a significantly greater contact (Table 2) angle without additional processing. Samples with the greatest polystyrene content showed the largest initial contact angle as the cyclohexane washing removed polystyrene from the matrix. When annealed, thin films with greater polystyrene compositions showed the least improvement in contact angle.

Table 2 Contact angle of water on PS/PMMA thin film mixtures with cyclohexane wash

Composition (% by weight)	Contact angle, raw	Contact angle, annealed	Contact angle, TiO_2
66/33 PS/PMMA	119.3	124.9	123.2
50/50 PS/PMMA	113.2	122.8	129.8
33/66 PS/PMMA	109.4	115.4	132.9

Effect of High Temperature Annealing

All spin-cast slides were annealed at 170 °C to determine the effect of annealing on the contact angle. Trapped solvent, THF, started evaporating at 66 °C. The effect of the evaporation roughens the surface by creating small pockets. Further, the glass transition temperature for polystyrene is 100 °C. The contact angle of each thin film slide was determined after annealing to observe the effects of this on the contact angle and is shown in Tables 1 and 2. Annealing showed the greatest effect on thin films that were not washed with cyclohexane. As all of the polystyrene content is still present in these thin films, there is a greater amount of trapped solvent. As this solvent evaporates, small pores are created in the thin film, roughening the surface. Thin films that were not washed with cyclohexane showed an average of a 16.7° increase in contact angle, while thin films that did receive a cyclohexane wash showed an average of a 6.7° increase contact angle.

Anisotropy

In several nanocomposites, we observed strong anisotropy. Figure 9 shows the actual shapes and anisotropy >7% for the composition 34/66% PS-PMMA and 2% anisotropy for the composition 66/34% PS-PMMA system. Glicksman et al. [13–16] have reported this type of surface energy anisotropy in several organic materials systems and their effects on the crystallization behavior and morphology. There is a slight possibility of anisotropic effects due to uneven thickness also in the film.

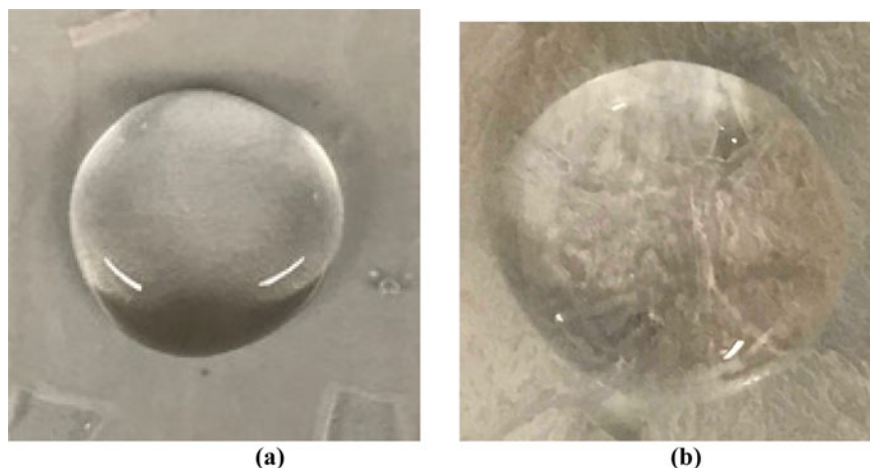


Fig. 9 **a** There was more than 7% anisotropy in 34/66% PS-PMMA composition and **b** 2% anisotropy in 66/34% PS-PMMA system. (Color figure online)

Other reasons of anisotropy can include uneven spatial orientation of nanoparticles in the thin film, differing size of nanoparticles due to a polydisperse size range being used, and uneven removal of film at certain points due to the cyclohexane washing. Anisotropy was most prevalent in thin films with higher polystyrene concentrations that had received cyclohexane washes. Further, anisotropy was observed regardless of whether TiO₂ nanoparticles were present in the thin films. When the titania nanoparticles were mixed with PMMA/PS solution spin casted onto the substrate, we observed slightly reduced anisotropy.

Summary

We synthesized nano particle filled composites for achieving hydrophobic characteristics and studied the surface behavior, interaction, wettability, and topographies of surface with fluids. We used semi-wet techniques to synthesize nanoparticles and prepared composites of different compositions to evaluate effects on wettability, which provided valuable information on achieving the lotus effect. Optical and light scattering methods were used to study the absorptions and particle size. We observed multiple compositions that yielded hydrophobic thin films. Certain stoichiometry material showed very high anisotropy, which diminished with loadings of nanoparticles. The effect of ultraviolet radiation for several hours on the surfaces did not show any effect on the hydrophobicity. This was supported by no change in the SEM morphology of the composite.

Acknowledgements We would like to thank NASA headquarters through NASA Langley Research Center for providing financial support for this research as fellowship to students.

References

1. Sundquist BE, Oriani RA (1962) Homogeneous nucleation in a miscibility gap system. *J Chemical Phys* 36:2604–2610
2. Sundquist BE, Oriani RA (1967) Thermodynamics of miscibility gap system and a test of nucleation theory. *Trans Faraday Soc* 63:561–568
3. Hillig WB, McCarroll B (1966) Physical cluster distribution during heterophase fluctuations. *J Chemical Phys* 45:3887
4. Cahn JW (1977) Critical point wetting. *J Chem Phys* 66:3677
5. Heady RB, Cahn JW (1973) Experimental test of classic nucleation theory in a liquid-liquid miscibility gap system. *Chem Phys* 58(3):896–8989
6. Lee HG, Kim J (2011) Accurate contact angle boundary conditions for Cahn-Hilliard equation. *Comput Fluids* 44(1):178–186
7. Wolfs M (2002) *Encyclopedia of Polymer Science and Technology*. Wiley, New York
8. Singh NB, Rai US, Singh OP (1985) Chemistry of monotectics; phenanthrene-succinonitrile system. *J Crystal Growth* 71:353–360
9. Rai US, Singh OP, Singh NB (1987) Some thermodynamic aspects of organic eutectics and monotectics. *Can J Chem* 65:2639–2642

10. Ma Y, Ca X, Feng X, Ma Y, Zou H (2007) Fabrication of super-hydrophobic film from PMMA with intrinsic water contact angle below 90. *Polymer* 48:7455–7460
11. Pant R, Singha S, Bandyopadhyay A, Khare K (2014) Investigation of static and dynamic wetting transitions of UV responsive tunable wetting surfaces. *Appl Surface Sci* 292:777–781
12. Bernagozzi I, Torrenzo S, Minati L, Ferrari M, Chiappini A, Aermellini C, Toniutti L, Lunelli L, Speranza G (2012) Synthesis and characterization of PMMA-based superhydrophobic surfaces. *Colloid Polym Sci* 290:315–322
13. Glicksman ME, Singh NB (1989) Effects of crystal-melt interfacial energy anisotropy on dendritic morphology and growth kinetics, *J Crystal Growth* 98:277–284
14. Singh NB, Glicksman ME (1989) Free dendritic growth in viscous melts: cyclohexanol. *J Crystal Growth* 3:534–540
15. Singh NB, Glicksman ME (1989) Determination of the mean solid-liquid interface energy of pivalic acid. *J Crystal Growth* 98:573–580
16. Sova S, Prasad N, Cooper C, Kelly L, Arnold B, Cullum B, Choa FS and Singh NB, (2019) Importance of lotus effect in surface sensing. In: Cullum B, Kiehl D, McLamore E (eds) *Proceedings SPIE 11020, “Smart Biomedical and Physiological Sensor Technology XVI, 1102005.* <https://doi.org/10.1117/12.2519738>

Temperature Dependence of Energy Gap in Semiconductors—Influence on Solar Cell Performance



**Rayan Daroowalla, Ritvik R. Rangaraju, Leqi Lin,
and Nuggehalli M. Ravindra**

Abstract An analysis of the temperature dependence of the energy gap in semiconductors is presented. Its influence on solar cell performance is examined for various semiconductor candidates. In particular, semiconductors belonging to groups IV, III–V, II–VI, as well as perovskites are considered. The results presented in this study are anticipated to be of direct applications to the utility of solar cells in space as well as in the design and manufacture of tandem solar cells.

Keywords Solar cells · Energy gap · Temperature · Efficiency · Semiconductors · Perovskites

Introduction

Given the huge global investments into photovoltaics, improving, and optimizing solar cell performance is a key focus for scientific and economic reasons. Significant academic and industrial research is currently underway to better understand the parameters that influence the solar cell performance. There are a large number of material and device parameters that influence the solar cell performance and its temperature dependence. A scientific consensus has emerged on the key parameters that influence the solar cell performance. From a fundamental perspective, the energy gap and its temperature dependence play a critical role in determining the solar cell efficiency.

R. Daroowalla
Department of Physics, University of Maryland, College Park, MD 20742, USA

R. R. Rangaraju
West Windsor-Plainsboro High School South, West Windsor, NJ 08550, USA

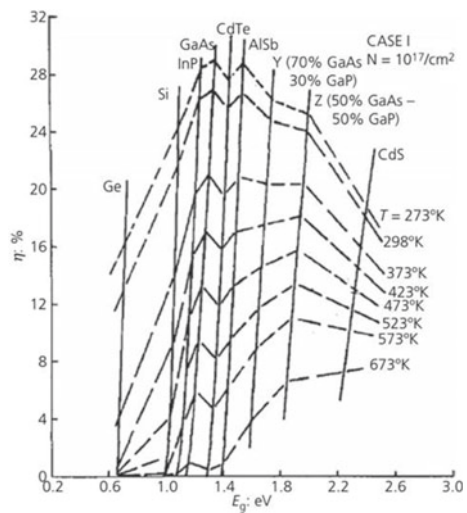
L. Lin
George Washington University, Washington, DC 20052, USA

N. M. Ravindra (✉)
Department of Physics, New Jersey Institute of Technology, Newark, NJ 07102, USA
e-mail: nmravindra@gmail.com

Practical interventions to improve solar cell performance can only happen when a deeper understanding of how these parameters interact and influence one another emerges across several materials. Early in the 1990s, O'Donnell and Chen [1] discussed the temperature dependence of the energy gaps of semiconductors. In their research, they formulated a three-parameter thermodynamic fit function to model the relationship between the bandgap and temperature for several technologically important semiconductors. Wysocki and Rappaport [2] explored the effect of temperature on solar cell energy conversion in their seminal paper. They concluded that the optimal material to use in a single-junction cell (in terms of what most closely matches the solar spectrum) is Gallium Arsenide (GaAs) although Cadmium Telluride (CdTe) is close to an optimal material (Fig. 1). Varshni [3] investigated and proposed an empirical model for the temperature dependence of the energy gap in various semiconductors. This model has become widely reputed as it most accurately predicts the energy gap of several semiconductors as a function of temperature.

This paper seeks to extend the understanding of the role of temperature by studying its impact on the energy gap and efficiency across a wide range of conventional semiconductor materials (Ge, Si, InP, GaAs, CdTe, AlSb, CdS), as well as Perovskites. The work presented in this paper will have particular use and relevance to the design of tandem (i.e., multi-junction) cells and the appropriate choice of materials therein. Theoretical models for predicting the solar cell performance for materials at varying temperature conditions have been reported in several studies in the literature, of which a few case studies will be discussed in this paper. Additionally, the analysis given here will be useful in developing the theoretical frameworks to model the effects of various environmental variables (for example, relative humidity) on the overall performance of the cell.

Fig. 1 η versus E_g for various semiconductors in the temperature range of 273–673 K as per the Wysocki–Rappaport model [2] (reproduced with permission from American Physical Society)



Models from the Literature

From a fundamental perspective, the energy gap of the semiconductor determines the energy threshold for absorption of photons in the semiconductor. Thus, due to its importance in the effective assessment of the performance of solar cells, the value of the energy gap parameter (E_g) across a wide range of temperatures (T) must be predicted with the highest accuracy possible. As such, several models have been proposed in the literature to interpret the change in E_g with T , each with varying degrees of adherence to real-world values. Among these are the Varshni relation [3], Bose–Einstein model [4], and the Pässler model [5]. The Wysocki–Rappaport model [2] considers the influence of temperature on photovoltaic solar energy conversion in the temperature range of 0 to 400 °C using semiconductor materials with bandgaps varying from 0.7 to 2.4 eV. While the results of this model were reported sixty years ago, they continue to be the fundamental basis for the understanding of the performance of homojunction solar cells, as function of temperature, today.

The Varshni relation [3] is given by the following equation:

$$E_g = E_g(0) - \frac{\alpha T^2}{T + \beta} \quad (1)$$

where E_g is the energy gap of the semiconductor at temperature T (in Kelvin), α and β are empirical constants that are characteristic of the semiconductor ($\beta \sim \theta_D$, the Debye temperature), and $E_g(0)$ is the energy gap at 0 K. With over 5000 citations in the literature, the Varshni relation is frequently used in the literature to estimate the nonlinear temperature dependence of the bandgap in semiconductors. In principle, it represents a combination of a quadratic low-temperature asymptotic behavior with a linear dependence of the bandgap, at high temperatures, in semiconductors.

Although the Varshni relation [3], Eq. (1) is the most widely accepted model to interpret the relationship between the bandgap and temperature, the Pässler and Bose–Einstein models [4, 5] also present alternative approaches for explaining the dependence of energy gap on temperature in semiconductors with relatively high accuracy.

The Pässler model [4], Eq. (2) is given by:

$$E_g(T) = E_g(0) - (\alpha/k) \int d\varepsilon \frac{w(\varepsilon)\varepsilon}{e^{\frac{\varepsilon}{k}} - 1} \quad (2)$$

where α is the slope of $E_g(T)$ versus T , as T approaches infinity, $w(\varepsilon)$ is the normalizing weightage function, and k is the Boltzmann constant.

The Bose–Einstein model [5], Eq. (3), uses the following equation to interpret the temperature dependence of the energy gap in semiconductors:

$$E_g(T) = E_g(0) - \frac{2a_B}{\left[\exp\left(\frac{\theta_E}{T}\right) - 1\right]} \quad (3)$$

where a_B represents the strength of the exciton-phonon interactions within the semiconductor and θ_E is an average temperature (\sim Einstein characteristic temperature). In general, irrespective of the models considered, the temperature dependence of the energy gap in semiconductors can be attributed to the following factors: (a) temperature dependent dilatation that leads to relative shift in the valence and conduction bands; (b) electron-phonon interactions.

Results and Discussion

Conventional Semiconductors

Based on the above models, the following significant aspects of the relationships between the three parameters (E_g , η , T) can be arrived at. The energy gaps and efficiencies of the semiconductors, considered in this study, decrease almost linearly with increasing temperature [6, 7]. In observing the relationship of η with respect to temperature according to the Wysocki-Rappaport model, several of the nine semiconductors behave significantly differently from one another. This is in stark contrast to the relationship of E_g with T for six of the semiconductors. Here, the average slopes of the lines are different. The efficiency-temperature plots for solar cell materials AlSb, 50–50% GaAs/GaP, 70–30% GaAs/GaP, and CdS all appear to intersect at 373 K, with the exception of CdS. On the other hand, in Fig. 2a, all four semiconductors have a more curved (and thus less linear) variance of efficiency with temperature. Though more prominent in Si and Ge, all four materials follow a linear degradation until approximately 450–500 K, where the efficiency begins to drop off with temperature.

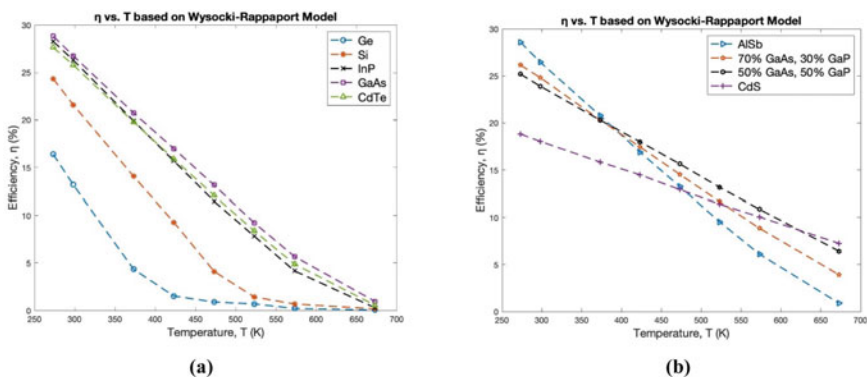


Fig. 2 a–b η versus T for several semiconductors in the temperature range 273–673 K—based on Wysocki-Rappaport model. (Color figure online)

Table 1 $[d\eta/dE_g]_T$ for nine semiconductors based on Wysocki–Rappaport model

Semiconductor	$[d\eta/dE_g]_T \times 10^{-2} \text{ (eV}^{-1}\text{)}$
Ge	3.01
Si	3.62
InP	1.99
GaAs	1.51
CdTe	1.83
AlSb	1.92
70% GaAs, 30% GaP	1.42
50% GaAs, 50% GaP	1.15
CdS	0.698

Also observed are the behaviors of η and E_g versus T in conjunction. Through plots created from the simulated results of Wysocki and Rappaport, as shown in Fig. 2a and b, the dependence of efficiency on temperature for the vast majority of semiconductors is best characterized as linear. However, using a first-degree polynomial fit, the R^2 value returned was only 0.945, indicating a sub-par fitting of the data. In an attempt to improve this, quadratic regression was used instead. This method was able to fit the data as perfectly as possible, with an R^2 value of 1. The $[d\eta/dE_g]_T$ for nine semiconductors, based on Wysocki–Rappaport model, are summarized in Table 1. In Fig. 3, comparisons of the temperature dependence of the energy gap of semiconductors, based on Varshni relation and Wysocki–Rappaport model, are presented.

In comparing these sets of values in Fig. 3, it may be noted that the values of E_g considered in the Wysocki–Rappaport model are consistently lower for all the semiconductors considered in the study except for Germanium (Fig. 4).

Perovskites

In recent years, there has been significant interest in pervoskites for their applications in the manufacture of solar cells. The promise of high efficiency and ease of fabrication of the cells are some of the reasons for this interest. Stability in perovskite solar cell performance over long durations and their chemical stability at moderate to high temperatures are some of the issues that are being addressed in research at this time. In this section, the temperature dependence of the energy gap and solar cell efficiencies of pervoskites are considered.

In Figs. 5 and 6, E_g versus T for the perovskites, methylammonium lead iodide ($\text{CH}_3\text{NH}_3\text{PbI}_3$) and cesium tin iodide (CsSnI_3), respectively, are presented. As can

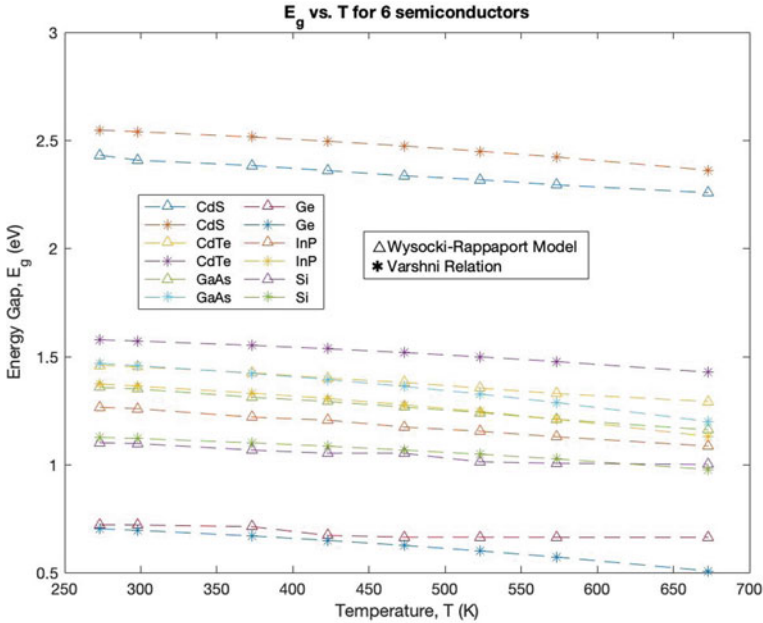


Fig. 3 Comparison of the energy gap as a function of temperature for six semiconductors, in the temperature range of 273–673 K, between calculated values from the Varshni relation and the Wysocki–Rappaport model. (Color figure online)

be seen in these figures, unlike most semiconductors, the energy gap increases with temperature in these perovskites.

This increase in E_g with temperature for perovskites is very similar to the behavior in lead chalcogenides—PbS, PbSe, and PbTe. As observed in the literature [9], the lead chalcogenides have dE_g/dT values of $\sim +4.0 \times 10^{-4}$ eV/K, which is in reasonable proximity to the value for CsSnI₃ (Table 2). The increase in E_g with temperature for lead chalcogenides has been attributed to the relatively high static dielectric constant, which is, in turn, the result of the material group’s ionic character [9]. Despite this, the same reasoning likely does not apply to perovskites due to their unique structure [10]. Perovskites are generally composed of some combination of a cation (denoted “A”), an anion (denoted “B”), and any halide (denoted “X”), in the form ABX₃. This intricate lattice structure gives rise to several new properties that are not present in conventional semiconductors and is likely the main cause of the perovskite’s unconventional behavior.

In Fig. 7, the energy gap for the perovskite, FAPbI₃, is plotted as function of temperature in the range of 298–523 K [11]. As can be seen in Fig. 6, dE_g/dT is negative until 473 K, after which there is a nearly 0.8 eV increase in E_g with temperature in the range of 473–523 K. FAPbI₃ solar cells follow the conventional trend of decreasing efficiency with increasing temperature, as shown in Fig. 8 [11].

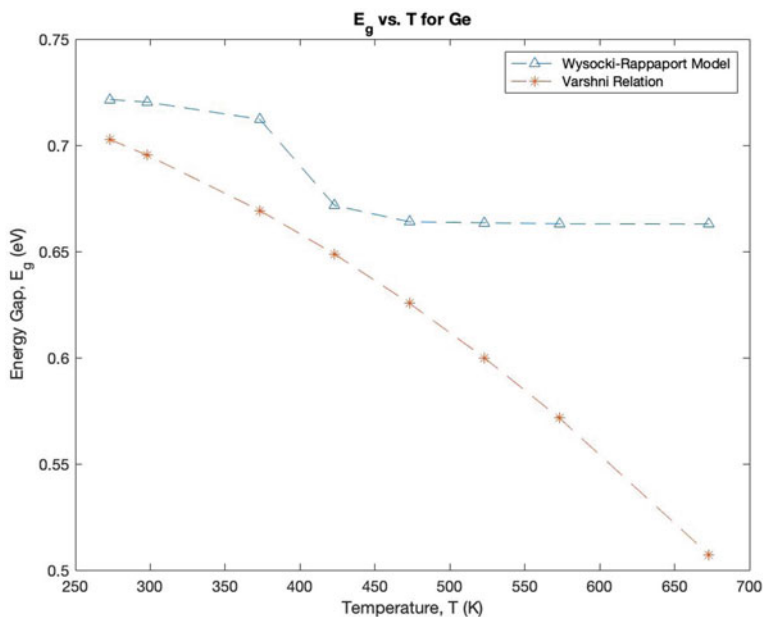


Fig. 4 Comparison of the energy gap as a function of temperature for Ge, in the temperature range of 273–673 K, between calculated values from the Varshni relation and the Wysocki–Rappaport model. (Color figure online)

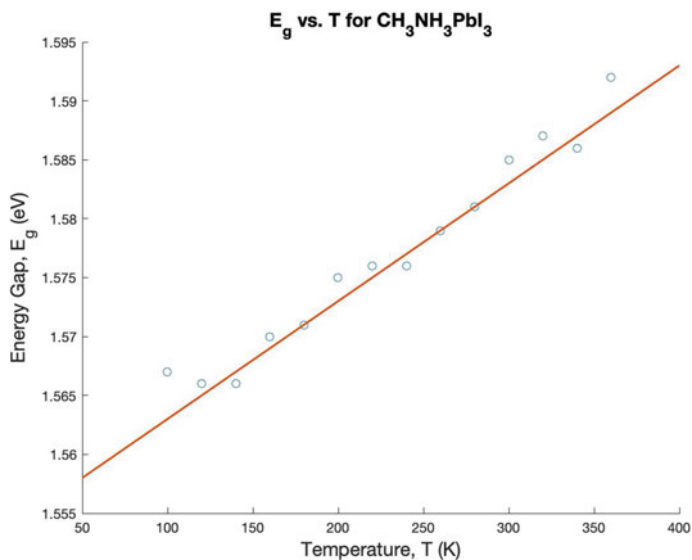


Fig. 5 Energy gap versus temperature for the perovskite—methylammonium lead iodide ($\text{CH}_3\text{NH}_3\text{PbI}_3$) [7]. Reproduced with permission from Springer. (Color figure online)

Fig. 6 Energy gap versus temperature for the perovskite—cesium tin iodide (CsSnI_3) from Yu et al. [8]. Reproduced with permission from the American Physical Society

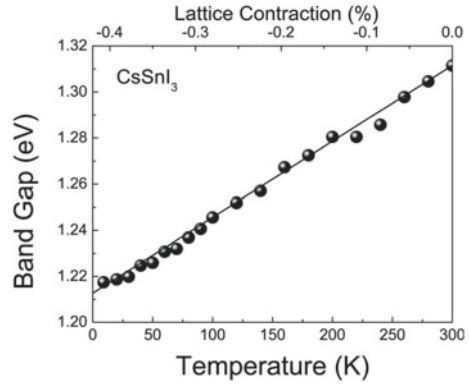


Table 2 dE_g/dT for various perovskites and lead chalcogenides

Semiconductor	$dE_g/dT \times 10^{-4} (\text{eV/K})$	References
$\text{CH}_3\text{NH}_3\text{PbI}_3$	1.00	Fig. 5—[7]
CsSnI_3	3.50	Fig. 6—[8]
PbS	4.0	[9]
PbSe	4.4	[9]
PbTe	4.3	[9]
FAPbI ₃ (298–473 K)	-3.57	Fig. 7—[11]
FAPbI ₃ (473–523 K)	174	Fig. 7—[11]

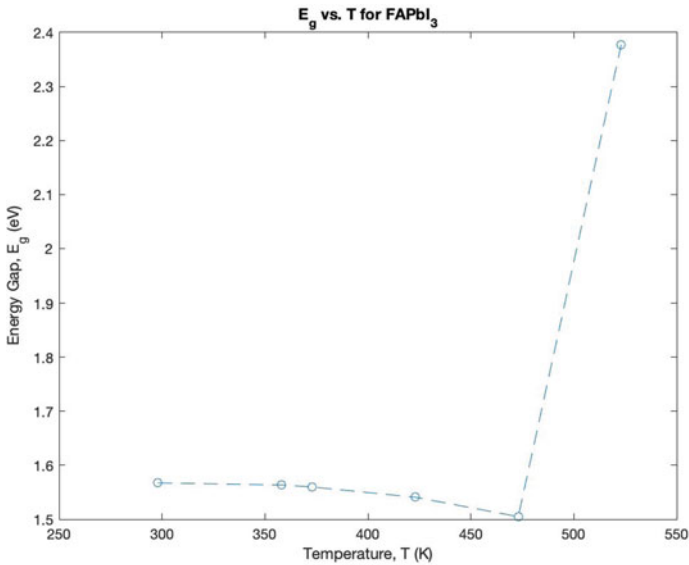


Fig. 7 E_g versus T for FAPbI₃ in the temperature range 298–523 K [11]. (Color figure online)

Fig. 8 Power conversion efficiency (η) versus temperature for FAPbI₃ in the temperature range 298–523 K (reproduced with permission from *Journal of Materials Science*) [11]. (Color figure online)

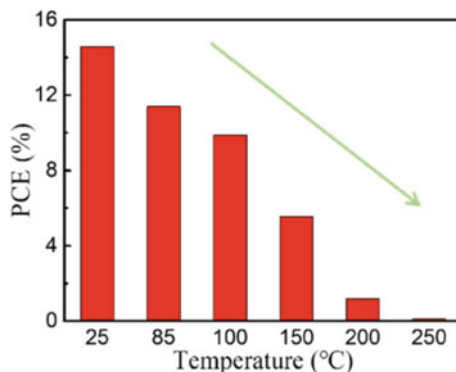


Table 3 $d\eta/dT$ for four variants of FAPbI₃ perovskite solar cells

Perovskite type	$d\eta/dT \times 10^{-2} (\text{K}^{-1})$	References
FAPbI ₃	-7.67	Figure 8—[11]
Ideal cells	-1451	[12]
Ideal thin-film cells	-1462	[12]
Real thin-film cells	-902	[12]

The change in efficiency with temperature for FAPbI₃ solar cells is summarized in Table 3.

Conclusions

In the above study, the relationships between the energy gap (E_g), power conversion efficiency (η) of solar cells, and temperature, of various semiconductor material candidates, have been qualitatively analyzed. While perovskite solar cells follow the conventional behavior of decreasing solar cell efficiencies with increasing temperature, the energy gaps of perovskites follow the behavior of lead chalcogenides in exhibiting a positive (dE_g/dT).

References

1. O'Donnell KP, Chen X (1991) Temperature dependence of semiconductor band gaps. *Appl Phys Lett* 58(25):2924–2926
2. Wysocki JJ, Rappaport P (1960) Effect of temperature on photovoltaic solar energy conversion. *J Appl Phys* 31(3):571–578
3. Varshni YP (1967) Temperature dependence of the energy gap in semiconductors. *Physica* 34(1):149–154

4. Pässler R (1997) Basic model relations for temperature dependencies of fundamental energy gaps in semiconductors. *Phys Status Solidi B* 200:155
5. Lautenschlager P, Garriga M, Logothetidis S, Cardona M (1987) Interband critical points of GaAs and their temperature dependence. *Phys Rev B* 35:9174
6. Singh P, Ravindra NM (2012) Temperature dependence of solar cell performance—an analysis. *Sol Energy Mater Sol Cells* 101:36–45
7. Lin L, Ravindra N (2020) Temperature dependence of CIGS and perovskite solar cell performance: an overview. *SN Appl Sci* 2
8. Yu C, Chen Z, Wang J, Pfenninger W, Vockic N, Kenney JT, Shum K (2011) Temperature dependence of the band gap of perovskite semiconductor compound CsSnI₃. *J Appl Phys* 110(6):063526
9. Ravindra NM, Srivastava VK (1980) Properties of PbS, PbSe, and PbTe. *Phys Status Solidi A* 58(1):311–316
10. Mei F, Sun D, Mei S, Feng J, Zhou Y, Xu J, Xiao X (2019) Recent progress in perovskite-based photodetectors: the design of materials and structures. *Adv Phys X* 4(1):1–30
11. Meng Q, Chen Y, Xiao YY et al (2020) Effect of temperature on the performance of perovskite solar cells. *J Mater Sci: Mater Electron*
12. Morales-Acevedo A (2019) Ultra-thin perovskite solar cells analytical model involving radiative and non-radiative carrier recombination mechanisms. *Phys Status Solidi (B)* 256:12. <https://doi.org/10.1002/pssb.201900340>

Part IX
Advanced High Strength Steels V

Correlation of Rolling Schedules, Mechanical Properties, and SCC Susceptibility of API X70 Steel



A. Roccisano, S. Nafisi, D. Stalheim, and R. Ghomashchi

Abstract The effect of thermomechanical rolling schedules on the development of crystallographic texture, mechanical properties, and SCC susceptibility were studied in an API X70 steel. The rolling temperatures and the magnitude of deformations (rough and finish rolling) were highly influential on the development of crystallographic texture and the resulting mechanical properties and SCC performance. Complete rolling above RLT (T_{nr}) resulted in the formation of large, equiaxed upper bainite and the highest yield strength and ultimate tensile strength. Finish rolling in the two-phase region increased the polygonal ferrite formation and deteriorated mechanical properties of the rolled steels. When finish rolling above the Ar_3 , an increase in the magnitude of the initial rough rolling deformation increased the proportion of granular bainite within the structure. Optimising the rolling strategy has shown to positively affect SCC performance.

Keywords TMCP · API X70 · Texture · EBSD · SCC

Introduction

The manufacturing process used to produce high strength low alloy (HSLA) steels for oil and gas transmission pipelines plays an important role in the strength and ductility of pipe steel. Thermo-mechanical control processing (TMCP) is a common manufacturing process used in the production of HSLA steels for oil and gas transmission pipelines that combines controlled rolling and cooling procedure to produce steels with the required mechanical properties. Various combinations of alloy design

A. Roccisano (✉) · S. Nafisi · R. Ghomashchi
The University of Adelaide, Adelaide, South Australia 5005, Australia
e-mail: a.roccisano@adelaide.edu.au

R. Ghomashchi
e-mail: reza.ghomashchi@adelaide.edu.au

D. Stalheim
DGS Metallurgical Solutions, Inc, Vancouver, WA, USA

and TMCP have been explored in the literature to produce high strength steels with desirable mechanical properties [1–8]. Whilst the link between the rolling conditions, the corresponding final microstructural/crystallographic texture and final mechanical property performance has been established [1–8], there is not much research in open literature linking processing conditions to corrosion susceptibility [9–11].

Stress corrosion cracking (SCC) is a form of environmental corrosion endemic in oil and gas pipelines. SCC forms in susceptible materials exposed to a corrosive environment under an applied or residual tensile stress [12, 13]. High pH SCC (SCC henceforth) propagates through combined film fracture and anodic dissolution. A passive oxide layer protects the steel from crack propagation, however, a sufficiently high tensile stress can fracture the brittle oxide layer, allowing anodic dissolution to occur [14, 15]. SCC in pipeline steels typically form highly branched, intergranular cracks that originate from the outer surface growing towards the inner wall [16]. As the cracks propagate, the integrity of the pipe is threatened due to a reduction in wall thickness, potentially leading to failure. By manufacturing pipelines in a way to optimise ductility/ crack arrest performance that minimises corrosion susceptibility, it may be possible to find a solution to decrease the likelihood of failure caused by SCC [17].

Experimental Procedure

Sections of API 5L X70 transfer bar (120 × 200 × 20 mm) of chemical composition outlined in Table 1 were rolled using a laboratory scale rolling mill equipped with a cooling runout table [18]. As outlined in Fig. 1, steel specimens were initially soaked to a temperature of 1180°C prior to being rough rolled at temperatures above the recrystallization lower temperature, RLT (often referred to as T_{nr}). Per pass deformation schedules were modified to affect the through-thickness austenite recrystallization behaviours and corresponding through-thickness austenite grain size formation/ homogeneity to evaluate the effect on final microstructure/texture formation and corresponding ductility/SCC performance. Samples were held in intermediate furnaces between rolling passes to prevent excessive heat loss. Following rough rolling, samples were finish rolled at temperatures below the recrystallization stop temperature, (RST) (often referred to as T_R), Fig. 1. Samples were water cooled in the runout table at a rate of 10°C/s to a temperature of 450 °C before being air cooled to room temperature. To ensure the development of sufficiently different material

Table 1 Chemical composition of supplied steel (wt. %), Fe balance

C	Mn	Si	Ni	Cu	Al	Mo	V
0.059	1.57	0.19	0.19	0.16	0.05	0.17	0.03
Nb	Ti	Cr	P	S	B	N	
0.05	0.01	0.03	0.01	<0.002	0.0005	0.004	

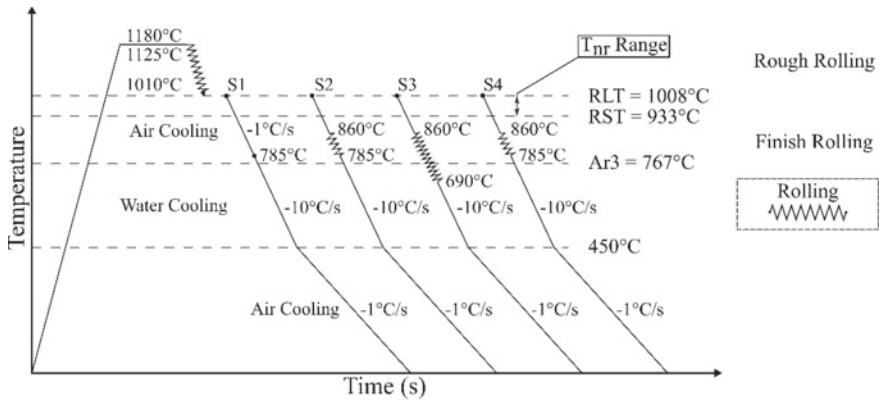


Fig. 1 Schematic diagram of thermomechanical rolling conditions of API 5L X70 steels [19]

Table 2 Rolling pass deformations data (rough rolling; finish rolling). (Color figure online)

	Pass 1	Pass 2	Pass 3	Pass 4
S1	20–17 mm (15%)	17–13.6 mm (20%)	13.6–10.2 mm (25%)	10.2–7 mm (32%)
S2	20–17.5 mm (12.5%)	17.5–12.25 mm (30%)	12.25–9.2 mm (25%)	9.2–7 mm (24%)
S3	20–14 mm (30%)	14–10.4 mm (26%)	10.4–8.2 mm (20.5%)	8.2–7 mm (15%)
S4	20–14 mm (30%)	14–10.4 mm (26%)	10.4–8.2 mm (20.5%)	8.2–7 mm (15%)

properties and crystallographic textures, different temperature ranges and per-pass rolling reductions were employed, outlined in Table 2.

Following rolling, samples had final dimensions of 500 × 120 × 7 mm. Specimens for optical microscopy and electron backscatter diffraction (EBSD) analysis were sectioned from ¼ of the width of the plate for consistency. All test pieces were evaluated from the quarter thickness plane. Specimens were prepared on an automatic polisher with diamond suspensions. Samples required for EBSD analysis were further polished with 0.04 µm colloidal silica. Optical microscopy specimens were etched with 2% Nital to aid in microstructure identification.

Tensile properties of three subsized tensile samples (ASTM E8 [20]) in three orientations, 0°, 45°, and 90° to the rolling direction, were measured on an MTS criterion model 45 universal testing machine. SCC testing was undertaken on a linearly increasing stress test (LIST) apparatus. LIST specimens underwent 10 cycles of loading from 90–95% of the measured yield stress at a rate of 24 N/hour. Specimens were exposed to a simulated high pH solution described by Parkins (2000) [12] for use in pipeline steel testing consisting of 1 M NaHCO₃ + 0.5 M Na₂CO₃ aqueous solution at 75 °C. The LIST specimens were held at an electrochemical potential of –575 mV versus Ag/AgCl. Once SCC testing was completed, samples were prepared for optical microscopy and SEM analysis to measure crack lengths; only cracks with an aspect ratio greater than 10 were considered.

Results and Discussion

Microstructures

Selected optical micrographs of the rolled samples, sourced from the quarter thickness, are shown in Fig. 2a. S1, which was rolled within the single austenite region above T_{nr} (i.e. above RLT), mainly consists of upper bainite (UB) with a limited fraction of granular bainite. The presence of upper bainite is clearly identified by sheaves of parallel ferrite crystals growing within the austenite grains in a blocky appearance. Dark etching carbides are observed between the ferrite pockets.

Steels S2 (Fig. 2b) and S4 (Fig. 2d) were finish rolled over the temperature range in the single austenite region and then cooled according to Fig. 1. Granular bainite (GB) and quasi-polygonal ferrite (QPF) are present in both S2 and S4 (granular bainite consists of islands of retained austenite or M/A dispersed in a ferrite matrix). Close examination revealed that S4 has higher concentrations of granular bainite than S2. Steel S3 (Fig. 2c) was rough rolled above RLT (i.e. above T_{nr}) and finish rolling was carried over to below Ar_3 temperature. This steel contains polygonal ferrite (PF) with limited fraction of granular bainite. Note that the prior austenite grain size of the rolled steels after initial soaking was approximately $61 \pm 19 \mu\text{m}$.

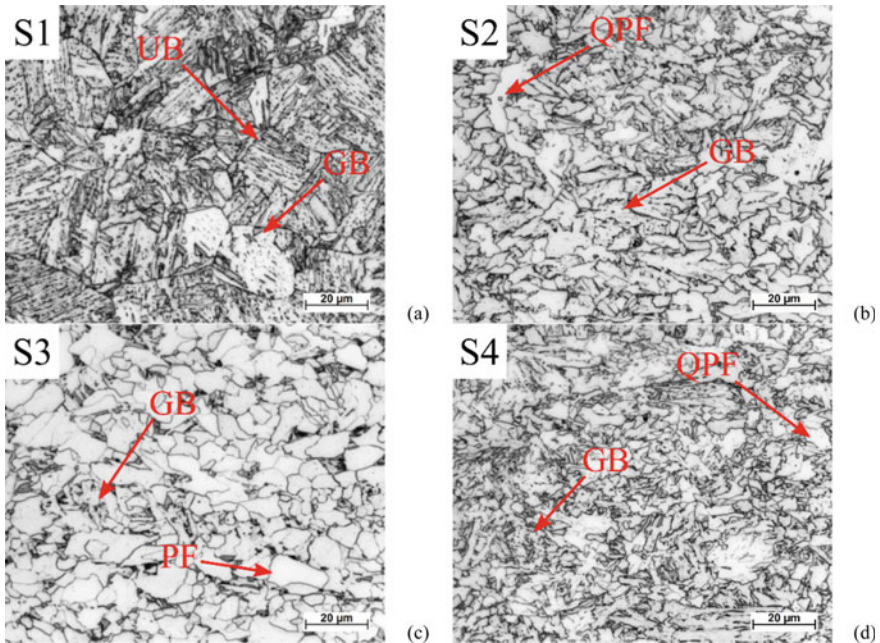


Fig. 2 Optical micrographs sourced from the quarter thickness plane. (Color figure online)

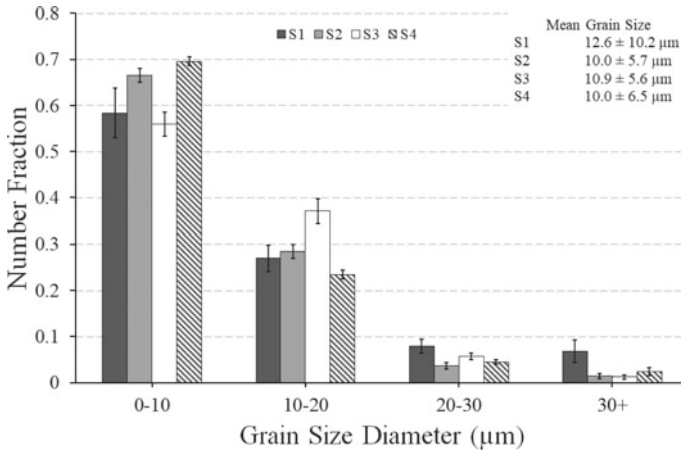


Fig. 3 Grain size distribution from the quarter thickness plane

Grain Size

The distribution of grain size at the quarter thickness is presented in Fig. 3 (EBSD results based on the equivalent circular area diameter with a critical misorientation of 15°). As stated earlier, steel S1 experienced recrystallization at rough rolling and did not undergo pancaking during finish rolling. This practice resulted in a coarse upper bainite microstructure. This is evident from the fraction of grains with equivalent circle diameters greater than 30 μm. S1 has the largest average grain size of 12.6 μm, as well as the largest standard deviation.

Steels S2 and S4, produced through conventional thermomechanical control processing, resulted in the same average grain size of 10 μm. Comparing these two, it is clear that S4 has a higher fraction of grains with diameter smaller than 10 μm and the smallest spread in each grain size fraction, a result of an optimum per-pass rolling strategy of the four strategies studied. Steel S3, that was finished rolled in the two-phase region, had an average grain size of 10.9 μm. S3 had the lowest fraction of grains below 10 μm and the highest fraction of grains between 10 and 20 μm. As S3 was finish rolled in the two-phase region, there was less austenite present to permit strain accumulation prior to transformation, resulting in a coarser grain size than those observed in S2 or S4.

Tensile Properties

One of the main requirements for linepipe design is the consideration of mechanical properties in both transverse and longitudinal directions to the pipe axis, TPA and LPA, respectively. Selected mechanical properties in three orientations 0°, 45°, and 90° with respect to the rolling direction are presented in Fig. 4.

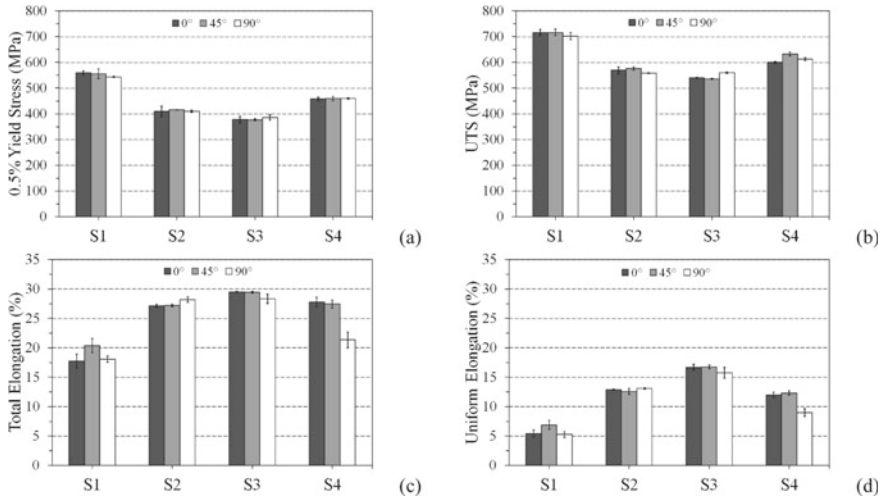


Fig. 4 Tensile properties of the laboratory rolled samples: **a** 0.5% yield stress, **b** UTS, **c** total elongation and **d** uniform elongation

Regardless of the sample direction, S1 had the highest yield strength of the investigated steels due to the presence of upper bainite. According to the literature, both YS and UTS increased with increasing proportions of upper bainite in two-phase ferritic steels [21]. S4 had the second highest YS and UTS of the remaining steels followed by S2 and S3. A similar trend was reported in an earlier investigation by one of the authors where the entire rolling schedule was carried out above T_{nr} resulted in higher YS and UTS than the steels produced through thermomechanical control processing [1]. The total and uniform elongation values are presented in Fig. 4c and Fig. 4d. The reported values for elongation are comparable with each other with the exception of S1, as expected; i.e., strength and ductility have opposite trends. A similar finding was reported in the previous publication where X100 steel completely rolled above RLT, T_{nr} , (with upper bainite microstructure) had the lowest total and uniform elongation [1]. S1 rolling strategy resulted in the coarsest and largest range of final ferrite grains that would also correspond to having a coarse and large range of austenite grains with higher hardenability characteristics during transformation. This resulted in a larger volume fraction of harder microstructural phases, negatively affecting the total and uniform elongation.

Crystallographic Textures—EBSD

The orientation distribution function (ODF) plots in Bunge notation [22], at the $\varphi_2 = 45^\circ$ section is shown in Fig. 5. Figure 5a presents the ODF plot from the quarter plane of S1. S1 shows the highest intensity of orientations at $\{001\}\langle 110\rangle$. The $\{001\}\langle 110\rangle$ textures are characteristic of a recrystallization process in austenite. These textures

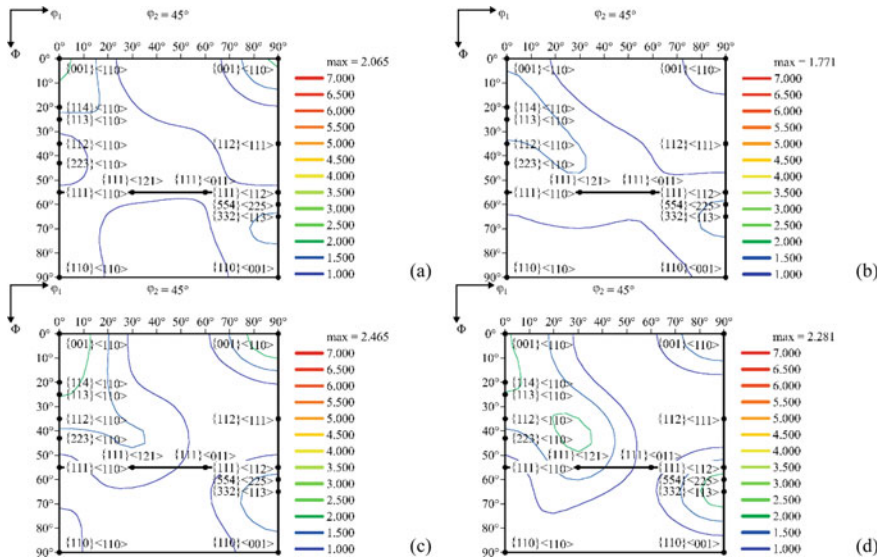


Fig. 5 Crystallographic textures at quarter plane determined through EBSD. **a** S1, **b** S2, **c** S3 and **d** S4. (Color figure online)

originate from the cube texture in austenite and rotate, upon transformation, to form the rotated cube textures (amongst others) in ferrite [8]. The presence of {332}<113> orientations indicate austenite deformation prior to transformation as this texture is the product of deformed austenite [22, 23]. Similar textures and intensities have been observed for high temperature rolling of low carbon steels in the literature [1, 22, 24]. The bulk texture of S2 at the quarter plane, Fig. 5b, shows the highest intensity at approximately the {113}<110> and {332}<113> orientations, expected for austenite deformation prior to transformation. In addition to the deformed austenite texture, weak {001}<110> orientations indicate austenite recrystallization prior to transformation, shown strongly in S1 [1, 8, 22].

The $\varphi_2 = 45^\circ$ ODF of S3 is presented in Fig. 5c and displays a high intensity of {001}<110> textures, indicating either austenite recrystallization (during rough rolling) or ferrite deformation (finish rolling below A_{r3}) [1]. Whilst the high intensity of {001}<110> in S3 would suggest significant austenite recrystallization, the high intensity of {113}<110> and {112}<110> textures in S3 are indicative of both austenite and ferrite deformation, as expected for S3 considering the two-phase finish rolling schedule for S3, outlined in Fig. 1 [22]. S4 in Fig. 5d displays similar overall textures to both S2 and S3, showing dominant {113}<110>, {332}<113> and {001}<110> orientations. As observed in Table 2, S3 and S4 have identical deformation profiles. The high % reduction during rough rolling results in a high level of austenite deformation prior to recrystallization above the RLT temperature. That high austenite deformation is the likely cause of the high intensity of {001}<110> textures observed in both S3 and S4. The formation of the {332}<113>

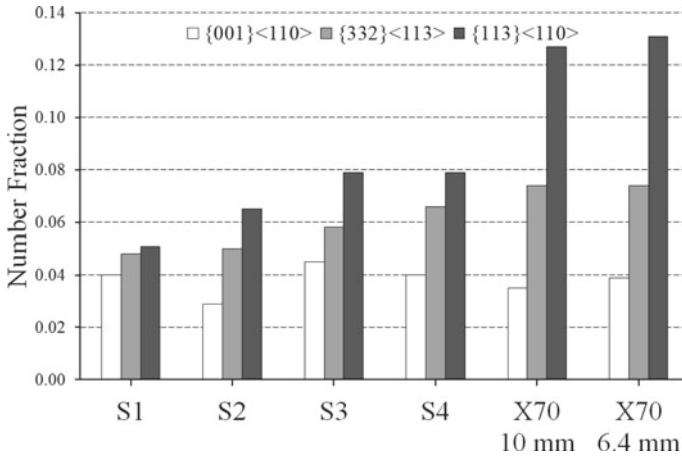


Fig. 6 Fraction of $\{001\}\langle 110\rangle$, $\{332\}\langle 113\rangle$ and $\{113\}\langle 110\rangle$ textures present in the investigated steels (measurements considered a 15° misorientation tolerance)

texture observed in S4 is higher than S2 because of the higher hot rolling deformation experienced by S4 that reduced the austenite grain size. Similarly, finish rolling below the RST temperature but above the A_{r3} increased the intensity of the $\{332\}\langle 113\rangle$ texture more than S3 which had the same deformation schedule as S4 as observed in the literature [22].

Ray et al. [22] reviewed rolling transformations in various steels and determined that amongst the texture components produced in controlled rolled steel, the $\{113\}\langle 110\rangle$ component causes major anisotropy in both strength and toughness, resulting in brittleness along the 45° plane, with respect to the rolling direction. On the other hand, the $\{332\}\langle 113\rangle$ component leads to minimum anisotropy and more desirable properties. Therefore, the fraction of these components could be an indication of the resulting properties. Figure 6 shows the most critical values for the laboratory rolled steels as well as a comparison with two industrial X70 steels.

Of the laboratory rolled steels, S4 has the highest fraction of $\{332\}\langle 113\rangle$ textures. S4 underwent more rough rolling reduction compared with S2 (30% compared to 12.5%) that contributed to the lower proportion of the highly beneficial $\{332\}\langle 113\rangle$ texture. S3 and S4 have identical rolling schedules, however, the fractions of texture components are different. It is believed that the difference is due to the lower finish rolling temperature of S3 within the two-phase region (i.e., higher fraction of $\{001\}\langle 110\rangle$ textures in S3). Whilst $\{001\}\langle 110\rangle$ textures are produced from recrystallized austenite, despite experiencing the same rough rolling deformation above RLT, finish rolling in the $(\gamma + \alpha)$ region has been observed to increase the intensity of $\{001\}\langle 110\rangle$ textures [22]. The fraction of $\{332\}\langle 113\rangle$, and $\{113\}\langle 110\rangle$ textures observed in S1 was low, common for hot rolled steel processed entirely above RLT which prevents any significant strain accumulation [24]. A similar trend was observed by the authors on X100 steel which was produced by RCR rolling schedule [1].

SCC Susceptibility

Laboratory testing can facilitate SCC crack formation and its growth under controlled conditions not possible through field testing. In addition, due to the constant, severe conditions, cracks can grow at a higher rate than is typical of field-grown cracks. There are two common laboratory methods used to produce SCC cracks; linearly increasing stress test (LIST) and slow strain rate test (SSRT) [25]. These tests mimic SCC forming conditions at a small scale so manageable tensile specimens can be used to gauge SCC susceptibility. The main difference between the two tests is that the SSRT is extension controlled (elongation rate is constant), whereas the LIST is load controlled (loading rate is constant); when loading to failure, the LIST test typically finishes faster [25]. One common method of gauging SCC susceptibility is by measuring the crack growth rate [26]. To account for different times spent corroding, the crack velocity is a common measure of normalising the crack length and is found by dividing the length of the longest crack in the test section by the total time spent in the corrosive environment [25]. Field grown cracks are typically larger than the size of cracks generated by LIST testing due to the difference in growth duration (days of LIST testing compared with decades in the field). An example of the growth characteristics of SCC in an ex-service pipe is presented in Fig. 7a whilst a cross-section of a field-generated crack, initiating at the base of a large pit, is presented in Fig. 7b. These images are from an API X65 pipe of nominal diameter 864 mm and wall thickness of 8.4 mm.

Figure 8 shows the average crack velocity of the LIST tested specimens. On average, S1 has the fastest SCC crack velocity amongst all the lab produced steels. Faster crack velocity is translated to more susceptible material as the crack could find easy paths through the steel microstructure. S1 has a significantly greater crack velocity in comparison to the others which is related to the recrystallized rolling schedule, and significantly different crystallographic texture, grain size, microstructure, and material properties. In contrast, S4 has the lowest average crack velocity

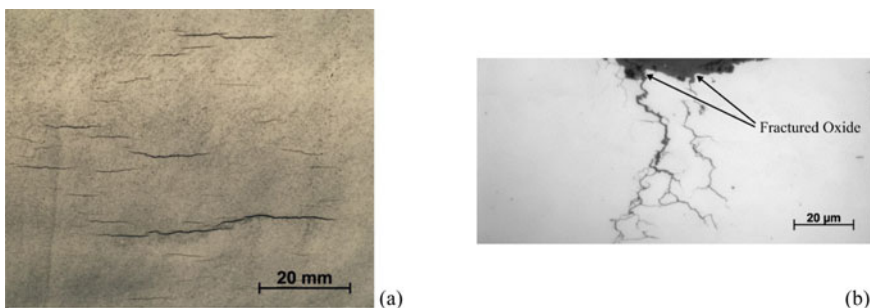


Fig. 7 a SCC cracks on the surface of an API X65 pipe, exposed using magnetic particle inspection, b Cross-section of a field-grown crack initiating from a pit in API X65. Adapted from [27]. (Color figure online)

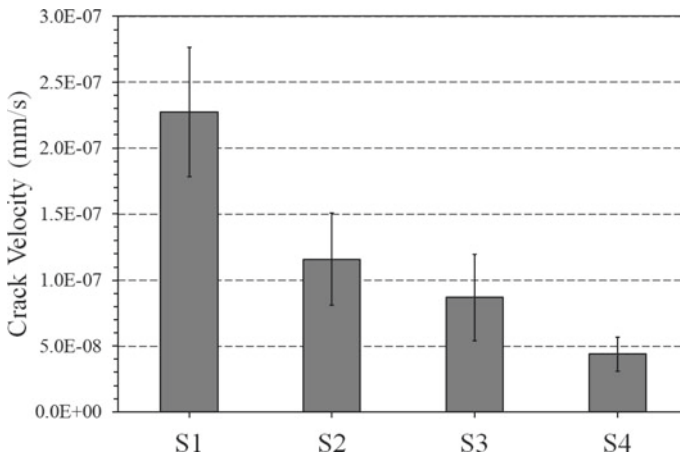


Fig. 8 Average SCC crack velocities of the investigated steels

indicating a higher resistance to cracking. The ability to minimise the SCC susceptibility of a pipeline steel through the rolling procedure has the potential to delay or prevent SCC failure over the lifetime of pipeline. This has a profound effect on the industry where millions of dollars are spent each year due to the occurrence of SCC.

Conclusions

The influence of various rolling schedules on microstructural evolution, crystallographic texture, mechanical properties, and SCC susceptibility of an API X70 steel has been studied and resulted in the following conclusions;

- Rolling above recrystallization lower temperature (RLT/ T_{nr}) in S1 showed predominantly upper bainite with high strength but low ductility (elongation) as well as the highest SCC susceptibility. Rolling schedule for S1 mainly offered $\{100\}\langle 011\rangle$ texture which was originated from recrystallized $\{100\}\langle 001\rangle$ cube austenite grains and therefore was more brittle than the other steels.
- When decreasing the finish rolling temperature, but remaining above the A_{r3} , an increase in the initial rough rolling deformation (S4 in comparison to S2) increased the proportion of granular bainite. There is also a major increase in the intensity of $\{332\}\langle 113\rangle$ component. S4 had the best mechanical properties of the conventional thermomechanical produced steels, along with the lowest SCC susceptibility.
- Per pass rolling and temperature strategies along with corresponding austenite recrystallization behaviours all play key roles in the texture development and influence mechanical properties of API X70 steel. Rolling below A_{r3} temperature facilitated formation of polygonal ferrite and led to lowest YS and UTS

and an improved elongation in comparison to the other steels. Optimising the rolling strategy for through-thickness optimum ductility performance has shown to positively affect SCC performance.

Acknowledgements This work was funded by the Energy Pipelines CRC, supported through the Australian Government's Cooperative Research Centres Program. The funding and in-kind support from the APGA RSC is gratefully acknowledged. The authors acknowledge the facilities, and the scientific and technical assistance, of the Australian Microscopy & Microanalysis Research Facilities at the University of Adelaide and Flinders University. The authors would like to acknowledge Professor Zhengyi Jiang and Mr Nathan Hodges of the school of mechanical and materials engineering of the University of Wollongong for access provision to the laboratory rolling mill.

References

1. Nafisi S, Arafin MA, Collins L, Szpunar J (2012) *Mater Sci Eng A* 531:2–11
2. Zhao M-C, Yang K, Shan Y (2002) *Mater Sci Eng A* 335(1–2):14–20
3. Shin SY, Hwang B, Lee S, Kim NJ, Ahn SS (2007) *Mater Sci Eng A* 458(1–2):281–289
4. Toth LS, Jonas JJ, Daniel D, Ray RK (1990) *Metall Trans Phys Metall Mater Sci* 21(11):2985–3000
5. Inagaki H (1994) *ISIJ Int* 34(4):313–321
6. Raabe D (2003) *Steel research* 74(5)
7. Haldar A, Ray RK (2005) *Mater Sci Eng A* 391(1–2):402–407
8. Jonas JJ (2009) 3–17
9. Ralston KD, Birbilis N (2010) *Corrosion* 66(7):075005–075005–13
10. Masoumi M, Silva CC, de Abreu HFG (2016) *Corros Sci* 111:121–131
11. Bauer J, Flüß P, Amoris E, Schwinn V (2005) *Ironmaking Steelmaking* 32(4):325–330
12. Parkins RN (2000) *CORROSION 2000*. NACE International
13. King A, Johnson G, Engelberg D, Ludwig W, Marrow J (2008) *Science* 321(5887):382–385
14. Song F (2008) *CORROSION 2008*. NACE International
15. Parkins RN (1996) *Corrosion* 52(5):363–374
16. Beavers JA, Christman TK, Parkins RN (1988) *Mater Perform* 27(4):22–26
17. National Academies of Sciences Engineering and Medicine (2018) *The National Academies Press*, Washington DC, p 144
18. Jiang ZY (2014) *Advanced materials and processes Iii*, Pts 1 and 2
19. Roccisano A (2020) *Manufacturing processes leading to improved high pH SCC resistance in pipes*. Ph.D. Thesis, The University of Adelaide, Adelaide
20. ASTM International (2016) *ASTM E8/E8M-16a*, Standard test methods for tension testing of metallic materials
21. Zhang X, Gao H, Zhang X, Yang Y (2012) *Mater Sci Eng A* 531:84–90
22. Ray RK, Jonas JJ, Butron-Guillen MP, Savoie J (1994) *ISIJ Int* 34(12):927–942
23. Nafisi S, Arafin M, Glodowski R, Collins L, Szpunar J (2014) *ISIJ Int* 54(10):2404–2410
24. Inagaki H (1981) *Proceedings of the sixth international conference on texture of materials*. Tokyo, Japan, pp 149–163
25. Atrens A, Brosnan CC, Ramamurthy S, Oehlert A, Smith IO (1993) *Meas Sci Technol* 4(11):1281–1292
26. Fang BY, Atrens A, Wang JQ, Han EH, Zhu ZY, Ke W (2003) *J Mater Sci* 38(1):127–132
27. Roccisano A, Nafisi S, Ghomashchi R (2020) *Metall Mater Trans A* 51(1):167–188

Part X
**Advanced Magnetic Materials for Energy
and Power Conversion Applications**

Magnetic Augmented Rotation System (MARS)—An Update



Tyler Brunstein-Ellenbogen, B. S. Mani, Tien See Chow,
and Nuggehalli M. Ravindra

Abstract Prior research conducted by the team at NJIT has shown that contactless torque transmission is possible and effective. In recent years, there has been significant development in materials, material systems, and materials processing for applications in contactless transmission. In minimizing material wear and tear due to minimal or zero friction, gearless systems require no lubrication, offer extended shelf-life and exhibit minimal noise. By utilizing 3D printing technologies such as fused deposition modeling and stereolithography, we are able to rapidly test new concepts and ideas. Growth opportunities of this evolving technology are summarized.

Keywords Magnetic augmented rotation system (MARS) · 3D printing · Gears · Electric vehicles · Magnetic levitation · Contactless torque transmission · Electromagnet · Coils

List of Abbreviations

MARS Magnetic Augmented Rotational System
EMF Electromotive Force/Electromagnetic Field
AC Alternating Current
DC Direct Current
AWG American Wire Gauge

T. Brunstein-Ellenbogen · B. S. Mani
Department of Mechanical & Industrial Engineering, NJIT, Newark, NJ, USA
e-mail: tb288@njit.edu

T. S. Chow
ETD Inc. New York, NY, USA

N. M. Ravindra (✉)
Department of Physics, NJIT, Newark, NJ, USA
e-mail: nmravindra@gmail.com

Introduction

The idea of magnetic gears (MG) was first introduced at the beginning of the twentieth century. In 1913, a US patent [1] described an electromagnetic gear, which was regarded as the first topology of electromagnetic gears. In this patent, the inventor provided a method and apparatus for coupling two shafts or rotatable elements together without the employment of any mechanical or tangible means connecting the shafts. However, this novel idea did not draw any attention at that time. People started to pay attention to MG because of another US patent by Faus in 1941 [2]. Faus magnetic gear had a geometric configuration analogous to ancient mechanical pin gears, with magnetic pins inserted in the base. Even though magnetic gears were more accepted at that time, the disadvantages still limited their application in industry. Since the gears were made by ferrite, the low mechanical and magnetic strength of ferrite seriously affected their performance and lifetime. With the appearance of the high-performance neodymium iron boron (NdFeB) material in the 1980s, the MGs aroused public attention again. Neodymium magnets are known to be the most commonly used type of rare-earth permanent magnets made from an alloy of neodymium, iron, and boron to form the Nd₂Fe₁₄B tetragonal crystalline structure [2]. Nagrial et al. [3–5] made use of NdFeB magnets to allow an external-type magnetic gear set to generate high magnetic flux densities within the air gap. Being the strongest type of permanent magnet, NdFeB has replaced many other types of magnets in applications today, especially in the area which require strong permanent magnets.

Magnetic augment rotation system, US patent No. 6356000 B1, was invented by Chun-Yuan Ho and Tien-See Chow. It was patented on March 12, 2002. The aim of MARS is to improve the efficiency of the drive wheel and the prime mover. The whole system includes several parts: wheel assembly, first magnetic polarity, second magnetic polarity, bearing assembly, magnetic biasing assembly, and anti-reversing gear assembly [6]. Like other magnetic gears, the power transform in the MARS system from one wheel to another is by magnetic coupling rather than mechanical contacts.

Unlike the prototype made by Chu-Yuan Ho and Tien-See Chow, the recent research is primarily focused on the application of MARS to an electric generator. The concept of magnetic levitation was applied to a generator in order to reduce the friction generated from the bearings used for axial balancing. In theory, a generator stator can be suspended in the air by magnets, further reducing wear related components. The motor design will be discussed in depth in the main concepts section.

Advantages of Contactless Transmission

Contactless mechanical gears and torque transmission components are proving to eclipse traditional meshed mechanical gears. The main advantage of magnetic gears is that they eliminate the need for lubrication. By reducing the amount of parts in

contact, we can reduce the wear and tear of mechanical parts, further improving their longevity. We also can allow the motor to spin at higher speeds without having to worry about over torquing the system. Because the transmission mode does not require mechanical teeth like that of a spur gear, we do not have to worry about damage due to shear stresses. In the case of the electric generator, the magnets provide a floating effect, which transmits the weight of the stator evenly through the casing to which the magnets are fixed. Another advantage is the magnet's strength in cold temperature and situations where the motor will be in a low pressure or vacuum environment. For this reason, MARS could be the answer to many problems in the aerospace industry that are plagued by mechanical friction.

Disadvantages of Contactless Transmission

Even though contactless gears have many advantages compared to traditional mechanical gears, MARS, as contactless, still has limitations in several areas. First, the material used in magnetic gears may not be as strong as that in mechanical gear; thus, they may be subjected to fatigue due to high cyclic load. Moreover, since MARS requires magnetic materials, it has Curie temperature, the temperature at which materials lose their magnetic properties. Hence, MARS cannot be used in extreme working conditions such as very high temperatures. Another limitation of MARS is its general instability. For the motor considered in this study, we are testing magnetic bearings to keep the central shaft aligned like it would be with the use of bearings. By using small neodymium magnets, the concept is very sporadic during operation and cannot run at low speeds. Another disadvantage of using this technology is the danger of cracking or breaking magnets during operation. When a magnet breaks, it will snap off and attract to the closest magnet with an opposite polarity. Fractures like this would certainly throw the system out of balance, which could lead to further problems throughout its lifetime caused by vibrations.

3D Printing and the Role of Rapid Prototyping

3D printing is a method of manufacturing in which materials such as plastic or metal are deposited onto one another in layers to produce a three-dimensional object, such as a pair of eyeglasses or other 3D objects. This creation has now become both an important instrument for research as well as a high-end household item. 3D printing has brought with it the potential to create objects that are virtually impossible to create otherwise. 3D printing, or additive manufacturing, has in recent years been able to accomplish the task of creating a simple solution to the problem of forming new structures that can be used in many technical and scientific fields; complex mechanical components varying in size, design, and shape can be printed with ease. This translates to cost reduction through the reduction of material waste. In metal 3D

printing, the raw material is added and formed layer by layer, rather than subtracting or cutting from a bulk solid chunk/figure. Gears are simple structures used within almost all types of mechanical devices. The process of replacing a single, discrete component such as a gear requires weeks of waiting for delivery. 3D printing simplifies delivery time hassles by allowing for the printing of the very same gear within a matter of less than a day or even an hour [7]. This solution could further be improved by using stronger materials to ensure that the new gear is stronger than its predecessor.

As desktop 3D printers have become affordable, they are readily available. In this study, our main focus was to bring the concepts discussed in relation to MARS into a tangible working model [8]. By using a homemade Creality Ender-3 printer, our team was able to rapidly test new ideas and concepts in only a few hours of printing. One amazing aspect of 3D printing is how cheap prototypes can be. Generally, a 1 kg spool of PLA filament will cost around \$20 USD. This means that we can get around 10 shell models and 5 stator models per roll. Traditionally, these concepts would need to be outsourced to a machine shop which would increase the price per test piece by tenfold. It should go without saying that the final version of the generator will be made from steel or another strong material, as the plastic cannot tolerate high heat.

That being said, our team was able to produce a model which outputs a small voltage and current, printed entirely from plastic without the use of ferromagnetic materials. PLA composite materials exist, which combine normal polylactic acid with a plethora of composite materials such as iron, bronze, nylon, polycarbonate shreds, and carbon fiber strands. Ideally, the outer shell of our printed motor would be printed in a ferromagnetic filament such as ProtoPasta LLC's iron core magnetic PLA [9]. Using a shell that is made from magnetic material would produce a back EMF which would induce more current through the coils.

Main Concepts of Motor

We will now discuss the concepts and theories used when designing the MARS motor. Simply put, the application for magnetic levitation is driven by putting two sets of neodymium magnets of the same polarity together. In our initial design, we placed magnets both on the motor shell and the stator, with identical magnet polarities facing up as seen in Fig. 1.

By doing this, we were able to float the shell on top of the stator core which fulfilled the levitation aspect, although, our next challenge is to make the central



Fig. 1 Theoretical principle for the magnetic levitation used in the motor. (Color figure online)

shaft of the stator balanced perfectly on the shell. It is worth noting that we do not have a finalized design yet due to material and time limitations with the Covid-19 pandemic. One theory that we have come up with to solve this balancing issue is to repeat the concept used for the base levitation, but to mount it 90° on the shaft. Pictured in Figs. 2 and 3, we are able to see the magnets mounted on the base shell and the stator. These magnets are packed as close together as possible which keeps the magnetic flux from the south poles of the magnets from interacting with each other. By doing this, we reduce the likelihood that the south pole on the stator magnets interacts with the north pole of the shell magnets; this would defeat the repulsion laws and would cause the magnets to attract, further locking the design into place. Figure 2 is a cross-sectional view of the stator and shell design which shows the cutouts for the permanent magnets; this also illustrates how they would be seated during operation through the central axis.

While this design was a significant indication that the magnetic levitation concept could work, the motor itself was obsolete. During testing with a 4 pole, 2 phase stator wound with 50 loops of 20 AWG wire, we were barely able to create 0.1 V AC. A winding jig was designed and 3D printed to help keep track of how many loops the stator core had before switching to the opposite pole, as shown below in Fig. 4. Keeping with the theme of this project, every piece aside from the arduino and stepper motor was printed using an inexpensive FDM printer.

Fig. 2 Cross-sectional cut away of the original motor design. (Color figure online)



Fig. 3 Polarity of the magnets when being placed inside the shell. The red dot on the top of the magnets represents the direction of the magnet face. (Color figure online)

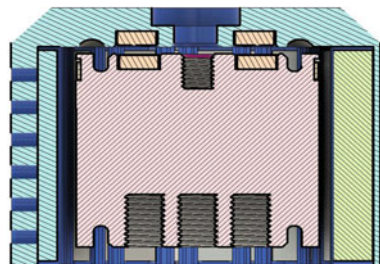
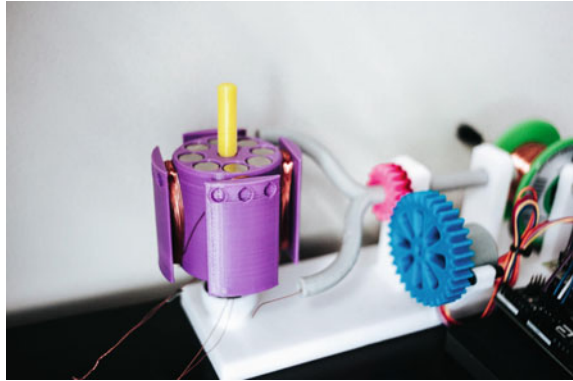


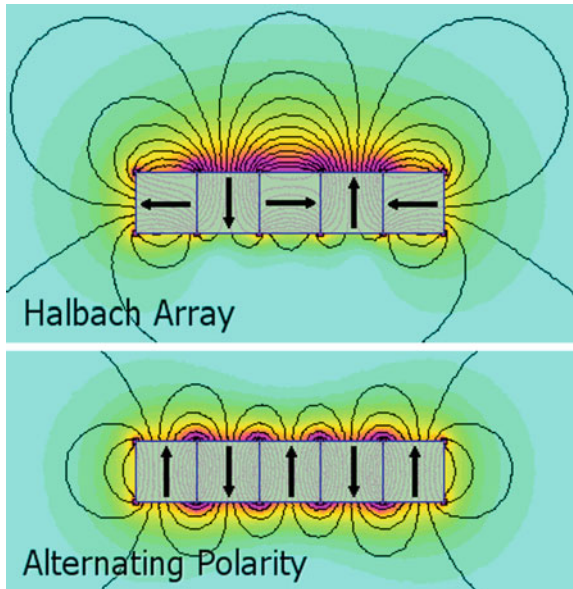
Fig. 4 Winding jig designed and printed to aid in winding the stator. (Color figure online)



While the stator winding pattern is important, it is worthwhile to note the pattern of the magnets used in the shell. The pattern used is called the Halbach Array [10]. This array was first discovered in 1973 by British Physicist John C. Mallinson. This discovery marked the very crucial turning point in the phenomena of single sided magnetic flux. By grouping bar magnets in groups of four and rotating each subsequent magnet 90°, such that the pattern goes North, South, East, and West, we can create a magnetic flux that is concentrated on one side and weak on the other. This is illustrated in Fig. 5.

Preliminary testing showed this effect when we measured the magnetic field strength (in Tesla) with respect to time. As can be seen in Fig. 6, magnetic field

Fig. 5 Magnetic flux of the Halbach array compared to the traditional alternating polarity array. (Color figure online)



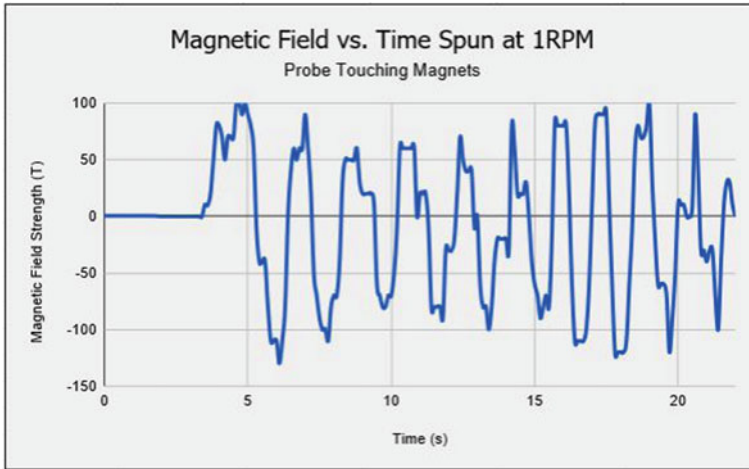


Fig. 6 Magnetic field as function of time. (Color figure online)

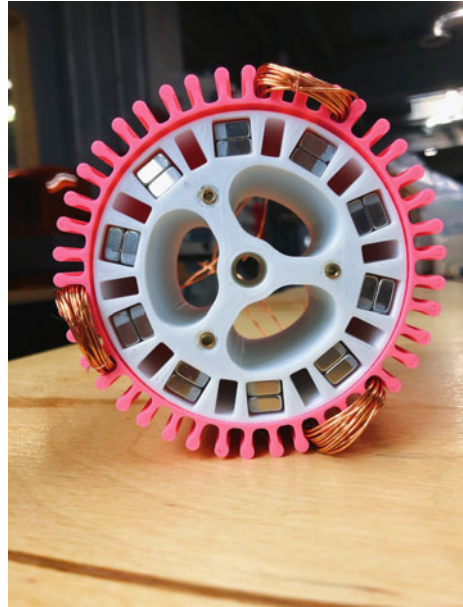
strength is oscillating every quarter turn, as it passes through one completed Halbach array. The red lines on the magnets were drawn while they were all connected in line to ensure proper orientation. The pattern resets itself after each four magnet grouping (Fig. 3). Testing with a homogenous magnetic array yielded significantly lower field strength on the inside of the shell and was not investigated further. This concept of the Halbach array has been used in each version of testing.

Since we have decided that the previous versions of the generator were not likely to produce the amount of voltage and current we had hoped for, we scrapped the idea and started over. The new design takes heavy influence from more conventional brushless motors, where the stator is loaded with permanent magnets, and the wire coils are placed along the outer perimeter of the shell. The magnets have been moved from the outer shell to the inner motor, which is now the spinning component. Conversely, the wires on the inner stator have been fastened to the non-moving outer shell in 3-phase configuration. A cutaway of the generator is pictured below in Fig. 7.

Preliminary testing with just these three windings provided phenomenal results. By using a drill spinning at 1500 rpm, we were able to spin the white stator piece on the inside of the coil pack. Testing this generator yielded 3.3V AC and 1 A of current. This is a nearly 3300% increase from the original model, which gives us confidence and we shall beat our expectations once the coil pack is completely populated.

Ideally, our team would like to integrate the magnetic levitation concept from the first version of the generator into the current model. The end goal of this project is to create a generator that does not require any bearings to center the stator inside of the coil pack. By using the concepts of magnetic levitation mentioned above, we think that we could integrate it into this model. A similar system will be used; we will have opposing magnets on the top of the central stator which would interfere with

Fig. 7 Outer coil holder (pink) with three wounds coils. The exposed view permits a look at the magnets inside of the stator as well. (Color figure online)



magnets situated on an endcap holding the coil pack in place. Theoretically, we will be able to create a stator that is frictionless resulting in a maximum energy transfer from the input into the windings.

Conclusion

By implementing MARS into large scale motors, we can reduce the need for lubrication and regular maintenance. This technology can be further applied to clean energy applications such as hydroelectric turbine generators and wind turbines. Further development of this concept will lead to a broader range of applications. Through rigorous testing of theoretical principles, it is within reason that our team will be able to accomplish our original goal. We will be able to produce a generator that is magnetically levitated, reducing the need for bearings or other friction generating components.

Acknowledgements The financial support of Mr. Tien-See Chow (ETD Inc.) and Prof. Nugehalli M. Ravindra is gratefully acknowledged. Tyler Brunstein-Ellenbogen would like to thank Professor B. S. Mani for the wonderful opportunity to work on this project as well.

References

1. Neuland AH (1916) US 1,171,351A, Apparatus for transmitting power. Google Patents
2. Faus HT (1941), US 2,243,355A, Magnet gearing. Google Patents
3. Fraden J (2004) Handbook of modern sensors: physics, designs, and applications. Springer Science & Business Media
4. Nagrial MH, Rizk J (2000) Proceedings of the IEEE international magnetics conference
5. Rizk J, Nagrial MH, Hellany A (2004) Analysis and design of magnetic torque couplers and magnetic gears. In: The 4th international power electronics and motion control conference, 2004, IPEMC 2004. IEEE
6. Nagrial M, Rizk J, Hellany A (2008) Design and performance of permanent magnet slotless machines. In: 18th international conference on electrical machines, 2008, ICEM 2008. IEEE
7. Ho CY, Chow T-S (2002), US 6,356,000B1, Magnetically augmented rotation system. Google Patents
8. <https://www.sciencedirect.com/science/article/pii/S0007681311001790>, accessed on 21 Sept 2020
9. <https://digitalcommons.njit.edu/theses/274>, accessed on 21 Sept 2020
10. ProtoPassta LLC (2020) Iron filled PLA technical data sheet. Retrieved 15 May 2020
11. <https://www.sciencedirect.com/science/article/abs/pii/S0029554X80900944?via%3Dihub>, accessed on 21 Sept 2020

Oxide Thin-Film Electronics for the Front-End Conditioning of Flexible Magnetic Field Sensors



Niko Münzenrieder, Giuseppe Cantarella, Luisa Petti, and Júlio Costa

Abstract Unobtrusive magneto-reception can enable innovative applications in diverse scenarios ranging from the interaction of humans with virtual objects to the controlled movement of micro-robots. The required bio-compatible magnetic sensor systems have to be cheap and able to conform to the movement of reconfigurable surfaces and biological tissue, while providing excellent performance. The key to realize such systems is the integration of magnetic sensors with on-site conditioning electronics directly on large-area plastic substrates. In fact, ad-hoc optimized oxide thin-film transistors provide a technology platform which is not affected by mechanical deformation or magnetic fields and can hence be used to boost the performance of magnetic sensor systems through front-end conditioning. Flexible oxide conditioning circuits provide voltage gains close to 50 dB at operation voltages down 1.7 V while bent to radii <4 mm. Fully flexible Co/Cu giant magnetoresistance sensors, Wheatstone bridges and amplifiers can be integrated on a single polymer foil and result in a $50\ \mu\text{m}$ -thin conformal system with a $25\ \text{V/V/kOe}$ sensitivity.

Keywords Flexible electronics · Oxide semiconductors · Conditioning · Thin-film transistors · Sensor technology

Introduction

Flexible systems operated in close proximity to the human body, manufactured using cost efficient large-area techniques, or based on bio-compatible transient materials are considered one of the next major steps in the development of environmentally-friendly and unobtrusive electronics [1, 2]. This applies particularly to the field of flexible magneto-electronics, which aims to provide accurate magnetic field mea-

N. Münzenrieder · G. Cantarella · L. Petti
Faculty of Science and Technology, Free University of Bozen-Bolzano, 39100 Bozen, Italy

N. Münzenrieder (✉) · J. Costa
Sensor Technology Research Centre, University of Sussex, Brighton, UK
e-mail: niko.muenzenrieder@unibz.it

surements for wearable systems in geometrically challenging environments [3, 4]. In this context, highly sensitive sensors [5] e.g. for geo-magnetic fields or virtual reality applications [6] have been demonstrated using flexible resistive sensors, as well as Hall sensors. To further push the performance of flexible magnetic sensor systems, flexible front-end amplifiers [7] conditioning the sensor signals are required. Fully flexible systems offer the advantage of being able to amplify the sensor output as close as possible to the sensor, before its output can be compromised by external noise or noise in the subsequent processing hardware. This paves the way to applications such as flexible magneto-encephalography with extremely demanding requirements such as fields around 10–1000 fT and frequencies up to 500 Hz [8, 9].

In order to realize such flexible active electronics, many novel semiconductors, such as organic materials, amorphous silicon, and oxides have been investigated in the last decades. Among the possible materials, low-temperature ($\lesssim 200^\circ\text{C}$) deposited amorphous In-Ga-Zn-O (IGZO) [10] is especially attractive as it combines compatibility with flexible substrates, excellent electrical properties, extreme bendability, as well as the possibility to realize integrated circuits [11–13]. Due to the above-mentioned advantages, IGZO based electronics is suitable to realize flexible front-end amplifiers. In fact, there are several examples of IGZO electronics interacting or being operated with magnetic fields such as: IGZO TFTs as magneto-resistive devices [14], IGZO with magnetic beads for enzymatic glucose biosensors [15], IGZO circuits for the conditioning of magnetic sensors [16], or IGZO electronics for magnetically coupled wireless power transmission systems [17].

Here, we present high-performance flexible IGZO electronics, evaluated especially in terms of their applicability for magnetic sensor systems. In particular, this work evaluates whether IGZO circuits are influenced by magnetic fields and how they can be integrated with B-field sensors to form highly sensitive sensor systems.

Flexible Active Oxide Electronics

Figure 1a shows fully processed amorphous IGZO based thin-film transistors on a flexible, $7.5\text{ cm} \times 7.5\text{ cm}$ large, plastic substrate.

Device Structure and Fabrication

The TFTs presented in this work employ a passivated bottom-gate inverted staggered geometry (see Fig. 1b). The devices were fabricated on free-standing $50\ \mu\text{m}$ thick polyimide foils, encapsulated by 50 nm PECVD grown SiN, using standard thin-film technologies and UV lithography as described in [18]. 35 nm thick evaporated Cr bottom gates were insulated by ALD deposited 25 nm of Al_2O_3 . Next, 15 nm IGZO

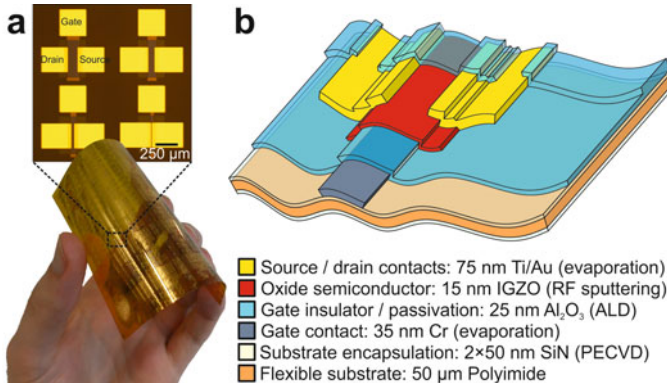


Fig. 1 Flexible IGZO TFTs: **a** photograph and micrograph of fully processed devices on a 7.5 cm × 7.5 cm polyimide foil. **b** Device structure of the presented bottom-gate inverted staggered thin-film transistors with layer thicknesses and employed deposition technique. (Color figure online)

were RF sputtered. Subsequently, Ti/Au source and drain contacts were evaporated. Finally, an additional 25 nm thick Al₂O₃ passivated the devices. The highest temperature was 150 °C.

Electrical and Mechanical Performance

All devices and circuits were characterized under ambient conditions using a semiconductor parameter analyzer. Performance parameters of TFTs were extracted using the Shichman-Hodges MOSFET model [19]. AC parameters were extracted from S-parameter measurements acquired using a vector network analyzer. The mechanical performance was evaluated using a custom-built bending setup [20].

DC and AC Performance

The measured relations between the drain current and the gate-source voltage as well as the drain-source voltage of a TFT are shown in Fig. 2a–c. The device exhibits a channel width/length ratio (W_{CH}/L_{CH}) of 280 μm / 115 μm, a field-effect mobility of 17.7 cm²V⁻¹s⁻¹, a threshold voltage of 0 V, a sub-threshold swing of 139 mV/dec, an on/off current ratio $> 1 \times 10^7$, and a maximum transconductance of 82 μS.

The AC performance of the devices is quantified by the transit frequency f_T and the maximum oscillation frequency f_{max} as the unity gain frequencies of the current gain and the maximum stable gain as shown in Fig. 2d. For short TFTs with a L_{CH} of 0.5 μm, f_T and f_{max} reach values of 135 MHz and 304 MHz, respectively [21]. As shown in Fig. 2e, the AC performance is influenced by the channel length, where easier to fabricate devices with $L_{CH} \gtrsim 5 \mu\text{m}$ provide significantly lower frequencies.

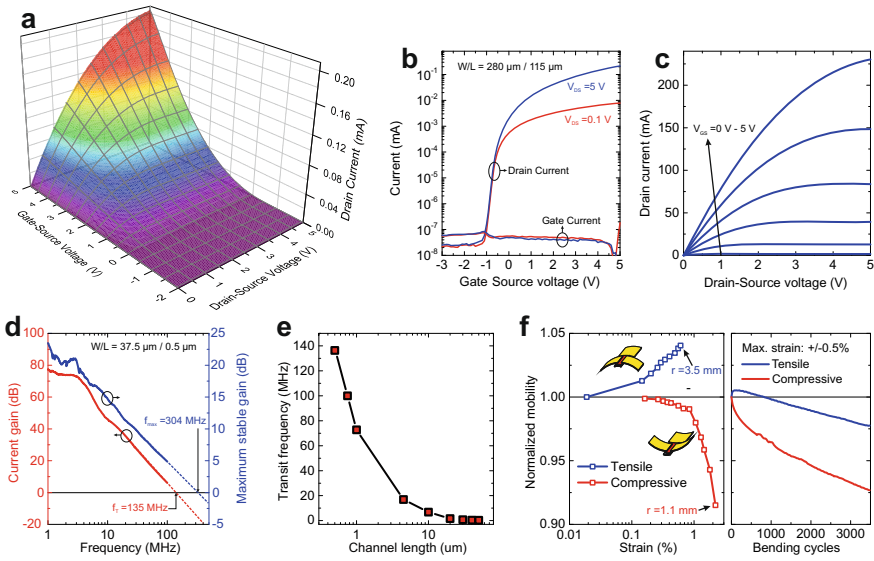


Fig. 2 Device performance: **a** measured drain current of a flexible IGZO TFT for various gate-source and drain-source voltages ($W_{CH}/L_{CH} = 280\mu\text{m} / 115\mu\text{m}$), and corresponding transfer (**b**) and output (**c**) characteristics. **d** Measured current gain and maximum stable gain of a flexible short channel TFT ($W_{CH}/L_{CH} = 37.5\mu\text{m} / 0.5\mu\text{m}$), and **e** channel length dependency of the transit frequency [21]. **f** Influence of tensile and compressive bending parallel to the channel on the effective mobility, and mobility change due to repeated bending and re-flattening cycles [23]. (Color figure online)

Mechanical Strain

The influence of mechanical deformation is a crucial aspect in flexible electronics. Extremely important parameters in this case are the minimum bending radius, the performance of bent devices, and the impact of repeated bending. Corresponding representative measurements for bent IGZO devices are shown in Fig. 2f. The presented IGZO TFTs exhibit a slight increase (decrease) of their effective mobility when exposed to tensile (compressive) strain, staying nevertheless fully functional down to bending radii of 3.5 mm (1.1 mm). These radii correspond to strain values of 0.7 % and 2.2 % [22], respectively. Furthermore, at these strain levels the effective TFT mobility changes by less than 10 % after more than 3500 tensile or compressive bending and re-flattening cycles [23]. More extreme bending radii down to 15 μm can be achieved by the use of pre-strained substrates [24]. Furthermore, the already small influence of strain can be considered and compensated when designing circuits, in order to create systems mostly unaffected by mechanical deformation [25, 26].

Integrated Analog Conditioning Circuits

Due to the lack of high-performance oxide p-type semiconductors [11], flexible oxide circuits typically use an NMOS topology [13]. In the case of circuits, the gate and source/drain metallic layers are used to realize circuit interconnections. There are numerous examples of unipolar digital and analog circuits e.g. for data processing or communication [12]; nevertheless for the front-end conditioning of sensors, amplifiers are more relevant. Figure 3 shows two examples of fully integrated flexible IGZO circuits: one differential amplifier optimized for high gain [27], and one common source amplifier optimized for high speed. These circuits cover a surface area of $\approx 2.3 \text{ mm}^2$ and $\approx 0.662.3 \text{ mm}^2$, respectively. They were measured by applying a DC supply voltage of 5 V, and input signals using a 2-channel function generator, while the output was monitored by an oscilloscope with an input impedance of $1 \text{ M}\Omega$. The measurements show that the common source circuit has a cutoff frequency of nearly 2 MHz, and a low frequency gain of 5.9 dB, resulting in a gain bandwidth product GBWP of 3.81 MHz, making this circuit very useful for resistive sensors (e.g. GMR elements) conditioning [28]. In contrast, the differential amplifier has a cutoff frequency of 150 kHz, and a low frequency gain of 19.5 dB (GBWP = 1.42 MHz). Additionally it converts double ended to single ended measurements, which is a feature extremely interest for the conditioning of Hall sensors or Wheatstone bridges.

IGZO Electronics in Magnetic Fields

It has been reported that IGZO TFTs can be sensitive to magnetic fields [14]. While it can be an advantage when the TFT is used as sensor, TFTs and circuits used for sensor conditioning should instead provide stable performance and not be influenced

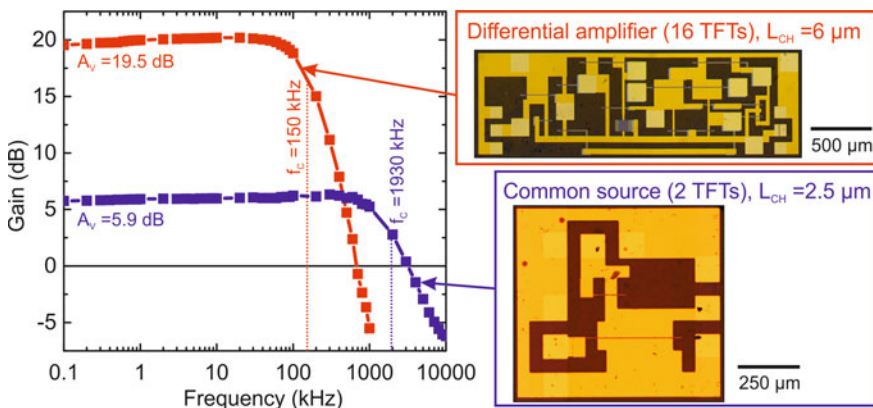


Fig. 3 Integrated circuits: voltage gain versus frequency and micrographs of a high gain (differential) amplifier and a high speed (common source) amplifier [27, 28]. (Color figure online)

by magnetic fields. To test the impact of an external magnetic field on the performance of the presented IGZO electronics, we characterized TFTs and circuits while they were exposed to a static magnetic field. This field was generated by an electromagnet, aligned as shown in Fig. 4a, and monitored using a commercial Hall magnetometer.

Devices

Figure 4b shows the influence of a magnetic field, with a flux density from 0 to 11 mT, perpendicular to the TFT channel on the effective mobility [29]. Furthermore, the inset shows the transfer characteristic of an IGZO TFT for 0 and 11 mT. The performance fluctuates by less than 1 % and it can be concluded that the presented TFTs are not influenced by magnetic fields. In the past the B-field sensitivity of certain IGZO TFTs has been attributed to the employed SiN and SiO gate insulators. However here the used Al₂O₃ leads to no observable magneto-resistive effect.

Circuits

Besides single devices, also the performance of circuits exposed to external fields was evaluated. In contrast to the circuits presented in Sect. “[Integrated Analog Conditioning Circuits](#)”, here a circuit with comparably large TFT channels was selected. The measured common source amplifier is constituted by 2 TFTs with W_{CH}/L_{CH} ratios of 700 μm / 20 μm (driver) and 20 μm / 700 μm (load). Even if these dimensions lead to less preferable electrical properties, the large circuit area is expected to maximize any potential influence of an external B-field and is therefore an interesting study case.

The performance under a magnetic field of 0 and 11 mT, together with a micrograph of the circuit, are shown in Fig. 4c. Additionally, representative input and output waveforms are given in Fig. 4d. The measurements show that the amplifier exhibits a cutoff frequency of 475 Hz, and an average low frequency gain of 6.4 dB independent of the external B-field. Hence this measurement further confirms the insensitivity of the presented IGZO electronics to magnetic fields.

Integration

To evaluate the integration of magnetic field sensors with front-end IGZO conditioning electronics on a flexible substrate, and to demonstrate the superior sensing performance of such a system, Cu/Co GMR sensors were combined with a high gain amplifier. A picture of the system as well as of the full circuit schematic is shown in Fig. 5a. The differential output of a Wheatstone bridge made from 2 Cu/Co

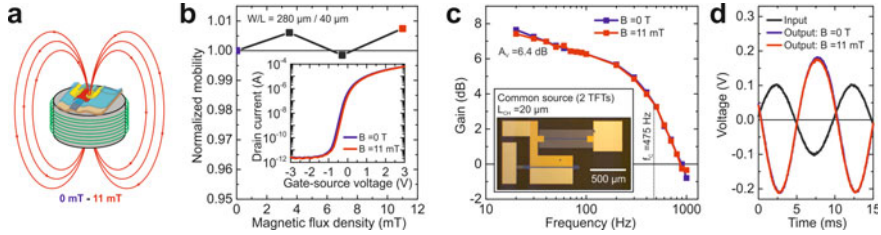


Fig. 4 IGZO electronics in magnetic fields: **a** measurement setup producing a variable magnetic field aligned perpendicularly to the device layer. **b** Influence of a magnetic field on the TFT mobility (inset shows a corresponding transfer characteristic measurement) [29]. **c** Influence of a magnetic field on a flexible integrated common source amplifier with extra long TFT channels (20 μ m). **d** Representative input and output waveforms with and without magnetic field. (Color figure online)

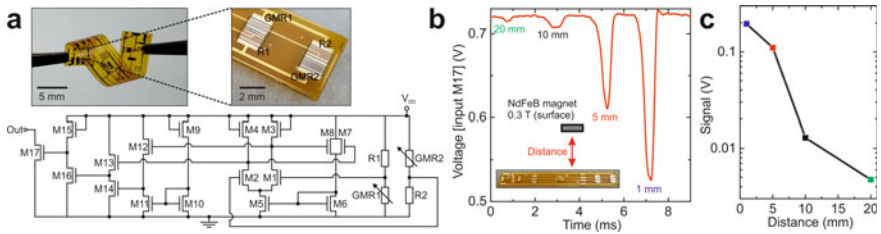


Fig. 5 Front end conditioning of magnetic sensors: **a** picture and circuit schematic of a fully flexible GMR sensor Wheatstone bridge integrated with a front end amplifier. The system consist of 2 Co/Cu GMR sensors, 2 Cu resistors and 17 TFTs. **b** Output voltage (measured at the input of M17) in the proximity of a permanent magnet, and **c** corresponding output signal [16]. (Color figure online)

GMR sensors and 2 Cu resistors is amplified by a differential amplifier made from 17 TFTs [16]. The sensing bridge alone has a sensitivity of 84 mV/V/kOe. The amplifier converts the differential output voltage of the bridge into a single ended signal. It also has a floating drain output able to output a current of 3 mA and enables driving high and low impedance loads such as an LED. Overall it provides voltage gain of up to 50 dB. The complete system can be operated using a single supply voltage 1.7 and 5 V, and exhibits a signal to noise ratio of 56 dB. The sensing performance of the GMR bridge together with the on-site voltage amplification leads to an overall sensitivity of 25 V/V/kOe. An intuitive demonstration of the system’s capabilities is given in Fig. 5c, d. Here, the full system is operated as a proximity sensor able to sense the presence of a permanent magnet. As shown, a magnet with a flux density 0.2 T on its surface can be detected even at a distance of 20 mm.

Conclusion

Flexible analog electronics based on IGZO simultaneously exhibit the electrical and mechanical properties needed to realize high-performance conformal systems. Additionally, the functionality of such circuits is not affected by the presence of external magnetic fields. The combination of these properties makes IGZO TFT based devices excellent candidates to fabricate front-end amplification circuits for the on-site conditioning of flexible magnetic field sensors. This is essential for the realization of fully integrated active magneto-electronics.

Acknowledgements This work was partially supported by EPSRC, GCRF, and NIHR under Grant EP/R013837/1 (SmartSensOtics). We would like to thank D. Karnaushenko, D. D. Karnaushenko, O. G. Schmidt, and D. Makarov for the collaboration on flexible GMR sensors and sensor systems.

References

1. Cherenack K, van Pieterse L (2012) *J Appl Phys* 112(9):091301
2. Nathan A, Ahnood A, Cole MT, Lee S, Suzuki Y, Hiralal P, Bonaccorso F, Hasan T, Garcia-Gancedo L, Dyadyusha A, Haque S, Andrew P, Hofmann S, Moultrie J, Chu D, Flewitt AJ, Ferrari AC, Kelly MJ, Robertson J, Amaratunga GAJ, Milne WI (2012) *Proc IEEE* 100(13):1486
3. Makarov D, Melzer M, Karnaushenko D, Schmidt OG (2016) *Appl Phys Rev* 3(1):011101
4. Costa JC, Spina F, Lugoda P, Garcia-Garcia L, Roggen D, Münzenrieder N (2019) *Technologies* 7(2):35
5. Granell PN, Wang G, Bermudez GSC, Kosub T, Golmar F, Steren L, Fassbender J, Makarov D (2019) *npj Flex Electron* 3(1):1
6. Ge J, Wang X, Drack M, Volkov O, Liang M, Bermúdez GSC, Illing R, Wang C, Zhou S, Fassbender J et al (2019) *Nat Commun* 10(1):1
7. Kondo M, Melzer M, Karnaushenko D, Uemura T, Yoshimoto S, Akiyama M, Noda Y, Araki T, Schmidt O, Sekitani T (2020) *Sci Adv* 6(4):eaay6094
8. Velmurugan J, Sinha S, Satishchandra P (2014) *Ann Indian Acad Neurol* 17(1):S113
9. Braun C (2007) *Z fur medizinische Phys* 17(4):280
10. Nomura K, Ohta H, Takagi A, Kamiya T, Hirano M, Hosono H (2004) *Nature* 432(7016):488
11. Petti L, Münzenrieder N, Vogt C, Faber H, Büthe L, Cantarella G, Bottacchi F, Anthopoulos TD, Tröster G (2016) *Appl Phys Rev* 3(2):021303
12. Myny K (2018) *Nature Electron* 1(1):30
13. Cantarella G, Costa JC, Meister T, Ishida K, Carta C, Ellinger F, Lugli P, Münzenrieder N, Petti L (2020) *Flexible Printed Electron* 5:4
14. Aoki K, Ozawa T, Chen YY, Fan CP, Cheng C, Kuo CW, Huang Y, Kuo CC, Matsumoto T, Yoshikawa A et al (2017) *IEEE Electron Dev Lett* 38(8):1143
15. Chou JC, Wu YX, Kuo PY, Lai CH, Nien YH, Lin SH, Yan SJ, Wu CY, Liao YH (2019) *IEEE Trans Electron Dev* 66(4):1924
16. Münzenrieder N, Karnaushenko D, Petti L, Cantarella G, Vogt C, Büthe L, Karnaushenko DD, Schmidt OG, Makarov D, Tröster G (2016) *Advanced Electronic Materials* 2(8):1600188
17. Chasin A, Volskiy V, Libois M, Myny K, Nag M, Rockelé M, Vandenbosch GA, Genoe J, Gielen G, Heremans P (2014) *IEEE Trans Electron Dev* 61(9):3289
18. Münzenrieder N, Petti L, Zysset C, Salvatore G, Kinkeldei T, Perumal C, Carta C, Ellinger F, Tröster G (2012) *IEEE Electron Dev Meeting (IEDM)* 5–2
19. Shichman H, Hodges DA (1968) *IEEE J Solid-State Circ* 3(3):285
20. Münzenrieder N, Cherenack KH, Tröster G (2011) *IEEE Trans Electron Dev* 58(7):2041

21. Münzenrieder N, Ishida K, Meister T, Cantarella G, Petti L, Carta C, Ellinger F, Tröster G (2018) *IEEE Electron Dev Lett* 39(9):1310
22. Gleskova H, Wagner S, Suo Z (2000) *J Non-Crystall Solids* 266:1320
23. Münzenrieder N, Cantarella G, Petti L (2019) *ECS Trans* 90(1):55
24. Cantarella G, Vogt C, Hopf R, Münzenrieder N, Andrianakis P, Petti L, Daus A, Knobelspies S, Büthe L, Tröster G, Salvatore G (2017) *ACS Appl Mater Interfaces* 9(34):28750
25. Bin Wan WMH, Zaidi, Costa J, Pouryazdan A, Abdullah WFH, Münzenrieder N (2018) *IEEE Electron Dev Lett* 39(9): 1314
26. Munzenrieder N, Zysset C, Kinkeldei T, Troster G (2012) *IEEE Trans Electron Dev* 59(8):2153
27. Zysset C, Münzenrieder N, Petti L, Büthe L, Salvatore GA, Tröster G (2013) *IEEE Electron Dev Lett* 34(11):1394
28. Münzenrieder N, Salvatore GA, Petti L, Zysset C, Büthe L, Vogt C, Cantarella G, Tröster G (2014) *Appl Phys Lett* 105(26):263504
29. Costa JC, Pouryazdan A, Panidi J, Spina F, Anthopoulos TD, Liedke MO, Schneider C, Wagner A, Münzenrieder N (2019) *IEEE J Electron Dev Soc* 7:1182

Part XI
Advanced Materials for Energy
Conversion and Storage VII

Aluminum-Ion Battery Made of AlCl₃-Trimethylamine Hydrochloride Ionic Liquid With Superior Performance



Kok Long Ng, Tony Dong, John Anawati, and Gisele Azimi

Abstract The excessive consumption of lithium and cobalt with increasing demand for lithium-ion batteries (LIBs) poses critical challenges in sustaining the cost-effectiveness of LIBs in the future. Among post-LIB systems, rechargeable aluminum batteries are particularly promising due to favorable properties including low material cost, high abundance, and high theoretical capacity. Most aluminum batteries utilize expensive alkylimidazolium/pyridinium chloride-based chloroaluminate ionic liquids. This greatly limits the commercialization of such systems, particularly for large-scale applications. Herein, we report a high-performance aluminum battery made of graphene nanoplatelets as the cathode and low-cost aluminum chloride-trimethylamine hydrochloride (AlCl₃-TMAHCl) ionic liquid as the electrolyte. The battery can be cycled for a few thousand cycles while delivering excellent specific capacity (~134 and ~80 mAh g⁻¹ at 2000 and 4000 mA g⁻¹, respectively) and coulombic efficiency. Through fundamental considerations, we demonstrate that Al/graphite battery employing AlCl₃-TMAHCl can achieve the highest cell-level energy density while maintaining comparable power density compared with conventional chloroaluminate ILs.

Keywords Al-ion battery · Energy storage · High-performance · Sustainable

Introduction

Rechargeable aluminum-ion batteries (AIBs) have been drawing substantial attention from the research and scientific community due to favorable features of aluminum (Al), including high theoretical capacities, low material cost, high abundance, high

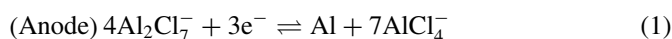
K. L. Ng · T. Dong · G. Azimi (✉)

Department of Materials Science and Engineering, University of Toronto, 184 College Street, Toronto, ON M5S34, Canada
e-mail: g.azimi@utoronto.ca

J. Anawati · G. Azimi

Department of Chemical Engineering and Applied Chemistry, University of Toronto, 200 College Street, Toronto, ON M5S35, Canada

stability in ambient environment, and nontoxicity. Most advanced AIBs employ graphitic and carbonaceous materials (GCMs) as the cathode. Numerous GCMs which include natural graphite [1, 2], pyrolytic graphite [3], edge-rich graphene paper [4], graphene aerogel [5], graphene nanoribbons on 3-D graphene foam [6, 7], graphene microflowers [8], 3-D graphite foam [9], zeolite templated carbon [10], carbon nanoscrolls [11], and graphene nanoplatelets (GNPs) [12] have been reported to demonstrate promising results in terms of operating voltage, rate capability, and long-term cyclability. On the other hand, chloroaluminate ionic liquids (ILs) by combining Lewis acidic aluminum chloride (AlCl_3) with Lewis basic dialkylimidazolium chlorides (in particular, 1-ethyl-3-methylimidazolium chloride; EMIMCl, and 1-butyl-3-methylimidazolium chloride; BMIMCl) are the most widely utilized electrolyte systems [13]. The working mechanism of Al/GCM batteries employing chloroaluminate ILs can be summarized in the following anodic and cathodic half-reactions during charging (\rightarrow ; forward direction) and discharging (\leftarrow ; backward direction):



where n represents the number of carbon atoms required to host one AlCl_4^- molecule. From extensive research on lithium-ion battery, it is generally known that graphite has a theoretical intercalation capacity of 372 mAh g^{-1} (considering $\text{Li}^+ + 6\text{C} + \text{e}^- = \text{LiC}_6$).

The major drawbacks of employing dialkylimidazolium chloride-based chloroaluminate ILs are associated with their high cost, corrosiveness, and low productivity. These undesirable characteristics negatively affect the scalability of AIBs, particularly for large-scale applications such as electric vehicles and grid storage systems. In exploring more industrially viable options, several reports including our previous works have identified widely available and cost-effective Lewis bases, such as urea [14–17], and triethylamine hydrochloride (TEAHCl) [18, 19].

In identifying a high-performance yet cost-effective electrolyte, we reported a room-temperature chloroaluminate IL prepared by combining AlCl_3 with trimethylamine hydrochloride (TMAHCl) at $\text{AlCl}_3/\text{TMAHCl}$ molar ratio of 1.7 [20]. The assembled AIB employing GNP cathode demonstrates excellent cell performance: a specific cathodic capacity of $\sim 134 \text{ mAh g}^{-1}$ at 2000 mA g^{-1} for over 3000 cycles with 98% CE and $\sim 80 \text{ mAh g}^{-1}$ with CE above 99.5% for over 4000 cycles at a current density of 4000 mA g^{-1} . Moreover, the Al/GNP battery demonstrates excellent fast-charging and slow discharging characteristics, delivering a specific discharge capacity of 83 mAh g^{-1} at 100 mA g^{-1} ($\sim 49.5 \text{ min}$) under a charge current density of 4000 mA g^{-1} ($\sim 1.2 \text{ min}$) while maintaining a CE of $\sim 97\%$. The Al/GNP battery shows remarkable low-temperature performance. At -10 and 0°C , a specific capacity of ~ 83 and 86 mAh g^{-1} (at 500 mA g^{-1}) is recorded, respectively. Through theoretical consideration coupled with the experimental results obtained, we demonstrate

that Al/GCM batteries employing AlCl_3 /TMAHCl IL exhibit the highest cell-level energy density compared with several existing chloroaluminate IL systems. Based on the results obtained in this work, we estimate that the experimentally achieved cell-level energy and power density of Al/GNP battery employing AlCl_3 -TMAHCl are in the range of 32 – 49 Wh kg^{-1} (equivalent to 53 – 76 Wh L^{-1}) and 500 – 5600 W kg^{-1} (800 – 9300 W L^{-1}), respectively.

Materials and Methods

Preparation of Electrolytes and GNP Electrodes

After extensive investigations of the effects of AlCl_3 /TMAHCl molar ratio (r) on battery performance, AlCl_3 /TMAHCl ($r = 1.7$) was chosen as the optimum composition that yielded the optimum capacity and coulombic efficiency [20]. Aluminum chloride (AlCl_3 , 99.985% purity; provided by Alfa Aesar) and TMAHCl (98%; Alfa Aesar) were mixed gradually in a glass beaker under constant magnetic stirring in an argon (Ar)-filled glove box (H_2O , $\text{O}_2 < 1$ ppm) for more than 12 h. The IL was subjected to vacuum (< -1 bar) for 10 min to remove unintended soluble gasses and other impurities prior to testing.

Graphene nanoplatelets were purchased from XG Sciences ($15 \mu\text{m} \times 15 \text{nm}$ (lateral size \times platelet thickness)). The GNP slurry contained 75 wt% of GNPs, 15 wt% of sodium alginate, 10 wt% of carbon black (Alfa Aesar), and 10 mL of distilled water as the solvent. The mixture was magnetically stirred until a homogenous slurry was obtained. The homogeneous slurry was subsequently coated onto a piece of molybdenum tab using a commercial doctor-blade film coater. The GNP mass loading of the cathode was standardized at 0.7mg cm^{-2} for all electrochemical testings.

Electrochemical Testing and Measurements

All battery fabrications were carried out in an Ar-filled glovebox. Coin cells (CR 2032) were assembled by stacking a 5 M HNO_3 -pretreated Al foil (99.9995%; Beijing Loyaltarget Technology Co.), a layer of glass microfiber separator (Whatman GF/A), a GNP-coated cathode, and approximately seven drops of AlCl_3 -TMAHCl = 1.7 electrolyte (equivalent to 350 μL).

Linear sweep voltammetry (LSV) and cyclic voltammetry (CV) were performed using a potentiostat (VersaSTAT 3; Princeton Applied Research). In LSV measurement, a tungsten (W) electrode was utilized as the working electrode, while a Mo rod and an Al wire were utilized as the counter and pseudo-reference electrodes, respectively. In CV measurement, an Al wire was employed as the working electrode, while an Al rod and Al wire were utilized as the counter and pseudo-reference

electrodes, respectively. Galvanostatic stripping/plating of Al-Al symmetrical cell was performed by using a multichannel battery tester (CT-4008, Neware), at an areal current density and stripping capacity of 0.5 mA cm^{-2} and 1.0 mAh cm^{-2} , respectively. Otherwise emphasized elsewhere in the text, the charge/discharge cut-off voltages for all room-temperature galvanostatic cycling were set at 2.37/0.50 V, respectively.

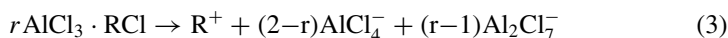
Characterization

The Raman spectrum of $\text{AlCl}_3/\text{TMAHCl}$ ($r = 1.7$) IL electrolyte was acquired by a Dispersive Raman Microscope (Bruker) using Ar^+ laser with 532 nm wavelength. The presented spectrum in this work was obtained by averaging five spectra that were acquired under the same conditions.

Results and Discussion

Characterization and Electrochemical Testing of AlCl_3 -TMAHCl IL

As presented in the inset in Fig. 1a, $\text{AlCl}_3/\text{TMAHCl}$ ($r = 1.7$) IL was a clear and homogenous liquid with light yellowish color at room temperature. In addition, the IL remained as a clear liquid even at -20°C . This enabled us to perform electrochemical testings at sub-zero degree Celsius temperatures. In characterizing anionic species (AlCl_4^- and Al_2Cl_7^-) in chloroaluminate ILs, Raman spectroscopy is widely known as a simple yet effective technique [18, 21, 22]. The Raman spectrum of the IL electrolyte is presented in Fig. 1a. The peaks at around 313 and 432 cm^{-1} correspond to dimeric Al_2Cl_7^- , while the peak at around 349 cm^{-1} can be assigned to monomeric AlCl_4^- . Studies have suggested that the Raman peak intensity ratio of Al_2Cl_7^- (at 313 cm^{-1}) to AlCl_4^- (at 349 cm^{-1}) provides quantitative information of the relative abundance/concentration of Al_2Cl_7^- over AlCl_4^- in chloroaluminate ILs [21, 22]. From a relative stronger Al_2Cl_7^- over AlCl_4^- peak intensity ratio observed in Fig. 1a, we can expect a relatively higher abundance of Al_2Cl_7^- as compared with AlCl_4^- in $\text{AlCl}_3/\text{TMAHCl}$ ($r = 1.7$) IL electrolyte. In general, the dissociation of Lewis neutral and acidic AlCl_3 -RCl (R: organic group) ILs can be expressed as [23]:



where r is the molar ratio of AlCl_3 to RCl and $1 \leq r \leq 2$. By using Eq. 3, the theoretical molar ratio of Al_2Cl_7^- to AlCl_4^- in $\text{AlCl}_3/\text{TMAHCl}$ ($r = 1.7$) IL electrolyte can be

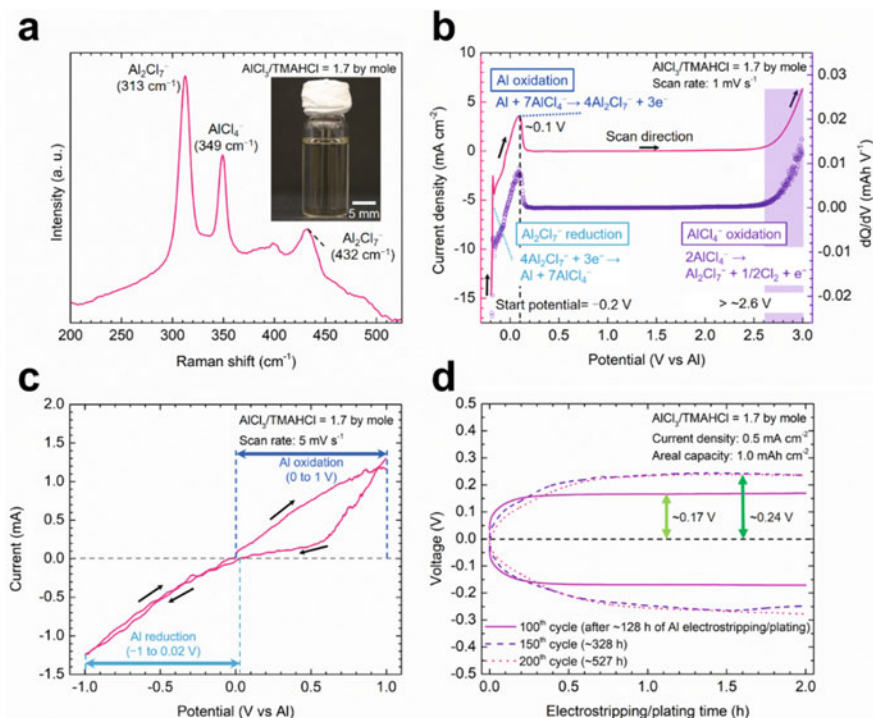
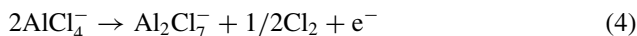


Fig. 1 **a** Raman spectrum of $\text{AlCl}_3/\text{TMAHCl} = 1.7$ (by mole) IL, inset: photo of the electrolyte at room temperature; **b** linear sweep voltammogram and differential capacity (dQ/dV) plot of the corresponding IL electrolyte; **c** cyclic voltammogram of the corresponding electrolyte in the range of -1.0 and 1.0 V (vs Al); **d** voltage profile of Al electroplating/stripping in an Al-Al symmetrical cell setup. (Color figure online)

determined as 2.33. This is in good agreement with the obtained experimental result, indicating a higher abundance of Al_2Cl_7^- over AlCl_4^- in the IL electrolyte.

Among several electrical properties of an electrolyte, the electrochemical stability window (ESW) is considered as one of the most important properties as it provides fundamental information on the operating limits of an electrochemical system. Among all, voltammetry (either LSV or CV) is the most widely employed technique to evaluate ESW of an electrolyte system. Figure 1b presents the LSV and the differential capacity (dQ/dV) plot for $\text{AlCl}_3/\text{TMAHCl}$ ($r = 1.7$) IL electrolyte from -0.2 to 3.0 V (vs Al). A negative/cathodic current at potentials below ~ 0 V suggests the reduction of Al_2Cl_7^- to form Al at the working electrode following Eq. 1 (forward direction). As the potential increased, an anodic peak at ~ 0.1 V indicating the electrostripping process of Al as given in Eq. 1 (backward direction) is observed. No appreciable electrochemical activities were observed in the range between ~ 0.2 and ~ 2.6 V. When the potential was further increased to above 2.6 V, a significant increase in oxidative current was observed. This is associated with the oxidation of AlCl_4^- as follows:



Hence, 2.6 V (vs Al) can be considered as the oxidation potential (E_{ox}) limit for this electrolyte. This value is higher than the E_{ox} (= 2.45 to 2.50 V vs Al) of AlCl_3 -EMIMCl IL electrolytes determined under similar scan rates [24, 25]. On the other hand, the bulk deposition of Al on Al working electrode started at ~ 0.02 V and the deposition continued until it reached the imposed cathodic limit at -1.0 V (Fig. 1c). When the scan was reversed, the reduction current continued to flow due to the continuous deposition of Al until the potential reached ~ 0 V. The oxidation of Al continued to the imposed anodic limit of 1.0 V. From the galvanostatic electrostripping/plating of Al-Al symmetrical presented in Fig. 1d, a slight increase in overpotential from ~ 0.17 (100th cycle, after 128 h of cycling) to ~ 0.24 V (150th cycle, after 328 h) was observed. This overpotential remained relatively stable even after 527 h (200th cycle) of continuous cycling; confirming the long-term stability of Al electrostripping/plating process in $\text{AlCl}_3/\text{TMAHCl}$ ($r = 1.7$) IL electrolyte.

Performance of Al/GNP Battery Employing AlCl_3 -TMAHCl IL

Figure 2a illustrates the galvanostatic cycling performance of Al/GNP battery employing $\text{AlCl}_3/\text{TMAHCl}$ ($r = 1.7$) IL electrolyte at 2000 and 4000 mA g^{-1} . At a lower current density of 2000 mA g^{-1} , the cell recorded a specific capacity of 134 mAh g^{-1} while maintaining an average CE above 98% across 3000 cycles. The increase in specific capacity with increasing number of cycles can be associated with the self-activating behavior of anion intercalation-based GCM cathodes [26, 27]. The successive intercalation and deintercalation of AlCl_4^- into/from graphene layers result in partial exfoliation of the GCM cathode over cycles. This partial exfoliation of graphene layers increases the electrochemical surface area, which enhances the (pseudo)capacitive charge storage contribution with increasing number of cycles [27]. At the current density of 4000 mA g^{-1} , the cell maintained a reasonable specific capacity of ~ 80 mAh g^{-1} with excellent CE above 99.5% for over 4000 cycles. Figure 2b presents the corresponding voltage profiles of the Al/GNP battery as a function of current density and cycle number. Despite significantly different capacities obtained at different charge–discharge current densities, the shape of the voltage profile remained relatively consistent with increasing the number of cycles. This was further evidenced by the average operating voltage obtained which was 1.47 and 1.44 V at 2000 and 4000 mA g^{-1} , respectively. A stable operating voltage at high current densities is particularly favorable for applications that require high power density.

The rate performance of the battery under fast charging (approximately 1.2 min at 4000 mA g^{-1}) and various slow discharging conditions was also investigated. As shown in Fig. 2c, the obtained specific capacity (~ 80 to 83 mAh g^{-1}) was consistent across all discharge rates. Even under a low discharge current density of 100 mA g^{-1} (equivalent to ~ 49.5 min of discharge time), the cell could still deliver a capacity of

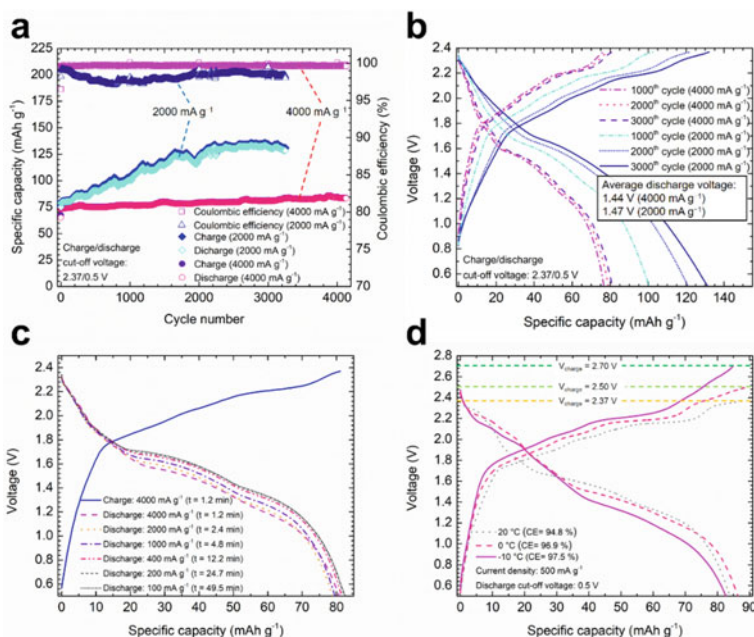


Fig. 2 **a** Long-term cyclability test of Al/GNP battery employing $\text{AlCl}_3/\text{TMAHCl} = 1.7$ (by mole) IL electrolyte at 2000 and 4000 mA g^{-1} , respectively; **b** corresponding voltage profiles at the 1000th, 2000th, and 3000th cycle; **c** voltage profile of Al/GNP battery under fast charging (at 4000 mA g^{-1}) and slow discharging (100 to 2000 mA g^{-1}) conditions, the discharge voltage profile at 4000 mA g^{-1} serves as a reference point for comparison; **d** voltage profile of Al/GNP battery in a temperature range between -10 and 20 $^{\circ}\text{C}$. (Color figure online)

83 mAh g^{-1} while maintaining a high CE at 97%. This clearly indicated the superior charge-retaining characteristics of Al/GNP battery employing TMAHCl-based IL electrolytes. The electrochemical performance of the battery at low temperatures was also tested, and the results are presented in Fig. 2d. To maximize the achievable capacity while maintaining a high CE, a voltage optimization approach was utilized to determine the optimum charging cut-off voltage at a particular temperature [11]. At -10 $^{\circ}\text{C}$, the cell could be charged to 2.70 V and deliver a specific capacity of ~ 83 mAh g^{-1} while maintaining a CE of 97.5%. Despite a lower charging cut-off voltage of 2.50 V at 0 $^{\circ}\text{C}$, the specific capacity delivered increased to ~ 86 mAh g^{-1} while maintaining 96.9% CE. From the specific capacity obtained at 20 $^{\circ}\text{C}$ (84 mAh g^{-1}), it is concluded that the cell could retain its full capacity even at low temperatures with an appropriate charging cut-off voltage.

Estimation of Cell-Level Energy and Power Density of Al/GCM Battery Employing Various AlCl_3 -RCl ILs

For Al battery employing chloroaluminate IL electrolytes, as the concentration of Al_2Cl_7^- in the electrolyte decreases during charging (Eq. 1), the electrolyte essentially behaves as an active materials for the anode (also known as a liquid anode or an anolyte) [28, 29]. As presented in our previous work [20], the cell-level specific energy density (E_{Cell}), energy density power density (P_{Cell}), cell-level volumetric energy density (e_{Cell}), and power density (p_{Cell}) can be expressed as:

$$E_{Cell} = \left(\frac{Fz(r-1)Q_{Cathode}}{Fz(r-1) + (rM_{\text{AlCl}_3} + M_{\text{RCl}})Q_{Cathode}} \right) V_{Avg} \quad (5)$$

$$P_{Cell} = \left(\frac{Fz(r-1)Q_{Cathode}}{Fz(r-1) + (rM_{\text{AlCl}_3} + M_{\text{RCl}})Q_{Cathode}} \right) \left(\frac{1}{t} \right) V_{Avg} \quad (6)$$

$$e_{Cell} = \left(\frac{2.266Fz(r-1)\rho_{r\text{AlCl}_3, \text{RCl}}Q_{Cathode}}{Fz(r-1)\rho_{r\text{AlCl}_3, \text{RCl}} + 2.266(rM_{\text{AlCl}_3} + M_{\text{RCl}})Q_{Cathode}} \right) V_{Avg} \quad (7)$$

$$p_{Cell} = \left(\frac{2.266Fz(r-1)\rho_{r\text{AlCl}_3, \text{RCl}}Q_{Cathode}}{Fz(r-1)\rho_{r\text{AlCl}_3, \text{RCl}} + 2.266(rM_{\text{AlCl}_3} + M_{\text{RCl}})Q_{Cathode}} \right) \left(\frac{1}{t} \right) V_{Avg} \quad (8)$$

where F is Faraday constant ($= 26.8 \text{ Ah mol}^{-1}$), z is the number of moles of electrons required per mole of Al_2Cl_7^- ($z = \frac{3}{4}$), and M_i is the molar mass of i (in kg mol^{-1}), $\rho_{r\text{AlCl}_3, \text{RCl}}$ is the density of the chloroaluminate IL in kg L^{-1} , $Q_{cathode}$ is the specific capacity of the CGM cathode obtained in Ah kg^{-1} , t is the total discharge time, and V_{Avg} is the nominal/average discharge voltage, respectively. The density of AlCl_3 -EMIMCl, -BMIMCl, -TEAHCl, and -TMAHCl IL as a function of r is given as $93.5r + 1204.4$ [30], $95.1r + 1148.3$ [30], $81.9r + 1147.2$ [31], and $124.6r + 1174.7$ (this work), respectively.

Figure 3a, b show the specific and volumetric Ragone plots (power density vs. energy density) of advanced Al/GCM battery systems employing various chloroaluminate ILs, respectively. Among all evaluated systems, the Al/GNP battery developed in this work delivers the highest E_{Cell} and e_{Cell} (in the range of 32–49 Wh kg^{-1} and 53–76 Wh L^{-1} , respectively) while maintaining a comparable P_{Cell} and p_{Cell} (500 – 5600 W kg^{-1} and 800 – 9300 W L^{-1} , respectively) compared with other systems. It is noteworthy that the most widely employed AlCl_3 /EMIMCl ($r = 1.3$ [13]) IL system generally shows a high power density feature, but the energy density remains relatively low compared with other systems. Lastly, from Eqs. 5–8, the molar ratio of AlCl_3 to RCl, r , is an important parameter to fundamentally improve the cell-level

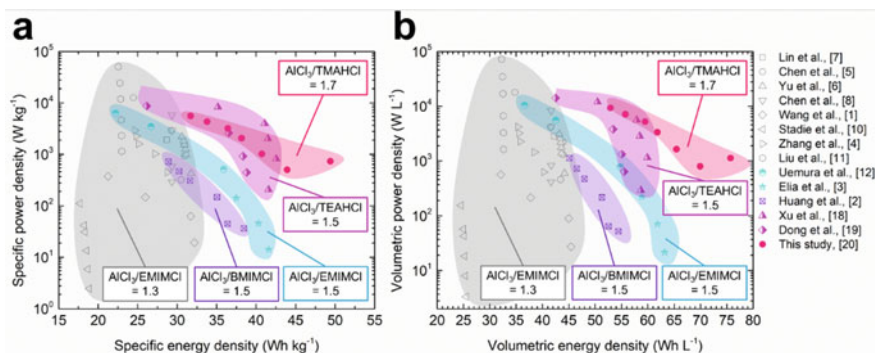


Fig. 3 Estimated **a** specific/gravimetric-; **b** volumetric cell-level Ragone plot (power density vs. energy density) of Al/GCM battery employing various room-temperature chloroaluminate ILs. (Color figure online)

energy density of Al/GCM batteries employing chloroaluminate ILs, as a higher r value is favorable to achieve higher E_{Cell} and e_{Cell} .

Conclusions

In summary, a high-performance Al/GNP battery employing cost-effective AlCl_3 -TMAHCl ($r = 1.7$) IL electrolyte was developed. This battery recorded a specific capacity of 134, and 80 mAh g^{-1} at 2000 and 4000 mA g^{-1} , over a few thousand cycles with excellent CE above 98%. In addition, the battery exhibited excellent fast charging (1.2 min at 4000 mA g^{-1}) and slow discharging (49.5 min at 100 mA g^{-1}) characteristics by delivering a specific capacity of $\sim 83 \text{mAh g}^{-1}$ with 97% CE. In addition, this battery can retain its full capacity (relative to near room-temperature condition) at -10 and 0°C without sacrificing CE. Through fundamental considerations, we showed that this battery offers the highest cell-level specific/volumetric energy density compared with other Al batteries utilizing the existing chloroaluminate ILs while maintaining high power density. The achieved cell-level energy and power density of Al/GNP battery employing AlCl_3 -TMAHCl were estimated to be in the range of 32 – 49 Wh kg^{-1} (equivalent to 53 – 76 Wh L^{-1}) and 500 – 5600 W kg^{-1} (800 – 9300 W L^{-1}), respectively. Given the cost-effectiveness and high performance of AlCl_3 -TMAHCl ILs, the results of this work contribute to the development of large-scale rechargeable Al energy storage devices.

Acknowledgements The authors acknowledge the financial support provided by Potent Group (Grant No. 503 355), Ontario Centres of Excellence (Grant No. 503760), and Mercedes-Benz Research and Development North America (MBRDNA) (Grant No. 208133). The authors sincerely thank Mr. Nick Di Pede, Mr. Dwight Gomes, Mr. Tony Alonzi, and Mr. Minos Lam for their collaboration throughout this project. The authors thank Dr. Peter Brodersen for the glovebox access.

References

1. Wang D, Wei C, Lin M, Pan C, Chou H, Chen H, Gong M, Wu Y, Yuan C, Angell M, Hsieh Y, Chen Y, Wen C, Chen C, Hwang B, Chen C, Dai H (2017) Advanced rechargeable aluminium ion battery with a high-quality natural graphite cathode. *Nat Commun* 8:14283. <https://doi.org/10.1038/ncomms14283>
2. Huang MC, Yang CH, Chiang CC, Chiu SC, Chen YF, Lin CY, Wang LY, Li YL, Yang CC, Chang WS (2018) Influence of high loading on the performance of natural graphite-based Al secondary batteries. *Energies* 11:12–16. <https://doi.org/10.3390/en11102760>
3. Elia GA, Ducros JB, Sotta D, Delhorbe V, Brun A, Marquardt K, Hahn R (2017) Polyacrylonitrile separator for high-performance aluminum batteries with improved interface stability. *ACS Appl Mater Interfaces* 9:38381–38389. <https://doi.org/10.1021/acsmi.7b09378>
4. Zhang Q, Wang L, Wang J, Xing C, Ge J, Fan L, Liu Z, Lu X, Wu M, Yu X, Zhang H, Lu B (2018) Low-temperature synthesis of edge-rich graphene paper for high-performance aluminum batteries. *Energy Storage Mater* 15:361–367. <https://doi.org/10.1016/j.ensm.2018.06.021>
5. Chen H, Guo F, Liu Y, Huang T, Zheng B, Ananth N, Xu Z, Gao W, Gao C (2017) A defect-free principle for advanced graphene cathode of aluminum-ion battery. *Adv Mater* 29:1605958. <https://doi.org/10.1002/adma.201605958>
6. Yu X, Wang B, Gong D, Xu Z, Lu B (2017) Graphene nanoribbons on highly porous 3D graphene for high-capacity and ultrastable Al-ion batteries. *Adv Mater* 29:1604118
7. Lin M-C, Gong M, Lu B, Wu Y, Wang DY, Guan M, Angell M, Chen C, Yang J, Hwang BJ, Dai H (2015) An ultrafast rechargeable aluminium-ion battery. *Nature* 520:324–328
8. Chen H, Chen C, Liu Y, Zhao X, Ananth N, Zheng B, Peng L, Huang T, Gao W, Gao C (2017) High-quality graphene microflower design for high-performance Li–S and Al-ion batteries. *Adv Energy Mater* 7:1700051
9. Wu Y, Gong M, Lin M-C, Yuan C, Angell M, Huang L, Wang D-Y, Zhang X, Yang J, Hwang B-J, Dai H (2016) 3D graphitic foams derived from chloroaluminate anion intercalation for ultrafast aluminum-ion battery. *Adv Mater* 28:9218–9222. <https://doi.org/10.1002/adma.201602958>
10. Stadie NP, Wang S, Kravchik KV, Kovalenko MV (2017) Zeolite-templated carbon as an ordered microporous electrode for aluminum batteries. *ACS Nano* 11:1911–1919. <https://doi.org/10.1021/acsnano.6b07995>
11. Liu Z, Wang J, Ding H, Chen S, Yu X, Lu B (2018) Carbon nanoscrolls for aluminum battery. *ACS Nano* 12:8456–8466
12. Uemura Y, Chen C-Y, Hashimoto Y, Tsuda T, Matsumoto H, Kuwabata S (2018) Graphene nanoplatelet composite cathode for a chloroaluminate ionic liquid-based aluminum secondary battery. *ACS Appl Energy Mater* 1:2269–2274. <https://doi.org/10.1021/acsaem.8b00341>
13. Zhang Y, Liu S, Ji Y, Ma J, Yu H (2018) Emerging nonaqueous aluminum-ion batteries: challenges, status, and perspectives. *Adv Mater* 30:1706310
14. Kim DJ, Yoo DJ, Otley MT, Prokofjevs A, Pezzato C, Owczarek M, Lee SJ, Choi JW, Stoddart JF (2019) Rechargeable aluminium organic batteries. *Nat Energy* 4:51–59. <https://doi.org/10.1038/s41560-018-0291-0>
15. Jiao H, Wang C, Tu J, Tian D, Jiao S (2017) A rechargeable Al-ion battery: Al/molten AlCl₃-urea/graphite. *Chem Commun* 53:2331–2334
16. Ng KL, Malik M, Buch E, Glossmann T, Hintennach A, Azimi G (2019) A low-cost rechargeable aluminum/natural graphite battery utilizing urea-based ionic liquid analog. *Electrochim Acta* 327:135031. <https://doi.org/10.1016/j.electacta.2019.135031>
17. Malik M, Ng KL, Azimi G (2020) Physicochemical characterization of AlCl₃-urea ionic liquid analogs: speciation, conductivity, and electrochemical stability. *Electrochim Acta* 354:136708
18. Xu H, Bai T, Chen H, Guo F, Xi J, Huang T, Cai S, Chu X, Ling J, Gao W, Xu Z, Gao C (2018) Low-cost AlCl₃/Et₃NHCl electrolyte for high-performance aluminum-ion battery. *Energy Storage Mater* 1–8. <https://doi.org/10.1016/j.ensm.2018.08.003>

19. Dong X, Xu H, Chen H, Wang L, Wang J, Fang W, Chen C, Salman M, Xu Z, Gao C (2019) Commercial expanded graphite as high-performance cathode for low-cost aluminum-ion battery. *Carbon* NY 148:134–140. <https://doi.org/10.1016/j.carbon.2019.03.080>
20. Ng KL, Dong T, Anawati J, Azimi G (2020) High-performance aluminum ion battery using cost-effective AlCl₃-trimethylamine hydrochloride ionic liquid electrolyte. *Adv Sustain Syst* 2000074:1–12. <https://doi.org/10.1002/adsu.202000074>
21. Zhu G, Angell M, Pan CJ, Lin MC, Chen H, Huang CJ, Lin J, Achazi AJ, Kaghazchi P, Hwang BJ, Dai H (2019) Rechargeable aluminum batteries: effects of cations in ionic liquid electrolytes. *RSC Adv* 9:11322–11330. <https://doi.org/10.1039/C9RA00765B>
22. Gilbert B, Olivier-Bourbigou H, Favre F (2007) Chloroaluminate ionic liquids: from their structural properties to their applications in process intensification. *Oil Gas Sci Technol Rev IFP* 62:745–759
23. Fannin AA, King LA, Levisky JA, Wilkes JS (1984) Properties of 1, 3-dialkylimidazolium chloride-aluminum chloride ionic liquids. 1. Ion interactions by nuclear magnetic resonance spectroscopy 2609–2614. <https://doi.org/10.1021/j150656a037>
24. Elia GA, Hasa I, Greco G, Diemant T, Marquardt K, Hoepfner K, Behm RJ, Hoell A, Passerini S, Hahn R (2017) Insights into the reversibility of aluminum graphite batteries. *J Mater Chem A* 5:9682–9690. <https://doi.org/10.1039/c7ta01018d>
25. Wang S, Kravchyk KV, Filippin AN, Müller U, Tiwari AN, Buecheler S, Bodnarchuk MI, Kovalenko MV (2018) Aluminum chloride-graphite batteries with flexible current collectors prepared from earth-abundant elements. *Adv Sci* 5:1–6. <https://doi.org/10.1002/advs.201700712>
26. Wang G, Yu M, Wang J, Li D, Löffler M, Zhuang X, Müllen K, Feng X (2018) Self-activating. Capacitive Anion Intercalation Enables High- Power Graphite Cathodes. <https://doi.org/10.1002/adma.201800533>
27. Xu H, Chen H, Lai H, Li Z, Dong X, Cai S, Chu X, Gao C (2019) Capacitive charge storage enables an ultrahigh cathode capacity in aluminum-graphene battery. *J Energy Chem* 45:40–44. <https://doi.org/10.1016/j.jechem.2019.09.025>
28. Kravchyk KV, Wang S, Piveteau L, Kovalenko MV (2017) Efficient aluminum chloride-natural graphite battery. *Chem Mater* 29:4484–4492
29. Elia GA, Kyeremateng NA, Marquardt K, Hahn R (2018) An aluminum/graphite battery with ultra-high rate capability. *Batter Supercaps* 83–90. <https://doi.org/10.1002/batt.201800114>
30. Fannin AA, Floreani DA, King LA, Landers JS, Piersma BJ, Stech DJ, Vaughn RL, Wilkes JS, Williams JL (1984) Properties of 1,3-dialkylimidazolium chloride-aluminum chloride ionic liquids. 2. Phase transitions, densities, electrical conductivities, and viscosities. *J Phys Chem* 88:2614–2621. <https://doi.org/10.1021/j150656a038>
31. Xia S, Zhang XM, Huang K, Le Chen Y, Wu YT (2015) Ionic liquid electrolytes for aluminium secondary battery: influence of organic solvents. *J Electroanal Chem* 757:167–175. <https://doi.org/10.1016/j.jelechem.2015.09.022>

Investigation of Cost-Effective AlCl₃-Urea Ionic Liquid Analog for Al-Ion Batteries



Monu Malik, Kok Long Ng, and Gisele Azimi

Abstract The present study investigates the physicochemical properties of cost-effective AlCl₃-urea ionic liquid analogs (ILAs) for aluminum (Al)-ion batteries. The neutral and the acidic regions for AlCl₃/urea molar compositions were investigated using nuclear magnetic resonance spectroscopy (NMR), linear sweep voltammetry (LSV), and electrochemical impedance spectroscopy (EIS) to determine the speciation of ionic moieties, electrochemical stability, and ionic conductivity of this complex system. The physical characterization shows that only 1.2–1.5 molar compositions are suitable for aluminum-ion batteries at room temperature, while 1.3 results in the highest ionic conductivity. The NMR results indicate that Al₂Cl₇⁻ is the dominating species for electrodeposition of aluminum at higher molar composition compared with AlCl₂·(urea)₂⁺, while the relative amount of AlCl₄⁻ remains almost unchanged across investigated compositions. The aluminum-ion battery prepared using aluminum anode and graphene nanoplatelets cathode delivered a specific capacity of 60 mAh g⁻¹ with 1.4 molar composition ILAs at 400 mA g⁻¹.

Keywords Aluminum ion battery · Ionic liquid analogues · AlCl₃-urea · Speciation · Ionic conductivity · Electrochemical stability · Graphene nanoplatelets

Introduction

Around the globe, the critical need for safe, cost-effective, long life, and sustainable battery technology for the electrification of the transportation sector, grid and renewable energy storage, leads to a research wave to develop low-cost and high-performing batteries using earth-abundant resources. Aluminum-based batteries are

M. Malik · G. Azimi (✉)

Department of Chemical Engineering and Applied Chemistry, University of Toronto, 200 College Street, Toronto, ON M5S3S5, Canada
e-mail: g.azimi@utoronto.ca

K. L. Ng · G. Azimi

Department of Materials Science and Engineering, University of Toronto, 184 College Street, Toronto, ON M5S34, Canada

particularly of interest among the emerging candidates for post lithium-ion batteries due to low cost, high recycling, high abundance, and high volumetric and gravimetric capacity. Since the electrodeposition of aluminum is only feasible in ionic liquids and organic solvents due to its high reactivity and high negative reduction potential [1], which significantly affects the battery performance, investigating the process at room temperature is of great importance. Several electrolytes have been proposed by researchers for electrodeposition of aluminum including aprotic polar organic solvents which were previously used in lithium and sodium batteries [2, 3] and molten salts eutectics [4]. However, the application of organic solvents remains limited because of their low thermal stability, narrow electrochemical window, and very low solubility of aluminum salts.

To overcome these drawbacks, ionic liquids (ILs) have been proposed and utilized for aluminum electrodeposition in recent years because of their high thermal stability, low volatility and flammability, and high solvability [5]. Various IL compositions were proposed using an aluminum salt and an organic solvent, where AlCl₃ was selected as the source of aluminum and several molecules such as 1-butyl-3-methylimidazolium trifluoromethanesulfonate, 1-ethyl-3-methylimidazolium bis (trifluoromethylsulfonyl) amide, 4-propylpyridine, and dicyanamide were considered for organic component [5–7]. Among these compounds, 1-ethyl-3-methylimidazolium chloride ([EMIm]Cl) is the most popular due to its wide stable electrochemical window, very low vapor pressure, and high electrical conductivity [8, 9]. Depending on AlCl₃ content, these chloroaluminate electrolytes made of [EMIm]Cl and AlCl₃ can be classified as basic, neutral, and acidic, where only the acidic compositions can participate in aluminum plating and stripping through the reversible reaction $4Al_2Cl_7^- + 3e^- \rightleftharpoons Al + 7AlCl_4^-$ [8, 9].

Although several studies utilized AlCl₃/[EMIm]Cl ILs as the electrolyte in aluminum-ion batteries and reported excellent performance [8, 10], the high cost of [EMIm]Cl impelled the search for alternative organic solvents. This research leads to the development of a new class of ionic liquids known as ionic liquid analogues (ILAs) [11] or deep eutectic solvents (DESSs) [12] obtained from mixing of AlCl₃ and an oxygen donor amide ligand. Abood et al. [13] showed the reversible electrodeposition of aluminum in such ILAs using the mixtures of AlCl₃ and urea. In recent years, a few groups including ours have investigated the application of AlCl₃/urea ILAs as the electrolyte in aluminum battery systems and reported excellent performance [14–16]. The application of urea in aluminum-ion batteries offers both economic and environmental benefits over ILs and other ILAs due to the large global production of urea and its environmental friendliness as a commercial fertilizer [17].

Although AlCl₃/urea ILAs have been investigated by a few researchers, only a few properties of this system such as density, electrical conductivity, and viscosity have been reported [1], while other properties are still missing. The present study investigates the physicochemical properties of AlCl₃-urea ILA through a multi-technique approach including nuclear magnetic resonance (NMR), linear sweep voltammetry (LSV), and electrochemical impedance spectroscopy (EIS). The neutral and the acidic regions of AlCl₃-urea were investigated to find the physical state at different temperatures, speciation, electrochemical stability, and ionic conductivity.

Finally, the compositions were tested in an electrochemical cell using aluminum as the anode and graphene nanoplatelets as the cathode. Based on the obtained results, the best compositional range of $\text{AlCl}_3/\text{urea}$ was identified.

Experimental Procedures

Chemicals and Materials

Urea and sodium alginate ($\geq 99.5\%$) were purchased from Bioshop Canada Inc. (Canada) and Landor Trading Co. Ltd. (Canada), respectively. Anhydrous aluminum chloride (99.985%) and aluminum shots (99.999%) were purchased from Alfa Aesar (USA). Aluminum foil (50 μm thick, 99.999%) and molybdenum sheet (130 μm thick, 99.95%) were obtained from Beijing Loyaltarget Tech. Co., Ltd. (China). Graphene nanoplatelets (GNP H15) were purchased from XG Science (USA). Whatman Glass microfiber separators (GF/A) were purchased from Sigma-Aldrich Co. (USA).

AlCl_3 -Urea ILAs

Urea was vacuum dried at 100 °C for 24 h before transferring to an argon-filled glovebox (O_2 and $\text{H}_2\text{O} < 1$ ppm), where it was slowly mixed with anhydrous AlCl_3 ($\text{AlCl}_3/\text{urea} = 1.0\text{--}1.6$) in a glass beaker under constant magnetic stirring. To prevent electrolyte decomposition, the temperature of the mixture was regulated by wrapping the glass beaker with ice gel patch. The mixture was stirred overnight at the ambient temperature inside the glovebox, resulting in a yellowish and transparent liquid, which was heated to 60 °C for 30 min, then subjected to vacuum for 10 min to remove gaseous impurities.

Linear Sweep Voltammetry and Electrochemical Impedance Spectroscopy

An in-house prepared Teflon cell was used to perform linear sweep voltammetry (LSV) with a potentiostat in a three-electrode configuration, where an aluminum wire was used as the reference electrode and molybdenum (Mo) rods of two different diameters were used as working and counter electrodes. The Teflon cell with all three electrodes was assembled inside the glovebox using the selected ILA compositions, and the scanning voltage range was set at -0.20 to 3.00 V (versus Al) to determine oxidation/reduction potential of aluminum and the electrochemical stability window

of the ILAs. The Teflon cells in the two-electrode configuration were also used for the electrochemical impedance spectroscopy (EIS) technique to measure the ionic conductivity of the considered ILA compositions at various temperatures (25–85 °C). The Mo rod was used as both working and counter electrodes, and EIS measurements were performed in a frequency range between 0.1 Hz and 100 kHz at a ± 10 mV amplitude versus open-circuit potential.

Nuclear Magnetic Resonance Analyses

The 1D ^{27}Al NMR spectra were acquired at 182.345 MHz on an Agilent DD2 spectrometer equipped with a 5 mm HFX probe (Agilent Technologies, Santa Clara, USA) with 512 transients and 5.0 s recycle delay. A coaxial insert with a 5-mm-diameter NMR tube (Wilmad-LabGlass) was used to prepare the samples inside the glovebox, and chloroform with 0.05% tetramethylsilane (TMS) was used as deuterium. The obtained NMR spectra were Fourier transformed with 1.0 Hz exponential line broadening using MestreNova software (v 12.0.3, Santiago de Compostela, Research S.L., Spain) followed by phase and baseline corrections. The chemical shifts were indirectly referenced to the spectrometer 2H lock.

Preparation of Battery Electrodes

The as-received graphene nanoplatelets (0.8 g) and carbon black (0.1 g) were mixed with a binder solution, which was previously prepared by mixing sodium alginate (0.1 g) and deionized (DI) water (2.5 mL), and a viscous slurry was obtained after overnight stirring at room temperature. The resulting slurry was coated on the Mo current collector of the known mass using a doctor-blade. The coated surface was restricted to a small particular area (1 cm (width) \times 1 cm (length)) by using a piece of Scotch tape, which was removed after drying the coated current collector under ambient conditions. The obtained cathode was dried overnight at 80 °C under vacuum and immediately weighted after removal from the oven to determine the amount of graphene nanoplatelet active material coated on the current collector. The coated surface of the Mo current collector was further determined using ImageJ software and used to find the loading of the active material. The average cathode material loading was limited to 1.0 mg cm $^{-2}$ for all compositions by controlling the height of the doctor blade.

Cyclic Voltammetry and Full-Cell Testing

The prepared graphene nanoplatelet cathode was placed inside a partially heat-sealed aluminum-laminated film pouch along with a piece of glass fiber membrane and vacuum dried overnight at 80 °C before transferring to the glovebox with an inert atmosphere. An L-shaped piece of aluminum foil (1 cm (width) × 3 cm (length) × 5 cm (length)) was inserted into the pouch and heat sealed immediately before being readmitted to the glovebox, where 1.5 mL electrolyte with known composition was injected into it using a glass pasteur pipette. The remaining open end of the cell was immediately heat-sealed after removal from the glovebox.

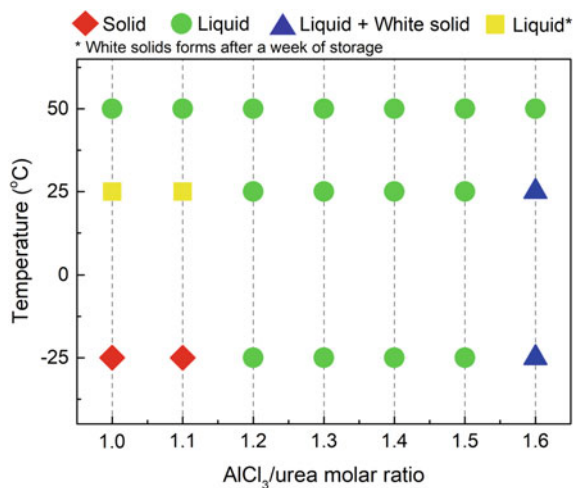
The assembled full cells were independently used for both cyclic voltammetry (CV) and rate capability test. For CV, the scanning voltage range was set at –0.50–2.40 V (versus Al) using a potentiostat, and aluminum anode was used as both auxiliary and reference electrodes. For rate capability test, the cells were charged/discharged to 2.20 V/1.00 V, respectively, using a multichannel battery tester (CT-4008, Neware), and the current density was varied from 100 to 1000 mA g⁻¹ for 25 cycles. For specific current densities (mA g⁻¹) and specific capacities (mAh g⁻¹) throughout this paper, only the mass of graphene nanoplatelet and carbon black are considered.

Results and Discussion

Physical State

The ILAs were prepared by mixing urea with certain mole equivalent AlCl₃ under an inert atmosphere. At room temperature, the obtained 1.0–1.5 compositions were clear liquids and some white solids observed beyond 1.5 molar composition (presumably AlCl₃ due to supersaturation) [18]. Although 1.0 and 1.1 molar compositions were originally clear liquids, they solidified after one week of storage. Therefore, only 1.2–1.5 molar compositions remained as a clear liquid at room temperature. The obtained ILAs compositions were further subjected to a controlled temperature environment in the range of –25 to 50 °C to evaluate their operating temperature range. Figure 1 shows the physical state of all studied ILAs, which indicate that only 1.2–1.5 molar compositions remained a clear liquid in the range of –25 to 25 °C, while all compositions including 1.6 molar were found to be clear liquids at 50 °C.

Fig. 1 Physical state of the AlCl₃-urea ILAs with 1.0–1.6 molar composition in a temperature range of –25 to 50 °C. (Color figure online)



Speciation

The characteristic of an ILA can be significantly affected by the type and relative concentration of species present. According to literature, the possible charged species in AlCl₃-urea ILAs are AlCl₂·(urea)_n⁺, AlCl₄⁻, Al₂Cl₇⁻, and Al₃Cl₁₀⁻ [16, 18–20].

The NMR measurements were performed for 1.0, 1.1, 1.2, and 1.4 molar compositions of AlCl₃-urea ILAs to determine species type and their relative concentration. Figure 2a shows the ²⁷Al NMR spectrum of 1.0 composition (neutral system), where the observed four peaks belong to charged species AlCl₄⁻ (chemical shift: 103.00 ppm) and AlCl₂·(urea)₂⁺ (73.75 ppm) and neutral species (AlCl₃·(urea) (89.64 ppm) and AlCl₃·(urea)₂ (54.54 ppm)). The peaks were assigned based on Coleman et al. [18] work, and the missing peak at a chemical shift of ~97 ppm indicates the absence of Al₂Cl₇⁻ in this composition, which is in agreement with our previous study [15]. The peak analysis in Fig. 1a allowed to evaluate the relative amount of four species in this composition which indicates AlCl₃·(urea) has the highest concentration, followed by AlCl₄⁻, AlCl₂·(urea)₂⁺, and AlCl₃·(urea)₂, respectively.

Figure 2b shows the ²⁷Al NMR spectrum of 1.2 molar compositions of the ILA, where the individual peaks that were observed in 1.0 composition start to broaden and some merge to a single peak. These peaks broaden due to several reasons such as the presence of Al₂Cl₇⁻ and its dynamic equilibrium with other species, changes in the electronic environment of the aluminum nucleus, and increased sample viscosity with an increase in the molar ratio [21]. The asymmetric environment of the aluminum nuclei in Al₂Cl₇⁻ in contrast to the cubic symmetry in AlCl₄⁻ could be another reason for peak broadening [22]. A few studies also suggest that the faster chemical exchange of AlCl₄⁻/Al₂Cl₇⁻ equilibrium than the time scale of NMR measurement

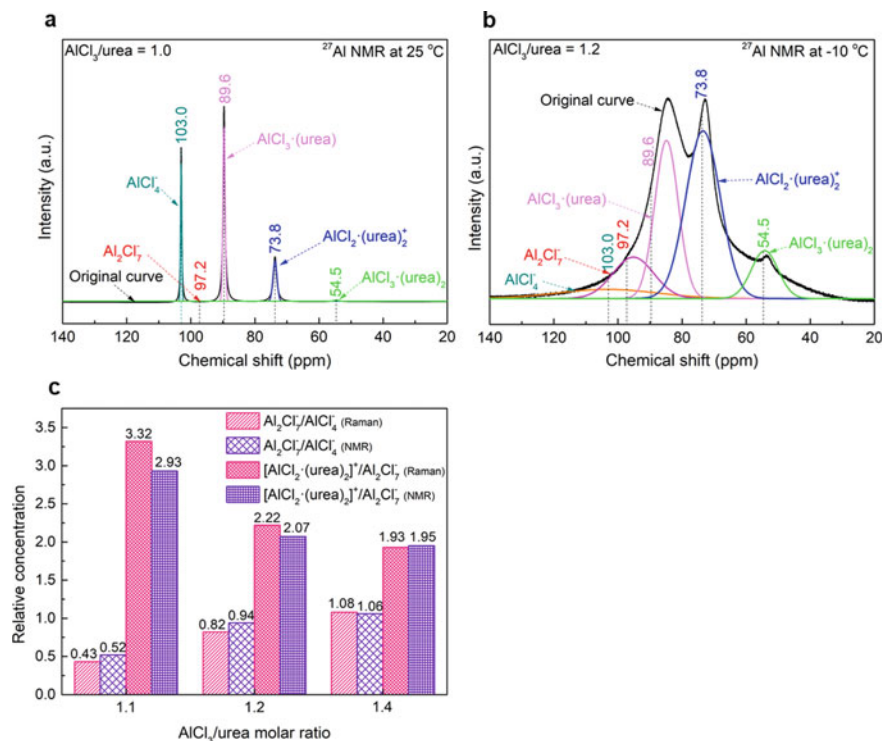


Fig. 2 A ^{27}Al NMR spectra for AlCl_3 -urea ILA of **a** 1.0 molar at 25°C , and **b** 1.2 molar at -10°C with deconvoluted curves. **c** Comparison of species relative concentration obtained from NMR and Raman spectroscopy. (Color figure online)

reduces the possibility of distinguishing the two separate signals [22, 23] and leads to one broad peak for both species as shown on Fig. 2b.

The obtained broadened peaks from various molar compositions were deconvoluted to determine the relative concentration of the five species in the system by considering their chemical shift in the 1.0 molar system as shown in Fig. 2b for 1.2 molar composition. For Al_2Cl_7^- , the chemical shift was referenced from 1.1 molar AlCl_3 -[EMIm]Cl IL as no data is available for this species in the present AlCl_3 -urea ILA. The best-fit analysis of obtained NMR spectra shows that an increased molar ratio from 1.0 to 1.1 resulted in a small decrease in the relative amount of AlCl_4^- species, but a significant increase in Al_2Cl_7^- from 0.0 to 11.3%. At the same time, the relative amount of cation species ($[\text{AlCl}_2 \cdot (\text{urea})_2]^+$) also increased from 22.1% to 33.0%, while neutral species ($\text{AlCl}_3 \cdot (\text{urea})$) reduced from 55.1% to 25.0%. This happens due to partial conversion of $\text{AlCl}_3 \cdot (\text{urea})$ to $[\text{AlCl}_2 \cdot (\text{urea})_2]^+$ and AlCl_4^- and then AlCl_4^- to Al_2Cl_7^- with the addition of more AlCl_3 [18]. With a further increase in the molar ratio to 1.2 and 1.4, the relative amount of AlCl_4^- species remains almost the same, while the amount of $[\text{AlCl}_2 \cdot (\text{urea})_2]^+$ and Al_2Cl_7^- increased.

Figure 2c shows the relative concentration ratio of electroactive species obtained from NMR analysis in this study and Raman spectroscopy results reported in our previous study [15] for 1.1, 1.2, and 1.4 molar compositions. While the relative amount of AlCl₄⁻ remained almost the same across the selected molar compositions of AlCl₃/Urea ILA (1.1, 1.2, 1.4), the results in Fig. 2c show that the relative ratio of Al₂Cl₇⁻/AlCl₄⁻ significantly increased and the relative ratio of AlCl₂·(urea)₂⁺/Al₂Cl₇⁻ decreased with an increase in the molar ratio. These results show that with increasing molar composition, Al₂Cl₇⁻ becoming the more dominating species contributing to the electrodeposition of aluminum compared with AlCl₂·(urea)₂⁺. A good agreement between the NMR and Raman spectroscopy results as shown in Fig. 2c authenticates the accuracy of the obtained NMR results.

Ionic Conductivity and Electrochemical Stability of AlCl₃-urea ILA

The ionic conductivity of 1.0–1.5 compositions was measured using EIS technique in a Teflon cell at 25 °C, where it first increases with increasing composition from 0.91 mS cm⁻¹ at 1.1 molar to 1.45 mS cm⁻¹ at 1.3 molar, and then decreases, as shown in Fig. 3. The initial increase in the ionic conductivity with an increase in AlCl₃ content is due to the increase in Al₂Cl₇⁻ concentration as Al₂Cl₇⁻ is the major ionic transport carrier among the two anionic species and therefore, has a more pronounced effect on ionic conductivity [23]. The decrease in ionic conductivity with a further increase in AlCl₃ content is due to the increase in the electrolyte viscosity at higher compositions [1]. The ionic conductivity was also measured at different temperatures (25–85 °C) for the considered AlCl₃-urea ILA compositions (1.1–1.5) and found to be increasing with increasing temperature for all compositions.

Fig. 3 Ionic conductivity of the AlCl₃-urea ILA at 25 °C with 1.1–1.5 molar composition. (Color figure online)

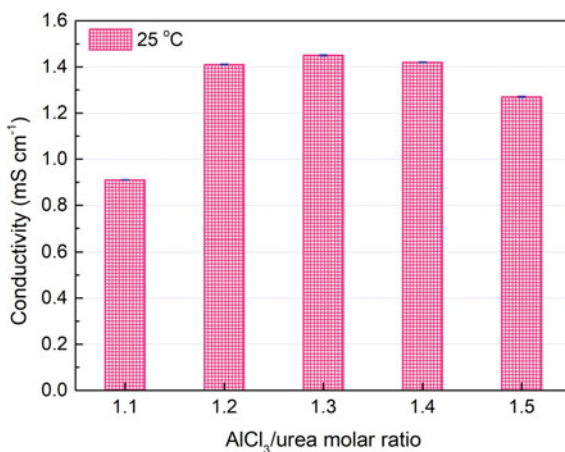
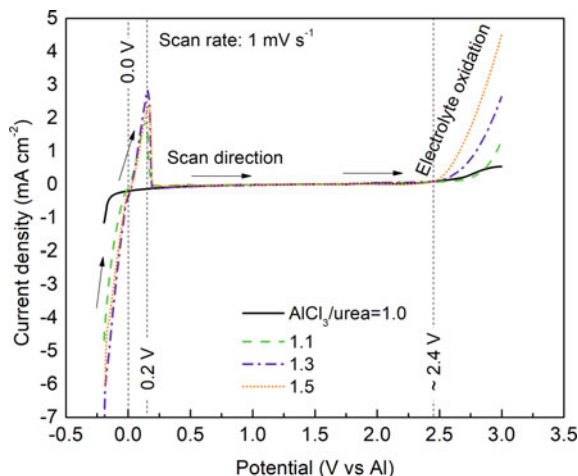


Fig. 4 Obtained LSV curve for the electrodeposition/stripping of aluminum and oxidation and electrochemical stability of the AlCl_3 -urea ILAs. (Color figure online)



The electrochemical stability window of the AlCl_3 -urea ILAs and electrodeposition/stripping of aluminum was investigated using linear scan voltammetry (LSV) for the considered composition in the -0.20 to 3.00 V (vs. Al/Al^{3+}) potential range with 1 mV s^{-1} scan rate, as shown in Fig. 4. With all compositions except 1.0, an increasing cathodic current (corresponding to aluminum plating) with onset potential at -0.20 V (vs. Al/Al^{3+}) and an anodic wave (corresponding to aluminum stripping) starting at ~ 0.00 V (vs. Al/Al^{3+}) with the highest current at ~ 0.20 V (versus Al/Al^{3+}) are observed. In the neutral composition ($\text{AlCl}_3/\text{urea} = 1.0$), no appreciable electrochemical activity was observed due to the absence of Al_2Cl_7^- (absence confirmed from NMR analysis in Fig. 2a). Similar behavior for neutral composition is also reported in other AlCl_3 -amide systems [24, 25] and well explained in our previous study [15].

In terms of electrochemical stability, no apparent oxidation or reduction peaks were observed for the studied ILAs between 0.25 and ~ 2.40 V, which shows that the studied AlCl_3 -urea ILAs are stable in this potential range. An oxidation peak was observed above 2.40 V due to the oxidation of AlCl_4^- ($4\text{AlCl}_4^- \rightleftharpoons 2\text{Al}_2\text{Cl}_7^- + \text{Cl}_2 + 2\text{e}^-$) [26] which indicates that the studied ILAs oxidize beyond this potential, as shown in Fig. 4. It was also observed that the oxidation potential of AlCl_3 -urea ILAs decreases with increasing AlCl_3 content, which can be linked to the increased concentration of Al_2Cl_7^- and increased activity of electrochemically active species at higher AlCl_3 content through Nernst equation for oxidation:

$$E = E^\circ - \frac{RT}{F} \ln \frac{[a_{\text{Al}_2\text{Cl}_7^-}] [\text{pCl}_2]^{\frac{1}{2}}}{[a_{\text{AlCl}_4^-}]^2} \quad (1)$$

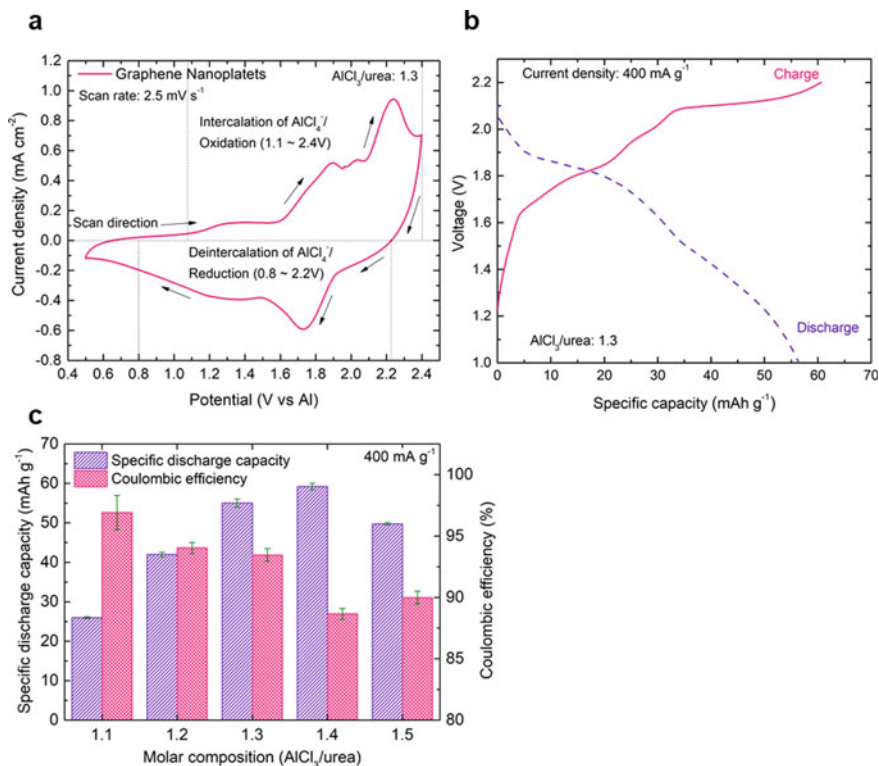


Fig. 5 Electrochemical performance analysis of AlCl_3 -urea electrolyte with graphene nanoplatelet working electrode; **a** cyclic voltammograms, **b** voltage profile during charge/discharge in 1.3 molar composition, **c** comparison of specific discharge capacity and coulombic efficiency across different molar composition at 400 mA g^{-1} . (Color figure online)

where E is the potential (V), E° is the standard oxidation potential (V), F is Faraday constant ($96,485 \text{ C mol}^{-1}$), T is temperature (K), R is the universal gas constant ($8.314 \text{ J mol}^{-1} \text{ K}^{-1}$), a is the activity, and p_{Cl_2} is the partial pressure of chlorine gas (Pa). Assuming the partial pressure of chlorine gas remains the same in the above equation, the oxidation potential will decrease with an increase in the activity of Al_2Cl_7^- , and the activity is linked to its concentration.

Full-Cell Testing

The full-cell testing was performed to verify the feasibility of the system where AlCl_3 -urea ILA with different compositions (1.1–1.5) was utilized as electrolyte and graphene nanoplatelet was used as the cathode. The reversibility of the aluminum insertion/deinsertion into the cathode active material was confirmed

through cyclic voltammetry as shown in Fig. 5a. For galvanostatic cycling, the cells were charged/discharged to 2.20 V/1.00 V, respectively, at different current densities. Figure 5b shows the voltage profile of the cell with 1.3 molar composition electrolyte during charging and discharging at 400 mA g⁻¹, where multiple voltage plateaus observed during the charge/discharge are consistent with the obtained CV results.

The electrochemical tests performed with the considered compositions show that the specific discharge capacity of the cell increases with increasing AlCl₃ concentration in the electrolyte up to 1.4 compositions and then decreases, as shown in Fig. 5c. This observation is due to the combined effect of increased electroactive ionic species concentration, particularly Al₂Cl₇⁻, and increased viscosity at higher AlCl₃ content. A balance is required between the increased concentration of ionic species (positive effect) and increased viscosity (negative effect) to achieve the optimum performance of the battery [14], which is why battery capacity first increases with increasing the molar ratio up to 1.4 molar and then decreases. In contrast, a small decrease in the coulombic efficiency with increasing the molar composition is observed in Fig. 5c. This is due to the reduction in the electrolyte oxidation potential at higher molar composition, resulting in electron loss because of electrolyte oxidation and side reactions. As shown in Fig. 5c, 1.4 molar composition delivers the highest specific discharge capacity (~60 mAh g⁻¹) followed by 1.3 composition (~55 mA g⁻¹) at 400 mA g⁻¹, while the Coulombic efficiency of 1.3 molar composition was higher (94%) than 1.4 molar (89%).

Conclusions

The present study investigates the physicochemical properties of AlCl₃-urea ILAs in the neutral and acidic range (AlCl₃/urea = 1.0–1.6). We determine the type of species in the AlCl₃-urea ILAs (AlCl₄⁻, Al₂Cl₇⁻, AlCl₃·urea, AlCl₂·(urea)₂⁺, AlCl₃·(urea)₂) and their relative composition using ²⁷Al NMR experiments. The obtained NMR results indicate that the relative amount of AlCl₄⁻ remains almost unchanged across the investigated molar compositions of AlCl₃-urea ILAs, while the relative ratio of AlCl₂·(urea)₂⁺/Al₂Cl₇⁻ decreases from 2.93 to 1.95 and the relative ratio of Al₂Cl₇⁻/AlCl₄⁻ increases from 0.52 to 1.05. These observations indicate that at higher molar compositions, Al₂Cl₇⁻ is the dominating species contributing to the electrodeposition of aluminum compared with AlCl₂·(urea)₂⁺. Furthermore, the electrochemical impedance spectroscopy shows that the ionic conductivity of the AlCl₃-urea ILAs first increases from 0.91 mS cm⁻¹ at 1.1 molar to 1.45 mS cm⁻¹ at 1.3 molar, and then decreases. The linear scan voltammetry results indicate that the studied ILAs are stable in the potential range of 0.25–2.4 V. The prepared ILAs were used as an electrolyte in an aluminum-ion battery made of aluminum anode and graphene nanoplatelets cathode, where 1.4 and 1.3 molar compositions were

selected as the best compositions delivering a specific capacity of 60 and 55 mAh g⁻¹ at 400 mA g⁻¹, respectively. Overall, the results indicate that AlCl₃-urea ILAs are suitable cost-effective electrolytes for aluminum-ion batteries.

Acknowledgements The authors acknowledge the financial support provided by Potent Group (No. 503355) and Ontario Centres of Excellence (No. 503760) for this project.

References

1. Liu C, Chen W, Wu Z, Gao B, Hu X, Shi Z, Wang Z (2017) Density, viscosity and electrical conductivity of AlCl₃-amide ionic liquid analogues. *J Mol Liq* 247:57–63
2. Bai L, Conway B (1990) Complex behavior of Al dissolution in non-aqueous medium as revealed by impedance spectroscopy. *J Electrochem Soc* 137:3737–3747
3. Licht S, Levitin G, Yarnitzky C, Tel-Vered R (1999) The organic phase for aluminum batteries. *Electrochem Solid-State Lett* 2:262–264
4. Zhao Y, VanderNoot T (1997) Electrodeposition of aluminium from nonaqueous organic electrolytic systems and room temperature molten salts. *Electrochim Acta* 42:3–13
5. Galiński M, Lewandowski A, Stepniak I (2006) Ionic liquids as electrolytes. *Electrochim Acta* 51:5567–5580
6. Rocher NM, Izgorodina EI, Rütther T, Forsyth M, MacFarlane DR, Rodopoulos T, Horne MD, Bond AM (2009) Aluminium speciation in 1-butyl-1-methylpyrrolidinium bis (trifluoromethyl-sulfonyl) amide/AlCl₃ mixtures. *Chem–A Eur J* 15:3435–3447
7. Giffin GA (2016) Ionic liquid-based electrolytes for “beyond lithium” battery technologies. *J Mater Chem A* 4:13378–13389
8. Lin MC, Gong M, Lu B, Wu Y, Wang DY, Guan M, Angell M, Chen C, Yang J, Hwang BJ (2015) An ultrafast rechargeable aluminium-ion battery. *Nature* 520:324
9. Jiang T, Brym MC, Dubé G, Lasia A, Brisard G (2006) Electrodeposition of aluminium from ionic liquids: Part I—electrodeposition and surface morphology of aluminium from aluminium chloride (AlCl₃)–1-ethyl-3-methylimidazolium chloride ([EMIm] Cl) ionic liquids. *Surf Coat Technol* 201:1–9
10. Yu X, Wang B, Gong D, Xu Z, Lu B (2017) Graphene nanoribbons on highly porous 3D graphene for high-capacity and ultrastable Al-ion batteries. *Adv Mater* 29:1604118
11. Haerens K, Matthijs E, Binnemans K, Van der Bruggen B (2009) Electrochemical decomposition of choline chloride based ionic liquid analogues. *Green Chem* 11:1357–1365
12. Smith EL, Abbott AP, Ryder KS (2014) Deep eutectic solvents (DESs) and their applications. *Chem Rev* 114:11060–11082
13. Abood HM, Abbott AP, Ballantyne AD, Ryder KS (2011) Do all ionic liquids need organic cations? Characterisation of [AlCl₂-nAmide]⁺AlCl₄⁻ and comparison with imidazolium based systems. *Chem Commun* 47:3523–3525
14. Malik M, Ng KL, Azimi G (2020) Physicochemical characterization of AlCl₃-urea ionic liquid analogs: speciation, conductivity, and electrochemical stability. *Electrochimica Acta* 136708
15. Ng KL, Malik M, Buch E, Glossmann T, Hintennach A, Azimi G (2019) A low-cost rechargeable aluminum/natural graphite battery utilizing urea-based ionic liquid analog. *Electrochim Acta* 327:135031
16. Jiao H, Wang C, Tu J, Tian D, Jiao S (2017) A rechargeable Al-ion battery: Al/molten AlCl₃-urea/graphite. *Chem Commun* 53:2331–2334
17. Antonetti E, Iaquaniello G, Salladini A, Spadaccini L, Perathoner S, Centi G (2017) Waste-to-chemicals for a circular economy: the case of urea production (waste-to-urea). *Chemsuschem* 10:912–920

18. Coleman F, Srinivasan G, Kwasny MS (2013) Liquid coordination complexes formed by the heterolytic cleavage of metal halides. *Angew Chem Int Ed* 52:12582–12586
19. Wang C, Li J, Jiao H, Tu J, Jiao S (2017) The electrochemical behavior of an aluminum alloy anode for rechargeable Al-ion batteries using an AlCl_3 -urea liquid electrolyte. *RSC Advances* 7:32288–32293
20. Angell M, Zhu G, Lin MC, Rong Y, Dai H (2019) Ionic liquid analogs of AlCl_3 with urea derivatives as electrolytes for aluminum batteries. *Advan Functional Mater* 1901928.
21. Estager J, Holbrey J, Swadźba-Kwaśny M (2014) Halometallate ionic liquids—revisited. *Chem Soc Rev* 43:847–886
22. Gray JL, Maciel GE (1981) Aluminum-27 nuclear magnetic resonance study of the room-temperature melt aluminum trichloride butylpyridinium chloride. *J Am Chem Soc* 103:7147–7151
23. Ferrara C, Dall'Asta V, Berbenni V, Quartarone E, Mustarelli P (2017) Physicochemical characterization of AlCl_3 -1-Ethyl-3-methylimidazolium chloride ionic liquid electrolytes for aluminum rechargeable batteries. *J Phys Chem C* 121:26607–26614
24. Li M, Gao B, Liu C, Chen W, Shi Z, Hu X, Wang Z (2015) Electrodeposition of aluminum from AlCl_3 /acetamide eutectic solvent. *Electrochim Acta* 180:811–814
25. Li M, Gao B, Liu C, Chen W, Wang Z, Shi Z, Hu X (2017) AlCl_3 /amide ionic liquids for electrodeposition of aluminum. *J Solid State Electrochem* 21:469–476
26. Wang S, Kravchuk KV, Filippin AN, Müller U, Tiwari AN, Buecheler S, Bodnarchuk MI, Kovalenko MV (2018) Aluminum chloride-graphite batteries with flexible current collectors prepared from earth-abundant elements. *Adv Sci* 5:1700712

Part XII
Advanced Real Time Imaging

In-Situ Quantitative Study of Heat Transfer Performance of Mold Flux by Using Double Hot Thermocouple Technology



Zhe Wang, Guanghua Wen, Wenbo Jiang, Ping Tang, and Shuheng Huang

Abstract The heat transfer ability of the mold flux is crucial for balancing the heat flux between the slab and mold. The double hot thermocouple technique (DHTT) is widely used for the qualitative determination of the heat transfer performance of the mold flux due to its advantages of rapid in-situ testing. However, the traditional DHTT cannot determine heat flux quantitatively, which limits the development of DHTT in the field of heat transfer measurement. In the current study, the in-situ quantitative investigation method based on DHTT was, for the first time, proposed to determine the heat transfer performance of mold flux. Herein, the heat flux of four mold fluxes with different $\text{Al}_2\text{O}_3/\text{SiO}_2$ mass (A/S) ratios was estimated by using the new DHTT. The result showed that the heat flux decreases with increasing A/S ratio, which is consistent with the result of the parallel-sided plate method.

Keywords Mold flux · Heat flux · Thermal resistance · Double hot thermocouple technique · In-situ quantitative method

Introduction

In continuous casting process, the mold flux plays an essential role in controlling the heat transfer between the billet/slab and the mold [1]. For many steels, especially advanced high strength steel (AHSS) [2], twin-induced plasticity (TWIP) [3], and transformation induced plasticity (TRIP) steels [4], controlling the heat transfer of film is critical to improving the quality of billet/slab. For instance, the thermal mismatch between ferrite and austenite phases can cause the longitudinal cracking problem in casting AHSS steel. It is therefore important to determine the heat transfer properties of the mold flux.

Z. Wang · G. Wen (✉) · W. Jiang · P. Tang · S. Huang
Chongqing University, Chongqing 400044, P. R. China
e-mail: wengh@cqu.edu.cn

Z. Wang
e-mail: zhewang@cqu.edu.cn

Currently, there are four main approaches to determine the heat transfer performance of the mold flux: the parallel plate method, the cold finger method, the infrared emitter technique (IET), and the double hot thermocouple technique (DHTT). Many groups take up with the research of the heat transfer properties of mold flux. Cho et al. [5] compared the heat transfer properties of low carbon steel (LC) and medium carbon steel (MC) mold fluxes by using the parallel plate method. The results showed that the interfacial thermal resistance is found to be about 50% of overall thermal resistance for the heat transfer. By using the cold finger method, Qi et al. [6] investigated the heat transfer performance of fluoride-free and titanium-bearing mold fluxes. The results suggested that the heat flux of fluoride-free mold fluxes reduces with increasing basicity (CaO/SiO₂ mass ratio). By employing the IET and the DHTT method, Wang et al. [7] explored the radiative heat transfer behavior and the heat transfer capability of the LC and MC mold fluxes. The results showed that glassy samples behave similar radiation heat transfer capability and the thermal diffusivity of fully crystalline LC mold flux is higher than MC mold flux under the same condition.

The hot thermocouple technique (HTT) is a kind of high-temperature measurement method which uses intermediate frequency chopper technology to realize both heating and temperature measurement [8]. Based on the HTT, the DHTT is further developed by doubling the U-shaped B-type thermocouple and its associated controlling system [9]. The simplicity and versatility of DHTT should make it very useful, especially for in-suit observation of the crystallization and heat transfer properties of mold flux for different temperature gradient. However, all DHTTs used to analyze the heat transfer of mold flux are qualitative analysis and cannot keep a stable temperature field (need the temperature pulse) [7, 9]. Thus, it is crucial to quantify the heat flux by using the DHTT.

Based on the new DHTT, this research provides a new approach to investigate the heat transfer performance of mold flux. The results suggested that the new DHTT results were consistent with results of the parallel plate method.

Experimental

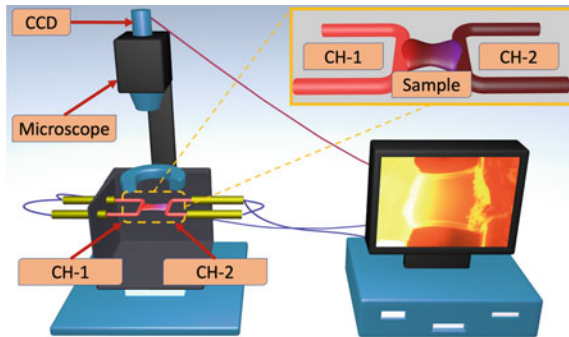
Pre-Melted Samples Preparation

The compositions of mold fluxes are listed in Table 1, which is the same as a previous Reference [10]. The mold fluxes for this study were made of pure chemical reagents. After mechanically mixed in a ball mill, these reagents were melted in an induction furnace at 1773 K for 20 min to homogenize their chemical compositions. Subsequently, the molten mold fluxes were quenched in a water cooled copper plate and crushed for the DHTT experiments.

Table 1 Chemical compositions of mold fluxes (wt%)

No	CaO	SiO ₂	Al ₂ O ₃	Na ₂ O	CaF ₂	A/S ratio	Heat flux / MWm ⁻²	Thermal resistance / 10 ⁻² K ² W ⁻¹
R1	20	45	5	10	20	0.11	0.449	0.246
R2	20	35	15	10	20	0.43	0.393	0.285
R3	20	25	25	10	20	1.00	0.368	0.302
R4	20	15	35	10	20	2.33	0.321	0.343

Fig. 1 Schematic of new DHTT. (Color figure online)



Experimental Procedure

Figure 1 shows the schematic diagram of the DHTT device. The details of DHTT have been described by Kashiwaya [11]. Based on the traditional DHTT, we add the duty cycle sensor in each channel, which can collect the output duty cycle. And the sample is heated by the lamps to keep the ambient temperature stable [12].

To test the heat transfer performance of mold flux, a temperature control curve was first designed. As shown in Fig. 2, the temperature of CH-1 and CH-2 was raised rapidly to 1773 K and keep 30 s to homogenize its composition. Then, the temperature of CH-1 and CH-2 rapidly cool down to 1673 K and 1073 K, respectively, remaining in agreement with the temperature gradient in the mold. Secondly, the pre-melted mold fluxes were added on the B-type thermocouple (between CH-1 and CH-2) and heated according to the temperature control curve (Fig. 2). When the temperature gradient is stable, the distance between CH-1 and CH-2 was kept constant at 2 mm. Finally, the duty cycle of CH-1 and CH-2 was collected.

In order to obtain the heat transfer performance of samples, the low-temperature channel (CH-2) was chosen as comparison criteria. In the comparison, if the duty cycle of low-temperature channel (CH-2) was assumed to be lower, estimating the heat flux was higher, and vice versa. In the quantitative study, each sample was repeated three times, and the mean duty cycle value (150 - 230 s of Fig. 2) was taken as the original parameters. However, the results are presented here only to provide

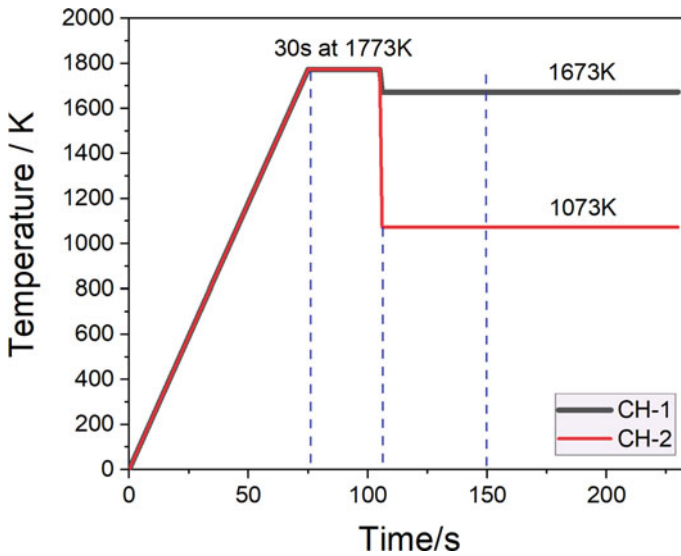


Fig. 2 Temperature control for DHTT test. (Color figure online)

a qualitative value of the heat transfer performance of mold flux. Therefore, further research is needed to quantify these parameters. Since the heat fluxes and thermal resistance of samples are known (Table 1), the conversion function can be obtained by the fitting.

Results and Discussion

Figure 3 shows the duty cycle result of each sample. It can be seen that the duty cycle and thermal resistance increase with increasing A/S ratio, while the heat flux decreases with increasing A/S ratio. These three parameters reflect the trend that the heat transfer performance of the mold flux reduces with the A/S ratio. Actually, this trend is related to the crystallization ratio of mold flux film. Figure 4 shows the in-situ observation results of mold flux film (R1 to R2) at 200 s in Fig. 2. It can be observed that the crystallization ratio increases with increasing A/S ratio. Therefore, the increase of crystallization of films inhibits the heat transfer, which is consistent with the previous studies [13–16].

For the purpose of quantification, the relationships between duty cycle and heat flux or thermal resistance was investigated to estimate the heat flow and thermal resistance of mold flux. As shown in Fig. 5a, it can be seen that the heat flux are significantly correlated with duty cycle, of which the R^2 is 0.992. Thus, the relationship between the heat flux and duty cycle can be estimated by fitting a linear regression model, which was expressed by the formula given below.

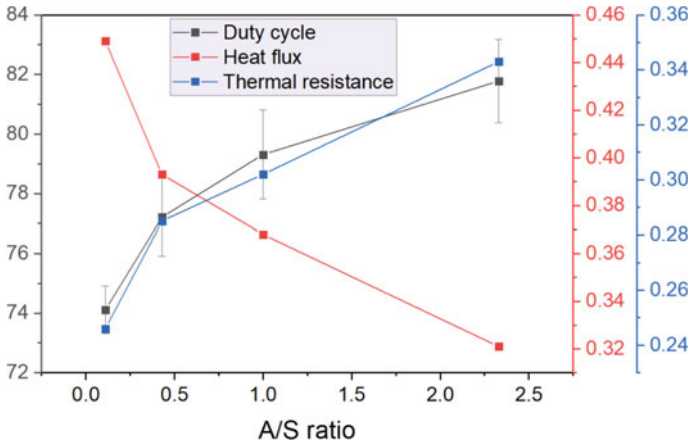
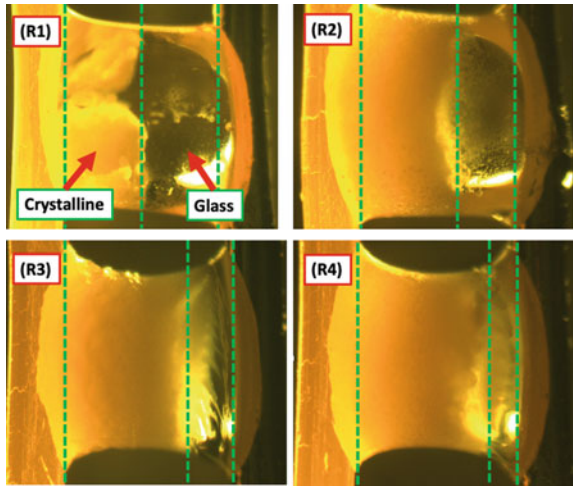


Fig. 3 Heat flux, duty cycle, and thermal resistance change with the A/S ratio. (Color figure online)

Fig. 4 In-situ DHTT observation of mold flux. (Color figure online)



$$q = -0.163 \frac{w}{10} + 1.660 \tag{1}$$

where q is the heat flux (MWm^{-2}), w is the duty cycle (%) obtained by new DHTT. As shown in Fig. 5b, the thermal resistance has an obvious positive correlation with the duty cycle ($R^2 = 0.980$). Thus, the conversion relationship between the thermal resistance and duty cycle is further established, as shown below.

$$R = 0.123 \frac{w}{10} - 0.665 \tag{2}$$

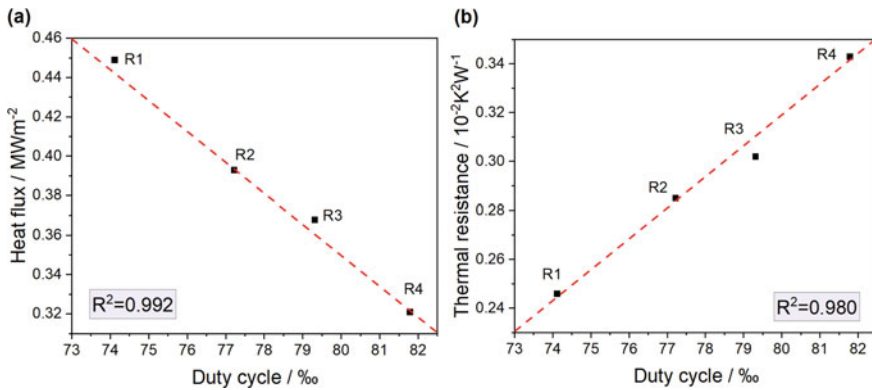


Fig. 5 Correlation analysis: **a** relationship between the heat flux and duty cycle, **b** relationship between the thermal resistance and duty cycle. (Color figure online)

where R is the thermal resistance ($10^{-2}\text{K}^2\text{W}^{-1}$). Thus, the new DHTT can be used quantitatively to evaluate the heat flux and thermal resistance of mold flux film by using Eqs. 1 and 2.

In this study, we proposed a new DHTT method to determine the heat transfer performance of mold flux. The results showed that the new DHTT not only solves the problem that traditional DHTT cannot be utilized in a quantitative study, but also establishes a stable temperature gradient during the experiment (no need for a temperature pulse). Collectively, the new DHTT provides a new approach to investigate the heat transfer performance of mold flux at high temperature.

Conclusion

In this paper, a new DHTT method was, for the first time, employed to quantitatively estimate the heat transfer performance of mold flux. The duty cycle of the low-temperature channel increases with increasing A/S ratio, reflecting the heat transfer performance of mold flux reducing with the increase of A/S ratio, which is consistent with the results obtained by the parallel plate method. The conversion formulas are further established, which enables the new DHTT to be used to estimate the heat flux and thermal resistance of mold flux.

Acknowledgements The authors greatly appreciate the funding from the Graduate Scientific Research and Innovation Foundation of Chongqing, China (Grant No. CYB19002).

References

1. Zhang SD et al (2019) Effect of substituting Na_2O for SiO_2 on the non-isothermal crystallization behavior of $\text{CaO-BaO-Al}_2\text{O}_3$ based mold fluxes for casting high Al steels. *Ceram Int* 45:11296–11303
2. Jia N et al (2009) An in situ high-energy X-ray diffraction study of micromechanical behavior of multiple phases in advanced high-strength steels. *Acta Mater* 57:3965–3977
3. Luo ZC et al (2018) The effect of deformation twins on the quasi-cleavage crack propagation in twinning-induced plasticity steels. *Acta Mater* 150:59–68
4. Wang WL, Lu BX, Xiao D (2016) A review of mold flux development for the casting of high-Al steels. *Metallurgical Mater Trans B-Process Metallurgy Mater Process Sci.* 47:384–389
5. Cho J et al (1998) Thermal resistance at the interface between mold flux film and mold for continuous casting of steels. *ISIJ Int* 38:440–446
6. Qi X, Wen GH, Tang P (2008) Investigation on heat transfer performance of fluoride-free and titanium-bearing mold fluxes. *J Non-Cryst Solids* 354:5444–5452
7. Wang WL et al (2011) Radiative heat transfer behavior of mold fluxes for casting low and medium carbon steels. *ISIJ Int* 51:1838–1845
8. Wang Z et al (2019) Novel method for determining the interfacial properties of melt slags based on single hot thermocouple technique. *ISIJ Int* 59:1806–1810
9. Wang WL et al (2018) High-temperature properties of mold flux observed and measured in situ by single/double hot-thermocouple technique. *Jom.* 70:1248–1255
10. Yan W et al (2015) Effect of slag compositions and additive on heat transfer and crystallization of mold fluxes for high-Al non-magnetic steel. *ISIJ Int* 55:1000–1009
11. Kashiwaya Y et al (1998) Development of double and single hot thermocouple technique for in situ observation and measurement of mold slag crystallization. *ISIJ Int* 38:348–356
12. Wang Z et al (2019) A novel method of surface tension test for melt slags based on hot thermocouple technique. Springer
13. Hayashi M, Abas RA, Seetharaman S (2004) Effect of crystallinity on thermal diffusivities of mould fluxes for the continuous casting of steels. *ISIJ Int* 44:691–697
14. Ozawa S et al (2006) Lattice and radiation conductivities for mould fluxes from the perspective of degree of crystallinity. *ISIJ Int* 46:413–419
15. Wang W, Cramb AW (2010) Study of the Effects of the Mold Surface and Solid Mold Flux Crystallization on Radiative Heat Transfer Rates in Continuous Casting. *Steel Res Int* 81:446–452
16. Cho JW et al (2013) Assessment of $\text{CaO-Al}_2\text{O}_3$ Based Mold Flux System for High Aluminum TRIP Casting. *ISIJ Int* 53:62–70

Synchronized High-Speed Microscopy and Thermoanalytical Measurement for Sub-mm/sub-ms-scale Cathodic Behavior in Molten Salt Electrolysis



Shungo Natsui, Ryota Shibuya, Hiroshi Nogami, Tatsuya Kikuchi, and Ryosuke O. Suzuki

Abstract The electrochemically deposited liquid metal (Me = Ca, Li, or their alloys) in the molten chloride works as powerful reductant for TiO_2 or other metal oxides; however, the electrolysis efficiency should be enough high if much lower oxygen level in metal phase was required. A detailed understanding of the cathodic behavior is necessary to control and optimize the electrolysis. In this study, to clarify the morphological and thermal characteristics of a cathodic electrode in a molten MeCl melt, we simultaneously performed electrochemical measurements and thermal measurements using an ultrafine thermocouple inserted inside a Mo electrode. Changes in the electrode interface were recorded at 500- μs intervals using a synchronized high-speed digital camera. It was possible to trace the change in the electrodeposition pattern in each potential quickly and sensitively, which was difficult to determine in only the electrochemical potential-current response.

Keywords Molten salt electrolysis · Colloidal metal · High-speed digital microscopy · Heat transfer

Introduction

In the prevailing Kroll process for titanium (Ti) production, which incurs an extremely high energy cost, TiO_2 must first be converted to TiCl_4 by Cl_2 gas, followed by use of liquid Mg as the reductant, and MgCl_2 as a by-product is circulated by electrolysis to give liquid Mg and gaseous Cl_2 . Thus, the Kroll process consists of many synchronized processes. Direct electrochemical reduction of solid TiO_2 in molten chloride (e.g. CaCl_2 , LiCl , and their mixtures) is a simple and straightforward electrolytic

S. Natsui (✉) · H. Nogami

Institute of Multidisciplinary Research for Advanced Materials, Tohoku University, Katahira 2-1-1, Aoba-ku, Sendai 980-8577, Japan
e-mail: natsui@tohoku.ac.jp

R. Shibuya · T. Kikuchi · R. O. Suzuki

Division of Materials Science and Engineering, Faculty of Engineering, Hokkaido University, Kita 13 Nishi 8, Kita-ku, Sapporo 060-8628, Japan

© The Minerals, Metals & Materials Society 2021

TMS 2021 150th Annual Meeting & Exhibition Supplemental Proceedings,

The Minerals, Metals & Materials Series,

https://doi.org/10.1007/978-3-030-65261-6_30

metallurgical method. This strategy is expected to simplify the processes separated in the Kroll process and thus reduce the amount of consumed energy. Among the present systems of titanium metal production, the direct electrochemical decomposition of TiO_2 in molten CaCl_2 has received special attention because of its simplicity and low energy cost. One successful example is the widely known “FFC Cambridge process”, in which the oxide anion from the solid TiO_2 pellet placed at the cathode transfers to the anode in the salt bath [1]. Another promising method (“OS process”) has been proposed that has better utilisation of the oxide anion transfer in CaCl_2 , because as much as 20 mol% CaO can dissolve in molten CaCl_2 at 1173 K [2]. The electrochemically deposited liquid Ca at the cathode also dissolves in the CaCl_2 melt (the solubility of Ca is reported as 2–4 mol% at 1123 to 1198 K) [3, 4]; and the dissolved Ca works effectively to reduce the oxide powder, even if the powder particles are electrical insulators or have no direct electrical contact with the cathode. In the mechanism of the OS process, metallothermic reduction by the dissolved liquid metal Me in the vicinity of the cathode is essential ($\text{Me}^{2+} + 2e^- \rightarrow \text{Me}$), where the oxide is placed close to the cathode. In the case of metallothermic reduction of solid titanium oxide using electrodeposited Me, the morphology of Me near the cathode is crucial. The liquid Me works effectively to reduce TiO_x , even though the latter does not have any direct electrical contact with the cathode. Therefore, the reduction efficiency in this method is thought to be greatly affected by the morphology of the interface between the electrolytically deposited Me and molten salt. It is widely known that a “metal fog” (colloidal metal) could be formed around the deposited Me without mechanical stirring, if a suitable emulsifier is present [5, 6]. Electrochemically deposited colloidal Me in molten salt has been considered to be particles formed by Me_x molecular clusters [7–9]. Despite its importance, however, there is only limited knowledge about the behaviour of colloidal Me due to the difficulty of in-situ observation [10, 11].

In this study, we investigated the dispersion characteristics of colloidal Me in molten LiCl-CaCl_2 system by examining images of the electrode surface obtained with high-speed digital microscopy synchronised to the electrochemical measurement with the thermoanalytical and electrochemical measurements.

Experimental

To observe the interfacial morphology of the working electrode, a quartz glass vessel 100 mm in diameter and 250 mm in height was employed, which has a barrel-vaulted shape with a flat surface. An electric resistance furnace was designed to control the inner vessel temperature with an accuracy of $\pm 1\text{K}$ for direct observation of processes within the vessel. A metal halide light (maximum light flux: 12,500 lm, main spectral peak: 550 nm) was used as an auxiliary light source. Time changes in the working electrode were recorded at 125 μs or more intervals, and a resolution of 640×480 pixels was obtained using a high-speed digital camera (Ditect Co., Ltd., HAS-D71, monochrome, main response spectral range: 500–600 nm) and a long-distance zoom

lens (VS Technology Co. Ltd., VSZ-10100, working distance: 95 mm, minimum field of view: $666 \mu\text{m} \times 500 \mu\text{m}$, and length per pixel: $1.04 \mu\text{m}$). The location of the tip of the liquid metal–electrode interface was tracked in each captured image by using image processing software (Photron Co., Ltd., PFV Viewer and ImageJ). Reagent-grade LiCl (>99.0 wt%) and CaCl₂ (>95 wt%) were used for the melt. Each chloride was dried under approximately 1 Pa at 573 K for more than 12 h. All the experiments were conducted in an Ar atmosphere (>99.9995 vol%). After melting the salt, the suspended electrodes were immersed in the melt while keeping the seal. Molybdenum (Mo) was employed as the material of the working electrode (WE), which must be inert and unreactive to the molten salt as well as the Ca and Li to be electrodeposited. One of the WE shape was a rod (ϕ 1.5 mm, 99.95 wt%) which was previously trimmed flatly in half by end-milling on the observation side, and the rod surface was polished with emery paper. Another one was a tube (i.d.: 1.57 mm, >99.95 wt%) and implanted K-type thermocouple are insulated by MgO nanopowder to record the temperature change due to the electrochemical reaction occurring on the Mo tube surface. The immersion depth of the working electrode was fixed at 10 mm by using an insulated protective Al₂O₃ tube. The counter electrode was a graphite rod (ϕ 10 mm). An Ag⁺/Ag reference electrode was employed, which consisted of a silver wire (ϕ 1.0 mm, 99.99%) immersed in each melt containing 0.5 mol% AgCl (99.5%) and set in a borosilicate tube [12]. Electrochemical measurements were performed using an automatic polarisation system (Hokuto Denko Corp., HZ-5000). The inter-electrode voltage and microscope images were synchronised with an error of 4 μs by using an analogue signal synchronous system. A “scopecoder” with a high noise-tolerant voltage measurement module (DL350, Yokogawa Electric Co.) was used to measure the thermoelectromotive analog signal of the TC in the electrodes and bath. The voltage measurement interval was constant at 100 μs . The minute thermoelectromotive force generated from TC was converted to a sharp waveform by an amplifier and a low-pass filter.

Results and Discussion

The molten CaCl₂ or LiCl electrolysis produces very high concentrations of metal fog [11]. In these cases, it was difficult to observe the electrode surface as the electrochemical reaction proceeded. Instead of these, the characteristic cathodic behavior can be discussed obviously in molten salt electrolysis of CaCl₂–LiCl eutectic system operating at low temperature. Photographs of the electrode surface along the current–time curves are shown in Fig. 1 [13]. The liquid-phase precipitate grew heterogeneously on the flat Mo surface, eventually generating a number of metal droplets. In contrast, colloidal Me was generated around the electrode. It showed that colloidal Me moves near the electrode surface to form a “cellular” network shape. After prolonged electrolysis, the cell structure collapsed due to excessive precipitation of colloidal Me and aggregation of the network structure. When the potential is more negative, the cells are larger for the same supplied charge, possibly because the convection field is

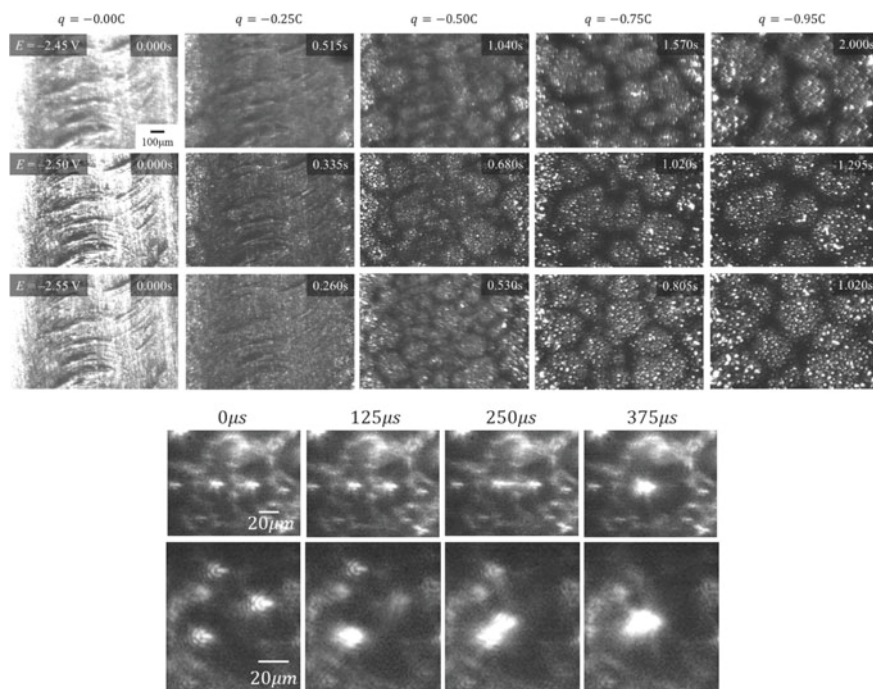


Fig. 1 Photographs of the electrodeposited melt and black colloidal metal formed on the flat Mo electrode at 823 K. (Reprinted from [13])

generated more rapidly. Further, a more negative potential promotes the aggregation of colloidal Me, and droplets can be clearly seen at the central portion of the cells.

As the amount of supplied charge increased, the droplets coalesced repeatedly; thus, their number density is decreased. A lower droplet number density was found at $E = -2.55\text{V}$ than at -2.50V , meaning that larger droplets were formed at the more negative potential. Supplying the same electric charge ($q = 0.95\text{C}$) took less time at $E = -2.55\text{V}$ than at -2.50V . Therefore, it is natural to consider that the static droplet diameter changes due to the effect of the potential on the interfacial tension balance (electric capillary phenomenon) [14]. After the network structure is formed, it has to be partially distorted for the coarsening of the cohesive structure. Although colloidal particles generally aggregate to minimize the local cohesive energy, this distortion process must also increase the local cohesive energy. Since the network aggregation structure has a tendency to shrink as a whole system, the spontaneously generated stress is stored instead. Thus, given the energy conservation, the hydrodynamic driving force must create distortion in the colloidal metal network. The famous cellular convection structure called “Bénard cells” is formed in the vertical direction driven by buoyancy. Interfacial tension-driven flow mechanism of two liquid phases

is known as “Marangoni–Bénard convection”. Considering a simplified hydrodynamic model, a relatively large flow velocity is expected to occur on this temporal and spatial scale even with a slight interfacial tension difference.

It has already been stated that the microscopic morphology of the dispersed fog can change with potential [15], and the authors are trying to quantify it from local calorimetric measurements. The macroscopic energy balance during the electrochemical reaction may have changed with the applied potential due to formation of metastable metal fog: the excess energy was probably required to create the dispersed metal-and-salt interface, and this energy depends on the microscopic fog morphology [16]. We analyzed the thermal behavior data to consider the effect of the morphology of the electrodeposited Me in molten MeCl. When the temperature T and the pressure P are constant and the chemical reaction proceeds, according to the first law of thermodynamics, the internal energy ΔU is expressed as $\Delta U = T\Delta S - (P\Delta V + W_e^0)$. Here, ΔS indicates the molar entropy change in a unipolar reaction. Herein, the electrochemical work is written as W_e^0 when the electrochemical system is in equilibrium. In an isobaric process, if the electrochemical reaction is in progress, the electrochemical work is written as W_e ; thus, the relationship of $Q = T\Delta S + W_e - W_e^0$ is obtained. In this case, Q is the heat absorbed when the electrochemical reaction is proceeding. We consider the current I and the heat dQ absorbed during time dt . Electrochemical work is the product of the potential difference (ΔE) and the electric charge ($I dt$); we denote the equilibrium potential of the cathode as E^0 , and we hence obtain $\Delta W_e^0 = (E - E^0)I dt$. Here, we must add the following generation term, because the Joule heating effect and the heat exchange at the reaction interface cannot be ignored while the electrochemical reaction proceeds. Therefore, the heat absorbed at the single electrode/electrolyte interface dQ can be written as:

$$\frac{dQ}{dt} = \frac{T\Delta SI}{nF} - |E - E^0|I + I^2 R_e - Q_t \quad (1)$$

where n is the valence of ion, F is the Faraday constant, R is the electrode/electrolyte resistance (\approx the electrolyte resistance [17]), η is the overpotential ($= E - E^0$), and q_t is the heat exchange between molten salt and electrode. The slope of the temperature change is approximated to a constant. Generally, the heat exchange between WE and molten salt bath Q_t can be calculated by the following equation to assume the temperature difference between the WE and bath, ΔT ($= T_{WE} - T_{bath}$):

$$Q_t = hA\Delta T; h \approx \frac{k \cdot Nu}{r_{WE}} \quad (2)$$

where k is the thermal conductivity of the bath [18], r_{WE} is the radius of the electrode, and Nusselt number, Nu ; the heat transfer coefficient between a WE and bath was given as 2.0 [19]. In the early stage of electrolysis, when dQ/dt can be assumed to be constant, we can analytically solve Eq. 1. Even in the electrolysis of the eutectic chloride melt, the metal deposition reactions are expected to be endothermic. Although

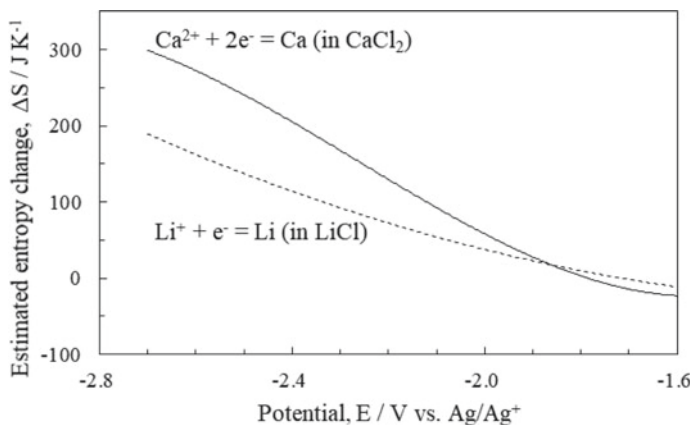


Fig. 2 Potential dependence of the molar entropy change of Me (=Ca, Li) electrodeposition from molten Me chloride melt at 1173 K due to electrochemical reaction estimated from thermal measurements

ΔS in this system is an unknown value, the apparent value can be estimated via the time integration; each application of the potential in Me precipitation gives the following equation (range of t' : 0–2 s):

$$\Delta S = \frac{1}{t'} \int_0^{t'} \frac{nF}{T_t I_t} \cdot \left(C_p \frac{dT}{dt} + I_t^2 R + \eta I_t + \frac{k \cdot Nu}{r_{WE}} A \Delta T_t \right) dt \quad (3)$$

Equation 3 can be solved by numerical integration, and Fig. 2 shows the estimated apparent ΔS of $\text{Me}^+ + e^- \rightarrow \text{Me}$ (in pure MeCl at 1173 K) at each potential. Both of ΔS were almost zero for (a) $E > -1.9$ V; however, for (b) $E < -2.0$ V, it was estimated as a positive value and clearly shows an increasing trend. In Case (a), the effects of the second to fourth terms on the right side of Eq. 5 are considered to be relatively large. In Case (b), the ΔS value was 100–300 $\text{JK}^{-1} \text{mol}^{-1}$. By simulating ΔS with the thermochemical software (FactSage7.0 was used for calculating the absolute entropy of Ca^{2+} or Li^+ in the melt, which was estimated with the help of approximations in aqueous solutions), we obtained 18.6 JK^{-1} for Ca, and -138.8 JK^{-1} for Li [20]. The experimental value was much higher than the simulated value. This is probably because the simulated value is for an ideal system; on the other hand, the electrodeposited morphology of Me in this system exhibits a unique dispersed phase. The excess energy was probably required to create the dispersed metal-and-salt interface and depends on the microscopic fog morphology. Unfortunately, no evidence has yet been obtained to support this hypothesis. The heat transport model represented in this section through the electrode/electrolyte interface is simplistic; it may be necessary to consider even smaller scale heat balances for a more detailed understanding.

Conclusions

We observed the sub-mm/sub-ms-scale convection with a colloidal network generated at the Mo cathode interface during electrolysis of CaCl_2 -LiCl system. The determined dependence of unit cell size of the network on the applied potential will make a significant contribution to high-temperature colloid chemistry in the future. Simultaneously, using a simplified hydrodynamic model, a relatively large flow velocity is expected to occur on this temporal and spatial scale even with a slight interfacial tension difference. This non-uniform interfacial flow caused by heat and mass transfer will make an effective contribution to the microscale mixing in the vicinity of the electrode.

References

1. Chen GZ, Fray DJ, Farthing TW (2000) Direct electrochemical reduction of titanium dioxide to titanium in molten calcium chloride. *Nature* 407:361
2. Ono K, Suzuki RO (2002) A new concept for producing Ti sponge: calciothermic reduction. *JOM* 54:59–61
3. Suzuki RO, Inoue S (2003) Calciothermic reduction of titanium oxide in molten CaCl_2 . *Metall Mater Trans B* 34:277–285
4. Suzuki RO, Ono K, Teranuma K (2003) Calciothermic reduction of titanium oxide and in-situ electrolysis in molten CaCl_2 . *Metall Mater Trans B* 34:287–295
5. Watanabe N, Nakanishi K, Komura A, Nakajima T (1968) Solubility of lithium in molten lithium chloride-potassium chloride system. *J Soc Chem Ind Jpn* 71:1599–1602
6. Watanabe N, Nakanishi K, Nakajima T (1974) The dissolution of lithium in molten lithium chloride. *Nippon Kagaku Kaishi* 1974:401–404
7. Heymann E, Martin RJL, Mulcahy MFR (1943) Distribution equilibria between molten metals and molten salts, with reference to the stability of intermetallic in the molten state. *J Phys Chem* 47:473–484
8. Merwin A et al (2016) Presence of Li clusters in molten LiCl-Li. *Sci Rep* 6:25435
9. Guo J, Merwin A, Benmore CJ, Mei ZG, Hoyt NC, Williamson MA (2019) Fluid Structure of Molten LiCl-Li Solutions. *J Phys Chem B* 123:10036–10043
10. Haarberg GM, Johansen SR, Melaas J, Tunold R (1990) Nucleation of droplets and metal fog during deposition of liquid Mg from molten chlorides. *ECS Proc* 1990:449–456
11. Zhuxian Q, Liman F, Grjotheim K, Kvande H (1987) Formation of metal fog during molten salt electrolysis observed in a see-through cell. *J Appl Electrochem* 17:707–714
12. Yasuda K, Nohira T, Ogata YH, Ito Y (2005) Electrochemical window of molten LiCl-KCl- CaCl_2 and the Ag+/Ag reference electrode. *Electrochim Acta* 51:561–565
13. Natsui S, Sudo T, Kaneko T, Tonya K, Nakajima D, Kikuchi T, Suzuki RO (2018) Spontaneous colloidal metal network formation driven by molten salt electrolysis. *Sci Rep* 8(1):13114
14. Prins MWJ, Welters WJJ, Weekamp JW (2001) Fluid control in multichannel structures by electrocapillary pressure. *Science* 291:277–280
15. Guo J, Merwin A, Benmore CJ, Mei ZG, Hoyt NC, Williamson MA (2019) Fluid Structure of Molten LiCl-Li Solutions. *J Phys Chem B* 123(47):10036–10043
16. Shibuya R, Natsui S, Nogami H, Kikuchi T, Suzuki RO (2020) Characterization of the cathodic thermal behavior of molten CaCl_2 and its hygroscopic chloride mixture during electrolysis. *J Electrochem Soc* 167(10):102507
17. Janz GJ, Tomkins RPT, Allen CB, Downey JR Jr, Garner GL, Krebs U, Singer SK (1975) *J Phys Chem Ref Data* 4:962

18. Nagasaka Y, Nakazawa N, Nagashima A (1992) Experimental determination of the thermal diffusivity of molten alkali halides by the forced Rayleigh scattering method. I. Molten LiCl, NaCl, KCl, RbCl, and CsCl. *Int J Thermophys* 13(4):555–574
19. Ranz WE, Marshall WR (1952) Evaporation from drops. *Chem Eng Prog* 48(3):141–146
20. Bale CW, Bélisle E, Chartrand P, Deckerov SA, Eriksson G, Gheribi AE, Hack K, Jung I-H, Kang Y-B, Melançon J, Pelton AD, Petersen S, Robelin C, Sangster J, Spencer P, Van Ende M-A (2016) Reprint of: FactSage thermochemical software and databases, 2010–2016. *Calphad* 55:1–19

X-ray Radiography Study on Defect Analysis of Electron Beam Welded Plain C-Steel and Fe-7% Al Alloy Joints



Soumitra Kumar Dinda, Prakash Srirangam, and Gour Gopal Roy

Abstract Low C-steel to Fe-7%Al alloy dissimilar joint by electron beam welding (EBW) was carried out using oscillating beam, without oscillating beam and by increasing welding speed condition. X-ray radiography technique at sub-micron resolution was employed to study the effects of scanning parameters on the defect formation. Detection and quantification of defects within welds were subsequently carried out from radiography images by image processing, segmentation of images and pattern recognition. X-ray radiography images showed the presence of porosity, wormhole and lack of fusion-type defects in the dissimilar joints. Quantitative analysis of weld defects demonstrated that beam oscillation provides better quality weld by decreasing approximately 58% porosity compared to its non-oscillating counterpart and 73% compared to higher welding speed. Wormhole and lack of fusion defects were observed at other two conditions, which did not observe in welds produced by beam oscillation.

Keywords Sub-micron X-ray radiography · Electron beam welding · Beam oscillation · ImageJ · Porosity · Circularity

Introduction

Nowadays, welding in dissimilar combinations is gaining prominence in automotive, aerospace, nuclear, engineering industries. Butt and tailor blank dissimilar welding of different steels to Al alloy fulfil that requirement [1]. Fuel saving and greenhouse gas emissions are now challenging and attractive task by reducing weight

S. K. Dinda (✉)

Materials Science and Engineering, University of Toronto, Toronto, Canada
e-mail: soumitra.dinda@utoronto.ca

P. Srirangam

Warwick Manufacturing Group (WMG), University of Warwick, Coventry, UK

G. G. Roy

Metallurgical and Materials Engineering, Indian Institute of Technology Kharagpur, Kharagpur, India

in these sectors. 7–8% addition of aluminium to steel reduces the density of steel approximately 17% [2]. In earlier days, dissimilar materials were bonded together by some mechanical assembling processes such as riveting, clinching and screwing. [3]. New welding techniques in the recent past such as friction welding or any other solid-state welding that bypass to fuse the materials were successfully employed. Different steels to Al alloy welding are quite difficult due to the differences in melting points, thermal expansion coefficients, thermal conductivities, corrosion potentials and mutual solubilities [4, 5]. Conventional list of fusion welding like gas tungsten arc, gas metal arc and submerged arc, etc., is available for the joining of different similar and dissimilar metals. With comparison to all others, laser beam welding (LBW) and electron beam welding (EBW) are considered one of the most sophisticated fusion welding techniques having contamination free weld, narrow heat-affected region, high depth-to-width ratio, less thermo-mechanical distorted, fewer defects, etc. [6–9]. Defect characterization and optimization by different non-destructive tests (NDT) are very important before going for any property-related study. Any types of joining defects like porosity, wormhole, microcracks, lack of proper fusion, etc., can be easily characterized by different techniques. Sub-micron X-ray radiography techniques emerge as one of the most appropriate NDT techniques and software also able to analysis and identify most all types of weld defects from the radiograph images. The main fundamental concept is that the defective/improper area absorbs more energy compared. As a result, defect portion appears to be darker portion within the image. Radiograph images can identify lots of weld defects and listed here in Fig. 1. Different mechanical weld properties greatly depend on various defect formations in the welded joints [10, 11]. Therefore, defect characterization is primitive steps to understand the influence of weld parameters on the quality assessment of the joints. From ImageJ user guide in process division for the quantification from its original digital images, techniques are available [12]. Nacereddine et al. [13] did weld defect detection by digital image processing technique of industrial radiography system. They characterized by standard image processing way, i.e., select of the region of interest, filtering, noising, contrast enhancement and thresholding. Wang et al. [14] detected different welding defects of radiographic images by using support vector machine (SVM) and also compared with other methods say k-means classifier, linear discriminant classifier, k-nearest neighbour classifier and feed-forward neural network. They conclude that the SVM method was best among all these lists of methods. Moghaddam et al. [15] recognized various linear defects such as lack of penetrations, incomplete fusion and external undercut by image processing technique of radiography images and compared with k-nearest neighbour (KNN) and support vector machine (SVM) classifiers. Madani et al. [16] detected different types of welding defects say crack, porosity, burn through and end crater by using image processing and MATLAB software. Murakami et al. [17] did segmentation analysis for detecting different types of weld defects of radiograph images by digital image processing, using smoothing filters, bridge filters, Sobel operations on contrast filters, etc. Saravanan et al. [18] did defects characterization of dissimilar friction stir aluminium to zinc-coated steel joints using digital X-ray radiography. They did noise cancellation by using filters and sharpen the images


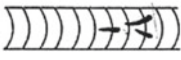



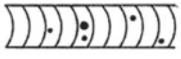

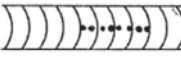

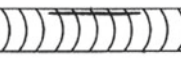

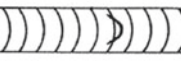



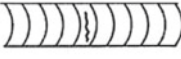


Description	Cross-section of weld	Radiogram
Worm hole		
Linear Slag Inclusion -		
Gas Pore		
Porosity (Linear)		
Lack of side-wall fusion - (lack of root fusion)		
Lack of inter-run fusion		
Longitudinal Crack		
Transverse Crack		
Radiating Cracks		

Fig. 1 Different types of weld defects (in cross section) can analyse from radiographic images. [22]

by gradient operation and contrast adjustment. They detected microcracks to see the effects of different welding parameters such as rotational speed, travel speed and penetration depth. Silva et al. [19] showed that pulsed GMAW produced better quality welds than double-pulsed GMAW technique by reducing porosity. They did porosity quantification and compare between the process by gravimetric and radiographic images. Igathinathane et al. [20] developed plugin for ImageJ in Java for determining length and width orthogonally of singulated particles to measure dimensions of food grains. Greater than 96.6% accuracy, they achieved for laboratory measurements and physical characteristic (dimensional), size-based grading and sieve analysis for size distribution of particles. Igathinathane et al. [21] studied and developed ImageJ plugin to extract the particle dimensions obtained from the digital image by identifying their shapes with their distribution. The plugin produces quick and accurate particle size distribution from its digital images, and it is also applicable for different various particle size studies.

From the previous studies and literature review, it was found that though X-ray radiography was employed in characterising defect formation in the weld joints by different methods, hardly, any paper related to these particular joints and analysis details of radiograph images with required resolution of sub-micron defects could be found. With the advent of laboratory X-ray machines at sub-micron resolution, it is now possible to characterize defects of the weld joints, which are in a size ranging from few microns to sub-micron size. In this study, we present the comprehensive characterisation of weld defect formation in electron beam welded dissimilar joint between plain C-steel and Fe-7% aluminium alloy by using oscillating beam and also by varying its welding speed.

Experimental Procedure

The composition of the parent materials used in the study was: plain C-steel (C = 0.3%, Mn = 0.92%, Si = 0.23%, Fe = rest) and Fe-Al alloys (C = 0.0045%, Al = 6.94%, Mn = 0.20%, Fe = rest). Fe-Al alloy is provided by Tata Steel, UK, and plain C-steel was purchased from market.

Figure 2 represents the schematic view of electron beam welding process using oscillating beam. Beam oscillation at definite periodic patterns alters the direction of the electromagnetic field as depicted in Fig. 2b. Using oscillating beam, improves weld geometry and by restricting molten pool to collapse by controlling root spiking of the weld [24]. Table 1 below shows the parameters used in this present study. Heat input rate was calculated by this formula ((Current*Voltage)/Welding speed)).

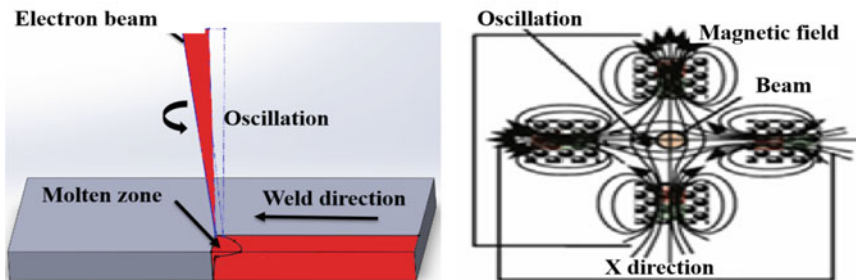


Fig. 2 Schematic of electron beam welding process with oscillating beam [23]. (Color figure online)

Table 1 EBW operating parameters (thickness = 1 mm each, keep beam voltage = 60 kV constant)

Joints	Applied current (mA)	Welding scanning velocity (mm/min)	Oscillation details		Heat input (calculated) (kJ/mm)
			Diameter	Frequency	
Joint 1	17	1000	1.0 mm	600 Hz	0.061
Joint 2	17	1000	–	–	0.061
Joint 3	19.3	1500	–	–	0.041

Table 2 Radiography scanning parameters used

Voltage (kV)	100
Power (W)	9
Exposure (s)	50
Optical magnification	4X
Voxel size (μm)	2.27

X-ray Radiography

Sub-micron X-ray radiography experiments were carried out by using the Zeiss Versa 520 scanning system. For 2D observation of any weld defects with their quantification, can easily characterized by using this system. The main principle of the study is that the material is fixed on the rotating platform within the X-ray source and detector where the exact position will be adjusted according to the material size and required observation. When X-ray beam on and into the material, they may pass through or attenuated. Thus, form the greyscale radiograph on the other side on the detector screen. Scanning parameters for radiography experiments used in this study are listed in below Table 2.

Image Processing

The radiography images and its quality are the main factor for different weld defect detections and identifications. Different machine parameters such as film type, film density, focus-film distance, source energy level, exposure time and developer temperature were controlled so that an image with satisfactory quality could be obtained for subsequent detection and defect classification [25]. The FFT band-pass filter had the best performance, and it is used here for noise reduction, without removing relevant defects and without decreasing image sharpness [26]. Parameters used in FFT band-pass filter are listed in Table 3 below. After using filter, adjust brightness/contrast for better vision of the images. Thresholding was the last stage in digital image processing of radiographs where it separates the regions of interest in the image. The main intention is to eliminate irrelevant information, which leaves

Table 3 Parameters used in FFT band-pass filter in this study

Filter large structures down to (pixels)	30
Filter small structures up to (pixels)	15
Suppress stripes	None
Tolerance of direction (%)	5

only portion of interest such as different types of defects by differentiating or partitioning of pixels having the relationship between pixel and threshold value [27]. Thresholding was done by automatic algorithm named ‘Otsu’ with dark background. After getting final images, particles were analyzed by giving size ranges from zero to infinity and circularity ranges from zero to 1.0 with outlines.

Results

Figure 3 depicts the radiography image that consists of original images, filtering images and segmented images after thresholding for different weld parameters. The first column represents the original radiography images of all joints. The second column was the intermediate steps during analysis of original images named filtered

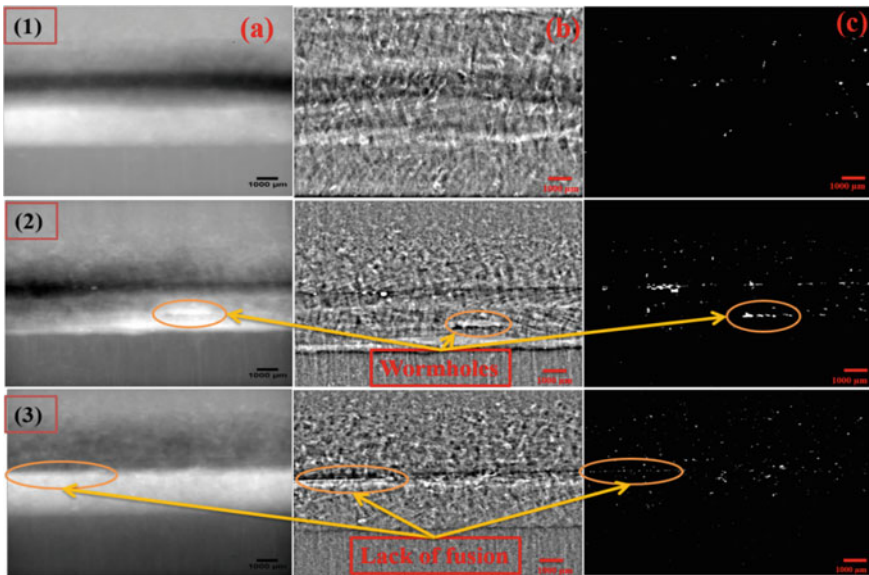


Fig. 3 Radiography images of column **a** original high resolution, **b** filtering images and **c** segmented images for welds: (1) Joint 1: first row: porosity having small diameter, (2) Joint 2: second row: porosity but large quantity (circle spot over the whole area) and wormhole, (3) Joint 3: third row: improper or lack of fusion (horizontal in middle portion). (Color figure online)

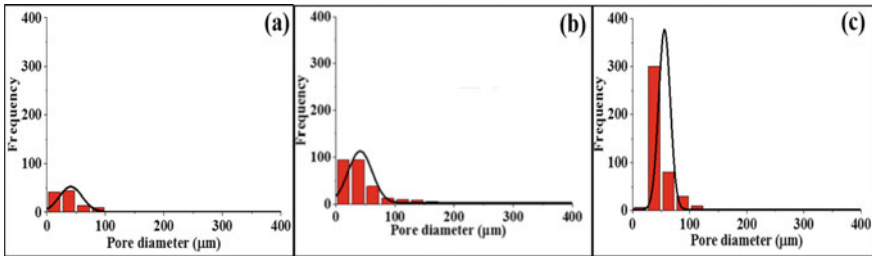


Fig. 4 Bar diagrams for pore size distribution for all three welded joints **a** Joint 1, **b** Joint 2, **c** Joint 3. (Color figure online)

images, and the third column was the final segmented images, which consists of different weld defects. Compared to the welds for Joint 2, the weld quality for Joint 1 obtained with beam oscillation showed only small-sized pores without any kind of other defects. Wormhole defects were seen in Joint 2, and also, the size of the pores was found to be larger. For Joint 3, pore density was found to be higher compared to other two joints. Lack of fusion or lack of penetration was also found to occur at the transition area of two base materials in case of Joint 3. Measured length for lack of fusion was estimated as 4594 μm approximately by ImageJ scale bar.

Figure 4 shows the pore size for all three joints in the same scale. It was seen that for Joint 1, the amount of pores was minimum, and the size is mostly below 50 μm . For Joint 2, the amount of pores is approximately twice that of Joint 1. Although the majority of pore size was mostly around 50 μm , bigger size pores were also significant. For Joint 3, the largest number of pores was seen. Here, also, 50 μm pores were more prevalent, but bigger size pores were also significant. Table 4 shows the comparative quantified results from radiograph images. It was seen that the average pore size for Joint 1 was 37.8 μm , while it was 42.7 μm for Joint 2. Maximum pore size in Joint 1 also reduced to 120.9 μm from 357.2 μm in Joint 2. Joint 1 provides 90% pores within 80 μm range compared to 175 μm range for Joint 2, and its decreased to 100 μm for Joint 3 (1500 mm/min). Found wormhole type of defects for Joint 2. That may be due to more gas entrapment, providing larger pores. Because of higher welding speed (Joint 3), maximum pore size decreased (175 μm) compared to the slower one (Joint 2) (357.2 μm), but the number of pores (427) and average pore size (48.4 μm) increased. Lack of fusion or lack of penetration found

Table 4 Quantitative comparison of pores among three different welded samples

Joints	Maximum diameter (μm)	Minimum diameter (μm)	Average diameter (μm)	No of pores	Pores > 75 μm diameter	Max % ranges (μm)
Joint 1	120.9	7.5	37.8	113	12	0–80
Joint 2	357.2	7.5	42.7	269	41	0–175
Joint 3	175	7.5	48.4	427	33	0–100

for Joint 3 is due to higher speed having less time for complete welding took place. From these radiography results, it can be summarized that beam oscillation reduced pores both qualitatively and quantitatively compared to both non-oscillating beams. Other type of defects was also not found with use of beam oscillation. For every joint, the percentage of pores having diameter above 75 μm was calculated, and the results were plotted in Fig. 5a and the corresponding pore numbers in Fig. 5b. As shown in Fig. 5a, Joint 3 contained minimum (7.7%) of larger pores (diameter above 75 μm) and maximum for Joint 2 (15.3%) and in between for Joint 1 (10.6%). Generally, above 75 μm diameter pores, it is considered as macrosize pores [28]. For Joint 2, macropores percentage was maximum. Figure 5b shows that in case of Joint 3, the number of pores is maximum, and it is minimum for Joint 1.

Equation 1 shows the equation of circularity index to identify pore morphology characteristics at different conditions. Figure 6 depicts the variation of the calculated circularity values with different sizes of pores in welded joints. Pore morphology in 2D way was characterized by circularity formula defined by Eq. 1 [29]. Small size pores mostly having circularity index close to 0.8 to unity indicate roughly circular

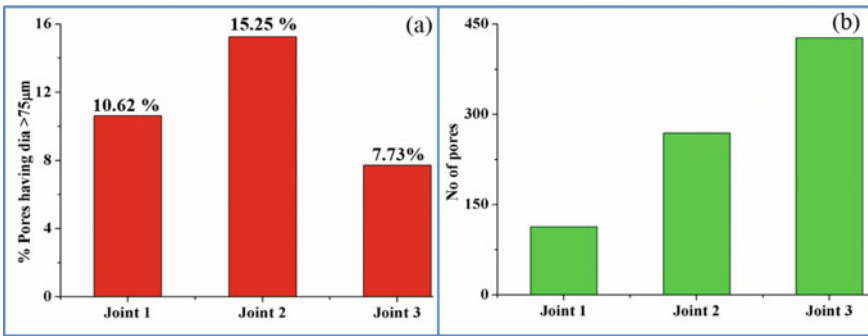
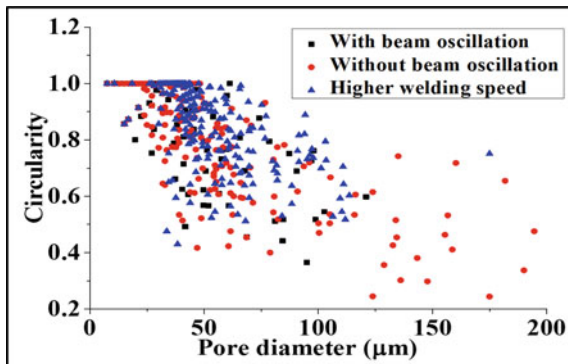


Fig. 5 Bar diagrams comparisons showing a pores % having diameter above 75 μm , b corresponding pore number for all three joints. (Color figure online)

Fig. 6 Pores circularity calculation of all joints from radiography data. (Color figure online)



pores, whereas for higher diameter pores, this value was generally between 0.5 and 0.8 indicating most irregular or anisotropic pores. Bubbles or pores having circularity index close to unity could be due to the gas entrapment within the welded joints.

$$Circularity = 4 \times \Pi \times \left(\frac{Area}{perimeter^2} \right) \quad (1)$$

Discussion

The goals of our present experiments are to optimize the weld parameters by weld defect characterization qualitatively and quantitatively. ImageJ software was used for analysis of sub-micron X-ray radiograph images at three different welded samples, i.e. oscillating beam, without oscillating beam at various welding speed. Porosity and other gas defects mainly happen possibly due to gas entrapment during solidification. In spite of keeping high vacuum in EBW process, it is still possible for very small air being trapped between two clamped surfaces of the materials [30]. One more phenomenon that might be responsible for porosity formation is the keyhole instability. Keyhole instability mechanism was not understood fully till date, and it is unlikely the phenomena in case of full penetration. Oscillating beam produced molten bath churning phenomena that aids more mixing of dissolved gases and remelting of a spot several times that facilitates more chance to remove or leave of gases from fusion weld bead. As an output, it leads to the generation of uniformly distributed pores having smaller in size compared to from non-oscillating counterparts. Wormhole type welding defects are formed due to insufficient materials flow during welding [31]. Due to improper mixing, less homogenization, lack of material flow may lead to the formation of wormhole type of defects at welds produced by non-oscillating beam. Keeping fixed power input, by increasing welding speed for normal beam (without oscillation), the input energy rate reduces and subsequently increases its cooling rates. As a result, entrapped gases faced insufficient time to release from the weld bead and effectively increase its porosity formation chances [32]. Due to the lower time, coalesce of pores is also not possible, which yields large pore density compared to lower welding speed. Percentages of macropores are reduced in this welding condition. Atwood et al. also reported that the higher solidification speed effectively reduced its porosity diameter and increase in pores number and porosity formed because of diffusion-controlled growth of hydrogen in Al-Si castings [33]. Fu et al. reported less defects and better quality of the welds produced by beam oscillation [34]. In our recent study on metallurgical and mechanical properties of same welded materials, it is demonstrated that beam oscillation provided more uniform and homogeneous structure which provides excellent mechanical performance compared to its non-oscillating counterpart. By increasing welding scanning speed, deteriorate its properties [35]. Thus, our present defect analysis strengthens our properties study.

Conclusions

1. Fe-7% aluminium alloy to plain C-steel plate dissimilar welding was successfully carried out using both oscillating and non-oscillating beams at different welding scanning velocities. Sub-micron range X-ray radiography study is performed to visualize the porosity and other defects with their quantifications.
2. By using oscillating beam, welded joints found better in quality by controlling porosity value with their diameter and number value of 58% compared to its non-oscillating counterparts at fixed welding speed. Wormhole and lack of fusion defects were observed for other two non-oscillating beam joints, which did not observe for oscillating one.
3. Quantification data from analysis also shows that non-oscillating joint having higher in scanning speed increases its porosity value approximately 73% and average size also from its lower welding speed joints.

Acknowledgements We acknowledge to Dr. Arunansu Halder, Tata steel for Fe-Al alloy, Prof. Mark A. Williams and Dr. Jason M. Warnett from WMG for allowing us to carry out the experiment and support during analysis. Authors thank to UKERI project (UK-India collaborative project) for financial support.

References

1. Chen YC, Bakavos D, Gholinia A, Prangnell PB (2012) *Acta Mater* 60:2816
2. Chaudhary S, Khaple S, Satya Prasad VV, Sambasiva Rao A, Baligheid RG (2015) *Trans. IIM* 68:809
3. Lee WB, Schmuecker M, Mercardo UA, Biallas G, Jung SB (2006) *Scripta Mater* 55:355
4. Bandi B, Dinda SK, Kar J, Roy GG, Srirangam P (2018) *Vacuum* 158:172
5. Dinda SK, Srirangam P, Roy GG (2019) TMS conference proceedings 239
6. Zhao X, Liu Y (2014) *Mater Des* 57:494
7. Zhang LC, Liu Y, Li S, Hao Y (2018) *Adv Eng Mater* 20:1
8. Dinda SK, Kar J, Jana S, Roy GG, Srirangam P (2019) *J Mater Process Tech* 265:191
9. Liu YJ, Li SJ, Wang HL, Hou WT, Hao YL, Yang R, Sercombe TB, Zhang LC (2016) *Acta Mater* 113:56
10. Potesser M, Schoeberl T, Antrekowitsch H, Bruckner J (2006) *EPD Congress* 167
11. Kar J, Dinda SK, Roy GG, Roy SK, Srirangam P (2018) *Vacuum* 149:200
12. Contributors I, Publications IR (2017) *D. R. History* 29:1
13. Nacereddine N, Zelmat M, Belaifa SS, Tridi M (2016)
14. Wang X, Wong BS, Tan C (2010) *Research journal of applied sciences. Engg Tech* 2:295
15. Moghaddam AA, Rangarajan L (2016) *Pattern Recogn Image Anal* 26:54
16. Madani S, Azizi M (2015) *CumhuriyetSci J* 36
17. Murakami K (1990) *Weld Int* 4:144
18. Saravanan T, Das H, Arunmuthu K, Philip J, Rao BPC, Jayakumar T, Pal TK (2014) *STWJ* 19:125
19. Da Silva CLM, Scotti A (2006) *J Mater Process Technol* 171:366
20. Igathinathane C, Pordesimo LO, Batchelor WD (2009) *Food Res Int* 42:76

21. Igathinathane C, Pordesimo LO, Columbus EP, Batchelor WD, Methuku SR (2008) *Comput Electron Agric* 63:168
22. Valavanis I, Kosmopoulos D (2010) *Expert Syst Appl* 37:7606
23. Dinda SK, Warnett JM, Williams MA, Roy GG, Srirangam P (2016) *Mater Des* 96:224
24. Mara GL, Funk ER, McMaster RC, Pence PE (1974) *Weld J* 246
25. Ahmadi RH, Matsuo H (1991) *Oper Res* 39:42
26. Ingale N, Borkar A (2013) *Inter J Sci Eng Res* 4:85
27. Chen S, Leung H (2004) *J Electron Imaging* 13:220
28. <https://www.soils.org/publications/soils-glossary>, (2017) 4
29. *Analyze/Set Measurements* (2017)
30. Huang JL, Warnken N, Gebelin JC, Strangwood M, Reed RC (2012) *Acta Mater* 60:3215
31. Kryukov I, Hartmann M, Mund M, Dilger K (1991) 32:50
32. Liu H, Wang H, Zhang Z, Huang Z, Liu Y, Wang Q, Chen Q (2019) *J Alloy Compd* 03:151937
33. Atwood RC, Sridhar S, Zhang W, Lee PD (2000) *Acta Mater* 48:405
34. Fu P, Mao Z, Zuo C, Wang Y, Wang C (2014) *Chin J Aeronaut* 27:1015
35. Dinda SK, BasiruddinMSk, Roy GG, Srirangam P (2016) *Mater SciEngg: A* 677:182

Part XIII
Advances in Powder and Ceramic
Materials Science

Biodegradability and Bioactivity of Porous Hydroxyapatite–Hardystonite–PCL for Using in Bone Tissue Engineering Application



Fariborz Tavangarian, Sorour Sadeghzade, and Rahmattollah Emadi

Abstract A study on the bioactivity and mechanical properties of the porous hydroxyapatite–hardystonite–PCL was performed, and the results were compared with the non-modified porous hydroxyapatite. Different apatite morphologies were observed in these two modified and unmodified scaffolds. The compression strength, modulus and toughness of the modified scaffolds showed 104, 14 and 38% improvement compared to unmodified scaffolds. This can be ascribed to the main role of thin polymer-ceramic coating layer applied on the surface of hydroxyapatite scaffolds on the mechanical and biological properties. These composite scaffolds showed a great potential to be used for bone tissue engineering application.

Keywords Hydroxyapatite · Hardystonite · Polymer · Coating · Scaffold

Introduction

In tissue engineering field, many attempts have been focused on preparing highly porous scaffolds with appropriate mechanical strength and bioactivity [1, 2]. An interconnected porous structure in scaffolds can mimic architecture and function of the extracellular matrix while providing a pathway for intercellular communication and allowing the exchange of nutrient and waste and ingrowth of cell and vascular [3, 4]. Various methods including phase separation, electrospinning, space holder method, and gel casting techniques are utilized to prepare porous scaffolds for bone tissue engineering applications [5, 6]. However, these methods are restricted by morphology, interconnectivity and size of pores. Hence, using the natural bovine bone scaffolds can be new methods for designing a scaffolds near the human bone

F. Tavangarian (✉)

Mechanical Engineering Program, School of Science, Engineering and Technology,
Pennsylvania State University, Harrisburg, Middletown, PA 17057, USA
e-mail: fut16@psu.edu

S. Sadeghzade · R. Emadi

Materials Research Group, Department of Materials Engineering,
Isfahan University of Technology, 84156-83111 Isfahan, Iran

© The Minerals, Metals & Materials Society 2021

TMS 2021 150th Annual Meeting & Exhibition Supplemental Proceedings,

The Minerals, Metals & Materials Series,

https://doi.org/10.1007/978-3-030-65261-6_32

[7]. Based on the literature, hydroxyapatite (HA) is widely used for bone tissue engineering applications. Despite its excellent biological properties, HA has shown a weak mechanical property and biodegradability [8, 9]. This is the drawback of these materials which restrict its use in load-bearing applications. Therefore, combination of hydroxyapatite with silicate-based ceramics and polymer coatings has been useful for obtaining nanocomposite materials with high mechanical and biodegradability properties of scaffolds [10]. The aim of this study was fabrication of nanocomposite porous hydroxyapatite-hardystonite-PCL using natural bovine bone to take the advantage of its high mechanical and biological properties.

Material and Methods

In this study, the spongy part of bovine bone was cut to rectangular samples with $10 \times 10 \times 18$ mm in size. First, all rectangular samples sintered at 900°C for 1 h. Then, all rectangular scaffolds were coated with 0, 5, 10 and 15 wt% nanostructured hardystonite/PCL composite. Briefly, PCL polymer (10 wt%) was dissolved in 50 cc dichloromethane. Then, the nanohardystonite with 0, 5, 10 and 15 wt% was added to the solution. Then, the samples are soaked for 30 min in solution, and the samples are heated at 45°C for 5 h in an oven.

To evaluate the morphology of pores, the scanning electron microscopy (SEM, Philips XL30 with acceleration voltage of 10–30 kV) coupled with energy-dispersive spectroscopy (EDS) was used. In order to evaluate the apatite formation ability, the optimum sample based on the mechanical properties was soaked in simulated body fluids (SBFs) with pH of 7.4 and at a temperature of 37°C . The functional groups of samples after immersion in simulated body fluid (SBF) for 21 days were evaluated by Fourier transform infrared spectroscopy (FTIR, JASCO 680 PLUS) in the range of $400\text{--}4000\text{ cm}^{-1}$. The percentage of porosity was measured using DahoMeter DE-120 M densimeter.

Results and Discussion

Table 1 shows the mechanical and physical properties of natural hydroxyapatite (NHA) scaffold compared to hydroxyapatite-hardystonite-PCL (NHA-HT-PCL) composite scaffolds with various wt% of hardystonite. The porosity of NHA, NHA-5wt%HT-PCL, NHA-10wt%HT-PCL and NHA-15wt%HT-PCL scaffolds was $95 \pm 1\%$, $94 \pm 2.5\%$, $91 \pm 1.5\%$ and $90 \pm 1.3\%$, respectively. As shown, after coating the samples a decreasing trend in porosity of scaffolds was observed. Also, applying the coating resulted in an increase in the compressive strength and modulus of NHA (0.5 ± 0.1 MPa and 112.13 ± 5.41 MPa) to 0.51 ± 0.1 MPa, 114.5 ± 4.31 MPa,

Table 1 Mechanical and physical properties of different samples

Sample	Compressive strength (MPa)	Compressive modulus (MPa)	Porosity (%)	Toughness (KJ/m ³)
NHA	0.5 ± 0.1	112.13 ± 5.41	95 ± 1%	0.71 ± 0.1
NHA-5 wt%HT-PCL	0.51 ± 0.1	114.5 ± 4.31	94 ± 2.5%	0.72 ± 0.1
NHA-10 wt%HT-PCL	1.02 ± 0.1	128.1 ± 5.21	91 ± 1.5%	0.98 ± 0.1
NHA-15 wt%HT-PCL	0.9 ± 0.1	171.12 ± 6.21	90 ± 1.3%	0.91 ± 0.1

1.02 ± 0.1 MPa, 128.1 ± 5.21 MPa, 0.9 ± 0.1 and 171.12 ± 6.21 MPa for NHA-5wt%HT-PCL, NHA-10 wt%HT-PCL and NHA-15wt%HT-PCL scaffolds, respectively. Increasing the toughness is another result of applying the composite coating on the surface of natural hydroxyapatite. The optimum samples based on mechanical properties with appropriate porosity are NHA-10 wt%HT-PCL. Using scaffold with close physical and mechanical properties to human spongy bone is really important to avoid stress shielding phenomenon. As shown in this study, the mechanical properties of the optimum scaffold were in the range of the low load-bearing compressive strength of natural spongy bone (the compressive strength and modulus of natural spongy bone are in the range of 0.2–4 and 120–1000 MPa), respectively [11].

Figure 1a–c shows the SEM micrographs of NHA and NHA-10 wt% HT-PCL composite scaffolds. As shown, the interconnected micropores (in the range of

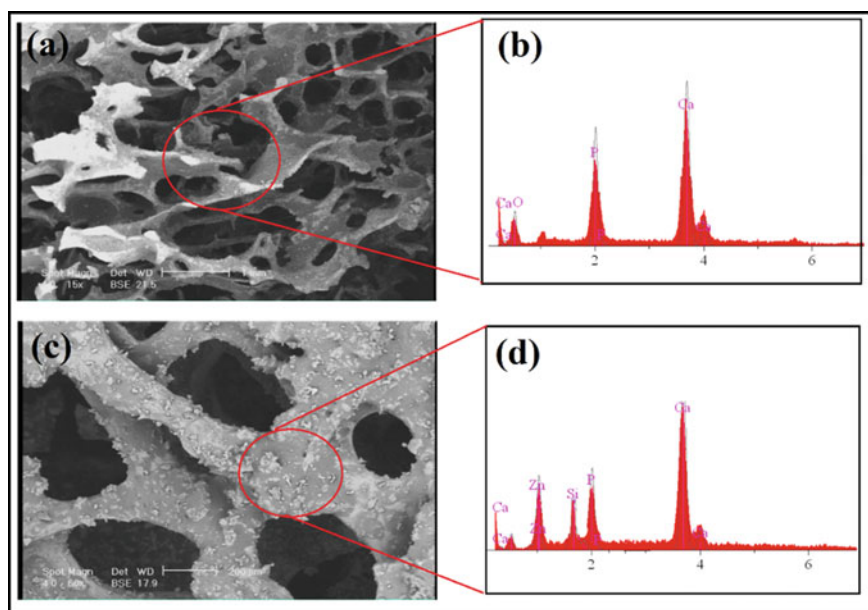


Fig. 1 a SEM micrograph and b EDS spectrum of NHA scaffold, c SEM micrograph and d EDS spectrum of NHA-10wt%HT-PCL scaffold. (Color figure online)

100–200 μm) and macropores (in the range of 800–1000 μm) can be observed in NHA scaffold. While applying the coating decreased the size of micropores as well as the size of macropores. As shown, applying the coating caused a soft and smooth surface without any crack on the NHA-10wt%HT-PCL composite scaffolds. A good agreement is observed between the results of SEM and mechanical properties. Figure 1b–d shows the EDS spectra of NHA scaffold compared to NHA-10wt%HT-PCL composite scaffolds. As shown, the observation of characteristic peaks of Si and Zn peaks confirmed the presence of hardystonite phases in the coating on the surface of NHA ceramic.

To evaluate the apatite formation ability of scaffolds before and after modification, the NHA scaffold and NHA-10wt%HT-PCL composite scaffolds were soaked in SBF for up to 21 days.

Figure 2a shows the SEM images of NHA scaffolds. Some white precipitates with spherical shape were observed on the surface of NHA. Applying the HT-PCL coating on the surface of scaffold resulted in the formation of a sticky layer on the entire surface of the scaffold. It seems that applying this coating led to an increase in biodegradability and bioactivity of NHA scaffold.

Figure 2c and d shows the FTIR patterns of NHA and NHA-10wt%HT-PCL composite scaffolds after 28-day soaking in SBF. The absorption peaks of OH and PO_4 were observed at 635 cm^{-1} and 1080, 1034, 602, 571 and 874 cm^{-1} [12]. In Fig. 2d, the vibration bands of Si–O–Si and Si–O were observed in the range of 1140–910 and $500\text{--}600\text{ cm}^{-1}$ which had an overlap with PO_4 group bands [13]. The

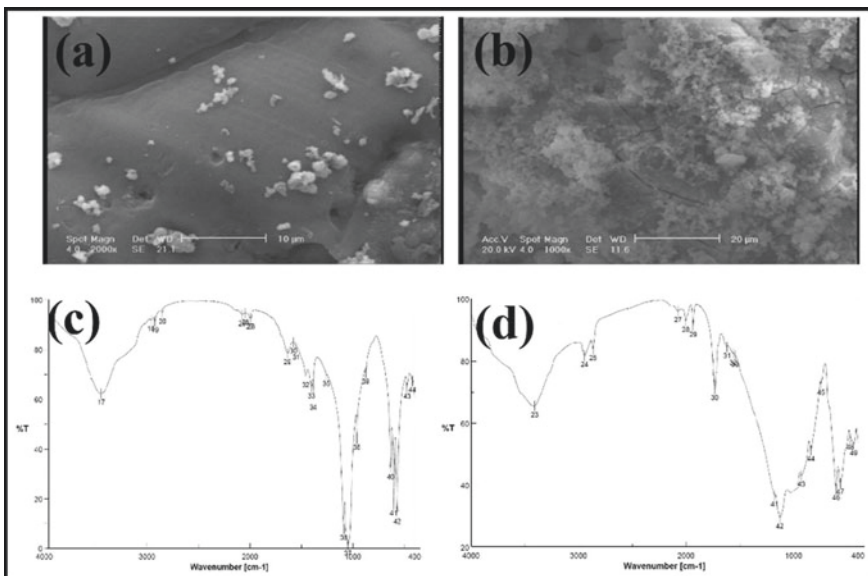


Fig. 2 SEM micrograph of **a** NHA scaffold and **b** NHA-10wt%HT-PCL scaffolds. FTIR spectrum of **c** NHA scaffold and **d** NHA-10wt%HT-PCL scaffold after 21-day soaking in SBF

characteristic peaks of Ca–O and Zn–O at 564 and 511 cm^{-1} confirmed the presence of hardystonite on the surface of scaffold [14, 15]. The new adsorption peaks related to phosphate groups were also detected at 1020, 980, 912, 689 and 614 cm^{-1} . The presence of the carbonate groups at 1400 and 831 cm^{-1} showed the formation of crystalline apatite [11, 12]. The formation of CO bands at 1727 cm^{-1} showed the presence of PCL on the surface of NHA-10 wt% HT-PCL composite scaffolds [10].

Conclusion

In this study, we successfully fabricated the hydroxyapatite–hardystonite–PCL nanocomposite scaffolds by using the natural bovine bone. Based on the mechanical and physical properties, the optimum sample was NHA-10 wt% HT-PCL with compressive strength, modulus, toughness and porosity 1.02 ± 0.1 MPa, 128.1 ± 5.21 MPa, 0.98 ± 0.1 kJ/m^3 and $91 \pm 1.5\%$. Based on the SEM results, modifying the surface of the scaffold results in improving the apatite formation ability of scaffolds. Furthermore, applying the polymer ceramic coating on the initial scaffolds increased the mechanical strength of the samples. Modifying the hydroxyapatite scaffolds with this procedure can result in a better mechanical properties that can match with the site of implantation and prevent the failure of the scaffolds after the surgery.

References

1. Arifvianto B, Zhou J (2014) Fabrication of metallic biomedical scaffolds with the space holder method: a review. *Mater (Basel)* 7:3588–3622
2. Roohani-Esfahani SI, Dunstan CR, Davies B, Pearce S, Williams R, Zreiqat H (2012) Repairing a critical-sized bone defect with highly porous modified and unmodified baghdadite scaffolds. *Acta Biomater* 8:4162–4172
3. Ni S, Chang J, Chou L (2008) In vitro studies of novel CaO–SiO₂–MgO system composite bioceramics. *J Mater Sci Mater Med* 19:359–367
4. Sadeghzade S, Emadi R, Labbaf S (2016) Formation mechanism of nano-hardystonite powder prepared by mechanochemical synthesis. *Adv Powder Technol* 27:2238–2244
5. Sadeghzade S, Emadi R, Ahmadi T, Tavangarian F (2019) Synthesis, characterization and strengthening mechanism of modified and unmodified porous diopside/baghdadite scaffolds. *Mater Chem Phys* 228:89–97
6. Soleymani F, Emadi R, Sadeghzade S, Tavangarian F (2019) Applying Baghdadite/PCL/Chitosan nanocomposite coating on AZ91 magnesium alloy to improve corrosion behavior. *Bioactivity, Biodegradability, Coatings* 9:789
7. Kim JY, Lee JW, Lee S-J, Park EK, Kim S-Y, Cho D-W (2007) Development of a bone scaffold using HA nanopowder and micro-stereolithography technology. *Microelectron Eng* 84:1762–1765
8. Ng AMH, Tan KK, Phang MY, Aziyati O, Tan GH, Isa MR, Aminuddin BS, Naseem M, Fauziah O, Ruszymah BHI (2008) Differential osteogenic activity of osteoprogenitor cells on HA and TCP/HA scaffold of tissue engineered bone. *J Biomed Mater Res A* 85:301–312

9. Sadeghzade S, Emadi R, Tavangarian F, Doostmohammadi A (2020) The influence of polycaprolactone fumarate coating on mechanical properties and in vitro behavior of porous diopside-hardystonite nano-composite scaffold. *J Mech Behav Biomed Mater* 101:103445
10. Joughehdoust S, Behnamghader A, Imani M, Daliri M, Doulabi AH, Jabbari E (2013) A novel foam-like silane modified alumina scaffold coated with nano-hydroxyapatite–poly (ϵ -caprolactone fumarate) composite layer. *Ceram Int* 39:209–218
11. Gerhardt L-C, Boccaccini AR (2010) Bioactive glass and glass-ceramic scaffolds for bone tissue engineering. *Mater (Basel)* 3:3867–3910
12. Ghomi H, Emadi R, Javanmard SH (2016) Fabrication and characterization of nanostructure diopside scaffolds using the space holder method: effect of different space holders and compaction pressures. *Mater Des* 91:193–200
13. Sadeghzade S, Emadi R, Tavangarian F, Doostmohammadi A (2020) In vitro evaluation of diopside/baghdadite bioceramic scaffolds modified by polycaprolactone fumarate polymer coating. *Mater Sci Eng C* 106:110176
14. Sadeghzade S, Emadi R, Labbaf S (2017) Hardystonite-diopside nanocomposite scaffolds for bone tissue engineering applications. *Mater Chem Phys* 202:95–103
15. Sadeghzade S, Emadi R, Tavangarian F (2016) Combustion assisted synthesis of hardystonite nanopowder. *Ceram Int* 42:14656–14660

Effect on Mechanical Properties of Porous Titanium by Adding Ferrovanadium Powder



Xu Wang, Guibao Qiu, Yilong Liao, Yuanhui Li, and Zhen Ma

Abstract As new structural and functional materials, porous materials have unparalleled advantages compared to dense materials because of their special pore structure. The powder metallurgy technique was utilized to prepare titanium foams by adding space holders to generate pores and FeV_{80} to modify the structure and properties of the materials. The results show that the Ti_xV_y ($x + y = 1$) phase exists in the sintering product after adding FeV_{80} powder. The content of FeV_{80} increases from 0% to 12%, resulting in the initial yield strength increasing from 190.08 MPa to 380.82 MPa; when the content of FeV_{80} is increased to 16%, the initial yield strength decreases to 331.77 MPa. Therefore, the improvement created in the mechanical properties of the porous titanium by adding ferrovanadium alloy is highly significant.

Keywords Yield strength · Powder metallurgy · Ferrovanadium · Property

Introduction

Porosity in materials provides them with many unparalleled functions and properties compared with those of dense materials, meaning that they have a wider range of applications. Generally, the utilization of porous metals can be divided into functional applications and structural applications [1]. Structural applications utilize the energy-absorbing property of metal and its functional applications; however, structural applications also take advantage of the physical traits of porous metals, such as acoustic, thermal, and electromagnetic properties. One of the aims in the field of modern materials is to reduce weight. Porous metal gives a superior performance in

X. Wang · Y. Liao (✉) · Y. Li · Z. Ma
Mingde College of Guizhou University, Gui Yang 550025, China
e-mail: liao Yong@sina.cn

G. Qiu (✉)
Chongqing University, Chongqing 400044, China
e-mail: qiuguibao@cqu.edu.cn

this regard and, at the same time, its abundant pore structure means that it will not lose strength.

Porous metals and their alloys are typically suited to functional applications due to their superior heat-resistance, conductivity, corrosion resistance and moreover their recyclability. These functional materials are widely applied in the aerospace industry, biological medicine, electronics and communications, the petrochemical chemical industry, environmental protection, construction, the automotive industry, heat exchangers, mufflers, shock absorbers, and biological bone substitutes. Their excellent high specific strength, high specific rigidity, good thermal conductivity, superior energy absorption effect, and good damping performance [2–4] add to the desirability of porous metals and their alloys in the wide range of applications for which they are suitable.

According to statistics, 10% of the total V resource is used in the titanium industry for the preparation of Ti alloys and then applied in the aerospace industry, examples of this are Ti6Al4V and Ti10V2Fe3Al. The adding of V alloy increases the strength and improves the plasticity of the material.

A study by Ge and Jinxi [6] reported on the mechanism of Al and V alloy on changing the properties of Ti alloys. The conclusion indicated that the binding force between Ti and V is larger than that of Ti and Ti. Therefore, the adding of V alloy could help to enhance the stability of β -Ti [5]. Huan et al. studied the enhancement effect on a variety of elements, and indicated that Fe alloys have the greatest significance for enhancing the strength of Ti alloys [6]. Niu Wenjuan studied the effect of different elements on improving the properties of porous Ti alloys. The conclusion implies that the adding of moderate Fe could contribute to the density of Ti powder [7]. This chapter mainly studies the increasing porosity of Ti by adding Fe and V alloys.

Experimental Methods and Raw Materials

Raw Materials

The raw materials used in the fabrication of porous titanium using the powder metallurgical technique are titanium (Ti), FeV80 powder, and carbamide. The basis of Ti powder is commercial pure titanium powder with an average particle size of 29.808 μ m and a purity of >99.5%. The FeV₈₀ powder chosen for the alloying element has an average particle size of 26.282 μ m, and the carbamide has an average particle size of 398.438 μ m. The SEM graphs of raw materials are shown in Fig. 1 and Tables 1, 2 depict the purity of the Ti and FeV80.

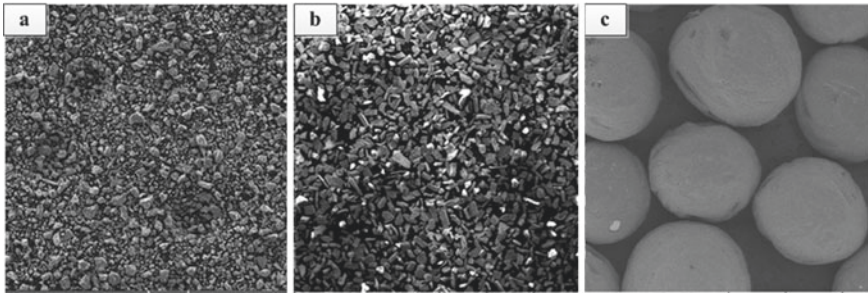


Fig. 1 Raw material: **a**-titanium powder, **b**-ferrovanadium powder, **c**-carbamide

Table 1 Chemical composition of titanium powder

钛粉	Ti	Fe	Si	Cl	C	N	O	H
含量	99.5	0.05	0.03	0.03	0.02	0.01	0.6	0.04

Table 2 Chemical composition of ferrovanadium powder

FeV ₈₀	V	Si	P	S	C	Al	余量
含量	77.58	0.91	0.032	0.046	0.2	0.91	20.32

Experimental Process

In this experiment, the carbamide is designed to comprise 40% in volume of the final product. The content of Ti and FeV₈₀ powders is figured in Table 3, in which entries 1 to 5 give the raw powder that did not have any pretreatment and entries 6 to 10 give the amount of raw powder milled in a high-energy ball-milling machine for the purpose of increasing the reactive interface of the powder.

The raw materials are then compressed into a sample under 200 Mpa pressure and sintered at 1250 °C for 2 h. During the sintering, the samples should be heated to 400 °C and held at that temperature for about 40 mins to ensure the maximum use of the carbamide. The sintering chamber is then filled with high-purity argon gas (99.99%) to prevent oxidation of the samples. After fabrication, the porosity is examined by ImageJ, the pore structure is examined using a scanning electron microscope, and the compressive strength is examined with universal electronic equipment. Finally, the effect of adding Fe and V elements together with the pretreatment on the mechanical properties of the samples is studied.

Table 3 The compositions of porous titanium alloys

Sample number	Alloying element(60vol%)		Carbamide content
	Ti	FeV ₈₀	
1#	100 wt% Ti	0 wt% FeV ₈₀	40 vol%
2#	96 wt% Ti	4 wt% FeV ₈₀	
3#	92 wt% Ti	8 wt% FeV ₈₀	
4#	88 wt% Ti	12 wt% FeV ₈₀	
5#	84 wt% Ti	16 wt% FeV ₈₀	
6#	100 wt% Ti	0 wt% FeV ₈₀	
7#	96 wt% Ti	4 wt% FeV ₈₀	
8#	92 wt% Ti	8 wt% FeV ₈₀	
9#	88 wt% Ti	12 wt% FeV ₈₀	
10#	84 wt% Ti	16 wt% FeV ₈₀	

Pretreatment of Raw Materials

The pretreatment of raw materials (i.e., ball milling) effectively increases the interface between the powders, eliminates microstructural flaws, enhances the activity of the raw materials, and therefore facilitates the sintering (Table 3).

Results and Discussion

The Effect of Ball Milling on Raw Materials

The Ti powder and FeV₈₀ powder are blended in a high-energy ball-milling machine for 1 hour using a rotation speed of 300 r/min to increase the interface energy of the powders and to make the powders homogeneous.

Through pretreatment, the powders are examined by laser particle size analyzer, and the size distribution is described in Fig. 2, from which we conclude that the particle size of the blending powders apparently augments owing to reunion of some small particles after 60 mins of ball milling (Fig. 2).

Figure 3 shows the SEM images of raw materials; image (a) is Ti powder before pretreatment, and image (b) is Ti and FeV₈₀ mixing powders after 60 mins of grinding. It is found that the particle size of raw powders decreases, forming various new surfaces. As the size of metal powders is now finer, and following the ball-milling process the interface energy is enhanced, leading to the recombination of some small particles.

Figure 4 shows the XRD pattern of raw powders after pretreatment. The powders are mixed with Ti and a 16 wt% content of FeV₈₀, and the ball-milling time is 60 mins.

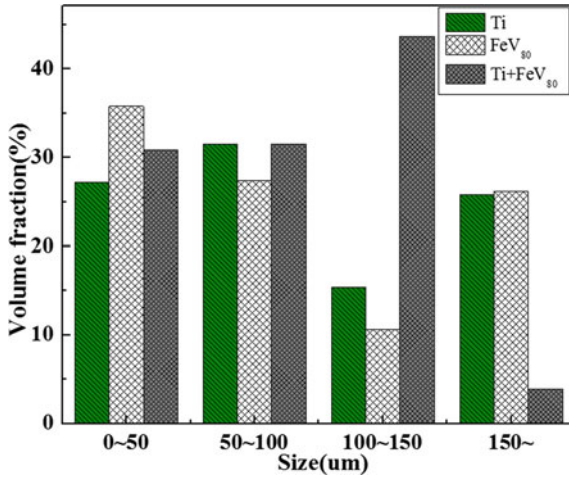


Fig. 2 Particle size distribution of raw material after pretreatment. (Color figure online)

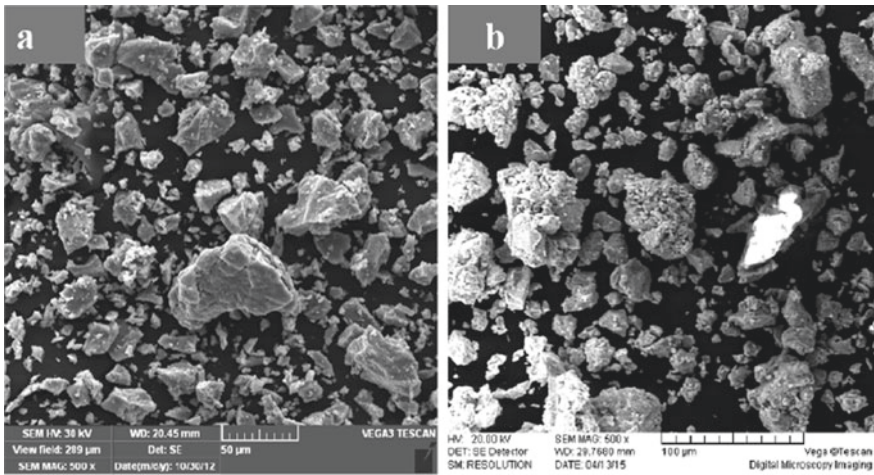
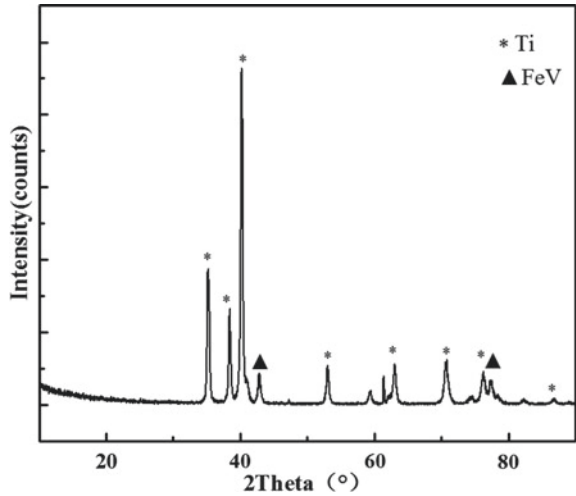


Fig. 3 SEM images of raw materials (a-titanium powder, b-mixing raw material after grinding with FeV₈₀ content of 16 wt%)

The aim of this procedure is to detect whether a new phase would be formed during the grinding process between Ti and FeV₈₀ powders. The conclusion obtained by this procedure is that no new phase forms after grinding.

Fig. 4 XRD pattern of mixing raw material after pretreatment

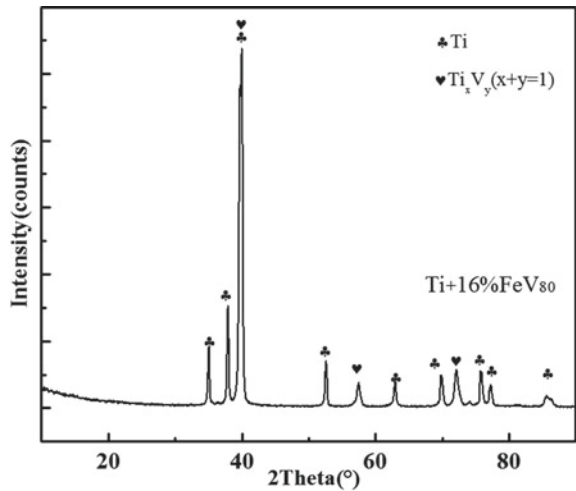


Effect on the Phase and Structure of Material by Adding FeV80 Powder

After sintering, the samples are processed by polishing and grinding to satisfy the requirement of XRD, the aim of which is to observe whether a new phase is formed.

Figure 5 shows the XRD pattern of Ti foams with the FeV₈₀ content equals 16%. The result shows that the sample exits the Ti_xV_y phase, mainly due to the bending force between Ti and V being greater than that of Ti, and that Ti leads to the V atoms replacing Ti atoms.

Fig. 5 XRD pattern of porous titanium



Effect on the Microstructure of Material by Adding FeV80 Powder

Figure 6 shows the powder samples obtained by varying the FeV₈₀ content images (a)–(d) show powders that have not been pre-treated; images (e)–(h) show pre-treated powders. The percentage content of FeV₈₀ is 0 wt% for images (a) and (e), 8 wt% for images (b) and (f), 12 wt% for images (c) and (g), and 16 wt% for images (d) and (h).

In images (a)–(d), the thickness of the sintering neck between particles varies in each image. The pore size is uniform, but the pores are distributed unevenly owing to incomplete sintering. In images (e)–(h), the sintering neck of the Ti is much thicker, from which we can conclude that pre-treatment increases the interface energy, improves the fluency of powders, and greatly enhances the activity of powder material, subsequently modifying the sintering. It can be concluded that the addition of FeV₈₀ and the pre-treatment process improve the properties obtained during sintering.

Fe is a stable element of the eutectoid-type β -Ti, and V is a stable element of eutectic-type β -Ti. Moreover, owing to a high rate of diffusion between Fe and β -Ti, which is about 103 to 105 times quicker than diffusion in β -Ti, the micropores that arise from incomplete sintering are quickly filled with nearby Fe atoms. However, too many Fe atoms cause the Kirkendall effect, mainly due to unequal diffusion between the two phases, leading to a decrease in the initial yield strength. Thus, a moderate amount of Fe helps to reduce the micropores and even promotes the densification of the structure.

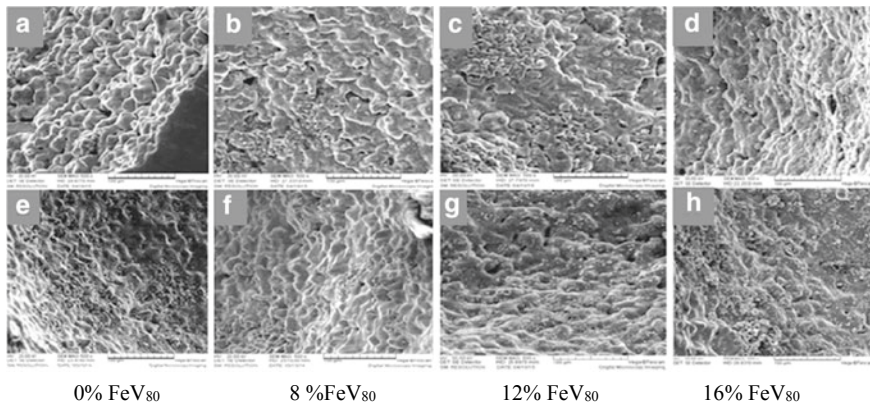


Fig. 6 Effect on microstructure of materials by adding various proportions of FeV₈₀ content ((a)–(d): without grinding; (e)–(h): after grinding)

Effect on the Pore Structure and Mechanical Properties of Material by Adding FeV80 Powder

The pores in the Ti formed after sintering can be divided into two types: macropores that arise from the space holder, and micropores that arise from incomplete sintering and are mainly due to particle size and interface energy. The pore structure is relative to the sintering process, the properties of the raw materials and the alloy elements.

Table 4 shows the initial yield strength of porous Ti alloys by adding different content of FeV80. It is found that porosity decreases as the content of FeV80 increases, indicating that a moderate amount of alloy powder is beneficial for densifying the samples.

The initial yield strength of pure Ti foam is 184.3 MPa; this increases to 281.4 MPa as the content of FeV80 increases to 12wt%. There are two reasons for this improvement. First, the addition of Fe and V promotes the density of the sample, refines the crystalline grain and therefore improves the compressive strength of the materials.

Second, the pre-treatment improves the interface properties, modifies the homogeneity of the mixture and facilitates the sintering of the raw powders. The form of the second phase, Ti_xV_y , helps to improve the properties of the materials. When the FeV80 content is increased to 16wt%, the strength decreases slightly to 277.3 MPa, which mainly due to the Kirkendall effect, which leads to the concentration of pores and therefore results in the reduction of strain (Table 4).

The initial yield strength of Ti foams is achieved by adding varying amounts of FeV₈₀ content to raw powders that were not pre-treated. It is clearly evident that the porosity and compressive strength are similar to those of samples that were pre-treated. However, the density and compressive strength of Ti foams achieved with pre-treatment are obviously superior to those that were not pre-treated, as can be seen by comparing Tables 4 and 5.

From Tables 4 and 5, it is easy to see that the initial yield strength increases with the increasing FeV₈₀ content. However, it should be mentioned that the decrease that occurred at an FeV80 content of 12–16 wt% may be attributable to the Kirkendall effect, which leads to the concentration of pores and subsequently diminishes the properties of the materials (Table 5).

Table 4 Effect of content of FeV₈₀ on porosity and initial yield strength

Alloying component	Porosity (%)	Initial yield strength (MPa)
Ti-0% FeV ₈₀	36.9	184.7
Ti-4% FeV ₈₀	34.8	218.6
Ti -8% FeV ₈₀	35.2	263.9
Ti -12% FeV ₈₀	34.7	281.4
Ti -16% FeV ₈₀	33.6	277.3

Table 5 Effect of FeV₈₀ content on porosity and initial yield strength

Alloy component	Porosity (%)	Initial yield strength (MPa)
Ti-0% FeV ₈₀	37.3	143.6
Ti-4% FeV ₈₀	36.4	183.5
Ti-8% FeV ₈₀	35.9	201.8
Ti-12% FeV ₈₀	36.1	194.6
Ti-16% FeV ₈₀	34.9	198.2

The Principle of Increasing Properties

The modification of the properties of Ti alloy material is achieved by adding an alloying element, the main effects of which are: (1) to change the crystal structure, increasing the crystal symmetry and decreasing the lattice resistance, thus improving the dislocation mobility: in other words, reducing the dislocation energy, with the corresponding alloy elements such as Cr, V, Mn and so on [8]; (2) to refine the microstructural structure, with corresponding alloy elements such as V, B [9]; (3) to instigate the second phase, improve the high-temperature creep resistance and hinder grain boundary migration, the corresponding alloy elements for which are Si, C [10].

The element of V powder not only improves the strength of the materials by refining the grain crystal but also prevents the transformation from β -Ti to α -Ti thereby enhancing the properties of the composites. The phase of β -Ti has the advantages of higher strength, better fatigue resistance performance and corrosion resistance performance, and vastly improved plasticity compared with other Ti alloys. Ge and Jinxu and others study the effect of the addition of V metal [6, 11]. Fe is a eutectoid stable element for β -Ti, indicating that the addition of the appropriate Fe powder is capable of effectively improving the properties of materials, being especially significant with regard to density and hardness [12].

As Fe and V are eutectoid stable elements for β -Ti, their effect on the hardness of Ti alloys is shown in Eqs. (1) and (2):

$$HV(Fe) = 170.660 + 204.023Fe - 86.8653Fe^2 + 16.8563Fe^3 \quad (1)$$

$$HV(V) = 173.029 + 30.375V \quad (2)$$

It may be concluded from the equations (1) and (2) that Fe and V are capable of improving the hardness of Ti alloys. The atomic radius of Ti is 0.147 nm, the atomic radius of Fe is 0.124 nm, and that of V is 0.136 nm, both of which measurements are smaller than that of Ti.

It is this difference in atomic radii and the discrepancy between the various valence electron structures of atoms that efficiently enhances the properties of alloys.

Conclusion

Ti foams were fabricated by means of the powder metallurgical technique using Ti powder and FeV80 powder with carbamide acting as the space holder. The pore structure, phases, microstructure, and compressive strength of products prepared under the temperature of 1250°C, the holding time of 2 h and the vacuum degree of 0.1 Pa were studied and analyzed. The conclusions of the study are as follows:

Pre-treatment helped the raw powder to refine the grain size, increased the roughness of the surface and even enhanced the interface energy, contributing to easy compression. The addition of an alloy element helped to improve the material's microstructure, promoted the densification of the structure, and boosted the strength of the materials.

The addition of FeV80 effectively contributed to speedier sintering of the compacts, improved and densified the structure of the pore wall, smoothed the sintering neck, and thus enhanced the properties of porous Ti. In addition, owing to the binding force between V and Ti atoms being greater than those of Ti and Ti atoms, the formation of Ti_xV_y ($x + y = 1$) simultaneously benefited the improvement properties of porous Ti alloys.

Acknowledgements The work described in this paper was supported by a grant from the Natural Science Foundation of China (Project no. 51174243), for which we are most grateful.

References

1. Lucai W, Fang W (2012) Processing, properties and application of metal foams [M]. National defense Industry Press, Beijing, p 10
2. Boqiong L, Deqing W, Xin L (2004) Study of porous Ti by powder metallurgy[J]. J DaLian Railway Inst 25(1):74–78
3. Lubin C (2007) Structure and properties of porous titanium by powder sintering [D]. Shandong University
4. Niu W, Bai C, Qiu GuiBao, Wang Q (2009) Processing and properties of porous titanium using space holder technique[J]. Mater Sci Eng, A 506(1):148–151
5. Huan W, Yongqing Z, Peng G (2012) Effect of β Stabilizing Elements on the Strengthening Behavior of Titanium α Phase[J]. Rare Metal Mater Eng 05:805–810
6. Honglin Ge, Jinxu Z (1990) Effect of the Al, V on valence electron structures and kinetic theory of phase transition of titanium alloy [J]. Shanghai Steel Res Inst 06:1–4
7. Wenjuan N, Bai C (2010) Preparation and properties of porous titanium using space holder technique [D]. Chongqing University
8. Oh I-H, Nomura N, Masahashi N, Hanada S (2003) Mechanical properties of porous titanium compacts prepared by powder sintering[J]. Scripta Mater 49(12):1197–1202
9. Peiyun H (1977) The principle of powder metallurgy [M]. Metallurgical Industry Press
10. Tuncer N, Arslan G (2009) Designing compressive properties of titanium foams[J]. J Mater Sci 44(6):1477–1484
11. Shouzhong Z (2010) Microstructural features and their influence on the properties of Ti-10V-2Fe-3Al titanium alloy [D]. Shandong University
12. Weidong L, Hua Q (2015) Valence electron structures of β solid solutions and mechanism of alloy elements in titanium alloy[J]. Special Casting Nonferrous Alloys 35(2)

Layered Ceramic Structures $\text{In}_{1+x}(\text{Ti}_{1/2}\text{Zn}_{1/2})_{1-x}\text{O}_3(\text{ZnO})_m$ ($m = 2, 4$ and 6 ; $x = 0.5$): Synthesis, Phase Stability and Dielectric Properties



Victor Emmanuel Alvarez Montaño, Subhash Sharma, Francisco Brown,
and Alejandro Durán

Abstract New ceramic materials with layered crystal structures and chemical formula $\text{In}_{1+x}(\text{Ti}_{1/2}\text{Zn}_{1/2})_{1-x}\text{O}_3(\text{ZnO})_m$ ($x = 0.5$; $m = 2, 4$ and 6), here named ITZO-II, ITZO-IV and ITZO-VI, have been synthesized by solid-state reaction method. The phase characterization, phase stability with temperature and their microstructure have been studied by X-ray powder diffractometry (XRD) and scanning electron microscopy (SEM). The XRD showed a hexagonal single phase at $1200\text{ }^\circ\text{C}$ whereas, at higher temperatures (1300 and $1400\text{ }^\circ\text{C}$), they decompose in secondary phases such as the $\text{In}_2\text{Zn}_7\text{O}_{10}$ solid solution and starting material traces. SEM micrographs showed an increase in grain size as the temperature of sintering increases, reducing the porosity and increasing the bulk density. Here, the dielectric spectra in a wide range of temperatures and frequencies are reported. The permittivity results seem to indicate a classical paraelectric behavior in this class of layered structural ceramic compounds.

Keywords $\text{In}_{1+x}(\text{Ti}_{1/2}\text{Zn}_{1/2})_{1-x}\text{O}_3(\text{ZnO})_m$ · ITZO · Microstructure · Layered crystal structure

V. E. Alvarez Montaño (✉)

Departamento de Ingeniería Química y Metalurgia, Universidad de Sonora, Rosales y Luis Encinas s/n Col. Centro, Hermosillo, Sonora 83000, México
e-mail: victor.alvarez@unison.mx

S. Sharma

CONACYT- Centro de Nanociencias y Nanotecnología, Universidad Nacional Autónoma de México, km. 107 Carretera Tijuana-Ensenada, Apartado Postal 14, 22860 Ensenada, Baja California, México

F. Brown

Universidad de Sonora, Departamento de Investigación en Polímeros y Materiales, Rosales y Luis Encinas s/n Col. Centro, Hermosillo, Sonora 83000, México

A. Durán

Centro de Nanociencias y Nanotecnología, Universidad Nacional Autónoma de México, km. 107 Carretera Tijuana-Ensenada, Apartado Postal 14, 22860 Ensenada, Baja California, México

© The Minerals, Metals & Materials Society 2021

TMS 2021 150th Annual Meeting & Exhibition Supplemental Proceedings,

The Minerals, Metals & Materials Series,

https://doi.org/10.1007/978-3-030-65261-6_34

Introduction

Technology advancement in many areas makes possible to build devices that require to investigate new materials with novel and better specific physical properties. The materials science demand looks into the relation between synthesis, structure and physical properties to impulse the modern technological applications. The investigation of new ceramic materials has been extended towards the study of ternary and quaternary systems [1–3].

Recently, a series of ternary compound-based indium has been studied since the layered crystal structures as well as the electronic properties are of great interest in the areas of electronic and optic properties [4–8]. A reference is the InGaZnO_4 compound, derived from the chemical formula $\text{InGaO}_3(\text{ZnO})_m$ ($m = \text{natural number}$) also known as IGZO [9, 10]. High-electron mobility and a low threshold voltage have proved to be an efficient material since it reduces the energy consumption for electronic devices applications [11–13]. Another derivation of the indium-based oxide systems is the $(\text{Sb}_{1/3}\text{Zn}_{2/3})\text{GaO}_3(\text{ZnO})_3$ which is homologous to the IGZO compound [14]. In both compounds, the structure is stacked in layered built up of trigonal bipyramidal layers sandwiched by InO_6 octahedral layers along the c -direction.

In this work, we report the synthesis of the $\text{In}_{1+x}(\text{Ti}_{1/2}\text{Zn}_{1/2})_{1-x}\text{O}_3(\text{ZnO})_m$ with $m = 2, 4$ and 6 ; $x = 0.5$, using the conventional solid-state reaction. The crystal structure and the phase stability with temperature were characterized by X-ray diffraction. The SEM analysis showed that the increase of sintering temperature from 1200 to 1400 °C increases the grain size. For these materials, the dielectric spectra in a wide range of temperatures and frequencies are presented for the first time.

Materials and Methods

Starting materials of high purity (99.9%), In_2O_3 , TiO_2 and ZnO were heated at 850 °C for 24 h to eliminate humidity. Later, specific starting materials with stoichiometric relations ($\text{In}_2\text{O}_3:\text{TiO}_2:\text{ZnO} = 3:1:9, 3:1:17$ and $3:1:25$) to form $\text{In}_{1.5}(\text{Ti}_{1/2}\text{Zn}_{1/2})_{0.5}\text{O}_3(\text{ZnO})_m$ ($m = 2, 4$ and 6) were weighed and mixed during 25 min in an agate mortar under ethanol. The dry mixture powder was compressed with a mold of stainless steel ($\phi = 13$ mm), applying 2.5 ton of pressure for 5 min using an uniaxial hydraulic press. The samples were placed in high alumina crucibles and calcined at 1200 °C for periods of 2 days, applying intermittent grinding heating cycles. In the final calcination, the samples were quenched (cooling in air) from 1200 °C, and afterwards, the phases were identified by X-ray diffraction. For this analysis, we used an X-ray diffractometer Phillips X'pert MPD, with $\text{Cu-K}\alpha$ radiation (1.5406 Å). The X-ray tube was operated to 45 kV and 40 mA, with a scanning rate of $2^\circ/\text{min}$ in 2θ . Lattice parameters were obtained by means of least-squares refinement. Once that each phase was identified, the powder samples were again

pelletized in a stainless steel die (6 mm diameter) applying a pressure of 0.5 metric tons using a hydraulic press. The disk samples were sintered at 1200, 1300 and 1400 °C in air by 24 h and then quenched in air from 1200 °C to room temperature. An LCR bridge (HP-4284A) was used to obtain the dielectric spectrum from room temperature to ~750 K in the frequency range of 1–100 kHz.

Results

Figure 1 shows the XRD for a) ITZO-II, b) ITZO-IV and c) ITZO-VI, after three different sintering temperatures (1200, 1300 and 1400 °C) and compared to the database IGZO homologous compounds. The database in the bottom XRD profile shows that the $\text{In}_{1.5}(\text{Ti}_{1/2}\text{Zn}_{1/2})_{0.5}\text{O}_3(\text{ZnO})_2$ (ITZO-II), $\text{In}_{1.5}(\text{Ti}_{1/2}\text{Zn}_{1/2})_{0.5}\text{O}_3(\text{ZnO})_4$ (ITZO-IV) were single phase at 1200 °C in air (see Fig. 1 a and b), while $\text{In}_{1.5}(\text{Ti}_{1/2}\text{Zn}_{1/2})_{0.5}\text{O}_3(\text{ZnO})_6$ (ITZO-VI) coexist with $\text{In}_2\text{Zn}_7\text{O}_{10}$ (Fig. 1 c). From this, we understand that more time of reaction is required as the value of m is increased, to get the complete reaction. On the other hand, the XRD profile shows the precipitation of second phases at higher temperature which were identified as $\text{In}_2\text{Zn}_7\text{O}_{10}$ and starting material traces. The results indicate that the phase stability occurs at ~1200 °C. The crystal structure of all compounds is built by layer with hexagonal structure and space group $P63/mmc$ (No. 194) (ICDD No. 00–038–1104). Table 1 shows the lattice parameter and volume which are compared with the IGZO counterpart. We can observe an increasing of the c -parameters and volume with increasing the $(\text{ZnO})_m$ layer. To understand this behavior, it is necessary recall the IGZO structure as is better illustrated in Fig. 2. There, it shows the crystal structure of (a) ITZO and how it is related to that one of IGZO (b). In the IGZO crystal structure instead of Ga/Zn in the trigonal bipyramidal sites, it is substituted by Ti/Zn in the ITZO compound. We can see (Ti/Zn or Ga/Zn) trigonal bipyramidal layers sandwiched by InO_6 octahedral layers along the c -axes. Thus, the lattice parameters (c and volume) grow with increasing the $(\text{ZnO})_m$ by the insertion of bipyramidal layers in the original chemical formula.

In Fig. 3, we present SEM images for the ITZO-II, ITZO-IV and ITZO-VI compounds after thermal treatments at 1200, 1300 and 1400 °C. It is evident that the grain size is notably increased as thermal temperature treatment is raised, reducing porosity and increasing density for samples. Likewise, crystal step patterns are presented with hexagonal forms, due the sintering process. These patterns indicate the presence of hexagonal phases, which is consistent with the X-ray diffraction results, where the ITZO-IV phase continues to be present. The same pattern occurs in phase VI with almost fused hexagonal crystal patterns at 1400 °C.

Figure 4 displays the temperature dependence of the dielectric properties of ITZO-II, ITZO-IV and ITZO-VI measured at several frequencies (50 kHz – 1 MHz) with temperature ranging from room temperature to 500 °C. As it is clear from the Figure, the dielectric constant for the samples decreases as frequency increases, which is the typical nature of dielectric materials [15, 16]. Moreover, It can be understood in terms

Fig. 1 XRD of **a** ITZO-II, **b** ITZO-IV and **c** ITZO-VI, after three different sintering temperatures (1200, 1300 and 1400 °C). (Color figure online)

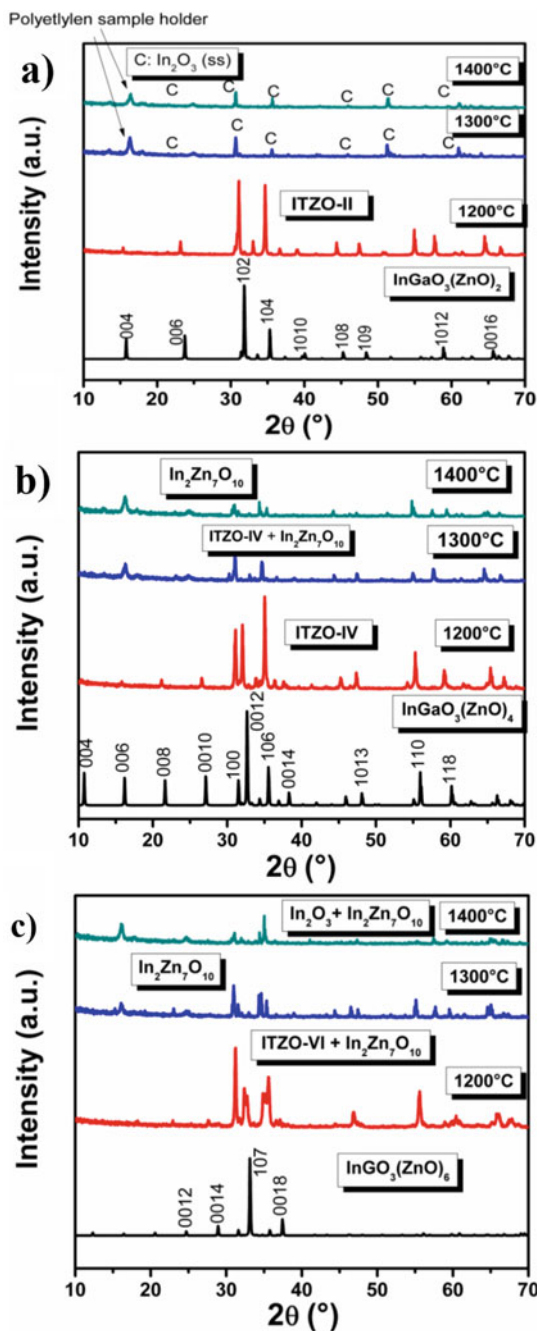
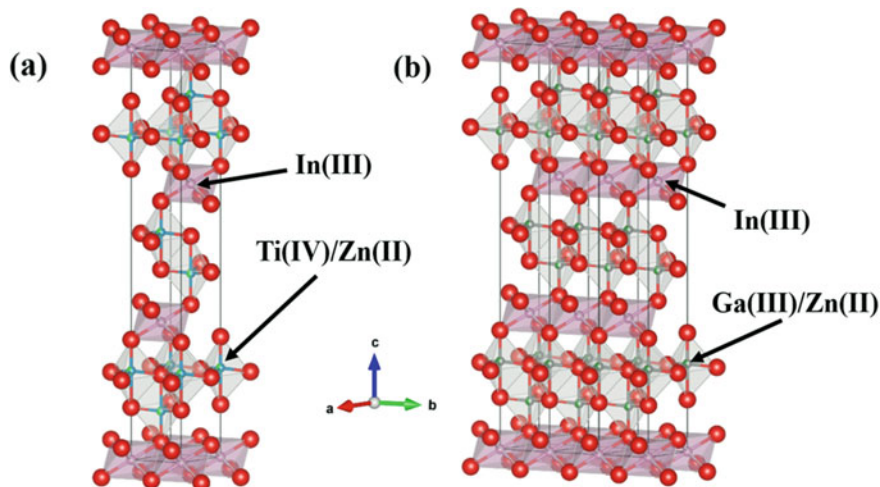


Table 1 Synthesis, crystal structure and lattice parameters of ITZO compounds

Sample	Compound	Crystal system	a(Å)	c(Å)	V(Å ³)
ITZO-II	$\text{In}_{1.5}\text{Ti}_{1/4}\text{Zn}_{1/4}\text{O}_3(\text{ZnO})_2$	Hexagonal	3.334(3)	22.915(2)	220.58(1)
ITZO-IV	$\text{In}_{1.5}\text{Ti}_{1/4}\text{Zn}_{1/4}\text{O}_3(\text{ZnO})_4$	Hexagonal	3.313(5)	33.326(3)	316.78(1)
ITZO-VI	$\text{In}_{1.5}\text{Ti}_{1/4}\text{Zn}_{1/4}\text{O}_3(\text{ZnO})_6$	Hexagonal	3.302(5)	43.064(7)	406.63(1)
IGZO ^a	$\text{InGaO}_3(\text{ZnO})$	Hexagonal	3.295	26.07	245.12

^aICDD PDF# 00–038–1104**Fig. 2** Crystal structure of **a** $\text{In}_{1+x}(\text{Ti}_{1/2}\text{Zn}_{1/2})_{1-x}\text{O}_3(\text{ZnO})$ and **b** $\text{InGaO}_3(\text{ZnO})$. (Color figure online)

of the role of different polarization mechanisms. In the low frequency side, electron displacement polarization, ion displacement polarization, orientational polarization and space charge polarization contribute to dielectric constant, whereas, at high frequency side, dielectric constant results from the electron displacement only or electronic polarization. Furthermore, the dielectric constant found to be increasing in temperature up to a particular temperature for ITZO-II simple may be due to the dielectric phase transition. However, for sample ITZO-IV and ITZO-VI, no such dielectric transition was observed. The dielectric loss of all materials around room temperature is nearly <1 , which is good for some device application; however, at high temperature, the loss becomes high for ITZO-II and ITZO-IV, whereas for ITZO-VI, the loss has been reduced in a significant way. Thus, the temperature dependence of permittivity shows a classical paraelectric behavior for all samples.

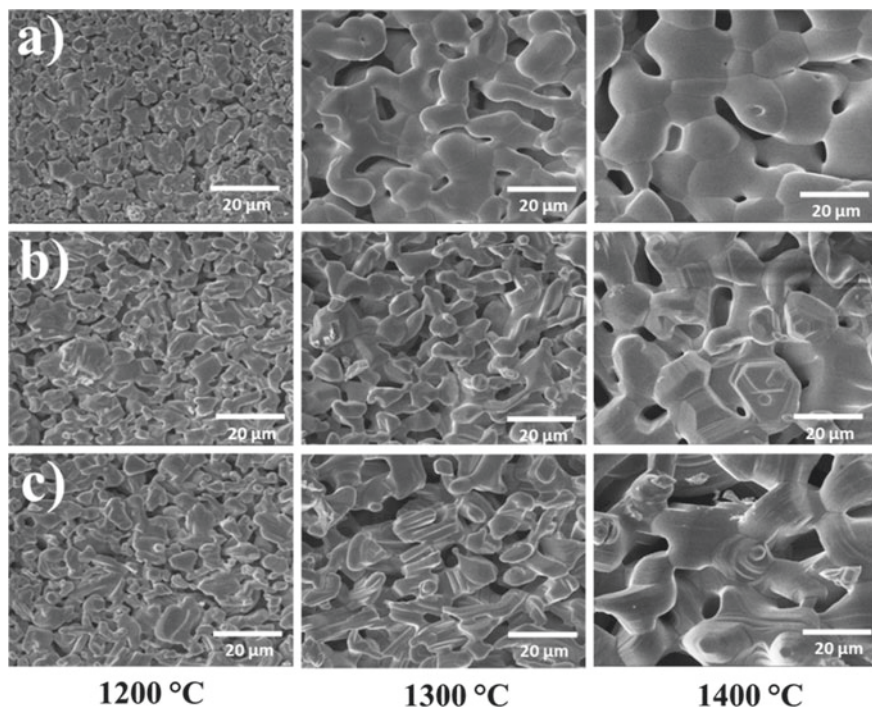


Fig. 3 Scanning electron images of **a** ITZO-II, **b** ITZO-IV and **c** ITZO-VI, after three different thermal treatments, 1200, 1300 and 1400 °C

Conclusion

The phases $\text{In}_{1.5}(\text{Ti}_{1/2}\text{Zn}_{1/2})_{0.5}\text{O}_3(\text{ZnO})_2$ (ITZO-II), $\text{In}_{1.5}(\text{TiZn}_{1/2})_{0.5}\text{O}_3(\text{ZnO})_4$ (ITZO-IV), and $\text{In}_{1.5}(\text{Ti}_{1/2}\text{Zn}_{1/2})_{0.5}\text{O}_3(\text{ZnO})_6$ (ITZO-VI) were successfully synthesized by the solid-state method. The XRD characterization showed that the studied samples crystallize in the hexagonal structure which is homologue to that of IGZO compound. The lattice parameters increase with increasing the $(\text{ZnO})_m$ composition. The compounds studied here are stable and maintain a single phase up to 1200 °C, beyond this temperature the compounds decompose into second phases. Microstructure analysis showed an increase in the grain size as sintering temperature was increased, and hexagonal step patterns were found at higher temperatures. The temperature dependence of the permittivity shows a classical paraelectric behavior without signal of relaxor or polar phase transition for all compounds.

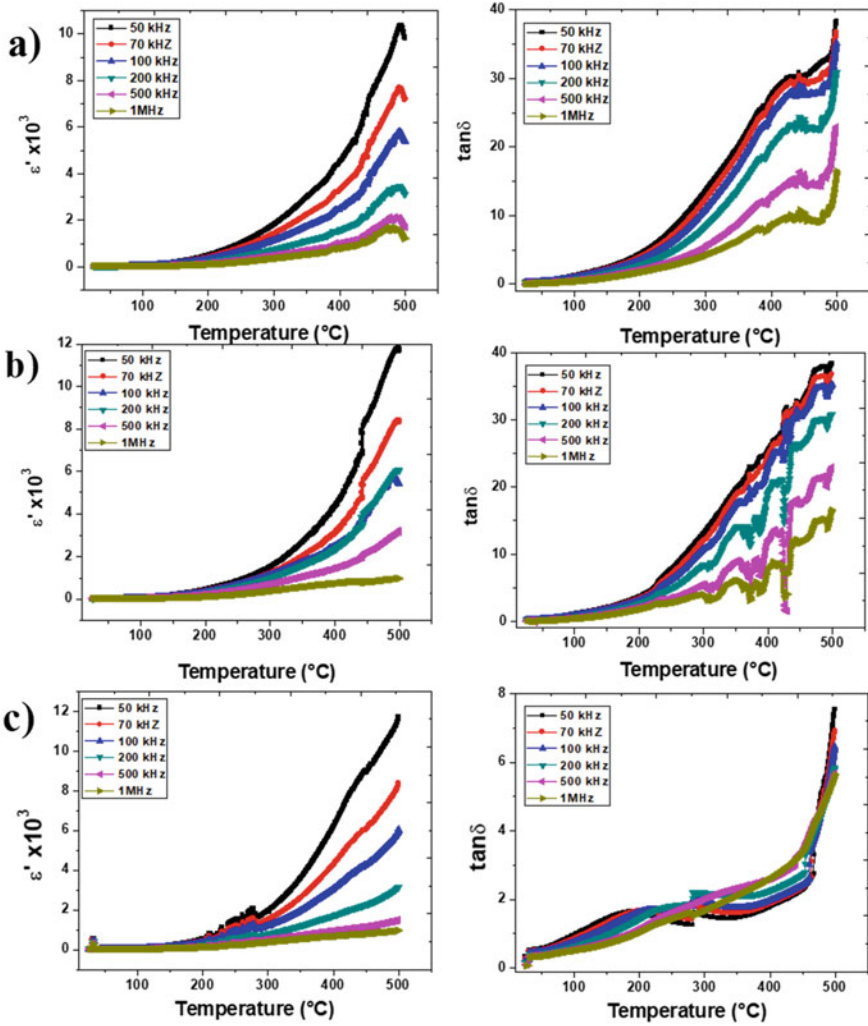


Fig. 4 Permittivity and loss tangent dependence with the temperature at several frequencies for ceramic compound **a** ITZO-II, **b** ITZO-IV, and **c** ITZO-VI. (Color figure online)

Acknowledgements VEAM thanks to University of Sonora, Department of Chemical Engineering and Metallurgy, for the support to this work. A.D. thanks project PAPIIT-UNAM IN101919.

References

1. Wang L, Hu P, Long Y, Liu Z, He X (2017) Recent advances in ternary two-dimensional materials: Synthesis, properties and applications. *Journal of Materials Chemistry A* 5:22855–22876
2. Lim JB, Zhang S, Kim N, ShROUT TR (2009) High-temperature dielectrics in the BiScO₃-BaTiO₃-(K^{1/2}Bi^{1/2})TiO₃ ternary system. *J Am Ceram Soc* 92:679–682
3. Castillón-Barraza FF et al (2019) Phase stability, microstructure, and dielectric properties of quaternary oxides In₁₂Ti₁₀A₂BO₄₂ (A: Ga or Al; B: Mg or Zn). *J Am Ceram Soc* 102:320–330
4. Brown F et al (2018) Phase relations in the pseudo ternary system In₂O₃-TiO₂-BO (B: Zn, Co and Ni) at 1200 °C in air. *J Solid State Chem* 258:865–875
5. Durán A, Martínez-Aguilar E, Conde-Gallardo A, Brown F, Alvarez-Montaña VE (2020) Dielectric and magnetic properties of InCr_{1-x}Ti_xO_{3+x/2} (x = 3/4, 5/7 and 2/3) solid solution. *Appl Phys a Mater Sci Process* 126:1–10
6. Piasecki M et al (2017) Band structure, electronic and optical features of Tl₄SnX₃ (X = S, Te) ternary compounds for optoelectronic applications. *J Alloy Compd* 710:600–607
7. Adachi S (2017) Iii-v ternary and quaternary compounds. In: Springer Handbooks 1. Springer. https://doi.org/10.1007/978-3-319-48933-9_30.
8. Hussain MI et al (2020) Investigations of structural, electronic and optical properties of YInO₃ (Y = Rb, Cs, Fr) perovskite oxides using mBJ approximation for optoelectronic applications: A first principles study. *Mater Sci Semicond Process* 113:105064
9. Tanaka Y et al (2019) Single crystal growth of bulk InGaZnO₄ and analysis of its intrinsic transport properties. *CrystEngComm* 21:2985–2993
10. Lahr D et al (2020) In_{1-x}Ga_{1+x}O₃(ZnO)_{0.5}: Synthesis, structure and cation distribution. *J Solid State Chem* 288:121341
11. Sheng J et al (2019) Amorphous IGZO TFT with high mobility of 70 cm²/(V s) via vertical dimension control using PEALD. *ACS Appl Mater Interfaces* 11:40300–40309
12. Physics and Technology of Crystalline Oxide Semiconductor CAAC-IGZO: application to LSI | Wiley. <https://www.wiley.com/en-us/Physics+and+Technology+of+Crystalline+Oxide+Semiconductor+CAAC+IGZO%3A+Application+to+LSI-p-9781119247340>
13. Yamazaki S, Tsutsui T (2016) Physics and technology of crystalline oxide semiconductor CAAC-IGZO. *Physics and technology of crystalline oxide semiconductor CAAC-IGZO: application to displays*. Wiley Ltd. <https://doi.org/10.1002/9781119247395>.
14. Garling J, Assenmacher W, Schmid H, Longo P, Mader W (2018) Real structure of (Sb^{1/3}Zn^{2/3})GaO₃(ZnO)₃, a member of the homologous series ARO₃(ZnO)_m with ordered site occupation. *J Solid State Chem* 258:809–817
15. Sharma S, Dwivedi RK (2017) Substitutionally driven phase transition and enhanced multiferroic and electrical properties of (1-x) BiFeO₃-(x) Pb(Zr_{0.52}Ti_{0.48})O₃ ceramics (0.0 ≤ x ≤ 1.00). *J Alloys Compounds* 692:770–773
16. Sharma S, Singh V, Dwivedi RK (2016) Electrical properties of (1-x) BFO - (x) PZT multiferroics synthesized by sol-gel method: transition from relaxor to non-relaxor. *J Alloy Compd* 682:723–729

Microwave Drying Behavior of Zinc Leaching Residue



Chengyu Sun, Xuemei Zheng, Yongguang Luo, Aiyuan Ma, and Song Li

Abstract To study the technological possibility of dehydration from zinc leaching residue by microwave heating, the temperature increasing characteristics of zinc leaching residue were studied. At the same time, the influences of the different material quantities, different drying time, and different microwave powers on the relative dehydration rate of zinc leaching residue were investigated, respectively. The results showed that the control temperature of 100 °C, the microwave power of 750 W, the mass of 50 g, the drying time of 21 min had the best drying effect, and the water removal rate was 95.45%. It was found that the heating rate is directly proportional to the power and inversely proportional to the material quantity.

Keywords Microwave drying · Zinc leaching residue · Dehydration

Introduction

Zinc leaching residue is presently obtained from a zinc hydrometallurgy process, which contains higher water content. Zinc leaching residue also contains a large number of valuable metals [1–3], which have great comprehensive recycling value. The valuable metals such as zinc (Zn) and indium (In) can be concentrated in a rotary kiln by roasting pretreated [4–6]. To meet the roasting pretreated requirement, the moisture content of zinc leaching residue should not exceed 5%. Thus, the removal of moisture from zinc leaching residue is an important pre-processing step.

C. Sun (✉) · Y. Luo · A. Ma
Faculty of Metallurgy and Energy Engineering, Kunming University of Science and Technology,
Kunming 650093, China
e-mail: qjlyg@163.com

X. Zheng · S. Li
School of Chemistry and Materials Engineering, Liupanshui Normol University, Liupanshui
553004, China

C. Sun · Y. Luo
Yunnan Chihong Zn and Ge Co Ltd., Qujing 655011, China

Compared with the traditional heating style, the microwave heating is a highly efficient, clean, and green metallurgy technology [7]. The unique microwave heating characteristics include the low processing time, the selective and volumetric heating, and the controllable heating process. When irradiated in a microwave field, moisture always quickly absorbs electromagnetic wave and is rapidly transferred to vapor [8]. The characteristics of microwave heating define the advantages of microwave drying, such as shortening the drying time and decreasing the environmental pollution. Microwave drying is a new technique and is widely used in woods [9], vegetables and fruits [10], and ores [11].

In this study, the removal of water from zinc leaching residue by microwave drying was investigated. The paper intends to investigate the influences of microwave power, microwave drying time, material mass on the dehydration rate.

Materials and Methods

Materials

The zinc leaching residue used in the experiments was received from zinc hydrometallurgical plant in Yunnan Province in China. The moisture in zinc leaching residue is almost all free water, with the initial moisture content 18.6%. The initial moisture content was measured using oven-drying method. The main chemical composition of the zinc leaching residue was characterized by X-ray fluorescence (XRF) measurements, as shown in Table 1.

Drying Apparatus and Procedure

The drying experiments were conducted in a power of 3 kW box-type microwave reactor designed by Kunming University of Science and Technology. See Fig. 1.

When carrying out the microwave drying experiment, a specific amount of zinc leaching residue was put into a corundum crucible, which was surrounded with thermal insulation material, and then the microwave power was set to the desired level, and the experiment started. Then, all of these were then transferred to the microwave reactor. A thermocouple was used to measure the temperature, in the range of 0–1300 °C. The starting of the experiment was marked by activating the microwave.

Table 1 Chemical compositions of zinc leaching residue (mass fraction, %)

Composition	Zn	Pb	Ca	Fe	Si	S	Mn	Mg
Content (%)	14.59	5.45	4.65	20.70	7.59	12.13	2.27	1.70

Fig. 1 Microwave drying equipment. (Color figure online)



Dehydration Ratio Analysis

The dehydration rate of zinc leaching residue after microwave drying was calculated. The dehydration rate (η) was expressed as,

$$\eta = \frac{M - M'}{M} \times 100\% \quad (1)$$

where M and M' represent the contents in the initial materials and samples after drying for water, respectively.

Results and Discussion

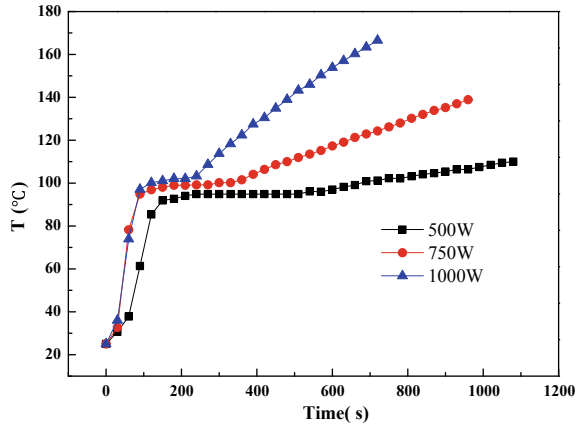
Microwave Heating Characteristics of Zinc Leaching Residue

Effect of Microwave Power on Temperature Increase Characteristics

The temperature increase characteristics and the microwave power in the microwave field are closely related to each other. In the microwave field, the microwave power of the zinc leaching residue affects the heating behavior under a sample mass setting of 50 g. The relationship between the temperature (T_m) of the zinc leaching residue and time for samples with different microwave powers of 500, 750, and 1000 W is illustrated in Fig. 2.

As can be seen from Fig. 2, the influence of microwave power on material heating behavior is mainly reflected in the increase of microwave power, the apparent average heating rate of zinc leaching residue increased as the microwave power increased

Fig. 2 Heating rate curves of zinc leaching residue at different microwave powers. (Color figure online)



from 500 to 1000 W, and higher microwave power required shorter heating time to reach the same temperature. The experimental result is similar to the reported results for microwave heating of low-grade nickel oxide ore [12]. This is because, within a certain range, with the increase of microwave output power, also will increase the temperature of the material. This value can be expressed as:

$$P_{ab} = \mu P \tag{2}$$

where P_{ab} , μ , and P represent the microwave power absorbed by material (W), absorption coefficient, and the output power of microwave (W), respectively.

Set C_p as heat capacity of the material, W as mass of the material, T as temperature of the material, t as microwave radiation time, and T_0 as initial temperature of the material, then according to the law of energy conservation:

$$C_p W dT = P_{ab} dt = \mu P dt \tag{3}$$

Integral,

$$T = T_0 + \int_0^t (\mu P / C_p W) dt \tag{4}$$

Equation (4) shows that, within a certain range, increasing the output power of microwave can increase the temperature of the material.

In addition, the per unit volume of the zinc leaching residue also absorbed microwave power or the microwave energy dissipated power in the dust. This value also can be expressed as [13],

$$P = 2\pi f \varepsilon'' E^2 \tag{5}$$

where f is the microwave frequency, GHz; E is the electric field strength, V/m; ϵ'' is the dielectric loss factor.

According to Eq. 5, when other conditions remain unchanged, increasing microwave heating power means increasing electric field intensity. With the increase of electric field intensity E , microwave can better and evenly penetrate into the interior of the material. At the same time, the microwave-absorption ability of zinc leaching residue was enhanced, and the temperature also increased. Therefore, appropriately increasing microwave heating power can shorten the heating time and increase the apparent average heating rate of zinc leaching residue.

Effect of Sample Mass on Temperature Increase Characteristics

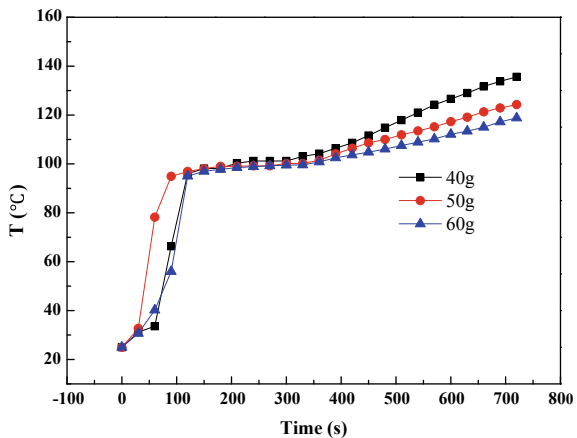
The temperature increase characteristics and the sample mass in the microwave field are closely related to each other. The control microwave output power is 750 W. The heating curves of zinc leaching residue and time for samples with different masses of 40, 50, and 60 g were presented in Fig. 3. The results show that a smaller mass of sample indicates a faster apparent heating rate.

In the microwave field, the effect of the sample mass of zinc leaching residue on the heating rate can be calculated as follows [14]:

$$\frac{dT}{d\tau} = \frac{T - T_0}{\tau} = \frac{2\pi f \epsilon_0 \epsilon'' E^2}{\rho V C_p} = \frac{2\pi f \epsilon_0 \epsilon'' E^2}{m C_p} \tag{6}$$

where T is the material heating temperature, K; T_0 is the material initial temperature, K; τ is the time, s; m is the mass of material, kg; C_p is the specific heat capacity of material, J/(K·kg); f is the frequency of the microwave, Hz; ϵ_0 is the vacuum permittivity; ϵ'' is the dielectric loss factor; E is the electric field strength, V/m.

Fig. 3 Heating rate curves of zinc leaching residue with different masses in microwave field. (Color figure online)



As shown in Eq. (6), the heating rate is decreased with the increase of the sample mass of zinc leaching residue. This observation is in accordance with the experimental results. When microwave power was constant, a larger amount of zinc leaching residue indicated a thicker sample and the need for more microwave power. In the experimental condition range, the power density of the sample decreased with the increase in the sample mass, which resulted in a slower rate of temperature increase.

Microwave Drying Experiment of Zinc Leaching Residue

To study the technological possibility of dehydration from zinc leaching residue by microwave heating, the effects of microwave power, material masses, and drying time on the dehydration rate of zinc leaching residue were investigated.

Effect of Sample Mass on Dehydration Rate

The dehydration rate curves of zinc leaching residue were evaluated using various masses in the range of 30–70 g. The dry conditions were as follows: microwave power is 750 W and dry temperature is 100 °C. The results are shown in Fig. 4. Figure 4 shows that the dehydration rate of zinc leaching residue increased with the mass was decreased, and the dehydration rate of zinc leaching residue increased with the drying time was increased. The entire drying time are much longer than those of the sample mass of 30 and 40 g when which were 50, 60, and 70 g. This may be related with the low power density and small steam diffusion rate inside residue layer. The temperature gradient also can affect the steam diffusion. The mass transfer process will be intensified by the same direction of temperature gradient and steam diffusion, and this intensifying effect will increases with the raise of temperature

Fig. 4 Dehydration rate curves of zinc leaching residue at different masses. (Color figure online)

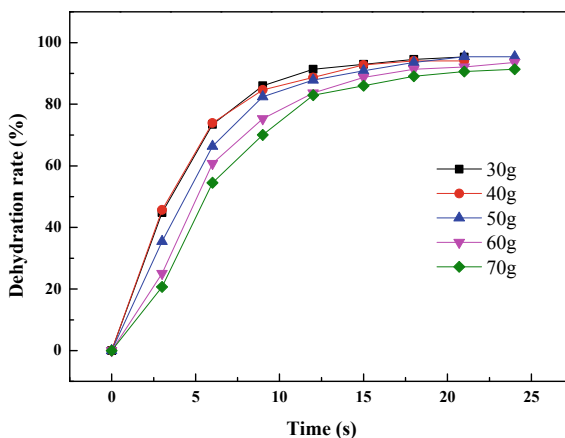
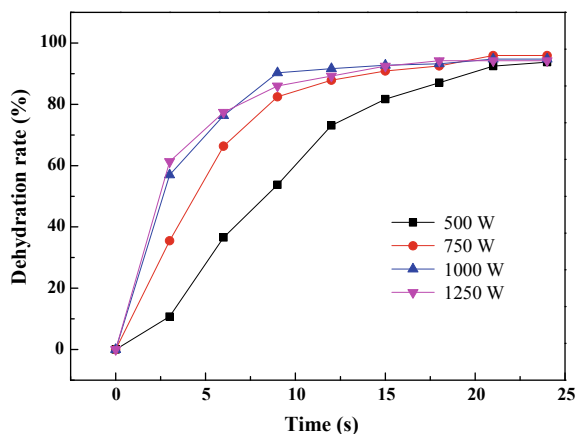


Fig. 5 Dehydration rate curves of zinc leaching residue at different microwave powers. (Color figure online)



gradient. The dehydration rate of zinc leaching residue increases significantly with the increase sample mass from 30 to 50 g, after the dehydration rate increased slowly. Thus, an appropriate sample mass of 50 g was selected to investigate the effect of the other parameters in the experiment.

Effect of Microwave Power on Dehydration Rate

Figure 5 describes the microwave drying curves on the dehydration rate of zinc leaching residue versus drying time at different microwave power levels. The dry conditions were as follows: sample mass is 50 g and dry temperature is 100 °C. It can be seen from Fig. 5, the dehydration rate of zinc leaching residue increased as the microwave power was increased. At the power of 500 W, the longest drying time was required, while at the power of 750 W, 1000 W, and 1250 W the shortest drying time was required. Figure 5 shows that the impact of microwave power levels on the drying rate were significant. The results showed that the control temperature of 100 °C, the microwave power of 750 W, the mass of 50 g, the drying time of 21 min had the better drying effect, and the dehydration rate of zinc leaching residue was 95.45%.

Conclusions

- (1) The effects of sample mass and microwave power on the temperature increase characteristics under the microwave field were also studied. The results show that the heating rate of the zinc leaching residue increases with the increase in microwave power and decreases with the increase in the sample mass. The temperature of the samples reaches approximately 100 °C after microwave

- treatment for 3 min, which indicates that the zinc leaching residue has strong microwave-absorption ability.
- (2) The drying characteristics of zinc leaching residue were made under microwave conditions using different power supplies and sample mass. The control temperature of 100 °C, the microwave power of 750 W, the mass of 50 g, the drying time of 21 min had the better drying effect, and the dehydration rate of zinc leaching residue was 95.45%.

Acknowledgements The authors are grateful for the financial support from Guizhou Provincial Colleges and Universities Science and Technology top-notch talent support program project (KY [2018]066), the Guizhou Province science and technology plan key project (No. [2019]1444), the Liupanshui Key Laboratory of Metallurgical Energy Saving, Environmental Protection and Recycling Economy (52020-2018-0304), the key cultivation disciplines of Liupanshui Normal University (LPSSYZDXK201901), the Science and Technology Innovation Group of Liupanshui Normal University (LPSSYKJTD201801), the excellent engineer training program of metallurgical engineering specialty in Liupanshui Normal University (LPSSYZzyjpyjh201801), and the Nonferrous Metal Electrodeposition Technology Provincial Innovation Team of Yunnan Chihong Zn & Ge Co., Ltd (201905E160007).

References

1. Ma AY, Zheng XM, Li SW et al (2018) Zinc recovery from metallurgical slag and dust by coordination leaching in $\text{NH}_3\text{-CH}_3\text{COONH}_4\text{-H}_2\text{O}$ system. *R Soc Open Sci* 5:180660
2. Rabah MA, El-Sayed AS (1995) Recovery of zinc and some of its valuable salts from secondary resources and wastes. *Hydrometallurgy* 37(1):23–32
3. Li XH, Zhang YJ, Qin QL et al (2010) Indium recovery from zinc oxide flue dust by oxidative pressure leaching. *Trans Nonferrous Metals Soc China* 20:s141–s145
4. Tsakiridis PE, Papadimitriou GD, Tsivilis S, Koroneos C (2008) Utilization of steel slag for portland cement clinker production. *J Hazard Mater* 152:805–811
5. Das B, Prakash S, Reddy PSR, Misra VN (2007) An overview of utilization of slag and sludge from steel industries. *Resour Conserv Recycl* 50:40–57
6. Trinkel V, Mallow O, Aschenbrenner P, Rechberger H, Fellner J (2016) Characterization of blast furnace sludge with respect to heavy metal distribution. *Ind Eng Chem Res* 55:5590–5597
7. Ma AY, Zheng XM, Peng JH et al (2017) Dechlorination of zinc oxide dust derived from zinc leaching residue by microwave roasting in a rotary kiln. *Braz J Chem Eng* 34(1):193–202
8. Ma AY, Zhang LB, Peng JH et al (2014) Dielectric properties and temperature increase of zinc oxide dust derived from volatilization in rotary kilns. *J Microwave Power Electromagn Energy* 48:25–34
9. Li XJ, Zhang BG, Li WJ (2008) Microwave-vacuum drying of wood: model formulation and verification. *Drying Technol* 26(10):1382–1387
10. Lupinska A, Koziot A, Araszkievicz M (2009) The changes of quality in rapeseeds during microwave drying. *Drying Technol* 27(7):857–862
11. Ganesapillai M, Regupathi I, Murgesan T (2008) Characterization and process optimization of microwave drying of plaster of paris. *Drying Technol* 26(10):1484–1496
12. Thostnson ET, Chou TW (1999) Microwave processing: fundamentals and applications. *Composites A* 30:1055–1071

13. Chen J, Lin WM, Zhao J (2007) The coking coal metallurgy technology [M]. Chemical Industry Press, Beijing (in Chinese)
14. Hua YX, Tan CE, Xie AJ et al (2000) Microwave-aided chloridizing of nickel-bearing garnierite ore with FeCl_3 . *Nonferrous Metals* 52(1):59–60 (in Chinese)

Synthesis of Willemite Bio-Ceramic by Mechanochemical Procedure



Sorour Sadeghzade, Rahmattollah Emadi, and Fariborz Tavangarian

Abstract Willemite is currently recognized as a bio-ceramic material for bone repair and bone tissue engineering applications. In this study, pure willemite powder was fabricated by mechanical alloying method. The starting materials were zinc oxide and silicon oxide. The results showed that pure willemite powder can be produced following 20 h of milling and subsequent sintering at 900 °C for 3 h. The obtained willemite powders had crystallite size and particle size in the range of 143–147 nm and 300–500 nm, respectively.

Keywords Bio-ceramic · Willemite · Nano-powders · Mechanochemical synthesis

Introduction

Ceramics are a new genre of biomaterials that can be used for various applications within the human body [1]. Many studies have shown that the mechanical and biological properties of various bio-ceramics including ZnO-SiO₂ groups have a significant advantage when compared with hydroxyapatite (HA) [2]. Furthermore, various studies have shown that bio-ceramics release beneficial ions such as zinc, phosphorus, silicon, into the body. Willemite (Zn₂SiO₄) is a member of orthosilicate substance with rhombohedral structure [3]. Due to its high bioactivity, willemite is a viable candidate to repair bone defects in the body. Willemite releases Zn²⁺ and Si⁴⁺ ions as it degrades [4]. These ions have been shown to increase collagen production and encourage bone growth. Based on the literature, zinc and silicon are beneficial for anti-inflammatory effects and stimulate bone formation by activating protein and promoting osteoblast growth [4–7]. The grain size of willemite

S. Sadeghzade · R. Emadi

Materials Research Group, Department of Materials Engineering, Isfahan University of Technology, 84156-83111 Isfahan, Iran

F. Tavangarian (✉)

Mechanical Engineering Program, School of Science, Engineering and Technology, Pennsylvania State University, Harrisburg, Middletown, PA 17057, USA

e-mail: fut16@psu.edu

© The Minerals, Metals & Materials Society 2021

TMS 2021 150th Annual Meeting & Exhibition Supplemental Proceedings,

The Minerals, Metals & Materials Series,

https://doi.org/10.1007/978-3-030-65261-6_36

influences its bioactivity. Nanostructured willemite bio-ceramics are expected to have better mechanical properties and biocompatibility than coarser crystals. It was reported that coarse grain ceramics had an extremely low degradation rate and was not bioactive [8]. Among all methods for fabrication of nanostructure ceramics, ball mill method is an economy, simple, mass product and powerful method in comparison with sol-gel method which is an expensive and time-consuming method [9]. Therefore, in this study, the willemite was synthesized by mechanochemical method and the mechanical properties of that were evaluated.

Materials and Methods

Willemite nano-powder was fabricated by mechanochemical synthesis. Zinc oxide (ZnO, 99% purity, Merck) and silicate oxide (SiO₂, 99% purity, Aldrich) powders were used as starting materials. The mixed powder was put in zirconia container in planetary ball mill machine with the ball/powder mass ratio of 10:1 and ball milled for 15 min, 1 h, 5 h, 10 h, and 20 h. The subsequent sintering temperature was 900 °C for 1 h to evaluate the phase transformation of powders at a different time and sintering temperature, and the X-ray diffraction (X'pert Philips) equipped with Cu K α radiation was utilized in the 2θ range of 20–80° ($\lambda = 0.154$, step size = 0.05°, time per step = 1 s). The crystallite size was measured by Scherrer equation. Transmission electron microscopy (TEM, Philips CM120) and scanning electron microscopy (SEM, Philips XL30, an acceleration voltage of 25 kV) were utilized to evaluate the morphology and particle size of synthesized powders.

Results and Discussion

XRD patterns of mixture powders with various ball milled times are shown in Fig. 1. As seen, the XRD patterns of initial materials (ball milled for 15 min) just show the characteristic peaks of ZnO (XRD data file No. 1-075-0576) and there are not the distinct peaks of SiO₂. In fact, this is due to the amorphous structure of this composition which was used in this study. The phase transformation was not occurred after 1 h and 5 h ball milled of raw materials. Milling for 10 h has caused reduction in peak intensity, and broadening of the XRD peaks was revealed. Increasing the internal strain and gradual transfer of the initial materials to amorphous structure is another reason which this phenomenon happened.

As shown in Fig. 1, new crystallite phase at 20 h ball milled was detected in XRD patterns. The characteristic peaks of willemite were observed after 20 h ball milled. But, ZnO peaks also can be detected in the structure. As observed, the willemite phases (XRD JCPDS data file No. 1-083-2270) can be formed just by ball milled method. However, the impurity phases in the structure are observed which can be removed with subsequent sintering process.

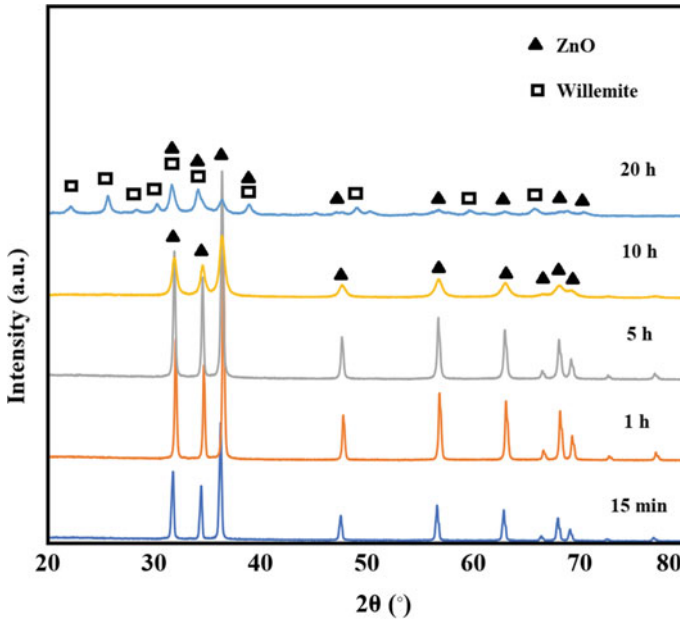
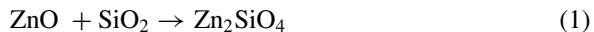


Fig. 1 XRD patterns of mixture powders after various times of ball milling. (Color figure online)

Figure 2 presents the XRD patterns of fabricated powders in various times of ball mill and sintered at 900 °C. As shown in XRD patterns of mixture powders after 15 min and 1 h milling, just the characteristic peaks of ZnO can be observed even with sintering at 900 °C. It shows that ball milling is an effective method in the formation of the desired phase in the structure. The sharp peaks of ZnO with SiO₂ amorphous can react together after 5 h ball milled and sintering at 900 °C. Nucleation of willemite peaks initiated after 5 h ball milled and sintering at 900 °C based on Eq. (1):



The XRD pattern of sample after 10 h milling and sintering at 900 °C for 1 h shows increase in the willemite peaks and reduction of ZnO peaks. The presence of impurity phases after 10 h milling and sintering at 900 °C can be due to un-homogeneity of mixture powders and long diffusion way between the ZnO and SiO₂ particles. ZnO peaks were disappeared from the system after 20 h ball milling and sintering at 900 °C. Complete transformation of ZnO and SiO₂ phases to willemite was happened at these conditions.

SEM images of mixture powders after 15 min, 20 h ball milling, and before and after sintering at 900 °C for 1 h are shown in Fig. 3a–c, respectively. Also, the TEM images of sample after 20 h ball mill and sintering at 900 °C for 1 h are presented in Fig. 3d. Figure 3a shows the ZnO with irregular morphology and average particle

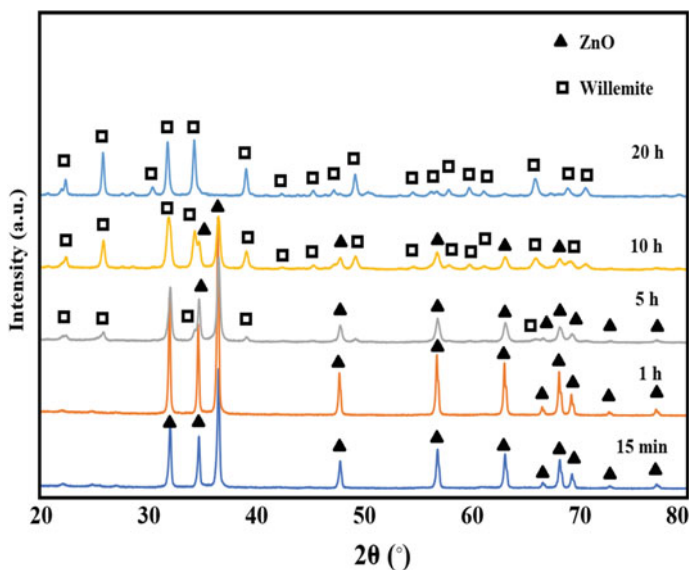


Fig. 2 XRD patterns of mixture powders after various times of ball milling with subsequent sintering at 900 °C for 1 h. (Color figure online)

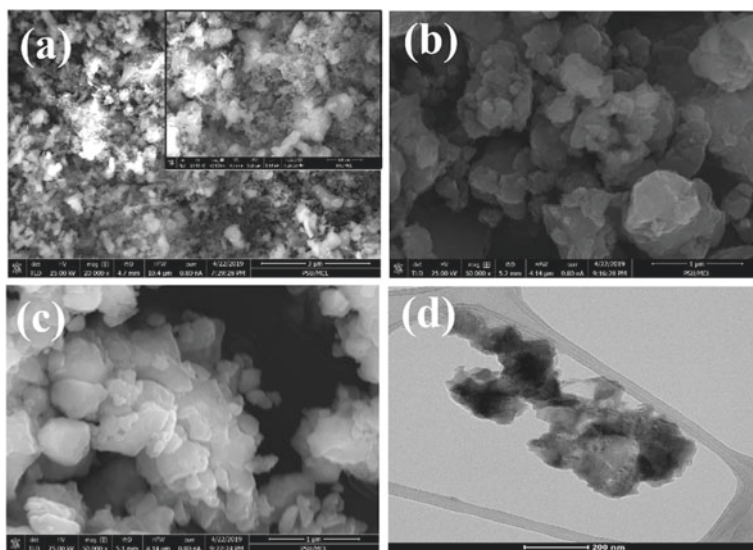


Fig. 3 SEM images of samples after **a** 15 min, **b** 20 h ball milled, **c** 20 h ball milled and sintered at 900 °C for 1 h, and **d** TEM image of pure willemite after 20 h ball milled and sintered at 900 °C for 1 h

size of 780 nm and SiO₂ with spherical structure and the average particle size of less than 100 nm as initial powders. By increasing the milling time from 15 min to 20 h, welding between the initial material particles occurs frequently and tendency of particles to agglomeration (due to high surface energy and surface area-to-volume ratio), increasing the average particle size of powder, can be observed. Also, the morphology of particles after 2 h ball mill is rather spherical. The mean agglomerated particle size of sample after 20 h ball mill was measured by ImageJ and to be in the range of 200–900 nm. After sintering of sample at 900 °C for 1 h, the morphology of powders did not change but the agglomerated particle size was measured to be in the range of 300–500 nm.

TEM was used to show the morphology and grain size of pure willemite after 20 h milling and sintering at 900 °C for 1 h. As shown in Fig. 3d, the spherical willemite particles show the high degree of agglomeration. The ImageJ software was used to measure the grain size of willemite and was found to be 145 ± 2 nm. Also, Scherrer equation shows the same crystallite size of willemite and the results were in good agreement with TEM.

Conclusion

In this study, pure willemite powder ceramic was successfully fabricated by mechanochemical synthesis. The best processing conditions for fabrication of pure willemite with 145 ± 2 nm grain sizes were 20 h ball milled and sintering at 900 °C. Based on the XRD results, the chemical reaction of willemite cannot be occurred just by heating process. The activation energy of this reaction is provided by both ball mill and subsequent sintering. Based on the SEM results, the agglomerate particle size for the pure willemite under 20 h milling and subsequent sintering at 900 °C for 1 h was found in the range of 300–500 nm.

References

1. Carter CB, Norton MG (2007) *Ceramic materials: science and engineering*. Springer
2. Roohani-Esfahani S-I, Chen Y, Shi J, Zreiqat H (2013) Fabrication and characterization of a new, strong and bioactive ceramic scaffold for bone regeneration. *Mater Lett* 107:378–381
3. Sadeghzade S, Emadi R, Labbaf S (2017) Hardystonite-diopside nanocomposite scaffolds for bone tissue engineering applications. *Mater Chem Phys* 202:95–103
4. Halabian R, Moridi K, Korani M, Ghollasi M (2019) Composite nanoscaffolds modified with bio-ceramic nanoparticles (Zn₂SiO₄) prompted osteogenic differentiation of human induced pluripotent stem cells. *Int J Mol Cell Med* 8:24
5. JamshidiAdegani F, Langroudi L, Ardeshiryajimi A, Dinarvand P, Dodel M, Doostmohammadi A, Rahimian A, Zohrabi P, Seyedjafari E, Soleimani M (2014) Coating of electrospun poly (lactic-co-glycolic acid) nanofibers with willemite bioceramic: improvement of bone reconstruction in rat model. *Cell Biol Int* 38:1271–1279

6. Sadeghzade S, Emadi R, Tavangarian F, Naderi M (2017) Fabrication and evaluation of silica-based ceramic scaffolds for hard tissue engineering applications. *Mater Sci Eng C* 71:431–438
7. Sadeghzade S, Emadi R, Tavangarian F, Doostmohammadi A (2020) The influence of polycaprolacton fumarate coating on mechanical properties and in vitro behavior of porous diopside-hardystonite nano-composite scaffold. *J Mech Behav Biomed Mater* 101:103445
8. Tavangarian F, Emadi R (2011) Nanostructure effects on the bioactivity of forsterite bioceramic. *Mater Lett* 65:740–743
9. Sadeghzade S, Emadi R, Labbaf S (2016) Formation mechanism of nano-hardystonite powder prepared by mechanochemical synthesis. *Adv Powder Technol* 27:2238–2244

Thermal Shock Resistance of Silica-Free Alumina–Spinel Castables



Yang Liu, Min Chen, Xianglan Yang, and Shan Wang

Abstract To improve the thermal shock resistance of ladle lining castable, silica-free alumina–spinel castables with an extensive range of calcium aluminate cement content (2–10 wt%) were prepared and the properties were investigated. The results showed that the card-house structures formed by the hexagonal flake calcium hexaluminate grains and the appropriate density of microcracks caused by the expansive reflection of calcium hexaluminate formation after firing at 1550 °C, which were beneficial to strengthen the aggregate–matrix combination and alleviate thermal stress. Consequently, the performance of the castables, including the retained moduli values and hot modulus of rupture, reached to the optimal values after 3 thermal cycles while 5–8 wt% cement was added. But while further increasing the cement content, these performances of the castables were degraded by the excessive volume expansion and density matrix due to the formation of calcium hexaluminate and the space occupation of calcium dialuminate respectively.

Keywords Cement content · Microstructure · Physical properties · Thermal shock resistance · Alumina–spinel castables

Introduction

Al₂O₃–MgO–CaO system alumina-rich castables are widely used as ladle lining materials due to their outstanding chemical stability and thermo-mechanical properties [1–5], and the structural spalling originate in poor thermal shock resistance caused by the large temperature gradient during ladles operation is considered to be one of the main reasons to affect the service life [6–8]. With the constantly progress of ladle refining technology, the service conditions of ladle refractories are becoming more severe, and the request to improve the thermal shock resistance of alumina-rich castables is very urgent.

Y. Liu · M. Chen (✉) · X. Yang · S. Wang
School of Metallurgy, Northeastern University, Shenyang 110819, China
e-mail: chenm@smm.neu.neu.cn

Considering this aspect, many research works on improving the thermal shock resistance of the materials have been carried out, and it is considered that the use of corundum aggregate with spinel is benefit to ladle lining castables, but the selection of spinel sources (pre-synthesized or in-situ generated) and binder system is still controversial. For the former, most previous works focused on the advantages of the in-situ reaction, whereas the different result showed by Kim et al. [9] that the alumina-spinel (pre-synthesized) castable could maintain stability without spalling after the field test. Meanwhile, the use of magnesia usually means the addition of silica fume which aim to increase the fluidity, inhibit the magnesia hydration and suppress volume expansion, while Ko [10] reported even small amounts of silica fume were detrimental for both thermo-mechanical properties and slag resistance. For the latter, compared with hydratable alumina, calcium aluminate cement (CAC) can reduce its drawbacks such as the longer mixing times as well as more water addition.

Furthermore, calcium aluminate cement, as the binder as well as the CaO source, their content would affect the microstructural evolution during the overall castable's processing step [11–14]. The earlier works on the series of noteworthy reactions among CaO- Al_2O_3 binary phases which involve calcium aluminate (CA), calcium dialuminate (CA_2) and calcium hexaluminate (CA_6), is considered well established. According to Xu [15], the platelet morphology of CA_6 can act as bridging sites in the wake of the cracks, enhancing the crack growth resistance. And the CA_2 is considered as a desirable phase in the refractory applications because of the extremely low thermal expansion coefficient, which benefits the releasing of the thermal stress. Take into account these, the cement content must be properly adjusted in order to obtain the stability without spalling when applying the material. But the study related to this subject has been little reported.

Thus, as mentioned above, silica-free alumina–spinel castables with optimized pre-synthesized spinel content and CAC were developed in this paper. The cement contents in an extensive range (from ultra-low to high) are selected to systematically assess their effects microstructural evolution (such as the quantity and morphology of in-situ CA_6 and CA_2) which directly connected with the material's thermal shock resistance. Moreover, the thermal shock resistance and its associated physical properties of samples were evaluated, so as to complete assessment of the cement content effect.

Experimental

Raw Materials and Composition

The raw materials used for this study were Tabular alumina (T60/T64, Almatiss), pure calcium aluminate cement (Secar 71; Imerys), Sintered spinel (AR78, Almatiss) and

Table 1 Chemical compositions of raw materials

Oxide (wt.%)	Tabular alumina	Spinel	Cement	Reactive alumina
Al ₂ O ₃	99.25	76.31	70.64	99.36
MgO	0.09	22.87	0.23	0.08
CaO	0.04	0.23	28.05	0.04
SiO ₂	0.01	0.06	0.22	0.06
Fe ₂ O ₃	0.12	0.17	0.12	0.06
Na ₂ O	0.35	0.1	0.33	0.05
TiO ₂	0.01	0.01	0.03	0.03
P ₂ O ₅	–	0.01	–	–
Cr ₂ O ₃	–	0.01	0.01	–
L.O.I	0.13	0.23	0.37	0.32

Table 2 Composition of cement bonded alumina–spinel castables (wt/%)

Raw materials		AS2	AS5	AS8	AS10
Tabular alumina	≤6 mm	50	50	50	50
	≤0.088 mm	17	14	11	9
Sintered spinel (mm)	1–0.2 mm	6	6	6	6
	≤0.088 mm	10	10	10	10
Calcium aluminate cement	d ₅₀ = 3.03 μm	2	5	8	10
Reactive alumina	d ₅₀ = 2.00 μm	5	5	5	5
Additives		0.5	0.5	0.5	0.5

reactive alumina powder (CL370, Almatix). Table 1 contains the chemical compositions of the raw materials. The composition used for alumina–spinel castable is listed in Table 2.

Sample Preparation and Testing

Table 2 displays the formulations of the castables with varied amounts of CAC. They were marked as AS2, AS5, AS8 and AS10, which correspond to cement additions of 2%, 5%, 8% and 10%, respectively. The starting powder mixtures were dry-mixed for 30 s, and then wet-mixed in a compulsory mixer with an appropriate amount of water for 180 s. After mixing, prismatic castables were cast into molds of 40 mm × 40 mm × 160 mm with vibration. Afterwards, the samples were cured at 20 °C and 95% relative humidity for 24 h. In order to remove the free water, binding water and release water vapor pressure sufficiently, the samples were dried for 24 h at 100 °C and 400 °C respectively. Then they were fired in a high temperature electric furnace

at a heating rate of $5\text{ }^{\circ}\text{C}\cdot\text{min}^{-1}$ up to $1550\text{ }^{\circ}\text{C}$ with a dwell time of 3 h and furnace cooled.

The bulk density (B.D.) and the apparent porosity (A.P.) of the material were measured by the Archimedes method with water as media. The permanent linear change (PLC) was calculated by measuring the dimensions of specimens before and after firing. The modulus of rupture (MOR) was measured on the bars using the three-point bending test. The thermal shock resistance (TSR) of the fired samples was evaluated using the air quenching method following GB/T3002-2004. Crystalline phases formed were analyzed by X-Ray power diffraction (XRD) using Cu $K\alpha 1$ radiation ($\lambda = 1.5406\text{ \AA}$) with a step of 0.02° (2θ). Microstructural analyses were also conducted by scanning electron microscopy (SEM) for samples fired at $1550\text{ }^{\circ}\text{C}$ for 3 h.

Results and Discussion

Physical Properties

The comparison of change in BD, AP, MOR and PLC with 2–10% cement bonded alumina–spinel castables at different temperature are given in Fig. 1(a–d). As

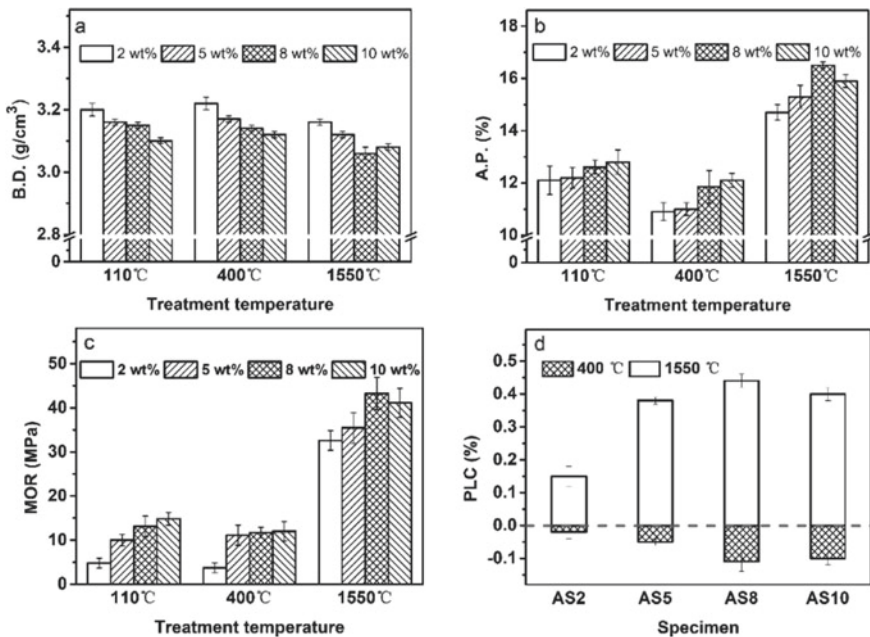


Fig. 1 The comparison of change in BD, AP, MOR, and PLC with different amounts of CAC addition

expected, the MOR of the castables continuously increase with the increase in CAC content after drying at 110 °C for 24 h (Fig. 1c). This improved castable strength with the higher CAC content can be ascribed to a higher amount of hydrates generated in the castables. With the treatment temperature elevates to 400 °C, a lightly loss of strength is showed due to a reduction of the special surface as well as to the formation of voids around the C_3AH_6 [16]. This coincides with the slight upward and downward trend of the B.D. and A.P. (Fig. 1a and b) that the castables demonstrate compared with the 110 °C, respectively. However, same trend doesn't show at 1500 °C, it carries out the tendency of ascending and then descending, with the maximum value of 43.2 MPa while the added 8% wt cement. Thus, it can conclude that excessive content of cement can reduce MOR at high temperature.

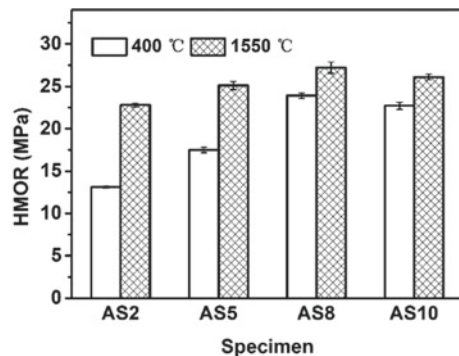
Figure 1d shows the permanent linear change of specimens after drying at 400 °C and firing at 1550 °C for 3 h. It can be seen that all specimens exhibit shrinkage after drying at 400 °C, which is attributed to the dehydration process of a series of hydration products such as C_3AH_6 and AH_3 [17]. After firing at 1550 °C for 3 h, specimens present an overall expansion, the expansion value increases from 0.15% to 0.44% with the increase of CAC from 2 to 8 wt%, and then decreased to 0.40%. That expansion is due to phase formation overpasses the sintering shrinkage. Combined with other physical properties of samples at the same treatment, it is not difficult to conclude that although the higher heat treatment temperature is favorable for the densification, the formation of new phase like CA_6 will result in a large volume expansion, which also leads to a higher porosity of castable as the Fig. 1b shown.

High-Temperature Mechanical Properties

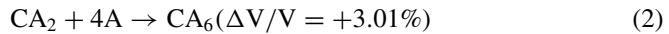
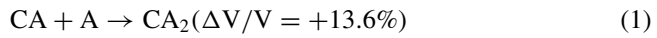
Hot Modulus of Rupture

The hot modulus of rupture of samples respectively treated at 400 °C and 1550 °C for 3 h is shown in Fig. 2. The HMOR of all the tested castables heated at 1550 °C are

Fig. 2 Hot modulus of rupture of specimens with different amounts of CAC addition



higher than those of the respective 400 °C treated samples, and also present the same rise-fall trend as the PLC of the samples mentioned before. Combine with the XRD patterns of samples after firing at 1550 °C for 3 h (Fig. 3), the CA₆ peaks emerge, the formation of CA₆ involves a series of reaction between the recrystallized CA and Al₂O₃ with obvious volume expansion, which has been verified by the result of the fired sample’s permanent linear change. The specific reaction and their theoretical volume expansion value are as follow [18]:



Meanwhile, the gradually increase of CA₆ peaks intensity explains the elevation of HMOR for the samples with the increasing addition of CAC. It should be noted that suitable calcium hexaaluminate formation is helpful to improve the high temperature bonding strength of the alumina–spinel castables, while excessive its formation will cause overexpansion and thus results in strength degradation. This is why specimen AS10 with a high amount of CAC addition, has a relatively lower HMOR. In addition, if the corundum aggregate is assumed not to react with CaO in the cement, the theoretical formation amount of CA₆ for each sample should be 6.69%, 16.74%, 23.63% and 22.98% according to the CaO content, and small amount of CA₂ will appear in samples AS8 and AS10 due to insufficient aluminum source in the matrix. From the Fig. 3, the CA₂ peaks are detected in the diffraction of samples AS8 and AS10, which partly verified the theoretical calculation and explained the PLC slightly

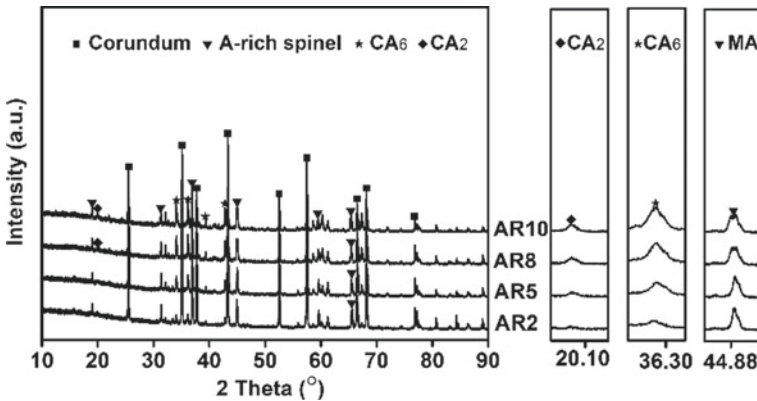
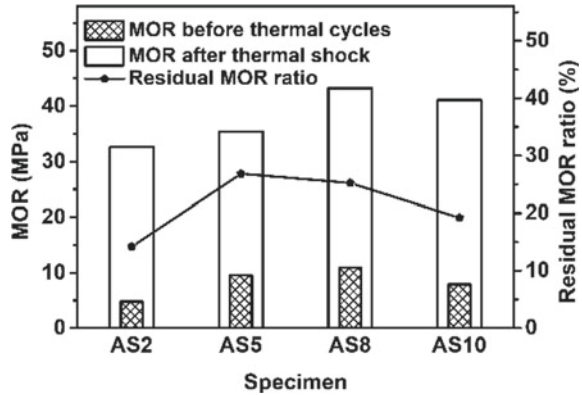


Fig. 3 XRD patterns of the specimens with different amounts of CAC addition firing at 1550 °C for 3 h

Fig. 4 Effect of different amounts of CAC addition on thermal shock resistance of specimens



decreased is due to contribution of the CA_2 with low theoretical expansion coefficient ($4.4 \times 10^{-6}/^{\circ}C$) to densification of the sample. Whereas the increasing trend of CA_6 peak intensity in diffraction contradicts the hypothesis, it is speculated that the corundum aggregate participates in the reaction of CA_6 formation.

Thermal Shock Resistance

The MOR and the residual MOR of fired samples after undergoing 3 thermal cycles at $1100^{\circ}C$ are depicted in Fig. 4. It can be observed that a great strength loss took place after thermal shock for each sample. The maximum residual MOR ratio value is 26.83% from the sample AS5 and the residual MOR ratio of sample AS8 (25.25%) has not significantly different from it. Hence, the results indicate that the optimum CAC addition range is 5–8 wt% to obtain better TSR of samples. Considering the distributions, sizes and amounts of CA_6 are highly influenced by the cement content, and further affect the TSR of specimens, SEM analysis of specimens is performed.

In the Fig. 5, it can be found that light gray reaction layers with different thickness attach to the aggregate edge of samples AS8 and AS10. Combined with energy spectrum analysis of the samples (Fig. 6), it can be conclude that the chemical composition of the reaction layer is calcium hexaluminate. A considerable amount of CA_6 grains could be defected both in the matrix and at the border of the alumina aggregates indicate their formation and binding effect on the matrix and aggregate made the castable obtain higher initial strength, which is also the premise to obtain nice TSR. In addition, CA_6 is prone to be formed only in the matrix of samples AS2 and AS5, and with the lack of fine alumina in the matrix, the formation of calcium hexaluminate will be carried out at the edges of tabular alumina aggregates, as shown in the Fig. 5c, d, which indicates the CA_6 formation is controlled by diffusion of Ca^{2+} ions. In fact, the Ca^{2+} ions diffusion in the solid phase limits the morphology and growth CA_6 [19]. To further study the effect of CAC addition on TSR, the fracture morphology of specimens need to be examined.

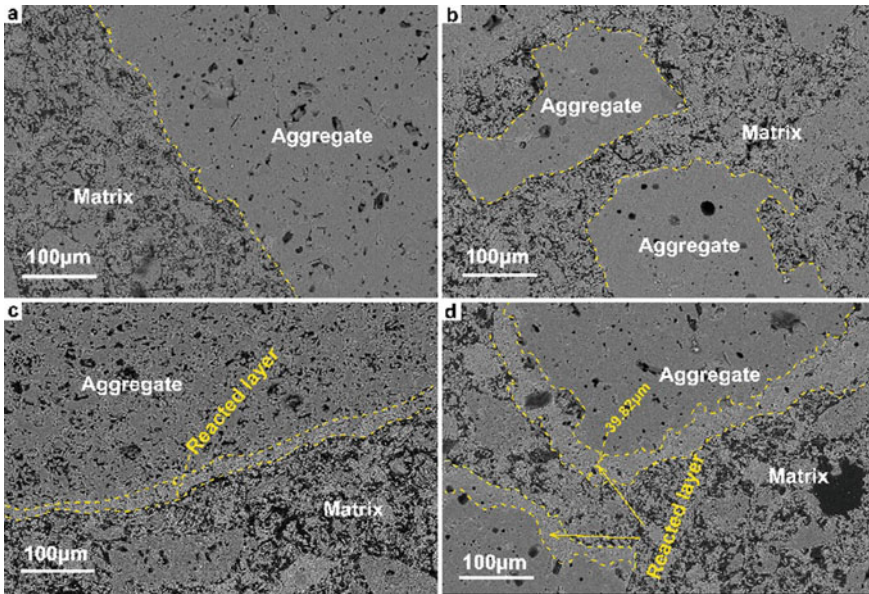


Fig. 5 SEM image of samples with different amounts of CAC addition firing at 1550 °C for 3 h: **a** AS2, **b** AS5, **c** AS8, **d** AS10. (Color figure online)

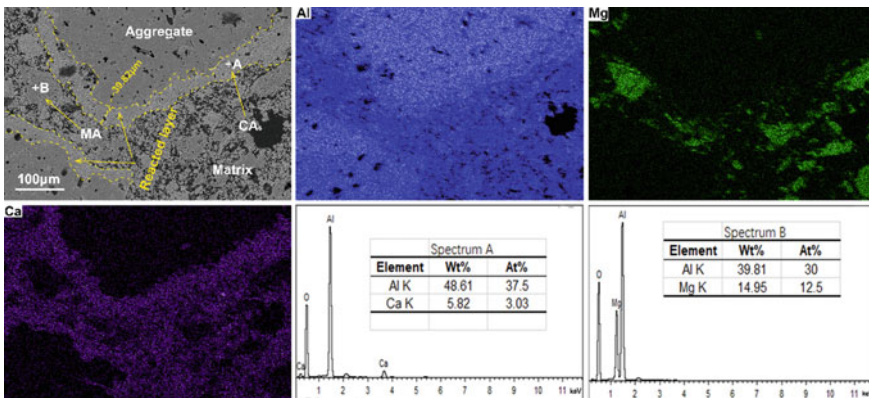


Fig. 6 SEM micrographs and energy spectrum analysis of cross section of corundum castables for AS10. (Color figure online)

The fracture surfaces of a castable after firing at 1550 °C for 3 h is given in Fig. 7 and the morphology of CA₆ can be compared with that shown in partial enlarged view. Notice from this figure that although CA₆ crystals develop to an interlocking structure between grain boundaries of corundum and spinel in each sample, the microstructure they involved exists obvious differences. The fracture surfaces of

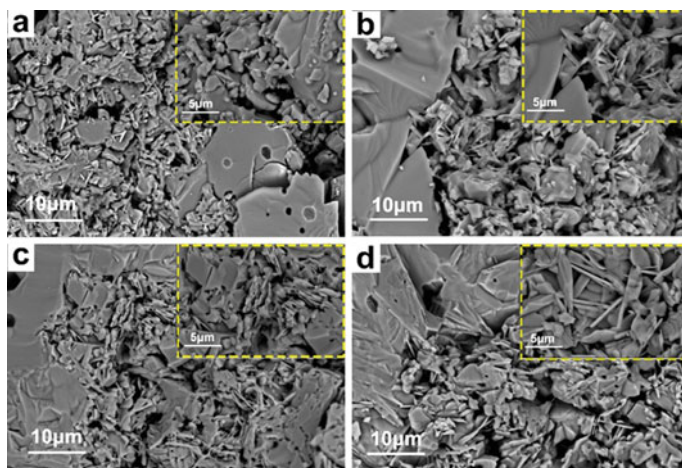


Fig. 7 SEM image of specimens fracture with different amounts of CAC addition firing at 1550 °C for 3 h: **a** AS2, **b** AS5, **c** AS8, **d** AS10. (Color figure online)

sample AS2 contains less amount and size of hexagonal flake CA_6 grains distribute in a disorderly manner in specimen, it is means that no strong bond exists between aggregates and matrix. This is the reason why it does not show a good thermal shock stability. In comparison, the platelet CA_6 grains gradually increase, grow up and distribute more and more uniformly for samples of AS5, AS8 and AS10 as seen in Fig. 7b–d, due to CA_6 grain nucleation agglomeration which lead to formation of pores and provide free space for CA_6 crystal growth. The sample AS5 does not give rise to a full and well defined reacted layer (Fig. 5b), it is still detected the direct bonding between corundum and MA by CA_6 crystals, which is beneficial to strengthen and accordingly leads to an increase in TSR. Moreover, with the cement content continuously increases, CA_6 grains show a tendency of equiaxial morphology which means the thickness of the hexagonal flake CA_6 increases. Sample AS10 forms a relatively dense body caused by the CA_2 occupation to the interlocking network structure by hexagonal flake CA_6 grains (Fig. 7d), which means that it is difficult to release thermal stress and further leading to the decrease of TSR.

In addition, it is well known that crack bridging and microcrack toughening are two approaches to promote the thermal shock resistance of castable. For the former, the in-situ CA_6 layer with card-house structures (partial enlarged view in Fig. 7b–d) can be regarded as a combination of alumina, spinel and the platelet CA_6 (bridges them), which is beneficial to alleviate thermal stress and induce the cracks deflection or branch. For the latter, the volume expansion caused by the formation of a series of calcium aluminate phases will form a certain amount of microcracks in the body. Appropriate density of microcracks can complicate crack propagation routes, and then the stress of crack tip can be released or absorbed. The two proposed mechanisms are in agreement with the observations in the AS5 and AS8 castables, that is why they obtain relatively favorable thermal shock resistance.

Conclusions

Cement contents significantly affect the microstructural evolution of cement-bonded silica-free alumina–spinel castables which is strongly related to TSR of this castables. With the increase of cement content, the number of nucleation of CA_6 was enlarged and provided more space for development of their hexagonal flake crystals, which is beneficial for the formation of an more strength interlocking network structure between grain boundaries of corundum and spinel. This card-house structure is beneficial to alleviate thermal stress as well as induce the cracks deflection or branch, and consequently improves the TSR of the alumina–spinel castable. Meanwhile, the microcracks caused by the expansion accompanying CA_6 formation can release the thermal stress, which is also contribute to enhance the TSR. It's important to note that excessive CAC addition will cause overexpansion and results in strength degradation. Consider the thermal shock resistance and its associated physical properties of the samples, the optimum CAC addition range is 5–8 wt% for the silica-free alumina–spinel castables.

Acknowledgements The authors gratefully acknowledge the National Natural Science Foundation of China (No. 51774072, 51774073, 51974080), which have made this research possible.

References

1. Martinez AGT, Luz AP, Braulio MAL, Sako EY, Pandolfelli VC (2017) Revisiting CA_6 formation in cement-bonded alumina–spinel refractory castables. *J Eur Ceram Soc* 37:5023–5034
2. Consonni LB, Luz AP, Pandolfelli VC (2019) Binding additives with sintering action for high-alumina based castables. *Ceram Int* 45(12):15290–15297
3. Braulio MAL, Rigaud M, Buhr A, Parr C, Pandolfelli VC (2011) Spinel-containing alumina-based refractory castables. *Ceram Int* 37:1705–1724
4. Long B, Xu G, Buhr A, Jin S, Harmuth H (2017) Fracture behavior and microstructure of refractory materials for steel ladle purging plugs in the system Al_2O_3 -MgO-CaO. *Ceram Int* 43:9679–9685
5. Kakroudia MG, Hugerb M, Gaultb C, Chotard T (2009) Damage evaluation of two alumina refractory castables. *J Am Ceram Soc* 29(11):2211–2218
6. Nag M, Agrawal T, Nag B, Singh B (2019) Study and post mortem analysis of steel ladle porous plug to improve bottom purging efficiency for cleaner steel. *Eng Fail Anal* 101:447–455
7. Kazemi N (2019) Reasons for crack propagation and strength loss in refractory castables based on changes in their chemical compositions and micromorphologies with heating: special focus on the large blocks. *J Asian Ceramic Soc* 7(2):109–126
8. Julio V, Nestor U, Luis L, Monica M, Lidia C (2020) The role of non-metallic Al_2O_3 inclusions, heat treatments and microstructure on the corrosion resistance of an API 5L X42 steel. *J Mater Res Technol* 18:5894–5911
9. Kim RH, Lee SJ, Jung SR, Lee SK (2013) Comparison of properties among spinel containing castables for steel ladle. Paper presented at the proceedings of UNITECR 2013, Canada, 10–13 Sep 2013
10. Ko YC (2010) Influence of the characteristics of spinels on the slag resistance of Al_2O_3 -MgO and Al_2O_3 -spinel castables. *J Am Ceram Soc* 83:2333–2335

11. Braulio MAL, Castro JFR, Pagliosa C, Bittencourt LRM, Pandolfelliz VC (2008) From macro to nanomagnesia: designing the insitu spinel formation. *J Am Ceram Soc* 91:3090–3093
12. Braulio MAL, Morbioli GG, Bittencourt LRM, Pandolfelli VC (2010) Novel features of nano-scaled particles addition to alumina-magnesia refractory castables. *J Am Ceram Soc* 93:2606–2610
13. Braulio MAL, Piva MFL, Silva GFL, Pandolfelli VC (2009) In situ expansion design by colloidal alumina suspension addition. *J Am Ceram Soc* 92:559–562
14. Long B, Buhr A, Xu G (2016) Thermodynamic evaluation and properties of refractory materials for steel ladle purging plugs in the system Al_2O_3 -MgO-CaO. *Ceram Int* 42:11930–11940
15. Xu L, Yin XL, Wang N, Chen M (2017) Effect of Y_2O_3 addition on the densification, microstructure and mechanical properties of MgAl_2O_4 - CaAl_4O_7 - $\text{CaAl}_{12}\text{O}_{19}$ composites. *J Alloy, Compd* 12:472–478
16. Banerjee SRD (1998) *Monolithic Refractories: A Comprehensive Handbook*. World Scientific, The American Ceramic Society, USA, Westerville
17. Luz AP, Pandolfelli VC (2011) Halting the calcium aluminate cement hydration process. *Ceram Int* 37:3789–3793
18. Asmi D, Low IM (1998) Processing of an in-situ layered and graded alumina/calcium hexaaluminate composite physical characteristics. *J Eur Ceram Soc* 18:1735–1738
19. Domínguez C, Chevalier J, Torrecillas R, Fantozzi G (2001) Microstructure development in calcium hexaluminate. *J Eur Ceram Soc* 21:381–387

Thermodynamic Analysis of Fe-FeAl₂O₄ Composite Material Prepared by Molten Salt Deoxidation



Yanke Xu, Hongyan Yan, Chao Luo, Hui Li, and Jinglong Liang

Abstract The Fe-FeAl₂O₄ composite material was prepared by molten salt electro-deoxidation method. It used mixed Fe₂O₃ and Al₂O₃ powder for tableting, and served as cathode electrolysis. The standard Gibbs free energy change (ΔG^\ominus) and theoretical decomposition voltage (E^\ominus) of each reactant in the system were calculated by FactSage. The results showed that the E^\ominus was in the range of -1.01 V to -2.31 V at 800°C , Fe₂O₃ reduced to FeO, formed FeAl₂O₄ spinel phase with Al₂O₃, and the remaining FeO continued to reduce to metallic phase Fe. By using FactSage to analyze the phase diagram of FeO-Al₂O₃ binary system, it can be determined that the molar ratio of Fe₂O₃ and Al₂O₃ was 2:1 and the best reaction temperature range for preparing Fe-FeAl₂O₄ composite material was $800\text{--}900^\circ\text{C}$.

Keywords Fe-FeAl₂O₄ composite material · Molten salt deoxidation · Thermodynamic

Introduction

Molten salt electric-deoxidation is a very important process technology in industry to prepare metals and alloys. This method is first published in Nature in 2000. The principle of this method is to use the reactant as the cathode and graphite as the anode to be electrolytically reduced to metal or alloy under a certain decomposition voltage. During this electrolysis process, oxygen ions would migrate from the anode to the molten salt and finally discharges at the anode. Compared with some traditional

Y. Xu · H. Yan (✉) · H. Li · J. Liang

College of Metallurgy and Energy, North China University of Science and Technology, Tangshan 063210, China

e-mail: xiaoniji@126.com

C. Luo

School of Materials and Metallurgy, Inner Mongolia University of Science and Technology, Baotou 014010, China

Hesteel Group Tangsteel Company, Tangshan 063000, China

© The Minerals, Metals & Materials Society 2021

TMS 2021 150th Annual Meeting & Exhibition Supplemental Proceedings,

The Minerals, Metals & Materials Series,

https://doi.org/10.1007/978-3-030-65261-6_38

processes, this method has a short process and low energy consumption. In recent years, people have successfully prepared Co [1], Ti [2], Cr [3], Ta [4] and other metals. Also a series of alloys such as TbNi₅ [5], NiTi [6], TiMo [7], FeTi [8] are prepared. Some alloys that are difficult to prepare were usually prepared by this method.

Cermet is a composite material composed of one or several metals and ceramic materials. It combines the excellent properties of ceramics and metals, such as high strength, high hardness, corrosion resistance, wear resistance, high temperature resistance and good thermal shock resistance [9]. With the development of new processes and materials, cermet is mainly used in aerospace, electric power, automobiles, building materials and other fields [10, 11]. The research on cermet has become an important research direction in the field of composite materials. Compared with magnesium-based cermet, aluminum-based cermet, and titanium-based cermet, iron-based cermet has problems such as high specific gravity, high sintering temperature, and low specific strength, and there are fewer research results on iron-based cermet.

In this paper, combined with the calculation and analysis of each reaction of molten salt electro-deoxidation by thermodynamic calculation, the influence of electrolysis temperature, decomposition voltage and other thermodynamic parameters on the electro-deoxidation process was investigated. It provided theoretical guidance for the preparation of Fe-FeAl₂O₄ composite materials by molten salt electro-deoxidation in Fe₂O₃-Al₂O₃ system.

Reaction Thermodynamics

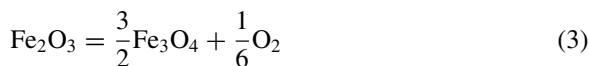
Electrode-Oxygenation Reaction

Fe₂O₃ and Al₂O₃ powders were mixed and pressed into tablets as the cathode, the anode was graphite flake, and the electrolyte was NaCl-KCl. The Fe-FeAl₂O₄ composite material was prepared by the molten salt electro-deoxidation method. Fe₂O₃ can be reduced from Fe₃O₄ to Fe step by step during electrified process [12]. The reduced low-valence iron oxide synthesizes iron-aluminum spinel with Al₂O₃, and then formed Fe-FeAl₂O₄ composite material with the reduced Fe. The reaction equations involved in the above process were given below.

Equation of Al₂O₃ electrified reactions,



Equation of Fe₂O₃ electrified reactions,



FactSage was used to calculate the standard Gibbs free energy of the possible reactions in the molten salt system at 0–1200 °C. The standard theoretical decomposition voltage E^\ominus could be calculated by following calculation formula.

$$\Delta G^\ominus = -nFE^\ominus$$

where, ΔG^\ominus was the standard Gibbs free energy (kJ mol^{-1}), E^\ominus was the theoretical decomposition voltage in the standard state (V), F was the Faraday constant ($96,485 \text{ C mol}^{-1}$), n was the number of electrons gained or lost in the reaction equation.

It can be seen from Fig. 1 that the decomposition reaction of iron oxide is easier to proceed in the process of electro-deoxidation in molten salt, while the decomposition reaction of alumina is more difficult to proceed.

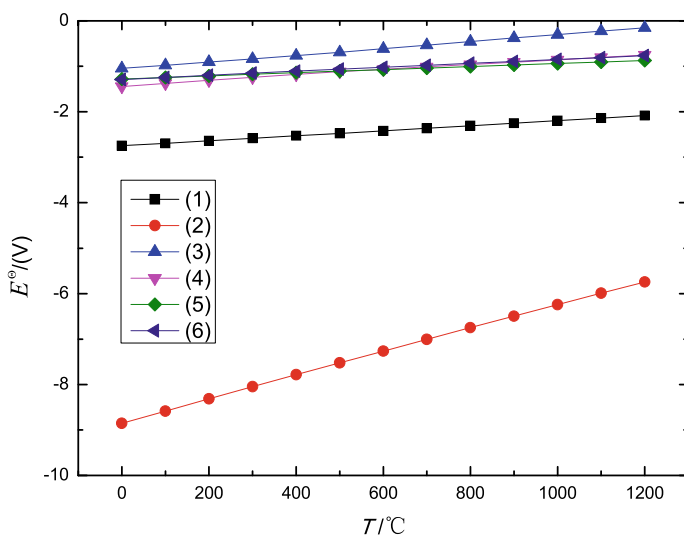
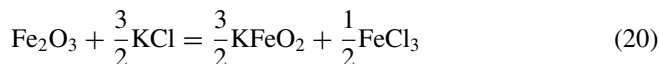
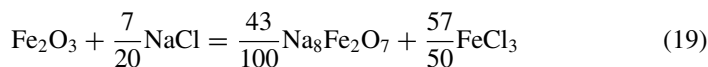
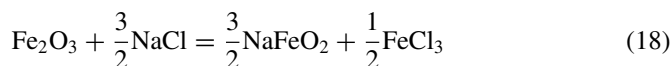
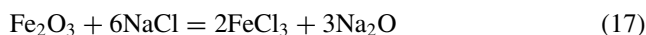
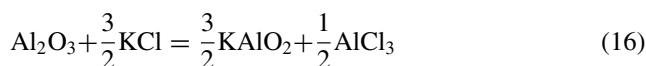
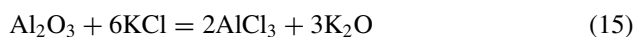
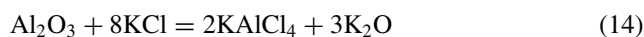
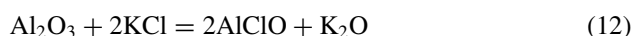
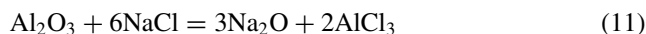
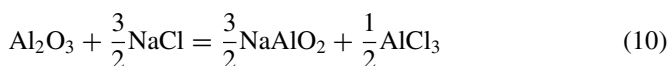
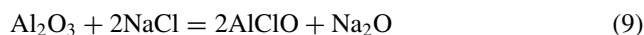
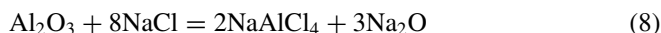
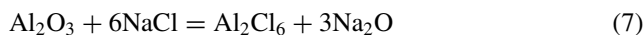


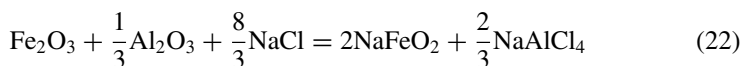
Fig. 1 The calculated results between E^\ominus and T at 0–1200 °C. (Color figure online)

Chemical Reactions with Molten Salt

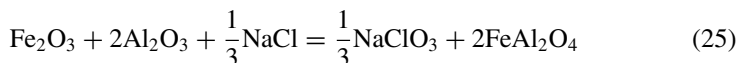
There is not only the electrochemical reaction in the molten salt system, but also the chemical reaction among reactants could be proceed. The following are the chemical reaction equations that may occur in molten salt.

No variety of valence state,





Variety of valence state,



According to thermodynamic calculations, the standard Gibbs free energy ΔG^\ominus from Eq. (7) to Eq. (26) at 0–1200 °C were all greater than zero. It was impossible to proceed spontaneously and there was no new material formation.

Influence of Electrolysis Reaction

Molten Salt System

There are many high temperature molten salt systems, such as chloride, fluoride salt, nitrate, etc. The chloride salt molten salt system, especially NaCl-KCl, is the commonly used system. Because NaCl-KCl is cheap and has the advantages, such as large specific heat capacity, low thermal conductivity, low viscosity, wide operating temperature range, good stability, high decomposition voltage, low cost [13]. It is widely used for extracting elemental metal or preparing synthetic materials (Fig. 2).



The theoretical decomposition voltage of NaCl was -3.24 V, and the theoretical decomposition voltage of KCl was -3.48 V at 800 °C. It was greater than the theoretical decomposition voltage of the reactant.

If a single chloride was used as the electrolyte, the melting point of KCl was 801 °C and NaCl was 770 °C. This required a higher electrolysis temperature. Not only wasted energy, but also accelerated the volatilization of molten salt, which posed

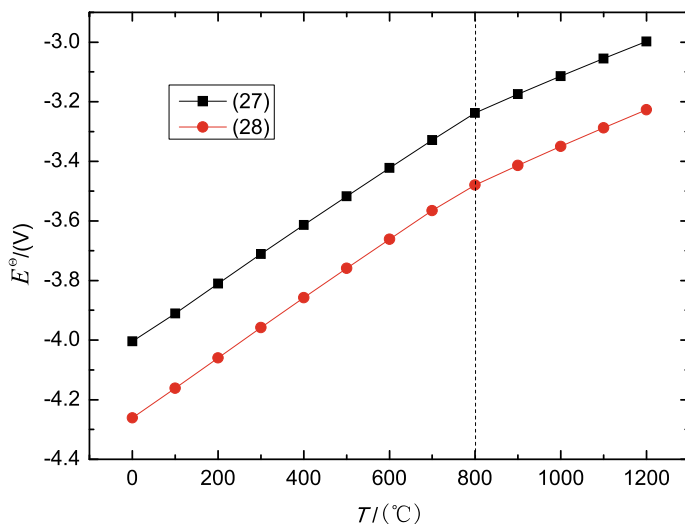


Fig. 2 Variation of E^{\ominus} with temperature. (Color figure online)

a safety hazard to the entire experiment. As shown in Fig. 3, using a mixed KCl-NaCl molten salt system, the eutectic point of the system was about 657 $^{\circ}\text{C}$. It improved the operating environment and reduced energy consumption costs and potential safety hazards. Especially the reaction product was not doped with other impurities, the viscosity was low and the cost was low. In this paper, the KCl-NaCl was selected.

Electrolysis Temperature

According to the phase diagram of the FeO- Al_2O_3 binary system, the metallic Fe-based and FeAl_2O_4 ceramic phases can be obtained within 1300 $^{\circ}\text{C}$ (Fig. 4).

As shown in Fig. 3, when the molar ratio of NaCl to KCl was 1:1, the molten salt reached the lowest eutectic point at about 657 $^{\circ}\text{C}$. The higher the electrolysis temperature, the better kinetic conditions were got. However, high temperature would cause rapid anodic oxidation and molten salt volatilization. Therefore, the electrolysis temperature was preferably 150–200 $^{\circ}\text{C}$ higher than 657 $^{\circ}\text{C}$, and the electrolysis temperature range was 800–900 $^{\circ}\text{C}$.

E^{\ominus} and Raw Material Ratio

In order to ensure that the cathode oxide was decomposed or reduced into a pure metal or alloy, while the molten salt electrolyte did not undergo electrochemical

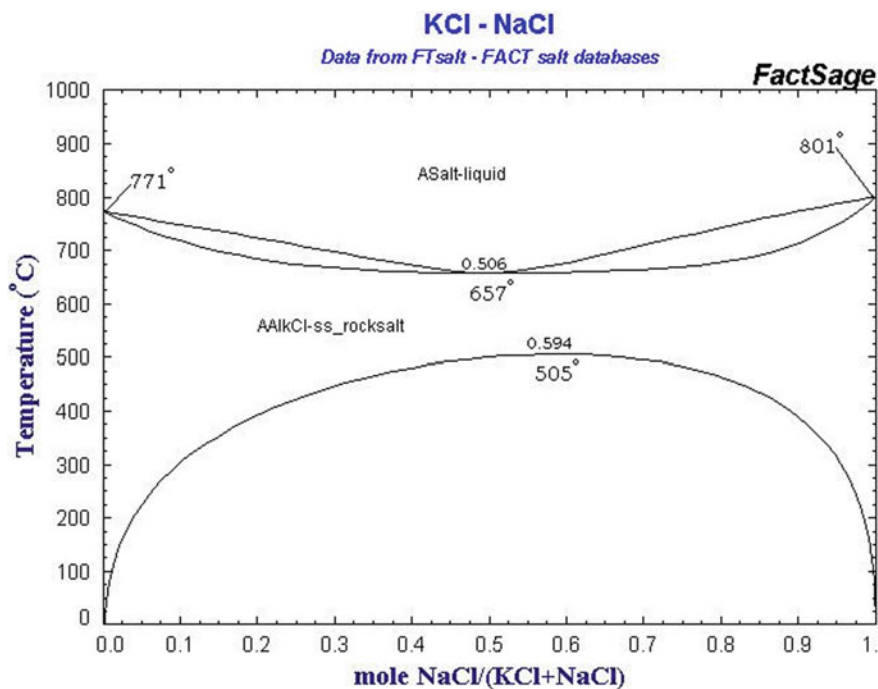


Fig. 3 KCl-NaCl molten salt phase diagram. (Color figure online)

reaction, the determination of the theoretical decomposition voltage was particularly important (Table 1).

The theoretical decomposition voltages of NaCl and KCl were -3.24 V and -3.48 V at 800 °C, respectively. The electrolysis voltage cannot be higher than the theoretical decomposition voltage of NaCl and KCl at 800 °C, otherwise the molten salt would be decomposed. The theoretical decomposition voltage of Al₂O₃ was -2.31 V. In order to combine Al₂O₃ and FeO to form FeAl₂O₄, Al₂O₃ cannot be decomposed. At 800 °C, Fe₂O₃ gradually reduced to Fe₃O₄, FeO and Fe, the theoretical decomposition voltages were -0.45 V, -0.96 V and -1.01 V respectively. To ensure that Fe₂O₃ can be decomposed into Fe element, the electrolysis voltage must be higher than -1.01 V. In summary, the decomposition voltage of this experiment should be between -1.01 V and -2.31 V.

During the experiment, when Fe₂O₃ was reduced to FeO, part of FeO combined with Al₂O₃ to form FeAl₂O₄, and the other part of FeO would continue to be reduced to Fe. At this time, excessive Fe₂O₃ powder was needed. Through the electrochemical Eqs. (3)–(5), the molar ratio of Fe₂O₃: FeO = 1:2 can be calculated. As shown in Fig. 2, when Al₂O₃/(Al₂O₃ + FeO) was 0.2, the molar ratio between Al₂O₃ and FeO was 1:4. It was known that the raw materials molar ratio Al₂O₃:Fe₂O₃ = 1:2.

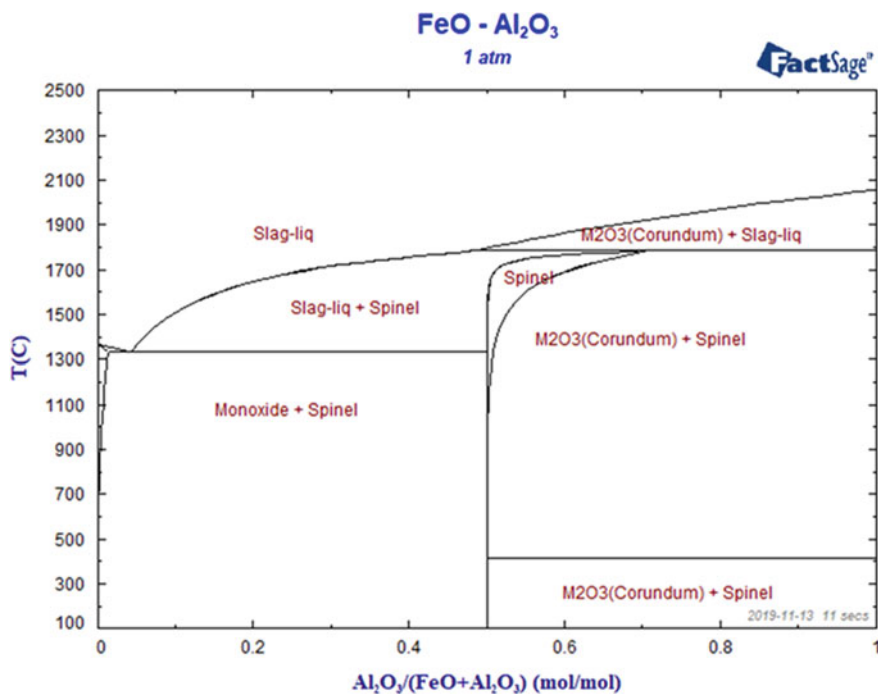


Fig. 4 Binary phase diagram with FeO–Al₂O₃. (Color figure online)

Table 1 Theoretical decomposition voltage of iron oxide

Iron oxide	E^{\ominus} (V)
Fe ₃ O ₄	–0.454
FeO	–0.96
Fe	–1.01

Conclusions

- (1) It was impossible to proceed reaction between reactants with molten salt, and no new material formation.
- (2) It was feasible to choose a mixed NaCl-KCl molten salt system, and the molar ratio was 1:1. The electrolysis temperature range was 800–900 °C. The raw material ratio was Al₂O₃:Fe₂O₃ = 1:2.
- (3) The decomposition voltage was between –1.01 V and –2.31 V at 800°C. Fe–FeAl₂O₄ composites can be prepared by the method of electro-deoxidation in molten salt.

Acknowledgements This work was supported by the National Natural Science Foundation of China (No.51804126) and Natural Science Foundation of Hebei Province (No. E2018209266).

References

1. Qingjun Z, Meiling Q, Ling W et al (2009) Preparation of Co alloy by direct electro-deoxidization in molten salt. *J Funct Mater* 40(5):830–832+835
2. Abdelkader AM, Kilby KT, Cox A et al (2013) Dc voltammetry of electro-deoxidation of solid oxides. *Chem Rev* 113(5):2863–2886
3. Bingjian Z, Ling W, Lei D et al (2008) Research of preparation of Cr by electro-deoxidation in molten salt. *Powder Metall Ind* 18(2):23–27
4. Xiaofeng H, Qian X (2006) Preparation of tantalum by electro-deoxidation in a CaCl₂-NaCl melt. *Acta Metall Sin* 42(3):285–289
5. Guodong Q, Dihua W, Xiabo J et al (2006) A direct electrochemical route from oxide precursors to the terbium–nickel intermetallic compound TbNi₅. *Electrochim Acta* 51(26):5785–5793
6. Jackson BK, Dye D, Inman D et al (2010) Characterization of the FFC Cambridge process for NiTi production using in situ X-Ray synchrotron diffraction. *J Electrochem Soc* 157(4):129–137
7. Bhagat R, Jackson M, Inman D et al (2008) The production of Ti-Mo alloys from mixed oxide precursors via the FFC cambridge process. *J Electrochem Soc* 155(6):63–69
8. Zhongren Z, Yixin H, Cunying X et al (2017) Synthesis of Micro-FeTi powders by direct electrochemical reduction of Ilmenite in CaCl₂-NaCl molten salt. *Ionics* 23(1):213–221
9. Miracle DB (2005) Metal matrix composites: from technology to science. *Compos Sci Technol* 65:2526–2540
10. Bains PS, Sidhu SS, Payal HS (2015) Fabrication and machining of metal matrix composites: a review. *Mater Manuf Processes* 31(5):553–573
11. Haghshenas M (2016) Metal-matrix composites. Elsevier, New York
12. Hui L, Lei J, Jinglong L et al (2019) Study on the Direct Electrochemical Reduction of Fe₂O₃ in NaCl-CaCl₂ Melt. *Int J Electrochem Sci* 14:11267–11278
13. Shixian Z, Xianping Z, Yungang L (2016) Application and researching progress of high temperature molten salt system. *Plating Finishing* 38(9):22–27

Part XIV
Advances in Surface Engineering III

Evaluation of the Surface Integrity of Titanium Nitride Coating Deposited on the Ni–Ti Substrate Through the Near-Dry Electrical Discharge Surface Coating Process



Ramver Singh, Akshay Dvivedi, and Pradeep Kumar

Abstract Having superior mechanical properties, nickel-titanium (Ni–Ti) based shape memory alloys are extensively used to make bio-implants. The existing literature suggests several surface modification techniques, including surface coating, for improving the bio-compatibility by reducing leakage of nickel from surface layers. Herein, an environmentally-friendly surface coating method, based on the concept of near-dry electric discharge machining (ND-EDM) process, was explored to deposit the titanium nitride (TiN) layer. Repeated spark discharges occurring in a two-phase dielectric medium of water and nitrogen gas were used for depositing the layer. The effect of process parameters like peak-current and pulse-on time on the surface integrity of deposited layers was evaluated. The deposited surfaces were characterized using the X-Rays diffraction (XRD), field-emission scanning electron microscopy (FE-SEM), and atomic force microscopy (AFM) techniques. The results show that the TiN layer can successfully be deposited onto Ni–Ti substrate.

Keywords Surface integrity · TiN · Coating · Near-dry · Nitriding · EDM · Nitinol

Introduction

Nickel-titanium (Ni–Ti) based shape memory alloy is an attractive material for biomedical applications due to its unique shape-memory and superelastic characteristics, high corrosion resistance, and suitable mechanical strength [1]. However, leaching of toxic nickel ions when in prolonged contact with human body's corrosive fluids engenders health risks such as cytotoxicity, allergic reactions, and inflammation [2, 3]. Therefore, different techniques have been explored to avoid these risks [4]. Surface coating is one of such techniques in which a layer of non-toxic and relatively inert material, such as titanium nitride (TiN), is deposited on the surface. The deposited layer breaks the physical contact between the material and corrosive fluids, and thereby prevents the leaching of nickel ions from the surface. There exists

R. Singh (✉) · A. Dvivedi · P. Kumar
Indian Institute of Technology (IIT) Roorkee, Roorkee 247667, India
e-mail: ramver.pme@gmail.com

© The Minerals, Metals & Materials Society 2021
TMS 2021 150th Annual Meeting & Exhibition Supplemental Proceedings,
The Minerals, Metals & Materials Series,
https://doi.org/10.1007/978-3-030-65261-6_39

a wide variety of surface coating processes, for instances, chemical vapour deposition (CVD), physical vapour deposition (PVD), plasma coating, and electric discharge coating, suitable for this purpose [5]. In particular, the EDC process is more suited. Since the machining of Ni–Ti alloys is difficult through conventional (i.e. contact-based) processes, and therefore, their machining is generally performed through advanced (i.e. “non-contact” based) processes, e.g., electric discharge machining (EDM). As the EDC can be performed on the same EDM facility with minimal modification, thus making it a suitable option.

During the EDC process, deposition is mainly accomplished by two routes: through a semi-sintered or green compact tool electrode, and using a powder suspended dielectric medium [6]. In the former route, the tool electrode plays the role of the material feed stock. The loosely held powder migrates from the tool towards the work surface under the influence of thermo-physical phenomena triggered by the initiation, growth and collapse of the plasma channel. A fraction of the eroded material is eventually embedded in the recast layer, and thus, enhancing the surface properties through deliberate surface alloying or coating. Whereas, in the later route, the dielectric medium itself plays the role of feed stock as far as coating material or alloying elements are concerned. Under the influence of electrical field, the powder particles arrange themselves in the inter-electrode gap (IEG) in order to form a conductive bridge of least electrical resistance which assists in triggering spark discharge. The entrapped particles in the plasma channel and molten puddle start melting and re-solidifies with the puddle.

In last decade, there are several investigation on surface modification following both the routes of EDC process. For example, Furutani et al. [7] successfully deposited a 150 μm thick layer of titanium carbide (TiC) on the steel substrate using the EDC procedure with TiC powder suspended in the kerosene [7]. They reported an improvement in the surface properties in terms of wear resistance and micro-hardness after the treatment. Otsuka et al. and Yang et al. [8, 9] studied various aspects of crystal structure and surface chemistry of the EDMed grade 2 and 5 titanium alloys, respectively [8, 9]. They concluded that the EDMed implant surface’s osseointegration response was better than that of the conventionally machined. Whereas, Wang et al. [10] used a green-compacted titanium to deposit the TiC coating by facilitating a reaction between the molten titanium from tool electrode and carbon released from kerosene disintegration [10]. They reported that formed TiC coating was three time harder than the substrate. Further, Shigyo and Nakano [11] developed an EDM tool electrode specifically built for surface coating operations [11]. They coated the surface of metal powder with nitride prior to the green compacting procedure to prevent the oxidation of the metal powder due to frictional heat, and thereby, led to more uniform distribution of surface characteristics.

It becomes clear from the above-cited literature that both of the EDC route mainly use liquid hydrocarbon-based dielectric mediums, such as kerosene and commercially available EDM oil. The disintegration of such oils produces carbon by-products and obnoxious fume which could led to health and safety risks. Hence, efforts have been made to develop operator and environmental friendly variants of the EDM process. The development of dry and near-dry EDM process variants are examples

of such efforts [12]. In year 1985, Ramani and Cassidenti developed the dry variant of the EDM process by using gaseous phase dielectric medium instead of traditionally used liquid phase to drill holes [13]. Since then, several investigations have been undertaken to assess and enhance the process capability. Yadav et al. and Kunieda et al. [14, 15] attempted to increase the material removal rate by supply additional oxygen in the dielectric media during the EDM of steel work material [14, 15]. The exothermic reactions involving oxidation of iron was attributed as a possible reason for the increase in MRR. However, the relatively poor flushing ability of gaseous dielectrics leads to the re-attachment of debris particles on the work and tool surfaces triggers frequent incidents of short-circuiting which in turn leads to poor surface integrity. The use of trace amount of liquid in the gaseous phase (i.e. two-phase dielectric mixture of liquid in gas) often eliminates this limitation in near-dry EDM variant. Tanimura et al. [16] researched on the feasibility of using water mist (water in air mixture) as the dielectric medium in the EDM process [16]. The presence of a liquid phase improves the dielectric medium's ability to dissipate heat. In this way, it helps in quick solidification of molten material ejected from the puddle. As a result, it impedes re-attachment of debris onto the tool and work surfaces which eventually improves the integrity of the surface.

The dry and near-dry concepts of EDM process are in research and development phase, and have the potential to replace the conventional EDM process. Literature on the use of these process variants for surface modification applications is rare. Chen et al. [17] assessed the effect of different process parameters during EDC treatment of 6061-T6 aluminum alloy under wet (kerosene) and dry (nitrogen gas) conditions using Ti-sintered tool electrode [17]. They observed that the modified surfaces embraced layer of titanium carbide and titanium nitride under wet and dry conditions, respectively. Huang et al. [18] explored the dry-EDM variant for depositing a coating of titanium nitride on Ni-Ti alloy [18]. Nitrogen gas was used as a dielectric medium. The presence of nitrogen gas shielded the molten material, and thus, prevented the formation of oxide and/or hydroxide in the recast layer. They observed that the treated Ni-Ti alloy work samples exhibited shape-memory effect even though the surface is coated with a thick and hard layer of TiN. Common observations among these investigations are poor integrity of the treated surface due to the presence of micro-cracks, voids and globules usually caused by the re-attachment of debris particles onto the tool and work surfaces. As a result, further post-processing becomes essential which ultimately increases the processing time and cost. Hence, there is a need to develop an environmentally-friendly EDC variant capable of producing surface free from such defects. The near-dry EDM process can be a potential solution.

In the current investigation, a layer of TiN coating was deposited on Ni-Ti substrate at different process parameters via near-dry EDC process. The experiments were conducted following one-factor-at-a-time (OFAT) scheme by varying the peak-current and pulse-on time at five levels. The effect of process parameters on the surface integrity in terms of crack density, and surface roughness of processed samples was evaluated. The deposited surfaces were characterized using the x-rays

diffraction (XRD), scanning electron microscopy (SEM), energy dispersive spectroscopy (EDS), and atomic force microscopy (AFM) techniques. The cross-sectional analysis of treated samples were done to measure the thickness of deposited layer.

Experimentation Details

Coating of TiN were deposited on Ni–Ti based shape memory alloy substrates which was selected due to its wide applications in the biomedical industry. Samples of 10mm × 20mm dimensions were cut from a flat sheet of 5 mm thickness using the wire-EDM process. To get rid of the thermal damages generated during the wire-EDM operation and to obtain uniform surface prior to the treatment, sample were initially subjected to mechanical polishing using abrasive papers (P400 to P2000) and then to cloth polishing in alumina colloidal solution. An Excetek ED30C three-axis CNC EDM machine was modified for performing near-dry surface coating experiments. Figure 1 depicts the schematic diagram of the modified experimental setup. A flushing unit to produce a two-phase mixture of glycerine in nitrogen gas was developed in-house. Measured quantities of liquid and gaseous phases were supplied into a mixing chamber using peristaltic pump and nitrogen gas cylinder, respectively. Tiny droplets of the liquid form when the liquid phase comes in contact with high velocity stream of nitrogen gas in the mixing chamber. The formed two-phase dielectric medium of glycerine in nitrogen mixture (hereinafter referred to as Gly-N₂ mist) was supplied into the IEG through the tubular-shaped tool electrode. Commercially pure titanium was selected as the tool material to minimize the possibility of foreign material inclusion in the TiN coating.

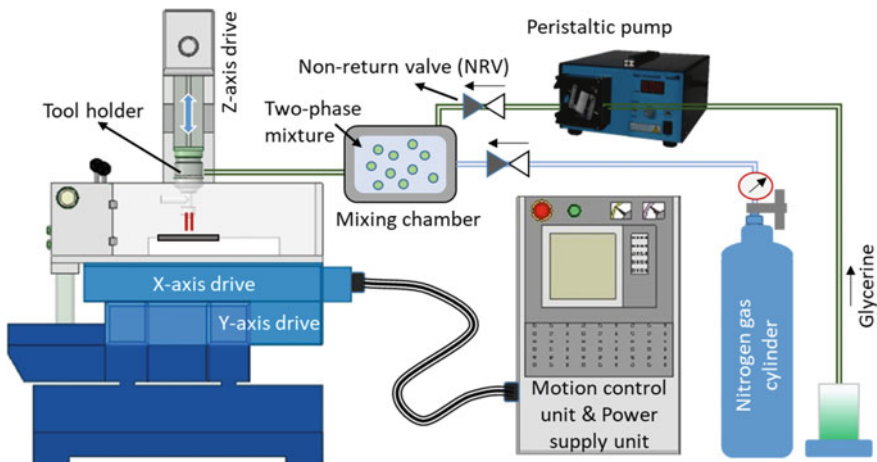


Fig. 1 Schematic diagram of the experimental setup. (Color figure online)

Table 1 Details pertaining the ranges and values of processing parameters

Parameters	Descriptions/values				
Tool material	Titanium (Green compacted)				
Tool geometry	Tubular (outer dia, 8 mm; inner dia, 6 mm)				
Polarity	Straight (Work, +)				
Machining time	2 min				
Sparking duration	30 s				
Dielectric media	Glycerin (liquid) + Nitrogen (gas)				
Gas pressure	40 psi				
Liquid flow rate	4 ml/min				
Peak current	1 A	2 A	3 A	4 A	5 A
Pulse-on time	10 μ s	30 μ s	50 μ s	70 μ s	90 μ s

The processing parameters used were chosen after preliminary experiments. The aim of these experiments was to obtain broad range of process parameters for which the coating can be successfully deposited. Table 1 provides details pertaining the ranges and values of variable and constant processing parameters used in this investigation. The peak current and pulse-on time were the variable parameters. The values of constant parameters were selected based on previous investigations for obtaining stable sparking conditions. The experiments were performed by following OFAT approach. In which, one parameter is varied at a time and another parameter was kept constant at their mid-level. Each experiment was performed thrice to obtain experimental results with minimal extent of experimental errors.

The surface integrity of the treated samples was examined using various characterization techniques such as XRD, EDX, FE-SEM, and AFM. An X-ray diffractometer (Bruker; D8) was operated in conventional $\theta/2\theta$ and glancing-angle modes. A FE-SEM (Carl Zeiss; Ultra plus) equipped with EDX detector was used for microscopic analysis of the deposited TiN coating. An atomic force microscope (INTEGRA; NT-MDT-INTEGRA) was used to obtain arithmetical mean surface roughness (R_a value) for corresponding scan area of $50 \mu\text{m} \times \mu\text{m}$. Cross-section analysis was conducted to find out the coating layer thickness.

Results and Discussion

The assessment of the effect of varying different process parameters such as peak current and pulse-on time on the surface integrity of coated samples is presented in this section. At first, the results of XRD analysis explaining the metallurgical aspects of the coating is presented and discussed. Then, the qualitative and quantitative assessments of the surface topography performed through the FE-SEM and AFM

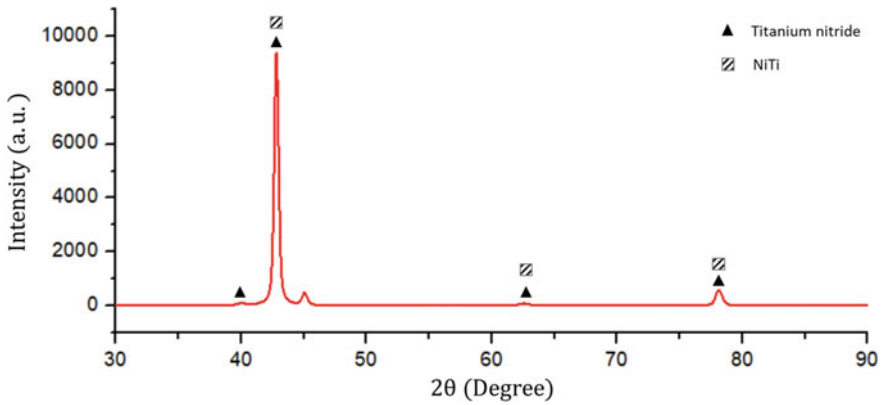


Fig. 2 Representative XRD spectrum of the coated surface. (Color figure online)

analyses, respectively, is presented. Lastly, the results of image processing analysis of the top and cross-sectional surfaces are presented and discussed.

Figure 2 displays the representative XRD spectrum of the TiN coating deposited on NiTi substrate. The reference data of JCPDS were used to assign the observed peaks. The presence of NiTi peaks may be attributed to the x-ray reflection from the work substrate as the coating may not be thick enough. The spark discharges triggers disintegration of nitrogen gas molecules in and around the plasma channel. The produced energetic nitrogen reacts with the molten titanium to produce titanium nitride.

Figures 3 and 4 show FE-SEM micrographs of the top and cross-sectional surfaces of the coated at different current settings and pulse-on time values, respectively. Microscopic pores were also found onto the surface of deposited surface. Besides, micro-cracks and peculiar splats-like features were observed onto the surfaces of samples coated at higher current settings. The surfaces coated at higher current settings appeared to be relatively rough in comparison to the surfaces coated at lower current settings. For shorter pulse-on time (i.e., 10 μ s), the surface appeared to be relatively uniform and embraced even-sized pores. Whereas, for longer pulse-on time values, the surface embraced micro-craters of varying sizes. The coating thickness increased notably on increasing the peak current; whereas, only a slight increase in it was observed upon increasing the value of pulse-on time. It is known that the thermal energy liberated from the spark discharge during the EDM process increases on increasing the values of both peak current and pulse-on time [19, 20]. Hence, higher discharge energy results in greater melting of work material and consequently may form thicker recast layer.

Figure 5 shows the effect of varying the peak current and pulse-on time on the average surface roughness (R_a) of the coated surface. The average R_a value of the coated surface increased approximately by 137% when the current settings were increased from 1 to 5 A, for a constant pulse-on time (50 μ s). Whereas, an approximate increase of 98% was observed when the duration of the pulse-on was prolonged

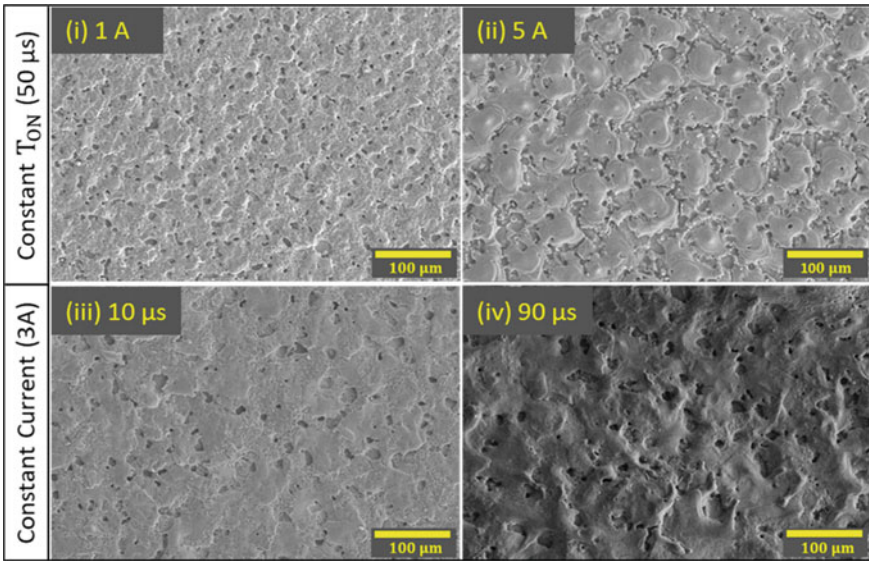


Fig. 3 FE-SEM micrographs of top surface of the coated sample under different processing conditions. (Color figure online)

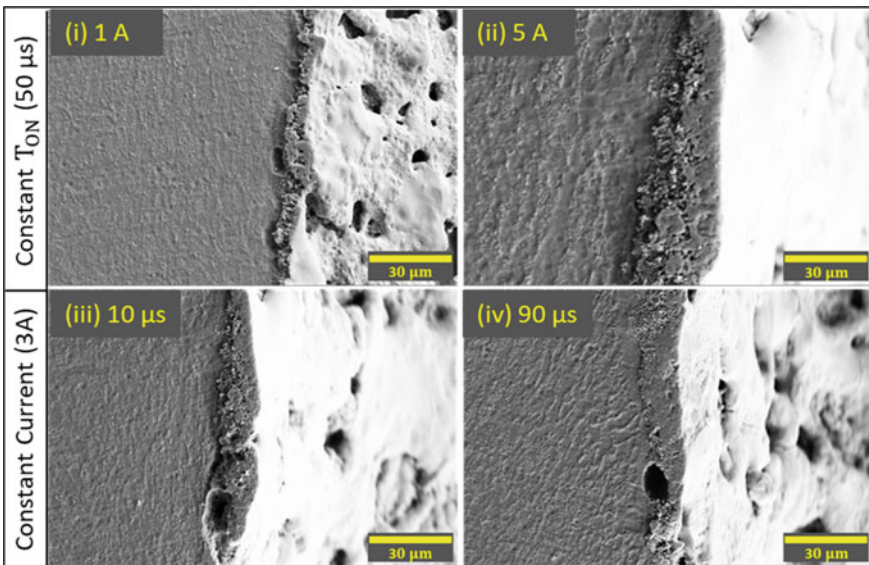


Fig. 4 FE-SEM micrographs of cross-sectional surface of the coated sample under different processing conditions. (Color figure online)

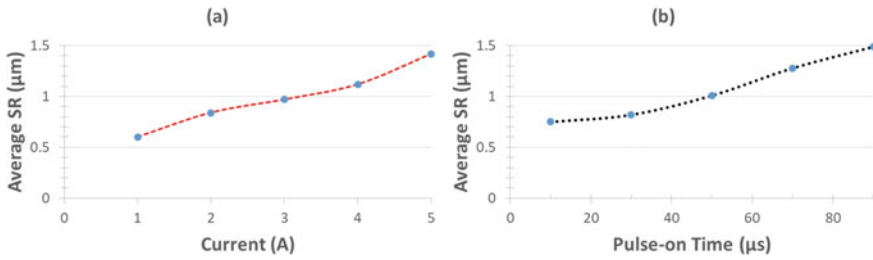


Fig. 5 Effect of varying **a** peak current from 1 to 5 A, and **b** pulse-on time from 10 μs to 90 μs on the average surface roughness (R_a) of the coated surface. (Color figure online)

from 10 μs to 90 μs , at same current settings of 3 A. As discussed earlier an increase in the current or pulse-on duration results in liberation of greater discharge energy which led to formation of deeper and larger size molten puddle. Subsequently, it can lead to generation of deeper and larger-sized micro-craters which can be a possible reason for this observed increase in the values of average surface roughness [21].

Conclusions

- This work has shown that a coating of TiN can be deposited onto Ni–Ti substrate using near-dry concept of EDM process.
- The average R_a value increased approximately by 137% and 98% on increasing the values of current from 1 to 5 A, and pulse-on time from 10 μs to 90 μs , respectively.
- Cross-sectional analysis revealed that on increasing the current settings from 1 to 5 A, a notably thicker coating was formed, whereas, only a slight increase in the thickness was observed when pulse-on duration was increased from 10 μs to 90 μs .

References

1. Pequegnat A, Michael A, Wang J, Lian K, Zhou Y, Khan MI (2015) Surface characterizations of laser modified biomedical grade NiTi shape memory alloys. *Mater Sci Eng C* 50:367–378
2. Zhang D, Zhang Z, Zi Z, Zhang Y, Zeng W, Chu PK (2008) Fabrication of graded TiN coatings on nitinol occluders and effects on in vivo nickel release. *Biomed Mater Eng* 18:387–393
3. Liu Y, Ren Z, Bai L, Zong M, Gao A, Hang R, Jia H, Tang B, Chu PK (2017) Relationship between Ni release and cytocompatibility of Ni-Ti-O nanotubes prepared on biomedical NiTi alloy. *Corros Sci* 123:209–216
4. Starosvetsky D, Gotman I (2001) Corrosion behavior of titanium nitride coated Ni-Ti shape memory surgical alloy. *Biomaterials* 22:1853–1859

5. Shabalovskaya S, Anderegg J, Van HJ (2008) Critical overview of nitinol surfaces and their modifications for medical applications. *Acta Biomater* 4:447–467
6. Simao J, Lee HG, Aspinwall DK, Dewes RC, Aspinwall EM (2003) Workpiece surface modification using electrical discharge machining. *Int J Mach Tools Manuf* 43:121–128
7. Furutania K, Saneto A, Takezawa H, Mohri N, Miyake H (2001) Accretion of titanium carbide by electrical discharge machining with powder suspended in working fluid. *Precis Eng* 25:138–144
8. Otsuka F, Kataoka Y, Miyazaki T (2012) Enhanced osteoblast response to electrical discharge machining surface. *Dent Mater J* 31:309–315
9. Yang TS, Huang MS, Wang MS, Lin MH, Tsai MY, Wang PY (2013) Effect of electrical discharging on formation of nanoporous biocompatible layer on Ti–6Al–4V alloys. *Implant Dent* 22:374–379
10. Wang ZL, Fang Y, Wu PN, Zhao WS, Cheng K (2002) Surface modification process by electrical discharge machining with a Ti powder green compact electrode. *J Mater Process Technol* 129:139–142
11. Shigyo K, Nakano Y (2013) Method of manufacturing electrical discharge surface treatment purpose electrode and electrical discharge surface treatment-purpose electrode
12. Yadav VK, Kumar P, Dvivedi A (2019) Effect of tool rotation in near-dry EDM process on machining characteristics of HSS. *Mater Manuf Process* 34:779–790
13. Ramani V, Cassidenti M (1985) Inert-gas electrical discharge machining. NASA Tech Briefs8, NPO-15660
14. Yadav VK, Kumar P, Dvivedi A (2019) Performance enhancement of rotary tool near-dry EDM of HSS by supplying oxygen gas in the dielectric medium. *Mater Manuf Process* 34:1832–1846
15. Kunieda M, Yoshida M (1997) Electrical discharge machining in gas. *CIRP Ann Manuf Technol* 46:143–146
16. Tanimura T, Isuzugawa K, Fujita I, Iwamoto A, Kamitani T (1989) Development of EDM in the Mist. In: Proceedings of the ninth international symposium of electro machining (ISEM IX); Nagoya, Japan
17. Chen H, Wu K, Yan B (2014) Characteristics of Al alloy surface after EDC with sintered Ti electrode and TiN powder additive. *Int J Adv Manuf Technol* 72:319–332
18. Huang TS, Hsieh SF, Chen SL, Lin MH, Ou SF, Chang WT (2015) Surface modification of TiNi-based shape memory alloys by dry electrical discharge machining. *J Mater Process Technol* 221:279–284
19. Ramver, Dvivedi A, Kumar P (2019) On improvement in surface integrity of μ -EDMed Ti-6Al-4V Alloy by μ -ECM Process. In: Proceedings of the TMS 2019 148th annual meeting and exhibition supplemental proceedings. Springer International Publishing Cham. pp 745–753
20. Singh R, Dvivedi A, Kumar P (2020) EDM of high aspect ratio micro-holes on Ti-6Al-4V alloy by synchronizing energy interactions. *Mater Manuf Process* 35:1188–1203
21. Ramver, Yadav VK, Kumar P, Dvivedi A (2020) Experimental investigation on surface morphology of micro-EDMed Ti-6Al-4V alloy. In: Parwani AK, Ramkumar P (eds) Recent advances in mechanical infrastructure, lecture notes in intelligent transportation and infrastructure. Springer Nature Singapore Pte Ltd., ISBN 978-981-32-9971-9

Part XV
Advances in Titanium Technology

Investigation to Hole Surface Microstructure Evolution in Drilling of Aerospace Alloys: Ti-5553



David P. Yan

Abstract Ti-5553 (Ti-5Al-5Mo-5V-3Cr-0.5Fe) is a newly developed near β titanium (Ti) alloy with excellent fatigue performance and corrosion resistance. Hence, it is of significant importance in several high-performance aerospace applications such as landing gear components and helicopter rotors. The machinability of Ti-5553 is low owing to its high strength at elevated temperature, low thermal conductivity and high chemical reactivity. Although there is a profound knowledge about the machinability of $\alpha + \beta$ Ti alloys (typically Ti-6Al-4V), there is a lack of understanding regarding the surface microstructure evolution during machining of Ti-5553. This paper presents experimental investigations on the microstructure evaluation in the hole surface produced from drilling of Ti-5553. A series of high-speed drilling tests were conducted to evaluate the influence of cutting conditions on the hole surface microstructure alternation in relation to the cutting temperature. Scanning electron microscopy (SEM) and X-ray diffraction (XRD) technique were used to characterize the hole surface microstructure evolution. The precipitation of new α phase from β matrix in the hole surface was observed in dry drilling; however, this phenomenon was not detected in wet drilling with a coolant supplied.

Keywords Microstructure evolution · Surface quality · Ti-5553 · High-speed drilling · Cutting temperature

Introduction

In recent years, Ti alloys have been increasingly used in the aerospace, biomedical and chemical engineering industries, owing to their superior mechanical properties, including excellent strength-to-weight ratio, ability to retain high strength at elevated temperature and good fatigue and corrosion resistance, etc. [1–3]. Accordingly, the β Ti alloys have been critically chosen for structural components applications in the aerospace industry, mostly due to their excellent performance-to-density ratio [4].

D. P. Yan (✉)

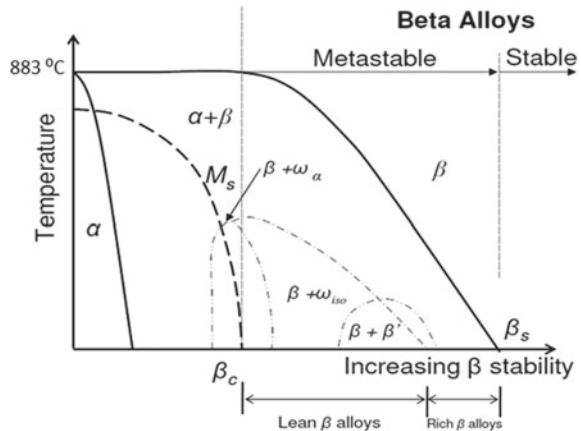
Department of Aviation and Technology, San Jose State University, San Jose, CA, USA
e-mail: david.yan@sjsu.edu

Despite offering higher strength levels and lower processing temperatures than $\alpha + \beta$ Ti alloys (typically Ti-6Al-4V), the machinability of metastable β Ti alloys is low [5, 6]. Since these aircraft structural components require high durability levels owing to fatigue being a predominant failure mechanism, thus, the quality of finish surface and surface microstructure are two critical aspects that can influence safety and durability concerns [7].

Ti-5Al-5Mo-5V-3Cr-0.5Fe (all in wt%), patented as Ti-5553, was publicly introduced in 1997 as an improved version of Russian near- β Ti alloy VT-22 [8]. Ti-5553 is expected to be applicable for thick section aerospace structural components such as landing gear due to its high strength, reported to be as high as 1250 MPa at room temperature for certain microstructures [9]. The properties of Ti-5553 can vary over a wide range and are critically dependent on the microstructure which is primarily described by the volume fraction, size, morphology and distribution of α precipitates within the β matrix [10]. Figure 1 shows a pseudo-binary phase diagram of β Ti alloys where Ti-5553 lies on the right of the martensitic transformation (M_s) line and has a metastable β structure. The phase components of Ti-5553, i.e. α , β , ω and martensite (Ms) phases can be varied significantly by different thermomechanical processes including heat treatment and cold working [11].

As the research on microstructural evolution of machined Ti-5553 component is limited, an understanding of the precipitation of new α phase from β matrix (i.e. β phase decomposition) during low temperature ageing of Ti-5553 can be insightful. Jones et al. [12] showed that the dot-shaped new α precipitates approximately 1–3 μm in diameter nucleated from β matrix, and the α phase appeared to form as strings, approximately 15 μm in length after solution treatment and ageing at 400 $^\circ\text{C}$ for 4 h. Their XRD data indicated that peaks corresponding to the (100) and (101) planes of α phase could be seen after 4 h of ageing at 400 $^\circ\text{C}$ and the precipitation of new (101) plane α phase was predominant. Dehghan-Manshadi and Dippenaar [13] reported that the precipitation of α phase was a function of ageing temperature at constant ageing time, and the volume fraction of α phase increased from around

Fig. 1 Pseudo-binary phase diagram of β Ti alloys showing the distribution of β stability, classification of β Ti alloys and location of α , β , ω and martensite (Ms) phases [11]



5% at 350 °C to more than 20% at 450 °C. In addition, increasing the isothermal ageing temperature caused changes in the morphology and size of α precipitates. In relation to the cutting temperature generated in machining process, Ugarte et al. [14] conducted milling tests on Ti-5553 and reported that the cutting temperature increased when increasing both cutting speed and feed rate, and the temperature on the tool side of tool-workpiece interface was around 630 °C.

To enhance the understanding of surface microstructure evolution in machining of Ti-5553, in this study, a series of high-speed drilling tests were conducted, and the cutting temperature was measured. Metallurgical characterizations including scanning electron microscopy (SEM) and X-ray diffraction (XRD) analysis were performed to reveal the effect of cutting conditions on the β to α phase transformation in the hole surface.

Experimental Procedure

A billet of Ti-5553 (non-heat treated) was used in this study with the chemical composition shown in Table 1. The drilling tests on Ti-5553 workpiece were carried out on a CNC machine under the dry and wet cutting conditions with varying cutting speeds and feed rates. A mineral oil-based cutting fluid emulsion was applied through drill's two internal cooling holes during wet drilling. Uncoated solid carbide drills (ϕ 12 mm), Seco Feedmax-T Geometry were used in this study, and the holes were continuously fed to the desired depth, and the depth of drilling was kept constantly at 22.5 mm in all trials.

The cutting zone temperature was measured by inserting a ϕ 1 mm K type thermocouple wire into a special made Ti-5553 workpiece (having a predrilled ϕ 1 mm hole at a designated drilling depth). Thus, the measured temperature was the temperature reading at which the thermocouple wire was just penetrated by the drill moving downward. After each drilling trial, the hole surface sample was made by sectioning the hole through the center of the hole to reveal the drilled surface and corresponding subsurface. G. Muller's three-step Ti metallographic preparations were applied, and Kroll's etchant (2 ml HF and 6 ml HNO₃ in 100 ml H₂O) was used for etching. Hitachi S-3000 N SEM and X'Pert PRO MRD XL XRD machine were used to determine the morphology and microstructure of the drilled hole surface.

In this present study, the volume fractions of α and β phase in the hole surface of Ti-5553 sample were quantified through the quantitative analysis of XRD patterns (i.e. the Rietveld method). In particular, for a drilled hole surface, the amounts of

Table 1 Chemical compositions of as-received Ti-5553 (in wt%)

Ti alloys	Element (wt%)								
	Al	Mo	V	Cr	Fe	O	Zr	C	Ti
Ti-5553	5.03	4.90	4.97	2.65	0.37	0.12	0.07	0.01	Bal

α phases were refined from the areas of the peak intensity line shape profile of three planes: (100), (101) and (201) α phase. The qualitative changes in the volume fractions of the phase suggested by the XRD data were coupled with the quantitative measurements (using Image J) of the volume fractions of the phase from the hole surface's SEM micrograph.

Results and Discussion

Microstructure and XRD Pattern of as-Received Ti-5553

Initial characterization of the as-received Ti-5553 billet (non-heat treated) involved light optical, scanning electron microscopy and XRD examinations. Figure 2a and b shows the light optical and SEM micrographs of the original Ti-5553 workpiece, where in the SEM image, the lighter region presents a β phase, and the darker region indicates an α phase. After quantitatively measuring the α phase (using Image J) from Fig. 2b, the volume fraction of α phase (i.e. V% of α) was 26.8% for the as-received Ti-5553. Figure 3 presents the XRD pattern of the as-received Ti-5553 showing the (110) and (101) main diffraction peaks of β and α phases, respectively. The intensity plotted in the figure is the square root of counts to help distinguish the weak peaks from the background. The observation and measurement of this present study were consistent with the findings of Arrazola et al. [15] and Jones et al. [16].

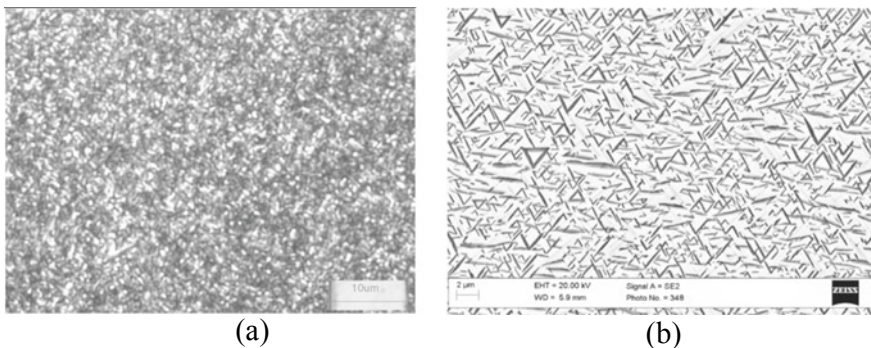


Fig. 2 a Light optical image and b SEM micrograph of the original Ti-5553 workpiece, in SEM image, the lighter and darker regions are the β and α phase, respectively

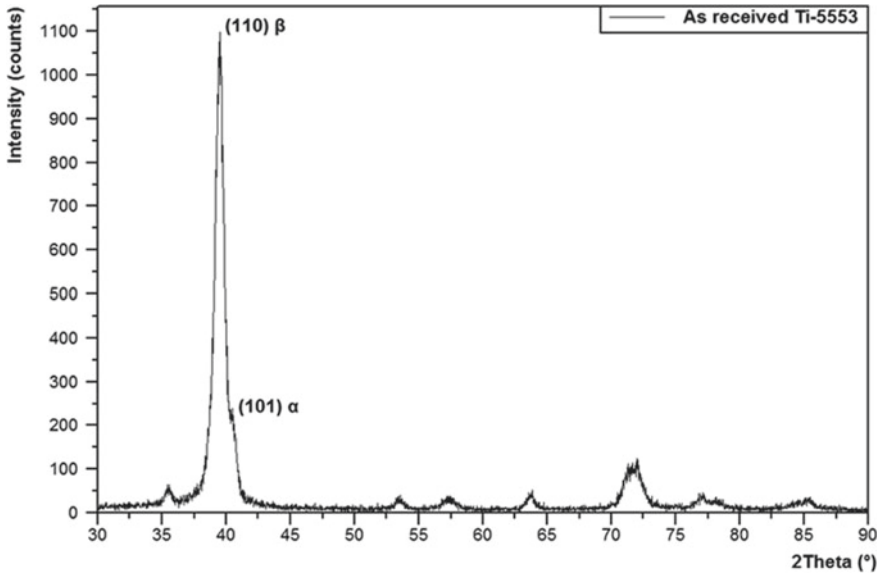


Fig. 3 XRD pattern of the as-received Ti-5553, showing the detected intensity peak of (110) β and (101) α phases

Effect of Coolant Supply on Microstructure Evolution in Hole Surface

Figure 4a–d shows the SEM micrographs of the drilled hole samples A and B produced with and without cutting fluid supply at cutting speed of 55 m/min and feed rate of 0.08 mm/rev, respectively. After quantitatively measuring the α phase (using Image J) from the higher magnification SEM micrographs of samples A and B shown in Fig. 4b and d, it was found that the V% of α phase were 32% and 61.5%, respectively. Thus, the results of this present study indicated that the coolant supply significantly influenced the β to α phase transformation, as the V% of α phase in sample B (i.e. 61.5% without coolant supply) was much higher than that of in sample A (i.e. 32% with coolant supply).

By comparing Fig. 4d to b and Fig. 2b, it can be seen that the size and morphology of small lath-shaped α phase in sample B, obtained about 10 μm away from the edge of the hole, were noticeably larger and coarser than those of two in the as-received workpiece and sample A. While the size and morphology of α phase in sample A shown in Fig. 4b, showing as homogenous small widely spaced laths, were similar to those in the as-received workpiece shown in Fig. 2b.

Figure 5 shows the comparisons of the detected XRD patterns between the wet and dry drilled samples A and B. It can be observed that a larger broadened peak intensity line shape profile of (101) plane α emerged in the dry drilled sample B (dot line) compared to the wet drilled sample A (solid line). The larger broadened

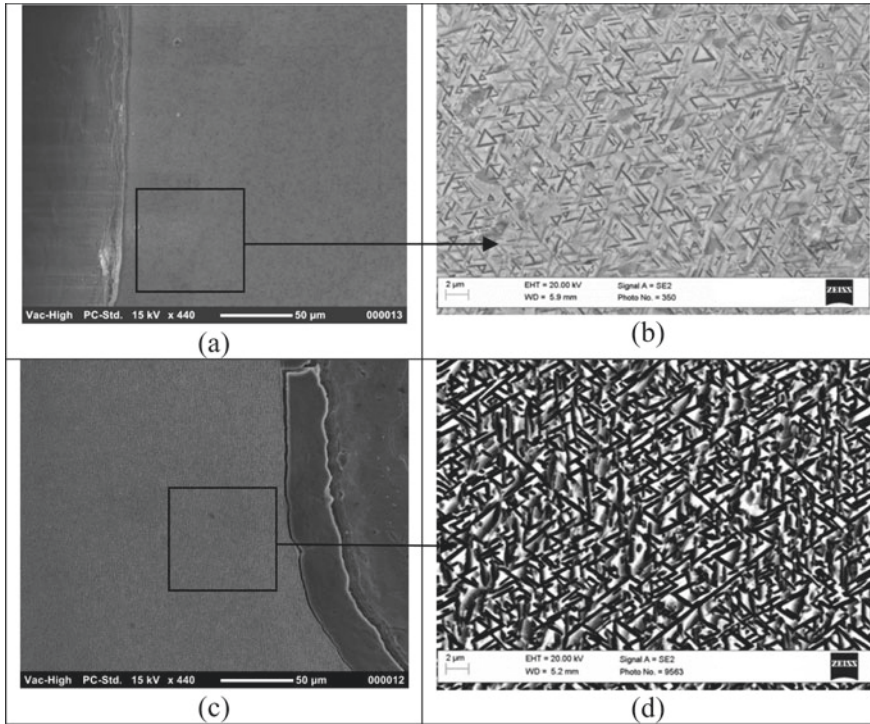


Fig. 4 **a** and **c** SEM micrographs of samples A and B produced with and without cutting fluid supply at cutting speed of 55 m/min and feed rate of 0.08 mm/rev, respectively, and **b** and **d** higher magnification SEM micrographs of the areas marked in **a** and **c**, showing the change of α phase morphology in these two samples obtained at different drilling conditions

peak intensity line shape profile of (101) plane α indicated a higher V% of α phase in the dry drilled sample than that of the wet drilled. The trend of the α phase changes obtained from the XRD patterns of samples A and B was well correlated with these two samples' V% of α phase measured from their higher magnification SEM micrographs as discussed above.

The cutting temperature histories of samples A and B corresponding to with and without cutting fluid supply in drilling process were plotted in Fig. 6. The maximum cutting temperature dramatically increased to 449 °C at the last four seconds of dry drilling of sample B, whereas the maximum cutting temperature just increased to 89 °C at the final two seconds in wet drilling of sample A (with cutting fluid supply). It appears that the cutting temperature of 449 °C in sample B was very close to the temperature that triggered the precipitation of new α phase from the β matrix during lower temperature ageing of Ti-5553 reported by Jones et al. [12].

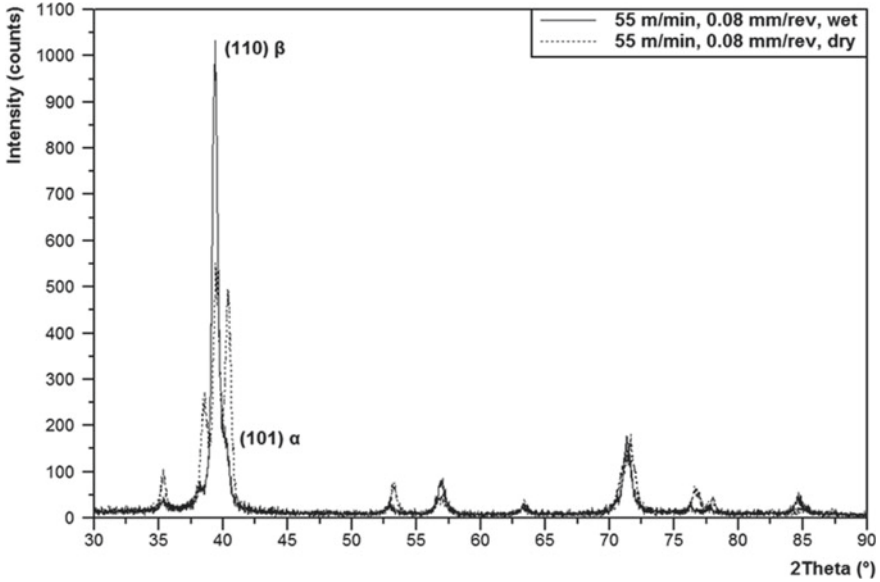


Fig. 5 XRD patterns of the wet and dry drilled samples A and B obtained under the same cutting speed, feed rate and depth of drilling, showing a more broadened the peak intensity line shape profile of (101) plane α (dot line) in the dry drilled sample B than the wet drilled sample A

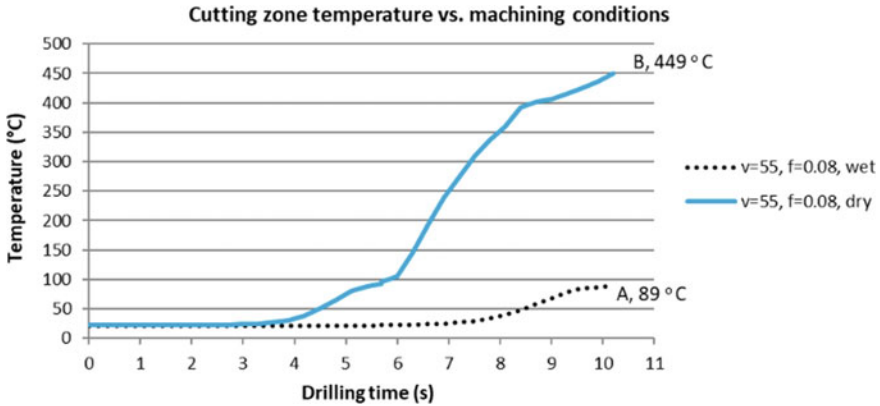


Fig. 6 Cutting temperature histories versus drilling conditions for samples A and B, obtained with and without cutting fluid supply, at 20 mm depth of drilling until the thermocouple wire was broken by the drill moving downward, showing the variation of cutting temperatures relating to cooling conditions. (Color figure online)

Effect of Cutting Speed on Precipitation of New α Phase in Hole Surface

Figure 7a–d shows the SEM micrographs of the dry drilled hole samples C and B produced at cutting speed of 27 and 55 m/min, respectively, at the same feed rate of 0.08 mm/rev without cutting fluid supply. The size and morphology of α phase in sample C (Fig. 7b) have a slightly smaller lath aspect ratio, while the size and morphology of α phase in sample B (Fig. 7d) have a larger and more closely spaced laths.

The V% of α phase in sample C (obtained at 10 μ m away from the edge of the hole) is 33.7% measured from the higher magnification SEM micrograph shown in Fig. 7b. After comparing the V% of α phase in samples C and B, it can be found that the sample B has a significantly higher V% of α (i.e. 61.5%) than sample C (i.e. 33.7%). This result seems to indicate the effect of the cutting speed on the precipitation of

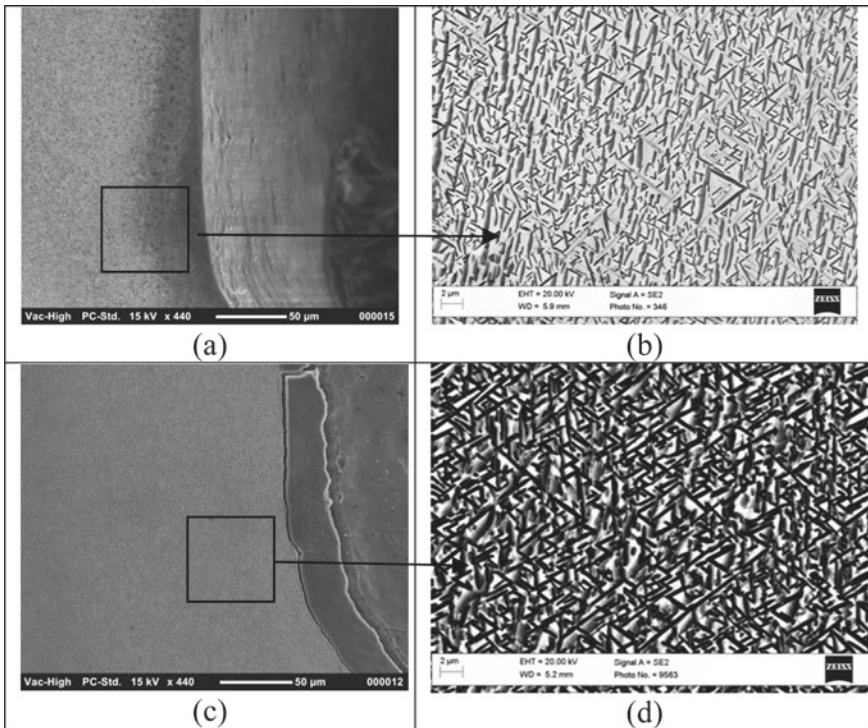


Fig. 7 a and c SEM micrographs of dry drilled samples C and B produced at cutting speed of 27 and 55 m/min, respectively, under the same feed rate of 0.08 mm/rev without cutting fluid supply, and b and d higher magnification SEM micrographs of the areas marked in a and c, showing the change of α morphologies relating to the cutting speeds during drilling process

new α phase, thus, the higher cutting speed, the more new- α precipitates from the β matrix.

Figure 8 shows the comparisons of the detected XRD patterns between the dry drilled samples C and B. It can be found that a larger broadened peak intensity line shape profile of (101) plane α emerged in the sample B (dot line) produced at a higher cutting speed of 55 m/min compared to the sample C (solid line) drilled at a lower cutting speed of 27 m/min. The larger broadened peak intensity line shape profile of (101) plane α indicated a higher V% of α phase in the sample B than that of the sample C. The trend of α phase changes obtained from the XRD patterns of samples C and B were consistent with the V% of α phase in these two samples measured from their higher magnification SEM micrographs discussed above.

The cutting temperature histories of samples B and C corresponding to varying cutting speeds were plotted in Fig. 9. It can be observed that the cutting temperature in sample B (i.e. 449 °C) was higher than that of sample C (i.e. 161 °C). The maximum cutting temperature increased 179% when increasing the cutting speeds from 27 to 55 m/min. This indicated that the effect of cutting speed on the cutting zone temperature was very significant. The result was consistent with the findings of Ugarte et al. [14] during machining of Ti-5553 and Ti-64. As discussed, the higher cutting temperature can assist on the new α phase precipitation and facilitate the growth of α precipitates. The highest cutting temperature of 449 °C in sample B can

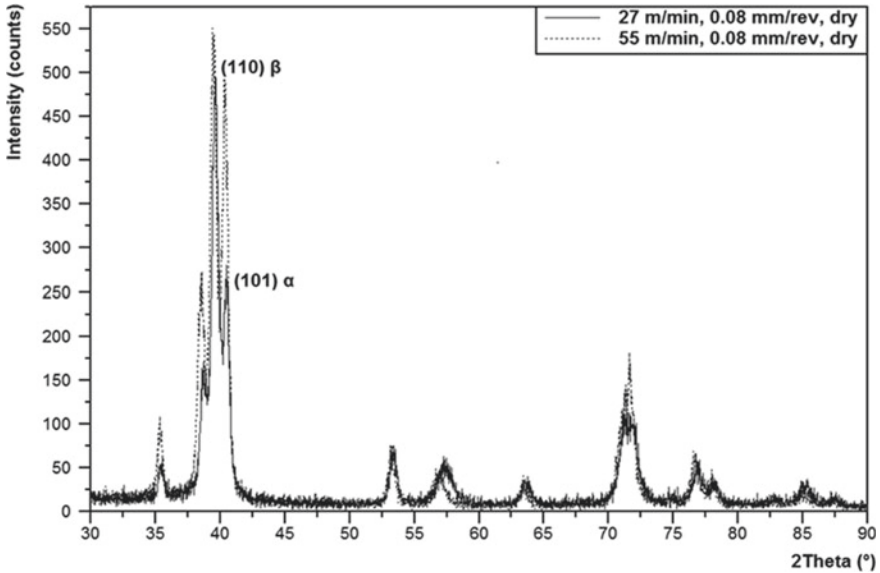


Fig. 8 XRD patterns of the dry drilled samples C and B obtained at cutting speed of 27 and 55 m/min, at the same feed rate of 0.08 mm/rev without cutting fluid supply, showing a more broadened the peak intensity line shape profile of (101) plane α (dot line) in sample B drilled at a higher cutting speed

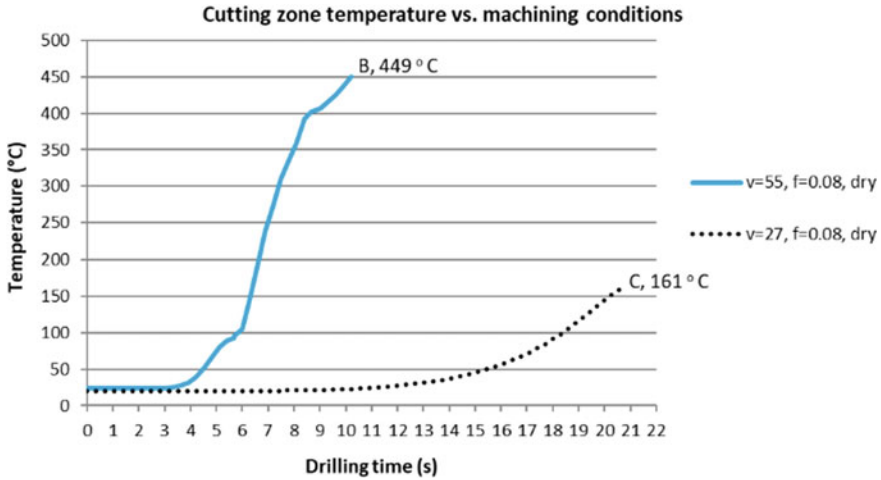


Fig. 9 Cutting temperature histories versus drilling conditions for samples B and C, obtained at cutting speed of 55 and 27 m/min, at 20 mm depth of drilling until the thermocouple wire was broken by the drill moving downward, showing the variation of cutting temperatures relating to cutting speeds. (Color figure online)

explain why it has the largest and most closely spaced α laths when comparing the size and morphology of these three samples, i.e. A, B and C.

Conclusions

The high-speed drilling of Ti-5553 trials were performed, and the SEM and XRD were used to characterize the hole surface microstructure of the drilled samples. The effect of drilling conditions on the hole surface microstructure evolution was studied in relation to the cutting temperature. Based on the results obtained from this present study, the following conclusions can be drawn:

1. The precipitation of new α phase from β matrix in the hole surface was observed in dry drilling; however, this phenomenon was not detected in wet drilling with a coolant supplied.
2. A higher cutting speed can lead to a higher cutting temperature during high-speed drilling of Ti-5553.
3. It has been found that a higher cutting temperature can assist on the new α phase precipitation and facilitate the growth of α precipitates.

Acknowledgements The author acknowledges the start-up funds from San Jose State University.

References

1. Kaynak Y, Gharibi A, Yılmaz U, Köklü U, Aslantaş K (2018) A comparison of flood cooling, minimum quantity lubrication and high pressure coolant on machining and surface integrity of titanium Ti-5553 alloy. *J Manuf Proc* 34:503–512. <https://doi.org/10.1016/j.jmapro.2018.06.003>
2. Zheng Y, Williams REA, Fraser HL (2016) Characterization of a previously unidentified ordered orthorhombic metastable phase in Ti-5Al-5Mo-5V-3Cr. *Scripta Mater* 113:202–205. <https://doi.org/10.1016/j.scriptamat.2015.10.037>
3. Barriobero-Vila P, Requena G, Schwarz S, Warchomicka F, Buslaps T (2015) Influence of phase transformation kinetics on the formation of α in a β -quenched Ti-5Al-5Mo-5V-3Cr-1Zr alloy. *Acta Mater* 95:90–101. <https://doi.org/10.1016/j.actamat.2015.05.008>
4. Boyer RR (1996) An overview on the use of titanium in the aerospace industry. *Mater Sci Eng, A* 213(1–2):103–114
5. Ezugwu EO, Bonney J, Yamane Y (2003) An overview of the machinability of aeroengine alloys. *J Mater Process Technol* 134(2):233–253
6. M'Saoubi R, Axinte D, Soo SL, Nobel C, Attia H, Kappmeyer G, Engin S, Sim W-M (2015) High performance cutting of advanced aerospace alloys and composite materials. *CIRP Ann Manuf Technol* 64(2):557–580. <https://doi.org/10.1016/j.cirp.2015.05.002>
7. Ahmed M, Li T, Casillas G, Cairney JM, Wexler D, Pereloma EV (2015) The evolution of microstructure and mechanical properties of Ti-5Al-5Mo-5V-2Cr-1Fe during ageing. *J Alloy Compd* 629:260–273. <https://doi.org/10.1016/j.jallcom.2015.01.005>
8. Fanning JC (2005) Properties of TIMETAL 555 (Ti-5Al-5Mo-5V-3Cr-0.6Fe). *J Mater Eng Perform* 14(6):788–791
9. Nag S et al. (2009) ω -Assisted nucleation and growth of α precipitates in the Ti-5Al-5Mo-5V-3Cr-0.5Fe β titanium alloy. *Acta Mater* 57(7):2136–2147
10. Jones NG et al (2008) Thermomechanical processing of Ti-5Al-5Mo-5V-3Cr. *Mater Sci Eng, A* 490(1–2):369–377
11. Cherukuri, B (2008) Microstructural stability and thermomechanical processing of boron modified beta titanium alloys. Wright State University, United States, Ohio. pp. 13–15
12. Jones NG et al (2009) Development of chevron-shaped α precipitates in Ti-5Al-5Mo-5V-3Cr. *Scripta Mater* 60(7):571–573
13. Dehghan-Manshadi A, Dippenaar RJ (2011) Development of α -phase morphologies during low temperature isothermal heat treatment of a Ti-5Al-5Mo-5V-3Cr alloy. *Mater Sci Eng, A* 528(3):1833–1839
14. Ugarte A et al (2012) Machining behaviour of Ti-6Al-4V and Ti-5553 alloys in interrupted cutting with PVD coated cemented carbide. *Procedia CIRP* 1:202–207
15. Arrazola PJ et al. (2009) Machinability of titanium alloys (Ti6Al4V and Ti555.3). *J Mater Process Technol* 209(5):2223–2230
16. Jones NG et al (2009) Beta Phase decomposition in Ti-5Al-5Mo-5V-3Cr. *Acta Mater* 57(13):3830–3839

Part XVI
AI/Data Informatics: Applications
and Uncertainty Quantification
at Atomistics and Mesoscales

Solving Stochastic Inverse Problems for Structure-Property Linkages Using Data-Consistent Inversion



Anh Tran and Tim Wildey

Abstract Process-structure-property relationships are the hallmark of materials science. Many integrated computational materials engineering (ICME) models have been developed at multiple length-scales and time-scales, where uncertainty quantification (UQ) plays an important role in quality assurance. In this paper, we applied our previous work [39] to learn a distribution of microstructure features that are consistent in the sense that the forward propagation of this distribution through a crystal plasticity finite element model (CPFEM) matches a target distribution on materials properties, which is given beforehand. To demonstrate the approach, DAMASK and DREAM.3D are employed to construct Hall-Petch relationship for a twinning-induced plasticity (TWIP) steel, where the average grain size distribution is inferred, given a distribution of offset yield strength.

Keywords Crystal plasticity · Uncertainty quantification · Bayesian statistics · Structure-property · ICME · Inverse problems

Introduction

Materials design and development is historically a long time process, where the gap between initial research to final commercialization could be decades. In that sense, the Materials Genome Initiative (MGI) [26] was proposed to significantly reduce the research and development time of new materials, by employing both integrated computational materials engineering (ICME) and machine learning (ML) approaches to establish process-structure-property linkages, where data plays a central and catalytic role to help accelerate the whole process. MGI successes have

This research was supported by the U.S. Department of Energy, Office of Science, Early Career Research Program.

A. Tran (✉) · T. Wildey
Optimization and Uncertainty Quantification Department, Center for Computing Research,
Sandia National Laboratories, Albuquerque, NM, USA
e-mail: anhtran@sandia.gov

been enabled by many sophisticated ML algorithms, including recent deep learning (DL) algorithms, to extract microstructure features that are beyond the understanding of human experts. However, much work remains to be done, particularly about understanding the microstructure, due to scarcity of datasets and its complicated stochasticity. To that end, uncertainty quantification (UQ) naturally rises as a fundamental mathematical toolbox to analyze, verify, and validate many ICME models within certain contexts. In the context of structure-property linkage, where the inputs are microstructures and outputs are materials properties, there has been a limited amount of work because of the challenge in microstructure representation, as well as the expensive computational cost of ICME models bridging the structure-property linkage. In this work, we applied data-consistent framework, which was initially proposed in Butler et al. [5, 6] to solve a stochastic problem. The problem can be succinctly stated as: given a target distribution of materials properties, and a map bridging between structure-property linkages, determine the distribution of microstructure features such that the forward propagation of this distribution matches a target distribution on materials properties.

Given the importance of UQ in forward ICME models, it has attracted much attention from researchers to predict materials behaviors under uncertainty, as reviewed by [15, 17, 19, 21]. For example, Paul et al. [22] optimized different materials properties for process-structure linkage, where microstructure orientation is considered. Johnson and Arróyave [16] proposed an inverse design framework for process-structure linkages for Ni-rich NiTi shape memory alloys. Yuan et al. [43] employed CPFEM as a forward ICME model to generate a training dataset and utilized principal component analysis and random forests to predict the stress-strain behavior. Tallman et al. [30, 31] utilized GPR to model the structure-property map from a CPFEM dataset. Acar et al. [1] proposed a linear programming approach to maximize a mean of materials properties under the assumption of Gaussian distribution for both inputs and outputs. Inductive design exploration method (IDEM) [7, 11, 20] has been introduced as a materials design methodology to identify feasible and robust design for microstructure features, which has been applied to many problems in practice. In our previous work, we have also addressed the forward UQ problem using polynomial chaos expansion [41] or inverse problems in process-structure relationship [35].

In the scope of this paper, we follow the framework proposed by Diehl et al. [9], which proposed an ICME workflow coupling DAMASK and DREAM.3D [14], to generate CPFEM dataset for a twinning-induced plasticity (TWIP) steel. Then, GPR is adopted as a ML model for structure-property linkages, as suggested by Tallman et al [30, 31]. Data-consistent framework, as proposed by Butler et al. [5, 6], is then employed to identify a distribution of microstructure features. In the case study, the microstructure feature is the average grain size, which is considered as the input, where the output is the ensemble-average offset yield strength at $\varepsilon = 0.2\%$. As the number of stochastic volume element (SVE) approaches infinity, the map between input and output can be considered deterministic, in the sense of asymptotic analysis.

The rest of this paper is organized as follows. Section “[Microstructure Generation](#)” provides a brief summary for constructing the CPFEM dataset using DREAM.3D

and DAMASK, as well as a brief introduction to GPR. Section “[A Stochastic Inverse Problem for Structure-Property Relationship in Materials Design](#)” introduces the theory and implementation of the stochastic inverse framework. Section “[Case Study: Equiaxed Grains for TWIP Steels Under Uniaxial Tension](#)” describes a Hall-Petch relationship obtained from CPFEM, as well as the structure-property GPR model, where stochastic inverse problem is solved based on the ML model. Section “[Discussion and Conclusion](#)” discusses and concludes the paper.

A Forward UQ Framework Employing ML for the Structure-Property Map Using CPFEM and Data Mining

We follow the principle of CPFEM, which assumes a deterministic behavior of a specific microstructure realization under a specific loading condition. To account for the randomness of microstructure, different microstructure realizations are generated using deterministic and statistical microstructure descriptors, which are sampled from their according probability density functions. As such, in the scope of this study, the map between inputs, i.e. microstructure, and outputs, i.e. materials properties, are considered as a deterministic map. In the scope of this study, assuming that such deterministic map exists, we solve the inverse problem to identify the distribution of microstructure descriptors such that under the deterministic structure-property map, the induced forward materials property distribution matches the target materials property distribution.

Microstructure Generation

Generating statistically equivalent microstructures is one of the main goals in microstructure generation and microstructure reconstruction. To rigorously define “statistically equivalent”, the statistical microstructure descriptors must be utilized to quantify microstructures represented as images and represent these images in terms of probability density functions. Two realizations of microstructures are said to be equivalent if two probability density functions of *any* microstructure descriptor applied on these two realizations are sufficiently close. The definition of “sufficient” is more loosely defined, as microstructure generation within finite domain is almost always biased because of the finite size effect. That is, to be perfectly unbiased, one needs to resort to an infinite domain, which is computationally intractable. Furthermore, there are so many norms and metrics to measure the distance between two probability density functions, which makes the definition even more ambiguous. Therefore, practically, the definition of “sufficiently close” is left for users to decide. Within the context of microstructure descriptors, numerous studies have been performed to describe the microstructure, both deterministically and statistically. Based

on the idea of minimization, microstructure reconstruction and generation is often casted as a numerical optimization problem such that microstructure realizations are within a tolerance from a referenced microstructure. Such approaches have been well studied in the literature, as reviewed by Bargmann et al. [3] and Liu et al. [18], and even applied to experimental microstructures [37]. Interested readers are referred to the works of Groeber et al. [12, 13], Bostanabad et al. [4], and Torquato [32] for comprehensive reviews of computationally characterizing microstructures. In this paper, the workflow proposed by Diehl et al [9] that couples a synthetic microstructure generation framework is adopted, where DREAM.3D [14] and DAMASK [23] is used as a forward ICME model, to bridge the structure-property relationship. This automated workflow is used to explore the microstructure space, while parallelization over and within the ensembles is utilized which exploits high-performance computing resources to generate the required datasets.

Synthetic microstructures are typically generated using a log-normal distribution for particle size as

$$f_D(d; \mu_D, \sigma_D) = \frac{1}{d\sigma_D\sqrt{2\pi}} e^{-\frac{(\ln d - \mu_D)^2}{2\sigma_D^2}}, \quad (1)$$

where μ_D and σ_D^2 are the mean and the variance, respectively, of the normally distributed $\ln(D)$, i.e. $\ln(D) \sim \mathcal{N}(\mu_D, \sigma_D^2)$, and D is the average grain diameter. The additional subscript in μ_D and σ_D is introduced to avoid a conflict of notation between the mean and variance for the particle size distribution and the mean and variance for the GP model described in Sect. [Gaussian Process Regression](#).

Dislocation-Based CPFEM

In this section, we follow the notation and description from Roters et al. [23, 25], Diehl [8], and Alharbi and Kalidindi [2] for the constitutive relations in the CPFEM model. For small deformations, the elasto-plastic decomposition can be computed additively, whereas for large deformations, a multiplicative decomposition is more appropriate,

$$\mathbf{F} = \mathbf{F}_e \cdot \mathbf{F}_p, \quad (2)$$

following by the elasto-plastic decomposition of the velocity gradient as

$$\mathbf{L} = \dot{\mathbf{F}} \cdot \mathbf{F}^{-1} = \dot{\mathbf{F}}_e \cdot \mathbf{F}_e^{-1} + \mathbf{F}_e \cdot \dot{\mathbf{F}}_p \cdot \mathbf{F}_p \cdot \mathbf{F}_e^{-1} = \mathbf{L}_e + \mathbf{F}_e \cdot \mathbf{L}_p \cdot \mathbf{F}_e^{-1}, \quad (3)$$

where \mathbf{L}_p and \mathbf{L}_e are the plastic and elastic velocity gradient, respectively. The 2nd Piola-Kirchoff stress tensor \mathbf{S} , which is a symmetric second-order tensor defined in the intermediate configuration, is given by

$$\mathbf{S} = \frac{\mathbb{C}}{2} : (\mathbf{F}_e^T \mathbf{F}_e - \mathbf{I}) = \mathbb{C} : \mathbf{E}_e = \mathbf{J} \mathbf{F}^{-1} \cdot \boldsymbol{\sigma} \cdot \mathbf{F}^{-T}, \quad (4)$$

where \mathbb{C} is the elasticity fourth-order tensor, \mathbf{F}_e is the elastic deformation gradient, \mathbf{F}_p is the plastic deformation gradient [25], $\mathbf{E}_e = \frac{1}{2} (\mathbf{F}_e^T \mathbf{F}_e - \mathbf{I})$ is the elastic Green's Lagrangian strain, $\boldsymbol{\sigma}$ is the Cauchy stress tensor (cf. [24], Sect. 3.3). Following Diehl et al. [8, 10, 28], we use the open-source DAMASK [23] package for the CPFEM model.

Gaussian Process Regression

In this section, we adopt the notation from Shahriari et al. [27] and Tran et al. [33, 34, 36, 38, 40] for its clarity and consistency. In the context of this paper, a Gaussian process is a spatially distributed collection of random variables, each of which is normally distributed. A $\mathcal{GP}(\mu_0, k)$ regressor is a nonparametric model which is fully characterized by a prior mean function, $\mu_0(\lambda) : \Lambda \mapsto \mathbb{R}$, and a positive-definite kernel or a covariance function $k : \Lambda \times \Lambda \mapsto \mathbb{R}$. In GPR, it is assumed that the output, f , is jointly Gaussian, and the observations, \mathcal{Q} , are normally distributed, leading to

$$f|\lambda \sim \mathcal{N}(m, \mathbf{K}), \quad (5)$$

$$\mathcal{Q}|f, \sigma^2 \sim \mathcal{N}(\mathcal{Q}, \sigma^2 \mathbf{I}), \quad (6)$$

where $m_i := \mu(\lambda_i)$, and $K_{i,j} := k(\lambda_i, \lambda_j)$. Equation (5) describes the prior distribution induced by the GP.

The prediction for an unknown arbitrary point is characterized by the posterior Gaussian distribution, which can be described by the posterior mean and posterior variance functions. These are given by

$$\mu(\lambda) = \mu_0(\lambda) + \mathbf{k}(\lambda)^T (\mathbf{K} + \sigma^2 \mathbf{I})^{-1} (\mathbf{y} - m), \quad (7)$$

and

$$\sigma^2(\lambda) = \sigma^2 - \mathbf{k}(\lambda)^T (\mathbf{K} + \sigma^2 \mathbf{I})^{-1} \mathbf{k}(\lambda), \quad (8)$$

respectively, where $\mathbf{k}(\lambda)$ is a vector of covariance $\mathbf{k}(\lambda)_i = k(\lambda, \lambda_i)$, $\sigma^2 = \frac{1}{n} (\mathbf{y} - \mu_0(\lambda))^T \mathbf{K}^{-1} (\mathbf{y} - \mu_0(\lambda))$ is the intrinsic variance. Here, we consider λ to be microstructure features, which are represented as random variables in the microstructure space Λ . The map $\mathcal{Q}(\lambda)$ is the quantities of interests (QoIs), which are the materials properties.

A Stochastic Inverse Problem for Structure-Property Relationship in Materials Design

Theory

The stochastic inverse problem utilized in this paper seeks a probability density on model input such that the forward propagation of this density through Q , often called a push-forward density, matches a given target probability density on the QoI. Of course, the solution to this inverse problem is not necessarily unique, i.e., multiple probability densities may satisfy this requirement. In [5], existence is guaranteed by a *predictability assumption* and uniqueness and stability are obtained by introducing prior information in the form of an initial probability density on the model input parameters. This initial density is similar to a prior in classical Bayesian inference, but there are important differences. A full discussion is beyond the scope of this paper, so we refer the interested reader to [5] for details. Given the initial density, $\pi_{\Lambda}^{\text{init}}$, and the corresponding push-forward density, $\pi_{\mathcal{D}}^{Q(\text{init})}$, we can define an *updated* probability density, $\pi_{\Lambda}^{\text{up}}$, given by

$$\pi_{\Lambda}^{\text{up}}(\lambda) = \pi_{\Lambda}^{\text{init}}(\lambda) \frac{\pi_{\mathcal{D}}^{\text{obs}}(Q(\lambda))}{\pi_{\mathcal{D}}^{Q(\text{init})}(Q(\lambda))} = \pi_{\Lambda}^{\text{init}}(\lambda) r(\lambda), \quad \lambda \in \Lambda, \quad (9)$$

where we use $r(\lambda)$ to denote the ratio of the observed density and push-forward of the initial density. While the expression in (9) resembles the posterior density in classical Bayesian inference, it is fundamentally different through the incorporation of the push-forward density in the denominator.

While the stochastic forward problem seeks a distribution on $Q(\lambda)$ given an assumed distribution on λ , the stochastic inverse problem assumes a target distribution on $Q(\lambda)$ is given and seeks a distribution on λ . In the context of the structure-property relationships, the stochastic inverse problem assumes that there is a desired/target distribution on the properties and seeks a distribution on the microstructure features such that the forward propagation of this distribution through the model matches the desired/target distribution.

Implementation and Diagnostics

In practice, direct numerical construction of the updated density, $\pi_{\Lambda}^{\text{up}}(\lambda)$, is impractical, so we often seek to generate a set of samples from this distribution. A straightforward approach for generating these samples is rejection sampling. The main objective in rejection sampling is to generate samples the target density $f(\lambda)$, using a proposal distribution $g(\lambda)$. An acceptance-rejection algorithm continuously draws samples from $g(\lambda)$ and accept the samples under certain conditions. A key assumption in

rejection sampling is the existence of a constant $M > 0$ such that $f(\lambda) \leq M g(\lambda)$ for all $\lambda \in \Lambda$. To generate samples from the updated density, $\pi_{\Lambda}^{\text{up}}(\lambda)$ using $\pi_{\Lambda}^{\text{init}}(\lambda)$ as the proposal density, we require the existence of a constant $M > 0$ such that

$$\pi_{\Lambda}^{\text{up}}(\lambda) = \pi_{\Lambda}^{\text{init}}(\lambda) \frac{\pi_{\mathcal{D}}^{\text{obs}}(Q(\lambda))}{\pi_{\mathcal{D}}^{Q(\text{init})}(Q(\lambda))} \leq M \pi_{\Lambda}^{\text{init}}(\lambda), \quad (10)$$

which is precisely the predictability assumption from [5].

We can gain more intuition and derive some computationally cheap diagnostics by considering the ratio, $r(\lambda)$, given in (9), which serves as re-weighting of the samples from the initial distribution. If we assume that we utilize P samples from initial distribution, $\{\lambda^{(i)}\}_{i=1}^P$ to construct the push-forward of the initial density (the initial forward UQ prediction), then we can re-use this information to estimate $M \approx \max_{1 \leq i \leq P} r(\lambda^{(i)})$ since we have already evaluated Q for these samples. Moreover, we can actually use this ratio evaluated at these samples to give a Monte Carlo estimates of the integral of the updated density,

$$\int_{\Lambda} \pi_{\Lambda}^{\text{up}}(\lambda) d\mu_{\Lambda} = \int_{\Lambda} \pi_{\Lambda}^{\text{init}}(\lambda) r(\lambda) d\mu_{\Lambda} \approx \frac{1}{P} \sum_{i=1}^P r(\lambda^{(i)}), \quad (11)$$

and the Kullback-Leibler divergence between the initial and updated densities,

$$\text{KL}(\pi_{\Lambda}^{\text{up}} || \pi_{\Lambda}^{\text{init}}) = \int_{\Lambda} \pi_{\Lambda}^{\text{up}}(\lambda) \log \left(\frac{\pi_{\Lambda}^{\text{up}}(\lambda)}{\pi_{\Lambda}^{\text{init}}(\lambda)} \right) d\mu_{\Lambda} \approx \frac{1}{P} \sum_{i=1}^P r(\lambda^{(i)}) \log(r(\lambda^{(i)})). \quad (12)$$

The integral of $\pi_{\Lambda}^{\text{up}}$ provides a numerical validation of the predictability assumption and the Kullback-Leibler divergence provides the relative entropy, or information gained, between the initial and updated densities.

In the scope of this paper, $Q(\lambda)$ is the map from the microstructure space Λ to the homogenized materials properties space \mathcal{D} . The push-forward and updated densities are approximated using a standard kernel density estimation (KDE) method. However, generating sufficient samples for an accurate KDE approximation using high-fidelity models is computationally expensive, so we employ the Gaussian process regression technique described in Sect. [Gaussian Process Regression](#) to approximate this map using a limited number of samples. In [6], we proved that under reasonable assumptions, the errors in the push-forward and updated densities are bounded by the error in the surrogate model.

Case Study: Equiaxed Grains for TWIP Steels Under Uniaxial Tension

TWIP steels have attracted significant attention lately due to their outstanding mechanical properties, including high strength and ductility. In this case study, we employ a CPFEM model to computationally probe the Hall-Petch relationship and apply the proposed framework to find the probability density of average grain size that induces a push-forward probability density that matches a target probability density of yield stress. We consider Fe-22Mn-0.6C TWIP steel and adopt the dislocation-density-based constitutive model with material parameters described in Steinmetz et al. [29], summarized in Sect. 6.2.3 and Tables 8 and 9 in Roters et al. [23], respectively. The constitutive model was validated experimentally by Wong et al. [42].

Figure 1 shows the Hall-Petch relationship for the TWIP steel considered in this study. As indicated in the plot, a linear regression model, given by $\sigma_Y = \sigma_0 + \frac{k}{\sqrt{D}}$, where $\sigma_0 = 483.46$ MPa, and $k = 0.09749$ MPa $m^{1/2}$, captures the main trend in this relationship. We also plot the GPR which we use to approximate the relationship to solve the stochastic inverse problem in structure-property linkages.

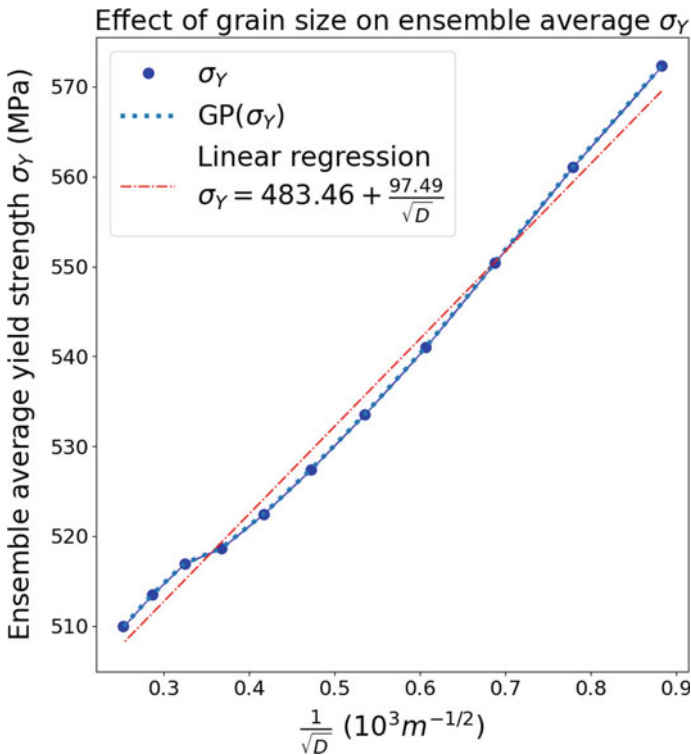


Fig. 1 Hall-Petch relationship for the TWIN steel considered. (Color figure online)

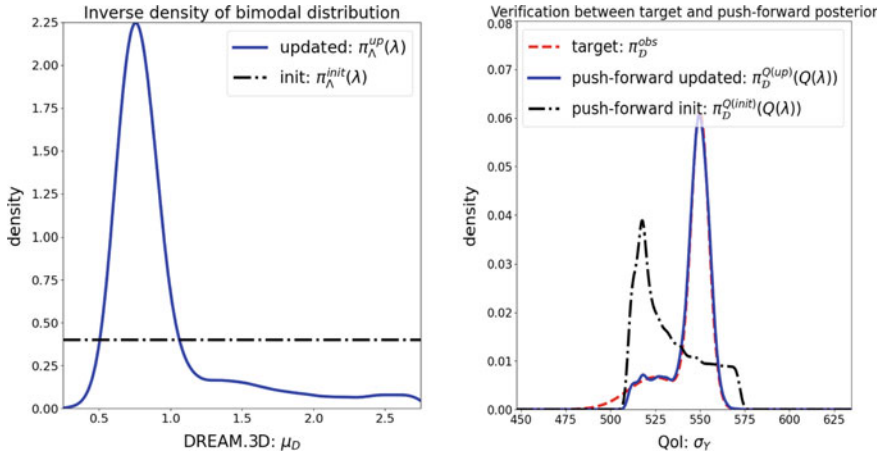


Fig. 2 On the left, the initial density, $\pi_\Lambda^{init}(\lambda)$, and updated density, $\pi_\Lambda^{up}(\lambda)$, on the microstructure feature. On the right, the target density on material properties and the push-forwards of the initial and updated densities. (Color figure online)

In this case study, we assume that the target density for σ_Y is a Gaussian mixture model, with 25% from $\mathcal{N}(525.0, 15.0)$, and 75% from $\mathcal{N}(550.0, 5.0)$. Figure 2 (left) shows the initial density $\pi_\Lambda^{init}(\lambda)$, which is uniform on $[0.25, 2.75]$ interval, and the updated density $\pi_\Lambda^{up}(\lambda)$, which is the solution of the stochastic inverse problem. Figure 2 (right) shows the comparison between the target density π_D^{obs} , as well as the push-forwards of the initial and updated density from microstructure $\pi_\Lambda^{up}(\lambda)$, respectively, i.e. π_Λ^{init} and π_Λ^{up} .

First, we note that while the push-forward of the updated density agrees very well with the larger peak in the observed density, we do not see good agreement in with the smaller peak. This is due to the fact that the predictability assumption is mildly violated, i.e. a portion of the support of the target density π_D^{obs} is outside the support of the push-forward prior π_Λ^{init} . In the context of rejection sampling, we are seeking samples from π_D^{obs} using samples generated from $\pi_D^{Q(init)}$, which is not possible in the regions where the model cannot predict the data. We can see this in Figure 2 (right) and this is confirmed numerically using the integral of the updated density, which is approximately 0.96. Therefore, the push-forward updated solution π_Λ^{up} simply ignores the portion outside the support, but tries to match the target density π_D^{obs} as closely as possible within the support. However, the fact that the push-forward of the updated density is a probability density implies that this missing probability must be redistributed which accounts for the small oscillations in the updated density.

Discussion and Conclusion

The goal of this paper was to define and solve a stochastic inverse problem in structure-property linkages using a combination of previously developed approaches, namely, Gaussian process regression and data-consistent inversion. We specifically chose a model problem where the predictability assumption was violated to discuss the utility of certain computationally cheap diagnostics to detect this violation and to assess the impact of this on the solution to the inverse problem. While these diagnostics are able to detect when this assumption is violated, they do not provide any guidance on what the root cause of this problem. Potential causes for the inability of the model to predict the data include an overly restrictive choice of initial density, errors in characterizing the observed density, and model-form uncertainty/error. Generally speaking, model-form uncertainty is ubiquitous in computational science. This is particularly true with CPFEM models where the high-fidelity dislocation-based constitutive models are much more expensive to simulate than the phenomenological constitutive models. If model-form uncertainty can be quantified, then, depending on the characterization of the uncertainty as either epistemic or aleatoric, we can still formulate and solve an appropriate stochastic inverse problem.

Acknowledgements The views expressed in the article do not necessarily represent the views of the U.S. Department of Energy or the United States Government. Sandia National Laboratories is a multimission laboratory managed and operated by National Technology and Engineering Solutions of Sandia, LLC., a wholly owned subsidiary of Honeywell International, Inc., for the U.S. Department of Energy's National Nuclear Security Administration under contract DE-NA-0003525. This research was supported by the U.S. Department of Energy, Office of Science, Early Career Research Program.

References

1. Acar P, Srivastava S, Sundararaghavan V (2017) Stochastic design optimization of microstructures with utilization of a linear solver. *AIAA J* 55(9):3161–3168
2. Alharbi HF, Kalidindi SR (2015) Crystal plasticity finite element simulations using a database of discrete Fourier transforms. *Int J Plast* 66:71–84
3. Bargmann S, Klusemann B, Markmann J, Schnabel JE, Schneider K, Soyarslan C, Wilmers J (2018) Generation of 3D representative volume elements for heterogeneous materials: a review. *Prog Mater Sci* 96:322–384
4. Bostanabad R, Zhang Y, Li X, Kearney T, Brinson LC, Apley DW, Liu WK, Chen W (2018) Computational microstructure characterization and reconstruction: review of the state-of-the-art techniques. *Prog Mater Sci* 95:1–41
5. Butler T, Jakeman J, Wildey T (2018) Combining push-forward measures and Bayes' rule to construct consistent solutions to stochastic inverse problems. *SIAM J Sci Comput* 40(2):A984–A1011
6. Butler T, Jakeman J, Wildey T (2018) Convergence of probability densities using approximate models for forward and inverse problems in uncertainty quantification. *SIAM J Sci Comput* 40(5):A3523–A3548
7. Choi HJ, McDowell DL, Allen JK, Mistree F (2008) An inductive design exploration method for hierarchical systems design under uncertainty. *Eng Optim* 40(4):287–307

8. Diehl M, A spectral method using fast Fourier transform to solve elastoviscoplastic mechanical boundary value problems
9. Diehl M, Groeber M, Haase C, Molodov DA, Roters F, Raabe D (2017) Identifying structure–property relationships through DREAM.3D representative volume elements and DAMASK crystal plasticity simulations: an integrated computational materials engineering approach. *JOM* 69(5):848–855
10. Eisenlohr P, Diehl M, Lebensohn RA, Roters F (2013) A spectral method solution to crystal elasto-viscoplasticity at finite strains. *Int J Plast* 46:37–53
11. Ellis BD, McDowell DL (2017) Application-specific computational materials design via multiscale modeling and the inductive design exploration method (IDEM). *Integr Mater Manuf Innov* 6(1):9–35
12. Groeber M, Ghosh S, Uchic MD, Dimiduk DM (2008) A framework for automated analysis and simulation of 3D polycrystalline microstructures. Part 1: Statistical characterization. *Acta Mater* 56(6):1257–1273
13. Groeber M, Ghosh S, Uchic MD, Dimiduk DM (2008) A framework for automated analysis and simulation of 3D polycrystalline microstructures. Part 2: synthetic structure generation. *Acta Mater* 56(6):1274–1287
14. Groeber MA, Jackson MA (2014) DREAM. 3D: a digital representation environment for the analysis of microstructure in 3D. *Integr Mater Manuf Innov* 3(1):5
15. Honarmandi P, Arróyave R (2020) Uncertainty quantification and propagation in computational materials science and simulation-assisted materials design. *Integr Mater Manuf Innov*, pp 1–41
16. Johnson L, Arróyave R (2016) An inverse design framework for prescribing precipitation heat treatments from a target microstructure. *Mater Des* 107:7–17
17. Kalidindi SR, Medford AJ, McDowell DL (2016) Vision for data and informatics in the future materials innovation ecosystem. *JOM* 68(8):2126–2137
18. Liu Y, Greene MS, Chen W, Dikin DA, Liu WK (2013) Computational microstructure characterization and reconstruction for stochastic multiscale material design. *Comput Aided Des* 45(1):65–76
19. McDowell DL (2007) Simulation-assisted materials design for the concurrent design of materials and products. *JOM* 59(9):21–25
20. McDowell DL, Panchal J, Choi HJ, Seepersad C, Allen J, Mistree F (2009) Integrated design of multiscale, multifunctional materials and products. Butterworth-Heinemann
21. Panchal JH, Kalidindi SR, McDowell DL (2013) Key computational modeling issues in integrated computational materials engineering. *Comput Aided Des* 45(1):4–25
22. Paul A, Acar P, Liao Wk, Choudhary A, Sundararaghavan V, Agrawal A (2019) Microstructure optimization with constrained design objectives using machine learning-based feedback-aware data-generation. *Comput Mater Sci* 160:334–351
23. Roters F, Diehl M, Shanthraj P, Eisenlohr P, Reuber C, Wong SL, Maiti T, Ebrahimi A, Hochrainer T, Fabritius HO et al (2019) DAMASK-The Düsseldorf Advanced Material Simulation Kit for modeling multi-physics crystal plasticity, thermal, and damage phenomena from the single crystal up to the component scale. *Comput Mater Sci* 158:420–478
24. Roters F, Eisenlohr P, Bieler TR, Raabe D (2011) *Crystal plasticity finite element methods: in materials science and engineering*. Wiley, New York
25. Roters F, Eisenlohr P, Hantcherli L, Tjahjanto DD, Bieler TR, Raabe D (2010) Overview of constitutive laws, kinematics, homogenization and multiscale methods in crystal plasticity finite-element modeling: Theory, experiments, applications. *Acta Mater* 58(4):1152–1211
26. Science N, (US), TC (2011) *Materials genome initiative for global competitiveness*. Executive Office of the President, National Science and Technology Council
27. Shahriari B, Swersky K, Wang Z, Adams RP, de Freitas N (2016) Taking the human out of the loop: a review of Bayesian optimization. *Proc IEEE* 104(1):148–175
28. Shanthraj P, Eisenlohr P, Diehl M, Roters F (2015) Numerically robust spectral methods for crystal plasticity simulations of heterogeneous materials. *Int J Plast* 66:31–45
29. Steinmetz DR, Jäpel T, Wietbrock B, Eisenlohr P, Gutierrez-Urrutia I, Saeed-Akbari A, Hickel T, Roters F, Raabe D (2013) Revealing the strain-hardening behavior of twinning-induced plasticity steels: theory, simulations, experiments. *Acta Mater* 61(2):494–510

30. Tallman AE, Stopka KS, Swiler LP, Wang Y, Kalidindi SR, McDowell DL (2019) Gaussian-process-driven adaptive sampling for reduced-order modeling of texture effects in polycrystalline alpha-Ti. *JOM* 71(8):2646–2656
31. Tallman AE, Swiler LP, Wang Y, McDowell DL (2020) Uncertainty propagation in reduced order models based on crystal plasticity. *Comput Methods Appl Mech Eng* 365:113009
32. Torquato S (2002) Statistical description of microstructures. *Annu Rev Mater Res* 32(1):77–111
33. Tran A, Eldred M, Wang Y, McCann S (2020) srMO-BO-3GP: a sequential regularized multi-objective constrained Bayesian optimization for design applications. In: Proceedings of the ASME 2020 IDETC/CIE, international design engineering technical conferences and computers and information in engineering conference, vol volume 1: 40th computers and information in engineering conference. American Society of Mechanical Engineers
34. Tran A, McCann S, Furlan JM, Pagalthivarthi KV, Visintainer RJ, Wildey T (2020) aphBO-2GP-3B: a budgeted asynchronously-parallel multi-acquisition for known/unknown constrained Bayesian optimization on high-performing computing architecture. arXiv preprint [arXiv:2003.09436](https://arxiv.org/abs/2003.09436)
35. Tran A, Mitchell JA, Swiler LP, Wildey T (2020) An active-learning high-throughput microstructure calibration framework for process-structure linkage in materials informatics. *Acta Mater* 194:80–92
36. Tran A, Sun J, Furlan JM, Pagalthivarthi KV, Visintainer RJ, Wang Y (2019) pBO-2GP-3B: A batch parallel known/unknown constrained Bayesian optimization with feasibility classification and its applications in computational fluid dynamics. *Comput Methods Appl Mech Eng* 347:827–852
37. Tran A, Tran H (2019) Data-driven high-fidelity 2D microstructure reconstruction via non-local patch-based image inpainting. *Acta Mater* 178:207–218
38. Tran A, Tranchida J, Wildey T, Thompson AP (2020) Multi-fidelity machine-learning with uncertainty quantification and Bayesian optimization for materials design: application to ternary random alloys. arXiv preprint [arXiv:2006.00139](https://arxiv.org/abs/2006.00139)
39. Tran A, Wildey T (2020) Solving stochastic inverse problems for property-structure linkages using data-consistent inversion and machine learning. *JOM*
40. Tran A, Wildey T, McCann S (2020) sMF-BO-2CoGP: a sequential multi-fidelity constrained Bayesian optimization for design applications. *J Comput Inf Sci Eng* 20(3):1–15
41. Tran AV, Liu D, Tran HA, Wang Y (2019) Quantifying uncertainty in the process-structure relationship for Al-Cu solidification. *Modell Simul Mater Sci Eng* 27(6):064005
42. Wong SL, Madivala M, Prah U, Roters F, Raabe D (2016) A crystal plasticity model for twinning-and transformation-induced plasticity. *Acta Mater* 118:140–151
43. Yuan M, Paradiso S, Meredig B, Niezgoda SR (2018) Machine learning-based reduce order crystal plasticity modeling for ICME applications. *Integr Mater Manuf Innov* 7(4):214–230

Part XVII
AI/Data Informatics: Design of Structural
Materials

Incorporating Historical Data and Past Analyses for Improved Tensile Property Prediction of 9% Cr Steel



Madison Wenzlick, Osman Mamun, Ram Devanathan, Kelly Rose, and Jeffrey Hawk

Abstract Data-driven analytical clustering and visualization techniques were applied to the dataset of 9% Cr experimental alloy data generated through the eXtremeMAT project. Techniques and results were compared with the resulting clusters obtained through similar analytical techniques on previous and reduced versions of the dataset. The principal components were generated in order to reduce the dimensionality of the complex dataset and to visualize the underlying trends in the data. Partitioning around medoids was performed on the resulting principal components to determine relevant clusters. Domain knowledge labels were further applied to the principal components to compare the labels with the trends identified through the clustering methods. The clusters can be used to compare the tensile properties of the alloys and to reduce the variation in the dataset.

Keywords Data analytics · Clustering · 9% Cr alloy · Data assessment

Introduction

Recent advancements in data collection, curation and analysis have increasingly enabled data-driven techniques to be applied in scientific discovery. The ability to parse and manipulate large volumes of data has improved the ability to identify and use relevant data from previous works in analysis. In the field of alloy design, the goal of understanding the complex connections between alloy processing, composition, microstructure and mechanical properties has been explored through experimentation and computation for many decades. Accessing and using this data to inform

M. Wenzlick · K. Rose · J. Hawk (✉)

National Energy Technology Laboratory, 1450 Queen Avenue SW, Albany, OR 97321, USA

e-mail: Jeffrey.Hawk@netl.doe.gov

M. Wenzlick

Leidos Research Support Team, 1450 Queen Avenue SW, Albany, OR 97321, USA

O. Mamun · R. Devanathan

Pacific Northwest National Laboratory, Energy and Environment Directorate, Richland, WA, USA

© The Minerals, Metals & Materials Society 2021

TMS 2021 150th Annual Meeting & Exhibition Supplemental Proceedings,

The Minerals, Metals & Materials Series,

https://doi.org/10.1007/978-3-030-65261-6_42

future work will enable more efficient alloy design, property prediction, and materials development.

However, data can be difficult to find and extract, as it is often stored in difficult to access forms when released to the public. Experimental data are found in journal manuscripts, reports, and patents, as well as data sheets and data repositories. The format of reported data varies widely, including which data attributes are reported, the methodologies for collecting data and conducting tests, and whether data are reported in graphical, tabular, digital or textual form.

Through eXtremeMAT, the United States Department of Energy (DOE) multi-laboratory consortium to improve alloy design, tools have been developed and tested for data identification and extraction. Work has been done to assess the variations in experimental data reporting and establish tools to rate the quality of reported data based on several metrics, namely the completeness, precision, standardization and usability of data.

9% Cr steel is a common alloy used in energy applications. Due to the wide availability of experimental creep, tensile and stress relaxation data, data science techniques were applied to understanding the connections between alloy processing and property performance. The insights gained from these analyses can be validated with domain expertise, simulation and modeling, and experimental results. As data-driven techniques are developed and validated with a known use case (9% Cr), the same techniques can be applied to alloys with more unknowns with improved confidence in the results. These data analytics can improve the design process by indicating where alloy processing-heat treatment-composition combinations can most likely result in desirable mechanical properties over time.

Previous iterations of the 9% Cr dataset have been used by researchers to explore connections and interactions between alloy attributes and the properties important to tensile strength.

In this work, we discuss the data collection, curation and analyses techniques used to curate a database of 9% Cr steel data and to investigate the relationships between alloy attributes and resulting tensile properties. We discuss the methodologies and necessary assumptions for leveraging previous analytical results and methods into future analytics with improved data. Further, we investigate the changes in analytical results with the addition of new data.

Methods

Data Collection

The data collection process to support data analytics has been underway for several years through eXtremeMAT. Researchers have applied both manual searches and automated search tools to identify relevant data. Resources containing information on alloy composition, processing, microstructure, heat treatment and mechanical

properties were identified and collected. Data sources include journal publications, online data repositories, national laboratory testing programs and reports, patents, and data sheets, as well as proprietary data from in house research and industry testing. The data used in this analysis include high quality data from national laboratory reports, in house research, and industry data [1–13] (Table 1).

Determining Data Quality

Data quality metrics for assessing the relative quality of experimental alloy data were developed through the eXtremeMAT program [14]. These metrics were designed to be appended to alloy metadata in order to enable data to be divided by quality for different uses. As the quality of data determines the quality of the analyses, assessing this metric helps to guide both the understanding of the uncertainty magnitude as well as where the uncertainty comes from. The sources of uncertainty include missing data, the use of a non-standard test technique, presenting data in a graphical form, among others. These aspects of uncertainty are captured in the different metrics for data quality.

For this work, only data with a quality rating of four or above were used. The high quality data were used to establish analytical relationships. Lower quality data can be used for comparison, as well as for verification of the model once established (Table 2).

Analytical Techniques

Several analyses have investigated processing-microstructure-property relationships using previous versions of the dataset, with more limited data [15–21]. These analyses include several correlation and clustering techniques that allow the data to be segmented into smaller groups with less variation in attributes.

Principal Component Analysis

Principal component analysis (PCA) was used to reduce the dimensions of the dataset and to consider trends in the data that occur through combinations of attributes [22]. The principal components of the dataset are obtained through linear combinations of attributes which are optimized to account for the maximum amount of variance in the data [22]. The number of principal components used in analysis or visualization can be determined either by number or by the total amount of variance explained. PCA was performed using the *prcomp* function in R, and the R library *factoextra* was used to visualize the resulting data.

Table 1 Overview of attributes and units included in the database

Field	Units	Field	Units	Field	Units	Field	Units
Alloy ID	–	Element sulfur (S)	wt%	Creep test temperature	°C	Low cycle fatigue test R-ratio	–
Element iron (Fe)	wt%	Element zirconium (Zr)	wt%	Creep stress	MPa	Low cycle fatigue test A-ratio	–
Element carbon (C)	wt%	Element yttrium (Y)	wt%	Creep rupture time	h	Low cycle fatigue test cycles to crack initiation	–
Element chromium (Cr)	wt%	Homogenization heat treatment	0/1	Elongation to failure	%	Low cycle fatigue test cycles to failure	–
Element manganese (Mn)	wt%	Normalization or austenization heat treatment temperature	°C	Reduction in area	%	High cycle fatigue test temperature	°C
Element silicon (Si)	wt%	Temper heat treatment 1	°C	Minimum creep rate	%/h	High cycle fatigue test stress concentration factor	–
Element nickel (Ni)	wt%	Temper heat treatment 2	°C	Time to reach 0.1% creep strain	h	High cycle fatigue test waveform	–
Element cobalt (Co)	wt%	Temper heat treatment 3	°C	Time to reach 0.15% creep strain	h	High cycle fatigue test frequency	Hz
Element molybdenum (Mo)	wt%	Temper heat treatment 4	°C	Time to reach 0.2% creep strain	h	Maximum stress	MPa
Element tungsten (W)	wt%	Austenite grain size number	#	Time to reach 0.25% creep strain	h	Minimum stress	MPa
Element niobium (Nb)	wt%	Austenite grain size	# grains/mm ²	Time to reach 0.5% creep strain	h	Stress amplitude	MPa
Element aluminum (Al)	wt%	Tensile test temperature	°C	Time to reach 1.0% creep strain	h	Mean stress	MPa

(continued)

Table 1 (continued)

Field	Units	Field	Units	Field	Units	Field	Units
Element phosphorous (P)	wt%	0.2% yield stress	MPa	Time to reach 2.0% creep strain	h	High cycle fatigue test R-ratio	–
Element copper (Cu)	wt%	Ultimate tensile strength	MPa	Time to reach 5.0% creep strain	h	High cycle fatigue test A-ratio	–
Element titanium (Ti)	wt%	Elongation to failure	%	Time to tertiary creep	h	High cycle fatigue test cycles to crack initiation	–
Element tantalum (Ta)	wt%	Reduction in area	%	Low cycle fatigue test temperature	°C	High cycle fatigue test cycles to failure	–
Element hafnium (Hf)	wt%	Charpy impact value	J/cm ²	Low cycle fatigue test stress concentration factor	–	Stress relaxation test temperature	°C
Element rhenium (Re)	wt%	Vickers hardness	Hv 196 N	Low cycle fatigue test waveform	–	Stress relaxation test total strain	%
Element vanadium (V)	wt%	Density	g/cm ²	Low cycle fatigue test frequency	Hz	Stress relaxation test initial stress	MPa
Element boron (B)	wt%	Elastic/Young's modulus	kN/mm ²	Low cycle fatigue test total strain amplitude	MPa	Stress relaxation test time running time	h
Element nitrogen (N)	wt%	Shear modulus	kN/mm ³	Low cycle fatigue test maximum strain amplitude	MPa	Stress relaxation test residual stress at specified running time	MPa
Element oxygen (O)	wt%	Poisson's ratio	–	Low cycle fatigue test minimum strain amplitude	MPa		

Table 2 Metrics to determine the rating of data quality in the categories of completeness, accuracy, usability and standardization from 1 to 5

Rating	Completeness	Accuracy	Usability	Standardization
1	<p>Only indication of the name of the material is reported</p> <p>Material manufacturing and processing data may or may not be provided:</p> <ul style="list-style-type: none"> • Material production process and/or material manufacturer specification • Heat treatment sequence, temperature, and time if applicable • Microstructure (grain size) • Product form and characteristic dimension 	<p>No data provided with exact values, all data are provided in graphs, averaged values, or nominal values</p> <p>Or more than 50% of values are difficult to read due to the low resolution of the document</p>	<p>Data require 100% manual extraction</p>	<p>Testing and measurement non-standard</p> <p>Testing organization non-accredited</p>
2	<p>Chemical composition is not complete or is given as nominal values only</p> <p>Material manufacturing and processing data may or may not be provided:</p> <ul style="list-style-type: none"> • Material production process and/or material manufacturer specification • Heat treatment sequence, temperature, and time if applicable • Microstructure (grain size) • Product form and characteristic dimension 	<p>Less than half of data, but more than 0%, are provided in exact values</p> <p>More than 50%, but less than 100% of data attributes are provided in average value only, or in graphical form</p>	<p>Data are located in physical copy only, requiring scanning to digitize</p>	<p>Accreditation and standard of testing and measurement unknown</p>

(continued)

Table 2 (continued)

Rating	Completeness	Accuracy	Usability	Standardization
3	<p>Some critical material manufacturing and processing data are provided (at minimum):</p> <ul style="list-style-type: none"> • Exact chemical composition <p>One of these attributes is not present:</p> <ul style="list-style-type: none"> • Material production process and/or material manufacturer specification • Heat treatment sequence, temperature, and time if applicable <p>These attributes may be provided:</p> <ul style="list-style-type: none"> • Microstructure (grain size) • Product form and characteristic dimension 	<p>50% of data are provided in exact values</p> <p>50% of data attributes are nominal or provided in averages or graphically</p> <p>Or, 1–2 attributes are unclear (provided but difficult to read)</p>	<p>Data are located in non-standard or hard to read tables. Or data requires OCR for extraction followed by error checking</p>	<p>Material testing organization and/or manufacturer is accredited. Standard of testing and measurement unknown</p>
4	<p>Some critical material manufacturing and processing data are provided (at minimum):</p> <ul style="list-style-type: none"> • Exact chemical composition • Material production process and/or material manufacturer specification • Heat treatment sequence, temperature, and time if applicable <p>One of these attributes are not present:</p> <ul style="list-style-type: none"> • Microstructure (grain size as minimum) or • Product form and characteristic dimension 	<p>More than 50%, but less than 100% of data are provided in exact values</p> <p>More than 0% but less than 50% of data attributes are nominal, or provided in an average value only, or in graphical form</p>	<p>Data in original source are organized in digital, tabular form, either in text-based files, data sheets, or in a database with relevant headers and/or metadata.</p> <p>However, data are unorganized (i.e., in multiple files) or requires manipulation to connect metadata with data</p>	<p>Standard of testing and measurement performed according to an accepted national standard accreditation unknown</p>

(continued)

Table 2 (continued)

Rating	Completeness	Accuracy	Usability	Standardization
5	<p>Critical material manufacturing and processing data are available:</p> <ul style="list-style-type: none"> • Exact chemical composition • Material production process and/or material manufacturer specification • Product form and characteristic dimension • Heat treatment sequence, temperature, and time if applicable • Microstructure (grain size as minimum) 	<p>All data and data attributes are provided as exact values (i.e. not nominal) No data are provided in an average value only, or in graphical form Document is in digital form or a high resolution scan Text and numbers are clear and are not required to be guessed</p>	<p>Data in original source are organized in digital, tabular form, either in text-based files, data sheets, or in a database with relevant headers and/or metadata Location of data is intuitive. Locations of relevant headers and metadata are intuitive Data are easy to extract and manipulate</p>	<p>Material testing organization and/or manufacturer are accredited Testing and measurement of the mechanical properties were performed according to an accepted national standard</p>

Partitioning Around Medoids/ K-Medoid Clustering

Once dimensionality reduction has been performed, the data were visualized and examined in the reduced-dimension space. Partitioning around medoids (PAM), a type of k-Medoid clustering, generates clusters of data by minimizing the distance between each data point to the center of the cluster [23]. In this case, the cluster center is assigned to one of the points. The number of clusters can be determined visually or optimized using several metrics. This analysis was performed in R using the *pam* function in the *cluster* library. The distance was minimized by using the Euclidean distance. The resulting clusters were compared to domain knowledge groupings of alloys based on elemental composition to validate and explore the results.

Results

Principal component analysis was performed several ways in the literature. In this work, PCA was performed on the 9% Cr data using the 18 compositional elements, as well as the heat treatment normalization and tempering temperatures. This subset of attributes follows the attributes in Verma, et al for clustering using t-SNE [21]. The resulting PCA was visualized using the first two principal components (Fig. 1). The points were colored according to the initial domain knowledge labels of the data, determined through analysis of the composition clusters resulting from t-SNE

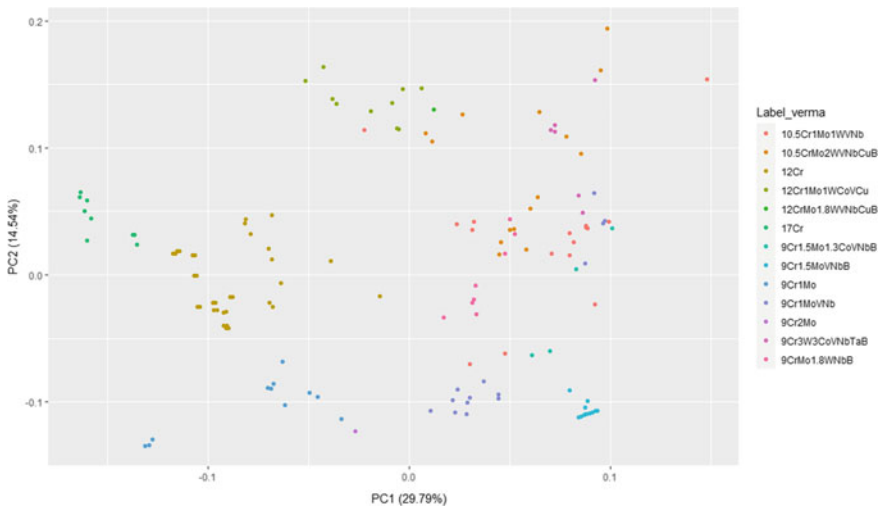


Fig. 1 PCA performed on 18 compositional elements and normalization and tempering heat treatment temperatures, and visualized using the first two principal components. The color of the point corresponds with the domain knowledge applied label [21]. (Color figure online)

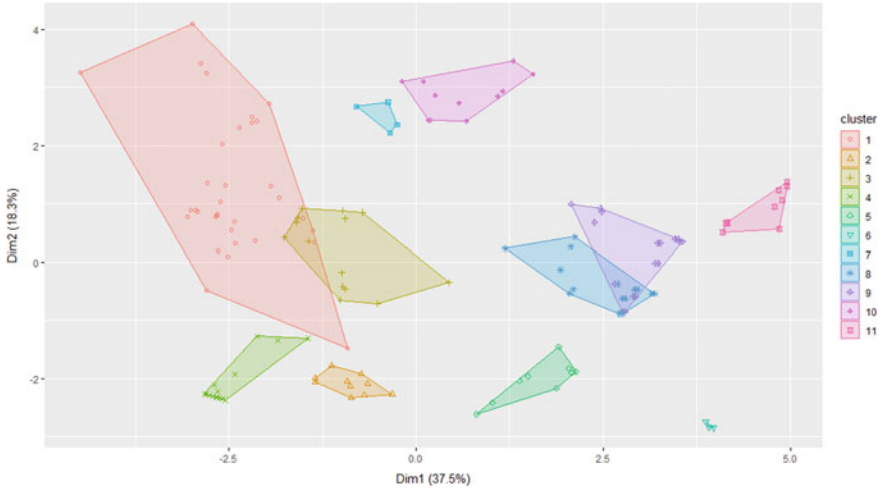


Fig. 2 PAM clustering results on the first seven principal components, visualized in 2D space. Note that the x -axis is flipped as compared to Fig. 1. (Color figure online)

analysis in [21]. In comparison, PAM was performed on the same data, using the first seven principal components, and visualized with 11 clusters (Fig. 2).

Discussion

The clustering results from PCA and PAM show interesting overlap with the domain knowledge applied labels. While the clusters are not as distinct as the t-SNE results shown in Fig. 1 from Verma et al. [21], the PAM clusters show similarity to the clustering groups identified in Fig. 4 in Romanov et al. [17]. However, in this work, we identify 11 clusters rather than the 9 identified by Romanov, et al. due to the addition of new data [17]. In Fig. 1, the 17% Cr cluster fully aligns with cluster 11 identified using PCA and PAM in Fig. 2. This indicates that this cluster is fairly distinct from the other data, which aligns with the alloy Cr composition being significantly higher than the other alloys in the dataset.

Further, cluster 1 in Fig. 2 contains a large number of points compared to some of the other clusters. This corresponds to an area where a number of domain knowledge labels are scattered in the PCA plot shown in Fig. 1, rather than forming a concise cluster. This shows good agreement between the two clustering labels that there should be a new domain label for that cluster as a whole. Alternatively, this cluster could be evaluated for several subgroupings with less variation than the entire cluster. The clusters can be evaluated for trends in tensile properties and used in machine learning to reduce the variation of the data across the dataset.

Some of the clusters identified by PAM appear to occupy two domain labels or to split one domain label into two groups. The composition of these groups of clusters can be evaluated and the domain label possibly adjusted. For example, the 12% Cr label appears in two clusters in the PAM visualization. This suggests that this label could be divided into two groups. The single 12% Cr grouping can be compared with the split subgroups and compared for reduction in variation among the composing elements and heat treatments.

Further, the domain knowledge labels can be evaluated for consistency, and the resulting trends in composition, heat treatment can be compared with how the clusters perform in predicting and correlation with tensile properties. Additionally, the clustering analysis can be used to identify outliers in the dataset through comparison of the cluster properties and the resulting influence on tensile behavior.

Conclusions

PCA and PAM are promising methods of reducing the dimensions of the experimental alloy dataset gathered on 9% Cr steel. Visualizing the resulting clusters from these methods against common alloy labels shows where the alloy groupings align with the patterns seen through PCA and where labels need to be adjusted to accommodate more variation. The data-driven exploration of the data space enables the analysis of underlying trends in the data, and to identify relationships between the composition, heat treatment and mechanical properties. As the development of the eXtremeMAT database continues, the analytics will continuously adjust to new data, providing new insights into the alloy design space.

Acknowledgements This work was performed in support of the US Department of Energy's Fossil Energy Crosscutting Technology Research Program. This work was supported by the NETL Crosscutting Research Program, Briggs White, NETL Technology Manager, and Regis Conrad, DOE-FE HQ Program Manager. The research was executed through the eXtremeMAT National Laboratory Field Work Proposal (NETL: FWP-1022433, LANL: FWP-FE85017FY17, ORNL: FWP-FEAA134, Ames: FWP-AL-17-510091, LLNL: FWP-FEW0234, INL: FWP-B000-17016, PNNL: FWP-71133). Research performed by Leidos Research Support Team staff was conducted under the RSS contract 89243318CFE000003.

Disclaimer

This work was funded by the Department of Energy, National Energy Technology Laboratory, an agency of the United States Government, through a support contract with Leidos Research Support Team (LRST). Neither the United States Government nor any agency thereof, nor any of their employees, nor LRST, nor any of their employees, makes any warranty, expressed or implied, or assumes any legal liability or responsibility for the accuracy, completeness, or usefulness of any information, apparatus, product, or process disclosed, or represents that its use would not infringe privately owned rights. Reference herein to any specific commercial product, process, or service by trade name, trademark, manufacturer, or otherwise, does not necessarily constitute or imply its endorsement, recommendation, or favoring by the United States Government or any agency thereof. The views and opinions of authors expressed herein do not necessarily state or reflect those of the United States Government or any agency thereof.

References

1. NIMS (1982) Fatigue data sheet series, no. 30. National Institute for Materials Science, Tsukuba-shi
2. NIMS (1982) Fatigue data sheet series, no. 29. National Institute for Materials Science, Tsukuba-shi
3. NIMS (1983) Fatigue data sheet series, no. 35. National Institute for Materials Science, Tsukuba-shi
4. NIMS (1994) Creep data sheet, no. 13B. National Institute for Materials Science, Tsukuba-shi
5. NIMS (1997a) Creep data sheet, no. 19B. National Institute for Materials Science, Tsukuba-shi
6. NIMS (1997b) Creep data sheet, no. 44. National Institute for Materials Science, Tsukuba-shi
7. NIMS (1998) Creep data sheet, no. 10B. National Institute for Materials Science, Tsukuba-shi
8. NIMS (2002) Fatigue data sheet series, no. 88. National Institute for Materials Science, Tsukuba-shi
9. NIMS (2005) Creep data sheet, no. 46A. National Institute for Materials Science, Tsukuba-shi
10. NIMS (2012) Creep data sheet, no. 48A. National Institute for Materials Science, Tsukuba-shi
11. NIMS (2013a) Creep data sheet, no. 51A. National Institute for Marine Science, Tsukuba-shi
12. NIMS (2013b) Creep data sheet, no. 52A. National Institute for Materials Science, Tsukuba-shi
13. NIMS (2014) Creep data sheet, no. 43A. National Institute for Materials Science, Tsukuba-shi
14. Wenzlick M et al (2020) Data assessment method to support the development of creep-resistant alloys. *Integrating Mater Manuf Innovation* 9(1):89–102. <https://doi.org/10.1007/s40192-020-00167-3>
15. Krishnamurthy N et al (2019) 9Cr steel visualization and predictive modeling. *Comput Mater Sci* 168:268–279. <https://doi.org/10.1016/j.commatsci.2019.03.015>
16. Krishnamurthy N et al. (2018) Data analytics for alloy qualification. National Energy Technology Lab. (NETL), Pittsburgh, PA, and Morgantown, WV
17. Romanov VN et al (2019) Materials data analytics for 9% Cr family steel. *Stat Anal Data Min ASA Data Sci J* 12(4):290–301
18. Verma A et al. (2018) Mapping multivariate influence of alloying elements presentation. in MSLE. Carnegie Mellon University
19. Verma AK et al (2019) Mapping multivariate influence of alloying elements on creep behavior for design of new martensitic steels. *Metall Mater Trans A* 50(7):3106–3120. <https://doi.org/10.1007/s11661-019-05234-9>
20. Verma AK et al (2020) Predictions of long-term creep life for the family of 9–12 wt% Cr martensitic steels. *J Alloy Compd* 815:152417. <https://doi.org/10.1016/j.jallcom.2019.152417>
21. Verma AK et al (2019) Screening of heritage data for improving toughness of creep-resistant martensitic steels. *Mater Sci Eng, A* 763:138142. <https://doi.org/10.1016/j.msea.2019.138142>
22. Wold S, Esbensen K, Geladi P (1987) Principal component analysis. *Chemometr Intell Lab Syst* 2(1–3):37–52
23. Rousseeuw PJ, Kaufman L (1990) Finding groups in data. Wiley Online Library, Hoboken, p 1

Prediction of the Mechanical Properties of Aluminum Alloy Using Bayesian Learning for Neural Networks



Shimpei Takemoto, Kenji Nagata, Takeshi Kaneshita, Yoshishige Okuno, Katsuki Okuno, Masamichi Kitano, Junya Inoue, and Manabu Enoki

Abstract The strengthening mechanism of the 2000 series aluminum alloy has been studied using neural networks. We have constructed a neural network for the simultaneous prediction of multiple mechanical properties, including ultimate tensile strength, tensile yield strength, and elongation at break. The replica-exchange Monte Carlo method, an improved Markov chain Monte Carlo (MCMC) method, has been applied for Bayesian learning of the optimal neural network architecture and hyperparameters. The obtained neural network, combined with the thermodynamic analysis using the Thermo-Calc software, enables us to identify a dominant combination of additive elements and heat treatments for strengthening alloys. We have also addressed an inverse problem for optimizing the process parameters. The approach we propose will accelerate the design of high strength alloys for high-temperature applications.

Keywords Aluminum alloy · Bayesian inference · Neural networks · Exchange Monte Carlo · Thermo-Calc

Introduction

Understanding the process–structure–property relationship (or the PSP relationship) is one of the goals of computational materials design. In this paper, we discuss the PSP relationship in aluminum alloys (Fig. 1). The major process parameters for aluminum alloys include the percentage of each additive element and the heat treatment

S. Takemoto (✉) · T. Kaneshita · Y. Okuno · K. Okuno · M. Kitano
Showa Denko K.K., 1-1-1 Ohnodai, Midori-ku, Chiba 267-0056, Japan
e-mail: takemoto.shimpei.xhmth@showadenko.com

K. Nagata
National Institute for Materials Science, 1-1 Namiki, Tsukuba, Ibaraki 305-0044, Japan
e-mail: Nagata.Kenji@nims.go.jp

J. Inoue · M. Enoki
Department of Materials Engineering, The University of Tokyo, Tokyo, Japan

time and temperature for annealing, solutionizing, and aging processes. Mechanical properties including ultimate tensile strength (UTS), tensile yield strength (TYS), and elongation at break (EB) are of our main interest for industrial applications. The structure factors include the percentage of each chemical compound, such as Al_2Cu , and size, shape, and spatial distribution of grains in aluminum alloys. The aluminum alloy structure is controlled by the process parameters and determines the mechanical properties, yet the process–structure relationship and the structure–property relationship are not clear. We believe understanding these relationships is inevitable for performing an inverse analysis for finding the best process parameters.

To approach this problem, we construct neural networks, which link the process parameters and mechanical properties. In analogy with the PSP relationship in Fig. 1, the neural networks have a single hidden layer, while input and output layer nodes correspond to the process parameters and the mechanical properties, respectively (Fig. 2). We expect hidden layer nodes in the neural networks to extract dominant structure features that determine the mechanical properties.

We apply the replica-exchange Monte Carlo (EMC) method for Bayesian estimation of the optimal neural network architecture and weights. Neural networks belong to singular learning machines, and it is known that Bayesian learning provides better generalization performance than the maximum-likelihood estimation [1, 2]. However, it needs huge computational cost to sample from a Bayesian

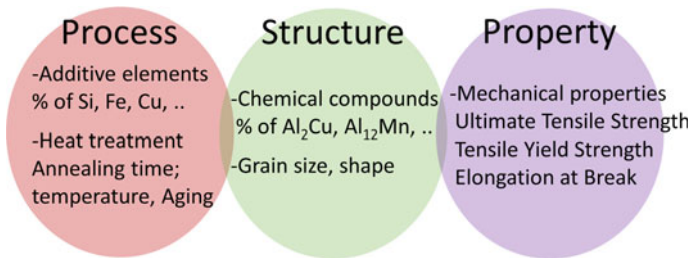


Fig. 1 Example of the PSP relationship in aluminum alloys. (Color figure online)

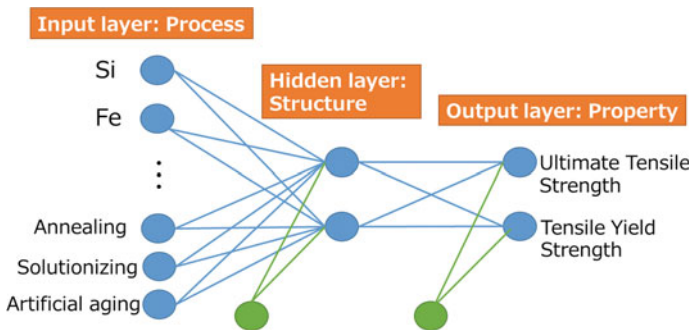


Fig. 2 Neural network architecture for predicting mechanical properties. (Color figure online)

posterior distribution of a singular learning machine by a conventional Markov chain Monte Carlo (MCMC) method, such as the metropolis algorithm because of singularities. The EMC method we use has a better effect on Bayesian learning in singular learning machines, which, in other words, converges to a global minimum faster when solving multimodal problems. For a detailed formulation of the EMC method, see, e.g., [3, 4].

This paper consists of four sections. In Sect. “[Bayesian Learning for Neural Networks](#)”, we formulate neural networks for the mechanical properties prediction. In Sect. “[Results](#)”, we show our main results for the simultaneous prediction of multiple properties. We discuss two (UTS and TYS) and three (UTS, TYS, and EB) properties cases. Using the obtained neural network, we discuss which combination of additive elements contributes to strengthening alloys. We also conduct a thermodynamic analysis of the phase fraction diagram using the Thermo-Calc software to analyze the alloy structure. In Sect. “[Discussions](#)”, we discuss further applications of our approach.

Bayesian Learning for Neural Networks

In this section, we formulate a neural network for predicting aluminum alloy mechanical properties. We focus on the analysis of the 2000 series aluminum alloy or the Al-Cu-Mg system. We prepare a clean dataset using the Matweb and the Japan Aluminum Association databases [5, 6]. The dataset has 68 records whose features and targets are summarized in Table 1. The corresponding neural networks have 13 input layer nodes (ten additive elements and three heat treatments) and three output layer nodes. The neural network has a single hidden layer.

Let f_i (Output), g_j (Input) and h_k (Hidden) represent the nodes, v_{ki} (Hidden-Output) and w_{jk} (Input-Hidden) represent the network weights, and c_{1i} (Output) and c_{2i} (Hidden) represent the biases. The relationships between the adjacent layers can be written as

Table 1 Features and targets in the 2000 aluminum alloy dataset

Category	Type of variables	#	Variables
Features	Continuous	10	Weight for Si, Fe, Cu, Mn, Mg, Cr, Ni, Zn, Ti, and Zr
Features	Binary (0 or 1)	3	Annealing, solutionizing, and artificial aging
Targets	Continuous	3	Ultimate tensile strength (UTS), Tensile yield strength (TYS), and Elongation at break (EB) at room temperature

$$f_i = v_{ki}h_k + c_{1i}, \quad (1)$$

$$h_k = w_{jk}g_j + c_{2k}, \quad (2)$$

where the summations over k and j are abbreviated.

We apply the EMC method as a sampling method for Bayesian estimation of the network weights. Let $\theta = (\theta_1, \theta_2, \dots, \theta_n)$ represent parameters of a neural network, or the network weights. The number of hidden layer nodes (K) is also estimated by the EMC method. The optimal number of K can be obtained by minimizing the Bayes free energy ($F(K)$):

$$F(K) = -\log Z(K), \quad (3)$$

$$Z(K) = \int d\theta \exp\left(-\frac{N}{\sigma^2}E(\theta, K)\right) \varphi(\theta), \quad (4)$$

$$E(\theta, K) = \frac{1}{2N} \sum_{i=1}^N (y_i - f_i)^2, \quad (5)$$

where $E(\theta, K)$ represents the mean squared error between the actual property values (y_i) and the neural network predictions (f_i). N and $\sigma (= 0.1)$ represent the number of records and the noise level of the dataset, respectively. $\varphi(\theta)$ represents the prior distribution of the parameter set θ and is set as n -dimensional normal distribution in this study.

Results

Prediction of Two Properties with a Linear Neural Network

In this subsection, we construct a linear neural network for the simultaneous prediction of two properties, UTS and TYS at room temperature. The activation function is linear for both hidden and output layer nodes. The Bayes free energy $F(K)$ is minimized at $K = 2$, meaning that the neural network is optimized at two hidden layer nodes. In other words, we have identified two dominant structure features, where UTS and TYS are expressed as a linear superposition of these features. Figure 3 shows that the linear neural network model with $K = 2$ predicts both UTS and TYS with good accuracy. The Monte Carlo ensemble in the EMC method also provides the probability distribution of the prediction.

The network weights of the optimal neural network are shown in Fig. 4. Every feature and target has been standardized before the Bayesian learning for the scale comparison of the network weights. Since both hidden layer nodes have positive weights with UTS and TYS, adding more (less) additive elements or heat treatments with positive (negative) weights strengthens alloys. Figure 4 also indicates which combinations of additive elements effectively control alloy strength. The hidden

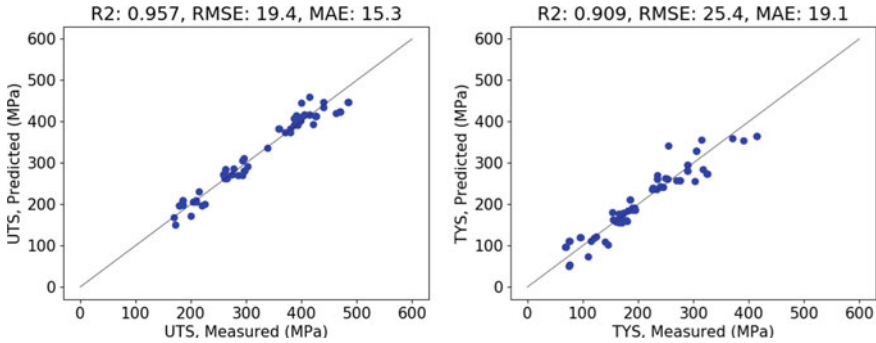


Fig. 3 Prediction of UTS (left) and TYS (right) with a linear neural network. (Color figure online)

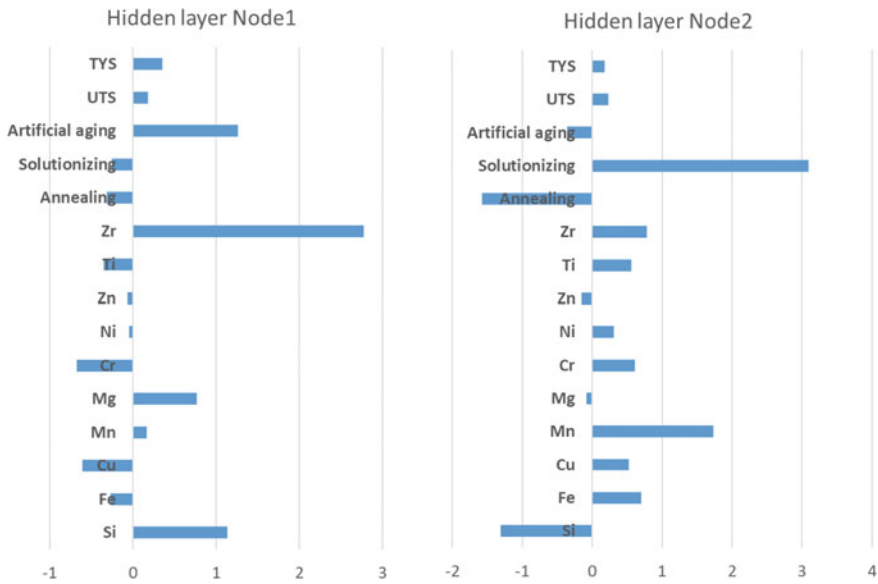


Fig. 4 Network weights of the optimal linear neural network for Node1 (left) and Node2 (right). (Color figure online)

layer node 2 (Node2) has strong positive weights with solutionizing and Mn, while the node has strong negative weights with annealing and Si. This result is consistent with that the aluminum alloys are strengthened with the solutionizing process and without the annealing process. This result is also consistent with that adding Mn in the 2000 series aluminum alloy causes a fine grain structure by forming the Al-Cu-Mn compound phase [7]. On the other hand, the hidden layer node 1 (Node1) has strong positive weights with artificial aging, Si, Mg, and Zr, while the node has strong negative weights with Cu and Cr. This behavior is similar to that of the 6000 series aluminum alloy or the Al-Mg-Si system, where we observe age-hardening by Mg and Si, and a fine grain structure by adding Zr and forming the Al-Zr compound

phase [8]. Thus, the 2000 aluminum alloy's strengthening mechanism appears to be the superposition of the Al-Cu system and the Al-Mg-Si system.

In order to analyze these observations in detail, we conduct thermodynamic calculations of the equilibrium phase fraction as a function of temperature using the Thermo-Calc software with the TCAL6 database. We draw two phase fraction diagrams—one is for Node2, and the other is for Node1 (Fig. 5). For Node 2, Fig. 4 suggests rich Mn and poor Si strengthen alloys, so we draw the phase fraction diagram with the maximum amount of Mn and the minimum amount of Si (median for other additive elements) listed in Table 2. At 500 °C, a typical solutionizing temperature, $\text{Al}_{28}\text{Cu}_4\text{Mn}_7$ appears in the phase fraction diagram. This result suggests that the formation of $\text{Al}_{28}\text{Cu}_4\text{Mn}_7$ causes a fine grain structure and strengthens alloys [7]. The composition of $\text{Al}_{28}\text{Cu}_4\text{Mn}_7$ is approximate to a stoichiometric composition $\text{Al}_{20}\text{Cu}_2\text{Mn}_3$ [9]. On the other hand, the formation of $\text{Al}_8\text{Fe}_2\text{Si}$ weakens alloys, which is consistent with the result that poor Si is preferred in Node2. For Node1, we draw the phase fraction diagram with the maximum amount of Si, Mg, and Zr and the minimum amount of Cu and Cr. We see Al_3Zr crystallizes at a higher temperature than α -Al, causing a fine grain structure and strengthening alloys [8]. At 180 °C, a typical artificial aging temperature, β - Mg_2Si and θ - Al_2Cu appear, which are associated with the Guinier–Preston zone and play major roles in age-hardening.

Once we obtain the optimal neural network, solving the inverse problem is straightforward. By plugging (2) into (1), we obtain

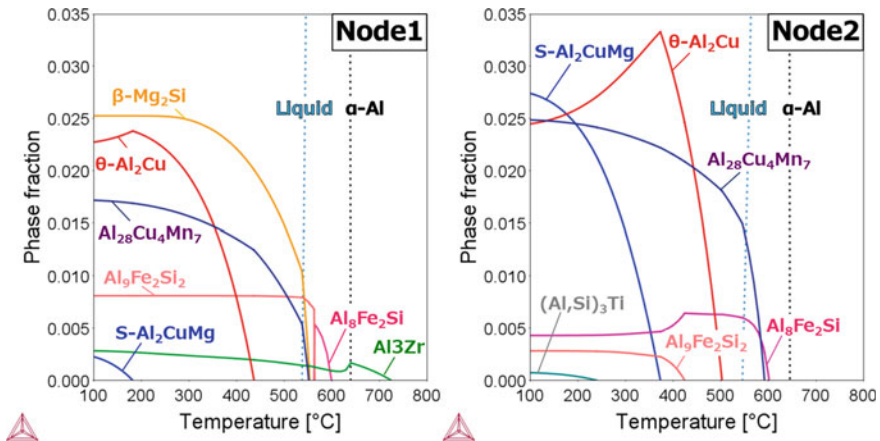


Fig. 5 Phase fraction diagrams for Node1 (left) and Node2 (right). (Color figure online)

Table 2 Range of each additive element in the dataset

Weight %	Si	Fe	Cu	Mn	Mg	Cr	Ni	Zn	Ti	Zr
Maximum	0.94	1.1	6.3	0.89	1.6	0.06	2.0	0.06	0.08	0.18
Median	0.54	0.25	4.0	0.62	0.61	0.04	0	0.05	0.03	0
Minimum	0.05	0.06	2.3	0	0	0	0	0.02	0.03	0

$$v_{ki}w_{jk}g_j = f_i - v_{ki}c_{2k} - c_{1i}. \tag{6}$$

Therefore, the optimal process condition g_j can be obtained from a set of required properties f_i by calculating the inverse matrix of X_{ij} ($\equiv v_{ki}w_{jk}$):

$$g_j = X_{ij}^{-1}(f_i - v_{ki}c_{2k} - c_{1i}), \tag{7}$$

when $\det X \neq 0$, which gives an analytical solution for the inverse problem. We could also get such solution for each sample of the Monte Carlo ensemble, which allows us to evaluate the probability of satisfying required properties.

Prediction of Three Properties

In addition to UTS and TYS, we would like to predict EB at room temperature with a linear neural network. When we predict these three properties simultaneously, the Bayes free energy $F(K)$ is minimized at $K = 3$, i.e., we have identified three structure features. Figure 6 shows that UTS and TYS are predicted with almost the same accuracy with the two properties case. The prediction accuracy for EB is lower, which is reasonable considering its larger measurement error.

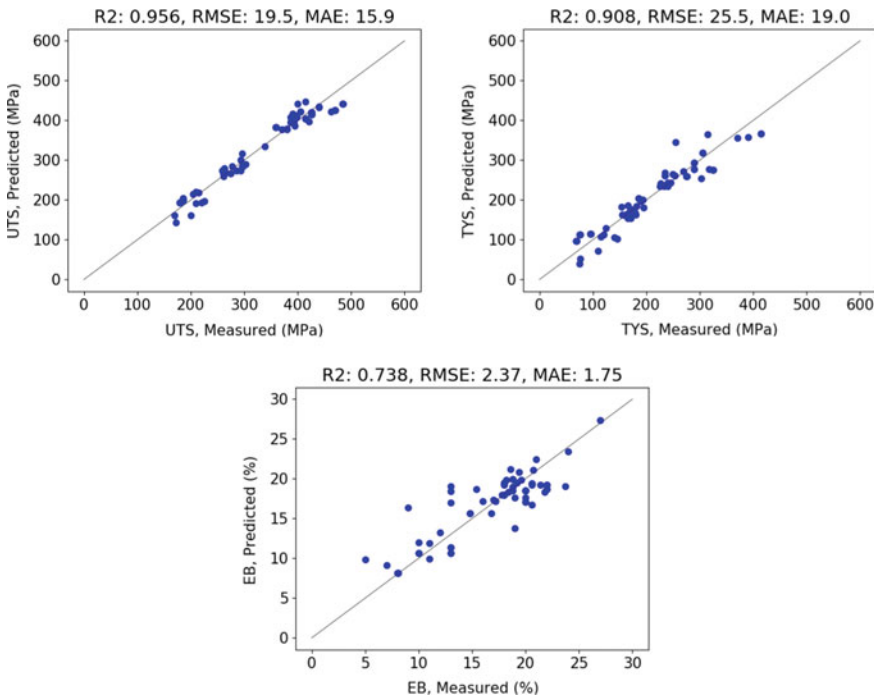


Fig. 6 Prediction of UTS (top left), TYS (top right) and EB (bottom) with a linear neural network. (Color figure online)

Discussion

In this paper, we have investigated the strengthening mechanism of the 2000 series aluminum alloy using Bayesian learning for neural networks and the thermodynamic analysis. Including more information such as time and temperature for each heating process or extrusion processing conditions is one direction to extend this analysis. Applying nonequilibrium thermal calculations such as the Langar–Schwartz model, the Kapman–Wagner (KWN) model, or the phase-field method is another direction. It is also of great interest to apply our approach to the analysis of alloys at high temperatures.

Acknowledgements This work was supported by Council for Science, Technology and Innovation(CSTI), Cross-ministerial Strategic Innovation Promotion Program (SIP), “Materials Integration for revolutionary design system of structural materials” (Funding agency:JST).

References

1. Nagata K, Watanabe S (2008) Exchange Monte Carlo sampling from Bayesian posterior for singular learning machines. *IEEE Trans Neural Netw* 19(7):1253–1266
2. Nagata K, Sumio W (2006) The exchange Monte Carlo method for Bayesian learning in singular learning machines. In: *The 2006 IEEE international joint conference on neural network proceedings*. IEEE
3. Nagata K, Sugita S, Okada M (2012) Bayesian spectral deconvolution with the exchange Monte Carlo method. *Neural Netw* 28:82–89
4. Iba Y (2001) Extended ensemble Monte Carlo. *Int J Mod Phys C* 12(05):623–656
5. MatWeb-MATERIALS PROPERTY DATA <http://www.matweb.com/index.aspx>
6. Aluminum Materials Property Database <http://metal.matdb.jp/JAA-DB/>
7. Takeda M et al (1998) The influence of Mn on precipitation behavior in Al-Cu. *Scripta Mater* 39(9)
8. Ebrahimi SHS et al (2010) The microstructure, hardness and tensile properties of a new super high strength aluminum alloy with Zr addition. *Mater Des* 31(9):4450–4456
9. Shen Z et al (2014) The structure determination of Al₂₀Cu₂Mn₃ by near atomic resolution chemical mapping. *J Alloys Comp* 601 (2014): 25–30

Solving Inverse Problems for Process-Structure Linkages Using Asynchronous Parallel Bayesian Optimization



Anh Tran and Tim Wildey

Abstract Process-structure linkage is one of the most important topics in materials science due to the fact that virtually all information related to the materials, including manufacturing processes, lies in the microstructure itself. Therefore, to learn more about the process, one must start by thoroughly examining the microstructure. This gives rise to inverse problems in the context of process-structure linkages, which attempt to identify the processes that were used to manufacturing the given microstructure. In this work, we present an inverse problem for structure-process linkages which we solve using asynchronous parallel Bayesian optimization which exploits parallel computing resources. We demonstrate the effectiveness of the method using kinetic Monte Carlo model for grain growth simulation.

Keywords Bayesian optimization · Microstructure descriptors · Process-structure · Grain growth · Kinetic Monte Carlo · ICME

Introduction

Process-structure-property linkages are the hallmarks of materials science, to which numerous efforts in experiments, theoretical models, computational simulations, and machine learning have been made to establish the relationship [8]. Since the Materials Genome Initiative [20] has been introduced to reduce the development time for new materials, machine learning has emerged as one of the most potential solutions to reduce experimental and computational efforts. Many integrated computational materials engineering (ICME) models and simulations [4, 14, 19] have been

A. Tran (✉) · T. Wildey
Optimization and Uncertainty Quantification Department, Center for Computing Research,
Sandia National Laboratories, Albuquerque, USA
e-mail: anhtran@sandia.gov

© The Minerals, Metals & Materials Society 2021
TMS 2021 150th Annual Meeting & Exhibition Supplemental Proceedings,
The Minerals, Metals & Materials Series,
https://doi.org/10.1007/978-3-030-65261-6_44

introduced and developed to simulate experiments as forward prediction computational toolboxes, the materials design should be addressed from the inverse problem perspective [1, 13, 21]. In this regard, microstructure is often bypassed, and the process-structure-property is then shortened to process-property linkage by ignoring the materials microstructure. However, it is often considered that microstructure is the great source of information, containing most, if not all, process-related information. Here, we applied our previous framework in solving inverse problem of structure-process linkages using asynchronous parallel Bayesian optimization (BO) on high-performance computing (HPC) platform. The problem statement can be succinctly described as follows. Given a microstructure and a predictive ICME model which allows simulations of the process-structure linkage, determine the process(es) and the associated processing parameters that were used to produce the given microstructure. We also assume that the manufacturing processes are parameterizable using continuous, discrete, and random variables.

Numerous studies have been conducted to optimize one or multiple materials properties, which are directly related to materials performance. Typical approaches often treat materials properties as scalar outputs, where manufacturing processes can be parameterized by either discrete or continuous variables. Recent advanced studies also include random variables to incorporate uncertainty quantification (UQ). Most commonly used methods are bio-inspired heuristic optimization methods, such as genetic algorithms, particle swarm optimization algorithms, and surrogate-based optimization methods, such as Bayesian optimization algorithms [31, 32], which is based on Gaussian process regression (GPR). In our previous work [27], we proposed asynchronous parallel BO, which is adopted to solve the grain growth problem in this paper.

While BO has been extensively used in literature, our approach [26] significantly leverages the computational effort in minimizing the wall-clock time deployment for computationally expensive simulations, by smartly submitting and retrieving results in an asynchronous manner, where the number of simulations queried is user-defined. For those with large computational resources, this framework allows one to run more simulations with different inputs and converge quicker with at least a factor of \sqrt{B} speedup, where B is the batch size. In this BO framework, the single-objective is scalarized from multiple objectives, where each objective measures the deterministic or statistical difference between the candidate and target microstructures. To measure the difference, we employ a number of microstructure descriptors, where the majority are statistical microstructure descriptors, such as grain size distribution, chord-length distribution, etc. The objective function can be regarded as the statistical metrics between two probability density functions (pdfs) of the same microstructure descriptors, applied on the target and candidate microstructures, respectively.

Methodology

In the context of process-structure-property linkages in materials science, process is usually referred to manufacturing process(es) and is often characterized by an exhaustive description to elaborate the procedure to produce a specific material, which in turns can be parameterized using continuous and discrete variables. In this regard, it is conventional to treat manufacturing process as deterministic variables, as they exhibit some sort of controllable behaviors that can use to reproduce the same materials. Structure, which is usually referred to microstructures, which is well-known to exhibit inherent randomness, for example, spatial variation on the same specimen. As such, it is conventional to characterize microstructure using an exhaustive set of microstructure descriptors to rigorously quantify the bound of these random behaviors. To this end, it is reasonable to treat microstructure descriptors as either deterministic or statistical variables.

Problem Formulation

In the asynchronous parallel BO workflow for process-structure linkage, the inputs are the parameterized processing parameters, and the output is the scalarized single-objective in solving the multi-objective optimization problem. For each proposed candidate microstructure, which is the output of the predictive ICME model coupling process-structure linkage that corresponds to the proposed input parameter, we applied the conditional microstructure descriptors on the target and candidate microstructures, respectively, to produce a set of probability density functions (pdfs) of conditional microstructure descriptors. We then use statistical functions to numerically measure the difference between two pdfs, which represents an objective in the multi-objective optimization problem. Multiple objectives can then be scalarized using the augmented Tchebycheff function. Each of the following subsections describes a key component of this BO workflow.

Materials Characterization by Microstructure Descriptors

Microstructure are inherently random, varying spatially from one location to another on the same specimen. The usage of microstructure descriptors on a sufficiently large microstructure to reduce bias is a well-known technique for computational characterization of microstructure. There are two types of microstructure descriptors: deterministic and statistical. Deterministic microstructure descriptors includes, but are not limited to, volume fraction, total surface area, number of cluster, number of grains, etc. Statistical microstructure descriptors are more commonly used

and represented in the form of probability density function, which includes, but are not limited to, equivalent radius distribution, compactness distribution, aspect ratio distribution, etc.

To compare between two microstructures quantitatively and measure how far they are away from each, one needs to impose many microstructure descriptors, including both statistical and deterministic. The microstructure descriptors must be able to distinguish one microstructure from another, quantitatively. Because of the stochastic nature of microstructure, the statistical microstructure descriptors are used more often than the deterministic ones. Suppose that there are s microstructure descriptors, denoted as $\{d_i\}_{i=1}^s$. Given a microstructure, one can collect a population of grains, and subsequently build a statistics on the grain population with a probability density function representation. For example, one can (i) compute the grain area for each grain in the microstructure, (ii) collect all the observations, and (iii) approximate the probability density function of the observational grain areas of the microstructure.

Measures of Differences Between Microstructures via Microstructure Descriptors

While both deterministic and statistical microstructure descriptors are very useful in characterize materials, they could be numerically ill-conditioned. In other words, to compare microstructures, one may impose other conditions to highlight the difference between target and candidate microstructures. If applied, such conditions would leverage the typical microstructure descriptors to the conditional microstructure descriptors, which only compare the difference between two microstructures if the condition is satisfied. For example, if the dominant grain population is very small, one may need to ignore the small grain population and compare only the larger grain population, which can be easily applied by thresholding. Such problems are fairly common in practice, such as in additive manufacturing via powder bed fusion.

If the microstructure descriptor is statistical and can be represented as a probability density function, some statistical metrics and divergences, for example, Wasserstein distance and Kullback-Leibler divergence, can be utilized to measure the difference between probability density functions. A list of statistical metrics is briefly discussed in [3, 6, 17]. We note that using statistical moments to characterize a probability density function is a poor approach due to numerically ill-conditioned of moments [10]. In particular, if the Kullback-Leibler divergence is utilized to measure the statistical difference $\mathcal{S}(\cdot)$, then the statistical difference between microstructures for a specific microstructure is computed as

$$\begin{aligned}
& S(p_D(d|\mathbf{candidateMs}), p_D(d|\mathbf{targetMs})) \\
&= \text{KL}(p_D(d|\mathbf{targetMs}) \parallel p_D(d|\mathbf{candidateMs})) \\
&= \int p_D(d|\mathbf{targetMs}) \log\left(\frac{p_D(d|\mathbf{targetMs})}{p_D(d|\mathbf{candidateMs})}\right) \partial d, \tag{1}
\end{aligned}$$

where $\text{KL}(\cdot)$ denotes the Kullback-Leibler divergence and d is the microstructure descriptor.

Objective Functions

The differences between these microstructure descriptors are then considered as the objective functions, i.e. $y_i = \mathcal{S}_i(p_{D_i}(d_i|\mathbf{targetMs}), p_{D_i}(d_i|\mathbf{candidateMs}))$, $i = 1, \dots, s$ where the goal is to minimize s objectives, $\{y_i\}_{i=1}^s$, simultaneously. It is noteworthy that these objective functions are typically noisy due to the fact that the microstructure considered is within finite domain, thus bias can be reduced but cannot be eliminated. As a result, one can regard that our framework [27] formulates the inverse problems in structure-property as a multi-objective optimization problem, where BO is used.

Asynchronous Parallel Bayesian Optimization Framework

In our previous work, we have extended the traditional Bayesian optimization framework into synchronously batch-sequential parallel Bayesian optimization [28] for constrained optimization problems, called pBO-2GP-3B, where the constraints are generalized to cover a broad spectrum of applications by considering both known and unknown constraints. We deployed a further improved implementation of pBO-2GP-3B, called aphBO-2GP-3B [26], to asynchronously parallelize on the high-performance computing environment with multiple acquisition functions considered. A brief description of BO is provided in the remainder of this section. Interested readers are further referred to our BO previous work [25, 29, 30].

Assume that f is a function of \mathbf{x} , where $\mathbf{x} \in \mathcal{X}$ is a d -dimensional input, and y is the observation. Let the dataset $\mathcal{D} = (\mathbf{x}_i, y_i)_{i=1}^n$, where n is the number of observations. A GP regression assumes that $\mathbf{f} = f_{1:n}$ is jointly Gaussian, and the observation y is normally distributed given f ,

$$f|\mathbf{X} \sim \mathcal{N}(\mathbf{m}, \mathbf{K}), \quad y|\mathbf{f}, \sigma^2 \sim \mathcal{N}(f, \sigma^2 \mathbf{I}), \tag{2}$$

where $m_i := \mu(\mathbf{x}_i)$ and $K_{i,j} := k(\mathbf{x}_i, \mathbf{x}_j)$. The covariance kernel \mathbf{K} is a choice of modeling covariance between inputs. At an unknown sampling location \mathbf{x} , the pre-

dicted response is described by a posterior Gaussian distribution, where the posterior mean is

$$\mu_n(\mathbf{x}) = \mu_0(\mathbf{x}) + \mathbf{k}(\mathbf{x})^T (\mathbf{K} + \sigma^2 \mathbf{I})^{-1} (\mathbf{y} - \mathbf{m}), \quad (3)$$

and the posterior variance is

$$\sigma_n^2 = k(\mathbf{x}, \mathbf{x}) - \mathbf{k}(\mathbf{x})^T (\mathbf{K} + \sigma^2 \mathbf{I})^{-1} \mathbf{k}(\mathbf{x}), \quad (4)$$

where $k(\mathbf{x})$ is the covariance vector between the query point \mathbf{x} and $\mathbf{x}_{1:n}$. The classical GP formulation assumes stationary covariance matrix, which only depends on the distance $r = \|\mathbf{x} - \mathbf{x}'\|$. While numerous kernels have been used in the literature, we focus on squared exponential kernel in this work. Optimizing the log-likelihood function yields the hyper-parameter θ at the computational cost of $\mathcal{O}(n^3)$ due to the cost to compute the inverse of the covariance matrix.

The acquisition function for probability of improvement (PI) [9] is defined as

$$a_{\text{PI}}(\mathbf{x}; \{\mathbf{x}_i, y_i\}_{i=1}^N, \theta) = \Phi(\gamma(\mathbf{x})), \quad (5)$$

where $\gamma(\mathbf{x})$ indicates the deviation away from the best sample. The acquisition function for expected improvement (EI) scheme [2, 11, 12, 22] is defined as

$$a_{\text{EI}}(\mathbf{x}; \{\mathbf{x}_i, y_i\}_{i=1}^N, \theta) = \sigma(\mathbf{x}; \{\mathbf{x}_i, y_i\}_{i=1}^N, \theta) \cdot (\gamma(\mathbf{x})\Phi(\gamma(\mathbf{x})) + \phi(\gamma(\mathbf{x}))) \quad (6)$$

The acquisition function for the upper-confidence bounds (UCB) scheme [23, 24] is defined as

$$a_{\text{UCB}}(\mathbf{x}; \{\mathbf{x}_i, y_i\}_{i=1}^N, \theta) = \mu(\mathbf{x}; \{\mathbf{x}_i, y_i\}_{i=1}^N, \theta) + \kappa \sigma(\mathbf{x}; \{\mathbf{x}_i, y_i\}_{i=1}^N, \theta), \quad (7)$$

where κ is a hyper-parameter describing the acquisition exploitation-exploration balance.

Multi-objective optimization problems are typically solved by converting a multi-objective problem to a single-objective problem, where the single objective is a weighted sum of multiple objectives [18]. While there is no restriction on the optimization method that can be used to minimize the difference between the candidate and the target microstructures, in this work, we use the aphBO-2GP-3B BO framework, which is an asynchronously parallel constrained multi-acquisition BO algorithm to further improve its efficiency on HPC platforms. The aphBO-2GP-3B subdivides the computational budget into three batches, supported by two GPRs. One GPR is used to model the objective function, whereas another GPR is used as a probabilistic binary classifier for hidden constraints. The first batch focuses on optimizing the objective functions by sampling at the locations where the acquisition function value of the Bayesian optimization is maximized. The second batch focuses on the exploration, by sampling at the locations where the posterior variance is maximized. The third batch focuses on the feasibility classification to learn hidden

constraints from the optimization problem. The acquisition function is sampled with probabilities exponentially scaled with rewards, in the same manner with GP-Hedge algorithm [7].

Case Study: Kinetic Monte Carlo Simulation

In this section, we demonstrate the applicability of asynchronous parallel BO in solving the inverse problem in process-structure linkages using kinetic Monte Carlo with numerical temperatures. Similar to the second case studies in our previous work [27], in this example, we set a different numerical temperature with $k_B T_s = 0.85$.

Kinetic Monte Carlo Simulation

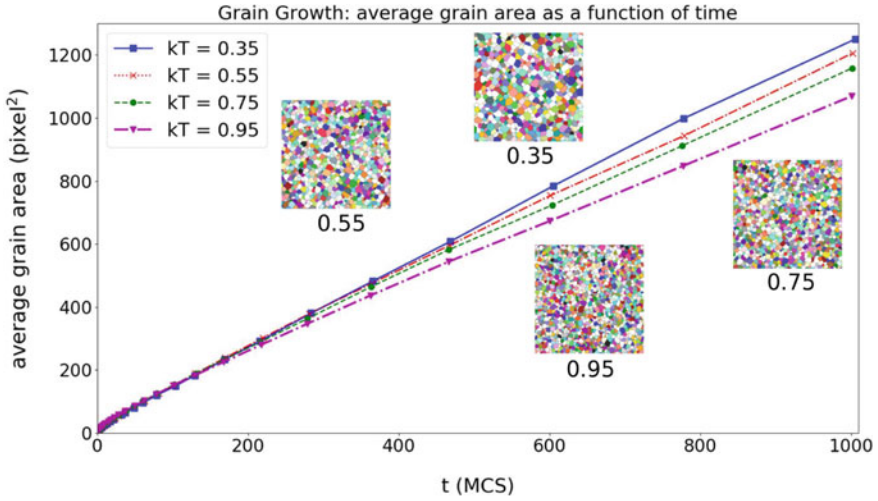
The details of temperature-dependent kMC simulation for grain growth and its implementation in Sandia/SPPARKS [15, 16] is described in Garcia et al. [5], and is summarized here for the sake of completeness. In the grain growth simulation, the Potts model [33] is used to simulate curvature-driven grain growth. The Arrhenius equation describes the relationship between grain boundary mobility and temperature and the Metropolis algorithm is used to determine the probability of successful change in grain site orientation as

$$P = \begin{cases} \exp\left(\frac{-\Delta E}{k_B T_s}\right), & \text{if } \Delta E > 0, \\ 1, & \text{if } \Delta E \leq 0, \end{cases} \quad (8)$$

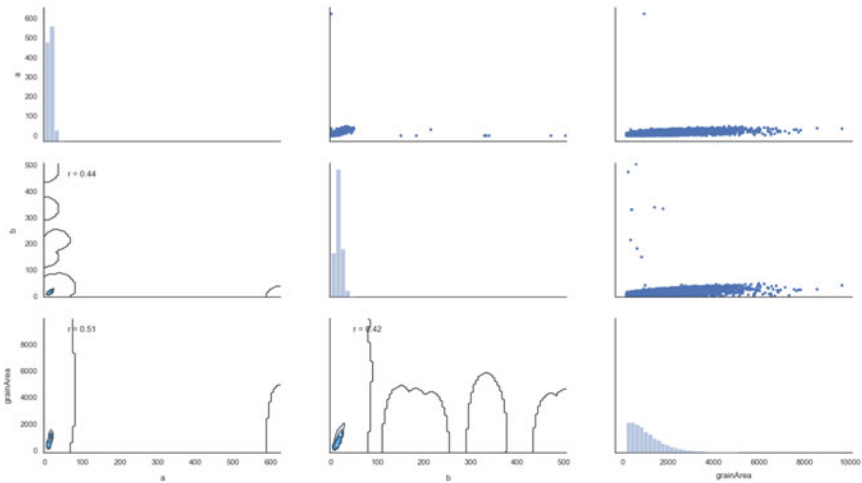
where E is the total grain boundary energy calculated by summing all the neighbor interaction energies, ΔE can be regarded as the activation, and T_s is the simulation temperature.

Statistical Microstructure Descriptors As Outputs

Figure 1a shows the effect of $k_B T_s$ on different grain growth microstructure. In particular, larger $k_B T_s$ is associated with microstructures with smaller grain size for (nearly) the same amount of time. This suggests that the grain size distribution may be a good microstructure descriptor to describe and distinguish one microstructure from another.



(a) Effects of the numerical temperature $k_B T_s$ in the kMC grain growth problem. Reprinted with permission from [27].



(b) Pair plot between microstructure descriptors: major dimensions of best-fit ellipse, minor dimensions of best-fit ellipse, and grain area.

Fig. 1 Grain growth and its dependence on temperature (a). Statistical microstructure descriptors and their pairwise correlations (b). (Color figure online)

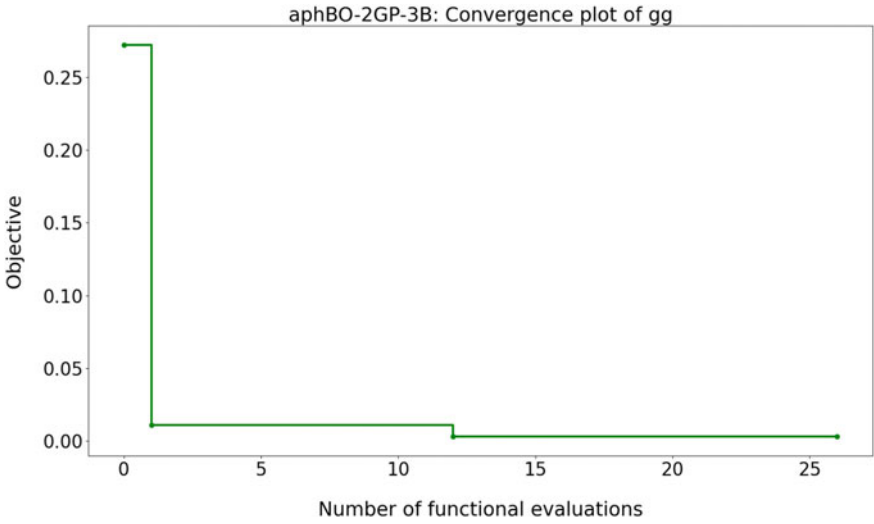
In this case study, the distribution of grain area is used as the microstructure descriptor, where the Kullback-Leibler divergence measuring the difference between candidate and target microstructures is used as an output, where $k_B T_s$ is the numerical input describing simulation temperature. Because the number of grains are fairly small (few thousands), no filter is imposed on the statistical microstructure descriptors. In the target microstructure, $k_B T_s$ is set as 0.70, where the range of candidate microstructures is [0.25, 0.95]. The size of the simulation domain is 1024×1024 , which takes about 300 s with 18 processors (≈ 1.5 CPU hours).

Numerical Results

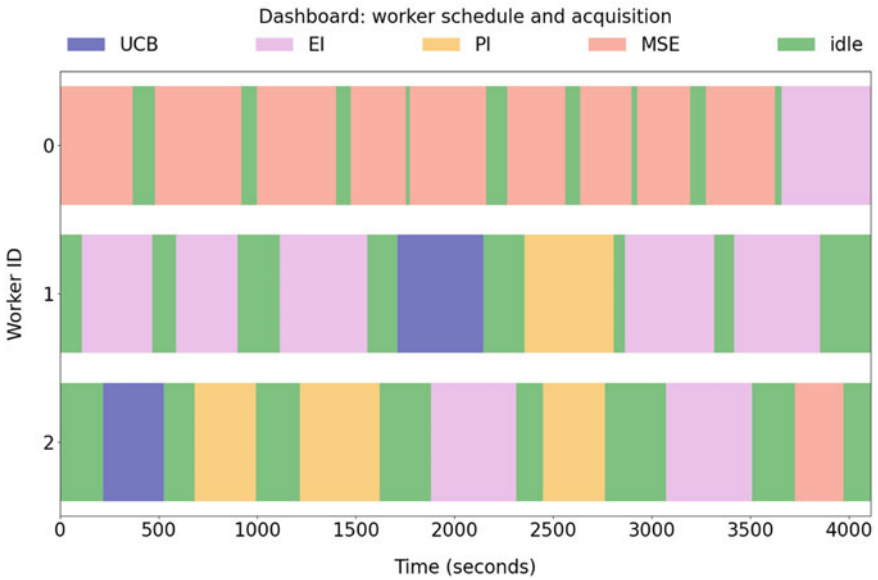
In this example, $k_B T_s$ is set at 0.85. A computational domain of $1024 \text{ pixel} \times 1024 \text{ pixel}$ is used to set up the numerical experiment. For consistency, all calculations are performed on Sandia's *Blake* cluster consisting of dual-socket Intel(R) Xeon(R) (Platinum) 8160 CPU with 24 cores per node. The upper and lower bounds of objectives for three optimization runs are plotted as blue envelope in Fig. 2a. Two sampling points at $k_B T_s \in \{0.25, 0.95\}$ are initialized. Here, one iteration corresponds to a single kMC simulation with different parameters. The single-objective y starts at 0.27194599 for iteration 0, 0.01099406 for iteration 1, and 0.00322190 for iteration 12. The optimal input parameter $k_B T_s$ is 0.85720249, which agrees very well with the target input parameter $k_B T_s$ of 0.85. Fig. 2b presents the state of specific workers, i.e. whether they are idle (green) or busy (blue, pink, yellow, or orange), which we refer to as the schedule. Furthermore, one can see what acquisition is being queried at specific time with the schedule. The optimization run ends when workers finish their last job.

Conclusions

In this paper, we applied our previous framework [27] to solve the inverse problem in process-structure linkages, where microstructure descriptors are used to characterize the microstructure on-the-fly. Statistical divergence, i.e. Kullback-Leibler divergence is then applied to measure the differences between candidate and target microstructure, respectively. To that end, an asynchronous parallel BO framework is applied to minimize their numerical differences. We demonstrate its application using kinetic Monte Carlo examples, where the numerical temperature is successfully recovered for our case study.



(a) Convergence plot of the microstructure calibration framework in kMC/grain growth problem.



(b) Scheduler for asynchronous parallel Bayesian optimization.

Fig. 2 Convergence plot (a) and scheduler (b) for the asynchronous parallel aphBO-2GP-3B [26] framework. (Color figure online)

Acknowledgements The views expressed in the article do not necessarily represent the views of the U.S. Department of Energy or the United States Government. Sandia National Laboratories is a multimission laboratory managed and operated by National Technology and Engineering Solutions of Sandia, LLC., a wholly owned subsidiary of Honeywell International, Inc., for the U.S. Department of Energy's National Nuclear Security Administration under contract DE-NA-0003525. This research was supported by the U.S. Department of Energy, Office of Science, Early Career Research Program.

References

1. Arróyave R, McDowell DL (2019) Systems approaches to materials design: past, present, and future. *Ann Rev Mater Res* 49(1):103–126
2. Bull AD (2011) Convergence rates of efficient global optimization algorithms. *J Mach Learn Res* 12(Oct):2879–2904
3. Cha SH (2007) Comprehensive survey on distance/similarity measures between probability density functions. *City* 1(2):1
4. Chaparro B, Thuillier S, Menezes L, Manach PY, Fernandes J (2008) Material parameters identification: gradient-based, genetic and hybrid optimization algorithms. *Comput Mater Sci* 44(2):339–346
5. Garcia AL, Tikare V, Holm EA (2008) Three-dimensional simulation of grain growth in a thermal gradient with non-uniform grain boundary mobility. *Scr Mater* 59(6):661–664
6. Gibbs AL, Su FE (2002) On choosing and bounding probability metrics. *Int Stat Rev* 70(3):419–435
7. Hoffman M, Brochu E, de Freitas N (2011) Portfolio allocation for bayesian optimization. In: *Proceedings of the twenty-seventh conference on uncertainty in artificial intelligence, UAI'11*. AUAI Press, Arlington, Virginia, USA, pp 327–336
8. Kalidindi SR, Medford AJ, McDowell DL (2016) Vision for data and informatics in the future materials innovation ecosystem. *JOM* 68(8):2126–2137
9. Kushner HJ (1964) A new method of locating the maximum point of an arbitrary multipeak curve in the presence of noise. *J Basic Eng* 86(1):97–106
10. Mnatsakanov RM (2008) Hausdorff moment problem: reconstruction of probability density functions. *Stat Prob Lett* 78(13):1869–1877
11. Mockus J (1975) On Bayesian methods for seeking the extremum. In: *Optimization techniques IFIP technical conference*. Springer, pp 400–404
12. Mockus J (1982) The Bayesian approach to global optimization. *Syst Model Optim* 473–481
13. Olson G (2013) Genomic materials design: the ferrous frontier. *Acta Mater* 61(3):771–781
14. Ong SP (2019) Accelerating materials science with high-throughput computations and machine learning. *Comput Mater Sci* 161:143–150
15. Plimpton S, Battaile C, Chandross M, Holm L, Thompson A, Tikare V, Wagner G, Webb E, Zhou X, Cardona CG et al (2009) Crossing the mesoscale no-man's land via parallel kinetic Monte Carlo. Sandia report SAND2009-6226
16. Plimpton S, Thompson A, Slepoy A (2012) SPPARKS kinetic monte carlo simulator
17. Rachev ST, Klebanov LB, Stoyanov SV, Fabozzi FJ (2013) Probability distances and probability metrics: definitions. In: *The methods of distances in the theory of probability and statistics*. Springer, pp 11–31
18. Rojas-Gonzalez S, Van Nieuwenhuysse I (2019) A survey on kriging-based infill algorithms for multi-objective simulation optimization. FEB research report KBI_1907
19. Salzbrenner BC, Rodelas JM, Madison JD, Jared BH, Swiler LP, Shen YL, Boyce BL (2017) High-throughput stochastic tensile performance of additively manufactured stainless steel. *J Mater Process Technol* 241:1–12

20. National Science and Technology Council (US) (2011) Materials genome initiative for global competitiveness. Executive Office of the President, National Science and Technology Council
21. Sinnott SB (2013) Material design and discovery with computational materials science. *J Vac Sci Technol A Vac Surf Films* 31(5):050812
22. Snoek J, Larochelle H, Adams RP (2012) Practical Bayesian optimization of machine learning algorithms. In: *Advances in neural information processing systems*, pp 2951–2959
23. Srinivas N, Krause A, Kakade SM, Seeger M (2009) Gaussian process optimization in the bandit setting: no regret and experimental design. arXiv preprint [arXiv:0912.3995](https://arxiv.org/abs/0912.3995)
24. Srinivas N, Krause A, Kakade SM, Seeger MW (2012) Information-theoretic regret bounds for Gaussian process optimization in the bandit setting. *IEEE Trans Inf Theory* 58(5):3250–3265
25. Tran A, Eldred M, Wang Y, McCann S (2020) SrMO-BO-3GP: a sequential regularized multi-objective constrained Bayesian optimization for design applications. In: *Proceedings of the ASME 2020 IDETC/CIE, international design engineering technical conferences and computers and information in engineering conference, vol 1. 40th computers and information in engineering conference*. American Society of Mechanical Engineers
26. Tran A, McCann S, Furlan JM, Pagalthivarathi KV, Visintainer RJ, Wildey T, Eldred M (2020) AphBO-2GP-3B: a budgeted asynchronous-parallel multi-acquisition for known/unknown constrained Bayesian optimization on high-performing computing architecture. arXiv preprint [arXiv:2003.09436](https://arxiv.org/abs/2003.09436)
27. Tran A, Mitchell JA, Swiler LP, Wildey T (2020) An active-learning high-throughput microstructure calibration framework for process-structure linkage in materials informatics. *Acta Mater* 194:80–92
28. Tran A, Sun J, Furlan JM, Pagalthivarathi KV, Visintainer RJ, Wang Y (2019) pBO-2GP-3B: A batch parallel known/unknown constrained Bayesian optimization with feasibility classification and its applications in computational fluid dynamics. *Comput Methods Appl Mech Eng* 347:827–852
29. Tran A, Tran M, Wang Y (2019) Constrained mixed-integer Gaussian mixture Bayesian optimization and its applications in designing fractal and auxetic metamaterials. *Struct Multi Opt* 1–24
30. Tran A, Tranchida J, Wildey T, Thompson AP (2020) Multi-fidelity machine-learning with uncertainty quantification and Bayesian optimization for materials design: application to ternary random alloys. *J Chem Phys* 153:074705
31. Tran A, Wildey T, McCann S (2019) SBF-BO-2CoGP: a sequential bi-fidelity constrained Bayesian optimization for design applications. In: *Proceedings of the ASME 2019 IDETC/CIE, international design engineering technical conferences and computers and information in engineering conference, vol 1. 39th computers and information in engineering conference*. American Society of Mechanical Engineers. V001T02A073
32. Tran A, Wildey T, McCann S (2020) SMF-BO-2CoGP: a sequential multi-fidelity constrained Bayesian optimization for design applications. *J Comput Inf Sci Eng* 20(3):1–15
33. Wu FY (1982) The Potts model. *Rev Mod Phys* 54(1):235

Part XVIII
Algorithm Development in Materials
Science and Engineering

2D Microstructure Reconstruction for SEM via Non-local Patch-Based Image Inpainting



Anh Tran and Hoang Tran

Abstract Microstructure reconstruction is a long-standing problem in experimental and computational materials science, for which numerous attempts have been made to solve. However, the majority of approaches often treats microstructure as discrete phases, which, in turn, reduces the quality of the resulting microstructures and limits its usage to the computational level of fidelity, but not the experimental level of fidelity. In this work, we applied our previously proposed approach [41] to generate synthetic microstructure images at the experimental level of fidelity for the UltraHigh Carbon Steel DataBase (UHCSDB) [13].

Keywords Microstructure reconstruction · SEM · Micrograph · Image processing · Image inpainting

Introduction

Microstructures are a crucial link between process and property, encoding nearly all information related to the processes used to manufacture the specimen. However, microstructures are naturally complicated to study due to its spatial stochasticity, which varies from one location to another, within certain bounds, usually referred to as aleatory uncertainty. This, in turn, leads to the concept of statistically equivalent microstructure, where the microstructure features are either deterministically or statistically measurable by microstructure descriptors, which are the key enablers for microstructure reconstruction and generation problems. While most of microstruc-

A. Tran (✉)

Optimization and Uncertainty Quantification Department, Center for Computing Research,
Sandia National Laboratories, Albuquerque, NM, USA
e-mail: anhtran@sandia.gov

H. Tran

Computer Science and Mathematics Division, Oak Ridge National Laboratory,
Oak Ridge, TN, USA
e-mail: tranha@ornl.gov

ture reconstruction and microstructure generation problems are already very well solved in the context of computational materials science, only a few attempts to generate and reconstruct microstructures that are equivalent to experimental level, such as images obtained from using scanning electron microscope, have been made.

Microstructure reconstruction and generation at the experimental level have high fidelity, because images are represented in either RGB or grayscale. It is fairly straightforward to threshold a RGB or grayscale image to produce a computational microstructure, which is a usual representation of phase-based microstructures for integrated computational materials engineering (ICME) workflow. However, it is nearly impossible to perform an inverse threshold to convert a binary or any phase-based microstructure back to a RGB or grayscale image, which is often a product of scanning electron microscope (SEM) or transmission electron microscope (TEM). The problem of microstructure reconstruction and microstructure generation at the level of experiment is mainly unsolved. However, its importance is found due to the scarcity of experimental materials data, which is well known to be resource-intensive, i.e. human labor, time and money [2].

There are mainly two approaches for this problem: the first one is based on machine learning (ML)/deep learning (DL) techniques, whereas the second one is based on conventional image processing techniques, which does not employ DL. While DL has been touted as a revolutionary technique to solve many problems, the lack of data repositories for experimental microstructures poses a significant challenge towards the adoption and application of DL in materials science in general. Notably, convolutional neural networks (CNN), including generative adversarial network (GAN) [19], are among popular choices for DL.

For example, Bostanabad [5] adopted VGG19 [34] to reconstruct 3D microstructure from 2D images using transfer learning. Iyer et al. [23] employed an auxiliary classifier Wasserstein GAN with gradient penalty to generate microstructure from UHCSDB, which is the same dataset considered in this work. Singh et al. [35] used Wasserstein GAN to generate and reconstruct microstructure with binary phases. DeCost et al. [12] applied VGG16 and t-SNE [48, 49] to visualize microstructure on their latent manifold space. DeCost et al. [14] applied a pre-trained VGG16 [34] for deep semantic segmentation in the same UHCSDB dataset. Ling et al. [28] also used VGG16 to extract features for SEM images between different datasets in the hope of generalization and interpretation. Li et al. [27] employed an auto-encoder (AE) approach to generate microstructures. Chun et al. [11] employed GAN to generate microstructures and showed that GAN is able to generate better quality images compared to AE, which is a well-known problem in computer vision. Mosser et al. [30] proposed a GAN to generate microstructure. Cang et al. [7, 8] employed deep belief network in reconstructing binary microstructure. Bostanabad et al. [6] proposed a tree-based ML technique for 2D stochastic microstructure reconstruction based on classification trees.

Zichenko [54] proposed an isotropic algorithm for random close packing of equi-sized spheres with periodic boundary conditions. Groeber et al. [20–22] proposed an automatic statistical framework to characterize [20] and to create statistically equivalent synthetic microstructures [21]. Fullwood et al. [17, 18] proposed a phase recovery

algorithm based on two-point correlation statistics to reconstruct the microstructure. Latief et al. [24] suggested a stochastic geometrical modeling approach to generate a μ -CT images of Fontainebleau sandstone. Staraselski et al. [36] demonstrated the application of two-point correlation function in constructing 3D representative volume element. Feng et al. [16] proposed a stochastic microstructure reconstruction for two-phase composite materials based on nonlinear transformation of Gaussian random fields that matches the marginal probability distribution function and the two-point correlation function. Chen et al. [9] employed simulated annealing method to reconstruct 3D multiphase microstructure and demonstrated with 2D and 3D reconstruction with three-phase sandstone. Xu et al. [52, 53] proposed a descriptor-based methodology using multiple microstructure descriptors as evaluation criteria to reconstruct 3D microstructure. Chen et al. [10] proposed a multiscale computational scheme to stochastically reconstruct the 3D heterogeneous polycrystalline microstructure from a single 2D electron backscattered diffraction (EBSD) micrograph. Li et al. [25, 26] conducted a comparison study on the effects of multiple objectives in the microstructure reconstruction problem.

In this paper, we adopt our previous approach [41], which is extended based on Newson et al. [32], using non-local patch-based image inpainting to produce texturally coherent microstructures and demonstrate its usage on UHCSDB [13]. The remaining of the paper is organized as follows. Section 45.2 presents the image inpainting methodology that is extensively used as a basic tool in this work. Section 45.3 presents the numerical demonstration on the publicly available UHCSDB dataset [13]. Section 45.4 discusses and concludes the paper.

Image Inpainting

The algorithm for image inpainting is described in details from our previous work [41], where we augment the algorithm from Newson et al. [32] for solving microstructure inpainting problems. For the sake of completeness, we briefly summarize the algorithm here. This line of research has been gradually developed and improved over years [15, 31, 32], where the PatchMatch algorithm [3] was employed to accelerate the nearest neighbor search. Figure 1 shows a schematic of the image inpainting problem, where image patches are denoted as gray squares, \mathcal{H} is the occluded region to be inpainted, and \mathcal{D} is the unoccluded region.

In patch-based inpainting approach, we fill in the missing region patch-by-patch by looking for well-matching replacement patches in the unoccluded part of the image and copying them to corresponding locations. In other words, let u be the image content and W_p be the image patch at position p , we find the map ϕ that locates its nearest neighbor $W_{p+\phi(p)}$, i.e. image patch in \mathcal{D} that is most similar to W_p . We need to do this for every position p in \mathcal{H} , therefore, the image reconstruction problem involves minimizing

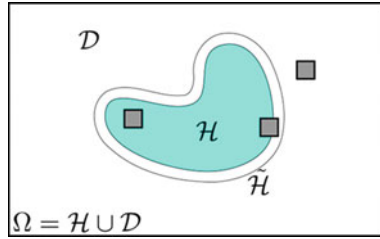


Fig. 1 Schematic of image inpainting problem, where the patches can be unoccluded, partially or completely occluded. Reprinted with permission from [41]. (Color figure online)

$$E(u, \phi) = \sum_{p \in \mathcal{H}} d^2(W_p, W_{p+\phi(p)}). \quad (1)$$

Here, d is a distance function formalizing the similarity between patches, [29, 37]. Unfortunately, (1) is a nonconvex, NP-hard optimization problem. To overcome this challenge, we adopt an iterated alternating approach. Specifically, we break the minimization of (1) into two separate minimization problems with respect to the shift map ϕ and the image content u , which are solved alternatively in iterations (see Algorithm 1). These two problems correspond to a nearest neighbor search and an image reconstruction process accordingly.

Algorithm 1 Minimization of $E(u, \phi)$ via iterated alternating approach. Reprinted with permission from [41].

Input: Initial guess u_0 and tolerance $\tau > 0$

Output: Inpainted image u_{k+1}

```

1: repeat
2:    $\phi_k \leftarrow \arg \min_{\phi} E(u^k, \phi)$  // Nearest neighbor search
3:    $u_{k+1} \leftarrow \arg \min_u E(u, \phi^k)$  // Image reconstruction
4:    $k \leftarrow k + 1$ 
5: until  $\|u_{k+1} - u_k\| < \tau$ 

```

For the **nearest neighbor search**, as in [32], only approximate, instead of exact, nearest neighbors (NN) are computed, due to the demanding cost of the later one. We use PatchMatch algorithm by Barnes et al. [3] for this goal. The process is initialized by randomly assigning each occluded pixel a candidate nearest neighbor in the unoccluded region. Then, for each iteration, each pixel is visited in lexicography order (on even iterations) and in inverse lexicography order (on odd iterations). At each pixel, we perform two operations for improving the shift map ϕ . First, we check the nearest neighbors of the adjacent pixels for better candidate nearest neighbor of the current pixel; and second, we look for better nearest neighbor at random in an increasingly small window around the current nearest neighbor. For more details, the readers are referred to the seminal work on PatchMatch algorithm

[3]. The PatchMatch pseudo-code for minimization with respect to ϕ is given in algorithm 2 and can also be found in [3, 15, 41].

For the **image reconstruction**, we reconstruct each pixel in the occluded area using a weighted mean scheme, initially proposed by Wexler et al. [51]. In particular, given fixed shift map ϕ , the pixel at position $p \in \mathcal{H}$ is assigned the color value

$$u(p) = \frac{\sum_{q \in \mathcal{N}_p} s_q^p u(p + \phi(q))}{\sum_{q \in \mathcal{N}_p} s_q^p}, \quad \forall p \in \mathcal{H}, \quad (2)$$

where \mathcal{N}_p is the patch neighborhood of p and the weight s_q^p is indicated by the ANN of W_q , $s_q^p = \exp(-d^2(W_q, W_{q+\phi(q)})/(2\sigma^2))$.

Finally, since microstructure images often have structures of different sizes, ranging from large objects to fine scale textures and details, our microstructure reconstruction problem is inherently multiscale. We finish the patch-based inpainting with a **multiscale scheme**, [1, 15, 32, 51]. Here, we sequentially apply the inpainting scheme on an image pyramid, starting at the coarsest scale. The result at each scale is upsampled and used as initialization for the next finer scale. We adopt the algorithm of Newson et al. [32], which upsamples the shift map rather than the image content and tunes the pyramid level according to the patch size and the occlusion size. For more details, we refer the interested reader to [32, 41].

Applications on UHCSDB Database

In this section, we demonstrate the application of our aforementioned method to the UHCSDB [13]. Scikit-image Python package [50] is used to create a series of occlusion images, in concert with the inpainting implementation from Newson et al. [32] to solve the original image inpainting. We note that the current implementation is limited to execute sequentially on one processor, thus hindering the possibility of parallelism on high-performance computing platforms. The patch size parameter is also noted to have a strong effect on the computational time; that is, larger patch is associated with longer computational time. The culprit of the patch size parameter is described in lines 12, 15 and 16 in algorithm 2, mainly due to the computation of patch distance, $d(\cdot, \cdot)$, which compares the values of pixels to pixels. Because the patch area scales as the square of the patch size parameter, the computational cost grows at least quadratically, which suggests a trade-off between efficiency and effectiveness in using inpainting method. To pre-process UHCSDB, original micrographs are cropped to eliminate the annotations, legends, as well as other metadata information, while retaining only the pure images. After cropping, the dimension of each micrograph is 484 pixel \times 645 pixel. The dimension is consistent across the whole dataset after the pre-process.

To rigorously quantify the effectiveness of the inpainting algorithm, the occluded regions \mathcal{H} are randomly created with as an ellipse with random major and minor

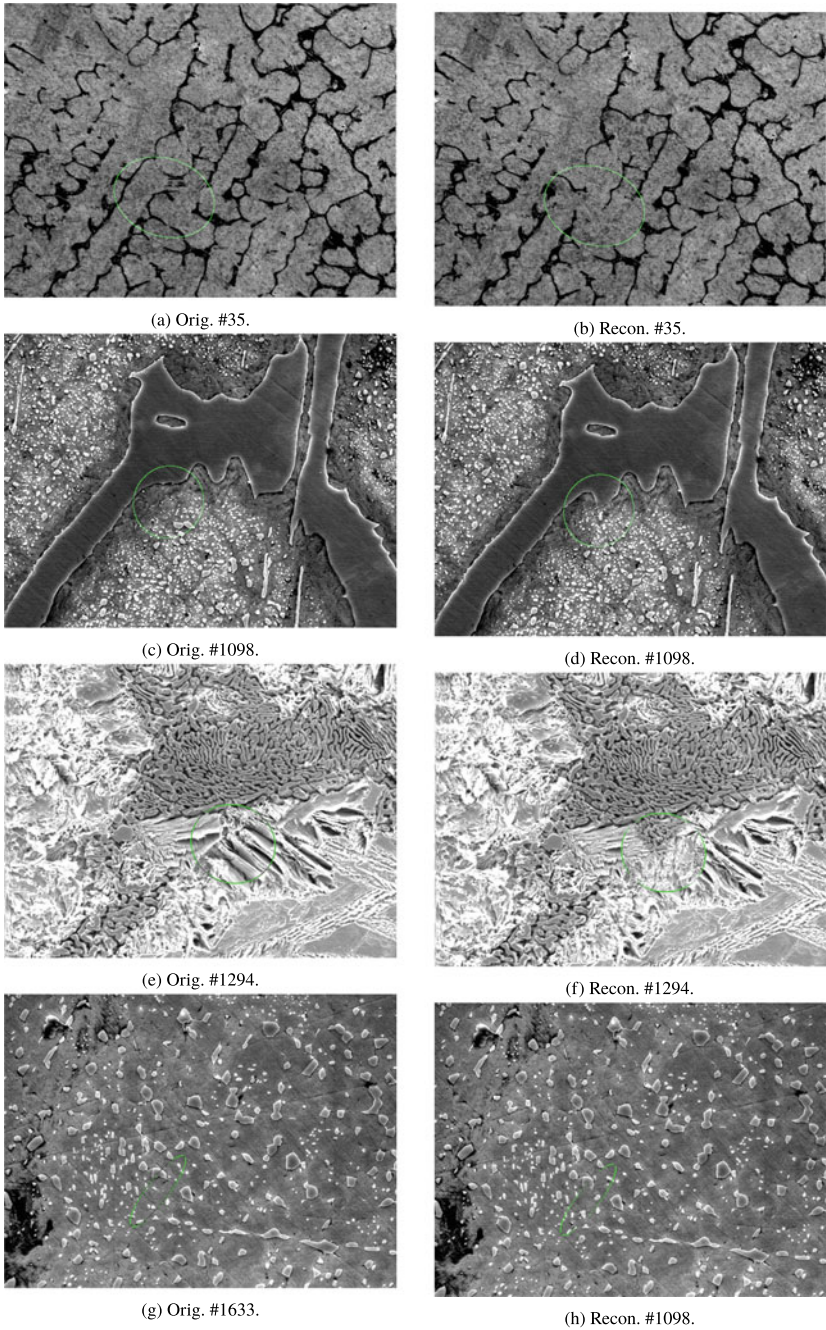


Fig. 2 Image inpainting for microstructure reconstruction. The difference is the region highlighted by the green border. Patch size of 7 pixel is used in this figure

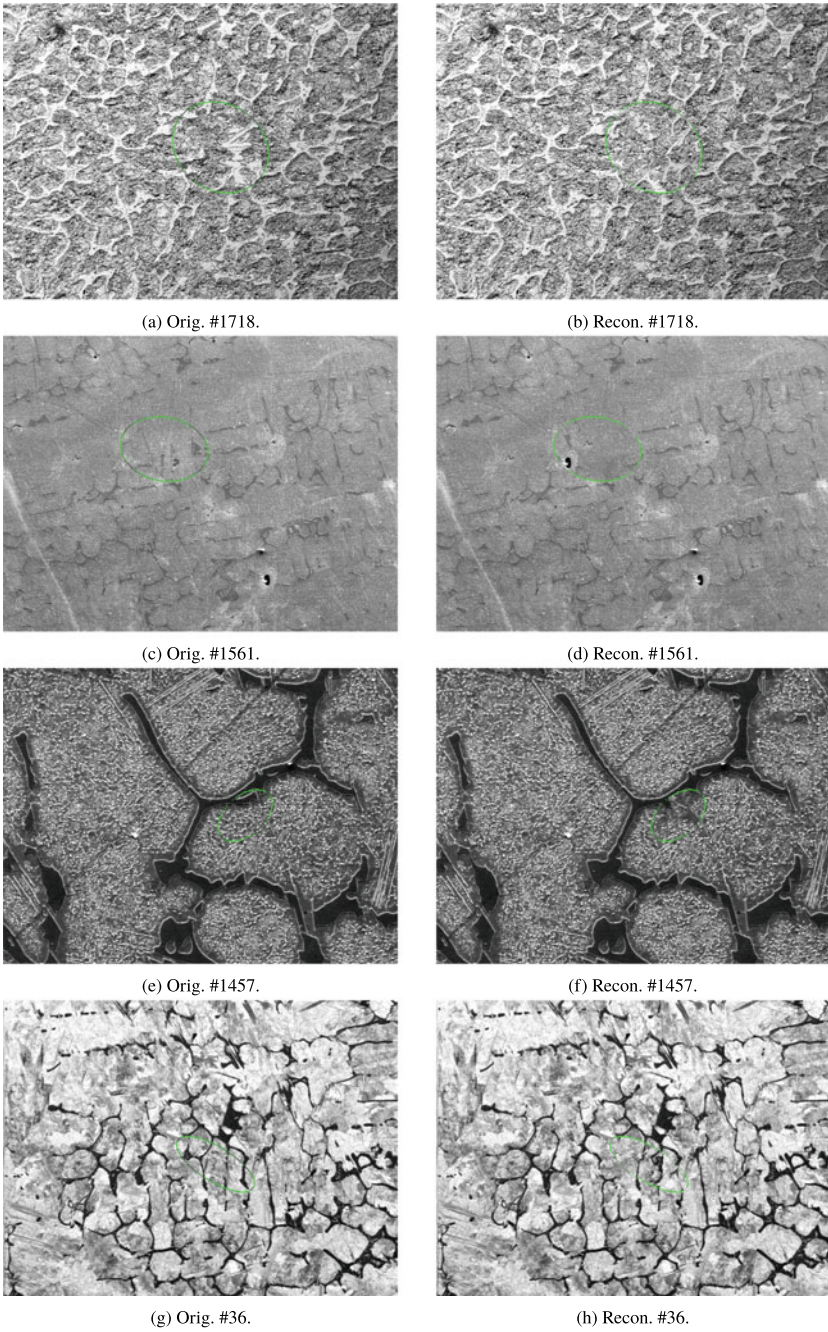


Fig. 3 Image inpainting for microstructure reconstruction. The difference is the region highlighted by the green border. Patch size of 3 pixel is used in this figure

dimensions, as well as orientation, which are shown as green ellipses. Figure 2 shows the comparison between original (left column) and reconstructed (right column) microstructures, respectively, for microstructures #35, #1098, #1294 and #1633. Figure 3 shows the comparison between original (left column) and reconstructed (right column) microstructures, respectively, for microstructures #1718, #1561, #1457 and #36. The texture in reconstructed microstructure is continuous between the occluded \mathcal{D} and unoccluded regions \mathcal{H} . The difference within the occluded regions between original and reconstructed microstructures is obvious when comparison is shown. Without the comparison, it is visually indistinguishable and difficult to classify if the microstructures are indeed real or fake, even for human experts. This highlights the impact of our inpainting algorithm to generate synthetic microstructures. Besides GAN, which is known to generate high-quality synthetic microstructure, our method provides an alternative option, without resorting to DL techniques.

Algorithm 2 Approximate nearest neighbor (ANN) search using PatchMatch [3, 15]. Reprinted with permission from [41].

Input: Current image u , occlusion \mathcal{H} , number of iteration J

Output: Shift map ϕ

```

1:  $\phi \leftarrow$  randomly initialize the shift map
2:  $(p_n), n = 1, \dots, |\mathcal{H}| \leftarrow$  lexicography ordering of the pixels in  $\mathcal{H}$ 
3: for  $j = 1, \dots, J$  do
4:   for  $n = 1, \dots, |\mathcal{H}|$  do
5:     if  $j$  is even then
6:        $p \leftarrow p_n$  // visit the occluded pixels by lexicography order
7:        $a \leftarrow p - (0, 1), b \leftarrow p - (1, 0)$  // check adjacent (up and left)
         pixels
8:     else
9:        $p \leftarrow p_{|\mathcal{H}|-n+1}$  // visit the occluded pixels by inverse order
10:       $a \leftarrow p + (0, 1), b \leftarrow p + (1, 0)$  // check down and right pixels
11:     end if
12:      $q \leftarrow \arg \min_{r \in \{p, a, b\}} d(W_p, W_{p+\phi(r)})$  // update candidate for NNs of
         current pixel
13:      $\phi(p) \leftarrow \phi(q)$ 
14:     // Random search for better NNs around the current one
15:      $\mathbb{S} \leftarrow$  Generate set of random 2D vectors around  $\phi(p)$ 
16:      $t \leftarrow \arg \min_{r \in \mathbb{S} \cup \{\phi(p)\}} d(W_p, W_{p+r})$ 
17:      $\phi(p) \leftarrow t$ 
18:   end for
19: end for

```

Discussion and Conclusion

In this paper, a microstructure reconstruction framework is applied based on our previous work [41] and the image inpainting algorithm of Newson et al. [32], which extensively uses the PatchMatch algorithm from Barnes et al. [3]. It is noteworthy

that our approach does not suffer from the lack of data, which is a common problem in experiments, particularly for experimental materials science. However, this does not mean to compete with and to be viewed as alternatives for ML/DL approaches, such as GAN and AE, for microstructure generation and reconstruction problems. Rather, we would like to view it as a complementary approach, which can further make it easier to apply ML/DL to bridge the gap between small and big data, as ML/DL techniques are well known to be data hungry. Intuitively, it is equivalent to bootstrapping method in statistics, because the patches are drawn within the limited dataset \mathcal{D} , thus samples and microstructure features are reused.

The inpainting algorithm plays an important role in generating statistically equivalent microstructures. To this end, UQ is utilized in materials science [2] to ensure that both aleatory and epistemic uncertainty are rigorously quantified. While two-point statistics and principal component analysis are among most popular choices for quantifying uncertainty associated with microstructures, it is noted that other methods also exist, such as intervals [44], sparse grid [47], Gaussian process regression [38, 40, 42, 46], with applications to other ICME models and simulations. Inverse problems in process structure [39] and structure property linkages [45] have also been explored for UQ where a single forward ICME model is considered. For multiple ICME models, multi-fidelity approaches [33, 43] remain a viable option for coupling multi-physics ICME models which share some common entities.

For the microstructure reconstruction in this paper, we note that small patch size parameter is good at boundary refinement, which in turn is used to ensure the microstructural continuity between the occluded and unoccluded regions. Large patch size parameter is typically used for outpainting problems in order to avoid excessive repetition of patches. Within the scope of this study, large patch size parameter is not considered.

Compared to prior works [20–22], the image inpainting method in this paper can generate microstructures at the same fidelity of the experiments, which are the state of the art in microstructure reconstruction and generation, beside ML/DL approaches. It should be also noted that there is a similar feature in the Adobe Photoshop commercial package, which is widely used in microscopy, which allows image inpainting as well. This proprietary implementation of the PatchMatch algorithm is known as “content-aware fill” operation [4] in the Adobe Photoshop package. Due to the license constraint, we did not compare the performance between our algorithm and the Adobe Photoshop package.

Acknowledgements The views expressed in the article do not necessarily represent the views of the U.S. Department of Energy or the United States Government. Sandia National Laboratories is a multimission laboratory managed and operated by National Technology and Engineering Solutions of Sandia, LLC., a wholly owned subsidiary of Honeywell International, Inc., for the U.S. Department of Energy’s National Nuclear Security Administration under contract DE-NA-0003525. Oak Ridge National Laboratory is a multiprogram science and technology national laboratory operated by UT-Battelle, LLC., for the U.S. Department of Energy under contract DE-AC05-00OR22725.

References

1. Arias P, Facciolo G, Caselles V, Sapiro G (2011) A variational framework for exemplar-based image inpainting. *Int J Comput Vis* 93(3):319–347
2. Arróyave R, McDowell DL (2019) Systems approaches to materials design: past, present, and future. *Ann Rev Mater Res* 49(1):103–126
3. Barnes C, Shechtman E, Finkelstein A, Goldman DB (2009) PatchMatch: a randomized correspondence algorithm for structural image editing. In: *ACM transactions on graphics (ToG)*, vol 28. ACM, p 24
4. Bedi A, Gupta S, Gupta S (2017) Content aware fill based on similar images. *US Patent* 9,697,595
5. Bostanabad R (2020) Reconstruction of 3D microstructures from 2D images via transfer learning. *Comput Aid Des* 128:102906
6. Bostanabad R, Bui AT, Xie W, Apley DW, Chen W (2016) Stochastic microstructure characterization and reconstruction via supervised learning. *Acta Mater* 103:89–102
7. Cang R, Ren MY (2016) Deep network-based feature extraction and reconstruction of complex material microstructures. In: *ASME 2016 international design engineering technical conferences and computers and information in engineering conference*. American Society of Mechanical Engineers, pp V02BT03A008–V02BT03A008
8. Cang R, Xu Y, Chen S, Liu Y, Jiao Y, Ren MY (2017) Microstructure representation and reconstruction of heterogeneous materials via deep belief network for computational material design. *J Mech Des* 139(7):071404
9. Chen D, He X, Teng Q, Xu Z, Li Z (2014) Reconstruction of multiphase microstructure based on statistical descriptors. *Phys A Stat Mech Appl* 415:240–250
10. Chen S, Kirubanandham A, Chawla N, Jiao Y (2016) Stochastic multi-scale reconstruction of 3d microstructure consisting of polycrystalline grains and second-phase particles from 2d micrographs. *Metall Mater Trans A* 1440–1450
11. Chun S, Roy S, Nguyen YT, Choi JB, Udaykumar H, Baek SS (2020) Deep learning for synthetic microstructure generation in a materials-by-design framework for heterogeneous energetic materials. *arXiv preprint* [arXiv:2004.04814](https://arxiv.org/abs/2004.04814)
12. DeCost BL, Francis T, Holm EA (2017) Exploring the microstructure manifold: image texture representations applied to ultrahigh carbon steel microstructures. *Acta Mater* 133:30–40
13. DeCost BL, Hecht MD, Francis T, Webler BA, Picard YN, Holm EA (2017) UHCSDB: ultrahigh carbon steel micrograph database. *Integr Mater Manuf Innov* 6(2):197–205
14. DeCost BL, Lei B, Francis T, Holm EA (2018) High throughput quantitative metallography for complex microstructures using deep learning: a case study in ultrahigh carbon steel. *arXiv preprint* [arXiv:1805.08693](https://arxiv.org/abs/1805.08693)
15. Fedorov V, Facciolo G, Arias P (2015) Variational framework for non-local inpainting. *Image Process On Line* 5:362–386
16. Feng J, Li C, Cen S, Owen D (2014) Statistical reconstruction of two-phase random media. *Comput Struct* 137:78–92
17. Fullwood D, Kalidindi S, Niezgodna S, Fast A, Hampson N (2008) Gradient-based microstructure reconstructions from distributions using fast Fourier transforms. *Mater Sci Eng A* 494(1–2):68–72
18. Fullwood DT, Niezgodna SR, Kalidindi SR (2008) Microstructure reconstructions from 2-point statistics using phase-recovery algorithms. *Acta Mater* 56(5):942–948
19. Goodfellow I, Pouget-Abadie J, Mirza M, Xu B, Warde-Farley D, Ozair S, Courville A, Bengio Y (2014) Generative adversarial nets. In: *Advances in neural information processing systems*, pp 2672–2680
20. Groeber M, Ghosh S, Uchic MD, Dimiduk DM (2008) A framework for automated analysis and simulation of 3D polycrystalline microstructures. Part 1: statistical characterization. *Acta Mater* 56(6):1257–1273

21. Groeber M, Ghosh S, Uchic MD, Dimiduk DM (2008) A framework for automated analysis and simulation of 3D polycrystalline microstructures. Part 2: synthetic structure generation. *Acta Mater* 56(6):1274–1287
22. Groeber M, Uchic M, Dimiduk D, Bhandari Y, Ghosh S (2007) A framework for automated 3d microstructure analysis & representation. *J Comput Aid Mater Des* 14(1):63–74
23. Iyer A, Dey B, Dasgupta A, Chen W, Chakraborty A (2019) A conditional generative model for predicting material microstructures from processing methods. arXiv preprint [arXiv:1910.02133](https://arxiv.org/abs/1910.02133)
24. Latief F, Biswal B, Fauzi U, Hilfer R (2010) Continuum reconstruction of the pore scale microstructure for Fontainebleau sandstone. *Phys A Stat Mech Appl* 389(8):1607–1618
25. Li D, Sun X, Khaleel M (2013) Comparison of different upscaling methods for predicting thermal conductivity of complex heterogeneous materials system: application on nuclear waste forms. *Metall Mater Trans A* 44(1):61–69
26. Li D, Tschopp MA, Khaleel M, Sun X (2012) Comparison of reconstructed spatial microstructure images using different statistical descriptors. *Comput Mater Sci* 51(1):437–444
27. Li X, Zhang Y, Zhao H, Burkhart C, Brinson LC, Chen W (2018) A transfer learning approach for microstructure reconstruction and structure-property predictions. *Sci Rep* 8(1):1–13
28. Ling J, Hutchinson M, Antono E, DeCost B, Holm EA, Meredig B (2017) Building data-driven models with microstructural images: generalization and interpretability. *Mater Discov* 10:19–28
29. Liu Y, Caselles V (2013) Exemplar-based image inpainting using multiscale graph cuts. *IEEE Trans Image Process* 22(5):1699–1711
30. Mosser L, Dubrule O, Blunt MJ (2017) Reconstruction of three-dimensional porous media using generative adversarial neural networks. *Phys Rev E* 96(4):043309
31. Newson A, Almansa A, Fradet M, Gousseau Y, Pérez P (2014) Video inpainting of complex scenes. *SIAM J Imag Sci* 7(4):1993–2019
32. Newson A, Almansa A, Gousseau Y, Pérez P (2017) Non-local patch-based image inpainting. *Image Process On Line* 7:373–385
33. Peherstorfer B, Willcox K, Gunzburger M (2018) Survey of multifidelity methods in uncertainty propagation, inference, and optimization. *SIAM Rev* 60(3):550–591
34. Simonyan K, Zisserman A (2014) Very deep convolutional networks for large-scale image recognition. arXiv preprint [arXiv:1409.1556](https://arxiv.org/abs/1409.1556)
35. Singh R, Shah V, Pokuri B, Sarkar S, Ganapathysubramanian B, Hegde C (2018) Physics-aware deep generative models for creating synthetic microstructures. arXiv preprint [arXiv:1811.09669](https://arxiv.org/abs/1811.09669)
36. Staraselski Y, Brahme A, Mishra R, Inal K (2014) Reconstruction of the 3D representative volume element from the generalized two-point correlation function. *Modell Simul Mater Sci Eng* 23(1):015007
37. Stickel JJ (2010) Data smoothing and numerical differentiation by a regularization method. *Comput Chem Eng* 34(4):467–475
38. Tran A, He L, Wang Y (2018) An efficient first-principles saddle point searching method based on distributed kriging metamodels. *ASCE-ASME J Risk Uncertainty Eng Syst Part B Mech Eng* 4(1):011006
39. Tran A, Mitchell JA, Swiler LP, Wildey T (2020) An active-learning high-throughput microstructure calibration framework for process-structure linkage in materials informatics. *Acta Mater* 194:80–92
40. Tran A, Sun J, Furlan JM, Pagalthivarthi KV, Visintainer RJ, Wang Y (2019) PBO-2GP-3B: a batch parallel known/unknown constrained Bayesian optimization with feasibility classification and its applications in computational fluid dynamics. *Comput Methods Appl Mech Eng* 347:827–852
41. Tran A, Tran H (2019) Data-driven high-fidelity 2D microstructure reconstruction via non-local patch-based image inpainting. *Acta Mater* 178:207–218
42. Tran A, Tran M, Wang Y (2019) Constrained mixed-integer Gaussian mixture Bayesian optimization and its applications in designing fractal and auxetic metamaterials. *Struct Multi Optim* 1–24

43. Tran A, Tranchida J, Wildey T, Thompson AP (2020) Multi-fidelity machine-learning with uncertainty quantification and Bayesian optimization for materials design: application to ternary random alloys. *J Chem Phys* 153:074705
44. Tran A, Wang Y (2015) A molecular dynamics simulation mechanism with imprecise inter-atomic potentials. In: *The 3rd TMS world congress on integrated computational materials engineering (ICME 2015)*. Colorado Springs, CO., May 31–June 4, 2015
45. Tran A, Wildey T (2020) Solving stochastic inverse problems for property-structure linkages using data-consistent inversion and machine learning. *JOM*
46. Tran A, Wildey T, McCann S (2020) SMF-BO-2CoGP: a sequential multi-fidelity constrained Bayesian optimization for design applications. *J Comput Inf Sci Eng* 20(3):1–15
47. Tran AV, Liu D, Tran HA, Wang Y (2019) Quantifying uncertainty in the process-structure relationship for Al–Cu solidification. *Modell Simul Mater Sci Eng* 27(6):064005
48. van Der Maaten L (2014) Accelerating t-SNE using tree-based algorithms. *J Mach Learn Res* 15(1):3221–3245
49. van der Maaten L, Hinton G (2008) Visualizing data using t-SNE. *J Mach Learn Res* 9(Nov):2579–2605
50. Van der Walt S, Schönberger JL, Nunez-Iglesias J, Boulogne F, Warner JD, Yager N, Gouillart E, Yu T (2014) Scikit-image: image processing in python. *PeerJ* 2:e453
51. Wexler Y, Shechtman E, Irani M (2007) Space-time completion of video. *IEEE Trans Pattern Anal Mach Intell* 3:463–476
52. Xu H, Dikin DA, Burkhart C, Chen W (2014) Descriptor-based methodology for statistical characterization and 3D reconstruction of microstructural materials. *Comput Mater Sci* 85:206–216
53. Xu H, Liu R, Choudhary A, Chen W (2015) A machine learning-based design representation method for designing heterogeneous microstructures. *J Mech Des* 137(5):051403
54. Zinchenko AZ (1994) Algorithm for random close packing of spheres with periodic boundary conditions. *J Comput Phys* 114(2):298–307

Dislocation Dipole Study on Material Hardening/Softening



Abu Bakar Siddique, Tariq Khraishi, and Hojun Lim

Abstract Dislocation dynamics simulations often reveal interesting phenomena in regard to material deformation, which may not be captured by experiments. In this work, we investigate the effect of dislocation dipoles on plastic material properties under different dipole configurations (i.e. the distance between active glide planes, and the signs of the two dislocations) using a 3D Discrete Dislocation Dynamics code. The simulations show that a dipole is causing a hardening effect when the Burgers vectors of the dislocations forming the dipole are of opposite sign and causing a hardening/softening effect when they are of the same sign. The distance between the two neighboring dislocations was also affecting the proportional limit for the material. Such hardening or flow stress results, as in this study, can be incorporated in larger-scale modeling work.

Keywords Dislocations · Dipoles · Plasticity · Hardening · Softening

Introduction

Line defects in the crystal (also known as dislocations) move, multiply and can interact with other types of defects present in the crystal. These interactions can be both elastic and inelastic. Plastic properties of material thus depend on the nature and scale of these interactions. A material can be hardened or softened as a consequence of these interactions. A dipole is formed when two dislocations in different slip planes interact as the distance between them closes in. Dipoles can contribute to elastic material hardening and softening [1].

Stokes and Olsen [2] and Kroupa [3] described the mechanism of dipole formation for both screw and edge dislocations. Gilman [4] and Neumann [5] studied the

A. B. Siddique · T. Khraishi (✉)
Department of Mechanical Engineering, University of New Mexico, Albuquerque, NM, USA
e-mail: khraishi@unm.edu

H. Lim
Sandia National Laboratories, Albuquerque, NM, USA

interaction between dislocations and dislocation dipoles, tripoles, and quadrupole. In the 2D study by Neumann [5], it was found that decomposition of the dipole occurs usually more often than trapping of the approaching dislocations.

To understand these phenomena in the plastic regime, researchers and scientists developed several codes that can simulate the dynamic behavior of dislocation interactions under simple to complex configurations, which are often not captured in real experiments. Kubin et al. [6] introduced a basic framework for 3D dislocation dynamics simulations. Later on, researchers and scientists developed other dislocation dynamics codes introducing more and more features. In the current study, the simulations are performed on a dislocation dynamics code developed by Zbib et al. [7], De La Rubia et al. [8], Khraishi et al. [9], and Siddique and Khraishi [10].

In this article, we present an interesting study on the hardening and softening due to a dislocation dipole feeling loading depending on the relative location and the separation distance between the two slip planes. In Sect. 2 we present some basic theory that helps us understand the reason for hardening or softening behaviors. In Sect. 3 we detail the simulation configuration, and in Sect. 4 we present the simulation outcomes and discuss the results.

Theory

Force \vec{F} (also known as Peach-Koehler force) acting on a dislocation can be calculated by [11]

$$\vec{F} = (\boldsymbol{\sigma}\vec{b}) \times \hat{e} \quad (1)$$

where $\boldsymbol{\sigma}$ is the stress tensor at a point on a dislocation line due to internal and externally-applied stresses, \vec{b} is the magnitude and direction of the crystal distortion by that dislocation (also known as the Burgers vector) and \hat{e} is a unit vector along the dislocation line (i.e. the line sense vector). Dislocations move in a slip plane when the Peach-Koehler force is high enough to overcome the internal friction in the crystal. A dislocation source multiplies when this force is large enough to overcome the line tension of dislocation. Line tension T of a dislocation is given by Bacon and Hull [12]

$$T = \alpha Gb^2 \quad (2)$$

where $\alpha \approx 0.5-1.0$ and b is the magnitude of the Burgers vector. In the multiplication of an initially straight Frank-Read source, it is assumed [5] that plastic flow occurs when the dislocation bows a half circle. This is also known as critical bowing. For critical bowing, the critical shear stress is calculated as,

$$\tau_{\text{crit}} = \alpha \frac{Gb}{R} \quad (3)$$

where R is the radius of the bowed dislocation.

Two dislocations of the same or opposite signs form a dipole when they interact elastically from some distance and are parallel to each other. Depending on the nature of this interaction, the extent of the elastic and plastic regimes in the material under loading can be changed. For two dislocations (in different slip planes) that are close to each other, having the same sign (i.e. same Burgers vector and line sense) can cause plastic deformation under deformation to happen at a smaller applied strain value than two dislocation of opposite sign. This could be explained in reference to theory on a dipole of infinite dislocations (i.e. 2D problem) [5]. For a dipole of the same sign, the stable configuration is when the two dislocations are stacked on top of each other, i.e. creating a 0° with respect to each other from the line perpendicular to their planes. If the angle between them increases to 45° then the configuration becomes unstable. In this configuration when the two dislocation are relatively close to each other, perturbations in the stress state can cause them to be at 45° with respect to each other. Once this degree is exceeded, they will repel each other and that will help ease the plastic flow. This situation causes the plastic flow for these two sources to occur at an earlier applied strain than a single Frank-Read source. The situation can be the opposite if the distance between the two dipole dislocations is high. In this case, a higher applied strain value is needed to reach a 45° separation with respect to each other. By that large strain value, more stabilization against flow is offered from the dipole and plastic flow can commence from the critical bowing of the sources.

Problem Configuration

To investigate the phenomena mentioned in the theory section, we perform many simulations by placing two Frank-Read sources in different parallel slip planes (see Fig. 1) and apply constant strain-rate using the code developed by [7–10]. The study intends to understand how the initial dipole configuration affects the elasto-plastic responses in the presence of external loading on the crystal. The shear modulus

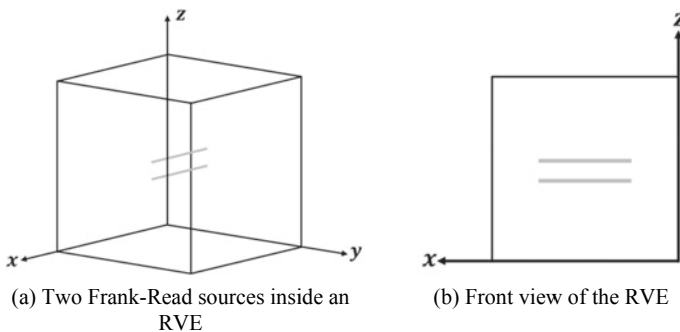


Fig. 1 Dipole configuration

for the selected material is set at 26.32 GPa and Poisson's ratio is taken as 0.33. The dimension of the representative volume element (RVE) for these simulations is $60,000b \times 60,000b \times 40,000b$. The Burgers vector of the Frank-Read sources is $[010]$. The shear load is applied in yz -direction, and the applied strain rate is 10 s^{-1} . Dislocations lie parallel to the x -axis with a separation distance d . The length of each dislocation is $4000b$.

The first set of simulations is conducted by changing the separation distance between active slip planes where the Burgers vectors are the same for both dipole dislocations. Initially, two Frank-Read sources are placed on two different slip planes as they make 0° angle with each other with respect to the vertical axis. This is a stable position for such dipole, as mentioned in the theory section. In the second set of simulations, the Burgers vectors of the two dislocations are set to $[010]$ and $[0\bar{1}0]$ and the separation distance between the active slip planes is varied. The initial position of the two Frank-Read sources was set to make 45° angle with each other with respect to the vertical axis (vertical to the two parallel planes).

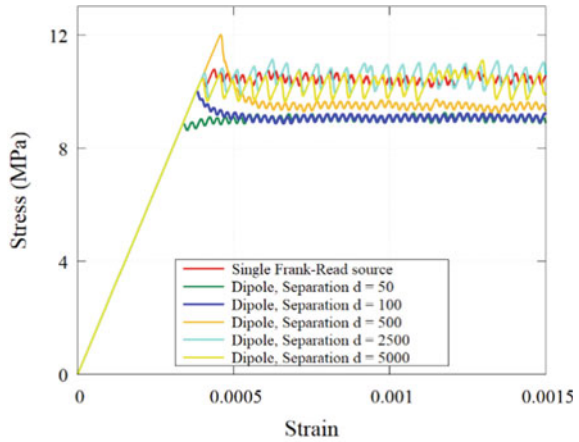
Results

Figure 2a shows the stress-strain responses of the RVE for different active slip plane separations for dipole configurations with the same dislocation sign. Figure 2b shows the proportional limit and flow stress as the separation between the two slip plane is varied. The curve shows both hardening and softening effect from the elastic interaction between two Frank-Read sources having the same Burgers vector.

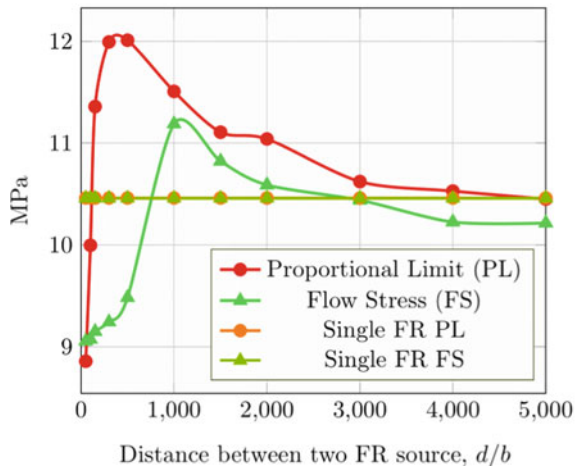
This result shows good agreement with the discussion in the theory section regarding small source separations. However, for large separations, the sources bow together trying to hold each other in equilibrium and this raises the proportional limit (i.e. the critical bowing of source(s)) and thus the flow stress. However, as the distance becomes much larger then the two sources start having less and less effect on one another during bowing resulting eventually in the proportional limit and flow stress being the same as if there was only one source. For this kind of interaction, two parameters play an essential role in conjunction with one another: one is the separation distance between two slip planes, and the other is the Peach-Koehler force due to the self-stress field created by the dislocations. This force, with perturbations in the self-stress of the dislocations, can cause the same-signed dislocation sources to either take longer to critically bow (i.e. a hardening or strengthening effect) or bow critically quickly, i.e. at lowered strain (i.e. a softening effect).

Figure 3 shows different results for the opposite-sign dipole configuration compared to the same-sign configuration. In this dipole configuration and for lower separation distances, both the proportional limit and the flow stress are significantly higher than for a single Frank-Read source. The reason for this is that for this dipole configuration the entire slip plane acts as a basin of attraction for both Frank-Read sources in accordance with theory [5]. Thus one should not expect any softening

Fig. 2 Dipole interaction with a dipole of same-sign dislocation sources. (Color figure online)



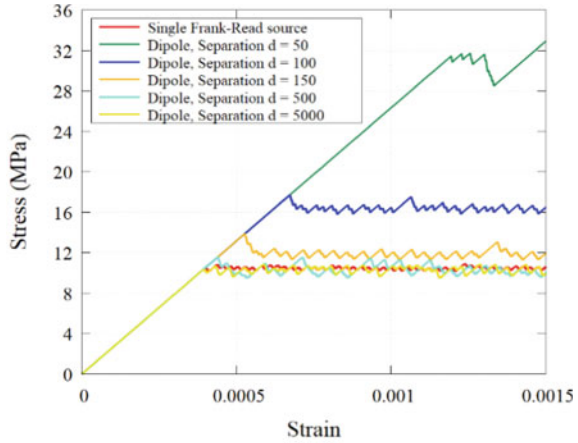
(a) Stress-strain curves



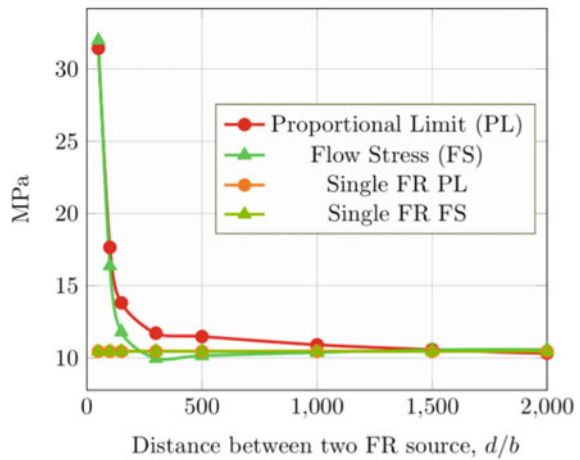
(b) Comparison of proportional limit and flow stress of a dipole with a single Frank-Read source

effect from this configuration because this continuing attraction hinders plastic flow. Figure 3 also shows a good agreement with the a study hypothesis: as the separation distance increases, the stress-strain response follows the single Frank-Read source response.

Fig. 3 Dipole interaction with a dipole of opposite-sign dislocation sources. (Color figure online)



(a) Stress-strain curves



(b) Comparison of proportional limit and flow stress of a dipole with a single Frank-Read source

Conclusion

In this article, the authors presented a study on dislocation dipoles that showed both hardening and softening behavior in the material. One of the main findings of this study is that opposite-signed dipoles contribute to hardening only. On the contrary, same-sign dipoles can cause either hardening or softening in the material depending on the separation distance between two slip planes where the dislocations move and multiply. For future studies, one could consider the initial source length as a

parameter as well as the number of dislocation sources stacked in the array, e.g. a tripole or more dislocations.

Acknowledgements This paper describes objective technical results and analysis. Any subjective views or opinions that might be expressed in the paper do not necessarily represent the views of the U.S. Department of Energy or the United States Government.

Sandia National Laboratories is a multi-mission laboratory managed and operated by National Technology and Engineering Solution of Sandia, LLC., a wholly owned subsidiary of Honeywell International, Inc., for the U.S. Department of Energy's National Nuclear Security Administration under contract DE-NA0003525.

References

1. Zbib H, Rhee M, Hirth J, Rubia TDL (1998) On dislocation reactions and hardening mechanisms in 3D dislocation dynamics. *MRS Online Proc Libr Arch* 538
2. Stokes RJ, Olsen KH (1963) Dislocation interactions and dipole formation. *Phil Mag* 8:957–965
3. Kroupa F (1996) Dislocation dipoles and dislocation loops. *Le J de Phys Colloques* 27(c3)
4. Gilman JJ (1964) Influence of dislocation dipoles on physical properties. *R Soc Chem* 38
5. Neumann PD (1971) Interactions between dislocations and dislocation dipoles. *Acta Metall* 19(11):1233–1241
6. Kubin LP, Canova G, Condat M, Devincere B, Pontikis V, Brechet Y (1992) Dislocation microstructures and plastic flow: a 3D simulation. *Solid State Phenom* 23–24:455–472
7. Zbib HM, Rhee M, Hirth JP (1998) On plastic deformation and the dynamics of 3D dislocations. *Int J Mech Sci* 40(2–3):113–127
8. de la Rubia TD, Zbib HM, Khraishi TA, Wirth BD, Victoria M, Caturla MJ (2000) Multiscale modelling of plastic flow localization in irradiated materials. *Nature* 406(6798):871–874
9. Khraishi TA, Zbib HM, de la Rubia TD, Victoria M (2002) Localized deformation and hardening in irradiated metals: three-dimensional discrete dislocation dynamics simulations. *Metall Mater Trans B* 33(2):285–296
10. Siddique AB, Khraishi T (2020) Numerical methodology for treating static and dynamic dislocation problems near a free surface. *J Phys Commun* 4(5):055005
11. Hirth JP, Lothe J (1982) *Theory of dislocations*. Wiley, Hoboken
12. Bacon DJ, Hull D (2011) *Introduction to dislocations*, Butterworth-Heinemann

Model and Improved Dynamic Programming Algorithm for Optimization of Unplanned Slab Allocation in the Steel Plant



Yongzhou Wang, Zhong Zheng, Cheng Wang, and Xiaoqiang Gao

Abstract The unplanned slab is the open orders slab produced by the steelmaking-continuous casting process, which will increase the inventory cost of enterprises. The unplanned slab allocation problem is to reasonably assign the unplanned slabs to the hot rolling supplementary orders, steelmaking supplementary orders, or customer orders in a given period. It can be considered as an extension of the multiple knapsack problem. Therefore, a 0–1 integer programming model is established to minimize the cost of differences between unplanned slab and order specification. In this paper, a decomposition method of problem solving process, an adaptive measurement method of order priority in different scenarios, and an improved dynamic programming algorithm considering the local search strategy are proposed for the unplanned slab allocation. The testing cases with data from a steel plant show that the optimization algorithm for the unplanned slab allocation is superior to the manual one in terms of solution quality and calculation time.

Keywords Unplanned slab · Allocation · Model · Multiple knapsack problem · Dynamic programming

Introduction

At present, the most of steel companies use make-to-order production mode. However, the contradiction between the multi-specification, multi-variety, and small-batch orders corresponding to the rapid changes in market demand and the mass production methods of steel plant may lead to the production of a large number of unplanned slabs. Generally speaking, unplanned slabs are produced mainly due to the following reasons: ① Changes in customer order requirements; ② Surplus materials

Y. Wang · Z. Zheng (✉) · C. Wang
College of Materials Science and Engineering, Chongqing University, Chongqing 400045, China
e-mail: zhengzh@cqu.edu.cn

X. Gao
School of Economics and Business Administration, Chongqing University, Chongqing 400045, China

added to meet the processing requirements of large-scale production equipment; ③ Slabs that do not meet the quality and composition of the production plan requirements; ④ Producing some slabs in advance to balance the production capacity of steelmaking and hot rolling. Unplanned slabs will inevitably have a certain negative impact on the company's production management, such as increasing capital occupation, increasing production costs, and affecting order delivery. Therefore, in addition to avoiding the production of unplanned slabs as much as possible, steel companies need to rationally optimize the utilization of unplanned slabs to reduce inventory and capital occupation.

There have been many studies on the optimization problem of unplanned slab allocation at home and abroad. Vasko et al. [1] first studied the unplanned slab allocation problem, and established an integer programming model with the goal of minimizing matching costs. The virtual order and virtual slab were added to convert the problem into a transportation problem, which was solved by Bertsekas network nodes. Kalgnam et al. [2] formulated the unplanned slab allocation problem with an interval value of order weight as a multi-choice knapsack problem. A nonlinear model with the goal of maximizing matching weight and minimizing matching residual material is established, and a heuristic algorithm based on bipartite graph matching and network maximum flow is designed to solve it. Since then, a large number of articles focusing on the unplanned slab allocation problem have been published Denton et al. [3], Forrest et al. [4], Yanagisawa [5], Song [6], Zheng et al. [7], Bai and Ji [8], Tian et al. [9], Zheng and Tang [10], Tang et al. [11], Xie et al. [12], Lv et al. [13]), and various models and solutions have been proposed. In addition to the above research, some relevant articles include the research done by Matsuda et al. [14], Li et al. [15], Zou et al. [16], Hu et al. [17, 18], Zheng and Tang [19], Wang [20], and Lv et al. [21]. They studied the matching of unplanned slabs and customer orders in different scenarios and proposed various solutions.

All of the above problems studied consider matching the unplanned slabs in stock to the existing customer orders at the current planning period. However, in the actual production of the steelmaking process or the hot rolling process, there are often some unexpected perturbations (e.g., insufficient temperature, unqualified composition, random machine breakdown) that cause some orders to fail to be successfully produced, and then it is necessary to match suitable unplanned slabs for these orders. Because the output of these orders is full of uncertainty, and their importance is usually not the same, when assigning unplanned slabs to these orders, the priority of different orders needs to be confirmed first, which is also a problem that is not considered in the current research.

This paper studied the unplanned slab allocation problem (USAP) of medium and heavy plates. The task of USAP is to select suitable slabs from unplanned slabs for the production order that requires slabs to meet its specification. For USAP, a 0-1 integer programming model is established with the goal of minimizing the amount of matching residual material under the condition of meeting the requirements of material properties such as steel grades and cross-section specifications, and meeting the constraints of order requirements and delivery dates. In this paper, the two-cut slabs and the unplanned slabs are grouped firstly, then the matching priority is confirmed for

the order that requires unplanned slabs, and finally a dynamic programming-based solution algorithm considering the local search strategy is designed to obtain an optimal solution for each group of unplanned slabs. Effectively solving this problem can not only avoid the prolonged production cycle of the order and improve customer satisfaction, but also ease inventory pressure of the enterprise and increase the capital turnover rate.

Problem Description

The unplanned slab allocation for medium and heavy plates is a process of determining a reasonable and optimized treatment method for unplanned slabs. Utilization of unplanned slabs mainly includes three methods. First, steelmaking supplementary orders. When the molten steel smelted by the converter does not meet the quality and composition requirements of the plan, it is necessary to select some suitable slabs from the unplanned slabs in the stock to replace the slabs that do not meet the requirements. Second, hot rolling supplementary orders. When unqualified rolling occurs in the hot rolling production process, it is necessary to select suitable slabs from unplanned slabs for rolling again. Third, some normal orders. When unplanned slab inventory is large, it is necessary to consume unplanned slab inventory through some normal orders.

For the production process of medium and heavy plates, the slab produced by the continuous caster is cut to obtain the two-cut slab, and the final product is obtained after hot rolling. The utilization of unplanned slabs is the opposite. The steel plates included in the order are first converted into two-cut slabs through plate and slab design, and then matched with unplanned slabs. Therefore, the unplanned slab allocation is also a process of combining the two-cut slabs included in the orders on unplanned slabs. The primary purpose of unplanned slab allocation is to ensure smooth production and avoid prolonged delivery. The unplanned slab allocation process is shown in the Fig. 1. When orders that require unplanned slabs are issued, the designer first groups two-cut slabs by steel grade and cross-section specifications and selects suitable unplanned slabs based on the suitability constraints, and then confirms the matching priority between unplanned slabs and the order. Finally, with the goal of minimizing the amount of residual material, the two-cut slabs included in the order are matched with unplanned slabs.

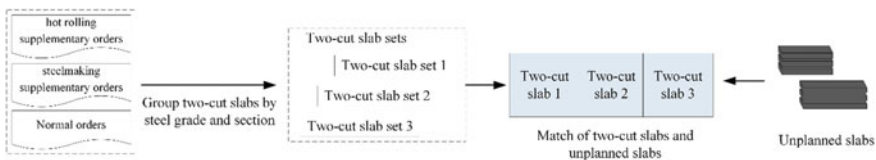


Fig. 1 The allocation process of the unplanned slab allocation problem. (Color figure online)

Mathematical Formulation and Solution Framework

Symbol Description

The symbol description of the parameters or variables in the formulation is as follows:

Parameter

- i The index of two-cut slab, $i \in \{1, 2, \dots, m\}$
- l_i The length of two-cut slab i
- j The index of unplanned slabUnplanned slab, $j \in \{1, 2, \dots, n\}$
- L_j The maximum length of unplanned slabUnplanned slab j .

Decision Variables

- $d_{i,j}$ A binaryDecision variables variable which is equal to 1 if a two-cut slab i is matched to a unplanned slabUnplanned slab j and 0 otherwise.

Preprocessing

According to the constraints of the USAP for medium and heavy plates, two-cut slabs of different steel grades and cross-section specifications cannot be matched to the same unplanned slab. Therefore, before applying the method, the two-cut slabs and unplanned slabs are grouped according to the matching rules. Each group of two-cut slabs and the corresponding unplanned slabs that can be matched are used as input to apply this method to solve the problem. Each group of two-cut slabs and unplanned slabs have the same requirements in terms of steel grade and cross-section specifications, and the relevant constraints are no longer discussed in the formulation.

Priority Confirmation in Different Scenarios

According to the source of the two-cut slab, the matching of the two-cut slab and the unplanned slab is divided into three different scenarios: rolling supplementary order priority, steel-making supplementary order priority and normal order priority. The matching priority in different scenarios is determined according to the urgency of the three types of supplementary orders and the production organization of the steel mill and hot rolling mill.

Mathematical Formulation

The matching problem of two-cut slabs and unplanned slabs can be regarded as a practical application of the multi-knapsack problem. The two-cut slabs are m items with a size of l_1, l_2, \dots, l_m , and the length of the two-cut slab is the weight of the item. The unplanned slabs are n backpacks with a capacity of L_1, L_2, \dots, L_n , and the length of unplanned slabs is the backpack capacity. Aiming at the conditions given in the problem description, the resulting formulation P is established with the goal of minimizing the residual material produced during the matching process.

$$\text{Formulation P } f = \min \sum_{j=1}^n (L_j - \sum_{i=1}^m d_{i,j} \cdot l_i) \quad (1)$$

$$\text{Subject to } \sum_{i=1}^m d_{i,j} \cdot l_i \leq L_j, j \in \{1, 2, \dots, n\} \quad (2)$$

$$\sum_{i=1}^m \sum_{j=1}^n d_{i,j} \leq 1 \quad (3)$$

$$d_{i,j} \in \{0, 1\}, \forall i \in \{1, 2, \dots, m\}, j \in \{1, 2, \dots, n\} \quad (4)$$

The objective function (1) is to minimize the residual material produced by the matching process; Constraint (2) indicates that the total length of the two-cut slab combined on the unplanned slab does not exceed the maximum length of the unplanned slab; Constraint (3) means that each two-cut slab can only be allocated to one unplanned slab at most; Constraint (4) means the value constraint of the corresponding variable. Solving the formulation P can obtain the optimized unplanned slab allocation result of the medium and heavy plate.

Solution Framework

The USAP for medium and heavy plates is a process of combining two-cut slabs on unplanned slabs. This paper decomposes this process into two stages for solution: two-cut slab and unplanned slab pretreatment stage and two-cut slab combination optimization stage. In the previous stage, the two-cut slabs and unplanned slabs were grouped according to suitability constraints, and each group of two-cut slabs was matched with a suitable set of unplanned slabs; In the latter stage, the problem of matching the two-cut slab and unplanned slab is stated as a multi-knapsack problem. A matching optimization algorithm based on dynamic programming (DP) algorithm is designed to combine the two-cut slabs to the unplanned slabs, and a local search strategy is designed to improve the quality of the solution. Among the unplanned

slabs remaining after the matching is completed, the local search strategy is used to check whether there are unplanned slabs that can replace the currently matched unplanned slabs and reduce the residual matching material, and if it exists, replace the currently matched unplanned slabs. The matching algorithm flow chart proposed in this paper is shown in Fig. 2.

Case Study

Case Design

In order to verify the effectiveness and practicability of the unplanned slab matching optimization method, taking the unplanned slab allocation problem of a steel mill as the object, 8 instances were selected to test the unplanned slab matching method based on DP, the unplanned slab matching method based on genetic algorithm (GA) proposed by Yu and Yang [22] and manual matching method for medium and heavy plates. The unplanned slab data included in each case are shown in Table 1. Other data during the test are based on the data provided by the steel mill. During the experimental test, it is assumed that the amount of the two-cut slabs is sufficient.

Result and Discussion

The parameters of the matching method based on GA are configured as follows: the population size $PS = 40$, iterations step size $step = 60$, crossover probability $CP = 0.8$, the mutation probability $MP = 0.15$. All the matching methods were implemented in C# language, and ran the 8 instances on a PC with CPU2.0 GHz and RAM8.00 GB using Windows10-64bit operating system. The final matching results are shown in Table 2.

In Table 2, columns 2, 6 and 10 are the number of unplanned slabs (USN) matched by the three matching methods, and all unplanned slabs are matched. Columns 3–4, 7–8 and 11–12 are the results of the residual material amount (RMA) and residual material rate (RMR) of the matching method based on DP, the matching method based on GA, and the manual matching method, respectively. Comparing the residual material rate of the three matching methods, the matching method proposed in this paper can greatly reduce the residual material rate of unplanned slab matching. This is because in the process of unplanned slab matching, the algorithm proposed in this paper can try different ways of matching the two-cut slabs and unplanned slabs among a large number of unplanned slabs, and can optimize the quality of the matching results by adjusting the strategy, so as to obtain a result with a smaller matching residual material rate. Columns 5, 9 and 13 are the matching time (MT) of the three matching methods, respectively. The manual matching time is determined

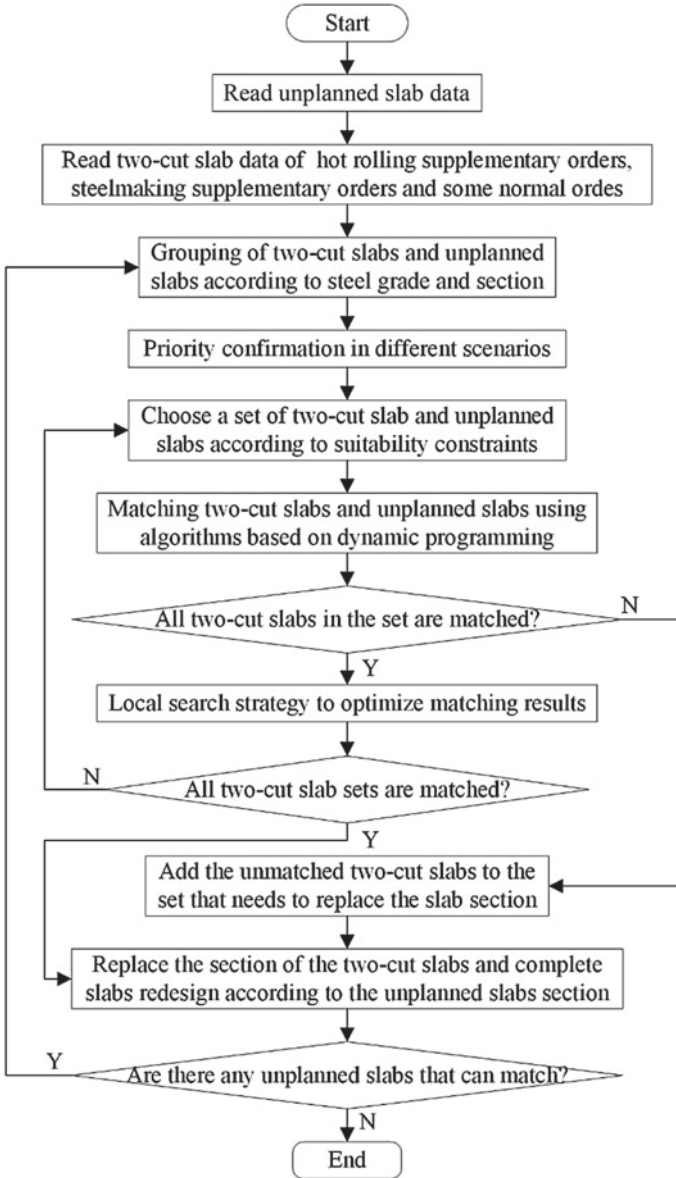


Fig. 2 The diagram of the unplanned slab allocation algorithm

Table 1 The unplanned slab data

No.	Steel grade	Thickness/mm	Width/mm	Length range/mm	Number
1	A	300	2010	6090–7600	14
2	B	230	1530	5400–9410	5
		300	2010	4800–8800	8
3	C	230	1530	9800	3
		200	2200	11,000	3
		300	2010	7600	2
4	D	230	1530	9800	5
		300	2010	3800–7700	12
5	E	200	2200	11,000	7
		300	2010	6280–7710	23
6	F	200	2200	7500–11,000	3
		300	2010	5300–7600	8
7	G	230	1530	9800	7
		200	2200	10,500–11,000	2
		300	2010	7600	4
8	H	230	1530	3640–10,700	11
		300	2010	5500–7600	5

based on the experience of the steel plant planner. The matching method proposed in this paper can greatly reduce the unplanned slab matching time. At the same time, compared with the manual matching method, the unplanned slab matching time is reduced from minutes to seconds, which can greatly improve the efficiency of unplanned slab allocation.

In summary, the unplanned slab matching optimization method proposed in this paper can improve the efficiency of unplanned slab matching and obtain matching results that are better than the other two methods. In this way, the unplanned slab produced by the iron and steel enterprises can be used reasonably, the unplanned slab inventory and the production cost of the iron and steel enterprises can be reduced.

Summary

This paper first introduces the unplanned slab allocation problem for medium and heavy plates, summarizes the source and utilization of unplanned slabs, and describes the optimization goals and constraints of unplanned slab matching. Then put forward reasonable assumptions, and established a multi-knapsack problem model. Finally, the expert experience is converted into solving rules, and an unplanned slab matching algorithm based on dynamic programming is designed to solve the problem, and

Table 2 The matching result of the unplanned slab allocation

No	Matching method based on DP				Matching method based on GA				Manual matching method			
	USN	RMA/t	RMR/%	MT/s	USN	RMA/t	RMR/%	MT/s	USN	RMA/t	RMR/%	MT/min
1	14	4.99	1.05	1	14	11.95	2.52	158	14	30.01	6.34	15
2	13	0	0	33	13	10.17	2.84	183	13	30.68	8.56	15
3	8	2.15	0.81	5	8	6.36	2.4	171	8	18.88	7.11	10
4	17	25.1	4.6	5	17	37.91	6.95	148	17	48.57	8.9	15
5	30	25.07	2.33	6	30	27.96	2.60	178	30	29.42	2.74	30
6	11	0	0	12	11	1.91	0.52	203	11	8.45	2.8	10
7	13	0	0	13	13	3.01	0.74	166	13	54.74	13.51	15
8	16	0.30	0.07	18	16	18.53	4.58	202	16	34.25	8.47	15

the residual material generated in the matching process is reduced by adjusting the strategy. A case test with unplanned slab data from a steel mill shows that the algorithm in this paper can complete all unplanned slab allocation. Compared with the other two methods, the residual material rate is reduced by 1.79% and 6.20% on average, respectively. And the matching time is reduced from minutes to seconds, which greatly improves the efficiency of unplanned slab distribution.

Acknowledgements The authors gratefully acknowledge the financial support of the Key Program of the National Natural Science Foundation of China (No. 51734004) and the General Program of National Natural Science Foundation of China (No. 51474044).

References

1. Vasko FJ, Cregger ML, Stott KL et al (1994) Assigning slabs to orders: an example of appropriate model formulation. *Comput Ind Eng* 26(4):797–800
2. Kalagnanam JR, Dawande MW, Trumbo M et al (2000) The surplus inventory matching problem in the process industry. *Oper Res* 48(4):505–516
3. Denton B, Gupta D, Jawahir K (2003) Managing increasing product variety at integrated steel mills. *Inform J Appl Anal* 33(2):41–53
4. Forrest JJH, Kalagnanam J, Ladanyi L (2006) A column-generation approach to the multiple knapsack problem with color constraints. *Inform J Comput* 18(1):129–134
5. Yanagisawa H (2007) The material allocation problem in the steel industry. *IBM J Res Dev* 51(3.4):363–374
6. Song SH (2010) A nested column generation algorithm to the meta slab allocation problem in the steel making industry. *Int J Prod Res* 47(13):3625–3638
7. Zheng XY, Shi CT, Zhang WX (2007) An inventory matching model and algorithm of production management in iron and steel enterprises. *Microcomput Inf* 36:9–10
8. Bai XZ, Ji SL (2008) Application of genetic algorithm to the match of no-entrusted slabs and contracts. *Control Eng China* 15(1):95–102
9. Tian ZB, Tang LX, Ren YM et al (2009) Solving open-order slab matching problem by ACO with compound neighborhood. *Acta Automatica Sinica* 35(02):186–192
10. Zheng YY, Tang LX (2009) Hybrid scatter search and tabu search for the mother plate design problem in the iron and steel industry. In: Paper presented at the 2nd international joint conference on computational sciences and optimization (CSO). Sanya, China, 24–24 Apr 2009
11. Tang LX, Luo JX, Liu JY (2013) Modelling and a tabu search solution for the slab reallocation problem in the steel industry. *Int J Prod Res* 51(14):4405–4420
12. Xie X, Li YP, Zheng YY et al. (2014) A mix-integer programming model for inventory slab allocation problem. In: Paper presented at international conference on materials engineering and mechanical automation (MEMA 2013). Shanghai, China, 01–02 Oct 2014
13. Lv YN, Wang GS, Tang LX (2014) Scenario-based modeling approach and scatter search algorithm for the stochastic slab allocation problem in steel industry. *ISIJ Int* 54(6):1324–1333
14. Matsuda K, Takai Y, Yoshida K et al (1995) Optimization of cutting stock schedule by simulated annealing method. *Trans Soc Instrum Control Eng* 31(5):544–552
15. Li ZQ, Huang R, Peng BL et al (2015) A divide-conquer heuristic search algorithm for cutting surplus steel plates of steel and iron companies. *Int J Innovative Comput Inf Control* 11(1):363–374
16. Zou F, Meng Y, Yang Y (2017) A hybrid differential evolution algorithm for open-order coil allocation problem in the steel industry. In: Paper presented at the 2017 13th IEEE conference on automation science and engineering (IEEE CASE). Xian, China, 20–23 Aug 2017

17. Hu KY, Chang CG, Zheng BL et al (2004) The model and algorithm for joint optimization of inventory matching and production planning in steel plant. *Inf Control* 02:177–180
18. Hu KY, Gao ZW, Wang DW (2004) Optimal multi-objective model and algorithm for order matching problems in iron and steel plants. *J Northeast Univ (Nat Sci)* 06:527–530
19. Zheng YY, Tang LX (2009) A branch-and-price algorithm for the dynamic inventory slab allocation problem in the steel industry. In: Paper presented at the 2nd international joint conference on computational sciences and optimization (CSO). Sanya, China, 24–24 Apr 2009
20. Wang C (2012) Column generation based method for dynamic inventory slab allocation problem. *Comput Eng Appl* 48(08):221–225
21. Lv YN, Tang LX, Meng Y et al (2015) Modeling and scatter search algorithm for dynamic slab allocation problem in iron and steel enterprises. *Control Decis* 30(01):17–24
22. Yu AB, Yang JB (2002) Genetic Algorithm for multi knapsack problem. *Comput Technol Autom* 02:59–63

Part XIX
Alloys and Compounds for Thermoelectric
and Solar Cell Applications IX

Order Parameter from the Seebeck Coefficient in Thermoelectric Kesterite $\text{Cu}_2\text{ZnSnS}_4$



Eleonora Isotta, Binayak Mukherjee, Carlo Fanciulli, Nicola M. Pugno, and Paolo Scardi

Abstract Kesterite (CZTS, $\text{Cu}_2\text{ZnSnS}_4$) is a quaternary chalcogenide which structural complexity leads to polymorphism and numerous kinds of disorder in cation sites, with interesting effects on thermoelectric properties. Tetragonal kesterite faces an order-disorder phase transition from $I-4$ to $I-42m$ crystal structures around 533 K, which causes a sharp increase in the Seebeck coefficient. The degree of order in the crystal structure determines the entity of this enhancement, locally influencing the steepness of the trend of thermopower in the transition region. The presence of secondary phases reduces the effect of the transition as well as causing a progressive reduction of the Seebeck coefficient. The present results show that a measurement of Seebeck coefficient provides direct and distinctive information on the degree of order and phase purity of kesterite samples, integrating results of Raman spectroscopy and X-ray diffraction.

E. Isotta (✉) · E. Isotta (✉) · B. Mukherjee · N. M. Pugno · P. Scardi (✉)
Department of Civil, Environmental and Mechanical Engineering, University of Trento, via
Mesiano 77, 38123 Trento, Italy
e-mail: eleonora.isotta@unitn.it

P. Scardi
e-mail: paolo.scardi@unitn.it

B. Mukherjee
e-mail: binayak.mukherjee@unitn.it

N. M. Pugno
e-mail: nicola.pugno@unitn.it

N. M. Pugno
Laboratory of Bio-Inspired, Bionic, Nano Meta Materials and Mechanics, University of Trento,
Trento, Italy

C. Fanciulli
National Research Council of Italy-Institute of Condensed Matter Chemistry and Technologies for
Energy (CNR-ICMATE), Lecco Unit, via Previati 1/E, 23900 Lecco, Italy
e-mail: carlo.fanciulli@cnr.it

N. M. Pugno
School of Engineering and Materials Science, Queen Mary University of London, Mile End Road,
London E1 4NS, UK

Keywords Kesterite $\text{Cu}_2\text{ZnSnS}_4$ CZTS · Order-disorder transition · Seebeck coefficient · Order parameter · Secondary phases · Thermoelectric materials

Introduction

The growing interest in waste heat recovery has drawn attention to thermoelectric (TE) materials, with increasing efforts to identify the best performing semiconductor materials [1–3]. The performance of TE materials is typically expressed through the figure of merit $zT = \alpha^2 T / (\rho k)$ where α is the Seebeck coefficient, T is the absolute temperature, ρ is the electrical resistivity and k is the thermal conductivity. This is composed of a lattice (k_L) and electronic (k_e) contribution ($k = k_L + k_e$) and typically experimentally determined as $k = dC_P a$ where d is the sample density, C_P the specific heat and a is the thermal diffusivity. The performance can also be assessed through the thermoelectric quality factor $\beta \propto N_V / (m_I^* k_L)$, with N_V band degeneracy, and m_I^* inertial effective mass along the conduction direction, which focuses on the fundamental and most independent material parameters to be optimized [4, 5]. The main approaches that have been investigated to improve the performance include nanostructuring [6, 7], that suppresses the lattice thermal conductivity due to increased density of grain boundaries, chemical doping and ion substitution [8, 9], which can primarily act on m_I^* through tuning of the carrier concentration, and crystal-structure engineering [4, 10]. Regarding this last issue, it has been shown that higher-symmetry structures can improve electronic properties due to band convergence, while typically a reduction of symmetry and larger unit cells can provide a reduction of lattice thermal conductivity [11–15]. Flat electronic bands, instead, can lead to an increase in thermopower due to higher effective band mass, although this typically decreases carrier mobility penalizing electrical conductivity [16].

Kesterite (CZTS, reference formula $\text{Cu}_2\text{ZnSnS}_4$) is a p-type chalcogenide material that has recently gained interest as a thermoelectric [12–14, 17–23], although historically studied for absorber layers in thin film photovoltaic devices [24–26]. CZTS is valued because composed of non-toxic, abundant and low-cost elements [27] as well as for its intrinsic low thermal conductivity [14, 17]. Furthermore, being a quaternary sulfide, it is characterized by a certain crystallographic complexity leading to polymorphism and diverse kinds of defects and disorder [14]. This makes the material interesting for the possibility of tuning electronic and thermal properties through defect engineering. When obtained from high-energy mechanical alloying, CZTS presents a disordered cubic $F\bar{4}3m$ crystal structure. This is similar to a sphalerite ZnS structure where the cation site is randomly occupied by Cu, Zn and Sn (2:1:1), coordinated with the sulfur sublattice. This polymorph, stable up to ~650 K, has been discovered recently [14, 17, 28] and shown to display interesting thermoelectric properties [14]. The generally reported crystallographic structure of kesterite is instead the tetragonal, and assumes an ordered tetragonal crystal structure (s.g. $I\bar{4}$) below 533 K, and a disordered tetragonal ($I\bar{4}2m$) above. The phase transition at 533 K

is known as order-disorder phase transition and causes the Cu^+ and Zn^{2+} cations in the intermediate planes to completely randomize their positions. This causes a remarkable effect on the Seebeck coefficient, which presents a sharp increase at the transition [12]. Recently, we have demonstrated that the transition to the disordered tetragonal polymorph increases the symmetry of the crystal structure thus promoting band convergence (N_V) and flatness, both responsible for the Seebeck enhancement [13].

Due to the low formation energy of the Cu_{Zn} and Zn_{Cu} antisites [29, 30], ambient temperature CZTS always reports some degree of disorder, the amount being dependent on the thermal history of the sample [31]. This transition has been thoroughly investigated for photovoltaic CZTS because deemed responsible for a loss in the open circuit voltage. For this reason, many groups have focused on methods to observe the order-disorder transition and quantify disorder. Some of the techniques that have been proposed are Raman spectroscopy [31, 32], bandgap measurements [33], neutron scattering [34] and solid-state nuclear magnetic resonance [32], but they all involve either expensive and sophisticated instruments, or a low accuracy. Even with neutron scattering techniques, the transition is just visible as a smooth increase in the cell parameters [34, 35]. In this sense the Seebeck coefficient measurement proves to be a simple and effective method [12]. Furthermore, it reveals efficient in observing the transition, as well as estimating the degree of order and phase purity, both affecting the steepness of the increase.

The aim of this work is to provide insights into the order-disorder transition of tetragonal CZTS and to highlight, also through a comparison with literature results, how the effect of the transition on Seebeck coefficient depends on phase purity and degree of order in the sample. Dually, we aim at showing how the thermopower measurement can be used to quantify secondary phases and estimate an order parameter.

Experimental Method

Kesterite sintered disks were produced according to previously described procedures [12, 17], starting from reactive ball milling of the elementary components, i.e., metals and sulfur in stoichiometric proportions. Some of the samples undergone a quenching process in air after the thermal treatment, either starting from the sintering temperature of 560 °C, or from a lower temperature reached with natural cooling, to room temperature. Absolute Seebeck coefficient measurements have been performed in 4-contact configuration and with Pt standard with a Linseis LZT Meter. X-Ray Diffraction (XRD) data have been collected using a Rigaku PMG diffractometer with $\text{Cu K}\alpha$ radiation. A Rietveld refinement of XRD data has been performed with the software TOPAS 7 [36].

Results and Discussion

Thermoelectric Behavior of Kesterite Polymorphs

As mentioned in the introduction, CZTS shows polymorphism. Different arrangements of atoms lead to changes in the chemical bonds inevitably resulting in differences in the electronic and thermal properties. The novel polymorph of low-temperature disordered cubic kesterite ($F-43m$), for example, presents an improvement in all the thermoelectric properties with respect to the ordered phases. This favorable but extremely uncommon condition in thermoelectricity seems to arise from a change in the chemical bond between some Sn atoms and sulfur. Indeed, disorder promotes a lone-pair localization in these Sn atoms leading to a rattling behavior that suppresses the thermal conductivity to ultra-low values. Simultaneously, this localization leads to electron-poor Sn-S bonds which deficiency is compensated by Cu electrons. This favors both the electronic properties as it causes sharp and localized gap states (improving the Seebeck coefficient) acting as acceptors, increasing carrier concentration and conduction, similarly to a p-type doping [14] (Figs. 1, 2 and 3).

Tetragonal kesterite, the commonly reported form, displays instead an order-disorder phase transition at ~ 533 K from the ordered $I-4$ to the disordered $I-42m$ tetragonal structures [31, 37]. It is a second-order and reversible transition [12], consisting in a full occupational disorder of Cu and Zn cations in the $4d$ Wyckoff positions. This transition appears to have a beneficial role for thermoelectric CZTS. Indeed, the measurement of Seebeck coefficient displays a sharp increase around the transition temperature, larger than $100 \mu\text{V/K}$ for our latest samples (see Fig. 4a in Ref. [12]). Many research groups have pointed out that there might be a connection between an increase in the symmetry of a crystal structure and band convergence, leading to a higher thermopower [5, 11, 38]. We have demonstrated that the order-disorder transition of CZTS is an example of this behavior [13]. Indeed, the increase in crystal structure symmetry for the disordered tetragonal polymorphs leads to a modification in the structure of the electronic bands, which tend to converge and flatten. This improves band degeneracy and increases the inertial effective mass of charge carriers, thus justifying the sharp growth of the Seebeck coefficient [12, 13]. As it will be discussed in the following, the manifestation of the order-disorder transition in the Seebeck trend is influenced by the amount of secondary phases and order degree in kesterite samples. These dependences can be used to derive an order parameter from the trend of Seebeck in temperature.

Dependence of Seebeck Coefficient on Phase Purity

Phase purity of samples affects the Seebeck coefficient curve and the appearance of the order-disorder transition. Sample 1, 2, 3, and 4 present different quantities of

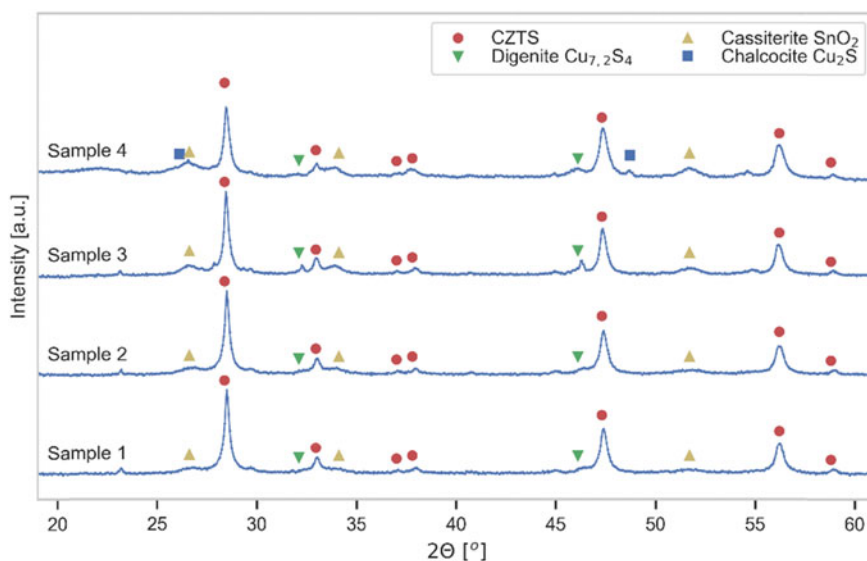


Fig. 1 XRD patterns collected for CZTS samples characterized by a different quantity of secondary phases (From sample 1–4 decreasing CZTS phase purity). Data partially reproduced from Refs. [12, 17]. (Color figure online)

secondary phases, as visible in the XRD patterns of Fig. 1. The samples have been obtained through the same production route, but the CZTS precursor powders were characterized by different levels of humidity. Humidity led to the development of cassiterite SnO_2 during the sintering process, and due to stoichiometry unbalances, CZTS has partially decomposed forming also copper sulfides such as digenite $\text{Cu}_{7.2}\text{S}_4$ and chalcocite Cu_2S . Sphalerite ZnS is probably present as well, to balance the overall stoichiometry, but the reflections of ZnS overlap with those of CZTS so it is not easy to distinguish the two phases with XRD.

A Rietveld refinement was performed on the XRD data and allowed to provide an estimate of the weight fraction for the different phases, visible in Table 1. Fractions of CZTS, tin oxide, and copper sulfides were obtained by the refinement procedure. For a more realistic estimate of CZTS purity, we have assumed a ZnS formation that would balance stoichiometrically the formation of the other secondary phases, and we have deducted this amount from the refined weight fraction of kesterite. The resulting phase purities for CZTS are reported in Table 1, and can be quantified as 81%, 76%, 68%, and 58%, respectively for samples 1, 2, 3 and 4. The main kesterite phase could have resent the formation of secondary phases and therefore partially be off-stoichiometric. A clue in this direction can be noticed in the relative intensity of the diffraction peaks of kesterite: for the less pure sample (sample 4) the first peak is less intense, which can be explained with a lower occupancy of the cation sites (Sn occupation is mainly affecting that peak intensity).

Table 1 Weight fractions (with standard deviation) for the different phases in CZTS samples obtained with a Rietveld refinement of XRD data

	CZTS (refined)	SnO ₂ (refined)	Cu _{7,2} S ₄ (refined)	Cu ₂ S (refined)	ZnS (estimated)	CZTS (estimated)
Sample 1	87(2)	9(1)	4(1)	–	7(3)	81(5)
Sample 2	84(2)	11(1)	5(1)	–	8(3)	76(5)
Sample 3	79(2)	11(1)	10(1)	–	11(2)	68(4)
Sample 4	72(3)	14(4)	7(2)	7(1)	14(4)	58(7)

A corrected CZTS weight fraction has been estimated by subtracting from the refined CZTS phase purity the weight fraction of ZnS, in turn obtained from stoichiometric balance. See text for details

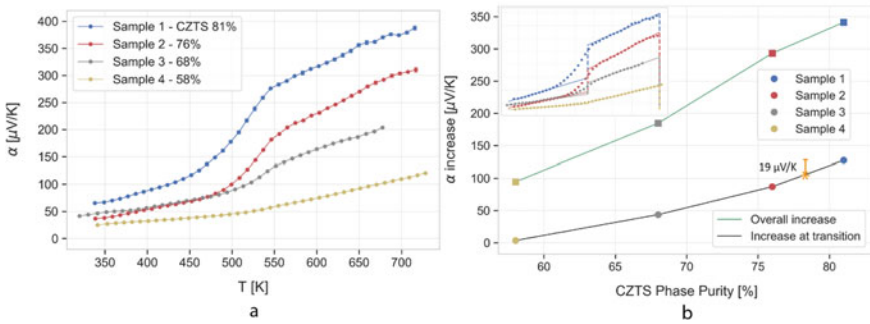


Fig. 2 **a** Absolute Seebeck coefficient measured for CZTS samples characterized by different phase purities (quantity in legend). The increase of Seebeck coefficient due to order-disorder transition gets suppressed as phase purity decreases, and a concurrent general depression of the curve occurs. Data partially reproduced from Refs. [12, 17]. **b** CZTS phase purity versus increase in Seebeck coefficient at the transition temperature (circular markers, solid black trend line) and over the whole temperature range (squared markers, solid green trend line) for the different samples. In the inset, trend lines of Seebeck coefficient for the different samples in the lower and upper temperature regions; the vertical displacements in Seebeck coefficient at the order-disorder transition temperature and through the whole temperature range have been highlighted with a dashed line. (Color figure online)

This dilution of the main CZTS phase has a remarkable effect on Seebeck (Fig. 2a): the order-disorder transition increase appears to be maximum for the purest sample, while it gets dampened as secondary phases increase, up to the point where the order-disorder transition is not visible anymore (sample 4). Furthermore, secondary phases cause a general and evident decrease in the Seebeck coefficient: a decrease of $\sim 20\%$ in the phase purity leads to values that are four times lower (see sample 1 and 4). It is to be stressed that Seebeck measurements of Fig. 2a are performed on samples that have undergone the same cooling history, so are possibly characterized by the same degree of order (see discussion in the next section). These considerations

assume that the formation of secondary phases leaves behind a roughly stoichiometric kesterite. Things might be different, as the remaining CZTS could instead partially be off-stoichiometric and therefore turn into a phase that does not display the order-disorder transition. This would further reduce the weight fraction of pure kesterite and help explaining the strong dependence of Seebeck coefficient on phase purity. Moreover, we are treating secondary phases as a dilution effect without distinguishing between them, which is a coarse simplification as they contribute differently to electrical properties such as thermopower. Nevertheless, this provides the idea of using the dependence to retrieve information on the phase purity of sample. Conversely, achieving a higher phase purity proves to be crucial to improve the thermoelectric performance.

To highlight the dependence of the Seebeck coefficient curve with phase purity, we have evaluated the increase in Seebeck both at the transition and through the whole temperature range. As visible in the inset of Fig. 2b, for each sample it was considered a linear trend of Seebeck coefficient in the lower and upper temperature regions unaffected by the transition, and the vertical displacement at 533 K was taken as the increase of Seebeck at the transition. The general increase of Seebeck was instead determined as the vertical displacement through the whole temperature range. Figure 2b shows the relationship between these vertical displacements and kesterite phase purity. Although we should not treat secondary phases merely as a dilution effect, as things might change according to the kind of secondary phases, these trends give an idea of what is the general effect of a lower phase purity. Furthermore, they could be used to estimate the phase purity of a sample from a Seebeck curve, which is a relatively simple and straightforward measurement.

Retrieval of an Order Parameter from Seebeck Curve

Kesterite is currently subject of intense studies as a possible absorber layer for thin film photovoltaic cells. In this sector, several studies have been conducted to identify the most suitable methods to estimate the degree of order of the samples, as disorder is considered one of the major causes of solar-cell efficiency losses. Anyway, it has proved hard to find an appropriate method to clearly distinguish between samples with different degrees of order. Indeed, diffraction is unsuitable to observe Cu-Zn disorder, as Cu^+ and Zn^{2+} are isoelectronic, so appear identical to X-rays. Other proposed techniques rely either on relatively weak signals, as Raman spectroscopy (via the quantification of the relative intensity of secondary peaks) [31, 37, 39, 40] and optical measurements [33, 41] (through slight differences in the bandgap), or require complex and expensive setups, as solid-state nuclear magnetic resonance [32] and neutron scattering [34]. In this context, we propose the Seebeck coefficient to identify and possibly quantify order in CZTS.

Experimental results show that the extent of the transition depends on the initial degree of order in the sample. Figure 3a shows the trends of Seebeck coefficient for some CZTS samples that have undergone different cooling processes, as the thermal

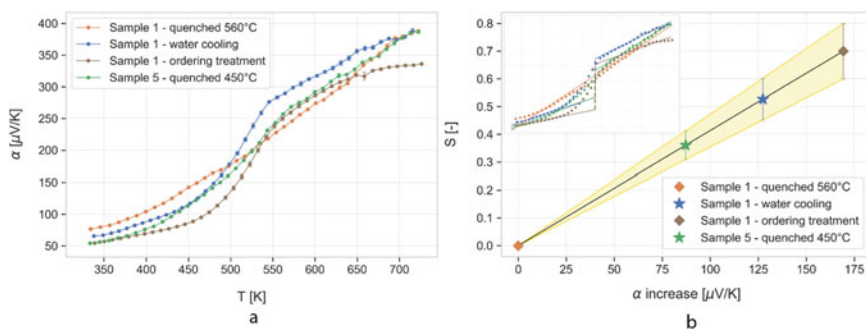


Fig. 3 **a** Absolute Seebeck coefficient α for some CZTS samples: quenched from 560 °C to preserve the disordered state, for the same sample after water cooling, for the same sample after an ordering treatment at 120 °C for 100 h, and for a another sample (sample 5), characterized by an intermediate disorder state. Data partially reproduced from Refs. [12, 13] with permission from MDPI and ACS. Copyright 2020 American Chemical Society. **b** Determination of the relationship between increase in Seebeck coefficient at the transition and order parameter S . The degree of order of the first and last points of the graph is given, and a linear relationship is assumed. This allows the determination of S for the other two samples. The golden area gives the confidence interval of results that is achieved assuming for sample 1 after the ordering treatment S in the range 0.6-0.8 (see text for further details). In the inset, trend lines of thermopower in the lower and upper temperature regions are plotted to show how the vertical displacement in Seebeck at the order-disorder transition temperature has been calculated (dashed lines). (Color figure online)

history of a sample greatly influences the degree of order [31, 37]. Sample 1 has been quenched from the sintering temperature of 560 °C to retain a fully disordered state. Indeed the sample, when heated up for the measurement, displays a flat trend of Seebeck coefficient with no sign of transition [12]. After the measurement, this same sample was cooled down slowly to room temperature (water cooled furnace, ~2 h long). On a second measurement, the Seebeck coefficient exhibits a sharp increase at the transition, pointing out that the slow cooling promoted a more ordered state in sample 1. Sample 5 has instead been obtained by natural cooling from the sintering temperature to 450 °C, followed by quenching to ambient temperature. This process leads to a partly disordered state, as the Seebeck coefficient curve shows only a small increase at the transition. It is to be remarked that sample 1–quenched, sample 1–after water cooling and sample 5–quenched, all present a comparable kesterite phase purity (~81% in weight). An ordering treatment has then been performed on sample 1 following literature guidelines [31] (annealing at 120 °C for 100 h in N_2 atmosphere). The measurement after this treatment displays the largest increment in the Seebeck coefficient at the transition, but generally depressed values with respect to the previous measurements. We attribute this to a development of secondary phases during the thermopower measurements and/or long annealing treatment (confirmed by XRD measurements of Fig. 4, see following discussion).

A long-range order parameter S can be introduced to express the degree of order, which ranges from $S=0$, meaning full disorder, to $S=1$, perfect order. It is defined in Eq. (1), where $P(\text{Cu}_{2c})$ is the probability of a Cu atom to be in its original $2c$ site,

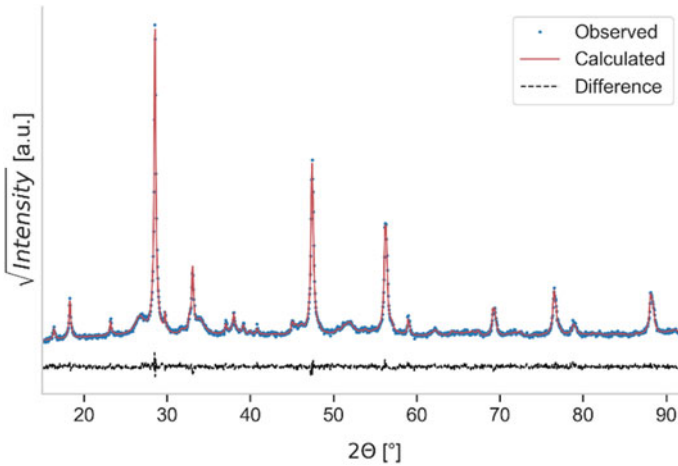


Fig. 4 Rietveld refinement of XRD data performed for sample 1-after the ordering treatment to allow for a phase purity estimation. Measured data (dotted blue), calculated profile (solid red) and difference (dashed black) are shown. (Color figure online)

$P(\text{Zn}_{2d})$ is the probability of a Zn atom to be in its original $2d$ site (being for both cases 0.5 for disordered, 1 for ordered), and a_{2c} is the total fraction of $2c$ site in the intermediate planes (at $z = 1/4$ and $z = 3/4$), being equal to 0.5 for a stoichiometric material [31].

$$S = \frac{P(\text{Cu}_{2c}) - a_{2c}}{1 - a_{2c}} = 2P(\text{Cu}_{2c}) - 1 = 2P(\text{Zn}_{2d}) - 1 \quad (1)$$

The maximum order that a sample can achieve depends on the temperature and thermal history, and perfect order is thought to be achieved only in the limit of an infinitely long cooling process down to 0 K [37]. The model that we propose to estimate the order parameter uses the increase of Seebeck coefficient at the transition as a second-order parameter. A linear interpolation of the lower and upper temperature regions of the Seebeck curve is used to determine the increase of thermopower at 533 K (see inset of Fig. 3b, where the trend lines and increase at transition are sketched). Sample 1 after the quenching from 560 °C has been assumed to be in a fully disordered state, therefore the order parameter is $S = 0$. And the increase in Seebeck at the transition for this sample is in fact 0 $\mu\text{V}/\text{K}$. For sample 1 after the ordering treatment, instead, an order parameter of $S = 0.7(1)$ was hypothesized, following the literature results for samples that undergone comparable ordering treatments [31]. A large confidence range has been considered to account for the effect of secondary phases and of a different production route with respect to the literature. The XRD pattern with Rietveld refinement for sample 1-after the ordering treatment is shown in Fig. 4. The estimated kesterite phase purity is 78(5)%, while, to be consistent with the other data of Fig. 3, the phase purity should have been 81%. For this reason,

in the determination of the Seebeck increase at the transition for sample 1-after the ordering treatment, we have added to the measured value ($150 \mu\text{V/K}$), an additional quota of $19 \mu\text{V/K}$ to compensate for this loss in phase purity, as illustrated in Fig. 2b (additional quota shown in orange). The trend of the order parameter, assuming a linear relationship with the increase in Seebeck coefficient, is shown in Fig. 3b. The solid black line is obtained with the assumption of $S = 0.7$ for sample 1-after the ordering treatment, while the golden area is the confidence interval of the results obtained assuming S in the range 0.6–0.8. This relationship allows us to estimate an order parameter of $S = 0.53(8)$ for sample 1-after water cooling and of $S = 0.36(5)$ for sample 2.

Seebeck Coefficient as an Effective Method to Observe and Distinguish the Effects of Phase Purity and Degree of Order

Both degree of order and phase purity appear to influence the behaviour of Seebeck coefficient in temperature. In the literature, different trends are reported for the Seebeck coefficient of CZTS, ranging from a flat curves (Liu et al. [18] and Yang et Al. [19]) to trends where the order-disorder transition increase is instead clearly visible (Sharma et al. [21, 22]). Given the experimental evidence presented here, we believe the cause of this divergence of results to be connected with differences in the degree of order and phase purity. Samples from the literature, characterized by different production processes and thermal histories, would differ in terms of degree of order and phase purity leading to diverse shaping of the Seebeck curve. Nevertheless, these strong dependences can be exploited to retrieve information on the sample. The Seebeck coefficient measurement proves to be suitable to not only to observe the transition, but also to estimate degree of order and phase purity. It is worth noticing that this method allows to distinguish among the two cases. In fact, a lower degree of order alone dampens the thermopower steepness at the transition (or, specifically, dampens the second derivative) but has little or no effects on the high-temperature values of Seebeck. Inversely, secondary phases appear to affect more the overall steepness of the curve, as they cause a general decrease in thermopower, if nothing else, for a dilution effect of the main CZTS phase.

Conclusion

In this work we have examined the effects of the order-disorder transition of CZTS on thermopower, which displays a sharp increase around 533 K. We have highlighted and distinguished the influence of degree of order and presence of secondary phases. A different level of order causes the increase of Seebeck coefficient characteristic of

the transition to be more (for more ordered) or less (for less ordered) sharp, up to disappear for completely disordered samples. This feature alone appears to not have an influence on the low and high-temperature values of Seebeck coefficient. A higher amount of secondary phases, instead, generally lowers the Seebeck coefficient curve and dampens the increase of the order-disorder transition. The curve of samples with a phase purity that is ~58% look almost flat and the maximum value of Seebeck coefficient is four times lower than the value of Seebeck for an 81% pure sample. These dependences help to understand why different authors in the literature report different trends for the Seebeck coefficient of CZTS, where not always the order-disorder transition is visible. The measurement of Seebeck coefficient has revealed to be a simple and efficient method to observe the order-disorder transition of kesterite. With this work we put forward it can also be used to estimate the phase purity and, separately, to evaluate the degree of order through the retrieval of an order parameter.

Acknowledgements This research was funded by the Autonomous Province of Trento, within the framework of the programmatic Energy Action 2015–2017. N.M.P. is supported by the European Commission under the FET Open (Boheme) grant No. 863179.

References

1. Seebeck TJ (1826) Ueber Die Magnetische Polarisation Der Metalle Und Erze Durch Temperaturdifferenz [Magnetic polarization of metals and ores by temperature differences], *Abhandlungen Der K. Akad. Der Wissenschaften Zu Berlin* (in Ger. 82:265
2. Peltier JCH (1834) Nouvelles Expériences Sur La Caloricité Des Courants Électrique [New experiments on the heat effects of electric currents]. *Ann Chim Phys* (in French) 56:371
3. Beretta D, Neophytou N, Hodges JM, Kanatzidis MG, Narducci D, Martin-Gonzalez M, Beekman M, Balke B, Cerretti G, Tremel W, Zevalkink A, Hofmann AI, Müller C, Döring B, Campoy-Quiles M, Caironi M (2018) Thermoelectrics: from history, a window to the future. *Mater Sci Eng R Reports*
4. Zeier WG, Snyder GJ, Zevalkink A, Gibbs ZM, Hautier G, Kanatzidis MG (2016) Thinking like a chemist: intuition in thermoelectric materials. *Angew Chemie Int Ed* 55:6826
5. Zeier WG (2017) New tricks for optimizing thermoelectric materials. *Curr Opin Green Sustain Chem* 4:23
6. Poudel B, Hao Q, Ma Y, Lan Y, Minnich A, Yu B, Yan X, Wang D, Muto A, Vashaee D, Chen X, Liu J, Dresselhaus MS, Chen G, Ren Z (2008) High-thermoelectric performance of nanostructured bismuth antimony telluride bulk alloys. *Science* (80-.) 320:634
7. Rowe DM (2012) Thermoelectrics and its energy harvesting
8. Sootsman JR, Chung DY, Kanatzidis MG (2009) New and old concepts in thermoelectric materials. *Angew Chemie - Int Ed* 48:8616
9. Chmielowski R, Bhattacharya S, Jacob S, Péré D, Jacob A, Moriya K, Delatouche B, Roussel P, Madsen G, Dennler G (2017) Strong reduction of thermal conductivity and enhanced thermoelectric properties in $\text{Cosbs}_{1-x}\text{Sex}$ paracostibite. *Sci Rep* 7:1
10. Snyder GJ, Toberer ES (2008) Complex thermoelectric materials. *Nat Mater* 7:105
11. Zeier WG, Zhu H, Gibbs ZM, Ceder G, Tremel W, Snyder GJ (2014) Band convergence in the non-cubic chalcopyrite compounds $\text{Cu}_2\text{MGeSe}_4$. *J Mater Chem C* 2:10189
12. Isotta E, Fanciulli C, Pugno NM, Scardi P (2019) Effect of the order-disorder transition on the seebeck coefficient of nanostructured thermoelectric $\text{Cu}_2\text{ZnSnS}_4$. *Nanomaterials* 9:762

13. Isotta E, Mukherjee B, Fanciulli C, Pugno NM, Scardi P (2020) Order-disorder transition in Kesterite $\text{Cu}_2\text{ZnSnS}_4$: thermopower enhancement via electronic band structure modification. *J Phys Chem C* 124:7091
14. Isotta E, Mukherjee B, Fanciulli C, Ataollahi N, Sergueev I, Stankov S, Edla R, Pugno NM, Scardi P (2020) Origin of a simultaneous suppression of thermal conductivity and increase of electrical conductivity and seebeck coefficient in disordered cubic $\text{Cu}_2\text{ZnSnS}_4$. *Phys Rev Appl* 14:064073. <https://doi.org/10.1103/PhysRevApplied.14.064073>
15. Lohani K, Isotta E, Ataollahi N, Fanciulli C, Chiappini A, Scardi P (2020) Ultra-low thermal conductivity and improved thermoelectric performance in disordered nanostructured copper tin sulphide (Cu_2SnS_3 , CTS). *J Alloys Compd* 830:154604
16. Pei Y, Wang H, Snyder GJ (2012) Band engineering of thermoelectric materials. *Adv Mater* 24:6125
17. Isotta E, Pugno NM, Scardi P (2019) Nanostructured kesterite ($\text{Cu}_2\text{ZnSnS}_4$) for applications in thermoelectric devices. *Powder Diffr.* 0:2
18. Liu ML, Huang FQ, Chen LD, Chen IW (2009) A wide-band-gap p-type thermoelectric material based on quaternary chalcogenides of $\text{Cu}_2\text{ZnSnQ}_4$ (Q = S, Se). *Appl Phys Lett* 94:202103
19. Yang H, Jauregui LA, Zhang G, Chen YP, Wu Y (2012) Non-toxic and abundant copper zinc tin sulfide nanocrystals for potential high temperature thermoelectric energy harvesting. *Nano Lett*
20. Kumar S, Ansari MZ, Khare N (2018) Influence of compactness and formation of metallic secondary phase on the thermoelectric properties of $\text{Cu}_2\text{ZnSnS}_4$ thin films. *Thin Solid Films* 645:300
21. Sharma SD, Neeleshwar S (2018) Thermoelectric properties of hot pressed CZTS micro spheres synthesized by microwave method. *MRS Adv* 3:1373
22. Sharma SD, Khasimsaheb B, Chen YY, Neeleshwar S (2019) Enhanced thermoelectric performance of $\text{Cu}_2\text{ZnSnS}_4$ (CZTS) by incorporating Ag nanoparticles. *Ceram Int* 45:2060
23. Jiang Q, Yan H, Lin Y, Shen Y, Yang J, Reece MJ (2020) Colossal thermoelectric enhancement in $\text{Cu}_2 + x\text{Zn}1 - x\text{SnS}_4$ solid solution by local disordering of crystal lattice and multi-scale defect engineering. *J Mater Chem A* 8:10909
24. Katagiri H, Jimbo K, Yamada S, Kamimura T, Maw WS, Fukano T, Ito T, Motohiro T (2008) Enhanced conversion efficiencies of $\text{Cu}_2\text{ZnSnS}_4$ -based thin film solar cells by using preferential etching technique. *Appl Phys Express* 1:0412011
25. Ataollahi N, Malerba C, Ciancio R, Edla R, Scardi P, Cappelletto E, Di Maggio R (2019) Control of composition and grain growth in $\text{Cu}_2\text{ZnSnS}_4$ thin films from nanoparticle inks. *Thin Solid Films* 674:12
26. Syafiq U, Ataollahi N, Di Maggio R, Scardi P (2019) Solution-based synthesis and characterization of $\text{Cu}_2\text{ZnSnS}_4$ (CZTS) thin films. *Molecules* 24:3454
27. S. Adachi (2015) Earth-abundant materials for solar cells
28. Kapusta K, Drygas M, Janik JF, Jelen P, Bucko MM, Olejniczak Z (2019) From magnetic cubic pre-kesterite to semiconducting tetragonal kesterite $\text{Cu}_2\text{ZnSnS}_4$ nanopowders via the mechanochemically assisted route. *J Alloys Compd* 770:981
29. Chen S, Gong XG, Walsh A, Wei S (2010) Defect physics of the kesterite thin-film solar cell absorber. *Appl Phys Lett* 96:021902
30. Chen S, Walsh A, Gong X, Wei S (2013) Classification of lattice defects in the Kesterite $\text{Cu}_2\text{ZnSnS}_4$ and $\text{Cu}_2\text{ZnSnSe}_4$ earth-abundant solar cell absorbers. *Adv Mater* 1522
31. Scragg JJS, Larsen JK, Kumar M, Persson C, Sendler J, Siebentritt S (2016) Cu–Zn Disorder and Band Gap Fluctuations in $\text{Cu}_2\text{ZnSn(S, Se)}_4$: Theoretical and Experimental Investigations. *Phys Status Solidi B* 253:247
32. Paris M, Lafond A, Guillot-deudon C (2014) Solid-state NMR and Raman spectroscopy to address the local structure of defects and the tricky issue of the Cu/Zn disorder in Cu-poor, Zn-rich CZTS materials. *Inorg Chem* 53:8646
33. Valentini M, Malerba C, Menchini F, Tedeschi D, Polimeni A, Capizzi M, Mittiga A (2016) Effect of the order-disorder transition on the optical properties of $\text{Cu}_2\text{ZnSnS}_4$. *Appl Phys Lett* 108:211909

34. Ritscher A, Hoelzel M, Lerch M (2016) The order-disorder transition in $\text{Cu}_2\text{ZnSnS}_4$ —A neutron scattering investigation, *J Solid State Chem* 238
35. Schorr S, Gonzalez-Aviles G (2009) In-situ investigation of the structural phase transition in kesterite. *Phys Status Solidi Appl Mater Sci* 206:1054
36. Coelho AA (2018) TOPAS and TOPAS-Academic: An optimization program integrating computer algebra and crystallographic objects written in C++. *J Appl Crystallogr* 51:210
37. Scragg JJS, Choubrac L, Lafond A, Ericson T, Platzer-Björkman C (2014) A low-temperature order-disorder transition in $\text{Cu}_2\text{ZnSnS}_4$ thin films. *Appl Phys Lett* 104:041911
38. Zhang Q, Song Q, Wang X, Sun J, Zhu Q, Dahal K, Lin X, Cao F, Zhou J, Chen S, Chen G, Mao J, Ren Z (2018) Deep defect level engineering: a strategy of optimizing the carrier concentration for high thermoelectric performance. *Energy Environ Sci* 11:933
39. Rudisch K, Ren Y, Platzer-Bjorkman C, Scragg J (2016) Order-disorder transition in B-Type $\text{Cu}_2\text{ZnSnS}_4$ and limitations of ordering through thermal treatments. *Appl Phys Lett* 231902
40. Rudisch K, Davydova A, Platzer-björkman C (2018) The effect of stoichiometry on Cu-Zn ordering kinetics in $\text{Cu}_2\text{ZnSnS}_4$ thin films 161558
41. Malerba C, Valentini M, Mittiga A (2017) Cation disorder in $\text{Cu}_2\text{ZnSnS}_4$ thin films: effect on solar cell performances. *Sol RRL* 1:1700101

Part XX
Biological Materials Science

Effect of Cobalt Metal on the Microstructure of Titanium Foam



Hanghang Zhou, Guibao Qiu, Ding Yang, and Tengfei Lu

Abstract Titanium foam has good biocompatibility and mechanical properties, and is often used as a bone replacement material. Cobalt can improve the density of titanium foam cell walls and help improve mechanical properties. In this paper, the effect of different cobalt contents on the microstructure of titanium foam was studied. Six sets of comparative experiments with different cobalt contents were carried out. The sintering temperature was 1100 °C and the holding time was 1.5 h. The samples were subjected to metallographic and SEM inspection. Between 0 and 10%, with the increase of cobalt content, the pores gradually become denser, which helps to improve the mechanical properties. Excessive cobalt powder will lead to the closure of microscopic pores, and the connectivity between the pores becomes poor. When the cobalt content increases from 10 to 14%, the porosity of titanium foam decreases from 45% to about 20%.

Keywords Titanium · Cobalt · Powder metallurgy · Porosity

Introduction

Metal titanium is often used in aerospace, automotive, biomedicine and other fields due to its advantages of low density, high specific strength, non-magnetic, corrosion resistance, good biocompatibility, and easier processing and forming [1–3]. With the advancement of science, higher requirements have been placed on the performance of materials. Titanium-based composite material is formed by adding a certain low-density, high-modulus and high-strength material as a reinforcement to a titanium alloy matrix [4, 5]. Compared with traditional titanium alloys, titanium-based composite materials have been enhanced in terms of specific strength, corrosion resistance, high temperature performance and biocompatibility, and can be used as structural materials in more complex environments, expanding the application of titanium materials field [6–9].

H. Zhou · G. Qiu (✉) · D. Yang · T. Lu

College of Materials Science & Engineering, Chongqing University, Chongqing 400044, China
e-mail: qiuuibao@cqu.edu.cn

© The Minerals, Metals & Materials Society 2021

TMS 2021 150th Annual Meeting & Exhibition Supplemental Proceedings,

The Minerals, Metals & Materials Series,

https://doi.org/10.1007/978-3-030-65261-6_49

The shortcomings of pure titanium are poor wear resistance and fracture resistance [10], but the addition of alloy elements can effectively improve the wear resistance and fracture resistance, and other properties will be further improved. The porous titanium alloy material has a structure of connected pores, allowing the growth of new bone cell tissue and the transmission of human tissue fluid. The three-dimensional porous structure can promote the growth of osteoblasts on the surface and pores of titanium and titanium alloy materials, and new bone tissue is implanted. The growth in the implant pores forms a staggered link state, which can strengthen the bonding strength between the implant and the human bone [11–13].

Metal cobalt is a metal with strong wear resistance, which can effectively improve the shortcomings of poor wear resistance of pure titanium [14]. In the preparation process of porous titanium, cobalt is used as an alloy element, which can make the porous titanium alloy matrix contain uniformly distributed titanium-cobalt intermetallic compounds, which can play a strengthening role. On the other hand, cobalt is the main component of vitamin B12, has hematopoietic function, can promote the metabolism of various substances, and is listed as an essential trace element for the human body [15, 16]. No matter from the point of view of medical application or material strengthening, metallic cobalt is a very suitable alloying element. This paper uses powder metallurgy to prepare titanium-cobalt alloy materials, and studies the effect of metallic cobalt on the microstructure of titanium foam.

Experimental

In this paper, urea is selected as the pore former, and the volume fraction of urea is controlled to 60%. In order to study the effect of different metal cobalt content on the microstructure of titanium alloys, 6 sets of experiments with different cobalt content were designed, and the cobalt mass fractions were 0, 6, 8, 10, 12, 14 wt%, as shown in Table 1, at the same time each group of experiments were repeated 3 times to reduce the experimental error. In order to mix the titanium and cobalt powders uniformly, a ball mill was used to mix the prepared powders at a rate of 200 r/min

Table 1 The compositions of porous titanium cobalt alloys

Sample number	Nominal compositions	Mass fraction (wt%)		Urea content (vol%)
		Ti	Co	
1#	Ti-0Co	100	0	60
2#	Ti-6Co	94	6	
3#	Ti-8Co	92	8	
4#	Ti-10Co	90	10	
5#	Ti-12Co	88	12	
6#	Ti-14Co	86	14	

for 2 h to make the cobalt and titanium powders uniformly mixed. At the same time, argon gas is used to protect it to prevent titanium and cobalt from being oxidized.

The uniformly mixed materials are pressed into a shape under a pressing pressure of 150 MPa, and a layer of zinc stearate is applied as a lubricant when using the mold. Finally, the obtained green compacts with different alloy compositions were raised from room temperature to 400 °C in a vacuum carbon tube furnace and held for 60 min to ensure complete removal of urea. After that, the temperature was raised to 1100 °C for high temperature sintering for 1.5 h, and the furnace cooled to obtain porous. The temperature rise curve of titanium-cobalt alloy is shown in Fig. 1.

The sintered samples are shown in Fig. 2. From left to right in the figure are 1# ~ 6# samples. The surface of the material has a metallic luster and good quality, indicating that it was not contaminated during the sintering process. At the same time, it can be seen that the surface is distributed with small pores, and the material

Fig. 1 Heating profile of porous material preparation

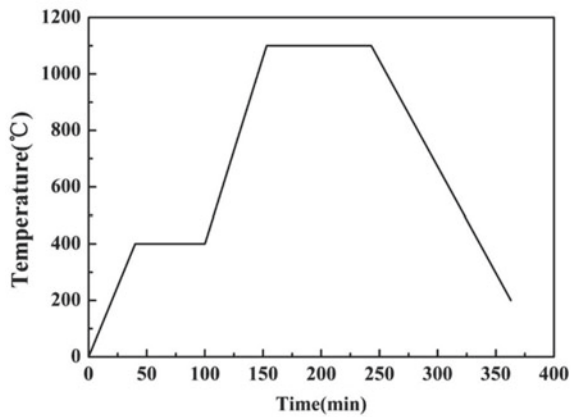
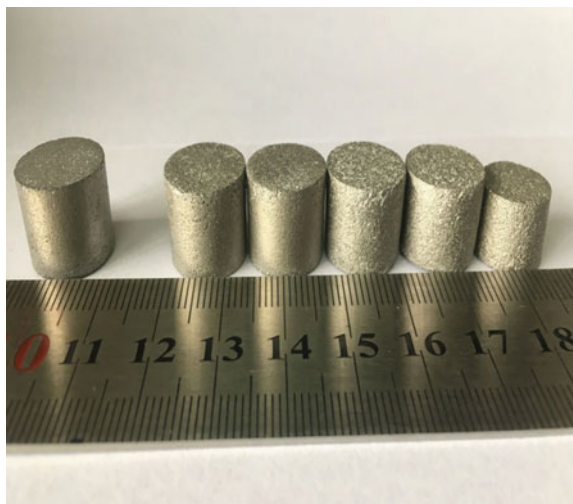


Fig. 2 Macroscopic morphology of porous titanium and porous titanium-cobalt alloys. (Color figure online)



has obvious pore characteristics, and as the cobalt content increases, the number of pores that can be observed on the surface is also greater. In addition, with the increase of the cobalt content, the volume of the sample has a tendency to gradually shrink, especially the 6# sample shrinks the most.

Results and Discussion

The sample obtained after sintering was cut in half transversely, and the internal microstructure was observed by SEM. Figure 3 is a diagram of the pore wall structure of the porous material. In the figure, a, b, c, and d are the SEM observation results of the addition of cobalt powder at 0 wt%, 6 wt%, 10 wt%, and 12 wt% respectively. As shown in the figure, as the content of cobalt powder increases, the number of microscopic pores in the pore wall of the porous material gradually decreases, and the pores on the pore wall also have a tendency to grow. The thickness of the pore wall increases when the cobalt content is less than 10 wt%. The general trend is not obvious, but when the cobalt powder content reaches 12 wt%, the pore wall thickness increases significantly. There are a large number of irregular pores and micropores distributed on the pore wall of pure porous titanium. With the increase of alloying elements, the pore wall can be clearly seen (the arrow refers to the figure): 1. Small

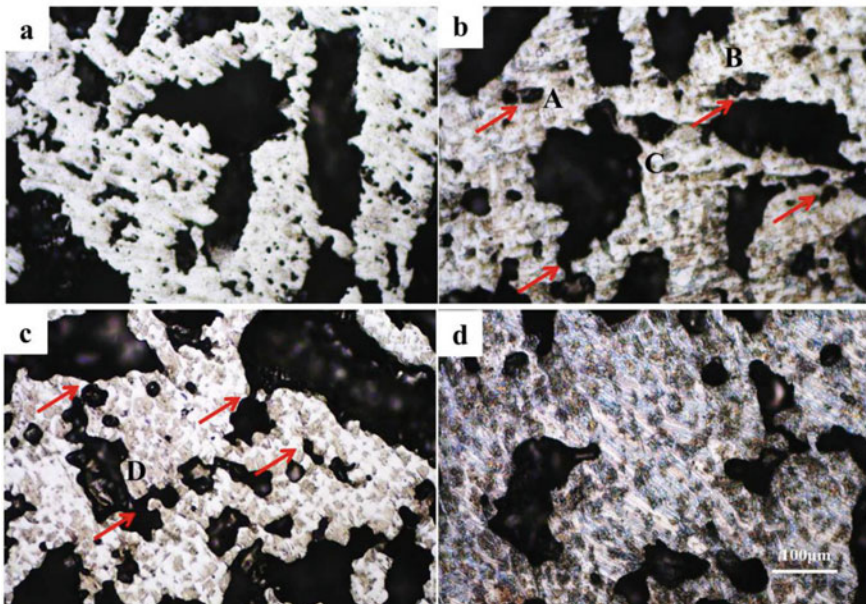


Fig. 3 Change of pore wall structure of porous materials **a** Ti-0Co; **b** Ti-6Co; **c** Ti-10Co; **d** Ti-12Co. (Color figure online)

holes on the pore wall. The pores are enlarged by mutual fusion, and a large number of microscopic pores are closed. The positions a and b in the figure show the state of pore fusion just finished. 2. The diffusion of atoms promotes the continuous smoothing of the edge of the hole, and also makes the small holes on the edge of the hole wall merge with each other. At the same time, it gradually approaches and merges to the large hole, changing from a closed cell to a structure with more than two holes interconnected., D shows this change process. Therefore, when the content of cobalt is less than 10 wt%, although in the pore structure, the small pores and micropores on the pore wall merge and close together so that the porosity decreases, but the size of the macroscopic macropores increases to a certain extent. Structural connectivity has improved. When the added amount of cobalt powder reaches 12 wt%, there are almost no microscopic pores in the pore wall, and the size of macroscopic pores is also greatly reduced.

Figure 4 shows the influence of different amounts of cobalt powder on the microstructure of porous materials. In the figure, a, b, c, d, e, and f correspond to the mass fractions of cobalt powder as 0 wt%, 6 wt%, 8 wt%, 10 wt%, 12 wt%, respectively. Samples prepared under 14 wt%.

The porous materials are all sintered under the same process. In the figure, a is the microstructure of pure porous titanium after sintering. The particles are connected to each other by sintering necks of different thicknesses, and there is a large amount of uneven distribution between the sintering necks. Microscopic pores of various sizes. In the microscopic group of samples b, c, and d, it can be seen that with the addition

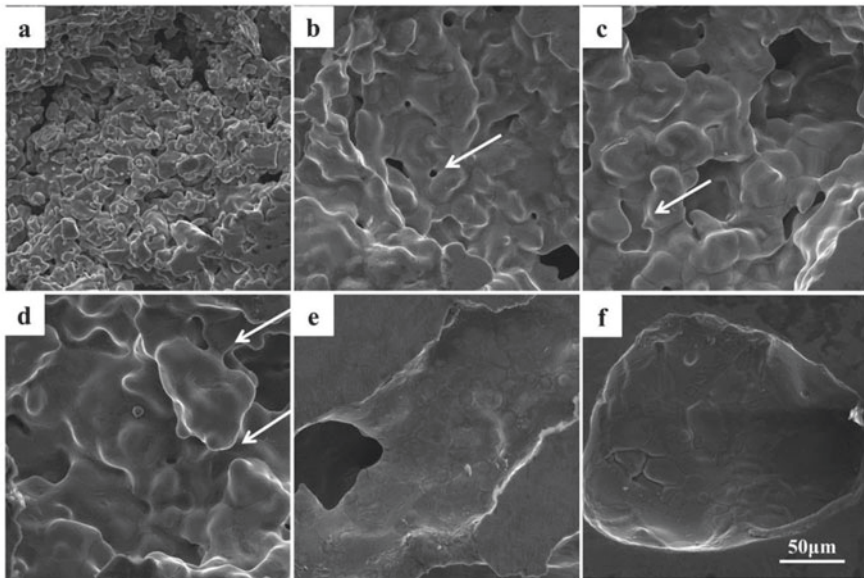


Fig. 4 Effect of different cobalt content on microstructure a Ti-0Co; b Ti-6Co; c Ti-8Co; d Ti-10Co; e Ti-12Co; f Ti-14Co

of cobalt, the sintering neck between the powder particles gradually becomes larger, the mutual fusion between the particles is more obvious, and the edges are passivated. The effect continues to increase, and the edges of the holes are further smoothed; a large number of microscopic pores left by the sintering of powder particles are closed and even merged with each other, as indicated by the arrow in the figure. The results show that with the addition of cobalt powder, the sintering quality is good, and the density of the pore walls increases. However, when the mass fraction of cobalt powder reaches 12 wt% and 14 wt%, the sintered neck structure formed by the granular connection is almost invisible on the pore wall, showing a smooth entire surface connection state, indicating that more liquid is produced during the sintering process. Phase, the atom has undergone a violent diffusion phenomenon.

From the analysis of the microstructure of the porous titanium-cobalt alloy, it can be seen that when the added mass fraction of cobalt powder is between 0 and 10 wt%, the sintering quality of the porous material has been significantly improved. This improvement effect mainly comes from the result of mutual diffusion of titanium and cobalt atoms at high temperatures. When 1020 °C, Co can be dissolved in β -Ti to a maximum of 14.5%, which makes the maximum amount of 14 wt% cobalt fully dissolved in β -Ti when the sintering temperature is 1100 °C, while adding alloy The element cobalt reduces the liquidus of the alloy, and the presence of cobalt increases the diffusion coefficient of the system at any temperature. Therefore, the diffusion coefficient of the alloy increases sharply with the increase of the cobalt content. The solute element cobalt can quickly fill the microscopic pores between the sintering necks, or promote the convective diffusion of solvent atoms and solute atoms to make the microscopic pores move, merge with each other or merge. Into the macroscopic large pores, but when the cobalt element is excessive, the severity of the above process will be greatly increased, and the sintering neck formed at the initial stage of sintering will be rapidly coarsened, and even the surface of a large number of particles will melt. Generally speaking, an appropriate amount of cobalt can promote the densification of the tissue while maintaining a good pore structure.

Conclusions

The addition of the alloying element cobalt can effectively increase the diffusion coefficient of the system.

- (1) The cobalt content is between 0 and 10 wt%. The macroscopic macropores of porous materials have little tendency to change, mainly reflected in the shrinkage and closure of small pores and micropores on the pore wall. With the increase of cobalt content, the pores The sintering neck on the wall is getting bigger and bigger, the micropores tend to be spheroidized, the number of small holes and micropores is greatly reduced.

- (2) When the cobalt content is 12 wt%, there are almost no microscopic pores on the pore wall, and the macroscopic pores tend to shrink, the pore wall is smooth, and the sintering neck tends to melt.
- (3) However, when the cobalt content is further increased to 14 wt%, a large amount of liquid phase is generated in the system, which causes a large number of macroscopic pores to shrink and close, and a large loss of porosity.

Acknowledgements The work described in this paper was supported by a grant from the Natural Science Foundation of China (Project no. 51674055).

References

1. Xinming R, Beiyue M, Bowen Z, Yaran Z, Jingkun Y (2017) Research progress of laser cladding coatings on titanium alloy and steel surface. *Mater Res Appl* 11(03):141–145+152
2. Guangming X, Jianqiao Z, Xiaobing M, Jing L (2012) Overview of coating technology and its engineering application. *Metallic Mater Metall Eng* 40(01):53–59
3. Beiyue Ma, Zhang Bowen Yu, Xuanhui Jingkun, Qu (2016) Progress in 3D printing technology and advanced applications. *Mater Res Appl* 10(04):233–237
4. Yuanfei H, Peikun Q, Xianglong S, Jiahao F, Liqiang W, Weijie L (2016) Preparation technology and research progress of discontinuous particle reinforced titanium matrix composites. *Aviat Manuf Technol* 2016(15):62–74
5. Shifeng Liu, Xi Song, Tong Xue, Ning Ma, Yan Wang, Liqiang Wang (2020) Application and development of titanium alloys and titanium-based composite materials in aerospace. *J Aeronaut Mater* 40(03):77–94
6. Yucheng Yang, Pan Yu, Lu Xin Yu, Aihua Hui Tailong, Yanjun Liu (2020) Research progress in the preparation of particle-reinforced titanium matrix composites by powder metallurgy. *Powder Metall Technol* 38(02):150–158
7. Yongtao Z, Hanyuan L, Chang W, Jun C, Jin S, Lan W, Zhentao Y (2017) The research and application status and development trend of biomedical metal materials. *Therm Process Technol* 46(04):21–26
8. Jianhong Wen, Guanjun Yang, Peng Ge, Xiaonan Mao, Yinghui Zhao (2008) Research progress of β titanium alloys. *Titanium Ind Prog* 01:33–39
9. Jie Yu, Mingkan Zhu, Ming Wen, Junmin Zhang (2017) Research progress of new medical titanium alloy materials. *J Kunming Univ Sci Technol (Nat Sci Ed)* 42(03):16–22
10. Lianpeng Fan, Huiping Shao, Donghua Yang, Zhimeng Guo, Tao Lin (2010) The effect of cobalt on gel injection molding of medical implanted titanium alloy materials. *Powder Metall Ind* 20(04):38–42
11. Haibo H, Huiqun L, Jieen W, Danqing Y, Shang F, Wuling S (2012) Research progress of biomedical porous titanium and titanium alloys. *Mater Rev* 26(S1):262–266+270
12. Jiangang Jia, Yongzhi Jing, Changqi Gao, Chang Liu, Genshun Ji, Tieming Guo (2019) Preparation methods and development of porous titanium materials for bone transplantation. *Chin J Nonferrous Metals* 29(06):1187–1197
13. Changjun Chen, Chao Zhang, Xiaonan Wang, Min Zhang, Hemin Jing (2014) Research progress in the preparation of biomedical porous tantalum. *Therm Process Technol* 43(04):5–8
14. Aihua Wu, Jiancheng Tang, Deqing Qin, Chunpeng Lei (2014) Development status of cobalt powder for cemented carbide. *Jiangxi Sci* 32(04):433–438

15. Yanhui W, Xuejun. W (2015) The biological effects of trace element cobalt and its application in livestock and poultry production. *Feed Expo* 06:10–13
16. Maojiang Wu (2013) Cobalt and human health. *Res Race Elem Health* 30(04):61–62

Part XXI
Characterization of Nuclear Materials
and Fuels with Advanced X-ray
and Neutron Techniques

Non-destructive Correlative 3D Characterization of Nuclear Graphite: From the Micro-scale to the Nano-scale



Stephen Kelly, Robin White, William Harris, Tobias Volkenandt,
Benjamin Tordoff, Giuliano Laudone, Katie Jones, and Ben Veater

Abstract Graphite is a key material in the design and operation of a wide range of nuclear reactors because of its attractive combination of thermal, mechanical, and neutron interaction properties. In all its applications, the microstructural evolution of nuclear graphite under operating conditions will strongly influence reactor lifetime and performance. However, measuring the 3D microstructural characteristics of nuclear graphite has traditionally faced many challenges. X-ray tomographic techniques face limitations in achievable resolution on bulk (mm-sized) specimens while serial sectioning techniques like FIB-SEM struggle to achieve adequate milling rates for tomographic imaging over representative volumes. To address these shortcomings, we present here a multiscale, targeted, correlative microstructural characterization workflow for nuclear graphite employing micro-scale and nano-scale x-ray microscopy with a connected laser milling step in between the two modalities. We present details of the microstructure, including porosity analysis, spanning orders of magnitude in feature size for nuclear graphite samples including IG-110.

Keywords Graphite · X-ray tomography · Porosity · Multiscale

Introduction

The advent of the femtosecond (fs) laser and its application to material ablation tasks has proven to be a game changer for materials research. With their extremely rapid milling rates (orders of magnitude faster than traditional ion beam approaches) and minimal heat affected zone (HAZ), the fs-laser has brought about a renaissance in

S. Kelly (✉) · R. White · W. Harris
Carl Zeiss X-ray Microscopy, Pleasanton, CA, USA
e-mail: steve.kelly@zeiss.com

T. Volkenandt · B. Tordoff
Carl Zeiss RMS, Oberkochen, Germany

G. Laudone · K. Jones · B. Veater
University of Plymouth, Plymouth, UK

advanced materials characterization capabilities. Recently, a fs-laser mill has been integrated into a commercial focused ion beam and scanning electron microscope (FIB-SEM) instrument, enabling numerous new capabilities, including access to deeply buried structures as well as production of extremely large trenches, cross sections, pillars, and TEM H-bars, all while preserving microstructure and avoiding or reducing FIB polishing. In addition to workflows utilizing the FIB-SEM instrument, this capability enables workflows that span between multiple instruments and the instrument can act as a rapid, targeted sample preparation station to enable a wide range of such workflows. For example, workflows moving from 3D imaging with x-ray microscopy (XRM) into high resolution 2D or 3D imaging with the FIB-SEM can now target deeply buried (more than 50–100 μm below the surface) structures for high resolution analysis via FIB-SEM. Also, workflows moving from micro-scale 3D XRM (samples generally a few millimetres in size) into nano-scale 3D XRM (samples generally $\sim 100 \mu\text{m}$ in size) can leverage the instrument to rapidly prepare nano-scale XRM samples in a targeted manner. This latter workflow is the subject of this work.

As a testbed for this workflow development and implementation, we use nuclear grade graphite. Nuclear grade graphites are high purity forms of graphite that have been engineered for several critical uses in a range of nuclear reactors. Graphite has a unique combination of properties that make it attractive for uses in nuclear energy generation, including robust thermal and mechanical properties, and attractive neutron interaction cross sections. Graphite finds uses as, for example, neutron moderators and structural components in fission reactors such as the high-temperature gas-cooled design, and neutron reflectors in developing fusion reactor designs.

In all these applications, the specific 3D microstructural properties of the graphite used can significantly affect the performance of the reactor and the ageing and degradation properties of the graphite itself. For example, the internal porosity of the graphite material can significantly affect several important material parameters relevant to reactor operation. The amount of porosity can affect the mechanical properties and thermal transport properties of the graphite. The structure and shape of the porosity can affect the way in which the graphite corrodes and oxidizes in the reactor, leading to a compromise in its integrity. As such, understanding the 3D microstructure of nuclear grade graphite is essential to understanding the performance and ageing characteristics of this critical material and providing insight for ways to engineer new forms of graphite through modelling and to improve performance in the future. Porosity in nuclear grade graphite and its evolution with exposure to operating conditions, including that studied here, has been studied extensively both computationally and experimentally [1, 2].

At the same time, however, nuclear grade graphite poses several challenges to traditional materials imaging techniques. First, the pore structure is highly multi-scale in nature, spanning over several orders of magnitude in pore size. Second, the low sputtering yields and extreme hardness of the material make large scale material removal, such as that leveraged in this workflow, impractical with ion beam based approaches.

The workflow and results outlined in this work overcome these challenges in two ways. The challenge of multi-scale pore structure imaging is addressed by leveraging both micro-scale and nano-scale XRM to provide the needed resolutions for comprehensive 3D imaging. Meanwhile, the material removal and sample preparation challenges are addressed by leveraging the capabilities of a connected, correlative fs-laser mill integrated into a FIB-SEM instrument to prepare a portion of the sample imaged with micro-scale XRM for subsequent imaging with nano-scale XRM.

Together, this 3D-to-3D x-ray imaging workflow spans over 10x in observable length scales and sample volumes imaged and enables a holistic multi-scale analysis not possible with one modality alone. While the analysis presented here reveals microstructural characteristics of nuclear graphite, the workflow itself is general enough to be applied to many other systems across materials science.

Methods

Materials

Commercial nuclear grade graphite of type IG-110 (Toyo Tanso Co., Ltd., Japan) was used for these experiments presented here. IG-110 is an isotropic graphite derived from petroleum coke and is manufactured by cold isotropic molding (isomolding) producing needle-shaped filler particles of $\approx 20 \mu\text{m}$. IG-110 grade graphite is used as a neutron moderator and reflector in components for high temperature gas-cooled reactors [3] and is currently in use in the High Temperature engineering Test Reactor (HTTR) in Japan [4] and the HTR-10 in China [5].

Sample Preparation

To facilitate the sample preparation, roughly $1 \times 1 \times 1 \text{ mm}$ sized pieces were manually cut from the bulk material using an IsoMet low speed precision cutter (Buehler, Lake Bluff, IL). Using 5-min epoxy, single pieces were glued on separate standard 5 mm SEM stubs for further sample preparation using Zeiss Crossbeam 350 laser (LaserFIB) (Carl Zeiss Microscopy GmbH, Jena, Germany). The LaserFIB features an integrated femtosecond laser for targeted laser preparation in a dedicated chamber attached to the airlock of the main FIB-SEM. After co-registering the laser and FIB-SEM sample chamber coordinate systems and selecting a region of interest by SEM imaging, the sample was transferred to the laser chamber and a two-step laser preparation process was carried out. Firstly, laser scanning pattern was setup using CAD software so that a layer of about $300 \mu\text{m}$ thickness was removed top-down over the whole sample area of about 1 mm^2 , leaving out a circular area of about $200 \mu\text{m}$ in diameter. This resulted in a remaining rough pillar of $300 \mu\text{m}$ in height protruding

from the sample surface. This pillar was laser polished towards suitable dimensions in the second step. Here, a ring-shaped (“donut”) laser pattern with a chosen inner diameter to give a final diameter of 50 μm at the top was positioned around the pillar. While the pattern of the first step was rastered line-wise with a rotation of the line direction by 19° after each complete layer to achieve homogeneous material removal, the second step used a spiral raster from outside to inside to polish the shape of the pillar. 250 raster layers at a scan speed of 200 mm/s were used in the rough milling step and the polishing step consisted of 300 raster layers at 50 mm/s. The laser power was set to 8 W and the pulse frequency to 50 kHz in both cases.

Micro-scale X-ray Imaging

X-ray tomographic imaging was performed using Zeiss Xradia 620 Versa X-ray Microscope (XRM) (Carl Zeiss X-ray Microscopy Inc., Pleasanton, CA). The XRM employs a tungsten target anode with potential accelerating voltage range of 30 kV to 160 kV. Here, an accelerating voltage of 60 kV was used. During the tomography, 2401 projection images were acquired over an angle range of -94 to $+94$ degrees utilizing the 4x optical magnification objective with an exposure of 10 s per image. This resulted in a pixel size 0.7 μm and field-of-view of 1.4 mm. Reconstruction was performed using commercial software package XMReconstructor (Carl Zeiss X-ray Microscopy Inc., Pleasanton, CA) utilizing a cone-beam filtered back-projection algorithm.

Nano-scale X-ray Imaging

High resolution X-ray tomographic imaging was performed using Zeiss Xradia 810 Ultra X-ray Microscope (XRM) (Carl Zeiss X-ray Microscopy Inc., Pleasanton, CA). The unique architecture of the XRM uses a sequence of x-ray optics to achieve spatial resolution of 50 nm or below allowing for high resolution imaging and high contrast sensitivity to nondestructively visualize the internal morphology. The XRM employs a Chromium target anode with pseudo-monochromatic x-rays at 5.4 keV, as well, Zernike phase contrast imaging was performed. Images were acquired with 64 nm pixels and a 64 μm field of view. For the tomography, 901 projection images collected at 60 s each were acquired. Reconstruction was performed using commercial software package XMReconstructor (Carl Zeiss X-ray Microscopy Inc., Pleasanton, CA) utilizing a parallel-beam filtered back-projection algorithm (Figs. 1, 2 and 3).

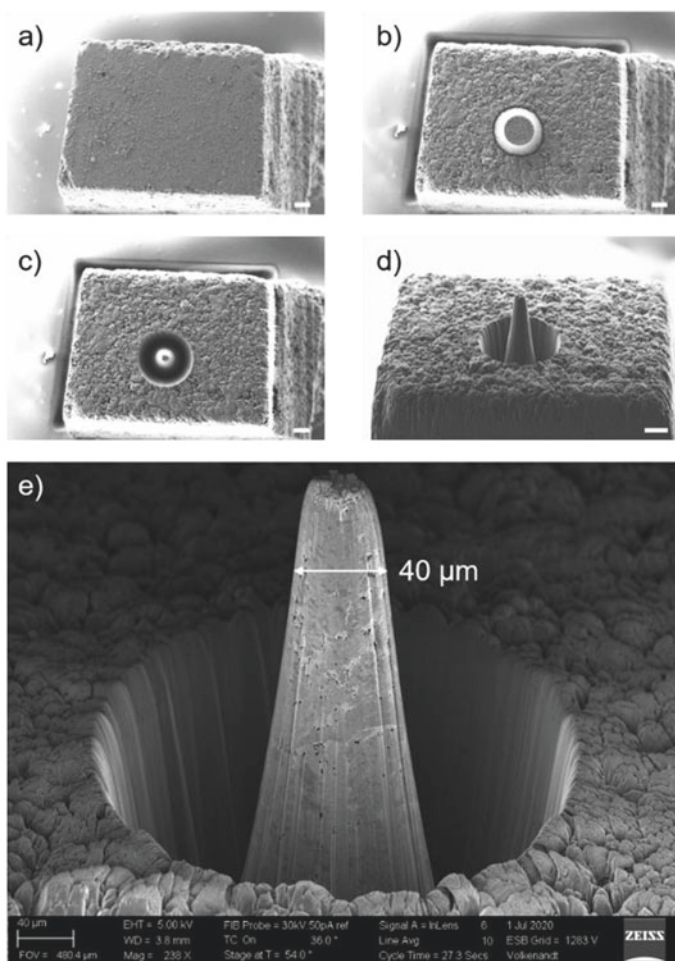


Fig. 1 SEM micrographs of the pillar preparation process. **a** the initial surface of the millimeter sized chunk, **b** after milling the $\sim 200\ \mu\text{m}$ diameter pillar into the surface, **c** after laser polishing to reduce the diameter to a suitable size for nano-scale XRM, **d** shows a side view of the pillar with the entire chunk in the background, **e** shows the completed pillar in detail, including the clean sidewalls resulting from the laser ablation. Scale bars in **a-d** are $100\ \mu\text{m}$

Image Processing/Analysis/Visualization

All visualization and image processing was performed using Dragonfly Pro software (ORS, Montreal, Canada). Versa and Ultra datasets were manually aligned. Large grains observed in the Versa data were isolated using a combination of grayscale thresholding, morphological operations, and a distance map transform to approximate the grain boundaries. Initially, pores were segmented by thresholding greyscale

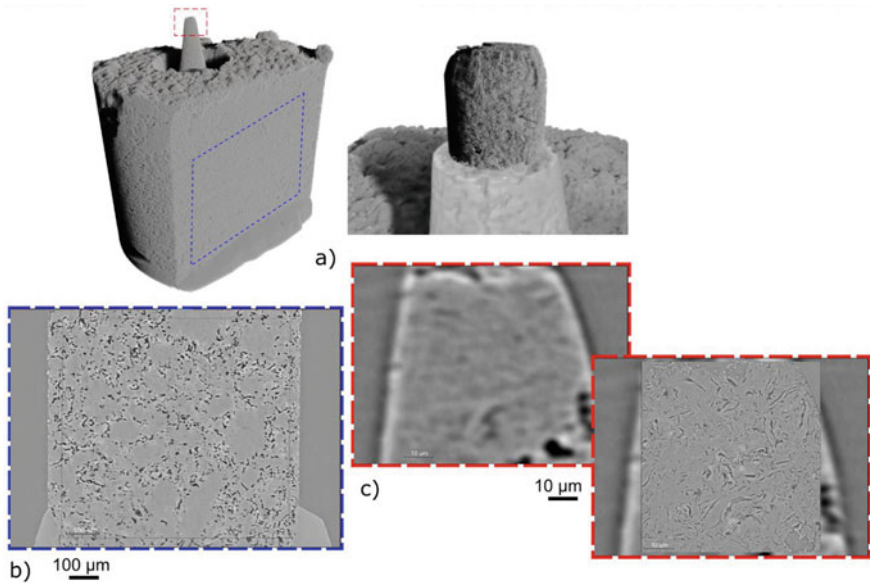


Fig. 2 Micro-scale and nano-scale XRM results, **a** shows a 3D rendering of the micro-scale (left) and nano-scale (right) XRM data, **b** shows a representative slice through the interior of the micro-scale XRM data, **c** shows the pillar region prepared via laser milling in both the micro-scale (left) and nano-scale (right) XRM data. (Color figure online)

values. Following this, an opening operation was used to remove small pores. Closing and dilation steps were performed to identify regions of high porosity density which define boundaries for the targeted grain regions. A pixel wise distance map was then calculated. This distance transform was segmented to form seeds of visual centers of the grain regions. A watershed transform was subsequently performed to grow the grain boundaries over the defined solid space. Porosity was quantified using grayscale thresholding followed by pore segmentation using the OpenPNM library implemented in Dragonfly Pro [6] for both Versa and Ultra datasets.

Results

As described in Sect. “[Sample Preparation](#)”, the millimeter-sized chunk of graphite was milled to form a pillar at the top of the sample suitable for measurement with nano-scale XRM. The steps taken to produce the pillar are shown in Fig. 1a–d, while the resulting pillar can be seen in Fig. 1e. The top portion of the pillar is $< 50 \mu\text{m}$ in diameter, ideal for imaging with nano-scale XRM. The graphite grain structure and porosity can be seen on the surface of the pillar, indicating the high quality of the laser-prepared surface. Total laser ablation time to produce the pillar was 750 s.

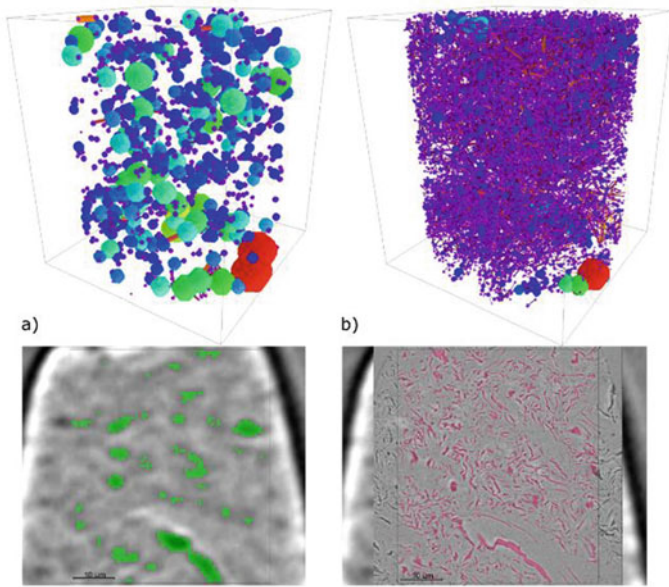


Fig. 3 Comparison of porosity segmented and measured in the same region for **a** micro-scale XRM and **b** nano-scale XRM. The lower images show an example slice through the data revealing the segmentation results in detail. The upper images show a connectivity diagram for the pore networks segmented in each volume where colored balls represent the pores and the sticks represent connectivity between the pores. (Color figure online)

Figure 2 shows the results of both the micro-scale and nano-scale XRM measurements on the IG-110 graphite sample. While the micro-scale XRM data captured information across the entire sample volume, the nano-scale XRM data is localized within the prepared pillar. Figure 2a shows a 3D rendering of the entire sample volume, with the side artificially clipped to reveal the interior of the millimeter sized base. The dotted blue and red insets show the regions highlighted in b) and c), respectively. Figure 2b shows the internal microstructure of the IG-110 graphite in detail. Distinct regions are visible in the image that represent high density graphite grains separated by a more porous region where the binder material has bound them together in the formation process. Very little porosity is visible in the more dense regions in the micro-scale XRM data. In Fig. 2c the resolution improvements between the micro-scale and nano-scale XRM are shown in detail.

Strikingly, the area shows a high degree of internal porosity in the nano-scale data which is not visible in the micro-scale XRM data. As a further example of the additional information revealed with the nano-scale XRM, Fig. 3a–b show pore segmentation for the same volume across both micro-scale and nano-scale XRM, respectively. The lower images of Fig. 3 clearly show the additional resolved porosity obtained in the nano-scale XRM data. Table 1 lists porosity values for this volume as measured in both the micro-scale and nano-scale XRM data. The micro-scale

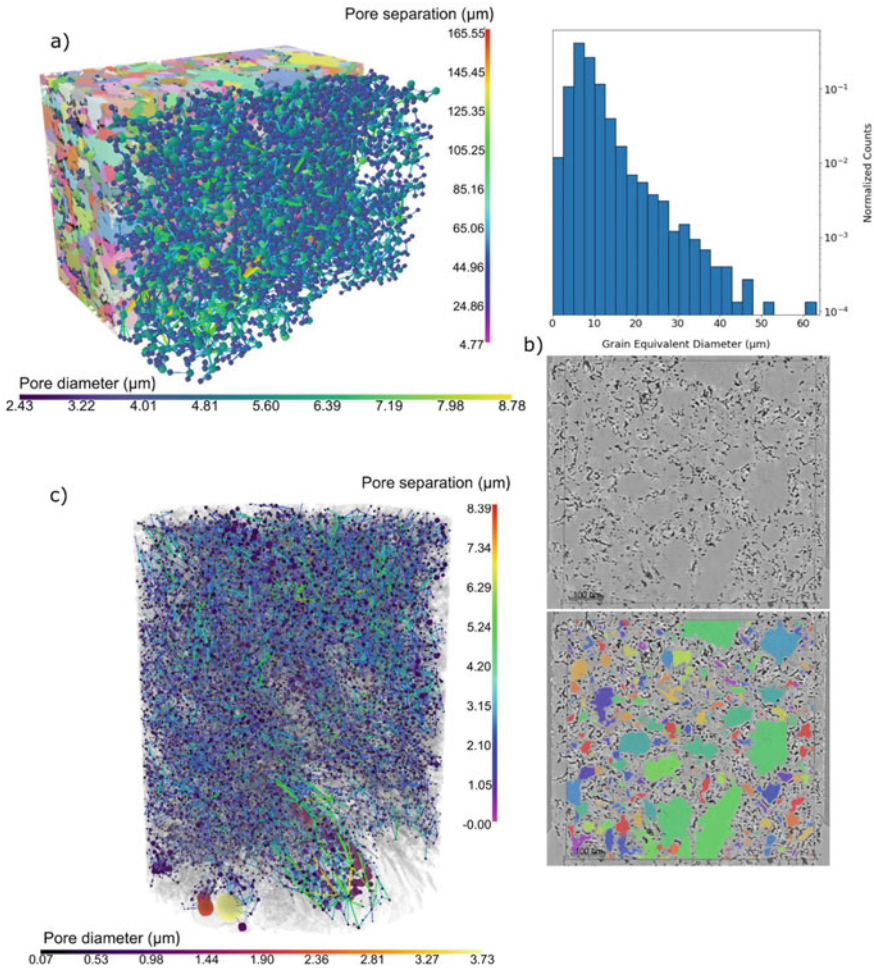


Fig. 4 Multiscale data analysis on the measured pore network. Part **a** shows the segmented dense grain regions (colored blocks in the rear) along with the 3D pore network model of the porosity in the micro-scale XRM data while the plot to the right shows the segmented grain size distribution. Part **b** shows the result of the grain segmentation overlaid in color (bottom) onto a single slice taken from the micro-scale XRM data (top). Part **c** shows the pore network model from the nano-scale XRM data. (Color figure online)

Table 1 Porosity metrics for the data described here

Dataset	Analysis sub volume (μm)	Porosity (%)	Grain Volume Fraction (%)	Total Interpolated Porosity (%)
Micro-scale XRM	$740 \times 730 \times 1055$	12.8	49.5	19.7
Micro-scale XRM	$24 \times 24 \times 56$	6.5		
Nano-scale XRM	$24 \times 24 \times 56$	15.5		

XRM data would indicate that this dense region contains only 6.5% porosity, while the (more accurate) nano-scale XRM data reveals the porosity to be over twice that amount at 15.5%. Furthermore, the pore network models of the two segmented data sets in the upper images of Fig. 3 reveal that not only are the larger pores from the micro-scale XRM data actually composed of several smaller pores, but that the micro-scale XRM data does not capture the connectivity of the pore network (absence of sticks connecting the spheres) while that character is well captured in the nano-scale XRM data. The connectivity and pore network character for the nano-scale XRM measurement is shown in more detail in Fig. 4c where the ball color represents the pore size and the stick color represents the pore separation distance. The connectivity of the pore network is an essential characteristic for understanding degradation properties in nuclear grade graphite as it dictates how gases can move through the structure and potentially react with the material.

Importantly, the volume analyzed by nano-scale XRM is from the interior of one of the dense grains visible from the micro-scale XRM images. As such, the metrics derived from this region can be used to enhance the metrics across the entire volume of the micro-scale XRM data to gain a much more complete picture of the overall material microstructure. To do this, the dense grain regions were first segmented from the porous regions in the micro-scale XRM data. This segmentation can be seen in the 2D images shown in Fig. 4b where the colored patches in the lower image represent the identified grains within the material. These grains are represented as the colored blocks in the background of the 3D rendering of Fig. 4a, with the grain size distribution plotted on the right side of Fig. 4a. The grain regions represent 49.5% of the total analyzed volume, while the total porosity measured in the micro-scale XRM data is found to be 12.8%, as tabulated in Table 1. Assuming the dense grain regions contain similar levels of porosity, we can take the 15.5% porosity metric from the nano-scale XRM data and use that to correct the measured 12.8% porosity from the micro-scale XRM data. For the grain regions, we assume the porosity is 15.5% (as measured from the nano-scale XRM data). For the porous regions, we use the porosity value measured from the micro-scale XRM data and assume this captures most of the porosity in this region. Then we sum the pore volume for the entire volume and rescale to the total analyzed volume to report a corrected porosity.

Table 1 summarizes the holistic, multiscale porosity analysis undertaken here. The total interpolated porosity measured with this approach is 19.7%, which matches well with the tabulated literature porosity value for IG-110 of 22.7% [7, 8]. The discrepancy between the two measurements could be due to segmentation variations, the particular regions analyzed, or finer scale porosity not captured by the nano-scale XRM data.

Aside from simply measuring the porosity value in this material, this multi-scale analysis approach delivers a comprehensive microstructural understanding of the pore network structure in nuclear graphite. This information is critical in developing a theoretical understanding of this critical material in its complex service environment. Additionally, as the sample is still intact following analysis, this approach can be used to track microstructure evolution with exposure to elevated temperatures, neutron irradiation, or corrosive environments. Future work will focus on refining

this workflow to deliver a more accurate microstructural representation, exploring other nuclear graphite forms, and extending the application of this method to other systems across materials science.

Conclusions

In conclusion, we present here a targeted, multiscale, correlative 3D imaging workflow spanning between micro-scale and nano-scale XRM and linked by the rapid sample preparation capabilities afforded by a fs-laser mill integrated onto a FIB-SEM instrument. The workflow has been used to analyze the multiscale porosity network present in the nuclear grade graphite IG-110. The measured porosity value of 19.7% from this method closely matches the reported literature value of 22.7% that was obtained from other methods, but yields a more complete picture of the porosity structure than can be obtained by non-imaging methods. The resulting multi-scale porosity representation makes useful input for modelling approaches that simulate the response of nuclear graphite to different operational conditions.

References

1. Jones KL, Laudone GM, Matthews GP (2018) A multi-technique experimental and modelling study of the porous structure of IG-110 and IG-430 nuclear graphite. *Carbon* 128(1):1–11
2. Snead L, Contescu C, Byun T, Porter W (2016) Thermophysical property and pore structure evolution in stressed and non-stressed neutron irradiated IG-110 nuclear graphite. *J Nucl Mater* 476(4):102–109
3. Xu Y, Zuo K (2002) Overview of the 10 MW high temperature gas cooled reactor—test module project. *Nucl Eng Des* 218(1–3):13–23
4. Shiozawa S, Fujikawa S, Iyoku T, Kunitomi K, Tachibana Y (2004) Overview of HTTR design features. *Nucl Eng Des* 233(1–3):11–21
5. Wu Z, Lin D, Zhong D (2002) The design features of the HTR-10. *Nucl Eng Des* 218(1–3):25–32
6. Gostick J et al. (2016) OpenPNM: A pore network modeling package. *Comput Sci Eng* 18(4):60–74
7. Oku T, Eto M, Ishiyama S (1990) Irradiation creep properties and strength of a fine-grained isotropic graphite. *J Nucl Mater* 172(1):77–84
8. Burchell T (1996) A microstructurally based fracture model for polygranular graphites. *Carbon* 34(3):297–316

Part XXII
**Computational Techniques for Multi-scale
Modeling in Advanced Manufacturing**

A Parametric Study of Grain Size and Its Volume Fraction Effect on Heterogeneous Materials Mechanical Properties



Khaled Adam and Tarek Belgasam

Abstract Tailoring the fraction and distribution of microstructural features computationally to achieve an optimized strength-ductility combination in heterogeneous materials is gaining importance. These microstructural features include grain size (GZ), geometrically necessary dislocation (GND), and crystallographic texture, among others. However, it is challenging to find the influence of an individual microstructural feature on the mechanical response experimentally due to cost limitations. In the current work, computational approaches and comprehensive statistical parametric study using response surface methodology (RSM) were combined to estimate the optimum fraction and distribution of microstructural features for coveted mechanical properties.

Keywords Heterogeneous structures · Grain size and fraction · Monte carlo potts · Model response surface methodology (RMS)

Introduction

In polycrystalline materials, high strength and ductility are commonly contradicting properties [1]. In a single-phase material the strength can be improved either by work hardening, or by finding the grain size or by performing the two techniques together. The large plastic deformation techniques, such as accumulative roll bonding (ARB), equal channel angular pressing (ECAP), or high-pressure torsion (HPT) can yield submicron grain size materials with tremendously high strength. Conversely, the large strength often was accompanied by low ductility [2]. However, creating a

K. Adam (✉)

Department of Mechanical Engineering, Kennesaw State University, Marietta, GA 30060, USA
e-mail: k-adem@wsu.edu

T. Belgasam

Materials Research Division | Honda R&D Americas Inc., 21001 State Route 739, Raymond, OH 43067-9705, USA
e-mail: tbelgasam@oh.hra.com

heterogeneous material that constitutes of domains of different phases or the same material of different structures can give a good strength and acceptable ductility [3].

Experiments have revealed that different grain size distributions can give rise to different material strengths particularly if the material is heterogeneous [4]. For single-phase materials, a spatial grain size gradient can origin local concentration and hardening, which in turn can cause a different strength [3]. In the present work, a combination of modeling and statistical techniques was proposed to analyze material behavior with include the effects of microstructural features such as grain size, and its volume fraction.

To generate the microstructure with a specific grain size distribution, we employed the Monte Carlo Potts model developed in references [5]. Then, by using a ViscoPlastic Fast Fourier Transformer model (VPPFFT) the strain and stress distribution are determined [6]. We also performed a series of simulations for different grain size distributions and different spatial distributions, and we picked the most appropriate to present in the current study. All in all, this work also delivers a nondestructive means of approximating the macroscopic properties of a heterogeneous material [4].

Methodology

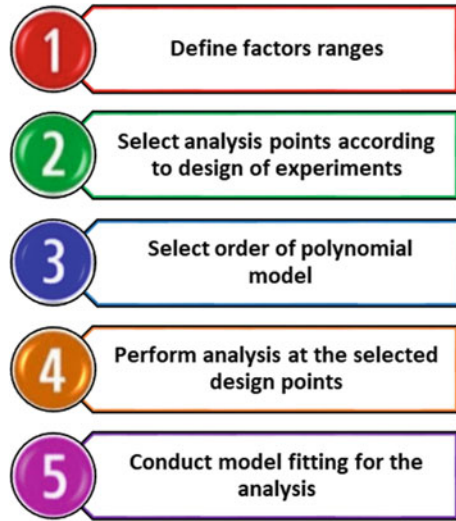
Response Surface Methodology (RSM)

Recently, the response surface methodology (RSM) has been utilized as a comprehensive statistical tool for parametric study and optimization in various kinds of analytical science fields and industrial processes in which a response is affected by many variables, and the purpose is to maximize/minimize this response [7]. For example, a strength-ductility combination in heterogeneous materials is affected by grain size of the small grains “SGZ” (x_1), grain size of the large grains “LGZ” (x_2), and their volume fraction of large grains “VFLG” (x_3). In this case, the strength-ductility combination (y) is the response variable and it is a function of the microstructure parameters as follows:

$$y = f(x_1, x_2, x_3) + e \quad (1)$$

where the variables x_1 , x_2 , and x_3 are independent variables and e is the experimental error, which the response y relies on them. This experimental error represents any estimates error on the response, as well as other type of variation not counted in the function f , which is a statistical error that is supposed to distribute data normally with zero average and variance. In this study, a statistical analysis of the RSM numerically and graphically was conducted using Minitab software. The calculations in matrix form were accomplished by faced CCD design where each RSM model was performed by detailed analysis (the number of factors and ranges) of each case study

Fig. 1 RSM model steps.
(Color figure online)



as shown in Fig. 1. The details of the used RSM technique for generation a parametric function (e.g., quadratic function, exponential function, logarithmic function) that models the output of interest (mechanical properties) as a function of the inputs (microstructure properties) are presented in the author's previous work [8–11].

Monte Carlo Potts Model

Monte Carlo method has been used considerably to simulate recrystallization, grain growth and texture evolution [12, 13]. In general, Monte Carlo also uses a discretized representation of microstructure; though, site interactions are energetically governed. Each lattice site is given a number, S_i , which resembles to the orientation of the grain in which it is embedded. Lattice sites that are next to sites having distinct grain orientations are viewed as being separated by a grain boundary, however a site bounded by sites with the similar orientation is in the grain inside. Each different couple of adjacent neighbors participates a unit of grain boundary free energy J to the system as already described in equation which called Hamiltonian, Eq. (1), is over all N sites in the system. The structure evolution is modeled by choosing a site and a new orientation at random from the set of allowable values. The change in total system energy ΔE for reorienting the site is calculated, and the reorientation is fulfilled with the transition probability Eq (2).

$$E = \sum_{i=1}^N \sum_{j=1}^Z \gamma(S_i, S_j) \quad (2)$$

where J_{\max} and M_{\max} are the maximum boundary energy and mobility in the system respectively. In the current simulation, we use $J_{\max} = 1$ and $M_{\max} = 1$. The lattice temperature (kT) was set to 0.2–0.3

$$(S_i, S_j, \Delta E, T) = \begin{cases} \frac{J(S_i, S_j)}{J_{\max}} \frac{M(S_i, S_j)}{M_{\max}} & \Delta E \leq 0 \\ \frac{J(S_i, S_j)}{J_{\max}} \frac{M(S_i, S_j)}{M_{\max}} \exp\left(\frac{-\Delta E}{kT}\right) & \Delta E > 0 \end{cases} \quad (3)$$

Results and Discussion

Potts Model simulation results are shown below in Fig. 2. The evolved structure is featured by multimodal distribution of grain sizes. The three-dimensional heterogeneous structure reveals that coarse grains are inconsistently distributed in fine grain structure in all directions. Figure 2b shows the grain size distribution with average in between 300 voxels for small grains and 3000 voxels for coarse grains, respectively (Fig. 2b). The grain size distribution, Fig. 1b, certifies the bimodality. As it is known that these coarse-grained comparatively have low strength, but high ductility. Whereas the fine size grains are characterized with high strength and low ductility, and this effect is normally comprehended in terms of the Hall–Petch effect of grain size

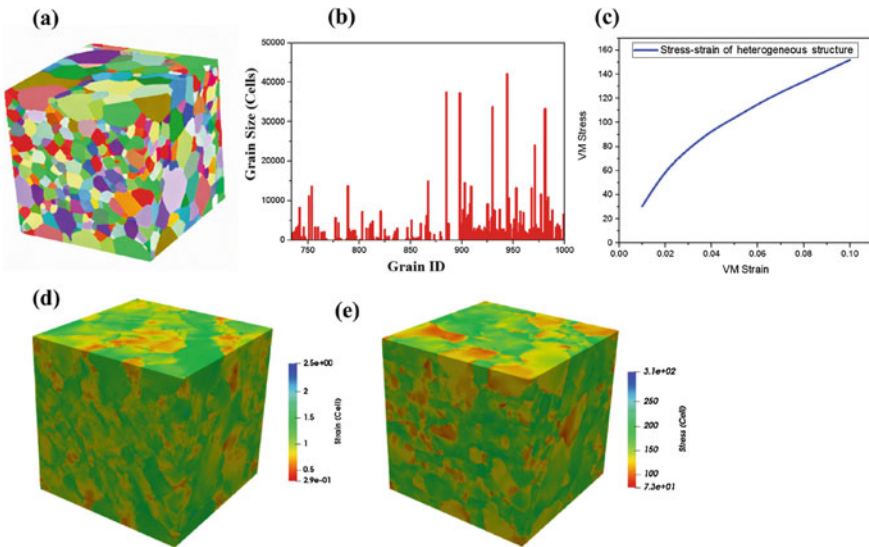


Fig. 2 Shows **a** heterogeneous grains with trans-modal grained structure with a uniform distribution of grain sizes in between 300 voxels and 3000 voxels. Grain is colored according to its orientation assigned randomly, **b** grain size distribution, **c** Engineering stress-strain curves of heterogeneous structure **d** Strain distribution, **e** stress distribution. (Color figure online)

strengthening. Thus, creating a material contains large grains randomly embedded among fine grains can provide enhanced combinations of strength and ductility that are not accessible to their homogeneous counterparts. Additionally, these developed digital heterogeneous microstructures are used for further analysis by microstructure sensitive computational models such as VPFPT [6]. However, to determine the deformation behavior of heterogeneous material, an investigation based on quantitative experimental results should be achieved. Lately, heterogeneous structure were studied in metals and alloys, and displayed excellent mechanical properties to their homogeneous counterparts [9]. Figure 1c displays the engineering stress–strain curves of the heterogeneous microstructures, indicating the heterogeneous structure has an excellent combination of strength and ductility compared to the homogeneous counterparts. Figure 2c and d shows the von Mises equivalent plastic strain and stress distribution in heterogeneous structure, measured by VPFPT. The results reveal clear strain partitioning along the fine and coarse boundary. More strain is determined on the coarse grain region than the fine grain region, which conveys a much lesser strain than the average. This strain partitioning between coarse grain and fine grain makes a benefit on the ductility. Normally, GNDs are produced adjacent grain boundaries to preserve the physical continuity between adjacent grains of dissimilar orientations since the directions of their slip systems are miscellaneous. Normally, once a material is toughened by grain refinement, the higher grain boundary fraction acts as a further barrier to dislocation movement.

Conclusion

The results show that introducing large grains randomly into fine matrix can be useful to enhance the strength and ductility of the material compared with its equivalent homogeneous microstructure. Also, it was found that grain sizes and volume fractions of both coarse and fine grains regions have a direct effect on mechanical properties of heterogeneous structure materials. This way of simulation has the benefit of being able to control the fraction and even spatial distribution of the coarse grains and fine grains regions. The deformation gradient appears along the fine/coarse grain boundary, since there are disparities in mechanical properties triggered by different grain sizes.

References

1. Park HK, Ameyama K, Yoo J, Hwang H, Kim HS (2018) Additional hardening in harmonic structured materials by strain partitioning and back stress. *Mater Res Lett* 6:5, 261–267
2. Ma E, Zhu T (2017) Towards strength–ductility synergy through the design of heterogeneous nanostructures in metals. *Mater Today* 20(6):323–331
3. Wu X, Zhu Y (2017) Heterogeneous materials: a new class of materials. with unprecedented mechanical properties. *Mater Res Lett* 5:8, 527–532

4. Salvatore T (2006) *Random heterogeneous materials: microstructure and macroscopic properties*. Springer, Berlin
5. Adam KF, Zöllner D, Field DP (2018) 3D microstructural evolution of primary recrystallization and grain growth in cold rolled single-phase aluminum alloys
6. Lebensohn RA (2001) N-Site modeling of a 3D viscoplastic polycrystal using fast fourier transform. *Acta Mater* 49:2723–2737
7. Montgomery DC (2012) *Design and analysis of experiments*. Wiley, Hoboken, NJ
8. Belgasam TM, Zbib HM (2018) Key factors influencing the energy absorption of dual-phase steels: multiscale material model approach and microstructural optimization. *Metall Mater Trans A* 49(6):1–22
9. Belgasam TM, Zbib HM. Microstructure characteristics optimization of dual phase steels using representative volume element method and response surface methodology : Parametric study
10. Belgasam T, Zbib H (2018) Multiscale material modeling and simulation of the mechanical behavior of dual phase steels under different strain rates: parametric study and optimization. *J Eng Mater Technol* Feb. 2018
11. Belgasam T (2018) Multiscale model analysis of the effects of martensite morphology and martensite volume fraction on the mechanical property of dual-phase (DP) steels: parametric study. In: 15th international LS-DYNA® users conference, pp 1–8
12. Adam KF, Long Z, Field DP (2017) Analysis of particle-stimulated nucleation (PSN)-dominated recrystallization for hot-rolled 7050 aluminum alloy *Metall. Mater Trans A* 48:2062–2076
13. Adam K, Root JM, Long Z et al (2017) Modeling the controlled recrystallization of particle-containing aluminum alloys. *J Materi Eng Perform* 26:207–213

Computational Multi-scale Modeling of Segregation and Microstructure Evolution During the Solidification of A356 Ingots Processed via a 2-Zone Induction Melting Furnace



Aqi Dong and Laurentiu Nastac

Abstract In the current study, a stochastic mesoscopic model was applied to predict the evolution of the A356 microstructure (e.g., dendritic morphologies and columnar-to-equiaxed transition formation) in a 2-Zone induction melting and solidification furnace. The influence of process and material parameters on microstructure, such as initial melting temperature, ultrasonic stirring and cavitation, fluid flow conditions, cooling rate, temperature gradient, and nucleation and growth kinetics parameters for both equiaxed and columnar phases, is studied. In addition, the initial transient of the macro-segregation of silicon during solidification of A356 in the crucible is also simulated. The results will be helpful for determining the solidification structure, mushy zone evolution in the crucible and assist in developing of comprehensive solidification maps of alloys used in additive manufacturing.

Keywords Segregation · 2-zone furnace · Microstructure · Numerical model · Solidification map

Introduction

Solidification of aluminum alloys is quite complex but vital to cast alloys because it is strongly affecting the mechanical properties of the processed alloys. Thus, modeling of the dendritic growth morphologies including the formation of the columnar-to-equiaxed transition (CET) during solidification is one of the most studied fields. Several solidification models were developed to study the nucleation and growth of dendrites, and CET formation in solidifying alloys [1–5]. These models can be used to visualize the evolution of solidification microstructures in relatively short time and make it possible to predict, evaluate and compare data against experiments.

The main objective of this research is to simulate the solidification process of A356 in bottom water-cooled graphite crucible and to study the effect of various process

A. Dong · L. Nastac (✉)

Department of Metallurgical and Materials Engineering, The University of Alabama,
Box 870202, Tuscaloosa, AL 35487, USA

e-mail: lnastac@eng.ua.edu

© The Minerals, Metals & Materials Society 2021

TMS 2021 150th Annual Meeting & Exhibition Supplemental Proceedings,

The Minerals, Metals & Materials Series,

https://doi.org/10.1007/978-3-030-65261-6_52

parameters such as initial melting temperature, geometry effect, boundary conditions, fluid flow conditions, cooling rate, temperature gradient, as well as nucleation and growth kinetics parameters of both equiaxed and columnar phases. In addition, the macro-segregation of silicon during solidification of A356 in the crucible is simulated. The results also include microstructure predictions, which are verified by the current experimental work.

Modelling and Experiment Settings

ANSYS's Fluent has been applied to simulate macro-segregation of silicon during solidification of A356 in a bottom water-cooled crucible, which is part of a 2-Zone induction melting and solidification furnace. The macro-segregation model is explained in detail in [6]. The geometry of the model is the graphite crucible size, and the modelling parameters is as follows: Height and diameter of the crucible are 305 and 75 mm, respectively, initial Si concentration in the melt is 7.0 wt%, alloy thermal conductivity is 90 W/(m K), alloy viscosity is 0.03 kg/(m K), the eutectic temperature (TE) and liquidus temperature (TL) are 565 °C and 617 °C, respectively. The alloy density is described as a piece-wise linear relationship with the temperature. The bottom and top coils are a mixed (e.g., convection and radiation) wall type with a heat transfer coefficient of 10 W/(m K) and an external emissivity of 0.9. External radiation temperature as measured during the current experiments is 423.15 K. The other wall is set as stationary wall with zero heat flux.

The Meso 2D software [2, 5] was employed to simulate the evolution of the A356 solidification microstructure in the crucible. The parameters used in the microstructure simulation are shown in Table 1.

Table 1 Parameters for microstructure simulation

Parameters	Value	Parameters	Value
Ingot height	0.305 m	Initial temperature	650 °C
Ingot diameter	0.075 m	Liquidus temperature	617 °C
Specific heat	963 J/kg/K	Initial Si concentration	7.0 wt%
Thermal conductivity	90 W/m/K	Partition coefficient	0.14
Latent heat	389,000 J/kg	Liquid diffusivity	3.0×10^{-9} m ² /s
Density	2490 kg/m ³	Solid diffusivity	1.0×10^{-12} m ² /s

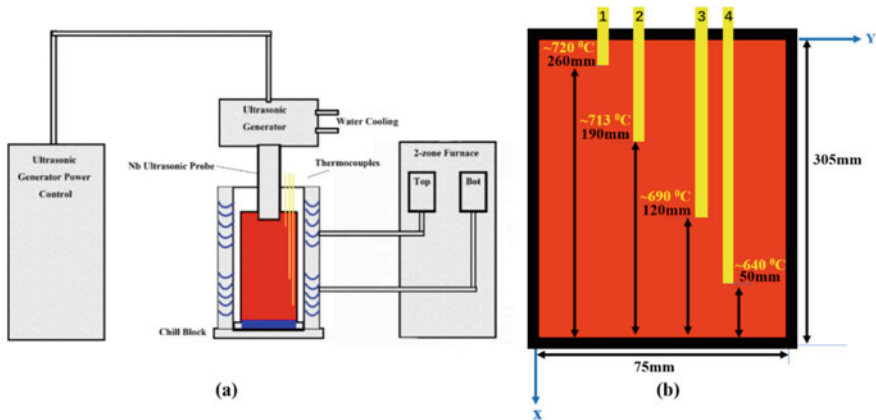


Fig. 1 **a** Sketch of the 2-Zone furnace system and **b** position of the thermocouples in the crucible. (Color figure online)

A schematic diagram of the 2-Zoneone furnace is shown in Fig. 1a. 4 K-type thermocouples were inserted at different positions inside the crucible to record the temperature profiles, as shown in Fig. 1b.

Results and Discussion

The Macro-Segregation of Silicon

The initial temperature contour of the ingot is shown in Fig. 2a, where the temperature gradient between the top and bottom is about 600 K/m, and the temperature gradient between the bottom thermocouples 1 and 2 is about 1700 K/m. The initial large gradient in the liquid is helpful to create a large mushy zone during the solidification/cooling process. The simulation shown in Fig. 2a was previously validated using the experimental cooling curves obtained with the setup in Fig. 1b [7]. After 50 s, the temperature contour is presented in Fig. 2b, which shows that the bottom portion of the A356 ingot started to solidify. Figure 3 shows the temperature profile of A356 ingot along the crucible. It can be seen the temperature decreases as the position approaches to the bottom and drops sharply as the temperature drops below the melting point. Figure 4 shows the liquid fraction and silicon concentration after 50 s at 3 different positions (ingot edge, ingot middle radius and ingot center) across the ingot diameter. Figure 5 shows the liquid fraction and silicon concentration plots after 50 s. As shown in Figs. 4 and 5, the L/S interface is at about 10 mm from the bottom after 50 s. The velocity magnitude, velocity vectors and the stream function during solidification of the vertical ingot after 50 s are presented in Fig. 6. The effect of the gap between the two induction coils can be clearly seen in Fig. 6. As also

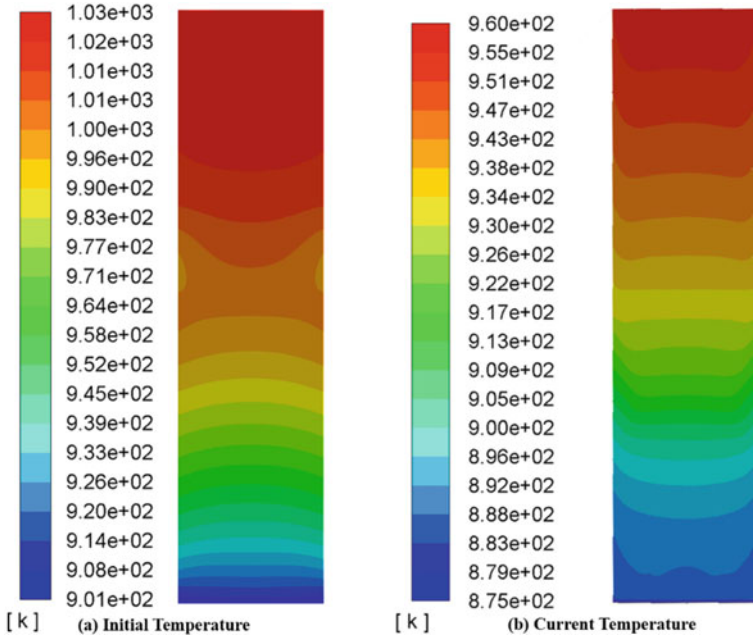


Fig. 2 Temperature plots at 0 s and after 50 s. (Color figure online)

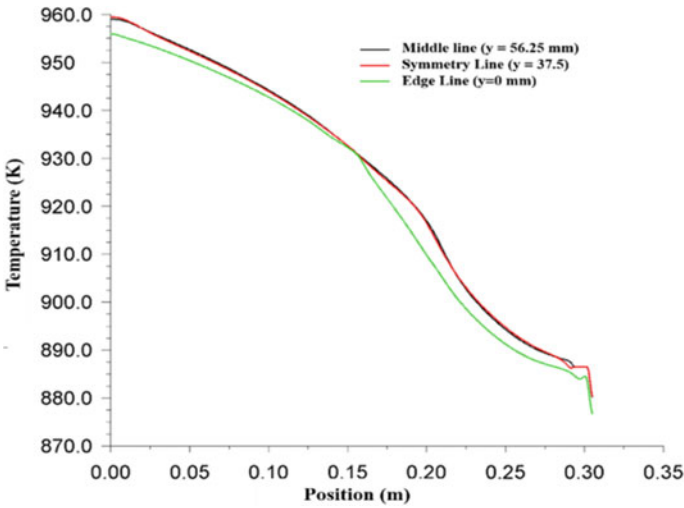


Fig. 3 Temperature plot of A356 along the crucible after 50 s. (Color figure online)

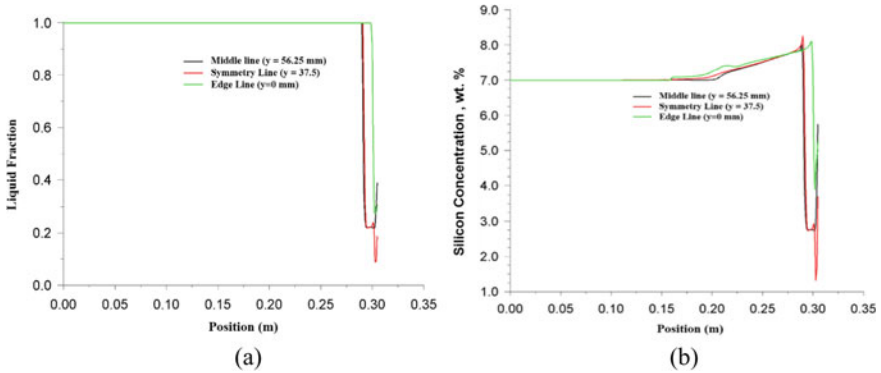


Fig. 4 **a** Liquid fraction and **b** silicon concentration profiles after 50 s. (Color figure online)

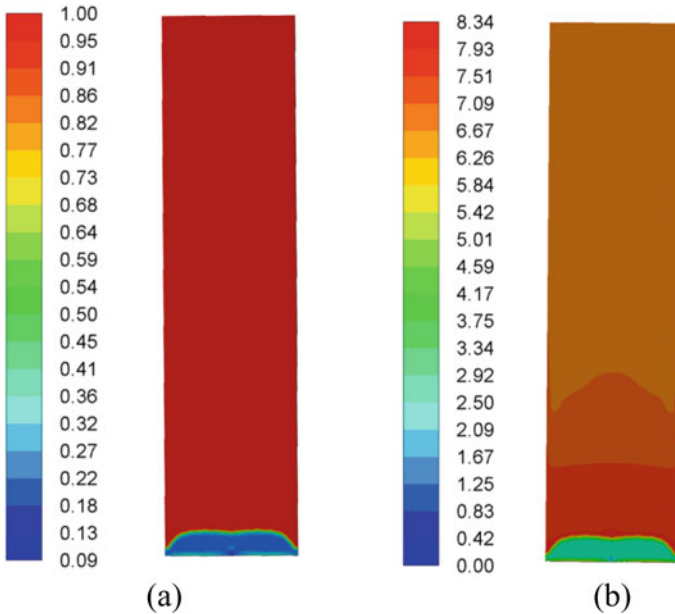


Fig. 5 **a** Liquid fraction and **b** silicon concentration (in wt%) contour plots after 50 s. (Color figure online)

shown in Fig. 6, the fluid flow dynamics is quite complex, which affects strongly the Si concentration (Figs. 4b and 5b).

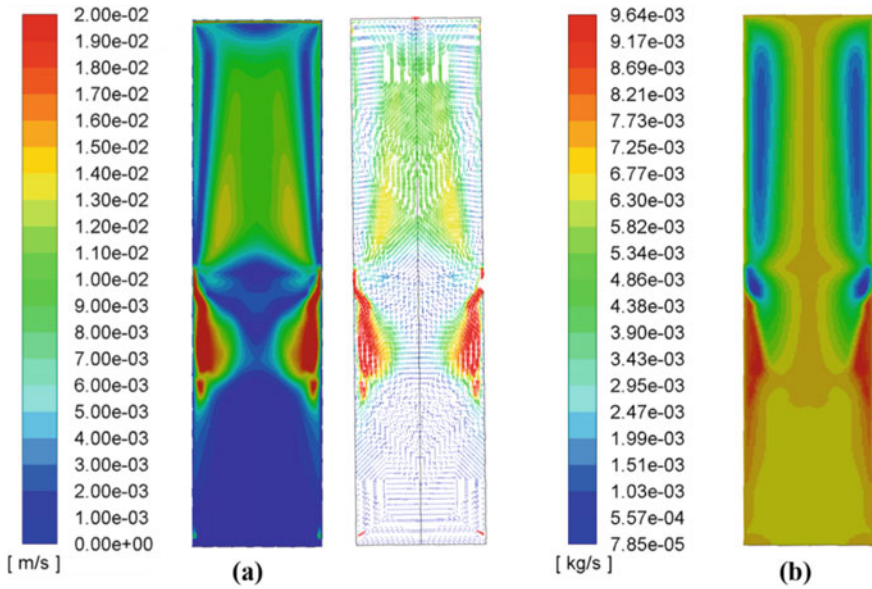


Fig. 6 **a** Velocity magnitude and velocity vectors and **b** stream function after 50 s. (Color figure online)

Microstructure Evolution

Simulated A356 microstructures with different parameters in a 2D domain are shown in Fig. 7. Based on the current simulation conditions (Fig. 7a is the morphology of the control group), CET is established around 25 mm from the bottom of the crucible and the simulated grain size in the middle of the ingot is about 500 μ .

It can be shown that with the decrease of the thermal gradient at the S/L interface, the CET region disappears gradually. Based on the current process conditions, the critical thermal gradient for CET formation, fluid flow, nucleation parameters for equiaxed and columnar grains, and the initial melt temperature are relevant parameters for solidification and CET formation. The microstructure shown in Fig. 7a is close to the real situation (Fig. 8).

Concluding Remarks

ANSYS’s Fluent was used to develop a fully coupled segregation model to simulate the initial transient of the macro-segregation of silicon during solidification of A356 in a water-cooled graphite crucible. The Si segregation, mushy zone evolution and fluid flow dynamics during the initial solidification in the crucible are shown to be quite complex. In addition, a stochastic mesoscopic model had been applied to predict

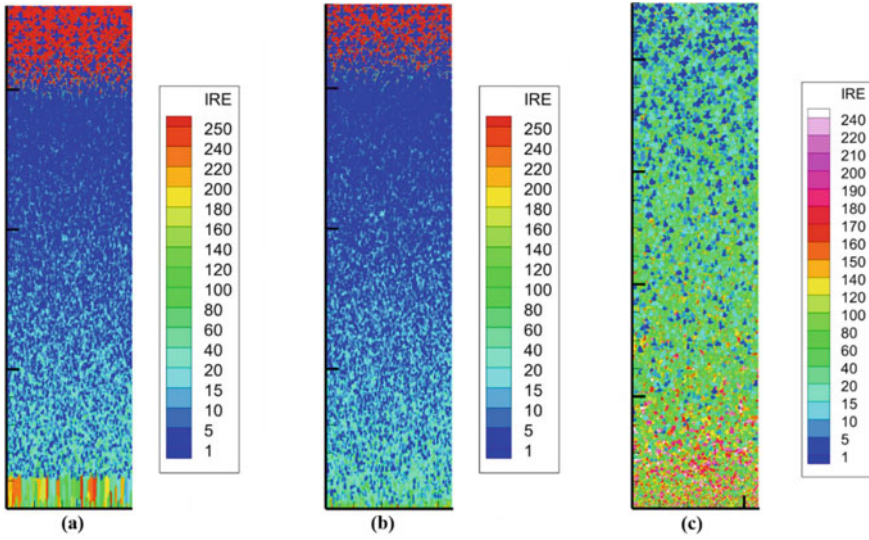


Fig. 7 Microstructure evolution with three different critical thermal gradients at the S/L interface for CET formation: **a** 5000 °C/m, **b** 3000 °C/m and **c** 1000 °C/m. (Color figure online)

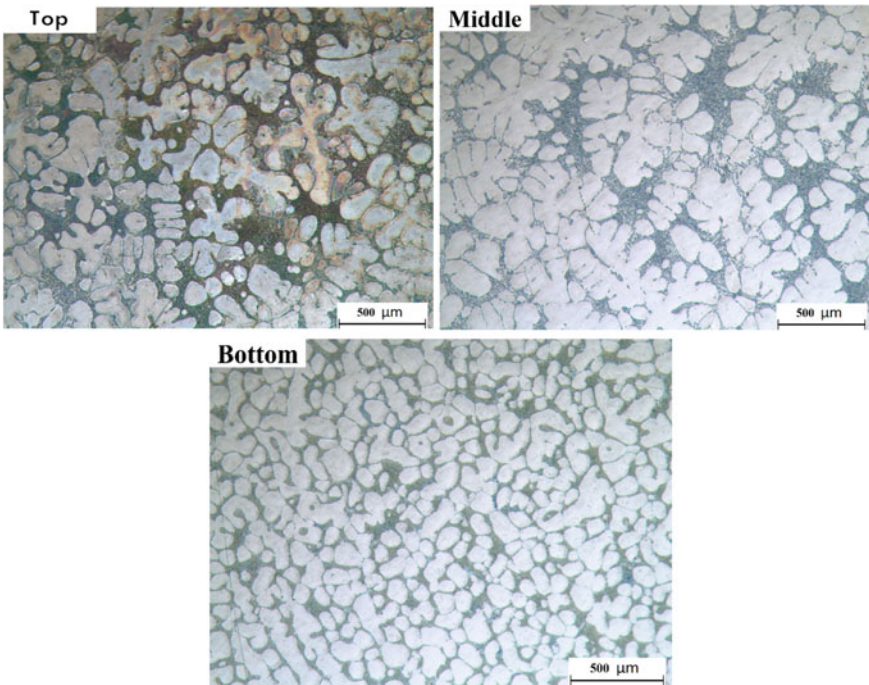


Fig. 8 Comparison of A356 microstructures at three different crucible positions. (Color figure online)

the evolution of the A356 microstructures and CET in the crucible. The influence of process and material parameters on the solidification microstructure, such as initial melting temperature, fluid flow conditions, cooling rate, temperature gradient, and nucleation and growth kinetics parameters for both equiaxed and columnar phases, is analyzed. It was found that, for the current solidification conditions, the critical temperature gradient at the S/L interface for CET formation is about 5000 K/m. The next step is to study the effect of ultrasonic stirring (see Fig. 1a) on the CET formation and macro-segregation of Si under similar process conditions. These results will be used to develop solidification maps for aluminum alloys processed with and without ultrasonic stirring.

References

1. Nastac L (2004) Modeling and simulation of microstructure evolution in solidifying alloys. Springer, Berlin. ISBN 978-1-4020-7832-3
2. Nastac L (2011) Mathematical modeling of the solidification structure evolution in the presence of ultrasonic stirring. *Metall Mater Trans B* 42(6):1297–1305
3. Mathiesen RH, Arnberg L, Ramsøskar K, Weitkamp T, Rau C, Snigirev A (2002) Time-resolved x-ray imaging of aluminum alloy solidification processes. *Metall Mater Trans B* 33(4):613–623
4. Lee PD, Chirazi A, See D (2001) Modeling microporosity in aluminum–silicon alloys: a review. *J Light Met* 1(1):15–30
5. Nastac L (1999) Numerical modeling of solidification morphologies and segregation patterns in cast dendritic alloys. *Acta Mater* 47(17):4253–4262
6. Fluent ANSYS (2011) ANSYS fluent theory guide. ANSYS Inc., USA, 15317, pp 724–746
7. Dong A, Nastac L (2020) The influence of ultrasound on the microstructure formation during the solidification of A356 ingots processed via a 2-zone induction melting furnace. In: TMS 2020 149th Annual Meeting & Exhibition supplemental proceedings, Springer, Cham, pp 1117–1126

Effect of Nozzle Injection Mode on Initial Transfer Behavior of Round Bloom



Pu Wang, Liang Li, Da-tong Zhao, Wei-dong Liu, Song-wei Wang, Hai-yan Tang, and Jia-quan Zhang

Abstract A coupled three-dimensional numerical model combining fluid flow, heat transfer, and solidification has been established to study the effect of two types of nozzle on the internal quality of LZ50 steel in a φ 690 mm sized continuously cast round bloom. The model is validated by measured data of the strand surface temperature for plant tests. According to the simulation and experimental results, it is found that the larger tangential velocity on meniscus and the higher vortex depth in the six-port nozzle is beneficial to melting mold powder and the floating removal of inclusions. When the injection mode is the six-port nozzle, the level fluctuation was an effective control to avoid slag entrapment, and the washing effect with multiple swirling flow reinforces both the heat exchange through the solidification front and the dendrite re-melting or fragmenting, stimulating the formation of an equiaxed crystal at the round bloom center. As the injection mode changes from the five-port nozzle to the six-port nozzle, the superheat degree in the round bloom center at the mold exit decreases by 9.3 K, which is one of the resulting increase in the center equiaxed crystal ratio is about 4.3% and the length of columnar decreases by 20 mm. A weaker impingement of the outlet flow on the shell has been observed as well, which can be expected to eliminate the popular subsurface white band phenomenon with an even shell thickness in the mold region. This suggests that the six-port nozzle can effectively improve the quality of large round bloom casting.

Keywords Nozzle injection mode · Level fluctuation · Superheat dissipation · Center equiaxed crystal ratio · Shell thickness

P. Wang · L. Li · H. Tang · J. Zhang (✉)

School of Metallurgical and Ecological Engineering, University of Science and Technology, Beijing, Beijing 100083, People's Republic of China
e-mail: jqzhang@metall.ustb.edu.cn

P. Wang

e-mail: wangpu_ustb@163.com

D. Zhao · W. Liu · S. Wang

Technology Center, Shanxi Taigang Stainless Steel Co., Ltd., Taiyuan 030003, People's Republic of China

© The Minerals, Metals & Materials Society 2021

TMS 2021 150th Annual Meeting & Exhibition Supplemental Proceedings,

The Minerals, Metals & Materials Series,

https://doi.org/10.1007/978-3-030-65261-6_53

Introduction

Since the C content of LZ50 railway axle steel for the production of large-sized round bloom bars is about 0.50%, its solidification end and columnar crystals were well developed prone to severe central shrinkage [1]. Given that mold electromagnetic stirring (M-EMS) is ineffective on casters with larger sized and the higher installation and maintenance costs of equipment. The new nozzle structure was designed to make the molten steel from a swirling flow in the mold, which has become an important research direction for improving the internal quality of the strand [2, 3].

Fang et al. [4] designed and installed a ceramic blade in the straight-through nozzle channel to obtain a horizontal rotating flow of the molten steel. The blade is difficult to process, but also to withstand the erosion of the molten steel, which can easily cause clogging of the nozzle and affect the stability of production. Wang et al. [5] found that a horizontal swirling flow can also be obtained by changing the outflow direction of the quad-furcated radial nozzle, which is conducive to the uniform growth of the initial solidified shell and the stability of the meniscus. Sun et al. [6] compared the flow and solidification behavior of molten steel in the mold with different nozzle types, and it is found that the quad-furcated swirling flow nozzle (SFN) can produce horizontal swirling flow in the mold and obtain the metallurgical effects similar to those of M-EMS. Currently, the SFN has been applied to a certain extent in special steel plants such as LW steel, which has effectively improved the internal quality of strand [7]. In numerical and physical simulation word on lager-sized round bloom casting, Wang et al. [8] found that the SFN is more beneficial than straight nozzle for superheat dissipation of molten steel and the melting of mold powder. Cheng et al. [9] carried out the comparison of the application effect of the straight-through nozzle and the SFN in bloom production practice. The SFN can significantly increase the center equiaxed crystal ratio of the strand, which can improve the center segregation, porosity and shrinkage. Wang et al. [10] combined numerical simulation with plant trials, and they found that the effect of five-port nozzle without M-EMS in improving the internal quality of the strand is far greater than that of straight-through nozzles plus M-EMS.

It has been shown that LZ50 steel has severe internal shrinkage defects when the five-port nozzle is used for large-sized round bloom casting, indicating that the size effect of the strand has an effect on the use of the nozzles. Taking the LZ50 steel of Φ 690 mm round bloom continuous casting as an example, based on the three-dimensional coupling model with fluid flow, heat transfer and solidification in the mold region, the level fluctuation and solidification behavior of the molten steel in the five-port and six-port nozzle injection mode are studied in order to provide theoretical guidance for the application of injection mode technology in the process of large-section special steel producing.

Model Description

Model Assumption and Governing Equations

In the continuous casting process, both the processing equipment and transport phenomena are very complex. To simplify the flow, heat transfer and solidification behavior of molten steel in the upper turbulent flow zone of the continuous casting, the following reasonable assumptions are necessary.

- (1) Regarding the constant casting speed and normal casting conditions, it is regarded as a steady-state process, and the low Reynolds number k-e model is used to simulate the turbulence effect of molten steel.
- (2) The molten steel is assumed to be an incompressible Newtonian fluid, the density during casting and solidification conforms to Boussinesq approximation, and other thermophysical parameters are regarded as average constants.
- (3) Since the latent heat of solid phase change of steel is much smaller than the latent heat of solidification, the arc in the upper turbulent zone of continuous casting is very small, and the influence of phase change and the arc of the caster is ignored.
- (4) Regarding the mushy zone as a porous medium zone, the flow of molten steel in the mushy zone obeys Darcy's law.

The mathematical details of the momentum conservation and energy equations in the casting strand are described in the previous publications [11, 12]. During the continuous casting process, the position of the solidification front changes continuously with the solidification and growth of the shell, and the position of the solid-liquid interface cannot be predicted in advance. The wall function is difficult to use rationally for the high Reynolds number standard k-e turbulence model. The low Reynolds number k-e turbulence model can be better applied to calculate the flow and solidification phenomena in the continuous casting process [13].

Boundary Condition and Solution Modes

Figure 1 presents the structures diagram of the five-port nozzle and the new six-port nozzle of the round bloom, and the main chemical composition of LZ50 steel is shown in Table 1. This continuous casting turbulence flow zone model uses a Cartesian coordinate system, where the Z-direction is the casting direction, and the X- and Y-directions are along the strand radial direction and parallel to the center line of the side port on the five-port nozzle.

In order to ensure the full development of turbulence flow, a total of 1.9 m in the mold region, foot roll zone and part of the secondary cooling zone is selected as the calculation domain. The molten LZ50 is assumed to enter the domain from the inlet with a constant velocity and a constant pouring temperature. The inlet velocity is calculated by the quantity of steel passing through the conservation of mass, and

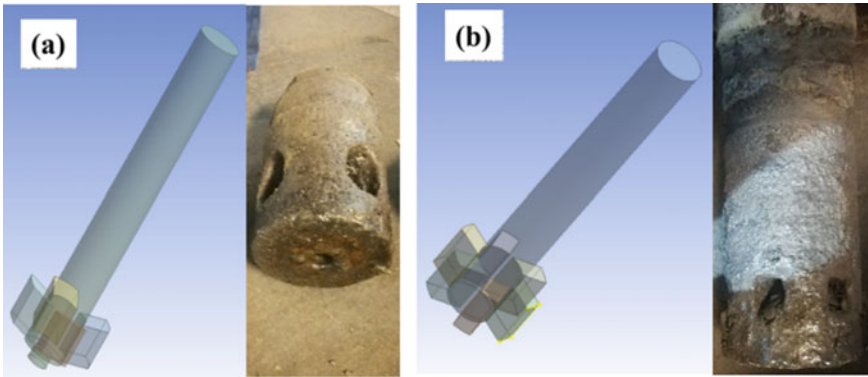


Fig. 1 Geometry structure diagram. **a** Five-port nozzle; **b** Six-port nozzle. (Color figure online)

Table 1 Main chemical composition of LZ50 steel (mass fraction, %)

C	Si	Mn	P	S	Cr	Mo
0.48–0.52	0.24–0.26	≤0.77	≤0.01	≤0.002	≤0.24	≤0.01

the inlet temperature is the sum of the superheat and the liquidus temperature of the molten steel. The turbulent kinetic energy and turbulent energy dissipation are calculated by semi-empirical formulas [14]. To maintain the pouring temperature on the free surface of the pool, the adiabatic condition is applied to the surface with zero shear force. The copper mold is applied on the side wall with a heat flux density [15]. When the round bloom is pulled out of the mold, the heat transfer coefficient of side wall is recommended in Refs. [16, 17]. The fully developed boundary conditions at the outlet of computational domain and solidified region continuously pull out the domain at a constant casting speed. Table 2 lists the physical parameters of material and the continuous casting process parameters of the round bloom.

Table 2 Continuous casting process parameters of round bloom and thermal properties of LZ50 steel

Parameters	Values	Parameters	Values
Section dimension	690 mm	Thermal conductivity	39 W
ID, OD of nozzle	50 mm, 105 mm	Density	7020 kg/m ³
Submergence length	125 mm	Viscosity	0.0055 kg/(m · s)
Nozzle angle	15°, upward	Liquidus temperature	1756 K
Side port	32 mm × 45mm	Solidus temperature	1694 K
Mold working length	620 mm	Specific heat	755 J/(kg · K)
Bottom port	24 mm	Latent heat	270000 J/kg
Casting speed	0.22 m/min	Superheat degree	30 K

In order to apply the low Reynolds number turbulence flow model more accurately, the grids are encrypted in areas with intense transmission intensity such as the nozzle boundary layer and solidification region. Around 470,000,0 hexahedral cells with a minimum mesh size of 1 mm are generated inside the calculation domain for all of the mathematical simulations. Grid-independent converged solutions are obtained using 380,000,0 cells. Considering that when the coefficient of the mushy zone is large, the residual curve is prone to oscillating and difficult to converge. The couple algorithm is used for pressure–velocity coupling. The discretization models for calculating the gradient, pressure and convection are green-Gauss cell-based, PRESTO and the PISO, separately. For the rest, the second-order upwind is used as the discretization model. The time step is gradually increased from 0.0005 to 0.01 s, and the total calculation time is 200 s. It should be mentioned that the residual values for energy are smaller than 10^{-6} and others are smaller than 10^{-4} in ANSYS Fluent 16.0 was used to judge the convergence during the calculation.

These comparisons between simulation and experiment indicate that results using present model have relatively high reliability [11–13]. Thus, the present numerical models of the flow, heat transfer and solidification behavior were used for further calculations.

Results and Discussion

Flow and Meniscus Behavior

Figure 2 reveals the molten steel streamline and phase distribution contour on the symmetry plane of the strand under different injection modes. It can be seen that the molten steel under the six-port nozzle outflows through the side ports to impact on the mold wall, and two recirculation zones are formed above and below the impact point, and the bottom port of the five-port nozzle also produces a recirculation zone. When the injection modes are five-port nozzle and six-port nozzle, respectively, the vortex core depth of the molten steel at the lower part of the mold is 0.68 m and 0.30 m, respectively. The circulation at the lower part of the nozzle helps to agitate the molten steel in the lower part of the mold, promote the movement of inclusions and bubbles, the higher the depth of the vortex is, more favorable the floating and removal of bubbles and inclusions [18].

Figure 3 shows the flow of molten steel on 150 mm below the meniscus under different injection modes. The maximum tangential velocity of molten steel is 0.1 m/s for five-port nozzle and 0.12 m/s for six-port nozzle. The higher tangential velocity with six-port nozzle of the solidification front helps to break the dendrite front, which is beneficial to generate more free crystal nuclei, and the broken dendrites flow freely in the molten steel to increase the equiaxed crystal nucleation opportunity [19].

The tangential velocity on the center line of the meniscus under different injection modes is shown in Fig. 4. As the injection modes are from the five-port to six-port

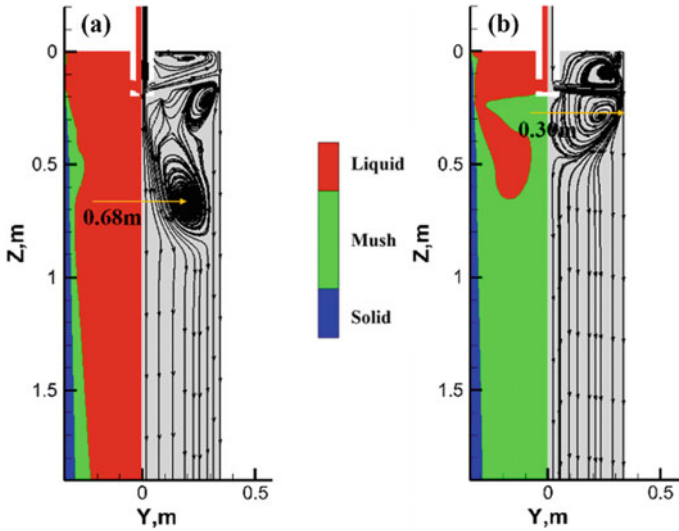


Fig. 2 Molten steel streamline and phase distribution contour on the symmetry plane of the strand. **a** Five-port nozzle; **b** Six-port nozzle. (Color figure online)

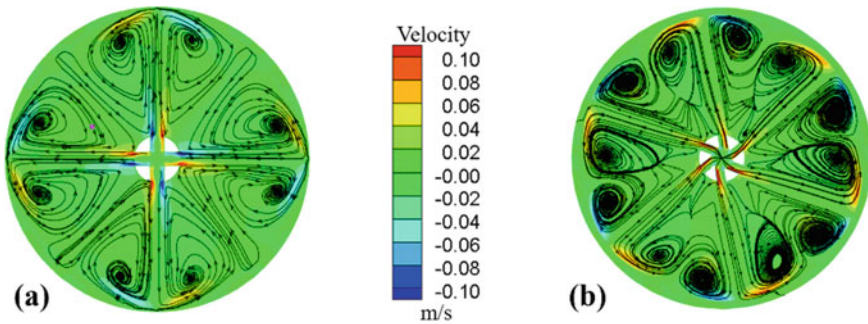


Fig. 3 Flow of molten steel in a cross section on 150 mm below the meniscus. **a** Five-port nozzle; **b** Six-port nozzle. (Color figure online)

nozzle, the maximum tangential velocity increases from 0.006 to 0.013 m/s. The tangential velocity of the molten steel at meniscus is too small that is easy to cause the meniscus to be too calm, which is not conducive to the melting of the mold powder. The tangential velocity of the molten steel at meniscus is too large that is easy to cause the surface of molten steel to be exposed, which can cause secondary oxidation and slag entrapment [17].

The fluctuation of molten steel at the meniscus of the mold can be described by the relative height difference Δh between the node and the free surface [20]. It can be observed in Fig. 5 that the maximum wave height difference of the liquid level is 4.5 mm fall to 1.3 mm under five-port and six-port nozzle. The upward jet flow from

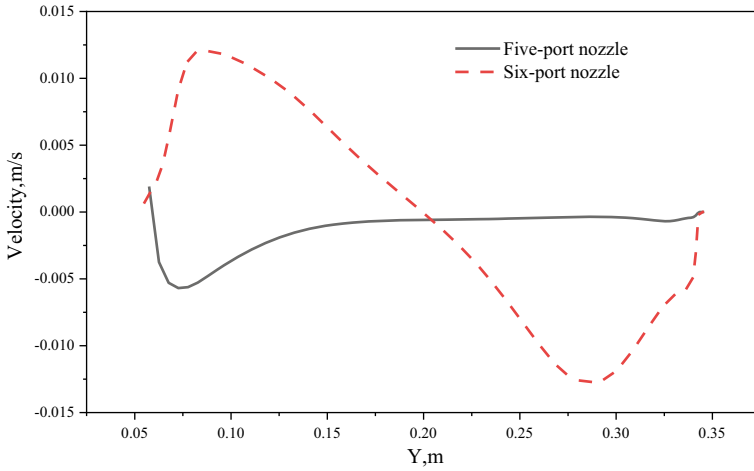


Fig. 4 Tangential velocity on the center line of meniscus under different cases. (Color figure online)

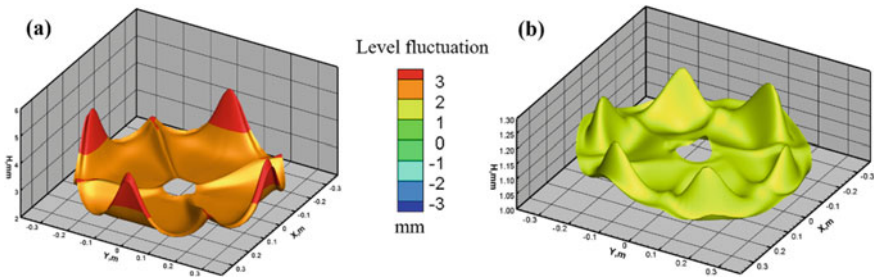


Fig. 5 Mold meniscus fluctuation. a Five-port nozzle; b Six-port nozzle. (Color figure online)

the side ports of the five-port nozzle leads to violent liquid-level fluctuations, which can easily cause the occurrence of slag entrapment influence on the surface quality of the strand.

Heat Transfer and Solidification Behavior

In Fig. 6, it can be seen that the distribution of the central molten steel temperature is in the casting direction under different injection modes. The temperature of molten steel at the mold exit is decreased from 1765.3 to 1756.0 K as the injection mode from five to six-port nozzle. The molten steel from the side ports of the six-port nozzle directly impacts the initial solidified shell for forced heat exchange, resulting in extremely fast superheat dissipation of the molten steel, which is beneficial to the formation of the central equiaxed crystal.

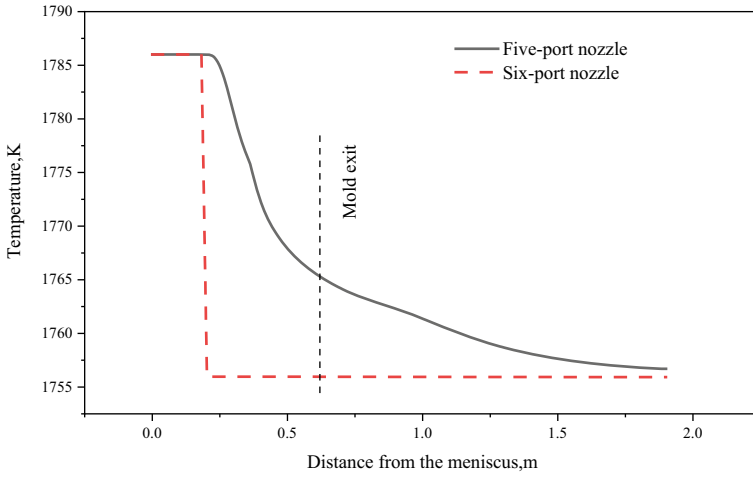


Fig. 6 Temperature distribution of molten steel on the strand centerline along the casting direction. (Color figure online)

Figure 7 indicates the comparison of the shell distribution under different injection modes, in which the liquid-phase fraction of 0.3 is defined as the solidification front. The results indicate that the shell thicknesses for injection modes five- and six-port nozzle are 25.6 and 31.1 mm, respectively. Meanwhile, the extreme difference of the circumferential shell is reduced by 0.4 mm from five to six-port nozzle. The jet flow of six-port nozzle has a certain angle, which effectively reduces the impact on the initial solidified shell and avoids the occurrence of the shell re-melting phenomenon caused by the direct impact of the five-port nozzle, it is of great significance to control strand depression and longitudinal cracks [21].

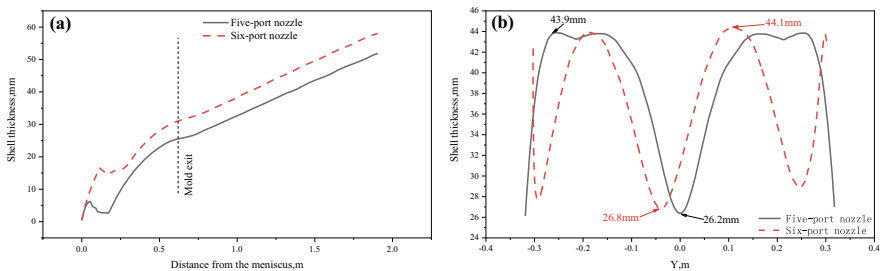


Fig. 7 Comparison of the shell distribution under different injection modes. **a** casting direction; **b** circumferential direction. (Color figure online)

Plant Trial Results

The morphologies of as cast round bloom cross sections with center region and outer arc side of strand under different injection modes are displayed in Figs. 8 and 9, respectively. The length of the equiaxed crystal zone on the inner arc side of the strand increases from 20 mm at five-port nozzle to 35 mm at six-port nozzle. The length and deflection angles of columnar crystals on the outer arc side decrease from 107 to 97 mm and increase from 17° to 20°, respectively, under five- and six-port nozzles. Define the center equiaxed crystal rate of the strand: $R_e = D_e/D$, then the equiaxed crystal rate is 5.8% and 10.1%, respectively.

Xu et al. [19] believe that the erosion of the solidification front by the molten steel may cause the melting of the dendrite arms, and the broken dendrite arms provide nucleation particles for the formation of equiaxed crystals, the certain strength of swirling flow can strengthen heat exchange of the molten steel with the initial solidified shell, which can promote superheat dissipation. Combined with the numerical

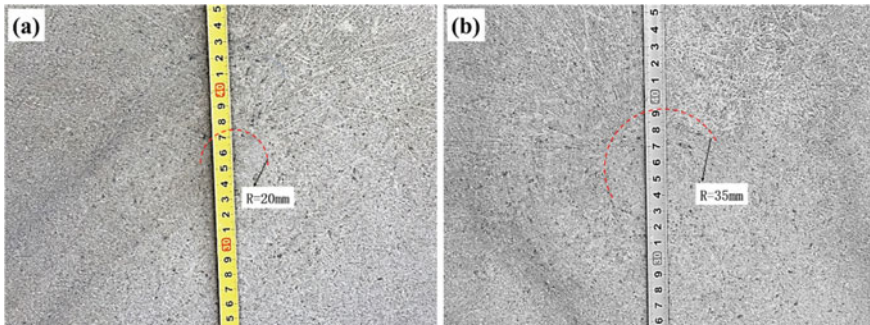


Fig. 8 Morphologies of as cast round bloom cross section with center region. **a** Five-port nozzle; **b** Six-port nozzle. (Color figure online)

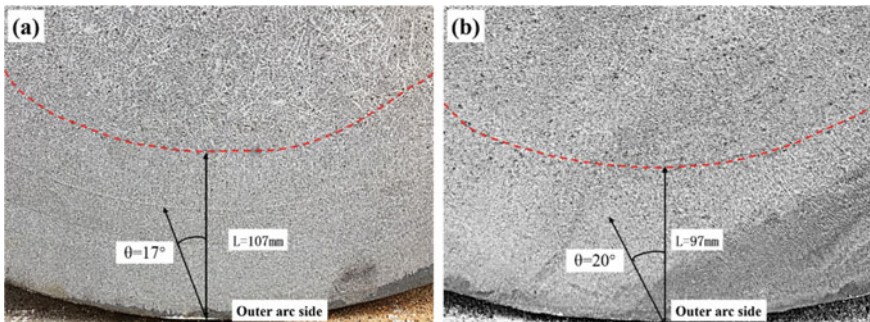


Fig. 9 Morphologies of as cast round bloom cross section at outer arc side. **a** Five-port nozzle; **b** Six-port nozzle. (Color figure online)

simulation results, it can be seen that the equiaxed crystal nucleation chance of the six-port nozzle is greater than the five-port nozzle. The solute washing effect will reduce the content of local elements and increase the temperature of the local liquidus, which is conducive to the liquid phase in the solidification front being in a state of supercooled composition and hindering the growth of columnar crystals [22]. The columnar crystals grow obliquely to the swirling direction, and deflect angles increase with flow rate [23].

Conclusions

Combined numerical simulation and plant trials, the effect of initial transfer behavior and macro-structure evolution were studied. The main conclusions are as follows:

- (1) The six-port nozzle keeps the meniscus of the mold at a certain tangential velocity, increases the depth of the vortex, which is beneficial to the floating and removal of inclusions and bubbles. It can also control the fluctuation range of the liquid level, avoid the occurrence of slag entrapment and improve the surface quality of the strand.
- (2) The side port of the six-port nozzle has a certain angle, which can effectively reduce the impact of the initial solidified shell by the side port jet flow, prevent the shell from re-melting, which can avoid breakout accidents and improve the surface depression of the strand.
- (3) The six-port nozzle can introduce more stranger swirling flow ahead of the solidification front than five-port nozzle, promoting the superheat dissipation of molten steel and columnar to equiaxed transition (CET).

Acknowledgements The authors wish to acknowledge the financial support of the National Natural Science Foundation of China (No. U1860111, and 51874033).

References

1. Cai KK (2008) Continuous casting mold. Metallurgical Industry Press, Beijing
2. Sun HB, Li L (2016) Application of swirling flow nozzle and investigation of superheat dissipation casting for bloom continuous casting. *Ironmaking Steelmaking* 43(3):228–233
3. Yamane H, Ohtani Y, Fukuda J, Kawase T, Nakashima J, Kiyose A (1997) *Steelmaking Conf Proc* 80:159–164
4. Fang Q, Ni HW et al (2017) The effects of a submerged entry nozzle on flow and initial solidification in a continuous casting bloom mold with electromagnetic stirring. *Metals Open Access Metall J* 7(4):146
5. Wang P, Li SX, Zhang JQ et al (2019) Swirling flow effect of radial outlet nozzle for bloom and its effect on initial solidification. *China Metall* 29(09):15–22
6. Sun HB, Han ZG, Qian HZ et al (2010) Effects of injection modes on the flow pattern and temperature distribution of molten steel in a bloom casting mould. *Chin J Eng* 32(9):1131–1137

7. Sun HB, Zhang JQ (2014) Macrosegregation improvement by swirling flow nozzle for bloom continuous castings. *Metall Mater Trans B* 45(3):936–946
8. Wang C, Zhang H, Ma Z W et al (2014) Simulation study on optimization of nozzle structure for round mould. *J Iron Steel Res* 026(003):15–20,26
9. Cheng XW, Fu QH, Dai FQ et al (2015) Application of swirling flow nozzle technology for bloom continuous castings. *Steelmaking* 031(005):32–37
10. Wang P, Zhang JQ et al (2019) Initial transfer behavior and solidification structure evolution in a large continuously cast bloom with a combination of nozzle injection mode and M-EMS. *Metals* 9(10):1083–1097
11. Wang P, Zhang JQ et al (2019) Effect of different types of nozzles on swirling flow development and shell growth behavior in a bloom casting mold. In: *AISTech2019*
12. Li SX, Zhang XM, Li L et al (2019) Representation and effect of mushy zone coefficient on the coupled flow and solidification simulation during continuous casting. *Chin J Eng* 41(2):199–208
13. Aboutalebi MR, Guthrie RIL, Seyedein SH (2007) Mathematical modeling of coupled turbulent flow and solidification in a single belt caster with electromagnetic brake. *Appl Math Model* 31(8):1671–1689
14. Lai KYM, Salcudean M, Tanaka S et al (1986) Mathematical modeling of flows in large tundish systems in steelmaking. *Metall Trans B* 17(3):449–459
15. Li SX, Lan P, Tang H et al (2018) Study on the electromagnetic field fluid flow and solidification in a bloom continuous casting mold by numerical simulation. *Steel Res Int* 89(12):1800071
16. Yuan Q, Vanka SP, Thomas BG et al (2004) Computational and experimental study of turbulent flow in a 0.4-scale water model of a continuous steel caster. *Metall Mater Trans* 35(5):967–982
17. Thomas BG (2006) Modeling of continuous casting defects related to mold fluid flow. *Iron Steel Technol* 3(7):127
18. Thomas BG, Zhang L (2007) Mathematical modeling of fluid flow in continuous casting. *Trans Iron Steel Inst Japan* 41(10):1181–1193
19. Xu ZG, Wang XH, Jiang M et al (2016) Investigation on formation of equiaxed zone in low carbon steel slabs. *Metall Res Technol* 113(1):106–116
20. Zhang LF et al (2010) Transient fluid flow phenomena in continuous casting tundishes. *Iron Steel Technol* 7(7):55
21. Li YQ, Liu JH, He Y et al (2019) Surface defects analysis and mechanism research of 15CrMoG steel bars and process improvement. *Special Steel* 40(6):1–6
22. Sun H, Li L, Wu X et al (2018) Effect of subsurface negative segregation induced by M-EMS on component homogeneity for bloom continuous casting. *Metall Res Technol* 115(6):603
23. Beckermann C, Diepers HJ (1999) Modeling melt convection in phase field simulations of solidification. *Comput Phys* 154:468–496

Study on the In-mold Flow Behavior Driven by a Subsurface Electromagnetic Stirring for IF Steel Slab Casting



Hong Xiao, Shao-xiang Li, Pu Wang, Hai-yan Tang, and Jia-quan Zhang

Abstract A three-dimensional numerical model coupling the electromagnetic field, fluid flow, and level fluctuation has been developed to investigate the flow behavior of molten steel in a slab continuous casting mold for interstitial-free (IF) steel. According to the industrial and modeling results, the swirls are generated on the cross-section due to the electromagnetic force (EMF) and its number relies on the magnetic pole pairs of electromagnetic fields. With the increase in current frequency, the EMF reaches the maximum at the current frequency of 4.5 Hz and then gradually decreases. When the current intensity increases from 0 to 600 A, the rate of slag entrapment related to the billet defects is decreased from 7.46 to 1.09%, but it increases to 6.09% when the current intensity reaches 650 A. The study suggests that the optimized current intensity of mold-electromagnetic stirring (M-EMS) can effectively prevent surface or subsurface defects for clean steel production.

Keywords Interstitial-free steel · Electromagnetic field · Fluid flow · Current intensity · Rate of slag entrapment

H. Xiao · P. Wang · H. Tang · J. Zhang (✉)
School of Metallurgical and Ecological Engineering, University of Science and Technology
Beijing, Beijing 100083, China
e-mail: jqzhang@metall.ustb.edu.cn

H. Xiao
e-mail: xiaohong199515@163.com

H. Xiao
Electromagnetic Center, Hunan Zhongke Electric Co., Ltd, Yueyang 414000, China

S. Li
School of Materials Science and Engineering, Tsinghua University, Beijing 100084, China

Introduction

With the development of clean steel production, the quality requirements for continuous casting products are becoming increasingly strict [1]. For interstitial-free (IF) steel production, which is widely used in the automobile industry due to its excellent deep-drawing property, the surface defects such as slivers and pencil blisters are the most frequent problems leading to rejections and downgrading of their final sheet products [2]. It is especially important to control the mold liquid level fluctuation during casting, and to avoid the subsurface inclusions collection related to the hook shell characteristic of the steels at the meniscus. In the recent decades, mold-electromagnetic stirring (M-EMS) has been recognized as an effective flow control technology, to improve surface qualities of both bloom and slab castings [3–5]. It is very difficult to investigate the molten steel flow with M-EMS by plant measurements and physical experiments, but the numerical simulation is a flexible way to provide an insight into the overall transport process. To reveal the characteristics in slab continuous casting process with M-EMS, much work on electromagnetic and flow fields of M-EMS has been carried out to date. In a series of work from Fujisaki and his co-authors [6–8], three-dimensional (3D) magnetohydrodynamic calculation models were well established to evaluate the characteristics of molten metal with the consideration of fluid flow, heat transfer, and solidification as well as free surface in a linear M-EMS for slab casters. The results revealed that the electromagnetic force (EMF) was eddy distributed, while the velocity was uniform at surface in case of the rotating stirring mold. The electromagnetic stirring makes the solidified shell more uniform with stable temperature deviation. Jin et al. [9] established a 3D mathematical model to calculate the fluid flow in the mold under electromagnetic stirring force and to compare the flow pattern and distribution characteristics under different continuous casting parameters and stirring electric current. Yin et al. [10] simulated the electromagnetic field, flow and solidification in a slab continuous casting mold with M-EMS, and discussed the influence mechanism of M-EMS on the fluid flow, initial solidification, and large inclusion capture.

Moreover, combined the application of numerical simulation and industrial plant trials with M-EMS for slab casting has been rarely reported. A new M-EMS has been introduced which can produce swirling stirring to clean the popular hook collected inclusions; coupled magnetohydrodynamics model has been developed to analyze the characteristics of the three-dimensional electromagnetic field, fluid flow, and level fluctuation phenomena in the 0.23 m × 1.6 m slab mold. The relationships between the EMF and the current intensity or frequency have been analyzed in detail. The influence of stirring current and stirrer position on the level fluctuation of molten steel is also studied. Finally, the various M-EMS parameters of coil current intensity are compared through a combined analysis to the mold flow behavior and the feedback from industrial plant trials.

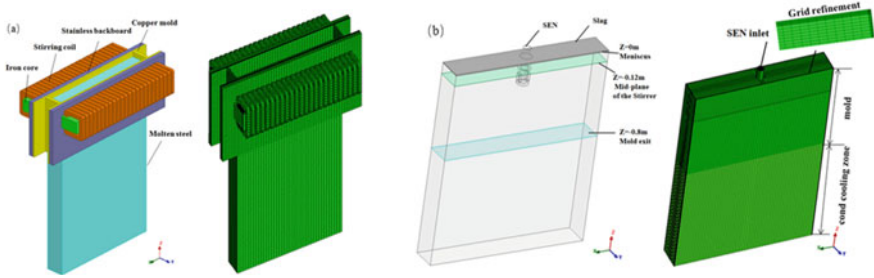


Fig. 1 Geometry model and finite element mesh: **a** electromagnetic simulation; **b** flow simulation. (Color figure online)

Model Description

Three-Dimensional Geometrical Model of M-EMS

The geometry model and finite element mesh in a slab strand with a traveling-wave electromagnetic stirrer are shown in Fig. 1. The model of M-EMS mainly includes molten steel, copper mold, stainless backboard, iron core, stirring coil, and air (not shown). The whole model except air adopts hexahedron element in the meshing process. The origin of the coordinates is at the center of the meniscus, and the casting direction is along the negative direction of Z-axis. Traveling-wave electromagnetic stirrer with 24 pairs of coils around the straight iron cores has been designed to stir the molten steel in the mold. All the coils are connected to three-phase AC current. The copper plate of the mold is 30 mm in thickness. As shown in Fig. 1b, a full geometry model has been developed for the flow simulation, a slab (0.9 m in mold, 1.5 m in second cooling zone) with a size of 1.6 m × 0.23 m × 2.4 m is divided into cells of which the minimum and maximum sizes are 0.001 m and 0.01 m, respectively. The mid-plane of the stirrer is located at Z = −0.12 m. The submerged depth of the nozzle is 0.26 m, and the nozzle inner diameter 0.08 m. The SEN port is rectangular, with a height of 0.08 m, a width of 0.065 m and pointing 15° down-wards. To simulate the level fluctuation in the mold, a liquid slag layer which is 30 mm in thickness is involved in the computation domain.

Basic Assumptions and Equations

To simplify the numerical model, the present work includes the following assumptions:

- (1) the molten steel is an incompressible and isotropic Newton fluid, and the slab is regarded as liquid state entirely.

- (2) the current frequency applied in M-EMS is usually <10 Hz, so the magnetic field is quasi-static and the displacement current in Maxwell's equations is ignored.
- (3) the influence of molten steel movement on electromagnetic field is ignored.
- (4) the molten steel flow in the mold is regarded as steady state.
- (5) the time variant EMF (EMF) is replaced by the time-averaged EMF.
- (6) the effects of the taper and vibration of the mold are not considered.

Electromagnetic field equations:

At the low frequency of M-EMS, the Maxwell's equations can be simplified as [11]:

$$\nabla \times E = -\frac{\partial B}{\partial \tau} \quad (1)$$

$$\nabla \times H = J + \frac{\partial E}{\partial \tau} \quad (2)$$

$$\nabla \cdot B = 0 \quad (3)$$

$$J = \sigma[E + (U + B)] \quad (4)$$

$$B = \mu H \quad (5)$$

Assuming that the electromagnetic field is harmonic, the EMF can be decomposed into time dependent and time-independent components. Because the electromagnetic field period is much shorter than the momentum response time of the molten steel, the time-averaged value can be used to couple with other variables. The time-averaged EMF is defined as follows:

$$F_{\text{mag}}^{\rightarrow} = \frac{1}{2} \text{Re}(\vec{j} \times \vec{B}) \quad (6)$$

where \vec{B} is conjugate complex number of B , and Re is the real part of a complex quantity.

Flow field equations include:

Continuity equation:

$$\frac{\partial}{\partial x_i} (\rho u_i) = 0 \quad (7)$$

where ρ is the density (kg/m^3), u is the flow velocity (m/s), and x is the coordinate system (m).

k and ε are turbulent kinetic energy and turbulent energy dissipation rate, respectively, which are calculated by the standard $k - \varepsilon$ turbulence model written in tensor form as follows:

$$\frac{\partial}{\partial \tau}(\rho_l k) + \rho_l(\nabla k \cdot \vec{u}) = \nabla \cdot [(\mu + \frac{\mu_\tau}{\sigma_k})\nabla k] + G_k - \rho_l \varepsilon \quad (8)$$

$$\frac{\partial}{\partial \tau}(\rho_l \varepsilon) + \rho_l(\nabla \varepsilon \cdot \vec{u}) = \nabla \cdot [(\mu + \frac{\mu_\tau}{\sigma_k})\nabla \varepsilon] + c_1 \frac{\varepsilon}{k} G_k - c_2 \rho_l \frac{\varepsilon^2}{k} \quad (9)$$

where G_k represents the production of turbulence kinetic energy due to the mean velocity gradients:

$$G_k = -\rho_l \overline{u'_i u'_j} \frac{\partial u_j}{\partial u_i} \quad (10)$$

and $C_1, C_2, C_k, C_\varepsilon$ are constants given by B. E. Launder and D. B. Spalding [12] as follows:

$$C_1 = 1.44C_2 = 1.92C_k = 1.0C_\varepsilon = 1.3 \quad (11)$$

The volume of fluid (VOF) model [13] can simulate two or more immiscible fluids by solving a single set of momentum equations and tracking the volume fraction of each of the fluids throughout the computational domain. Ignoring the flux layer, there is an obvious interface between steel and slag, where the VOF model is competent to track the wave.

Boundary Conditions and Solution Methods

During the calculation of electromagnetic field, three-phase alternating current is connected to the coils of M-EMS, and the phase difference is 120° . The boundary condition of electromagnetic field is assumed that the magnetic lines of force are parallel to the outer surface of the air surrounding the stirrer. The distribution of electromagnetic field is solved by the method of magnetic vector potential. Prepared for the calculation of flow field in the next step, the time-averaged EMF needs to be extracted. During the calculation of flow field, the boundary conditions of electromagnetic field are as follows:

- (1) the inlet: the inlet velocity is converted from casting speed by the continuity equation; the turbulent kinetic energy and the dissipation rate at the inlet are calculated by the semi-empirical equations [14].
- (2) the outlet: the boundary condition of mass flow is adopted to guarantee the mass conservation of molten steel.

Table 1 Geometry and material properties for the numerical simulation

Parameter	Values	Units
Mold cross-section	1.6×0.23	m^2
Mold thickness	0.03	m
Mold length	0.9	m
Stainless backboard thickness	0.07	m
Second cooling zone length in geometry model	1.5	m
Casting speed	0.02	m s^{-1}
Length of stirrer	2.0	m
Width of stirrer	0.3	m
Liquid steel magnetic conductivity	$1.257\text{e-}6$	H m^{-1}
Liquid steel electric conductivity	$7.14\text{e}5$	S m^{-1}
Steel density	7020	kg m^{-3}
Slag density	2700	kg m^{-3}
Molecular viscosity of the molten steel	0.0055	$\text{kg s}^{-1} \text{m}^{-1}$
Molecular viscosity of the liquid slag	0.2	$\text{kg s}^{-1} \text{m}^{-1}$
Specific heat of steel	680	$\text{J kg}^{-1} \text{K}^{-1}$
Thermal conductivity	31	$\text{W m}^{-1} \text{K}^{-1}$

- (3) the top surface: the normal derivatives of all variables are set to zero at the free surface.
- (4) the wall surface: the non-slip boundary condition is utilized.

The geometry and material properties used in the present work are listed in Table 1.

The geometry and material properties used in the present work are listed in Table 1.

Results and Discussion

Validity of Developed Model

To ensure the validity of the mathematical model, the computed results for the magnetic flux density along $Y = 0.1$ m line at the mid-plane of the stirrer were compared with the measured data in a plant, which is shown in Fig. 2. The measured data was obtained by the Hunan Zhongke Electric Co., Ltd through a Lake Shore 475 DSP Gauss meter. From this figure, the tendencies of the magnetic flux density are centrally symmetrical distribution. The calculated results are in good agreement with the measured data, which indicates that the developed mathematic model is reasonable for this stirring system and the calculated results could be used to provide

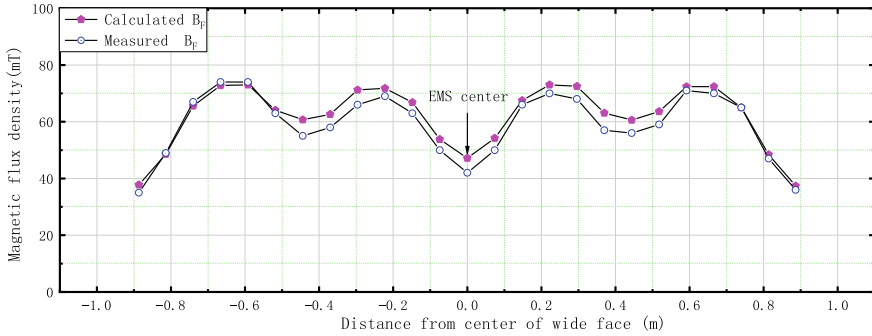


Fig. 2 Comparison between the calculated and measured values of magnetic flux intensity. (Color figure online)

theoretical guidance for optimizing stirring operation parameters in actual production. Besides, the measured magnetic flux density is a little lower than that calculated, owing to the magnetic field leakage and measured or computed error. However, this error is small and can be neglected.

Magnetic Flux Density

Figure 3 shows the magnetic flux density along lines for $Y = -0.1$ m (BF), $Y = 0.1$ m (BL), $Y = 0$ m (BO) at the mid-plane of the stirrer with and without stainless backboard. It can be observed that the BF is almost equal to BL. For the case with the stainless backboard in Fig. 3a, its magnetic flux density is more uniform and smaller than that without stainless backboard, which plays a role of electromagnetic shield from the coils. The average values of BF are, respectively, 61.92 mT and 122.26 mT for with and without stainless backboard, so it is not accurate to ignore stainless backboard in the M-EMS geometry model.

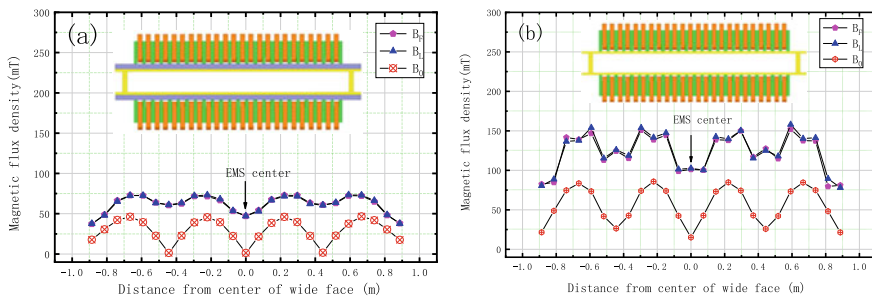


Fig.3 Magnetic flux density (BF, BL, BO). **a** with stainless backboard; **b** without stainless backboard. (Color figure online)

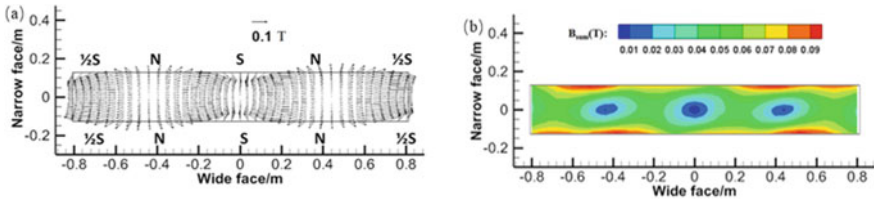


Fig. 4 Distribution of magnetic flux density on the stirrer mid-plane ($Z = -0.12$ m). **a** Vector; **b** contour. (Color figure online)

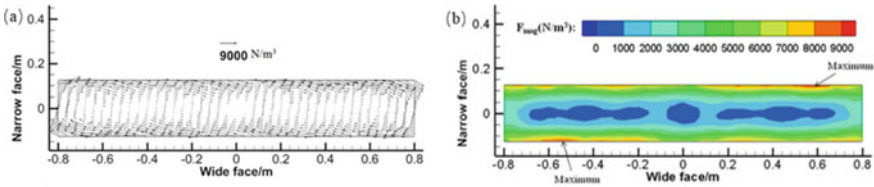


Fig. 5 Vector and contour plots of time-averaged EMF on the stirrer mid-plane ($Z = -0.12$ m). **a** vector; **b** contour. (Color figure online)

Figure 4 shows the vector and contour plots of magnetic flux density at the mid-plane of the stirrer ($Z = -0.12$ m). It is seen that the vector and contour of magnetic flux density of the initial phase distribute centrosymmetric. The magnetic flux density is larger at the edge of wide face, and it decreases gradually from the exterior to the interior. The maximums are located in the vicinity of the mold wide edge ($Y = 0.125$ m or $Y = -0.125$ m).

Figure 5 shows the vector and contour of the time-averaged EMF on the stirrer mid-plane ($Z = -0.12$ m). It is seen that the distribution of EMF is centrosymmetric due to the centrosymmetric distribution of the magnetic flux density. The tangential components of the EMFs in the vicinity of the edges are greater than that in the inner part of the cross-section, and the tangential components of the EMFs at the two parallel edges of the wide face are equal in value with opposite direction. Four transverse swirls of the time-averaged EMF exist in the interior of cross-section. The maximum of the time-averaged EMF is 9000 N/m^3 , which appears at the points $X = 0.57 \text{ m}$, $Y = 0.125 \text{ m}$ and $X = -0.57 \text{ m}$, $Y = -0.125 \text{ m}$. The minimum of the time-averaged EMF is lower than 1000 N/m^3 , which appears in the interior.

Figure 6a shows the distribution of magnetic flux density for different current at 4.5 Hz. The magnetic flux density increases with the increasing current intensity, and they are in approximate proportional relationship. Figure 6b shows the distribution of tangential EMF for different current frequencies at 600 A. In the range of applied current frequencies for M-EMS (1.0–5.5 Hz) at 600 A, the tangential EMF increases with the increasing current frequency and reaches the maximum at the current frequency 4.5 Hz and then decreases gradually.

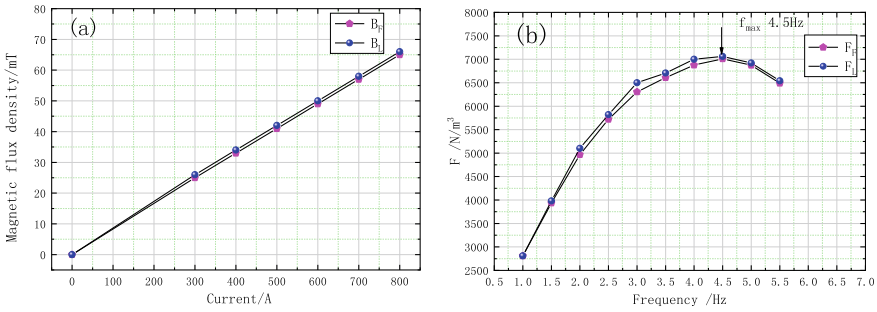


Fig. 6 Distribution of magnetic flux density and tangential EMF. **a** different currents; **b** different frequencies. (Color figure online)

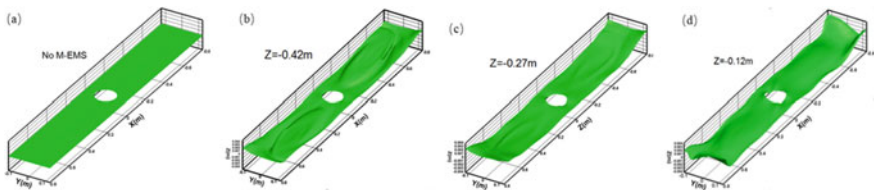


Fig. 7 Comparison of three-dimensional level fluctuations: **a** M-EMS off; **b** with M-EMS, $Z = -0.42$ m; **c** with M-EMS, $Z = -0.27$ m; **d** with M-EMS, $Z = -0.12$ m. (Color figure online)

Figure 7 shows the three-dimensional level fluctuations under different positions of stirrer mid-plane, in which the plane of steel volume fraction value 0.5 is chosen to express the status of level fluctuation. It can be intuitively seen that the steel/slag interface is nearly flat as the M-EMS off. The swirling flow from the effect of M-EMS increases the fluctuation of the free surface, and the highest-level fluctuations for M-EMS happen at four corners of the mold-free surface. In the local regions, the maximum height of level fluctuation for M-EMS at $Z = -0.42$ m, -0.27 m, -0.12 m are 1.0 mm, 2.4 mm, and 2.9 mm, respectively. The height of the stirrer increases, which can easily induce the fluctuation of the free surface. The results indicate that as the height of the stirrer is increased, the level fluctuation is aggravated. The largest value of level fluctuation under M-EMS at $Z = -0.12$ m is acceptable for the movement of slag, which the range of level fluctuation within ± 4 mm is acceptable for plant [15]. Therefore, the optimum stirrer position for the mid-plane of M-EMS is at $Z = -0.12$ m below the meniscus.

Figure 8 indicates the effect of stirring current on the level fluctuation. With the increase of stirring current, the level fluctuation is intensified due to the obvious transversal swirling flow induced by the M-EMS, which may lead to slag entrapment. In the local regions, the maximum height of level fluctuation for current 500 A, 550 A, 600 A, 650 A are 2.1 mm, 2.8 mm, 3.6 mm, and 4.2 mm, respectively. When the current is 650 A, the level fluctuation exceeds ± 4 mm, the aggravation of the level fluctuation may lead to the slag entrapment.

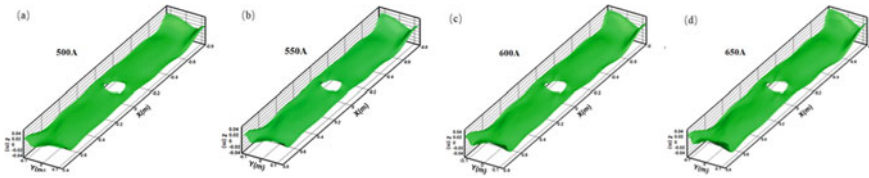


Fig. 8 Comparison of three-dimensional level fluctuations: **a** 500 A; **b** 550 A; **c** 600 A; **d** 650 A. (Color figure online)

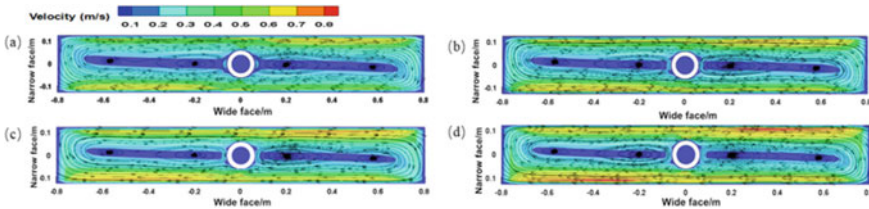


Fig. 9 Vector distribution at the center of EMS **a** 500 A; **b** 550 A; **c** 600 A; **d** 650 A. (Color figure online)

Figure 9 reveals the flow pattern on the mid-plane of M-EMS under various currents. The tangential velocity rises with the increasing current intensity. Four transverse swirls of the molten steel are symmetrically distributed, which almost coincide with the four magnetic pole pairs.

Quality of Slab with Different Process Parameters

According to the simulation results above, four current intensities were chosen to test for a interstitial-free steel slab produced by a steel plant in China, the blocking rate of slag entrapment was counted in Table 2, which is one of the main sources of inclusions in the final product, and will greatly harm the clean steel production. When the M-EMS is powered on, the blocking rate of flux entrainment obviously decreases. At the current intensity 600 A, the blocking rate of slag entrapment is only 1.09%, which is decreased by 85% compared with the situation M-EMS off. Therefore, the industrial results agree well with the calculated results, and thus verify the success of the present model.

Table 2 Blocking rate for slag entrapment with different current intensities

Stirring current intensity	0 A	500 A	550 A	600 A	650 A
Blocking rate of slag entrapment (%)	7.46	6.86	2.80	1.09	6.90

Conclusions

Combined numerical simulation and plant trials, the effect of M-EMS on the electromagnetic field, fluid flow, and level fluctuation were studied. The main conclusions are as follows:

- (1) The magnetic flux density and the EMF distribute centrally symmetrical on the wide face of mold. The EMF generates the swirls on the cross-section and its number is corresponding to the magnetic pole pairs of electromagnetic field. With the increase in current frequency, the EMF reaches the maximum at the current frequency of 4.5 Hz and then gradually decreases.
- (2) With the increase in the height of the stirrer position, the level fluctuation aggravates, which may lead to the flux entrainment. When the mid-plane of M-EMS is at $Z = -0.12$ m, the level fluctuation is ± 4 mm, which is accepted by the plant.
- (3) According to the statistical results of the entrainment blocking rate for different process parameters in industrial plant trials, the optimized current intensity is 600A, and at this current intensity, the blocking rate of slag entrapment is only 1.09%, far lower than the case with M-EMS off.

Acknowledgements The authors wish to acknowledge the financial support of the National Natural Science Foundation of China (No. U1860111, and 51874033), the National key research and development program (No. 2016YFB0601302), and Hunan province science and technology plan major project (2016GK1002).

References

1. Takechi H (1994) The development of interstitial-free steel in Japan. *Iron Steel Inst Japan* 34:1
2. Tripathy PK, Das S, Jha MK, Singh JB, Kumar AM, Das AK (2006) Migration of slab defects during hot rolling. *Ironmaking Steelmaking* 33:477
3. Yamane H, Ohtani Y, Fukuda J, Kawase T, Nakashima J, Kiyose A (1997) High power in-mold electromagnetic stirring—improvement of surface defects and inclusion control. *Steelmaking Conf Proc* 80:159
4. Ohtani Y, Fukuda J, Ishiwata N, Ishiwatari N, Funato K (1994) Improvement of surface quality with in-mold electromagnetic stirring. *CAMP-ISIJ* 7:1194
5. Okano S, Nishimura T, Ooi H, Chino T (1975) Relation between large inclusions and growth directions of columnar dendrites in continuously cast slabs. *Tesu-To-Hagane* 61:2982–2989
6. Fujisaki K (2001) In-mold electromagnetic stirring in continuous casting. *IEEE Trans Ind Appl* 37:1098–1104
7. Fujisaki K, Ueyama T, Okazawa K (1997) Magnetohydrodynamic calculation of in-mold electromagnetic stirring. *IEEE Trans Magn* 33:1642–1647
8. Fujisaki F, Ueyama T, Takahashi K, Satoh S (1997) Phase characteristics of electromagnetic stirring. *IEEE Trans Magn* 33:4245–4247
9. Jin XL, Zhou YM, Let ZS (2016) Numerical simulation of fluid flows in a slab continuous casting mold under electromagnetic stirring. *Baosteel Tech Res* 10:10–15

10. Yin YB, Zhang JM, Lei SW, Dong QP (2017) Numerical study on the capture of large inclusion in slab continuous casting with the effect of in-mold electromagnetic stirring. *ISIJ Int* 57:2165–2174
11. Li S, Lan P, Tang H et al (2018) Study on the electromagnetic field, fluid flow, and solidification in a bloom continuous casting mold by numerical simulation. *Steel Res Int* 89(12):1800071
12. Launder BE, Spalding DB (1972) *Lectures in mathematical models of turbulence*. Academic Press, London
13. Hirt CW, Nichols BD (1981) Volume of fluid (VOF) method for the dynamics of free boundaries. *J Comput Phys* 39:201–225
14. Lai KYM, Salcudean M, Tanaka S, Guthrie RIL (1986) Mathematical modeling of flows in large tundish systems in steelmaking. *Metall Mater Trans B* 17:449–459
15. Thomas BG (2006) Modeling of continuous casting defects related to mold fluid flow. *Iron and Steel Technol* 3(7):127–141

Part XXIII
Corrosion in Heavy Liquid Metals
for Energy Systems

Corrosion Investigations of Materials in Antimony–Tin and Antimony–Bismuth Alloys for Liquid Metal Batteries



Tianru Zhang, Annette Heinzl, Adrian Jianu, Alfons Weisenburger, and Georg Müller

Abstract Liquid metal batteries are discussed as stationary electrical energy storage for renewable energies, in order to compensate their fluctuating supply of energy. A liquid metal battery consists of three different liquids, which stay segregated due to density differences and mutual immiscibility. The negative electrode is the low-density liquid metal, and in our case sodium, a medium density molten salt, is the electrolyte and positive electrode is a high-density liquid metal. For the latter, Sb–Sn and Sb–Bi alloys are selected. However, one issue is the compatibility of structural materials with the used liquids. In a first step, the behavior of potential structural materials in Sb_3Sn_7 and SbBi_9 at the temperature of 450 °C up to 750 h was tested. The results showed that the corrosion in SbBi_9 was significantly less than in Sb_3Sn_7 and the most promising materials were molybdenum meta and Max-phase coatings.

Keywords Corrosion · Sb–Sn alloy · Sb–Bi alloy · Liquid metal batteries

Introduction

Liquid metal batteries (LMBs) are an intriguing energy storage technology because of their advantages including low cost, simply assembly, high kinetics on liquid–liquid boundaries, potential for large capacity and long lifespan, etc. [1, 2]. Nowadays, it has attracted great interest to be applied as one of the most promising large-scale electricity storage devices to smooth over the intermittency of renewable energy production such as wind and solar, in order to integrate them into grid [3–6].

Despite the excellent electrochemical performance of Li-based LMBs, lithium is not an abundant element, and there are considerable concerns about the rare natural resources of lithium in the Earth's crust (only 0.0017wt %), uneven global distribution (predominantly in Chile, Bolivia, and China) of lithium, and expected increasing cost of lithium-ion-containing minerals (Li_2CO_3) [7, 8], which make low-cost Na-based LMBs more competitive in large-scale energy storage for the future energy system.

T. Zhang (✉) · A. Heinzl · A. Jianu · A. Weisenburger · G. Müller
Karlsruhe Institute of Technology, Karlsruhe, Germany
e-mail: tianru.zhang@kit.edu

© The Minerals, Metals & Materials Society 2021
TMS 2021 150th Annual Meeting & Exhibition Supplemental Proceedings,
The Minerals, Metals & Materials Series,
https://doi.org/10.1007/978-3-030-65261-6_55

605

Therefore, the aim of our research is to realize low-cost Na-based LMBs with good electrochemical performance and long lifetime.

Based on recent researches, Sb is the most promising positive electrode candidate because of its low cost and relatively higher cell voltage, but its high melting point (631 °C) requires undesirable higher cell operating temperature and herein results in higher corrosion rates. Some researchers found that alloying Sb with Pb can significantly decrease the melting point of positive electrode as well as the cell operating temperature without a decrease in cell voltage [3, 6]. However, considering about the potential environmental concerns might be brought by large-scale application of Pb, Sn and Bi were selected to alloy with Sb, to create an environmentally friendly positive electrode material, with promising thermodynamic and electrochemical performance [6].

The higher operating temperature (usually above 300 °C) of LMBs brings one of the biggest scientific issues to be solved: the compatibility of structural materials with those effective compositions/corrosion behavior of structural materials with heavy liquid metal, molten salt, and liquid sodium as well.

Up to now, 10 kinds of materials: T91 steel, 304 steel, 316L steel, 4J33 alloy, high-entropy alloy (HEA), Mo metal, Cr metal, 3 max-phase coatings on Al₂O₃ substrate (Ti₂AlC, Ti₃AlC₂ and Cr₂AlC) were chosen to evaluate their corrosion resistance against heavy liquid metal Sb₃Sn₇ and SbBi₉, respectively [6], at 450 °C with the duration of 1 month, in order to investigate their potential to be applied as positive current collector (PCC) material in LMBs.

Experimental

Except for those three kinds of max-phases, all test materials were ground before exposure. All specimens were fixed on an Al₂O₃ holder by Mo wires and then exposed to liquid Sb₃Sn₇ and SbBi₉, respectively.

The used facility for this corrosion test is the COSTA facility in the Institute of High power and Microwave Technology/Karlsruhe Institute of Technology (IHM/KIT) laboratory [9]. It consists of a furnace, which is applied to regulate the isothermal condition for the exposure, and two separately quartz tubes, which are set inside the furnace. The quartz tubes are connected with a gas control system and flow meters to adjust the gas flow and to control the atmosphere.

At the first step, an appropriate temperature gradient was regulated in the three-zone furnace of COSTA facility to achieve the largest possible uniform temperature distribution inside the quartz tubes at the temperature of 450 °C.

The used composition of heavy metal was gained by mixing the individual heavy metals Sb, Sn, and Bi in their solid forms together (90 g for both Sb₃Sn₇ and SbBi₉) in Al₂O₃-crucibles. For this, granular of the metals was used. In the case of Sn, the granular had a size of 2–4 mm and a purity of 99.99%. It was delivered by the company HMW Hauner GmbH & Co. KG; Sb and Bi were delivered by Haines & Maassen. The Sb granular had a purity of 99.65% and a size of 1–10 mm, and the Bi

granular had a purity of 99.99% and a size of 1–3 mm. Unfortunately, the surface of the Bi granular was a bit oxidized, so it had been first melted in a Mo-crucible and the slag layer on top was removed. After that, the desired amount of molten Bi was poured into the Al_2O_3 -crucibles and cooled down in room temperature.

After the crucibles were filled, they were put into the furnace at room temperature. Additionally, the atmosphere inside the quartz tubes were pre-purged with 100 ml/min $\text{Ar}5\%\text{H}_2$ for 2 days. Then, the temperature was raised up to 700 °C to melt as well the Sb (melting point: 631 °C) which has the highest melting point of the three metals. The high temperature was hold for 2 h, afterward the temperature was decreased to the test temperature of 450 °C. To get a reducing environment inside the liquid metal, it was hold under 100 ml/min $\text{Ar}5\%\text{H}_2$ gas flow.

For loading and unloading of the specimens, a glove box was connected to the quartz tubes. To maintain the atmosphere inside the furnace, the globe box was also purged before with $\text{Ar}5\%\text{H}_2$ gas until an oxygen content of 2×10^{-14} ppm was reached. For the exposure, each specimen was put into the glove box, separately added and full-immersed/sub-immersed (depends on the shape and size of specimens) in one Al_2O_3 -crucible through the globe box with inert atmosphere. Then all Al_2O_3 -crucibles were set back into COSTA facility and held isothermally at 450 °C for exposure duration of 750 h.

After 750 h exposure in Sb_3Sn_7 and SbBi_9 , all specimens were extracted from the COSTA facility, cooled down in glove box to room temperature and analyzed by XRD, LOM, and SEM with EDX.

Results and Discussion

The appearance of all samples after exposure to liquid Sb_3Sn_7 and SbBi_9 , respectively, are shown in Fig. 1a, b. As shown in this graph, regardless of the two different compositions of the liquid metal systems, the immersed part of all metallic samples was more or less covered by a layer of liquid metal. In contrast, all three kinds of max-phases showed no attachment of liquid metal and all retained their original appearance.

The SEM images of all samples after expose are shown in following paragraphs. After the exposure, all metallic tested specimens (Mo, Cr, steels, and alloys) were cut,

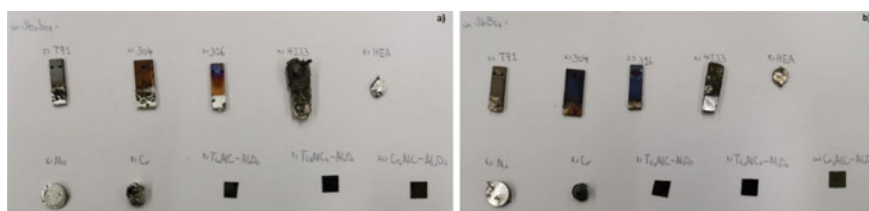


Fig. 1 Appearance of all samples after exposure in the circumstance of (a) Sb_3Sn_7 and (b) SbBi_9 . (Color figure online)

embedded into resin, ground, and then polished for the observation and examination of cross sections with the help of SEM. Due to the fact, that nearly no heavy metals was sticking on the three kinds of max-phases, an investigation of the surface of these materials after exposure was possible and done, an investigation of the cross section was not done so far.

The observation and examination of cross sections of specimens reveal the microstructure of the interface between the specimen surface and the layer attached and/or formed on the specimen surface during the exposure, which indicates the penetration of heavy liquid metals and the dissolution/destruction of specimen during the exposure likewise.

The elemental mapping/point scanning/line scanning on cross sections or on surface morphologies determines the distribution of diverse elements including liquid metals at certain spots in specimens.

304 Steel

304 steel was taken as an example, and other metallic samples (all the other steels, 4J33 alloy, HEA, and Cr) showed similar corrosive performance like 304 steel in Sb_3Sn_7 and in SbBi_9 environment, except for Mo, which has an outstanding corrosion resistance in both environments.

In Sb_3Sn_7 Environment

Figure 2 shows the cross sections of 304 steel specimen and its EDX elemental mapping analysis after exposure in Sb_3Sn_7 . A layer of heavy liquid metal (bright part in the first image) was attached on the steel surface and showed on one side a partly enormous penetration into 304 steel. After 750 h exposure in Sb_3Sn_7 , the maximal penetration depth in 304 steel is larger than 1 mm. EDX elemental maps reveal that Fe, Cr, and Ni were intensively dissolved after exposure in Sb_3Sn_7 . Furthermore, both Sb and Sn in Sb_3Sn_7 showed evident penetration into 304 steel.

In SbBi_9 Environment

As shown in Fig. 3, the surface of 304 steel specimen immersed in SbBi_9 was attached by a layer of heavy liquid metal (bright part in the first image) as well. Furthermore, these images also indicate that 304 steel specimen suffered distinct dissolution attack during exposure in SbBi_9 ; however, compared with Sb_3Sn_7 , SbBi_9 exhibited much slighter penetration into 304 steel, the maximal penetration depth after 750 h exposure is around 20 μm .

EDX elemental mapping analysis across the specimen surface indicates that compared with the specimen in Sb_3Sn_7 , dissolution and destruction of 304 steel

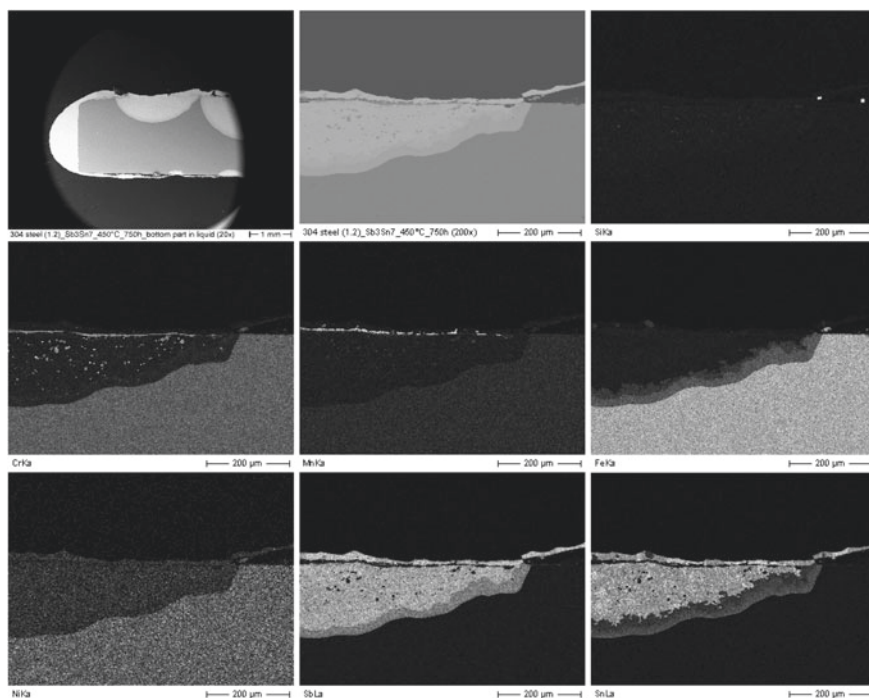


Fig. 2 Cross sections and elemental maps of 304 steel after exposure in Sb_3Sn_7

occurred during the exposure in SbBi_9 is more drastic; however, compared with the Sb_3Sn_7 , both Sb and Bi in SbBi_9 did not show severe penetration into 304 steel; furthermore, in comparison to Sb, Bi showed less penetration depth into 304 steel.

Mo Metal

In Sb_3Sn_7 Environment

Figure 4 shows the cross sections of Mo specimen and its EDX elemental mapping analysis after exposure in Sb_3Sn_7 . Obviously, a layer of heavy liquid metal was attached on the surface of Mo metal; however, no penetration of Sb_3Sn_7 or development of second phases can be observed into Mo metal. In addition, EDX elemental maps clarify that Mo metal suffered no dissolution attack during the exposure in Sb_3Sn_7 for 750 h. Furthermore, those images also indicate that both Sb and Sn in Sb_3Sn_7 showed no penetration into Mo metal.

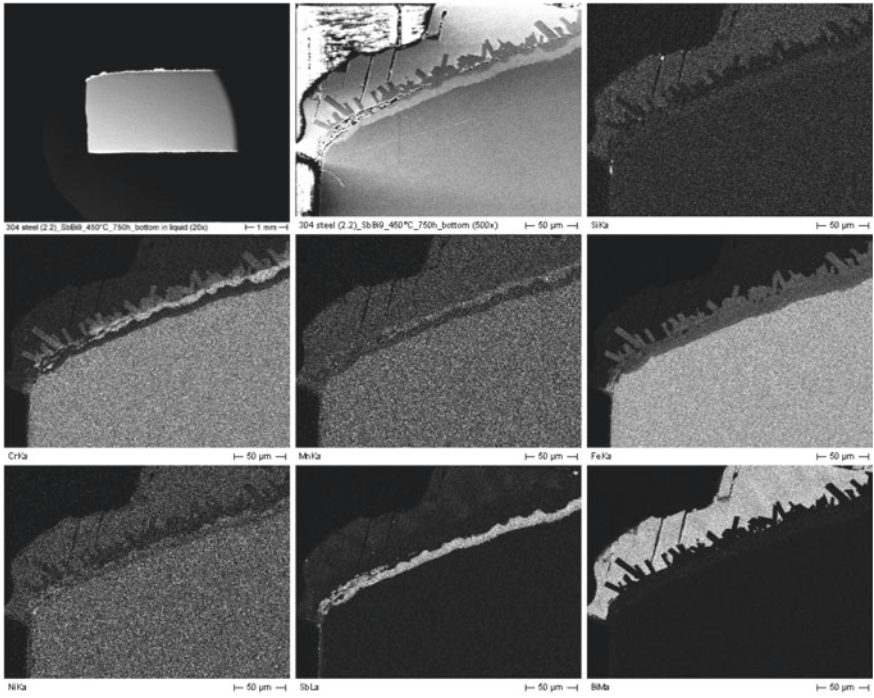


Fig. 3 Cross sections and elemental maps of 304 steel after exposure in SbBi₉

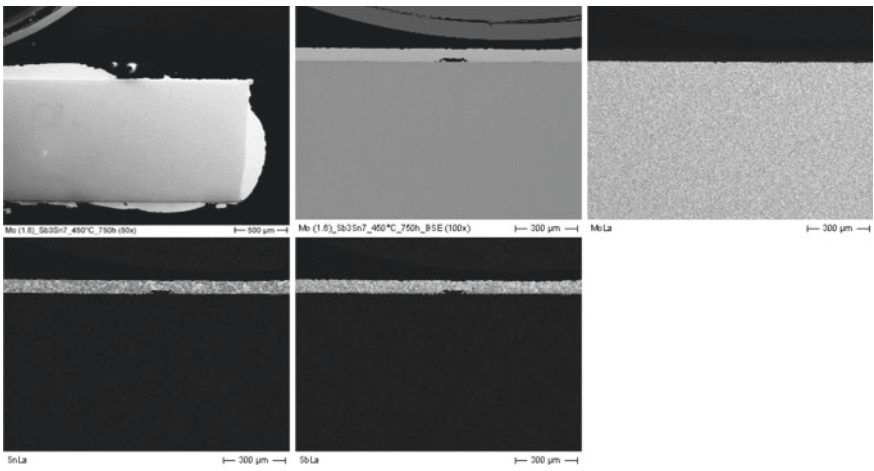


Fig. 4 Cross sections and elemental maps of Mo after exposure in Sb₃Sn₇

In SbBi₉ Environment

Figure 5 presents the cross sections and the elemental mapping analysis of Mo after exposure in SbBi₉, the surface of Mo specimen immersed in SbBi₉ was attached by an extremely thin layer of heavy liquid metal. Similarly, no penetration of SbBi₉ can be observed into Mo metal in this case. In addition, these images also indicate that Mo metal specimen suffered no dissolution attack and developed no second phases during the 750 h exposure in SbBi₉ as well. Furthermore, both Sb and Bi in SbBi₉ showed no penetration into Mo metal.

Figure 6 shows the line scan across the surface layer of Mo metal after exposed in SbBi₉ for 750 h, which also reveals that both Sb and Bi in SbBi₉ showed no penetration into Mo metal. The Mo specimen surface was still in good condition after exposure. Therefore, the Mo attached on sample surface might come from Mo powder generated when the sample was cut.

Cr₂AlC–Al₂O₃ (Max-Phase on Al₂O₃ Substrate)

Cr₂AlC coated on Al₂O₃ substrate was also cited as an example, since the other 2 Max-phases showed great similarities on corrosion performance to Cr₂AlC–Al₂O₃ after exposure in those two heavy liquid metal environments.

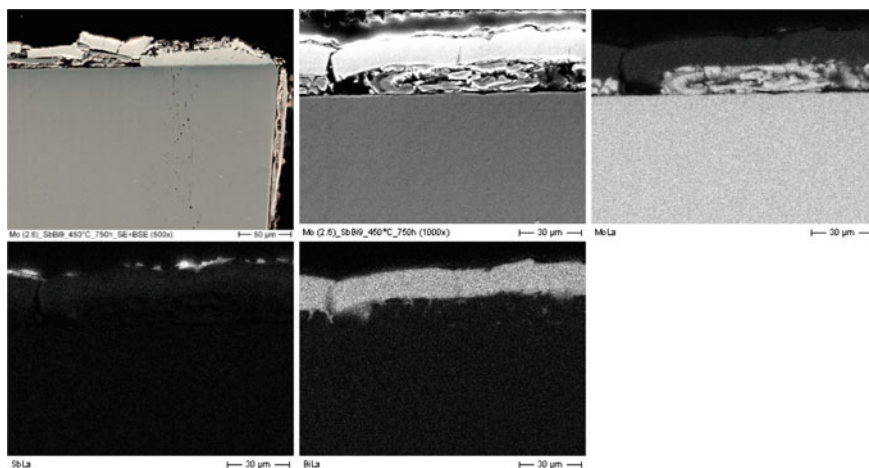


Fig. 5 Cross sections and elemental maps of Mo after exposure in Sb₃Sn₇. (Color figure online)

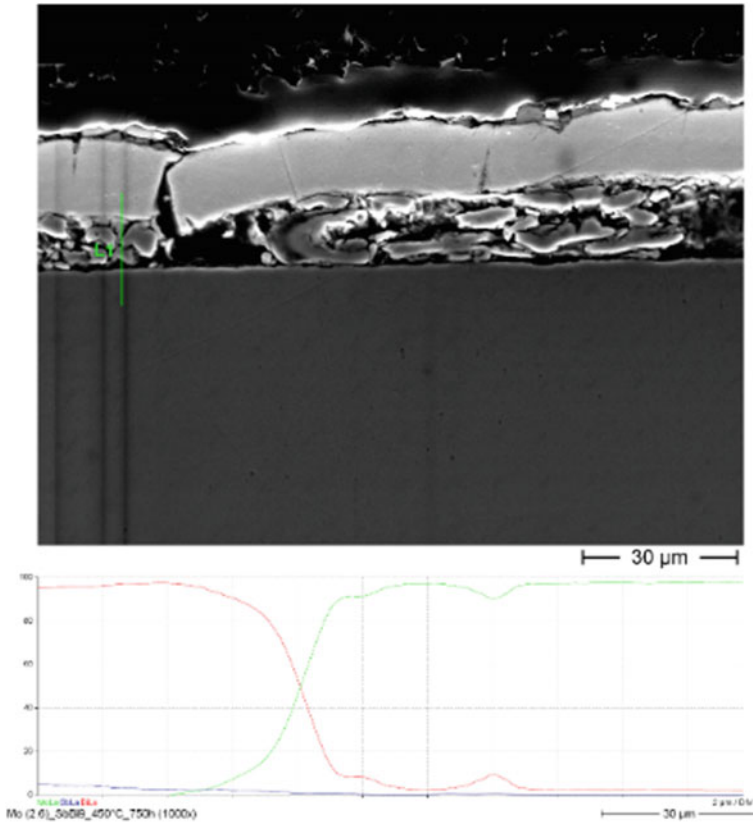


Fig. 6 Line scan across the surface layer of Mo after exposure in SbBi_9 . (Color figure online)

In Sb_3Sn_7 Environment

Figure 7 presents the surface morphology of Cr_2AlC coated on Al_2O_3 substrate after exposure in Sb_3Sn_7 . It can be seen from this figure that the surface of $\text{Cr}_2\text{AlC}-\text{Al}_2\text{O}_3$ specimen kept perfect and smooth; no dissolution attack or penetration of liquid metal were observed after exposure in Sb_3Sn_7 . Obviously, some small, bright particles were attached on specimen surface, which were evidenced by EDX elemental mapping analysis, are drops of Sb and Sn.

In SbBi_9 Environment

As shown in Fig. 8, the surface morphology of Cr_2AlC coated on Al_2O_3 substrate immersed in SbBi_9 also remained perfect and smooth. No dissolution attack or penetration of liquid metal was observed on $\text{Cr}_2\text{AlC}-\text{Al}_2\text{O}_3$ specimen after exposure in

Fig. 7 Surface morphology of $\text{Cr}_2\text{AlC}-\text{Al}_2\text{O}_3$ after exposure in Sb_3Sn_7

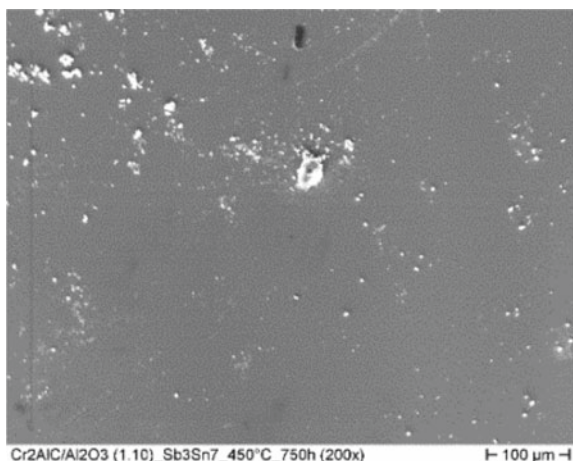
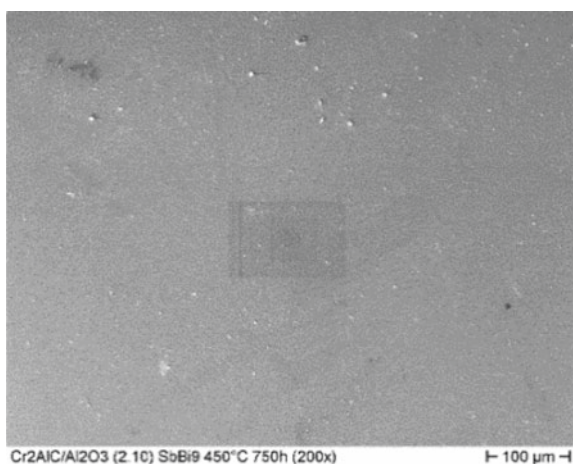


Fig. 8 Surface morphology of $\text{Cr}_2\text{AlC}-\text{Al}_2\text{O}_3$ after exposure in SbBi_9



SbBi_9 . However, compared with Sb_3Sn_7 , the amount of small and bright particles attached on specimen surface in the circumstance of SbBi_9 was much less. Those drops were confirmed by qualitative EDX analysis, as remained Sb and Bi drops.

Conclusion

It can be seen from the results of all specimens after 750 h exposure in these two different heavy liquid metal systems (Sb_3Sn_7 and SbBi_9) at 450 °C that each composition of heavy liquid metal system has its own corrosion property. In comparison to the Sb–Bi system, the Sb–Sn system is highly aggressive and corrosive, which

also indicate that it is necessary for us to compare their electrochemical performance when applied as positive electrode in future experiments.

Among all the test materials, all specimens of steels and alloys (T91 steel, 304 steel, 316L steel, HEA, 4J33 alloy) as well as Cr could not meet the corrosion resistance requirements in such heavy liquid metal environments. One exception is Mo, the only tested metallic material which shows outstanding corrosion-resistant performance during the exposure; however, for the application of Mo, its higher price (\$ 26,000/ton) has to be taken into consideration, which makes the coating of Mo on steel substrate the appropriate method.

All 3 max-phases (Ti_2AlC , Ti_3AlC_2 and Cr_2AlC) also present promising corrosion resistance in those heavy liquid metal environments. The coating of those Max-phases on steel substrate could also be possible; however, the electrical conductivity, thermal conductivity and mechanical properties of those Max-phases must also be under consideration.

In summary, the results of our present research confirms that among all test materials, Mo metal and those 3 kinds of Max-phases (Ti_2AlC , Ti_3AlC_2 and Cr_2AlC) are the most promising candidates to be applied as PCC material in liquid metal batteries. In addition, considering about the price and manufacture of the battery cell, coating of those promising materials on a suitable substrate might be the most economically reasonable method.

References

1. Li HM, Yin H, Wang KL, Cheng SJ, Jiang K and Sadoway DR (2016) Liquid metal electrodes for energy storage batteries. *Adv Energy Mater* 6(1600483):1–19. <https://doi.org/10.1002/aenm.201600483>
2. Kim HJ, Boysen DA, Newhouse JM et al (2013) Liquid metal batteries: past, present and future. *Chem Rev* 113:2075–2099
3. Wang K, Jiang K, Sirk AHC, Sadoway DR (2014) Lithium-antimony-lead liquid metal battery for grid-level energy storage. *Nature* 514:348–350. <https://doi.org/10.1038/nature13700>
4. Wittingham MS (2012) History, evolution, and future status of energy storage. *Proc IEEE* 100:1518–1534
5. Nardelli PHJ et al (2014) Models for the modern power grid. *Eur Phys J Special Topics* 223:2423–2437. <https://doi.org/10.1140/epjst/e2014-02219-6>
6. Li HM, Wang KL, Cheng SJ and Jiang K (2016) High performance liquid metal battery with environmentally friendly antimony-tin positive electrode. *ACS Appl Mater Interfaces* 8:12830–12835. <https://doi.org/10.1021/acsami.6b02576>
7. Vikström H, Davidsson S, Höök M (2013) Lithium availability and future production outlooks. *Appl Energy* 110:252–266
8. Gruber PW, Medina PA, Keoleian GA, Kesler SE, Everson MP and Wallington TJ (2011) Global lithium availability: a constraint for electric vehicles? *J Ind Ecol* 15(5):760–775. <https://doi.org/10.1111/j.1530-9290.2011.00359>
9. Heinzl A, Weisenburger A, Müller G (2017) Corrosion behavior of austenitic steel AISI 316L in liquid tin in the temperature range between 280 and 700 °C. *Mater Corros* 68:831–837. <https://doi.org/10.1002/maco.201609211>

Engineering Model of the Kinetics of the Steel Oxide Layer in a Flow of a Heavy Liquid Metal Coolant Under Various Oxygen Conditions



A. V. Avdeenkoy, A. I. Orlov, and Nafees Kabir

Abstract An engineering model is presented for a self-consistent calculation of the growth of an oxide film in circulation loops with a heavy liquid metal coolant and concentrations of impurities using STAR-CCM+ software complex. The modeling of thermohydraulic and physicochemical processes is based on solving the associated three-dimensional equations of hydrodynamics, heat transfer, convective-diffusive transport, and the formation of chemically interacting impurity components in the coolant volume, and on the surface of steels. The parabolic constant, which is determined by the degree of steel oxygen consumption, obviously significantly depends on this steel grade. For a more adequate justification of the evolution of the oxide film, a semi-empirical model is proposed for using the empirical parameterization of the parabolic constant not only in the equation for changing the thickness of the oxide film but also in the mass balance equation associated with it.

Keywords Coolant · Corrosion · Films · Heavy liquid metal coolant · Impurities · Lead · Lead–bismuth · Mass transfer

Kinetics of corrosion processes of steel components in a heavy liquid metal coolant (HLMC) is determined by the associated processes of hydrodynamics and the interaction of dissolved components, primarily such as oxygen and iron. Justification and appropriate modeling of these processes is an important component for substantiating heavy liquid metal coolant technology [1–18].

The use of commercial CFD (STAR CCM + in the present case) codes in this area has not yet been widely applied because of the need to build some apparatus of user

A. V. Avdeenkoy (✉)

All-Russian Research Institute for Nuclear Power Plants Operation, JSC, Moscow, Russia

e-mail: avdeyenkov@mail.ru

A. I. Orlov

Proryv JSC, Moscow, Russia

N. Kabir

MEPhI, Obninsk, Russia

© The Minerals, Metals & Materials Society 2021

TMS 2021 150th Annual Meeting & Exhibition Supplemental Proceedings,

The Minerals, Metals & Materials Series,

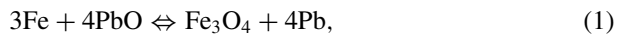
https://doi.org/10.1007/978-3-030-65261-6_56

functions for coordinated calculation of thermal hydraulics and processes of interaction and formation of impurities. For example, the works [19, 20] on modeling physicochemical processes in lead coolant show the possibility of using this approach. At the same time, the general accuracy of the calculations is mainly determined by the accuracy of the equations of physicochemical processes.

Oxidative kinetics leading to the parabolic law of growth of an oxide film is usually used when the effective diffusion of reagents is independent of time and size of the film. The oxidation mechanism of ferritic-martensitic steels is determined by the diffusion of Fe ions in the direction of the coolant and variations in the oxygen potential. In this approach, oxidation of the surface of steels is described by the parabolic velocity equation with the rate constant predicted by Wagner's theory if the resulting oxide film has an "ideal" crystal lattice, and ion diffusion is dominant.

For simplicity, we consider the growth of a single-layer film. In the developed [21–23] model of the growth of a single-layer film, at the first stage, the iron flux "remaining" in the wall layer is determined as the difference between the fluxes through the oxide film and the flux that has gone into the coolant. The "oncoming" oxygen flow from the coolant is determined according to the stoichiometry of the resulting magnetite.

In this approximation, it is unambiguously assumed that the growth of the film (magnetite) occurs due to the reaction on the surface of the oxide layer:



and at the same time, all four components of the reaction are in chemical equilibrium. Since the rate of chemical reactions is much higher than the characteristic rates of all other physical processes, the chemical equilibrium can be considered steady in the volume of the coolant at each moment of time and the distribution of components substantially depends on thermohydraulic processes.

Let us consider a model assuming the presence of a diffusion "reaction" layer at the interface between the oxide film and the coolant. The main components interacting with oxygen are iron and lead. We consider the oxide film as a single layer and consisting of magnetite. At the steel-coolant boundary, we distinguish four subregions: steel (conventionally Fe), oxide, an intermediate diffusion layer, and HLMC.

Intermediate layer is a virtual layer where the surface reaction (1) is carried out. For flows of components and sources of impurities in the media, we use the notation: $J_{O,Fe}^\beta$ —oxygen (PbO), iron flux in the coolant; $J_{O,Fe}^\delta$ —oxygen, iron flux in oxide film; $J_{O,Fe}^\gamma \sim \frac{\partial v_{O,Fe}^\gamma}{\partial t}$ —oxygen, iron flux (source) in the intermediate layer; $v_{O,Fe}^\gamma$ —the amount of oxygen and iron in the intermediate layer.

The condition of chemical equilibrium in the intermediate layer during the formation of magnetite:

$$\frac{v_O^\gamma}{v_{Fe}^\gamma} = \frac{\partial v_O^\gamma}{\partial v_{Fe}^\gamma} = \frac{4}{3} = \frac{J_O^\gamma}{J_{Fe}^\gamma} \quad (2)$$

The formulas for the sources of oxygen and iron in the surface layer γ , J_0^y and J_{Fe}^y , are proportional to the growth rate (or degradation) of this “reaction” layer, which in turn is proportional to the amount of oxygen and iron substance in it.

The source of oxygen in the system is the coolant (oxygen content is regulated through external sources). Therefore, “diffusion” of oxygen from the coolant to the steel-coolant surface section and the formation of a conventional oxide film (magnetite in our model) are initially assumed.

Using standard definitions for fluxes, we get:

$$\frac{4M_O}{3M_{Fe}} \left(D_{Fe}^\delta \frac{C_{Fe}^\delta - C_{Fe}^\gamma}{\delta} - \chi_{Fe} (C_{Fe}^\gamma - C_{Fe}^\beta) \right) = \chi_O (C_O^\beta - C_O^\gamma) - 2D_O^\delta \frac{C_O^\delta - C_O^\gamma}{\delta}, \tag{3}$$

where C_{Fe}^δ —iron concentration in the layer δ , C_{Fe}^β —iron concentration in the coolant flow, C_{Fe}^γ —iron concentration in the layer γ , C_O^β —oxygen concentration in the coolant flow, C_O^δ —oxygen concentration in the layer δ , where $\chi_{Fe,O}$ —iron, and oxygen mass transfer coefficient [24–26].

Using relation (3) and the relationship between the activities of oxygen and iron in the wall layer γ , we can obtain a nonlinear equation for the concentration (or activity) of oxygen in the wall layer in which the concentrations of iron and oxygen, C_{Fe}^β and C_O^β , are calculated with use of STAR CCM + hydrodynamics module. Concentrations C_{Fe}^δ and C_O^δ are calculated based on the properties of magnetite, namely the activity of iron in magnetite is assumed equal to one. The activity of oxygen in magnetite is found from the condition of chemical equilibrium. Thus, the equation obtained from relation (3) will contain one unknown parameter, namely the film thickness δ . Note that the obtained equation for the concentration C_O^γ (or the activity corresponding to it) parametrically depends only on the concentrations in other regions (β and δ), which in turn depend on time.

Then the film growth equation takes the following form:

$$\frac{d\delta}{dt} = \frac{K_p}{2\delta} - \frac{\chi_{Fe}(C_{Fe}^\gamma - C_{Fe}^\beta)}{C_{Fe}^\delta} \tag{4}$$

The derivation of the film growth rate constant of the parabolic law is based on the model [27], where, when modeling the diffusion of iron cations, the assumption was made that the concentration of vacancies and interstitial ion concentrations are independent of porosity and grain size of magnetite, that is, ion diffusion within the framework of the vacancy model for ideal “magnetite [28]. Such models are quite fundamental in nature and allow one to calculate the diffusion coefficient of iron ions, which is necessary for calculating the film growth rate constant in the framework of the Wagner model. The main result of the model [27] and similar ones [29] is that in the region of low partial oxygen pressures $K_p \sim P_{O_2}^{2/3} \sim (a_O^\gamma)^{4/3}$. Experimental

studies of film growth on various alloys show slightly different dependences of the film growth constant on the partial pressure of oxygen than was obtained for pure magnetite using models of the type [27, 28].

Since in reality the film for the overwhelming majority of materials under consideration is not pure magnetite, but is at least two-layer, the models developed in [27, 28] it is not necessary to describe the dependence of the film growth rate constant (conditional name) on the partial oxygen pressure like $K_p \sim P_{O_2}^{2/3}$. Since in the works [30–33], the dependencies $P_{O_2}^{0.145}$, $P_{O_2}^{0.135}$, $P_{O_2}^{0.141}$ and $P_{O_2}^{0.279;0.313}$ have been experimentally found for different types of steel correspondingly. These empirical estimates imply the fulfillment of the parabolic law of film growth (31), i.e., without taking into account possible mass transfer processes leading to its dissolution (corrosion). The latter was taken into account in (33) and for large times provides a nonparabolic change in the growth of the oxide film. Such a different dependence of the film velocity constant is determined by both the composition of the metal so that by the properties of the grains, which leads to the failure of the theoretical dependence $K_p \sim P_{O_2}^{2/3}$, characteristic to the “ideal” magnetite [29]. In [33], it was assumed that the film growth rate constant is generally determined by the diffusion of chromium ions in chromium oxide, the theoretical dependence of which $K_p \sim P_{O_2}^{3/16}$, which, in principle, is somewhat closer to the experimental values.

Note that in [29–33], the oxidation of steel surface was carried out at low partial oxygen pressures typical for partial pressures in liquid lead, but in a gaseous medium. Therefore, the processes of film dissolution and erosion, in principle, could not play a significant role. The results of experiments in a stationary coolant [10, 11] led to an empirical dependence $P_{O_2}^{0.125}$ for steels EP823 and E302. For T91 steel, the available experimental data shows a dependence of the type $P_{O_2}^{0.11}$.

The parabolic dependence of the film growth, in principle, is quite well confirmed experimentally, if corrosion-erosion processes have low intensity (for example, in a gaseous medium), and the Wagner approach is currently the only reasonably substantiated approximation. Deviations from the parabolic law can be explained within the framework of the approach [34, 35].

In the general case, the film growth constant can be written as:

$$K_p = A \exp\left(-\frac{Q}{RT}\right) \left((P_{O_2}^\gamma)^n - (P_{O_2}^\delta)^n \right) \quad (5)$$

$P_{O_2}^\gamma$, $P_{O_2}^\delta$ —partial oxygen pressure at the interface between the coolant-oxide and steel oxide media, respectively, while unknown parameters are determined empirically.

The value of the partial pressure at the oxide-steel interface is much smaller than the value of the partial pressure of oxygen at the surface and can be neglected [2]. In the case of lead–bismuth coolant, it can be estimated that since the binding energy of bismuth oxide is much lower than the binding energy of lead oxide, the formation of the former does not occur until a significant amount of lead oxide is formed.

Therefore, in all calculations, the formation of bismuth oxide is neglected for its smallness.

When describing the film growth constant using formula (4), the ratio of fluxes at the boundary (3) takes the following form:

$$\frac{4M_O C_{Fe}^\delta}{3M_{Fe}} \left(\frac{K_p}{2\delta} - \frac{\chi_{Fe}(C_{Fe}^\gamma - C_{Fe}^\beta)}{C_{Fe}^\delta} \right) \approx \chi_0 (C_0^\beta - C_0^\gamma) \quad (6)$$

That is, upon reaching the maximum value of the film $\delta_c = K_p / (2 \frac{\chi_{Fe}(C_{Fe}^\gamma - C_{Fe}^\beta)}{C_{Fe}^\delta})$, the oxygen concentrations in the film and in the volume are equal. That is, the global isoconcentration regime is established.

In the empirical determination of the parameters of the parabolic constant, the assumption of a parabolic growth of the oxide film in the static mode is fundamental. This assumption works fine provided that the diffusion yield of steel components in the coolant is small. In passivation mode in the initial period of formation of oxide films [36], the diffusion yield of metal components into the coolant is very intense, and its fraction can reach ~50% and the diffusion flux does not have to be proportional to the oxygen flux. According to the data of [36], for an oxidation duration of more than 400 h, the proportion of steel components entering the coolant of the total amount of oxidized is ~1% and less, with an oxidation duration of 200–400 h, this proportion is ~10%. Therefore, during long campaigns, at least more than several hundred hours, oxygen consumption occurs only on the surface and parabolic film growth in static experiments should be manifested to a greater extent than, for example, in dynamic ones. Thus, the empirical determination of the parabolic constant in the best way can be made by the thickness of the film after a sufficiently long oxidation (more than ~400 h) and when using the static mode. Unfortunately, there are extremely few such experimental data.

Such experiments were carried out at JSC “SSC RF-IPPE” [10], where a technique was developed that made it possible to estimate the flows of oxygen consumed for the oxidation of the steel surface under variations in temperature and oxygen conditions of the coolant. There is a matrix of various experimental values of the flow of oxygen consumed for steel oxidation, and the temperature and partial pressure of oxygen in the coolant [10, 11].

Based on the available experimental data [10, 11], the following dependence was proposed for EP-832 steel:

$$K_p = \exp(39.5) p_{O_2}^{0.125} \exp\left(-\frac{30000}{T}\right), [\mu\text{m}^2 / \text{чac}], \quad (7)$$

Similar experimental studies, by definition, were also carried out for EP-302 steel. The following dependence is proposed for a parabolic constant:

$$K_p = \exp(31) p_{O_2}^{0.125} \exp\left(-\frac{20000}{T}\right), [\mu\text{m}^2 / \text{чac}] \quad (8)$$

For comparison, we present the dependences of parabolic constants for the basic oxygen regime, obtained in [10], based on an analysis of the available experimental data [1, 2, 13–18, 37].

In [24], the following dependences were also obtained for HT9 and T91 steels that take into account the partial pressure at the interface between media, namely steel T91:

$$K_p = 2.096 \times 10^{-5} c_o^{0.27} \exp\left(-\frac{157802}{RT}\right), [M^2 / \text{cek}], \quad (9)$$

where c_o (ppm, millionth share)—mass fraction of oxygen.

The joint solution of Eqs. (4) and (6) within the framework of the point model, that is, without taking into account the exact geometry (Tadmon's approach), allows a reasonable accuracy to estimate the film growth rate depending on temperature and coolant velocity. For this, we used the film growth parameters selected for EP-823 steel, since for this grade of steel, there is a fairly large amount of experimental data.

Figure 1 shows the calculations for steels EP-823, T91 for which both static and dynamic experiments were performed [18, 37, 38], which allow a consistent analysis of these data, that is, the same parameterization of the parabolic constant is used for both types of tests. The coolant speed in the dynamic test is 1.9 m/s. Below is an analysis for $T = 600^\circ\text{C}$. Taking into account the numerical errors from the variation of the parameters, we obtain fairly good agreement with the experimental data. An interesting feature of the above calculations and experimental data is that although the steels EP-823 and T91 are quite close to each other in composition, the growth and thickness of the film for them is significantly different, which determines the adequacy of our engineering approach.

Test calculations of the elementary model of HLMC flow in a pipe were carried out using the commercial StarCCM + code and MASKA-LM code of own design.

The STAR CCM + code interface allows you to use user-defined functions to model certain physical and chemical processes. The system of Eqs. (4), (6), functions dependent on them, and semi-empirical dependencies of type (7–9) were incorporated into the code for joint solution with the STAR CCM + thermohydraulic models. For numerical analysis, a simple model was chosen for the flow of lead coolant of a given temperature in the pipe of EP-823 steel: the length of the computational domain is 1 m; diameter 50 mm; design; Reynolds number is 10^5 ; input mass concentration of oxygen 10^{-8} kg/kg.

Figures 2 and 3 show the calculations for different temperatures, oxygen concentrations, and average speeds in the pipe using the MASKA-LM and STAR CCM + codes.

Figure 2 shows film growth versus time. All models, in accordance with Zhang's approach, demonstrate the approximation of the film thickness to the maximum possible value. The calculation shown by the black solid line is made taking into account only the parabolic constant (there is no dependence on the coolant speed through taking into account mass transfer). As can be seen, for calculations at a speed of 1.8 m/s, the film growth rate close to the parabolic behavior is observed

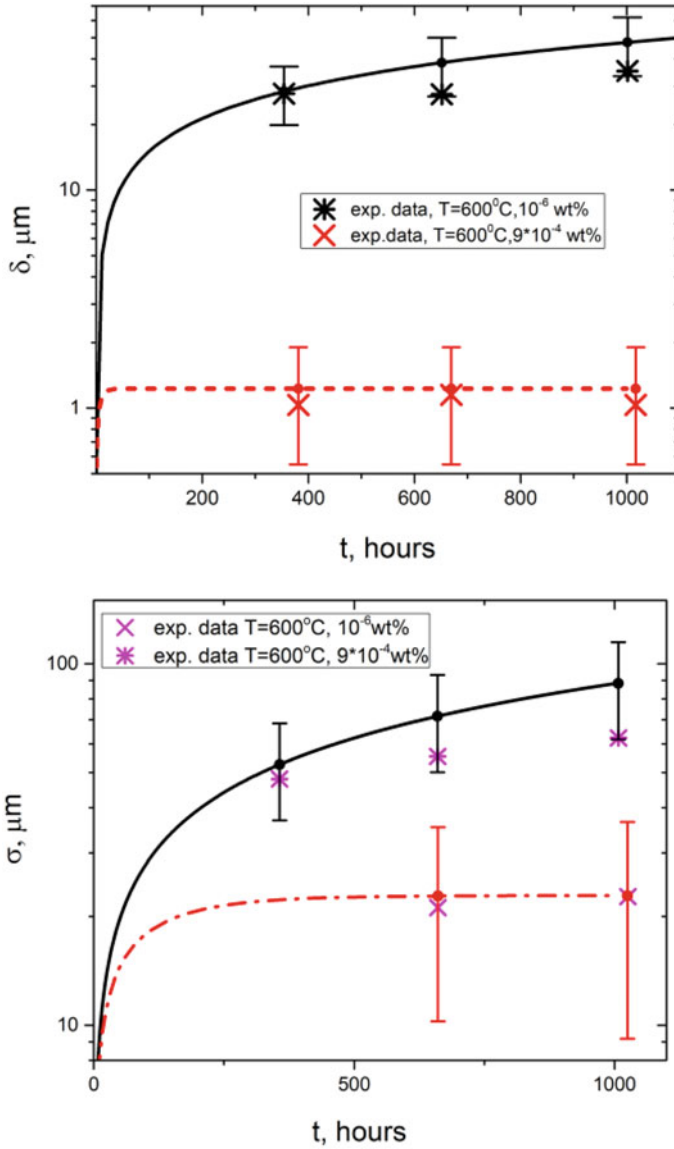


Fig. 1 Calculated results and experimental data for oxide film growth based on static and dynamic experiments for steel EP-823 and T91. The calculated error is 55% for a dynamic experiment and 30% for a static. (Color figure online)

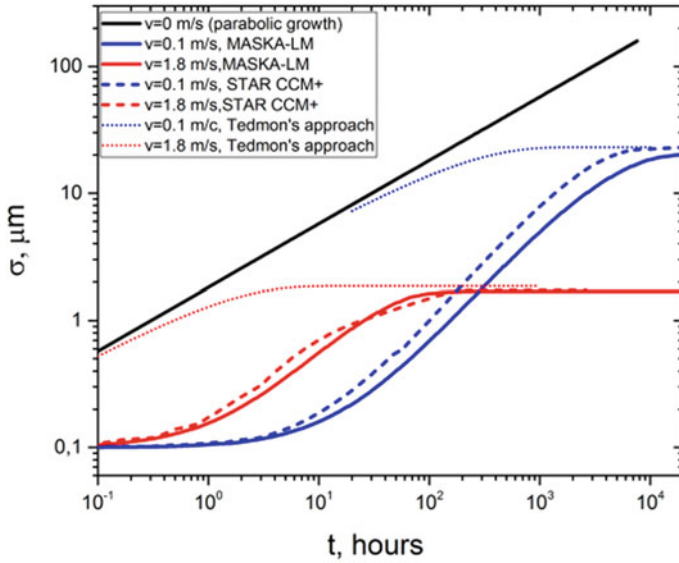


Fig. 2 Results of calculations of film growth carried out with MASKA-LM, STAR-CCM + , and the solution of the Tedmon's approach at a temperature of $T = 650$ °C. Mass oxygen concentration -10^{-8} kg/kg. (Color figure online)

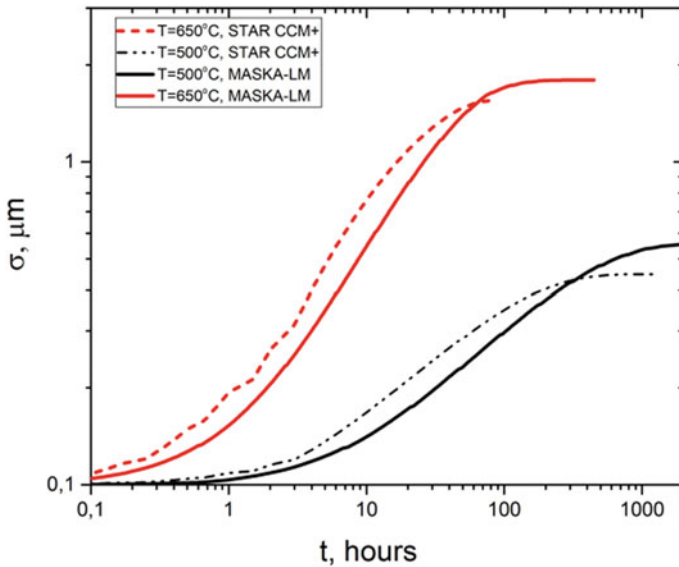


Fig. 3 Results of calculations of film growth carried out in the framework of MASKA-LM, STAR-CCM + at temperatures $T = 650$ °C and $T = 500$ °C. Mass oxygen content is -10^{-8} kg/kg. The curves are trimmed after the thickness of the films reaches the saturation value. (Color figure online)

only from about 1 to 50 h, while at a speed of 0.1 m/s, it is observed up to several thousand hours. The Tedmon's approach fairly well describes only areas close to saturation in film growth.

Figure 3 shows the calculation results for the thickness of the oxide film at various temperatures. As in the previous case, the difference in the obtained calculations does not exceed 20%.

In conclusion, the change in the thickness of the oxide film on the metal surface and the corresponding exit of steel components into the coolant substantially depend on the steel grade. For a more adequate justification of the evolution of the oxide film, a semi-empirical model is proposed for using the empirical parameterization of the parabolic constant not only in the equation for changing the thickness of the oxide film but also in the mass balance equation associated with it. The parabolic constant, which is determined by the degree of oxygen consumption by the steel, obviously significantly depends on the type of this steel and on the method of its preparation. Therefore, the direct application of the Wagner approach is unlikely to adequately describe such differences in steels, while the experimental parametric dependences on oxygen consumption by steel depending on temperature and oxygen partial pressure are obviously unique for each steel.

For an adequate experimental determination of the parametric dependences for a parabolic constant, at least two conditions are necessary: the experiment should be carried out for a static case or the average coolant velocity should be low in order to exclude the influence of corrosion-erosion processes; steel should have a sufficient initial oxide film to exclude the influence of the initial large flow of iron, and possibly corrosion of steel, since with a large yield of iron the film growth does not have to obey the parabolic law even in the static case.

The developed approach regarding accounting for the main physical and chemical processes is used not only in our MASKA-LM code but is also implemented as user-defined functions in the STAR CCM + code. The cross-verification calculations of the two test models showed a fairly good agreement between the results in terms of describing the increase in the thickness of the oxide film.

References

1. Handbook on lead-bismuth eutectic alloy and lead properties, materials compatibility, thermal-hydraulics and technologies, 2015 Edition
2. Martinelli L et al (2008) *Corros Sci* 50:2537–2548
3. Zhang J (2013) Long-term behaviors of oxide layer in liquid lead-bismuth eutectic (LBE), part I: model development and validation. *Oxid Met* 80:669–685
4. Zhang J, Li N (2007) *Corros Sci* 49:4154–4184
5. Weisenburger A, Heinzel A, Mueller G, Muscher H, Rousanov A (2008) *J Nuclear Mater* 376:274–281
6. Tsisar V, Schroer C, Wedemeyer O, Skrypnik A, Konys J (2017) *J Nuclear Mater* 494:422–438
7. Schroer C, Konys J (2009) Proceedings of the 17th international conference on nuclear engineering ICONE17, Brussels, Belgium
8. Schroer C, Wedemeyer O, Skrypnik A, Novotny J, Konys J (2012) *J Nuclear Mater* 431:105–112

9. Steiner H (2009) *J Nuclear Mater* 383:267–269
10. Askhadullin RS et al (2011) Evaluation of the intensity of oxidation processes of structural steels of the first circuit of a nuclear power plant with heavy coolants. *Izvestiya vuzov. Yadernaya energetika*. No. 4. C. 121
11. Ivanov KD, Niyazov SA, Lavrova OV, Salaev SV, Askhadullin RS (2017) Development of a method for determining the oxidation rate of structural steels in heavy liquid metal coolants. *Izvestiya vuzov. Yadernaya energetika*. No. 4. C. 127
12. Salaev SV et al (2018) Experimental processing of methods for studying the kinetics of oxidation of structural steels in TZhMT and the main results. *VANT: Nuclear-reactor constants*, pp 4–104
13. Hwang IS, Lim J (2010) The 25th KAIF/KNS annual conference, World Trade Center, COEX, Seoul, Korea
14. Fazio C et al (2001) *J Nuclear Mater* 296:243
15. Aiello A et al (2004) *J Nuclear Mater* 335:169
16. Lim J et al (2008) 10th information exchange meeting on actinide and fission product partitioning and transmutation. Mito, Japan
17. Zhang J et al (2005) *J Nuclear Mater* 336:1
18. Barbier F et al (2001) Corrosion behavior of steels in flowing lead-bismuth. *J Nuclear Mater* 296:231
19. Marino A, Lim J, Keijers S, Deconinck J, Aerts A (2018) Numerical modeling of oxygen mass transfer in a wire wrapped fuel assembly underflowing lead bismuth eutectic. *J Nuclear Mater* 506:53
20. Marino A (2015) Numerical modeling of oxygen mass transfer in the MYRRH. System Brussels University Press. ISBN 978-9-4619730-5-3
21. Kumaev VY, Lebezov AA, Pyshin IV, Alekseev VV (2002) MASKA-LM—code for calculating the mass transfer of impurities in liquid metal circuits. Heat and mass transfer and properties of liquid metals: materials conf. Obninsk, vol 1, pp 295–298
22. Kumaev V, Lebezov A, Alexeev V (2005) Development and application of MASKA-LM code for calculation of thermal hydraulics and mass transfer of lead cooled fast reactors. In: The 11th international topical meeting on nuclear reactor thermal-hydraulics (NURETH-11), Paper: 191. (Avignon, France, October 2–6, 2005) pp 191/1–191/6
23. Alekseev VV, Orlova EA, Kozlov FA et al (2010) Modeling of mass transfer and corrosion of steels in nuclear power plants with lead coolant: preprint SSC RF-IPPE No. 3128. Obninsk, 2008, Calculation and theoretical analysis of the process of steel oxidation in a lead coolant *Issues of Atomic Science and Technology, Series: Nuclear Constants, Issue 1–2*, p 56
24. Berger FP, Hau KF-FL (1977) Mass transfer in turbulent pipe flow measured by electrochemical method. *Int J Heat Mass Transf* 20:1185–1194
25. Silverman DC (1984) Rotating cylinder electrode for velocity sensitivity testing. *Corrosion* 40:220
26. Harriott P, Hamilton RM (1965) Solid liquid mass transfer in turbulent pipe flow. *Chem Eng Sci* 20:1073
27. Topfer J, Aggarwal S, Diekmann R (1995) *Solid-state ionic* 81:251
28. Hallstrom S et al (2011) *Acta Materialia* 59:53–60
29. Diekmann R (1998) *J Phys Chem Solids* 59:507
30. Surman P. *Corrosion science – 1973*. – Vol. 13, p 852.
31. Smith AF (1973) *Corros Sci* 22:857
32. Saito M, Furuya H, Sugisaki M (1985) *J Nuclear Mater* 135:11
33. Sato I et al (2002) *J Nuclear Mater* 304:21
34. Zhang J et al (2005) Oxidation mechanism of steels in liquid-lead alloys. *Oxid Metals* 63
35. Steiner H, Schroer C, Voss Z, Wedemeyer O, Konys J (2008) *J Nuclear Mater* 374:211–219
36. Ivanov KD, Lavrova OV, Salaev SV (2005) Using the developed methodology for assessing the diffusion yield of metal components from steels to study the corrosion resistance of these steels in heavy fluids: Abstract. dokl. Thermohydraulic safety aspects of nuclear power plants with fast reactors, p 117

37. Balbaud-Celerier F et al (2004) High-temperature corrosion of steels in liquid Pb-Be alloy. Mater Sci Forum 461–464:1091
38. Balbaud-Celerier F, Terlain A (2004) Influence of the Pb–Bi hydrodynamics on the corrosion of T91 martensitic steel and pure iron. J Nuclear Mater 335:204–209

Exposure Tests of Different Materials in Liquid Lead for LFRs: Effect of the Dissolved Oxygen on Corrosion



S. Bassini, C. Sartorio, A. Antonelli, S. Cataldo, A. Fiore, M. Angiolini, D. Martelli, M. R. Ickes, P. Ferroni, I. Di Piazza, and M. Tarantino

Abstract Corrosion studies in high-temperature liquid Pb of conventional materials such as Fe–Cr and Fe–Cr–Ni steels for LFRs have demonstrated that they are prone to corrode affecting their structural integrity. Corrosion is minimized by using oxygen in Pb to form a protective Fe–Cr oxide layer on steels, but its protectiveness works well only up to 450–480 °C limiting their applicability in LFRs. The present work shows preliminary corrosion results of alternative materials (Ni alloys, FeCrAl ODS, Zr and Mo alloys, and SiC) for potential use in Pb, obtained by ENEA and Westinghouse Electric Company. Tests were performed in static Pb at 550 and 750 °C and different oxygen concentrations. The results demonstrated the potential availability in Pb of some of these materials and confirmed the key influence of oxygen on corrosion, imposing oxygen control in Pb coolant to prevent critical damage of materials. About oxygen control, some ENEA activities will be illustrated.

Keywords LFR · Lead corrosion · Oxygen control

Introduction

One of the major issues in the development of commercial LFRs (lead-cooled fast reactors) lies in the compatibility of the component structures with the Pb coolant. Conventional steels—such as T91 ferritic/martensitic steel and 316L austenitic stainless steel—in contact with liquid Pb suffer from corrosion phenomena due to dissolution of the constituting alloying elements (Ni, Cr, Fe) and oxidation of the surface with formation of an oxide scale [1]. Both phenomena are detrimental since they

S. Bassini (✉) · C. Sartorio · A. Antonelli · S. Cataldo · A. Fiore · M. Angiolini · D. Martelli
ENEA C.R. Brasimone, FSN-ING, Camugnano, BO, Italy
e-mail: serena.bassini@enea.it

M. R. Ickes · P. Ferroni
Westinghouse Electric Company, 1332 Beulah Road, Pittsburgh, PA 15235, USA

I. Di Piazza · M. Tarantino
FSN-PROIN, ENEA C.R. Brasimone, Camugnano, BO, Italy

affect the structural integrity of the components and create slugs which may cause occlusions in the cold and narrow sections of the reactor. Oxide scale formation may also reduce the heat transfer capability [1].

Corrosion phenomena are strongly dependent on the oxygen content dissolved in Pb [2–4]. Dissolution in particular could be reduced by operating with an “active oxygen” concentration range, which consists of having continuously a sufficient amount of oxygen in Pb capable to form a protective oxide layer over the steel structures (passivation). The oxide layer, made of external Fe_3O_4 magnetite and internal Fe–Cr spinel oxide, acts as a barrier against dissolution corrosion. However, steel passivation with “active oxygen” seems to be effective against dissolution only when the structures are exposed below to a critical temperature, which in lead–bismuth eutectic (LBE) is identified around 450 °C, whereas in Pb reasonably lies around 450–480 °C [2–4]. Below this temperature, it is possible the formation of a protective oxide layer able to slow down the diffusion of ionic species inwards and outwards. On the contrary, if the steel is exposed to Pb above this temperature, the oxide formed loses its effectiveness as diffusion barrier.

The combination of temperature and oxygen concentration is thus a key point for the compatibility of steels and materials in Pb [4, 5]. On the importance of the oxygen, several efforts were undertaken in the last years by the international research community to implement methods aimed at controlling its concentration in Pb/LBE to a target optimal value [6]. Potentiometric oxygen sensors based on ceramic solid electrolytes were developed for laboratory use and for loop facilities to monitor the oxygen concentration during the operation. Gas-phase control methods such as the injection of H_2/O_2 and $\text{H}_2/\text{H}_2\text{O}$ mixture and solid-phase methods such as oxygen getters and dissolution of PbO particles were investigated for laboratory and loop facility scale [6]. Studies about sensors and control methods are still ongoing to transfer the present knowledge to larger-scale facilities.

Nevertheless, in spite of the strategy based on oxygen control, the corrosion of steels above 450–480 °C in Pb coolant is a big issue which limits their applicability in LFR. The present paper investigates the corrosion behavior of alternative materials and alloys for the potential use in high-temperature Pb, such as Ni-based alloys, Fe–Cr–Al ODS alloy, Zr and Mo refractory metal alloys, and SiC material. Screening exposure tests have been performed in static Pb at high temperature and different oxygen concentrations to investigate the effect of the combination of oxygen and temperature, in the frame of a collaboration between ENEA and Westinghouse Electric Company. The results demonstrated the potential availability of some of these materials, in terms of corrosion, for the employment in high-temperature Pb, and show also the effect of oxygen on the corrosion of materials different from conventional steels, confirming the need for controlling oxygen during LFR operation. R&D activities carried out by ENEA in the last years on oxygen sensors and gas-phase control methods are illustrated and discussed.

Corrosion of Materials in Lead

Materials and Methods

The materials exposed to liquid Pb are enlisted in Table 1 together with the elemental composition detected by EDX (energy-dispersion X-ray spectrometry, EDAX—Genesis). The list of materials comprises two Ni-based alloys (HAYNES 214 and 242), a ferritic FeCrAl ODS (oxide-dispersion-strengthened alloy, MA 956), two Mo alloys (pure Moly and TZM), three Zr alloys (Zr IV, Zr 702 and 704), and a SiC alloy (SiC Hexaloy). The samples were in the form of plates about 40 mm long with a hole (3.5 mm) at one of the end. Ra values were between 0.5 and 1.8 μm , evaluated by a profilometer (Mahr) on virgin samples.

The tests in liquid Pb were performed in RACHEL laboratory in ENEA Brasimone inside large capsules for the exposure in static liquid metals up to 750 °C. The capsules consist of a stainless steel cylinder ($h = 500$ mm) heated on the outer surface. A large alumina crucible ($d = 110$ mm, $h = 220$ mm) is placed at the bottom of the steel cylinder to prevent the contact with the steel walls of the capsule. Solid pieces of Pb from ingots (about 5.5 kg) are introduced inside the alumina crucible, then melted and heated up to the working temperature (heating rate 0.5 °C/min). The Pb used has a nominal purity of 99.99%. The cover lid of the capsule is equipped with penetrations for the insertion of components in the melt: K-type thermocouple inside an alumina one-end closed tube, alumina open tube for gas bubbling in Pb, fitting for the outgas, oxygen sensor, and sample-holder bars in stainless steel. The gas injection to manage the oxygen concentration in Pb is provided to the capsules by means of a gas line fed with Ar–H₂ mixture for tests at low oxygen, Ar gas for tests at oxygen saturation,

Table 1 Elemental composition by EDX (% wt.) and Ra value (μm) of the materials tested in liquid Pb

Material	Al	Cr	Fe	Ni	Mo	Zr	Y	Ti	C	Si	Sn	Nb	Ra (μm)
HAYNES 214	4.9	16.2	3.9	75									1.80
HAYNES 242		7.2	1.3	55.4	36.2								1.20
MA 956	5.2	20.1	73.8				0.3	0.6					1.41
Moly					100.0								1.54
TZM Moly					94.1	0.9		0.4					1.76
Zr IV			0.4			97.8					1.8		0.80
Zr 702			0.2			98.7							1.30
Zr 705			0.2			94.4						3.9	1.32
SiC Hexaloy									37	63			0.52

and Ar–H₂–O₂ mixture for tests at medium oxygen. Oxygen sensors with YPSZ tube (Yttria Partially Stabilized Zirconia, $L = 700$ mm) and air reference electrode were used to monitor the oxygen concentration in the Pb during the tests. The sensors were all equipped with a stainless steel sheet tube, used to distribute the heat along the ceramic tube and prevent thermal shocks.

The samples were exposed under different conditions of temperature and oxygen concentration as follows:

- (1) 550 °C, 1000 h, high oxygen 10⁻³% wt. (all the materials)
- (2) 550 °C, 1000 h, low oxygen 10⁻⁸–10⁻¹⁰% wt.; (HAYNES 214, HAYNES 242, MA 956, TZM, SiC)
- (3) 550 °C, 1000 h, very low oxygen 10⁻¹⁸–10⁻²⁰% wt.; (Zr IV, Zr 702, Zr 705, Moly)
- (4) 750 °C, 670 h, high oxygen 10⁻³% wt.; (Zr IV, Moly, TZM, SiC)
- (5) 750 °C, 660–690 h, medium oxygen 10⁻⁶% wt. (all the materials).

In some tests at 550 °C, oxygen deviates from the target concentration (10⁻⁸–10⁻¹⁰% wt.) and reached values 10⁻¹⁸–10⁻²⁰% wt. After the exposure tests, sample cross sections were mechanically prepared by cutting, embedding in conductive resin, grinding with abrasive papers and polishing with diamond suspensions, and then analyzed by scanning electron microscopy (SEM) and EDX. X-ray diffraction (XRD) analysis was performed on some samples after removing residual Pb from the surfaces with the chemical solution acetic acid/hydrogen peroxide/ethanol in ratio 1:1:1 diluted at 50% vol.

Corrosion Results

Ni-Based Alloys

HAYNES 214 and 242 samples were exposed to Pb at 550 °C for about 1000 h at high oxygen concentration (1×10^{-3} % wt.). Figure 1 illustrates the cross-sectional morphology for the materials. The surface of both HAYNES 214 and 242 alloys is affected by deep Pb penetration and dissolution attack (120–160 and 50 μm, respectively). Within the dissolution area, there are several layers or islands made of Ni and Fe elements only. EDX analysis indicates that Ni is almost completely absent near the surface (high solubility of Ni in Pb) and, although the high Al content makes HAYNES 214 material a potential alumina-forming alloy, no effective alumina layer has been detected but only a non-protective layer of a mixed oxide of Al, Cr, and Fe. In HAYNES 242 sample, the oxygen is present across the whole layer, and there is an external area where Fe, Cr, and Ni are present in a stratified structure.

HAYNES 214 and 242 samples were exposed to Pb at 550 °C for 1000 h at low oxygen concentration (3×10^{-10} % wt.). The results are shown in Fig. 2. Concerning HAYNES 214, no oxide layer seems to be present but only an outer Ni-depleted area

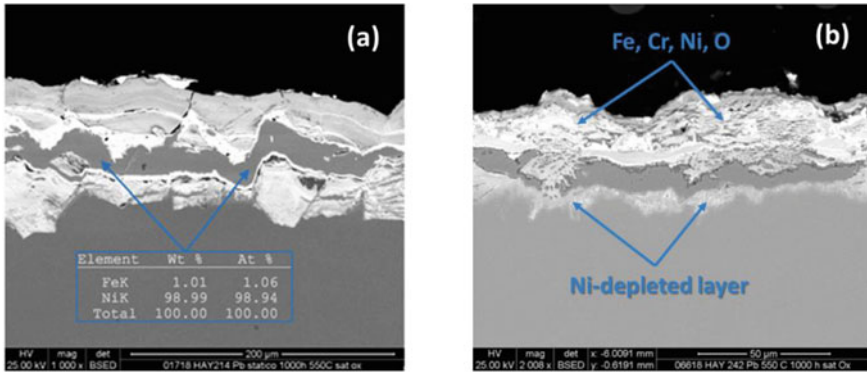


Fig. 1 SEM images of **a** HAYNES 214 and **b** HAYNES 242 exposed in Pb at 550 °C for 1000 h with high oxygen. (Color figure online)

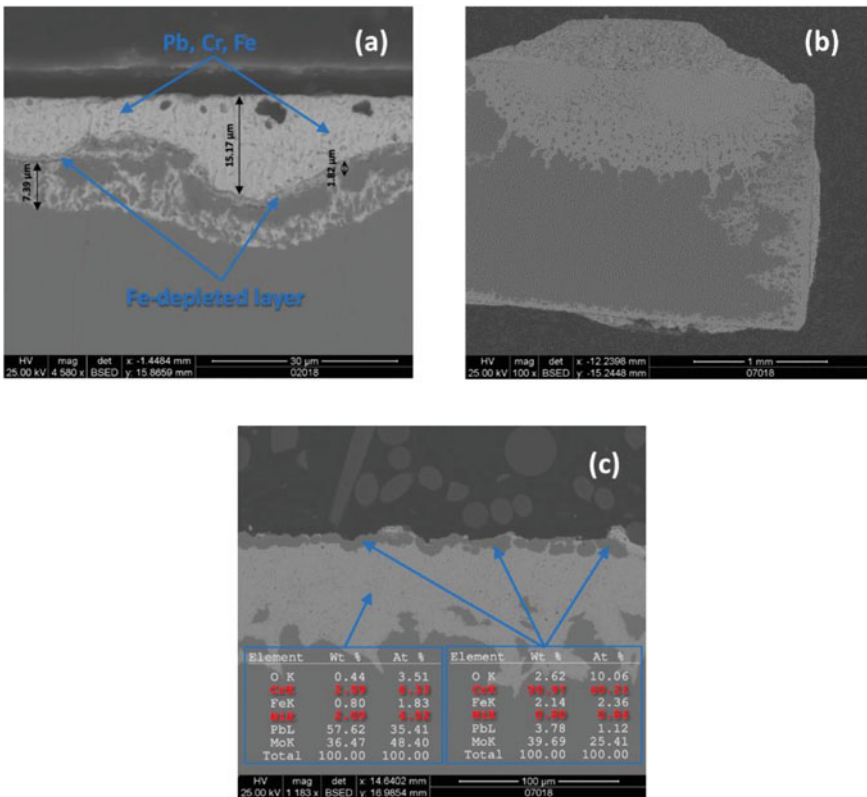


Fig. 2 SEM images of **a** HAYNES 214 and **b, c** HAYNES 242 exposed in Pb at 550 °C for 1000 h with low oxygen. (Color figure online)

(10–15 μm thick) attacked by Pb and rich in Cr and Fe, and an inner one (about 7 μm thick) where Pb penetration is lower and from which is separated by a thin Fe-depleted layer (<2 μm) (Fig. 2a). For HAYNES 242, a considerable Pb penetration with strong Ni leaching, up to approximately 1 mm of depth (about half of the thickness of the sample), has been observed in a large area (Fig. 2b). Analyzing carefully the regions where the dissolution attack is not so deep, it is possible to observe some areas, placed above the Ni-depleted layer, rich in Cr (Fig. 2c).

HAYNES 214 and 242 samples exposed in Pb for 660 h at 750 °C and medium oxygen concentration ($6 \times 10^{-7}\%$ wt.) were found completely dissolved for the portion dipped in the Pb melt.

FeCrAl ODS Alloy (MA 956)

MA 956 was exposed to Pb at 550 °C for about 1000 h at high ($1 \times 10^{-3}\%$ wt.) and low oxygen concentrations ($3 \times 10^{-10}\%$ wt.). For the test at high oxygen (Fig. 3b), no Pb penetration and chemical modifications have been detected on the entire surface. EDX analysis (here not reported) did not show elemental gradients along the cross section, and the composition near the surface is the same as the bulk. Even after the exposure at low oxygen concentration (Fig. 3c), no general corrosion or localized attack sites have been found, and again, the surface of the MA 956 sample seems the same as the one observed before the exposure in Pb (Fig. 3a). The excellent performances of this material are likely due to a very thin alumina layer, which protects from dissolution and which unfortunately was not possible to identify and detect with our SEM–EDX due to resolution limits.

Mo Alloys

Moly and TZM samples were exposed to Pb at 550 °C for 1000 h at high oxygen ($1 \times 10^{-3}\%$ wt.). Concerning Moly samples, no Pb penetration occurs in the bulk material. Two oxide layers were formed: a thin film 2–3.5 μm thick at the Pb/bulk interface and an outer crystalline layer 22–26 μm thick (see Fig. 4a). XRD analysis on the sample confirmed that these layers correspond to MoO_2 and PbMoO_4 . Similar results have been observed for TZM samples: no Pb penetration or elemental gradients along the cross section has been detected. Over the entire analyzed surface, a layer 2–3 μm thick of MoO_2 mixed with Pb is detected at the Pb/bulk interface and above a thicker crystalline layer of about 8–11 μm , corresponding to PbMoO_4 .

Exposure in Pb at 550 °C and low oxygen concentration for about 1000 h was performed for Moly and TZM samples. During the Moly test, the oxygen concentration deviated from the fixed target and reached a value between 10^{-18} and $10^{-20}\%$ wt., whereas, during the TZM test, the average concentration was $1 \times 10^{-8}\%$ wt. Figure 5 shows the cross-sectional SEM images of the samples after the exposure.

There is no appreciable difference in the surface before and after the exposure in Pb for both materials: No oxide layer has been detected and no signs of degradation appear on the surface (negligible solubility of Mo in Pb). However, Moly surface is entirely covered by adherent Pb, whereas TZM appears completely free from residual Pb. This is likely due to the different oxygen conditions to which the materials were exposed, as the low oxygen condition generally promotes wetting.

Moly and TZM samples were then exposed to Pb at 750 °C for 670 h at high oxygen concentration ($4 \times 10^{-3}\%$ wt.) and 667 h at medium oxygen concentration ($1 \times 10^{-6}\%$ wt.). Concerning the test at high oxygen concentration, the results for both materials are similar to those obtained at 550 °C and high oxygen concentration. No Pb penetration has been detected, and the elemental composition near the surface is the same as the bulk (see Fig. 6).

Again, there does not seem to be any evidence of corrosion damages both for Moly and TZM samples (see Fig. 7). However, no compact oxide film was detected but only small traces of MoO_2 at the bulk/Pb interface and above a crystalline layer

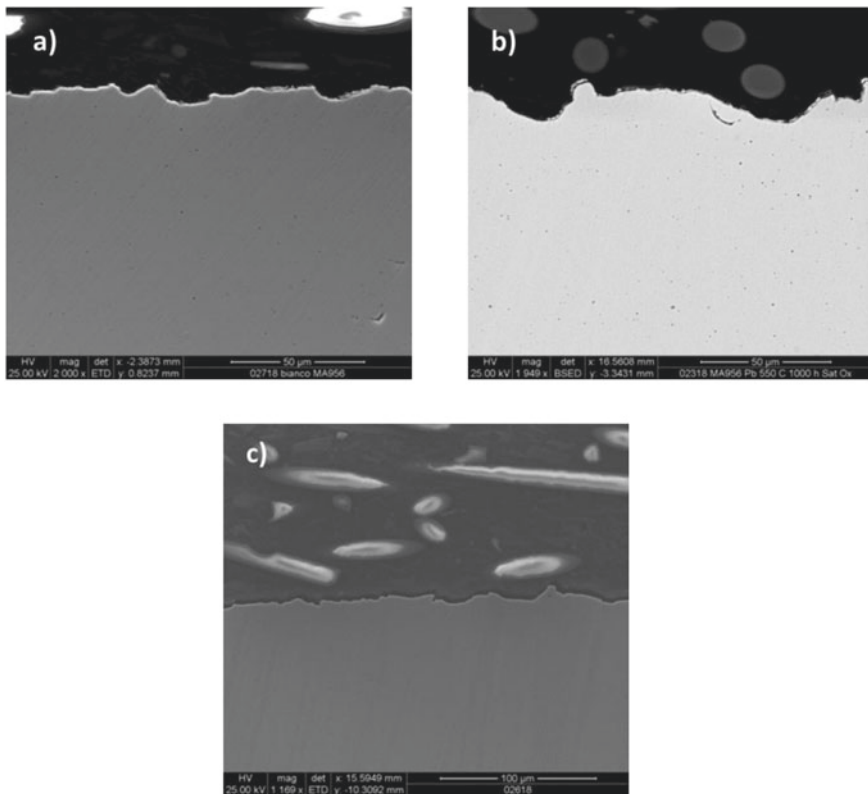


Fig. 3 SEM images of MA 956 **a** as virgin material, and after exposure in Pb at 550 °C for 1000 h, **b** with high oxygen and **c** with low oxygen. No corrosion or chemical degradation of the surface observed

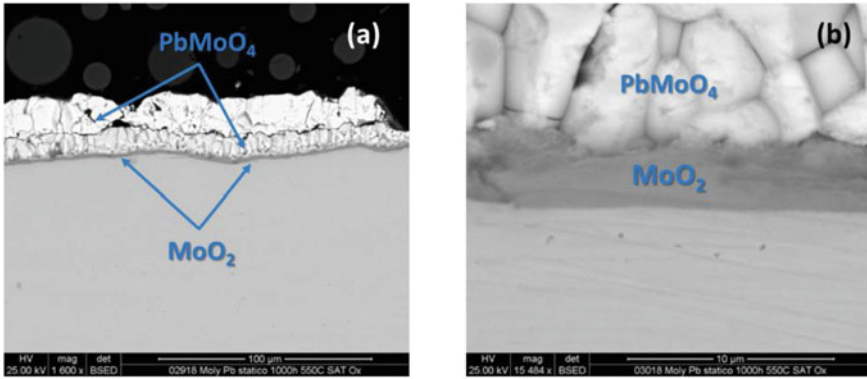


Fig. 4 SEM images of Moly exposed in Pb at 550 °C for 1000 h with high oxygen at low and high magnification. (Color figure online)

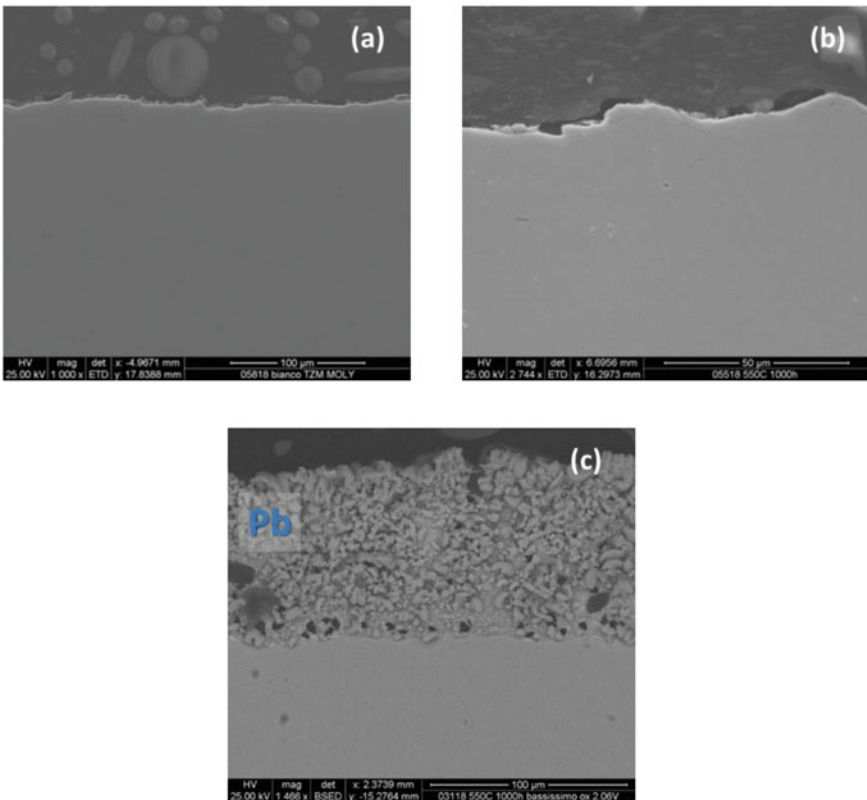


Fig. 5 SEM images of TZM **a** before and **b** after the exposure in Pb at 550 °C for 1000 h with low oxygen and **c** SEM image of Moly after the exposure in Pb at 550 °C for 1000 h with very low oxygen. (Color figure online)

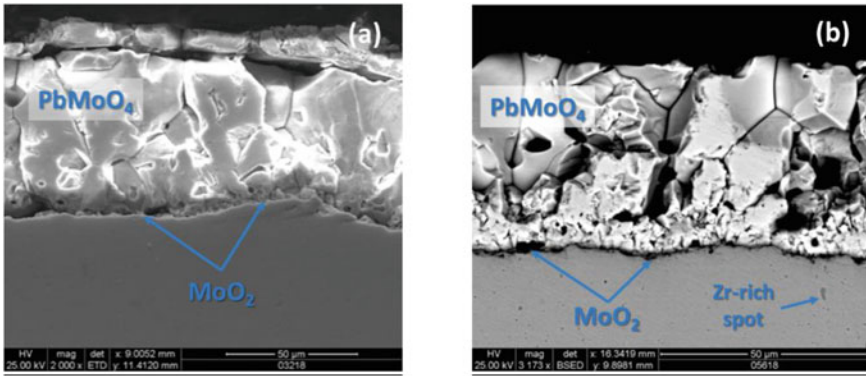


Fig. 6 SEM images of Moly **a** and TZM **b** exposed in Pb at 750 °C for 670 h with high oxygen. In TZM bulk sample, it is possible to see dark spots enriched in Zr. (Color figure online)

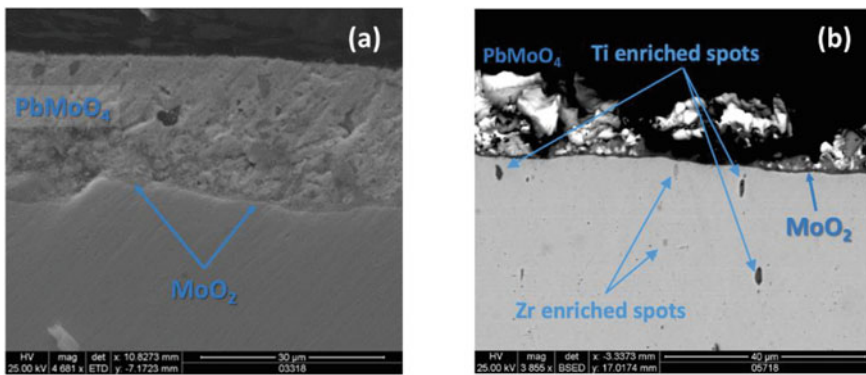


Fig. 7 SEM images of Moly **a** and TZM **b** exposed in Pb at 750 °C for 667 h with medium oxygen. In TZM bulk sample, it is possible to see dark spots enriched in Zr and Ti. (Color figure online)

about 70 and 50 μm thick, respectively, for Moly and TZM samples, most likely PbMoO_4 , whereas, at 550 °C, this layer has been found thick between 8 and 26 μm . Interestingly, after the exposure at 750 °C and medium oxygen, traces of MoO_2 layer are still detectable in several points at the Pb/bulk interface in the TZM sample. In addition, all the surfaces are covered by solid Pb, indicating a good wetting of the samples in these operating conditions.

Zr Alloys

Zr IV, Zr 702, and Zr 704 samples were exposed to Pb at 550 °C for 1000 h at high ($1 \times 10^{-3}\%$ wt.) and very low oxygen concentrations (10^{-18} – $10^{-20}\%$ wt.). Cross-sectional morphologies are reported in Fig. 8 for Zr IV and Zr 702, respectively, in high and low oxygen conditions. Similar results were obtained by all the Zr alloys for a specific condition, in spite of the differences in the bulk concentration. In the high oxygen test, the materials do not show dissolution and Pb penetration, and the surface is covered by a uniform oxide layer of ZrO_2 with thickness from 8 to 16 μm (Fig. 8a).

At very low oxygen concentration (Fig. 8b), a very thin oxide layer of a few μm is detected but completely spalled off from the interface. Below this oxide layer, there is a thick Pb layer with a Zr content which gradually increases from the detached oxide to the Zr bulk interface. This appearance may be due to the weird oxygen conditions obtained in Pb during the test: After the first 150 h when the oxygen concentration was sufficiently high to form the Zr oxide layer (about $10^{-8}\%$ wt.), the gettering effect of Zr prevails, lowering the oxygen concentration down to value which cannot provide the stability of ZrO_2 layer (10^{-18} – $10^{-20}\%$ wt.). Here, Pb penetrated through the oxide layer interacting with Zr bulk below. In addition, at the bulk/oxide interface, there are black areas with a significant fluorine %. These F-rich areas have also been detected in cavities or cracks on the virgin surface before the exposure in Pb, and their presence is most likely due to the manufacturing process of the alloy.

Figure 9 shows the results for Zr IV and Zr 702 exposed to Pb at 750 °C, respectively, for 670 h at high oxygen ($4 \times 10^{-3}\%$ wt.) and 667 h at medium oxygen ($1 \times 10^{-6}\%$ wt.). Again, the high oxygen promotes the formation of a ZrO_2 layer 70–120 μm thick, which is spalled off from the surface. Near the interface, a Zr concentration gradient is visible, indicating some dissolution in Pb at high temperature (Fig. 9a).

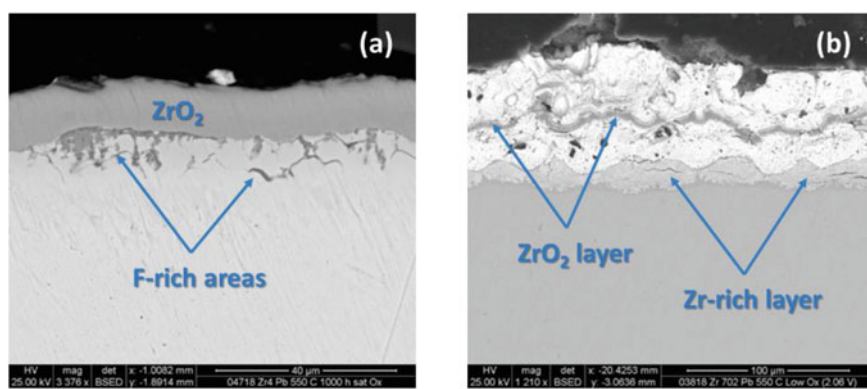


Fig. 8 SEM images of **a** Zr IV exposed in Pb at 550 °C for 1000 h at high oxygen, and **b** Zr 702 exposed in Pb at 550 °C for 1000 h at very low oxygen. F-enriched areas are detected in the bulk below the oxide layer. (Color figure online)

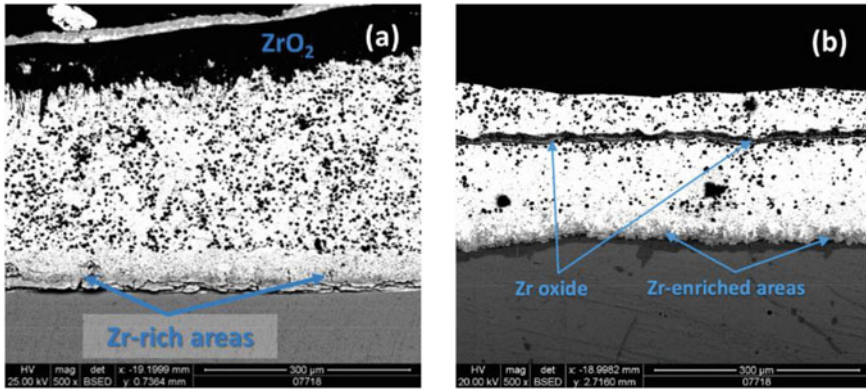


Fig. 9 SEM images in Pb at 750 °C of **a** Zr IV for 670 h at high oxygen, and **b** Zr 702 for 667 h at medium oxygen. (Color figure online)

Unfortunately, solubility data in literature about Zr in liquid Pb are scarce. Reference [7] gives only one data point of solubility, $1.2 \times 10^{-9}\%$ wt. at 500 °C, which appears to be low if compared to the present results. Similar results were obtained at low oxygen, where the detached Zr oxide layer is only a few μm thick (Fig. 9b).

SiC Hexaloy

In all the testing conditions—550 °C with high ($1 \times 10^{-3}\%$ wt.) and low oxygen concentrations ($2 \times 10^{-8}\%$ wt.) for 1000 h (Fig. 10), and 750 °C for 670 h with high oxygen ($4 \times 10^{-3}\%$ wt.) and 690 h in medium oxygen ($1 \times 10^{-6}\%$ wt.) (Fig. 11)—SiC samples seem not to show any chemical degradation of the surface or Pb penetration.

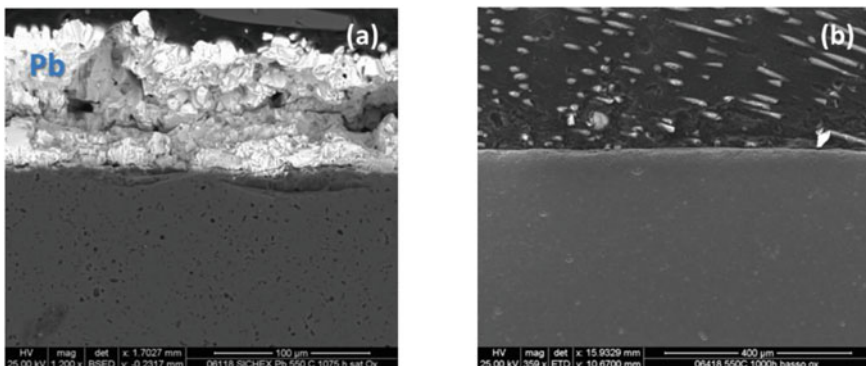


Fig. 10 SEM images of SiC Hexaloy after exposure in Pb at 550 °C for 1000 h, **a** with high oxygen and **b** with low oxygen. (Color figure online)

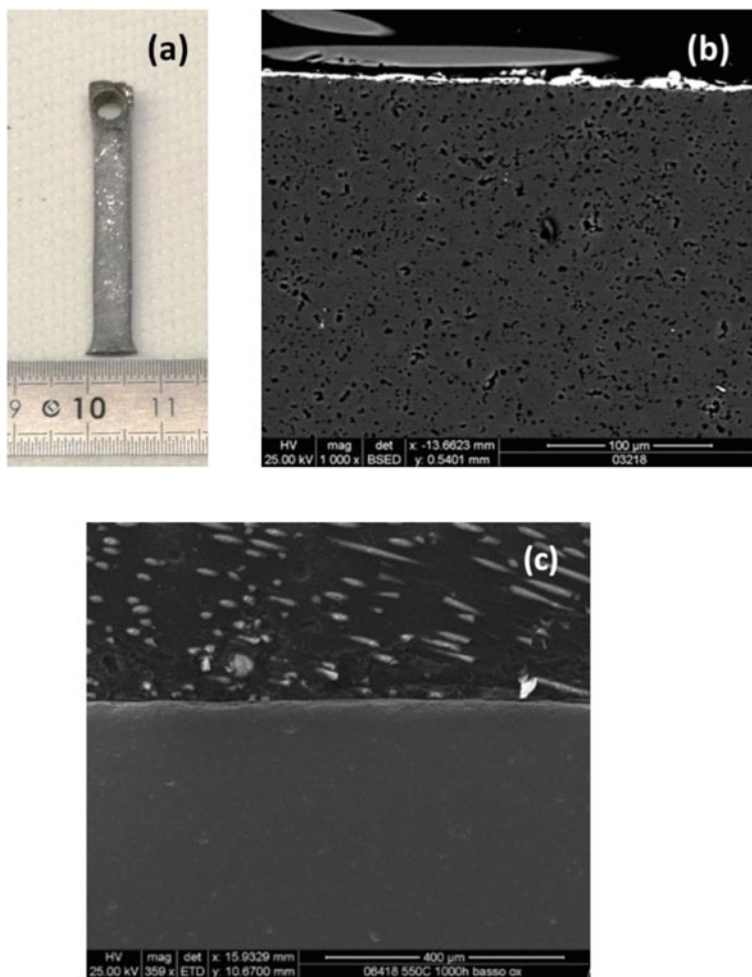


Fig. 11 SiC Hexaloy after exposure in Pb at 750 °C, **a, b** appearance of the sample and SEM images after the exposure with high oxygen for 670 h, and **c** with low oxygen for 690 h. (Color figure online)

However, after the exposure at 750 °C in high oxygen, the sample was heavily thinned for almost about 30% of the thickness (Fig. 11a). This is likely ascribable to strong oxidation undergone at high oxygen concentration in Pb at 750 °C, with formation of volatile SiO and CO. Traces of SiO₂ have been found in the surfaces, detected by XRD.

Oxygen Control Activities in Pb Alloys

From some years, ENEA has been involved in Pb chemistry activities and in particular about oxygen monitoring and control. Potentiometric sensors based on ceramic solid electrolytes, measuring an electric voltage at null current, are the devices devoted to the monitoring the oxygen concentration in Pb coolant, and several types with different configurations were implemented and tested for different scale systems (laboratory scale, loop and pool facility). For laboratory scale and capsules, small oxygen sensors with length 400 mm were calibrated and tested using different internal reference electrodes (Pt-air, Bi/Bi₂O₃, and Cu/Cu₂O) and using YPSZ as solid ceramic O²⁻ conductive material [8]. The type of internal reference electrodes used influences the “minimum reading temperature” in Pb/LBE, and the internal electrodes investigated were Cu/Cu₂O (200 °C) < Bi/Bi₂O₃ (300 °C) < Pt-air (400–450 °C). Alternative internal air-based references such as Lanthanum-Strontium-Manganite—Godolinium-Doped Ceria (LSM-GDC) and Lanthanum-Strontium-Cobalt-Ferrite—Godolinium-Doped Ceria (LSCF-GDC) powders were recently tested in 400 mm sensors improving the minimum reading temperature compared to Pt-air reference (Fig. 12). The result of the calibration, performed in oxygen-saturated LBE, shows that LSM-GDC and LSCF-GDC sensors exhibit an electric voltage E in agreement with the expected theoretical voltage down to 220 and 260 °C, respectively, whereas the minimum reading temperature of the Pt-air sensor is above 400 °C.

Scale-up of sensors is fundamental to investigate oxygen control methods in larger facilities such as large Pb/LBE pools and in view of its application in LFR systems. ENEA started to work on sensors for the operation in large pools and storage tanks and tested a sensor prototype with Pt-air reference 1100 mm long [9]. Although the configuration needs some improvements (e.g. in electrode connection and tightness), the sensor was successfully tested in Pb storage tank containing a large volume of Pb (about 285 L), with good calibration results in the range 400–480 °C (Fig. 13).

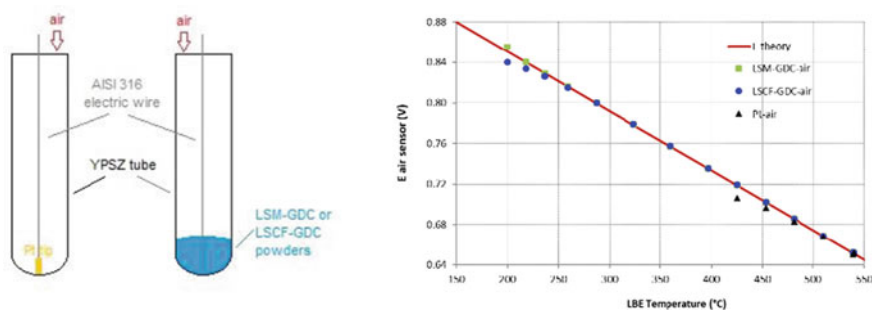


Fig. 12 Calibration of air-based sensors 400 mm long with LSM-GDC, LSCF-GDC, and Pt-air reference electrodes and YPSZ solid electrolyte in oxygen-saturated LBE in the range 200–550 °C

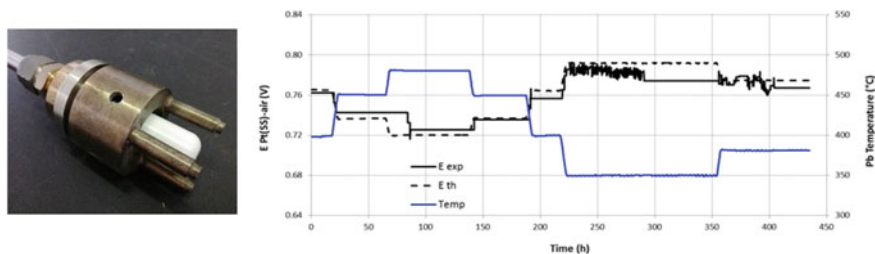


Fig. 13 Calibration of Pt-air sensors 1100 mm long in oxygen-saturated Pb in the range 380–480 °C. (Color figure online)

About control methods, gas injection with H_2 and O_2 is a solution to have almost instantaneous oxygen control, and it is now under implementation in ENEA facilities. In particular, the combination $H_2 + O_2$ diluted in argon seems to be effective in balancing the concentration, by exploiting automated injection based on sensor voltage. On the contrary, single Ar- H_2 injection is not able to control the oxygen concentration since it is not able to balance the oxygen gettering effect of materials, which tend to capture oxygen from Pb to passivate. An example is given by the oxygen concentration obtained during the corrosion tests here reported. Tests of Zr alloys and Moly samples at 550 °C reach a very low oxygen concentration (see Fig. 14a), which did not increase even by bubbling pure Ar gas during the tests. To the opposite, Ar- $H_2 + O_2$ gas used during exposure tests at 750 °C was able to perfectly control the concentration to the target value of $10^{-6}\%$ wt. (Fig. 14b).

Conclusions

Different materials were exposed to Pb up to 1000 h at different temperatures—550 and 750 °C—and oxygen concentrations—from $10^{-3}\%$ to very low oxygen $10^{-20}\%$ wt.—to investigate the effect of oxygen on corrosion behavior, and to assess their potential applicability as structural materials in high-temperature LFR units. The results of the exposures are summarized as follows:

- HAYNES 214 and 242 Ni-based alloys show strong dissolution at 550 °C at both high and low oxygen concentrations and completely dissolve at 750 °C, due to the high solubility of Ni in liquid Pb. The 5% of Al content in HAYNES 214 is not able to form a protective alumina layer protective against dissolution.
- MA 956 FeCrAl ODS exhibits excellent corrosion behavior at 550 °C in both high and low oxygen conditions, showing no dissolution. Exposure at 750 °C is required to investigate the behavior at very high temperature.
- Moly and TZM alloys exhibit good corrosion resistance at 550 and 750 °C in low and very low oxygen thanks to the low solubility of Mo in Pb. In high oxygen conditions, the formation of a thick layer of $PbMoO_4$ was detected.

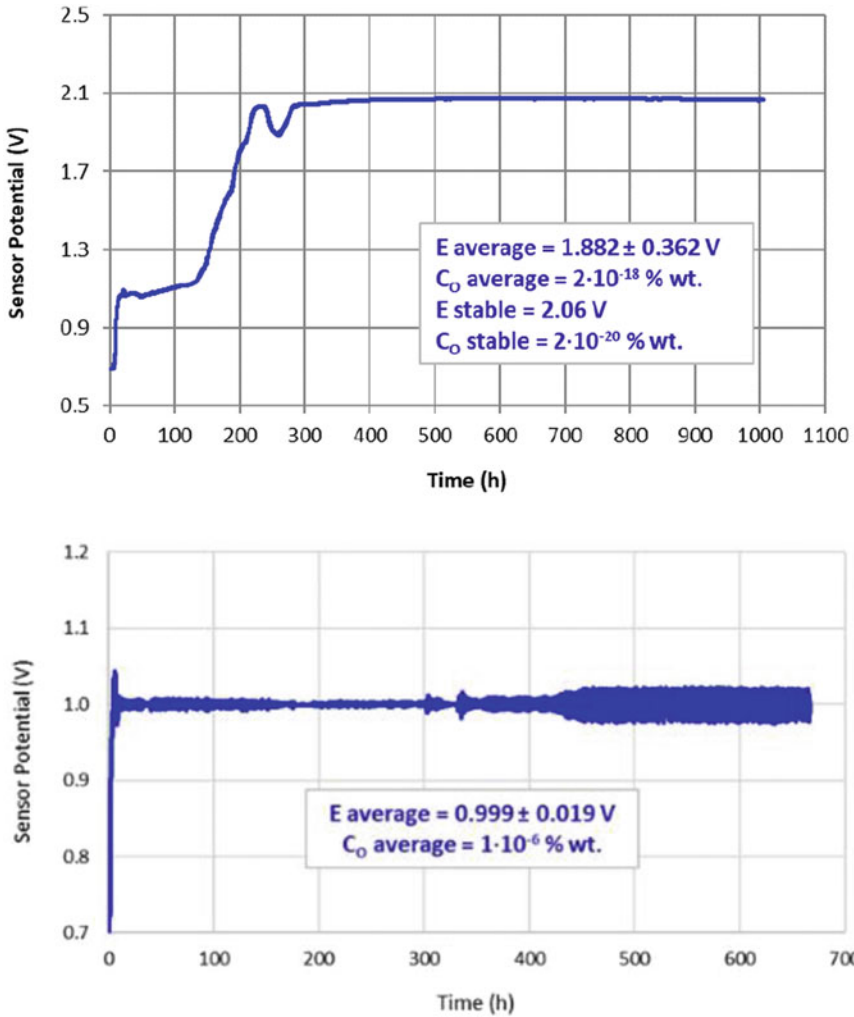


Fig. 14 Oxygen sensor output during exposure tests in Pb showing **a** very low oxygen concentration for Zr and Moly samples at 550 °C with Ar-H₂/Ar gas and **b** precise oxygen control during the test at 750 °C with Ar-H₂-O₂ gas. (Color figure online)

- Zr alloys exhibit oxidation and no dissolution at 550 °C in high oxygen, and some dissolution effects in very low oxygen at 550 °C and in high/medium oxygen at 750 °C.
- SiC alloy shows good resistance in medium/low oxygen conditions at 550 and 750 °C. In high oxygen at 750 °C, the alloys show break-way oxidation with high consumption of sample.

The results obtained show that materials such as Mo alloys, FeCrAl ODS, and SiC alloy are promising for the use in high-temperature Pb, and the effect of oxygen on the corrosion resistance of these materials is confirmed. The need for monitoring and controlling oxygen during LFR operation is then mandatory, and R&D activities on oxygen monitoring with potentiometric sensors and oxygen control with gas-phase methods are ongoing in ENEA to manage this issue.

References

1. OECD/NEA (2015) Handbook on lead-bismuth eutectic alloy and lead properties, materials compatibility, thermal-hydraulics and technologies
2. Muller G et al (2004) Behavior of steels in flowing liquid PbBi eutectic alloy at 420–600°C after 4000–7200h. *J Nucl Mater* 335:163–168
3. Schroer C et al (2014) Selective leaching of nickel and chromium from type 316 austenitic steel in oxygen-containing lead-bismuth eutectic (LBE). *Corros Sci* 84:113–124
4. Schroer C et al (2011) Aspects of minimizing steel corrosion in liquid lead-alloys by addition of oxygen. *Nucl Eng Des* 241:4913–4923
5. Li N (2002) Active control of oxygen in molten lead–bismuth eutectic systems to prevent steel corrosion and coolant contamination. *J Nucl Mater* 300:73–81
6. Li N (2008) Lead-alloy coolant technology and materials e technology readiness level evaluation. *Prog Nucl Energ* 50:140–151
7. IAEA (2002) Comparative assessment of thermophysical and thermohydraulic characteristics of lead, lead-bismuth and sodium coolants for fast reactors. IAEA-TECDOC-1289
8. Bassini S et al (2017) Oxygen sensors for Heavy Liquid Metal coolants: calibration and assessment of the minimum reading temperature. *J Nucl Mater* 486:197–205
9. Martelli D et al (2017) CIRCE-ICE experimental activities in support of LMFR Design. In: 17th international conference on fast reactors and related fuel cycles (FR17), Yekaterinburg, Russian Federation

Fundamental Interactions of Steels and Nickel-based Alloys with Lead-based Liquid Alloys or Liquid Tin



Carsten Schroer

Abstract The solution of elements from metallic alloys is analysed and compared with observations for steels and nickel-based alloys after exposure to lead-based liquid alloys or liquid tin. Furthermore, the influence of dissolved oxygen and formation of intermetallic compounds are addressed.

Keywords Liquid metal · Corrosion · Solution · Selective leaching · Oxidation · Intermetallic phase

Introduction

Application of lead (Pb)-based liquid alloys or liquid tin (Sn) to thermal energy conversion or storage opens the avenue to compact in design, highly efficient components in the high-temperature section of respective plants, however, at the cost of increased corrosion of metallic materials of construction, namely nickel (Ni)-containing steels or Ni-based alloys. Experimental studies and corresponding theoretical work identify selective leaching of constituent parts, especially Ni, as an intermediate stage of complete dissolution [1], with the near-surface depletion zone originating in the solid alloys being dependent on the alloy composition [2, 3], the liquid metal [3] and temperature [1–3]. If the oxygen content in the liquid allows, formation of solid oxides is likely to interfere with the leaching process or even changes the corrosion mode to oxidation. A similar role intermetallic compound may play.

As to fundamental interactions, the focus is on the transfer to and transport in the liquid metal of dissimilar metals [4]. The dissimilarity primarily refers to the solubility or maximum enrichment the elements may achieve if dissolving from the pure solid, and this solid constitutes the thermodynamically stable solid modification

C. Schroer (✉)

Karlsruhe Institute of Technology (KIT), Institute of Applied Materials—Applied Materials Physics (IAM-AWP), Hermann-von-Helmholtz-Platz 1, 76344 Eggenstein-Leopoldshafen, Germany

e-mail: carsten.schroer@kit.edu

of the element under consideration. However, in the case of metals dissolving from an alloy, concentrations in the liquid metal cannot reach the solubility, except for the element that would remain at the solid/liquid interface after complete leaching of the other elements. Of major alloying elements in steels or Ni-based alloys, the possible enrichment of Ni in liquid metals typically is clearly higher than for iron (Fe) or chromium (Cr), which is illustrated in Fig. 1 for liquid lead–bismuth eutectic (LBE) [5–7].

After analysing the elemental steps that result in the transition of alloying elements to the bulk of the liquid, whilst others stay behind, the theoretical implications are compared to experimental observations. The influence of oxygen dissolved in the liquid metal and the formation of intermetallic compounds are relatively briefly discussed. The observations evaluated with respect to fundamental interactions stem from experiments in Pb-based alloys [1, 3, 8–19] and liquid Sn [20–23] at 400–750 and 500–1000 °C, respectively.

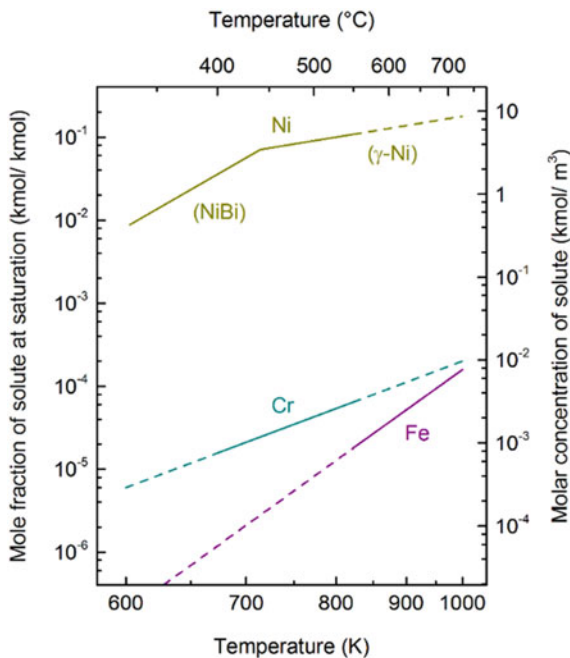


Fig. 1 Solubility of Fe [5], Cr [6] and Ni [6, 7] in LBE as a function of temperature. The solid section of the data plots indicates the temperature range in which experimental data is actually available. It should be noted that at temperature less than about 450 °C, the thermodynamically stable Ni-containing solid is intermetallic NiBi rather than pure nickel [2, 7]. (Color figure online)

Metal Solution and Selective Leaching from Alloys

Analysis of Element Transfer, Transport and Re-Precipitation

The most typical interaction between liquid metals and solid metallic materials certainly is the solution of material elements in the liquid. In the case of alloys, it seems reasonable to assume that the elements initially dissolve in proportion to their concentration in the alloy (general solution of the alloy), so that, after transfer of i mol of alloy to j mol of liquid, the mole fraction x in the liquid is

$$x = \frac{i}{i+j}y + \frac{j}{i+j}x_0 \quad (1)$$

Equation (1) applies to each element with mole fraction y in the solid alloy and initial concentration x_0 in the liquid. A restriction to general solution arises when for one of the alloying elements the thermodynamic activity in the liquid phase approaches that in the solid, or

$$f \times y = \frac{x}{x_s} \quad (2)$$

f is the activity coefficient in the solid corresponding to y , and the inverse of the solubility x_s of the element under consideration replaces the activity coefficient in the ideal diluted liquid solution that is assumed to form. For negligible initial concentrations x_0 , inserting Eq. (1) in (2) and rearranging gives

$$i = \frac{f \times x_s}{1 - f \times x_s} j \quad (3)$$

Equation (3) implies $f \times x_s < 1$ ($i, j > 0$), and that the element with smallest $f \times x_s$ (smallest i) first imposes a limit to general solution of the alloy. Especially, in the Cr–Fe–Ni system, activity coefficients in solid alloys seem to be < 5 [2, 24] so that for differences in solubility of more than about half an order of magnitude, it is the alloying element with lowest solubility that is likely to stop general solution. The influence of concentration in the alloy is relatively weak. The criterion for negligible x_0 is

$$\frac{x_0}{f \times y} \ll x_s \quad (4)$$

the violation of which means that the limit to general solution occurs earlier, at smaller i than predicted by Eq. (3). This is again more likely for the element with lowest solubility x_s , and especially if its concentration in the alloy is low.

The process of solution in a certain volume of liquid metal, however, involves not only the transfer across the solid/liquid interface but also diffusion of the transferring elements in the liquid. The analysis so far tacitly assumes that either the liquid volume is small or diffusion fast enough for absorbed elements to disperse uniformly. Any delay in element transport in the liquid leads to accumulation at the solid/liquid interface so that, at this interface, the activity in the liquid approaches the limit earlier. If the diffusion flux into the bulk of the liquid is proportional to the alloy composition just like element transfer in the case of general solution, only the effective volume (j in Eqs. (1) and (4)) becomes smaller, and the equality of activities at the interface is reached earlier. If the diffusion coefficients in the liquid of the transferred elements have similar value, the flux is higher for elements with high concentration in the solid, especially for the parent element of the alloy (generally highest concentration in the liquid at the interface). For the parent element having the lowest solubility in the liquid, this means that another constituent of the solid alloy may equally be responsible for a transition from general to selective solution, possibly the one with the next highest solubility. According to the hydrodynamic approach to diffusion (Stokes–Einstein), the case of similar diffusion coefficients in the liquid is likely to apply to Cr–Fe–Ni alloys, because the atoms have approximately same size. Experimental evidence is available for the diffusion coefficients of Fe and Ni in LBE [25].

At the point of one element prohibiting further solution in proportion to the concentrations in the alloy, something must change. The first and most obvious option is disproportionate, i.e. preferential solution of the other elements that accordingly deplete in the near-surface zone of the solid (depletion zone). At the same time, thermodynamic limits alter with the change in alloy composition, and especially, the element that once has stopped general solution will continue to dissolve as it enriches in the solid at the solid/liquid interface. Furthermore, this element tends to diffuse in the solid towards the bulk of the alloy, whereas the elements that deplete diffuse from the bulk towards the surface. If counterdiffusion is balanced, the surface of the depletion zone recedes rather than porosity develops (Fig. 2a). As diffusion in the solid is likely to be slow in contrast to diffusion in the liquid phase and probably also in comparison with element transfer across the solid/liquid interface. This means, selective solution tends to retard and concentration gradients develop between the bulk of the alloy and the solid/liquid interface. Element transfer across the solid/liquid interface being generally faster than diffusion in the liquid leads to the elements approaching the equality of activity on both sides of the interface one by one. For similar diffusion coefficients in the liquid, the transport away from the interface that is necessary for further solution is relatively fast for elements that are able to enrich in the liquid more than others do, which increases the selectivity of solution for elements with high solubility. The latter naturally applies only if concentrations in the bulk of the liquid are, respectively, low.

Figure 2b extends the view to possible formation of voids in the depletion zone and preferential progress along grain boundaries. Because of crystallographic mismatch between abutting grains and, respectively, stretched or compressed bonds, the atoms at grain boundaries are more likely to transfer to the liquid in contrast to the interior

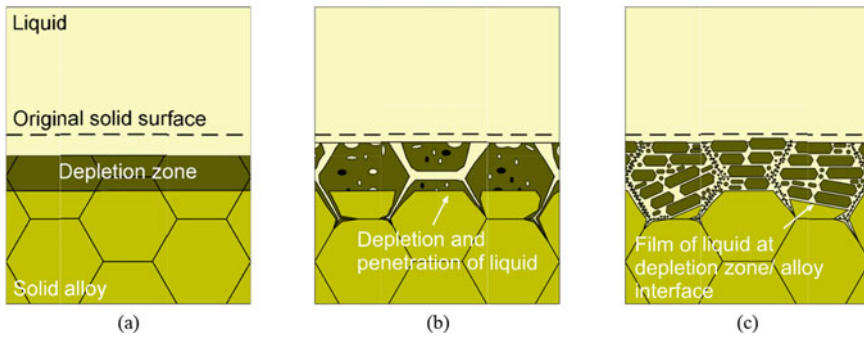


Fig. 2 Schematic illustration of depletion zones as expected to develop in the course of selective leaching for **a** disproportionate element transfer with balanced counterdiffusion in the depletion zone, **b** preferential progress along grain boundaries, and voids forming both at the surface and inside the depletion zone, and **c** re-precipitation of elements of low solubility. (Color figure online)

of the grains. This gives rise to intergranular solution and penetration as especially evident for pure Fe in flowing LBE at 400 [8] and 450 °C [9], but the principle will not change if the material exposed to the liquid is an alloy. In case of disproportionate transfer, the grains deplete in the preferentially transferred elements on both sides of the boundary, and depletion proceeds from this boundary into the adjacent grains. Transport in the finite volume of liquid that penetrates the grain boundary eventually limits further element transfer so that the process of solution retards and the share of intragranular consumption of the alloy gradually increases. However, the notion that solution and especially penetration of the liquid have begun at grain boundaries may persist. Relatively slow diffusion of the elements of low solubility towards the unaffected alloy, i.e. fast diffusion of highly soluble elements in the opposite direction, is likely to maintain voids in the surface as well as create porosity inside the depletion zone. The higher the porosity inside the depletion zone, the smaller the (average) surface recession, which equally applies to concentration in the solid of elements of high solubility being high or low. Pores may allow the liquid to penetrate the depletion zone in addition to the grain boundaries. But the necessary prerequisite for the liquid reaching the alloy in original composition by this means is a continuous network of pores crossing the depletion zone.

The alternative to dispersion in the bulk of the liquid is re-precipitation, possibly after some short-range diffusion [1]. Re-precipitation of elements nearby the site of solution necessitates that, through solution from the alloy, these elements achieve a concentration or activity in the liquid that is higher than in a solid phase that may newly form. For precipitation of a pure solid element, this means enrichment to above solubility or activity >1 , whereas the required element activity is lower if an alloy precipitates. Activity >1 in the liquid implies activity >1 also in the original solid alloy that, for the primarily settled element, then is a metastable modification such as austenite for Fe at temperature less than about 900 °C. Thermochemical data suggests a value of 1.2 for Fe activity in hypothetical pure γ -Fe (austenite) at

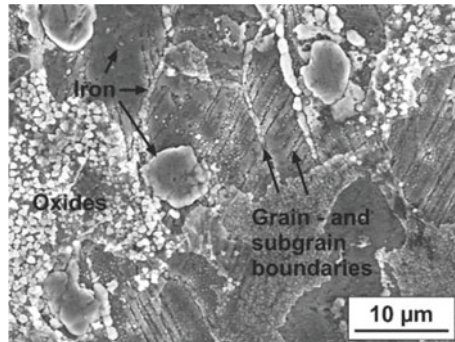
800 K (527 °C) [26], a temperature at which α -Fe (ferrite) clearly is the stable modification. If re-precipitation at a minimum of diffusion is an option especially for elements that have only low solubility in the liquid, they are less likely to restrain proportional transfer across the solid/liquid interface. In this case, the depletion zone does not originate from disproportionate solution as such but through precipitation along with dispersion in the liquid of those elements that enter the newly formed solid in only minor amounts. This solid being interspersed with the liquid is inherent to the formation mechanism, and a thin layer of liquid separating it from the original alloy is probably characteristic [1]. Allotropic transformation, however, is not an exclusive feature of re-precipitation, but possible also if the elements stabilising a metastable original alloy preferentially transfer to the liquid.

Figure 2c illustrates the re-precipitation of elements of low solubility after element transfer to the liquid in proportion to the alloy composition. The grain boundaries are again the sites where the processes most likely start. Necessary element transport, especially of the highly soluble alloying elements, in the liquid volume that penetrates the grain boundaries is hampered by the first precipitates of the newly formed phase. Consequently, the solution and subsequent precipitation on the grain face gain in importance. The precipitates above the interior of the grains are likely to be large in comparison with particles forming at and especially inside the limited space along grain boundaries, so that the original alloy microstructure is traced through small between large precipitates. Growth of large at the cost of small particles (Ostwald ripening) may clear the former grain boundaries from precipitates, by which the original alloy structure becomes even more apparent in the depletion zone. In contrast to depletion by disproportionate transfer to the liquid, there is no diffusion towards the alloy of the elements remaining in the depletion zone, because their activity in the precipitating solid is at most equal if not less than in the alloy. Accordingly, for the surface of the depletion zone to recede, repeated transfer to and dispersion in the liquid are required [1]. As mentioned above, the presence of a newly formed phase is not distinctive for the re-precipitation mechanism. It rather is the missing depletion below the deepest penetration of the liquid that excludes disproportionate element transfer to the liquid. A film of liquid separating precipitated particles from the alloy is a necessary indication for short-range diffusion in the liquid before precipitation, but also establishes if nucleation occurs immediately on the alloy surface and further solution proceeds around the formed particle. The latter is an option especially in the initial stage, whereas, in the long run, the growth of the existing particles is likely to be more favourable.

Observations from Experiments

A large part of experimental investigations in which material solution in liquid metal is evident has been performed on steels. Significantly different solubility of the major alloying elements, as illustrated in Fig. 1 for LBE, especially occurs in the case of austenitic grades. At moderately high temperature, namely <900 °C, ferrite is the

Fig. 3 Surface of 15–15 Ti steel 1.4970 (40% cold work, flat surface, polished) after exposure for about 5000 h to flowing LBE at 400 °C and 10^{-7} % dissolved oxygen [10]

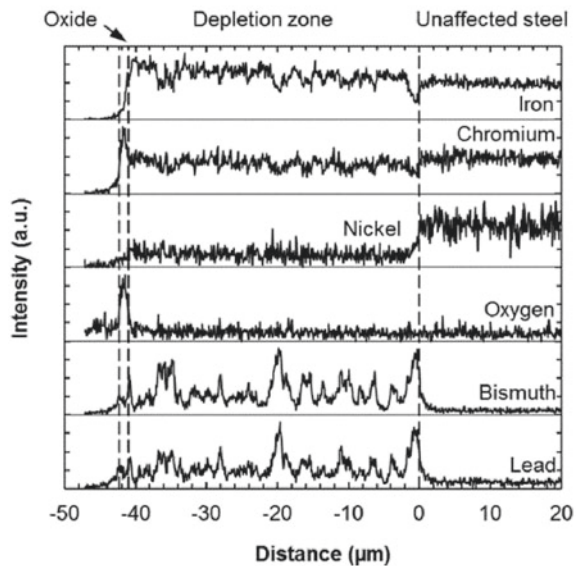
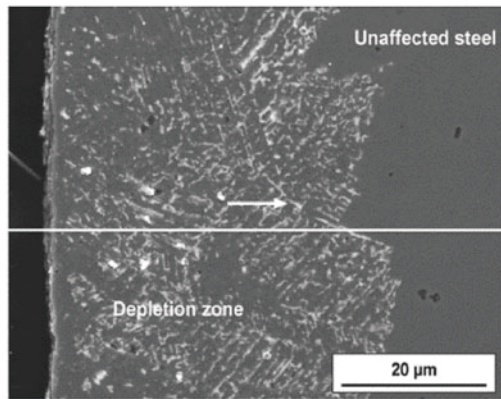


generally more stable modification of the parent element of the alloy, so that, from the purely thermodynamic point of view, selective element transfer or the precipitation primarily of Fe is equally likely to occur. An indication of the latter (Fig. 3) has been found in 15–15 Ti steel 1.4970 after exposure to flowing LBE at 400 °C, on the flat, polished surface of the material both in the solution annealed and cold-worked (40%) state [10]. In the particular experiment, the LBE contained 10^{-7} % (by mass) oxygen so that the solution typical for the interaction with liquid metal competes with surface oxidation. Figure 3 constitutes an early stage of solution that has started after a period dominated by the formation of surface oxides. As other materials, especially technically pure Fe [8], have been tested in the same experimental run, it may not be excluded that the accumulated Fe has partially deposited from the flowing liquid metal, the temperature of which may (slightly) decrease as it passes the exposed samples one after another. However, the interaction of the austenitic steel and the liquid metal is obvious from cross-sectional analyses, especially for grain and subgrain boundaries [10], and re-precipitation of Fe seems all the more required for maintaining proportional element transfer from the steel if the Fe concentration in the liquid is already high.

Figure 3 also exhibits indications of preferential attack along grain and subgrain boundaries. Accelerated element transfer and liquid–metal penetration facilitated by high local defect density in the solid are generally more likely to occur at high-angle grain boundaries, for which the crystallographic mismatch of the neighbouring grains certainly is largest. However, solution and penetration may be clearly more apparent along subgrain boundaries, most notably the deformation twins in cold-worked austenitic steels that have been exposed to LBE at 450 [11] or 500 °C [12]. While highest potential energy or highest mobility of atoms cannot immediately explain this striking observation, the formation of low-energy liquid/solid interfaces possibly favours the penetration of liquid into a subgrain boundary if this boundary divides the grain parallel to crystallographic planes with special affinity to the liquid. Along former twin boundaries and where the latter would intersect each other, electron microscopy [11] reveals ferrite with reduced Ni and Cr content in comparison with the original steel, always enclosed by solidified LBE. Transport of Ni and Cr in the penetrated liquid is evident, whereas element depletion on the side remote

from the ferrite is not apparent from the presented elemental maps and other microanalyses, and not particularly addressed in the evaluations. A mechanism has been proposed for depletion and transformation into ferrite of narrow twins of submicron thickness, starting with penetration of the liquid metal along two almost adjacent twin boundaries [11]. The idea that a narrow austenite twin widens through selective leaching of elements, which opens the space for further ingress of liquid metal [11], may apply analogously for a single twin boundary, considering the loss of material in connection with the removal of atoms via the penetrating liquid. An advanced state of selective leaching in austenitic steel is exemplified in Fig. 4 that stems from experiments in oxygen-containing flowing LBE at 550 °C [13]. Liquid metal that has penetrated the depletion zone seems to trace at least a part of the grain boundaries in

Fig. 4 Cross section of a depletion zone that has formed in austenitic steel 1.4571 during exposure for 5012 h to oxygen-containing flowing LBE at 550 °C [13]



the original microstructure of the steel, but progress at the depletion zone/steel interface is largely transgranular. The results from energy-dispersive *X*-ray spectroscopy (EDS) performed across the near-surface portion of the steel imply that depletion is confined by the deepest penetration of the liquid metal. The particular shape of the depletion zone/steel interface depends on temperature [1], the concentration and orientation of deformation twins in the material [12] or other special features of the microstructure of the steel [14]. The formed surface oxide (Fig. 4) may have retarded [1] but could obviously not suppress selective leaching.

Most notably if the oxygen concentration (activity) in the liquid metal suffices to stabilise oxides of the material elements, solution needs an incubation period during which surface oxides are destroyed. For austenitic steel exposed to static LBE at 500 °C [3] or flowing LBE at 400–550 °C [15], the kinetics of the processes that then take place may initially be described by a linear rate law. In the long run, however, the instantaneous velocity with which selective leaching consumes the steel decreases with time [1, 14]. The duration of apparently linear degradation depends on temperature and the specific austenitic material under consideration [15]. Albeit different in the quantitative outcome, weight change as a function of time determined at 700 °C in flowing sodium (Na) corroborates that, on average, the rate of selective leaching decreases with time for various austenitic steels [27–29]. The identification of the rate determining elemental step in the overall process naturally depends on the mechanism that is presumed being active, but, as a basic principle, it must be the slowest of the subprocesses that are necessary to maintain element transfer from the solid to the liquid phase. For selective element transfer, this would be either diffusion in the gradually depleting steel towards or transport of the preferentially dissolving elements in the liquid. A network of former grain boundaries and, possibly, pores that are penetrated by the liquid (Fig. 2b) reduces the distance to cover by means of diffusion in the solid state. In the case of the re-precipitation mechanism (Fig. 2c), again the transport in the liquid phase imposes a limit on continuing (non-selective) element transfer, but, in the effect of removing dissolved elements from the liquid at the site of dissolution, is supported by the precipitation of the elements of low solubility [1]. Finally, it cannot be excluded that depending on local pre-requisites for dispersion via the liquid (thickness of liquid films), resupply through diffusion in the depleting solid (microstructure, element concentration) or re-precipitation (available space) temporarily take turns, which seems all the more likely if selective leaching preferentially proceeds along grain boundaries or narrow subgrains. In general, however, non-selective element transfer along with re-precipitation should enable faster progress, because it works without solid-state diffusion [1]. Austenitic steels are predestined to gradually dissolve according to this mechanism especially at temperature at which austenite is the metastable solid modification of Fe.

Austenitic steel exposed to liquid Sn [20] shows ferrite formation only at >650 °C and most notably at >840 °C. Both Cr in the steel and Sn stabilise the ferritic phase that is still observed at >1050 °C. At >1050 °C, not only the surface recession of the depletion zone becomes prominent but also the formed ferrite tends to recrystallise into a continuous layer. Additionally, a preference for Ni removal and phase transformation near twins in the austenitic structure is found. The habitus of ferrite

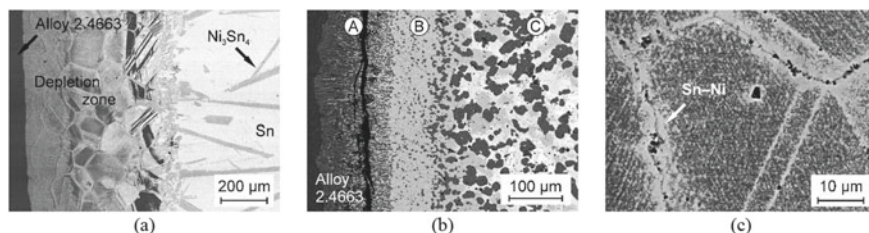


Fig. 5 Selective leaching in Ni-based alloy 2.4663 (Ni–22Cr–12Co–9Mo) after contact with static liquid Sn **a** for 25 h at 700 °C and **b** for 50 h at 1000 °C. **c** Detail of the innermost part of the depletion zone in Fig. 5a [21]

changes from globular to columnar if conditions are adverse to the removal of Ni, i.e. after pre-saturation of the liquid with Ni, for comparatively small volume of liquid or decreasing temperature. Ferrite interspersed with liquid is most obvious in the temperature range from 950 to 1050 °C and occurs for both shapes of ferrite grains. Especially at <950 °C, the austenite at the interface with columnar ferrite does not show Ni depletion [20], which complies with slow Ni transport in the austenite in contrast to diffusion across the ferritic zone even in the absence of penetrated liquid. Besides the presence of intermetallic compounds, e.g. Ni₃Sn₂ that seems to have formed at up to 1050 °C [20], Sn entering and stabilizing the ferritic phase is likely to influence the detailed mechanism of ferrite formation. At >900 °C, solid-state diffusion becomes increasingly faster, whereas the precipitation of Fe-rich ferrite from the liquid is rather improbable.

Figure 5 presents examples of selective leaching in Ni-based alloy as observed after exposure to static liquid Sn at 700 and 1000 °C, respectively [21]. At 700 °C (Fig. 5a), the body of the depletion zone mainly consists of a conglomerate of Sn–Ni and Cr–molybdenum (Mo) phases. The Sn–Ni part is likely to be at least partially liquid at 700 °C, whereas Cr and Mo are major alloying elements of low solubility in the particular Ni-based material. The microstructure of the original alloy is largely conserved. In the outer portion, Cr–Mo has more clearly separated from Sn–Ni and accumulated in the domains that appear dark in the backscatter electron (BSE) micrograph depicted in Fig. 5a. The latter certainly results from ageing of the depletion zone. At 1000 °C (Fig. 5b), three subzones can be distinguished: (A) the innermost part, showing columnar Cr–Mo interspersed with Sn–Ni; (B) a transition zone characterised by high percentage of Sn–Ni and small particles that seem to have originated from disintegration of the columnar Cr–Mo in subzone A; and (C) comparatively large particles enclosed by Sn–Ni. The large particles have gained in size partly through absorption of Fe from the liquid Sn [21]. The most obvious difference between the two scales is the percentage of Sn–Ni via which Ni and other alloying elements of rather high solubility in Sn, such as cobalt (Co), defect from the original alloy. Columnar Cr–Mo formed at 1000 °C is reminiscent of the ferrite structure attributed to relatively low velocity of Ni transfer to the bulk of the liquid metal [20]. At 300 °C lower temperature, at which the original microstructure of

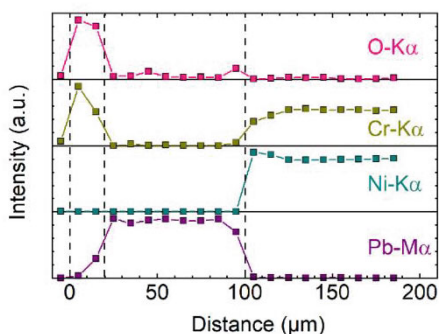
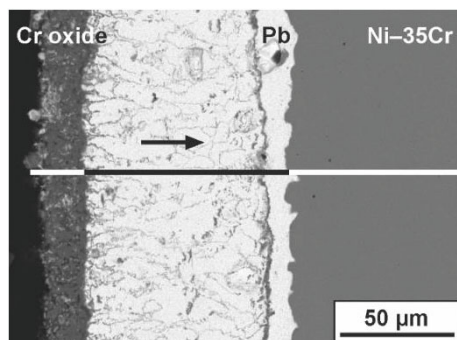
the alloy is conserved, not only the rate of element removal is significantly reduced but also the capacity of the liquid Sn for dissolving Ni as well as other alloying elements is clearly lower. Both favour elements of low solubility staying behind in the depletion zone. The re-precipitation mechanism could explain the generally fine dispersion but accumulation of Sn along the grain boundaries of the original alloy (Fig. 5c), and precipitation of Cr–Mo after transport only over a short distance would comply with reproduction of the original microstructure.

Influence of Dissolved Oxygen

At the time of the first exposure to the liquid metal, the surface of solid metallic materials is rarely clean in the sense that there is no adsorption layer or precursor of a surface scale formed during storage and handling. Surface oxides are of particular importance in this respect. Depending on the oxygen concentration, or more precisely, oxygen activity in the liquid metal, they tend to degrade, grow or transform. Surface oxide that is stable under the prevailing conditions may effectively suppress the interaction with the liquid metal [16]. However, along with growth of an oxide film, defects accumulate which renders the oxide prone to local failure [30, 31], i.e. the interaction with the liquid metal is only delayed [17] rather than completely avoided.

The influence of oxygen that is dissolved in the liquid metal is not confined to the formation of surface oxides. Where such an oxide scale remains discontinuous or locally loses its protective properties, solid oxides may also form after transfer of the respective material element to and transport in the liquid metal. This gives rise to the precipitation of oxide in some distance from the site of element solution as, e.g., observed for austenitic steel at 450 °C in the presence of static LBE containing $10^{-7}\%$ oxygen [17]. The formation of solid oxide is an alternative way of a dissolved element leaving the solution, and the concentration of this element in the liquid is rather low at the site where the precipitation occurs. Accordingly, concentration gradients become steeper which supports element transport and, therefore, further solution from the solid alloy. For selective leaching this means, oxidation improves the conditions for transport in the liquid specifically for oxide-forming elements, which suggests oxidation of Fe and Cr as an explanation for different ferrite contents in depletion zones formed in austenitic steel at 450 and 550 °C, in flowing LBE with $10^{-6}\%$ dissolved oxygen in both cases [1]. Likewise, lower Cr content in the depletion zone and overall higher material loss have been attributed to higher oxygen activity in Pb–lithium (Li) alloys with different Li concentrations [18]. Oxide formation may even reverse the situation as to selective leaching in the sense that elements with generally high solubility stay in the alloy, whilst elements of low solubility preferentially transfer to the liquid and subsequently precipitate. An example is the performance of binary Ni–Cr alloys, especially Ni with 35% Cr in static liquid Pb at 750 °C and $10^{-6}\%$ dissolved oxygen [19]. The EDS linescan presented in Fig. 6 indicates near-surface enrichment of Ni, and Cr depletion in the alloy, although Ni

Fig. 6 Ni–35Cr model alloy after exposure for 120 h to oxygen-containing static Pb at 750 °C: BSE micrograph and results of qualitative EDS analyses performed along the indicated line [19]. (Color figure online)



solubility in Pb is clearly higher than the solubility of Cr [32]. Cr has re-precipitated to form an oxide layer that finally encloses the liquid metal.

Oxygen enrichment above the threshold for the formation of oxides of the alloying elements in steels and Ni-based alloys is also possible for liquid Sn, giving rise to suppression of element solution as well as only local occurrence of solution [22].

Formation of Intermetallics

The formation of intermetallic compounds is particularly important in the Fe–Sn [33] and Ni–Sn systems [34]. At temperature in the range of 500 °C, Ni in austenitic steel primarily transfers to the liquid metal, but a significant share of Fe is retained as FeSn₂, and FeSn to lesser extent, in a solid surface scale on the steel [21–23]. Consumption of the steel is non-selective, which changes, if temperature increases to around 700 °C. Furthermore, austenitic steels now develop the depletion zone at the instantaneous surface that is typical for selective leaching especially of Ni. The removal of Ni is likely to still occur through a solid intermetallic layer that, in this temperature range, predominantly consists of FeSn [21–23]. This layer is interspersed with particles that are rich in Cr and Mo. Their Fe content and size decrease with

increasing distance from the alloy [21]. Ferrite that has formed in the depletion zone is columnar, similar to Fig. 5b, and the notion that the particles enclosed by FeSn have separated from the columnar ferrite equally arises. The removal of Ni through the intermetallic layer requires an adequate solubility in FeSn₂ or FeSn and is driven by the high solubility of Ni in liquid Sn. Ni–Sn intermetallics alternatively form if the bulk of the liquid is Ni-saturated. In pits originating from local initiation of the interaction with liquid Sn, Cr–Mo forms a network, as the ratio of Sn available inside the pit and active alloy surface area is rather small [22].

Also in the case of Ni-based alloys, the stability of intermetallic compounds with Sn changes the initially liquid Sn/solid alloy interaction into a solid/solid interaction with Ni₃Sn₄ being the dominant intermetallic at 700 °C [21, 22]. As the growth of Ni₃Sn₄ primarily consumes Ni, the qualitative outcome, i.e. formation of a conglomerate of Sn–Ni and Cr–Mo similar to Fig. 5c, does not significantly change in comparison with selective leaching caused by liquid Sn, but the consumption of material is clearly lower if there is a Ni₃Sn₄ layer on the surface, as experiments with Ni-saturated Sn show [22]. The solubility of Cr and Mo in the intermetallic may be equally low or even lower than in liquid Sn, and diffusion of these elements is slower. At high concentration of Fe in the alloy and temperature at which Fe–Sn intermetallics are stable, the formation of the latter competes with the development of ferrite that, for austenitic steel, completely vanishes at 500 [21, 22] or the amount of which is reduced at 700 °C [21, 22].

In contrast to liquid Sn, the formation of intermetallic phases plays a negligible role in the performance of steels or Ni-based alloys in the presence of liquid Pb or LBE. This especially applies to the typical temperatures of interest. However, precipitation of the bismuth (Bi)–Ni intermetallics NiBi or NiBi₃ is to be taken into account if LBE absorbs Ni from materials in a non-isothermal system.

Conclusions

The analysis of dissimilar metal transfer from a solid alloy to the bulk volume of a liquid shows that the process becoming selective for certain alloying elements depends on the solubility of the metals under consideration, but only weakly on their concentration in the alloy. The re-precipitation of elements of low solubility is generally favoured over disproportionate transfer to the liquid if, for the re-precipitating elements, the alloy is not the thermodynamically most stable modification under the prevailing conditions such as austenite in the case of Fe at <900 °C. This especially applies to temperature too low for significant diffusion in solids. Re-precipitation is indicated by a film of liquid separating a zone depleted in the elements of high solubility from the alloy in its original composition.

Experimental observations as to selective leaching are more numerous for austenitic steel and Pb-based alloys, most notably LBE, if compared with Ni-based alloys or liquid Sn. The results from high-resolution microscopy available for narrow twins [11] show the characteristics of re-precipitation most clearly, for austenitic steel

after exposure to LBE at 450 °C. Selective leaching caused by Sn without influence of the formation of intermetallic phases is to be expected at temperatures high enough for remarkable solid state diffusion, so that one of the main arguments against disproportionate solution loses validity. Furthermore and unlike Pb or Bi, Sn contributes to the ferritic phase that is the product of the decomposition of austenitic steels [20], so that same mechanism of selective leaching as in LBE at moderately high temperature is not a matter of course. The identification of re-precipitation as the prevailing mechanism for Ni-based alloy and Sn at 700 °C has, at this stage, preliminary character and partly bases on the contrast to observations at 1000 °C.

Dissolved oxygen supports leaching of elements that form solid oxides. The formation of intermetallic compounds of alloying elements that exhibit high solubility in the liquid metal reduces the rate of selective leaching, but apparently has weak influence on the structure of the depletion zone that develops. The latter is in contrast to elements of low solubility forming intermetallics with the constituent parts of the liquid metal.

References

1. Schroer C, Wedemeyer O, Novotny J et al (2014) Selective leaching of nickel and chromium from Type 316 austenitic steel in oxygen-containing lead–bismuth eutectic (LBE). *Corros Sci* 84:113–124
2. Gossé S (2014) Thermodynamic assessment of solubility and activity of iron, chromium, and nickel in lead bismuth eutectic. *J Nucl Mater* 449(1–3):122–131
3. Yamaki E, Ginestar K, Martinelli L (2011) Dissolution mechanism of 316L in lead–bismuth eutectic at 500°C. *Corros Sci* 53(10):3075–3085
4. Manly WD (1956) Fundamentals of liquid metal corrosion. *Corrosion* 12(7):336t–342t
5. Weeks JR, Romano AJ (1969) Liquidus curves and corrosion of Fe, Ti, Zr and Cu in liquid Bi–Pb alloys. *Corrosion* 25(3):131–136
6. Rosenblatt G, Wilson JR (1970) The solubilities of several transition metals in liquid lead–bismuth eutectic. In: Draley JE, Weeks JR (eds) *Corrosion by liquid metals: proceedings of the sessions on corrosion by liquid metals of the 1969 Fall meeting of the Metallurgical Society of AIME, October 13–16, 1969, Philadelphia, Pennsylvania*. Plenum Press, New York, London, pp 469–477
7. Martinelli L, Vanneroy F, Diaz Rosado JC et al (2010) Nickel solubility limit in liquid lead–bismuth eutectic. *J Nucl Mater* 400(3):232–239
8. Schroer C, Tsisar V, Durand A et al (2019) Corrosion in iron and Steel T91 caused by flowing lead–bismuth eutectic at 400 °C and 10⁻⁷ mass% dissolved oxygen. *J Nucl Eng Radiat Sci* 5(1)
9. Schroer C, Skrypnik A, Wedemeyer O et al (2012) Oxidation and dissolution of iron in flowing lead–bismuth eutectic at 450 °C. *Corros Sci* 61:63–71
10. Tsisar V, Schroer C, Wedemeyer O et al (2018) Effect of structural state and surface finishing on corrosion behavior of 1.4970 austenitic steel at 400 and 500 °C in flowing Pb–Bi eutectic with dissolved oxygen. *J Nucl Eng Radiat Sci* 4(4)
11. Hosemann P, Frazer D, Stergar E et al (2016) Twin boundary-accelerated ferritization of austenitic stainless steels in liquid lead–bismuth eutectic. *Scripta Mater* 118:37–40
12. Klok O, Lambrinou K, Gavrilov S et al (2018) Effect of deformation twinning on dissolution corrosion of 316L stainless steels in contact with static liquid lead–bismuth eutectic (LBE) at 500 °C. *J Nucl Mater* 510:556–567

13. Schroer C, Wedemeyer O, Novotny J et al (2011) Long-term service of austenitic steel 1.4571 as a container material for flowing lead–bismuth eutectic. *J Nucl Mater* 418(1–3):8–15
14. Lambrinou K, Charalampopoulou E, van der Donck T et al (2017) Dissolution corrosion of 316L austenitic stainless steels in contact with static liquid lead–bismuth eutectic (LBE) at 500 °C. *J Nucl Mater* 490:9–27
15. Tsisar V, Schroer C, Wedemeyer O et al (2016) Long-term corrosion of austenitic steels in flowing LBE at 400 °C and 10^{-7} mass% dissolved oxygen in comparison with 450 and 550 °C. *J Nucl Mater* 468:305–312
16. Asher RC, Davies D, Beetham SA (1977) Some observations on the compatibility of structural materials with molten lead. *Corros Sci* 17(7):545–557
17. Klok O, Lambrinou K, Gavrilov S et al (2018) Effect of lead–bismuth eutectic oxygen concentration on the onset of dissolution corrosion in 316 L austenitic stainless steel at 450 °C. *J Nucl Eng Radiat Sci* 4(3):31019
18. Barker MG, Coen V, Kolbe H et al (1988) The effect of oxygen impurities on the behaviour of type 316 stainless steel in Pb–17Li. *J Nucl Mater* 155–157:732–735
19. Picho O (2014) Beständigkeit von Nickel–Chrom–Legierung und Eisenaluminidschichten in sauerstoffhaltigen flüssigen Bleilegierungen. Karlsruhe. <https://doi.org/10.5445/IR/1000043553>
20. Duc D, Marchive D, Treheux D et al (1974) Ferritic transformation of an austenitic stainless steel by hot dipping in liquid tin or tin–nickel alloys. *J Cryst Growth* 24–25:559–562
21. Emmerich T, Schroer C (2017) Corrosion in austenitic steels and nickel-based alloys caused by liquid tin at high temperature. *Corros Sci* 120:171–183
22. Emmerich T, Durand A, Tsisar V et al (2018) Aspects of corrosion of iron- and nickel-based materials by liquid tin: oxygen dissolved in the melt and saturation with the parent element. *Mater Corros* 69(7):832–849
23. Heinzel A, Weisenburger A, Müller G (2017) Corrosion behavior of austenitic steel AISI 316L in liquid tin in the temperature range between 280 and 700 °C. *Mater Corros* 68(8):831–837
24. Mazandarany FN, Pehlke RD (1973) Thermodynamic properties of solid alloys of chromium with nickel and iron. *Metall Trans* 4(9):2067–2076
25. Gao Y, Takahashi M, Nomura M (2015) Characteristics of iron and nickel diffusion in molten lead–bismuth eutectic. *Mech Eng J* 2(6):15–00149 (9 pages)
26. Chase MW, Davies CA, Downey JR et al (1985) JANAF thermochemical tables, third edition. *J Phys Chem Ref Data* 14, Suppl. 1:1–1856
27. Suzuki T, Mutoh I (1989) A revisit to “steady-state corrosion rate of type 316 stainless steel in sodium in a non-isothermal loop system. *J Nucl Mater* 165(1):83
28. Suzuki T, Mutoh I (1988) Steady-state corrosion rate of type 316 stainless steel in sodium in a non-isothermal loop system. *J Nucl Mater* 152(2–3):343–347
29. Suzuki T, Mutoh I, Yagi T et al (1986) Sodium corrosion behavior of austenitic alloys and selective dissolution of chromium and nickel. *J Nucl Mater* 139(2):97–105
30. Lin LF, Chao CY, Macdonald DD (1981) A point defect model for anodic passive films: II. Chemical breakdown and pit initiation. *J Electrochem Soc* 128(6):1194–1198
31. Chao CY, Lin LF, Macdonald DD (1981) A point defect model for anodic passive films: I. Film growth kinetics. *J Electrochem Soc* 128(6):1187–1194
32. Alden T, Stevenson DA, Wulff J (1958) Solubility of nickel and chromium in molten lead. *T Metall Soc AIME* 218(2):15–17
33. Predel B (1995) Fe–Sn (Iron–Tin). In: Madelung O (ed) Dy–Er—Fr–Mo. Springer, Berlin, pp 1–5
34. Predel B (1998) Ni–Sn (Nickel–Tin). In: Madelung O (ed) Ni–Np—Pt–Zr. Springer, Berlin, pp 1–4

Numerical and Analytical Research of the Formation and Accumulation of Deposits on the Circuit with HLM Coolant Within the Consistent Model for Physical and Chemical Processes



A. V. Avdeenkov, O. I. Achakovsky, and A. I. Orlov

Abstract We analyze an engineering model for a self-consistent calculation of the growth of an oxide film in circulation circuits with a heavy liquid metal coolant and concentrations of impurities (oxygen, iron, magnetite) from the point of view of possible uncertainty in determining the activity of oxygen. The modeling of thermo-hydraulic and physicochemical processes is based on solving the associated three-dimensional equations of hydrodynamics, convective-diffusive transport, and the formation of chemically interacting impurity components in the coolant volume and on the surface of steels. Model calculations of the influence of the uncertainty of oxygen activity on the rate and integral yield of iron, which under the given conditions of the oxygen regime after interaction with oxygen determine the appearance of magnetite. It is numerically demonstrated that in the saturation mode, there is a model-independent characteristic, which is determined by the parabolic constant and thickness of the oxide film characteristic of steel.

Keywords Mass transfer · Impurities · Oxide film · Fast reactor · Lead coolant · MASKA-LM code · Iron yield · Oxygen regime · Saturation

Introduction

The experience of operating circulation loops with HLHC has shown that impurities enter the coolant that interact with each other, with the coolant and structural materials, and the products of these interactions spread around the loop and could localize in specific areas. As a result of these interactions and mass transfer processes,

A. V. Avdeenkov (✉)

All-Russian Research Institute for Nuclear Power Plants Operation, JSC, Moscow, Russia

e-mail: avdeykov@mail.ru

A. I. Orlov

Proryv JSC, Moscow, Russia

A. V. Avdeenkov · O. I. Achakovsky

JSC "SSC RF-IPPE", Obninsk, Russia

© The Minerals, Metals & Materials Society 2021

TMS 2021 150th Annual Meeting & Exhibition Supplemental Proceedings,

The Minerals, Metals & Materials Series,

https://doi.org/10.1007/978-3-030-65261-6_59

disruptions to the performance of the circuits are possible, which are expressed in the following:

- deterioration of thermohydraulic characteristics due to the deposition on surfaces of the circuit of phases containing oxides of coolant components and circuit materials.
- violation of the tightness of the circuit or the appearance of various defects and destruction of its materials due to the aggressive action of the coolant.

The composition, physical state, and amount of impurities largely depend on the stage and operating conditions of circuits. The presence of particles of structural materials (SM) in slags is associated with the release of materials from them due to the occurrence of diffusion and corrosion–erosion processes during the contact of HLHC with SM. As shown by the results of numerous studies of the composition and chemical properties of slags in most cases, the bulk share consists of the components of the phases PbO, Pb (and Bi for Pb-Bi HLHC). Slag also contains oxide phases from Bi_2O_3 , Fe_3O_4 , Fe_2O_3 and oxides of other elements.

The purpose of this work is to study only one, but an important component of the formation of impurities, namely the yield of iron and the formation of magnetite, since this process is precisely due to the specificity of self-consistent physicochemical processes in the oxide film and at the interface between the media, while the other processes are due to the specifics of the design and operation of the circuits.

The paper presents model calculations of the influence of the uncertainty of oxygen activity on the rate and integral yield of iron, which, under the given conditions of the oxygen regime, after interaction with oxygen, causes the formation of magnetite.

Since at the moment, there is no sufficient amount of data on the behavior of magnetite in the circuit (the degree of deposition, coagulation, solubility), modeling allows us to make only calculated estimates of the rate of its generation and its integral amount in the circuit by the emission of iron into a circuit.

When calculating and analyzing physicochemical processes, it is necessary to take into account that oxygen activity can be measured (indirectly calculated) only with some error.

The article presents the results of corrosion processes kinetics and changes in the oxide layer modeling using MASKA-LM software complex. The complex is intended for numerical simulation of three-dimensional non-stationary processes of mass transfer and interaction of impurity components in a heavy liquid metal coolant (HLHC: lead, lead–bismuth). The software complex is based on numerical solution of coupled three-dimensional equations of hydrodynamics, heat transfer, formation and convective-diffusive transport of chemically interacting components of impurities.

A system of three-dimensional equations of an incompressible multicomponent medium in a Cartesian coordinate system was used to describe the processes of formation, transformation, and transfer of impurities in the primary circuit of a reactor with HLHC. The system includes hydrodynamic equations in the Boussinesq approximation, equations of conservation and transfer of thermal energy, equations of physicochemical kinetics of impurities [1–4], equations of conservation, and transfer of

components of a multicomponent medium. The system of equations is solved by finite-difference methods.

For simplicity, a system is considered only with the formation of magnetite and the release of iron. This approach is fully justified, since the mobility of iron is an order of magnitude higher than that of, for example, chromium, and its release into the coolant is at least an order of magnitude more intense. In the developed model, at the first stage, the iron flux “remaining” in the near-wall layer is determined as the difference between the fluxes through the oxide film and the flux that has gone into the coolant. The “counter” flow of oxygen from the coolant is determined according to the stoichiometry of the magnetite formed. In this approximation, it is unambiguously assumed that the growth of the film (magnetite) occurs due to the reaction on the surface of the oxide layer:



and at the same time, all four components of the reaction are in chemical equilibrium. Since the rate of chemical reactions is much higher than the characteristic rates of all other physical processes, then in the volume of the coolant at each moment of time, chemical equilibrium can be considered steady and the distribution of components depends significantly on thermohydraulic processes.

Basic equations of the model for the growth of a conventionally single-layer film δ , fluxes, and concentrations of impurities at the steel–coolant interface:

$$\frac{4M_O}{3M_{Fe}} \left(J_{Fe}^\delta - J_{Fe}^\beta \right) = J_O^\beta - J_O^\delta, \tag{1a}$$

or

$$\frac{4M_O C_{Fe}^\delta}{3M_{Fe}} \left(\frac{K_p}{2\delta} - \frac{\chi_{Fe} (C_{Fe}^\gamma - C_{Fe}^\beta)}{C_{Fe}^\delta} \right) \approx \chi_0 (C_0^\beta - C_0^\gamma), \tag{1b}$$

$$\frac{d\delta}{dt} = \frac{K_p}{2\delta} - \frac{\chi_{Fe} (C_{Fe}^\gamma - C_{Fe}^\beta)}{C_{Fe}^\delta} \tag{2}$$

where

- $J_{O,Fe}^{\beta,\delta}$ oxygen and iron flows in the coolant flow and the film, respectively,
- C_{Fe}^δ concentration of iron in the oxide film (designation δ),
- C_{Fe}^β iron concentration in the coolant flow,
- C_{Fe}^γ concentration of iron on the surface of the oxide layer due to the reaction (designation γ),
- C_O^β oxygen concentration in the coolant flow,
- C_O^δ oxygen concentration in the oxide film,
- χ_{Fe}, χ_O mass transfer coefficients for iron and oxygen, M_O, M_{Fe} —molar masses of oxygen and iron, K_p —parabolic constant.

Parametrizations of parabolic constants for EP-823, T91, 316L and others are given in [5–11].

From expression (2), it follows that the film thickness reaches its limit value (saturation thickness):

$$\delta_c = \frac{K_p}{2 \frac{\chi_{Fe}(C_{Fe}^\gamma - C_{Fe}^\beta)}{C_{Fe}^\delta}} \quad (3)$$

The joint solution of the equations of thermal hydraulics, the equations of chemical equilibrium processes describing the formation of oxide, and the equations of film change (1a, 1b, 2) of the MASKA-LM code make it possible to determine the thickness of the oxide film and the fluxes of impurities at the interfaces at any time.

Model Calculations for Different Steels

For numerical analysis, a simple model of the flow of lead coolant of a given temperature in a pipe was chosen: the length of the computational domain is 1 m; diameter 50 mm; Reynolds number 10^5 , which corresponds to the coolant flow velocity $v = 1.736$ m/s. Pipe surface area $S = 0.157$ m².

To estimate the iron yield, it is sufficient to know its flux at the boundary of the oxide film J_{Fe}^β , which can be obtained from the solution of the above-described model equations. Knowing the flow, it is possible to determine the total yield of iron from the surface per unit of time and its integral yield as a function of time.

In further calculations, the scatter of oxygen concentration values is assumed: ± 20 and $\pm 50\%$ [12].

In the present analysis, most of the model calculations were carried out for the basic mode and coolant temperature of 650 °C to assess the scale of iron release into the coolant.

As is well known, the oxygen regime for the coolant is selected based on currently available experimental material for bench tests of structural steels and can be further adjusted. The upper limit of the range is selected based on prevention of conditions for formation of a solid phase of lead oxide in the “cold” part of the circuit. The lower limit is determined based on the oxygen content corresponding to the level of potential destruction of the outer layer of protective oxide coatings on the surfaces of structural steels. When the concentration of dissolved oxygen in the coolant drops below the critical value, i.e., less than the lower limit of the concentration range, reliable anti-corrosion protection of structural steels is not provided. Exceeding the upper limit of the concentration range, i.e., the presence of a significant amount of oxygen in the loop, can lead to the accumulation of an unacceptable amount of slag deposits on the heat exchange surfaces of the loop and equipment.

Figure 1 shows the rate of iron yield, its integral yield, and the spread of values with an uncertainty of oxygen concentration up to $\pm 50\%$. Just as for the thickness of

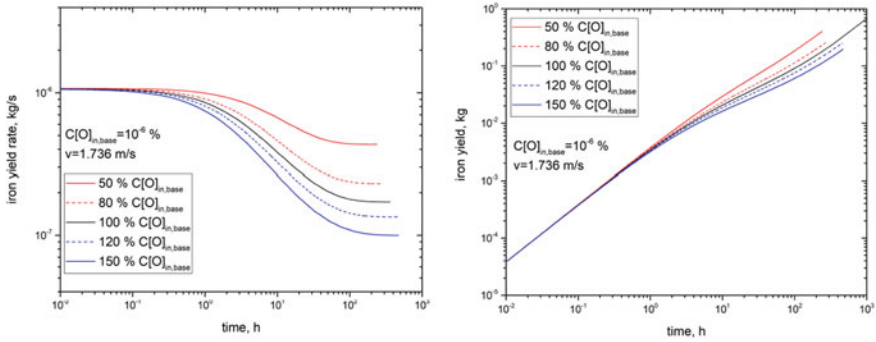


Fig. 1 Spread of values of iron yield rate rate(left panel) and integral yield (right panel) in the tube made of EP-823 steel with the spread of oxygen concentration values ± 20 and $\pm 50\%$ of the base value 10^{-6} mass%. $T = 650^\circ\text{C}$. (Color figure online)

the oxide film, the numerical range of the studied values is from ~ 30 to $\sim 100\%$ for the lower and upper values. Figure 2 shows the results of comparative calculations of the amount of iron in the film and the amount of iron released into the coolant. The released iron, due to the constancy of the maintained oxygen concentration, quickly reacts with oxygen, forming magnetite, which in the form of deposits can stay in the circuit. The results show that most of the iron is released into the coolant, which obviously needs constant filtration.

Figure 2 shows the results of calculations of the release of iron into the coolant at different temperatures. At a temperature of 500°C , the integral yield of iron is approximately three orders of magnitude less than at 650°C , which is obviously explained by the higher mobility of iron cations in steel and film at high temperatures.

Figure 3 show the same as Fig. 1, but for increased oxygen concentration. The proportions in uncertainty of 30 and 100% are also the same as for the basic oxygen

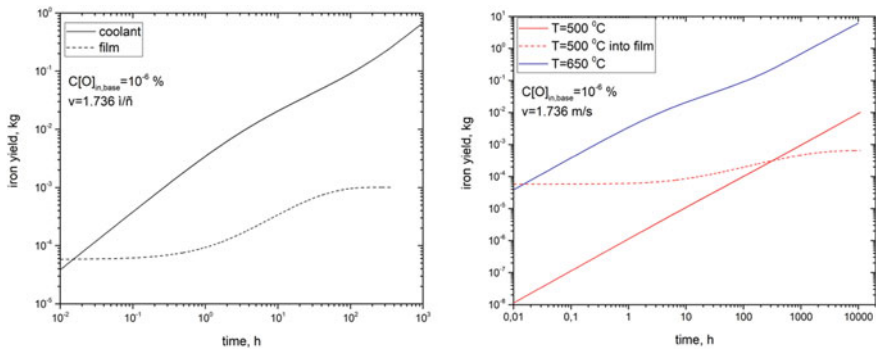


Fig. 2 Comparison of integral yield of iron in the film with the amount of iron released into the coolant. Steel EP-823 (left panel). Integral iron yield at different temperatures for EP-823 steel (right panel). $T = 650^\circ\text{C}$. (Color figure online)

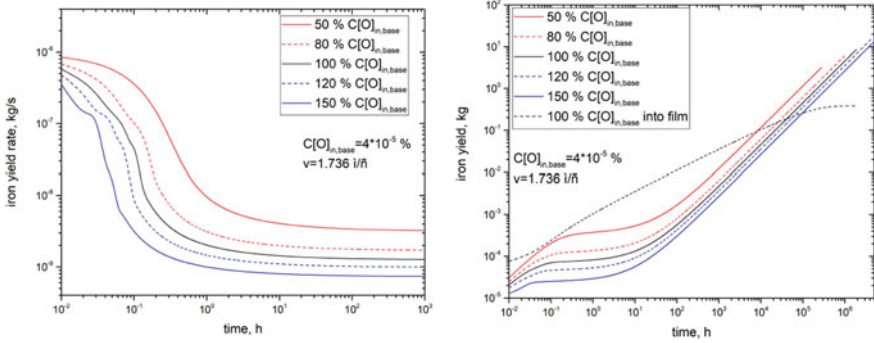


Fig. 3 Spread of the values of iron yield rate and the integral yield in a tube made of EP-823 steel with the spread of the oxygen concentration values $\pm 20\%$ and $\pm 50\%$ from 4×10^{-5} mass%. $T = 650^\circ\text{C}$. (Color figure online)

regime. A significant difference from the basic oxygen regime is the result that a comparable part of iron goes into the oxide film, and the actual release of iron into the coolant is several orders of magnitude smaller, then at the basic oxygen regime for the same times. It should be noted here that at an increased oxygen concentration, the film grows for a long time (up to tens of thousands of hours) according to a parabolic law and reaches values of up to several millimeters, which, based on the available experimental data and general concepts, is hardly possible, since erosion processes should “rip off” such thick film. But now, the model does not take into account the erosive processes of film stripping due to the lack of experimental information.

Figures 4, 5 and 6 show the results of comparative calculations of the iron yield for different steels at different temperatures and different rates of coolants. All the carried-out calculations confirm the above observations and conclusions for other steels as well. But here it is necessary to make an essential remark. As can be seen from these figures, starting from a certain moment in time, the rate of release of iron

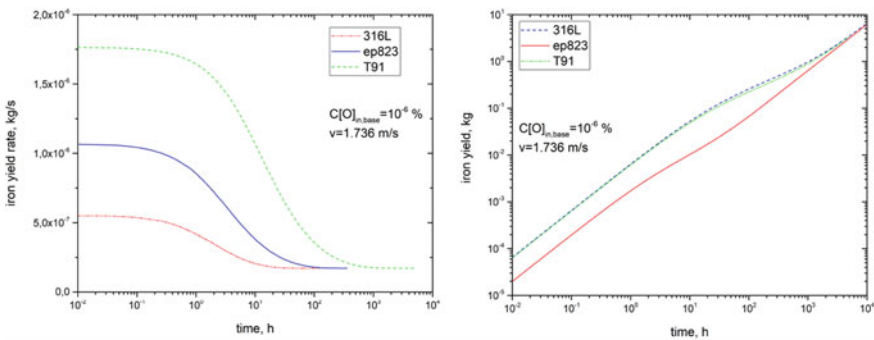


Fig. 4 Comparison of values of iron yield rate (left panel) and the integral yield (right panel) for different steels. $T = 650^\circ\text{C}$. (Color figure online)

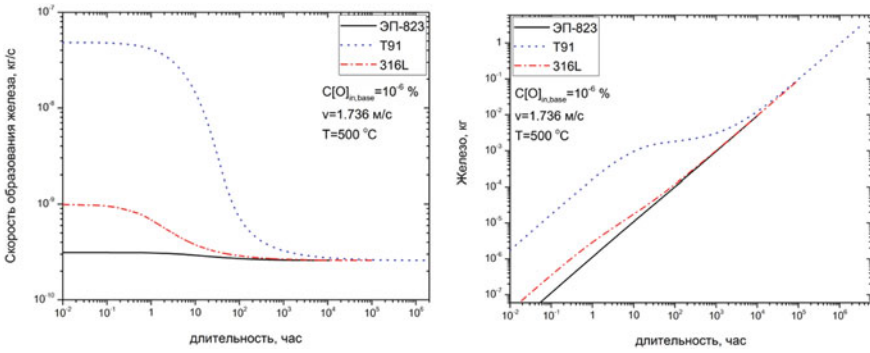


Fig. 5 Comparison of values of iron yield rate (left panel) and the integral yield (right panel) for different steels. $T = 500\text{ }^{\circ}\text{C}$. (Color figure online)

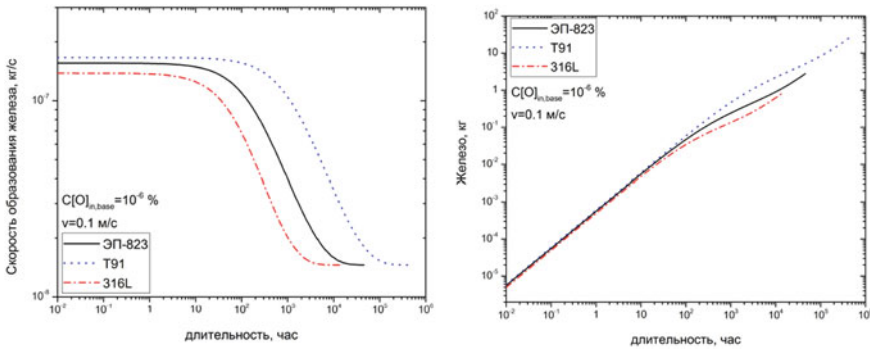


Fig. 6 Comparison of values iron yield rate (left panel) and the integral yield (right panel) for different steels. $T = 650\text{ }^{\circ}\text{C}$ at an average speed of the coolant $v = 0.1\text{ м/с}$. (Color figure online)

no longer depends on the type of steel and is the same for all of them. This moment in time is the moment when the thickness of the oxide film reaches the saturation value. For different steels, this moment occurs at different times.

It is obvious that the result obtained is a consequence of the assumption that the film is the same for all steels, that is, magnetite. And since upon reaching saturation, the film thicknesses no longer change, the differences in the properties of the steels behind the film no longer affect the iron yield, and it is determined by magnetite itself. It is also obvious that if we consider that for each steel, its film will have a different composition, then such an exact coincidence will not happen. It should be noted that since the density of spinel and the density of magnetite differ quite slightly (less than 10%), the expected differences will also be insignificant.

Calculations confirm the statement about the consistency of the value

$$\frac{J_{Fe}^{\beta}}{S \cdot C_{Fe}^{\delta}} = \frac{K_p}{S \cdot 2\delta_c} \quad (4)$$

and reaching a certain constant rate of iron release, which is determined by the ratio of the parabolic constant and the thickness of the oxide film in saturation mode, K_p/δ_c .

For the considered example of the growth of an oxide film in a tube, the ratio of the volume of the coolant in the tube to the steel surface area is rather large and amounts to ~12.5 mm. We considered another example, where this ratio is much smaller (~2.7 mm), namely a bundle of rods in a triangular package with a diameter of 10 mm, a length of 0.97 m, with a pitch of 14 mm. The results obtained with an accuracy of the ratio of the surface areas of steels of these two geometries repeat the results for the tube.

Thus, as for the thickness of the oxide film, the geometry itself has no significant effect on the magnitude and rate of iron release, and small differences are determined by a small difference in the coolant flow rate. However, this is obviously the expected result that the properties of the coolant (velocity and temperature fields) determine the features of physicochemical processes at the steel–coolant interface and are necessary preliminary data obtained directly from 3D thermohydraulic calculations.

Estimation of Relative Loss of Iron in Steel

The calculated values of the rate of iron yield and the integral yield of iron obtained above can be used in assessing the conditionally removed steel material. The iron left from the sample can be converted to the volume of the removed steel. For a tube, this volume can be equivalently converted to the “eaten” steel thickness by diameter. For a tube with a diameter of 50 mm, the “expansion” of the tube due to the loss of steel lies in the region of 5 mm for different steels at $T = 650\text{ }^{\circ}\text{C}$ (Table 1). In this case, the contribution of iron transferred into the film is insignificant in comparison with the contribution of iron released into the coolant. Thus, the yield of iron with such parameters is very noticeable.

Table 1 Iron loss from the tube surface

Tube, diameter 50 mm, $v = 1.736\text{ m/s}$, $T = 650\text{ }^{\circ}\text{C}$, oxygen concentration 10^{-6} mass\% , surface square $S = 0.157\text{ m}^2$			
Steel	Total flow of iron into the coolant at a moment in time 10,000 h, kg/s	Iron, kg	«Eatable» thickness, mm
EP-823	1.72E-7	6.2	5.05
T91	1.72E-7	6.45	5.25
316L	1.72E-7	6.15	5.0

Table 2 Iron loss from the tube surface at low coolant velocity

Tube, diameter 50 mm, $v = 0.1$ m/s, $T = 650$ °C, surface square $S = 0.157$ m ²			
Steel	Total flow of iron into the coolant, kg/s	Iron, kg	«Eatable» thickness, mm
EP-823	1.55E-8	9.1E-01	7.45E-01
T91	3.5E-08	2.2	1.8
316L	1.45E-08	6.2E-01	5.05E-01

Table 3 Iron loss from the tube surface at $T = 500$ °C

Tube, diameter 50 mm, $v = 1.736$ m/s, $T = 500$ °C, surface square $S = 0.157$ m ²			
Steel	Total flow of iron into the coolant, kg/s	Iron, kg	«Eatable» thickness, mm
EP-823	2.6E-10	1.00E-2	8.2E-3
T91	2.75E-10	3.70E-02	3.0E-02
316L	2.60E-10	1.20E-2	9.8E-3

At low speed of coolant (Table 2), the “eatable” tube thickness is much smaller, while the thickness of the oxide film is much larger. This is quite understandable, since the main amount of iron comes out already after the oxide film reaches the saturation value and according to the ratio (3)

$$J_{Fe}^{\beta} \sim 1/\delta_c \quad (3)$$

At a temperature of 500 °C (Table 3), the iron yield is almost three orders of magnitude lower than at 650 °C and the thinning of steel is only 8–10 microns after 10,000 h.

It should be noted that the numbers are approximate since they do not take into account, for example, the yield of chromium and the change in material properties in time. It is possible that structural changes in steel occurring over time due to the release of iron also affect the rate of formation and structure of the film, which in turn affects the rate of release of iron. But for the implementation of these processes now, there is not enough experimental data.

Conclusion

The release of iron and the formation of magnetite is managed by the specificity of self-consistent physicochemical processes in the oxide film and at the interface.

Model calculations of the influence of the uncertainty of oxygen activity on the rate and integral yield of iron have been carried out, which, under given conditions of the oxygen regime, after interaction with oxygen, causes the formation of magnetite.

The scatter of the calculated values of iron yield is essentially determined by the accuracy of measurements of oxygen activity and varies from several tens of percent to values close to one hundred percent in case of unsatisfactory calibration of the oxygen sensor. The calculated values of the release of iron from the coolant have the same errors as the thickness of the oxide at a given oxygen regime and temperature.

It is numerically demonstrated that temperature significantly affects the yield of iron and can make significant influence on the changes in the structure of steel due to the high intensity of the process.

It is numerically demonstrated that in the saturation mode, there is a model-independent characteristic, which is determined by the parabolic constant and the thickness of the oxide film typical to this steel.

A simple model relationship is proposed for assessing the power of the mass transfer apparatus.

References

1. Alekseev VV, Kozlov FA, Kumaev VY, others (2010) Modeling the processes of mass transfer and corrosion of steels in nuclear power plants with lead coolant: Obninsk, preprint FEI-3179
2. Kumaev VY, Lebezov AA, Pyshin IV, Alekseev VV (2002) MASKA-LM is a code for calculating the mass transfer of impurities in liquid metal circuits. Heat and mass transfer and properties of liquid metals: materials conf. Obninsk, T. 1. S., pp 295–298
3. Kumaev V, Lebezov A, Alexeev V (2005) Development and application of MASKA-LM code for calculation of thermal hydraulics and mass transfer of lead cooled fast reactors. In: The 11th international topical meeting on nuclear reactor thermal-hydraulics (NURETH-11), Paper: 191 (Avignon, France, October 2–6, 2005) pp 191/1–191/6
4. Alekseev VV, Orlova EA, Kozlov FA, others (2010) Modeling the processes of mass transfer and corrosion of steels in nuclear power plants with lead coolant: preprint SSC RF-IPPE No. 3128. Obninsk, 2008; Computational and theoretical analysis of the process of steel oxidation in a lead coolant, Questions of Atomic Science and Technology, Series: Nuclear constants, issue 1–2, p 56, Martinelli L. et al. Corros Sci 50:2537–2548
5. Hwang IS, Lim J (2010) The 25th KAIF/KNS annual conference, World Trade Center, COEX, Seoul, Korea
6. Fazio C et al (2001) J Nuclear Mater 296:243
7. Aiello A et al (2004) J Nuclear Mater 335:169
8. Lim J et al (2008) 10th Information exchange meeting on actinide and fission product partitioning and transmutation. Mito, Japan
9. Zhang J et al (2005) J Nuclear Mater 336:1
10. Barbier F et al (2001) Corrosion behavior of steels in flowing lead–bismuth. J Nuclear Mater 296:231
11. Balbaud-Celier et al F (2004) High-temperature corrosion of steels in liquid Pb-Be alloy. Mater Sci Forum 461–464:1091
12. Handbook on Lead-bismuth Eutectic Alloy and Lead Properties, Materials Compatibility, Thermal-hydraulics and Technologies, 2015 Edition

Part XXIV
Deformation Induced Microstructural
Modification

Analysis of Al 6061 and Mild Steel Joints from Rotary Friction Welding



Nikhil Gotawala and Amber Shrivastava

Abstract This work focuses on the microstructure evolution upon rotary friction welding of Al 6061 to mild steel and resulting joint strength. Material deforms plastically during rotary friction welding; however, temperatures are low enough to prevent melting, which limits intermetallic compound formation. Displacement-controlled rotary friction welding of circular workpieces is performed with combinations of three friction times (48, 24 and 16 s) and two rotation speeds (1200 and 1400 rpm). Significant grain refinement is observed at the centre on Al 6061 side, which indicates dynamic recrystallization. However, only recovery is observed at the mild steel side, which is attributed to low temperatures. The maximum joint strength of 136 MPa is achieved. The fractured surfaces from tensile tests reveal sticking of Al 6061 on mild steel at the centre region. The fractured surfaces suggest ductile fracture in the centre region and brittle fracture close to the periphery.

Keywords Rotary friction welding · Dissimilar material joining · Dynamic recrystallization

Introduction

Many industries like aerospace, automotive, marine, etc. desire to reduce the fuel consumption, for achieving lower operational cost and environmental impact. Lightweighting of structures without compromising strength is a potential way forward. Al alloys are light in weight with high specific strength. However, complete replacement of steel components by Al alloys is difficult due to higher price of Al alloys. This makes it desirable to join Al alloys and steel. Fusion welding of Al alloys and steels leads to large amount of brittle intermetallic compounds (IMC) in the joint, which deteriorate the joint's mechanical performance [1, 2]. The solid-state joining techniques, such as friction stir welding can be used for joining dissimilar

N. Gotawala · A. Shrivastava (✉)
Department of Mechanical Engineering, Indian Institute of Technology Bombay, Mumbai
400076, India
e-mail: ashrivastava.me@iitb.ac.in

materials [3]. Many researchers have successfully joined aluminium alloys and steel using friction stir welding [4, 5]. However, friction stir welding is limited to sheet- or plate-type components. Rotary friction welding (RFW) is a solid-state joining process, which can be used for joining circular components [6]. During RFW, one of the workpiece rotates about its axis and plunges into the stationary workpiece. The friction at the interface of the two workpieces leads to heat generation and the temperature rises, material deforms plastically and workpieces are forged together to create the joint. For dissimilar materials, the diffusion between two materials at the interface leads to the formation of IMC [7]. Further in the vicinity of the interface, dynamic recrystallization due to high temperature plastic deformation results in the grain refinement [8].

Over the last decade, many researchers have tried RFW with different combinations of materials. Liag et al. RFWed Al 1060 and Mg AZ 31 alloys at different friction pressures. Al_3Mg_2 and $\text{Al}_{12}\text{Mg}_{17}$ IMCs were observed at the interface and the joint tensile strength improved with increase in friction pressure up to a certain value [9]. Guo et al. also found Al_3Mg_2 and $\text{Al}_{12}\text{Mg}_{17}$ IMCs in RFWed joints of 7A04 Al alloy and Mg AZ 31 alloy [10]. The IMC thickness decreased significantly with increase in friction pressure. Ma et al. successfully joined 1045 carbon steel and 304 stainless steel with RFW, and analysed formation of carbide layer (CrC and Cr_{23}C_6) at the interface due to diffusion [11]. Similarly, Celik et al. performed RFW of AISI 4140 and AISI 1050 steels. The joint tensile strength was comparable to the parent materials and hardness improved near interface due to grain refinement [12]. Satyanarayana et al. optimized the tensile strength of RFWed austenitic and ferritic steel with respect to process parameters [13]. Li et al. studied effect of tool rotation speed on RFW Ti alloy and stainless steel joints [14]. The joint strength increased with increase in tool rotational speed up to a critical value and decreased thereafter. FeTi and Fe_2Ti IMCs were reported at the interface of Ti alloy and stainless steel [14]. Dev et al. also observed comparable joint strength of RFWed Ti and SS 304 joints as compared against the Ti. However ductility was extremely poor upon bend test due to presence of IMCs at the interface. Post-weld heat treatment led to improvement in the ductility of the RFWed joints [15].

Some researchers have also attempted to weld aluminium alloys with steels using RFW. Sundaresan et al. performed RFW of aluminium alloy and austenitic stainless steel [16]. Fe_2Al_5 and FeAl_3 IMCs were reported at the joint interface [16]. Taban et al. reported Fe_2Al_5 and FeAl IMCs in RFWed joints of Al 6061 and AISI 1081 steel [17]. Fukumoto et al. noticed Fe_2Al_5 , FeAl_3 and FeAl IMCs at the interface of Al 1050 and austenitic stainless steel joints from RFW [18]. The elongation of aluminium grains was observed in the vicinity of weld interface due to deformation during process. The flying surface of stainless steel also underwent austenite to martensite phase transformation [18]. Fukumoto et al. observed that the joint tensile strength is maximum for a certain friction time and decreases on either increasing or decreasing the friction time, for RFWed Al 5052 and SS 304 joints [19]. Fukumoto et al. also found an amorphous layer at the interface of Al 5052 and SS 304 RFWed joints [20]. For majority of the existing work, RFW is performed in the pressure control mode. In the present work, RFW of Al 6061 and mild steel is attempted

with displacement control. The RFWed joints of Al 6061 and mild steel are prepared with different rotation speeds and friction times. The RFWed joints are subjected to tensile test and microstructure at the joint interface is analysed. The fracture surfaces of tensile specimens are also studied to determine the fracture mechanism of the weld.

Experimental Work

RFW of Al 6061 and mild steel were performed on three-axis CNC mill (LMW LV55). The length and diameter of the mild steel and Al 6061 rods are 100 mm and 12 mm, respectively. Figure 1 shows the schematic diagram of RFW of Al 6061 and mild steel. During RFW, mild steel rod was rotating and Al 6061 rod was held stationary. A dwell time of 5 s was provided to remove initial oxide layer and improve the heat generation. Next, the rotating mild steel rod was plunged to a depth of 8 mm into the Al 6061 rod (Friction action). The RFWed joints were created with three feed rates during 'Friction action': 10 mm/min, 20 mm/min, and 30 mm/min, which corresponded to friction times of 48 s, 24 s, and 16 s, respectively (for plunge to a depth of 8 mm). After 'Friction action', mild steel rod stopped rotating motion and plunged further by 10 mm into the Al 6061 rod at a feed rate of 100 mm/min (Forging action). Finally, the joint is allowed to cool. The Al 6061-mild steel RFW joints were performed at two rotation speeds: 1200 and 1400 rpm.

To determine the joint strength, tensile test was performed as per ASTM E8/E8M standard on Instron tensile testing machine. The gauge length and diameter of the tensile test specimen were 45 mm and 6 mm, respectively. Welding specimen cross section cut using wire EDM to see microstructure at interface of both material. The joints were cross-sectioned and polished. These samples were electro-polished used as a final polishing. Electro polishing performed on Buehler Electromet 4 with electrolyte (700 ml ethanol + 200 ml perchloric acid + 100 ml butanol) at 15 V and

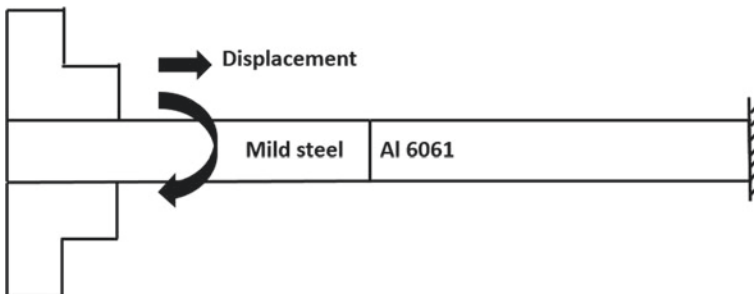


Fig. 1 Schematic of rotary friction welding of Al 6061 and mild steel

–10 °C for 20 s. Electron back scattered diffraction (EBSD) was done to analyse the microstructure at the joint interface. Gemini SEM 300 with EBSD detector was used for EBSD scans. EBSD scan was performed over $250\ \mu\text{m} \times 250\ \mu\text{m}$ with step size of $0.5\ \mu\text{m}$. Aztec HKL was used to analyse the EBSD scans.

Results and Discussion

Microstructure Evolution at Al 6061 and Mild Steel Interface

Figures 2 and 3 show the EBSD results at the interface of Al 6061 and mild steel RFWed joint prepared with rotation speed of 1200 rpm and friction time of (a) 48 s (b) 24 s (c) 16 s. For this analysis, a misorientation angle greater than 10° is considered as for identifying grains. Al 6061 and mild steel sides are shown in red and blue colours, respectively. A variation in grain size from interface towards Al 6061 side can be noticed. This is attributed to the dynamic recrystallization due to high temperature plastic deformation et al. 6061 side during RFW. In a similar observation, Winiczenko et al. also noticed dynamic recrystallization of Al 5454 alloy upon RFW with a tungsten heavy alloy [21]. From Figs. 2 and 3, finer grains can be noticed near the interface at the Al 6061 side. From the samples welded at 1200 rpm rotation speed and friction time of 48 s, 24 s, and 16 s, the average size of Al 6061 alloy grains are $3.3\ \mu\text{m}$, $3.4\ \mu\text{m}$, and $5.2\ \mu\text{m}$, respectively. Similarly, from the samples welded at 1400 rpm rotation speed and friction time of 48 s, 24 s, and 16 s, the average size of Al 6061 alloy grains are $6.1\ \mu\text{m}$, $5.3\ \mu\text{m}$, and $4.4\ \mu\text{m}$, respectively.

During RFW, higher rotation speed and friction times lead to higher temperatures [9, 14], which encourage grain growth after recrystallization. Also, higher rotation speed and friction times lead to more accumulation of strain, which promotes grain refinement [22]. The interplay of these effects is well reflected by the average grain size of Al 6061 (near joint interface) across the RFWed Al 6061-mild steel joints. At higher rotation speed of 1400 rpm, the average Al 6061 grain size increases with increase in friction time, and this suggests that the grain growth owing to higher temperatures is significant. At the lower rotation speed of 1200 rpm, the grain size reduces as the friction time increases from 16 to 24 s. This suggests that the accumulation for strain at higher friction time of 24 s is more pronounced than the additional grain growth that would be achieved due to increased temperature (compared to friction time of 16 s at 1200 rpm). However further increase in friction time to 48 s from 24 s at 1200 rpm affects the average Al 6061 grain size minimally. This suggests that the increased accumulation of strain at higher friction time of 48 s is countered by the additional grain growth owing to higher temperature (compared to friction time of 24 s at 1200 rpm).

At the steel side of the joint interface, a non-indexed region is observed in EBSD scans of all the RFWed joint samples. This is expected to be a high dislocation density

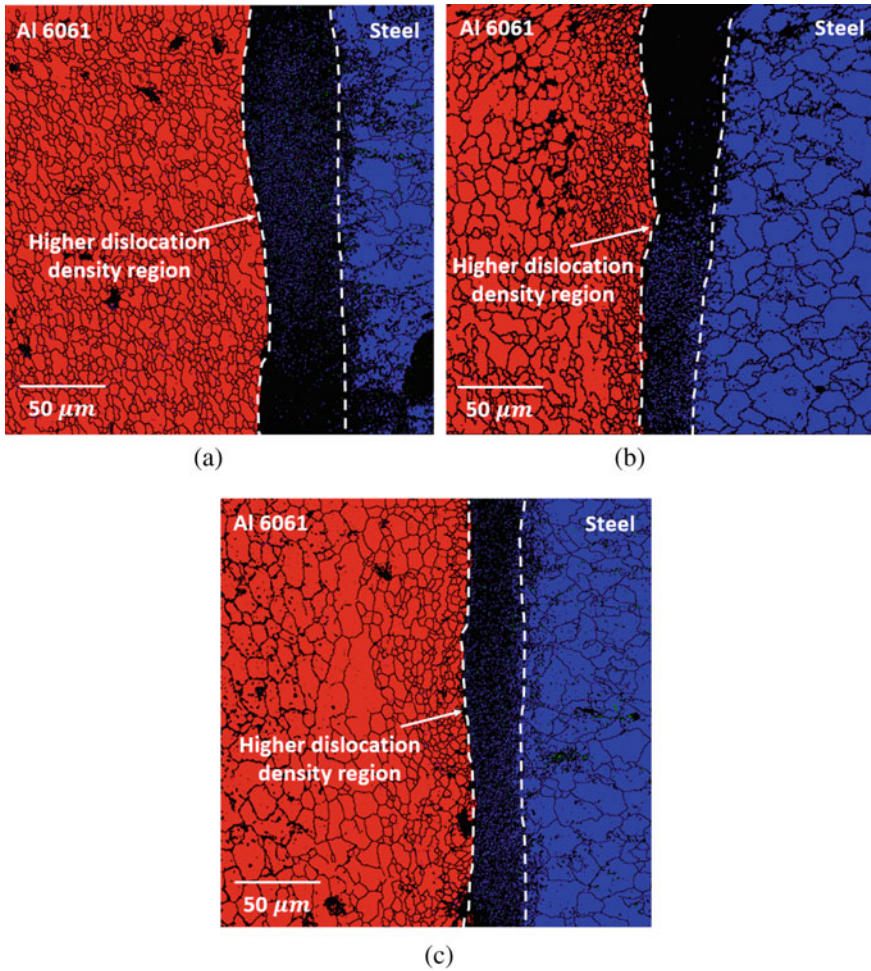


Fig. 2 EBSD et al. 6061 and mild steel interface of RFWed joint performed at 1200 rpm and friction time of **a** 48 s **b** 24 s and **c** 16 s. (Color figure online)

region on the steel side of the joint interface. The non-indexed region suggests that there was no dynamic recrystallization on the steel side. This is suspected due to process temperatures lower than the dynamic recrystallization temperature for steel. For the joints RFWed at 1200 rpm rotation speed and friction times of 48 s, 24 s, and 16 s, the average width of the non-indexed regions are 53.8 μm , 34.6 μm , and 28.9 μm , respectively. Similarly, for the joints RFWed at 1400 rpm rotation speed and friction times of 48 s, 24 s, and 16 s, the average width of the non-indexed regions are 18.3 μm , 9.9 μm , and 5.6 μm , respectively. The width of the non-indexed region reduced with increase in rotation speed. This is anticipated due to more recovery at

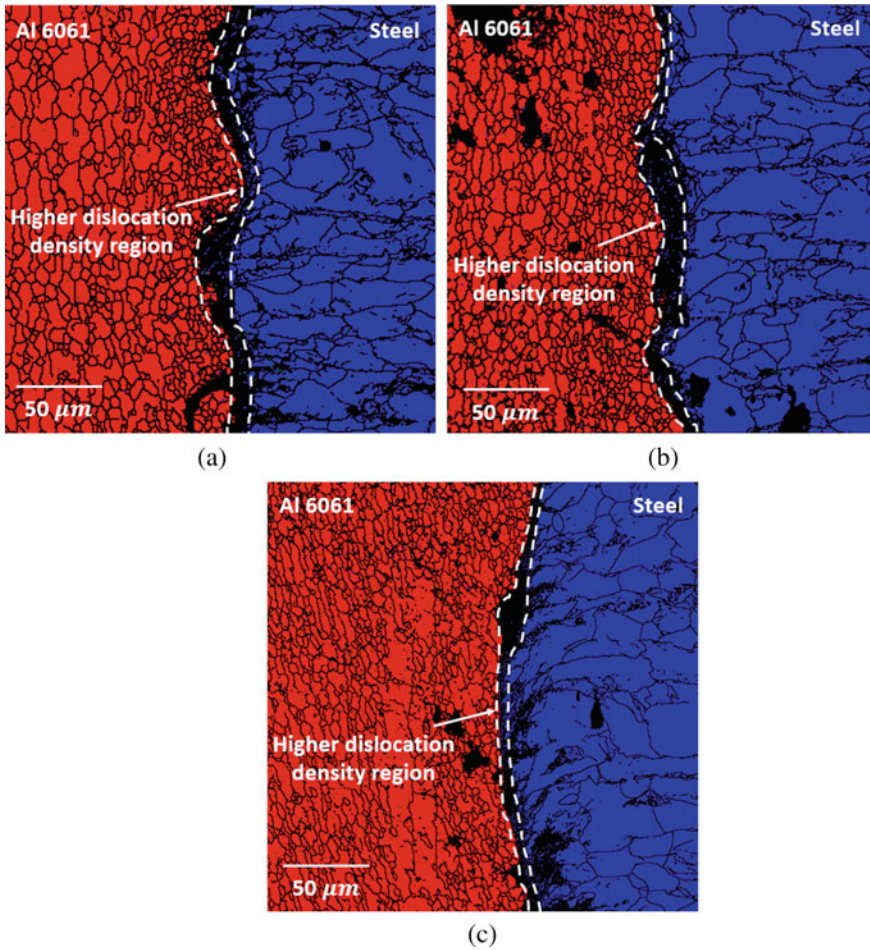


Fig. 3 EBSD et al. 6061 and mild steel interface of RFWed joint performed at 1400 rpm and friction time of **a** 48 s **b** 24 s and **c** 16 s. (Color figure online)

higher temperature with increase in rotation speed. There is also reduction in non-indexed region with decrease in friction time. This is due to reduction in accumulation of strain with decrease in friction time.

Tensile Strength and Fracture Surface Analysis

Figure 4 shows tensile strength of RFWed joints prepared with different rotation speeds and friction times. The maximum tensile strength of observed all the joint samples is 136 MPa. As figure shows the tensile strength of weld is higher for the

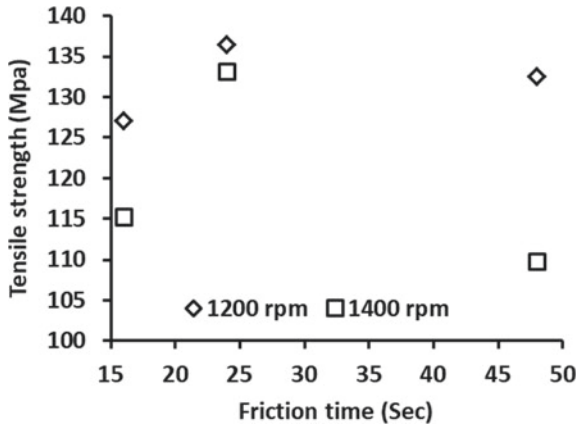


Fig. 4 Tensile strength of RFWed joints prepared with different rotation speeds and friction times

samples joined at 1200 rpm as compared to the samples joined at 1400 rpm, for all the friction times. This may be due to smaller amount of brittle IMC formation at lower temperatures, owing to lower rotation speed. With respect to friction time, the maximum tensile strength is recorded for the samples joined with 24 s, for both the rotation speeds. This suggests that diffusion at Al6061-steel interface is not sufficient at lower friction time (16 s), while excessive diffusion at higher friction (48 s) would have led to more brittle IMCs.

Fracture surfaces from tensile tests are analysed to study the nature of failure. Figure 5a–c shows the fractured Al6061 surfaces from the joints prepared at 1200 rpm with friction time of 48 s, 24 s, and 16 s, respectively. Similarly, Fig. 6(a–c) shows the fractured Al6061 surfaces from the joints prepared at 1400 rpm with friction time of 48 s, 24 s, and 16 s, respectively. Circular marks can be noticed at the fractured surfaces of all the samples. Circular marks appear to follow the material flow during the process and rough surface indicates towards possible brittle failure. From Figs. 5b

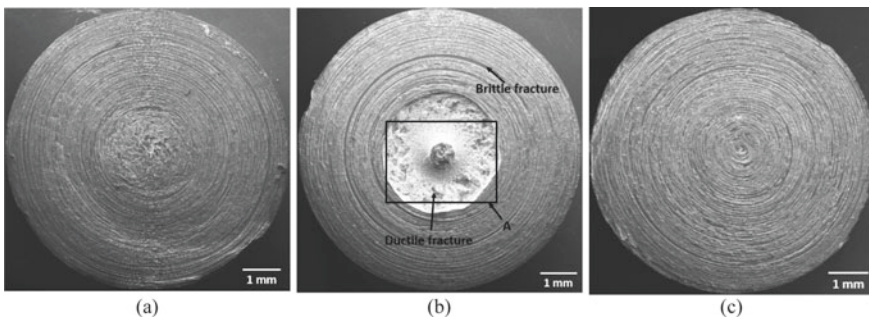


Fig. 5 Fractured Al6061 surface from the joint prepared at 1200 rpm with friction time of **a** 48 s **b** 24 s and **c** 16 s

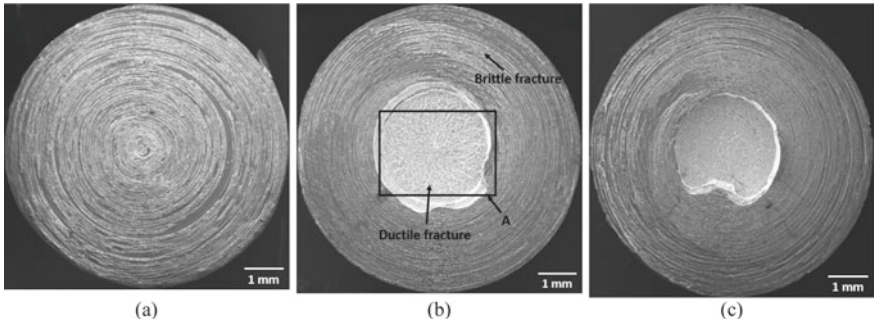


Fig. 6 Fractured Al6061 surface from the joint prepared at 1400 with friction time of **a** 48 s **b** 24 s and **c** 16 s

and **6b**, it can be noticed that the chunk of aluminium alloy broke away from the centre region (location A). Figures **7** and **8** shows the locations A of Fig. **5a** and **6a** at higher magnification. The presence of dimple features at locations A suggests

Fig. 7 Fractured Al6061 surface at location A of the joint prepared with 1200 and 24 s friction time

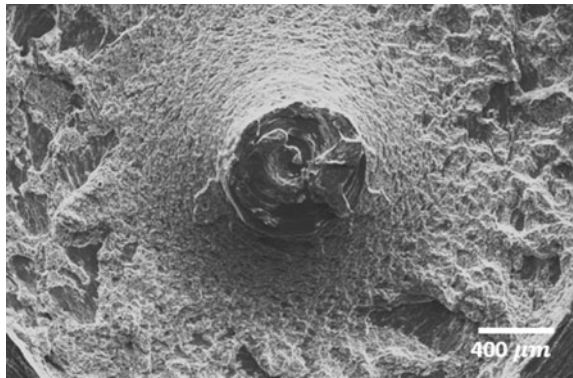
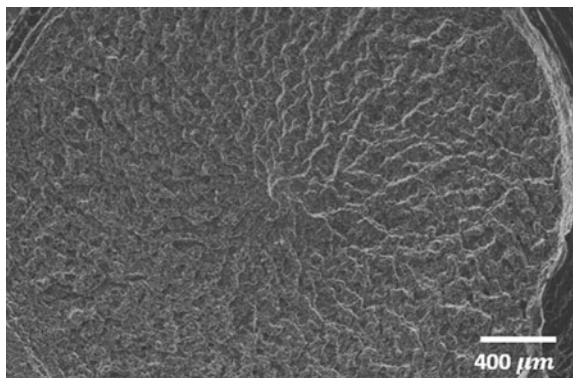


Fig. 8 Fractured Al6061 surface at location A of the joint prepared with 1400 and 24 s friction time



the ductile nature of failure at the centre and nearby regions of the samples joined with 24 s friction time. This implies that the ductile fracture occurred at the centre and brittle fracture occurred at the peripheral locations, for the sample with the maximum tensile strength in this study. This observation is consistent with variation in IMC thickness observed by Fukumoto et al. along the radius for RFWed samples [20]: minimum IMCs at the centre and along the radial direction increase towards periphery. This can be attributed to lower heat generation in the centre region due to slower relative motion between two materials.

Conclusions

The present work is focused on RFW of Al 6061 and steel with the displacement control mode. The RFW was performed with the combinations of two rotation speeds (1200 and 1400 rpm) and three friction times (48, 24 and 16 s). Microstructural analysis by EBSD at the Al6061-steel interface of the joints suggests dynamic recrystallization et al. 6061 side and grain size of Al 6061 in the vicinity of the interface depends on the RFW process parameters. However, recrystallization is not observed at the steel side of the Al6061-steel interface. Instead, a non-indexed region is noticed at the steel side next to the joint interface. This is expected due to accumulation of strains upon plastic deformation during RFW. The size of non-indexed region reduced with increase in rotation speed, due to improved recovery at higher temperatures at higher rotation speed. The maximum tensile strength of 136 MPa is recorded for the joint prepared at 1200 rpm rotation speed and 24 s friction time. The inspection of fracture surface revealed that ductile fracture occurred at the centre and brittle fracture occurred at the peripheral locations, for the sample with the maximum tensile strength in this study. This observation is consistent with the variation in IMC thickness along the radius for RFWed samples observed in previous study.

Acknowledgements The authors gratefully acknowledge the partial support of this work by the Science & Engineering Research Board, Department of Science & Technology, Government of India (File No. ECR/2017/000727/ES), Department of Mechanical Engineering, Microstructural Mechanics and Microforming Lab and Machine Tools Lab at Indian Institute of Technology.

References

1. Mukherjee S, Chakraborty S, Galun R, Estrin Y, Manna I (2010) Transport phenomena in conduction mode laser beam welding of Fe–Al dissimilar couple with Ta diffusion barrier. *Int J Heat Mass Transf* 53(23–24):5274–5282
2. Sierra G, Peyre P, Deschaux-Beaume F, Stuart D, Fras G (2007) Steel to aluminium key-hole laser welding. *Mater Sci Eng, A* 447(1–2):197–208
3. Murr LE (2010) A review of FSW research on dissimilar metal and alloy systems. *J Mater Eng Perform* 19(8):1071–1089

4. Movahedi M, Kokabi AH, Reihani SS, Najafi H (2012) Effect of tool travel and rotation speeds on weld zone defects and joint strength of aluminium steel lap joints made by friction stir welding. *Sci Technol Weld Joining* 17(2):162–167
5. Chen TP, Lin WB (2010) Optimal FSW process parameters for interface and welded zone toughness of dissimilar aluminium–steel joint. *Sci Technol Weld Joining* 15(4):279–285
6. Li W, Vairis A, Preuss M, Ma T (2016) Linear and rotary friction welding review. *Int Mater Rev* 61(2):71–100
7. Lee WB, Bang KS, Jung SB (2005) Effects of intermetallic compound on the electrical and mechanical properties of friction welded Cu/Al bimetallic joints during annealing. *J Alloy Compd* 390(1–2):212–219
8. Liu FC, Nelson TW (2018) Grain structure evolution, grain boundary sliding and material flow resistance in friction welding of Alloy 718. *Mater Sci Eng, A* 710:280–288
9. Liang Z, Qin G, Wang L, Meng X, Li F (2015) Microstructural characterization and mechanical properties of dissimilar friction welding of 1060 aluminum to AZ31B magnesium alloy. *Mater Sci Eng, A* 645:170–180
10. Guo W, You G, Yuan G, Zhang X (2017) Microstructure and mechanical properties of dissimilar inertia friction welding of 7A04 aluminum alloy to AZ31 magnesium alloy. *J Alloy Compd* 695:3267–3277
11. Ma H, Qin G, Geng P, Li F, Fu B, Meng X (2015) Microstructure characterization and properties of carbon steel to stainless steel dissimilar metal joint made by friction welding. *Mater Des* 86:587–597
12. Celik S, Ersozlu I (2009) Investigation of the mechanical properties and microstructure of friction welded joints between AISI 4140 and AISI 1050 steels. *Mater Des* 30(4):970–976
13. Satyanarayana VV, Reddy GM, Mohandas T (2005) Dissimilar metal friction welding of austenitic–ferritic stainless steels. *J Mater Process Technol* 160(2):128–137
14. Li X, Li J, Liao Z, Jin F, Zhang F, Xiong J (2016) Microstructure evolution and mechanical properties of rotary friction welded TC4/SUS321 joints at various rotation speeds. *Mater Des* 99:26–36
15. Dey HC, Ashfaq M, Bhaduri AK, Rao KP (2009) Joining of titanium to 304L stainless steel by friction welding. *J Mater Process Technol* 209(18–19):5862–5870
16. Sundaresan S, Murti KGK (1993) Friction welding of aluminium to austenitic stainless steel. *Int J Joining Mater* 5:66–66
17. Taban E, Gould JE, Lippold JC (2010) Dissimilar friction welding of 6061-T6 aluminum and AISI 1018 steel: properties and microstructural characterization. *Mater Des* (1980–2015), 31(5):2305–2311
18. Fukumoto S, Tsubakino H, Okita K, Aritoshi M, Tomita T (1998) Microstructure of friction weld interface of 1050 aluminium to austenitic stainless steel. *Mater Sci Technol* 14(4):333–338
19. Fukumoto S, Tsubakino H, Okita K, Aritoshi M, Tomita T (1999) Friction welding process of 5052 aluminium alloy to 304 stainless steel. *Mater Sci Technol* 15(9):1080–1086
20. Fukumoto S, Tsubakino H, Okita K, Aritoshi M, Tomita T (2000) Amorphization by friction welding between 5052 aluminum alloy and 304 stainless steel. *Scripta Materialia* 42(8)
21. Winiczenko R, Goroch O, Krzyńska A, Kaczorowski M (2017) Friction welding of tungsten heavy alloy with aluminium alloy. *J Mater Process Technol* 246:42–55
22. Midling OT, Grong Ø (1994) A process model for friction welding of Al–Mg–Si alloys and Al–SiC metal matrix composites—I. Haz temperature and strain rate distribution. *Acta Metallurgica et Materialia* 42(5):1595–1609

Investigation of Mechanical Properties and Microstructural Valuation Under Different Heat Treatment Parameters of AA6060 Alloy Used in Crash Boxes



Murat Konar, Salim Aslanlar, Erdinç Ilhan, Cagatay Bölükbaşı, Melih Kekik, Mehmet Buğra Güner, and Görkem Özcelik

Abstract The crash boxes used in cars are the connection elements that absorb the impact energy that occurs in the event of an accident and provide the energy released by the accident to the car at the minimum level (Sharifi et al. in *Thin-Walled Structures* 89:42–53, 2015). In the study, the effects of heat treatments on the mechanical properties of the crash boxes were investigated in order to reach the optimum levels of AA6060 alloy box profiles produced by extrusion method. F, T4, T5, T6, and T7 heat treatments were applied to crash boxes. As a result of compression loads, force–displacement graphs were obtained and total absorbed energies were calculated from these graphs. Samples that were able to absorb the highest energy in samples produced for use in crash boxes were obtained in T6 heat treatment.

Keywords Aluminum · Crash box · Energy absorption

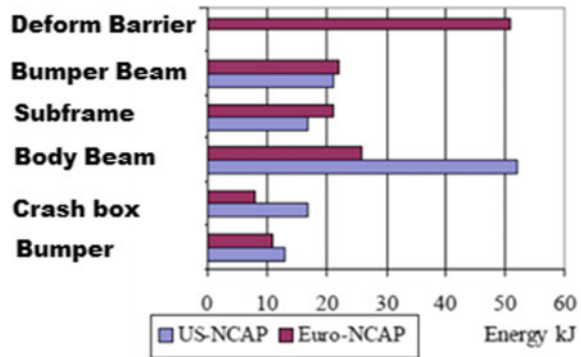
Introduction

Crash boxes are one of the fastening elements that absorb the impact first in the event of a front or rear impact accident, and ensure that the energy is not transmitted to the interior of the automobile at the lowest possible level. US-NCAP and EURO-NCAP (New Car Assessment Program), which are accepted as important references by automobile manufacturers and have international validity with their data, determined the distribution of the energy generated as a result of a crash test according to the parts on the vehicle. As seen in Fig. 1, crash boxes absorb a significant portion of this energy [1].

M. Konar (✉) · S. Aslanlar · E. Ilhan · C. Bölükbaşı · M. Kekik
Sakarya University of Applied Sciences, Sakarya, Turkey
e-mail: murat.konar@asastr.com

M. B. Güner · G. Özcelik
ASAŞ Aluminium San. Ve Tic. A. Ş., Sakarya, Turkey

Fig. 1 Energy distribution on different parts of automobiles during crash. (Color figure online)



Various studies have been carried out from past to present for increasing the energy absorption capacity of crash boxes [2–9]. The crash boxes used in the studies generally have circular, square, and rectangular cross-sections. Aktay et al. [10] filled the circular cross-section crash boxes with honeycomb structure and investigated their energy absorption capacity under applied loads. Isaac et al. [11] studied the effect on the energy absorption capacity of circular cross-section crash boxes against axial and different angle deformation loads. Langseth and Hopperstad [12] investigated the performance of square cross-sections extruded at different tempering temperatures and with different wall thicknesses under static and dynamic loads. Nagel and Thanbiratman [13] examined the changes in energy absorption capacity under dynamic loads at different speeds by changing the wall thickness and cone angles of rectangular crash boxes. In some studies [14–17], energy absorption capacities of crash boxes with different geometries were investigated by using different parameters (wall thickness, cone angle etc.). Various changes have been made to improve the performance of the crash boxes. One of them is to cut holes on crash boxes. It is known that the initial deformation force required for the initiation of folding in crash boxes is reduced by the opened cavities and accordingly the crushing force efficiency is increased [18, 19].

Crash boxes have an important place on the automobile in terms of the task they have undertaken. Various R & D studies have been carried out to increase the energy absorption capacity of crash boxes from past to present. In these studies, variable

Fig. 2 Empty and foam filled aluminum crash boxes. (Color figure online)



parameters such as wall thickness, geometric properties and material used of crash boxes were used. Metallic foam materials are placed in crash boxes as shown in Fig. 2, due to their high energy absorption capacity and lightness in recent years [10].

Materials and Methods

The 6XXX series contains magnesium (Mg) and silicon (Si) as the main alloying elements, but like every alloy, there are different elements in trace amounts other than magnesium and silicon. Chemical composition of AA6060 alloy is given in Table 1 [4].

Thanks to the precipitate phases (Mg_2Si) formed by the magnesium and silicon elements in AA6060; it turns into an alloy that can be hardened by precipitation hardening and as a result, good mechanical properties are revealed. Mechanical properties for AA6060 alloy are given in the related literature as in Table 2.

The square prisms we obtained from extrusion, with dimensions of $80 \times 80 \times 300$ mm, consisting of EN AW 6060 material whose chemical composition is given in Table 2, have a wall thickness of 2 mm. The samples were subjected to T4, T5, T6, T7 heat treatments in the temperature-controlled Nabertherm furnace. A total of 16 samples, four samples for each heat treatment, were heat treated. Comparisons with condition F will be made to interpret the effects of heat treatment. The experiment plan is given in Table 3.

Samples for T4 heat treatment; They were solutionized at $540^\circ C$ for half an hour, then quenched and left at room temperature for 1 week to allow natural aging.

Samples for T5 heat treatment; They were kept at $490^\circ C$ for 15 min and then quenched and kept at $180^\circ C$ for 6 h for artificial aging.

Table 1 Chemical composition limits of EN AW 6060

	Si	Fe	Cu	Mn	Mg	Cr	Al
EN 573-3	0.3-0.6	0.1-0.3	0.10	0.10	0.35-0.6	0.05	Rem

Table 2 Mechanical properties of EN AW 6060

Temper	Yield stress (MPa) min-max	Tensile stress (MPa) min-max	Elongation $A_{50\%}$ min-max	Brinell hardness min-max
F	50	100	26	25
T4	90	160	21	50
T5	110-175	150-215	12	60
T6	170-210	205-245	12	75
T7	240	260	9	80

Table 3 Heat treatment parameters on experimental study

Sample	Heat treatment	Heat treatment condition
N1	F	As extruded
N2	F	As extruded
N3	F	As extruded
N4	F	As extruded
N5	T4	Solutionizing on 540 °C for 30 min + quenching + natural aging
N6	T4	Solutionizing on 540 °C for 30 min + quenching + natural aging
N7	T4	Solutionizing on 540 °C for 30 min + quenching + natural aging
N8	T4	Solutionizing on 540 °C for 30 min + quenching + natural aging
N9	T5	Solutionizing on 490 °C for 15 min + quenching + artificial aging at 185 °C for 5.30 h
N10	T5	Solutionizing on 490 °C for 15 min + quenching + artificial aging at 185 °C for 5.30 h
N11	T5	Solutionizing on 490 °C for 15 min + quenching + artificial aging at 185 °C for 5.30 h
N12	T5	Solutionizing on 490 °C for 15 min + quenching + artificial aging at 185 °C for 5.30 h
N13	T6	Solutionizing on 540 °C for 30 min + quenching + artificial aging at 185 °C for 5.30 h
N14	T6	Solutionizing on 540 °C for 30 min + quenching + artificial aging at 185 °C for 5.30 h
N15	T6	Solutionizing on 540 °C for 30 min + quenching + artificial aging at 185 °C for 5.30 h
N16	T6	Solutionizing on 540 °C for 30 min + quenching + artificial aging at 185 °C for 5.30 h
N17	T7	Solutionizing on 540 °C for 30 min + quenching + artificial aging at 200 °C for 4 h
N18	T7	Solutionizing on 540 °C for 30 min + quenching + artificial aging at 200 °C for 4 h
N19	T7	Solutionizing on 540 °C for 30 min + quenching + artificial aging at 200 °C for 4 h
N20	T7	Solutionizing on 540 °C for 30 min + quenching + artificial aging at 200 °C for 4 h

The process applied to samples subjected to T6 heat treatment; After keeping them at 540 °C for half an hour, quenching was carried out and then it was held at 180 °C for 6 h.

In T7 heat treatment; They were solutionized at 540 °C for half an hour, then quenching was carried out and it was kept at 200 °C for 4 h.

On Zwick/Roell Allround Series Z250 universal tensile testing device, 15 pieces 300 mm length specimens were subjected to compression loads along 200 mm. Tests were carried out according to the standards of international automotive OEMs and

Fig. 3 Compression test of box profiles. (Color figure online)



tested under a maximum load of 250 kN. Then the results of the load/displacement data were exported (Fig. 3).

From the samples subjected to F, T4, T5, T6, T7 heat treatments, one profile is separated for hardness test. The diameter of the ball in the Brinell hardness device is 2.5 mm. Then, the hardness of the samples was measured from three different parts and reported.

Results and Discussion

Compression test chart for Condition F is given in Fig. 4. Condition F is the same as it is produced, so its mechanical properties are expected to be low. When the average of the total energies absorbed is taken, the value of 5794.265 J was reached; this

Fig. 4 Compression test plot for F conditioned profile. (Color figure online)

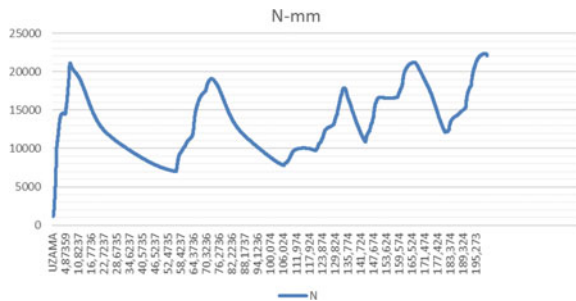
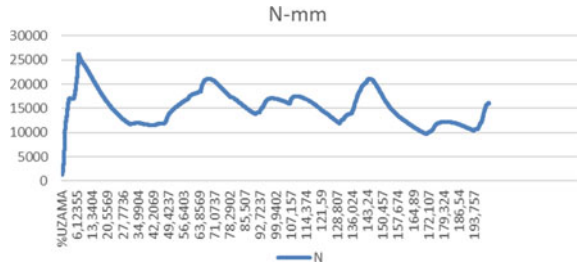


Fig. 5 Compression test plot for T4 conditioned profile. (Color figure online)



value is the lowest among the values obtained in other samples. When the hardness values were averaged, higher values were obtained than the data in the literature. Brinell hardness value is 35.3 HBW. Since the important detail in Crash Boxes is the absorbed energy, it is not appropriate to use the F condition in crash boxes.

The compression graph obtained as a result of T4 heat treatment is given in Fig. 5. After quenching is done and then natural aging is performed. The longer the natural aging time, the better the solutions will disperse. In this study, the natural aging period is 1 week and gave sufficient results for this period and hardness; the hardness results are on average 49.7 HBW. Hardness value of 45 HBW was given for brinell T4 heat treatment in the literature. The total absorbed energy increased to 6667.207 J. It is approximately 1000 J higher than the F condition, but these results are not sufficient for crash boxes when compared with the data from other samples.

The compression graph obtained for the T5 heat treatment is given in Fig. 6. Solutionizing was done at 490° C for 15 min + quenching + 185 °C for 5.30 h. As a result of the T5 heat treatment, the hardness value reached approximately 48 HBW. The hardness value is given as 50 HBW in the literature. As a result of the compression test, the total energy absorbed increased to 8018,547 J. This value is the highest value after T6 heat treatment. It is a desirable feature since its hardness is not very high, does not show brittle behavior, and there is no breakage. For this reason, the results obtained gave much better results than other treatments except T6 condition. Nevertheless, the more energy absorbed, the more the energy released as a result of the accident is absorbed, and both vehicle and passenger safety are ensured. Therefore, T5 is not the preferred heat treatment.

Fig. 6 Compression test plot for T5 conditioned profile. (Color figure online)

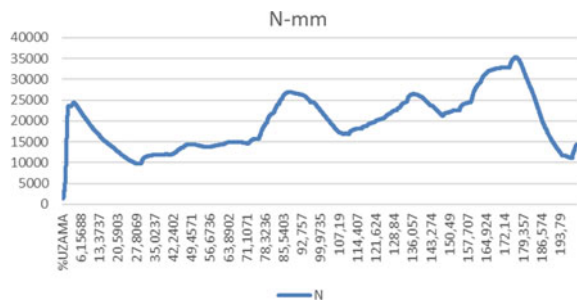
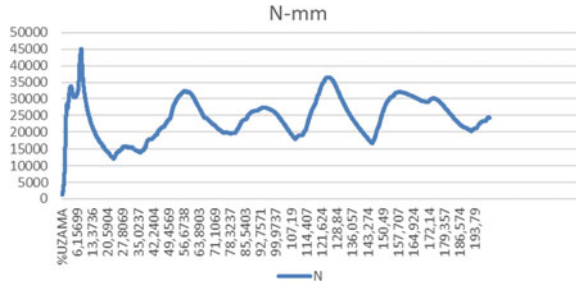


Fig. 7 Compression test plot for T6 conditioned profile. (Color figure online)



For the T6 heat treatment, half an hour of solutionizing at 540 °C + quenching + 185 °C for 5.30 h of artificial aging was carried out. The compression plot obtained for the compression test after T6 heat treatment is given in Fig. 7. As a result of the compression test, the arithmetic average of the energies that three separate samples can absorb is 9656,138 J. This value is the highest value obtained among the F, T4, T5, and T7 samples. The average of brinell hardness values taken from three different points was 80 HBW. The hardness value is higher than the values given in the literature, but this situation did not cause any brittleness or cracking on the surface of the crash boxes. As a result of the T6 heat treatment in this study, it is understood that more efficient energy absorbers are obtained.

The compression graph obtained for T7 heat treatment is given in Fig. 8. The processes applied for T7 heat treatment are solution heat treatment + quenching and then artificial over-aging. As a result of T7 heat treatment, the average of Brinell hardness values taken from three different parts of the samples separated for hardness were measured as 53.16 HBW. The hardness value was lower than the value given in the literature for T7 heat treatment. However, the highest hardness value obtained after T6 was obtained in T7 heat treatment. The total energy absorbed as a result of this heat treatment is on average 7045,166 J. This value is lower than T6 and T5 heat treatment. However, even if higher values were obtained than T4 and F conditions, this value is not sufficient for using crash boxes.

In this study, the effect of heat treatment parameters (solution temperature, aging temperature and time) on the mechanical properties (hardness) and impact performance of AA6060 alloy were investigated. The targeted result aims to find the most

Fig. 8 Compression test plot for T6 conditioned profile. (Color figure online)

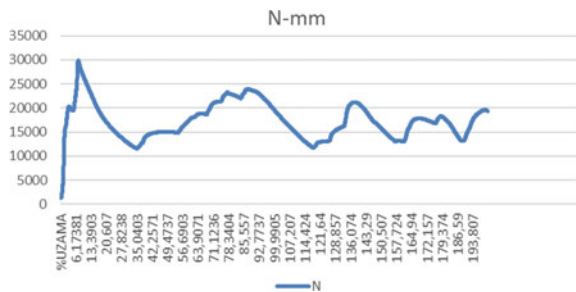


Table 4 Total absorbed energies during compression tests and hardness values

Sample	Absorbed energy (J)	Hardness (HBW)
F1	5405	33,9
F2	6252	35
F3	5725	37
T4-1	6103	49,3
T4-2	7226	50
T4-3	6672	49,8
T5-1	7977	47,4
T5-2	8182	45,8
T5-3	7896	47
T6-1	9769	82
T6-2	9352	78
T6-3	9846	80
T7-1	6968	52,9
T7-2	7152	53,5
T7-3	7014	53,1

suitable heat treatment for crash boxes by comparing the energies that AA6060 alloy can absorb as a result of F, T4, T5, T6, and T7 heat treatments. Total energies absorbed as a result of compression test are given in Table 4 and brinell hardness measurement results are given in Table 5. In TL 116 Standards, it is required to comply with DIN EN 755–1 standards for surface texture. No problem was encountered in the surface texture. No tearing was observed in the folding areas as a result of the compression test. Total energies absorbed as a result of compression test;

References

1. Sharifi S, Shakeri M, Fakhari HE, Bodaghi M (2015) Experimental investigation of bitubal circular energy absorbers under quasi-static axial load. *Thin-Walled Struct* 89:42–53
2. Othman A, Abdullah S, Ariffin AK, Mohamed NAN (2016) Investigating the crushing behavior of quasistatic oblique loading on polymeric foam filled pultruded composite square tubes. *Compos Part B Eng* 95:493–514, [4] Mohammadiha O. and Ghariblu H
3. Mohammadiha O, Ghariblu H (2016) Crush response of variable thickness distribution inversion tubes under oblique loading. *Thin-Walled Struct* 109:159–173
4. Rezvani M, Nouri M (2014) Axial crumpling of aluminum frusta tubes with induced axisymmetric folding patterns. *Arab J Sci Eng* 39(3):2179–2190
5. Sun G, Xu F, Li G, Li Q (2014) Crashing analysis and multiobjective optimization for thin-walled structures with functionally graded thickness. *Int J Impact Eng* 64:62–74
6. Zhu G, Li S, Sun G, Li G, Li Q (2016) On design of graded honeycomb filler and tubal wall thickness for multiple load cases. *Thin-Walled Struct* 109:377–389
7. Xiong Z, Zhang H (2015) Relative merits of conical tubes with graded thickness subjected to oblique impact loads. *Int J Mech Sci* 98:111–125

8. Zhang X, Zhang H (2012) Experimental and numerical investigation on crush resistance of polygonal columns and angle elements. *Thin-Walled Struct* 57:25–36
9. Aktay L, Çakıroğlu C, Güden M (2011) Quasi-static axial crushing behavior of honeycomb-filled thin-walled aluminum tubes. *Open Mater Sci J* 5:184–193
10. Isaac W, Oluwole O (2016) Energy absorption improvement of circular tubes with externally press-fitted ring around tube surface subjected under axial and oblique impact loading. *Thin-Walled Struct* 109:352–366
11. Langseth M, Hopperstad OS (1996) Static and dynamic axial crushing of square thin-walled aluminium extrusions. *Int J Impact Eng* 18:7–8
12. Nagel GM, Thambiratnam DP (2005) Computer simulation and energy absorption of tapered thin-walled rectangular tubes. *Thin-Walled Struct* 43(8):1225–1242
13. Abbasi M, Reddy S, Nazari GA, Fard M (2015) Multiobjective crashworthiness optimization of multicornered thin-walled sheet metal members. *Thin-Walled Struct* 89:31–41
14. Jusuf A, Dirgantara T, Gunawan L, Putra IS (2015) Crashworthiness analysis of multi-cell prismatic structures. *Int J Impact Eng* 78:34–50
15. Tarlochan F, Samer F, Hamouda AMS, Ramehs S, Khalid K (2013) Design of thin wall structures for energy absorption applications: Enhancement of crashworthiness due to axial and oblique impact forces. *Thin-Walled Struct* 71:7–17
16. Xiong Z, Zhang H (2013) Energy absorption of multi-cell stub columns under axial compression. *Thin-Walled Struct* 68:156–163
17. Deepak A, Rawat S, Upadhyay AK (2016) Crashworthiness of circular tubes with structurally graded corrugations. SAE technical paper, No. 2016-28-0050
18. Asanjarani A, Dibajian SH, Mahdian A (2017) Multiobjective crashworthiness optimization of tapered thinwalled square tubes with indentations. *Thin-Walled Struct* 116:26–36
19. Rawat S et al (2017) Collapse behavior and energy absorption in elliptical tubes with functionally graded corrugations. *Proc Eng* 173:1374–1381

Part XXV
Electronic Packaging and Interconnections
2021

On Interface Formation in Zr-Based BMG/6061 Al Interconnects Joined by μ FSSW



David Yan and Logan Vahlstrom

Abstract Bulk metallic glasses (BMGs) are very attractive to a range of micro-electronic applications including sensing elements, precision optics, and micro-gear motors due to their high strength, elasticity, corrosion resistance, and soft magnetic properties. Although joining BMGs to dissimilar materials to manufacture interconnects for micro-electronic devices is a great challenge, micro-friction stir spot welding (μ FSSW) is a novel solid-state joining process which makes it a strong candidate for joining BMGs or BMGs to other crystalline materials to fabricate various types of interconnects. However, studies on the dissimilar μ FSSW of BMGs to aluminum (Al) alloys are limited. This paper presents experimental investigations on interface formation in μ FSSW of dissimilar Zr-based BMGs (i.e. LM105) to 6061 Al alloys. A series of μ FSSW of dissimilar 1.5 mm thick LM105 BMGs-to-6061Al-T6 sheets trials were conducted and the stir zone temperature was measured. The obtained joint cross sections were characterized by scanning electron microscopy equipped with energy dispersive X-ray spectroscopy, and the effect of μ FSSW conditions on the joint interface's microstructure evolution was evaluated. It has been found that the BMGs materials were stirred into the Al side in the stir zone and reacted with the Al to form the Al-rich phase.

Keywords Dissimilar joining · BMG/Al interconnects · Joint interface microstructure · Micro-friction stir spot welding

Introduction

Bulk metallic glasses have origins of long-range disordered atomic configurations and multicomponent characteristics. Thus, they possess superior properties such as high strength and hardness, wide elasticity range, excellent wearing and corrosion resistance, and suitable magnetic properties [1, 2]. Joining of dissimilar materials is

D. Yan (✉) · L. Vahlstrom

Department of Aviation and Technology, San José State University, One Washington Sq, San Jose, CA 95192, USA

e-mail: david.yan@sjsu.edu

© The Minerals, Metals & Materials Society 2021

TMS 2021 150th Annual Meeting & Exhibition Supplemental Proceedings,

The Minerals, Metals & Materials Series,

https://doi.org/10.1007/978-3-030-65261-6_62

often required for semiconductor industrial and micro-electronic applications due to the demand for hybrid components and interconnects made of different materials [3]. For example, a diameter of 4 mm micro-gear motor made of the Zr-based BMGs gears in conjunction with various types of connection adapters of curved sections and circularly piping has been used in advanced medical equipment, including micro-pump, precision optics, and micro-machines [4]. Therefore, joining BMGs to crystalline metallic materials is an important method for broadening the applications of the BMGs [5]. However, BMGs are generally regarded as non-weldable materials, which greatly limit their applications as engineering materials [6]. Recently, joining of BMGs by various welding methods has been developed, generally speaking, both liquid phase and solid state welding methods have been used for the welding of BMGs. Nevertheless, the liquid phase approach could induce the crystallization from the amorphous structure or change of chemical composition in the BMGs as its processing temperature reaches the BMGs' crystallization temperature. Therefore, the solid-state welding method such as friction stir welding (FSW) is a promising solid-state technique for joining BMGs, as the temperature increase is relatively low and an excellent metallurgical joint can be achieved without any crystallization in the BMGs [7].

Sun et al. [8] successfully carried out dissimilar FSW of Zr-based BMGs to pure Al (A1050-H24) under various welding conditions. They found that a clear and straight BMG/Al interface was formed and no intermetallic compounds caused either by chemical reaction or crystallization from the amorphous phase can be detected within the entire stir zone. Li et al. [7] joined a 2 mm thick Zr-based BMGs plate to a 4.5 mm thick pure Al plate by FSW and found that some BMGs particles were stirred into the Al side in the stir zone and reacted with the Al to form the Al-rich phase. The residues of the BMGs particles still maintained the amorphous structure. However, no crystallization and reaction layer were detected at the interface between the BMGs and Al. Shin [9] conducted dissimilar friction stir spot welding (FSSW) of Zr-based BMGs (Vit-1) to Al alloy (A5052-H32) and evaluated the effect of tool geometry on the weld zone temperature in relation to the crystallization of the BMGs. Shin reported that by using the round pin tool, the vertical load increased with friction time, but it dropped suddenly in magnitude when the pin contacted to the lower-positioned BMG sheet, because the temperature at the stirred zone had reached its supercooled liquid state wherein the BMG starts to show a superplastic deformation.

Moreover, Shin et al. [10] performed dissimilar friction stir spot welding (FSSW) of Zr-based BMGs (LM-1) to Mg alloy (AZ31B) to study the influence of welding conditions on the weld zone temperature. They reported that by using the round pin tool, the increment in the tool rotation speed increased the heat input into the stir zone and, as a result, produced a higher temperature around the stir region. As for the micro-friction stir spot welding (μ FSSW), it is a spot-like joining process utilizing a tool shoulder, with or without tool pin, to generate frictional heat and join multilayer materials under the solid-state condition. However, μ FSSW of Zr-based BMGs such as LM 105 and 6061 Al plates is limited and has still not been systematically investigated.

In this study, experimental studies were performed on μ FSSW of 1.5 mm thick Zr-based BMGs-LM 105 and 1.5 mm thick 6061Al-T6 plates. The mechanism of the joint interface formation was investigated, and the effect of μ FSSW conditions on the joint microstructure evolution was studied in relation to the processing temperature.

Experimental Procedure

A HAAS CNC mill (TM-1) was employed to perform μ FSSW trials with a custom-made rigid clamping and steel backing. A non-tilted tool including one scroll flat shoulder with diameter of 6 mm and cylindrical thread pin at diameter of 2.5 mm and length of 1.5 mm was made of heat-treated H13 tool steel and utilized during μ FSSW. Zr-based BMGs-LM 105 and 6061Al-T6 plates, both with the thickness of 1.5 mm and width of 15 mm, were selected to form a dissimilar workpiece used in μ FSSW trials. Per the Liquidmetal Technologies Inc., Zr-based BMGs-LM 105 has a composition (in wt. %) of: Zr 65.7, Cu 15.6, Ni 11.7, Al 3.7, Ti 3.3 with 399 °C of glass transition temperature (T_g) and 468 °C of crystallization temperature (T_x).

These two plates were overlapped by 15 mm in length with the Al plate on the top and μ FSSW was conducted in the center of the overlapped area. A series of μ FSSW trials were conducted when the tool was rotating at rotational speed (ω) of 3000 and 3600 rpm, respectively, and plunging into the workpiece at a constant speed of 3 mm/min (V) with tool dwell time (T) of 2 s. A constant 0.5 mm depth of shoulder plunging (D) was used in all experiments. Figure 1 shows experimental setup, a scroll tool, and a dissimilar BMGs-to-Al weldment joined by μ FSSW.

The stir zone temperature was measured by embedding a tip of 0.127 mm diameter thermocouple wire (OMEGA 5TC-TT-E-36-72) at the faying surface of the Zr-based BMGs and Al plates, with 2.75 mm away from the welding centerline. After each μ FSSW trial, the produced BMGs-to-Al weldments were sectioned in the transverse direction through the welding centerline. All cross-sectional samples were mounted and polished with standard metallographic practice followed with 0.3 μ m alumina-water slurry for final polishing, and then etched using Kroll's etchant (2 ml HF and 6 ml HNO₃ in 100 ml H₂O). Subsequently, the etched samples were examined via optical microscope and scanning electron microscope (SEM) equipped with energy dispersive spectroscopy (EDS).

Results and Discussion

Post-Joint Profile and Cross-Sectional Configuration

Figure 2a–d shows two post-joint profiles and lower magnification SEM micrographs of joint cross sections made using scroll tool with rotational speed (ω) of 3000 and

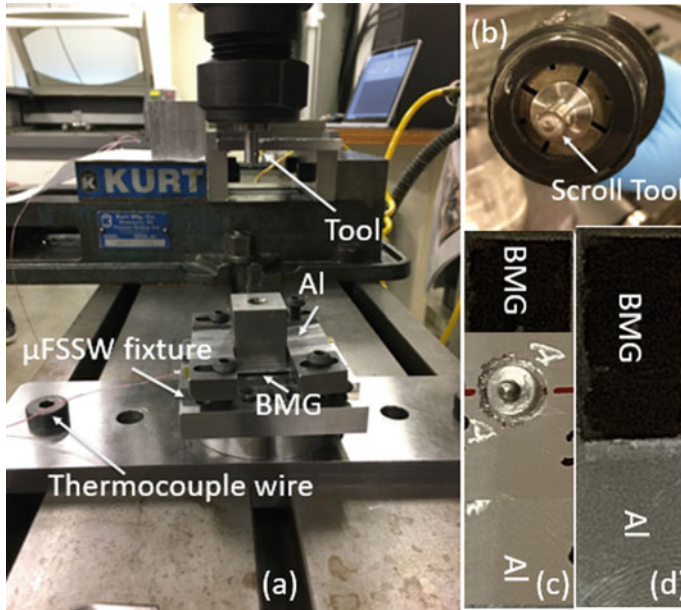


Fig. 1 Photographs of **a** μ FSSW experimental setup, **b** a scroll tool, **c** and **d** front and back view of BMGs-to-Al weldment joined via μ FSSW. (Color figure online)

3600 rpm, respectively, at a constant tool plunging speed (V) of 3 mm/min, 0.5 mm depth of shoulder plunging (D) and dwell time (T) of 2 s. Observation of these two post-joint profiles shows that surface-defect-free joints were achieved under the current μ FSSW conditions. It can also be seen from Fig. 2a, c that some Al metals were extruded outside the stir zone by the high-speed rotating tool to form flash due to the overwhelming softening of the materials induced during μ FSSW, though the position control mode, i.e. a constant depth of 0.5 mm plunging was used.

Examination using SEM in Fig. 2b, d has shown the common features in μ FSSW such as stir zone (SZ) and hook structures. It can be found that a BMGs hook was extruded upward from the lower BMGs plate into the upper Al plate, and the shape of the hook varied due to different tool rotational speeds as depicted in the figure. In fact, at a lower tool rotating speed, a smaller hook is formed at the interface due to smaller amount of frictional heat input compared to a larger hook developed under a higher tool rotating speed. Also, the geometry of BMGs-to-Al interface is quite different, in which a flat feature was formed under the lower tool rotating speed while a concave nature was generated at the higher tool rotating speed. The appearances of these two post-joint profiles and cross-sectional structures were similar to the findings of Shin et al. [10], although they performed dissimilar FSSW of Zr-based BMGs (LM-1) to Mg alloy (AZ31B). Apparently, a continuous metallurgical bonding could be achieved under suitable μ FSSW conditions.

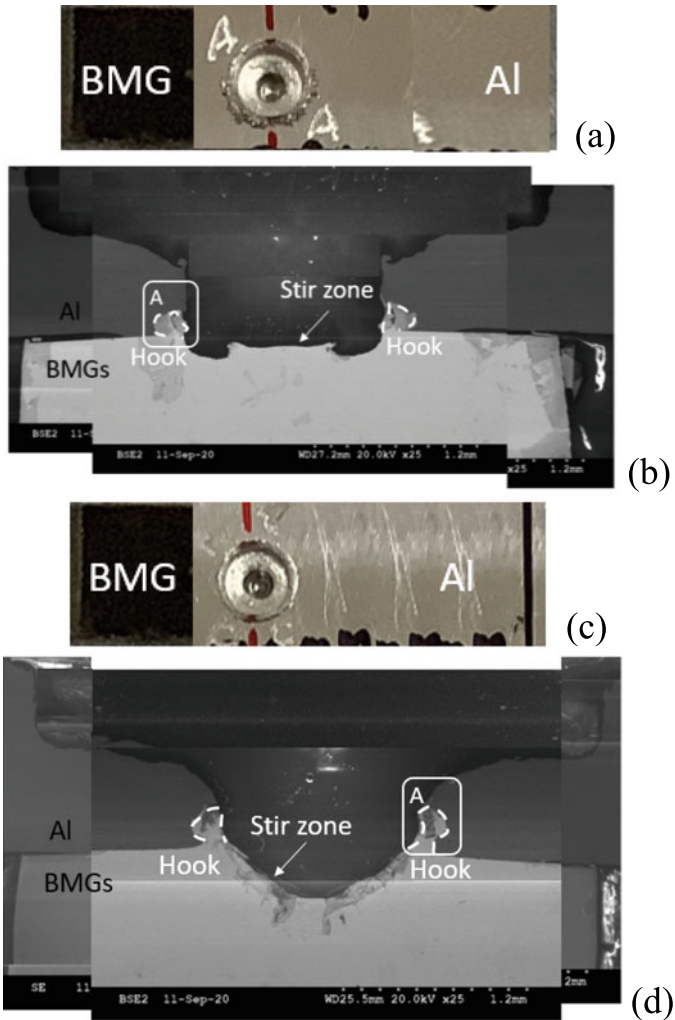


Fig. 2 Photographs of two post-joint profiles obtained at **a** $\omega = 3000$ rpm and **c** $\omega = 3600$ rpm, and two SEM micrographs of joint cross sections produced at **b** $\omega = 3000$ rpm, showing a flat BMGs-to-Al interface, and **d** $\omega = 3600$ rpm, showing a concave BMGs-to-Al interface, in conjunction with $V = 3$ mm/min, $D = 0.22$ mm and $T = 2$ s used during μ FSSW. (Color figure online)

Stir Zone Temperature History Relating to Joint Interface Formation

It is crucial to study the thermal history during μ FSSW of BMGs or BMGs to other crystalline materials, as the elevated temperature is the most critical parameter to case BMGs’ structural relaxation and crystallization of the original amorphous

structure [6, 8]. The temperature histories of above two joints corresponding to the tool rotational speed of 3000 and 3600 rpm were plotted in Fig. 3a, b. It can be seen from the figure that the peak temperature of 170 °C was recorded at tool rotational speed of 3000 rpm, while the maximum temperature of 125 °C was obtained at tool rotational speed of 3600 rpm. Thus, our study has shown that increasing tool rotational speed led to a higher peak temperature. These stir zone temperature records also indicated that no structural relaxation and crystallization occurred along the interface produced during μ FSSW of BMGs to Al in this present study. As the glass transition temperature (T_g) and crystallization temperature (T_x) for BMGs-LM 105 are 399 and 468 °C, respectively, according to the data provided by the BMGs manufacturer.

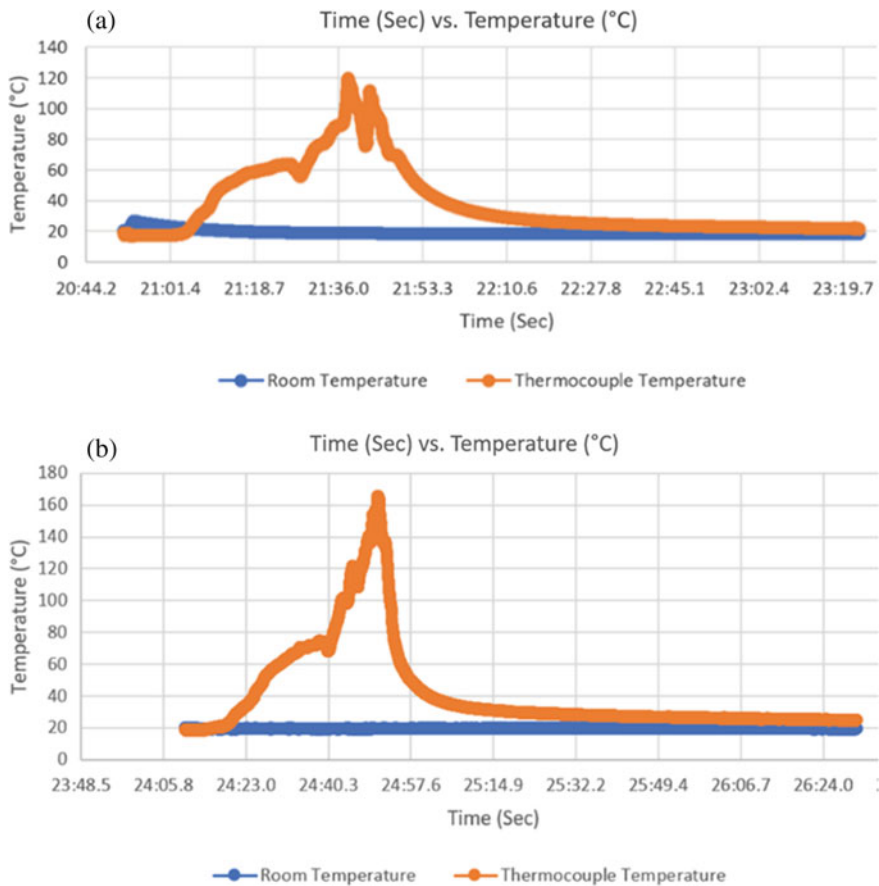


Fig. 3 Stir zone temperature history during μ FSSW obtained at **a** $\omega = 3000$ rpm, and **b** $\omega = 3600$ rpm, showing the effect of tool rotational speed on the peak temperature of stir zone, in conjunction with $V = 3$ mm/min, $D = 0.22$ mm and $T = 2$ s. (Color figure online)

The stir zone temperature curves shown in Fig. 3a, b indicated that the temperature increasing included two-steep rises. The first steep rise was due to the initial contact between the scroll tool pin and upper surface of the Al plate that generated a large amount of frictional heat. While the second steep increase was a result of the contact between the scroll tool shoulder and the upper surface of the Al plate and partial softened Al workpiece, in which the frictional area was more than five times larger than that of the first steep rise after comparing the diameters of the tool shoulder and pin.

Compositional Analysis of BMGs-to-Al Joint Interface

Figure 4a presents a higher magnification SEM micrograph of area A marked in Fig. 2b, showing a hook structure and some bright particles near the interface in the Al side, and (b) back scattering SEM micrograph of area A marked in (a), showing a clear interface between the BMGs and Al. Energy dispersive spectroscopy (EDS) analyses were conducted at two different spots: A is at the BMGs side and B is along the BMGs-to-Al joint interface marked in Fig. 4c, and the EDS spectra at these two spots are shown in Fig. 4d.

The EDS analysis results revealed that the spot A contains 68.06%Zr, 14.70%Cu, 13.1%Ni, 4.14%Al (in wt. %), while the spot B contains 55.62%Al, 18.4%Zr, 16.74%Cu, 7.14%Ni, 2.1%Ti (in wt. %). By comparing the composition of the original (as received) BMGs-LM105 (Zr 65.7, Cu 15.6, Ni 11.7, Al 3.7, Ti 3.3 in wt. %) with the results at spot A, it can be found that the composition at A is almost identical to the composition of the original BMGs-LM105 matrix. However, after comparing the composition of the spot B, original BMGs-LM105 and 6061Al-T6 (Al 97.33, Mg 1.17, Si 0.57, Cu 0.26, Fe 0.45, Cr 0.22 in wt. %), there is significant composition difference at the spot B, i.e. BMGs-to-Al joint interface in relation to those two original BMGs and Al alloy. This result indicated that a larger degree of stirring and mixing between the BMGs and Al during μ FSSW that resulted in some BMGs being stirred and reacted with the Al. Consequently, the Al-rich phase with the obtained chemical composition was formed in the BMGs-to-Al joint interface. The finding of this present study was consistent with the results of Li et al. during FSW of Zr-based BMGs to pure Al alloy [7].

Evolution of BMGs-to-Al Joint Interface

Figure 5a shows a higher magnification SEM micrograph of area A marked in Fig. 2d, showing a hook structure and some workpiece fragments appeared within the hook region, and (b) backscattering SEM micrograph of area A marked in (a), showing a clear and straight BMGs-to-Al interface. Energy dispersive spectroscopy (EDS) line scan analysis was conducted across the BMGs-to-Al interface illustrated in Fig. 5c, and the EDS line scan result was shown in Fig. 5d.

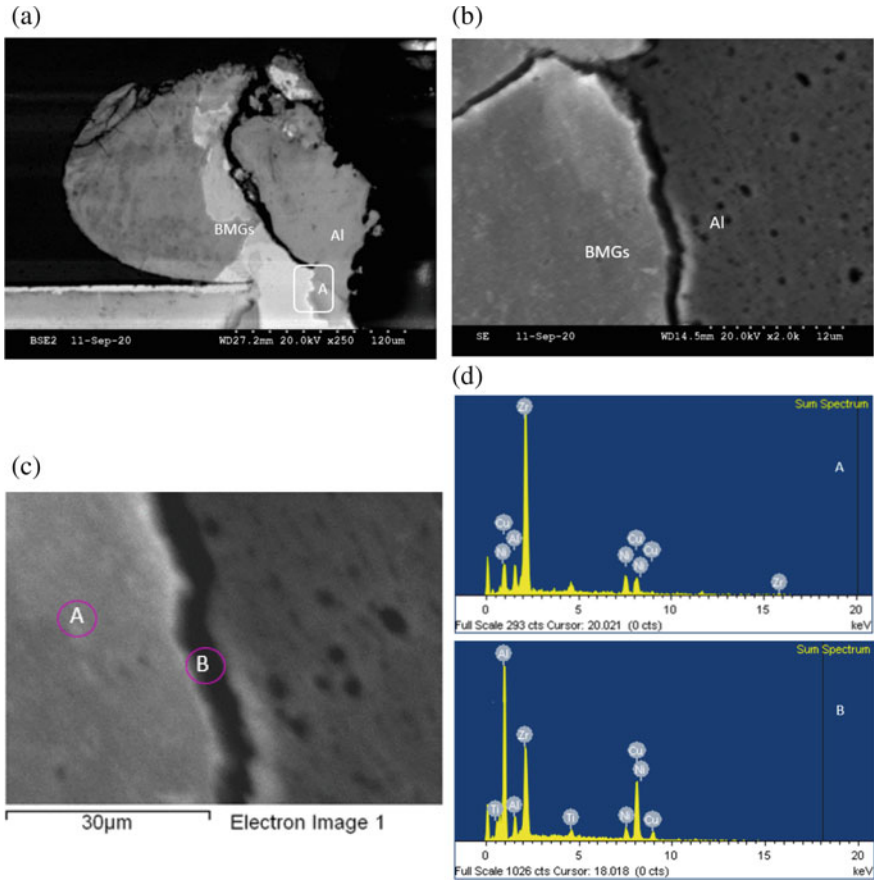


Fig. 4 **a** Higher magnification SEM micrograph of area A marked in Fig. 2b, showing a hook structure, **b** back scattering SEM micrograph of area A marked in **a**, showing the BMGs-to-Al interface, **c** higher magnification image of **b**, indicating A and B spots selected for EDS analysis, **d** EDS spectra at A and B spots marked in **c**, respectively, showing the chemical compositions. (Color figure online)

Apparently, higher BMGs signal count and lower Al signal count were observed along the interface on the BMGs side in Fig. 5d and different elemental gradients and interface thicknesses can be observed as well. The redistribution of elements suggested that Zr element from the BMGs side diffused into the Al side. The different chemical composition from Fig. 5d confirmed that there was a reaction layer with width of $9\ \mu\text{m}$ across the BMGs-to-Al interface. The distinct decrease of Zr signal and increase of Al signal also revealed the boundaries of the diffusion zone in relation to the BMGs and Al matrix. The results of line scan analysis obtained from this current study was similar to the finding of Shin et al. [10] during FSSW of BMGs to Mg alloy.

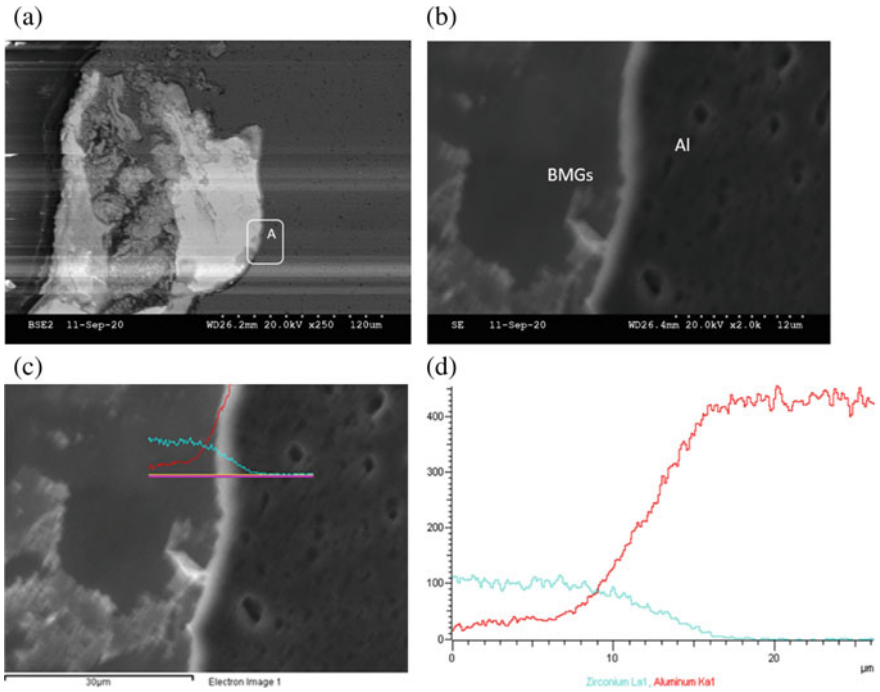


Fig. 5 **a** higher magnification SEM micrograph of area A marked in Fig. 2 **d**, showing a hook structure, **b** backscattering SEM micrograph of area A marked in **a**, showing the BMGs-to-Al interface, **c** higher magnification image of **b**, indicating the location selected for EDS line scan analysis, and **d** the result of EDS line scan analysis, illustrating variation in elemental composition across the BMGs-to-Al interface. (Color figure online)

Conclusions

The dissimilar Zr-based BMGs and 6061 Al plates were successfully joined utilizing μ FSSW and the effect of μ FSSW conditions on the joint microstructure evolution was studied in relation to the processing temperature. Based on the results obtained from this present study, the following conclusions can be drawn:

1. Two μ FSSW joints possess a BMG hook extruded upward by the tool pin from the lower BMGs plate into the upper Al plate.
2. BMGs materials were stirred into the Al side in the stir zone and reacted with the Al to form the Al-rich phase.
3. No crystallization and reaction layer can be detected at the BMGs-to-Al interface.
4. The higher tool rotational speed and the higher peak temperature in the stir zone.

Acknowledgements The authors are grateful to the Undergraduate Research Grants of San Jose State University for the financial support.

References

1. Jamili-Shirvan Z et al (2020) Non-isothermal crystallization kinetics investigation of different zones at the joining area of a bulk metallic glass welded by friction stir spot welding (FSSW). *J Non-Cryst Solids* 533:119904
2. Karmakar B (2017) 12-Functional bulk metallic glasses. In: Karmakar B (ed) *Functional glasses and glass-ceramics*. Butterworth-Heinemann, pp 365–390
3. Kar A et al (2020) Role of plastic deformation mechanisms during the microstructural evolution and intermetallics formation in dissimilar friction stir weld. *Mater Charact* 164:110371
4. Inoue A, Kong FL (2016) Bulk metallic glasses: formation and applications. In: *Reference module in materials science and materials engineering*. Elsevier
5. Wang D et al (2009) Friction stir welding of Zr₅₅Cu₃₀Al₁₀Ni₅ bulk metallic glass to Al–Zn–Mg–Cu alloy. *Scripta Mater* 60(2):112–115
6. Sun Y et al (2010) Microstructure and mechanical properties of friction stir welded joint of Zr₅₅Cu₃₀Al₁₀Ni₅ bulk metallic glass with pure copper. *Mater Sci Eng, A* 527(15):3427–3432
7. Li FP et al (2013) Microstructure and mechanical properties of friction stir welded joint of Zr₄₆Cu₄₆Al₈ bulk metallic glass with pure aluminum. *Mater Sci Eng, A* 588:196–200
8. Sun Y et al (2012) Interface microstructure and mechanical properties of dissimilar friction stir welded joints between Zr₅₅Cu₃₀Ni₅Al₁₀ bulk metallic glass and pure Al. *Mater Trans* 53(6):1106–1112
9. Shin H-S (2014) Tool geometry effect on the characteristics of dissimilar friction stir spot welded bulk metallic glass to lightweight alloys. *J Alloy Compd* 586:S50–S55
10. Shin H-S, Jung Y-C, Lee J-K (2012) Influence of tool speeds on dissimilar friction stir spot welding characteristics of bulk metallic glass/Mg alloy. *Met Mater Int* 18(4):685–689

Reliability Evaluation of Ag Sinter-Joining Die Attach Under a Harsh Thermal Cycling Test



Zheng Zhang, Chuantong Chen, Aiji Suetake, Ming-Chun Hsieh, Aya Iwaki, and Katsuaki Suganuma

Abstract Ag sinter-joining is an ideal connection technique for next-generation power electronics packaging due to its excellent high-temperature stability and excellent thermal conductivity. In this work, we applied Ag sinter-joining to die attach of power electronics and focused reliability of Ag sinter-joining under a harsh thermal cycling condition, which ranges from -50 to 250 °C. The bonding quality of as-sintered die attach had a shear strength of over 45 MPa and remained over 25 MPa after a 500-cycle test. However, the shear strength drastically degraded to less than 10 MPa due to a failure of metallization layer detachment between dummy chip and sputtering layer after 750 cycles. Meanwhile, thermal resistance of die attach with different bonding materials was also evaluated by a T3ster, which suggests the Ag sinter-joining owns a superior property of thermal conduction than the traditional solder joining. This investigation indicates that the Ag sinter-joining has a long lifetime under a severe operating condition of power electronics.

Keywords Ag paste sinter-joining · Thermal cycling test · Reliability · Thermal resistance · Die attach

Introduction

Wide bandgap (WBG) semiconductors such as SiC and GaN are important in dealing with an increasing power density and cutting down power losses due to their excellent physical properties such as high breakdown voltage, high junction temperature, and low on-resistance [1]. In the last decade, the rapid development of production process of WBG semiconductors allows a widespread application of WBG semiconductors in more scenarios like aerospace, electric vehicles, and even a tiny super-fast charger. However, a higher junction temperature of WBG semiconductors, even up to 250 °C, brings new challenges for packaging of power electronics, especially

Z. Zhang (✉) · C. Chen · A. Suetake · M.-C. Hsieh · A. Iwaki · K. Suganuma
Institute of Scientific and Industrial Research, Osaka University, Mihogaoka 8-1, Ibaraki
567-0047, Osaka, Japan
e-mail: zhangzheng@sanken.osaka-u.ac.jp

for the packaging of die attach that is the most critical component in the power electronics. Typically, the WBG semiconductor bonds to a substrate or lead frame via solder or conductive adhesive. Although a preferable bonding quality can be achieved by these traditional die attach materials, it is almost incapable of dealing with the severe junction temperature. Currently, Ag sinter-joining technique, which has excellent high-temperature resistance and electrical properties, is regarded as one of promising approaches for the WBG die attach in power electronics [2, 3].

Ag sinter-joining technique is based on sintering of Ag paste to realize interconnection between die and substrate. The Ag paste, consisting of Ag particles and organic solvents, owns a low sintering temperature of below 250 °C, whereas it can withstand severe high temperature even over 900 °C after being sintered into a micron porous structure. The sintered Ag structure has low electrical resistance in the order of $1 \times 10^{-5} \Omega\text{-cm}$ and high thermal conductivity of over 200 W/m·K on account of superior electrical and thermal properties of Ag [4, 5]. Besides, the Ag sinter-joining technique can bare various chemical conditions due to the stability of Ag. These merits perfectly meet the requirements for WBG die attach packaging, making the Ag sinter-joining technique increasingly important in the packaging of power electronics. Currently, massive efforts have been made on the Ag sinter-joining. For instance, Ag paste exhibits feasible bond-abilities on various surface metallizations like Ag, Au, Ni, and Al, which significantly extend application scenarios of Ag paste sintering [6–8]. Bonding quality of die attach with Ag sinter-joining reaches a shear strength of over 40 MPa, showing a better bonding quality than soldering or adhesive joining. However, there is still limited knowledge on the reliability variation of Ag sinter-joining after a harsh thermal reliability test.

In this work, we took an in-depth investigation of reliability changes of Ag sinter-joining after a series of harsh thermal cycling test (TCT, -50 to 250 °C). Die attach was achieved by sintering a micron Ag flake paste. Sintering behavior of the Ag flake paste was initially investigated through TG–DTA curves, and thermal diffusivity of the sintered structure was measured through a flash method. Shear strength of die attach after the TCT and thermal resistance of die attach were studied as well.

Experiments

Ag flake paste, consisting of micron-sized Ag flakes (Fukuda Metal Foil and Powder Co. Ltd) and organic solvent (Daicel Corporation), was applied as Ag sinter-joining material. Thermal properties of the Ag flake paste were investigated through a thermogravimetric (TG)-differential thermal analysis (DTA) equipment (2000SE Netzsch, Germany) and LFA 467 Hyperflash (Netzsch, Germany). Figure 1a shows a schematic drawing of the die attach with the Ag paste sinter-joining. Dummy Si die ($3 \text{ mm} \times 3 \text{ mm}$) and AMB substrate ($30 \text{ mm} \times 30 \text{ mm}$) were sputtered with Ni/Ti/Ag coating and then used for die attach packaging. The sintering process was conducted on a hotplate at the ambient atmosphere at a sintering temperature of 250 °C for 60 min. The prepared die attaches were put on a thermal cycling machine (ESPEC

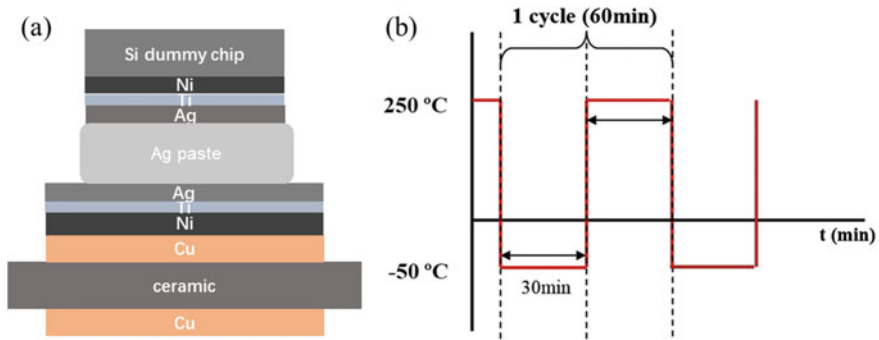


Fig. 1 **a** Schematic drawing of die attach structure with Ag sinter-joining; **b** Diagram of thermal cycling condition. (Color figure online)

CORP.) with a temperature range from -50 to 250 °C. The dwell time in each zone is 30 min as shown in Fig. 1b. Shear strength of sintered die attachment was tested by a shear tester (Dage 4000, Japan) with a shear speed at 50 $\mu\text{m/s}$ and a shear height at 100 μm . Cross sections of die attach before and after thermal cycling test (TCT) were prepared via ion milling (IM-4000; Hitachi, Japan) initially and then observed by a scanning electron microscopy (SU-8020 Hitachi, Japan). Au80Sn20 and SAC305 were also selected as die attach materials for a comparison thermal resistance of die attach. SiC Schottky Body Diode (SBD) with a size of 5 mm \times 5 mm was packaged on active metal brazing (AMB) substrate and then bonded through Al ribbons for a topside connection. The thermal resistance of die attach was measured by a T3Ster (Mentor Graphics).

Results and Discussion

Figure 2a shows an SEM observation of the original morphology of Ag flakes. The Ag flakes achieved via a cold-working process exhibit a compressed structure with an irregular and shape edges. Figure 2b presents a cross section of Ag paste after sintering at 250 °C for 1 h. These Ag flakes merge entirely into a uniform porous structure, suggesting full sintering of Ag flakes. In order to further investigate the sintering behavior of the Ag flake paste, TG-DTA of the Ag flake paste was conducted and shown in Fig. 2c. A noticeable weight loss can be found from 50 to 125 °C in the TG curve, which is attributed to evaporation and decomposition of organic solvents in the paste. The DTA curve reveals a tiny exothermic peak at around 125 °C and a significant exothermic at 275 °C, respectively. The slight exothermic peak is mainly due to the decomposition of the organic solvent at low temperature. With the increase of temperature, the Ag grains in flakes begin to recrystallize and grow under the affection of oxygen along with an extraordinary thermal release as observed in the DTA curve [9, 10]. The TG-DTA curves confirm the Ag flake paste owns a preferable

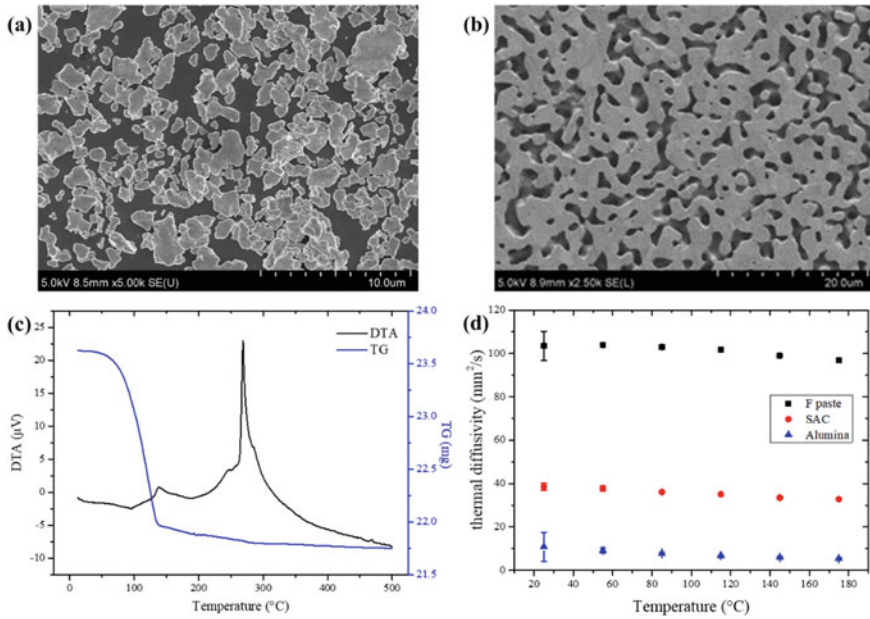


Fig. 2 Original morphology of Ag flakes; **b** Cross section of sintered Ag paste; **c** TG–DTA curves of Ag paste; **d** thermal diffusivity of sintered Ag, SAC305, and alumina from 25 to 175 °C. (Color figure online)

sinter-ability at a low-temperature sintering condition. Figure 2d shows a comparison of thermal diffusivity of sintered Ag structure, SAC305, and alumina from room temperature to 175 °C. Even though the thermal diffusivity of sintered Ag degrades due to a porous structure, it remains at 105 mm²/s at room temperature (solid Ag 160 mm²/s), which is over twice as much as the SAC305 solder and almost ten times of alumina (11 mm²/s) [11]. Thermal diffusivity of different materials is reduced as an increase in temperature. However, the sintered Ag structure still possesses a high thermal diffusivity of around 100 mm²/s, suggesting an excellent performance in thermal conduction even at high temperatures.

Shear strength of die attach before and after thermal cycling test is presented in Fig. 3. The initial shear strength of die attach is over 45 MPa, which is superior to solder joining or adhesive bonding [12]. The shear strength gradually decreases as the cycle number increases, and the shear strength of the die attach is still over 30 MPa after 500 cycles. However, a drastic decrease in shear strength occurs after 500 cycles. The shear strength degrades to 10 MPa after 750 cycles. In order to understand this degradation, the structure of die attach was investigated via CT and SEM cross-sectional images.

Figure 4 presents CT images and cross-sectional SEM images of the die attach structure before and after the TCT. It can be seen that the sintered Ag appears as a uniform layer with very few voids inside. After 750 TCT, the sintered layer has

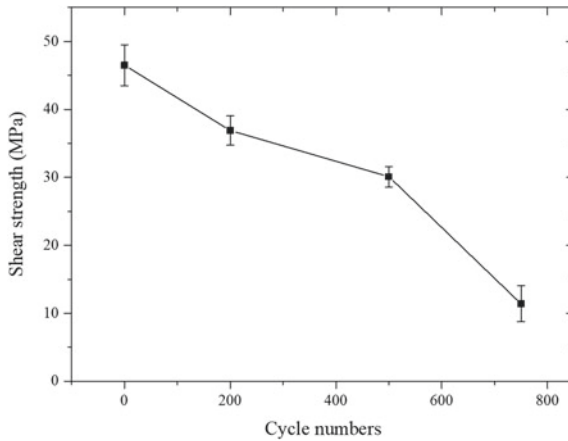


Fig. 3 Shear strength variation of die attach after different cycle numbers

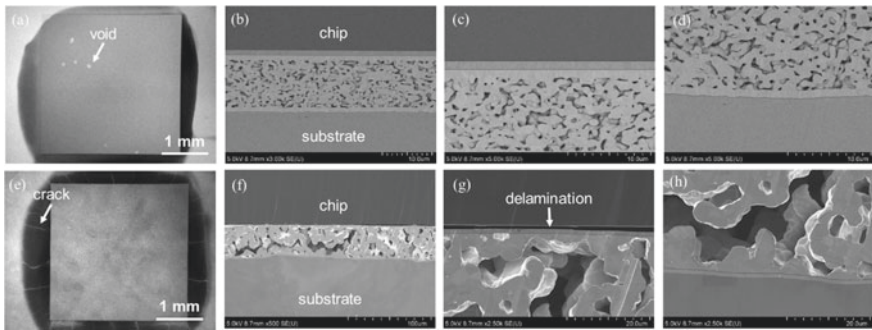
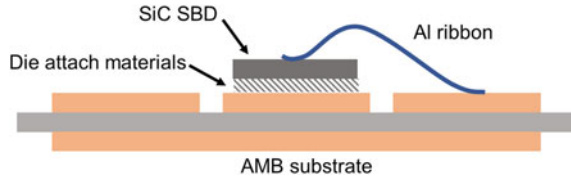


Fig. 4 CT and cross-sectional SEM images of die attach structure before **a–d** and after 750 cycles **e, h**

become a crazing structure with obvious cracks at the edges of chip. The cracks and crazing structure generated during the TCT are ascribed to massive stress induced during the harsh cycling condition [13].

In the cross section of the initial die attach specimen, Ag appears as a well sintered porous structure (Fig. 4b). With a magnified observation of top and bottom bonding interface (Fig. 4c, d), it can be observed that the sintered Ag has completely connected to surface metallization of substrate and chip, which is in accordance with the superior initial bonding strength of over 45 MPa. After 750 cycles, the die attach structure presents dramatic changes (Fig. 4f). The sintered Ag structure exhibits denser connection necks and larger pore size compared with the initial Ag structure. An apparent crack can also be observed in the cycled Ag structure due to the severe cycling stress, and the substrate is drastically deformed as well. Figure 4e, f gives a detailed view of the top and bottom bonding interface. A delamination layer occurs between the

Fig. 5 Schematic graph of module for thermal resistance measurement. (Color figure online)



dummy die and the sputtering layer. At the bottom bonding interface, the sintered Ag still intimately connects to the surface metallization even through significant deformation happened to the substrate. Due to different material properties of metal and Si, massive stress generates during the cycling process, which leads to deformation and cracks in the die attach structure. However, it is worth to notice that the failure of die attach is attributed to the delimitation layer between the sputtering layer and the die rather than the sintered layer. The figures in the die attach structure suggest that the Ag sintered layer is capable of withstanding harsh thermal cycling condition even from -50 to 250 °C.

The thermal resistance of die attach with Ag paste joining is tested via a T3Ster and compared with solder sintered die attaches. Figure 5 shows a schematic diagram of a packaged module for the thermal resistance measurement. A $5\text{ mm} \times 5\text{ mm}$ SiC (SBD) die bonds with an AMB substrate by using Ag flake paste, Au80Sn20 solder, and SAC305 solder, separately. The topside connection is realized by Al ribbon bonding. The packaged module was set on an isothermal cooling plate and heated via a stress current of 20 A. Cooling curve of the module is acquired by a sensing current of 50 mA.

Figure 6a shows a cumulative structure function of the cooling process. The cumulative structure function shows an identical variation initially, which is ascribed to the same SiC SBD die structure. There is a significant increase in thermal resistance of die attach with Au80Sn20 and SAC305 solder. Then, the cumulative structure functions appear as a similar variation once again. The difference of cumulative structure function is arguably attributed to the different die attach material since the packaged die attach structure has the same design except for the die attach materials. Figure 6b

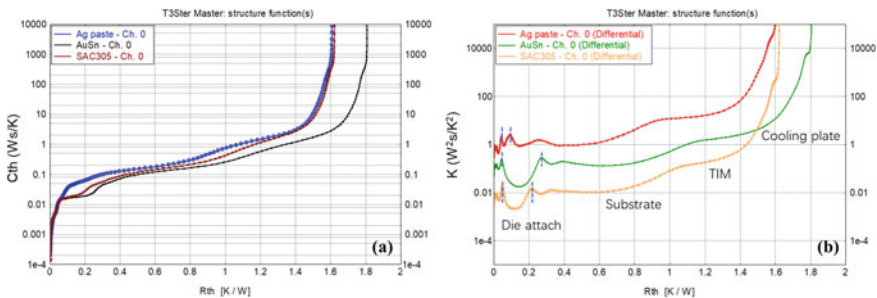


Fig. 6 Cumulative structure function **a** and differential structure function **b** of the module with Ag paste, Au80Sn20, and SAC 305. (Color figure online)

depicts differential structure functions of the different modules. The curves present two obvious peaks with different gap distances at the initial stage, which is due to the different thermal diffusivity die attach materials. Thermal resistance of the sintered Ag paste layer is 0.050 K/W, which is much lower than that of AuSn (0.177 K/W) and SAC305 (0.123 K/W).

Conclusions

In this work, we systematically investigated the bonding performance and thermal performance of the Ag flake paste sinter-joining. The Ag flake paste possesses a superior sinter-ability at low sintering temperature, which provides a precondition for a reliable die attach structure. The die attach structure with the Ag flake sinter-joining has an excellent initial shear strength of over 45 MPa and remain at 30 MPa after 500 cycles TCT. However, due to a delamination layer between the chip and sputtering layer, the bonding quality was severely degraded after 750 cycles. Meanwhile, the sintered Ag structure has lower thermal resistance (0.05 K/W) than the soldering layer due to the excellent thermal diffusivity. The Ag paste sinter-joining can be regarded as an ideal candidate for the die attach packaging in high-temperature applications.

Acknowledgements This paper is based on results obtained from a project (JPNP14004) commissioned by the New Energy and Industrial Technology Development Organization (NEDO). The author acknowledges the Comprehensive Analysis Center of Osaka University for the use of and TG-DTA, Daicel Company in Japan for providing the solvent, and the Network Joint Research Centre for Materials and Devices, Dynamic Alliance for Open Innovation Bridging Human, Environment and Materials.

References

1. Yoder MN (1996) Wide bandgap semiconductor materials and devices. *IEEE Trans Electron Devices* 43:1633–1636
2. Yu F, Johnson RW, Hamilton MC (2015) Pressureless sintering of microscale silver paste for 300 °C applications. *IEEE Trans Compon Packag Manuf Technol* 5:1258–1264
3. Zhang Z, Chen C, Yang Y, Zhang H, Kim D, Sugahara T, Nagao S, Sugauma K (2019) Low-temperature and pressureless sinter joining of Cu with micron/submicron Ag particle paste in air. *J Alloys Compd* 780:435–442
4. Sugauma K, Sakamoto S, Kagami N, Wakuda D, Kim K-S, Nogi M (2012) Low-temperature low-pressure die attach with hybrid silver particle paste. *Microelectron Reliab* 52:375–380
5. Wang S, Li M, Ji H, Wang C (2013) Rapid pressureless low-temperature sintering of Ag nanoparticles for high-power density electronic packaging. *Scripta Mater* 69:789–792
6. Zhang Z, Chen C, Kim D, Suetake A, Nagao S, Sugauma K (2020) Bonding and high-temperature storage performance of die attachment with Ag paste sintering on bare direct bonding aluminum (DBA) substrate. In: *TMS 2020 149th annual meeting & exhibition supplemental proceedings*. Springer, pp 697–706

7. Zhang Z, Chen C, Suganuma K, Kurosaka S (2019), Effect of substrate preheating treatment on thermal reliability and micro-structure of Ag paste sintering on Au surface finish. In: 2019 IEEE 69th electronic components and technology conference (ECTC), IEEE, pp 474–478
8. Chew LM, Schmitt W, Dubis M (2018) High bonding strength of silver sintered joints on non-precious metal surfaces by pressure sintering under air atmosphere using micro-silver sinter paste. In: 2018 IEEE 20th electronics packaging technology conference (EPTC), IEEE, pp 125–131
9. Jiu J, Zhang H, Nagao S, Sugahara T, Kagami N, Suzuki Y, Akai Y, Suganuma K (2016) Die-attaching silver paste based on a novel solvent for high-power semiconductor devices. *J Mater Sci* 51:3422–3430
10. Presland A, Price G, Trimm D (1972) Hillock formation by surface diffusion on thin silver films. *Surf Sci* 29:424–434
11. Parker W, Jenkins R, Butler C, Abbott G (1961) Flash method of determining thermal diffusivity, heat capacity, and thermal conductivity. *J Appl Phys* 32:1679–1684
12. Manikam VR, Cheong KY (2011) Die attach materials for high temperature applications: a review. *IEEE Trans Compon Packag Manuf Technol* 1:457–478
13. Amalu EH, Ekere N (2012) Damage of lead-free solder joints in flip chip assemblies subjected to high-temperature thermal cycling. *Comp Mater Sci* 65:470–484

Part XXVI
Environmentally Assisted Cracking:
Theory and Practice

A Multiphysics Model of Synergistic Environmental Exposure-Assisted Damage of Composite Using Homogenization-Based Degradation Variables



Zhiye Li and Michael Lepech

Abstract The adoption of fossil-based hydrocarbon polymer composites has been successful in both the automotive and aircraft industries and is rapidly expanding into buildings and civil infrastructure. One challenge to broader adoption of polymer composites in buildings and civil infrastructure is a limited ability to model the synergistic effects of the combined physical/chemical processes of environmental exposure and mechanical loading. Unlike other building materials, long-term experience and field performance data of polymer composites in buildings and civil infrastructure applications do not exist. The first and largest composite building system used in a high-rise exterior in the USA is the facade of the San Francisco Museum of Modern Art (SFMOMA) completed in 2015. Since historical, experience-based service life models for composite building applications are not available, it is crucial to build multi-physical-based models in order to predict composite service life performance on a semi-centennial or centennial time scale. This study is to build a physics-based model to predict synergistic effect of environmental exposure to damage of the composite. Based on the authors' previous UV/moisture exposure experiment-computational study, this extended study couples degradation-induced material weakening to continuum damage model. Results of this study indicate that the synergistic effect of combined UV and moisture exposure on composite material degradation is more severe than simple linear superposition of each exposure's damage. A comparison and analysis of UV and moisture exposure degradation mechanisms indicate that these environmental exposures caused material degradation by weakening the polymer matrix, along with weakening the interface between the polymer matrix and fiber reinforcing yarns. Moreover, the interface weakening is more critical than the former one.

Keywords Fiber-reinforced composites · UV · Moisture · Temperature · Deterioration · Damage · Multiphysics · Multiscale modeling · Structural scale

Z. Li (✉) · M. Lepech
Department of Civil and Environmental Engineering, Stanford University, Stanford, CA, USA
e-mail: zli88@stanford.edu

M. Lepech
e-mail: mlepech@stanford.edu

Introduction

The degradation of fiber-reinforced polymer (FRP) composite materials used in buildings and other civil infrastructure is the synergistic result of a number of physical loads, chemical loads, ultraviolet (UV) exposures, and other mechanisms of deterioration acting simultaneously over decades of service life. Such synergistic material degradation exacerbates creep and fatigue [1–3] of structural members and limits the accuracy of existing phenomenological service life prediction tools [2].

The first and largest architectural application of fiberglass-reinforced plastic (FRP) in the USA is the facade of the San Francisco Museum of Modern Art (SFMOMA) completed in 2015. The SFMOMA enclosure, which has won many awards, is the result of a collaborative union between architect Snøhetta, leading FRP manufacturer Kreysler & Associates of American Canyon, California, and Enclos, one of the largest facade contractors in the USA [4, 5]. When predicting the sustainability of this new material in a very long future time span, a lack of long-term historical performance data limits the application of experience-based design tools, prevents reliance on long-standing design heuristics (i.e., “rules of thumb”), and calls into question the reliability of predictions or assessments of future in-service performance. Due to these circumstances, the development of multiphysics and multiscale models of material and structural degradation phenomena can be crucial to assessing the safety and durability of newly adopted or proposed material and structural systems. [1, 2]

In this paper, a multiscale modeling technique is used to upscale the usage of material model prediction into structural and system levels. In the multiscale computational model, there are two levels: materials level and structure level. The material level model has the smallest length scale. It consists of woven fiber microstructure, periodic boundary conditions, and coupled multi-physical processes (radiation heat transfer, moisture condensation, polymer deterioration, and solid material behavior), which ultimately affect the mechanical performance of the material. In a previous study [6], these mechanisms were computationally modeled using COMSOL® Multiphysics modeling software. An equivalent homogenized model is generated from previous research [6], so that it can be used at the structural level efficiently while maintaining the same accuracy. The micromechanics RVE model has been validated by UV/moisture exposure and mechanical experiment.

In Section “[Results and Discussion](#)”, a computational model of the SFMOMA façade panels is constructed, including all of deterioration mechanisms and solid continuum damage mechanism applied simultaneously. This effort consists of three steps: (i) use the theory of synergistic effects between ultraviolet exposure and moisture exposure degradation processes developed by the authors to generate a residual deterioration induced damage variable field, (ii) implement the residual damage field as the initiation of continuum damage model (CDM) at structure length scale, and (iii) recreate one 3D façade plate of the SFMOMA and perform parametric damage analysis. In the long term, the models developed in this study will be combined with life-cycle assessment (LCA) tools to better support sustainability focused design of new material, thus reducing costs and environmental impacts of the built environment.

More broadly, this paper expands the physics-based modeling thrust of the sustainable integrated materials, structures, and systems (SIMSS) framework proposed by

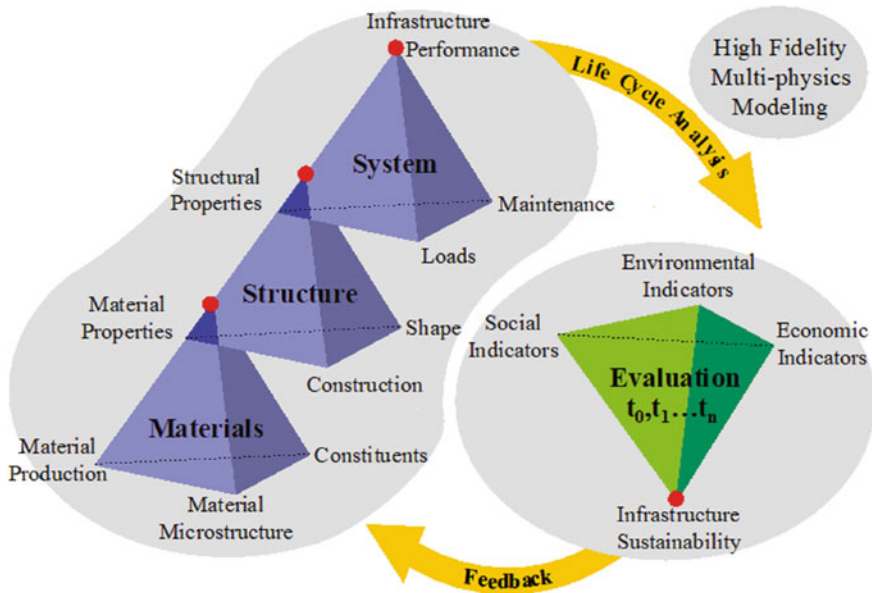


Fig. 1 Sustainable integrated materials, structures, and systems (SIMSS) framework adapted from [2]. (Color figure online)

Lepech et al. [2] and shown in Fig. 1. As seen, the SIMSS framework integrates multi-physics and multiscale considerations in the design of sustainable built environments. Specifically, the multiphysics models developed in this paper provide a foundation for the consideration and performance prediction of new building materials and elements (i.e., fiber-reinforced polymer composite elements) at the micromechanics level of the SIMSS paradigm, further advancing the fundamental design of sustainable built environments.

In Fig. 1, at the material level of the research, water condensation and polymer degradation models are established and calibrated separately. The synthetic model is calibrated after a single physics model is validated. From a comparative study of the three control groups, researchers discovered that the synthetic effect of moisture on polymer degradation can be fit into a Weibull cumulative distribution function family [7]. Hierarchical homogenized models [6] have been widely used to study damage in composites and guide design in structural components. However, their application in multiphysics models, which are as complicated as the proposed research, still waits to be explored and cultivated.

Multiphysics Modeling of GFRPS

Moisture Transportation

The model for moisture absorption used in this study is based on the conservation of mass, provided as Eq. (1)

$$\frac{\partial c}{\partial t} + \nabla \cdot (-D\nabla c) = R \quad (1)$$

where c is the moisture concentration, and R is the internal generation of moisture per unit volume per unit time. In this study, R is equal to zero since no moisture is internally generated within the composite materials. The diffusion coefficient tensor, D , is a diagonal matrix with its components calibrated with data obtained from homogenizing micromechanical state variables in [6, 7].

Hygroscopic swelling is an internal straining of the polymer composite caused by changes in moisture content. This strain can be calculated as shown in Eq. (2).

$$\varepsilon_{ij}^{(hs)} = \beta_h M_m (c_{mo} - c_{mo,ref}) \delta_{ij} \quad (2)$$

where β_h is the coefficient of hygroscopic swelling, M_m is the molar mass of the polymer resin, c_{mo} is the moisture concentration, and $c_{mo,ref}$ is the strain-free reference moisture concentration. δ_{ij} is the Kronecker delta function.

UV Radiation Model

Internal damage due to ultraviolet radiation exposure is caused by radiative heating, and the associated internal strains are caused by this internal heating. The net inward radiative heat flux, q^{rad} , is the difference between the irradiation, G , and the radiosity, J , shown in Eq. (3).

$$q^{rad} = G - J \quad (3)$$

The overall heat flux is then transferred to the solid material, following Eq. (4).

$$\rho C_p \frac{\partial T}{\partial t} + \nabla q = Q \text{ with } q = -k\nabla T \quad (4)$$

where C_p is the specific heat capacity of the polymer material, and q is the heat flux by conduction. Since inward heat flux and heat conduction both lead to temperature change, the total thermal strain can then be calculated following [8], and shown as Eq. (5).

$$\varepsilon_{ij}^{(T)} = \alpha(T - T_0) \delta_{ij} \quad (5)$$

where α is coefficient of thermal expansion of the polymer composite and T_0 is a reference temperature.

Solid Mechanics Model at Structural Level

To calculate the induced stress field resulting from moisture absorption and UV exposure, it is assumed that both the polymer matrix and fiber are isotropic, homogeneous, and elastic. Thus, the constitutive law follows [9] and is shown as Eq. (6) through Eq. (9)

$$\sigma_{ij} = C_{ijkl}\varepsilon_{kl} \quad (6)$$

where σ_{ij} and ε_{ij} in Eq. (6) are the Cauchy stresses and strain components, respectively. The fourth-order stiffness tensor C_{ijkl} is a function of the elastic modulus, E_i , Poisson's ratio, ν_i , the shear modulus, G_i . The strain is the superposition of mechanical, thermal, and chemical strain tensor [7].

$$\varepsilon_{ij} = \varepsilon_{ij}^{(M)} + \varepsilon_{ij}^{(T)} + \varepsilon_{ij}^{(hs)} \quad (7)$$

Strain-Based Fatigue Model

The strain-based fatigue model can be described by a relation between strain amplitude $\varepsilon_a = \varepsilon/2$ and fatigue life N . In this paper, a combined Basquin and Coffin-Manson model with Morrow's mean stress correction is applied to study the continuum damage model-related fatigue life. Morrow proposed a mean stress correction to the Basquin part of the combined Basquin and Coffin-Manson relation according to

$$\varepsilon_a = \frac{\sigma'_f - \sigma_m}{E} \cdot (2N_f)^b + \varepsilon'_f \cdot (2N_f)^c \quad (8)$$

where σ'_f is the fatigue strength coefficient, $\sigma_m = \frac{\sigma_{\min} + \sigma_{\max}}{2}$ is the mean stress of the load cycle, b is the fatigue strength exponent, ε'_f is the fatigue ductility coefficient, c is the fatigue ductility exponent, and E is the Young's modulus. N_f is the number of load reversals, and thus $2N_f$ is the number of full cycles. In Eq. (8)

$$\varepsilon = \begin{cases} \varepsilon_1, \varepsilon_1 \geq |\varepsilon_3| \\ \varepsilon_3, \varepsilon_1 < |\varepsilon_3| \end{cases} \quad (9)$$

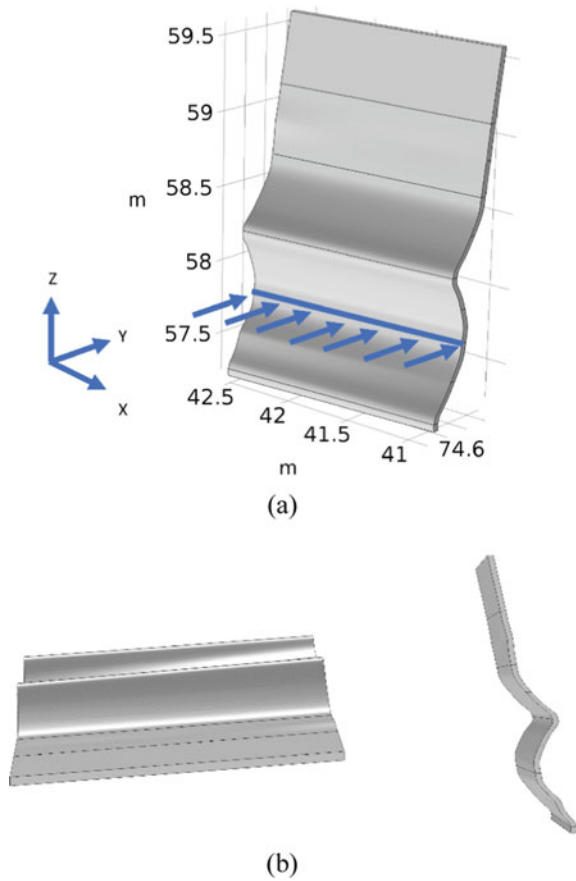
and

$$\sigma = \begin{cases} \sigma_1, \sigma_1 \geq |\sigma_3| \\ \sigma_3, \sigma_1 < |\sigma_3| \end{cases} \quad (10)$$

Results and Discussion

In this section, a finite element (FEM) model (see Fig. 2) of a SFMOMA façade plate is established, with its geometry model recreated based on a CAD model. The CAD model is imported from the building information model (BIM) of the SFMOMA façade. The analysis consists of three steps: (I) solves for curvilinear coordinates filed. (II) solves the thermo-chemical–mechanical problem of the model subject to 1000 hours of cyclic UV/moisture exposure for a scalar damage variable field. (III) solves the damage-fatigue problem of the deteriorated plate model under cyclic deformation. The equivalent outdoor exposure time can be correlated from laboratory exposure time and UV settings. Simplified UV correlation for accelerated UV experiments and natural weathering can be found in [10]. In previous study [11], the author has discussed how to solve step (I) and (II) on a sample plate. Also,

Fig. 2 a Geometry of one SFMOMA façade plate and displacement load. The load is applied in Y direction of global coordinates. b Left: Top view (XY view in global coordinates). Right: Side view (YZ view in global coordinates). (Color figure online)



the previous study discussed the continuum damage behavior of plate under time-dependent deformation loading using time dependent solver. In this study, a strain-based fatigue model is added to the previous model. As a result, damage-fatigue behavior is discussed in the step (III) using static solver (Fig. 3).

It is easy to see in Fig. 2, each SFMOMA façade plate is designed as an elegant surface but has very complicated curvature everywhere. However, in this situation, anisotropic material parameter tensor in all physics introduced in Section “**Multiphysics Modeling of GFRPS**” needs to be defined along the streamline where the global coordinate system is inapplicable. In the step (I), a coordinate system following the curves of the geometry is solved. In this coordinate system shown in Fig. 4, anisotropic material properties, anisotropic constrains and anisotropic physics can be defined in step (II) and (III).

In step (II) of this paper, only the irreversible degradation of the polymeric matrix is assumed to affect the material performance of the composites. Reversible moisture absorption and desorption are assumed to not play a role in weakening the material. To implement these assumptions, moisture causes strain and the stress field change is isolated from the data, solved from step (II), that will be imported to step (III) as the initiation of step (III). The deterioration model in Section “**Multiphysics Modeling of GFRPS**” is implemented in the FEM model. Diffusion coefficient tensor D_{ij} is homogenized from material length scale model in [6]. In previous research [6], the multiphysics model, which was experimentally calibrated and validated by the authors in [7] (see Fig. 3a), is used to build an RVE model for a single-layer, plain weave, woven polymer composite (see Fig. 3b) used in the construction of the facade of SFMOMA. The microstructure of the RVE is built using details of the micromorphology of the fiber-reinforced polymer composite panels supplied by Kreyser Associates for the SFMOMA façade [4, 5]. For the interface of this RVE, it

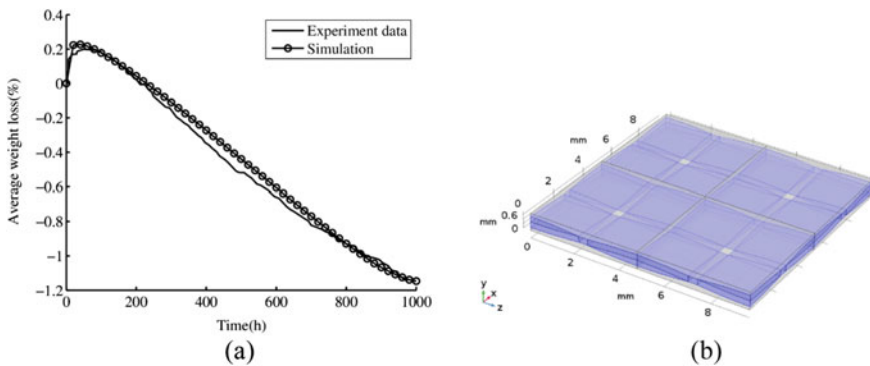
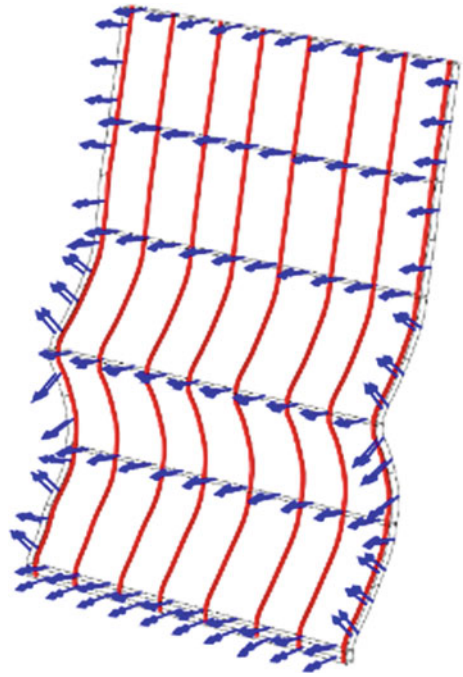


Fig. 3 **a** Experimentally determined and computationally simulated mass change of fiber-reinforced polymer composite specimens, as a function of time, subjected cyclic exposure in 6-h increments to both UV radiation and water condensation (experimental results from [17]). The comparison shows that the multiphysics model is able to capture the underlying synergy of these combined deterioration phenomena [7]. **b** Geometry of plain woven RVE [6]. (Color figure online)

Fig. 4 Curvilinear Coordinates. Red: vector field in material frame. Blue: Second basis vector (Y -axis) in curvilinear coordinates. (Color figure online)



is assumed that the glass fiber yarn and matrix are perfectly bonded. The model does not include the protective gel coat used in the actual building. Detailed parameter references can be found in Table 1.

In the model of step (III), the top and bottom surfaces are fully constrained. The two lateral surfaces are constrained by symmetric boundary conditions. The specific boundary where displacement is applied is shown in Fig. 2a. The applied displacement is 0, 5, -5 , and 0 mm for one cycle. The continuum damage model is implemented in a COMSOL external material library written in C code [16].

The authors want to emphasize that the target of Step (III) is to test the properties of only the GFRPs plate, not the façade-steel frame system. In reality, the façade is fixed on a steel frame. Displacement loads in 4 are very large and they will rarely occur. As

Table 1 Material parameters of the orthotropic woven glass fiber-reinforced polymeric composite model at structural length scale

Parameters	References
Stiffness tensor C_{ijkl}	[12]
Diffusion coefficient tensor D_{ij}	[6, 7]
Evolution function of scalar damage variable S_D	[8, 13]
Material parameter for CDM	[14, 15]
Material parameter for combined Basquin and Coffin-Manson model	[6, 7, 16]

a starting point for more broadly parametric studies, the damage initiation threshold of effective strain in this example is arbitrarily set to be a very low value at $1.05\text{e-}4$. In future studies, the damage parameters should be calibrated from experiments. Also, the simulation in step (II) assumes a situation that the GFRPs plate is not protected by gel coat.

The result of material degradation after step (II) and step (III) is shown in Figs. 5 and 6, respectively. The scalar damage variable S_D represents the defects in the local material. The damage variable is bounded by 0 and 1. $S_D = 0$ represents the undamaged material, while $S_D = 1$ means fully broken material into two parts. In the time-dependent deformation process, the damage variable S_D increases accumulatively and irreversibly. Figure 6 shows the contour of S_D on the surface of plate in both front and back view at the end of first cycle loading in step (III). From the back-surface view of Fig. 5, it shows that there is slightly deformation concentrated at the back of the plate. The damage variables in this region are less than 0.4.

After a full cycle of deformation, the much more severe damage accumulates at the two lateral sides and propagates into the center of the plate. Figure 7 shows the number of cycles to failure base on strain-life fatigue model in Eq. (8). In the figures, the location and minimum number of cycles to failure is labeled. Compare the contour of failure cyclic number with the damage contour after one cycle of displacement load, it is obvious that the weakest point from fatigue model falls in the high damage area ($S_D > 0.8$).

In future studies, the non-local effects of damage increment can be implemented into the CDM model to get mesh independent non-local damage analysis results. And the damage-fatigue model should be calibrated from experiments. This model is ready for further development to predict the performance of GFRPS under very high cycle fatigue.

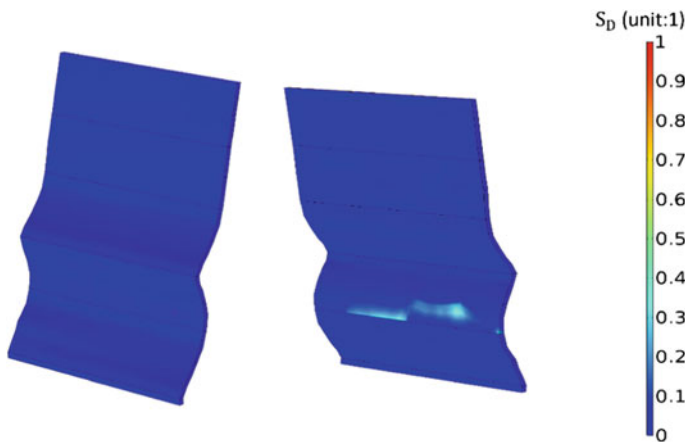


Fig. 5 Contour of scalar damage variable S_D (unit: 1) after environmental exposure, without prescribed deformation. Left: Top surface. Right: back surface. (Color figure online)

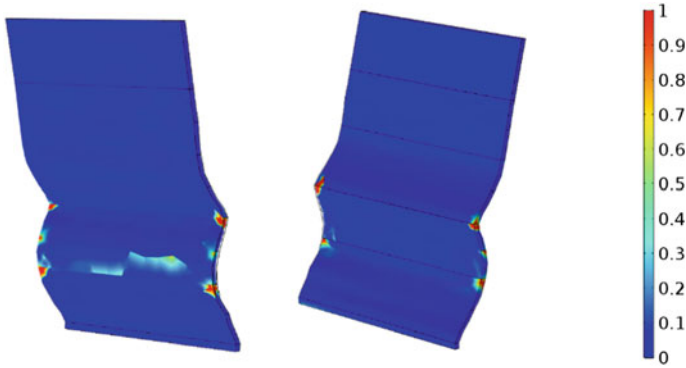


Fig. 6 Contour of scalar damage variable S_D (unit: 1) after environmental exposure and prescribed deformation. Left: Top surface. Right: back surface. (Color figure online)

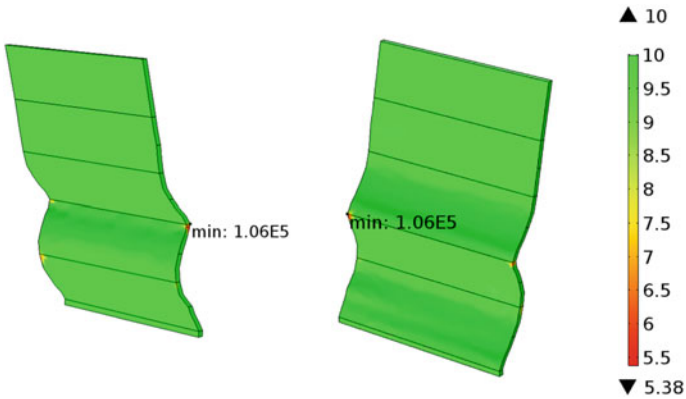


Fig. 7 Number of cycles to failure in \log_{10} . Left: Top surface. Right: back surface. (Color figure online)

Conclusion

This paper develops a thermo-chemical–mechanical model at the structural length scale of SFMOMA facade, using diffusion coefficient tensor and stiffness tensor homogenized from a plain-woven RVE at mesoscale length scale. The results show that environmental exposure causes material degradation, which leads to mild material performance weakening after 1000 h of accelerated cyclical UV/moisture exposure. Although these local material weakening are not fatal in limited hours, in the long term, their effect on the structural stability and the nucleation and propagation of fatal damage is considerable. The minimum number of cyclic loads from strain-based fatigue model is calculated and the weakest point is highlighted for the sample plate. Compare the contour of failure cyclic number with the damage contour after one

cycle of displacement load, it is obvious that the weakest point from fatigue model falls in the high damage area. This model can be incorporated into many commercial finite element codes for a sustainability study of composite structures/systems, e.g., [3]. In future work, the models developed in this study will be combined with life-cycle assessment (LCA) tools to better support sustainability focused design of new material, thus reducing costs and environmental impacts of the built environment.

Acknowledgements This work was supported by ExxonMobil through its membership in the Stanford Strategic Energy Alliance. The authors would also like to thank the Thomas V. Jones Engineering Faculty Scholarship at Stanford University for continued support. Computational support of this work has been provided by the John A. Blume Earthquake Engineering Center at Stanford University. The BIM data and material properties were obtained thanks to Kreysler & Associates, Snøhetta, Enclos and San Francisco Museum of Modern Art.

References

1. Hollaway LC, Teng JG (eds) (2008) Strengthening and rehabilitation of civil infrastructures using fibre-reinforced polymer (FRP) composites
2. Lepech M, Keoleian GA, Li VC (2007) Integrated structure and materials design for sustainable concrete transportation infrastructure
3. Wu J, Lepech M (2020) Incorporating multi-physics deterioration analysis in building information modeling for life-cycle management of durability performance
4. Kreysler & Associates, <https://www.kreysler.com/> (last check on May 5, 2020)
5. Enclos, <https://www.enclos.com/projects/san-francisco-museum-of-modern-art-expansion> (last check on May 5, 2020)
6. Li Z, Lepech M (2020) Environmental accelerated deterioration modeling of large glass fiber reinforced polymer composite structures/systems
7. Li Z, Lepech M (2019) Deterioration modeling of large glass fiber reinforced polymer composite structures/systems
8. Li Z, Ghosh S (2020) Micromechanics modeling and validation of thermal-mechanical damage in DER353 epoxy/borosilicate glass composite subject to high strain rate deformation
9. Jin H, Lu WY, Nissen A, Nelson K, Briggs T (2018) Mechanical properties of woven composites at ambient temperature
10. Shokrieh MM, Bayat A (2007) Effects of ultraviolet radiation on mechanical properties of glass/polyester composites. *J Compos Mater* 41(20):2443–2455
11. Li Z, Lepech M (2020) Development of a model of synergistic effects between deterioration mechanisms and damage in woven glass fiber reinforced polymeric composite structure. In: ASME international mechanical engineering congress and exposition. American Society of Mechanical Engineers
12. Zhang X, Li Z, Ghosh S, O'Brien D (2016) Parametric homogenization based continuum damage mechanics model for composites
13. Li Z, Ghosh S, Getinet N, O'brien DJ (2016) Micromechanical modeling and characterization of damage evolution in glass fiber epoxy matrix composites
14. Lemaitre J (2012) A course on damage mechanics
15. Murakami S (2012) Continuum damage mechanics: a continuum mechanics approach to the analysis of damage and fracture
16. COMSOL Multiphysics® v. 5.3a. www.comsol.com. COMSOL AB, Stockholm, Sweden
17. Kumar BG, Singh RP, Nakamura T (2002) Degradation of carbon fiber-reinforced epoxy composites by ultraviolet radiation and condensation

Assessing the Susceptibility of Existing Pipelines to Hydrogen Embrittlement



Tim Boot, Ton Riemslag, Elise Reinton, Ping Liu, Carey L. Walters, and Vera Popovich

Abstract With fossil fuels being phased out and growing global interest in a hydrogen economy, there is demand for re-purposing existing pipelines for transportation of hydrogen gas. However, hydrogen embrittlement (HE) can limit pipeline steel's performance. In this study, the effect of hydrogen on the mechanical properties of an X60 base metal (polygonal ferrite/pearlite) and its girth weld (acicular ferrite/pearlite) was measured with a novel slow strain rate tensile (SSRT) test in which hollow pipe-like specimens were internally pressurised with nitrogen and hydrogen gas from 0 to 100 bars. Results showed that exposure to H₂ gas at 100 bars reduced the ductility of the base metal by up to 40% and the weld metal by 14%. Reduction in cross-sectional area (%RA) reduced by up to 28% in the base metal and 11% in the weld metal. Fracture surface analysis showed micro-void coalescence as well as quasi-cleavage fracture characteristic of HE. Susceptibility to HE was also observed in the form of secondary longitudinal and internal transverse cracks.

Keywords Hydrogen embrittlement · Pipeline steel · In situ testing · Fractography

Introduction

Hydrogen has never been as relevant globally as it is today since it is a cost-effective and energy-efficient way of transporting and storing energy sustainably. Implementation of hydrogen as an energy carrier is now being pushed for on a global scale like in the European Green Deal [1]. A cost and material-efficient way of transporting hydrogen would be to use existing natural gas pipelines. Since natural gas is expected to be phased out in the coming decades, these pipelines would become available to transport hydrogen instead. However, current knowledge of the effect of hydrogen

T. Boot (✉) · T. Riemslag · E. Reinton · C. L. Walters · V. Popovich
TU Delft Department of Materials Science and Engineering, Mekelweg 2, Delft, Netherlands
e-mail: t.boot@tudelft.nl

P. Liu
IntecSea BV, Wilhelmina van Pruysenweg 2, Den Haag, Netherlands

gas on pipeline steels and especially their weldments is lacking. This research studies the effects of hydrogen gas on the mechanical properties of X60 pipeline steel and its girth weld and assesses the HE susceptibility of both.

Through several mechanisms, gaseous hydrogen that is absorbed into a steel will embrittle it, reducing its ductility and possibly its strength. This is called hydrogen embrittlement (HE). Because hydrogen diffuses towards regions of high stress triaxiality like notches and areas in front of crack tips, they can cause extra deterioration of mechanical properties leading to a loss of strength [2]. The fracture mechanisms related to HE can be fundamentally plastic in nature, even though the behaviour that is observed in the material on a larger scale appears to be brittle [3–5]. Standardised tests to assess HE susceptibility of metals are listed in, for example, ASTM F1624 [6], which describes an incremental step loading technique to assess a HE threshold stress, and ASTM G142, which describes a slow strain rate tensile (SSRT) test to assess HE susceptibility [7]. Both tests are performed in situ in a hydrogen environment to eliminate any desorption of hydrogen during the test. SSRT or constant load tests are preferred since a high strain rate can limit HE, because sufficient hydrogen diffusion towards regions of high stress triaxiality is required in order to cause HE [8]. Many studies in the literature test their materials in situ in an electrochemical charging environment. This environment is often not representative of gaseous hydrogen environments because the hydrogen concentrations are often much higher in an electrochemical charging environment, as shown by Zhao et al. [9].

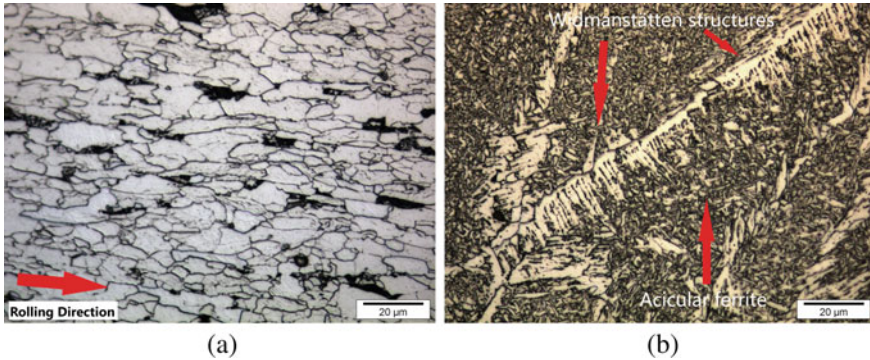
To assess the susceptibility of pipelines that are used to transport gaseous hydrogen, it is necessary to adequately represent the hydrogen environment that would be in place during operation. Therefore, in situ SSRT testing in a high-pressure gaseous hydrogen environment is desired. In this research, a novel test setup was designed that allows for assessment of both the base and weld metals to HE. The design removes the need of a pressure vessel around the sample to charge it with hydrogen, thereby providing an easy and cost-effective way of testing metals in a hydrogen environment and greatly reducing the amount of gas required. Fracture surface investigation by microscopy (SEM) was used in this study to determine HE mechanisms.

Materials

This research considers an X60 pipeline steel, including a girth weld that was made according to industrial pipeline welding procedures. The alloy contents of both steels are listed in Table 1. The start/stop regions of the girth weld as well as the longitudinal weld regions were both excluded from the research. The base metal as shown in Figure 1a consists of mainly polygonal ferrite with small regions of pearlite with an average grain size on the order of 10 μm . The weld metal, shown in Figure 1b, has a microstructure consisting of mainly acicular ferrite and pearlite with grain boundary Widmanstätten ferrite. The acicular ferrite phase makes up the bulk of the weld microstructure with an average grain size on the order of 1 μm . The base metal

Table 1 Alloy contents the base and weld metals in weight %, where rest is Fe

Element	C	Mn	Si	Cr	Nb	Al	P	S	Rest
Base metal	0.06	1.66	0.26	0.06	0.04	0.04	<0.01	<0.01	97.88
Weld metal	0.07	1.45	0.58	0.05	0.01	0.01	0.01	0.01	97.81

**Fig. 1** **a** Microstructure of the base metal with ferrite (white) and pearlite (black) regions, and **b** the weld metal where the acicular and Widmanstätten structures are indicated. (Color figure online)

and weld metal have an HV1 hardness of 200 ± 3.7 and 248 ± 9.9 , respectively. The X60 base metal has a yield strength of 461 MPa.

Methods

A novel test setup and specimen were designed in this research. The specimens, shown in Fig. 2, were machined from the X60 pipeline wall in longitudinal direction. Both specimens consisting of just the base metal as well as specimens including the girth weld zone were manufactured, in which case the weld metal was present in the notch region. The blunt notch was introduced to the specimen to enforce fracture in the weld zone without causing high stress triaxialities that will result in exaggeration of the HE susceptibility. A blind hole was machined into the specimen, so that it can be charged with hydrogen gas from the inside. In this way, the specimen acts as a miniature pipe where hydrogen gas is present on the inside, while the outside is left open to the laboratory environment. The specimens are machined in such a way that the girth weld remains in the same orientation as in the pipeline.

SSRT testing was performed on smooth base metal specimens, notched base metal and weld metal specimens under the following conditions: without any internal pressure, at 100 bar N_2 pressure and at different levels (0–100 bar) of H_2 pressures.

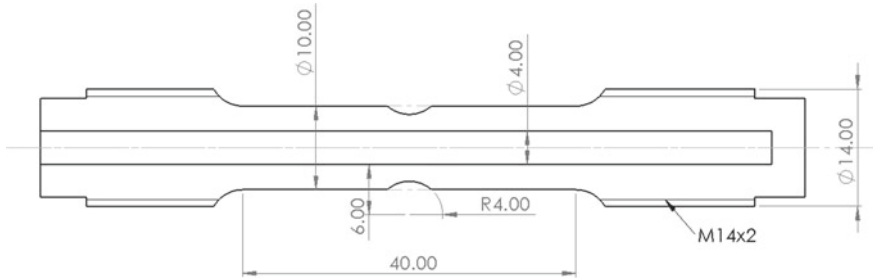


Fig. 2 Schematic drawing of the samples used in this research. Dotted lines in the notch represent the measurements of smooth samples

Every test was performed at a cross-head displacement speed of 1.5 mm/h, which translates to a strain rate of 10^{-5} s^{-1} for smooth (un-notched) specimens. Tests that were performed in H_2 gas also included a pre-charging step in which the sample was kept at the testing pressure for 17 h before the start of the test. At least three repetitions were tested for each combination of sample type and pressure, after which the tensile data was analysed. Fractographic analysis was performed in a SEM to highlight the differences in fracture behaviour between the different specimens. Furthermore, the area of each fracture surface was measured using a digital optical microscope so that reduction in cross-sectional area (%RA) could be calculated.

In addition to the experimental setup, two FEA models were created to support the design. Both models use the same geometry based upon an axisymmetric mesh type to model the cylindrical notched specimen. A diffusion model was used to estimate the pre-charging time, and a deformation model was created to model the behaviour of the sample during the tensile test. The deformation model shows the emergence of a zone inside the specimen wall where the stress triaxiality approaches 0.75 as a consequence of the notch and the axisymmetry of the specimen.

Results and Discussion

A significant influence of H_2 on the base metal and weld metal was found from tensile data and SEM fractography.

Effect of Hydrogen on Mechanical Properties

Representative tensile curves of the different specimens are shown in Fig. 3. The most prominent effect of hydrogen that was found is a reduction in ductility of both the base and weld metal. As can also be seen in Table 2, no apparent influence of the

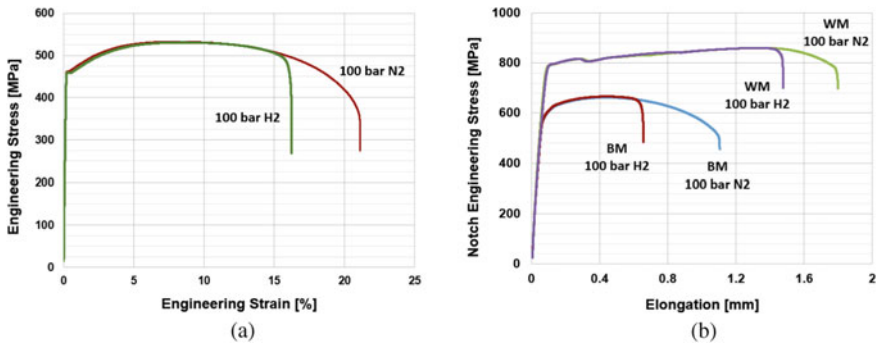


Fig. 3 **a** Tensile curves of smooth BM samples tested in 100 bar N₂ and 100 bar H₂, and **b** tensile curves of notched BM and notched WM samples tested in 100 bar N₂ and 100 bar H₂. (Color figure online)

hydrogen on either the yield strength or the UTS of the specimens was discovered. The notched base metal specimens lost 40.4% in ductility when subjected to 100 bar hydrogen gas. This is higher than that of the smooth specimens (27%), because of the higher stress triaxialities present in the notch root compared to a smooth specimen. Both the yield strength and the UTS of the weld metal exceed that of the base metal by approximately 30%. Moreover, the elongation of the weld metal samples at failure is 1.72 mm compared to 1.08 mm for the base metal. This means the weld metal is stronger and more ductile than the base metal, but still retains much more ductility when subjected to gaseous hydrogen. The specimens only lose 14% in ductility at 100 bar of H₂ pressure. This is because the weld metal has a more refined microstructure of small interlocking acicular ferrite grains and a high grain boundary density. This structure creates maximum resistance to brittle crack propagation which leads to a smaller reduction in elongation under influence of hydrogen compared to the base metal.

The notched base metal specimens showed a 28% reduced %RA in H₂ as compared to N₂. The weld metal specimens show an 11% decrease in %RA in H₂ compared to N₂. The %RA values for the weld metal were constant over different pressures, meaning that the trend that was observed of a reduction in elongation with increasing hydrogen pressure is not present in the %RA values. This can be explained by looking at the fracture surfaces.

Fractography

The reduction in %RA values for both steels in hydrogen is a direct consequence of the HE fracture mechanisms. Martin et al. study characteristic smooth features and ridges that arise on so-called quasi-cleavage (QC) fracture surfaces that is typical of hydrogen enhanced fracture [4, 5]. They observe nanoscale dimples on the smooth

Table 2 Yield strength, UTS, elongation until failure and %RA values for the notched base metal (BM) and weld metal (WM) specimens. Values are averages \pm standard deviations of each set

	Notched BM 100 bar N ₂	Notched BM 100 bar H ₂	Notched WM 100 bar N ₂	Notched WM 100 bar H ₂
Yield strength (MPa)	626 \pm 24.6	631 \pm 18.3	810 \pm 5.9	812 \pm 4.8
UTS (MPa)	674 \pm 15.1	677 \pm 12.9	857 \pm 6.4	861 \pm 1.5
Elongation at failure (mm)	1.08 \pm 0.04	0.64 \pm 0.06	1.72 \pm 0.16	1.48 \pm 0.11
Reduction (%)	–	40.4	–	14.0
%RA	72.1 \pm 1.0	52.0 \pm 2.0	48.2 \pm 1.5	43.0 \pm 3.0
Reduction (%)	–	28.0	–	10.8

QC areas and a high density of dislocations under the fracture surface, pointing to a very localised ductile mode of failure rather than a brittle one. As can be seen in Fig. 4a, similar features were found on the base metal samples tested under 100 bar H₂ pressure. Such highly localised ductile failure acts before larger-scale necking and causes a reduction in %RA for the specimens. Both smooth and notched base metal specimens showed near identical %RA values, which could be explained by their fracture surfaces that were both QC dominated. It was also found that notched specimens show more secondary cracking perpendicular to the fracture surface in the zones of large triaxiality, but this does not influence the cross-sectional area.

As shown in Fig. 4b, weld specimens were found to only partially fracture in the QC mode before reverting back to a more ductile microvoid coalescence (MVC) mode near the outer surface. The size of the QC fracture area was found similar for

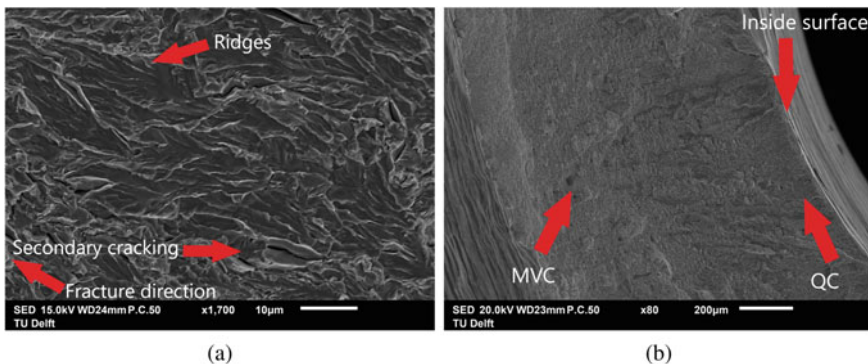


Fig. 4 **a** SEM image of the fracture surface of a smooth base metal sample tested in 100 bar H₂ gas showing smooth quasi-cleavage (QC) facets with ridges and secondary cracking, and **b** an overview of the fracture surface of a weld sample tested in 100 bar H₂ gas showing partial QC and partial microvoid coalescence (MVC) cracking. (Color figure online)

weld specimens tested in different hydrogen pressures, which could explain their similar %RA values. Because of the weld metal's small grain size, no characteristic QC features could be identified on their fracture surfaces. The fact that there is a transformation from QC to MVC fracture could be attributed to a more abruptly occurring fracture in the weld metal specimens. The base metal specimens showed a more gradual decrease in force before failure, pointing to a slower advancing crack front, while a faster advancing crack in the weld specimens might not have allowed the QC fracture mode to form over the entire fracture surface.

Secondary cracking (of up to 100 μm) parallel to the fracture surface was frequently observed in smooth samples tested in H_2 gas. In a gaseous hydrogen environment, the sensitivity of the material to sharp defects increases, and crack initiation can be accelerated. It is suspected that the secondary cracks initiated from machining defects. Although the inside surface of the smooth samples was mechanically reamed, it was still sensitive to accelerated cracking in a hydrogen environment. The outside surface, which was not reamed, did not show any signs of secondary cracking. It should be noted that notched specimens showed less secondary cracking, likely because strain in these samples was localised to the notch root where fracture occurred.

Conclusions

The following conclusions can be drawn from this research:

- A novel SSRT setup featuring in situ hydrogen gas and samples representing miniature pipelines was successfully applied for assessing HE susceptibility of both base and weld metals of pipeline steels.
- Both the base and weld metal were found susceptible to HE. Although the behaviour before fracture (yield strength and UTS) was found to be unaffected by H_2 , a substantial reduction in ductility of 40% for base and 14% for weld metal under 100 bar H_2 was observed.
- The weld metal was found less susceptible to HE due to its fine acicular ferrite microstructure with its inherent resistance to crack propagation.
- Reduction in elongation of the weld specimens showed an increasing trend with increasing H_2 pressure. It should also be noted that %RA values did not show this trend, which indicates that %RA is not a suitable parameter to assess the effect of hydrogen pressure on the extent of HE.

Some aspects that are essential for the assessment of pipelines to HE were not researched in this work, but remain as recommendations for future work:

- Pipelines rarely operate in high plastic strain regimes, but rather at lower strains in cyclic loading. Therefore, cyclic testing is necessary to fully characterise the effect of HE on a pipeline in its application environment.

- Existing pipelines can have existing defects. These could be simulated by altering the notch geometry in the samples discussed in this work and thus result in useful fracture toughness data.

Details regarding the development of the test setup will be discussed in a follow-up journal paper.

Acknowledgements The authors would like to thank IntecSea for sharing their knowledge to make this research possible.

References

1. European Commission, “A European Green Deal” (2020). Retrieved from https://ec.europa.eu/info/strategy/priorities-2019-2024/european-green-deal_en. Accessed on 30 Aug 2020
2. Song EJ, Baek SW, Nahm SH, Baek UB (2017) Notched-tensile properties under high-pressure gaseous hydrogen: comparison of pipeline steel X70 and austenitic stainless type 304L, 316L steels. *Int J Hydrogen Energy* 42:8075–8082
3. Lynch SP (2011) Hydrogen embrittlement (HE) phenomena and mechanism. In: *Stress corrosion cracking: theory and practice*, vol i, pp 90–130
4. Martin ML, Fenske JA, Liu GS, Sofronis P, Robertson IM (2011) On the formation and nature of quasi-cleavage fracture surfaces in hydrogen embrittled steels. *Acta Materialia* 59(4):1601–1606
5. Martin ML, Robertson IM, Sofronis P (2011) Interpreting hydrogen-induced fracture surfaces in terms of deformation processes: a new approach. *Acta Materialia* 59(9):3680–3687
6. ASTM (2018) F1624-12, standard test method for measurement of hydrogen embrittlement threshold in steel by the incremental step loading technique. American Association for Testing and Materials
7. ASTM (2013) G142, standard test method for determination of susceptibility of metals to embrittlement in hydrogen containing environments at high pressure, high temperature, or both. American Association for Testing and Materials
8. Wang M, Akiyama E, Tsuzaki K (2005) Crosshead speed dependence of the notch tensile strength of a high strength steel in the presence of hydrogen. *Scripta Materialia* 53:713–718
9. Zhao, Seok MY, Choi IC, Lee YH, Park SJ, Ramamurty U, Suh JY, Jang JZ (2015) The role of hydrogen in hardening/softening steel: influence of the charging process. *Scripta Materialia* 107:46–49

Combined Ab Initio and Experimental Study of Hydrogen Sorption in Dual-Phase Steels



Saurabh Sagar, Vera Popovich, Pascal Kömmelt, and Poulumi Dey

Abstract Controlling the detrimental effect of hydrogen on the mechanical behaviour of advanced high strength steels is decisive for their application. Precipitates in steels can be useful in irreversibly trapping the hydrogen atoms, thereby preventing their diffusion to critical regions in the microstructure where they can be most detrimental. In this work, the capability of precipitates of transition metals in limiting the amount of diffusible hydrogen has been examined. A combined ab initio–experimental approach was used to study the hydrogen sorption in two DP800 steel grades with different concentrations of titanium and vanadium using cyclic voltammetry. Under the same charging conditions, diffusible hydrogen concentration was found to be higher in the vanadium grade as compared to the titanium grade. Scanning electron microscope characterisation revealed a more compact layer of oxide on the vanadium grade which contributed to more hydrogen absorption on the surface. Density Functional Theory calculations were performed to determine the trapping strength of precipitates of titanium and vanadium. C vacancy in titanium carbide was found to be the strongest hydrogen trap, but the C vacancy formation energy was much lower in vanadium carbide. At finite temperatures, however, both precipitates are experimentally known to be off-stoichiometric. Our DFT-based finding of the titanium grade being irreversible hydrogen trap is thus in agreement with the experimental results.

S. Sagar (✉) · V. Popovich · P. Dey
Department of Materials Science and Engineering, TU Delft, Delft, The Netherlands
e-mail: s.sagar@tudelft.nl

V. Popovich
e-mail: V.Popovich@tudelft.nl

P. Dey
e-mail: P.Dey@tudelft.nl

P. Kömmelt
Tata Steel Europe, Amsterdam, The Netherlands
e-mail: pascal.kommelt@tatasteelurope.com

Keywords Advanced high strength steels · Hydrogen trapping · Cyclic voltammetry · Density functional theory

Introduction

Advanced High Strength Steels are widely used for manufacturing structural components in the automotive industry owing to their high strength and ductility [1, 2]. It has been well documented that when hydrogen is absorbed in steels, even in small concentrations of the order of 1 ppm, it causes a severe loss in strength and ductility [3–6]. The intricate phenomena of deterioration of mechanical properties of a material in the presence of hydrogen is commonly referred as hydrogen embrittlement (HE). The exact role of hydrogen in causing embrittlement is ambiguous and various mechanisms of embrittlement have been proposed to explain instances of hydrogen embrittlement [7]. However, it is understood that diffusible hydrogen which can evolve out from specimens during exposure at service temperature is responsible for HE of high strength steels [6]. Diffusible hydrogen tends to migrate towards critical regions in the microstructure such as the crack tip zone or voids surrounding inclusions, where it exerts its deleterious effect. One possible solution to improving a material's resistivity to hydrogen embrittlement is to limit the amount of diffusible hydrogen by introducing benign hydrogen *traps* in the microstructure [6, 8].

Microstructural features such as defects or impurities play a crucial role in HE. A hydrogen atom interacts with the distinct electrostatic fields around defects and can possibly bind to such a location. When the hydrogen atom is strongly bound at a site, such that it does not diffuse out upon the applied conditions of stress and temperature, it is said to be irreversibly trapped. On the other hand, reversibly trapped hydrogen atoms can diffuse out at ambient conditions and contribute to embrittlement. The distinction between a reversible and irreversible trap is not exact and depends upon the environment that the material is in. However, it has been established that defects such as grain boundaries and dislocations are reversible traps [9, 10], while second phase particles such as precipitates of alloying elements may be irreversible traps depending upon several factors such as size, stoichiometry and type of interface [11, 12]. It has been reported in a number of experimental studies [11, 13] that steels with uniform distributions of fine carbide and nitride precipitates indeed have a lower susceptibility to HE. Therefore, carbides and nitrides of transition metals seem to be prime candidates for improving resistivity to HE of steels and consequently significant research has been dedicated to this aspect. Takahashi et al. directly imaged hydrogen isotopes in VC and TiC precipitates using atom probe tomography [14]. These studies revealed that most hydrogen atoms are located within the precipitate and along the broad interfaces of these precipitates. Laureys et al. [12] compared the trapping capability of TiC and VC precipitates through hot and melt extraction in generic Fe-C-Ti and Fe-C-V steel specimen. It was observed that hydrogen was trapped more strongly in Fe-C-Ti than in the Fe-C-V alloy, indicating that TiC was a stronger trap. However, a direct comparison of trapping capacity of TiC and VC

precipitates could not be obtained through these methods. In a first-principles study on the interaction of hydrogen with TiC precipitates in α -Fe, Di Stefano et al. found that a large variety of possible trapping sites for hydrogen are possible [15]. Such sites can be associated with the particle-matrix interface, misfit dislocation cores and other defects at the interface as well as interstices and carbon vacancies within the precipitate. Trapping at the semi-coherent interfaces was moderate while carbon vacancies in the interior of the precipitate were the strongest traps.

While atomistic simulations have been able to provide fundamental insights into the trapping of hydrogen, a direct correlation between the theoretical and experimental findings has not been established thus far. In the present work, we validate the potential usability of precipitates of titanium and vanadium in irreversibly trapping absorbed hydrogen in dual-phase steels, thereby limiting the amount of diffusible hydrogen. Trapping of hydrogen in TiC, TiN, VC and VN was studied using Density Functional Theory (DFT)-based ab initio calculations and the precipitate with better trapping efficiency was identified. Simultaneously, two steel grades with different concentrations of titanium and vanadium were loaded with hydrogen under the same conditions and the amount of diffusible hydrogen was subsequently measured using Cyclic Voltammetry (CV). CV has recently been applied for measuring diffusible hydrogen in electrochemically hydrogen charged specimen [16–18]. The method is relatively fast and simple and can be performed with in situ hydrogen charging, which is a big advantage over hot extraction methods in which a large proportion of hydrogen can diffuse out between the charging and measurement steps [18].

Materials and Methods

Two commercial grades of DP800 steel with different concentrations of titanium and vanadium were chosen for this study. The chemical composition of the two grades is listed in Table 1. As can be seen, the grade with higher titanium concentration has been referred to as T-Grade while the other is called V-Grade. By selecting steel grades with these specific compositions, it was possible to ensure that a high number density of titanium carbides and nitrides would be present in the T-grade and similarly vanadium precipitates in V-grade. Carbides in dual phase steel are known to be in the size range of 4 nm up to 50 nm for (semi) coherent nano-precipitates while incoherent precipitates ranging up to 150 nm have been reported [19, 20].

Dual-phase (DP) steels studied herein have a microstructure of mainly soft ferrite with islands of hard martensite dispersed throughout the matrix. For both materials,

Table 1 Concentration of elements of interest in the two DP800 steel grades

	C (wt%)	N (ppm)	Ti (wt%)	V (wt%)
Grade T	0.148	45	0.020	0.004
Grade V	0.158	44	0.009	0.062

grain sizes were in the range of 5–10 μm . Semi-quantitative XRD analysis of the steel samples revealed a microstructure consisting of $4 \pm 1\%$ retained austenite for both grades.

Experimental Approach

CV experiments with in situ hydrogen charging were conducted on both materials to compare the amount of diffusible hydrogen sorbed under specified charging conditions. The as-received material had been hot-dip galvanised beforehand. For performing electrochemical experiments, the steel specimens were de-coated by immersing in 1:1 HCl solution following which they were rinsed with isopropanol. One side of the sample, which was to be exposed to the electrolyte was sanded and polished to a surface finish of 1 μm . A three-electrode setup was used with the steel sample as the working electrode, a double junction saturated Ag/AgCl reference electrode (+0.197 V versus SHE) and a platinum mesh as counter electrode. A circular area of diameter 1 cm on the sample surface was exposed to the electrolyte. The electrolyte consisted of a solution of 8 g/l thiourea in 1 M NaOH. Thiourea is an organo-sulphur compound with the formula $\text{SC}[\text{NH}_2]_2$ which is known to function as a recombination poison. It facilitates the retention of protons in the electrolyte during the test thereby promoting the ability of atomic hydrogen to enter steel.

Electrochemical measurements were performed with a Bio-Logic VSP300 potentiostat. The test consisted of three steps—(i) two initial cyclic voltammetry scans from -1.25 V to -0.2 V at a scan rate of 10 mV/s. The first scan was done to ensure that the sample surface was consistent for all tests, while the second scan was used to generate a baseline. (ii) Immediately after the second CV scan, cathodic hydrogen charging was carried out by applying a constant potential of -1.25 V. Charging was done for three different durations of 30, 60 and 120 min. (iii) For detecting the absorbed hydrogen, hydrogen charging was followed by two CV scans. For quantifying the amount of hydrogen, instead of the CV scans, a static potential of -0.9 V versus Ag/AgCl was applied to the cell after hydrogen charging. The choice of this potential was based on results from CV experiments and will be explained later. Three sets of tests were performed for each grade.

Theoretical Approach

DFT calculations were performed to compute the trapping efficiency of TiC, TiN, VC and VN. All DFT calculations were carried out using the Vienna Ab initio simulation package (VASP) [21, 22]. The generalised gradient approximation (GGA) parameterised by Perdew, Burke and Ernzerhof [23] was employed for exchange correlation. The Methfessel-Paxton method [24] with a smearing width of 0.15 eV has been used for the Fermi surface smearing. The single-electron wave functions

were expanded by using plane waves up to an energy cutoff of 500 eV. All lattice vectors and atomic positions were relaxed until the residual forces acting on each atom were below 0.01 eV/Å. An energy tolerance of 10^{-6} eV was defined as a convergence criterion for the self-consistent electronic loop. The Brillouin zone was sampled using Monkhorst-Pack grids [25] with a $24 \times 24 \times 24$ grid for the 8 atom unitcell and $6 \times 6 \times 6$ grid for the 64 atom supercell.

The formation energy of studied compounds was calculated as the difference between the total energy of the compound phase and that of its constituent elements. Equation 1 depicts this relation, where M is the metal atom, X is a carbon or nitrogen atom and a and b are the number of atoms of the two constituents of the compound.

$$E_f = E[M_a X_b] - aE[M] - bE[X] \quad (1)$$

To determine the propensity of the compounds to form vacancies, the vacancy formation energy was calculated as:

$$E_v = E[MX_{\text{vacancy}}] - E[MX_{\text{perfect}}] + \mu_X^0 \quad (2)$$

where μ_X^0 is the chemical potential of an X atom in BCC iron. Hydrogen trapping was characterised by the solution energy of hydrogen at a trap site. Solution energy was calculated at interstitial sites and vacancies according to:

$$E_H = E[MXH] - E[MX] - \frac{1}{2}\mu_{H_2}^0 \quad (3)$$

where $\mu_{H_2}^0$ is the ground state energy of a hydrogen molecule. The energies used in Eqs. 1, 2 and 3 were obtained from DFT calculations.

Results and Discussion

Experimental Results

The voltammograms obtained for the both materials, before and after hydrogen charging are shown in Fig. 1. The shape of the voltammogram was similar for both materials which was to be expected owing to the similarity in composition of the materials. For the uncharged specimen, two peaks were formed in the anodic direction. The first peak, labelled as A1 occurs at a potential of -0.86 V. This peak was also observed in the work of Ozdirik et al. and was determined to be arising from thiourea related oxidation processes [18]. The second peak, A2, was observed at a potential of -0.7 V and is attributed to the oxidation of iron. Oxidation of iron was visible on the sample as a reddish-brown layer over the exposed area. When the sweep direction was reversed, peak B1 formed in the cathodic branch at a potential

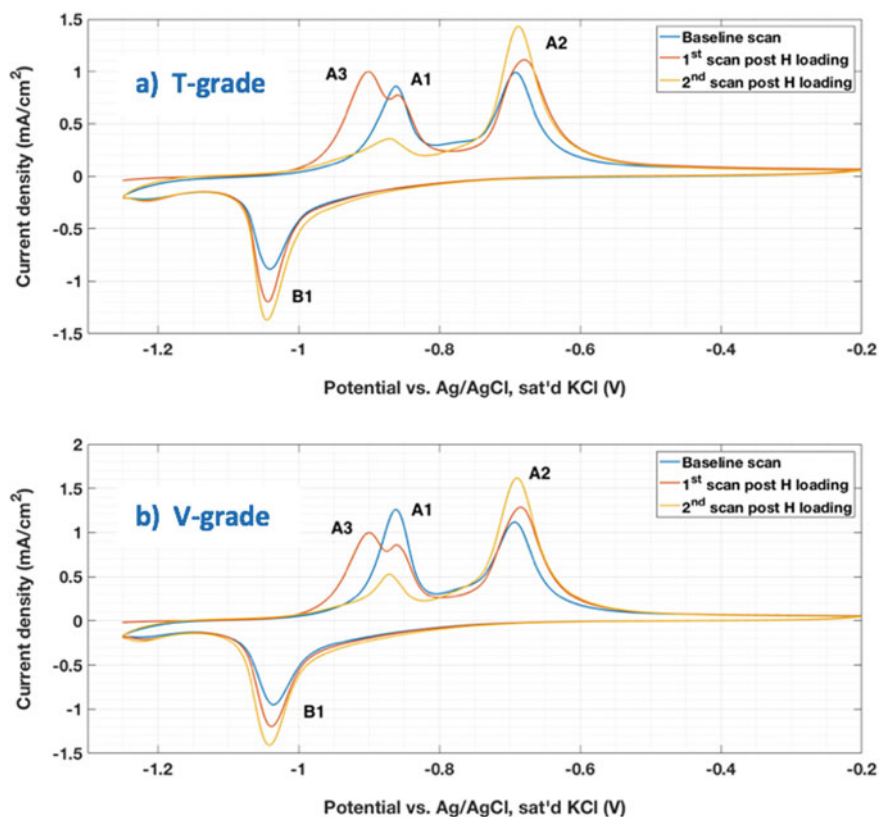


Fig. 1 CV plots obtained a T-grade and a V-grade sample. Baseline scan was done on uncharged samples followed by two scans after 30 min of hydrogen charging. (Color figure online)

of -1.04 V. The areas of peak A2 and B1 were found to be quite similar. Thus, peak B1 was arising due to the reduction of iron which was oxidised during the forward scan.

For the hydrogen charged samples, peaks A1, A2 and B1 occurred at exactly at the same potentials as the uncharged case. However, a previously unknown peak A3 was formed at a potential of -0.9 V for both materials. This potential corresponds to the evolution of hydrogen. During the charging step, hydrogen was evolved from the electrolyte. The hydrogen atoms were first adsorbed or chemisorbed on the sample surface and subsurface followed by diffusion into the bulk where it may get trapped. Thus, peak A3 is attributed to diffusible hydrogen that is desorbed from the specimen. Hydrogen that is detected via this method includes contributions from surface and subsurface sites and possibly reversible traps, such as grain boundaries, in the bulk of the specimen. Upon subsequent scanning, the hydrogen related peak disappeared, which suggested that hydrogen was completely desorbed during the previous scan. Peak A1 which was attributed to thiourea is also diminished significantly. This is to

be expected as some thiourea from the electrolyte is consumed to prevent hydrogen recombination.

For quantification of the absorbed hydrogen, current transients obtained from the potentiostatic discharging step were integrated. The potential was chosen as -0.9 V, which was the potential at which the hydrogen peak had formed. Although discharging was done for a duration of 30 min, after an instantaneous rise in current, it began to drop significantly and within 100 s, it was almost zero. For this reason, the current-time plot was integrated up to 100 s. The surface charge density thus obtained was divided by the charge on an electron to obtain the number density of electrons. As each electron reacts with one hydrogen atom, the number of hydrogen atoms is equal to that of electrons. The number density of hydrogen atoms was then divided by the atomic density of iron to yield the concentration of hydrogen in atomic ppm. A comparison of hydrogen content with charging duration for the two materials is presented in Fig. 2. The observed diffusible hydrogen content in V-grade steel was consistently higher (by around 25%) than in T-grade. Since the phase compositions are similar for both materials, the bulk diffusion constants for hydrogen in both materials is expected to be the same. Hence, kinetics of diffusion does not play a role in the observed difference in hydrogen concentration. It is also notable that the scatter in values obtained for T-grade was consistently higher than that in V-grade.

SEM imaging of the sample post experiments revealed an oxide layer on both materials are shown in Fig. 3. The thickness of the oxide layer was around $2 \mu\text{m}$ for both materials. However, V-grade steels exhibited a uniform oxide layer throughout the activated area while that for T-grade steels was sparse and irregular. Upon contrasting the oxide film morphology against the measured hydrogen content, it was seen that the material with a larger scatter in data had a more irregular oxide morphology. As the oxide layer on T-grade was more susceptible to irregularities, the number density of hydrogen trap sites on the surface would also vary significantly between multiple samples, which possibly led to a large scatter in the

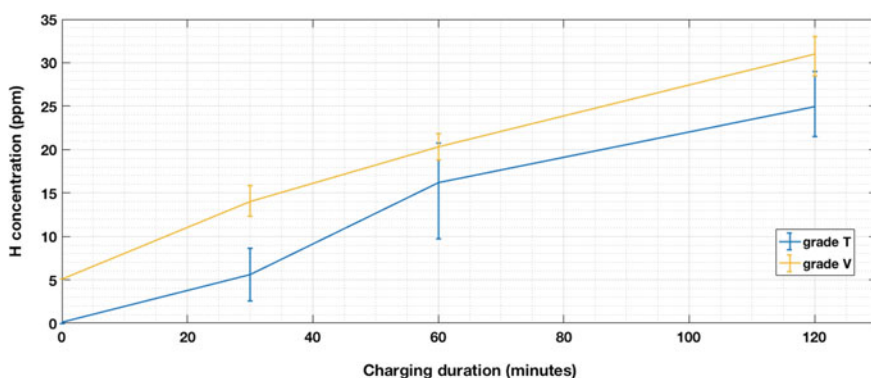


Fig. 2 Comparison of diffusible hydrogen content in both grades as measured from potentiostatic discharging experiments. Hydrogen content in V grade was consistently higher than in T grade samples. (Color figure online)

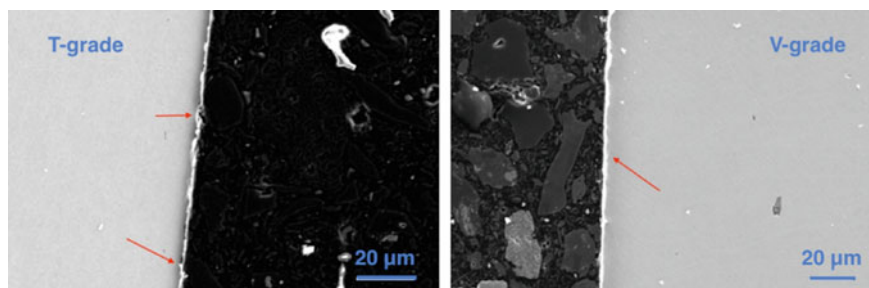


Fig. 3 Oxide layer morphology on samples of both grades. The arrows on T-grade indicate voids at the oxide-metal interface. (Color figure online)

measured hydrogen content. This observation therefore offers evidence for trapping of hydrogen by the oxide layer. Additionally, the dense layer on V-grade would offer more trap sites, and correspondingly, more hydrogen was absorbed by this grade.

DFT Results

Both titanium carbide/nitride and vanadium carbide/nitride crystallise in the rock salt crystal structure (Fig. 4). The equilibrium lattice parameters, formation energy and vacancy formation energy obtained for the four compounds are listed in Table 2. The values obtained for lattice parameter and formation enthalpy are comparable with previously reported works [26–28] and the references used therein. The formation of each compound is exothermic indicating the phases are stable. However, the vacancy formation energy in both titanium compounds as well as VN is endothermic, indicating that these compounds would remain stoichiometric (with respect to C and N) in the absence of any kind of applied plastic strain and at zero temperature. This

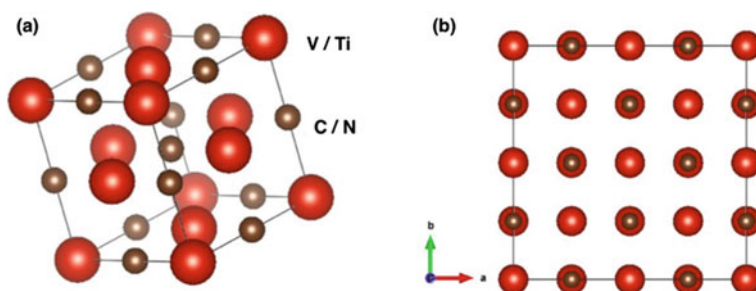


Fig. 4 **a** Unit cell of the studied compounds depicting the rocksalt type crystal structure. Simulations were carried out on $2 \times 2 \times 2$ supercells **(b)** generated by repeating the unit cells twice along each lattice vector. (Color figure online)

Table 2 Structural parameters and energies of the studied compounds from calculations on a $2 \times 2 \times 2$ supercell

Parameter	Compound			
	TiC	VC	TiN	VN
Lattice Constant (Å)	4.33	4.15	4.25	4.12
Structure Formation Energy (eV/f.u)	-9.44	-6.32	-14.08	-8.16
Vacancy Formation Energy (eV)	1.29	-0.24	2.44	1.16

is in contrast to VC, which is known to precipitate in the off-stoichiometric V_4C_3 composition [29].

Hydrogen solution energies in the studied compounds were firstly calculated at the interstitial sites. As the octahedral sites are fully occupied by C or N atoms, only the tetrahedral sites can accommodate hydrogen atoms. As can be seen from Table 3, hydrogen solubility at interstitial sites was endothermic, indicating that occupation of these sites by hydrogen is a thermally activated process. Hydrogen solubility in a C/N vacancy within the precipitate was also calculated according to Eq. 3. Hydrogen solution energy is negative for all compounds, indicating exothermic dissolution in vacancies. Comparison with interstitial sites clearly shows that vacancies within a precipitate are stronger traps for a hydrogen atom as compared to tetrahedral interstices. A carbon vacancy in TiC is seen to have the strongest affinity for hydrogen. Vacancy-hydrogen complex formation energy is the energy required to form a C/N vacancy in the compound and the energy required to dissolve a hydrogen atom in the vacancy. The C vacancy formation in VC was found to be exothermic, unlike the other compounds (refer to Table 2).

The values obtained for vacancy-hydrogen complex formation energy would suggest that irreversible trapping during hydrogen charging should be more effective in the V-grade material, and consequently, the amount of diffusible hydrogen should be lesser than the T-grade. This is, however, in contradiction to the experimental results. Following are the key factors for the observed contradiction between theory and experiments. It has already been mentioned that the oxide layer is contributing to some reversible hydrogen trapping which can alter the results of the experiments. Other possible reasons are the finite temperature effects and/or the elastic strain between coherent precipitates and matrix. To elaborate, C (N) vacancy formation is energetically feasible at finite temperatures because of configurational entropy, which

Table 3 Hydrogen trapping related energetics in studied compounds for a $2 \times 2 \times 2$ supercell

Parameter	Compound			
	TiC	VC	TiN	VN
H-Solution energy in interstices (eV)	1.33	1.99	2.30	1.23
H-Solution energy in vacancy (eV)	-0.96	-0.06	-0.38	-0.26
Vacancy-H complex formation energy (eV)	0.33	-0.30	2.06	0.90

holds true for both Ti and V precipitates. Furthermore, the elastic strain between coherent precipitates embedded in matrix plays a significant role in driving out C or N atoms from the precipitates to the surrounding matrix, even at zero temperature. Hence, Ti and V precipitates are expected to be off-stoichiometric with respect to C or N. It is worthwhile to mention here that the Ti or V precipitates are indeed experimentally observed to be off-stoichiometric [29, 30]. This implies that the DFT-based finding of TiC and TiN precipitates being stronger hydrogen traps than their V counterpart is consistent with the experimental observation.

Conclusions

This work was focused on examining the capability of precipitates in trapping hydrogen thereby limiting the amount of diffusible hydrogen in the material. CV results showed that the amount of diffusible hydrogen after two hours of hydrogen charging was approximately 25% higher in V-grade steel than in T-grade steel. However, the method has a shortcoming since the oxide layer formed during CV scans can also contribute to reversible trapping of hydrogen. It is thus recommended that for establishing the method for measuring hydrogen sorption, the contribution of oxide layer to trapping needs to be quantified. DFT calculations were carried out to compare the hydrogen trapping efficiency of carbides and nitrides of vanadium and titanium. It was observed that H solubility in interstitial sites was endothermic, indicating that trapping was unfavourable. However, H solubility in a C/N vacancy was found to be exothermic. C vacancy in TiC was found to be the stronger trap than that in VC (-0.91 eV versus -0.06 eV for VC). This was, however, counterbalanced by the high C vacancy formation energy in TiC. It is noteworthy that both compounds are experimentally known to be off stoichiometric. It is thus concluded from our combined ab initio—experimental approach that the contribution of precipitates of Ti in irreversible hydrogen trapping is higher in T-grade steel, than the corresponding role played by V precipitates in the V-grade steel.

Acknowledgements We would like to thank Tata Steel Europe for supporting the work through knowledge sharing and providing materials for the study.

References

1. Horvath CD (2010) Advanced steels for lightweight automotive structures. In *Materials, design and manufacturing for lightweight vehicles*. Woodhead Publishing Series in Composites Science and Engineering, pp 35–78
2. Hilditch T, de Souza T, Hodgson P (2015) Properties and automotive applications of advanced high-strength steels (AHSS). In *Welding and joining of advanced high strength steels (AHSS)*. Woodhead Publishing, Cambridge, pp 9–28

3. Fan D, Pielet H (2018) Bend failure mechanism of zinc coated advanced high strength steel. *ISIJ Int* 58:1528–1544
4. Hagihara Y, Shobu T, Hisamori N, Suzuki H, Takai K, Hirai K (2012) Delayed fracture using CSRT and hydrogen trapping characteristics of V-bearing high-strength steel. *ISIJ Int* 52(2):298–306
5. Mohtadi-Bonab M, Eskandari M, Rahman K, Ouellet R, Szpunar J (2016) An extensive study of hydrogen-induced cracking susceptibility in an API X60 sour service pipeline steel. *Int J Hydrogen Energy* 41:4185–4197
6. Takai K, Watanuki R (2003) Hydrogen in trapping states innocuous to environmental degradation of high-strength steels. *ISIJ Int* 43(4):520–526
7. Barrera O, Bombac D, Chen Y, Daff T, Galindo-Nava E, Gong P, Haley D, Horton R, Katzarov I, Kermodé J, Liverani C, Stopher M, Sweeney F (2018) Understanding and mitigating hydrogen embrittlement of steels: a review of experimental, modelling and design progress from atomistic to continuum. *J Mater Sci* 53:6251–6290
8. Bhadeshia H (2016) Prevention of hydrogen embrittlement in steels. *ISIJ Int* 56(1):24–36
9. McEniry EJ, Hickel T, Neugebauer J (2017) Hydrogen behaviour at twist {110} grain boundaries in α -Fe. *Philosophical Trans Royal Soc A* 375(2098)
10. Hagi H, Hayashi Y (1987) Effect of dislocation trapping on hydrogen and deuterium diffusion in iron. *Trans Jpn Inst Met* 28(5):368–374
11. Cui Q, Wu J, Xie D, Wu X, Huang Y, Li X (2017) Effect of nanosized NbC precipitates on hydrogen diffusion in X80 pipeline steel. *Materials* 10(7)
12. Laureys A, Claeys L, Seranno TD, Depover T, Eeckhout EVd, Petrov R, Verbeken K (2018) The role of titanium and vanadium based precipitates on hydrogen induced degradation of ferritic materials. *Mater Charact* 144:22–34
13. Valentini R, Solina A, Matera S, De Gregorio P (1996) Influence of titanium and carbon contents on the hydrogen trapping of microalloyed steels. *Metall Mater Trans A* 27:3773–3780
14. Takahashi J, Kawakami K, Kobayashi Y, Tarui T (2010) The first direct observation of hydrogen trapping sites in TiC precipitation-hardening steel through atom probe tomography. *Scripta Mater* 63(3):261–264
15. Stefano DD, Nazarov R, Hickel T, Neugebauer J, Mrovec M, Elsässer C (2016) First-principles investigation of hydrogen interaction with TiC precipitates in alpha-Fe. *Phys Rev B* 93(18)
16. Uluc V (2015) Hydrogen sorption and desorption properties of Pd-alloys and steels investigated by electrochemical methods and mass spectrometry. TU Delft, Netherlands
17. Flores KSE (2019) Study of hydrogen sorption/desorption effect on austenitic iron-based alloys. TU Delft, Netherlands
18. Ozdirik B, Depover T, Vecchi L, Verbeken K, Terryn H, Graeve ID (2018) Comparison of electrochemical and thermal evaluation of hydrogen uptake in steel alloys having different microstructures. *J Electrochem Soc* 165(11):787–793
19. Kamikawa N, Hirohashi M, Sato Y, Chandiran E, Miyamoto G, Furuhashi T (2015) Tensile behavior of ferrite-martensite dual phase steels with nano-precipitation of vanadium carbides. *ISIJ Int* 55(8):1781–1790
20. Li CH, Chen CY, Tsai SP, Yang (2019) Microstructure characterization and strengthening behavior of dual precipitation particles in Cu-Ti microalloyed dual-phase steels. *Mater Design* 166
21. Kresse G, Hafner J (1993) Ab initio molecular dynamics for open-shell transition metals. *Phys Rev B* 48(17):13115–13118
22. Kresse G, Furthmüller J (1996) Efficient iterative schemes for ab initio total-energy calculations using a plane-wave basis set. *Phys Rev B* 54(16):11169–11186
23. Perdew JP, Burke K, Ernzerhof M (1996) Generalized gradient approximation made simple. *Phys Rev Lett* 77(18):3865–3868
24. Methfessel M, Paxton A (1989) High-precision sampling for Brillouin-zone integration in metals. *Phys Rev B* 40(6):3616–3621
25. Monkhorst HJ, Pack JD (1976) Special points for Brillouin-zone integrations. *Phys Rev B* 13(12):5188–5192

26. Restrepo SE, Di Stefano D, Mrovec M, Paxton AT (2020) Density functional theory calculations of iron—vanadium carbide interfaces and the effect of hydrogen. *Int J Hydrogen Energy* 45(3):2382–2389
27. Yang R, Zhu C, Wei Q, Du Z (2016) Investigations on structural, elastic, thermodynamic and electronic properties of TiN, Ti₂N and Ti₃N₂ under high pressure by first-principles. *J Phys Chem Solids* 98:10–19
28. Li H, Zhang L, Zeng Q, Guan K, Li K, Ren H, Liu S, Cheng L (2011) Structural, elastic and electronic properties of transition metal carbides TMC (TM = Ti, Zr, Hf and Ta) from first-principles calculations. *Solid State Commun* 151(8):602–606
29. Epicier T, Acevedo D, Perez M (2008) Crystallographic structure of vanadium carbide precipitates in a model Fe-C-V steel. *Phil Mag* 88(1):31–45
30. Dong B-X, Qiu F, Li Q, Shu S-L, Yang H-Y, Jiang Q-C (2019) The synthesis, structure, morphology characterizations and evolution mechanisms of nanosized titanium carbides and their further applications. *Nanomaterials* 9(1152)

Stress Corrosion Cracking of TRIP Fe₃₉Mn₂₀Co₂₀Cr₁₅Si₅Al₁ (at. %) High Entropy Alloy



P. Varshney, R. S. Mishra, and N. Kumar

Abstract Stress corrosion cracking (SCC) can adversely affect the life of any engineering component. The study of high entropy alloys (HEA) shows excellent mechanical properties but SCC susceptibility is unknown. We have studied SCC behavior of a transformation-induced-plasticity (TRIP) Fe₃₉Mn₂₀Co₂₀Cr₁₅Si₅Al₁ (at. %) HEA in 3.5 wt% NaCl solution using slow strain-rate tensile testing (SSRT) on smooth tensile specimens along with the electrochemical behavior of the alloy. The microstructural characterization of the alloy was carried out in as-received condition and after corrosion test using advanced characterization tools including X-ray photoelectron spectroscopy. The polarization test of the alloy done in 3.5 wt% NaCl solution revealed corrosion current density as 8.05×10^{-8} A/cm², markedly lower than the 304 stainless steel (76×10^{-8} A/cm²). The pitting potential of the alloy was 0.089 V. The SSRT result shows a decrease in the elongation and ultimate tensile strength. Further, experiments are in-progress to understand mechanistic origin of decrease in ductility of the alloy.

Keywords Corrosion · Stress corrosion cracking · High entropy alloy · Slow strain rate tensile test

P. Varshney · N. Kumar (✉)

Department of Metallurgical and Materials Engineering, The University of Alabama, Tuscaloosa, AL 35487, USA

e-mail: nkumar@eng.ua.edu

P. Varshney

e-mail: pvarshney@crimson.ua.edu

R. S. Mishra

Department of Materials Science and Engineering, University of North Texas, Denton, TX 76203, USA

e-mail: Rajiv.Mishra@unt.edu

© The Minerals, Metals & Materials Society 2021

TMS 2021 150th Annual Meeting & Exhibition Supplemental Proceedings,

The Minerals, Metals & Materials Series,

https://doi.org/10.1007/978-3-030-65261-6_67

Introduction

Stress corrosion cracking (SCC) is a phenomenon in which corrosive environment and tensile stress (internal or external) acting on the material play a crucial role in the material deformation or fracture [1]. External stresses include monotonic load, low amplitude cycling whereas internal stresses correspond to the stresses introduced during processing of the material, i.e., cold working, welding. The SCC mechanism suggests that cracks nucleate and coalesce together to form a bigger crack and propagate through the material leading up to fracture of a material. The failure in SCC is sudden and poses a significant threat to structures and life [2, 3]. For instance, in nuclear power plants, the operating temperature is very high and high-energy radiation environment that provides satisfactory conditions for the SCC [4]. The failure of any component due to SCC may lead to radiation leakage and sudden fracture of the material can cost even human lives. To counter SCC, researchers have designed advanced alloys [5]. For instance, Dutta et al. mention in their work that nuclear power plants use austenitic steels (304, 316), Alloy 600, Alloy 800, and Alloy 690 as the tube materials for steam generators. However, in austenitic steels, chloride-induced SCC is a major concern that led to replacement of some of these alloys with better alloys [6]. Zinkle et al. in their published work have stated that Alloy 600 contains 78% Ni and is highly susceptible to SCC even in pure water that led to the use of Alloy 690 in place of Alloy 600 as it provided better resistance to SCC [5].

Conventionally, the alloy contains one principal element, and the remaining elements are present in minor proportion. For instance, Al 2045 alloy, contains aluminium as its principal alloying element. Similarly, different alloys like Mg, Ti, Cu, Ni alloys have one principal element. In 1995, a new alloying concept emerged considering multiple principal alloying elements and led to the development of a new class of alloys referred to as high-entropy alloys (HEA) [7]. The HEAs show the excellent properties that make these alloys potential candidates for various critical applications. A review of published literature on HEA over one and half decades suggests that some of the HEAs show an excellent combination of mechanical and electrochemical properties [8–10]. However, to date, there is no work reported addressing SCC behavior of HEAs.

In this work, we studied a newly designed $\text{Fe}_{39}\text{Mn}_{20}\text{Co}_{20}\text{Cr}_{15}\text{Si}_5\text{Al}_1$ TRIP HEA. The published work so far on this alloy suggests that the alloy contains hcp (ϵ) and fcc (γ) phase. The hcp (ϵ) phase is harder than fcc (γ) phase and is responsible for the increased strength. The studied HEA show excellent mechanical properties, but many of the properties are still unexplored and need to be understood. The focus of the current work is on the SCC behavior of the alloy. To understand the SCC behavior, we have carried out experiments using linear polarization technique, scanning electron microscopy technique, and slow strain-rate testing (SSRT), and corresponding results are reported here.

Experimental

Material Processing Route

The HEA Fe₃₉Mn₂₀Co₂₀Cr₁₅Si₅Al₁ studied in this paper was produced by vacuum arc melting in a cold-copper crucible. The chamber was filled with Ar at 1 atm before melting the pure metals. The pure metal composition was Fe₃₉Mn₂₀Co₂₀Cr₁₅Si₅Al₁ (at. %). The as-cast alloy was homogenized at 900 °C for 2 h followed by water quenching. The produced alloy was warm rolled at 500 °C until 70% reduction. The dimensions of the rolled alloy plate were 50 × 25 × 5 mm³. The rolled alloy was further cut into thin sheets of thickness 1.2–1.4 mm using wire electrical discharge machining (EDM) from Mitsubishi for further characterization.

Microstructural, Electrochemical, and SCC Characterization

Microstructure

In this work, 1.5–2.0 mm thick sheets were used to machine out specimens of size 10 × 5 mm², polished from 240 (abrasive grit size) to 0.05 μm surface finish using colloidal silica solution. The polished specimen was etched using aqua regia etchant. Optical micrographs (Amscope-ME520TA) were used for grain size determination. Another polished specimen was characterized for the phase identification and phase fraction determination using X-ray Diffraction (XRD) technique (Philips X'Pert MRP) operated at 40 kV, 30 mA having a Cu source. The data was analyzed using EVA software for phase determination and TOPAS software for the phase fraction determination.

Linear Polarization and Passive Layer Characterization

A specimen of 22 mm diameter and 1.5 mm thickness size was used to study the corrosion behavior by performing a linear polarization test using Gamry 1010 E. The specimen was mirror-polished to 0.05 μm surface finish using colloidal silica. The specimen was cleaned with acetone to remove impurity and grease content from the surface before starting the test. The test was performed in 3.5 wt% NaCl solution with potential ranging from –0.5 V to 1 V with a scan rate of 0.167 mV/s. The corroded sample was characterized using scanning electron microscopy (SEM) of APREO S to understand the microstructural characteristics of the corroded sample including pit size and morphology.

The information concerning the chemical composition in the film was obtained using X-ray photoelectron spectroscopy (XPS) of Kratos AXIS 165 having Al Kα X-ray source, operated at 15 kV and 10 mA. The pressure maintained in the chamber

was $\sim 10^{-7}$ torr. The survey spectra were generated at 160 eV pass energy to get the elemental information present in the corroded sample (linear polarized). The analysis of the data was performed using CasaXPS software.

Slow Strain Rate Tensile Test (SSRT)

The specimen of gauge section $5.00 \times 3.07 \text{ mm}^2$ having a thickness of 1.2 mm was machined out using a micro mill from the HEA sheet. The specimen was polished using the standard metallographic technique from 240 (abrasive grit size) to $0.05 \mu\text{m}$ using a colloidal silica solution. The machined sample was tested using the universal tensile testing set up of ADMET. One tensile specimen was tested in air and another with the same dimension in the presence of 3.5 wt% NaCl solution. The cross-head velocity for both the test was $6.45 \times 10^{-5} \text{ mm/s}$.

Results and Discussion

Figure 1 shows the optical micrograph of the $\text{Fe}_{39}\text{Mn}_{20}\text{Co}_{20}\text{Cr}_{15}\text{Si}_5\text{Al}_1$ HEA, etched with aqua regia. The analysis of the micrograph provided the average grain size as $220 \mu\text{m}$. Figure 2 shows the XRD data plot for $\text{Fe}_{39}\text{Mn}_{20}\text{Co}_{20}\text{Cr}_{15}\text{Si}_5\text{Al}_1$ HEA. The analysis of the XRD data revealed the existence of two phases, i.e., fcc (γ) and hcp (ϵ) phases consistent with information available in the published literature [11–15]. The phase fraction of γ and ϵ phases were $\sim 24\%$ and $\sim 76\%$, respectively. The lattice parameter for the γ phase was estimated to be $a = 3.6 \text{ \AA}$, and for ϵ phase $a = 2.54 \text{ \AA}$ and $c = 4.12 \text{ \AA}$. Nene et al. in his work on $\text{Fe}_{39}\text{Mn}_{20}\text{Co}_{20}\text{Cr}_{15}\text{Si}_5\text{Al}_1$ reported 2 phases, i.e., γ and ϵ . The phase fractions reported in their work was different from what was observed in this work. It could be due to the difference in the processing parameter used in the rolling of the as-cast alloy [7]. TRIP literature suggests that the ϵ phase is hard and provides strength to the alloy [7, 14, 16].

Figure 3 shows the Tafel plot for the $\text{Fe}_{39}\text{Mn}_{20}\text{Co}_{20}\text{Cr}_{15}\text{Si}_5\text{Al}_1$ HEA. The obtained corrosion potential (E_{corr}) and corrosion current density (i_{corr}) values were -0.185 V and $8.05 \times 10^{-8} \text{ A/cm}^2$, respectively. The corrosion rate of the alloy was estimated to be $1 \times 10^{-3} \text{ mmpy}$ or 0.04 mpy . The pitting potential (E_{pit}) of the alloy was $+0.089 \text{ V}$. The E_{corr} and i_{corr} value indicated better corrosion resistance in 3.5 wt% NaCl solution in comparison with conventional alloys and some of the HEAs reported in the literature. The anodic polarization curve did not show the active-passive transition and directly attains the passivation. This shows better corrosion resistance towards uniform corrosion. Very close to E_{pit} , we observe the current fluctuation that can be attributed to the formation and repassivation of the metastable pits. The sudden increase in the current after E_{pit} relates to the formation of the stable pits. Kumar et al. in their work on $\text{Al}_{0.1}\text{CoCrFeNi}$ HEA have mentioned the presence of current

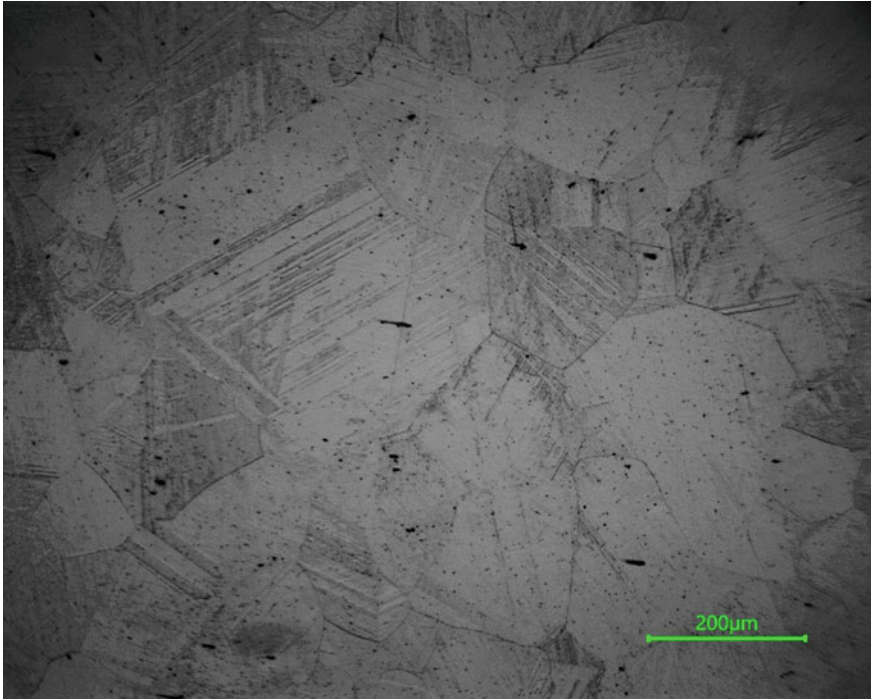


Fig. 1 Optical micrograph of the $\text{Fe}_{39}\text{Mn}_{20}\text{Co}_{20}\text{Cr}_{15}\text{Si}_5\text{Al}_1$ HEA after etching with aqua-regia. (Color figure online)

Fig. 2 XRD plot for $\text{Fe}_{39}\text{Mn}_{20}\text{Co}_{20}\text{Cr}_{15}\text{Si}_5\text{Al}_1$ HEA showing the two phases present. (Color figure online)

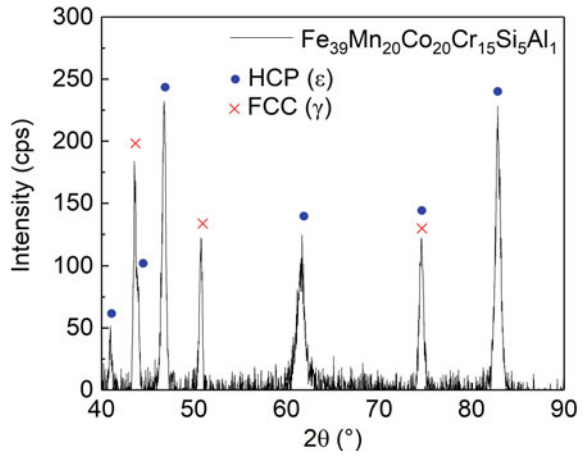
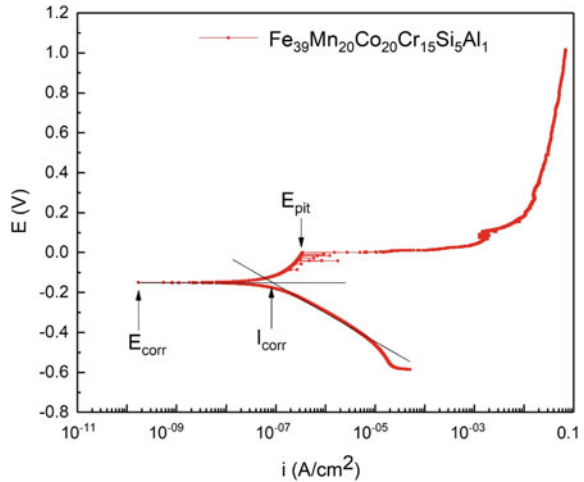


Fig. 3 Linear polarization plot for $\text{Fe}_{39}\text{Mn}_{20}\text{Co}_{20}\text{Cr}_{15}\text{Si}_5\text{Al}_1$ HEA in 3.5 wt% NaCl solution. (Color figure online)



fluctuation and attributed it to the formation and repassivation of the metastable pits [17].

Figure 4 shows the SEM micrographs of the linear polarized sample that shows the presence of a corrosion pit. The alloy showed extensive localized pitting. The size of the pit varied considerably. The smaller pits had a perforated layer on the surface whereas, in the bigger pit, we did not observe such layer. This might be due to the fracture and dissolution of the layer in general. In general, the perforated layer acts as a diffusion barrier and does not allow the dilution of the anolyte. This leads to the growth of the pit. The perforated layer fractures when the pit depth becomes very large and the growth conditions are sufficient for stable pit formation [18]. Pradhan et al. in their work on austenitic 304 stainless steel observed the fracture layer on the pit surface in case of larger pits [18].

The XPS is an effective method for the analysis of the elemental composition and its chemical state present in the alloy surface or the passive layer formed. The

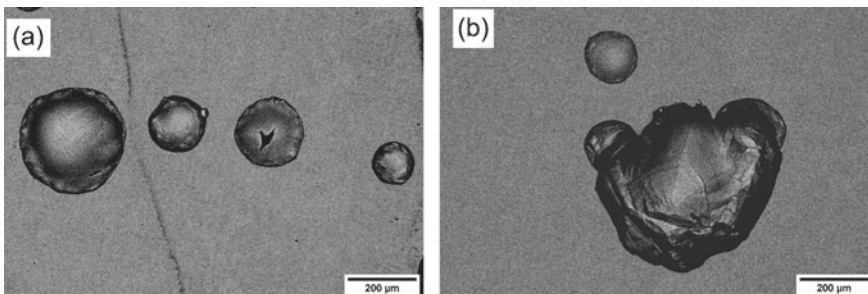


Fig. 4 SEM micrograph of the linear polarized sample showing the pits formed in 3.5 wt% NaCl solution

survey spectra give information about the elements present at the surface from a very low thickness of ~ 5 nm. Figure 5 shows the XPS survey spectra for linear polarized $\text{Fe}_{39}\text{Mn}_{20}\text{Co}_{20}\text{Cr}_{15}\text{Si}_5\text{Al}_1$ HEA. We observed the presence of Si, Cr, Mn, Co, Fe, O, and C. The carbon position in the spectra on comparison with standard spectra gives the accurate position of the other element and their oxidation states position. The presence of the metal elements and oxygen indicates the presence of a metal oxide layer. Biesinger et al. worked on the XPS analysis of the Cr, Mn, Fe, Co, and Ni for their oxides and hydroxides formation and observed metal oxides [19]. The in-depth analysis of the oxides present in the surface film and their quantification requires core level information as the surface film plays an important role in the SCC behavior of any alloy. Further analysis of the XPS spectra is currently underway to characterize and quantify the chemical make-up of the passivation film.

Figure 6 shows the stress-strain curve of $\text{Fe}_{39}\text{Mn}_{20}\text{Co}_{20}\text{Cr}_{15}\text{Si}_5\text{Al}_1$ HEA obtained after SSRT in air and 3.5 wt% NaCl solution. The yield strength (YS) and % elongation of the alloy, tested in air, were found to be 299 MPa and 23.5%, respectively. However, in 3.5 wt% NaCl solution, the YS and elongation were noted to be 293 MPa and 19.7%, respectively. In air, the ultimate tensile strength (UTS) was 641 MPa whereas in 3.5 wt% NaCl solution UTS was 586 MPa. So, we observed a decrease in UTS and ductility. The YS of the alloy is more or less the same and the alloy properties changed after the onset of plastic deformation. The decrease in elongation and tensile strength of the alloy may be related to the rupture of the stable passive film and subsequent SCC of the alloy. The rupture of the film will allow easy attacking of the Cl^- ion. Logan suggested the film rupture slip dissolution model and mentioned that the film rupture took place during SCC and dissolution of the metal caused the initiation of the crack [20].

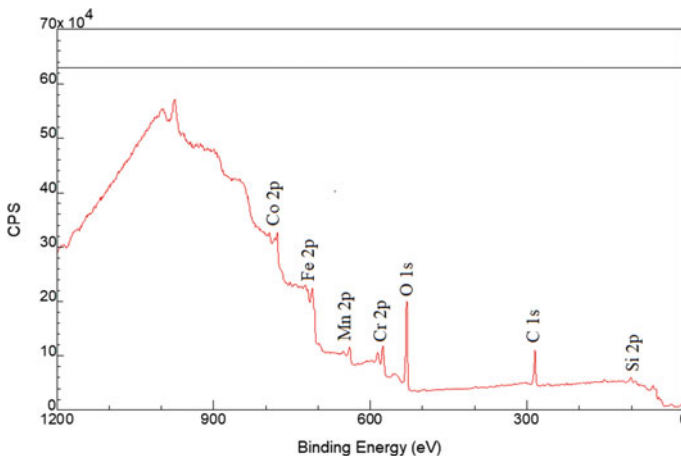
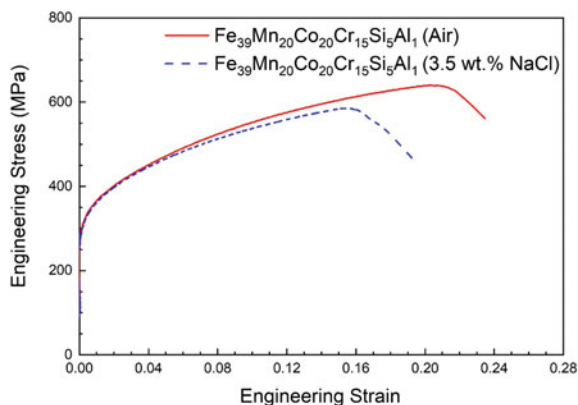


Fig. 5 XPS survey spectra of $\text{Fe}_{39}\text{Mn}_{20}\text{Co}_{20}\text{Cr}_{15}\text{Si}_5\text{Al}_1$ HEA at 160 eV. (Color figure online)

Fig. 6 Engineering stress—engineering strain curves obtained from the slow strain rate tensile test for $\text{Fe}_{39}\text{Mn}_{20}\text{Co}_{20}\text{Cr}_{15}\text{Si}_5\text{Al}_1$ HEA tested in air and 3.5 wt.% NaCl solution; initial strain-rate: $1.3 \times 10^{-5} \text{ s}^{-1}$. (Color figure online)



Conclusion

In this work, the $\text{Fe}_{39}\text{Mn}_{20}\text{Co}_{20}\text{Cr}_{15}\text{Si}_5\text{Al}_1$ HEA exhibited a coarse grain size of $220 \mu\text{m}$. The HEA shows better corrosion resistance towards the uniform corrosion resistance as corrosion current density is very low, i.e., $8.05 \times 10^{-8} \text{ A/cm}^2$ whereas the alloy showed extensive pitting as evident from the presence of large pits formed on the surface during the corrosion test. The XPS analysis showed the presence of metal oxides on the surface that could be the reason for the better uniform corrosion resistance. The SCC result showed a decrease in the UTS and % elongation that can be attributed to the fracture of the passive film. The detailed surface and fractographic study of the alloy will give a better understanding of the mechanism responsible for SCC of the alloy.

References

1. Popov BN (2015) Chapter 9—Stress corrosion cracking. In: Popov BN (ed) Corrosion engineering. Elsevier, Amsterdam, pp 365–450
2. Parkins RN (1989) The application of stress corrosion crack growth kinetics to predicting lifetimes of structures. *Corros Sci* 29:1019–1038
3. Turnbull A, McCartney LN, Zhou S (2006) A model to predict the evolution of pitting corrosion and the pit-to-crack transition incorporating statistically distributed input parameters. *Corros Sci* 48:2084–2105
4. Li Z, Lu Y, Wang X (2019) Modeling of stress corrosion cracking growth rates for key structural materials of nuclear power plant. *J Mater Sci* 55:439–463
5. Zinkle SJ, Was GS (2013) Materials challenges in nuclear energy. *Acta Mater* 61:735–758
6. Dutta RS (2009) Corrosion aspects of Ni–Cr–Fe based and Ni–Cu based steam generator tube materials. *J Nucl Mater* 393:343–349
7. Nene SS, Liu K, Frank M, Mishra RS, Brennan RE, Cho KC, Li Z, Raabe D (2017) Enhanced strength and ductility in a friction stir processing engineered dual phase high entropy alloy. *Sci Rep* 7:16167

8. Kumar N, Ying Q, Nie X, Mishra RS, Tang Z, Liaw PK, Brennan RE, Doherty KJ, Cho KC (2015) High strain-rate compressive deformation behavior of the $Al_{0.1}CrFeCoNi$ high entropy alloy. *Mater Des* 86:598–602
9. Komarasamy M, Kumar N, Tang Z, Mishra RS, Liaw PK (2014) Effect of microstructure on the deformation mechanism of friction stir-processed $Al_{0.1}CoCrFeNi$ high entropy alloy. *Mater Res Lett* 3:30–34
10. Ayyagari A, Hasannaemi V, Grewal H, Arora H, Mukherjee S (2018) Corrosion erosion and wear behavior of complex concentrated alloys: a review. *Metals* 8:603
11. Li Z, Pradeep KG, Deng Y, Raabe D, Tasan CC (2016) Metastable high-entropy dual-phase alloys overcome the strength–ductility trade-off. *Nature (London)*. 534:227–230
12. Nene SS, Sinha S, Frank M, Liu K, Mishra RS, McWilliams BA, Cho KC (2018) Unexpected strength–ductility response in an annealed, metastable, high-entropy alloy. *Appl Mater Today* 13:198–206
13. Nene SS, Frank M, Liu K, Sinha S, Mishra RS, McWilliams B, Cho KC (2018) Reversed strength-ductility relationship in microstructurally flexible high entropy alloy. *Scripta Mater* 154:163–167
14. Li Z, Tasan CC, Springer H, Gault B, Raabe D (2017) Interstitial atoms enable joint twinning and transformation induced plasticity in strong and ductile high-entropy alloys. *Sci Rep* 7:40704
15. Nene SS, Frank M, Liu K, Mishra RS, McWilliams BA, Cho KC (2018) Extremely high strength and work hardening ability in a metastable high entropy alloy. *Sci Rep* 8:9920–9928
16. Li Z, Tasan CC, Pradeep KG, Raabe D (2017) A TRIP-assisted dual-phase high-entropy alloy: grain size and phase fraction effects on deformation behavior. *Acta Mater* 131:323–335
17. Kumar N, Fusco M, Komarasamy M, Mishra RS, Bourham M, Murthy KL (2017) Understanding effect of 3.5 wt.% NaCl on the corrosion of $Al_{0.1}CoCrFeNi$ high-entropy alloy. *J Nucl Mater* 495:154–163
18. Pradhan SK, Bhuyan P, Mandal S (2019) Influence of the individual microstructural features on pitting corrosion in type 304 austenitic stainless steel. *Corros Sci* 158:108091
19. Payne BP, Grosvenor AP, Lau LWM, Gerson AR, Smart RSC (2011) Resolving surface chemical states in XPS analysis of first row transition metals, oxides and hydroxides: Cr, Mn, Fe, Co and Ni. *Appl Surf Sci* 257:2717–2730
20. Logan HL (1952) Film-rupture mechanism of stress corrosion. *J Res Natl Bur Stan* 48:99–105

Part XXVII
**Fatigue in Materials: Fundamentals,
Multiscale Characterizations
and Computational Modeling**

Microstructure and Fatigue Damage Evolution in Additive-Manufactured Metals Using Enhanced Measurement Techniques and Modeling Approaches



M. Awd, F. Walther, S. Siddique, and A. Fatemi

Abstract Process-induced microstructures have a high impact on the fatigue strength of engineering materials. Advanced materials testing builds the base for the design and manufacturing of reliable, high-performance products for various technical applications. Combining modern analytical and intermittent testing strategies with applied enhanced measurement techniques, i.e., physical instrumentation of testing specimens during loading, allows the characterization of process-structure-property relationships in various fatigue damage stages. Further, in situ mechanical testing in analytical devices like micro-computed tomography (μ -CT) enables the immediate correlation of material's physical reactions with the applied loading conditions. The focus of the presented studies. Using the proposed technique, the characterization of fatigue damage evolution and progression before failure depending on environmental as well as material specific microstructural characteristics is carried out. Investigations on additively manufactured Al alloys revealed the interaction between porosity and microstructure under very high-cycle fatigue (VHCF) loading conditions. Measurement-based fatigue damage tracking during testing of SLM aluminum alloys revealed the interaction between porosity and microstructure under loading in the very high-cycle fatigue (VHCF) regime. The grain boundary strengthening of the microstructure increased VHCF strength by 33%.

Keywords Selective laser melting · Platform heating · Remnant porosity · Plastic damage

M. Awd (✉) · F. Walther
Department of Materials Test Engineering (WPT), TU Dortmund University, Baroper Str. 303,
44227 Dortmund, Germany
e-mail: mustafa.awd@tu-dortmund.de
URL: <http://www.wpt-info.de>

S. Siddique
Department of Mechanical Engineering, The University of Lahore, Raiwind Road, Lahore 53700,
Pakistan

A. Fatemi
Mechanical Engineering Department, University of Memphis, 3720 Alumni Ave, Memphis, TN
38152, USA

Introduction

Laser powder bed fusion processes (LPBF) to which selective laser melting (SLM) belongs makes manufacturing of low volume overly complex components feasible, which otherwise are extremely expensive by conventional methods such as forming or machining [1]. SLM metallic parts are usually used in the aerospace industry as well as medical implants such as hip replacement or ball joint replacement. The highest advantage offered in these industries is the extremely short time from design to functional products [2]. To prevent contamination of the melt pool and build-up of impurities inside the structure, an inert gas such as argon is usually used [3]. The minimization of geometrical deviation, residual stresses, and distortions imposed the need of including support structures in the printing process. In addition, the platform on which the structure is being built is similar material. The component cleaning process follows by blowing air as well as separation from the support structure by electrical discharge machining (EDM) [1].

The intricate interaction of process parameters in SLM inflicts detrimental influences on residual stresses, structural integrity, surface roughness, and consequently, fatigue strength, and on-site service can enhance fatigue performance. Concerning microstructure, the dendritic width in aluminum alloys can be down to sub-micron [4, 5]. In-process control measures such as platform heating reduce thermal gradients, which promotes microstructural coarsening [6]. Secondly, porosity, which forms from unstable melt pools, becomes a dominant fatigue failure source. The failure mechanisms become highly influenced by stress concentration resulting from pores, which is otherwise a microstructure dominated phenomenon [7]. Thirdly, residual stresses come into play, which has the influence of accelerating or delaying the failure progression by locally opening or closing cracks. Residual stresses are induced by the local thermal gradient between the melt pool and the surrounding solids or powder [8].

The intense dynamics of melt pools form porosity due to the entrapment of gas [9]. The total energy density being lower or higher than optimum leads to the formation of linear or spherical porosity, both of which accelerate fatigue failure [10]. The nature of pore formation with respect to size, shape, and location is highly statistical in nature and imposes significant scatter on fatigue life [11]. Additionally, the layer by layer nature of the SLM process imposes the stair-case morphology on specimens and components, which means that for applications that require a smooth surface, machining becomes necessary [12]. Aluminum silicon alloys are known for their machinability and high specific strength as well as corrosion and wear resistance, which promotes wide use in aerospace and automotive industries [13]. Frequently, AlSi10Mg is used in SLM applications since its microstructure tolerates high thermal gradients without hot cracking, unlike EN AW 7075 [14].

In this paper, the issue of the influence of microstructure and remnant porosity on fatigue strength and failure mechanisms, especially in the very high-cycle fatigue

regime, is revisited. By presenting two material batches of AlSi12, one of which is built with platform heating, thermal gradients are reduced and dendritic growth is enhanced which leads to the alternation of failure mechanisms in the low cycle (LCF) to the very high cycle fatigue (VHCF) regime.

Materials and Methods

Cylindrical specimens of AlSi12 were manufactured perpendicular to the building platform with powder provided by SLM solutions on the machine SLM 250^{HL}. Control of the laser source was achieved through SLM-AutoFabCAM software. The build chamber was filled with argon gas to avoid contamination of melt pools with impurities and oxides. Control over the cooling rate and microstructural thermal history were achieved through platform heating up to 200 °C, which is approx. 30% of the melting temperature of this alloy for batch B only as two batches are analyzed according to Table 1.

Process-induced residual stresses and geometrical distortions were counter measured by dividing the current layer into islands of perpendicular scanning vector in a chessboard fashion, according to Fig. 1a. Every chessboard at the current layer *n* is a rotation of the previous layer *n* – 1 by 79 °C, according to Fig. 1b. All specimen was stress-relieved at 240 °C for four hours, followed by slow cooling in the oven.

The investigation and quantification of remnant gas porosity were carried out by X-ray microcomputed tomography (μ -CT). The advantage provided by μ -CT is

Table 1 Scanning parameters used of the current specimen batches according to [4]

Batch	Factors		
	Energy density [J/mm ³]	Platform heating [°C]	Stress-relief [°C]
A	39.6	0	240
B	39.6	200	240

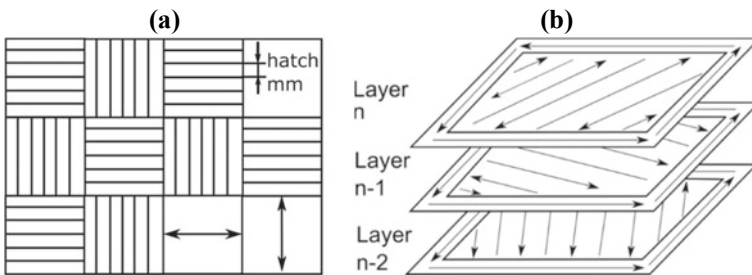


Fig. 1 a The schematic of chessboard scanning strategy for specimen building [4]; b alternative rotation of layers to minimize distortion [15]



Fig. 2 Testing setup for ultrasonic fatigue testing [15]

the representation of internal defects in a three-dimensional fashion. The specimen is 360° rotated by the manipulator. Meanwhile, a stream of electrons will excite a tungsten target, which will subject the specimen to continuous X-rays penetration that is projected on the panel. The footprint of the bulk of the specimen and the internal defects is used for quantification in this analysis by VGStudio Max 2.2.

Tensile tests were carried out on machined specimens using an Instron 3369 system with a 50 kN load cell. For monitoring specimen extension and deduction of strain, a 10 mm gauge length extensometer was applied at the specimen, which is strained at $1.67 \cdot 10^{-3} \text{ s}^{-1}$. Fatigue tests are classified into continuous load increase tests (C-LIT) and constant amplitude tests (CAT). In C-LIT, a cyclic test is started at a stress amplitude, which is lower than the expected critical resolved shear stress of the material, and the amplitude is gradually increased with a constant ramp. This test is carried out along with CATs in early high-cycle fatigue at a Instron 8872 servohydraulic testing system with a load cell of 10 kN. The strain characteristics of the specimens were monitored by a dynamic extensometer with a 10 mm gauge length at stress ratio $R = -1$. The specimen geometry used in these tests is to be seen in Fig. 3.

Very high-cycle fatigue tests were carried out at an ultrasonic fatigue testing system of Shimadzu USF-2000A with a characteristic displacement amplitude of $\pm 50 \mu\text{m}$. The principle relies on the ultrasonic frequency actuation of a piezo-electric sensor connected to a horn that excites the specimen at the frequency and displacement amplitude, as shown in Fig. 2.

A special specimen geometry which relies on linear elastic properties is a prerequisite to achieving ultrasonic resonance at this system. The specimen can be seen in Fig. 4.

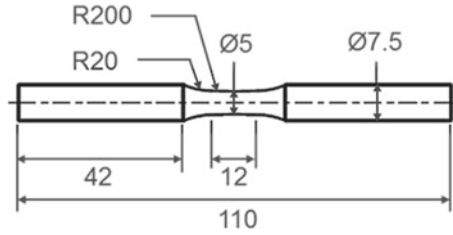


Fig. 3 Technical drawing of specimen geometry in tensile testing and fatigue testing up to 20 Hz [16]

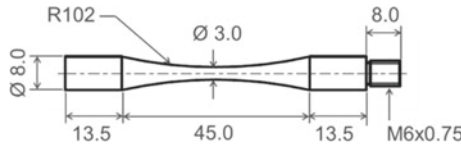


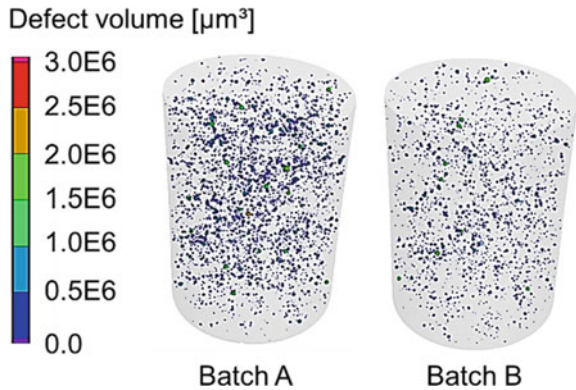
Fig. 4 Technical drawing of specimen geometry in ultrasonic fatigue testing up to 20 kHz [17]

Results and Discussion

The three-dimensional scans of μ -CT enabled quantification of remnant porosity associated with the cooling rate of which is influenced by the platform heating that reduced thermal gradients significantly. In Fig. 5, batch A displays a significantly higher amount of remnant porosity in addition to larger average defect size. One mechanism responsible for this phenomenon would be the stabilized melt pool induced by lower thermal gradients, which leads to longer cooling time.

Consequently, remnant gas from powder humidity due to storage is more likely to escape the melt pool into the atmosphere of the building chamber. Moreover, the increased stability implies that the sphericity of pores is higher, which undermines the formation of pores with sharper corners or notches that are more likely to initiate

Fig. 5 Three-dimensional defect distribution as revealed by the microcomputed tomography (μ -CT): A (SR); B (SR + PH). (Color figure online)



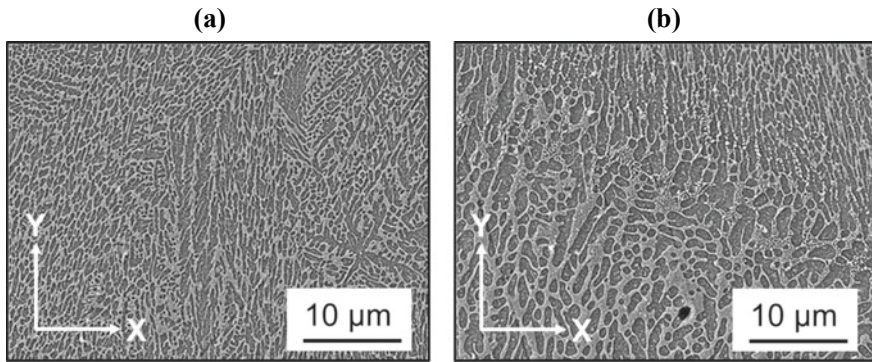


Fig. 6 Dendritic growth of the microstructure in the direction of building: **a** batch A (SR); **b** batch B (SR + PH)

failure. However, another factor comes into effect in relation to cooling rates, which is the growth of dendrites under lower cooling rates. In Fig. 6, a comparison is presented between dendrites in the vertical direction of the specimen build-up following the Y-axis in Fig. 6, where coarser columnar dendrites are observed for batch B, as revealed by scanning electron microscopy (SEM).

The growth of the microstructure compounded by the decrease of remnant porosity influences mechanical properties in the quasi-static and fatigue loading cases. In Fig. 7a, higher elastic modulus, yield strength, and ultimate tensile strength are to be seen in batch A although fracture strain was approximately 1% lower.

The latter observation is probably attributed to coarser columnar dendrites in the build direction. In Fig. 7b, the accumulation of plastic strain amplitude is presented, which shows a lower build-up of plasticity in batch B at earlier stages of the test that is inherent from the microstructural morphology. Wider dendrites present a stronger obstacle for movement of dislocations along with the Al matrix which delays macroplasticity build-up. However, as load amplitude increases, plastic strain accumulation increases in batch B in the range between 100 and 140 MPa that indicates a change in the plastic deformation state in the microstructure and formation of physical cracks across several grains. It has the effect of lower fatigue life in CATs at stress amplitude of 140 MPa, as shown in Fig. 8a. The alternation of plastic deformation mechanisms evident by the plastic strain amplitude accumulation in the LIT implied the existence of a transition point in the Woehler curve were under the same frequency and loading conditions, fatigue is very close in value, which we see in Fig. 8a at stress amplitude of 120 MPa. This is affected by the interaction of two factors, which are microstructure and remnant porosity compensating each other in this load range. At lower loads in very high-cycle fatigue tests (VHCF), Fig. 8b indicated the influence of remnant porosity becomes more dominant to the extent that at $1E9$ cycles, the run-out stress drops by 30%.

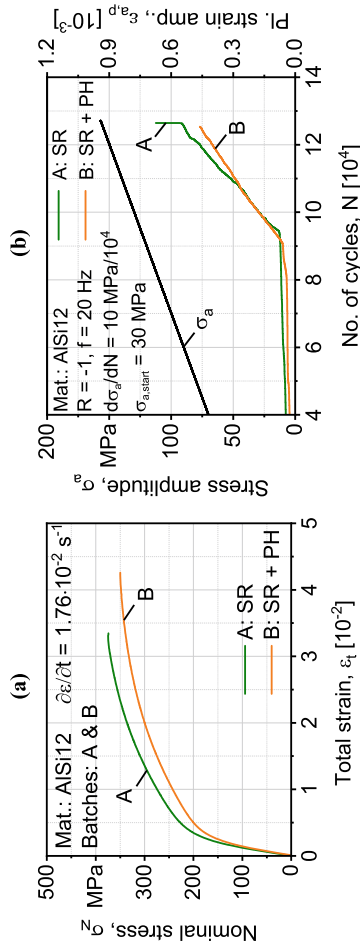


Fig. 7 **a** Tensile testing curves comparison between batches A and B; **b** accumulation of plastic deformation in a continuous load increase test [18]. (Color figure online)

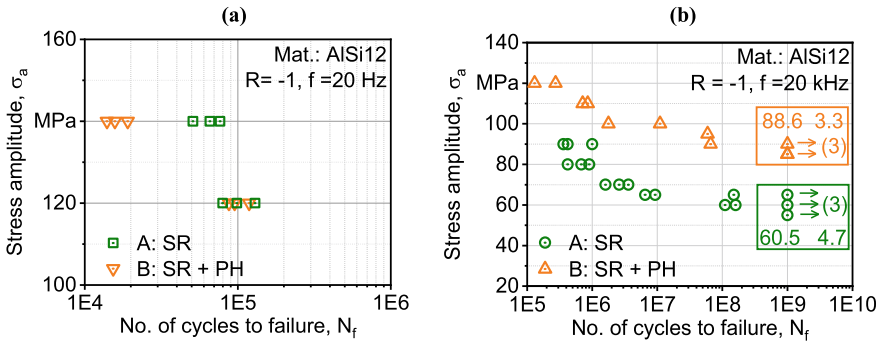


Fig. 8 **a** Experimental fatigue results for low-frequency testing at 20 Hz; **b** extension of Woehler curves by ultrasonic fatigue testing at 20 kHz. (Color figure online)

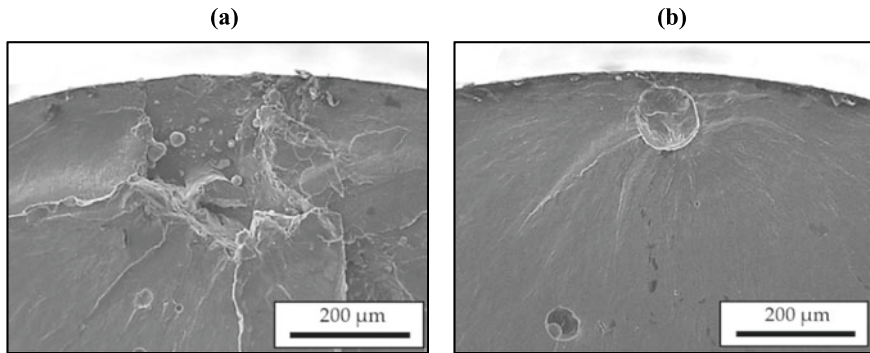


Fig. 9 Crack initiation defects revealed by fractography for batch A in VHCF regime: **a** $\sigma_a = 70$ MPa, $N_f = 1.6E6$; **b** $\sigma_a = 70$ MPa, $N_f = 3.2E8$

Analysis of fracture surfaces of batch F in Fig. 9 shows that smaller size, more uniform porosity that is spherical in shape, increase fatigue life in the VHCF region by two orders of magnitude.

Conclusions and Outlook

The issue of interaction of the influence of microstructure and remnant porosity on the fatigue properties in high-cycle to very high-cycle fatigue is revisited. Two batches of selective laser melted AISi12 studied for which one of them platform heating was applied to reveal the influence of thermal history. The study applied X-ray micro-computed tomography, scanning electron microscopy as well as mechanical testing in quasi-static and fatigue load cases. The reduced cooling rate by platform heating led to stabilized melt pools. Consequently, remnant gas in the powder was allowed to

escape, which decreased the number of pores. Additionally, the stabilized melt pools avoided the formation of porosity with notched roots that are more detrimental to fatigue strength. The microstructure was also coarsened by platform heating and the reduced cooling rate. Consequently, platform-heated specimens had wider columnar dendrites, which lead to higher fracture strain in the quasi-static tests. However, fatigue strength in early high-cycle fatigue was lower. On the contrary, the combination of improved remnant porosity and coarse columnar dendrites led to significant improvement of fatigue strength in very high-cycle fatigue. The study highlights the possibility of tailor fatigue properties by the usage of in-process techniques such as surface remelting. The influence of thermal history can be monitored by thermal cameras to quantify a relation between thermal input in the melt pool and resulting fatigue strength.

Acknowledgements The authors thank the German Research Foundation (Deutsche Forschungsgemeinschaft, DFG) for its financial support within the research project “Mechanism-based understanding of functional grading focused on fatigue behavior of additively processed Ti-6Al-4V and Al-12Si alloys” (WA 1672/25-1), and the reaseach partners from Institute of Laser and System Technologies (ILAS) for production of the specimens within the framework of an excellent collaboration.

References

1. Mueller B (2012) Additive manufacturing technologies—rapid prototyping to direct digital manufacturing. *Assem Autom* 32(2). ISBN: 978-1-4419-1119-3
2. Luisa S, Contuzzi N, Angelastro A, Domenico A (2010) Capabilities and performances of the selective laser melting process. In: *New trends in technologies: devices, computer, communication and industrial systems*, Sciyo, INTECH, pp 233–252
3. Gebhardt A (2013) Generative Fertigungsanlagen für rapid prototyping, direct tooling und direct manufacturing. In: *Generative Fertigungsanlagen*. Carl Hanser Verlag GmbH & Co. KG, Düsseldorf, pp 101–307
4. Siddique S, Imran M, Wycisk E, Emmelmann C, Walther F (2015) Influence of process-induced microstructure and imperfections on mechanical properties of AlSi12 processed by selective laser melting. *J Mater Process Technol* 221:205–213
5. Baufeld B, Brandl E, Biest D (2011) Wire based additive layer manufacturing: comparison of microstructure and mechanical properties of Ti-6Al-4V components fabricated by laser-beam and shaped metal deposition. *J Mater Process Technol* 211(6):1146–1158
6. Prashanth K, Scudino S, Klauss H, Surredi K, Löber L, Wang Z, Chaubey A, Kühn U, Eckert J (2014) Microstructure and mechanical properties of Al-12Si produced by selective laser melting: effect of heat treatment. *Mater Sci Eng A* 590(10):153–160
7. Awd M, Labanie F, Möhring K, Fatemi A, Walther F (2020) Towards deterministic computation of internal stresses in additively manufactured materials under fatigue loading: part I. *Materials* 13(10):1–15
8. Kruth J, Badrossamay M, Yasa E, Deckers J, Thijs L, Humbeeck J (2010) Part and material properties in selective laser melting of metals. In *16th international symposium on electromachining (ISEM XVI)*, Shanghai
9. Qiu C, Adkins N, Attallah M (2013) Microstructure and tensile properties of selectively laser-melted and of HIPed laser-melted Ti-6Al-4 V. *Mater Sci Eng A* 578(20):230–239
10. Hosford W (2005) *Mechanical behavior of materials*. Cambridge University Press, New York

11. Leuders S, Thoene M, Riemer A, Niendorf T, Tröster T, Richard H, Maier HJ (2013) On the mechanical behaviour of titanium alloy TiAl6V4 manufactured by selective laser melting: fatigue resistance and crack growth performance. *Int J Fatigue* 48:300–307
12. Brandl E, Michailov V, Viehweger B, Leyens C (2011) Deposition of Ti–6Al–4V using laser and wire part I: microstructural properties of single beads. *Surf Coat Technol* 206(6):1120–1129
13. Ahmad Z (2012) Aluminum alloys new trends in fabrication and applications. INTECH, Islamabad
14. Monter-Sistiaga M, Mertens R, Vrancken B, Wang X, Hooreweder B, Kruth J-P, Humbeeck J (2016) Changing the alloy composition of Al7075 for better processability by selective laser melting. *J Mater Process Technol* 238:437–445
15. Siddique S (2018) Reliability of selective laser melted AlSi12 alloy for quasistatic and fatigue applications. Springer Vieweg, Dortmund. ISBN: 978-3-658-23424-9
16. Siddique S, Walther F (2017) Fatigue and fracture reliability of additively manufactured Al-4047 and Ti-6Al-4V alloys for automotive and space applications. In: Innovative design and development practices in aerospace and automotive engineering. Springer, Singapore, pp 19–25
17. Siddique S, Imran M, Walther F (2017) Very high cycle fatigue and fatigue crack propagation behavior of selective laser melted AlSi12 alloy. *Int J Fatigue* 94(2):246–254
18. Awd M, Siddique S, Hajavifard R, Walther F (2018) Comparative study of defect-based and plastic damage-based approaches for fatigue lifetime calculation of selective laser-melted AlSi12. In: Proceedings of the 7th international conference on fracture fatigue and wear, Singapore

Part XXVIII
Frontiers in Solidification Science VIII

Research on Solidification and Heat Transfer Characteristics of Molten Converter Slag in Air Quenching Granulation Process



Wen-Feng Gu, Jiang Diao, Jing Lei, Liang Liu, and Bing Xie

Abstract The physical and mathematical model of molten converter slag particle has been established in this paper. The laws of solidification and heat transfer of molten converter slag particles with the diameter of 2 mm in the process of air quenching granulation at different air velocity have been simulated by FLUENT, which the conclusion is as follows: the transformation order of molten converter slag particles is upwind point → upper point and lower point → leeward point → center point. When the air velocity is 200 m/s and 1 m/s, the time of temperature maintaining phase transformation at the center point is about 0.5 s and 1 s, respectively. Under the conditions of forced cooling and natural cooling, the maximum value of internal temperature difference of converter slag particles is reached after 0.5 s and 2 s, respectively. When $v = 200$ m/s and $v = 1$ m/s, the internal maximum temperature differences of converter slag particles were 645 K and 162 K, respectively. Moreover, the maximum internal temperature point is deviated to the right with different cooling conditions. When the air velocity was 200 m/s and 1 m/s, the starting solidification time was 0.05 s and 0.35 s, respectively, and it severally took 0.55 s and 1.80 s to complete the solidification.

Keywords Molten converter slag · Air quenching granulation · Numerical simulation · Waste heat recovery · Solidification and heat transfer

Introduction

Molten converter slag is a byproduct of the steelmaking process. Its waste heat also has a high recovery value. The processing methods of molten converter slag can directly affect heat recovery and the recycling of converter slag [1–3]. At present, the

W.-F. Gu · J. Diao (✉) · J. Lei · L. Liu · B. Xie
College of Materials Science and Engineering, Chongqing University, Chongqing 400044,
People's Republic of China
e-mail: diaojiang@163.com

Chongqing Key Laboratory of Vanadium-Titanium Metallurgy and Advanced Materials,
Chongqing University, Chongqing 400044, People's Republic of China

© The Minerals, Metals & Materials Society 2021
TMS 2021 150th Annual Meeting & Exhibition Supplemental Proceedings,
The Minerals, Metals & Materials Series,
https://doi.org/10.1007/978-3-030-65261-6_69

most widely used molten converter slag treatment processes are hot sealing method and hot pouring method. Both of them have the advantages of high degree of mechanization and simple operation, but they could not realize the waste heat recovery of molten converter slag. The air quenching granulation process of molten converter slag can effectively granulate the molten converter slag. At the same time, the heat of converter slag can be recovered with air as the medium, so that the converter slag resources can be applied to the maximum extent [4, 5]. The process of air quenching granulation is to use high-pressure air to impact molten converter slag. The molten converter slag is broken into small droplets. The converter slag droplet is cooled rapidly in the flight process, and then solidified into small particles. The molten converter slag is granulated by high-pressure air and carries out convective heat transfer with surrounding air during flight. Waste heat recovery is realized by recycling high-temperature air. The injection air can be recycled, so that it has good environmental friendliness [6, 7].

At present, most of the research is based on experimental methods to study heat recovery of molten converter slag. However, such methods have a narrow range. In addition, the results are mostly dependent on the experimental conditions and the experimental conditions could not be widely changed. There are also errors in the measurement. Moreover, such full scale experiments are extremely expensive and often difficult to achieve [8–10]. Therefore, in this paper, the numerical simulation method was used to simulate the cooling and solidification process of molten converter slag particles, and the heat transfer law and the evolution law of liquid-solid phase of molten converter slag under different cooling conditions are studied. What's more, the solidification time of molten converter slag particles is determined, which was helpful for the control optimization of air quenching granulation process and provided theoretical support for the heat of molten converter slag recycling.

Mathematical Modeling

Model Hypothesis

In the actual process of air quenching granulation, the solidification and phase transformation process of molten converter slag was very complicated. In order to efficiently solve the heat transfer problem, it was necessary to simplify some specific conditions and made necessary assumptions. Based on the heat conduction model of phase transformation in the process of converter slag granulation, this study has the following assumption:

- (1) Because of the small size of converter slag after air quenching granulating, it was regarded as a small ball with uniform particle size and well-distributed initial temperature inside the particles.

- (2) The phase transformation temperature of the molten converter slag particle was constant. Since the latent heat of solid phase transformation was much less than that of solidification, the effect of solid phase transformation was ignored;
- (3) Heat transfer in phase transformation medium was dominated by heat conduction so that the influence of natural convection was ignored.
- (4) The process of phase transformation started from the outer layer to the inner layer and did not consider the floatation and deposition of central equiaxed crystals.

Model Formulation

The flow of air in the process of air quenching granulation of molten converter slag is three-dimensional turbulent flow. The selection models are Solidification/Melting model, $k - \varepsilon$ turbulence model and DO model, which the mass equation, momentum equation, energy equation, and turbulent kinetic energy equation used in the calculation are as follows:

Continuity equation:

$$\frac{\partial \rho}{\partial t} + \frac{\partial(\rho u_i)}{\partial x_i} + \frac{\partial(\rho u_j)}{\partial x_j} = 0 \tag{1}$$

Momentum equation:

$$\frac{\partial(\rho u_i u_j)}{\partial x_j} = \frac{\partial P}{\partial x_j} + \frac{\partial}{\partial x_j} \left[\mu_{\text{eff}} \left(\frac{\partial u_i}{\partial x_j} + \frac{\partial u_j}{\partial x_i} \right) \right] + \rho g_i \tag{2}$$

Energy equation related to temperature field calculation:

$$\rho C_p \left(u_i \frac{\partial t}{\partial x_i} + u_j \frac{\partial(\rho u_j)}{\partial x_j} \right) = \frac{\partial}{\partial x_i} \left(k_{\text{eff}} \frac{\partial t}{\partial x_i} \right) + \frac{\partial}{\partial x_i} \left(k_{\text{eff}} \frac{\partial t}{\partial x_j} \right) \tag{3}$$

Standrad $k - \varepsilon$ equation describing the turbulent viscosity coefficient:

$$\frac{\partial(\rho k)}{\partial t} + \frac{\partial(\rho k u_i)}{\partial x_i} = \frac{\partial}{\partial x_i} \left[\left(\mu + \frac{\mu_t}{\sigma_k} \right) \frac{\partial k}{\partial x_i} \right] + G_k - \rho \varepsilon \tag{4}$$

$$\frac{\partial(\rho \varepsilon)}{\partial t} + \frac{\partial(\rho \varepsilon u_i)}{\partial x_i} = \frac{\partial}{\partial x_i} \left[\left(\mu + \frac{\mu_t}{\sigma_\varepsilon} \right) \frac{\partial \varepsilon}{\partial x_i} \right] + \frac{\varepsilon C_{1\varepsilon}}{k} G_k - C_{2\varepsilon} \rho \frac{\varepsilon^2}{k} \tag{5}$$

where ρ is the density, kg m^{-3} ; u_i and u_j are the velocity of molten steel in the i and j directions, m s^{-1} ; P is the pressure, Pa; μ_{eff} is the effective viscosity, $\text{kg m}^{-1} \text{s}^{-1}$; k_{eff} is the effective thermal conductivity, $\text{W m}^{-1} \text{K}^{-1}$; $C_{1\varepsilon}$, $C_{2\varepsilon}$, σ_k , σ_ε , are empirical constants, and their values are 1.44, 1.93, 1.0, 1.3.

Simulation Scheme

Because the calculation of solidification heat transfer model was more complex in three-dimensional space, in order to facilitate the calculation, the model was further simplified into a two-dimensional axisymmetric plane model. The physical model of molten converter slag with particle size of 2 mm was constructed by Gambit, as shown in Fig. 1. The distances between the upper and lower wall surfaces, the left inlet, and the slag droplet surface were 1 mm, and the distance between the right outlet end and the slag particle surface was 3 mm. Due to the converter slag particles will be affected by the air flow in the flight process, the inlet of the auxiliary area was taken as the air inlet that the type was set as the speed inlet. The initial air speed, respectively, was set to 200 m/s and 1 m/s under the forced cooling and natural cooling state. The outlet was set as the pressure outlet, which the gauge pressure was set to 0 Pa. The upper and lower boundary conditions were the default wall. The simulation parameters involved in the numerical simulation were shown in Table 1. In addition, the initial temperatures of air and molten converter slag particles were set at 300 K and 1700 K, respectively.

Fig. 1 Geometry of converter slag particle.
(Color figure online)

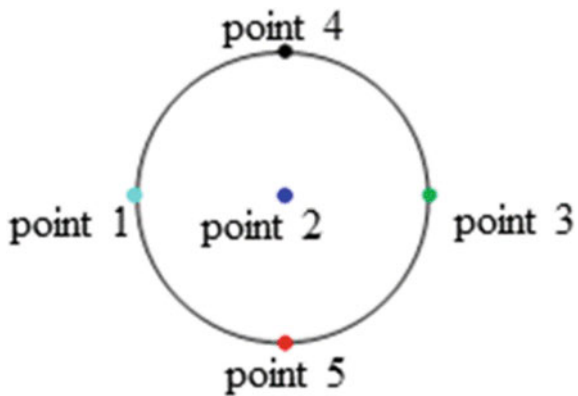


Table 1 Important physical parameters of molten converter slag

Parameters	Values	Parameters	Values
Density	3200 kg m ⁻³	Latent heat	209015 j kg ⁻¹
C _p	1340 j kg ⁻¹ K ⁻¹	Solidus temperature	1537 K
Thermal Conductivity	2.33 W m ⁻¹ K ⁻¹	Liquidus temperature	1557 K
Viscosity	0.06 kg m ⁻¹ s ⁻¹	–	–

Results and Discussion

The Temperature Distribution

Figures 2, 3 show the temperature field changes of molten converter slag particles with diameter $D = 2$ mm at air velocity of 200 m/s and 1 m/s, respectively. It can be seen from the figures that the convection heat transformation with the particles made the temperature of the outside air on the particle surface increased rapidly when the air flowed through the high temperature slag particles, so that the temperature of the air near the particle surface and the flow wake area increased obviously. When the air flow rate was 1 m/s, the particle surface temperature was even as high as 1600 K. When the air flow rate is 200 m/s, the heat exchange air with slag particles was heated and transferred rapidly resulted in the air for heat exchange with slag particles is always kept at low temperature. Because the surface heat transfer coefficient of molten converter slag particles changed along the direction of air flow, the internal temperature distribution of molten converter slag particles varied greatly, which the temperature of molten converter slag on the leeward side was lower than that on the windward side.

The relationship between temperature and cooling time of molten converter slag particles at different air flow rates was shown in Fig. 4. It can be seen from the figure that the temperature reduction rate in different regions was obviously slowed down when the temperature of converter slag particles reached the phase transformation temperature, for the heat lost by the particles was compensated by the latent heat in the solidification process. When the air velocity is 200 m/s and 1 m/s, the time of maintaining phase transformation temperature at point 2 is about 0.5 s and 1 s,

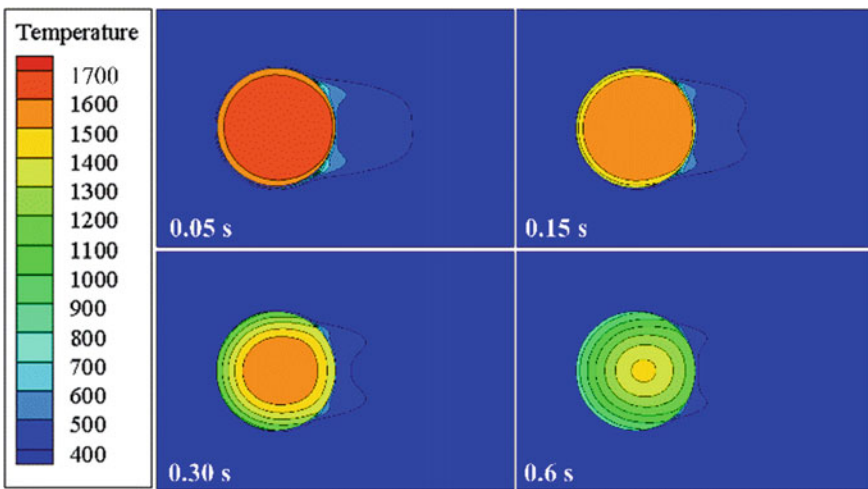


Fig. 2 Distribution of temperature field at different time under $v = 200$ m/s. (Color figure online)

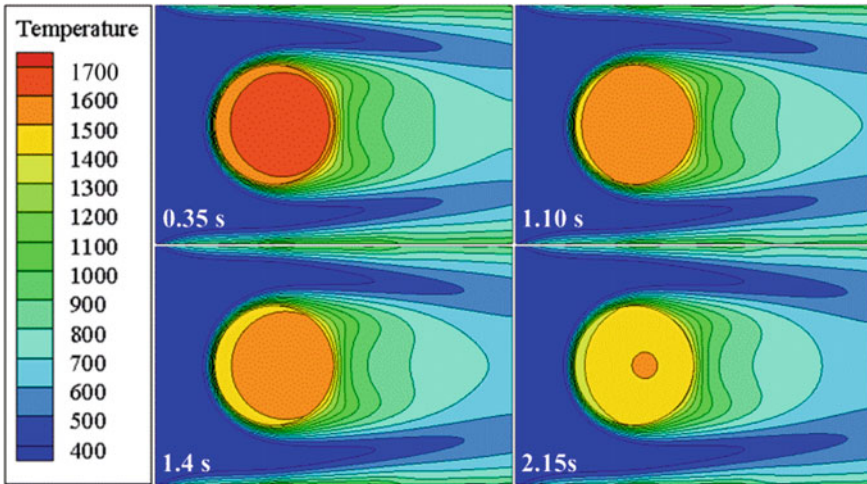


Fig. 3 Distribution of temperature field at different time under $v = 1$ m/s. (Color figure online)

respectively. It can be seen that the solidification reaction of slag particles took place from the outside to the inside, which the temperatures of upwind point (point 1), upper point and lower point (point 4 and point 5), leeward point (point 3), and central point (point 2) reached the phase transformation temperature in turn. The solidification of slag particles was not uniform to the internal development. Moreover, the temperature difference inside the converter slag particles under forced cooling was significantly higher than that under slow cooling.

The internal temperature difference of converter slag particles in the cooling and solidification process tended to increase first and then decrease under different air velocity conditions. When the cooling time is 0.5 s, the maximum internal temperature difference under 200 m/s air velocity reached 645 K. It was obviously higher than the maximum internal temperature difference (162 K) at 2 s under 1 m/s air velocity. What's more, when the air velocity was 200 m/s and 1 m/s, the transverse coordinates of the internal maximum temperature points were 2.08 mm and 2.14 mm, respectively. Under the condition of natural cooling, the offset of the highest temperature point was slightly higher than that of forced cooling.

Evolution Law of Liquid-Solid Phase

Figures 5, 6 show the distribution of liquid-solid phase during the solidification process of molten converter slag particles with diameter of 2 mm. It can be seen from Fig. 5 that when $v = 200$ m/s, the first 0.05 s was liquid cooling, the solidification started at 0.05 s and solidification was completed in 0.6 s that took 0.55 s. As shown in Fig. 6, when $v = 1$ m/s, the solidification started 0.35 s and the solidification was

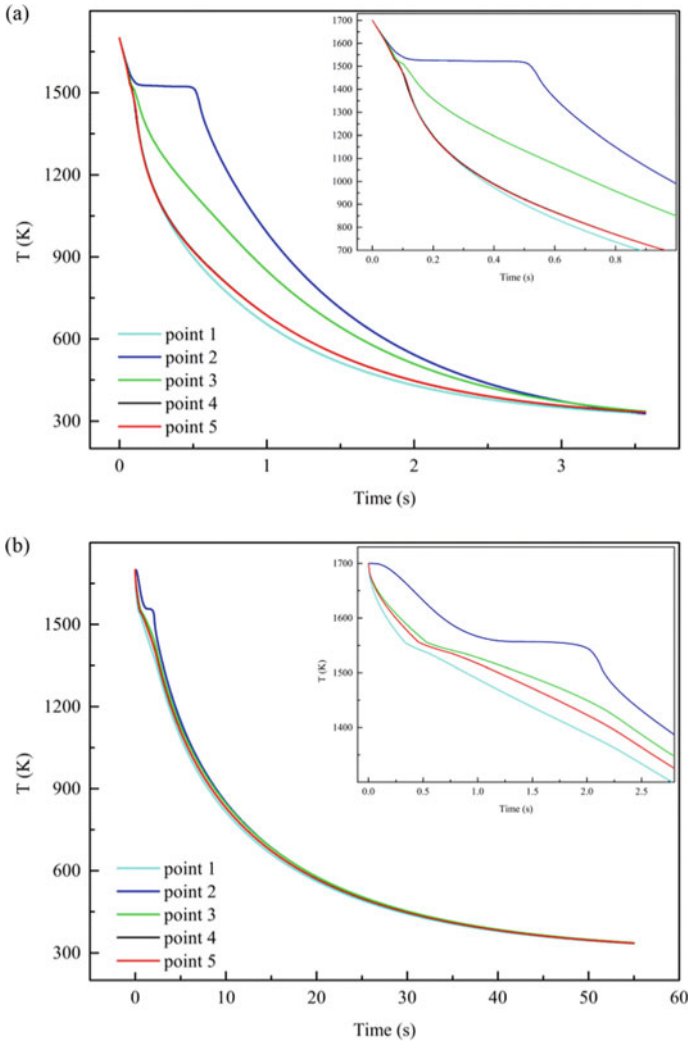


Fig. 4 Temperature curves of monitoring points: **a** $v = 200$ m/s; **b** $v = 1$ m/s. (Color figure online)

completed at 2.15 s that took 1.80 s. During forced cooling, the heat exchange of air with converter slag particles was transferred rapidly after being heated resulting in large temperature difference between converter slag particles and air, which is conducive to the rapid cooling of converter slag particles. In natural cooling, due to the low air velocity, it was easy to cause the accumulation of heat, which made the temperature difference between converter slag particles and air smaller. There was reduced heat transfer efficiency between converter slag particles and air so that prolonged the solidification time of molten converter slag particles. In addition, the temperature span on the same section is larger and the liquid-solid phase is relatively

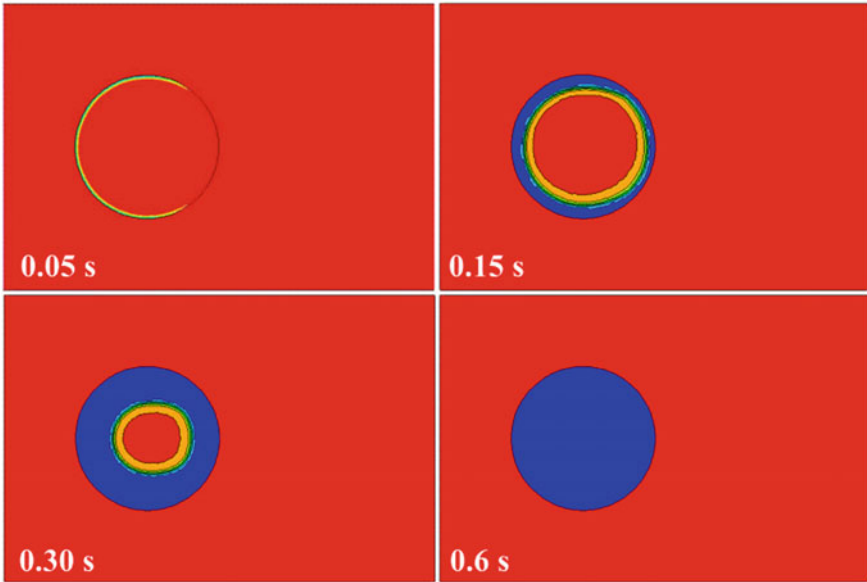


Fig. 5 Distribution of liquid-solid phase at different time under $v = 200$ m/s. (Color figure online)

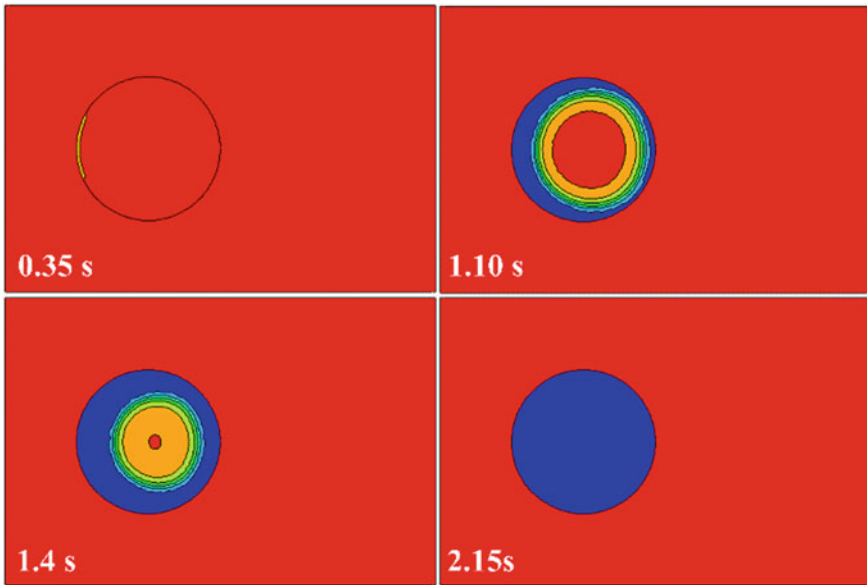


Fig. 6 Distribution of liquid-solid phase at different time under $v = 1$ m/s. (Color figure online)

clear under $v = 200$ m/s. When $v = 1$ m/s, the temperature on the same section was almost the same, all around 1557 K, indicating that the boundary of liquid-solid phase was fuzzy and it is mostly liquid-solid mixture before the solidification was completed.

Conclusion

In order to study the solidification and heat transfer characteristics and the evolution law of liquid-solid phase of molten converter slag during air quenching granulation process, the cooling and solidification process of molten converter slag particles were simulated and calculated in this paper. The conclusions are as follows:

- (1) When the air velocity was 1 m/s, the maximum surface temperature of particles was about 1600 K. However, when the air velocity was 200 m/s, the surface temperature of particles was kept in a low range.
- (2) Under different cooling conditions, the temperatures of the upwind point, upper point and lower point, leeward point, and the center point reached the phase transformation temperature then solidified successively. When the air velocity was 200 m/s and 1 m/s, the time for maintaining the phase transformation temperature at the center point was about 0.5 s and 1 s, respectively.
- (3) When $v = 200$ m/s, the internal maximum temperature differences of converter slag particles were 645 K after cooling time of 0.5 s. When $v = 1$ m/s, the internal maximum temperature differences of converter slag particles were 162 K after cooling time of 2 s. Under different cooling conditions, the internal maximum temperature point shifted to 2.08 mm and 2.14 mm to the right.
- (4) When $v = 200$ m/s, the solidification started at 0.05 s and completed at 0.6 s. when $v = 1$ m/s, the solidification started from 0.35 s and completed at 2.15 s. It took 0.55 s and 1.80 s to complete the solidification process under different cooling conditions.

Acknowledgements This work was supported by the National Natural Science Foundation of China (No. 51974047) and Natural Science Foundation of Chongqing, China (cstc2020jcyj-msxmX0043).

References

1. Wang Q, Yan P (2010) Hydration properties of basic oxygen furnace converter slag. *Constr Build Mater* 24(7):1134–1140
2. Yi H, Xu G, Cheng H et al (2012) An overview of utilization of converter slag. *Procedia Environ Sci* 16:791–801
3. Jiang Y, Ling T, Shi C (2018) Characteristics of converter slags and their use in cement and concrete—a review. *Resour Conserv Recycl* 136:187–197

4. Gao J, Li SQ, Zhang Y (2011) Process of re-resourcing of converter slag. *J Iron Steel Res Int* 18(12):32–39
5. Leuchtenmuller M, Antrekowitsch J, Steinlechner S (2019) A kinetic study investigating the carbothermic recovery of chromium from a stainless-converter slag. *Metall Mater Trans B* 50(5):2221–2228
6. Xing HW, Wu JF, Li GL (2012) Experimental study on fluidization characteristics of gas quenching converter slag. *Adv Mater Res* 531:7–13
7. Zong YB, Cang DQ, Zhen YP (2009) Component modification of converter slag in air quenching process to improve grindability. *Trans Nonferrous Metal Soc China* 19(supp-S3):834–839
8. Ishaqa H, Dincera I, Naterer GF (2019) Exergy and cost analyses of waste heat recovery from furnace cement slag for clean hydrogen production. *Energy* 172:1243–1253
9. Yue Long, Zhenlei Cai, Yuzhu Zhang (2013) Numerical simulation of flow fields for gas quenching of converter slag. *Iron Steel Vanadium Titanium* 034(004):30–35
10. Hiroyuki T, Yasutaka T (2015) Development of continuous steelmaking slag solidification process suitable for sensible heat recovery. *ISIJ Int* 55(4):894–903

Part XXIX
Functional Nanomaterials: Functional
Low-Dimensional Materials (0D, 1D, 2D)
Driving Innovations in Electronics, Energy,
Sensors, and Environmental Engineering
and Science 2021

Silicon Carbide Biotechnology: Carbon-Based Neural Interfaces



Chenyin Feng, Mohamad Beygi, Christopher L. Frewin,
Md Rubayat-E Tanjil, Ashok Kumar, Michael Cai Wang,
and Stephen E. Saddow

Abstract Implantable neural interfaces (INI) have gained significant interest since the 1970s. However, the materials currently utilized for neural interfaces suffer from limitations such as degradation, induce a foreign body response, and experience a loss of target neurons in close proximity. Therefore, the development of new implantable device materials for biomedical applications continues to be an important direction of research and development. Carbon-based nanomaterials are promising candidates and also interesting since carbon has many allotropes with different structures and properties, many of which have also been developed for biomedical devices. Moreover, many carbon allotropes have excellent electrical conductivity and mechanical properties. In this framework, the biocompatibility of graphene, carbon nanotubes, and pyrolyzed-photoresist films, which are three very promising carbon-based nanomaterials (CBN), will be discussed. The neural probe fabricated solely using amorphous silicon carbide as support and pyrolyzed photoresist film (PPF) will be presented as this system represents a highly robust, thin, and flexible neural interface using well-known neurocompatible materials.

Keywords SiC · Carbon-based nanomaterials · Implantable neural interface · Pyrolyzed-photoresist film

C. Feng · M. R.-E. Tanjil · A. Kumar · M. C. Wang
Department of Mechanical Engineering, University of South Florida, Tampa, FL 33620, USA

C. Feng · M. Beygi · S. E. Saddow (✉)
Department of Electrical Engineering, University of South Florida, Tampa, FL 33620, USA
e-mail: saddow@usf.edu

C. L. Frewin
NeuroNexus LLC, Ann Arbor, MI 48108, USA

S. E. Saddow
Department of Medical Engineering, University of South Florida, Tampa, FL 33620, USA

Introduction

A comprehensive understanding of the brain (the most complex organ/ecosystem of the human body) is still far from complete. Since the nineteenth century, much research has been dedicated to developing devices that connect with the human nervous system through electrical, mechanical, and optical means. The electrical connection has gained the most attention because of the ability of electrical recording and stimulation of the nervous system which can help neuroscientists to understand neural electrophysiological processes. Subsequently, INI can contribute to developing effective treatments for various nervous system diseases (such as depression, addiction, Parkinson's, Alzheimer's, and Poliomyelitis) and subdue the damage that affects more than hundreds of millions of people and cost more than trillions of dollars annually [1]. Overall, developing a cost-effective treatment for nervous system diseases is essential, for which, the implantable neural interface, or INI, is a viable candidate [2].

For more than two decades, silicon and noble metals have been used for the fabrication of INIs to stimulate neurons and record neural signals, thanks to their excellent mechanical and electrical properties [3]. However, due to the relatively low impedance and small detection window, noble metals and silicon-based INIs have limited application during neural stimulation [4]. Furthermore, long-term implantable performance is poor due to the foreign body response, loss of target neurons, and scar (i.e., gliosis) formation. Moreover, noble metals introduce irreversible dissolution during neurostimulation, which can cause undesirable damage to the human body [5].

Recently, nanomaterials and nanotechnology have gained significant interest in biomedical applications because of their ability to control and modulate the electrical, mechanical, and chemical properties of devices fabricated at the micro- and nanoscale levels [6]. This has motivated the development of nanomaterials for biomedical applications, including neural implants such as the INI. Carbon, one of the most versatile elements in the periodic table, can covalently bond with itself or with other elements because it has four bonds that can form into different compounds and forms [7]. Furthermore, there are many allotropes of carbon, attributed to the different hybridized carbon electron orbitals, like sp , sp^2 , and sp^3 [6]. In this framework, we are focusing on carbon-based nanomaterials (CBN) as the conductive layer for implantable neural interfaces, which includes graphene, graphene oxide (GO), reduced graphene oxide (rGO), carbon nanotubes (CNT), and pyrolyzed-photoresist-films (PPF).

Graphene continues to be a revolutionary material and since Geim and Novoselov first exfoliated graphene from highly oriented pyrolytic graphite (HOPG), there have been more than 600,000 publications on this carbon allotrope [8]. Moreover, graphene has many excellent intrinsic properties such as atomic-scale thickness, structurally lightweight at 0.77 mg/m^2 , high tensile stiffness ($\sim 10^3 \text{ GPa}$), high heat conductivity (5000 W/mK) at room temperature, and very high carrier mobility of $15,000 \text{ cm}^2\text{v}^{-1}\text{s}^{-1}$ [9]. A decade ago our group reported early biocompatibility

results from graphene in vitro. Recently, Park and collaborators demonstrated the long-term biocompatibility of graphene electrodes [10, 11]. They successfully fabricated a carbon-layered electrode array (CLEAR) based on graphene and Parylene C for neurophysiological recording [12] (Fig. 1a). The optical transparency of this device has been characterized at >90% transmission from the ultraviolet to the infrared part of the optical spectrum. In their work, they achieved optogenetic activation of cortical areas under the electrodes and imaging of blood vasculature by fluorescence microscopy at the same time. In addition, their research demonstrated that graphene substrates can promote neurite sprouting and outgrowth, which indicates that graphene can reduce the tissue inflammatory response [13, 14]. Furthermore, graphene-derived materials such as GO and rGO have also proven to be suitable for biomedical and bioelectrical applications. Tian et al. reported a GO doped poly(3,4-ethylenedioxythiophene)(PEDOT) hybrid film on a gold wire electrode,

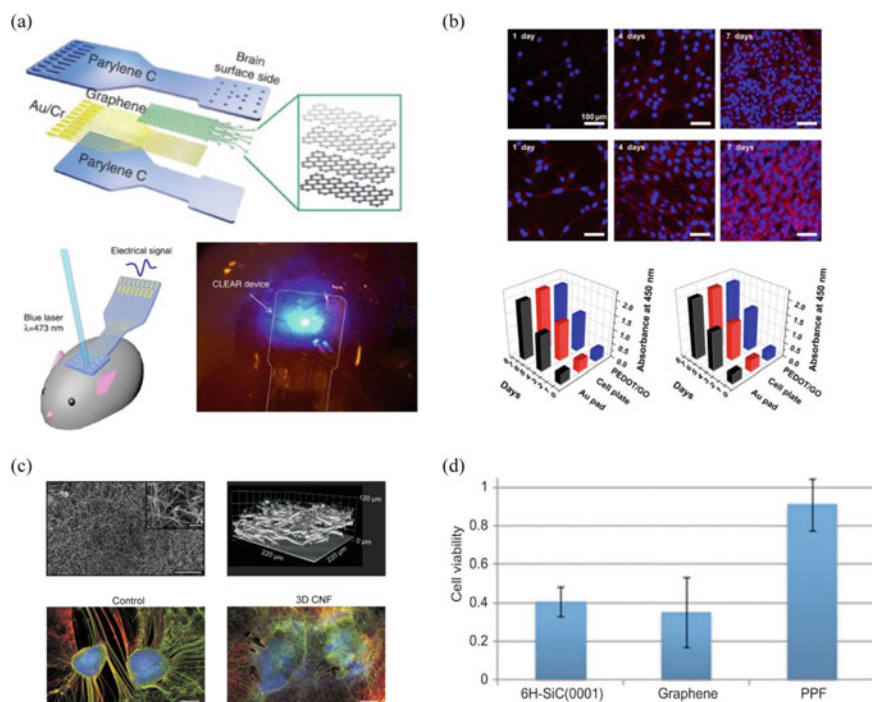


Fig. 1 The biocompatibility of different carbon-based nanomaterials. **a** graphene electrode for neural imaging and optogenetic device. Reprinted with permission from ref. [12] under Creative Commons Attribution 4.0 International License. **b** confocal laser scanning microscope on the cell growth on GO/PEDOT. Reprinted with permission from ref. [15], **c** spinal cord cell growth and reconnection on 3D CNT foam. Reprinted with permission from ref [16] under Creative Commons Attribution 4.0 International License, and **d** in vitro cell viability assays comparing the viability of human keratinocyte (HaCaT) cells on 6H-SiC, Graphene and PPF. Reprinted with permission from ref. [17]. (Color figure online)

which showed enhanced mechanical and electrochemical impedance performance [15].

The impedance at 1 kHz of GO/PEDOT gold electrode demonstrates a two order of magnitude decrease compared with bare gold electrodes. In addition, they also illustrated the biocompatibility of GO/PEDOT coated gold electrode using PC-12, and NIH/3T3 cells which were cultured on GO/PEDOT electrodes for several days to investigate the cell proliferation. Figure 1b shows cell morphology from a confocal laser scanning microscope (CLSM) after cell growth versus time. These results indicate both cell lines thrive on GO/PEDOT electrodes, demonstrating that the system neither facilitates nor restrains cell proliferation compared with gold pads and cell plates and indicates that GO/PEDOT has excellent biocompatibility such as gold and cell culture plates.

In 1991, the CNT was first observed by Ijima which exhibits excellent electrical, mechanical, and thermal transfer properties [18]. The CNT was made of single- or multilayer graphene rolled into a cylindrical shape. The diameter and wall layer of the CNT can be tuned by controlling various parameters during synthesis. Because of the high surface area, great mechanical properties, and excellent chemical and thermal stability, CNTs are a promising material for bio-electronic devices [19]. Usmani et al. demonstrated that 3D CNT foam (CNF) could help spinal cord cell growth and reconnection, as shown in Fig. 1c [16]. The top left image shows an SEM image of the CNF, and the top right is the confocal 3D reconstruction of this CNF. The bottom two images show two weeks ex vivo cultured spinal organotypic slices in the control group and CNF group. It shows a significant outgrowth of nerves in both groups. Several studies suggest exposure to CNTs may lead to risks for biomedical applications [20]. This is mainly due to the Fe, Ni, and Co particle contaminants from the synthesis process. Another critical issue is the potential of CNTs to damage and induce mutation in DNA, possibly resulting in cancer or other severe genetic diseases [21]. However, we still believe CNTs are a cutting-edge nanomaterial well suited for biomedical applications, and this issue can be solved with more research but is not the focus of this paper.

Pyrolyzed photoresist film (PPF) is another promising material for biomedical applications [17]. Photoresists are a type of polymer resin that contains photoactive compounds and is an essential material for IC fabrication. The main advantage of using PPF for biomedical applications is that it can enable facile patterning by standard photolithography processes and then converted to a conductive carbon film via thermal annealing. In addition, PPF is electrically conductive, chemically inert, and biocompatible. In Fig. 1d, a previous result from our group demonstrated that PPF can promote cell viability [17]. Human keratinocyte (HaCaT) cells were used for cell viability testing. Graphene and 6H-SiC were used as a comparison group. The HaCaT cells were seeded with a density of 30,000 cells/cm². After 72 h incubation, the viability value of HaCaT cells was 0.35 ± 0.18 (standard deviation of the mean), 0.41 ± 0.08 , and 0.91 ± 0.13 for graphene, 6H-SiC, and PPF, respectively. This study illustrated that PPF is more biocompatible than graphene and 6H-SiC and thus a possible candidate for implantable devices. Thus, our current research is focusing

Table 1 The properties of the most commonly used carbon-based nanomaterials [22–27]

Carbon material	Electron mobility (cm ² /V s)	Young's modulus (GPa)	Electrical conductivity (S/m)	No. of Dimensions
Graphene	15,000	856	10 ⁷ –10 ⁸	2
CNT	15,000	1000	10 ⁶ –10 ⁷	1
PPF	–	–	–	3
3C-SiC ^a	800	433	~10 ^{4b}	3
4H-SiC ^a	1000	444	~10 ^{3b}	3

^an-doped material^bActual conductivity depends on doping density

on the PPF-based neural interface, which will be discussed in Sect. 3. The main properties of the most commonly used CBNs and other materials for biomedical devices have been summarized in Table 1 [22–27].

Synthesis Methods of CBN

Methods for Graphene Growth

Since graphene was reported in 2004, researchers have discovered various methods for large scale fabrication of graphene such as mechanical, liquid, and gas exfoliation, chemical vapor deposition (CVD), epitaxial growth (EG) on silicon carbide, laser-induced graphene (LIG), etc. (Figure 2) [8, 25–35]. CVD graphene is the most commonly used method because it can enable large-area growth, crystallinity, and layer controllability. Typically, single-crystal copper (Cu)(111) foil is used to obtain single-crystal monolayer graphene. The graphene can be grown onto Cu foil under 1000 °C by CVD. Methane and hydrogen are used as precursor gases and argon as a carrier gas. Nickle can also be used as a substrate for CVD graphene growth [24]. However, since the carbon atoms solubility of Ni is higher than Cu, the graphene growth on Ni is multilayer. After CVD graphene growth, it can be transferred to an arbitrary substrate by various transfer techniques (e.g., wet transfer). Laser-induced-graphene (LIG) is a novel method which does not require harsh conditions such as high ambient temperature, methane, and a hydrogen environment. Lin et al. reported LIG on a polyimide (PI) substrate, which is a cost-effective, one-step, and scalable approach for porous graphene film fabrication [25]. They utilized a CO₂ laser (wavelength ~10.6 μm) directly writing on the PI substrate, the energy of the laser irradiation can lead to an extremely high, but very localized, temperature, which can be up to 2,500 °C. At this temperature, the C–O, C=O, and C–N bonds can be broken easily. Then, the oxygen and nitrogen will be recombined and released as gases,

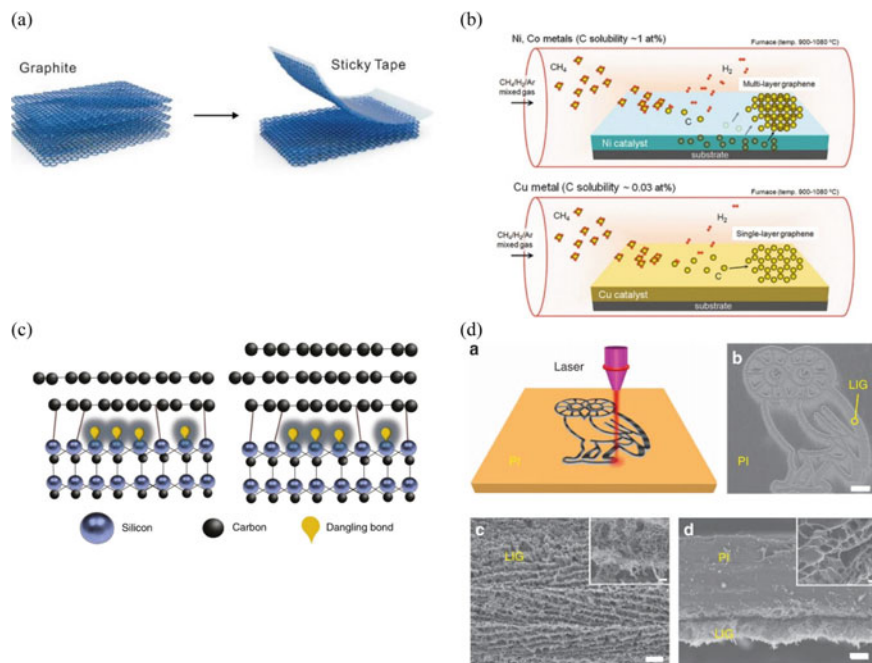


Fig. 2 Different methods to obtain graphene **a** mechanical exfoliation. Reprinted with permission from ref. [26], **b** chemical vapor deposition graphene. Reprinted with permission from ref. [27], **c** epitaxial growth graphene on SiC. Reprinted with permission from ref. [28], **d** laser-induced graphene. Reprinted with permission from ref. [25]. (Color figure online)

and the rest of the carbon atoms form aromatic compounds which rearrange to form porous graphene.

Methods for GO Synthesis

GO can be obtained by several different methods. The most commonly used is the Hummer's method, which was discovered in 1958 by Hummers and Offeman [29, 30]. In their work, they used graphite flake powder, potassium permanganate (KMnO_4), and sodium nitrate (NaNO_3) stirred into sulfuric acid to obtain GO. Nowadays, this method has been slightly changed, called the modified Hummers method. The NaNO_3 is replaced with phosphoric acid (H_3PO_4) and nitric acid (HNO_3), incorporating H_2SO_4 as an intercalating agent. Then, hydrogen peroxide (H_2O_2) was added and with KMnO_4 as the oxidizing agents [29]. Figure 3 shows the synthesis process of GO; graphite flake powder was added into H_2SO_4 , HNO_3 , and H_3PO_4 mixture, then a 0 °C ice bath will be utilized to carefully control the temperature. KMnO_4 was added slowly during this time, followed by a 2 h oil bath at 45 °C. Finally, deionized

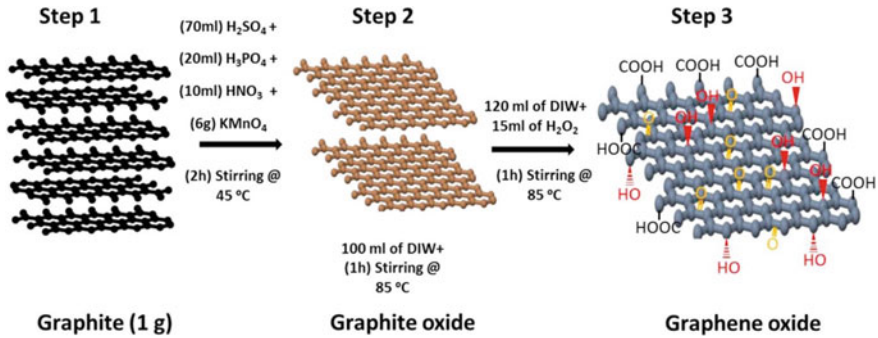


Fig. 3 Modified Hummer's method for GO production. Reprinted with permission from ref. [29]. Bulk graphite powder transforms into few-layer graphene flakes and is oxidized into graphene oxide (GO), as shown via wet chemical processing. (Color figure online)

(DI) water with H_2O_2 as added, and the solution was centrifuged and washed with DIW until the solution reached a neutral pH.

Synthesis of Pyrolyzed Photoresist Films (PPF)

PPF can be obtained by annealing photoresist under high temperatures [17]. Spin-coating a substrate with photoresist and patterning it to the desired shape allows one to achieve a film with a thickness related to the photoresist thickness and associated shrinkage during annealing. Film annealing is normally performed at between 500 °C and 1000 °C in a tube furnace with an inert environment, such as Ar, for one hour. As the photoresist starts heating, the color changes from transparent to black. The solvent and free phenols in the photoresist are evaporated out of the resist by the time the temperature reaches 300 °C. A cross-linking reaction starts in the photoresist film when the temperature exceeds 300 °C, whereby the $C=O-H$ bonds will break and form $C-O-C$ bonds. The bond reforming results in a significant thickness reduction, producing nanometer-scale films [31]. Furthermore, Campo et al. demonstrated PPF fabrication using a rapid thermal process (RTP), which indicates that the annealing temperature and the annealing time are more critical to fabricate PPF than the actual heating rate. Currently, our research focuses on PPF conductive traces formed on SiC substrates for the neural interface applications. Details of the fabrication process and preliminary results will be discussed in the next section.

Amorphous Silicon Carbide (a -SiC) Supported PPF INI

Biocompatibility of a -SiC

Silicon carbide is a semiconductor material which has more than 250 polymorphs, exhibits high tolerance to harsh environments, including long-term stability in acid/base solutions, at high temperatures, and in high radiation environments [32, 33]. These excellent properties give SiC the ability to be utilized as an INI material. In our work, the amorphous form, a -SiC, was chosen as the substrate and capping layer for our PPF electrodes because of its robust chemical inertness, high electrical conductivity, and observed biocompatibility. Previous work from our group had demonstrated the biocompatibility and hemocompatibility of a -SiC [33–35]. To investigate the chronic implantation of a -SiC, a control Si probe along with the a -SiC probe was implanted in the same rat brain for four weeks. Figure 4a shows an immunohistochemically stained horizontal slices from an a -SiC and Si implant. The white circle indicates the probe locations, glial fibrillary acidic protein (GFAP) labeling in green, and the deep cortical tissue is labeled in red. By comparing the a -SiC-coated probe with the control Si probe, the a -SiC-coated probe showed a significant decrease in GFAP intensity at the insertion site, which means a decreased level of activated astrocytes. Figure 4b shows the summary data of GFAP intensity

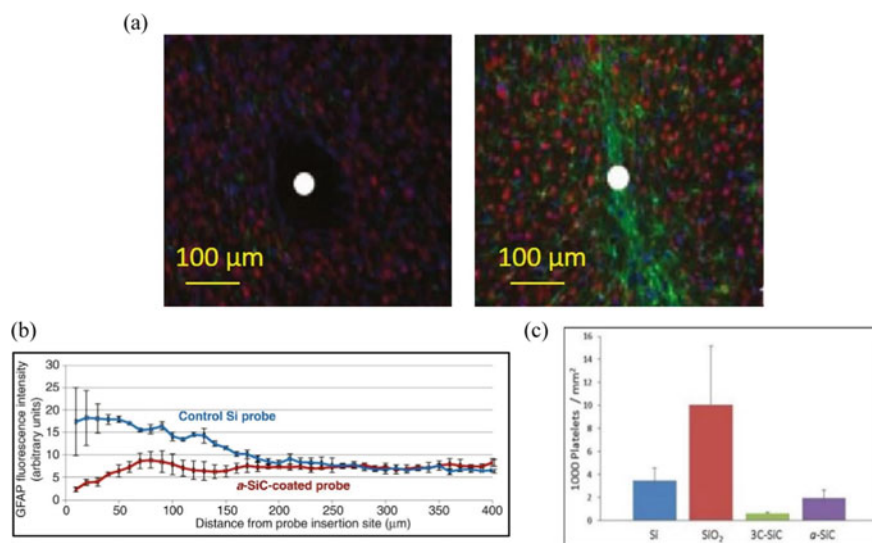


Fig. 4 **a** Biocompatibility of a -SiC fluorescent images from deep cortical tissue with a -SiC-coated probe (left) and Si probe (right) inserted. **b** Plot of GFAP intensity with distance from the probe insertion site. **c** Hemocompatibility of Si, 3C-SiC, SiO₂, and a -SiC. Note that 3C- and a -SiC displayed a lower concentration of platelets bound to the surface than Si and SiO₂ indicating that these materials more hemocompatible. Reprinted with permission from ref. [33, 34]. (Color figure online)

with distance from the insertion site for both the α -SiC and Si probes. The hemocompatibility was examined by the number of attached platelets to the material [33]. A lower concentration of attached platelets indicates that the material is more hemocompatible since platelets will trap blood cells and form a thrombus. In a separate work, all samples were exposed to platelet-rich plasma for 15 min afterward the presence of attached platelets was studied by fluorescent microscopy. Comparison data of platelet attachment to Si, 3C-SiC, SiO₂, and α -SiC is shown in Fig. 4c. The results indicate 3C-SiC has the lowest platelet binding followed by α -SiC which displayed slightly higher platelet binding than 3C-SiC, whereas SiO₂ and Si had a much higher number of bound platelets. This result further indicates that Si and SiO₂ are not suitable for biomedical applications, especially when the devices are in contact with the vascular system [33].

PPF Electrode Fabrication on α -SiC

An α -SiC supported PPF electrode can be fabricated using standard semiconductor micromachining processes. First, a 500 nm thick α -SiC layer is deposited by plasma-enhanced chemical vapor deposition (PECVD) on the SiO₂/Si wafer. The deposition conditions are a platen temperature of 300 °C, with a process pressure of 1100 mTorr, and 200 W of RF power. The precursors are CH₄ (200 sccm), %5 SiH₄ in H₂ (300 sccm), all diluted in 700 sccm He. Figure 5 shows the fabrication process of single-ended electrodes with different recording site areas. Positive photoresist (AZ12xt) was used to fabricate the devices. AZ12xt will be spin-coated on the α -SiC wafer with 500 rpm for 20 s, then 3000 rpm for 50 s, and finally 11000 rpm for 2 s. The first spinning stage is to distribute the photoresist on the wafer uniformly, the second stage determines the thickness of the photoresist (in this case, 7.4 μ m as measured with

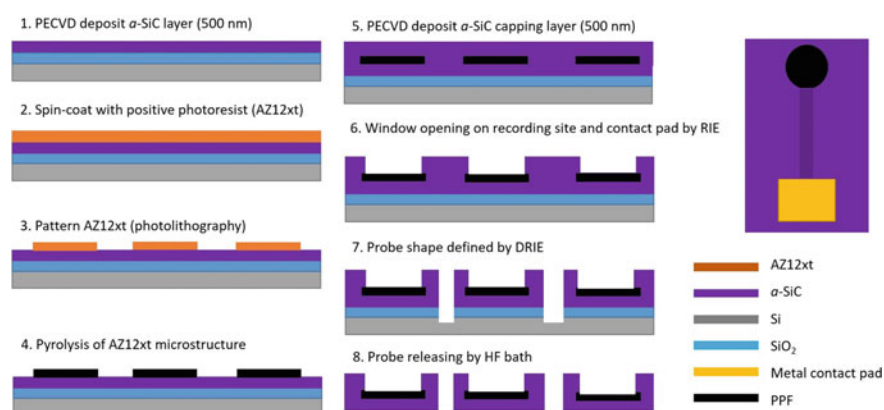


Fig. 5 Cross-section view of the fabrication process of the α -SiC/PPF device. Top view of the completed device shown for reference on the right. (Color figure online)

an optical profilometer), and the last stage is to eliminate any die edge effects. The coated substrate was then soft-baked at 120 °C for 3 min, followed by UV exposure at an intensity of ~ 120 mJ/cm² and a one-minute post-exposure bake at 95 °C. Once the pattern has been transferred to the resist, the *a*-SiC wafer was annealed in a tube furnace at different temperatures from 600 °C to 900 °C under an Ar and H₂ environment of 100 sccm and 5 sccm, respectively. The ramp-up rate was 10 °C/min, followed by a long thermal soak at the desired temperature for an hour. Afterward, the wafer was cooled down to room temperature under an Ar and H₂ ambient. To investigate the influence on recording area size, we fabricated four different recording area sized single-end electrodes with an area of 125 k μ m², 7.8 k μ m², 1.9 k μ m², and 314 μ m², respectively. This was followed by capping the electrodes with another layer of *a*-SiC (500 nm thickness) deposited by PECVD. The contact and electrode windows were then opened by RIE etching with 37 sccm CF₄ and 13 sccm O₂ for 20 min (both electrode tip and bonding pad areas were etched at the same time). To facilitate packaging 20 nm of Ti (adhesion layer) was e-beam evaporated followed by 150 nm of Au (without breaking vacuum) on the electrode site for packaging. To obtain Ohmic contact, the whole device will be annealed at 500 °C in a rapid temperature process (RTP) furnace with a ramping rate of 10 °C/s. Another Ti/Au metal layer was deposited on the annealed contacts to facilitate wire bonding, thus completing the electrode fabrication. The single-end electrode fabrication will end here, and for the *a*-SiC/PPF neural probe will require another step to release the probe from the SiO₂ substrate by HF bath. Thus, we can obtain free-standing *a*-SiC supported PPF-based neural probes.

Preliminary Results of a-SiC/PPF Device

Figure 6 shows our preliminary data for the *a*-SiC supported PPF conductor neural probe. In Fig. 6a, a planar SEM image of 16 PPF conductor traces on one probe. The width of each trace and the gap between them is 10 μ m with a 20 μ m recording site as shown in the inset. Figure 6b is a cross-section SEM image of the PPF sample before annealing. The thickness of the top layer AZ12xt was 7.4 μ m before annealing, and the inset image is after annealing under 700 °C for 1 h. The photoresist shrank from 7.4 μ m to 332 nm or approximately 95% shrinkage after annealing. Raman spectroscopy was used to investigate the crystalline and carbonization degree of the synthesized PPF versus annealing temperature and is shown in Fig. 6c. All of the PPF traces exhibited peaks at 1360 and 1580 cm⁻¹, which are called the D band (for disorder) and G band (for graphite), respectively. With increasing annealing temperature, the D band and G bands become slightly more distinguishable which indicates that the PPF structure became more crystalline. Furthermore, the I_D/I_G ratio of annealed at 800 °C was ~ 1 , while at 500 °C ratio was ~ 0.85 . The observed ratio increase with temperature illustrates an increase in the material's structural order. Figure 6d shows preliminary electrochemical impedance spectroscopy (EIS) data from the PPF single-ended electrodes with different recording areas, ranging from

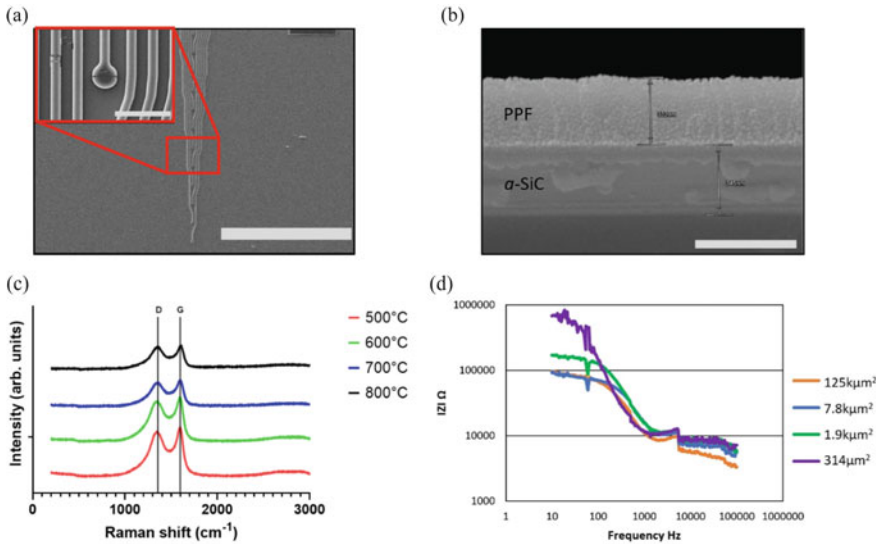


Fig. 6 Preliminary data of an α -SiC/PPF free-standing probe **a** plan-view SEM image, scale bar 1 mm (50 μm for inset), **b** cross-section SEM image after annealing, scale bar 500 nm. Initial photoresist thickness 7.4 μm prior to annealing at 700 $^{\circ}\text{C}$. **c** Raman spectra of PPF annealed versus temperature, and **d** Electrochemical (EIS) data versus recording area. Note impedance ~ 10 k Ω at 1 kHz for all electrodes tested. (Color figure online)

314 to 125 $\text{k}\mu\text{m}^2$. The impedance at the frequency of 1 kHz is critical since it is associated with the electrode recording efficiency due to 1 kHz being the neurons' spiking frequency. For all of our PPF electrodes, the impedance at 1 kHz is about 10 k Ω , which is an order of magnitude lower than for Pt electrode with the same recording area [36]. This result indicates the PPF has an excellent impedance range for neural recording applications and is worthy of further development.

Conclusion and Future Work

Carbon-based nanomaterial (CBN) has already been applied to several different fields, including neural interfacing. Many CBNs exhibit excellent electrical and biocompatible properties when they interact with the bio-environment. In this framework, we have discussed the application of graphene, GO, CNT, and PPF in the field of implantable neural interface (INI). In particular, PPF supported by α -SiC as a neural interface is an interesting possibility because the other CBNs require either harsh or complicated fabrication steps. Furthermore, most of the current devices fabricated using graphene, GO, and CNTs are based on Si or polymer substrates. As we discussed above, Si substrates are not biocompatible, which stimulates the body's immune response. Polymer substrates are known to degrade during chronic

implantation and require other delivery techniques or temporary support structures to eliminate buckling during insertion [37]. With *a*-SiC supported PPF, has all materials resident in the brain display suitable chronic biocompatibility, possess excellent preliminary electrochemical properties, and do not require assistive devices to implant into the tissue.

For future work, the free-standing neural probes based on the *a*-SiC/PPF devices as well as complete electrochemical testing of single-ended planar MEAs made with this material system will be completed. We strongly believe that CBN has a great future in the biomedical field and will continue our studies of other CBN systems using *a*-SiC as a support/insulating layer.

References

1. Gooch CL, Pracht E, Borenstein AR (2017) The burden of neurological disease in the United States: a summary report and call to action. In: *Annals of neurology*, vol 81, no 4. John Wiley and Sons Inc., Hoboken, pp 479–484. <https://doi.org/10.1002/ana.24897>.
2. Shih JJ, Krusienski DJ, Wolpaw JR (2012) Brain-computer interfaces in medicine. In: *Mayo clinic proceedings*, vol 87, no 3. Elsevier Ltd, Amsterdam, pp 268–279. <https://doi.org/10.1016/j.mayocp.2011.12.008>
3. Campbell PK, Jones KE, Huber RJ, Horch KW, Normann RA (1991) A silicon-based, three-dimensional neural interface: manufacturing processes for an intracortical electrode array. *IEEE Trans Biomed Eng* 38(8):758–768. <https://doi.org/10.1109/10.83588>
4. Chen B et al (2020) Penetrating glassy carbon neural electrode arrays for brain-machine interfaces. *Microdevices, Biomed*. <https://doi.org/10.1007/s10544-020-00498-0>
5. Park H, Zhang S, Steinman A, Chen Z, Lee H (2019) Graphene prevents neurostimulation-induced platinum dissolution in fractal microelectrodes. *2D Mater*. <https://doi.org/10.1088/2053-1583/ab2268>
6. Rauti R, Musto M, Bosi S, Prato M, Ballerini L (2019) Properties and behavior of carbon nanomaterials when interfacing neuronal cells: how far have we come? *Carbon*, vol 143. Elsevier Ltd, Amsterdam, pp 430–446. <https://doi.org/10.1016/j.carbon.2018.11.026>.
7. Silva GA (2008) Nanotechnology approaches to crossing the BBB.pdf. *BMC Neurosci* 4(S3):1–4. <https://doi.org/10.1186/1471-2202-9-S3-S4>
8. Novoselov KS, et al. (2004) Electric field in atomically thin carbon films. *Science* (80-) 306(5696):666–669. <https://doi.org/10.1126/science.1102896>
9. Demczyk BG et al (2002) Direct mechanical measurement of the tensile strength and elastic modulus of multiwalled carbon nanotubes. *Mater Sci Eng A* 334(1–2):173–178. [https://doi.org/10.1016/S0921-5093\(01\)01807-X](https://doi.org/10.1016/S0921-5093(01)01807-X)
10. Oliveros A, Coletti C, Frewin CL, Locke C, Starke U, Sadow SE (2011) Cellular interactions on epitaxial graphene on SiC (0001) substrates. In *Materials science forum*, vol 679–680, pp 831–834. www.scientific.net/MSF.679-680.831
11. Sadow SE (2016) Chapter 1: silicon carbide materials for biomedical applications, Second edn. Elsevier Inc., Amsterdam
12. Park D-W et al (2014) Graphene-based carbon-layered electrode array technology for neural imaging and optogenetic applications. *Nat Commun* 5(1):5258. <https://doi.org/10.1038/ncomms6258>
13. Song Q et al (2014) Anti-inflammatory effects of three-dimensional graphene foams cultured with microglial cells. *Biomaterials* 35(25):6930–6940. <https://doi.org/10.1016/j.biomaterials.2014.05.002>

14. Convertino D et al (2020) Graphene promotes axon elongation through local stall of nerve growth factor signaling endosomes. *Nano Lett* 20(5):3633–3641. <https://doi.org/10.1021/acs.nanolett.0c00571>
15. Tian HC et al (2014) Graphene oxide doped conducting polymer nanocomposite film for electrode-tissue interface. *Biomaterials* 35(7):2120–2129. <https://doi.org/10.1016/j.biomaterials.2013.11.058>
16. S. Usmani et al. (2016) 3D meshes of carbon nanotubes guide functional reconnection of segregated spinal explants. *Sci Adv* 2 (7). <https://doi.org/10.1126/sciadv.1600087>
17. Oliveros A, Coletti C, Sadow SE (2012) Carbon based materials on SiC for advanced biomedical applications. *Silicon Carbide Biotechnol* 431–458, <https://doi.org/10.1016/b978-0-12-385906-8.00012-x>
18. Iijima S (1991) Helical microtubules of graphitic carbon. *Nature* 354(6348):56–58. <https://doi.org/10.1038/354056a0>
19. Yang N, Chen X, Ren T, Zhang P, Yang D (2015) Carbon nanotube based biosensors. *Sensors and Actuators, B: Chemical*, vol. 207, no. Part A. Elsevier, Amsterdam, pp 690–715. <https://doi.org/10.1016/j.snb.2014.10.040>.
20. Pulskamp K, Diabaté S, Krug HF (2007) Carbon nanotubes show no sign of acute toxicity but induce intracellular reactive oxygen species in dependence on contaminants. *Toxicol Lett* 168(1):58–74. <https://doi.org/10.1016/j.toxlet.2006.11.001>
21. Schins RPF (2002) Mechanisms of genotoxicity of particles and fibers. *Inhal Toxicol* 14(1):57–78. <https://doi.org/10.1080/089583701753338631>
22. Sun Z, Yan Z, Yao J, Beitler E, Zhu Y, Tour JM (2010) Growth of graphene from solid carbon sources. *Nature* 468(7323):549–552. <https://doi.org/10.1038/nature09579>
23. Chyan Y, Ye R, Li Y, Singh SP, Arnusch CJ, Tour JM (2018) Laser-induced graphene by multiple lasing: toward electronics on cloth, paper, and food. *ACS Nano* 12(3):2176–2183. <https://doi.org/10.1021/acs.nano.7b08539>
24. Losurdo M, Giangregorio MM, Capezzuto P, Bruno G (2011) Graphene CVD growth on copper and nickel: role of hydrogen in kinetics and structure. *Phys Chem Chem Phys* 13(46):20836–20843. <https://doi.org/10.1039/c1cp22347j>
25. Lin J et al (2014) Laser-induced porous graphene films from commercial polymers. *Nat Commun* 5(1):1–8. <https://doi.org/10.1038/ncomms6714>
26. Lee J-H, Park S, Choi J-W (2019) Electrical property of graphene and its application to electrochemical biosensing. *Nanomaterials* 9(2):297. <https://doi.org/10.3390/nano9020297>
27. Ago H (2015) CVD growth of high-quality single-layer graphene. In *Frontiers of Graphene and Carbon Nanotubes: Devices and Applications*. Springer, Japan, pp 3–20. https://link.springer.com/chapter/10.1007/978-4-431-55372-4_1
28. Guy OJ, Walker KAD (2016) Chapter 4: Graphene Functionalization for Biosensor Applications, Second edn. Elsevier Inc., Amsterdam, p 2016. <https://doi.org/10.1016/B978-0-12-802993-0.00004-6>
29. Al-Gaashani R, Najjar A, Zakaria Y, Mansour S, Atieh MA (2019) XPS and structural studies of high quality graphene oxide and reduced graphene oxide prepared by different chemical oxidation methods. *Ceram Int* 45(11):14439–14448. <https://doi.org/10.1016/j.ceramint.2019.04.165>
30. Hummers WS, Offeman RE (1958) Preparation of graphitic oxide. Available: <https://pubs.acs.org/sharingguidelines> Accessed on 06 Sept 2020 [Online]
31. Ranganathan S, McCreery R, Majji SM, Madou M (2000) Photoresist-derived carbon for micro-electromechanical systems and electrochemical applications. *J Electrochem Soc* 147(1):277. <https://doi.org/10.1149/1.1393188>
32. Phan H-P et al. (2019) Long-lived, transferred crystalline silicon carbide nanomembranes for implantable flexible electronics. *ACS Nano*. <https://doi.org/10.1021/acs.nano.9b05168>
33. Sadow SE, et al (2014) 3C-SiC on Si: a bio- and hemo-compatible material for advanced nano-bio devices. In: 2014 IEEE 9th Nanotechnol. Mater. Devices Conf. NMDC, pp 49–53. <https://doi.org/10.1109/NMDC.2014.6997419>

34. Knaack GL, Charkhkar H, Cogan SF, Pancrazio JJ (2016) Chapter 8: amorphous silicon carbide for neural interface applications, Second edn. Elsevier Inc., Amsterdam, p 2016. <https://doi.org/10.1016/B978-0-12-802993-0.00008-3>
35. Beygi M et al (2019) Fabrication of a monolithic implantable neural interface from cubic silicon carbide. *Micromachines* 10(7):430. <https://doi.org/10.3390/mi10070430>
36. Bernardin EK, Frewin CL, Everly R, Ul Hassan J, Saddow SE (2018) Demonstration of a robust all-silicon-carbide intracortical neural interface. *Micromachines* 9(8):1–18. <https://doi.org/10.3390/mi9080412>
37. Deku F, et al. (2018) Amorphous silicon carbide platform for next generation penetrating neural interface designs. *Micromachines* 9(10). <https://doi.org/10.3390/mi9100480>

Part XXX
Heterostructured and Gradient Materials
(HGM IV): Tailoring Heterogeneity
for Superior Properties

Gradients, Singularities and Interatomic Potentials



K. Parisi and E. C. Aifantis

Abstract After a brief review on the ability of continuum gradient elasticity (GradEla) to eliminate singularities from dislocation lines and crack tips, we present an extension to its fractional counterpart by replacing the classical Laplacian in the gradient-enhanced Hooke's Law by a fractional one. Then, a discussion on implications of fractional gradient elasticity to eliminate stress/strain singularities from a screw dislocation is given, followed by the derivation of the fundamental solution of the governing fractional Helmholtz equation, for addressing more general problems. Finally, an elaboration is provided on using these ideas to revisit interatomic potentials used in materials science simulations.

Keywords Gradient elasticity · Interatomic potentials · London modification · Fractional laplacian

Introduction

Among the various generalized continuum theories, the GradEla model developed by the second author [1] has found prominent applications due to its robustness and simplicity. These include the removal of singularities from dislocation lines and crack tips, as well as the interpretation of size effects [2–4]. The GradEla model consists of a straightforward generalization of Hooke's Law through the Laplacians of stress and strain multiplied by corresponding scalar internal length parameters [2, 3]. With this modification, it turns out that nonsingular solutions for dislocation lines can be derived through the solution of an inhomogeneous Helmholtz equation (Ru-Aifantis theorem [5]), where the classical (singular) solution acts as a source term (see [3])

K. Parisi · E. C. Aifantis (✉)

Aristotle University of Thessaloniki, Thessaloniki 54124, Greece
e-mail: mom@mom.auth.gr

E. C. Aifantis

Michigan Technological University, Houghton, MI 49931, USA

Friedrich-Alexander University, Erlangen-Nürnberg, Fürth 90762, Germany

© The Minerals, Metals & Materials Society 2021

TMS 2021 150th Annual Meeting & Exhibition Supplemental Proceedings,

The Minerals, Metals & Materials Series,

https://doi.org/10.1007/978-3-030-65261-6_71

for a review). More recently, the GradEla approach was applied to revisit classical interatomic potentials by enhancing London’s quantum mechanical potential with an extra gradient term [6] that allows the resolution of the missing “repulsive” branch (at small interatomic separations), which is empirically introduced, for example, by the $1/r^{12}$ term of Lennard–Jones potential. Here, we extend the aforementioned gradient London’s potential to its fractional counterpart by using the formalism of [7–9], i.e. by employing a fractional Laplacian of Riesz type (Sect. “[Fractional Gradient Elasticity and Dislocations](#)”). The fundamental solution of the resulting fractional Helmholtz equation is then obtained through special functions (Sect. “[The Fundamental Solution of the Fractional Helmholtz Equation](#)”). The corresponding fractional gradient-enhanced interatomic potentials are then derived through the solution of an inhomogeneous fractional Helmholtz equation with the London’s potential as source (Sect. “[Fractional Gradient Interatomic Potentials](#)”).

Fractional Gradient Elasticity and Dislocations

A fractional generalization of gradient elasticity (GradEla) has previously been developed in [7–9] through the introduction of a fractional Laplacian of Riesz-type $(-\Delta)^{\alpha/2}$ and a corresponding fractional internal length ℓ^α . This is most efficiently obtained through a Taylor series expansion in Fourier space [9] of the constitutive kernel in the following nonlocal stress–strain relation

$$\sigma_{ij}(\mathbf{r}) = \int_{\mathbb{R}^3} K(|\mathbf{r} - \mathbf{r}'|) C_{ijkl} \varepsilon_{kl}(\mathbf{r}') d\mathbf{r}'. \tag{1}$$

Here $\sigma_{ij}(\mathbf{r})$ is the stress tensor, $\varepsilon_{ij}(\mathbf{r})$ is the linear strain field tensor, C_{ijkl} is the elastic stiffness tensor, while $K(|\mathbf{r} - \mathbf{r}'|)$ denotes the fractional interaction constitutive kernel accounting for power-law-type nonlocality. In order to facilitate the description of fractional gradient elasticity theories, it is necessary to employ the Fourier transform method, defined by the pair

$$\mathcal{F}\{f(\mathbf{r})\}(\mathbf{k}) = \tilde{f}(\mathbf{k}) = \int_{\mathbb{R}^3} f(\mathbf{r}) e^{-i\mathbf{k}\cdot\mathbf{r}} d\mathbf{r}, \tag{2}$$

$$\mathcal{F}^{-1}\{\tilde{f}(\mathbf{k})\}(\mathbf{r}) = f(\mathbf{r}) = \frac{1}{(2\pi)^3} \int_{\mathbb{R}^3} \tilde{f}(\mathbf{k}) e^{i\mathbf{k}\cdot\mathbf{r}} d\mathbf{k}. \tag{3}$$

The symbol $f(\mathbf{r})$ denotes any physical quantity, such as $\sigma_{ij}(\mathbf{r})$ or $\varepsilon_{ij}(\mathbf{r})$, for which the above integrals exist, while \mathbf{k} denotes the wave vector. A superimposed tilde over $\tilde{f}(\mathbf{k})$ denotes the Fourier transform of $f(\mathbf{r})$.

Through application of the Fourier transform in Eq. (1) via Eq. (2), along with the convolution property $\mathcal{F}\{(K * \varepsilon_{jk})(\mathbf{r})\}(\mathbf{k}) = \tilde{K}(|\mathbf{k}|) \tilde{\varepsilon}_{jk}(\mathbf{k})$ and a subsequent

fractional Taylor series expansion of the transformed interaction kernel $\tilde{K}(|\mathbf{k}|)$ in Fourier space up to the $|\mathbf{k}|^\alpha$ order (neglecting higher-order terms), one obtains

$$\tilde{\sigma}_{ij}(\mathbf{k}) = C_{ijkl} (1 + c_\alpha |\mathbf{k}|^\alpha) \tilde{\varepsilon}_{kl}(\mathbf{k}), \quad (4)$$

where c_α is a fractional gradient coefficient, which is determined through application of the Caputo fractional derivative in Eq. (4), evaluated at $k = 0$. It is given by the expression $c_\alpha = \text{sgn}(c_\alpha) \ell^\alpha$, where $\ell^\alpha = \frac{1}{\Gamma(\alpha+1)} \left| ({}_0^C D_k^\alpha \tilde{K})(0) \right|$ is the fractional internal length, and ${}_0^C D_k^\alpha$ denotes the Caputo fractional derivative with respect to the magnitude¹ of the wave vector $k = |\mathbf{k}|$, defined as ${}_0^C D_k^\alpha = \frac{1}{\Gamma(m-\alpha)} \int_0^k \frac{f^{(m)}(\kappa)}{(k-\kappa)^{\alpha-m+1}} d\kappa$ for $m-1 < \alpha < m$. Then, by applying the inverse Fourier transform of Eq. (3) into the reduced relation of Eq. (4) in Fourier space, along with the definition of the Riesz fractional Laplacian

$$\mathcal{F} \left\{ (-\Delta)^{\alpha/2} \varepsilon_{kl}(\mathbf{r}) \right\}(\mathbf{k}) = |\mathbf{k}|^\alpha \mathcal{F} \left\{ \varepsilon_{kl}(\mathbf{r}) \right\}(\mathbf{k}), \quad (5)$$

we obtain the following fractional constitutive equation

$$\sigma_{ij}(\mathbf{r}) = C_{ijkl} (1 + \ell^\alpha (-\Delta)^{\alpha/2}) \varepsilon_{kl}(\mathbf{r}), \quad (6)$$

where $\text{sgn}(c_\alpha) > 0$ is assumed for stability purposes. For a linear isotropic medium $C_{ijkl} = \lambda \delta_{ij} \delta_{kl} + \mu (\delta_{ik} \delta_{jl} + \delta_{il} \delta_{jk})$, where λ and μ are the Lamé constants, the constitutive relation of Eq. (6) is written as

$$\sigma_{ij}(\mathbf{r}) = \lambda \varepsilon_{kk}(\mathbf{r}) \delta_{ij} + 2\mu \varepsilon_{ij}(\mathbf{r}) + \ell^\alpha (-\Delta)^{\alpha/2} [\lambda \varepsilon_{kk}(\mathbf{r}) \delta_{ij} + 2\mu \varepsilon_{ij}(\mathbf{r})]. \quad (7)$$

It is noted that for $\alpha = 2$, Eq. (7) reduces to the well-known GradEla stress-strain constitutive equation involving the ordinary Laplacian operator $\Delta = \nabla^2 = \sum_{j=1}^3 \partial_j^2$ in a three-dimensional space. By substitution of Eq. (7) into the equilibrium equation $\partial_j \sigma_{ij} = 0$, along with the observation that the Riesz fractional Laplacian $(-\Delta)^{\alpha/2}$ commutes with the divergence operator, we obtain the fractional generalization of the Ru-Aifantis theorem [5]

$$(1 + \ell^\alpha (-\Delta)^{\alpha/2}) \varepsilon_{ij}(\mathbf{r}) = \varepsilon_{ij}^0(\mathbf{r}), \quad (8)$$

where $\varepsilon_{ij}^0(\mathbf{r})$ denotes the corresponding classical solution (singular for the case of dislocations). In fact, the fractional inhomogeneous Helmholtz equation in the form of Eq.(8) has been successfully employed to remove singularities from dislocation lines. In particular, the strain field of a screw dislocation turns out to be [10]

$$\varepsilon_{xz}(\mathbf{r}) = \frac{b_z}{4\pi} \left[-\frac{y}{r^2} + \frac{y}{r\ell} K^\alpha \left(\frac{r}{\ell} \right) \right]; \quad \varepsilon_{yz}(\mathbf{r}) = \frac{b_z}{4\pi} \left[\frac{x}{r^2} - \frac{x}{r\ell} K^\alpha \left(\frac{r}{\ell} \right) \right], \quad (9)$$

¹The usage of the Caputo fractional derivative ${}_0^C D_k^\alpha$ is introduced for convenience as a consequence of the assumed spherical symmetry of the interaction kernel.

where b_z is the magnitude of the Burgers vector, r is the radial distance from the dislocation line, and K^α is a fractional generalization of the modified Bessel function given by the relation $K^\alpha(r) = \int_0^\infty \frac{k^2 J_1(kr)}{k^{2-\alpha}(1+k^\alpha)} dk$, where J_ν denotes the Bessel function of order $\nu = 1$. It is noted that the strain field of Eq. (9) remains non-singular, as in the non-fractional GradEla solution, due to the asymptotic behavior $K^\alpha \rightarrow \ell/r$ near the origin. Moreover, for $\alpha \rightarrow 2$ we have $K^\alpha|_{\alpha \rightarrow 2} = \int_0^\infty \frac{k^2 J_1(kr)}{1+k^\alpha} dk = K_1(r)$ and, thus, the previous non-fractional GradEla results [11, 12] are recovered.

The self-energy of a fractional GradEla screw dislocation W_s turns out to be given by the equation

$$W_s = \frac{\mu b_z^2}{4\pi} \left[\ln\left(\frac{R}{r_0}\right) - \mathbb{K}^\alpha\left(\frac{r_0}{\ell}\right) + \mathbb{K}^\alpha\left(\frac{R}{\ell}\right) \right], \tag{10}$$

where $\mathbb{K}^\alpha(r) = \int_0^\infty \frac{k J_0(kr)}{k^{2-\alpha}(1+k^\alpha)} dk$, while r_0 and R are the inner and outer body radii, respectively. In the limit of $r_0 \rightarrow 0$, $\mathbb{K}^\alpha\left(\frac{r_0}{\ell}\right) \rightarrow -\gamma + \ln\left(\frac{r_0}{2\ell}\right)$, and thus, Eq. (10) gives $W_s = \frac{\mu b_z^2}{4\pi} \left[\gamma + \ln\left(\frac{R}{2\ell}\right) + \mathbb{K}^\alpha\left(\frac{R}{\ell}\right) \right]$, which again recovers the GradEla expression for the non-fractional case when $\alpha \rightarrow 2$, also independent of an initially assumed cutoff radius r_0 .

The Fundamental Solution of the Fractional Helmholtz Equation

In this section, the fundamental solution of the fractional counterpart of the Helmholtz equation is provided, as it appears in key problems resolved by gradient theory. By definition, the fundamental solution, $G^\alpha(\mathbf{r})$, is obtained as the response to a concentrated point source $\delta(\mathbf{r})$, through the governing equation

$$(1 + \ell^\alpha (-\Delta)^{\alpha/2}) G^\alpha(\mathbf{r}) = \delta(\mathbf{r}), \tag{11}$$

Equation (11) is most efficiently solved by applying the Fourier transform method of Eq. (2), along with the transformed Riesz fractional Laplacian through Eq. (5), and the Delta function property $\mathcal{F}\{\delta(\mathbf{r})\} = 1$. The resulting algebraic equation $(1 + \ell^\alpha |\mathbf{k}|^\alpha) \tilde{G}^\alpha(\mathbf{k}) = 1$ is readily solved, and after subsequent inversion, we obtain

$$G^\alpha(\mathbf{r}) = \frac{1}{(2\pi)^3} \int_{\mathbb{R}^3} \frac{1}{1 + \ell^\alpha |\mathbf{k}|^\alpha} e^{i\mathbf{k}\cdot\mathbf{r}} d\mathbf{k}. \tag{12}$$

Equation (12) is the required integral representation of $G^\alpha(\mathbf{r})$. On using the well-known Lemma 25.1 of Samko-Kilbas [13] involving the Fourier transform of spherically symmetric functions,

$$\frac{1}{(2\pi)^n} \int_{\mathbb{R}^n} f(|\mathbf{k}|) e^{i\mathbf{k}\cdot\mathbf{r}} d\mathbf{k} = \frac{1}{(2\pi)^{n/2} |\mathbf{r}|^{n/2-1}} \int_0^\infty k^{n/2} f(k) J_{n/2-1}(k|\mathbf{r}|) dk, \quad (13)$$

followed by a direct application to Eq. (12) for $n = 3$, we obtain

$$G^\alpha(\mathbf{r}) = \frac{1}{(2\pi)^{3/2} \sqrt{|\mathbf{r}|}} \int_0^\infty \frac{k^{3/2} J_{1/2}(k|\mathbf{r}|)}{1 + \ell^\alpha k^\alpha} dk. \quad (14)$$

Equation (14) is recognized as the Mellin convolution [14] in the form $(f \otimes g)(x) = \int_0^\infty f(k) g(kx) dk$. By employing the Mellin transform property $\mathcal{M}((f \otimes g)(x))(s) = \mathcal{M}(f(x))(1-s) \mathcal{M}(g(x))(s)$, along with $\mathcal{M}((1+k^\alpha)^{-1})(s) = \frac{1}{\alpha} \Gamma(\frac{s}{\alpha}) \Gamma(1 - \frac{s}{\alpha})$, and $\mathcal{M}(k^{3/2} J_{1/2}(k))(s) = 2^{1/2+s} \Gamma(1 + \frac{s}{2}) / \Gamma(\frac{1}{2} - \frac{s}{2})$ (see Sect. 6.8 of [15]), we obtain the following Mellin–Barnes integral representation [16]

$$\begin{aligned} G^\alpha(\mathbf{r}) &= \frac{1}{2\alpha\pi^{3/2} \ell |\mathbf{r}|^2} \frac{1}{2\pi i} \int_{\gamma-i\infty}^{\gamma+i\infty} \frac{\Gamma(\frac{1}{\alpha} - \frac{s}{\alpha}) \Gamma(1 - \frac{1}{\alpha} + \frac{s}{\alpha}) \Gamma(1 + \frac{s}{2})}{\Gamma(\frac{1}{2} - \frac{s}{2})} \left(\frac{|\mathbf{r}|}{2\ell}\right)^{-s} ds \\ &= \frac{1}{2\alpha\pi^{3/2} \ell |\mathbf{r}|^2} H_{1,3}^{2,1} \left[\frac{|\mathbf{r}|}{2\ell} \left| \begin{matrix} (1 - \frac{1}{\alpha}, \frac{1}{\alpha}) \\ (1 - \frac{1}{\alpha}, \frac{1}{\alpha}), (1, \frac{1}{2}), (\frac{1}{2}, \frac{1}{2}) \end{matrix} \right. \right]. \end{aligned} \quad (15)$$

In Eq. (15), the fundamental solution $G^\alpha(\mathbf{r})$ is expressed in terms of the H-function, commonly utilized in fractional calculus (see, for example, [13, 17, 18]). It consists of the fractional generalization of the modified Bessel function of the second kind K_ν , which has many notable implications in physical systems. In particular, the terms K_ν of integer order ν (such as K_1 and K_2) enable the removal of singularities from dislocations and disclinations [12], while of half-integer order $\nu = n + 1/2$ (such as $K_{1/2}$ and $K_{5/2}$) can eliminate singularities from crack tips [19–21]. More recently, it was employed to represent significant deviations from Newtonian gravity [4], with related applications in subatomic systems, such Yukawa-type nuclear potentials (see also [22, 23]). In the integer-order case $\alpha \rightarrow 2$, $G^\alpha(\mathbf{r})$ reduces to $K_{1/2}(|\mathbf{r}|/\ell)$, and more generally to $K_{n+1/2}(|\mathbf{r}|/\ell) = \sqrt{\pi \ell / 2|\mathbf{r}|} e^{-|\mathbf{r}|/\ell} \sum_{j=0}^n \frac{(n+j)!}{j!(n-j)!} \left(\frac{\ell}{2|\mathbf{r}|}\right)^{2j}$ (6.565 and 8.468 of [24]) in \mathbb{R}^n .

Fractional Gradient Interatomic Potentials

In this section, we apply the fractional GradEla formalism in order to generalize a recently derived gradient modification of London’s quantum mechanical interatomic potential [6] where a detailed discussion on generalized gradient interatomic poten-

tials and an extension to their fractional counterparts is given, while the special London’s case was treated as a preliminary assignment in [25] see acknowledgements. Motivated by the fractional counterpart of the Ru-Aifantis theorem [5], a gradient-enhanced London’s potential, denoted as w_{LG}^α , is obtained [6, 25] by the following Riesz-fractional inhomogeneous Helmholtz equation

$$(1 + \ell^\alpha (-\Delta)^{\alpha/2}) w_{LG}^\alpha(\mathbf{r}) = w_L(\mathbf{r}), \tag{16}$$

where \mathbf{r} is the interatomic distance, and $w_L(\mathbf{r})$ the denotes the classical London’s potential. The classical (non-gradient) London’s potential is given by the expression $w_L(\mathbf{r}) = -\frac{C_L}{|r|^6}$; $C_L = 3\alpha_0^2 h \nu / 4(4\pi\epsilon_0)^2$, where α_0 is the electronic polarizability, ϵ_0 the vacuum dielectric permittivity, while h, ν denote the Planck constant and the electron orbital frequency respectively [26, 27]. A local relation between the induced dipole moment μ_i and the electric field E_i of the form $\mu_i = \alpha_0 E_i$ is assumed. For non-local and fractional generalizations, the reader can consult [28] and [29], respectively. Using Eq. (14), a particular solution of Eq. (16) can be expressed in convolution form as

$$\hat{w}_{LG}^\alpha = \int_{\mathbb{R}^3} G^\alpha(\mathbf{r} - \mathbf{r}') w_L(\mathbf{r}') d\mathbf{r}'. \tag{17}$$

By applying, in addition, the well-known theorem of Bessel functions (8.532 of [24])

$$\frac{J_\nu(kR)}{R^\nu} = \left(\frac{2}{k}\right)^\nu \Gamma(\nu) \sum_{m=0}^\infty (m + \nu) \frac{J_{m+\nu}(kr)}{r^\nu} \frac{J_{m+\nu}(k\rho)}{\rho^\nu} C_m^\nu(\cos\theta), \tag{18}$$

where $R = |\mathbf{r} - \mathbf{r}'|$ and $\nu = 1/2$, along with subsequent evaluation of the angular integral in Eq. (17) through the orthogonality of the Gegenbauer polynomials $\int C_m^\nu(\cos\theta) d\Omega = 4\pi \delta_{m,0}$, the general solution of Eq. (16) is obtained as

$$w_{LG}^\alpha = A G^\alpha(r) + \int_0^\infty (r\rho)^{-1/2} \mathcal{K}^\alpha(r, \rho) w_L(\rho) \rho^2 d\rho, \tag{19}$$

where we defined $\mathcal{K}^\alpha(r, \rho) = \int_0^\infty k (1 + \ell^\alpha k^\alpha)^{-1} J_{1/2}(kr) J_{1/2}(k\rho) dk$; G^α is given by Eqs (14), (15), while A is an adjustable parameter. We note that $\mathcal{K}^\alpha|_{\alpha \rightarrow 2} = K_{1/2}(\frac{r_>}{\ell}) I_{1/2}(\frac{r_<}{\ell})$ (6.541 of [24]), where $r_> = \max(r, \rho)$, $r_< = \min(r, \rho)$, and hence Eq. (19) reduces to the gradient solution obtained by variation of parameters [6], which reads

$$w_{LG}^\alpha|_{\alpha \rightarrow 2} = \frac{A \ell}{r} e^{-r/\ell} + \frac{C_L}{48\ell^6} \left\{ \frac{4\ell^4}{r^4} + \frac{2\ell^2}{r^2} + \frac{\ell}{r} \left[e^{r/\ell} Ei\left(-\frac{r}{\ell}\right) - e^{-r/\ell} Ei\left(\frac{r}{\ell}\right) \right] \right\}. \tag{20}$$

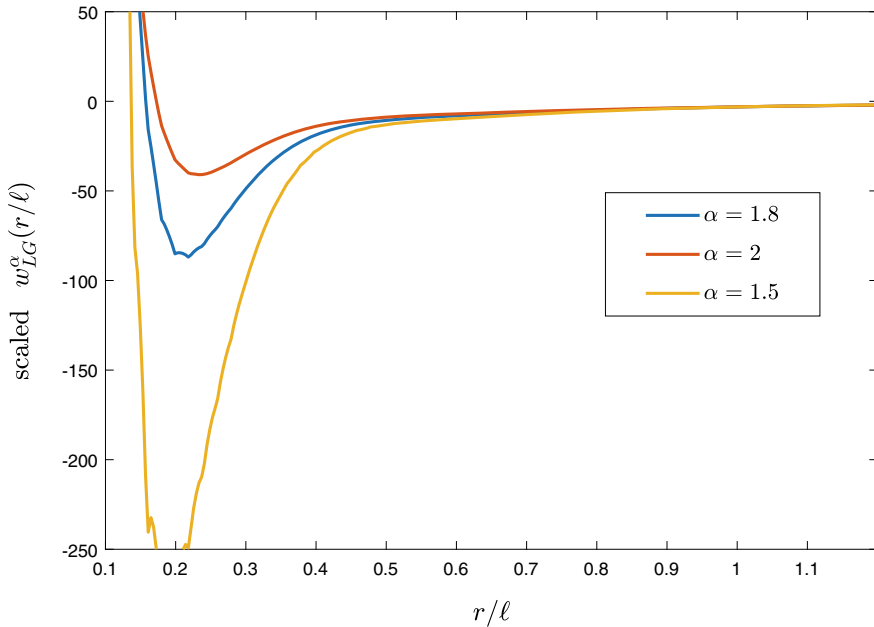


Fig. 1 Qualitative plots of the fractional gradient potential for $\alpha = 1.5, 1.8, 2$. The scaling factor is $C_L \ell^{-6}$. (Color figure online)

Again, the fractional interatomic potential of Eq. (19) includes both an “attractive” (for large r) and a “repulsive” (for small r) branch, as in the integer order case of Eq. (20). A qualitative plot for Eq. (19) is provided in Fig. 1.

Acknowledgements This work was benefited from research interactions with the beneficiaries and partners of the RISE European projects FRAMED no. 734485 (<https://cordis.europa.eu/project/rcn/207050/factsheet/en>), and ATM2BT no. 824022 (<https://cordis.europa.eu/project/rcn/219192/factsheet/en>). The work was initiated during a visit of E.C. Aifantis to the University of Florida which was supported in part by FRAMED and in part by the following regional grants of NSRF 2014–2020: MIS 5005134 “Nano-chemomechanics in Deformation and Fracture: Theory and Applications in LIBs and SGS”, and MIS 5005454 “Material Instabilities, Size Effects and Morphogenesis: Nanomaterials and Brain”. An extended version of this work is included in the review [6], whereas the special London’s non-fractional gradient case was discussed in [25]. In fact, the article in [25] was advanced in order to realize the aforementioned research collaboration between Aristotle University (E. C. Aifantis team) and the University of Florida (K. E. Aifantis team).

References

1. Aifantis EC (1992) On the role of gradients in the localization of deformation and fracture. *Int J Eng Sci* 30(10):1279–1299

2. Aifantis EC (2011) On the gradient approach—relation to Eringen's nonlocal theory. *Int J Eng Sci* 49(12):1367–1377
3. Aifantis EC (2016) Internal length gradient (ILG) material mechanics across scales and disciplines. *Adv Appl Mech* 49:1–110
4. Aifantis EC (2020) A concise review of gradient models in mechanics and physics. *Front Phys* 7:1–8
5. Ru CQ, Aifantis EC (1993) A simple approach to solve boundary-value problems in gradient elasticity. *Acta Mech* 101(1–4):59–68
6. Aifantis EC (2021) Gradient extension of classical material models: from nuclear condensed matter scales to earth & cosmological scales. In: Ghavanloo E, Fazelzadeh SA, Marotti de Sciarra F (eds) *Size-dependent continuum mechanics approaches: theory and applications*. Springer
7. Tarasov VE, Aifantis EC (2014) Toward fractional gradient elasticity. *J Mech Behav Mater* 23(1–2):41–46
8. Tarasov VE, Aifantis EC (2015) Non-standard extensions of gradient elasticity: fractional non-locality, memory and fractality. *Commun Nonlinear Sci Numer Simul* 22(1–3):197–227
9. Tarasov VE, Aifantis EC (2019) On fractional and fractal formulations of gradient linear and nonlinear elasticity. *Acta Mech* 230(6):2043–2070
10. Parisi K, Konstantopoulos I, Aifantis EC (2018) Non-singular solutions of GradEla models for dislocations: an extension to fractional GradEla. *J Micromech Mol Phys* 03(03n04):1840013
11. Yu M, Gutkin, Aifantis EC (1996) Screw dislocation in gradient elasticity. *Ser Mater* 35(11):1353–1358
12. Yu M, Gutkin, Aifantis EC (1999) Dislocations and disclinations in gradient elasticity. *Phys Status Solidi* 214(2):245–284
13. Samko SG, Kilbas AA, Marichev OI (1993) *Fractional integrals and derivatives theory and applications*. Gordon and Breach, New York
14. Marichev OI (1982) *Handbook of Integral transforms of higher transcendental functions: theory and algorithmic tables*. Ellis Horwood, New York
15. Erdelyi A (1955) *Tables of integral transforms I*. McGraw-Hill, New York
16. Aifantis EC Fractional generalizations of gradient mechanics. In: Tarasov VE (ed) *Handbook of fractional calculus with applications*. De Gruyter, Berlin, Boston
17. Kilbas AA, Srivastava HM, Trujillo JJ (2006) *Theory and applications of fractional differential equations*. Elsevier, Amsterdam
18. Mathai AM, Saxena RK, Haubold HJ (2010) *The H-function*. Springer, New York, NY
19. Aifantis EC (2012) A note on gradient elasticity and nonsingular crack fields. *J Mech Behav Mater* 20(4–6):103–105
20. Konstantopoulos I, Aifantis EC (2013) Gradient elasticity applied to a crack. *J Mech Behav Mater* 22(5–6):193–201
21. Aifantis EC (2014) On non-singular GRADELA crack fields. *Theor Appl Mech Lett* 4(051005):1–7
22. Fischbach E (2015) The fifth force: a personal history. *Eur Phys J H* 40(4–5):385–467
23. Rowlinson JS (1989) The Yukawa potential. *Phys A Stat Mech Appl* 156(1):15–34
24. Gradshteyn IS, Ryzhik IM (2015) *Table of integrals, series, and products*, 8th ed. Academic Press
25. Parisi K, Shuang F, Wang B, Hu P, Giannakoudakis A, Konstantinidis A (2020) From gradient elasticity to gradient interatomic potentials: the case-study of gradient London potential. *J App Math Phys* 8:1826–1837
26. Israelachvili J (2011) *Intermolecular and surface forces*, 3rd edn. Elsevier, San Diego
27. London F (1937) The general theory of molecular forces. *Trans Faraday Soc* 33:8–26
28. Bardhan JP (2013) Gradient models in molecular biophysics: progress, challenges, opportunities. *J Mech Behav Mater* 22(5–6):169–184
29. Tarasov VE, Trujillo JJ (2013) Fractional power-law spatial dispersion in electrodynamics. *Ann Phys* 334:1–23

Part XXXI
High Temperature Electrochemistry IV

Investigation on Preparation of Fe–Al Alloys by Direct Reduction of Fe₂O₃–Al₂O₃ Powder in CaCl₂–NaCl Molten Salt System



Jinrui Liu, Hui Li, and Jinglong Liang

Abstract Fe–Al alloys have been synthesized directly from Fe₂O₃–Al₂O₃ powder by electro-deoxidation in the CaCl₂–NaCl molten salt at 800 °C. The thermodynamic decomposition voltages of Fe₂O₃, Al₂O₃ and compounds in molten salt to their corresponding metal in 800 °C have been analyzed. Constant voltage electrolysis has been utilized to investigate the formation process of Fe–Al Alloys. The results indicated that Fe₂O₃ is decomposed into Fe earlier. It is found that with the first reduction product Fe, the later reduction product Al will immediately form Fe₃Al and FeAl which are more refractory, avoiding the loss of Al due to its low melting point thereby.

Keywords Fe–Al alloys · Electrochemical reduction · Reduction mechanism · Constant voltage electrolysis

Introduction

Fe–Al alloys with their, low density, high strength-to-weight ratios, good wear resistance, ease of fabrication and resistance to high temperature oxidation and sulfurization are very attractive as a kind of potential materials in the field of high-temperature materials [1, 2]. Currently, the preparation method of Fe–Al alloys is mainly traditional molten casting method [3] and emerging powder metallurgy such as thermal explosion method [4], all of which are using metal Fe and Al as raw material. Since both metal Fe and Al can react with oxygen easily, methods mentioned above have limitations in raw material storage.

In 2000, Chen et al. [5] reported a new process in which Ti can be produced by direct electrochemical reduction of solid TiO₂ in molten salts. After that, various

J. Liu · H. Li (✉) · J. Liang
College of Metallurgy and Energy, North China University of Science and Technology, 063210
Tangshan, Hebei, China
e-mail: lh@ncst.edu.cn

metals and alloys have also been synthesized from corresponding oxide by electro-deoxidation in molten salt [6]. In this report, Fe–Al alloy is directly prepared from the solid Fe_2O_3 – Al_2O_3 in CaCl_2 – NaCl as a molten salt system at 800 °C.

Calculation Method and Experiment

The theoretical composition voltages (U^\ominus/V) were obtained by Eq. (1):

$$U^\ominus = -\frac{\Delta G^\ominus}{nF} \quad (1)$$

where ΔG^\ominus is the standard Gibbs free energy change (kJ mol^{-1}) calculated by the HSC thermodynamic software, and n is the electron transfer number, and F is a Faraday's constant (96485 C mol^{-1}).

The analytical grade powders of Fe_2O_3 and Al_2O_3 were each weighted and mixed thoroughly according to the molar ratio of 53:47 by ball milling for 2 h. The mixture was weighted and pressed at a pressure of 8 MPa for 2.5 min into small porous pellets with diameter of about 15 mm, thickness of about 2 mm and mass of 1 g. The pellets were sintered in air in a tubular resistance furnace at 800 °C for 4 h to achieve stronger mechanical strength. After cooling, a pellet was wrapped with a stainless steel mesh to form a composite cathode. A high-purity graphite rod polished by sandpaper was used as anode.

A corundum crucible containing CaCl_2 – NaCl (150 g, molar ratio 58:42) was placed in a tube heating furnace and heated to 400 °C at a rate of 8°C min^{-1} and kept for 4 h to remove the surface water. Later, the mixed salt was heated to 800 °C at a rate of 5°C min^{-1} and maintained at this temperature during the experiment under argon. Pre-electrolysis was carried out for 4 h at 2.5 V using a stainless steel foil as cathode to remove moisture and impurities remaining in the molten salt. Subsequently, the oxide pellet cathode was inserted in the molten salt to undergo constant voltage electrolysis.

To investigate the reduction mechanism, the constant voltage electrolysis was carried out using a Taiwan GWINSTEK PSM-3004DC power supply. After individual electrolysis, the product was cooled with distilled water and washed in distilled water to remove residual chlorine salt on ultrasonic for 30 min, followed by vacuum drying. The obtained sample was characterized by X-ray diffraction spectrum (XRD, X-ray 6000 with Cu $K\alpha 1$ radiation at $\lambda = 1.5405 \text{ \AA}$).

Results and Discussion

Thermodynamic Analysis on the Electrochemical Reduction of Fe₂O₃–Al₂O₃ to Fe–Al Alloys in CaCl₂–NaCl Molten Salt

CaCl₂–NaCl molten salt is regarded as an ideal electrolyte for the electrochemical reduction of oxides with its low melting point, good conductivity, wide electrochemical window and acceptable cost. However, the metal oxides may react with CaO contents in the molten salt, resulting in the formation of intermediate phases. The standard Gibbs free energy changes (ΔG^\ominus) of possible reactions of CaO with Fe₂O₃ (reaction (2) and (3)) and Al₂O₃ (reaction (4)–(9)) are shown in Fig. 1.

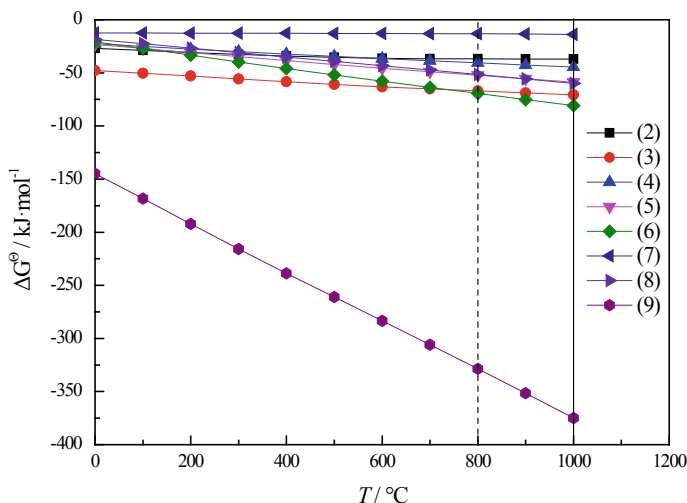
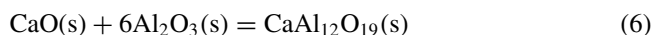
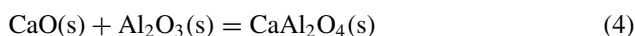
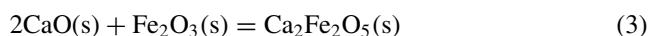
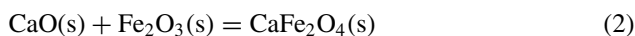
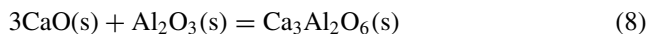
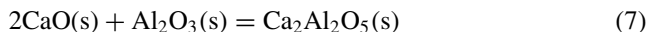


Fig. 1 Standard Gibbs free energy changes (ΔG^\ominus) of possible reactions of CaO with Fe₂O₃ and Al₂O₃ versus temperature (T). (Color figure online)



According to Fig. 1, the standard Gibbs free energy changes to form intermediate phases are all negative to 0 and keep decreasing as a function of temperature. Among all the reactions, the curve of reaction(9) has the largest slope, and the value of reaction (9) is much lower than those of others at 800 °C, which means that the formation of $\text{Ca}_{12}\text{Al}_{14}\text{O}_{33}$ is more thermodynamically favorable at the experimental temperature.

Commonly, the electrochemical reduction sequence of metal oxides/compounds can be judged by its theoretical decomposition voltage (U^\ominus). It is confirmed by the thermodynamic analysis in Fig. 1 that the formation of intermediate phases of CaO and Fe_2O_3 or Al_2O_3 can proceed spontaneously according to reaction (2) to (9) in $\text{CaCl}_2\text{-NaCl}$. Therefore, it is reasonable to take the decomposition of the intermediate phases into account. In the previous work, it was found that the reduction mechanism of solid Fe_2O_3 mainly consists of three steps: chemical formation of $\text{Ca}_2\text{Fe}_2\text{O}_5 \rightarrow \text{Fe}_3\text{O}_4 \rightarrow \text{FeO} \rightarrow \text{Fe}$ [7]. However, considering the content of CaO in $\text{CaCl}_2\text{-NaCl}$ and CaO is more inclined to combine with Al_2O_3 , the formation of $\text{Ca}_2\text{Fe}_2\text{O}_5$ is not inevitable, so as other intermediate phases. Thus, the thermodynamic analysis on the electrochemical reduction of Fe_2O_3 , Al_2O_3 and their intermediate phases to their low-valence and oxides (reaction (10) to (21)) was conducted, and the results are shown in Fig. 2.

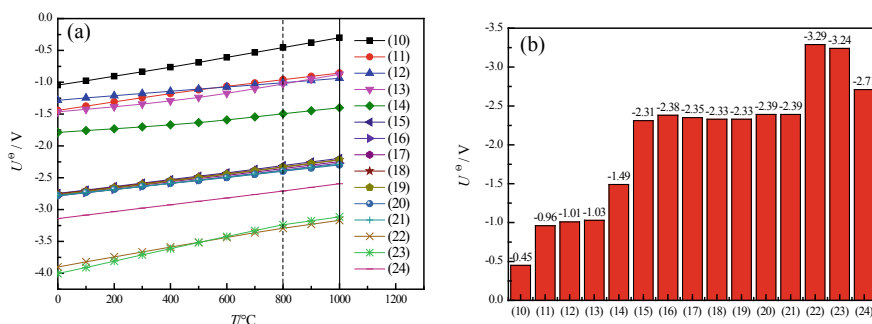
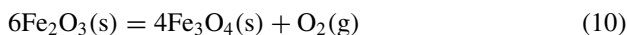
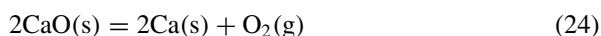
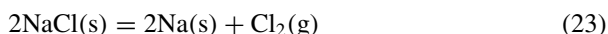
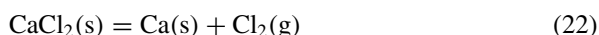
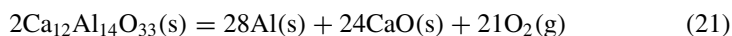
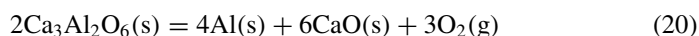
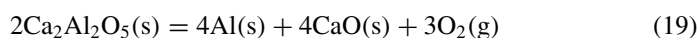
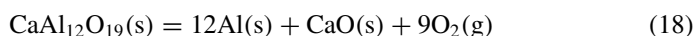
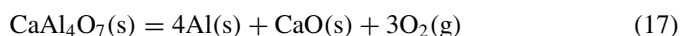
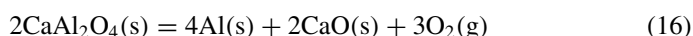
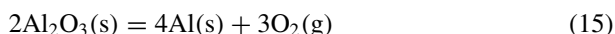
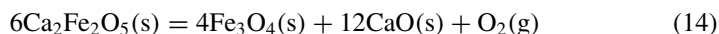
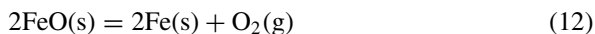
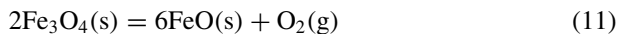


Fig. 2 **a** Theoretical decomposition voltages (U^\ominus) of Fe_2O_3 , Al_2O_3 , their intermediate phases, CaCl_2 , NaCl and CaO versus temperature (T); **b** theoretical decomposition voltages(U^\ominus) at 800 °C. (Color figure online)



The theoretical decomposition voltages of all the oxides, intermediate phases and CaCl_2 – NaCl molten salt decrease as the temperature rises. Figure 2b presents the theoretical decomposition voltages at 800 °C. It can be seen that CaCl_2 – NaCl molten salt has the largest value of the theoretical decomposition voltages, which indicates that CaCl_2 – NaCl is suitable as molten salt electrolyte for electrolysis of Fe_2O_3 – Al_2O_3 to prepare Fe–Al alloys. Furthermore, when taking graphite as the anode material, the anode products are CO/CO_2 instead of O_2 , and the theoretical decomposition voltages of reactants would be even lower. The theoretical decomposition voltages of all the Fe-containing compounds are lower than those of Al-containing compounds, so the theoretically calculated Fe would be reduced first.

In addition, the formation of the intermediate phases will increase the theoretical decomposition voltage of the corresponding metal oxide, as can be seen from Fig. 2. Therefore, by using methods such as pre-electrolysis, reducing the concentration of CaO in the molten salt as much as possible will facilitate the electrolysis of $\text{Fe}_2\text{O}_3\text{-Al}_2\text{O}_3$. However, CaO is in the form of Ca^{2+} and O^{2-} in the molten salt, as long as it is not saturated. Thus, in addition to the hydrolysis of CaCl_2 , CaO may also come from the deoxygenation of oxides. This means that the concentration of CaO near the cathode may be higher than that of the molten salt body, and the formation of intermediate phases will be inevitable.

Effects of Electrolysis Voltage on the Product

In this work, the impact of electrolysis voltage on the product was investigated. The applied voltages were 2.4, 2.8 and 3.2 V, and the electrolysis time was fixed for 12 h. Figure 3 shows that Fe_2O_3 which exists in sintered precursor was converted to metal Fe basically, after electrolyzed at 2.4 V for 12 h. However, no metal Al or Fe–Al alloy phases were observed in the product, suggesting that it is difficult to reduce Al_2O_3 to Al metal under this condition, even if the electrolysis voltage is higher than the theoretical decomposition voltage of its compounds. This may be due to the insufficient over potential. The intermediate phase $\text{Ca}_{12}\text{Al}_{14}\text{O}_{33}$ was

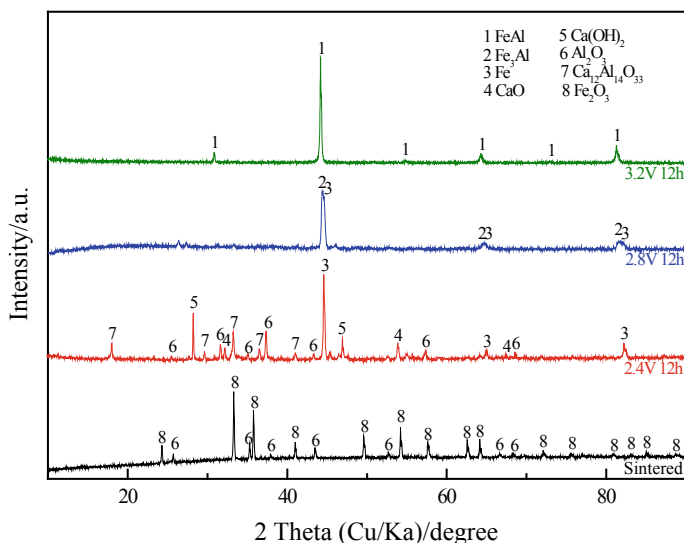


Fig. 3 XRD patterns of precursor $\text{Fe}_2\text{O}_3\text{-Al}_2\text{O}_3$ and electrolytic products obtained from constant voltage electrolysis at 2.4, 2.8 and 3.2 V for 12 h in 800 °C NaCl-CaCl_2 molten salt (molar ratio 42:58). (Color figure online)

formed in the meanwhile, which was consistent with thermodynamic analysis. As the results, on the one hand, since the reduction of Fe_2O_3 to Fe increased the porosity and conductivity of the precursor pellet, the reduction of Al_2O_3 should be much easier; on the other hand, O^{2-} released by the electro-deoxygenation reaction of Fe_2O_3 increased the concentration of CaO nearby the cathode, which would result in a basically unavoidable increase in forming intermediate phases such as $\text{Ca}_{12}\text{Al}_{14}\text{O}_{33}$.

When the voltage was increased to 2.8 V, XRD patterns revealed that the product was dominated by the Fe and Fe_3Al phases, suggesting that Al_2O_3 could be reduced to Al at this voltage. It is worth mentioning that considering the content of Al_2O_3 in the precursor, there should still exist a small amount of aluminum compounds which have not been reduced. By further increasing the voltage to 3.2 V, there was only FeAl phase observed in the cathode product. However, this voltage is close to the molten salt decomposition voltage (3.24 V). Therefore, to prepare a purer FeAl alloy in a short time, the electrolysis voltage could be selected as 3.0 V.

Preparation of Fe–Al Alloy by Molten Salt Electrolysis

A typical current–time plot recorded during electrolysis is presented in Fig. 4 which also shows the detail in the first 90 min. It can be seen from the current curve that in the stage 1, as the metal/solid oxide/molten salt three-phase reaction boundary extending on the surface of the pellet, the value of current rises slightly within 0–5 min. After that, the deoxidation and reduction of iron spread deep into the pellet, and the value of current rapidly drops within 5–10 min due to the increasing resistance of O^{2-}

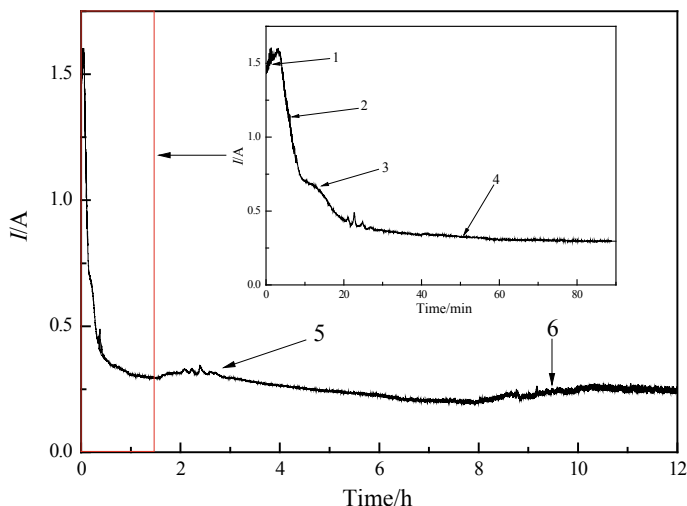


Fig. 4 Current–time plot of preparation of the FeAl alloy by electrolysis (800 °C, 3.0 V, 12 h). (Color figure online)

diffusing into the bulk of molten salt. At stage 3, the metal Fe formed on the surface of the pellet had a partial sintering phenomenon, resulting in a dense metal layer which slowed down the mass transfer and reaction speed. The value of current in the stage 4 is close to the background current, suggesting the reduction of Fe_2O_3 was basically completed. The rise of the current in the stage 5 should correspond to the reduction of Al_2O_3 or intermediate phases. The relatively low current and longer electrolysis time indicate that the reduction rate of Al_2O_3 is much lower than that of Fe_2O_3 . When the electrolysis time reached 8 h, as the electrode polarization phenomenon became more obvious, part of the molten salt started to decomposing, causing the value of current to rise slightly, as shown by the curve at stage 6. It is worth mentioning that due to the earlier production of a large amount of Fe, the post-produced Al can quickly alloy with Fe to form Fe_3Al or FeAl phase with higher melting points, so as to avoid the large loss of Al from cathode due to low melting point (660 °C) [8].

Conclusion

The feasibility for the production of Fe–Al alloys from Fe_2O_3 – Al_2O_3 by electrolysis in CaCl_2 – NaCl molten salt is analyzed thermodynamically. It is found that the theoretical voltage for decomposing Fe_2O_3 and Al_2O_3 to Fe and Al is only 1.01 V and 2.31 V at 800 °C, both of which are much lower than those of CaCl_2 – NaCl molten salts. However, the intermediate phases spontaneously generated in thermodynamics will increase the theoretical decomposition voltage, making the electrochemical decomposition reaction more difficult.

To further investigate the reduction mechanism, the electrolysis of Fe_2O_3 – Al_2O_3 was performed in the CaCl_2 – NaCl molten salt. In the process of Fe_2O_3 – Al_2O_3 , the production of Fe came first and could act at a lower electrolysis voltage. The formation of $\text{Ca}_{12}\text{Al}_{14}\text{O}_{33}$ occurred in the meanwhile. Al_2O_3 was not reduced until Fe_2O_3 was basically reduced. Al is produced later and relatively slowly, making Al with low melting point which can quickly alloy with Fe to form phases with higher melting point.

Acknowledgements The study is financially supported by the National Science Foundation of China (Project No. 51674120).

References

1. Kratochvíl P, Málek P, Cieslar M et al (2007) High-temperature mechanical properties of Zr alloyed Fe_3Al -type iron aluminide. *Intermetallics* 15(3):333–337
2. Jin Z, Yaping B, Chao C et al (2019) Research status of FeAl intermetallic with B2 structure. *Foundry Technol* 40(8):858–861

3. Jin Z, Yaping B, Chao C et al (2020) Effect of holding time of hot pressing sintering on microstructure and properties of B2 structure FeAl intermetallics. *J Xi'an Technol Univ* 40(03):274–281
4. Liu YN, Sun Z, Cai XP et al (2018) Fabrication of porous FeAl-based intermetallics via thermal explosion. *Trans Nonferrous Met Soc China* 28(6):1141–1148
5. Chen GZ, Fray DJ, Farthing TW (2000) Direct electrochemical reduction of titanium dioxide to titanium in molten calcium chloride. *Nature* 407(6802):361–364
6. Chen GZ, Fray DJ (2020) Chapter 11—Invention and fundamentals of the FFC Cambridge process. *Extr Metall Titanium*. 227–286
7. Jia L, Li H, Cai Z et al. (2020) Electrochemical behavior of Fe_2O_3 in electro-deoxygenation in NaCl-CaCl_2 molten salt system. In: TMS 2020 149th annual meeting and exhibition supplemental proceedings
8. Yan XY, Fray DJ (2009) Direct electrolytic reduction of solid alumina using molten calcium chloride-alkali chloride electrolytes. *J Appl Electrochem* 39(8):1349–1360

Liquid Bipolar Electrode for Extraction of Aluminium and PGM Concentrate from Spent Catalysts



Andrey Yasinskiy, Peter Polyakov, Dmitriy Varyukhin,
and Sai Krishna Padamata

Abstract Liquid bipolar electrodes (LBE) were proposed for the extraction of noble metals from spent catalysts by the electrometallurgical method with the production of aluminium and oxygen. The two-sectioned electrolysis cell divided by the LBE for the one-step extraction was designed. The first section acts as the aluminium reduction cell; the second one plays the role of the aluminium refinery cell. The noble metals are collected in the LBE, while the carrier (Al_2O_3) is decomposed to oxygen and aluminium which is transferred through the second section to be collected in the cathode. The effect of the spent catalysts content in the melt on the electrode processes and carrier dissolution kinetics was studied for molten fluoride systems at 800 °C. The dissolution rate lays in the range from 0.0123 to 0.0291 $\text{g kg}^{-1} \text{s}^{-1}$. The extraction of Pt to the LBE reached more than 99%. This method can be applied for the treatment of catalyst based on $\gamma\text{-Al}_2\text{O}_3$ carrier with a minor content of other oxides (SiO_2 , Fe_2O_3 , MgO , TiO_2 , CeO_2).

Keywords Spent catalyst · PGM · Electrolysis · $\text{KF}\cdot\text{AlF}_3$ · Molten salt · Dissolution

Introduction

The platinum group metals (PGMs) play the role of catalysts in the processes of the petrochemical industry and automotive catalytic converters. Petrochemical catalysts often consist of an Al_2O_3 -based carrier and 0.05–1% of noble metals (PGMs and rhenium) as the active components [1]. The catalysts gradually lose their catalytic activity during the operation. The deactivated (or spent) catalysts require processing to extract valuable components.

A large number of pyro- and hydrometallurgical methods of noble metals extraction from the spent catalysts were reported [2, 3]. Some of them are realized on an industrial scale. Common significant drawbacks of these methods often are the high

A. Yasinskiy · P. Polyakov · D. Varyukhin · S. K. Padamata (✉)
Siberian Federal University, Krasnoyarsk, Russia
e-mail: saikrishnapadamata17@gmail.com

© The Minerals, Metals & Materials Society 2021
TMS 2021 150th Annual Meeting & Exhibition Supplemental Proceedings,
The Minerals, Metals & Materials Series,
https://doi.org/10.1007/978-3-030-65261-6_73

812

cost of equipment and consumables, the high specific energy consumption and the huge amount of waste. The recent advances in this field are discussed below.

Antonov et al. [4, 5] presented an electrochlorination technology for the industrial processing of spent diesel automotive catalysts containing PGM and SiC carrier. The direct yield of platinum and palladium was 80 and 90%, respectively, without prior heat treatment. Subsequent operations with the catalyst after electrochlorination showed the possibility of increasing the extraction of Pt up to 98.7% and Pd up to 98.9% by increasing the treatment temperature to 160 °C (electrolysis under pressure). The specific energy consumption was 0.8 kWh/kg.

Diac et al. [6] showed that platinum can be electrochemically recovered from spent automotive catalysts in different electrolytes. An acidic pH and the presence of chlorides are mandatory in achieving high dissolution rates. Pt dissolution is achievable even at neutral pH, as long as the electrolyte contains chlorides. The recovery rates were as high as 50% in 24 h.

Ding et al. [7] proposed technology for recovery of Pt, Pd, and Rh by iron melting with iron powder. The recovery efficiency of PGMs was 99.25% under the conditions: the mass ratio of CaO/Na₂O = 35:20, CaF₂ 5 wt%, Na₂B₄O₇ 8.5 wt%, collector Fe 15 wt%, and 5 wt% C, where the concentration of Pt, Pd and Rh in slag phase was 2.398, 3.879, and 0.976 g/t, respectively. 50 kg pilot-scale experiments achieved over 99% recovery efficiency of PGMs.

A method for PGMs determination in spent automobile catalysts without chemical separation was discussed in [8]. An approach for the microwave dissolution with the mixture of HCl and H₂O₂ (4:1) was developed for the further high-resolution continuum source graphite furnace atomic absorption spectrometry. It was found that within 20 min at 210 °C PGMs quantitatively and simultaneously transferred to the solution.

HCl leaching followed by the selective precipitation of Pt and Pd has been investigated by Ilyas et al. [9]. The efficient formation of metal-chloro complexes was achieved by the addition of 3 vol% H₂O₂ with 8.0 mol/l HCl solution at 55 °C and 180 min of leach time. Approximately 94% Pd and 90% Pt extraction were achieved. The leaching process was diffusion-controlled with the apparent activation energy of Pd and Pt 14.4 kJ/mol and 10.8 kJ/mol, respectively. The leach liquor was processed to selectively recover platinum salt by adding a 300 g/l solution of NH₄Cl, precipitating (NH₄)₂PtCl₆.

The effect of ultrasound-assisted nitric acid pretreatment on enhancing the leaching of PGMs from spent catalysts by cyanogenic bacteria was investigated by Karim and Ting [10]. Samples were pretreated using ultrasonication and acid to remove competing metals. The optimal ultrasound power was 80%, nitric acid concentration—6M, ultrasound duration—50 min, and ultrasound frequency—37 kHz. Mesophilic bacteria *Pseudomonas fluorescens* and *Bacillus megaterium* were used to bioleach PGMs. Pretreated samples showed a higher recovery of PGMs. Using two-step bioleaching at a pulp density of 1% (w/v) and at pH 9, *P. fluorescens* yielded a maximum recovery of Pt (38%), Pd (44%), and Rh (91%) for pretreated samples. The corresponding values for *B. megaterium* were Pt (35%), Pd (41%), and Rh (82%).

The possibility of selective chlorination of PGM contained in spent catalysts, using molten salt as reaction media, was investigated by Martinez et al. [11]. Chlorination yields of the PGMs were found to be 40–50% after 2–3 h of passing chlorine gas through the eutectic LiCl–KCl and the equimolar CaCl₂–NaCl melts at 100 ml min⁻¹. Increasing the temperature did not lead to better chlorination yields, but the evaporation losses were significantly higher. The most suitable molten chloride system is the eutectic LiCl–KCl melt, allowing working at a relatively low temperature of 450 °C.

A pyrometallurgical iron matte process was adopted to separate PGMs from spent catalytic converters in [12]. The highest recovery percentages were 99% Pt, 99% Pd, and 97% Rh at 950 °C for 75 min. with the addition of 3 times flux (0.72 wt/wt, B₂O₃/Na₂O) of spent catalytic converters and 10 g of FeS₂ with a corresponding enrichment factor of around 6.0. Wen et al. [13] applied the electrolytic refining method on Fe-PGMs alloy for separating PGMs from iron. Fe-PGMs alloy and titanium plates are used as anode and cathode. The main electrolyte is ferrous sulfate. During electrolysis, iron is electrolytically migrated to the cathode and electrodeposited, while PGMs settle to form anode slime. Appropriate parameters ranges for electrolysis are: potential (0.5–0.8 V), concentration of Fe²⁺ (1.0–1.5 mol/l), temperature (60–80 °C), pH (3.0–3.5). The recovery efficiency reached nearly 100%.

The recovery of PGMs from spent catalysts using potassium bisulfate fusion pretreatment and hydrochloric acid leaching was performed by Prasetyo and Anderson [14]. Optimization on the fusion and leaching parameters resulted in 106% ± 1.7%, 93.3% ± 0.6%, and 94.3% ± 3.9% recovery for Pd, Pt, and Rh, respectively. These results were achieved at fusion conditions: temperature 550 °C, potassium bisulfate/raw material mass ratio 2.5, and fusion time 30 min. The leaching conditions were: HCl concentration 5 M, temperature 80 °C, and time 20 min.

Novel macrocyclic extractants were synthesized and employed in liquid–liquid extraction by Torrejos et al. [15] for Pd/Pt separation in the aqueous feed source. Dioxadithia-benzo-crown ether diols (BCES₂O₂) 2 g–2i were prepared through bis-epoxide cyclization with aqueous 1,2-benzenedithiol under mild basic conditions. 2 g–2i was alkylated to afford dimethoxy-BCES₂O₂ 3 g–3i. Experiments reveal their high stability, extraction efficiency, and separation performance ($\beta_{\text{Pd}^{2+}/\text{Pt}^{2+}} = 10^4 - 10^5$) in highly acidic feed solutions (~6 M HCl). The high extraction efficiency (99.5%) and purity (98.5%) of recovered Pd²⁺ from simulated acidic spent catalyst liquor demonstrated the potential of 3i [in toluene] system for selective Pd²⁺ recovery from automotive wastes.

A hydrometallurgical process is proposed by Yakoumis et al. [16] resulting in recovery rates for Pt (100%), Pd (92%) and Rh (~60%) in low acidity reagents, namely 3 M HCl, 4.5 M NaCl, 1% v/v H₂O₂, under mild temperature conditions (70 °C). The highest S/L ratio achieved (S/L = 0.7) leads to high catalyst mass dissolution.

Thiophosphate- and phosphate-based extractants, 1,3-bis (diethoxythiophosphinoxy) benzene (Ext 1) and 1,3-bis(diethoxyphosphinoxy) benzene (Ext 2), respectively, were synthesized and studied for their ability to extract Pd(II) from

HCl and HNO₃ media by Yamada et al. [17]. Ext 1 (0.1 M) in 1-octanol selectively extracted 90–99.9% of Pd(II) in HCl (0.1–8.0 M) and 99.8% of Pd(II) in HNO₃ (0.1–8.0 M) single-metal solutions, whereas Ext 2 demonstrated negligible Pd(II) extraction in either solution. Back-extraction of Pd(II) was performed using a solution of 0.1 M thiourea and 1.0 M HCl, allowing Ext 1 to be reused for five cycles.

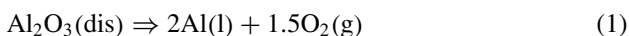
Zhang et al. [18] proposed an integrated process based on the capture of copper scrap and electrodeposition process to recycle Pd in spent catalysts. The process consisted of two procedures: the capture of copper scrap to enrich palladium and electrodeposition process to separate and purify palladium. The appropriate parameters for the capture of copper scrap are the melting temperature reached 1400 °C, adding 20% of copper scrap and 2 of the mass ratio of SiO₂/Al₂O₃ and for the electrodeposition process, nearly 100% of palladium was deposited on the cathode under 0.1 M concentration of HNO₃, −0.042 V of electrodeposition potential and 25 °C reaction temperature with 9 h.

Zhao et al. [19] developed a new method for the recovery of cerium from spent catalysts. Sulfuric acid (2 mol/l) and hydrofluoric acid (0.9 mol/l) were used as a mixed acid leaching agent to successfully decompose the ceria-zirconia solid solution of the catalyst, which is resistant to dissolve in acids. The leaching efficiency of Ce reached 99.25% under the optimal conditions of a catalyst particle size range of 76–96 μm, an S/L of 1/10 (w/v), a leaching temperature of 70 °C, a leaching time of 4 h, and 200 rpm. The results indicated that 87.23% of Ce⁴⁺ was extracted into the D2EHPA-kerosene solution with a concentration of 0.8 mol/l D2EHPA, a stoichiometric quantity of KMnO₄ of 175%, and contact for 15 min at room temperature. Reduction stripping was performed using hydrochloric acid (2 mol/l) with 3% H₂O₂ to obtain the CeCl₃ solution. The recovered amount of Ce was 85.54% with high purity.

A few decades ago, Belov et al. [20] proposed an electrochemical method for the extraction of Pd from spent Al₂O₃-based catalysts which was carried out in several stages based on the Hall–Heroult process for the primary aluminium production and the three-layer refining process for the high-purity aluminium production.

Recently, the new idea of one-step electrochemical method which can be used at 700–850 °C was presented [21]. A liquid bipolar electrode (LBE) dividing the cell into two parts can be used. The first part would act as an electrolysis cell where catalyst carrier dissolves and decomposes into oxygen and aluminium, and PGMs are accumulated in LBE. The second part would act as refinery cell where aluminium dissolves from the LBE and is reduced at the liquid aluminium cathode. The concentration of PGMs would increase in time due to the equal (more or less) partial currents of aluminium cathodic reduction and anodic dissolution at the LBE.

The promising candidate for the electrolyte, the molten 1.3KF-AlF₃ system has the high solubility of Al₂O₃ and high limiting current density of Al reduction. The metallic anode, which enables oxygen evolution by the reaction (1), can be used:



The process can be implemented for aluminium reduction with oxygen-evolving anodes simply by using alumina instead of spent catalysts. In that case, the liquid bipolar electrode will be used to collect the anode corrosion products that sounds beneficial because the proper cathode metal purity remains one of the most difficult and important tasks in the inert anode research [22, 23]. The following improvements can make this process applicable to aluminium production:

- A decrease in interelectrode spaces especially in the refinery part;
- An increase in alumina dissolution rate in low-temperature electrolytes;
- A decrease in overvoltages by decreasing the current densities;
- Design of the continuous alumina feeding system.

The electrochemical characterization of the LBE is studied in various molten salts systems [21, 24]. The rate of catalyst dissolution and the effect of catalyst concentration in the 1.3KF-AlF₃ melts on the polarization curves recorded at LBE at 800 °C are studied in this work. The results of the first 29 h laboratory-scale electrolysis test are reported. This study supplements scarce data on the kinetics of aluminium deposition, oxidation and oxide dissolution in fluoride melts.

Experimental

Materials Preparation

The electrolyte was synthesized at 900 °C from the dried chemically pure (p.a.) salts KF and AlF₃. Drying lasted for 4 h at 400 °C. The prepared melt was purified during 2 h electrolysis with a graphite electrode under the potential of 1.5 V (for the removal of oxygen ions before the dissolution studies) and 0.2 V (for the removal of electronegative metals ions, namely Fe, Si, etc., before the cyclic voltammetry on tungsten electrode) relative to the aluminium electrode potential. The spent catalysts supplied by JSC “Kratsvetmet” (Krasnoyarsk, Russia) were calcined at 800 °C under air atmosphere for 30 min to remove organic compounds. The mechanical activation of the catalysts was performed after the heat treatment in planetary mills with a duration of 10 s.

Dissolution Rate

The electrical conductivity κ_l of the molten cryolite is known to be decreased with the increase of the dissolved alumina concentration C_A . Different models predict the value $\partial\kappa_l/\partial C_A \cong -0.05\Omega^{-1}\text{cm}^{-1}\text{wt}\%^{-1}$. Addition of 1 wt% of alumina will cause a change in cell resistance of 2.5–5%. The resistance-time dependence was

used to estimate the alumina dissolution rate. The resistance was measured by electrochemical impedance spectroscopy (EIS) in the cell described in [25]. The resistance R of the electrochemical system was calculated out of impedance Z , given by the expression:

$$Z = R - j \cdot \frac{1}{\omega \cdot C} = Z' - jZ'' \quad (2)$$

where $j = \sqrt{-1}$, $Z' = R$ is the real part of the impedance, $Z'' = \frac{1}{\omega \cdot C}$ is the imaginary part of impedance, ω is the frequency of the AC polarization, C is the capacitance of the electrochemical system. The phase angle, φ , is given by the equation:

$$\operatorname{tg} \varphi = \frac{Z''}{Z'} = \frac{1}{R \cdot \omega \cdot C} \quad (3)$$

The EMF of the galvanic cell is given by the Nernst equation:

$$E^{\text{rev}} = E^0 - \frac{RT}{nF} \ln \frac{a_O^{\nu_O}}{a_R^{\nu_R}} \quad (4)$$

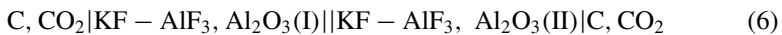
where E^0 is the standard EMF, a is the activity, ν is the stoichiometric coefficient, subindexes O and R denote oxidation and reduction forms.

If the activities of the species are unknown, the EMF can be expressed as a function of dissolved alumina (for cryolite-alumina melts) concentration by the semi-empirical formula:

$$E^{\text{rev}} = -\frac{\Delta G^0}{6F} + \frac{RT}{6F} \ln \left(\frac{C_{A(\text{sat})}}{C_A} \right)^{2.77} \quad (5)$$

where ΔG^0 is the change of Gibbs energy in the corresponding reaction.

For the concentration cell



the EMF can be expressed by the equation:

$$E^{\text{rev}} = \frac{RT}{6F} \ln \left(\frac{C_{A(II)}}{C_{A(I)}} \right)^{2.77} \quad (7)$$

where $C_{A(I)}$ and $C_{A(II)}$ are alumina concentration in the half-cells I and II .

The noted relations were used to measure the dissolution rate indicated by EMF of the concentration cell [25] as a function of time after addition of alumina into one of the half-cells.

Electrode Processes Characterization

The electrochemical measurements were carried out in a three-electrode graphite cell under air atmosphere in the temperature range of 700–850 °C. The graphite crucible served as an auxiliary (counter) electrode. Tungsten rod with a diameter of 2 mm placed into a BN tube was used as a working electrode. The working electrode potential was measured vs. the potential of the aluminium reference electrode encapsulated into a BN case. The cell was heated by the vertical electric furnace. The temperature of the electrolyte was measured by the k-type thermocouple in a BN case and maintained constant (± 2 °C). The current and the potential were supplied or measured using AutoLab PGSTAT 302n and NOVA 2.1 Software (The MetrOhm, Netherlands).

Cyclic voltammograms were obtained at different potential sweep rates in the range 0.01 – 0.1 V s⁻¹. The ohmic voltage drop of the measuring circuit was determined by the current interrupt technique and compensated during the sweep. The stationary polarization dependencies were determined by recording the steady-state value of the electrode potential at different cathodic current densities in the range of 0.01–1.5 A cm⁻².

Electrolysis Test

The cell for the electrolysis test (graphite crucible) consisted of two sections: electrolysis and refining. The sections were separated by a vertical graphite plate. The lower part of the plate and the crucible (bottom and 1 cm of walls) were coated with a TiB₂ layer to improve the wettability by aluminium.

In the electrolysis part, the electrolyte consisted of a KF-AlF₃ system with a cryolite (molar) ratio [KF]/[AlF₃] = 1.3 mol/mol. In the refining part, the electrolyte consisted of an equimolar mixture of NaCl-KCl and 5 wt% AlF₃. The sections were connected through a liquid bipolar aluminium electrode located at the bottom of the cell. The test was performed at 800 °C with a current of 13.9 A for 29 h. The temperature was measured in the refining part using a k-thermocouple. The catalyst was loaded in portions of 4.3 g every 30 min (with interruptions due to technical problems during testing). The voltage was measured with a voltmeter. The content of Pt and Re in cathode aluminium and the LBE was determined.

Results and Discussion

Dissolution of Catalysts

The rate of catalyst dissolution plays an important role in the process. Low rates may lead to the sludge formation, increase in the apparent viscosity and decrease in the electrical conductivity. The dissolution takes more time in the laboratory cells when compared to the industrial ones due to the suppressed convection. However, it can be used for the comparison purpose. The resistance and EMF values indicating the change in the concentration of dissolved alumina carrier in the 1.3KF-AlF₃ melt at 800 °C are shown in Fig. 1.

The resistance was changing in the range from 0.56 to 0.64 Ω. The first measurement was done immediately after the addition of 1 g (1 wt%) of regular catalyst. Several stages can be distinguished. They are indicated by the sections in the graph. In section *B0–B1*, a rapid drop (0.04 Ω or 7% in 90 s) in the resistance was observed due to the heating of the melt cooled by the cold catalyst added. The similar drop (section *A0–A1*) was observed in the EMF which reduced from ~100 to ~70 mV in 150 s. The resistance and the EMF were increasing in section *B1–B2* and *A1–A2*. The $\partial R/\partial \tau$ value was less. The reason is probably the dissolution rate being controlled by the heat transfer stage. In section *B2–B3*, the $\partial R/\partial \tau$ value rapidly increased that indicates the change in the dissolution mechanism from heat transfer controlled to mass transfer controlled. This stage lasted 150 s during which the sample was completely dissolved. The resistance was more or less constant during section *B3–B4*. The complete dissolution took 812 s. The EMF reached a local maximum value of 98 mV at *A2*, stayed constant for ~40 s and started to reduce in the section *A3–A4*. The resistance change after the addition of the catalyst sample corresponds

Fig. 1 Resistance (squares) and the EMF (solid line) of the cell recorded during 1000 s after the addition of a regular catalyst to the 1.3KF-AlF₃ melt containing 3 wt% of dissolved catalyst. (Color figure online)

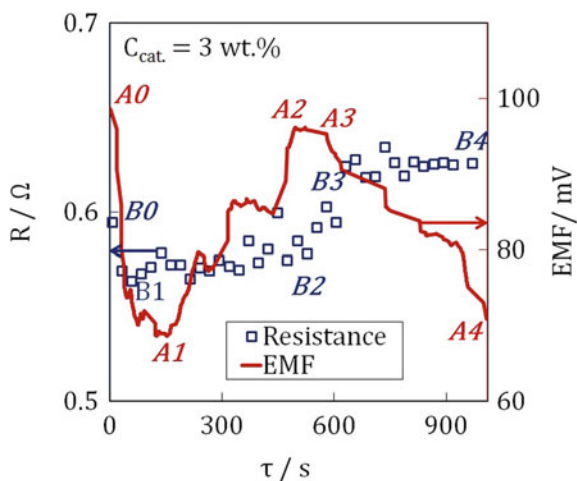
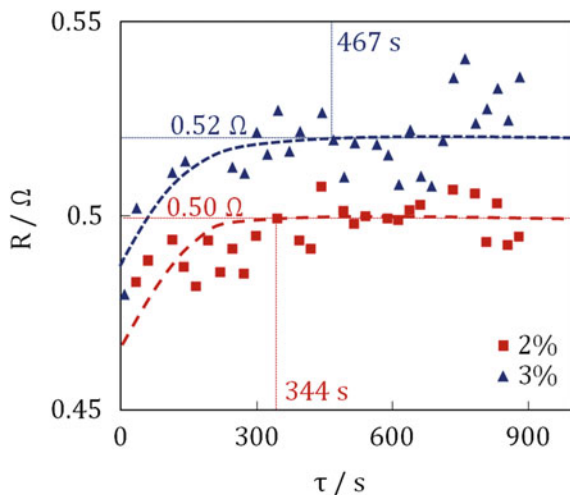


Fig. 2 Resistance of the cell recorded during 1000 s after the addition of an activated catalyst to the 1.3KF-AlF₃ melt containing 2 (squares) and 3 (triangles) wt% of dissolved catalyst. (Color figure online)



to the expected dissolution behaviour, while the EMF change sometimes gives the inexplicable data.

In previous work [25], it was shown that the special treatment (namely, mechanical activation) done over the oxide material may increase its dissolution rate. The same treatment was performed over the spent catalyst. The resistance change after addition of an activated catalyst to the melt containing 2 and 3 wt% of the dissolved catalyst is shown in Fig. 2.

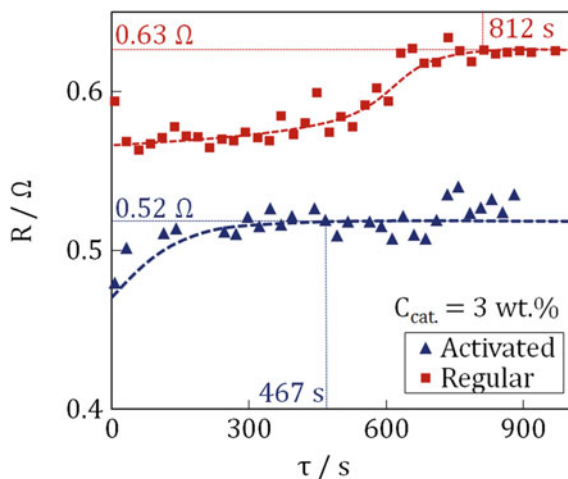
The resistance was changing in the range from 0.47 to 0.51 Ω and from 0.47 to 0.54 Ω for the melts containing 2 and 3 wt% of dissolved catalyst. It is difficult to find the precise value of dissolution time due to the fluctuations in the resistance caused by the varying temperature and the local volume fractions of solid particles. The dash lines represent the averaged data. The time at which this line becomes horizontal is considered as an estimated dissolution time. The dissolution time increases with the initial concentration of dissolved catalyst in the melt that evidences the mass transfer control.

The comparison of the regular and activated catalysts dissolution under the same conditions is presented in Fig. 3.

The heat transfer stage is almost absent in case of the dissolution of activated catalyst. As a result, the total dissolution time is almost two times less when compared to the dissolution of regular catalyst (467 and 812 s respectively).

The estimated dissolution rates were in the range from 0.0123 to 0.0291 $\text{g kg}^{-1} \text{s}^{-1}$ which are almost five times less when compared to the dissolution rate of alumina under the similar conditions presented in [25]. The reason might be the presence of organic residues after the catalyst calcination and PGMs inhibiting the dissolution. The presented data are not sufficient for making the conclusions but aim at drawing the attention to the dissolution of the oxide in the molten halides. To perform an

Fig. 3 Resistance of the cell recorded during 1000 s after the addition of regular (squares) and activated (triangles) catalyst to the 1.3KF-AlF₃ melt containing 3 wt% of dissolved catalyst. (Color figure online)



electrolysis test, the activated catalyst was chosen as a fed material. The concentration should be maintained between 2 and 3 wt%.

Electrode Processes at the LBE

The cyclic voltammetry was performed to study the effect of the catalyst concentration in the melt on the parameters of anodic dissolution and cathodic reduction of aluminium. These parameters are reduction and oxidation onset potential, peak potentials (if obtained), peak current densities. The voltammograms (CVs) recorded on the tungsten substrate are shown in Fig. 4.

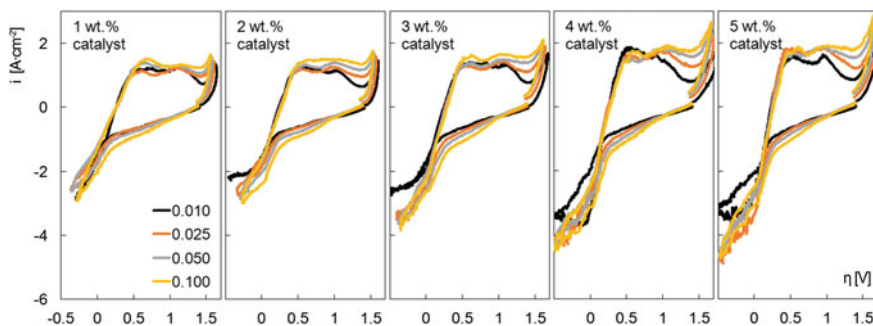
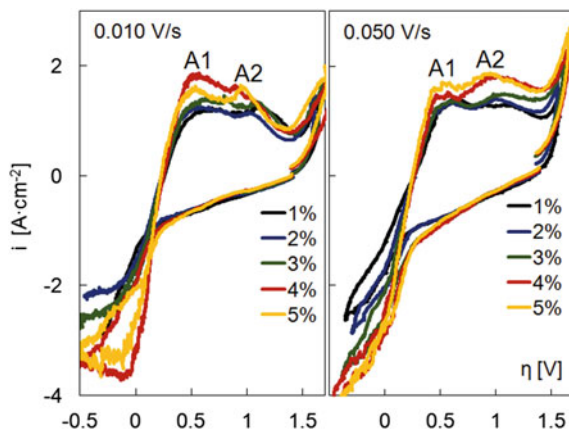


Fig. 4 CVs recorded on tungsten in the 1.3KF-AlF₃ melt with different catalyst content at different sweep rates from 10 to 100 mV/s. (Color figure online)

Fig. 5 Comparison of the CVs recorded on tungsten in the 1.3KF-AlF₃ melt with different catalyst content at the same sweep rate. (Color figure online)



The aluminium reduction onset potentials were around +0.1 V versus Al/Al³⁺ reference electrode. The cathodic peaks were not found in the studied range of potentials. The reason is mixed kinetics and was discussed the previous work [NJC, NFM]. The cathodic current densities at the reverse potential (−0.5 V) were increasing with an increasing catalyst concentration in the range from 2.9 to 4.9 A cm^{−2}. The sweep rate slightly affected the current density in the cathodic part of the CV. In the anodic part, two peaks at +0.5 and +1.0 V were recorded with the peak current densities in the range from 1.2 to 1.8 A cm^{−2}. The first peak currents did not depend on the sweep rate and were related to the aluminium oxidation. The current of the second peak increased with increasing sweep rate indicating the mass transfer dominance. This peak may be correlated with the aluminium oxidation from the intermetallic compound in the system Al-W. However, the potential gap of 0.5 V between these peaks makes this explanation questionable. The tungsten oxidation onset potential was recorded at +1.5 V.

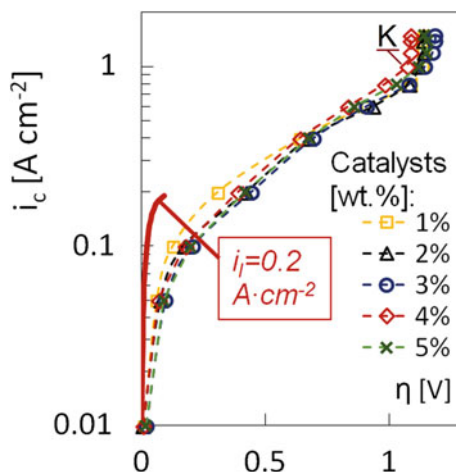
The CVs recorded at different catalysts concentration were plotted on the same graph and shown in Fig. 5.

The currents of anodic peaks A1 and A2 are slightly affected by the catalyst concentration. Besides that, no drastic difference was observed on the CVs. The chosen range of dissolved catalyst concentration in the melt between 2 and 3 wt% may be approved for the electrolysis test.

No significant difference was observed in the stationary galvanostatic polarization curves shown in Fig. 6.

The polarization curves recorded are not typical for the diffusion-controlled process. The solid line represents the calculated values for the limiting current of 0.2 A cm^{−2}. These results support the idea of mixed kinetics. Reduction of potassium occurs at a potential of −1.1 V versus reference electrode. The overvoltage can be sufficiently high in the studied system, so the limiting current should be lower than usually used for the liquid aluminium cathode. For the electrolysis test, the current density of 0.4 A cm^{−2} was chosen.

Fig. 6 Stationary polarization curves recorded for the cathodic process on tungsten in the 1.3KF-AlF₃ melt with different catalyst content. (Color figure online)



Electrolysis Test

An electrolysis test was performed at the following parameters:

- Current 13.9 A
- Duration 29 h
- Current densities ~ 0.4 A cm⁻²
- Temperature 800 ± 10 °C
- Electrolyte in the electrolysis part 1.3KF-AlF₃ +(2÷3) wt% cat.
- Electrolyte in the refinery part NaCl-KCl +5 wt% AlF₃
- The weight of each fed portion 4.3 g
- The frequency of feeding 30 min⁻¹
- Anode 90Cu-10Al/graphite;
- The distance between the anode and the LBE 2 cm.

The photo of the cell during the electrolysis is shown in Fig. 7.

The electrolysis test started with metallic anode which was replaced by the graphite one after 15 h due to the possible short circuiting. During the process, the cell voltage was about 4.6 V with the metallic anode. The bubbles were observed in the electrolysis part. After 15 h of electrolysis, the viscosity in the electrolysis section arose that indicated a high content of the solid phase. A dense film was formed on the surface of the melt in the electrolysis section. The melt in the refining section remained transparent.

After the test, the content of Pt and Re was measured. The results are presented in Table 1.

Pt and were accumulated in the LBE. Less than 1 wt% of Pt entered the liquid aluminium cathode. The content of Re in the products was less because a significant part of it might form a volatile oxide and left the cell with the outlet gases.

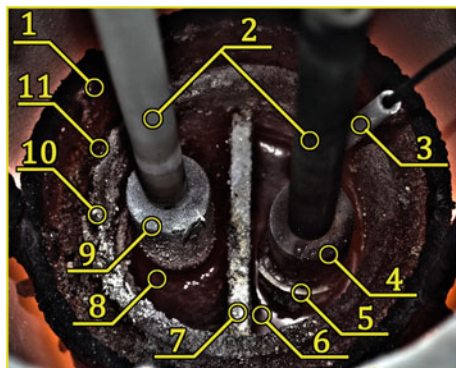


Fig. 7 Photo of the cell during the 29 h electrolysis test: (1) steel container; (2) current leads in alumina tubes; (3) k-type thermocouple; (4) graphite cathode; (5) alumina vessel for cathodic metal; (6) electrolyte in the refinery part; (7) the wall dividing the parts; (8) electrolyte in the electrolysis part; (9) graphite anode; (10) graphite crucible; (11) graphite powder. (Color figure online)

Table 1 Distribution of Pt and Re in the cell

Element	Mass in electrolysis part of LBE, mg	Mass in the refinery part of LBE, mg	Mass in cathodic metal, mg
Pt	1107.2	101.8	11.0
Re	708.6	not found	not found

Conclusions

The possibility of the extraction of PGMs and Re from spent catalysts by molten salt electrolysis is shown. The main findings are as follows:

- Mechanical activation of the spent catalyst and calcination at 800 °C for 30 min is required before the extraction;
- The dissolution rate lays in the range from 0.0123 to 0.0291 g kg⁻¹ s⁻¹ which is less when compared to the dissolution rate of alumina under similar conditions;
- The organic residue and noble metals on the surface of the catalyst may inhibit the dissolution of the carrier;
- The sufficient current densities are about 0.4 A cm⁻²;
- More than 99% of Pt and up to 100% of Re can be accumulated in the LBE.

Further work should be aimed at finding optimal conditions for the extraction of noble metals from spent catalysts.

Acknowledgements The reported study was funded by RFBR according to the research project No. 18-29-24,122.

References

1. Trinh HB, Lee JC, Suh YJ, Lee J (2020) A review on the recycling processes of spent autocatalysts: towards the development of sustainable metallurgy. *Waste Manag* 114:148–165. <https://doi.org/10.1016/j.wasman.2020.06.030>
2. Padamata SK, Yasinskiy AS, Polyakov PV, Pavlov EA, Varyukhin DY (2020) Recovery of noble metals from spent catalysts: a review. *Metall Mater Trans B*. <https://doi.org/10.1007/s11663-020-01913-w>
3. Nazanin BH, Mousavi SM (2020) Comprehensive characterization and environmental risk assessment of end-of-life automotive catalytic converters to arrange a sustainable roadmap for future recycling practices
4. Antonov A, Samotaev N, Tietz A, Tsarev G, Veselov D, Kirichenko A (2020) Effective method for the platinum group metals extracting from spent diesel autocatalysts. *Mater Sci Forum* 977:218–222. <https://doi.org/10.4028/www.scientific.net/MSF.977.218>
5. Antonov A, Tietz A, Samotaev N, Kirichenko A (2020) Electrochlorination as the basis for an efficient technique for extracting platinumoids from spent diesel catalysts. *Tsvetn Metall* 4:30–36. <https://doi.org/10.17580/tsm.2020.04.03>
6. Diac C, Maxim FI, Tirca R, Ciocanea A, Filip V, Vasile E, Stamatin SN (2020) Electrochemical recycling of platinum group metals from spent catalytic converters. *Metals* 10:822. <https://doi.org/10.3390/met10060822>
7. Ding Y, Zheng H, Zhang S, Liu B, Boyu W, Jian Z (2020) Highly efficient recovery of platinum, palladium, and rhodium from spent automotive catalysts via iron melting collection. *Resour Conserv Recycl* 155:104644. <https://doi.org/10.1016/j.resconrec.2019.104644>
8. Eskina VV, Dalnova OA, Filatova DG, Baranovskaya VB, Karpov YA (2020) Direct precise determination of Pd, Pt and Rh in spent automobile catalysts solution by high-resolution continuum source graphite furnace atomic absorption spectrometry. *Spectrochim Acta, Part B* 165:105784. <https://doi.org/10.1016/j.sab.2020.105784>
9. Ilyas S, Srivastava RR, Kim H, Cheema HA (2020) Hydrometallurgical recycling of palladium and platinum from exhausted diesel oxidation catalysts. *Sep Purif Technol* 248:117029. <https://doi.org/10.1016/j.seppur.2020.117029>
10. Karim S, Ting YP (2020) Ultrasound-assisted nitric acid pretreatment for enhanced biorecovery of platinum group metals from spent automotive catalyst. *J Clean Prod* 255:120199. <https://doi.org/10.1016/j.jclepro.2020.120199>
11. Martínez AM, Osen KS, Støre A (2020) Recovery of platinum group metals from secondary sources by selective chlorination from molten salt media. In: Azimi G, Forsberg K, Ouchi T, Kim H, Alam S, Baba A (eds) *Rare metal technology 2020. The minerals, metals and materials series*. Springer, Cham. pp 221–233. https://doi.org/10.1007/978-3-030-36758-9_21
12. Morcali MH (2020) A new approach to recover platinum-group metals from spent catalytic converters via iron matte. *Resour Conserv Recycl* 159:104891. <https://doi.org/10.1016/j.resconrec.2020.104891>
13. Wen Quan, Ding Yunji, Zheng Huandong, Liu Bo, Zhang Shengen (2020) Process and mechanism of electrolytic enrichment of PGMs from Fe-PGMs alloy. *J Clean Prod* 271:122829. <https://doi.org/10.1016/j.jclepro.2020.122829>
14. Prasetyo E, Anderson C (2020) Platinum group elements recovery from used catalytic converters by acidic fusion and leaching. *Metals* 10:485. <https://doi.org/10.3390/met10040485>
15. Rey EC, Torrejos GM, Nisola SH, Min JW, Han SPL, Chung WJ (2020) Highly selective extraction of palladium from spent automotive catalyst acid leachate using novel alkylated dioxo-dithiacrown ether derivatives. *J Ind Eng Chem* 89:428–435. <https://doi.org/10.1016/j.jiec.2020.06.015>
16. Yakoumis I, Moschovi A, Panou M, Paniais P (2020) Single-step hydrometallurgical method for the platinum group metals leaching from commercial spent automotive catalysts. *J Sustain Metall* 6:259–268. <https://doi.org/10.1007/s40831-020-00272-9>

17. Yamada M, Gandhi MR, Kunda UMR, Mori T, Haga K, Shibayama A (2020) Recovery of Pd(II) from leach solutions of automotive catalysts by solvent extraction with new thiophosphate extractants. *Hydrometallurgy* 191:105221. <https://doi.org/10.1016/j.hydromet.2019.105221>
18. Zhang L, Song Q, Liu Y, Zhenming X (2020) An integrated capture of copper scrap and electrodeposition process to enrich and prepare pure palladium for recycling of spent catalyst from automobile. *Waste Manag* 108:172–182. <https://doi.org/10.1016/j.wasman.2020.04.013>
19. Zhao Z, Qiu Z, Yang J, Ma B, Li Z, Lu S, Xu Y, Cao L, Zhang W (2020) Recovery of rare earth element cerium from spent automotive exhaust catalysts using a novel method. *Waste Biomass Valorization* 11:4967–4976. <https://doi.org/10.1007/s12649-019-00783-x>
20. Belov SF, Igumnov MS, Lovchinovsky IYu (1997) Electrochemical technique for processing of deactivated aluminium-palladium catalysts during fabrication of pure aluminium and palladium concentrate. *Tsvetnye metally* 5:39–41
21. Yasinskiy AS, Krishna PS, Polyakov PV, Varyukhin DY (2019) Electrochemical characterization of the liquid aluminium bipolar electrode for extraction of noble metals from spent catalysts. *Non-ferrous Met* 47(2):23–30. <https://doi.org/10.17580/nfm.2019.02.04>
22. Yasinskiy AS, Padamata SK, Polyakov PV, Shabanov AV (2020) An update on inert anodes for aluminium electrolysis. *Non-ferrous Metals* 48(1):15–23. <https://doi.org/10.17580/nfm.2020.01.03>
23. Padamata SK, Yasinskiy AS, Polyakov PV (2020) Anodic process on Cu–Al Alloy in KF–AlF₃–Al₂O₃ Melts and Suspensions. *Trans Nonferrous Met Soc China* 30(5):1419–1428. [https://doi.org/10.1016/S1003-6326\(20\)65307-9](https://doi.org/10.1016/S1003-6326(20)65307-9)
24. Padamata SK, Yasinskiy AS, Polyakov PV (2020) Electrode processes in KF–AlF₃–Al₂O₃ Melts. *New J Chem* 44(13):5152–5164. [10.1039/D0NJ00016G](https://doi.org/10.1039/D0NJ00016G)
25. Yasinskiy AS, Suzdaltsev AV, Polyakov PV, Padamata SK, Yushkova OV (2020) Behaviour of aluminium oxide in KF–AlF₃–Al₂O₃ melts and suspensions. *Ceram Int* 46(8, Part B):11539–11548. <https://doi.org/10.1016/j.ceramint.2020.01.180>

Part XXXII
Materials for High Temperature
Applications: Next Generation Superalloys
and Beyond

Open Die Forging Simulation of Superalloy NIMONIC 115 Using DEFORM 3D Software



Swarup Jana, Jyoti Mukhopadhyay, Rajashekar Rao, and Venkatesh Meka

Abstract Nimonic 115 is a Ni-based superalloy that contains major alloying elements such as Cr, Co, and Mo. The alloy is used in the manufacturing of turbine blades for aerospace engines. The blades should have high fatigue strength and creep resistance at elevated temperature along with excellent wear and oxidation resistance properties. The presence of γ' phase with carbide precipitates in the γ phase matrix leads to high strength of Nimonic 115 even at high temperature. The product obtained either casting or powder metallurgy route needs to be thermo-mechanically processed to obtain the improved mechanical properties. Nimonic 115 has a very narrow working range with respect to temperature and strain rate. The reason may be due to the high phase stability of γ' phase at elevated temperature. During open die forging, Nimonic 115 is prone to surface defect, due to high local flow stress. In the present research work, the effect of heat transfer on deformation due to the transfer of billet from furnace to the forging setup has been examined. The combined effect of reduction and strain rate on the deformation has also been studied. Based on the simulation results using DEFORM 3D software, the optimum forging conditions have been estimated.

Keywords NIMONIC 115 · DEFORM 3D · Simulation

Introduction

Nimonic 115 is a nickel (Ni)-based superalloy with major alloying elements such as Cr, Co, and Mo which is used for high-temperature applications. High strength, better creep resistance along with excellent wear and corrosion resistance properties at high temperature make Nimonic 115 suitable for its use in aerospace industry

S. Jana · J. Mukhopadhyay (✉)
IIT Gandhinagar, Gandhinagar, Gujarat 382355, India
e-mail: jm@iitgn.ac.in

R. Rao · V. Meka
Mishra Dhatu Nigam Ltd, Hyderabad, Telangana 500058, India

[1–3]. Nimonic 115 is precipitation-hardened alloy with Ti and Al which form an inter-metallic compound $\text{Ni}_3(\text{Ti}, \text{Al})$ or γ' and carbide phase in the γ matrix [3]. The superior mechanical properties of Nimonic 115 greatly depend upon γ/γ' microstructure and volume fraction of γ' [1–3]. The increase in operating temperature of an aero-engine improves the efficiency of gas turbine. Thus, the components of the engine are required to sustain high thermal fatigue load and creep. Accordingly, Nimonic 115 is used in the manufacturing of turbine blades of aero-engine [1–3]. The failure of turbine disc leads to catastrophic failure of the engine. To achieve the high efficiency of the aero-engine, the components are made of superalloy which takes 50% of its total weight. The cast or wrought product obtained through casting (VIM) or powder metallurgy process requires further rolling/forging operation to obtain improved mechanical properties. During metal forming processes, failure occurs due to ductile mode rather than brittle failure. Several researchers had estimated the fracture experimentally or by numerical simulation or both. The failure in simulation can be modelled considering the ductile damage criteria, and a comparison is made between them considering compression test data [4–7]. Polakova et al. [8] discussed the open die forging simulation of Nimonic 80A considering the effective strain and standard Cockroft–Latham damage model. Furthermore, the fracture prediction during forging is also evaluated by simulation of upsetting using critical strain rate from experimental test [9–11]. In this present research work, open die forging simulation of Nimonic 115 has been carried out using DEFORM 3D. Based on simulation result, the optimum forging conditions are estimated while analysing the stress field after deformation in a single stroke.

Simulation Modelling

The open die forging operation was simulated in DEFORM 3D using DEFORM multiple operation (DEFORM MO). The operations consist of initial heat transfer operation due to transfer of the billet from the furnace to the forging setup followed by cogging operation between top and bottom die.

Heat Transfer Operation

The workpiece was only simulated in this operation with time step of 1 s per step for 120 s using explicit solver. The initial workpiece temperature was taken as 1175 °C i.e. above γ' solvus temperature [2] and the material as plastic. Tetrahedral mesh was used with 220,215 no of elements for the simulation. The specifications of the workpiece are shown Table 1. Material properties such as the flow stress, thermal conductivity and volumetric specific heat were obtained using JMatPro software using the chemical composition shown in Table 2. Heat transfer boundary conditions

Table 1 Workpiece specifications

Specifications	Value (mm)
Diameter	280
Length	500
Corner radius	20

Table 2 Chemical composition of Nimonic 115 [2]

Elements	C	Si	Cu	Fe	Mn	Cr	Ti	Al	Co	Mo	Zr	Ni
Composition	0.14	0.14	0.02	0.3	0.08	14.34	3.79	4.98	13.3	3.26	0.057	*balance

were applied at the surface and two end surfaces, with surrounding temperature as 30 °C and heat transfer coefficient 20 W/m²-K.

Cogging Operation

The workpiece data was extracted from the previous heat transfer operation database for cogging operation. Finer mesh was used near the surface and at the corner edges with mesh windows value as 0.5. IN 718 6um[1650-2200F(900-1200C)] was taken as rigid die material with preheat temperature 100 °C. The die specifications used for the simulation are shown in Tables 3 and 4. No manipulator was considered for the simulation. The load for deformation was applied using hydraulic press by the movement of the top die which was manipulated by constant strain rate. Friction coefficient between the workpiece and dies was considered as 0.69 [12] and heat

Table 3 Top die specifications

Dimensions	Value (mm)
Length	800
Width	350
Height	500
Corner radius	50

Table 4 Bottom die specifications

Dimensions	Value (mm)
Length	800
Width	350
Height	750
Corner radius	50

transfer coefficient was taken as 11 W/m-K. The cogging operation was simulated for 0.5 mm top die movement per unit step with explicit solver.

Results and Discussion

Effect of Temperature Gradient

To consider the effect of temperature gradient, two simulations were carried out (i) without heat transfer operation (ii) with heat transfer operation. For the later case, temperature gradient takes place near the surface of the workpiece before cogging operation. The sections are taken after one stroke of the top die and at the centre of the stroke. From the displacement contour (Fig. 1), it is seen that the maximum displacement in r - and z -directions takes place in the perpendicular direction of stroke at the surface, whereas maximum displacement in θ -direction takes place near the die contact. A comparison of displacement is made by taking point in perpendicular direction of the stroke from center to the surface (Fig. 2). Displacement in θ -direction (Fig. 2b) is small compared to r - and z -direction (Fig. 2a and 2c). The displacement in r -direction increases for the later case due to no restriction for material to flow, whereas the displacement in z -direction reduced as plastic deformation is nearly incompressible (Fig. 2a and 2c).

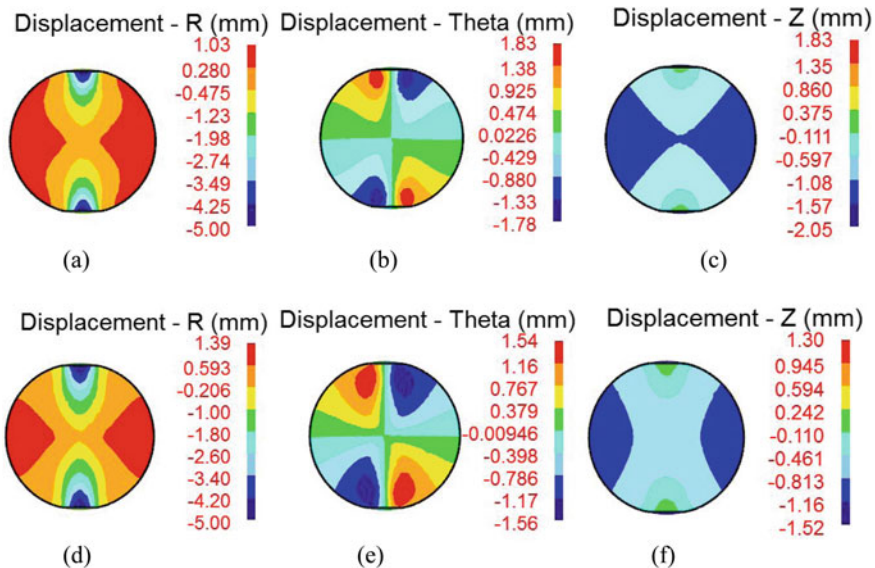


Fig. 1 Displacement contour (a),(b),(c) without temperature gradient and (d), (e), (f) with temperature gradient in r -, θ - and z -direction for strain rate 0.1 s^{-1} and 10 mm reduction. (Color figure online)

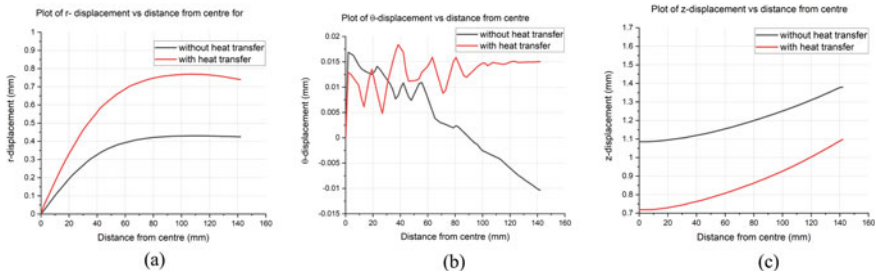


Fig. 2 Comparison of displacement field in **a** *r*- **b** θ - and **c** *z*-direction for strain rate 0.1 s^{-1} and 10 mm reduction. (Color figure online)

Due to heat transfer, temperature gradient takes place near the surface, and temperature is minimum at the surface. Hence, the flow stress is increased near the surface. Stresses $\sigma_{\theta\theta}$ and σ_{zz} increase near the surface as the material is restricted to flow in θ - and *z*-direction. But material is not restricted to flow in *r*-direction; as a result, value of stress σ_{rr} is reduced with heat transfer operation (Fig. 3). The value of stress $\sigma_{\theta\theta}$ and σ_{zz} near the surface are tensile in nature and become maximum at the surface (Fig. 4b and 4c). However, maximum value of stress $\sigma_{\theta\theta}$ is low compared to stress σ_{zz} , whereas stress σ_{rr} is zero at the surface due to no traction (Fig. 4).

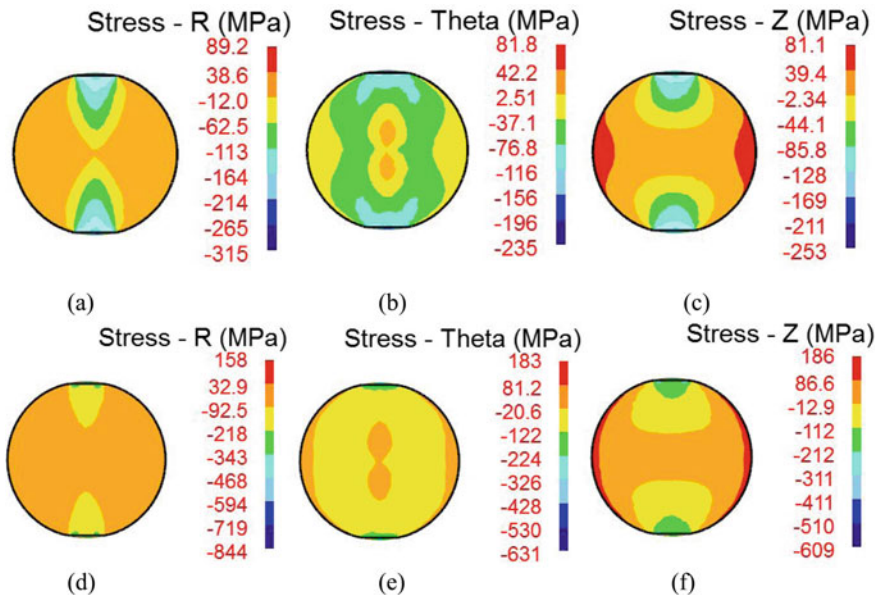


Fig. 3 Stress contour (a), (b), (c) without temperature gradient and (d), (e), (f) with temperature gradient in *r*-, θ - and *z*-direction for strain rate 0.1 s^{-1} and 10 mm reduction. (Color figure online)

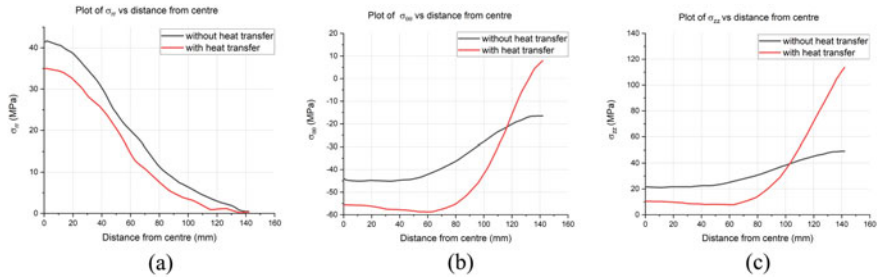


Fig. 4 Comparison of stress in **a** r -, **b** θ - and **c** z -direction with and without temperature gradient for strain rate 0.1 s^{-1} and 10 mm reduction. (Color figure online)

Effect of Reduction and Strain Rate

To consider the effect of strain rates and reductions, nine simulations were carried out with reductions 10, 20 and 30 mm and strain rates 0.01, 0.1 and 1 s^{-1} . The value of stress σ_{zz} is increased with increase in both strain rate and reduction (Figs. 5 and 6).

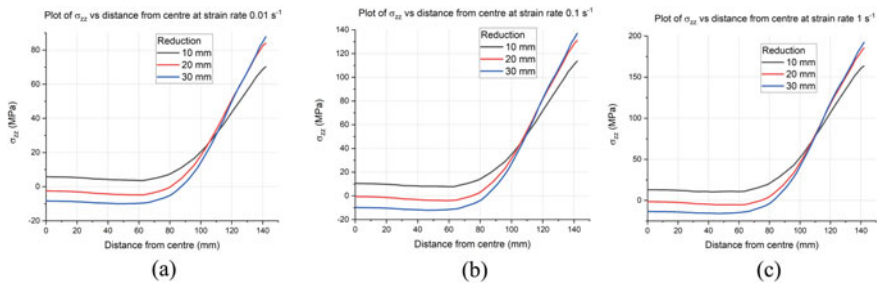


Fig. 5 Comparison of stress in z -direction for various reductions with strain rate **(a)** 0.01 s^{-1} , **(b)** 0.1 s^{-1} and **(c)** 1 s^{-1} . (Color figure online)

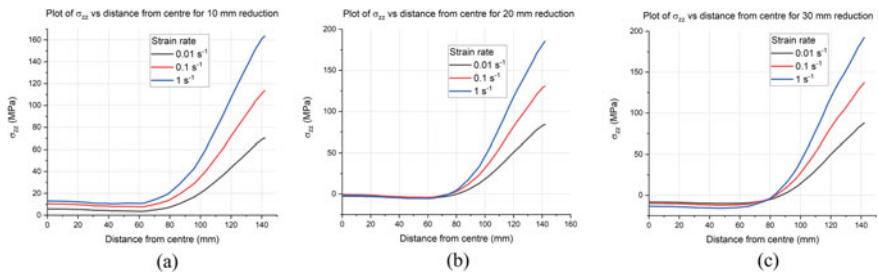


Fig. 6 Comparison of stress in z -direction for various strain rates with **(a)** 10 mm, **(b)** 20 mm and **(c)** 30 mm reduction. (Color figure online)

Fig. 7 Comparison of maximum value of stress σ_{zz} for different combinations of strain rate and reduction

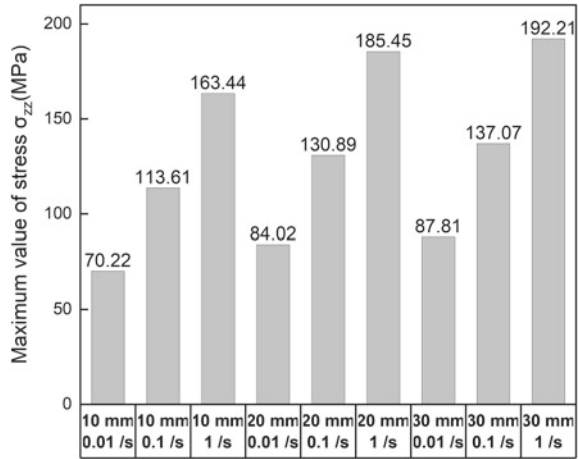


Table 5 Top die speed for different strain rates

Strain rate for deformation (s ⁻¹)	Top die velocity (mm/s)
0.01	2.8
0.1	28
1	280

Now, a comparison is made for the maximum value of stress σ_{zz} at the surface after one stroke for different combinations of strain rates and reductions. It is evident that maximum value of stress σ_{zz} is increased significantly with increase in strain rate rather than increase in reduction (Fig. 7).

Top die speed during the deformation at a constant strain rate is obtained from the post-processor result (Table 5). Top die speed at strain rate 1 s⁻¹ is 280 mm/s which is not practically achievable during forging, and 2.8 mm/s at strain rate 0.01 s⁻¹ is too slow for an industrial forging process. Thus, for an actual forging process, the top die speed will be 28 mm/s i.e. at strain rate 0.1 s⁻¹.

Conclusions

The initial heat transfer operation strongly affects the deformation behaviour of the material. Due to the temperature gradient, stresses σ_{zz} and $\sigma_{\theta\theta}$ increase rapidly near the surface. The maximum value of stress σ_{zz} is restricted to the ultimate tensile strength value to avoid crack at the workpiece surface. Based on simulation result, optimal forging condition will be 10 mm reduction at a strain rate of 0.1 s⁻¹ with an initial forging temperature of 1175 °C.

Acknowledgements The simulation in DEFORM 3D was done at Mishra Dhatu Nigam (MIDHANI) Ltd., Telangana, India, 500058.

References

1. Bruni C, Forcellese A, Gabrielli F (2002) Hot workability and models for flow stress of NIMONIC 115 Ni-base superalloy. *J Mater Process Technol* 125:242–247
2. Shahriari D, Sadeghi MH, Akbarzadeh A (2009) γ' Precipitate dissolution during heat treatment of nimonic 115 superalloy. *Mater Manuf Processes* 24(5):559–563. <https://doi.org/10.1080/10426910902746820>
3. Shahriari D, Sadeghi MH, Akbarzadeh A, Cheraghzadeh M (2009) The influence of heat treatment and hot deformation conditions on γ' precipitate dissolution of Nimonic 115 superalloy. *Int J Adv Manufact Technol* 45(9–10):841
4. Gouveia BPPA, Rodrigues JMC, Martins PAF (1996) Fracture predicting in bulk metal forming. *Int J Mech Sci* 38(4):361–372
5. Jeysingh J, Rao B, Reddy A (2008) Development of a ductile fracture criterion in cold forming. *Mater Sci Res J* 2(3&):4
6. Yu S, Feng W (2011) Experimental research on ductile fracture criterion in metal forming. *Front Mech Eng* 6(3):308
7. Zheng C, Pires F (2007) A comparison of models for ductile fracture prediction in forging processes. *Comput Methods Mater Sci* 7(4):389–396
8. Poláková I, Duchek M, Malencek L (2014) FEM simulation of open die forging of a plate from material NIMONIC 80A in DEFORM 3D. *Arch Mater Sci Eng* 66(1):31–36
9. He G, Liu F, Huang L, Jiang L (2016) Analysis of forging cracks during hot compression of powder metallurgy nickel-based superalloy on simulation and experiment. *Adv Eng Mater* 18(10):1823–1832
10. Yu S, Xie X, Zhang J, Zhao Z (2007) Ductile fracture modeling of initiation and propagation in sheet-metal blanking processes. *J Mater Process Technol* 187:169–172
11. Zhang W, Liu Y, Wang L, Liu B (2012) Numerical simulation and physical analysis for dynamic behaviors of P/M TiAl alloy in hot-packed forging process. *Trans Nonferrous Metals Soc China (English Edition)* 22(4):901–906. 10.1016/S1003-6326(11)61263-6. [http://dx.doi.org/10.1016/S1003-6326\(11\)61263-6](http://dx.doi.org/10.1016/S1003-6326(11)61263-6)
12. Shahriari D, Amiri A, Sadeghi MH (2010) Study on hot ring compression test of Nimonic 115 superalloy using experimental observations and 3D FEM simulation. *J Mater Eng Perform* 19(5):633–642. <https://doi.org/10.1007/s11665-009-9522-7>

Part XXXIII
Mechanical Behavior of Nuclear Reactor
Components

In-situ Scanning Electron Microscopic Observation of Creep and Creep-Fatigue of Alloy 709



Amrita Lall, Rengen Ding, Paul Bowen, and Afsaneh Rabiei

Abstract Alloy 709 is a 20Cr-25Ni advanced austenitic stainless steel developed as an improvement over the existing advanced austenitic stainless steels. The alloy's high Ni content provides increased austenite stability, while its high Cr content improves its corrosion resistance at extreme environments of nuclear structures. In this study, in-situ scanning electron microscope (SEM) tensile, creep and creep-fatigue tests at various temperatures from room temperature to 1000 °C will be reported. Electron backscatter diffraction (EBSD) and energy dispersive X-ray spectrometry (EDS) were used to observe the microstructural evolution and phase change during the in-situ heating and loading at different temperatures and strain rates and identify the dominant deformation mechanisms in each environmental condition.

Keywords In-situ SEM characterization · High-temperature test · Advanced steel alloy 709

Introduction

In a nuclear power plant, structural materials are exposed to high temperatures with temperature gradients for extended periods of time. This can result in aging of the microstructure along with creep damage and creep-fatigue loading. Advanced nuclear power plants are being developed as a part of the US Department of Energy's Generation IV reactor program initiative to increase lifespan, safety and efficiency by utilizing higher temperatures, higher neutron flux, more aggressive coolants/moderators [1]. Hence, new structural material needs to be developed to address the need of such structures.

A. Lall · A. Rabiei (✉)

Advanced Materials Research Laboratory (AMRL), Department of Mechanical and Aerospace Engineering, North Carolina State University, Raleigh, NC 27606, USA
e-mail: arabiei@ncsu.edu

R. Ding · P. Bowen

School of Metallurgy and Materials, University of Birmingham, Edgbaston, Birmingham B15 2TT, UK

Alloy 709 (Fe-20Cr-25Ni) is a nitrogen-stabilized niobium-strengthened advanced austenitic stainless steel that is being considered as potential material for structural applications in sodium-cooled fast reactors due to its high-temperature strength, weldability and high corrosion resistance [2]. Alloy 709 needs to undergo tensile, creep and creep-fatigue tests so that its capabilities and limitations can be documented in support of fast reactor licensing activity. Aged Alloy 709 should also be evaluated and compared with as-received material as aging is expected during service.

In-situ heating–loading and scanning electron microscope (SEM) imaging will be used to study the “real-time” crack growth of alloy 709 under plane stress conditions under tensile, creep and creep-fatigue loading at various temperatures from room temperature to 850 °C. The SEM is equipped with energy dispersive spectroscopy (EDS) and electron backscatter diffraction (EBSD). Crack propagation modes will be studied and compared, primarily at elevated test temperatures to evaluate crack initiation and growth. Some of the important features of defect nucleation and growth within the specimen will also be addressed by the subsequent fractographic assessments. This will combine the advantages of in-situ SEM observation to reveal the “real-time” fracture behavior and fractography to assess the failure mechanisms of Alloy 709 under various service conditions.

Experimental Procedure

Alloy 709 used in this study was fabricated by Carpenter Technologies in the form of ingots using vacuum-induction melting (VIM) and electro-slag remelting (ESR). These ingots were hot-forged, hot rolled and annealed at 1100 °C and then water quenched. The composition of Alloy 709 provided by the manufacturer is shown in Table 1. As-received Alloy 709 was aged at 650 °C for 2000 h in air to reveal microstructural changes similar to those during service. Aging at higher temperature than service expedites the aging process. Before cutting aged test samples, the material was skinned to remove any oxidized or decarburized layer at the surface [3].

The heating–loading stage shown in Fig. 1a (Kammrath and Weiss GmbH) consists of a 10 kN load cell and a ceramic heater that can heat up to 1000 °C which was installed inside a Hitachi SU 3500 SEM. Flat dog-bone samples were designed for tensile and creep-fatigue tests as per the constraints of the in-situ heating and loading stage and following the ASTM E-8 standard as shown in Fig. 1b. Flat samples with continuously reducing cross section were designed for creep tests as per ASTM E466-15 as shown in Fig. 1c. Samples with continuously reducing cross section were used to ensure that the maximum stress and the failure occurs at the center and SEM observations can be focused in that region. All samples were cut out of the plate along the rolling direction using electric discharge machining.

For SEM and EBSD observations, the samples were prepared to a near-perfect surface finish by grinding progressively using 320–2400 grit SiC sandpaper on

Table 1 Composition of alloy 709

TP310MoCbN	C	Mn	Si	P	S	Cr	Ni	Mo	N	Ti	Cb/Nb	B
Composition wt%	0.063	0.88	0.28	<0.005	<0.001	19.69	25.00	1.46	0.14	<0.01	0.23	0.0022

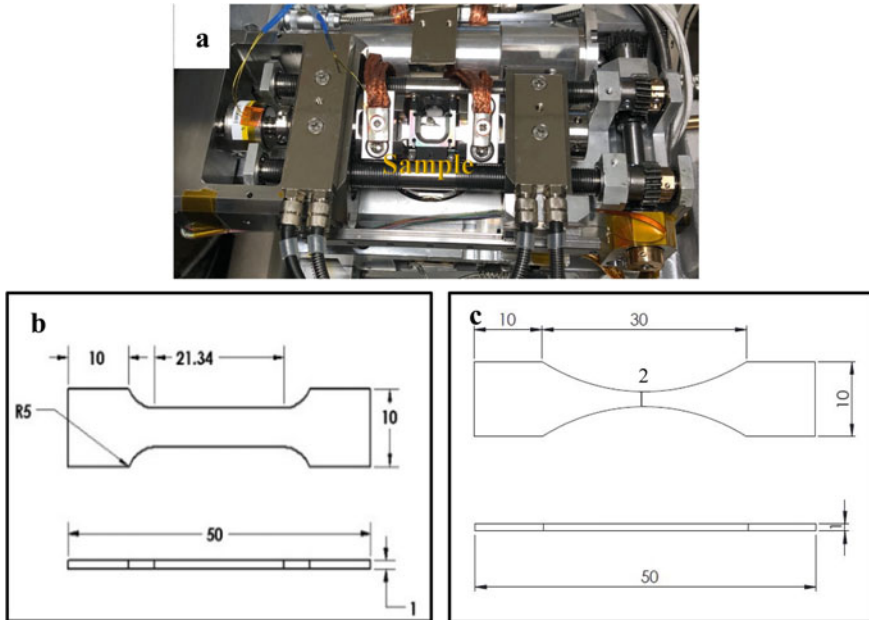


Fig. 1 a. Heating–loading stage with sample loaded. b Design and dimensions (mm) of the tensile and creep-fatigue test sample used in in-situ SEM heating and loading experiments c. Design and dimensions (mm) of the creep test sample. (Color figure online)

Buehler Automet grinding machine followed by either ion-milling or electro-polishing. For creep-fatigue crack growth (CFCG) tests, a small notch of 0.7–0.85 mm was added by machining, and then, a pre-crack was introduced at the tip of the notch by high frequency cyclic loading at room temperature.

High-temperature tensile, creep and creep-fatigue tests were performed at various temperatures from room temperature to 850° C in an in-situ heating–loading scanning electron microscope (SEM) equipped with Oxford Nordlys Max² Electron Backscatter Diffraction (EBSD) and Oxford X-Max^N Energy Dispersive Spectroscopy (EDS).

The as-received and aged Alloy 709 underwent in-situ SEM uniaxial tensile tests at temperatures between room temperature and 850 °C. All the tests were conducted along the rolling direction and at a strain rate of 5.02×10^{-3} /min as per the ASTM E21 standard for tensile tests at elevated temperatures. Next, uniaxial accelerated creep tests were conducted at higher temperature and greater stresses than the expected service condition. Creep tests were conducted by using blocks of constant load. The load was increased when creep deformation reached secondary stage. As such, a significant amount of data could be generated in a timely fashion [4]. One constant load creep test was also performed at 850 °C. Finally, in-situ creep-fatigue tests were done at 750 °C with dwell times of 1-second and 1 h introduced at the maximum tensile stress of 95% of yield stress. The crack path was monitored during the entire

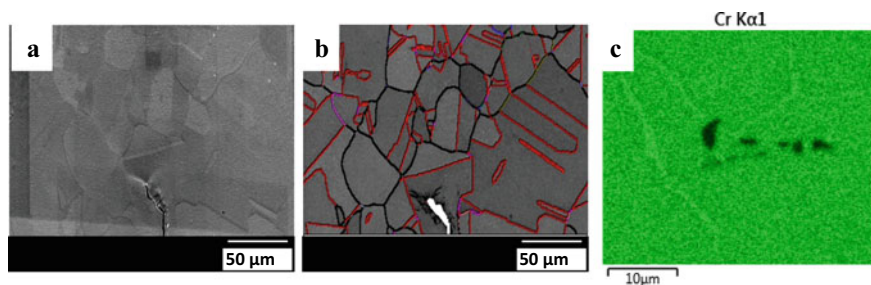


Fig. 2 a. SEM image of Alloy 709 test sample with pre-crack at the bottom of the picture. b. CSL map of the same area showing all boundaries. c. Cr EDS map of aged Alloy 709 showing Cr precipitation at grain boundaries. (Color figure online)

loading time. After all the tests, fractography was also performed on each sample using SEM to correlate the failure mechanism observations made on the surface during the in-situ test with those within the sample.

Results and Discussion

Microstructural Observations

SEM image and coincident site lattice (CSL) maps of Alloy 709 map of as-received Alloy 709 are shown in Fig. 2. As can be seen, the microstructure is comprised of equiaxed grains of 50 microns size. The red boundaries represent $\Sigma 3$ twin boundaries. The figure shows that 50% of all boundaries are twin boundaries. Some precipitates were also observed. EDS analysis confirms that these precipitates are mainly Nb and Mo rich carbides. EDS mapping of aged sample reveals the formation of chromium carbides in the form of globular particles at grain boundaries as shown in Fig. 2c.

Tensile Properties

Stress–strain curves obtained from tensile tests of all as-received and aged samples at a constant strain rate of 5.02×10^{-3} /min at various temperatures from room temperature (25 °C) to 850 °C are shown in Fig. 3. The sudden large drops in stress in the stress–strain curve occur when the test was paused for approximately 5 min to allow SEM imaging which resulted in stress relaxation. At room temperature, there were no serrations in plastic flow at any point in both the tests. As the temperature increases, serrations in plastic flow occur depending on the heat treatment condition of the alloy. For as-received Alloy 709, serration occurs at temperature between 550 °C

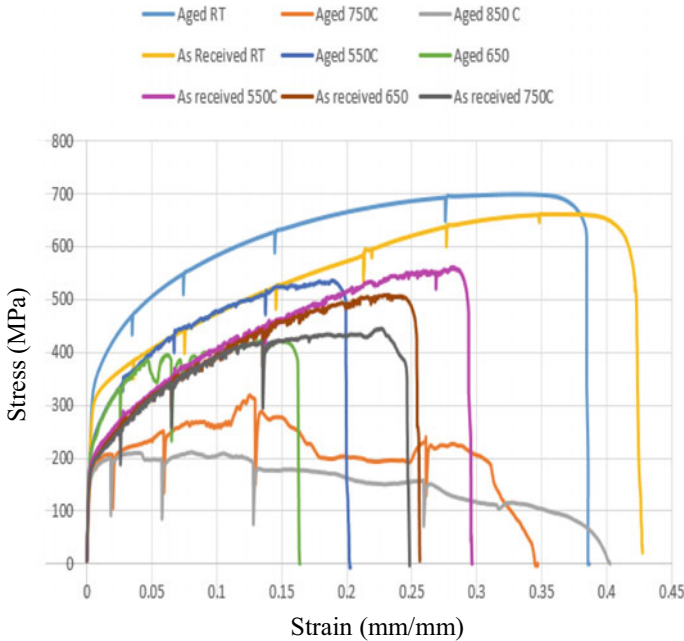


Fig. 3 a Stress–strain curves obtained from tensile test of all as-received and aged samples. (Color figure online)

and 750 °C, and for aged Alloy 709, serrations occur between 550 and 650 °C. In both as-received and aged Alloy 709, serrations start at a critical strain level after yield but continue till ultimate tensile strength only in as-received Alloy 709 and not in aged Alloy 709 where it ends sooner. The critical strain at which plastic flow also begins depends on temperature [5] and heat treatment conditions. As temperature increases, the strain at which serrations stop exhibiting reduces.

Serrations occur due to dynamic strain aging (DSA) [6] when there is pinning and unpinning of mobile dislocation at obstacles such as solute atoms [7]. Solute atoms obstruct the movement of dislocation but as loading continues, dislocation density increases which allows them to overcome the obstruction to their motion. At room temperature, solute atoms do not diffuse with respect to dislocations. When temperature increases, solute atoms become more energetic and are able to diffuse through the matrix. During tensile tests, dislocation density increases, and their motions become obstructed by solute atoms. Heat and load allow the solute atoms to diffuse within the matrix and interact with dislocations resulting in unpinning and re-pinning of dislocations. As the test continues and strain increases, speed of dislocation motions surpasses the speed of solute atoms, thus ending the serrated plastic flow.

At the beginning of the test, Type A serrations were observed. They are caused due to the formation of deformation bands such as Lüders bands repeatedly. As the test continues, the type of serrations changes to A+B in the aged samples, where the stress oscillates at about the general level or A+C in as-received Alloy 709 samples,

where the stress drops below the general level of stress. Type B serrations result from dislocation pinning and unpinning at diffusing solute atoms of high mobility such as carbon, whereas Type C serrations are associated with substitutional atoms such as chromium, molybdenum and niobium. Hence, Type C serration needs higher activation energy to get set in motion. Less serrations were observed in aged samples as compared to the as-received sample. During aging, some of the interstitial and solute atoms in the matrix diffuse to the grain boundary to form chromium carbide, which reduces the density of interstitial and solute atoms in the matrix, and less dislocation locking and unlocking effect is observed in aged sample compared to as-received sample.

Figure 3 also shows that there is very little to no necking strain at temperatures where there is dynamic strain aging (DSA) or Portevin–Le Chatelier effect. As temperature increases, usually thermally activated processes allow stress relaxation. In Alloy 709, DSA results in strengthening, and therefore, the strength does not drop within the DSA temperature between 550 and 750 °C regime, but a sharp decrease in strength is seen beyond the DSA regime.

Microstructural Evolution During Tensile Tests at Various Temperature

Pre-DSA Regime: Room Temperature

Figure 4a and b shows the SEM images of the as-received and aged sample, tested at room temperature. Both samples show formation of slip lines. The density of slip lines was found to be less in the aged sample than in the as-received sample. This can be attributed to the brittle carbide particles present on the grain boundaries of aged Alloy 709. During the test, these carbides do not allow plastic deformation resulting in void nucleation at the grain boundaries. Fractured surface of as-received Alloy 709 (Fig. 4c) shows dimpled fracture indicating failure by multi-void coalescence. Fractured surface of aged Alloy 709 (Fig. 4d) shows intergranular failure formed by debonding of brittle carbides on the grain boundaries. Crack propagation takes place by coalescence of all the voids nucleated around de-bonded and fractured carbides.

DSA Regime 550–750 °C

Between 550 and 750 °C, similar mechanism of failure is observed. As can be seen in Fig. 5, multiple micro-voids were formed on the surface. As temperature increases, mechanism of failure, during the test, shifts from slip mechanism to void nucleation at grain boundaries and at the site of nano and micro-scale precipitates. Grain boundaries perpendicular to the loading direction are acted upon by a higher resolved normal stress, and therefore, it separates more. Grain boundaries parallel

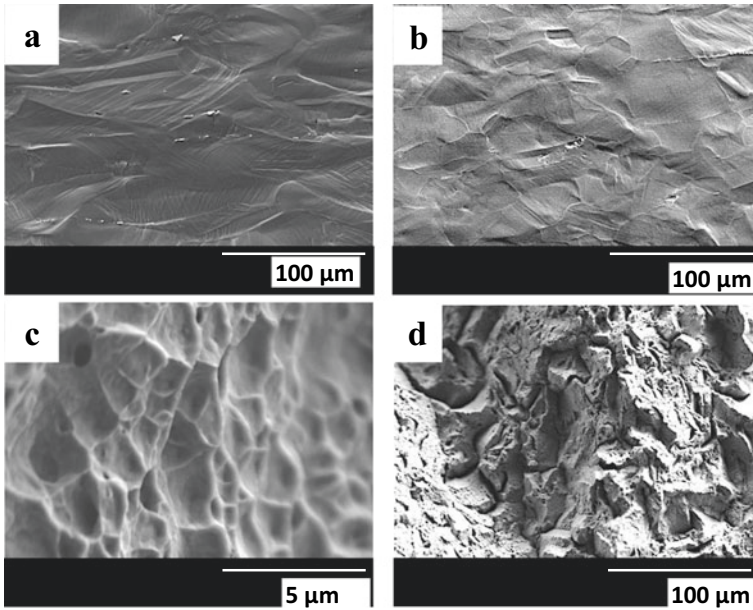


Fig. 4 In-situ SEM image of **a** as-received Alloy 709 tested at room temperature at about 35% strain **b** aged Alloy 709 tested at room temperature at about 35% strain **c** Fractograph of as-received Alloy 709 showing multi-void coalescence **d** Fractograph of aged Alloy 709 showing intergranular cracking

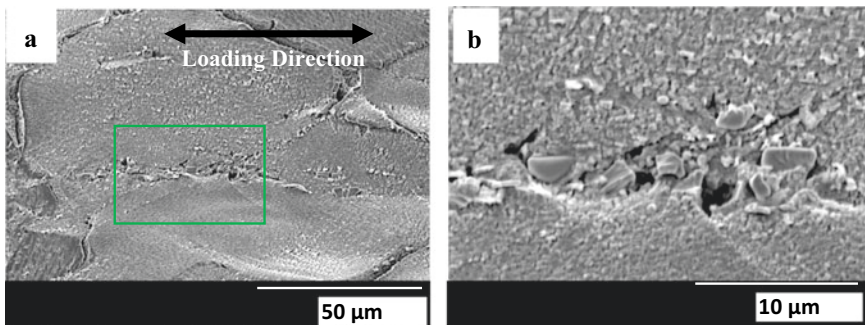


Fig. 5 In-situ SEM image of **a** as-received Alloy 709 tested at 750 °C showing intergranular cavitation **b** Zoom in image of the marked area on image a, showing trans-granular crack initiating at grain boundaries growing into the grains. (Color figure online)

to loading direction have a lower resolved stress acting on those resulting in less separation of these grain boundaries. Next, new crack starts from the grain boundaries and grows into the grains perpendicular to the loading direction. These cracks cause the final failure which take place in trans-granular fashion.

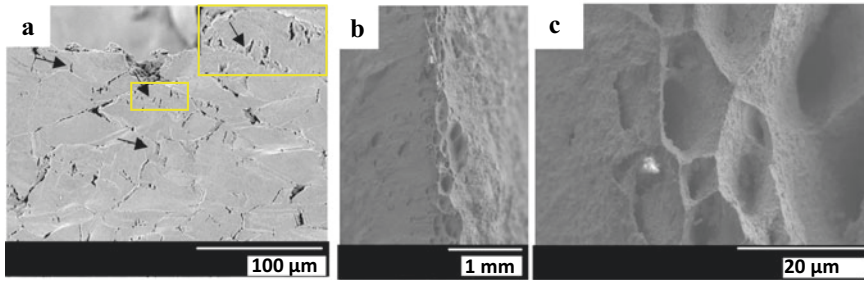


Fig. 6 a SEM image of aged Alloy 709 tested at 850 °C showing many trans-granular crack originating from grain boundary growing into grains with inset showing a high magnification image of the trans-granular cracks b entire fractured surface of aged Alloy 709 tested at 850 °C and c showing higher magnification of fractured surface. (Color figure online)

Beyond DSA Regime: 850 °C

At 850 °C, void nucleation and growth takes place at a much higher rate. Many trans-granular cracks originate from the grain boundary into the grains as marked with arrows in Fig. 6a. The in-situ SEM image of aged Alloy 709 in Fig. 6a suggests the formation of sub-grains at grain boundaries where the dislocation network forms and the density of dislocations decreases resulting in work softening. At 850 °C, high temperature and lack of dynamic strain aging result in large amount of necking and ductility as indicated by extended thinning of fracture surface as shown in Fig. 6b and the presence of deep dimples on its fracture surface as observed on Fig. 6c.

Creep-Rupture Tests

Creep Properties

Creep-rupture curves for the two tests at 750° C and one test at 850 °C are shown in Fig. 7a. During the creep tests, each stress level is associated with three regions: a primary creep regime with decreasing creep rate and a secondary creep regime with a constant creep rate and a tertiary creep regime at the end with increasing creep rate until failure. The creep parameters were calculated using equation 1 [8].

$$\text{Creep Rate } \dot{\epsilon} = A\sigma^n \exp\left(-\frac{Q}{RT}\right)$$

where Q is the activation energy, n is the stress exponent, A is a constant, R is the gas constant, n is the stress exponent and T is absolute temperature. Stress exponent, n , was calculated to be 5.6 by using elongation rates at different stresses which suggests that the underlying mechanism of creep for Alloy 709 at 750 °C could be dislocation

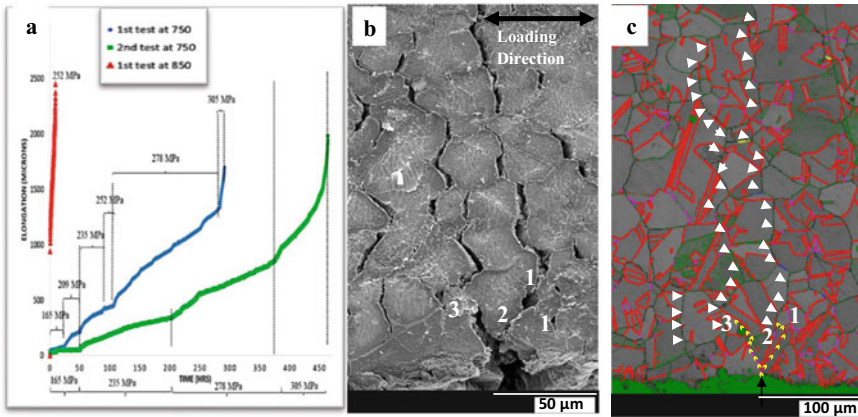


Fig. 7 a. Creep curves of all the creep tests. b. In-situ SEM image of the grain boundary separation due to the increasing creep stress level. c. CSL map showing the propagation of the cavitated grain boundaries. (Color figure online)

climb.. Activation energy, Q , was also calculated using elongation rates in tests at different temperatures to be 366 kJ/mol which can be attributed to self-diffusion in face-centered cubic in austenitic steel. Therefore, a vacancy-controlled climb of dislocations type of mechanism can be expected [8].

Since the creep test samples were designed to have constantly reducing cross section, gauge length needs to be determined. A simulation was conducted using SolidWorks/Ansys using the setup of the stage and heater. This simulation gives temperature distribution on the sample. To find the gauge length, stress and strain were calculated at various vertical slices of 0.5 mm throughout the sample. A gauge length value of 10 mm was chosen as the central 10 mm of the sample was calculated to include 97.41% of the total strain.

Creep Test Microstructural Observation

Figure 7b shows an in-situ SEM image taken during creep tests at 750 °C. As can be seen, the figure shows creep cavitation damage (marked by arrows) in the grain boundary perpendicular to loading direction. Figure 7c shows CSL map of the same area in the sample. It shows that the black boundaries represent random boundaries separate easily, while the red boundary, or $\Sigma 3$ twin boundaries, do not separate easily. Site marked 1 shows crack becoming trans-granular and parallel to $\Sigma 3$ twin boundary until it reaches a random grain boundary. Site marked 2 shows crack deflection away from $\Sigma 3$ twin boundaries, whereas site 3 shows crack arrest due to the presence of $\Sigma 3$ twin boundaries.

Creep-Fatigue Crack Growth Tests

1-Second Dwell Loading

Figure 8a shows the CSL map of the sample subjected to a creep-fatigue loading with a dwell time of 1 s and a maximum load of 95% of yield strength. During the test, crack path was studied with respect to the CSL and grain boundaries. The crack path is indicated with yellow arrow heads on CSL maps in Fig. 7a. With a hold time of 1-second, the crack growth was found to be primarily trans-granular at lower ΔK values (up to 20 MPam^{1/2}) with small regions of intergranular crack growth at higher ΔK (above 20 MPam^{1/2}). A closer look into the crack path also reveals that the crack propagation occurs with the help of slip mechanism, which is indicated by the presence of slip lines in the vicinity of the crack. Crack propagation was observed to be parallel to slip lines in the presence of twin boundaries and perpendicular to slip lines and the loading direction in the absence of twin boundaries. Hence, twin boundaries had a strengthening effect by resisting cracking under the load and delaying the crack growth.

As the test progressed, long exposure to high temperature resulted in grain boundaries cavitation. As such, towards the end of the test, a combination of intergranular and trans-granular failure was observed.

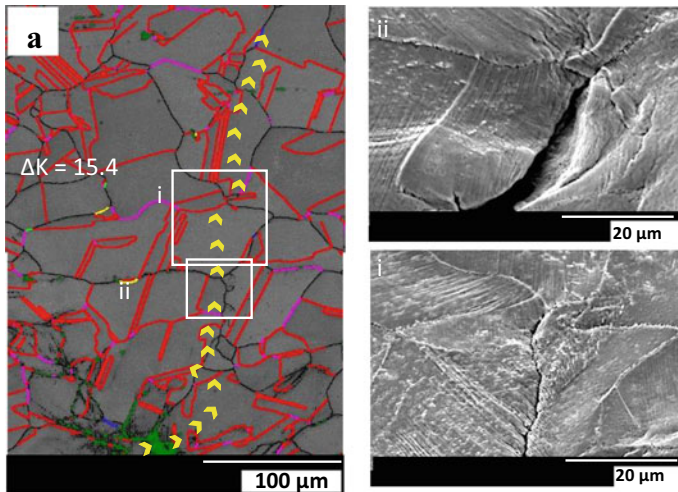


Fig. 8 a. CSL map of Alloy taken before the creep-fatigue test with crack path marked arrows (i) showing crack growing at an angle to the slip lines (ii) showing crack growing parallel to the slip lines. (Color figure online)

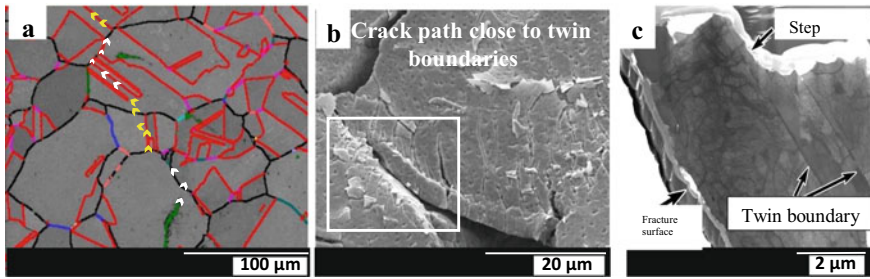


Fig. 9 a. CSL map of creep-fatigue test sample with 1-hour dwell with crack path marked on it. b. Higher magnification image showing crack growing very close to the twin boundary c. BF-STEM confirms crack parallel to the twin boundary and the presence of dislocations cells on one side of the twin boundary. (Color figure online)

1-Hour Dwell Loading

Figure 9 shows a CSL map from the sample subjected to creep-fatigue loading with a dwell time of 1 h and a maximum load of 95% of the yield stress. Blocks of 1-second dwell cycles were also added between the 1-hour dwell cycles to expedite crack growth and sharpen the crack tip after crack tip blunting. The white arrowheads indicate crack path during 1-hour dwell loading cycles, whereas the yellow arrowheads show the crack path during 1 s dwell loading cycles. In this case, most of the crack propagation was in intergranular mode. Addition of 1-hour dwell time in the fatigue cycle allows extensive creep damage and cavitation along grain boundaries. There was a negligible amount of slip line formation. It was observed that on multiple occasions, the crack approached a twin boundary and reached very close, but did not pass through it. Transmission electron microscopy (TEM) foil from a crack path near one of these twin boundaries (Fig. 9b) was lifted, and bright field scanning transmission electron microscopy (BF-STEM) study was conducted for further observation. The TEM image clearly shows that the fracture surface was parallel to the twin plane (Fig. 9c). Also, dislocation density, dislocation cells/walls and sub-grains were less on one side of the twin boundary. This can be attributed to the fact that coherent twin boundaries do not allow dislocations to pass through them due to discontinuity of slip systems [9, 10]. This is because of the high resistance created by the misorientation angle of 60° between matrix and twin boundary [11, 12]. As such, dislocations pile up on one side of the twin boundary, which activates planar slip and the crack propagates in a direction parallel to the twin boundary.

Conclusion

In-situ SEM tensile tests of as-received and aged Alloy 709 were conducted. During tensile tests, both as-received and aged samples showed serrated plastic flow and reduction in ductility over the temperature range of 500–750 °C. This was attributed

to dynamic strain aging (DSA). The aged sample undergoes dynamic strain aging in narrower range of temperature because of reduced concentration of solute atoms as compared to as-received Alloy 709. Aged Alloy 709 was found to be less ductile at all temperatures because of the brittle globular carbide precipitates formed at grain boundaries, which do not allow plastic deformation and result in void nucleation. At room temperature, the failure occurs by slip mechanism. At higher temperatures of 550 and 650 °C, the failure mechanism was controlled by void nucleation and coalescence at grain boundaries and at the site of precipitates. As temperature increases to 750 and 850 °C, the failure mechanism shifted to grain boundary sliding and formation of sub-grains at grain boundaries due to the formation of dislocation networks and failure along the grain boundaries.

In-situ SEM accelerated creep tests were done to observe microstructural damage mechanism and the interaction of the crack with grain and CSL boundaries (twin boundaries). Accelerated creep loading with multiple blocks of constant load with increasing load was used. As such, more data can be collected in reasonable amount of time. Real-time observations suggest that $\Sigma 3$ twin boundaries have a strengthening effect. Stress exponent, n , was calculated to be 5.6, whereas the activation energy was found to be 366 kJ/mol which suggests that the underlying mechanism was vacancy-controlled climb of dislocations.

Real-time observations of creep-fatigue crack growth, microstructural evolution and interaction of cracks with grain and CSL boundaries were conducted in an in-situ heating-loading SEM. The effect of varying dwell time and grain boundary character on creep-fatigue behavior of Alloy 709 was studied. With a lower dwell times, the crack grows mainly in a trans-granular fashion, with the help of slip mechanism. When the dwell time increases, creep cavitation damage occurs. As such, crack growth mechanism changes from trans-granular to intergranular. The high-temperature CFCG tests reveal that twin boundaries produce a strengthening effect by obstructing dislocation motion due to a discontinuity in the slip system and the fact that 50% of grain boundaries in alloy 709 are twin boundaries explain its high creep resistance and strength at high temperatures.

Acknowledgements This study is partially funded by the United States Department of Energy Nuclear Energy University Program award 2015–1877/DE-NE0008451, and Research Council of the United Kingdom (RCUK) award number EP/N016351/1.

References

1. Abram T, Ion S (2008) Generation-IV nuclear power: a review of the state of the science. *Energy Policy* 36(12):4323–4330
2. Sham TL, Natesan K (2017) Code qualification plan for an advanced austenitic stainless steel, alloy 709, for sodium fast reactor structural applications
3. Hong SH, Seo MG, Jang CH, Lee KS (2015) Evaluation of the effects of thermal aging of austenitic stainless-steel welds using small punch test. *Procedia Eng* 130:1010–1018
4. Porter T, Findley K, McMurtrey M. Assessment of Creep-Fatigue Behavior of Alloy 709

5. Peng K, Qian K, Chen W (2004) Effect of dynamic strain aging on high temperature properties of austenitic stainless steel. *Mater Sci Eng, A* 379(1–2):372–377
6. Hong SG, Lee SB (2005) Mechanism of dynamic strain aging and characterization of its effect on the low-cycle fatigue behavior in type 316L stainless steel. *J Nucl Mater* 340(2–3):307–314
7. Cottrell AH (1953) *Dislocations and plastic flow in crystals*, Clarendon. p 90
8. Monteiro SN, Luz FSD, Pinheiro WA, Brandão LPM, Braga FDO, Assis FSD (2017) Creep parameters and dislocation substructure in AISI 316 austenitic stainless steel From 600 to 800 °C. *Mater Res* 20:231–235
9. Zhang P, Zhang ZJ, Li LL, Zhang ZF (2012) Twin boundary: stronger or weaker interface to resist fatigue cracking? *Scripta Mater* 66(11):854–859
10. Tran HS, Tummala H, Péron-Lühns V, Fivel M, Habraken AM (2015) Interaction between dislocation and coherent twin boundary by quasicontinuum model. In: *COMPLAS XIII: proceedings of the XIII international conference on computational plasticity: fundamentals and applications*. CIMNE, pp 992–1002
11. Christian JW, Mahajan S (1995) Deformation twinning. *Prog Mater Sci* 39(1–2):1–157
12. Lu L, Shen Y, Chen X, Qian L, Lu K (2004) Ultrahigh strength and high electrical conductivity in copper. *Science* 304(5669):422–426

Simulation of Intergranular Void Growth Under the Combined Effects of Surface Diffusion, Grain Boundary Diffusion, and Bulk Creep



John W. Sanders, Negar Jamshidi, Niloofar Jamshidi, Mohsen Dadfarnia, Sankara Subramanian, and James Stubbins

Abstract Creep rupture is currently a major concern for next-generation nuclear reactor components, and many commonly used lifetime estimates are based on how quickly intergranular voids grow. Void growth is caused by three processes: diffusion along the void surface, diffusion along the grain boundary, and creep of the surrounding grains. Previous modeling efforts have only considered two of these three processes at a time. Here we present finite element simulations of void growth under the influence of all three mechanisms simultaneously. To our knowledge, these are the first such simulations to be reported in the literature. Based on our simulations, we develop quantitative criteria for quasi-equilibrium and crack-like void growth and compare them to previous results. Furthermore, we find that void growth is highly accelerated during the primary creep regime. Our results promise to aid in the development of microstructure-sensitive material strength models for next-generation nuclear reactor components.

J. W. Sanders (✉) · N. Jamshidi · N. Jamshidi
Department of Mechanical Engineering, California State University, Fullerton, 800 North State College Boulevard, Fullerton, CA 92831, USA
e-mail: jwsanders@fullerton.edu

N. Jamshidi
e-mail: negarjms@csu.fullerton.edu

N. Jamshidi
e-mail: niloofarjms@csu.fullerton.edu

M. Dadfarnia
Department of Mechanical Engineering, Seattle University, 901 12th Street, Seattle, WA 98122, USA
e-mail: dadfarniamoh@seattleu.edu

S. Subramanian
PhotoGAUGE, 13A/209, Velachery Main Road, Chennai 600042, India
e-mail: shankar_sj@iitm.ac.in

J. Stubbins
Department of Nuclear, Plasma, and Radiological Engineering, University of Illinois at Urbana-Champaign, 216 Talbot Laboratory, 104 South Wright Street, Urbana, IL 61801, USA
e-mail: jstubbin@illinois.edu

Keywords Cavitation · Creep · Diffusion · Grain boundary · Rupture · Superalloys · Void growth

Introduction and Background

One leading design for next-generation nuclear power plants is the very high-temperature reactor (VHTR), in which temperatures are expected to reach 650–950 °C [1]. Such high temperatures promise increased thermal efficiency compared to current energy conversion systems while facilitating the production of hydrogen gas. However, such conditions will also place a severe burden on plant components, and creep rupture is expected to be the primary failure mechanism. It is well known that creep rupture is caused by intergranular cavitation: the nucleation, growth, and coalescence of voids along grain boundaries [2]. This fact has been established based on decades of experiments on a myriad of structural metals.

The seminal work of Hull and Rimmer [3] was one of the first to suggest that matter diffusion plays a significant role in the void growth process, with atoms migrating along the void surface (“surface diffusion”) and along the grain boundary (“grain boundary diffusion”). It is now well known that the relative strengths of surface diffusion and grain boundary diffusion determine the shape assumed by a growing void. When surface diffusion occurs much more rapidly than grain boundary diffusion, a void maintains its original shape as it grows (“quasi-equilibrium void growth”). Conversely, when grain boundary diffusion occurs much more rapidly than surface diffusion, the void becomes elongated in the direction of the grain boundary (“crack-like void growth”) [4–6]. Hull and Rimmer [3] were also among the first to estimate the rupture time of a specimen or component based on the rate at which voids grow. Denote by a the mean void radius and by $2b$ the center-to-center void spacing, and suppose that the grain boundary ligament will fail when $a = \lambda b$, where $\lambda \in (0, 1]$. Then one may estimate the rupture time as

$$t_r = \int_{a_0}^{\lambda b} \dot{a}^{-1} da, \quad (1)$$

where a_0 is the initial void radius, a superscribed dot denotes differentiation with respect to time, and \dot{a} is a function of the system parameters. Such models provide the basis for commonly used lifetime estimates (e.g. [7]). The functional form of \dot{a} is often based on the results of void growth simulations, and over the last several decades much effort has been devoted to accurate simulations of void growth.

Kagawa [5] and Chuang et al. [6] were the first to investigate void growth analytically in the presence of both surface diffusion and grain boundary diffusion, allowing the shape of the void to be determined by the analysis. Kagawa [5] considered cylindrical voids under remotely applied uniaxial tension, and treated the grains as rigid,

neglecting creep of the surrounding material. By linearization, Kagawa [5] derived three solutions for the void profile: one for quasi-equilibrium void growth, another for crack-like void growth, and a third solution whose predictions agree with those of the quasi-equilibrium solution or the crack-like solution, depending on the value of a dimensionless parameter $\chi = a^3 \dot{a} / \mathcal{D}_s \gamma_s$, where γ_s is the surface free energy, and $\mathcal{D}_s = D_s \delta_s \Omega / kT$ is the surface diffusivity, where $D_s \delta_s$ is the void surface diffusion coefficient, Ω is the atomic volume, k is Boltzmann's constant, and T is the absolute temperature. According to Kagawa [5], quasi-equilibrium void growth should occur under remote stresses S satisfying

$$Sa/\gamma_s < \psi (1 - a/b) \left[1 + \frac{4}{9} (b/a - 1) \chi_0 \Delta \right], \quad (2)$$

where ψ is the angle, in radians, the void tip makes with the grain boundary ($\psi = \pi/2$ for a circular void), and $\Delta = D_s \delta_s / D_b \delta_b$ is the ratio between the surface and grain boundary diffusion coefficients. Similarly, crack-like void growth should occur under remotely applied stresses S satisfying

$$Sa/\gamma_s > \psi (1 - a/b) \left[\chi_0^{1/3} + \frac{2}{3} (b/a - 1) \chi_0^{2/3} \Delta \right]. \quad (3)$$

The parameter χ_0 that appears in both (2) and (3) is an appropriate value for χ that describes the ‘‘cutoff’’ between quasi-equilibrium and crack-like void growth, for which Kagawa [5] suggested $\chi_0 = 5$.

Needleman and Rice [8] were the first to study how creep deformation of the grains interacts with grain boundary diffusion to bring about void growth. They performed finite element simulations of axisymmetric voids in uniaxial tension under the influence of both grain boundary diffusion and bulk creep, without accounting for surface diffusion explicitly, but assuming that surface diffusion occurred rapidly enough to maintain quasi-equilibrium void growth. The seminal contribution of Needleman and Rice [8] was the introduction of a grain boundary *diffusion length*

$$L_b = (\mathcal{D}_b S / \dot{\epsilon}_\infty)^{1/3}, \quad (4)$$

where $\mathcal{D}_b = D_b \delta_b \Omega / kT$ is the grain boundary diffusivity and $\dot{\epsilon}_\infty$ is the remote creep strain rate. For remote power-law creep, $\dot{\epsilon}_\infty = \dot{\epsilon}_0 (S/\sigma_0)^n$, where $\dot{\epsilon}_0 = 10^{-6} \text{ s}^{-1}$ is the conventional reference strain rate, σ_0 is the reference stress, and n is the creep exponent. The dimensionless ratio L_b/a gives a measure of the relative importance of grain boundary diffusion *vis-à-vis* bulk creep. Grain boundary diffusion is more significant than bulk creep in bringing about void growth when this ratio is large (> 20), and vice versa when this ratio is small (< 4). Virtually all subsequent work [9–11] has been based on the extension of Needleman and Rice [8] to triaxial stress states.

One limitation to the literature cited above is consideration of only two of the three fundamental void growth mechanisms (surface diffusion, grain boundary diffusion, and bulk creep) at a time. Another is that, when creep was accounted for, it

was modelled using power-law (secondary) creep, without addressing primary creep effects [8, 9, 11]. In the present work, we will consider all three void growth mechanisms acting in tandem, and we will investigate the effects of both primary and secondary creep.

Problem Formulation

Following Kagawa [5], we will consider cylindrical voids with an initially circular cross section ($\psi = \pi/2$) of radius a_0 and an initial center-to-center spacing of $2b$. Due to the symmetry of the problem, it suffices to consider only one quarter of a unit cell centered on a single void, as shown in Fig. 1, in which the grain boundary is aligned along the x -axis. Along the top edge of the unit cell (denoted S_T), the material is subjected to a uniform and constant tensile stress S corresponding to the remotely applied load, and S_T is constrained to remain horizontal at all times.

The void surface (denoted S_s in Fig. 1) is subjected to an outward normal stress $\gamma_s \kappa$, where γ_s is the surface free energy and κ is the curvature of the void surface [6]. Due to chemical potential gradients, matter diffuses along the void surface and is deposited along S_s . Let j_s denote the volumetric flux (i.e. the volume of matter diffused per unit out-of-plane length per unit time) along the void surface, and let α be the thickness of matter deposited *onto* the void surface by this process (when $\alpha < 0$, matter is depleted from the void surface). Conservation of mass dictates that

$$\frac{d}{ds} j_s + \dot{\alpha} = 0 \quad \text{along } S_s, \tag{5}$$

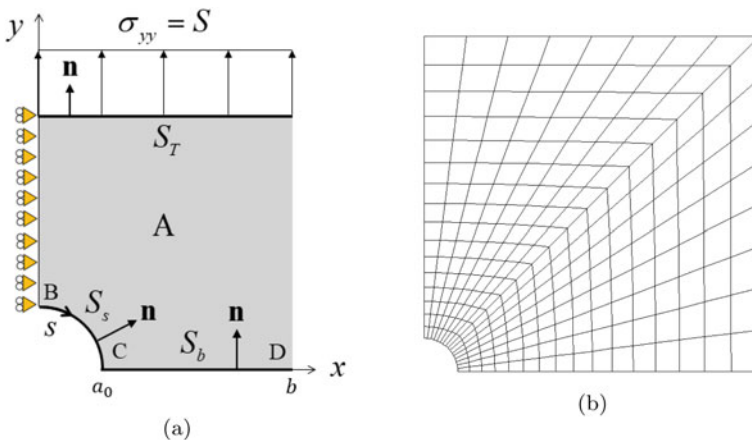


Fig. 1 **a** Quarter unit cell model of an intergranular void. **b** Finite element mesh. (Color figure online)

where s is the arc length along S_s , starting from zero at point B , and j_s is taken to be positive in the direction of increasing s . According to Fick's law,

$$j_s = \mathcal{D}_s \gamma_s \frac{d}{ds} \kappa \quad \text{along } S_s, \quad (6)$$

where \mathcal{D}_s is the surface diffusivity, and we assume that γ_s is independent of arc length.

Matter arriving by surface diffusion is deposited on, and continues to diffuse along, the grain boundary (denoted S_b in Fig. 1). Let j_b denote the volumetric flux along the grain boundary. Following Needleman and Rice [8], we assume that there is no grain boundary sliding or cracking, so that the rate at which matter is deposited onto the grain boundary coincides with the normal velocity v_n of the grain boundary surface. Conservation of mass requires that

$$\frac{d}{ds} j_b + v_n = 0 \quad \text{along } S_b, \quad (7)$$

where we are taking the unit normal to the void surface and grain boundary to point *into* the surrounding material, in order to remain consistent with Needleman and Rice [8] (see Fig. 1). Fick's law states that

$$j_b = \mathcal{D}_b \frac{d}{ds} \sigma_n \quad \text{along } S_b, \quad (8)$$

where \mathcal{D}_b is the grain boundary diffusivity and σ_n is the tensile stress normal to the grain boundary.

Following a similar numerical approach to Subramanian and Sofronis [12], we treat matter deposition along the void surface separately from the other deformation. In particular, we decompose the displacement of the void surface as $u_i^s = u_i^0 - \alpha n_i$, where u_i^0 is the "baseline" displacement of the void surface arising from processes other than surface diffusion, α is the thickness of matter that has accumulated on the void surface, and n_i is the inward unit normal vector to the void surface, as shown in Fig. 1 (we are employing indicial notation, whereby subscript indices label tensor components and vary from 1 to 3). At a given time step t_n , the following two problems are solved sequentially:

- (i) *Deformation without surface diffusion.* Following Needleman and Rice [8], we construct the integral form of local static equilibrium using the principle of virtual work in rate form:

$$\iint_A \sigma_{ij} \delta \dot{\epsilon}_{ij} dA = \int_{S_T} T_i \delta v_i ds - \int_{S_s} \gamma_s \kappa \delta v_n ds - \int_{S_b} \sigma_n \delta v_n ds, \quad (9)$$

where σ_{ij} is the stress field, δv_i is a virtual velocity field, $\delta \dot{\epsilon}_{ij} = \text{sym}(\delta v_{i,j})$ is the associated virtual strain rate field, T_i is the applied traction on S_T , and $\delta v_n = \delta v_i n_i$ (we are employing the Einstein summation convention, whereby repeated indices are summed over). By finite element discretization, (9) is

converted into a set of finite element equations, which are solved incrementally in time via Newton–Raphson iteration using custom FORTRAN code. The finite element mesh used in the present work is shown in Fig. 1(b). A total of 256 eight-noded, biquadratic quadrilateral elements were used. The solution to (9) yields displacement increments for each node, which determine the *baseline* displacement increments Δu_i^0 for the void surface. Once these are known, the mass flux along the entire grain boundary $j_b(s)$ is evaluated by integrating (7).

- (ii) *Matter deposition along the void surface.* Equations (5) and (6) are then solved simultaneously for the rate $\dot{\alpha}$ at which matter is being deposited onto the void surface, and thus the thickness $\Delta\alpha = \dot{\alpha}\Delta t$ deposited during the time increment Δt . Once $\Delta\alpha$ is known, the new shape of the void is constructed according to $\Delta u_i^s = \Delta u_i^0 - \Delta\alpha n_i$. This determines the curvature κ along the entire void surface for use in (9) at the next time step $t_{n+1} = t_n + \Delta t$.

For the full mathematical details of this solution procedure, we refer the reader to Appendix F of Sanders [13].

Simulation Results

To be definite, we consider material parameters representative of 2 1/4 Cr-1 Mo Steel, a high-temperature alloy used in liquid metal cooled fast breeder reactor components, at 566 °C [14]. The limiting chemical composition of 2 1/4 Cr-1 Mo Steel is shown in Table 1. In order to generalize our results to other materials at other temperatures, we will consider suitable dimensionless groups. Straightforward dimensional analysis on the system parameters a_0 , b , \mathcal{D}_s , \mathcal{D}_b , $\dot{\epsilon}_\infty$, γ_s , S , and ψ yields five independent dimensionless groups:

$$(\mathcal{D}_b S / \dot{\epsilon}_\infty a_0^3)^{1/3}, \quad (\mathcal{D}_s S / \dot{\epsilon}_\infty a_0^3)^{1/3}, \quad S a_0 / \gamma_s, \quad a_0 / b, \quad \text{and} \quad \psi. \quad (10)$$

We recognize the first group as Needleman and Rice’s [8] normalized grain boundary diffusion length L_b/a_0 , and it is only natural to define an analogous surface diffusion length $L_s = (\mathcal{D}_s S / \dot{\epsilon}_\infty)^{1/3}$, making the second group L_s/a_0 . Here we will consider an initial void radius of $a_0 = 1 \mu\text{m}$ and an initial half-spacing of $b = 10 \mu\text{m}$, fixing $a_0/b = 0.1$. Based on Frost and Ashby’s deformation mechanism maps [15], we estimate that, for 2 1/4 Cr-1 Mo Steel at 566 °C, $\mathcal{D}_b \sim 5 \times 10^{-33} \text{ m}^6/\text{J s}$. From experimental creep test data [14], we find that the power-law reference stress and creep exponent are $\sigma_0 \approx 550 \text{ MPa}$ and $n \approx 4.4$, respectively. We will consider an applied stress of $S = 100 \text{ MPa}$. Using these values, we estimate that $L_b/a_0 \sim 10$, and we will consider values of L_b/a_0 in this neighborhood. As for L_s/a_0 , we will consider values up to 80, which we will see is sufficient to observe both quasi-equilibrium and crack-like void growth. For metals at high temperatures, $\gamma_s \sim 0.5 \text{ J/m}^2$ [16], so with $S = 100 \text{ MPa}$, we have that $S a_0 / \gamma_s \sim 200$, and we will consider values on that order of magnitude. Finally, we will only consider $\psi = \pi/2$ in the present work.

Table 1 Approximate chemical composition of 2 1/4 Cr-1 Mo steel [17]. All values are percentage by mass

C	Cr	Fe	Mn	Mo	P	S	Si
0.05–0.15	2.0–2.5	95 (balance)	0.3–0.6	0.9–1.1	0.025	0.025	0.5

Power-Law Creep

We begin with results obtained using the power-law creep model, which only accounts for secondary creep. In the power-law model, the strain rate tensor is given by

$$\dot{\epsilon}_{ij} = \frac{3}{2} \dot{\epsilon}_0 (\sigma_e / \sigma_0)^n (\sigma'_{ij} / \sigma_e), \tag{11}$$

where $\dot{\epsilon}_0 = 10^{-6} \text{ s}^{-1}$ is the conventional reference strain rate, σ_0 is the reference stress, n is the creep exponent, a subscript e denotes a von Mises equivalent quantity such that, for any tensor T_{ij} , $T_e = \left(\frac{3}{2} T'_{ij} T'_{ij}\right)^{1/2}$, a prime denotes the deviatoric part of a tensor such that $T'_{ij} = T_{ij} - \frac{1}{3} T_{kk} \delta_{ij}$, and δ_{ij} is the Kronecker delta. Recall that, for 2 1/4 Cr-1 Mo Steel at 566 °C, $\sigma_0 \approx 550 \text{ MPa}$ and $n \approx 4.4$ [14].

Figure 2a shows representative simulation results for model parameters $L_s/a_0 = 20$, $L_b/a_0 = 8$, and $Sa_0/\gamma_s = 200$. The times are normalized by a reference time $\tau = 320 \text{ hr}$, a number which will become meaningful in the next section. In this case, the void only expands in the x -direction (the direction parallel to the grain

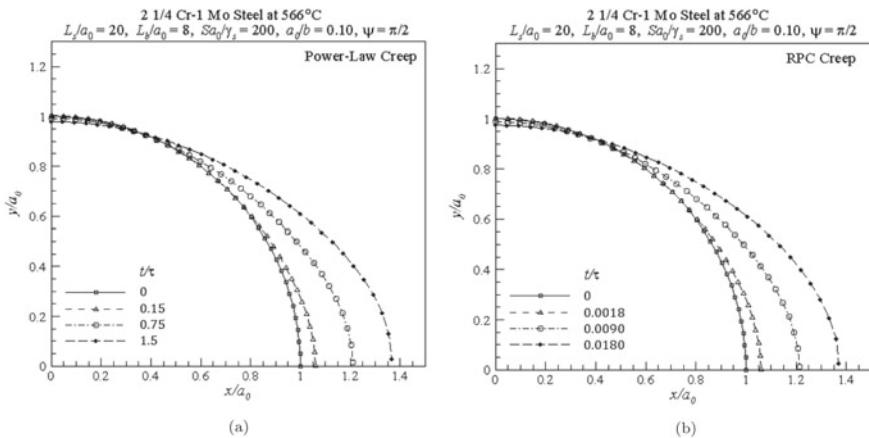


Fig. 2 Simulated void profiles at various times for $L_s/a_0 = 20$, $L_b/a_0 = 8$, $Sa_0/\gamma_s = 200$, $a_0/b = 0.10$, and $\psi = \pi/2$, using **a** power-law creep and **b** RPC creep. The material parameters represent 2 1/4 Cr-1 Mo Steel at 566 °C

boundary), which is the hallmark of crack-like void growth. Quasi-equilibrium void growth was observed for sufficiently higher values of L_s/a_0 .

Primary Creep Effects

To see the effects of primary creep, we employ a unified creep-plasticity model due to Robinson, Pugh, and Corum [14] (henceforth the ‘‘RPC model’’). This model accounts for both primary and secondary creep, with a smooth transition in between. In the RPC model, the strain rate tensor is given by

$$\dot{\epsilon}_{ij} = \frac{3}{2} A \Sigma_e^m (\Sigma'_{ij} / \Sigma_e), \quad (12)$$

where the scalars A and m are temperature-dependent material parameters, and the effective stress $\Sigma_{ij} = \sigma_{ij} - \alpha_{ij}$ is the difference between the local Cauchy stress tensor σ_{ij} and the local flow stress tensor α_{ij} . The flow stress α_{ij} is an internal state variable which represents the local material microstructure in that $\alpha_e = B\sqrt{\rho}$, where B is another temperature-dependent material parameter and ρ is the local dislocation density. The time dependence of the flow stress is governed by the following evolution equation:

$$\dot{\alpha}_{ij} = \frac{2}{3} (C/\alpha_e) \dot{\epsilon}_{ij} - D \alpha_e^2 \alpha_{ij}, \quad (13)$$

where C and D are additional temperature-dependent material parameters. As discussed in detail by Sanders et al. [17], the first and second terms on the right-hand side of (13) represent strain hardening and recovery of the material, respectively. It is the competition between strain hardening and recovery that brings about the transition from primary to secondary creep, which is characterized by the time scale

$$\tau = [ACD (S - B\sqrt{\rho_0})^m]^{-1/2}, \quad (14)$$

where ρ_0 is the initial dislocation density [17]. For 2 1/4 Cr-1 Mo Steel at 566 °C, Robinson et al. [14] give $A = 4.87 \times 10^{-40} \text{ Pa}^{-4} \text{ s}^{-1}$, $B = 8.76 \text{ Pa m}$, $C = 7.9031 \times 10^{17} \text{ Pa}^2$, $D = 2.382 \times 10^{-23} \text{ Pa}^{-2} \text{ s}^{-1}$, $m = 4$, and $\rho_0 = 2.79 \times 10^{11} \text{ m} / \text{m}^3$. With these material parameters and $S = 100 \text{ MPa}$, the transition time comes out to about $\tau = 320 \text{ hr}$.

Figure 2b shows the analogous plot to Fig. 2a using the RPC model instead of the power-law creep model. Evidently, primary creep does not affect the shape of the void. However, when primary creep is accounted for, the void initially grows about $1.5/0.018 \approx 83$ times faster than it does when primary creep is neglected. This same acceleration factor of 83 was observed for all simulations with $S = 100 \text{ MPa}$, regardless of the values of L_b/a_0 , L_s/a_0 , and Sa_0/γ_s . This has important implications for microstructure-based creep rupture models. Recall that rupture time is often estimated using (1), with \dot{a} informed by void growth simulations such as those of Van

der Giessen et al. [11]. However, the simulations on which \dot{a} is based do not account for primary creep. It is possible that, when primary creep is present, the current models are underestimating the void growth rate, and therefore *overestimating* component lifetimes. More accurate lifetime estimates may be obtained by correcting the void growth rate during the primary creep phase.

Our results also suggest a strategy for reducing the computation time required for void growth simulations. The simulations performed using the RPC model [14] took about four times longer to finish than the corresponding simulations using the simpler power-law model. But once the acceleration factor (83 for $S = 100$ MPa) has been identified, it seems that it is no longer necessary to use the RPC model, since identical void profiles are obtained with both models. Significant time could be saved by using the power-law model and simply scaling all times by the acceleration factor.

Criteria for Quasi-equilibrium and Crack-Like Void Growth

To establish quantitative criteria for quasi-equilibrium versus crack-like void growth, we have performed a parametric study on the dimensionless groups L_b/a_0 , L_s/a_0 , and Sa_0/γ_s . Over 130 simulations were performed (half with the power-law model and half with the RPC model [14]), and each simulation was categorized as primarily quasi-equilibrium, crack-like, or “dynamic” (something in between). The void growth was categorized as quasi-equilibrium if the void grew the same amount ($\pm 0.05a_0$) in both the x - and y -directions during the entire course of the simulation; crack-like if the void grew at least $0.20a_0$ in the x -direction without growing more than $0.05a_0$ in the y -direction during the entire course of the simulation; and dynamic otherwise. The two constitutive models yielded identically shaped void profiles for every set of parameters considered here. Figure 3 summarizes the results for $Sa_0/\gamma_s = 100$ and 200.

For fixed values of Sa/γ_s , a/b , and ψ , (2) and (3) define lines that separate the L_bL_s -plane into three regions, corresponding to quasi-equilibrium void growth, crack-like void growth, and a combination of the two (which we have called “dynamic” void growth). These lines are illustrated in grey in Fig. 3. Not surprisingly, our results do not align with Kagawa’s [5] criteria. However, there still appear to be linear boundaries between the regions of crack-like, quasi-equilibrium, and dynamic void growth defined by the data points in Fig. 3. This suggests that the void shape may depend on L_s and L_b only in their ratio, even when creep is accounted for. That is, the void shape may be a function of just four dimensionless groups (L_s/L_b , Sa_0/γ_s , a_0/b , and ψ), not the five dimensionless groups (10) identified using dimensional analysis. With $Sa/\gamma_s = 100$, we find that the quasi-equilibrium region is well approximated by the condition $L_s/L_b > 5.63$, and that the crack-like region is well approximated by the condition $L_s/L_b < 3.05$. With $Sa/\gamma_s = 200$, we find that the quasi-equilibrium region is well approximated by the condition $L_s/L_b > 6.50$, and that the crack-like region is well approximated by the condition $L_s/L_b < 4.40$. The

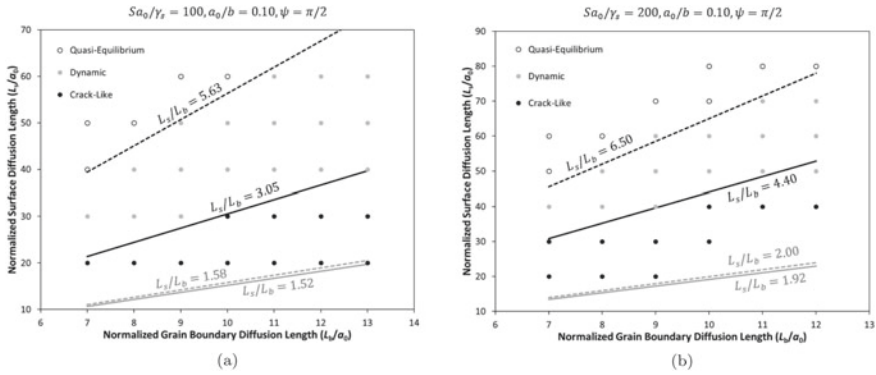


Fig. 3 Summary of results for **a** $Sa_0/\gamma_s = 100$ and **b** $Sa_0/\gamma_s = 200$, with $a_0/b = 0.10$ and $\psi = \pi/2$. The grey lines represent the criteria derived by Kagawa [5] for rigid grains using nominal values $a/b = 0.10$ and $\chi_0 = 5$ in (2) and (3). The black lines represent criteria consistent with our results

corresponding boundaries are illustrated in black in Fig. 3. Our threshold values for L_s/L_b are *higher* than the corresponding values given by Kagawa [5]. This suggests that crack-like void growth may be more common than previously thought.

Summary and Conclusion

We have presented here the first finite element simulations of intergranular void growth under the combined effects of surface diffusion, grain boundary diffusion, and bulk creep. Perhaps the most important insight to be gleaned from our results is that voids grow significantly faster in the presence of primary creep than would be expected based on the power-law creep model. This could have serious implications for current microstructure-based creep rupture models, which are based on power-law creep and may consequently overestimate component lifetimes. Another important insight is that the threshold for crack-like void growth appears to be higher than prior estimates obtained assuming rigid grains, suggesting that crack-like void growth may be more common than previously thought. This could also have implications for creep rupture models, which assume that surface diffusion occurs rapidly enough to maintain quasi-equilibrium void growth. Interestingly, primary creep does not affect the shape that a void assumes as it grows, and we have established quantitative criteria for quasi-equilibrium and crack-like void growth for a range of realistic model parameters, summarized in Fig. 3. Finally, our results suggest that future void growth simulations can save computation time by using the power-law model and scaling time by an acceleration factor that can be determined *a priori*. These results promise to aid in the development of microstructure-sensitive material strength models for next-generation nuclear reactor components.

References

1. Chersola D, Lomonaco G, Marotta R (2015) *Prog Nucl Energy* 83:443
2. Argon AS (1982) Recent advances in creep and fracture of engineering materials and structures, pp 1–52
3. Hull D, Rimmer DE (1959) *Phil Mag* 4:673
4. Chuang TJ, Rice JR (1973) *Acta Metall* 21:1625
5. Kagawa KI (1976) Models of slow intergranular void growth due to void surface and grain boundary self-diffusion. Master's thesis, Brown University
6. Chuang TJ, Kagawa KI, Rice JR, Sillis LB (1979) *Acta Metall* 27:265
7. Sanders JW, Dadfarnia M, Stubbins JF, Sofronis P (2017) *J Mech Phys Solids* 98:49
8. Needleman A, Rice JR (1980) *Acta Metall* 28:1315
9. Sham TL, Needleman A (1983) *Acta Metall* 31(6):919
10. Tvergaard V (1984) *J Mech Phys Solids* 32:373
11. Van der Giessen E, Van der Burg MWD, Needleman A, Tvergaard V (1995) *J Mech Phys Solids* 43(1):123
12. Subramanian SJ, Sofronis P (2002) *Int J Mech Sci* 44:2239
13. Sanders JW (2017) Modeling and simulation of creep rupture in high-temperature alloys. PhD thesis, The University of Illinois at Urbana-Champaign
14. Robinson DN, Pugh CE, Corum JM (1976) Proceedings of specialist meeting on high-temperature structural design technology of LMFBRs, IAEA Report IWGFR/11
15. Frost HJ, Ashby MF (1982) Deformation-mechanism maps: the plasticity and creep of metals and ceramics. Pergamon Press
16. Chattopadhyay R (2001) Surface wear: analysis, treatment, and prevention, ASM International
17. Sanders JW, Dadfarnia M, Sehitoglu H, Stubbins J, Sofronis P (2020) *Int J Solids Struct* 193–194:455

Part XXXIV
Mechanical Response of Materials
Investigated Through Novel In-Situ
Experiments and Modeling

In Situ Characterization of the Damage Initiation and Evolution in Sustainable Cellulose-Based Cottonid



R. Scholz, A. Delp, and F. Walther

Abstract The usage of environmentally friendly materials based on sustainable resources is nowadays more important than ever, especially in technical applications. Cottonid is based 100% on cellulose, therefore sustainable and due to its excellent properties a promising alternative material in terms of eco-friendliness. Within this study, the deformation and damage behavior of two Cottonid variants, an industrial standard as well as the structurally optimized variant M60Z50, is characterized for the first time using innovative in situ testing techniques. Quasi-static tensile tests were comparatively performed in a scanning electron microscope as well as a microfocus computer tomograph, and the development of defects present in the initial condition of the materials were investigated on surface and in volume. In general, in the elastic region, no visible damage initiation on the surface and a decrease of overall void volume within the gauge length could be detected for Cottonid. When reaching the yield strength, cracks initiate on the surface at critical areas, like pores and microcracks, which propagate and assemble until total loss of structural integrity. Further, in the plastic region, an increase in void volume could be shown in the gauge length until final failure. Compared to an industrial standard, M60Z50 exhibits a clearly lower percentage in overall void volume and shows increased mechanical properties, like yield strength and ultimate tensile strength. The structural optimization of M60Z50 seems to result in a more sufficient bonding of the paper layers during the manufacturing process, which improves the deformation and damage behavior under quasi-static loading.

Keywords Cottonid · Cellulose · In situ testing · Scanning electron microscope · Microfocus computer tomograph · Microstructure · Quasi-static loading · Damage evolution · Damage mechanisms · Crack initiation

R. Scholz (✉) · A. Delp · F. Walther
Department of Materials Test Engineering (WPT), TU Dortmund University, Dortmund, Germany
e-mail: ronja.scholz@tu-dortmund.de

Introduction

The material Cottonid is manufactured by parchmentizing of unsized filter paper layers using a catalyst solution (e.g. based on ZnCl_2) for a superficial etching of the cellulose fibers contained in the paper to create a chemical bonding. After washing out of the chemicals and planning and drying the material, a 100% sustainable cellulose based polymer is produced. The mechanical and hygroscopic properties of Cottonid alter as a function of the material thickness, which is a result of the amount of paper layers fed into the process, respectively. So either, a rather flexible and hygroscopically adaptive material is produced, when e.g. using just one paper layer, or with material thicknesses of $\sim t_{\text{mat}} > 2$ mm Cottonid is dimensionally stable and rigid. The procedure for Cottonid production was developed in 1844 by J. Mercer and patented by T. Taylor in 1859 [1]. The cellulose can be derived from any plant resource, whereas cotton linters are very efficient, since they contain nearly 100% cellulose without any by-products like hemicelluloses or lignin. During the chemical reaction of the cellulose with the tempered catalyst bath, new intra- and intermolecular hydrogen bonds are formed, which amount influences the material properties immense. Cottonid was the first plastic and used in several applications, like motor or rail insulation, furniture or tubes for power distribution, but with development of synthetic plastics in the beginning of the twentieth century, Cottonid was replaced in most technical applications [2]. Therefore, research activities remain static over a long time. Today, Cottonid is a resource-efficient alternative to conventional construction materials again. The industrial standard is still used as carrier material for e.g. grinding disks and is produced using the old and proven recipe, e.g. concerning the temperature of the catalyst bath T_{cat} or the reaction time t_{react} of the paper in it. So it lies great potential in new research activities on this material concerning the influence of single manufacturing parameters on its application-oriented mechanical behavior. By using current standards and advanced and innovative testing strategies, Scholz et al. [3,4] characterized material properties of Cottonid and its deformation behavior in dependence of chosen manufacturing parameters to derive application potential for adaptive or constructive issues. Industrially manufactured material is contrasted with structurally optimized Cottonid, where manufacturing parameters, e.g. T_{cat} or t_{react} are adjusted for characterization of their influence on resulting material properties [5].

In general it could be shown, that the cellulose fibers in Cottonid have a preferred orientation in manufacturing direction due to the upstream papermaking process. So, Cottonid exhibits a direction-dependent deformation behavior, where highest mechanical strength and toughness (ultimate tensile strength UTS, tensile modulus E_T) can be obtained in manufacturing direction and is comparable to common technical plastics, like PA or PVC, and wood-based materials [6–8]. Further, T_{cat} and t_{react} have a huge influence on the crystallinity of Cottonid and therefore on its swelling and shrinking properties. For now, a cotton-based (“M”) single layer Cottonid variant, parchmentized by a ZnCl_2 -solution (“Z”) with $T_{\text{cat}} = 50$ °C and $t_{\text{react}} = 60$ s—labelled

as “M60Z50”—showed comparatively strong hygroscopic reactions, which is a very promising approach towards climate-adaptive architectural elements [3,5,9].

For characterization of microstructural changes during loading and correlation with the macroscopic deformation behavior, the combination of mechanical testing with analytical techniques, like scanning electron microscopy (SEM) or microfocus computer tomography (μ CT), is very efficient [10,11]. By using in situ SEM [12,13] and μ CT [14–16], the microstructure of the specimen can be analyzed in a loaded state, since the mechanical testing module is directly integrated into the test chamber of the analytical device. This technique leads to a basic understanding of effective damage mechanisms leading to final failure of the specimen [17]. It has been already shown in various studies on the example of fiber-reinforced structures [18,19] or wood tissue [20,21], that high-resolution computed tomography is very efficient for visualizing the microstructure of low density polymeric materials, like Cottonid. Theories regarding the damage propagation in laminated [22] composite materials were further used as scientific basis for interpretation of monitored microstructural changes due to mechanical loading.

With this work, a first approach is made to comparatively evaluate the deformation and damage behavior of the structurally optimized Cottonid variant M60Z50 with an industrially manufactured standard Cottonid material under quasi-static tensile loading. The results are used for validation of application-oriented structural optimization of Cottonid through adjustment of single manufacturing parameters, e.g. the temperature of the catalyst bath T_{cat} or the reaction time t_{react} of the paper in it. To assess the microstructure in initial condition as well as changes during loading, qualitative and advanced optical surface and volume analyses via in situ SEM and μ CT techniques were performed.

Materials and Methods

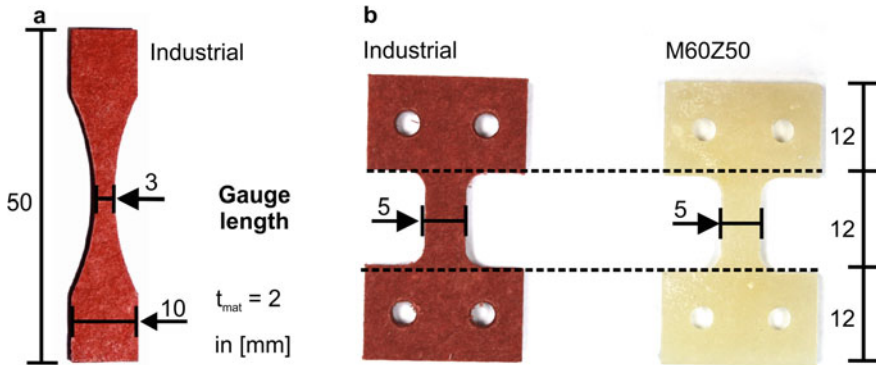
Sample Preparation

Specimens for in situ investigations have been milled out of a plate of industrial Cottonid material (Ernst Krueger GmbH & Co. KG, Geldern, Germany) as well as a plate of structurally optimized Cottonid of the variant M60Z50. Both plates had a thickness of $t_{\text{mat}} \sim 2$ mm. The raw paper for the production of M60Z50 was obtained from Hahnemuehle FineArt GmbH (Dassel, Germany) and has a weight of 320 g/m^2 with a material thickness $t_{\text{mat}} = 0.9$ mm. It consists of 100% cotton linters, subsequently marked as “M”. A 70 wt-% Zinndichloride (ZnCl_2) solution, hereinafter referred to as “Z”, is used as the chemical catalyst for parchmentizing. The sample designation of the resulting Cottonid variants consists out of the chosen manufacturing parameters (Table 1) [5].

The samples are then smoothed and dried in a calander (Sumet, Denklingen, Germany) under pressure and temperature. In order to prevent a dimensional change of the material due to water absorption from the environment, the samples are stored

Table 1 Manufacturing parameters of cottonid variant M60Z50

Cottonid variant	Manufacturing parameters			
	Cellulose source	Reaction time	Catalyst	Temperature
M60Z50	Cotton linters (“M”)	60 s	Zinedichloride solution (“Z”)	50 °C

**Fig. 1** Specimen geometry for in situ tensile tests in a scanning electron microscopy (SEM) and μ CT, following [17]. (Color figure online)

under weight in a dry atmosphere until further analysis [5]. For mechanical in situ investigations in a SEM and μ CT, geometries were chosen in respect to the assembly dimensions of the in situ testing machines (Fig. 1). For conditioning, specimens were stored under laboratory conditions (temperature $T = 23 \pm 2$ °C, relative humidity $\varphi = 35 \pm 5\%$) for a time $t > 48$ h before testing [17].

Test Setup for Microstructural In Situ Investigations

For microstructural investigations on the surface of Cottonid specimens (Fig. 1a) a FE-SEM (MIRA 3, Tescan GmbH, Dortmund, Germany) was used. Beam voltage was set at $U_B = 10$ kV, while magnification settled between $M = 50$ and $5 \cdot 10^3$. Using a micro tensile testing module ($F_{\max} = 5$ kN, Kammrath and Weiss GmbH, Dortmund, Germany), tensile loading during surface observation with SEM was applied with a testing speed of $v = 0.12$ mm/min. Figures 2a and b show the test chamber of the SEM with integrated in situ module and mounted Cottonid specimen, here on the example of the industrially manufactured material. Further, exemplary SEM micrograph of specimen's surface in gauge length after failure (Fig. 2c) is given, to illustrate the in situ testing technique for characterization of damage development [17].

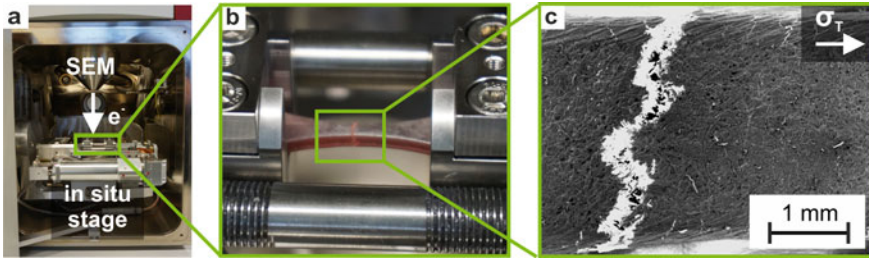


Fig. 2 In situ tensile test in SEM: **a** Integrated micro tension module (Kammrath & Weiss GmbH, Dortmund, Germany), **b** mounted Cottonid specimen; **c** SEM micrograph of gauge length's surface after failure; following [17]. (Color figure online)

Microstructural investigations in the volume of specimen's gauge length (Fig. 1b), were performed in a microfocus computer tomograph (μ CT, X TH 160, Nikon Metrology GmbH, Alzenau, Germany) with maximum beam energy of $U_{max} = 160$ kV and maximum power of $P_{max} = 60$ W. For in situ tensile tests during a μ CT scan, a micro tensile/compression testing module ($F_{max} = 5$ kN, CT5000TEC, Deben UK Ltd, UK) was used.

Figure 3a shows the in situ module—without housing to visualize the internal construction—in front of the the μ CT with mounted M60Z50 specimen, whereas Fig. 3b shows the assembled testing module integrated in the test chamber of the μ CT. Further, exemplary 3D volumes of specimen's gauge length are shown (Fig. 3c), one opaque and one in 50% transparency to visualize a treshold defect analysis performed in the volume of the gauge length. Scanning parameters for μ CT scans were $U_{scan} = 125$ kV and $P_{scan} = 6.4$ W resulting in an effective pixel size of $7 \mu\text{m}$. Testing speed was $v = 0.5$ mm/min. During one scan, 1583 projections were captured, each with an exposure time of $t_{ex} = 250$ ms. The obtained data was reconstructed and post processed with industrial CT software (VGStudio Max V.2.2) via threshold defect analysis [17].

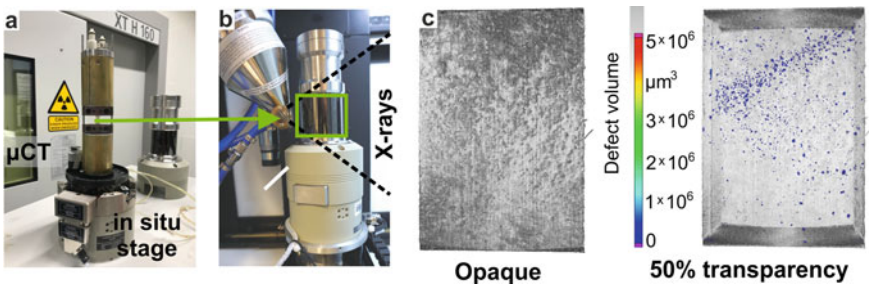


Fig. 3 In situ tensile test in μ CT: Micro tension/compression module (CT5000TEC, Deben UK Ltd, UK) **a** with mounted μ CT specimen; **b** integrated in μ CT; **c** 3D volume of specimen's gauge length, opaque and with 50% transparency to visualize defect analysis; following [17]. (Color figure online)

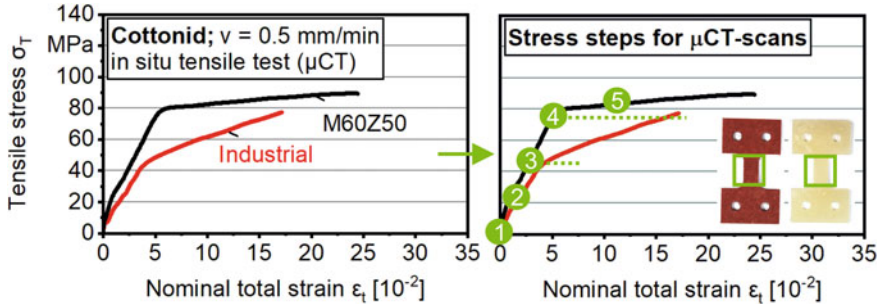


Fig. 4 Determination of stress steps in significant ranges in the stress–strain behavior of two Cottonnid variants to visualize damage development in volume. (Color figure online)

For characterization of damage development in the different Cottonnid variants, i.e. industrially manufactured material and structurally optimized material M60Z50, due to quasi-static tensile loading, a comparative evaluation of the microstructure on surface and in volume at different load steps was performed in comparison to the initial condition of the specimens. The obtained SEM micrographs were therefore analyzed for characteristic defects, like pores or microcracks, which could be monitored during the in situ test. On the reconstructed 3D volumes from μ CT scans, threshold defect analyses for comparison of void volumes in specimens ‘gauge lengths’ were applied [17].

Test Strategy for Characterization of Damage Development on Surface and in Volume

Based on the stress (σ)–strain (ε) behavior of the Cottonnid variants, when applying quasi-static tensile loading under laboratory conditions, characteristic loads steps, where SEM micrographs and 3D volumes, respectively, should be taken, were determined (Fig. 4). The materials show a significant difference in deformation behavior, e.g. M60Z50 is characterized by an increase in yield strength σ_Y of $\sim 30\%$. The adjustment of manufacturing parameters for structural optimization obviously resulted in an improved deformation behavior as well as optimized mechanical properties for M60Z50, i.e. an increased yield strength σ_Y and ultimate tensile strength UTS. Therefore, the applied tensile stresses cause divergent deformation stages for each specimen and e.g. step 5 ($\sigma_T \sim 85$ MPa), which lies in the plastic region of M60Z50, could not be performed on the industrially manufactured material, since the specimen has already reached its UTS. Significant microstructural changes due to mechanical loading in comparison to the initial condition (1) of the specimens were expected in the elastic region (2), at the yield strength (3, 4) and in the plastic region (4, 5).

Results and Discussion

In Situ *Quasi-Static Tensile Tests in SEM*

Figure 5a visualizes the surface of the gauge length of the SEM in situ specimen in initial condition and significant structural characteristics to visualize damage development due to quasi-static tensile loading are marked. It consists out of bound and partly bound, protruding cellulose fibers, pores, microcracks and amorphous areas.

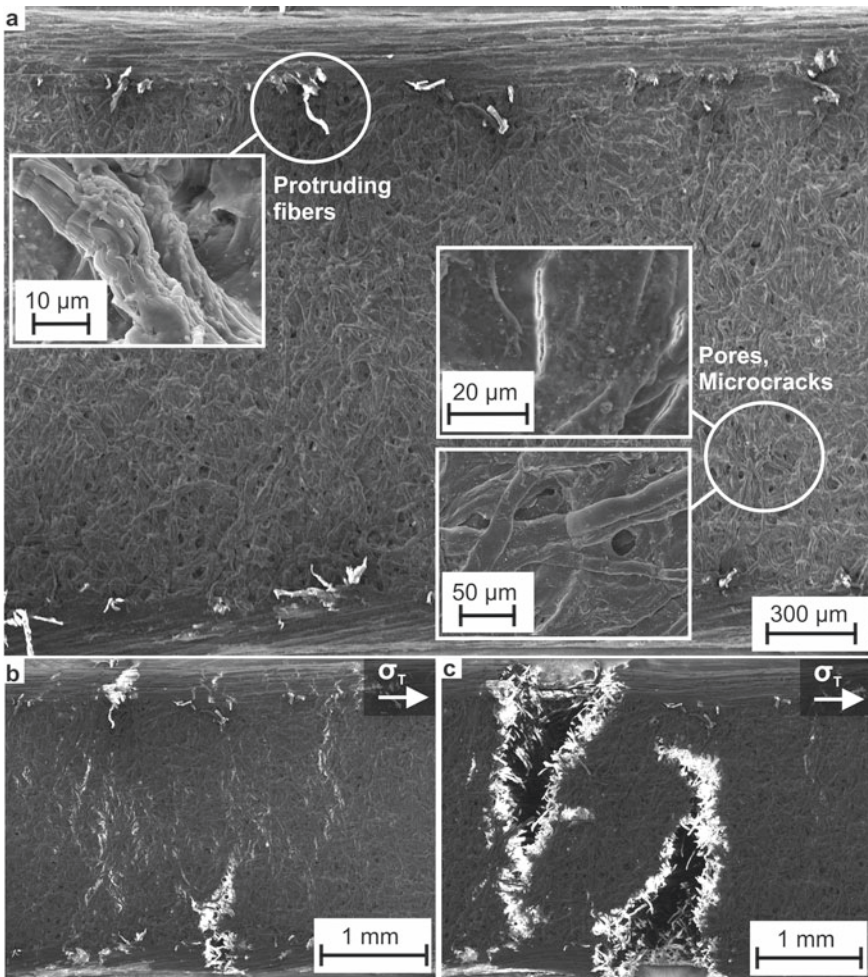


Fig. 5 SEM micrographs of Cottonid's surface in gauge length: **a** Field of view in in situ test in initial condition with marked structural characteristics; **b** crack initiation and **c** crack propagation during in situ tensile test

An exemplary monitoring of the gauge length is presented in Fig. 5b and c. The identified imperfection of Cottonid's surface leads to crack initiation at critical areas, like pores or already existing microcracks. Cracks propagate with increasing tensile stress σ_T throughout the whole structure by cutting cellulose fibers and assemble then, which leads to a complete loss of structural integrity and final failure of the specimen [17].

In Situ Quasi-Static Tensile Tests in μ CT

Figure 6 comprises the results of the in situ tensile tests in μ CT by correlating observed void volumes in specimen's gauge length to the applied tensile stress σ_T . In Fig. 6a the chosen stress steps, where 3D volumes are taken, are classified based on the σ - ε curves of the industrially manufactured and the M60Z50 Cottonid variant, whereas in Fig. 6b the detected void volume percentages in relation to the initial condition are plotted over the applied tensile stresses σ_T , which are comparable for both variants (1–4). In initial condition (1), both Cottonid variants already exhibit an amount of voids, which could be explained by the manufacturing process, where several paper layers, which already contain defects, are layered over each other and bonded by a chemical process. If areas are insufficiently bonded, additional delaminations/voids are present within the final bulk material. It is noticeable, that M60Z50 shows much less overall void volume than the industrially manufactured variant. It could be derived, that the optimized mechanical behavior of M60Z50 (Fig. 4) is related to the structural optimization by adjustment of the manufacturing parameters, which obviously lead to a more sufficient bonding of the interfaces between the paper layers and less delaminations/voids, respectively, in the final bulk material [5]. The comparatively small amount of overall void volume in M60Z50 may therefore only originate from the defects within the paper layers (Fig. 5a). For the industrial material, in the elastic region (2), the overall void volume first decreases until reaching the yield strength (3), because of deformation-induced closing of the voids. With further loading into the plastic region (4), the overall void volume increases until final failure of the specimen at $\sigma_{T,f,ind} = 77.10 \text{ MPa}$ ($\varepsilon_{n,f,ind} = 17.00 \cdot 10^{-2}$) [17]. For M60Z50, the detected overall void volume percentages in relation to the initial condition nearly stay the same (Fig. 7b) until final failure of the specimen at $\sigma_{T,f,M60} = 89.31 \text{ MPa}$ ($\varepsilon_{n,f,M60} = 24.42 \cdot 10^{-2}$).

The development of void volume for both specimens is exemplary visualized for three loading stages (initial condition, yield strength, plastic region) in Fig. 7. To focus on void development due to the mechanical loading, the material itself is rendered invisible, whereas the different colours represent the maximum void volume. In correlation to the surface defects obtained in in situ SEM investigations, the void volume in initial condition could be explained by insufficiencies in the material originating from defects within the paper layers ($\sim 10,000$ – $1,000,000 \mu\text{m}^3$), besides insufficiently bonded areas between the paper layers caused by the manufacturing

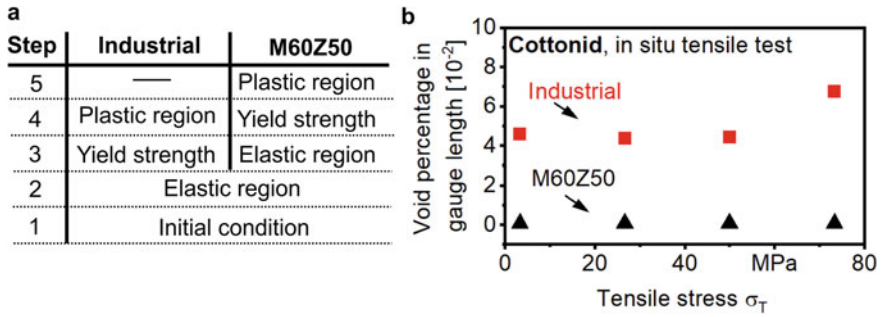


Fig. 6 **a** Classification of stress steps based on deformation behavior of the two Cottonid variants; **b** percentage development of void volume in comparable stress steps. (Color figure online)

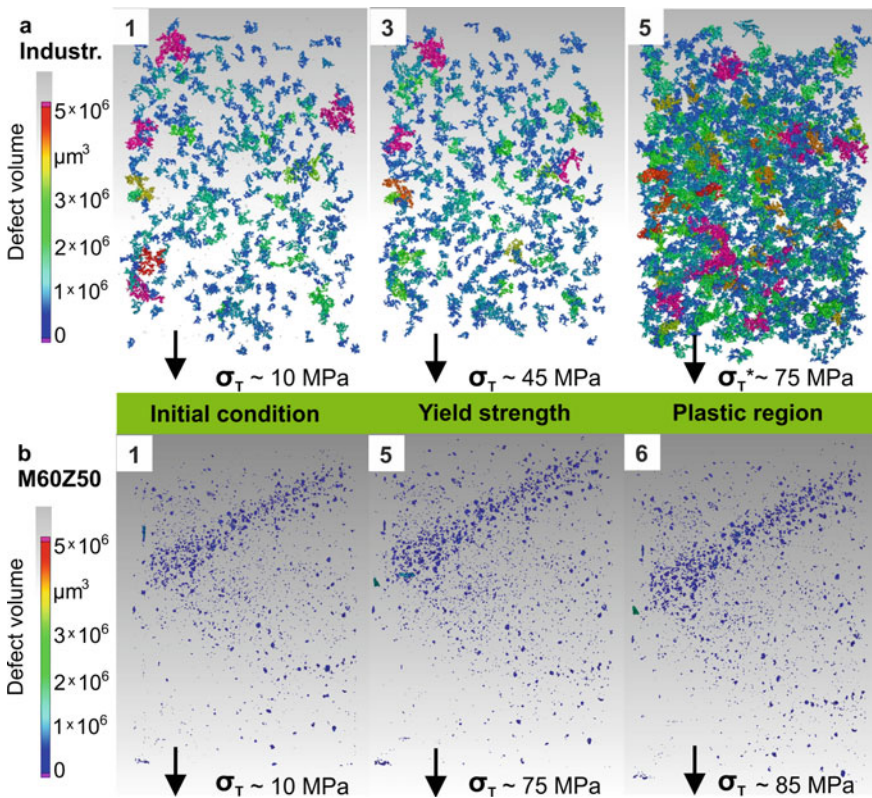


Fig. 7 Visualization of void volume in specimen’s gauge length for chosen stress steps: **a** Industrially manufactured Cottonid; **b** Cottonid variant M60Z50. (Color figure online)

process ($>1,000,000 \mu\text{m}^3$). A further delamination of the chemically bonded paper layers at the interface within the plastic region starting from insufficiently bonded areas in initial condition is expected for the industrial standard. This hypothesis correlates to μCT studies of Arif et al. [15], where also debonding of interfaces in a PA66/GF30 composite was identified as critical failure mechanism due to a mechanical tensile load.

This damage development could not be observed for M60Z50, since much smaller void volumes ($<1,000,000 \mu\text{m}^3$) are present, which may only originate from the defects within the paper layers. Structural optimization therefore obviously leads to a strengthening of interfaces between the paper layers and therefore to smaller defects in initial condition, which propagate less intensive under a quasi-static mechanical load. These findings correspond to the improved mechanical behavior of M60Z50 (Fig. 4).

Conclusions and Outlook

Within this study, advanced in situ scanning electron microscope and microfocus computer tomography techniques were applied to characterize and comparatively evaluate microstructural damage development due to quasi-static tensile loading on the surface and in the volume of two variants of the polymeric material Cottonid. The materials observed are an industrial standard and the structurally optimized variant M60Z50. Via optical monitoring of microstructural characteristics of the materials in initial condition, the progression of defects like pores, microcracks or delaminations could be correlated with applied tensile loads. Therefore, the deformation, damage and failure behavior of industrially manufactured Cottonid and the impact of structural optimization on the material behavior could be interpreted for different regions of the stress–strain curve.

In situ investigations revealed, that in the elastic region, no visible damage occurs on the surface, whereas in the volume present delaminations/voids first decrease due to deformation-induced closing. When passing the yield strength, cracks initiate at critical areas on the surface (pores, microcracks) and in the volume (delaminations/voids) and propagate throughout the whole structure with increasing load. The assembly of these cracks leads to loss of structural integrity and final failure of the specimen. Corresponding to studies on fiber-reinforced composites, microcrack propagation starts after reaching the yield strength, but it is not characterized by known phenomena, like propagation along fiber-matrix interfaces. In fact, microcracks initiate variously on the surface and propagate by cutting fibers and amorphous areas, equally [17]. Similar to laminated composites [22], present voids detected in the volume seem to increase within the interfaces between the paper

layers, which macroscopically are not visible anymore after the chemical treatment during parchmmentizing.

Structural optimization through adjustment of manufacturing parameters resulted in an improved deformation and damage behavior for M60Z50, since a much less amount of overall void volume with comparatively small defect size was detected, which propagation is less pronounced until final failure of the specimen. Structural optimization therefore obviously leads to a strengthening of interfaces between the paper layers and therefore to smaller defects in initial condition, which improves the mechanical behavior of Cottonid. Since Cottonid is hygroscopic, further studies will focus on the influence of relative humidity on the damage behavior.

Acknowledgements The authors thank the German Research Foundation (Deutsche Forschungsgemeinschaft, DFG) for its financial support within the research project “Biomechanical qualification of the structurally optimized functional material Cottonid as an adaptive element” (WA 1672/23-1; ZO 113/22-1), and the Hahnmuehle FineArt GmbH (Dassel, Germany) and the Ernst Krueger GmbH & Co. KG (Geldern, Germany) for providing raw material for Cottonid manufacturing and industrial reference material, as well as the research partners M. Langhansl, C. Zollfrank (TUM Campus Straubing) for providing „M60Z50” material within the framework of an excellent collaboration.

References

1. Taylor T (1871) Improvement in the treatment of paper and paper-pulp. US. Patent 114,880, 16 March 1871
2. Schoenen F (1965) 3. Cellulose as resource (in German). In: Vieweg R, Becker E (eds), Plastic handbook volume 3 modified natural products Manufacturing, properties, processing and applications. Carl Hanser, Munich, Germany
3. Scholz R, Langhansl M, Zollfrank C, Walther F (2019) Cottonid—An efficient functional material for humidity-driven actuators (in German). In: Wiedemann M, Melz T (eds), Smart structures and systems—conference manuscript of the 4 smarts symposium. Shaker, Germany, p 63–75. ISBN: 978–3–8440–6425–4
4. Scholz R, Langhansl M, Zollfrank C, Walther F (2019) Experimental study on the actuation and fatigue behavior of the biopolymeric material Cottonid. *Mater Tod Proc* 7:476–483. <https://doi.org/10.1016/j.matpr.2018.11.112>.
5. Scholz R, Langhansl M, Zollfrank C, Walther F (2020) Humidity-sensing material Cottonid—microstructural tuning for improved actuation and fatigue performance. *Front Mater* 7(156):1–10. <https://doi.org/10.3389/fmats.2020.00156>
6. Scholz R, Mittendorf R-M, Engels J, K, Hartmaier, A, Kuenne, B, Walther, F, (2016) Direction-dependent mechanical characterization of cellulose-based composite vulcanized fiber. *Mater Test* 58(10):813–817. <https://doi.org/10.3139/120.110929>
7. Scholz R, Delp A, Kaplan A, Walther F (2016) Comaparative evaluation of the temperature-dependent mechanical properties of vulcanized fiber and technical plastics (in German). In: Christ H-J (ed), *Materials testing 2016—progress in materials testing for research and practice*. Stahl Eisen, Germany, p 245–250. ISBN: 978–3–514–00830–4
8. Frey M, Widner D, Segmehl J, S, Casdorff, K, Keplinger, T, Burgert, I, (2018) Delignified and densified cellulose bulk materials with excellent tensile properties for sustainable engineering. *ACS AMI* 10(5):5030–5037. <https://doi.org/10.1021/acsami.7b18646>

9. Poppinga S, Zollfrank C, Prucker O, Ruhe J, Menges A, Cheng T, Speck T (2018) Toward a new generation of smart biomimetic actuators for architecture. *Adv Mater* (Deerfield Beach, Fla.) 30(19) e1703653:1–10. <https://doi.org/10.1002/adma.201703653>
10. Tenkamp J, Awd M, Siddique S, Starke P, Walther F (2020) Fracture-mechanical assessment of the effect of defects on the fatigue lifetime and limit in cast and additively manufactured aluminum-silicon alloys from HCF to VHCF regime. *Metals* 10(7)943:1–18. <https://doi.org/10.3390/met10070943>
11. Striemann P, Hulsbusch D, Mrzljak S, Niedermeier M, Walther F (2020) Systematic approach for the characterization of additive manufactured and injection molded short carbon fiber-reinforced polymers under tensile loading. *Mater Test* 626:561–567. <https://doi.org/10.1016/j.ijfatigue.2011.12.005>
12. Niederberger C, Mook W, M, Maeder, X, Michler, J, (2010) In situ electron backscatter diffraction (EBSD) during the compression of micropillars. *Mater Sci Eng A* 527:4306–4311. <https://doi.org/10.1016/j.msea.2010.03.055>
13. Liu Y, Tanaka Y (2003) In situ characterization of tensile damage behavior of a plain-woven fiber-reinforced polymer-derived ceramic composite. *Mater* 57:1571–1578. [https://doi.org/10.1016/S0167-577X\(02\)01034-0](https://doi.org/10.1016/S0167-577X(02)01034-0)
14. Scott A, E, Mavrogordato, M, Wright, P, Sinclair, I, Spearing, S. M. (2011) In situ fibre fracture measurement in carbon-epoxy laminates using highresolution computed tomography. *Compos Sci Technol* 71(12):1471–1477. <https://doi.org/10.1016/j.compscitech.2011.06.004>
15. Arif M, F, Meraghni, F, Chemisky, Y, Despringre, N, Robert, G, (2014) In situ damage mechanisms investigation of PA66/GF30 composite: effect of relative humidity. *Compos Part B-Eng* 58:487–495. <https://doi.org/10.1016/j.compositesb.2013.11.001>
16. Hulsbusch D, Mrzljak S, Walther F (2019) In situ computed tomography for the characterization of the fatigue damage development in glass fiber-reinforced polyurethane. *Mater Test* 61(9):821–828. <https://doi.org/10.3139/120.111389>
17. Scholz R, Delp A, Walther F (2012) In situ characterization of damage development in Cottonid due to quasi-static tensile loading. *Mater* 13(9)2180:1–12. <https://doi.org/10.3390/ma13092180>
18. Little J, E, Yuan, X, Jones, M, I, (2012) Characterisation of voids in fibre reinforced composite materials. *NDT&E Intern* 46:122–127
19. Yu B, Bradley R, Soutis C, Hogg P, Withers P (2015) 2D and 3D imaging of fatigue failure mechanisms of 3D woven composites. *Compos Part a* 77:37–49. <https://doi.org/10.1016/j.compositesa.2015.06.013>
20. Patera A, Derome D, Griffa M, Carmeliet J (2013) Hysteresis in swelling and in sorption of wood tissue. *J Struct Biol* 182:226–234. <https://doi.org/10.1016/j.jsb.2013.03.003>
21. Adey-Johnson R, Mclean J, P, Van den Bulcke, J, Van Acker, J, McDonald, P, J, (2020) Micro-CT measurements of within-ring variability in longitudinal hydraulic pathways in Norway spruce. *IAWA J* 1:12–29. <https://doi.org/10.1163/22941932-00002104>
22. Barbero E, J, Cosso, F, A, Campo, F, A, (2013) Benchmark solution for degradation of elastic properties due to transverse matrix cracking in laminated composites. *Comp Struct* 98:242–252. <https://doi.org/10.1016/j.compstruct.2012.11.009>

Non-destructive Inspection of Contaminated Epoxy Plates Using Propagating Acoustic Waves



I. M. McBrayer and F. Barsoum

Abstract The increased use of composites demands the development of repair processes that can guarantee lasting strength restoration so as to minimize the frequency of expensive downtime. Weak bonds are a concern for ensuring the structural integrity of a repair and although epoxy resins are continuously being developed to have higher strengths than their predecessors, factors such as contamination levels in the repair bond may result in poor adherence and inhibit overall bond strength. This research compares the response of virgin epoxy plates to short duration acoustic excitation with that of epoxy with varied levels of contamination (0.5, 1 and 10%). Acoustic events were simulated at multiple distances from a high-fidelity displacement sensor, using the Hsu-Nielsen technique, and the experimental signals were then assessed in the time–frequency domain, using the wavelet transform. Results were then compared with previous research on unidirectional carbon fiber laminates with a single contaminant in between plies.

Keywords Acoustic emission · Hsu-nielsen · Bond quality · Contamination · Epoxy · Wavelets · Time–frequency · Weak bonds

Introduction

Adhesive bonds, used in both repairs and bonded structure, are used across multiple industries, including aircraft, marine craft, wind turbines and high performance cars; however, unknown quantities of weak adhesion can influence designers to supplement bonds with mechanical fasteners, increasing cost and weight of installations. The large size of many of the structures within these industries, and difficulties associated with transportation, may often require certain repairs and modifications to be performed “in situ”, which could cause several quality assurance related issues, notably, imperfections due to ingress of contaminants and voids in a bond line. Such imperfections can have a significant detrimental impact on the overall integrity of

I. M. McBrayer (✉) · F. Barsoum
Aerospace Blvd, Daytona Beach, FL 32136, USA
e-mail: birdi@my.erau.edu

© The Minerals, Metals & Materials Society 2021
TMS 2021 150th Annual Meeting & Exhibition Supplemental Proceedings,
The Minerals, Metals & Materials Series,
https://doi.org/10.1007/978-3-030-65261-6_78

the adhesive bond as discussed by [1–6]. Consequently, weak bonds have become a topic of great interest in industry. Possible sources of contamination when a bonding operation is performed under non-clean room conditions include skin oil, bagging materials, release agents, engine oils, dust, and grease. If the quality of the bond or level of contamination present is unknown, it becomes challenging to predict the strength and life of the bond.

The aim of this research is the detection of dispersed, low-level contamination of epoxy resin bonds using NDI techniques. Experimental techniques are incorporated to assess multiple epoxy resin plates with varying levels of contamination, by inducing a broadband excitation to simulate an acoustic event. The effects of the presence of contamination on the signal picked up by a single acoustic sensor are investigated to assess the validity of acoustic NDI techniques for this purpose.

Materials and Methods

Test Specimens

The test specimens were a series of plates provided by PTM&W industries that were manufactured from MVS 610/615 epoxy and hardener mixture. The contamination in the “worst case scenario” was mineral oil at a 10% total contamination. Determination of percentage of contamination was based on 300 grams of mixed material, thus for the 10% contamination, 270 g of mixed epoxy and hardener were mixed with 30 g of mineral oil. Three additional specimens with contamination levels of 1, 0.5, and 0% were manufactured following the same guidelines. Plate dimensions were 381 mm × 121 mm × 3.175 mm.

Experimental Techniques

The experimental set up for this investigation incorporated use of a Micro-II comprehensive acoustic emission system alongside two S9208 High Fidelity Displacement Sensors, all supplied by Mistras.

Tests were conducted using a pencil lead break methodology. The technique involves the breaking of a pencil lead at a replicable angle and distance from the sensor to produce a repeatable signal, which simulates an acoustic event and is otherwise known as a “Hsu-Nielsen” source. It is typically used for calibration purposes to check the calibration of an acoustic emission sensor, for defining thresholds for acoustic studies and in propagation studies to identify dominant frequencies of symmetric and antisymmetric wave modes. Testing was set up in accordance with ASTM E976 procedures, with respect to the use of a 0.3 mm 2H pencil lead, as well as a “Nielsen

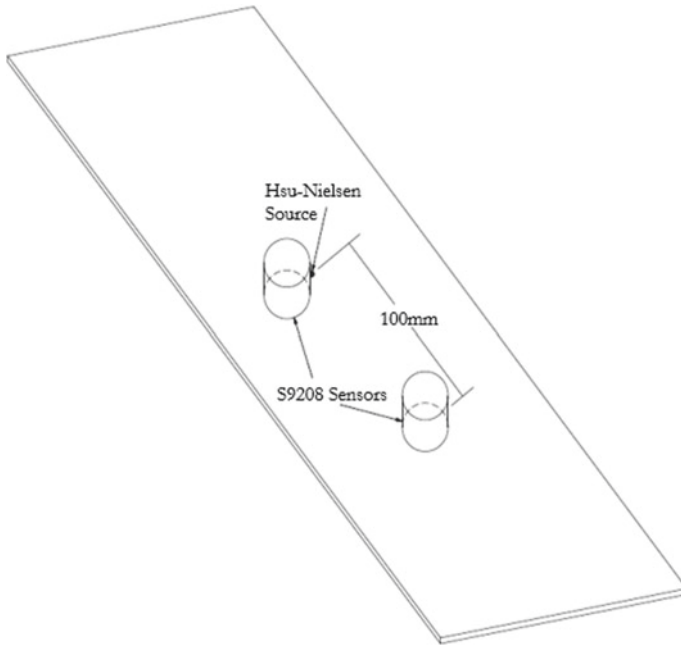


Fig. 1 Test setup

shoe” (a small Teflon guide ring of standard specified dimensions to aid in ensuring the pencil lead is broken at a consistent angle).

The technique was applied across the length instead of through thickness (Fig. 1) to allow for industry scenarios in which both sides of a panel are not easily accessible and through thickness pitch catch type signals are, therefore, made difficult. 10 Hsu-Nielsen source responses were gathered for each specimen at distances between the pencil lead break location and the pick-up sensor of 100, 200, and 250 mm, to ensure ample interaction of the signal with the structure.

Results and Discussion

Signal Consistency

Initial review of the temporal signal (Fig. 2) demonstrates the replicability of the propagating waves due to pencil lead break excitation. Two separate randomly selected signals from Hsu Nielsen excitation are plotted in each graph for both the 10% oil contamination and the 0% contamination. The signals are plotted for the first 350 microseconds to limit the effects of edge reflections. Results show high agreeability

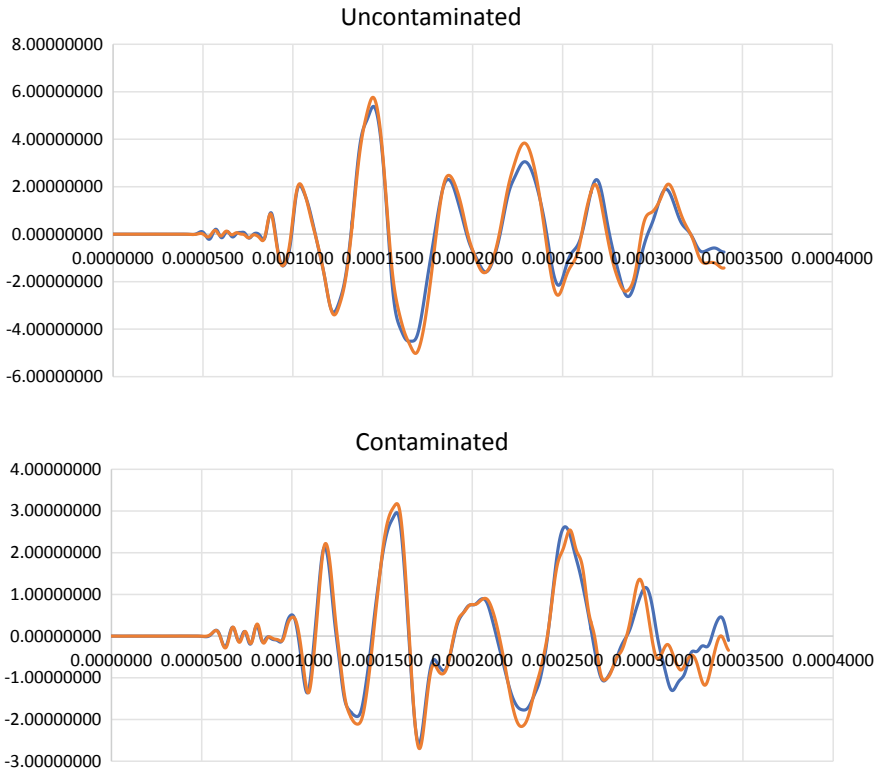


Fig. 2 Initial part of signal for both 10% contamination and 0% contamination. (Color figure online)

during the initial part of the signal. Higher amplitudes may also be observed in the signal obtained from the uncontaminated specimen.

Time–Frequency Analysis

In addition to looking at waveform features in the temporal domain, Wavelet analysis using Morlet wavelet transform was performed to extract further information on the recorded signals by observation in the time–frequency domain. The capability to identify features such as frequency components allows for a more in-depth interrogation of a signal. Wavelet transforms have become increasingly popular as a technique for assessing as well as denoising signals and have been used for the processing of Acoustic Emission signals as well as those produced by guided lamb waves. Wavelet transforms are similar in theory to the Fourier transform in that they allow us to break up a signal into components of frequency; however, they go one step further

by adding in a temporal function, seen in the basis functions for the continuous Morlet wavelet transform and the Fourier transform (Eqs. 1 and 2 respectively).

$$\varphi(t) = e^{i\omega t} e^{-\frac{t^2}{2}} \tag{1}$$

$$\varphi(t) = e^{i\omega t} \tag{2}$$

This allows the user to identify frequency discontinuities with respect to time. Whereas a Fourier transform breaks up a signal into constituent sinusoidal waves of different frequencies, a wavelet transform depends on the application of a selected “mother wavelet” across the signal and allows the user to measure the degree of stretch and compression (scale) of this mother wavelet at different times within the signal. The Morlet “mother” wavelet (Fig. 3) has exhibited favorable characteristics for acoustic emission and guided wave applications [7], and has been shown to provide the greatest resolution in both the frequency and time domain.

Figure 4 exhibits the time domain signals for both the highly contaminated (10% oil) specimen and the uncontaminated specimen at a 200 mm propagation distance, respectively, along with their associated wavelet scalograms. On initial inspection it is noted that shorter duration of the signal may be associated with contamination increases. Scalograms were used for the identification of frequency regions of interest, with the dark red regions conveying higher energy components of the signal. Regions of interest were identified as the low frequency range of 20-30 kHz and the high frequency range of 50–60 kHz.

Closer inspection of the wavelet coefficient modulus at both ranges showed significant variations in peak values between test specimens at low frequencies but less significant at higher frequency. Wavelet coefficients at the 25 kHz frequency range

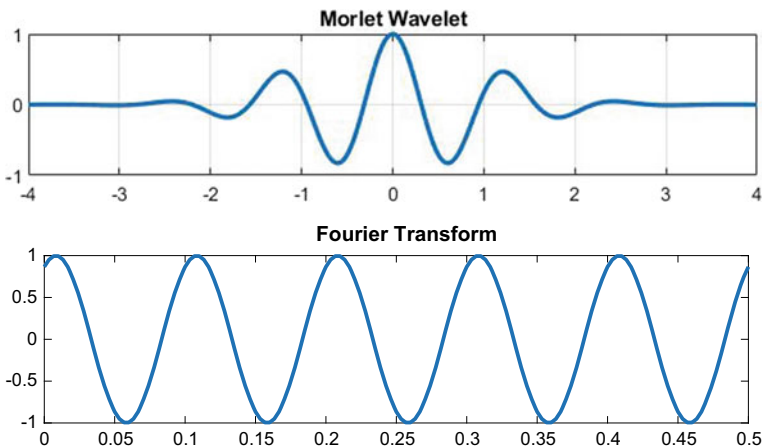


Fig. 3 Morlet wavelet and Fourier basis function generated in MATLAB. (Color figure online)

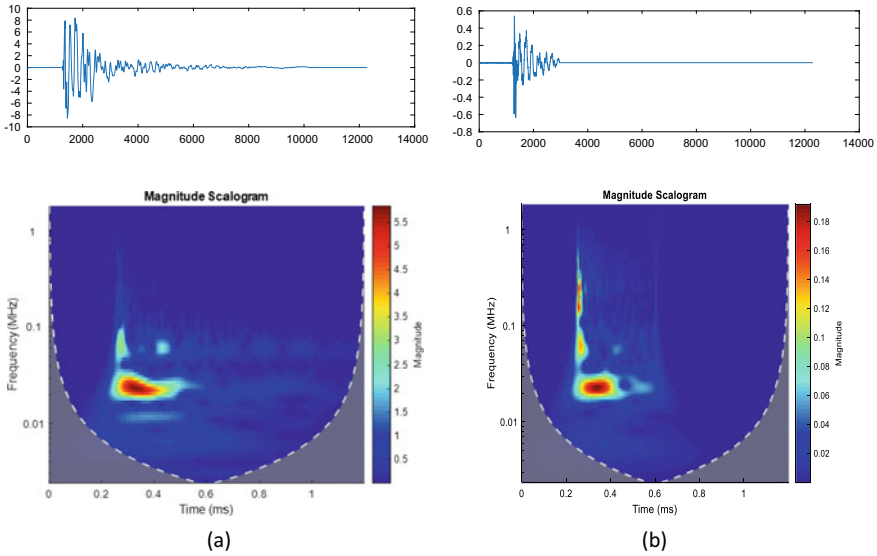


Fig. 4 Temporal signal and Morlet Continuous wavelet Transform scalogram for MVS 610/615 cast epoxy plates with **a** 0% contamination and **b** 10% contamination. (Color figure online)

were plotted for all four specimens (Fig. 5) and exhibit a correlation between a decrease in energy associated with the arrival of the signal at low frequencies along with an increase in levels of contamination, present within the specimen. Coefficients were observed to decrease significantly for the signal obtained for the specimen with very high levels of contamination.

Both the lower duration of the signal and lower energy of low frequency components associated with higher levels of contamination are indicative of an increase in attenuation properties. This is potentially due to interaction of the epoxy and oil during cure creating an increase in porosity, causing scattering, or the combined mechanical properties increasing the absorptive properties of the material.

Comparison of these plots of wavelet coefficient modulus with those previously obtained by experimentation on contaminated, thin unidirectional carbon fiber plates can be conducted by observation of Fig. 6. These plots also show a decrease in energy of first arrival for the contaminated specimen, albeit a much smaller change as the overall attenuation of the low frequency signal components is lower for these specimens versus the low contamination epoxy specimens.

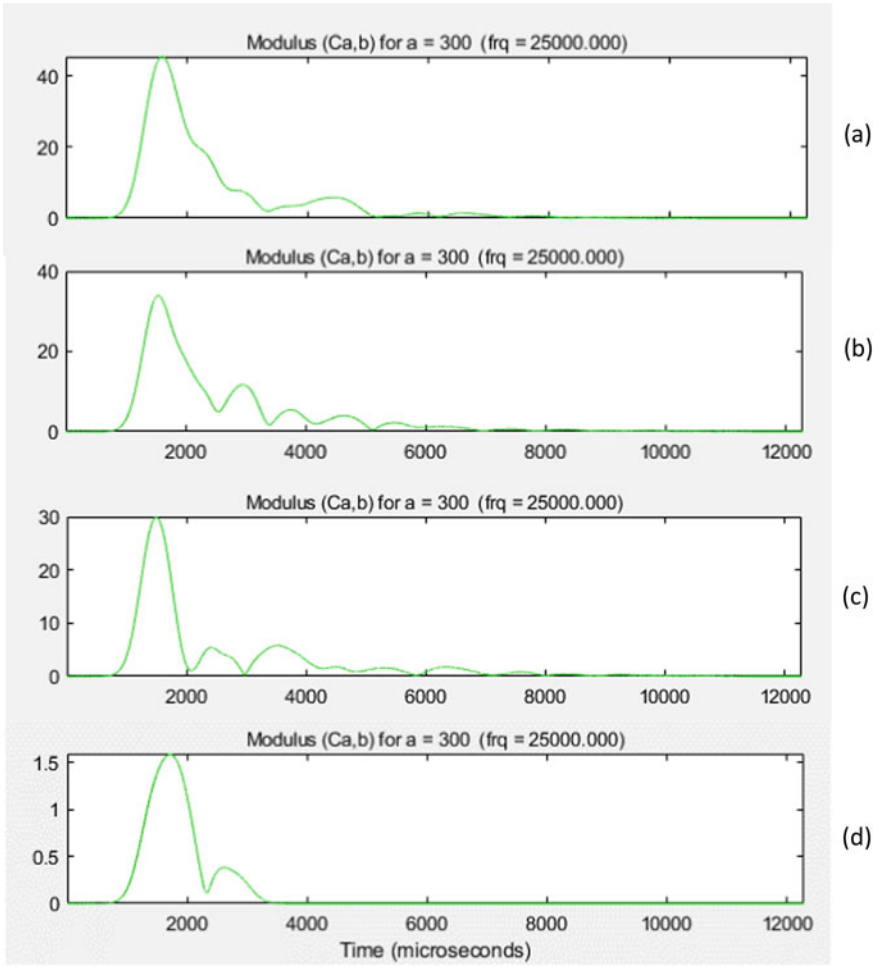


Fig. 5 Morlet wavelet coefficients at 25 kHz for MVS 610/615 epoxy resin cast plates with **a** 0% contamination, **b** 0.5% contamination, **c** 1% contamination and **d** 10% contamination. (Color figure online)

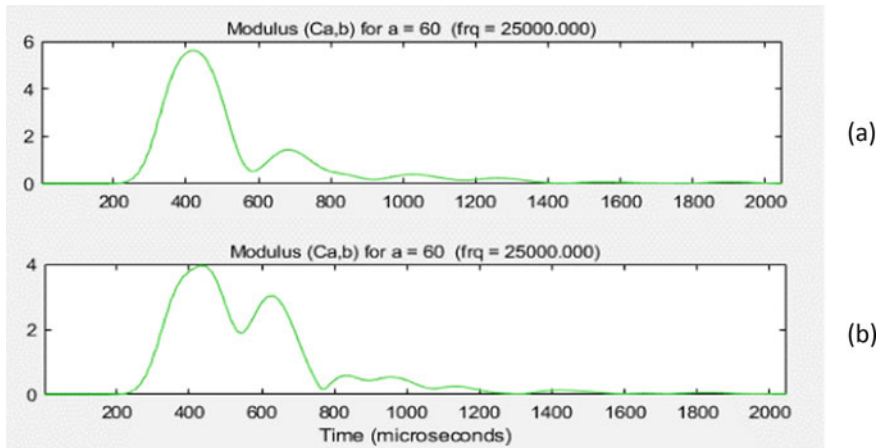


Fig. 6 Unidirectional CFRP plates with **a** No contamination and **b** a 5 mm by 5 mm single contaminant between plies. (Color figure online)

Summary and Key Takeaways

Varied levels of low-level dispersed oil contamination in cast epoxy plates have been excited by an artificial acoustic source known as the Hsu-Nielsen source to study the effects of contamination on the signal received by a broadband sensor. Signal contrasts, resulting from introduced contamination, were successfully identified and findings of this study may be summarized as follows:

1. Hsu-Nielsen source gave very consistent results on each specimen, particularly in the initial arrival of the signal. Clear differences can also be observed within the temporal signals between contaminated and uncontaminated specimens, although perhaps not quantifiable. Excitation by Hsu-Nielsen source can therefore be justified as a technique to be further researched in the domain of contaminant identification.
2. Mode discrepancies show correlation between epoxy plates and UD CFRP tensile specimens, although signals received for the larger, single piece contaminant could also be observed to contain a second arrival of low frequency components, which suggests further research into the minimum contaminant particle size that would cause a second arrival may be warranted.
3. Attenuation of the signals increased with decreasing contamination levels, particularly of the low frequency signal components. This was observed by a faster arrival time of the signal for non-contaminated specimens alongside higher energy of low frequency components of the received signal.

References

1. Pribanic T, et al Effect of surface contamination on composite bond integrity and durability, p 23
2. McDaniel D, Musaramthota V, Pribanic T, Zhou, X Effect of surface contamination on composite bond integrity and durability, p 35
3. Phark J-H, Duarte S Jr, Kahn H, Blatz MB, Sadan A (Dec. 2009) Influence of contamination and cleaning on bond strength to modified zirconia. *Dent Mater* 25(12):1541–1550. <https://doi.org/10.1016/j.dental.2009.07.007>
4. Anderson GL, Stanley SD, Young GL, Brown RA, Evans KB, Wurth LA (Nov. 2010) The effects of silicone contamination on bond performance of various bond systems. *J Adhes* 86(12):1159–1177. <https://doi.org/10.1080/00218464.2010.529380>
5. Vittitow MP Adhesion impact of silicone contamination during encapsulation, p 32
6. Shang X Role of contamination on the bondline integrity of composite structures, p 143
7. Mostavi A, Kamali N, Tehrani N, Chi S-W, Ozevin D, Indacochea JE (Aug. 2017) Wavelet based harmonics decomposition of ultrasonic signal in assessment of plastic strain in aluminum. *Measurement* 106:66–78. <https://doi.org/10.1016/j.measurement.2017.04.013>

Part XXXV
Phase Transformations
and Microstructural Evolution

Application of High-Throughput Experimental Techniques in Metal Materials Research



Hui-cheng Li, You Xie, Jing Yuan, and Xiang-yang Deng

Abstract With the development and popularization of material genome engineering, the application of high-throughput experimental technology in metal materials research has attracted more and more attention due to its high efficiency and systematization. This paper briefly introduces the experimental process of high-throughput (HT) technology and its application in metal materials research, especially the application of in-situ metal analysis technology in high-throughput metal materials research, and looks forward to the application of high-throughput (HT) technology in metal materials research.

Keywords Materials genome initiative (MGI) · High-throughput (HT) · Metal materials

Introduction

In June 2011, the Obama administration in the White House announced the launch of a “Materials Genome project” (the Materials Genome Initiative, MGI), and high-throughput experiments and calculated by the material integrating database construction, and speed up the development and application of advanced materials, the plan is the “Advanced Manufacturing Partnership” (the Advanced Manufacturing Partnership) is an important part of the plan. In December 2011, the Chinese academy of sciences and the Chinese academy of engineering hosted the 14th Xiangshan scientific conference entitled “materials science systems engineering - China’s version of material genome project” to study the technical understanding of MGI. In 2014, the Chinese Academy of Sciences and Chinese Academy of Engineering, respectively, the consulting report submitted to the state council, suggest that launched the Chinese materials genome project as soon as possible, and in September that year was held in Xi’an “2014 new material development trend of international top BBS - genome project research progress on BBS,” during the academicians of the Chinese version

H. Li (✉) · Y. Xie · J. Yuan · X. Deng
Technical Center of Zenith Steel Group Company Limited, Changzhou 213011, China
e-mail: lihuicheng@zt.net.cn; castlhc@163.com

© The Minerals, Metals & Materials Society 2021
TMS 2021 150th Annual Meeting & Exhibition Supplemental Proceedings,
The Minerals, Metals & Materials Series,
https://doi.org/10.1007/978-3-030-65261-6_79

of the materials genome project team leader Chen in our country to carry out the importance and urgency of the MGI is introduced, and put forward the suggestions to develop the Chinese version material genome project [1, 2].

The core idea of material genome is to clearly put forward the deep fusion of “computation-preparation-representation-database,” and combine the development of high-throughput experimental techniques and methods such as calculation, preparation, and characterization, so as to realize the scientific and accelerated development of new material research and development. High-throughput experimental technology to pursue material finished in a short time a large number of sample preparation and characterization of the traditional materials research in the order of the iteration method is used to parallel processing, qualitative to quantitative change materials research efficiency, and to achieve material research and development from the traditional “experience to guide the experiment” model to “theoretical predictions and experimental verification” new paradigm shift, can greatly improve the efficiency of study. In addition, as one of the three elements of “material genome technology,” high-throughput experiments can provide a large amount of basic data for material simulation calculation, so as to enrich and improve the material database. At the same time, high-throughput experiments can provide strong experimental verification for the results of material simulation calculation, so that the simulation model can be continuously optimized and modified to accelerate the optimization and development of materials.

High-throughput experimental technology originated in the 1970s, the first applied in the field of biological and chemical high-throughput sequencing and high-throughput screening [3–5], the beginning of the twentieth century 90 years, high-throughput experimental technology applied in the field of metal material, after entering the twenty-first century, is a special offer commercial high-throughput experimental instruments and equipment research and development company.

Metal materials are the important material basis for the survival and development of human society. Throughout the history of the development of human society, the discovery and application of each important metal material can make human’s ability to transform nature get a new promotion. Metal materials not only laid the material foundation of social and industrial development, but also marked the development level of a country’s economic strength. With the rapid development of science and technology, the development of every major science and technology depends on the breakthrough of corresponding materials to a great extent. In particular, the research and development and application of new metal materials can greatly improve the scientific and technological level of a country. The new metal materials industry has become an important industry in the twenty-first century, which can strongly support the development of energy-saving and environmental protection, high-end equipment manufacturing, new energy vehicles, petrochemical, and other industries.

Metal materials are the most widely used materials in modern society. Compared with materials in other fields, the development and performance improvement of metal materials are relatively slow. With the increasing demand for high-performance metal materials in various industries in society, the research and development requirements for new high-quality metals are becoming more and more urgent, and the

requirements for the composition of metal materials are becoming more and more complex [6]. The various chemical components constitute a complex phase space of materials, which makes it difficult for traditional metal material development methods to effectively find new materials that can meet the needs in such a complex space. Therefore, a more efficient method is needed to improve the speed of material development and application. In this context, high-throughput experimental technology emerges.

High-Throughput Experimental Procedure

The core of high-throughput experimental technology lies in the simulation and calculation of experiment and material intelligence, the optimization of combined experimental design, the improvement of characterization efficiency of material testing, and the improvement of massive intelligent database. The high-throughput experimental flow is shown in Fig. 1.

High Flux Simulation and Calculation of Experiment and Materials

High-throughput multi-scale material simulation and calculation are an important part of the “Materials Genome project” announced in the United States in 2011. It is an important means to realize the rapid development and industrialization of materials in the future, and can integrate theoretical design, experimental research, and application industrialization more efficiently. High flux material calculation and design, is based on the material chemical composition and other basic information,

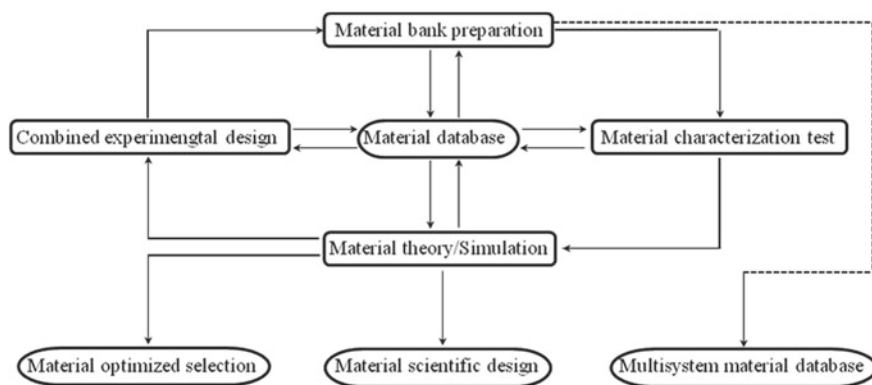


Fig. 1 Schematic diagram of material high-flux experimental flow [7]

then according to the requirements of the basic theoretical research method and material design, and application of known algorithm or develop new algorithm, the algorithm into the code or the integration of the existing theory, or develop new computational simulation software, to achieve the purpose of materials design. Multi-scale calculation is mainly aimed at the research requirements of different scales and different experimental environments of materials, so as to improve the calculation speed while maintaining the calculation accuracy, so as to study the properties of materials at different scales [8].

The four basic elements of metal materials include synthesis, structure, property, and service performance, which are independent and correlated with each other, and are usually expressed as the four vertices of a tetrahedron [9]. In order to develop metal materials that meet specific application requirements, the structural composition, synthesis method and preparation process of the materials should be reverse-designed based on the corresponding service performance and service environment [10]. Material simulation and computational design include two main contents: One is the computational simulation of materials, that is, the actual service process of materials is simulated by building a physical model; the other is the computational design of materials, that is, the design of new material components directly through the theoretical model of materials and the results of numerical calculation. The most commonly used tools for studying the properties of materials are density functional theory, molecular dynamics, first-principles calculation, phase diagram calculation, phase field simulation, and finite element analysis, as well as various simulation tools for material processing and properties. According to the relevant calculation, the relevant parameters such as thermodynamics, dynamics, crystal structure and defects of materials, as well as the response to the service environment, were obtained. Material simulation calculation and design build a bridge from microstructure to macroscopic properties, from basic research to engineering application with the rapid development of materials science and computer technology, researchers can realize the multi-scale material simulation and design calculation, this will help to understand the relationship between the structure and performance of materials, building materials of atomic structure—the connection between the microstructure and macro properties, shortening the period of new materials research and development, reduce the cost of new material research and development process [10]. Therefore, the high-throughput multi-scale simulation based on the basic theory will become a powerful means of material design. There are relatively mature materials design simulation computing software at home and abroad, such as materials project high-flux computing platform [11], mat cloud high-flux materials integrated computing platform [12], automatic flow (AFLOW) computing platform [13], and powerful material structure prediction software crystal structure analysis by particle swarm optimization (CALPSO) [14] developed by professor Ma Yanming's research group in Jilin University.

At present, the established theories and methods can predict the microstructure from the composition, but the theories and methods of predicting the macroscopic properties of materials from the microstructure need to be improved. For metallic structural materials, it is particularly necessary to establish scientific theories and

databases of various properties of material phase components varying with composition and temperature, establish theoretical basis for predicting macroscopic properties of materials from the perspective of organizational distribution, and establish and effectively integrate multi-scale models [15].

High-Throughput Preparation of Experimental Samples

The core of high-throughput preparation lies in the efficiency, systematization, and consistency of sample preparation. The sample preparation of multi-component target material multi-factor system should be completed in one experiment. High-throughput preparation of experimental samples is generally divided into two steps: composition design and obtaining samples under set experimental conditions. A variety of experimental factors should be considered comprehensively in sample preparation, and the arrangement and combination of experimental variables should be scientifically designed and formulated. High-throughput sample preparation requires the maximization of sample preparation under controllable factors or fixed conditions, and the sample can be compared in as many forms at various levels as possible under various forms or variables. As for the preparation of high-throughput samples, a number of scholars in China have carried out preliminary exploration, forming the preliminary process of continuous chemical industry production of materials and metals from molding to heat treatment and then to application, as well as the research on intelligent and scientific preparation of supply chain (Fig. 2).

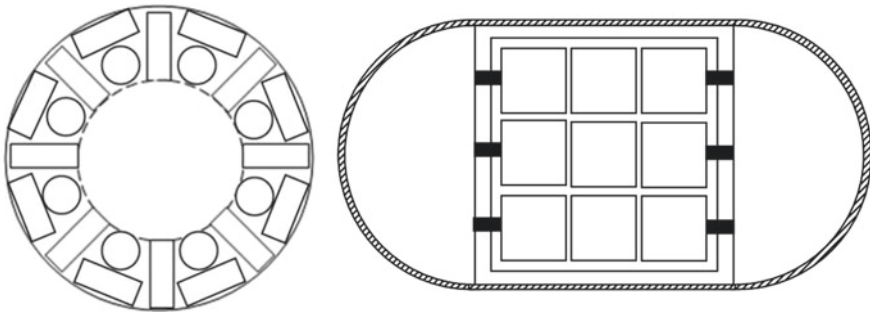


Fig. 2 Sample combination form example

High-Throughput Detection and Characterization of Experimental Samples

High throughput testing and characterization of experimental samples requires rapid analysis testing and characterization technology with scanning, automation, and intensification as the core. For metal material samples, the main contents of detection include composition structure, tissue performance, and various thermal property parameters (Fig. 3).

The composition and structure of metal materials are usually characterized by the electromagnetic spectrum method of X-ray, ultraviolet, infrared, and other wavebands, but the characterization rate is controlled by the sample and the beam, and the efficiency is not high. Synchrotron radiation source can achieve full spectrum high brightness micro focusing, with high collimation, full spectrum, high polarization, high purity, and other prominent characteristics, can meet the requirements of multi-scale and multi-quantization of high-flux samples, so it is an ideal and efficient means of high-flux sample testing and characterization. The hard X-ray synchrotron radiation has the advantages of high flux, strong penetrating power, thus, it can be dynamically observed engineering materials under the condition of the limit of physical, chemical, and mechanical properties of micro scale change process, and then understand them produce macro creep, cracking and deformation, and the change of optical and electrical properties of the internal mechanism [16].

The materials in practical application are non-uniform, multi-component, and complex, with different components and structures at different locations and different properties at different scales. Therefore, the final performance of the material is closely related to the statistical distribution characterization of the original position information.

Wang et al. proposed a characterization technique of high-throughput in-situ statistical distribution analysis based on quantitative statistical distribution rules of chemical composition and morphology in a large scale. The technology to the production of new materials research or related actual samples as the object, using a variety of

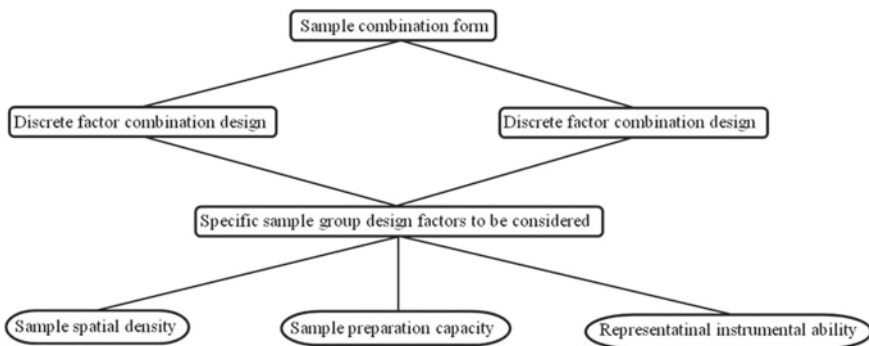


Fig. 3 Reference factors for sample combination scheme design

high-throughput characterization techniques, such as in-situ statistical distribution of laser induced breakdown spectroscopy analysis technology (LIBS-OPA) [17], laser ablation inductively coupled plasma mass spectrometry in-situ statistical distribution analysis technology (LA-icp-ms-OPA) [18], X-ray fluorescence in-situ statistical distribution analysis (XRF-OPA) and high-flux mapping characterization technique in-situ statistical distribution analysis (OPA-RM) [19], edm in-situ statistical distribution analysis (SPARK-OPA) [20], etc., Gaining mass in-situ in material composition, structure and properties, such as information, based on the material samples in area within the scope of in-situ composition distribution and statistical analytic representation of the original information [21], realize micro-mesoscopic-macro comprehensive statistical characterization of quantitative distribution across scales, can get material/structure distribution and in-situ quantitative parameters such as distribution, state distribution information, such as the content of each element in material in different positions of quantitative statistic; Quantitative calculation of the segregation degree of each element in the material. At the same time can achieve material characterization of evenness, elements of different content in the material of weight ratio of in-situ, statistical uniformity and segregation, loose materials, degree of quantitative characterization of statistical density, and apparent density at the same time, as well as the material statistics and quantitative distribution of the inclusions and inclusions in different particle size distribution of quantitative statistics, etc. [22, 23] capture, which reflect the heterogeneity of material. This comprehensive statistical characterization method is combined with the macroscopic average characterization method and the microscopic composition/structure characterization method to realize the composition distribution analysis of metal samples, the positioning of large defects, the distribution and statistics of small defects, and the distribution and statistical analysis of inclusions. The characterization technique can more fully reflect service from different parts of the material properties, helps to parse phenomena and problems in the process and materials, can be used in the design of material calculation, modification and optimization of high-throughput screening and verification, shorten the cycle analysis, lowering the cost analysis is a kind of a combination of macro analysis and micro analysis of the statistical power technology [24].

Zhao and coauthors developed a new measurement technique based on femtosecond laser surface reflection to accurately scan and test several key physical properties, such as thermal conductivity [25], thermal expansion coefficient [26], and specific heat capacity [27]. Other properties, such as elastic constants [28], specific heat fusion (CP) and curie temperature, can also be measured efficiently with the composition. In addition, nano-indentation can be used to measure the hardness and elastic modulus at the micro scale [29].

High-Throughput Analysis of Experimental Data

High-throughput analysis of experimental data required to make full use of the computer data processing and analysis function, based on the sample of the inhomogeneity and the factors of preparation, the difference of the retrieve samples within a large number of composition, microstructure, structure and properties, such as data and information, through the study of the statistical parsing of data information and mapping physical model is established for screening and verification, so as to obtain the valuable target research the basic sample unit body, finally got the ideal sample preparation process optimization parameters. This high-throughput analysis method is conducive to the systematic and rapid comparative analysis of mass data with the help of computer operation. It has the characteristics of advanced manufacturing, which aims at the properties of practical materials, covers the entire process of preparation process, and effectively accelerates the research and development and application of materials. The in-situ statistical analysis method of in-situ metal analyzer can be applied to the analysis of casting billet, which can quickly, accurately and intuitively analyze the composition, and at the same time, it can also analyze the types, contents, distribution characteristics of inclusions, density of sample surface, and defects, such as porosity and shrinkage. It is a typical high-throughput analysis technique that combines macroscopic analysis with microscopic analysis. Applying the in-situ metal analyzer to the analysis of high-flux samples of metal materials, the quality of samples can be analyzed comprehensively and accurately in a short time and in a large range. The analysis of composition distribution, quantitative determination of density, and statistics of inclusions are of great guiding significance for material preparation, production, and improvement of process conditions. In addition, Luo et al. combined the capillary X-ray lens focusing technique and the energy dispersive X-ray diffraction technique to conduct qualitative high-flux X-ray structure and component analysis.

Construction, Improvement and Application of Material Database

Material database system used to store and manage all kinds of data, including the basic properties, crystal structure data, the simulation calculation data, experiment, process data, etc., as the materials research, production and application of the data sharing and data application development platform, has become the world's countries technology development and strategic resources, is playing an increasingly important role. At the same time, the material database construction and management is the key link in high-throughput experiments; the database can be a huge number of high-throughput experimental data using intelligent storage and output, the effectiveness and accuracy of the calculation of material and a large number of experiments, the production and the scientific nature of the product data verification, to accelerate

the material to provide effective data to support the research and development and application of materials.

At present, some scientific research institutes, colleges and universities all over the world began to set up their own material database including mechanical properties, metal elastic performance data center, material corrosion database, the database of material friction and wear, high temperature materials database, HT-DB collection of all kinds of metal, nonmetal and composite materials mechanics and thermodynamics data, and so on. Materials database provides users with rich data resources and convenient query methods, designers can quickly query the required material characteristics and related information, thus, saving a lot of time to browse the manual. The establishment of material database is conducive to the reduction of repeated experiments and tests of materials, and plays a very positive role in shortening the research and development period of new materials and saving the research and development cost of new materials. From the current situation of the development of the majority of single function, database data quantity is less, the coverage is narrow, and sharing is poor, therefore, the creation of a large material database, and assisted in the rapid development of network technology make materials greatly improve the data sharing function, make the database has more important application value.

Summary and Prospects

- (1) With the wide spread and acceptance of material genome method, high-throughput experimental technology, as an advanced experimental technology, will enter a new stage of rapid development.
- (2) The progress of high-throughput experimental technology requires the innovation and development of related preparation and characterization equipment technology and related intellectual support. The development of a series of universal, accurate and rapid preparation and characterization instruments based on the particularity of metal materials and the cultivation of relevant scientific research reserve talents are crucial to the sustainable development of the promotion and application of high-throughput experimental technology.
- (3) The high-throughput multi-scale metal material theory is used to calculate and enrich and improve the data content of relevant experiments. In particular, the metal material thematic database is established, and the material database is applied to the aspects of metal material optimization design, defect diagnosis and quality control, performance and life prediction, etc.

References

1. Wang H, Xiang Y et al (2015) Materials genome enables research and development revolution. *Sci Technol Rev* 33(10):13–19
2. Zhao JC (2013) High-throughput experimental tools for the Materials Genome Initiative. *Chin Sci Bull (Chin Ver)* 58:3647–3655
3. Hanak J (1970) The, “multiple-sample concept” in materials research: synthesis, compositional analysis and testing of entire multicomponent systems. *J Mater Sci* 5(11):964–971
4. Xiang X, Wang H et al (2015) Applications of combinatorial material chip technology in research and development of new materials. *Sci Technol Rev* 33(10):64–78
5. Xiang XD, Sun X, Briceno G et al (1995) A combinatorial approach to materials discovery. *Science* 268(5218):1738–1740
6. Li JC, Wang BF, Ma YL et al (2009) Theoretical research on four-frequency electromagnetic field. *J Inner Mongolia Univ Sci Technol* 28(1):76–80
7. Wang HZ, Wang H, Ding H et al (2015) Progress in high-throughput materials synthesis and characterization. *Sci Technol Rev* 33(10):31–49
8. Liu LM (2015) Genetic engineering of materials: material design and simulation. *J New Ind* 12:71–88
9. Flemings MC (1990) Materials science and engineering for the 1990’s. *Adv Mater* 2(4):165–166
10. Fan XL (2015) Materials genome initiative and first-principles high-throughput computation. *Mater China* 34(09):689–695
11. Jain A, Ong SP, Hautier G et al (2013) Commentary: the materials project: a materials genome approach to accelerating materials innovation. *APL Mater* 1(011002):1–11
12. Wang XY, Yang XY, Chi XB (2015) A computational material database system. *Res Inf Technol Appl* 6(2):12–17
13. Curtarolo S, Setyawan W, Hart GLW et al (2012) AFLOW: an automatic framework for high-throughput materials discovery. *Comput Mater Sci* 58:218–226
14. Wang Y, Lv J, Zhu L et al (2010) Crystal structure prediction via particle-swarm optimization. *Phys Rev B* 82(09):094–116
15. Zhao JC (2014) Introduction to the materials genome project. *Chin J Nat* 36(2):89–104
16. Wang HZ (2007) Original position statistic distribution analysis (OPA)-novel statistic characterization method of different chemical compositions and its states of the materials. *Mater Sci Forum* 539:4446–4451
17. Chen YH, Yuan LJ, Wang HZ (2009) Investigation on original statistic distribution analysis of flat-bulb steel by laser ablation inductively coupled plasma mass spectrometry. *Metall Anal* 29(9):1–5
18. Wang HZ (2002) In situ statistical distribution analysis—a new technique for material research and quality criteria. *Sci China (B)* 32(6):481–485
19. Li D, Wang H (2014) Original position statistic distribution analysis for the sulfides in gear steels. *ISIJ Int* 54(1):160–164
20. Luo QH, Li DL, Ma FC et al (2013) Original position statistic distribution analysis for inclusion of cross section of stainless steel continuous casting slab. *Metall Anal* 33(12):1–7
21. Yang ZJ, Wang HZ (2003) Research on segregation and inclusion of continuous casting slab by original position analysis. *Iron Steel* 38(3):61–63
22. Yang ZJ, Wang HZ (2003) Original position analysis for low alloy steel billets with different microstructure. *Iron Steel* 38(9):67–71
23. Yang ZJ, Wang HZ (2003) In situ metal analysis system. *China Metall* 38(9):67–71
24. Cahill DG (2004) Analysis of heat flow in layered structures for time-domain thermoreflectance. *Rev Sci Instrum* 75:5119–5123
25. Huxtable S, Cahill DG, Fauconnier V et al (2004) Thermal conductivity imaging at micrometer-scale resolution for combinatorial studies of materials. *Nat Mater* 3:298–301

26. Wei C, Zheng X, Cahill DG et al (2013) Micron resolution spatially-resolved measurement of heat capacity using dual-frequency time-domain thermoreflectance. *Rev Sci Instrum* 84(7):071301
27. Oliver WC, Pharr GM (1992) An improved technique for determining hardness and elastic modulus using load and displacement sensing indentation experiments. *J Mater Res* 7(6):1564–1583
28. Doerner MF, Nix WD (1986) A method for interpreting the data from depth-sensing indentation instruments. *J Mater Res* 1(4):601–609
29. Zhao JC (2001) A combinatorial approach for efficient mapping of phase diagrams and properties. *J Mater Res* 16(6):1565–1578

Dilatometric Analysis of Tempering Kinetics in a Cr–Mo–V Medium-Carbon Steel



E. F. Barrera-Villatoro, O. Vázquez-Gómez, A. I. Gallegos-Pérez,
H. J. Vergara-Hernández, E. López-Martínez, and P. Garnica-González

Abstract Tempering kinetics of the martensite was determined using the Johnson–Mehl–Avrami model in a Cr–Mo–V alloyed medium-carbon steel by dilatometry. Tempering temperatures were determined by non-isothermal analysis at constant heating rate. From these temperatures, isothermal tempering was carried out. The reaction stages were associated with the transformation of retained austenite in bainitic ferrite and cementite, and the conversion of transition carbides into cementite. For the third stage, through dilatometric analysis and the normalization relation, the grade of reaction was calculated and compared with the estimated with JMA model. Finally, this stage was related with the kinetic tempering parameters reported in the literature.

Keywords Tempering · Kinetics · Dilatometry · Medium-carbon steel

Introduction

Martensitic steels are widely used in engineering because they possess greater hardness and abrasive wear resistance compared to steels with softer microstructures. However, with the increase in hardness, certain mechanical properties and behavior may not be, in a certain way, beneficial for its optimal performance. Therefore, some heat treatments can be effectively used to relieve internal stresses to improve

E. F. Barrera-Villatoro · O. Vázquez-Gómez (✉) · A. I. Gallegos-Pérez ·
H. J. Vergara-Hernández · P. Garnica-González

Tecnológico Nacional de México/I.T. Morelia, Av. Tecnológico 1500, Lomas de Santiaguito,
Morelia, Michoacán 58120, México

e-mail: ovazquezgo@gmail.com; ovazquezgo@conacyt.mx

O. Vázquez-Gómez

Consejo Nacional de Ciencia y Tecnología, Av. Insurgentes 1582, Crédito Constructor, Ciudad de México 03940, México

E. López-Martínez

Universidad del Istmo, Campus Tehuantepec, Ciudad Universitaria s/n, Barrio Santa Cruz, 4a. Secc. Sto. Domingo Tehuantepec, Oaxaca 70760, México

© The Minerals, Metals & Materials Society 2021

TMS 2021 150th Annual Meeting & Exhibition Supplemental Proceedings,

The Minerals, Metals & Materials Series,

https://doi.org/10.1007/978-3-030-65261-6_80

toughness [1]. Another heat treatment is tempering, which consists of subjecting a quenched steel to temperatures lower than that of martensite decomposition. However, there are a series of stages that are carried out as the temperature increases during the tempering treatment. These stages consist of phase transformation and precipitation/dissolution of carbides controlled by diffusive processes mainly by iron and carbon [2]. In this way, the tempering treatment can be delimited by four stages, which take place in different temperature ranges [3–5]. In principle, in plain steels, the first stage is carried out in a range from 373 to 473 K with the precipitation of transition carbides such as carbides $\eta(\text{Fe}_2\text{C})$ or $\varepsilon(\text{Fe}_{2.4}\text{C})$ contributing to carbon supersaturation reduction in martensite and partial loss of tetragonality [2]. Subsequently, in an interval of 473–573 K, the second tempering stage or retained austenite decomposition into bainitic ferrite and cementite occurs. The third tempering stage occurs between 473 and 623 K where transition carbides are replaced by cementite (Fe_3C) and martensite loses tetragonality. Above 773 K conversion and coarsening of lath-like to spheroidal cementite and alloy carbides precipitation occurs [2], these processes conform the fourth stage. The aim of this work is to analyze the isothermal kinetics of the third tempering stage in a Cr–Mo–V medium-carbon steel.

Experimental Procedure

Material

A Cr–Mo–V medium-carbon steel was used to carry out dilatometric tests with a Linseis L75–V equipment, and the composition is indicated in Table 1. Cylindrical specimens of 5 mm in diameter and 15 mm in length were machined, which were initially annealed at 1273 K, using a heating rate of 0.33 K s^{-1} and a dwell time of 20 min. Subsequently, these were cooled at a rate of 0.08 K s^{-1} at room temperature; Fig. 1a shows the as-annealed microstructure. After annealing, quenching was performed, using an austenitization temperature of 1273 K for 25 min in a Felisa F-340 muffle and brine with stirring as cooling medium; Fig. 1b shows the as-quenched microstructure.

Table 1 Experimental Cr–Mo–V medium-carbon steel composition, in % weight

C	Mn	Si	Cr	Mo	V	Ni
0.378	0.719	0.236	0.940	0.191	0.292	0.071

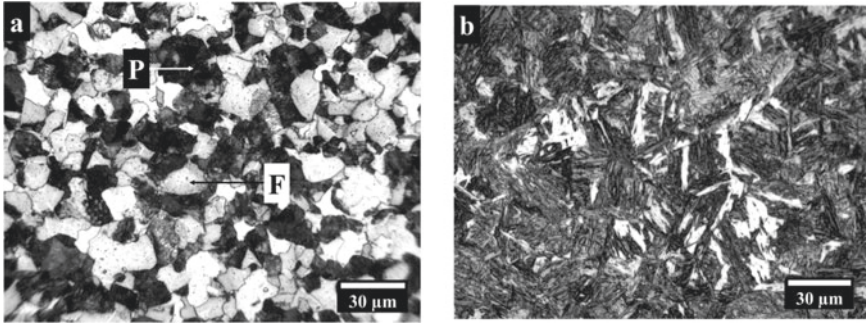


Fig. 1 Microstructure of Cr–Mo–V medium-carbon steel: **a** as-annealed and **b** as-quenched microstructures

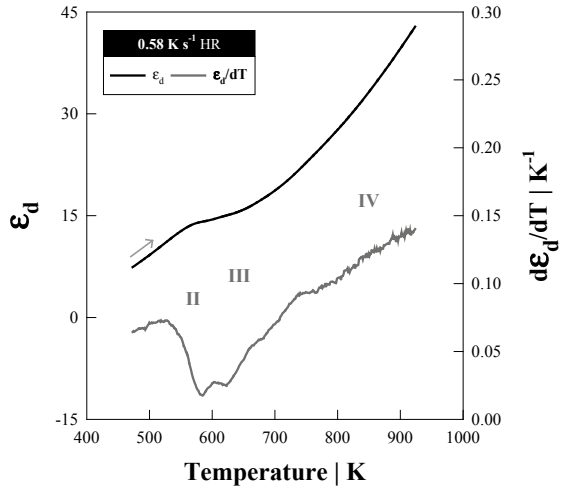
Dilatometric Analysis

From the quenched specimens, the tempering stages were identified by continuous heating cycles at a rate of 0.58 K s^{-1} to a temperature lower than martensite decomposition onset temperature. Subsequently, the zone corresponding to the third tempering stage, where transition carbides are replaced by cementite, was selected. Within this zone, a temperature was established considering the peaks (*minimum points*) of the first derivative of the dilation strain with respect to temperature. The isothermal tempering cycle was carried out for 50 min using the same heating rate employed in the determination of the stages. After tempering, the specimens were cooled to room temperature.

Results and Discussion

The behavior of the dilation strain and its first derivative with respect to temperature are indicated in Fig. 2. From the dilation strain, a slope change (*contraction*) after 500 K is appreciated, which is verified with the change of the first derivative where this phenomenon is magnified. These changes indicate the start of the second tempering stage associated with the decomposition of retained austenite. In the same way, the first derivative evidences the start and finish of a contiguous reaction, denoted as the third tempering stage; however, this effect is not as perceptible in the behavior of the dilation strain over the same temperature range. These stages are directly related since they are processes that overlap by the temperature range where they occur. The second stage, as mentioned, involves the decomposition of retained austenite into bainitic ferrite and cementite, while the third stage involves the conversion of transition carbides into cementite [6, 7]. Due to this, these processes are contiguous giving the impression that it will be a single process. Moreover, a last process associated with

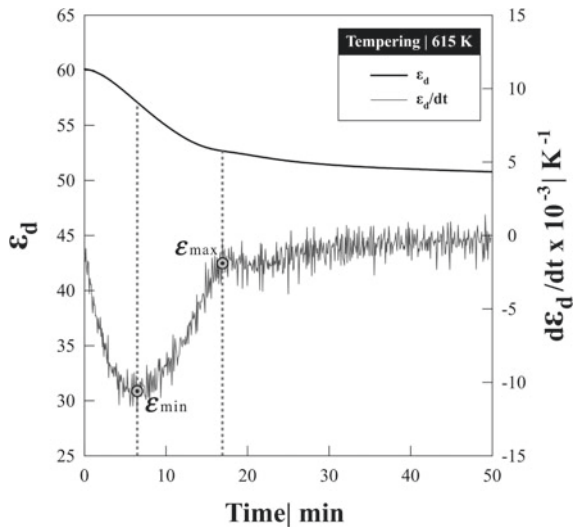
Fig. 2 Behavior of the dilation strain and its first derivative with respect to the temperature of Cr–Mo–V medium-carbon steel in as-quenched condition subjected to continuous heating at a rate of 0.58 K s^{-1}



the fourth tempering stage is observed, where in this case could be related to the alloy carbide precipitation.

Throughout Fig. 2, the tempering temperature within the third stage was selected in order to evaluate the isothermal reaction kinetics. Based on the minimum point criterion [8], a temperature of 615 K corresponding to the minimum point after the start of the third stage was established. Maintaining the heating rate of 0.58 K s^{-1} , isothermal tempering was carried out at the indicated temperature for 50 min. Figure 3 shows the behavior of the dilation strain and its first derivative (*dilation strain rate*, $\dot{\epsilon} = d\epsilon/dt$) with respect to time. From the figure, it can be seen that the tempering

Fig. 3 Behavior of dilation strain and its first derivative with respect to time of Cr–Mo–V medium-carbon steel at a tempering temperature of 615 K and a time of 50 min



is completed in the times indicated on the curve of dilation strain rate, considering the start time at the point of minimum rate $\dot{\epsilon}_{\min}$ and the end time at the point where the rate reaches a constant maximum value $\dot{\epsilon}_{\max}$.

Once the start and end tempering times were established, the grade of reaction was calculated considering the points of minimum and maximum dilation strain rate, through the following normalization relationship [9]:

$$\varphi = \frac{\dot{\epsilon} - \dot{\epsilon}_{\min}}{\dot{\epsilon}_{\max} - \dot{\epsilon}_{\min}} \tag{1}$$

The grade of tempering reaction φ was adjusted with the Johnson–Mehl–Avrami (JMA) model, which has been used previously to determine the grade of reaction during the tempering stages, considering nucleation and growth processes [7, 10]:

$$\varphi = 1 - \exp(-k^n \cdot t^n) \tag{2}$$

where k and n are kinetics parameters associated with reaction mechanisms and t is the isothermal tempering time.

In Fig. 4, the estimated tempering reaction grade is compared with the JMA model transposed to the data calculated from the dilation strain rate curve and Eq. (1). The fit done for the steel shows a agree correlation, since the determination coefficient R^2 is 0.99 (Table 2). In this case, the parameter n should approaches a value of 3–4, a range in which a process of nucleation and growth of pure particles is considered [11]. However, this value can also be influenced by the content of the alloying elements.

Fig. 4 Comparison between the grade of reaction calculated from the data on dilation strain rate and the JMA model for the third tempering stage at 615 K for 50 min

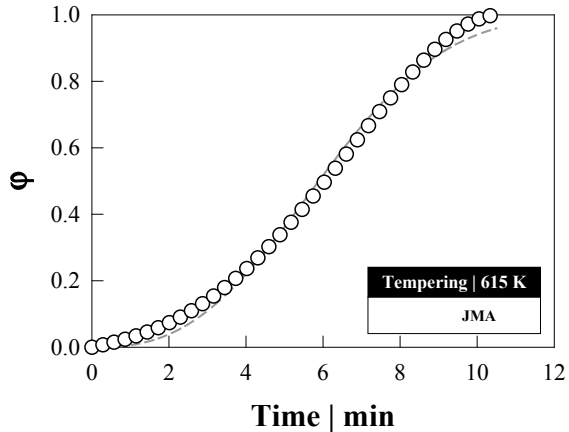


Table 2 Kinetic parameters of the JMA model

k	n	Adjusted R^2
0.15	2.65	0.99

Biro et al. [10] report values between 1.60 and 1.73 for dual-phase steels with Cr and Cr/Mo contents, which retard the growing kinetics of cementite, so it is to be expected that higher Cr, Mo and V contents could further increase the value of n as is the case of the steel studied. Finally, the parameter k maintains similarity with the values reported by Biro et al. [10] between 0.14 and 0.20 for dual-phase steels alloyed with Cr and Cr/Mo.

Conclusions

From the results obtained, the tempering reaction stages for a Cr–Mo–V medium-carbon steel were determined by non-isothermal analysis. Subsequently, the grade of reaction was calculated by isothermal tempering and the behavior of the dilation strain rate for the third stage. Finally, the tempering kinetics was estimated using the JMA model, obtaining values of 0.15 and 2.65 for the kinetic parameters k and n , respectively, which were compared with the literature suggesting that the content of alloying elements retards the reaction kinetics by increasing the value of n .

Acknowledgements E. F. Barrera-Villatoro (No. 465236) and A. I. Gallegos-Pérez (No. 494883) would like to thank National Council for Science and Technology of Mexico (CONACYT) for their postgraduate scholarship. The authors are also grateful to the support projects for Scientific and Technological Research-TecNM/ITM (7726.20-P) and Cutting-Edge Science-CONACYT (377862) for the financial support and the National Laboratory SEDEAM-CONACYT for the use of equipment acquired with support for projects No. 235780, 271878 and 282357.

References

1. Krauss G (2015) Steels: processing, structure, and performance, 2nd edn. ASM International
2. Porter DA, Easterling KE (2009) Phase transformations in metals and alloys (revised reprint). CRC Press, Boca Raton
3. Ju Y, Goodall A, Strangwood M, Davis C (2018) Characterisation of precipitation and carbide coarsening in low carbon low alloy Q&T steels during the early stages of tempering. *Mater Sci Eng A* 738:174–189
4. Primig S, Leitner H (2011) Separation of overlapping retained austenite decomposition and cementite precipitation reactions during tempering of martensitic steel by means of thermal analysis. *Thermochim Acta* 526(1):111–117
5. Liu Q, Qian D, Hua L (2018) Transformation from non-isothermal to isothermal tempering of steel based on isoconversional method. *J Mater Sci* 53(4):2774–2784
6. Cheng L, Brakman CM, Korevaar BM, Mittemeijer EJ (1988) The tempering of iron- carbon martensite; dilatometric and calorimetric analysis. *Metall Trans A* 19(10):2415–2426
7. LeivaJAV, Morales EV, Villar-Cociña E, Donis CA, Bott IDS (2010) Kinetic parameters during the tempering of low-alloy steel through the non-isothermal dilatometry. *J Mater Sci* 45(2):418–428
8. Liu F, Sommer F, Mittemeijer EJ (2004) An analytical model for isothermal and isochronal transformation kinetics. *J Mater Sci* 39(5):1621–1634

9. Mittemeijer EJ (1992) Analysis of the kinetics of phase transformations. *J Mater Sci* 27(15):3977–3987
10. Biro E, McDermid JR, Embury JD, Zhou Y (2010) Softening kinetics in the subcritical heat-affected zone of dual-phase steel welds. *Metall Mater Trans A* 41(9):2348–2356
11. Christian JW (2002) Formal theory of transformation kinetics, Chap 12. In: Christian JW (ed) *The theory of transformations in metals and alloys*. Pergamon, Oxford, pp 529–552

Thermal and Mechanical Characterization of Non-isothermal Tempering of an Experimental Medium-Carbon Steel



P. G. Díaz-Villaseñor, O. Vázquez-Gómez, H. J. Vergara-Hernández, A. I. Gallegos-Pérez, E. López-Martínez, and B. Campillo

Abstract A medium-carbon steel alloyed with vanadium was analyzed by differential dilatometry, microhardness and nanoindentation to characterize the fourth tempering stage or secondary hardening zone. From isochronal heating paths at different tempering temperatures, the secondary hardening zone preceding the martensite decomposition initiation temperature was delimited. A progressive increase in microhardness was observed proportional to continuous tempering temperature increase with respect to start temperature of fourth tempering stage at the lowest heating rate. This increase was related to secondary hardening zone by alloy carbides precipitation. Likewise, isothermal tempering was carried out at the start of the fourth tempering stage to verify secondary hardening. After the thermal cycles, nanoindentation tests were performed to determine the nanohardness and prove the precipitates presence by scanning probe microscopy. A decrease in the nanohardness of the steel was observed, as well as different size and distribution precipitates depending on the heating rate.

Keywords Tempering · Secondary hardening · Dilatometry · Nanoindentation

P. G. Díaz-Villaseñor · O. Vázquez-Gómez (✉) · H. J. Vergara-Hernández · A. I. Gallegos-Pérez
Tecnológico Nacional de México/I.T. Morelia, Av. Tecnológico 1500, Lomas de Santiaguito,
58120 Morelia, Michoacán, México
e-mail: ovazquezgo@gmail.com; ovazquezgo@conacyt.mx

O. Vázquez-Gómez
Consejo Nacional de Ciencia y Tecnología, Av. Insurgentes 1582, Crédito Constructor, 03940
Ciudad de México, México

E. López-Martínez
Universidad del Istmo, Campus Tehuantepec, Ciudad Universitaria s/n, Barrio Santa Cruz, 4a.
Secc. Sto. Domingo Tehuantepec, 70760 Oaxaca, México

B. Campillo
Facultad de Química, Universidad Nacional Autónoma de México, Av. Universidad 3000, Cd.
Universitaria, Ciudad de México 04510, México

Instituto de Ciencias Físicas, Universidad Nacional Autónoma de México, Av. Universidad 1001,
Col. Chimalpa, Cuernavaca, Morelos 62209, México

Introduction

Nowadays, there is a wide development of ultra-high strength steels (UHSS) of medium-carbon low-alloy (MC-LA) in structural components manufacture for the aeronautical industry such as gears and bearings. MC-LA steels emphasize its structural character and its optimal of strength-hardenability combination due quenching and tempering treatments [1], due to the controlled addition of alloying elements such as Mn, Ni, Cr, Si, Mo and V. These treatments are used to obtain the final desired mechanical properties. Among the main tempering characteristics are to reduce brittleness, increase ductility, toughness and relieve internal stresses, as well as reduce hardness and increase tensile strength [2]. Tempering is carried out at a temperature lower than that of austenite formation temperature, so it is feasible to obtain an endless number of microstructures and mechanical properties dependent on thermal parameters [2]. Microstructural changes during tempering have been studied by different authors, establishing different reactions according to the transformation mechanisms [3–9]. The first reaction that takes place during tempering is known as zero stage, where the carbon atoms are redistributed and segregated to form clusters [3, 5, 7]. Later, the first, second and third tempering stages are presented, which are characterized by the precipitation of transition carbides, the decomposition of austenite retained in ferrite and cementite, and the conversion of transition carbides to stable carbides, respectively [7–12]. The cementite growth contributes to steel softening during third stage [4]. However, it has been reported that steels containing carbide-forming alloying elements present a fourth tempering stage that is characterized by an increase in hardness, known as secondary hardening. [3, 9, 13]. Gündüz and Cochrane [14] reported that this increase is due to the fact that the alloying elements produce fine precipitates that are located very close to each other. On the other hand, alloying elements have been shown to retard the cementite coarsening kinetics [4]. The present work aims are to determine the hardening zone of the fourth tempering stage, as well as to demonstrate the secondary hardening existence through carbides presence in an experimental medium-carbon steel alloyed with vanadium through differential dilatometry, microhardness and nanoindentation.

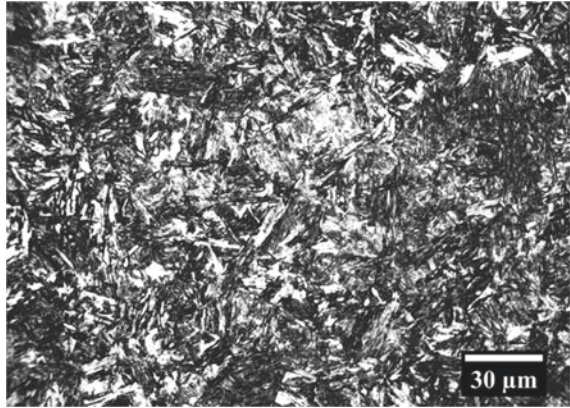
Experimental Procedure

Material

From an experimental medium-carbon martensitic steel alloyed, dilatometry tests were carried out to determine the secondary hardening zone during tempering, the composition is presented in Table 1. Figure 1 shows the initial microstructure with a 606.80 ± 49.04 HV 0.3/15 microhardness. The standard deviation magnitude is attributed to a typical steels quenched variation, where there are acicular ferrite and retained austenite regions composed. For dilatometry tests, solid cylindrical

Table 1 Experimental medium-carbon steel alloyed composition, in % weight

C	Mn	Si	Mo	Cr	V	Ni
0.378	0.719	0.236	0.191	0.940	0.292	0.071

Fig. 1 Initial microstructure of experimental steel alloyed in quenched condition

specimens of 5 mm in diameter and 15 mm in length were machined. Each specimen contact surfaces were prepared by SiC sandpaper grinding, from extra to micro-fine (6–23 μm) and polished with 0.5 μm particle size alumina.

Differential Dilatometry

Dilatometry tests were implemented on a L75–V Linseis vertical dilatometer. In order to determine the tempering and austenite formation temperatures as a heating rate function, a pre-heating was carried out at 308.15 K for 15 min in each specimen, subsequently, there were heated at different rates: 0.58, 0.75 and 0.91 K s^{-1} until reach 1273.15 K without dwell time. Finally, they were cooled at 0.41 K s^{-1} rate until reaching room temperature. Above these temperatures, continuous tempering treatments were performed, whereby the specimens were heated at different rates: 0.58, 0.75 and 0.91 K s^{-1} until reaching the continuous tempering temperature T_{CT} and there were cooled at 0.41 K s^{-1} rate until reaching room temperature. The dilatometry tests were done in duplicate with a constant flow industrial argon atmosphere.

Micro and Nanohardness

Subsequently, microhardness and nanohardness tests were performed. Microhardness measurements were scanned with a Vickers MVK-HVL Mitutoyo microdurometer with a 2.94 N (300 gf) and an application time of 15 s, the diamond indenter footprints were observed with a 40× objective len. Measurements were made on the entire surface of each specimen with a distance between footprints of approximately 0.5 mm. Besides, nanohardness measurements were made with a TI 750 Hysitron nanoindenter with a Berkovich type tip calibrated with a standard sample of fused silica. A maximum force of 9000 μN was established using a triangular type force function and an application time of 50 s. Once the test conditions were established, the measurements were made on the inner surface of the specimen with a distance between footprints of 0.2 mm.

Results and Discussion

Continuous Heating Dilatometry

On the basis of martensitic microstructure, the first derivative of the change in strain dilation with respect to temperature was calculated $d\varepsilon_d/dT$, Fig. 2a–c. In figures, it is pointed T_{S-IV}^s as the start temperature of the fourth tempering stage; according to literature, it is established that fourth stage is presented above 773.15 K for steels with alloying elements [3, 14, 15]. From the figures, a slight contraction is observed around this temperature, which displaces to higher values as a function of the heating rate. On the other hand, the start and end austenite formation temperatures are also indicated, A_s and A_f , respectively, which also increase as a heating rate function, while the interval between T_{S-IV}^s and A_s tends to decrease. Table 2 shows associated temperatures with the hardening zone as a heating rate function.

Continuous Tempering

Using the temperatures as indicated in Table 2 and Eq. (1), the temperatures T_{CT} were determined as a heating rate function, assuming that the zone delimited by T_{S-IV}^s and A_s is associated with precipitation and dissolution region of alloy carbides. Continuous tempering temperatures are indicated in Table 3.

$$T_{CT} = \frac{A_s - T_{S-IV}^s}{2} + T_{S-IV}^s \quad (1)$$

Fig. 2 Dilation change behavior with respect to temperature $d\varepsilon_d/dT$ as a temperature T function at different heating rates: **a** 0.58, **b** 0.75, and **c** 0.91 K s^{-1}

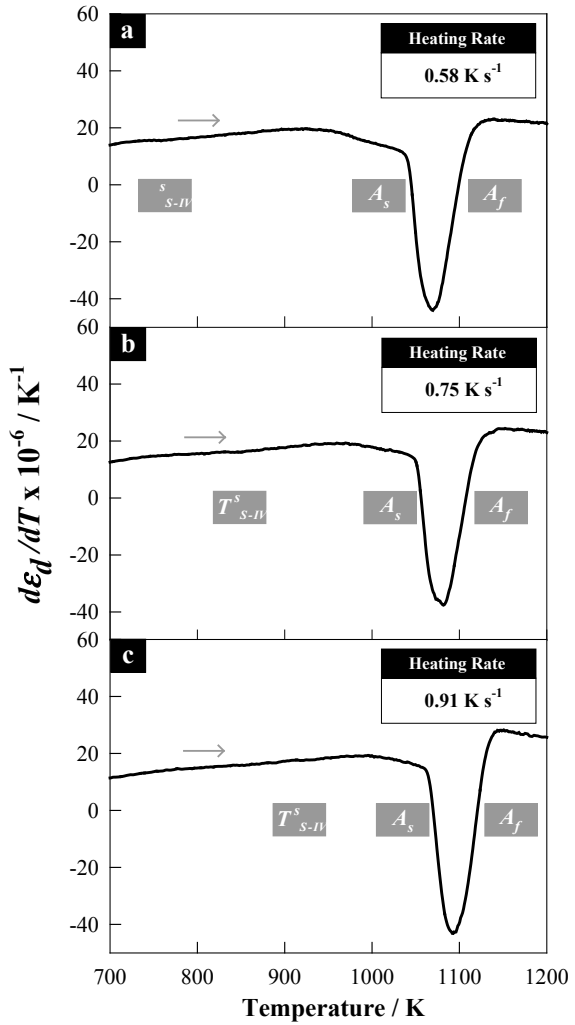


Table 2 Start tempering temperature T_{S-IV}^s ; start and end austenite formation temperatures A_s and A_f , respectively

HR (K s^{-1})	T_{S-IV}^s (K)	A_s (K)	A_f (K)
0.58	760.9 ± 3.18	1035.4 ± 0.21	1129.2 ± 3.54
0.75	846.4 ± 1.70	1044.6 ± 0.28	1135.9 ± 4.31
0.91	918.6 ± 2.55	1057.0 ± 1.34	1144.7 ± 1.13

Table 3 Continuous tempering temperatures and microhardness as a heating rate function

HR (K s ⁻¹)	T _{CT} (K)	HV 0.3/15
0.58	913	403.00 ± 11.15
0.75	963	372.15 ± 8.99
0.91	1008	313.05 ± 6.70

Table 4 Isothermal tempering parameters and microhardness at 15 and 120 min at heating rate of 0.58 K s⁻¹

HR (K s ⁻¹)	T _{S-IV} ^s (K)	HV 0.3/15 (15 min)	HV 0.3/15 (120 min)
0.58	757.15	348.47 ± 8.93	355.67 ± 10.03

According to Table 3, it is observed that T_{CT} temperature increases proportionally to heating rate augment due to transition temperatures displacement as indicated in Fig. 2. After the continuous tempering, microhardness measurements were done, Table 3, which tend to decrease as increases rate from ~400 to ~310 HV 0.3/15. However, it is possible that vanadium affects the microhardness given conditions tempering, due to carbides precipitation and/or dissolution and its carbon affinity.

The vanadium effect has been reported in the literature [2, 3] for which isothermal tempering was carried out in duplicate for 15 and 120 min at the temperature T_{S-IV}^s (757.15 K) at heating rate of 0.58 K s⁻¹. In Table 4, microhardness values are indicated after isothermal tempering, where it can be seen that the microhardness remains practically constant around 350 HV 0.3/15 regardless of dwell time. Compared to continuous tempering at the same heating rate and 913 K (T_{CT} at heating rate of 0.58 K s⁻¹), microhardness is less by at least 50 units. This is opposed to the ordinary effect of temperature on the microhardness during tempering; i.e., the higher the tempering temperature, the lower the steel microhardness. However, microhardness after continuous tempering increases with respect to isothermal tempering, so it can be inferred that the observed hardening is due to a existence of carbide precipitation region (secondary hardening) from temperature T_{S-IV}^s .

Microstructures after continuous tempering at different heating rates are shown in Fig. 3a–c, where a martensitic microstructure with a finer and more homogeneous morphology with regard to microstructure quenched is appreciated (cf. Fig. 1), since in each of the cases a standard deviation less than ±6–11 units compared to quenched condition.

Nanoindentation

To provide the carbides presence in the continuous tempering treatments, nanohardness measurements were performed using scanning probe microscopy and nanoindentation. Considering that there is a hardening caused by carbides precipitation

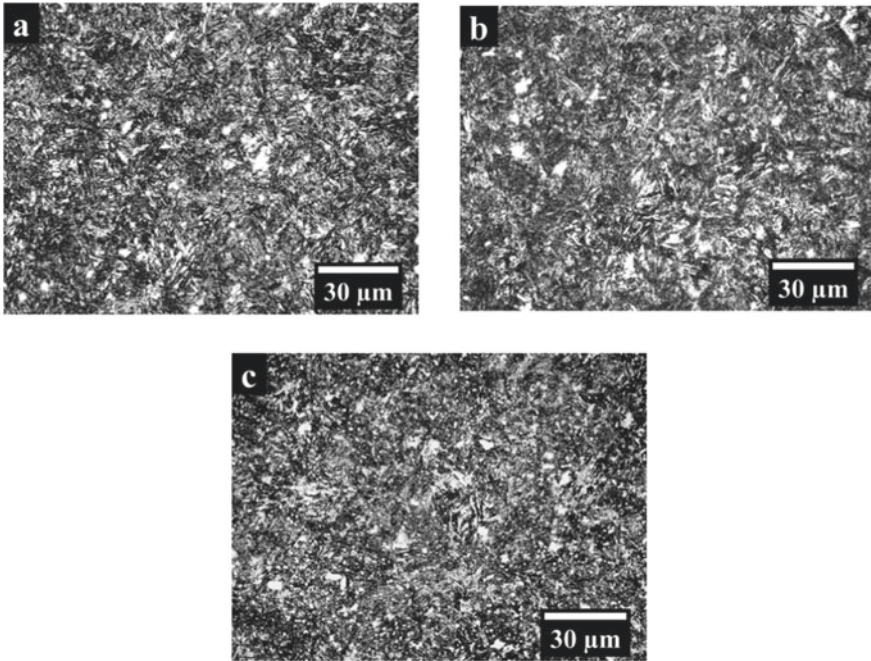


Fig. 3 Experimental steel microstructure after continuous tempering at different heating rates: **a** 0.58, **b** 0.75 and **c** 0.91 K s⁻¹

from alloying elements during heating and at temperature tempering, the results obtained by nanoindentation tests are presented at established treatment conditions, Fig. 4a–c. The figures show different sizes (<1 μm) carbides presence (pyramidal reliefs) around footprints as a heating rate function and continuous tempering temperature. The carbides amount tends to decrease without any definite tendency regarding carbide size, since for intermediate heating rate (0.75 K s⁻¹) carbides are remarkably small compared to other two rates. However, there is a trend in the nanohardness H and maximum depth (h_{\max}) as shown in Table 5.

Data as shown in Table 5 agree with the tendency of the obtained microhardness measurements (Table 3), nanohardness is decreased. Moreover, in Fig. 5, force–displacement curves corresponding to quenching condition and continuous tempering footprints as shown in Fig. 4 for each heating rate. It is appreciated that quenching condition presents a greater opposition to indenter penetration, since it presents a less displacement (~156 nm) with respect to other curves, where a softening is observed according to the maximum depth, as shown in Table 5. This effect is attributed to carbides presence formed during tempering, since as heating rate increases, the amount and shape of the carbides change.

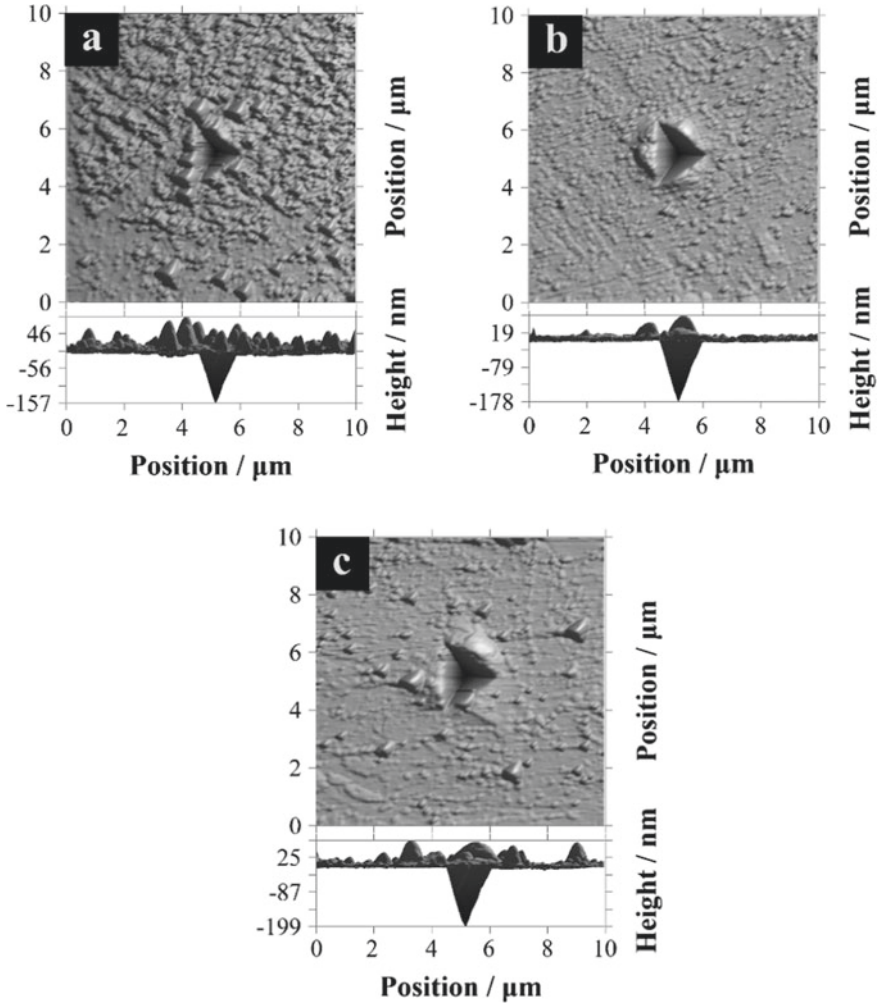
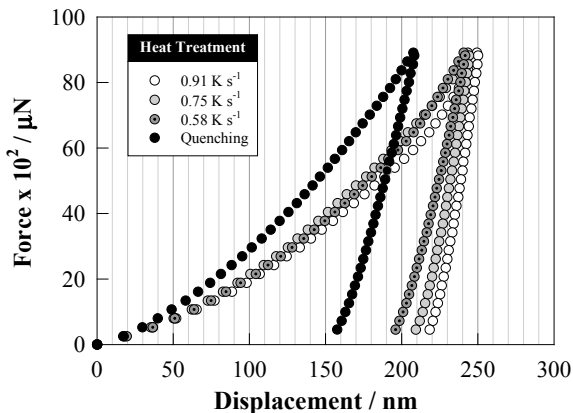


Fig. 4 Indentation footprints on the specimens during continuous tempering at different heating rates: **a** 0.58, **b** 0.75 and **c** 0.91 K s⁻¹

Table 5 Maximum depth and nanohardness for the continuously tempered specimens

HR (K s ⁻¹)	<i>h</i> _{max} (nm)	<i>H</i> (GPa)
Quenching	114.80 ± 23.13	8.32 ± 0.41
0.58	166.72 ± 13.13	5.73 ± 0.04
0.75	177.41 ± 0.44	5.69 ± 0.21
0.91	197.31 ± 2.17	4.80 ± 0.08

Fig. 5 Force–displacement curves after continuous tempering at different heating rates: 0.58, 0.75 and 0.91 K s^{-1} with a $9000 \mu\text{N}$ constant force



Conclusions

From results, it is concluded that by means of continuous heating cycles and dilatometric analysis, secondary hardening zone associated with fourth tempering stage was determined. Also, the effect of the heating rate on the start temperatures of hardening zone and those concern to austenite formation was showed.

Through isothermal tempering, it was observed that the microhardness remains constant at the beginning of the hardening zone, which demonstrates the secondary hardening during continuous tempering at T_{CT} temperature verified by microhardness measurements.

Finally, it was shown that by increasing the heating rate during continuous tempering, both the microhardness and the nanohardness of the steel decrease.

Acknowledgements P. G. Díaz-Villaseñor would like to thank National Council for Science and Technology of Mexico (CONACYT) for their postgraduate scholarship. The authors are also grateful to the support projects for Scientific and Technological Research-TecNM/ITM (7726.20-P) and Cutting-Edge Science-CONACYT (377862) for the financial support and the National Laboratory SEDEAM-CONACYT for the use of equipment acquired with support for projects No. 235780, 271878 and 282357.

References

1. Sankaran KK, Mishra RS (2017) Ultrahigh strength steels, Chap 6. In: Sankaran KK, Mishra HM (eds). Elsevier, pp 289–343
2. Krauss G (2015) Steels processing, structure, and performance
3. Porter DA, Easterling KE, Sherif MY (2009) Phase transformations in metals and alloys, 3rd edn
4. Biro E, McDermid JR, Embury JD et al (2010) Softening kinetics in the subcritical heat-affected zone of dual-phase steel welds. *Metall Mater Trans A* 41(9):2348–2356

5. Cheng L, Brakman CM, Korevaar BM et al (1988) The tempering of iron-carbon martensite; dilatometric and calorimetric analysis. *J Polit Sci Educ* 19A:2415–2426
6. Yan Z, Liu K, Eckert J (2020) Effect of tempering and deep cryogenic treatment on microstructure and mechanical properties of Cr–Mo–V–Ni steel. *Mater Sci Eng A* 787:139520
7. Liu Q, Qian D, Hua L (2018) Transformation from non-isothermal to isothermal tempering of steel based on isoconversional method. *J Mater Sci* 53(4):2774–2784
8. Primig S, Leitner H (2011) Separation of overlapping retained austenite decomposition and cementite precipitation reactions during tempering of martensitic steel by means of thermal analysis. *Thermochim Acta* 526(1–2):111–117
9. Ju Y, Goodall A, Strangwood M et al (2018) Characterisation of precipitation and carbide coarsening in low carbon low alloy Q&T steels during the early stages of tempering. *Mater Sci Eng A* 738:174–189
10. Hoyos J, Ghilarducci A, Salva H et al (2012) Evolution of martensitic microstructure of carbon steel tempered at low temperatures. *Procedia Mater Sci* 1:185–190
11. Díaz-Villaseñor PG, Vázquez-Gómez O, Barrera-Villatoro EF et al (2020) Dilatometric analysis of the martensite decomposition by stages during continuous heating. In: TMS 2020 149th Annual Meeting & Exhibition supplemental proceedings, pp 1861–1870
12. Kaiser D, de Graaff B, Jung AM et al (2017) A dilatometric study on the influence of compressive stresses on the tempering of martensitic AISI 4140 steel—evidence of transformation induced plasticity during cementite precipitation. *Mater Sci Eng A* 705:114–121
13. Djebaili H, Zedira H, Djelloul A et al (2009) Characterization of precipitates in a 7.9Cr-1.65Mo-1.25Si-1.2V steel during tempering. *Mater Charact* 60(9):946–952
14. Gündüz S, Cochrane RC (2005) Influence of cooling rate and tempering on precipitation and hardness of vanadium microalloyed steel. *Mater Des* 26(6):486–492
15. Vieweg A, Povoden-Karadeniz E, Ressel G et al (2017) Phase evolution and carbon redistribution during continuous tempering of martensite studied with high resolution techniques. *Mater Des* 136:214–222

Part XXXVI
**Phonons, Electrons and Dislons: Exploring
the Relationships Between Plastic
Deformation and Heat**

Unified Analysis of Temperature Fields Arising from Large Strain Deformation and Friction in Manufacturing Processes



Harish Singh Dhama, Priti Ranjan Panda, Debapriya Pinaki Mohanty, Anirudh Udupa, James B. Mann, Koushik Viswanathan, and Srinivasan Chandrasekar

Abstract We consider the contact between a sliding wedge/tool and a metal surface prototypical of material removal and deformation processing operations such as forming, cutting, and wear. We show how heat generated at the contact is partitioned into each of the bodies involved: tool, workpiece, removed chip, and surrounding fluid (if any). By performing thermal analysis and heat partition via temperature matching on global and local scales, we show how temperature fields in all four bodies can be easily calculated. The analysis framework involves a heat source moving over a body (Jaeger) and energy partition at the contact into tool, workpiece, fluid, and chip/wear particle (Blok). We present temperature solutions for two cases—incremental forming and grinding—while providing a simple method for solving the thermal problem in other deformation processing applications.

Keywords Heat partition · Grinding · Thermal analysis · Deformation processing · Metal forming

Introduction

Thermal phenomena play an important role in manufacturing processes and tribology [1–3]. These phenomena range from phase transformations to microstructure changes to alterations in mechanical and frictional behavior of solids. The key parameters that control these phenomena often involve the temperatures that the material being processed and the die/tool experience. This includes their instantaneous temperature distributions, temperature history, and temperature gradients. Knowledge of the

H. S. Dhama · P. R. Panda · K. Viswanathan
Department of Mechanical Engineering, Indian Institute of Science, Bangalore, India

D. P. Mohanty · A. Udupa · S. Chandrasekar (✉)
Center for Materials Processing and Tribology, Purdue University, West Lafayette, IN, USA
e-mail: chandy@purdue.edu

J. B. Mann
M4 Sciences Corporation, Lafayette, IN, USA

temperature field and underlying heat sources thus becomes critical for predicting component material properties and microstructure, as well as die/tool wear. In a large class of materials processing operations such as bulk and sheet metal forming, machining, abrasive processes, and friction stir processing, where material shape changes or new surfaces are produced due to action of a die/tool (henceforth tool) interacting with a workpiece, the heat generation is due to two primary sources: firstly, friction between the tool and workpiece at a sliding-type contact, including surface plasticity; and secondly from work done in large strain plastic deformation of the workpiece material. In this paper, we describe a general framework for analysis of the former, i.e., contact temperature fields arising from (large-strain) surface plastic deformation and friction, which is typically the more difficult analysis problem. Accounting for heat arising from large strain plastic flow constitutes a logically simple extension.

Analysis of the contact temperature problem in processing usually involves two sub-problems: (1) the temperature field produced by a moving heat source and (2) the heat partitioning problem—how to apportion the heat generated at the interfaces and surfaces between the various bodies in sliding contact. The bodies in contact typically include the tool, workpiece, chip/wear particle, and fluid (lubricant/coolant). Of the aforementioned sub-problems, the heat partitioning problem is by far the most difficult one. And it is with analysis of this partitioning, specifically, that this paper is concerned with. We present a framework and associated methodology for accurately estimating the fractions of heat being conducted into the various contacting bodies involved. Once this estimation (partitioning) is done, the various temperature fields in tool, workpiece, etc., can be obtained by straightforward application of the theory of moving heat sources [4, 5]. It may be of interest to note here that the heat partitioning sub-problem does not arise in processing operations wherein a tool is not used, such as welding and laser cutting (die-less operations); in these instances, all of the heat being used or generated is conducted solely into the workpiece, and the temperature field solution is in principle much simpler, requiring only application of moving heat source theory.

Our conceptual framework and treatment of the contact temperature problem is an analytical one—that is examine the possibility of obtaining analytical expressions for the temperature fields. Such an approach is attractive for two reasons. Firstly, analytical expressions directly reveal parameter dependencies unlike FE simulations. One can then better understand the relative importance of different parameters in influencing the temperature fields. Secondly, analytical models allow us to perform quick first-order computations without having to take recourse to a commercial simulation package. Overall, the temperature analysis can be quite useful for predicting component properties and performance, as well as for process design and optimization.

We illustrate the temperature analysis, especially the heat partitioning problem treatment using typical examples from forming and machining processes. Logically, the various partitioning cases may first be classified based on the number of bodies interacting thermally, and the heat sources estimated using a unit interaction model for the tool–workpiece contact. Standard results on heat partition between contacting bodies (due to Blok [6]) are then invoked to partition the generated heat and obtain estimates for the final temperatures in the tool and workpiece. The manuscript is

organized as follows. The basic ideas behind the thermal analysis are outlined using a unit interaction model in Section “[Unit Interaction Model](#)”. This is then applied to a variety of processing configurations in Section “[Applications](#)” to obtain temperature field estimates. Some concluding remarks are presented in Section “[Conclusions and Outlook](#)”.

The Heat Partition Problem

We begin by discussing a simple partition problem involving two semi-infinite rods brought into contact along their length. Assume the two rods are one-dimensional and that they interact in such a manner that frictional heat q_n is generated at the contact interface. This heat must be conducted away from the contact area either by conduction into rod 1 or rod 2. If ε_1 denotes the fraction of q_n that goes into rod 1 and ε_2 denotes the fraction of q_n going into rod 2, then from conservation of energy:

$$\varepsilon_1 + \varepsilon_2 = 1 \tag{1}$$

By solving the 1D heat conduction equation in each rod separately, we can express the temperatures $T_1(x)$, $T_2(x)$ in rods 1, 2 as a function of distance x from the contact interface. Note that $T_1(x)$, $T_2(x)$ will also be a function of $\varepsilon_1 q_n$ and $\varepsilon_2 q_n$, respectively. In order to determine the partition fractions, we simply equate the temperatures of rods 1 and 2 at the contact interface $x = 0$. This gives one equation relating ε_1 , ε_2 which, along with Eq. (1), can be solved for both partitions. For two stationary or quasi-static rods, the ratio $\varepsilon_1/\varepsilon_2$ is thus determined to equal K_1/K_2 , the ratio of the thermal conductivities of the two. The same scheme of matching the contact temperatures to estimate the partition coefficients applies irrespective of whether the two bodies are 1D, 2D, or 3D [6].

When the two contacting bodies are moving with respect to each other, heat is conducted into each one but this conducted heat is also constantly “convected” away inside the body. The larger the relative velocity, the greater this heat removal. Consequently, one should expect ε_1 , ε_2 to change from the static case. In fact, this is also easily evaluated—one then solves the heat conduction equation again in each body, but now in a moving frame. By evaluating $T_1(x = 0) = T_2(x = 0)$ as before, and using Eq. (1), one finds that the fractions are now determined not by the conductivities alone, but instead by the thermal diffusivities of the two rods [6].

Unit Interaction Model

We now cast this idea in the context of multi-body thermal contact as occurs in deformation processing. Irrespective of the particular geometry or deformation configuration involved, one can idealize the tool–workpiece contact zone as being represented

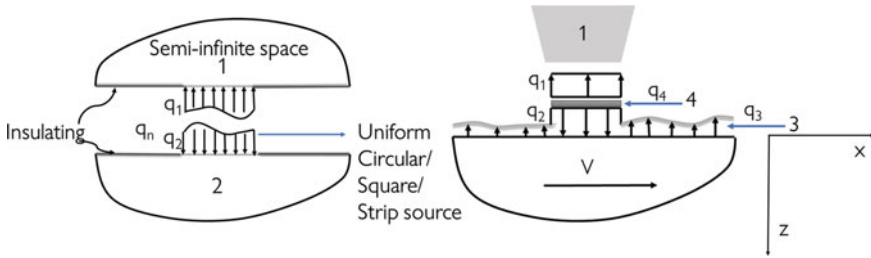


Fig. 1 Unit interaction model showing global scale (left) and local scale (right) heat partition. Here, 1 represents the tool/die/wedge and 2 is the workpiece. (Color figure online)

by the unit interaction shown in Fig. 1. Here, the tool (marked 1) is kept stationary while the workpiece (marked 2) is moving with constant relative speed V . In a more general situation, one can envisage two additional bodies—a chip or wear fragment (marked 3) and a surrounding lubricant or cooling fluid (marked 4). In Fig. 1, two schematics are shown—the left one is a “global” version where the tool and workpiece alone interact and the right one is the local variant, where details of the fluid and chip are also incorporated. In the latter, the actual contacting area between the tool and the workpiece is small, the ratio to the real to nominal tool–workpiece contact areas being ξ .

Let the total heat generated at the contact interface is q_n , and denoted by q_1, q_2, q_3, q_4 the heat going into the tool, workpiece, fluid, and removed material, respectively. If the nominal and real contact areas between the tool and workpiece differ significantly (the ratio $\xi \ll 1$), one must clearly distinguish between the local and global scale conduction problem. At the local scale, tool–workpiece interaction occurs only via asperities on the tool. Consequently, each of these local contacts generates a fraction $q_l = \xi q_n$ of the total global heat q_n .

Depending on the exact context involved, one must first obtain an expression for q_n . The objective of the analysis then is to determine the values q_1 to q_4 and use this to obtain approximate values for the temperature distribution in the four bodies. We define the partition coefficients $\varepsilon_1, \varepsilon_2, \varepsilon_3, \varepsilon_4$ as heat fractions corresponding to each body, for instance $\varepsilon_1 = q_1/q_n, \varepsilon_2 = q_2/q_n, \varepsilon_3 = q_3/q_n, \varepsilon_4 = q_4/q_n$. From conservation of energy, partition coefficients must obey the relation

$$\varepsilon_1 + \varepsilon_2 + \varepsilon_3 + \varepsilon_4 = 1 \tag{2}$$

The coefficients can be used with a temperature model to estimate the final temperature in body i as a function of ε_i and distance x along the contact interface (assumed for simplicity as being 1D). For this, standard moving 1D/2D/3D heat source solutions may be employed [4, 5], depending on the exact configuration of interest. Consequently, we have temperature fields T_1, \dots, T_4 that are a function of (x, z) in the body (see Fig. 1) and also depend on $\varepsilon_1, \dots, \varepsilon_4$.

The amount of heat generated locally is $q_l = \xi q_n$ as discussed earlier. Since the workpiece is in thermal equilibrium with the surrounding fluid (if present),

the local temperature in the workpiece can be taken to be the mean of the global workpiece and fluid temperatures. Furthermore, heat conducted into the chip is just $q_4^L = \xi q_4$ and the local heat going into the tool q_1^L can be obtained from local heat balance. Consequently, we have the following equations for the unknowns $\varepsilon_1, \varepsilon_2, \varepsilon_3, \varepsilon_4, q_1^L, q_2^L$

$$q_2^L = \xi(q_2 + q_3) = \xi(\varepsilon_2 + \varepsilon_3)q_n$$

$$\xi q_n = q_1^L + q_2^L + \xi \varepsilon_4 q_n$$

Recall that q_n is assumed to be known a priori. Including Eq. (1), we have 3 equations for the six unknowns so that three more relations are necessary to fully determine the coefficients ε_i individually. This determination depends critically on how many bodies are interacting and is discussed next.

Tool and Workpiece (2-Body Problem)

When the wear fragment and fluid do not exist, such as in dry rolling, the local fields are redundant and one can simply match the temperatures all along the contact interface as we discussed in the introductory example [6]. Therefore, $T_1(x) = T_2(x)$, and this can be used with Eq. (1) to determine $\varepsilon_1, \varepsilon_2$. The problem is fully solved and the complete temperature fields $T_1(x, z), T_2(x, z)$ can be determined everywhere inside the two bodies.

Tool, Workpiece and Chip (3-Body Problem)

When three bodies are present, as in say dry machining, temperature matching must be performed more carefully. Since the fluid is not present, we set $\varepsilon_3 = 0$ so that we now only have five unknowns and three equations. The system is completed by matching local temperatures in the chip and workpiece, and at the tool–chip interface:

$$T_2(x) + T_2^L(x) = T_4(x)$$

$$T_4(x) = T_1^L(x)$$

where T_1^L, T_2^L are obtained using the local heat flux expressions $q_1^L(x), q_2^L(x)$, respectively. Now the system is complete and the temperatures in the tool, workpiece, and chip are determined.

Tool, Workpiece and Fluid (3-Body Problem)

In situations where material is not being removed, as for instance, in lubricated rolling, we can set $\varepsilon_4 = 0$ but now we have to account for the fluid explicitly. As before, we have five unknowns with three equations so that two additional conditions are necessary. For this, the local temperature in the tool and workpiece is first matched. Depending on whether the fluid boils or not, we then match the global temperatures in the workpiece and fluid since they must be in thermal equilibrium. Consequently, we have the following relations:

$$\begin{aligned} T_2(x) + T_2^L(x) &= T_1^L(x) \\ T_3(x) &= T_2(x) \quad \text{no boiling} \\ T_3(x) &= 0 \quad \text{if boiling occurs} \end{aligned}$$

This scheme must be implemented iteratively—it is initially assumed that the fluid does not boil and the above relations are used to determine the temperature. If the resulting $T_3(x) > T_b$ the boiling point at some location along the interface, these values are set to zero explicitly and the calculation repeated. This process is continued until the resulting field is everywhere either below the boiling point or equal to zero. One can use these constraints to again completely solve for the temperature fields in the three bodies.

Tool, Workpiece, Fluid and Wear Fragment (4-Body Problem)

The most general case consists of four-way heat partition between the tool, workpiece, fluid and any removed material or chip, and involves six unknowns with three equations already specified. This partition problem is solved by combining the conditions presented above for the three-body case [7]. First, the local temperature in the tool, workpiece and chip are matched individually. Following this, we apply the boiling condition to determine the temperature fields in the fluid. The conditions are now as follows:

$$\begin{aligned} T_2(x) + T_2^L(x) &= T_4(x) \\ T_4(x) &= T_1^L(x) \\ T_3(x) &= T_2(x) \quad \text{no boiling} \\ T_3(x) &= 0 \quad \text{if boiling occurs} \end{aligned}$$

which completes the system for the six unknowns. Here, again, the fluid temperature problem is solved iteratively until the temperature fields are self-consistent.

In summary, workpiece/tool temperature fields in deformation processing may be obtained by mapping the particular geometry of interest to the unit problem described above. This unit problem is then solved systematically in the following sequence:

- The total heat generation q_n is determined based on the tool–workpiece interaction mechanics. There are typically two contributions—one from friction and the other due to large strain plastic deformation.
- Suitable moving heat source models are used to obtain temperature fields $T_1(x), T_2(x), T_3(x), T_4(x)$ in terms of the unknown partition functions $\varepsilon_1(x), \varepsilon_2(x), \varepsilon_3(x), \varepsilon_4(x)$.
- Depending on how many bodies are thermally interacting in the problem, one of the four cases above is solved to obtain $\varepsilon_i(x)$ and, consequently, $T_i(x)$ for all bodies involved.

Applications

We briefly illustrate these general ideas by applying them to two specific deformation processing applications—incremental forming and grinding.

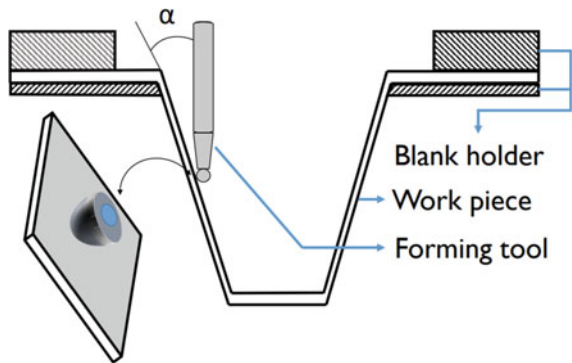
Incremental Forming

As a first example, we consider the process of incremental forming of sheet metal, shown in Fig. 2, where a predefined path is traversed by a rotating tool to deform material locally. A large single step forming operation is broken down into smaller “incremental” steps, with frictional heat generation occurring locally due to tool–workpiece interaction. Since no chip formation occurs and a lubricant is also absent, this configuration presents a two-body partition problem.

First, the frictional heat generated can be computed as:

$$q_n = F_f V_s$$

Fig. 2 Schematic of incremental forming showing circular contact geometry between tool and workpiece. (Color figure online)



where F_f is the frictional force between the tool and workpiece, V_s is the relative sliding velocity. The friction force can be evaluated from the horizontal and vertical force components which can be obtained by geometric considerations and the material's yield stress σ_Y . In order to illustrate the process, we only use the horizontal force given by [8]:

$$F_f \simeq F_H = r t \sigma_Y (\sin \alpha + 1 - \cos \alpha)$$

and the corresponding relative sliding velocity consists of contributions from the tool angular velocity ω and the tool feed f ,

$$V = 2\pi r \omega + f$$

where r is the tool radius.

The frictional heat q_n is partially conducted away by the workpiece and the rest is conducted into the tool. Ideally, the contact geometry is circular (see Fig. 2) and the heat must be distributed within this contact zone. One must then match the temperatures in the tool and workpiece point by point in the contact zone and proceed to obtain the corresponding ε values, which are now a function of position in the contact zone. However, a good approximate solution for the partition coefficients is obtained by matching the average or maximum temperatures in the contact zone, see Refs. [6, 7]. In this latter case, the ε values are effective values and independent of location.

In order to illustrate, we consider mild steel plate of thickness 1.6 mm, with $\sigma_Y = 350 \text{ N/mm}^2$ and tool radius (r) of 15 mm, semi-cone angle (α) of $\pi/6$ and tool-tip velocity of 40 mm/s. For this situation, we obtain a corresponding horizontal force of $F_H = 5.3 \text{ kN}$.

Further, assuming that the tool is made of 440C stainless steel (hardened and tempered $\sim 60 \text{ HRC}$), with $K_T = 24.2 \text{ W/m}^2\text{C}$, $\alpha_T = 6.74 \times 10^{-6} \text{ m}^2/\text{s}$ and for mild steel $K_{MS} = 31 \text{ W/m}^2\text{C}$, $\alpha_{MS} = 3.598 \times 10^{-6} \text{ m}^2/\text{s}$. The maximum contact zone diameter (Fig. 2) is determined from the tool geometry and the heat source is assumed to be distributed over this region.

Using a uniform circular heat source solution and matching maximum temperatures in the tool and workpiece, the temperature rise in the workpiece is obtained as $\Delta T \sim 70 \text{ }^\circ\text{C}$. The corresponding partition coefficient is ~ 0.21 . This procedure shows the ease with which temperature rises may be calculated.

Surface Grinding

We now turn to an application involving a four-body problem. Consider a wet grinding process, where all four bodies—tool, workpiece, chip, and lubricant—interact thermally, see Fig. 3.

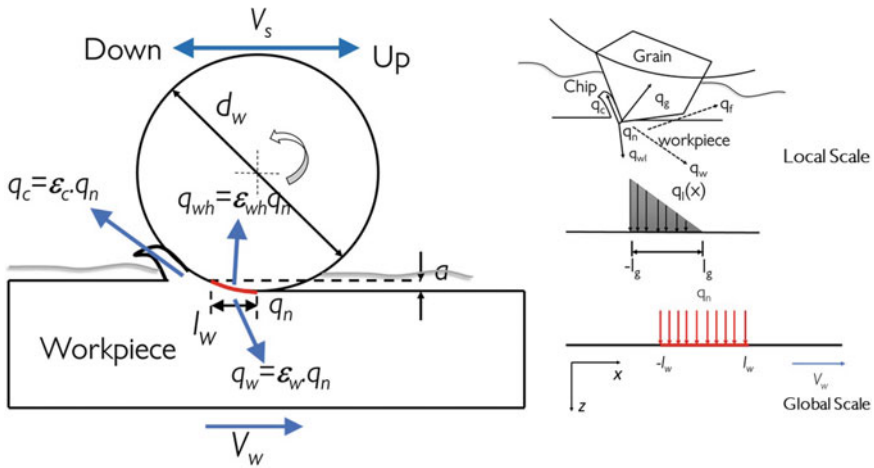


Fig. 3 Heat partition in a typical grinding process showing global scale (left) and local scale (right) interactions. (Color figure online)

Usually, the grinding wheel rotates at very high angular velocity so that the interaction between the wheel and the workpiece can be extreme even if the latter is fed at a low rate. Figure 3 shows both the local interaction between an abrasive grain and the workpiece (right) as well as the global interaction at the wheel level (left). Process parameters involved are the linear velocity of the wheel V_s , translation velocity of workpiece V_w , depth of cut a and length of contact zone l_w .

We now use four partition coefficients $\epsilon_w, \epsilon_{wh}, \epsilon_f, \epsilon_c$, corresponding to the workpiece, wheel, fluid, and chip, respectively. All of them are functions of distance x along the contact zone. The temperatures in the four bodies are obtained by using suitable moving heat source models as discussed by Ju et al. [7]. They are determined in terms of conductivities K_w, K_g of the workpiece and wheel, thermal diffusivities of the workpiece α_w and wheel α_g , as well as the density and specific heat of workpiece ρ_w and C_w , respectively.

Using the four-body heat partition formulation presented in Section “The Heat Partition Problem”, we obtain the heat partition functions as a function of x by solving the full six-variable system. The resulting partition coefficients are evaluated numerically and the results are shown in Fig. 4. The data in the figure corresponds to up-grinding. Several features are immediately evident. Firstly, it shows that the fraction of heat going into the fluid and the chip is quite negligible for the parameters chosen. This in fact a posteriori justifies the use of composite models for grinding in the literature. The heat going into the workpiece and tool together constitutes nearly 92–95% of the total heat generated.

From the partition coefficients, we obtain the equivalent temperature distribution in, say, the workpiece, see Fig. 5. Values for each of the parameters are taken from Ref. [7]. Such a plot can be very useful in determining maximum temperatures on

Fig. 4 Partition functions determined along the contact length.

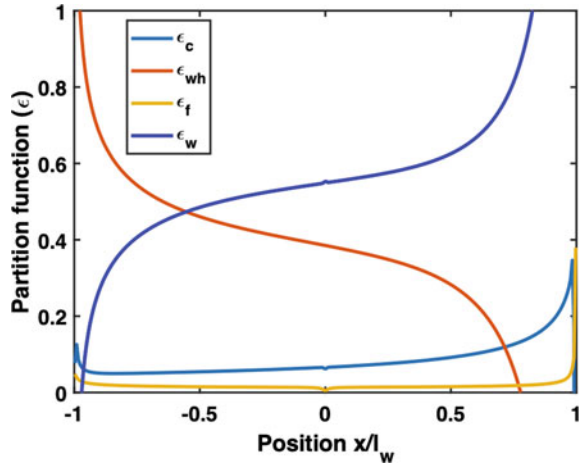
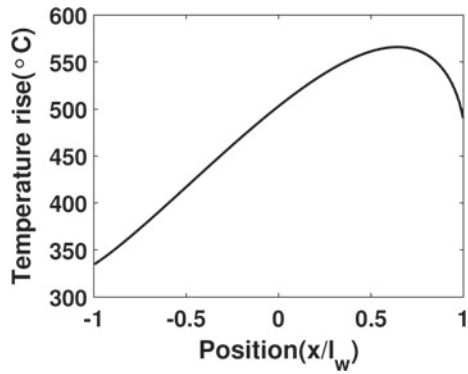


Fig. 5 Workpiece temperature distribution along the contact length with the grinding wheel.



the surface of the ground workpiece and, consequently, for evaluating defects such as grinding burns.

Conclusions and Outlook

The techniques for heat partition described in the present manuscript provide a practical method to evaluate temperature fields in deformation processing applications. Unlike in other materials processing applications that involve directed energy sources alone (e.g., laser-based manufacturing), deformation processing applications inherently involve multiple contacting bodies. Hence the method used to estimate the partition of heat is central to the problem of determining temperature fields. This has the inherent advantage that the resulting fields are either analytical or, at worst, semi-analytical, making them far more desirable than voluminous time-consuming

finite element simulations. It is hoped that the exposition presented will help apply some of these ideas to various applications in deformation processing and material removal processes.

References

1. Rosenthal D (1946) The theory of moving sources of heat and its application to metal treatments. *Trans ASME* 68:849–866
2. Backofen WA (1972) *Deformation processing*. Addison-Wesley Publishing Company
3. Shaw MC (2005) *Metal cutting principles*. Oxford University Press, New York
4. Jaeger JC (1942) Moving sources of heat and the temperature of sliding contacts. *Proc R Soc New South Wales* 76:203–224
5. Carslaw HS, Jaeger JC (1959) *Conduction of heat in solids*. Clarendon Press, Oxford
6. Blok HP (1937) Theoretical study of temperature rise at surfaces of actual contact under oiliness lubricating conditions. *Proc Inst Mech Eng* 2:222
7. Ju Y, Farris TN, Chandrasekar S (1998) Theoretical analysis of heat partition and temperatures in grinding. *J Tribol* 120:789–794
8. Jackson K, Allwood J (2009) The mechanics of incremental sheet forming. *J Mater Process Technol* 209(3):1158–1174

Part XXXVII
Powder Materials for Energy Applications

Thermodynamic Behavior Analysis of Fe-FeAl₂O₄ Cermet Prepared by Zinc Kiln Slag



Chao Luo, Jun Peng, Hongyan Yan, Hui Li, and Jinglong Liang

Abstract The use of zinc kiln slag to prepare Fe-FeAl₂O₄ cermet can realize the recycling of zinc kiln slag and promote sustainable development. The thermodynamic behavior was analyzed by XRD, XRF and using FactSage. The results showed that reaction temperature was higher than 710 °C, 7% of C contained in the zinc kiln slag can reduce the iron oxide to Fe, and the reduced Fe₃O₄ and FeO could be reacted with Al₂O₃ to synthesize FeAl₂O₄. Complex oxide ores presented in zinc kiln slag were advantageous to the preparation of Fe-FeAl₂O₄ cermet. The thermodynamic conditions for preparing Fe-FeAl₂O₄ cermet from zinc kiln slag are feasible.

Keywords Zinc kiln slag · Fe-FeAl₂O₄ cermet · Powder metallurgy · Thermodynamics

Introduction

Cermet is a composite material composed of one or several metals and ceramic materials [1, 2]. It combines the excellent properties of ceramics and metals, such as high strength, high hardness, corrosion resistance, wear resistance, high-temperature resistance, and good thermal shock resistance [3]. With the development of new processes and materials, cermet is mainly used in aerospace, electric power, automobiles, building materials, and other fields [4, 5]. The research on cermet has become an important research direction in the field of composite materials. Due to the high cost of raw materials for preparing cermet, it limits its wide-scale promotion

C. Luo · J. Peng (✉)

School of Materials and Metallurgy, Inner Mongolia University of Science and Technology, Baotou 014010, China
e-mail: pengjun@imust.com

C. Luo

Hesteel Group Tangsteel Company, Tangshan 063000, China

H. Yan · H. Li · J. Liang

College of Metallurgy and Energy, North China University of Science and Technology, Tangshan 063210, China

© The Minerals, Metals & Materials Society 2021

TMS 2021 150th Annual Meeting & Exhibition Supplemental Proceedings,

The Minerals, Metals & Materials Series,

https://doi.org/10.1007/978-3-030-65261-6_83

and application. In particular, compared with magnesium-based cermet, aluminum-based cermet, and titanium-based cermet, iron-based cermet has problems such as high specific gravity, high sintering temperature, and low specific strength, and there are fewer research results on iron-based cermet.

With the increase in steel output, the amount of zinc kiln slag has also increased significantly. The accumulation of countless slag mountains has brought environmental pollution, large area, and increased investment. High value-added, resource-based treatment of zinc kiln slag is an urgent problem to be solved now [6–8]. Zinc kiln slag is rich in oxides such as Fe and Al, which can be considered as a raw material for preparing Fe-FeAl₂O₄ cermet. The use of zinc kiln slag for the preparation of Fe-FeAl₂O₄ cermet will simultaneously solve the resource of zinc kiln slag and the cost of metal-based cermet. It has huge social, economic, and scientific value. In this paper, the thermodynamic behavior was analyzed by using FactSage. The feasibility of using zinc kiln slag to prepare cermet was studied.

Experimental

The zinc kiln slag samples were mixed in a ball mill, ground to 100 μm, and dried and then subjected to XRD and XRF detection. FactSage was used to analyze the thermodynamic conditions of cermet prepared from zinc kiln slag.

Results and Discussion

Analysis of Physical Properties of Zinc Kiln Slag

The sample composition of the zinc kiln slag used in this study was shown in Table 1. The zinc kiln slag was mainly composed by Fe₂O₃, SiO₂, CaO, Al₂O₃, and C. Preparation of Fe-FeAl₂O₄ cermet needed to use Fe and Al₂O₃, and Fe and Al₂O₃ could be got from zinc kiln slag.

Table 1 Zinc kiln slag composition table (mass fraction)

Composition	Content	Composition	Content
Slag	100	MnO ₂	0.76
Fe ₂ O ₃	23.74	Na ₂ O	0.59
SiO ₂	15.71	K ₂ O	0.20
CaO	15.74	SO ₃	18.80
Al ₂ O ₃	6.04	As ₂ O ₃	7.07
MgO	2.88	C	7.00
TiO ₂	0.36	other	1.11

Fig. 1 XRD results of zinc kiln slag

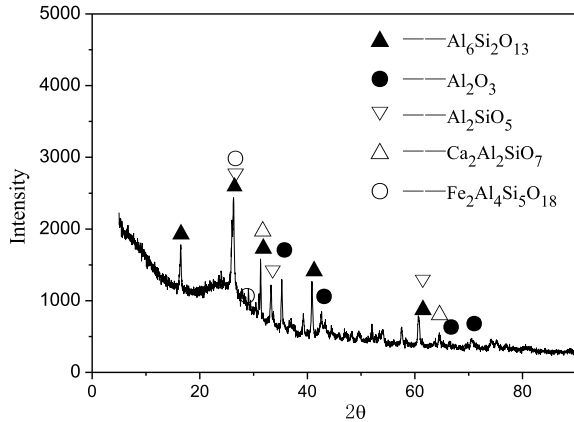


Figure 1 shows the XRD results of zinc kiln slag. The main phases were Al₂O₃, iron cordierite (Fe₂Al₄Si₅O₁₈), mullite phase (Al₂SiO₅, Al₆Si₂O₁₃), and calcium aluminosilicate (Ca₂Al₂SiO₇). The iron cordierite phase was beneficial to lower the sintering temperature of the cermet, and promoted the formation of FeAl₂O₄. Also, the thermal expansion coefficient of the iron cordierite phase was small, it was a favorable component for the preparation of iron-based cermet. Al₂SiO₅ and Al₆Si₂O₁₃ belonged to the mullite phase. Al₂SiO₅ was intermediate phase and Al₆Si₂O₁₃ was stable binary compound. They could inhibit the growth of crystal grains and prevented the propagation of cracks in cermet.

Research found that suitable amount of SiO₂ could promote the formation and growth of FeAl₂O₄ [9]. TiO₂ could be used as a nucleating agent for composite materials to accelerate the crystallization of FeAl₂O₄. MgO could replace Fe²⁺ in Fe₃O₄, and Fe²⁺ and MgO can form continuous solid solution (Mg-Fe)O, which is beneficial to the stability of Fe²⁺ in FeAl₂O₄ synthesis [10, 11]. The above results showed that the components in zinc kiln slag that were conducive to the excellent performance of iron-based cermet. It had certain advantages as a raw material for preparing iron-based cermet.

Carbothermal Reduction

Iron Oxide Reduction Reaction

At present, the common point in the synthesis of FeAl₂O₄ was to adjust the reaction atmosphere by doping or burying carbon. It converted Fe³⁺ to Fe²⁺ and reacted with Al₂O₃ to synthesize FeAl₂O₄, then FeAl₂O₄ and Fe bond to form a metal matrix composite material. The C contained in zinc kiln slag could reduce Fe₂O₃ and reacted with Al₂O₃ to obtain Fe-FeAl₂O₄ cermet.

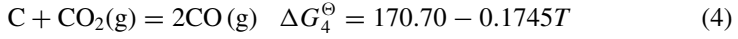
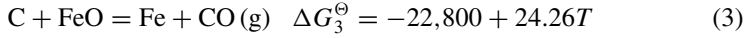
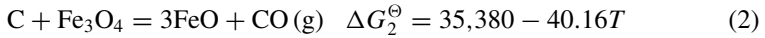


Figure 2 shows the equilibrium reaction between C and iron oxide. It can be seen that the gasification reaction curve of carbon did not intersect with the two lines that before point b, Fe₂O₃ was reduced and the product was Fe₃O₄. Between point b and a, the gasification reaction curve of carbon intersects with curve 1, Fe₂O₃ was reduced to FeO. When the temperature raised to 710 °C (point a), the corresponding CO content of the reaction was 62%, and the reaction product was Fe. When temperature raised to 950 °C, the CO content was 100%, Fe₂O₃ was completely reduced to Fe. Therefore, in order to obtain Fe, the sintering temperature should be higher than 710 °C.

Other Oxide Reduction Reactions

In order to further study the changes in substances during the preparation of iron-based cermet from zinc kiln slag, the reaction of C with other oxides was studied. The standard Gibbs free energy of each reaction was compared, and the results shown in Fig. 3.

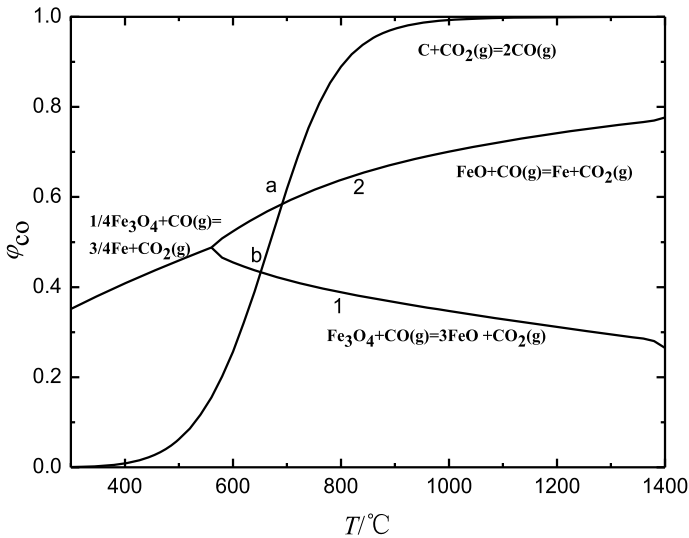


Fig. 2 Phase equilibrium result diagram of the reaction between iron oxide and C

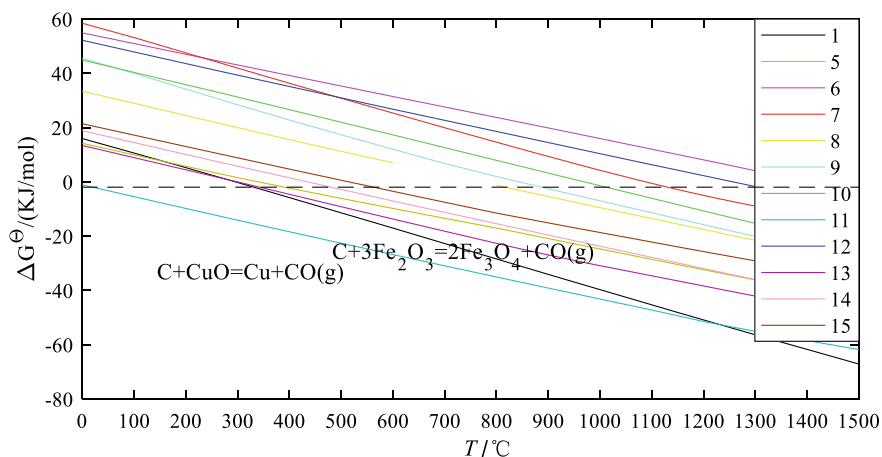
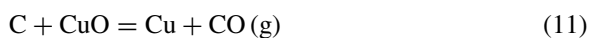
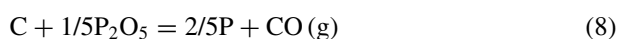
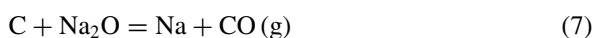
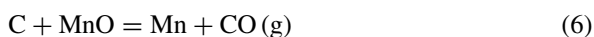


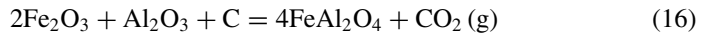
Fig. 3 Standard Gibbs free energy variation curve of oxides in zinc kiln slag. (Color figure online)



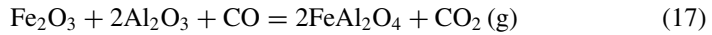
It can be seen from Fig. 3 that C could reduce oxides in zinc slag within a certain temperature range. Before 1200 °C, the CuO line is the lowest, followed by Fe₂O₃. It indicated that CuO undergoes C reduction before Fe₂O₃. Since the content of copper oxide in the zinc extraction kiln slag was only 0.17%, the copper oxide could be completely reduced in a short time, and then the carbon reduced iron oxide.

FeAl₂O₄ Synthesis Reaction

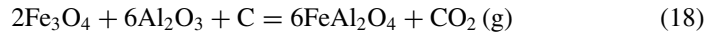
Zinc kiln slag contains Fe₂O₃, Al₂O₃, and C in Table 1. The synthesis of iron-aluminum spinel in a reducing atmosphere involved the following reactions.



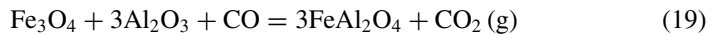
$$\Delta G_{16}^{\ominus} = -31,839.86 + 6.66T \ln T - 381.16T \\ + 48.70 \times 10^{-3}T^2 - 23.14 \times 10^5T^{-1}$$



$$\Delta G_{17}^{\ominus} = -73,874.39 + 1.09T \ln T - 68.82T \\ + 23.07 \times 10^{-3}T^2 - 7.47 \times 10^5T^{-1}$$



$$\Delta G_{18}^{\ominus} = -34,346.67 - 98.82T \ln T + 301.42T \\ + 116.40 \times 10^{-3}T^2 - 12.37 \times 10^5T^{-1}$$



$$\Delta G_{19}^{\ominus} = -106,994.08 - 51.56T \ln T + 259.15T \\ + 81.63 \times 10^{-3}T^2 - 2.08 \times 10^5T^{-1}$$



$$\Delta G_{20}^{\ominus} = -34,577.94 + 10.07T \ln T - 64.66T \\ - 2.58 \times 10^{-3}T^2 - 2.70 \times 10^5T^{-1}$$

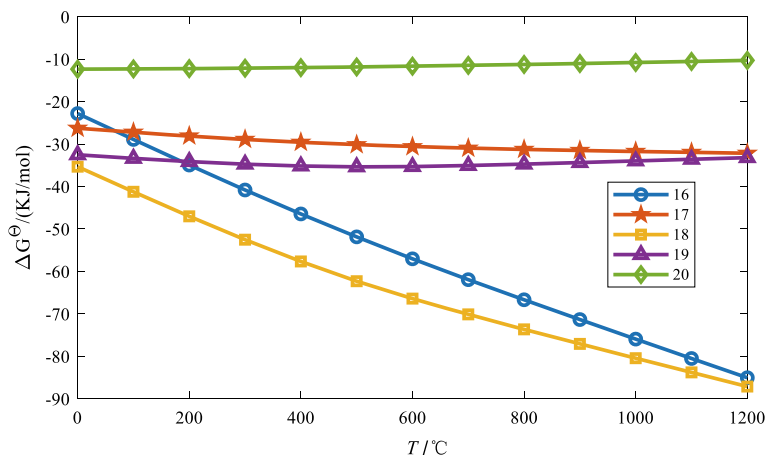


Fig. 4 Standard Gibbs free energy curves. (Color figure online)

Figure 4 shows that $\Delta G_{18}^{\ominus} < \Delta G_{16}^{\ominus} < \Delta G_{19}^{\ominus} < \Delta G_{17}^{\ominus} < \Delta G_{20}^{\ominus} < 0$ at 200–1200 °C, $\Delta G_{18}^{\ominus} < \Delta G_{16}^{\ominus} < \Delta G_{17}^{\ominus} < \Delta G_{19}^{\ominus} < \Delta G_{20}^{\ominus} < 0$ at 1200–1500 °C. Reaction (18) proceeded first, followed by reaction (16), and finally reaction (20). It indicated that Fe₂O₃ and Fe₃O₄ were more likely to form iron-aluminum spinel than FeO.

Conclusions

By analyzing the thermodynamic behavior of zinc-lifting kiln slag, the following conclusions were obtained.

- (1) The XRD results showed that the presence of the mineral phase of the zinc extraction kiln slag was beneficial to the preparation of metal-based ceramics, and the zinc extraction slag could be used to prepare metal-based ceramics.
- (2) The synthesis reaction of FeAl₂O₄ phase had been analyzed by thermodynamics. It was possible to synthesize five reactions of the iron-aluminum spinel phase during the preparation of metal-based ceramics. The standard Gibbs free energy of each reaction at different temperatures was compared. It was concluded that the order of the reaction to form the iron-aluminum spinel phase was Fe₂O₃ > Fe₃O₄ > FeO.
- (3) The thermodynamic analysis of the carbothermal reduction reaction showed that in order to reduce the metal phase Fe, the reaction temperature reached 710 °C, and CO concentration was greater than 62%. Among other oxides in zinc kiln slag, only CuO reacted with C prior to iron oxides. Because the content of CuO in the slag was low, carbon could basically completely react iron oxides.

Acknowledgements This work was supported by the National Natural Science Foundation of China (No. 51804126) and Natural Science Foundation of Hebei Province (No. E2018209266).

References

1. Di Z, Dingguo Z, Zhiqiang L (2010) The current state and trend of metal matrix composites. *Mater China* 29(4):78–84
2. Rittner MN (2000) Metal matrix composites in the 21st century. Paper presented at the 2nd annual aluminum metal matrix composites meeting, Orlando, 26 May 1999
3. Miracle DB (2005) Metal matrix composites: from technology to science. *Compos Sci Technol* 65:2526–2540
4. Bains PS, Sidhu SS, Payal HS (2015) Fabrication and machining of metal matrix composites: a review. *Mater Manuf Process* 31(5):553–573
5. Haghshenas M (2016) *Metal-matrix composites*. Elsevier, New York
6. Hongping L (2009) Surveying the disposal process of zinc leaching-slag. *Yunnan Metal* 38(4):34–47
7. Jing L, Niu H, Peng J et al (2008) Present situation and prospect about comprehensive utilization of zinc kiln slags. *Multi Utiliz Min Res* 6:44–48
8. Kaideng Z (2004) Study on comprehensive utilization of zinc volatilization kiln slag. Central South University, Hu Nan
9. Chen JH, Yan MW, Su JD et al (2015) Effect of SiO₂ addition on the synthesis of hercynite with high purity. *J Ceram Soc Jpn* 123(1439):595–600
10. Johnson RE, Muan A (1965) Phase equilibria in the system CaO-MgO-iron oxide at 1500 °C. *J Am Ceram Soc* 48(7):359–364
11. Paladino AE (1960) Phase equilibria in the ferrite region of the system FeO-MgO-Fe₂O₃. *J Am Ceram Soc* 43(4):183–191

Tunable Morphology Synthesis of Lithium Iron Phosphate as Cathode Materials for Lithium-Ion Batteries



Yin Li, Keyu Zhang, Li Wang, Meimei Yuan, and Yaochun Yao

Abstract Tailor-designed structure is an essential method to improve energy density capacity retention and energy density of lithium-ion batteries. Herein, we designed and synthesized lithium iron phosphate (LiFePO_4) with ellipsoidal, hierarchical, and nanosheets morphologies by a solvothermal using phytic acid as phosphorus source. The influence of mole ratio on the morphologies and electrochemical performances were studied. The results illustrated that phytic acid dosage plays a vital role in the tunable morphology syntheses process. Additional, electrochemical measurement confirms that hierarchical LiFePO_4 exhibits higher initial discharge capacity ($162.09 \text{ mAh g}^{-1}$, 0.1C), more excellent high-rate discharge capability ($114.13 \text{ mAh g}^{-1}$, 10C), and better cycle stability (97.2% at 1C after 150 cycles). This satisfactory electrochemical performance could be ascribed to the moderate size and fast ion transport kinetics, which caused by the changing of thermodynamics and kinetics in synthesis process.

Keywords Lithium iron phosphate · Phytic acid · Solvothermal · Lithium-ion batteries

Introduction

Olivine structured LiFePO_4 has attracted vast attention due to its excellent thermal stability, good theoretical specific capacity (170 mAh g^{-1}), low cost, environmental compatibility, and superb stability [1–5]. However, the main drawbacks, such as low intrinsic electronic conductivity and sluggish lithium-ion transport, are the causes of poor electrochemical capacity [6–8]. In recent years, tremendous efforts have been

Y. Li · K. Zhang · L. Wang · M. Yuan · Y. Yao (✉)

The National Engineering Laboratory for Vacuum Metallurgy, Kunming University of Science and Technology, Kunming 650093, China

e-mail: yaochun9796@163.com

Engineering Laboratory for Advanced Battery and Materials of Yunnan Province, Kunming University of Science and Technology, Kunming 650093, Yunnan Province, China

© The Minerals, Metals & Materials Society 2021

TMS 2021 150th Annual Meeting & Exhibition Supplemental Proceedings,

The Minerals, Metals & Materials Series,

https://doi.org/10.1007/978-3-030-65261-6_84

made to overcome these disadvantages, for instance, coating with a conductive layer, reducing particle size and obtaining kinetically favorable morphology [9–13].

It is well known that the electrochemical performances are closely related to their morphologies [14, 15]. To obtain favorable crystal orientation and optimize the particle morphology of LiFePO_4 , various synthetic methods such as hydrothermal synthesis, sol–gel, and solid-state method have been used. Among these many synthetic methods reported, hydrothermal synthesis has been widely used to prepare various materials which occurs a lower cost of precursors, simpler process, and the possibility for large-scale production [16]. During the solvothermal synthesis, the morphology and particle size of the LiFePO_4 are determined by many experiment parameters such as precursor types, pH, use of additives or surfactants, temperature, concentration, molar ratios, and solvent types [17–21].

Previous study has reported that LiFePO_4 with different morphologies including spindles [22], hollow [23], plates [24] and starfish [25] has been prepared by adjusting the experiment parameters. Generally, a nanostructure is necessary to obtain good electrochemical performance. However, the synthesis of nanostructured LiFePO_4 is usually more complicated. In this work, we reported a facile method to obtain various morphologies of LiFePO_4 to nanoscale with PhyA as phosphorus source by simply changing the molar ratio. Here PhyA was aimed as phosphorus source, antioxidant as well as structure directing agent. The effects of molar ratio on the morphological transformation and electrochemical performances of olivine LiFePO_4 has been discussed in detail.

Experimental

Preparation of Sample

The samples were synthesized by hydrothermal method and heat-treatment. The stoichiometric amounts of $\text{LiOH}\cdot\text{H}_2\text{O}$, PhyA, and $\text{FeSO}_4\cdot 7\text{H}_2\text{O}$ were dispersed in the ethylene glycol, respectively. Next, the solution was mixed and stirred for 30 min at room temperature. Then, the above mixture was transferred into a Teflon-lined stainless steel autoclave and was kept 180 °C for 4 h. After cooling to room temperature, the precursor was collected after centrifuging and washing by deionized water for 3 times and ethanol for 1 time. Finally, it was mixed with source in the mortar. The resultant product was heated in a vacuum oven at 650 °C for 6 h under flowing Ar atmosphere. According to the molar ratios of LiFePO_4 (Li:Fe:P = 3: 1: 1, 3: 1: 1.5, 3: 1: 2 and 3: 1: 2.5), the corresponding materials were denoted as LFP-1, LFP-1.5, LFP-2, and LFP-2.5, respectively.

Materials Characterization

X-ray diffraction (XRD) analyses were identified with a D/Max-RA X-ray diffractometer with Cu K α radiation. The morphology of samples was characterized by scanning electron microscopy (SEM, FEI Quanta-430) with field emission SEM operated at 10 kV.

Electrochemical Characterization

The electrochemical measurements of the cathode materials were performed using the CR2025 coin cell assembled in argon-filled glovebox with lithium foils as reference electrode and Celgard 2400 as the separator. The cathode consists of 80 wt% active material, 10 wt% conductive additive (Super P), and 10 wt% polyvinylidene fluoride (PVDF). The substance was dissolved in N-methyl pyrrolidone (NMP) as a binder. Then, the slurry was coated onto an aluminum foil current collector and dried at 80 °C under vacuum for 12 h. The dried electrode was cut into a circle with the diameter of 14 mm. Galvanostatic charge–discharge cycling tests were carried out by a battery test system (XWJ Neware Tech. Co., BTS3000, China) in the 2.0–4.2 V (vs. Li/Li⁺) under 25 °C. Electrochemical impedance spectra (EIS) acquired by PMC-1000DC electrochemical workstation in the frequency range from 100 kHz to 10 MHz. Cyclic voltammetry (CV) was performed by an electrochemical workstation (Ametek, PMC-1000DC, America) from 2.5 to 4.3 V at room temperature.

Results and Discussion

In the process of preparing LiFePO₄ by hydrothermal method, the ratio of ingredients should be considered. As reported, only by choosing the proper ratio of ingredients can be get pure LiFePO₄ and save the raw materials. The XRD patterns of the LiFePO₄ prepared in various molar ratios are shown in Fig. 1. It is clearly that all samples can be indexed to an orthorhombic olivine-type phase LiFePO₄ (JCPDS card No. 83-2092), indicating that molar ratio has no effect on phase purity. Moreover, the relative intensity of the diffraction peaks gradually increases with increased molar ratio, which demonstrate that higher purity and better crystallization materials are obtained.

The SEM results confirm the significant changes in surface morphology, as displayed in Fig. 2. From Fig. 2a, it can be seen that the precursor synthesized at 3: 1: 1 exhibits irregular shape composed of micrometer-sized ellipsoidal (100–200 nm width and 200–500 nm length) and many immature flakes. When the molar ratio increases to 3: 1: 1.5, a loose spherical morphology assembled with nanoparticles is

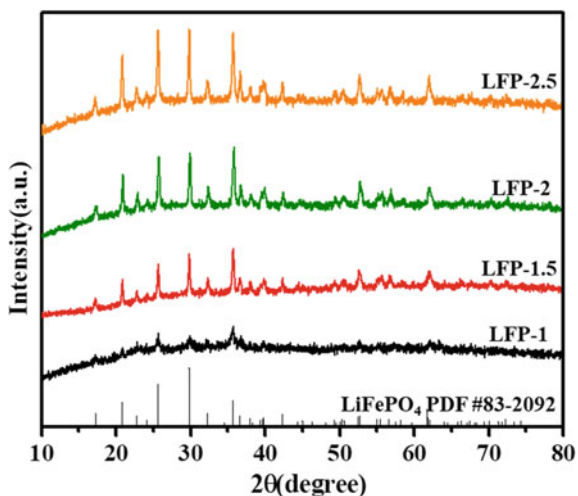


Fig. 1 XRD patterns of these samples prepared in different molar ratios. (Color figure online)

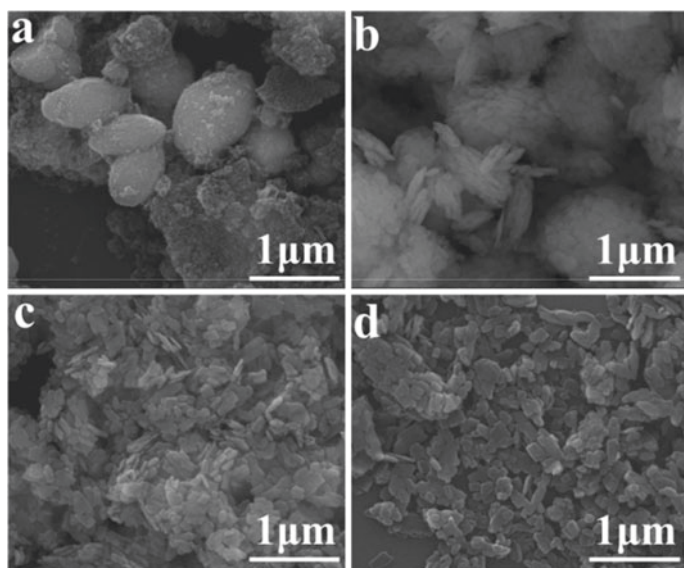


Fig. 2 SEM images of these samples prepared in different molar ratios **a** 3:1:1; **b** 3:1:1.5; **c** 3:1:2; **d** 3:1:2.5

obtained (Fig. 2c), which might be beneficial to the electrical resistance and electrochemical performance. As the molar ratio goes on 3: 1: 2, those particles convert to numerous nanosheets. Further increasing the molar ratio to 3: 1: 2.5 resulted in a size increment of LiFePO_4 nanosheets. Clearly, the molar ratio significantly influenced the

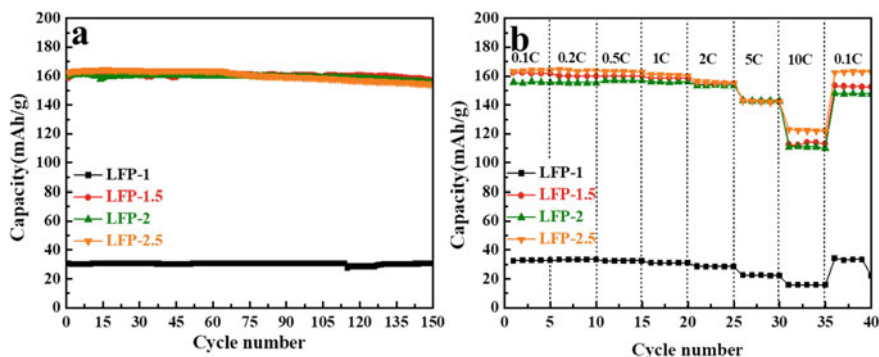


Fig. 3 The cycling and rate performances of these samples prepared in different molar ratios. (Color figure online)

morphology of LiFePO_4 . The particle shape of all sample changed from ellipsoid-shape to a hierarchical structure, then to a nanosheets, and finally to a larger nanosheet with increasing the molar ratio. As we all know that the electrochemical performance of materials is directly affected by the morphology of the sample. Considering the phase structure and morphology, we hypothesize that when phytic acid dosage is 1.5, 2, and 2.5, the samples have excellent electrochemical performance. Because the tiny particle size can provide preconditions for the rapid transmission of lithium ions and electrons.

In order to evaluate the molar ration on the electrochemical performance of LiFePO_4 , the cells were charged and discharged at 25°C . Before the electrochemical performance test, carbon coating is carried out to improve conductivity. Figure 3a displays the detailed cyclic properties of the four electrodes. LFP-1 shows the lowest discharge specific capacity of 30.3 mAh/g at 1C, whereas the other samples show improved capacities: 160.5, 159.9, and 162.3 mAh/g for LFP-1.5, LFP-2, and LFP-2.5, respectively. After 150 cycles, the LFP-1.5, LFP-2, and LFP-2.5 exhibit the reversible capacities of 157.1, 155.4, and 154.3 mAh/g with the capacity retention ratios of 97.9%, 97.1%, and 95.1%, respectively. Obviously, the proper phosphorus dosage can greatly improve the cyclic stability of LFP cathode. In addition, the LFP-1.5, LFP-2, and LFP-2.5 showed a good rate property. As displayed in Fig. 3b, the LFP-1 exhibits a lowest capacity than other samples at various current. The reversible capacity of LFP-1.5, LFP-2, and LFP-2.5 can reach 159.9, 156.8, and 163.1 mAh/g at 0.5C, 153.9, 153.3, and 156.2 mAh/g at 2C, 143.1, 142.9, and 142.9 mAh/g at 5C. At high current rates of 10C, the capacities of those electrodes are 112.4, 110.9, and 123.0 mAh/g, which are 70.2%, 70.7%, and 75.4% of its capacity at 0.5C. When the discharge rate returns from 10C to 0.1C, the capacity almost has no fading, suggesting that the materials have a stable structure that is suitable for high-rate cycling. The good electrochemical properties of LFP-1.5, LFP-2, and LFP-2.5 can be attributed to their unique structure. The excellent electrochemical performance depends on the good particle morphology (consistent with SEM results), which enables the material

to maintain a stable structural state during charging and discharging, and improves the de-intercalation ability of lithium ions and ensures the safe performance of the battery.

Electrochemical impedance spectroscopy (EIS) examination was analyzed to further explain the electrochemical kinetic performance of LFP-1 and LFP-1.5 materials. Figure 4a presents the EIS spectra for the studied cathode materials in fresh lithium cells. It can be seen that each plot consists of a semicircle and a sloping line. The semicircle in the high-frequency region represents the charge transfer impedance (R_{ct}) due to the diffusion of Li^+ ion in the electrode/electrolyte interface, and the line in the low-frequency region is the solid-state diffusion of ion. As seen in Fig. 4a, the very small high-frequency semicircle for the LFP-1.5 implies its low charge-transfer resistance (139.3Ω) at the electrolyte/electrode interface. As for the LFP-1, the R_{ct} is calculated to be 240Ω , which indicate that reaction kinetics of LFP-1.5 is remarkably improved and the transport of electron/ion were facilitated. These results are also in good agreement with electrochemical performance exhibited in Fig. 3. A simple equivalent circuit is constructed to analyze the impedance spectra, as shown in Fig. 4b.

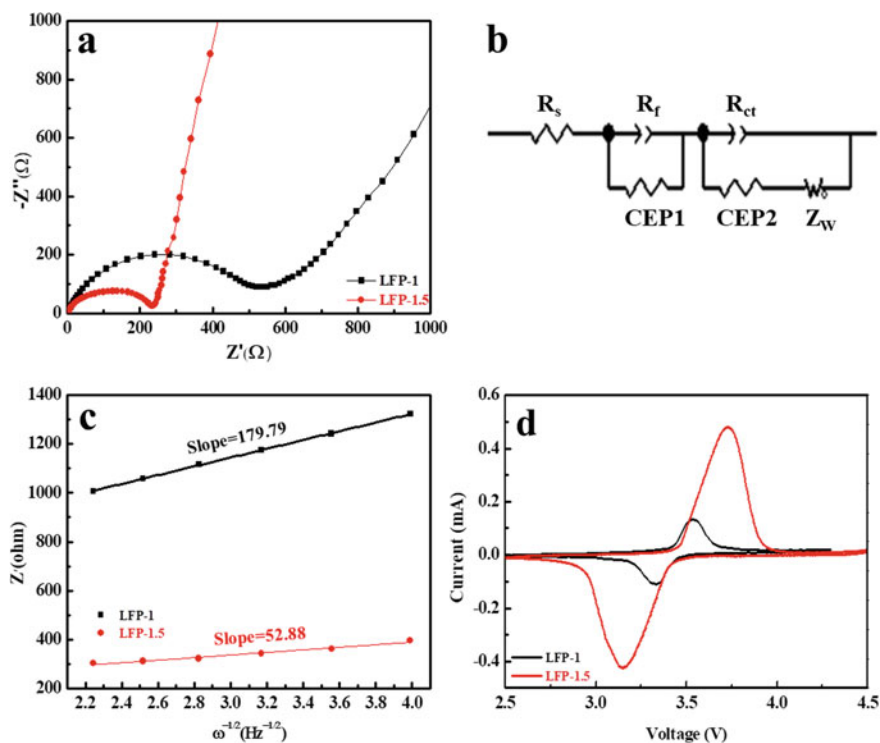


Fig. 4 **a** Nyquist plots of LFP-1 and LFP-1.5 electrodes for the fresh cells; **b** the corresponding equivalent circuit; **c** the relationship between Z' and $\omega^{-1/2}$ at low frequency; **d** cyclic voltammograms for LFP-1 and LFP-1.5. (Color figure online)

The lithium-ions diffusion coefficient (D_{Li^+}) can be calculated using the following equation [26]:

$$D_{\text{Li}^+} = 0.5 \left(\frac{RT}{AF^2\sigma_w C} \right)^2 \quad (1)$$

where R is gas constant, T is the absolute temperature, A is the electrode area, n is the number of electron per molecule during the redox reaction, F is the Faraday constant, C is the concentration of lithium ions, and σ_w is the Warburg factor associated with the Z' and $\omega^{-1/2}$ according to the following equation:

$$Z' = R_e + R_{\text{Ct}} + \sigma_w \omega^{-1/2} \quad (2)$$

According to Eq. (1), the lithium ions diffusion coefficients of LFP-1 and LFP-1.5 were 7.62×10^{-15} , 9.46×10^{-14} $\text{cm}^2 \text{s}^{-1}$, confirming that the suitable molar ratio is beneficial to increase the ionic conductivity.

The cyclic voltammograms (CV) of the LFP-1 and LFP-1.5 composite at a scan rate of 0.1 mV s^{-1} are shown in Fig. 4d. A pair of anodic and cathodic peaks, which correspond to the oxidation/reduction transformation between Fe^{2+} and Fe^{3+} , is observed. Compared with LFP-1, LFP-1.5 exhibits higher redox peak current, which indicates higher Li insertion capacity and is consistent with previous charge/discharge tests and SEM result.

Conclusions

Olivine lithium iron phosphate with various morphologies is successfully synthesized via a solvothermal strategy using PhyA as phosphorus source. The morphology of LiFePO_4 is closely dependent on the Li: Fe: P molar ratio. At low ratios, the LiFePO_4 has an irregular shape composed of micrometer-sized ellipsoidal (100–200 nm width and 200–500 nm length) and shows poor electrochemical performance. As the molar ratio gradually increases, the particles shape change into a hierarchical structure, then to a nanosheets, and finally to a larger nanosheet. When molar ratio of Li: Fe: P is 3:1:1.5 in the precursor, the product after carbon coating yields a superior discharge capacities of 162.09, 114.13 mAh g^{-1} at 1C and 10C. After 150 cycles at current rate of 1C, it can retain 97.2% of its initial capacity. Therefore, this work provides a facile method to prepare various morphologies LiFePO_4 with different electrochemical performance by simply changing the molar ratios of the starting ingredients.

Acknowledgements The authors gratefully acknowledge the financial support from the National Natural Science Foundation of China (Grant No. 51364021) and the Project of Natural Science Foundation of Yunnan Province (Grant No. 2018HB012).

References

1. Padhi AK, Nanjundaswamy KS, Goodenough JB (1997) Phospho-olivines as positive-electrode materials for rechargeable lithium batteries. *J Electrochem Soc* 144:1188–1194
2. Wang GX, Bewlay S, Yao J (2004) Characterization of $\text{LiM}_x\text{Fe}_{1-x}\text{PO}_4$ ($\text{M}=\text{Mg}, \text{Zr}, \text{Ti}$) cathode materials prepared by the sol-gel method. *Electrochem Solid State Lett* 7:A503–A506
3. Julien CM, Zaghib K, Mauger A (2006) Characterization of the carbon coating onto LiFePO_4 particles used in lithium batteries. *J Appl Phys* 100:063511-1–063511-7
4. Huang H, Yin SC, Nazar LF (2001) Approaching theoretical capacity of LiFePO_4 at room temperature at high rates. *Electrochem Solid State Lett* 4:A170–A172
5. Sauvage F, Baudrin E, Gengembre L (2005) Effect of texture on the electrochemical properties of LiFePO_4 thin films. *Solid State Ionics* 176:1869–1876
6. Arico AS, Bruce PG, Scrosati B (2005) Nanostructured materials for advanced energy conversion and storage devices. *Nat Mater* 4:366–377
7. Amin R, Balaya P, Maier J (2007) Anisotropy of electronic and ionic transport in LiFePO_4 single crystals. *Electrochem Solid-State Lett* 10:A13–A16
8. Saravanan K, Reddy MV, Balaya P (2009) Storage performance of LiFePO_4 nanoplates. *J Mater Chem* 19:605–610
9. Du GD, Zhou YK, Tian XH (2018) High-performance 3D directional porous LiFePO_4/C materials synthesized by freeze casting. *Appl Surf Sci* 453:493–501
10. Hu GR, Xie XM, Cao YB (2019) Ultrasonic-assisted synthesis of LiFePO_4/C composite for lithium-ion batteries using iron powder as the reactant. *J Alloys Compd* 773:1165–1171
11. Deng YF, Yang CX, Zou KX (2017) Recent advances of Mn-rich $\text{LiFe}_{1-y}\text{Mn}_y\text{PO}_4$ ($0.5 < y < 1.0$) cathode materials for high energy density lithium ion batteries. *Adv Energy Mater* 1601958
12. Gao LB, Xu ZR, Zhang S (2018) The co-doping effects of Zr and Co on structure and electrochemical properties of LiFePO_4 cathode materials. *J Alloys Compd* 739:529–535
13. Zhou YK, Tian XH, Wang PC (2016) Freeze-drying of “pearl milk tea”: a general strategy for controllable synthesis of porous materials. *Sci Rep* 6:26438
14. Lee MH, Kim TH, Kim YS (2011) Precipitation revisited: shape control of LiFePO_4 nanoparticles by combinatorial precipitation. *J Phys Chem C* 115:12255–12259
15. Wang, L, He X, Sun W (2012) Crystal orientation tuning of LiFePO_4 nanoplates for high rate lithium battery cathode materials. *Nano Lett* 12:5632–5636
16. Dokko K, Koizumi S, Nakano H, Kanamura K (2007) Particle morphology, crystal orientation, and electrochemical reactivity of LiFePO_4 synthesized by the hydrothermal method at 443 K. *J Mater Chem* 17:4803–4810
17. Lemmer S, Ruether F (2012) Habit prediction of succinic acid influenced by two solvents using build-in method. *Chem Eng Sci* 77:143–149
18. Chen JJ, Whittingham MS (2006) Hydrothermal synthesis of lithium iron phosphate. *Electrochem Commun* 8(5):855–858
19. Qin X, Wang XH, Xiang HM (2010) Mechanism for hydrothermal synthesis of LiFePO_4 platelets as cathode materials for lithium-ion batteries. *Phys Chem C* 114(39):16806–16812
20. Ni JF, Morishita M, Kawabe Y (2010) Hydrothermal preparation of LiFePO_4 nanocrystals mediated by organic acid. *J Power Sources* 195(9):2877–2882
21. Kanamura K, Koizumi S, Dokko K (2008) Hydrothermal synthesis of LiFePO_4 as a cathode material for lithium batteries. *J Mater Sci* 43:2138–2142
22. Yang X, Zhang WK, Huang H (2011) Self-assembled mesoporous LiFePO_4 with hierarchical spindle-like architectures for high-performance lithium-ion batteries. *J Power Sources* 196(13):5651–5658
23. Zheng ZM, Pang WK, Tang XC (2015) Solvothermal synthesis and electrochemical performance of hollow LiFePO_4 nanoparticles. *J Alloys Compd* 640:95–100
24. Mei RG, Song XR, Yang YF (2014) Plate-like LiFePO_4 crystallite with preferential growth of (010) lattice plane for high performance Li-ion batteries. *RSC Adv* 4:5746–5752

25. Chen MF, Wang XY, Shu HB (2015) Solvothermal synthesis of monodisperse micro-nanostructure starfish-like porous LiFePO_4 as cathode material for lithium-ion batteries. *J Alloys Compd* 652:213–219
26. Takami N, Satoh A, Hara M (1995) Structural and kinetic characterization of lithium intercalation into carbon anodes for secondary lithium batteries. *J Electrochem Soc* 142:371–379

Part XXXVIII
Recent Advances in Functional Materials
and 2D/3D Processing for Sensors, Energy
Storage, and Electronic Applications

3D Printed Passive Sensors—An Overview



Vishal R. Mehta and Nuggehalli M. Ravindra

Abstract Recent advances in 3D printed passive sensors have opened up new markets in a variety of applications. In order to function, passive sensors do not need any outside power and directly create an output response. These sensors either measure pressure or humidity or temperature or smoke or gases such as ammonia, SO₂, CO, and CO₂. Advanced 3D filaments/materials are enabling industry to design and manufacture reliable, accurate, and cost-effective sensors rapidly to address the requirements of food and drug industry, monitoring the environment, and biomedical, renewable energy, soft robotics-related applications. The paper will highlight improvements in the manufacture of these sensors and present various case studies. A summary of the market shares of 3D printed sensors will be presented.

Keywords Passive · Sensors · 3D printing

Introduction

A sensor identifies and responds to the surrounding changing physical environment. Sensors can be contact and non-contact type. They can be further classified as active and passive sensors. Active sensors require an energy source to be able to detect change in the physical environment. Passive sensors either receive power from outside or get stimulated from interactions with the surrounding environment. Numerous force measuring sensors have also been additively manufactured or more commonly known as 3D printed and used in various applications. These sensors are widely used in industry such as in consumer electronics, automotive, IT, and telecom. Many consumer handheld portable devices, nowadays, include sensors such

V. R. Mehta (✉)
Ohio Northern University, Ada, OH, USA
e-mail: v-mehta@onu.edu

N. M. Ravindra
New Jersey Institute of Technology, Newark, NJ, USA
e-mail: nmravindra@gmail.com

as accelerometers, gyroscopes, ambient light sensors, gas sensors, proximity sensors, and temperature detectors for feedback on various constraints.

3D printing was initially developed for rapid prototyping; but, due to the rapid progress in technology, its development has enabled quick transition as a manufacturing method of choice for sensors. During the last decade, there has been a tremendous development in the types of materials and technologies involved in additive manufacturing [1–3]. Techniques such as fused deposition modeling (FDM), ink-jet printing, stereolithographic printing, digital light printing (DLP), laminated object manufacturing (LOM), selective laser sintering (SLS) and selective laser melting (SLM), photopolymer jetting (Ploy jet), and 3D powder binder jetting (3DP) have been modified and used for mass production. 3D printed active sensors for different fields of applications have also been reviewed [4–9]. Case studies of selected 3D printed passive sensors are presented here.

Gas Sensors

3D printing has been used in fabricating gas sensors as it has benefits of rapid prototyping, less mold formation, and customization. Additive manufacturing has been used to create sensors to detect CO, CO₂, methane, methanol, acetone, NO₂, and NH₃. Zhou et al. created a 3D printed resistive ammonia gas sensor. They used a digital light printer (DLP) to create ceramic lattice structures (CLS) [10]. Polyaniline (PANI), a stable, conductive polymer was used as a NH₃ detector. CLS structures were modified by depositing PANI on it. Ag nanoparticle ink was added for increasing the sensitivity of PANI for ammonia (Fig. 1). Material characterization, mechanical properties, and selectivity of the ammonia sensor was tested. The sensor showed a high sensitivity of 9.7 for 100 ppm of NH₃.

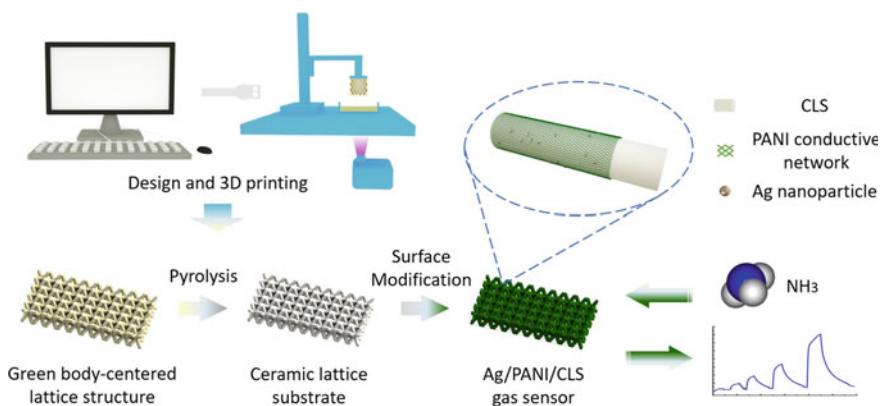


Fig. 1 Flow diagram for fabrication of ceramic-based ammonia sensor. With permission from Elsevier [10]. (Color figure online)

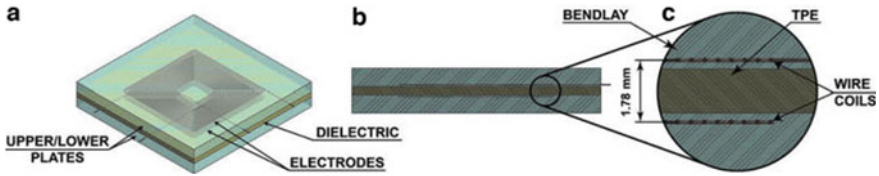


Fig. 2 **a** Design of the prototype capacitive force sensor using additive manufacturing, **b** cross-sectional view of the sensor, and **c** close up view of the cross-section showing the constituents of the sensor. With permission from Mary Ann Liebert Inc Publishers [12]. (Color figure online)

Force Sensor

Kisic et al. used additive manufacturing and made force sensor parts from polylactic acid (PLA) using fused deposition method. They studied variation of the inductance caused by distance changes of smooth ferrite close to the inductor [11]. The manufactured sensor was characterized in the force range of 0–2 N.

Saari et al. created a composite capacitive force sensor by using a combination of copper (Cu) fiber encapsulation and thermoplastic elastomer via additive manufacturing [12]. In customized 3D printer setup, Cu wire was encapsulated using a liquid dielectric on a thin ABS layer. The flexible core of the capacitor was built by a specifically designed screw extruder. The thermoplastic elastomer core forms the yielding component, that is, responsible for the change in the distance between plates under load (Fig. 2). A single 3D printer was used to create the entire capacitor using these three materials. The fabricated sensor was tested using a tensile tester and LCR meter at a frequency of 1 kHz.

Conductive Wires

3D printed sensors typically use metal inks (e.g., silver nanoparticle or carbon-based composites). Kwok et al. used a thermoplastic composite of carbon black (25% by wt.) and polypropylene. Optical and electrical characterization was carried out. The composite showed a positive temperature coefficient. Kwok et al. fabricated temperature sensor by embedding the conductive thermoplastic inside a hollow acrylonitrile butadiene styrene (ABS) body, as shown in Fig. 3.

Wu et al. used erbium-doped strontium aluminum oxide to create mechanoluminescent material to create stretching/strain sensor. Depending on whether it is static or dynamic state of stress, the device will generate luminescence [14]. The fabricated devices were mounted in a stretchable elastomer, and this composite structure accomplished sensing both strain level and stretching states as shown in Fig. 4.

Dharmarwardana et al. used temperature-responsive organic single crystals along with organic thermo-polymeric filaments (butoxyphenyl N-substituted derivative,

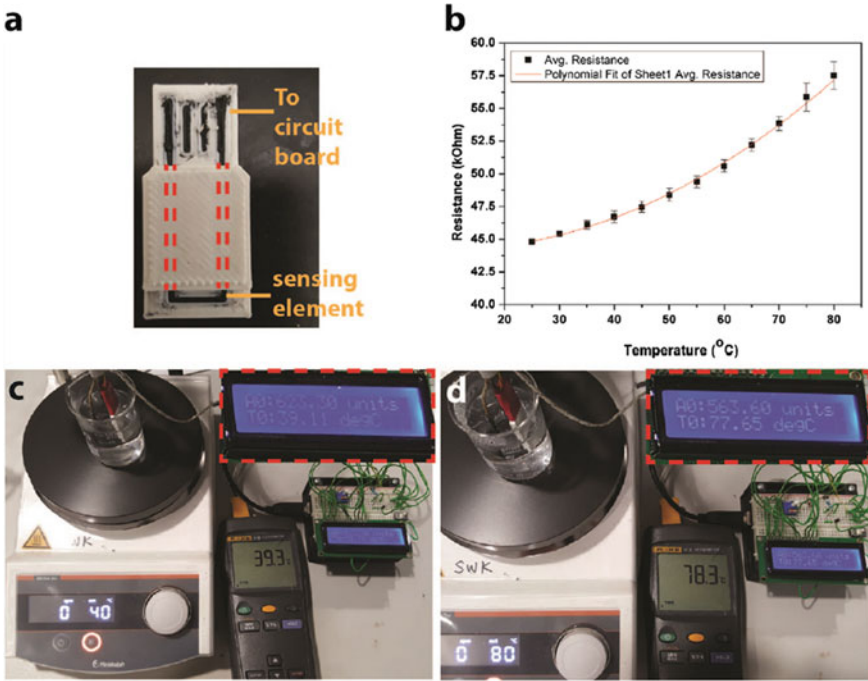


Fig. 3 3D printed temperature sensor. **a** Image of a temperature sensor. **b** Resistance versus temperature of a 3D-printed thermometer. **c, d** The printed sensor, connected to a potentiometer circuit and Arduino for measurement and display. With permission from Elsevier [13]. (Color figure online)

BNDI) and polylactic acid (PLA) and demonstrated 3D printed temperature sensors as shown in Fig. 5 [15].

Kato and Miyashita used a FDM-based 3D printer to create grid having multiple contact points. When touched by the user, an input is produced [16]. The input is displayed on an XY plane. A diverse interface can be recognized by modifying the wiring inside the 3D printed object.

Recent advances in additive manufacturing of wearable radiofrequency identification (RFID) sensor tags have enabled their usage in a wide range of applications. Colella and Catarinucci used a polylactic acid (PLA), copper strip, and circuit board to create RFID sensor for body temperature monitoring as shown in Fig. 6 [17].

Trangkanukulij et al. designed and manufactured a passive RFID tag that works at 910 MHz suitable for North American market [18]. A silver nanoparticle-based conductive ink was used for creating a dipole antenna on a flexible polyimide (PI) film substrate. This is shown in Fig. 7.

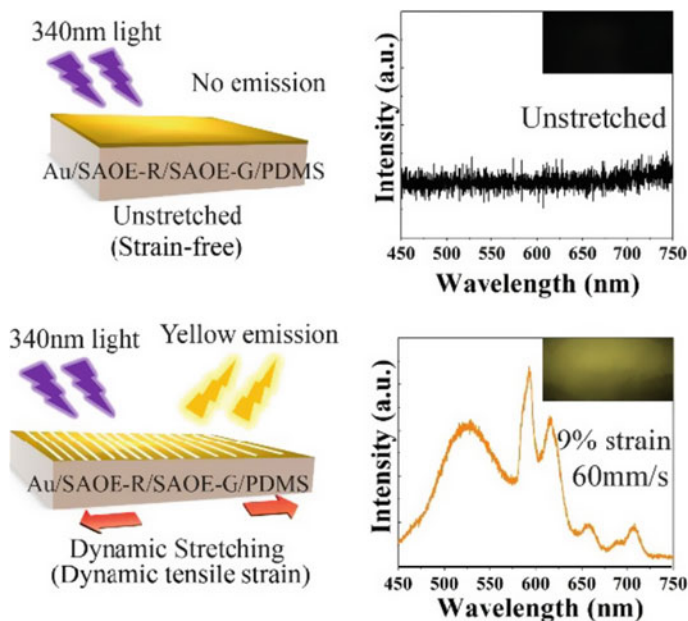


Fig. 4 Schematic structure and corresponding mechanical responsive luminescence of the bi-layered stretching/strain sensor under conditions of unstretched (strain-free) and dynamic stretching. With permission from John Wiley & Sons, Inc. [14]. (Color figure online)

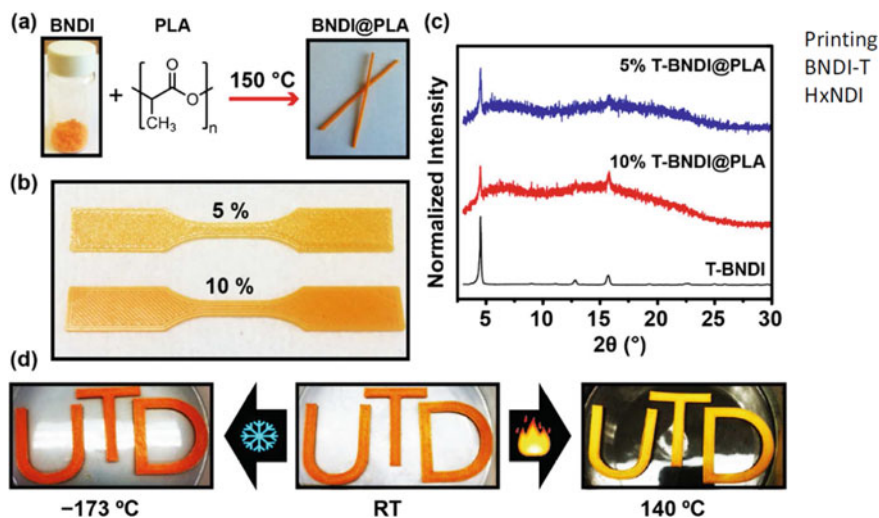


Fig. 5 a Schematic diagram of the fabrication of BNDI-T@PLA filaments, b varying ratios of BNDI-T incorporated into PLA, c PXRD data for BNDI-T@PLA composites, and d thermochromics behavior of BNDI-T@PLA. With permission from Royal Society of Chemistry [15]. (Color figure online)

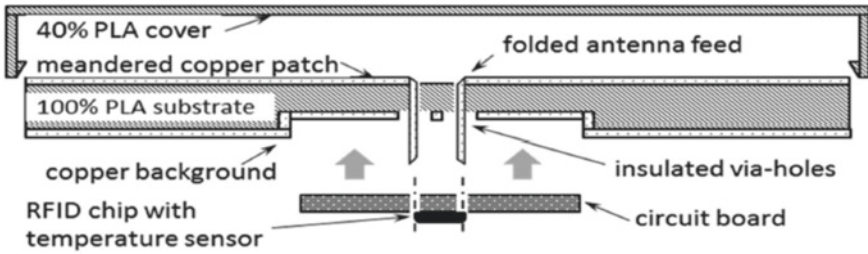
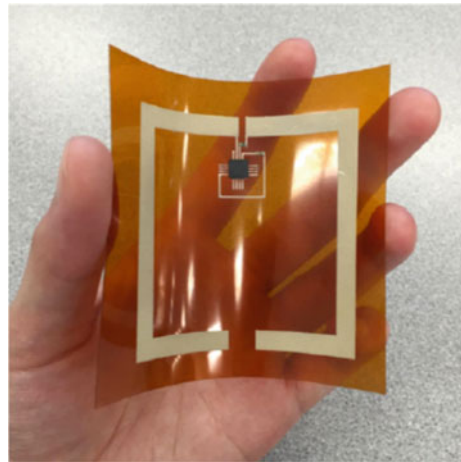


Fig. 6 Schematic of 3D printed wearable sensor tag. With permission from IEEE [17]

Fig. 7 Photo of completed RFID tag. With permission from IEEE [18]. (Color figure online)



Offline Sensing

Offline sensors are a type of passive sensors that identify one time interactions. These sensors do not have active electronics or any power requirement. Schmitz et al. have designed and fabricated 3D printed offline sensors that have conductive liquid embedded within the structure of the sensors [19]. The sensors are manufactured with pre-defined interaction via user interface. Sensors have a user electrode and touch screen electrode. A capacitive touch screen is utilized to extract information if the sensor has been exposed to a pre-defined interaction. These sensors react to load, pressure, acceleration, tilt, flip, and change in temperature. The operative principle is shown in Fig. 8.

At Ohio Northern University, while the emphasis on 3D printing continues to be along the lines of in-class instruction, work has begun to formulate a research program that is focused on 3D printing and prototyping of pressure sensors for utilization by the sports-related industry.

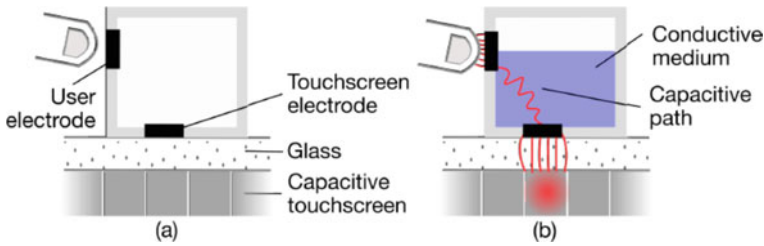


Fig. 8 Operating principle of offline sensor. The state of the sensor determines if there is a conductive path (a) or not (b) With permission from Association for Computing Machinery [19]. (Color figure online)

Market Share

Global sensor market has been growing rapidly and is expected to be about \$287 billion dollars by 2025 [20]. It is expected to grow at a compound annual growth rate (CAGR) of 13.3% [21]. The global 3D sensor market was valued \$1997.14 million in the year 2017 and is anticipated to grow with a CAGR of 26.54% from the year 2018 to 2023 [22]. The 3D printer market size in 2019 was 11.58 billion and expected to grow at 14% from 2020 to 2027. The current USD 739 million 3D printer filament market is projected to reach USD 2552 million by 2025, at a CAGR of 28.1% from 2020 to 2025 [23]. It is important to note that the ongoing COVID-19 pandemic can affect the future market growth projections.

Conclusion

3D printed or additive manufactured sensors have seen rapid development and deployment as they offer both manufacturer and user a high level of customization for a given application. A variety of material and deposition techniques have been developed to address the market needs. The feature resolution, ability to deposit multiple materials simultaneously, adhesion between layers of different materials, deposition rates, and in-situ process monitoring and control remain the challenges to overcome.

References

1. Ngo TD, Kashani A, Imbalzano G, Nguyen KTQ, Hui D (2018) Additive manufacturing (3D printing): a review of materials, methods, applications and challenges. *Compos Part B Eng* 143:172–196. <https://doi.org/10.1016/j.compositesb.2018.02.012>
2. Ligon SC, Liska R, Stampfl J, Gurr M, Mülhaupt R (2017) Polymers for 3D printing and customized additive manufacturing. *Chem Rev* 117(15):10212–10290. <https://doi.org/10.1021/acs.chemrev.7b00074>

3. Scordo G, Bertana V, Scaltrito L, Ferrero S, Cocuzza M, Marasso SL, Romano S, Sesana R, Catania F, Pirri CF (2019) A novel highly electrically conductive composite resin for stereolithography. *Mater Today Commun* 19:12–17. <https://doi.org/10.1016/j.mtcomm.2018.12.017>
4. Lambert A, Valiulis S, Cheng Q (2018) Advances in optical sensing and bioanalysis enabled by 3D printing. *ACS Sens* 3(12):2475–2491. <https://doi.org/10.1021/acssensors.8b01085>
5. Xu Y, Wu X, Guo X, Kong B, Zhang M, Qian X, Mi S, Sun W (2017) The boom in 3D-printed sensor technology. *Sensors* 17:1166
6. Han T, Kundu S, Nag A, Xu Y (2019) 3D printed sensors for biomedical applications: a review. *Sensors* 19(7):1706. <https://doi.org/10.3390/s19071706>
7. Hunter GW, Akbar S, Bhansali S, Daniele M, Erb PD, Johnson K, Liu C-C, Miller D, Oralkan O, Hesketh PP, Manickam P, Vander Wal RL (2020) A critical review of solid state gas sensors. *J Electrochem Soc* 167(3), art. no. 037570
8. Khosravani MR, Reinicke T (2020) 3D-printed sensors: current progress and future challenges. *Sens Actuators A Phys* 305:111916. <https://doi.org/10.1016/j.sna.2020.111916>
9. Ota H, Emaminejad S, Gao Y, Zhao A, Wu E, Challa S, Chen K, Fahad HM, Jha AK, Kiriya D, Gao W, Shiraki H, Morioka K, Ferguson AR, Healy KE, Davis RW, Javey A (2016) Application of 3D printing for smart objects with embedded electronic sensors and systems. *Adv Mater Technol* 1:1600013. <https://doi.org/10.1002/admt.201600013>
10. Zhou S, Mei H, Lu M, Cheng L (2020) 3D printed and structurally strengthened ammonia sensor. *Compos Part A Appl Sci Manuf* 139:106100. <https://doi.org/10.1016/j.compositesa.2020.106100>
11. Kisic M, Blaz N, Zivanov L, Damjanovic M (2020) Elastomer based force sensor fabricated by 3D additive manufacturing. *AIP Adv* 10:015017. <https://doi.org/10.1063/1.5130065>
12. Saari M, Xia B, Cox B, Krueger P, Cohen AL, Richer E (2016) Fabrication and analysis of a composite 3D printed capacitive force sensor. *3D Print Addit Manuf* 3(3):136–141
13. Kwok SW, Goh KHH, Tan ZD, Tan STM, Tjiu WW, Soh JY, Ng ZJG, Chan YZ, Hui KH, Goh KEJ (2017) Electrically conductive filament for 3D-printed circuits and sensors. *Appl Mater Today* 9:167–175. <https://doi.org/10.1016/j.apmt.2017.07.001>
14. Wu C, Zeng S, Wang Z, Wang F, Zhou H, Zhang J, Ci Z, Sun L (2018) Efficient mechanoluminescent elastomers for dual-responsive anti-counterfeiting device and stretching/strain sensor with multi-mode sensibility. *Adv Funct Mater* 28:1803168. <https://doi.org/10.1002/adfm.201803168>
15. Dharmarwardana M, Arimilli BS, Luzuriaga MA, Kwon SL, Hamilton A, Gayan A, McCandless GT, Smaldone RA, Gassensmith JJ (2018) The thermo-responsive behavior in molecular crystals of naphthalene diimides and their 3D printed thermochromic composites. *United Kingdom*. <https://doi.org/10.1039/C8CE00798E>
16. Kato K, Miyashita H (2016) UIST' 16 adjunct: proceedings of the 29th annual symposium on user interface software and technology, Oct 2016, pp 47–49. <https://doi.org/10.1145/2984751.2985700>
17. Colella R, Catarinucci I (2018) Wearable UHF RFID sensor tag in 3D-printing technology for body temperature monitoring. In: 2018 2nd URSI Atlantic radio science meeting (AT-RASC), Meloneras, 2018, pp 1–4. <https://doi.org/10.23919/URSI-AT-RASC.2018.8471562>
18. Trangkanukulij R, Kim T, Kim WS (2018) A 3D printed flexible passive RFID for temperature sensing. In: 2018 international flexible electronics technology conference (IFETC), Ottawa, ON, 2018, pp 1–3. <https://doi.org/10.1109/IFETC.2018.8583913>
19. Schmitz M, Herbers M, Dezfuli N, Günther S, Mühlhäuser M (2018) Off-line sensing: memorizing interactions in passive 3D-printed objects. In: Proceedings of the 2018 CHI conference on human factors in computing systems (CHI' 18). Association for Computing Machinery, New York, Paper 182, pp 1–8. <https://doi.org/10.1145/3173574.3173756>
20. <https://www.alliedmarketresearch.com/sensor-market>. Downloaded on 9/5/2020
21. <https://www.bccresearch.com/market-research/instrumentation-and-sensors/sensors-technologies-markets-report.html>

22. <https://www.industryarc.com/Report/244/global-3D-sensor-market-analysis-report.html>.
Accessed on 9/8/2020
23. <https://www.grandviewresearch.com/industry-analysis/3d-printing-industry-analysis>.
Accessed on 9/8/2020

Modeling of Rheological Properties of Metal Nanoparticle Conductive Inks for Printed Electronics



Patrick Dzisah and Nuggehalli M. Ravindra

Abstract Of late, printed electronics continues to experience an increased demand due to enhanced use of flexible electronics, RFID devices, gas sensors, antennas, and intelligent food packaging devices. Due to this demand, the use of inkjet printers and conductive inks, with desirable properties, is on the rise. Conductive nanomaterials, such as metal nanoparticles and nanowires, carbon nanotubes, and graphene, are promising building blocks for synthesizing conductive inks for printed electronics. In order to develop printing devices that are optimized for flexible electronics, numerical studies on the ink flows and the associated rheological properties are crucial. Therefore, it is critical to provide accurate conductive ink properties for reliable numerical results. However, it is difficult to find such data in the literature since conductive inks for printed electronics contain precious metal nanoparticles and they are not only non-Newtonian but expensive. To address this challenge, this paper aims to utilize common viscosity–shear rate models such as the power law model to study rheological properties such as viscosity, shear rate, and shear stress of conductive inks. Notably, conductive inks made from metal nanoparticles such as silver, copper, gold, nickel, and aluminum are considered in this study. The results obtained from this model have been compared with experimental data. To further understand the effects of temperature and viscosity on synthesized ink, the viscosity–temperature relationship of the conductive ink is also modeled using Arrhenius’s law and compared with experimental data. The benefits of using this model for performing numerical simulations of desirable rheological properties of conductive inks for printed electronics are discussed.

Keywords Power law model · Viscosity · Shear stress · Shear rate · Temperature · Conductive ink · Printed electronics · Inkjet printing

P. Dzisah (✉) · N. M. Ravindra
New Jersey Institute of Technology, Newark, NJ, USA
e-mail: pd59@njit.edu

N. M. Ravindra
e-mail: nmravindra@gmail.com

Introduction

In recent years, the demand for functional devices such as flexible, wearable, and printed electronics has been rising exponentially. This is in part due to the promising technology such as inkjet printing which is suitable for printing functional inks on various substrates. For example, printing techniques like gravure printing, slot-die coating, or inkjet printing have been applied to fabrication of solar cells, radio frequency identifier (RFID) tags, antennas, gas sensors, electroluminescent devices, controlled-release drug delivery devices, and refractive micro-lenses in order to reduce their production costs [1–5]. Coupled to this demand is the use of inkjet printers and conductive inks with desirable properties. Conductive nanomaterials, such as metal nanoparticles and nanowires, carbon nanotubes, and graphene, are promising building blocks for synthesizing conductive inks for printed electronics.

In order to develop printing devices that are optimized for flexible electronics, numerical studies on the ink flow and rheological properties are crucial, and therefore, it is critical to provide accurate conductive ink properties for reliable numerical results. However, these data are rarely available since conductive inks for printed electronics contain precious metal nanoparticles and they are not only non-Newtonian but expensive. However, the related physical and rheological properties of inks, provided by most commercial manufacturers, are only indicative of viscosity values that exhibit either Newtonian or non-Newtonian fluid properties. Thus, developing a reliable and economic method to evaluate the rheological behaviors of conductive inks and providing benchmark data for the ink quality would be highly desirable. Only few studies have reported the characteristics of conductive inks. Lee et al. [6] reported that the viscosity and surface tension of nano-sized silver colloids depend on the contents of Ag particles. Tseng and Chen reported a relationship between the shear strain rate and viscosity of nickel nanoparticle inks [7]. To develop a direct ceramic inkjet printing technique, Prasad et al. studied the rheology of ceramic inks and spread of ink droplets and observed shear-thinning behaviors of the inks [8]. Izu et al. also studied the rheological behaviors of core-shell type cerium oxide/polymer hybrid nanoparticles [9]. To obtain ink viscosities, these studies utilized a commercial viscometer or rheometer, which generally consumes a large amount of ink (at least several milliliters per experiment), leading to high experimental costs. To address this challenge, microfluidic chip methods with microparticle image velocimetry (μ PIV) have been suggested to reduce sample consumption and experimental costs in studying particulate flows such as colloidal gel flow, DNA solution, polymer solution, and glass-forming liquid [10–13]. Mortazavi analyzed the flow of pseudoplastic power law fluid under different power law exponents in the microchannel plate by computational fluid dynamics (CFD) simulations [14]. The results showed that the pseudoplastic fluid in the microheat exchanger can reduce the pressure drop and increase the heat transfer efficiency than Newtonian fluid. The radial flow numerical simulation of non-Newtonian power law fluid in the rough wall fracture shows that, when the flow behavior index changes, the flow pattern has slight but systematic change. When the index drops, the fluid becomes more radial, and the fluid becomes shear

thinning [15]. As a non-Newtonian fluid, it is necessary to analyze the rheological characteristics and heat transfer characteristics of the synthesized conductive ink. To study the viscosity-temperature effects on conductive inks, Huang et al. obtained the viscosity-temperature relationship of yellow ink through experiments and simulated the influence of ink viscosity on the ink temperature field at steady state. However, the influence of the viscosity-temperature relationship and the properties of the interface material on the ink heat transfer were not considered [16].

In this paper, the non-Newtonian fluid characteristics of the metal nanoparticle conductive inks of Ag, Cu, Au, Al, and Ni are considered. The relationships between the rheological properties such as viscosity, shear stress, and shear strain rate are simulated using the power law model. The ink viscosity and temperature characteristics under the interaction of viscous dissipation are studied.

Materials and Methods

Printable Conductive Nanomaterials

In order to fabricate high quality and functional electronics, the ink development step is critical and cannot be compromised for the specific printing process. The synthesized ink should have desired properties such as high electrical conductivity, good stability without aggregation, desirable viscosity, and surface tension for high printing resolution and accuracy.

The most widely researched materials for conductive ink development for printed electronic applications are metal nanomaterials and organic nanomaterials. Among these nanomaterials, metal nanoparticles and nanowires of Ag, Cu, Au, Al, and Ni are the preferred choice for ink development. Due to high electrical conductivity at room temperature, AgNPs and AgNWs are the most extensively studied metal nanostructures as conductors or electrodes for printed electronics [17–23]. Another promising metal nanomaterial for ink development for printed electronics is CuNPs and CuNWs which possess a very high conductivity (only 6% less than that of Ag) and is much cheaper in comparison with Ag. Furthermore, metal grids that are based on metal NPs and NWs show high transmittance, good conductivity, and excellent mechanical compliancy. In addition to metal nanomaterials, carbon nanomaterials, including graphene and CNTs, are also promising materials for flexible and stretchable printed electronic applications due to their unique properties, such as high intrinsic current mobility and mechanical flexibility [24–32].

Inkjet Printing Processes

Printing various conductive patterns, thin films, and circuits in a single step at low temperature on compatible substrates such as paper, plastics, and glass is simplified using inkjet printing technique. This method is also suitable for large-area and roll-to-roll production of films. There are many reports on producing inks from Ag NPs [33–36], Au NPs [37–39], Cu NPs [40, 41], Al NPs [42], and Sn NPs [43], and subsequent deposition of conductive thin films and circuits from these nanomaterials by inkjet printing methods [44–48].

Rheological Properties of Conductive Ink

Rheological properties such as shear stress, shear rate, surface tension, and viscosity can either be measured experimentally or simulated by mathematical modeling. Rheological behaviors of non-Newtonian fluids can be modeled using the following four well-known models—power law model (Ostwald model), Herschel–Bulkley model for Bingham plastic fluid, Carreau model for pseudoplastic fluid, Cross–William model according to Zhang [49] and Moreno et al. [50]. The most widely used model is the power law model to predict the rheological behavior of non-Newtonian fluids due to its simplicity, accuracy, and consistency. The model of choice for this research is the power law model to study the rheological behavior of conductive inks of various metal NPs.

Power Law Model of Conductive Ink

For an incompressible Newtonian fluid, the relationship between the shear stress and the shear rate is in accord with the law of Newtonian inner friction. The kinetic viscosity (viscosity for short) is a constant, independent of the shear stress and the shear rate.

The relationship of the three parameters can be expressed as,

$$\tau = \eta \dot{\gamma} \quad (1)$$

where τ is shear stress, η is the fluid viscosity, and $\dot{\gamma}$ is the shear rate. For non-Newtonian fluid, the relationship between the shear stress and the shear rate is no longer consistent with the law of Newtonian inner friction. Its viscosity is not only related to the shear rate, but also varies with the change in temperature. The viscosity of a non-Newtonian fluid can be expressed as,

$$\eta = \eta(\dot{\gamma})H(T) \quad (2)$$

In relation (2), η is the fluid viscosity (Pascal-Second—Pa s); it can not only represent the fixed viscosity of Newtonian fluid in Formula (1) but also describes the apparent viscosity of non-Newtonian fluid in Eq. (2). $\dot{\gamma}$ is the shear rate and also known as the velocity gradient, expressed as $\dot{\gamma} = du/dy$, and its unit is s^{-1} . $\eta(\dot{\gamma})$ is the viscosity–shear rate function and has different expressions under different models. $H(T)$ is related to the viscosity–temperature function, and it indicates the relationship between the viscosity and the temperature of the fluid as in Eq. (3),

$$H(T) = \frac{\eta(T)}{\eta(T_\alpha)} \tag{3}$$

$\eta(T)$ is the viscosity–temperature function, and $\eta(T_\alpha)$ is the viscosity–temperature relationship at reference temperature, T_α as shown in Eq. 6.

Model of Shear Stress-Shear Rate Relation

Shear stress-Shear rate data were obtained using shear stress, shear rate and viscosity relation in Eq. (1). Experimental results of offset ink based on shear stress and shear rate, at 20 °C, are shown in Table 1.

Model of Viscosity-Shear Rate Relation

The power law model (Eq. 4) was used to establish viscosity-shear rate relationship of conductive inks of five metal nanoparticles which are non-Newtonian fluids.

Table 1 Relationship between shear stress and shear rate at normal temperature 20 °C [51]

No.	Shear stress (Pa)	Shear rate (s ⁻¹)	Viscosity (Pa s)	No.	Shear stress (Pa)	Shear rate (s ⁻¹)	Viscosity (Pa s)
1	18.26	0.1160	157.42	11	246.54	0.8595	286.84
2	41.09	0.1855	221.51	12	269.37	0.9378	287.23
3	63.92	0.2273	281.21	13	292.2	1.0349	282.35
4	86.75	0.2733	317.42	14	315.03	1.1581	272.02
5	109.58	0.3482	314.70	15	337.86	1.1714	288.42
6	132.4	0.4254	311.24	16	360.69	1.4320	251.88
7	155.23	0.5031	308.55	17	383.51	1.5341	249.99
8	178.06	0.5730	310.75	18	406.34	1.7313	234.70
9	200.89	0.6739	298.10	19	429.17	1.8427	232.90
10	223.72	0.7435	300.90	20	452	2.0400	221.57

Power Law Model (Ostwald Model)

$$\eta = k\dot{\gamma}^{(n-1)} \quad (4)$$

In Eq. (4), k is the consistency coefficient (Pa s^n), n is the power law index, which is a dimensionless quantity that characterizes the deviation degree between the shear-thickening [$(n > 1)$; dilatant fluids], shear-thinning fluid [$(n < 1)$; pseudo-plastics], and Newtonian fluid ($n = 1$).

Modeling of Viscosity-Temperature Relation

Temperature characterizes the degree of molecular heat movement, and the temperature increase makes the free volume of the polymer increase, which leads to decrease in viscosity. For most fluids, Arrhenius's law [52] can be used to interpret its viscosity-temperature relationship

$$\eta = \eta(T) = Ae\left(\frac{E_a}{RT}\right) \quad (5a)$$

$$\ln \eta = \ln A + \frac{E_a}{R} \frac{1}{T} \quad (5b)$$

In relations (5a) and (5b), A is the pre-exponential factor also called as experimental constant (Pa s). E_a is the viscous flow activation energy (KJ/mol). R is the gas constant (thermodynamic constant); usually, $R = 8.314 \text{ J/(mol K)}$. T is the absolute temperature (K).

And,

$$H(T) = \exp \frac{E_a}{R} \left(\frac{1}{T} - \frac{1}{T_\alpha} \right) \quad (6)$$

Analysis of Rheological Properties of Metal NPs Conductive Ink

In order to study the changes in both shear stress-shear rate and viscosity-shear rate behaviors, experimental data from offset ink experiments were used as a baseline for our model. Offset ink is a high-viscosity mixture. Its rheological properties mainly include viscosity, yield value, fluidity, and so on. Among them, the viscosity is the internal friction that obstructs the flow of itself between the layers. The printability of

the ink requires stable viscosity when it is on the plate, but when the ink is transferred to the substrate, it would be better that the viscosity becomes larger quickly [53].

The relationship between the viscosity and the stress rate of offset ink was studied by Liu [53, 54]; it indicates that, using the power law model or the Bingham plastic fluid model can better describe the rheological characteristics of offset ink. Using Brookfield rheometer, the relationship between shear stress and shear rate of yellow ink under shear stress mode was determined by Chu et al. [51]. The results of the experimental data are shown in Table 1. It is observed that, as the shear stress and shear rate increases, the ink viscosity first increases to 317.42 Pa s and then decreases.

The experimental data of the ink at normal temperature have been analyzed and fitted in accordance with Eq. (4) and tested against other models. The results are shown in Fig. 1. The model parameters are illustrated in Table 2. Because the shear rate and shear stress begin to change from 0, the (0, 0) is seen as a data point to ensure that the fitted model passes through this point. Figure 1 indicates that the fitting results of Bingham model are the most unsatisfactory. The best fitting models are power law model and Carreau model, and their stability indices, R^2 , are 0.9872 and 0.9965, respectively. The closer the stability index is to 1, the better the consistency of the curve fitting and the experimental data. Because there are many parameters in the Carreau model, the relationship between the shear rate and the shear stress is more complicated and difficult to solve [51]. Therefore, the power law model is used to interpret the behavior of metal NP conductive inks in this paper. At normal temperature, the consistency coefficient k is 270.08 Pa s, and power law index, n , is 0.7939.

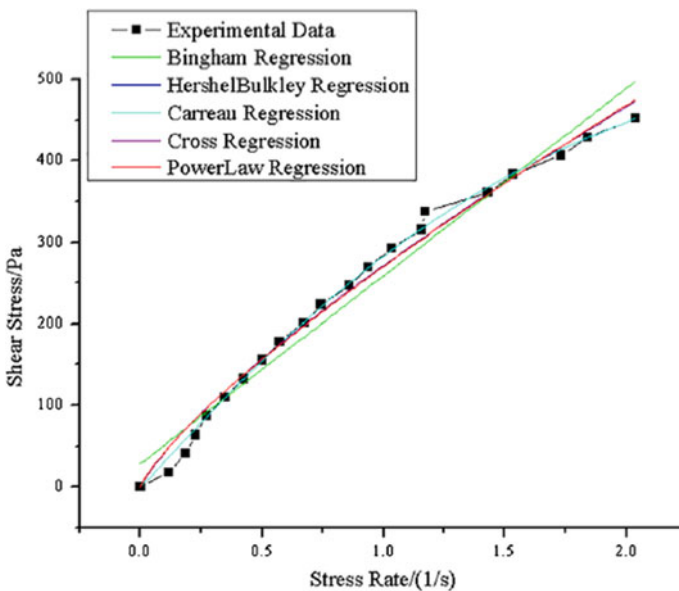


Fig. 1 Rheological model fitting of conductive ink at normal temperature [51]. (Color figure online)

Table 2 Fitting parameters of ink fluid model [51]

Rheological model	k (Pa s ⁿ)	n	η_0 (Pa s)	η_∞ (Pa s)	λ (s)	τ_0 (Pa)	η_p (Pa s)	R^2
Bingham						28.74	230.14	0.9697
Herschel-Bulkley	270.08	0.7938				1.1×10^{-21}		0.9855
Carreau		0.9	317.68	1.49×10^{-10}	0.543			0.9965
Cross		0.7184	1140.95	8.76×10^{-12}	32.57			0.9868
Power law	270.08	0.7939						0.9872

Table 3 Fitting of shear stress-shear rate model of metal NP conductive ink

Shear rate (s ⁻¹)	[Ag] Shear stress (Pa)	[Cu] Shear stress (Pa)	[Au] Shear stress (Pa)	[Al] Shear stress (Pa)	[Ni] Shear stress (Pa)
0.1160	3.06	0.40	3.70	0.68	0.94
0.1855	8.88	1.20	10.26	1.77	2.42
0.2273	15.66	2.10	17.34	2.85	3.90
0.2733	24.16	3.29	26.20	4.19	5.75
0.3482	36.61	5.25	39.86	6.39	8.76
0.4254	51.50	7.71	56.28	9.04	12.39
0.5031	68.64	10.66	75.22	12.11	16.60
0.5730	86.98	13.86	95.25	15.31	20.99
0.6739	111.30	18.49	123.01	19.94	27.33
0.7435	133.71	22.63	147.55	23.88	32.72
0.8595	165.02	29.06	183.98	30.07	41.21
0.9378	192.92	34.58	215.10	35.14	48.17
1.0349	226.00	41.48	252.94	41.47	56.84
1.1581	266.12	50.38	300.21	49.60	67.98
1.1714	287.73	53.94	320.75	52.36	71.76
1.4320	359.97	72.33	412.72	69.28	94.95
1.5341	403.96	82.46	463.95	78.00	106.90
1.7313	470.83	99.82	547.89	93.32	127.90
1.8427	522.21	112.33	608.72	103.84	142.33
2.0400	595.92	132.25	701.91	120.98	165.81

To establish similar relationships between shear stress, shear rate, and ink viscosity of our chosen metal nanoparticle conductive inks, Eqs. (1) and (4) have been used to determine both shear stress and specific viscosity values of each metal NPs ink. The results are shown in Tables 3 and 4, respectively. The results of these relationships are shown in Figs. 2 and 3, respectively.

Viscosity and Temperature of Conductive Ink

The relationship between the viscosity and temperature of offset ink, reported by Zhang [49] and Versteeg and Malalasekera [55], shows that the viscosity–temperature relation of offset ink can be expressed as in Eqs. (5a) and (5b). The viscosity of the yellow ink was measured at different temperatures. The relevant experimental data are shown in Table 5. The relationship between viscosity and thermodynamic temperature was obtained by refitting the data. The results are illustrated in Fig. 4. The specific model parameters are shown in Table 6. The relationship between the viscosity and the absolute temperature can be represented as follows,

Table 4 Fitting of viscosity-shear rate model of metal NP conductive ink

Shear rate (s ⁻¹)	[Ag] Specific viscosity (Pa s)	[Cu] Specific viscosity (Pa s)	[Su] Specific viscosity (Pa s)	[Al] Specific viscosity (Pa s)	[Ni] Specific viscosity (Pa s)
0.1160	26.37	3.48	31.90	5.90	8.09
0.1855	47.88	6.48	55.30	9.53	13.06
0.2273	68.88	9.26	76.30	12.52	17.16
0.2733	88.41	12.04	95.88	15.35	21.03
0.3482	105.13	15.08	114.47	18.35	25.15
0.4254	121.06	18.13	132.29	21.26	29.14
0.5031	136.44	21.19	149.52	24.07	32.99
0.5730	151.80	24.19	166.24	26.72	36.63
0.6739	165.16	27.44	182.53	29.59	40.56
0.7435	179.83	30.43	198.45	32.11	44.01
0.8595	191.99	33.81	214.05	34.98	47.95
0.9378	205.72	36.87	229.36	37.47	51.36
1.0349	218.38	40.08	244.41	40.07	54.92
1.1581	229.79	43.50	259.22	42.83	58.70
1.1714	245.63	46.05	273.82	44.70	61.26
1.4320	251.38	50.51	288.21	48.38	66.31
1.5341	263.32	53.75	302.42	50.84	69.69
1.7313	271.95	57.66	316.46	53.90	73.88
1.8427	283.39	60.96	330.34	56.35	77.24
2.0400	292.12	64.83	344.07	59.30	81.28

$$\eta = 5.45 \times 10^{-8} e^{\left(\frac{6134.2}{T}\right)} \tag{7}$$

$$\ln \eta = -16.725 + \frac{6134}{T} \tag{8}$$

The experimental data of offset ink, obtained by Zhang [49], are as follows: ln A: (-30.89) to (-16.1), E_a/R: 5506.17–10,926.63. By comparison, it is found that the values of A and E_a/R, in the viscosity-temperature relationship (Eqs. 7 and 8) are reasonable. Therefore, the viscosity-temperature relationship of offset ink can be represented in the form as in relations (7) and (8).

Results and Discussion

In order to evaluate the rheological models that are suitable for the five metal NPs conductive inks, out of the four common models that are most commonly used for low strain rate flows—the power law model, Cross-Williamson model, Carreau model,

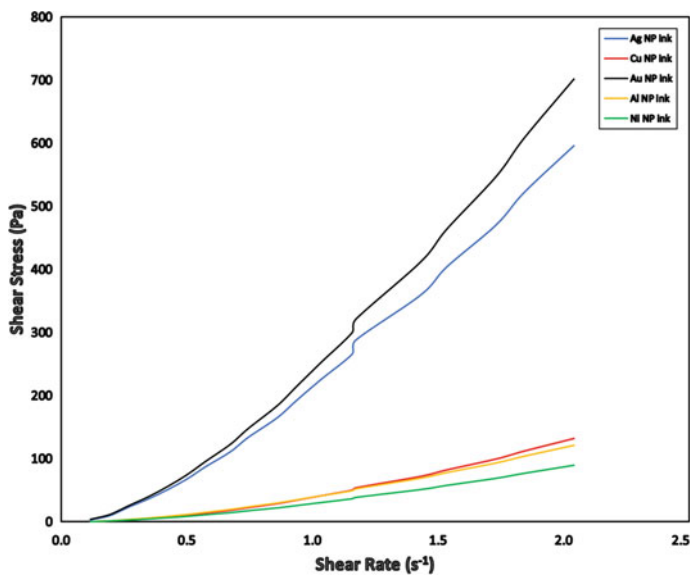


Fig. 2 Rheological model fitting of metal NP conductive inks at normal temperature. (Color figure online)

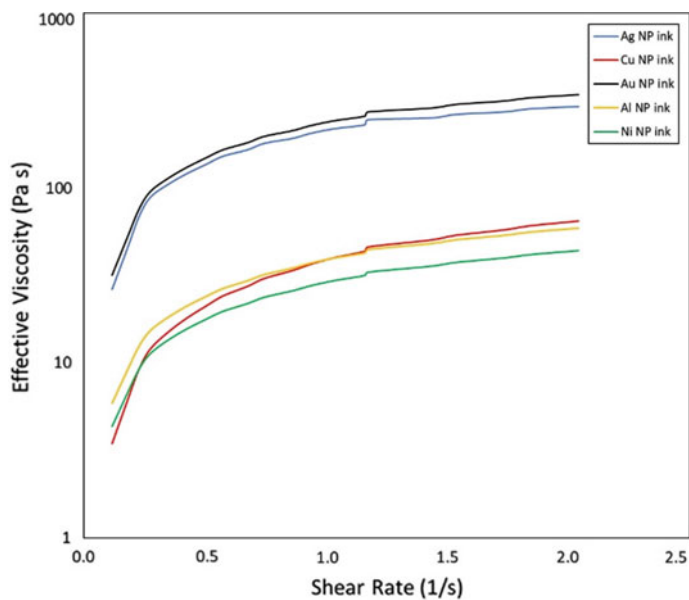


Fig. 3 Rheological model fitting of viscosity-shear rate relationship between different metal NP conductive inks. (Color figure online)

Table 5 Experimental data of viscosity and temperature relationship [49]

T ($^{\circ}\text{C}$)	T (K)	$1/T$ (K^{-1})	Viscosity η (Pa s)	$\ln \eta$ (ln(Pa s))
19.4	292.55	0.003418	69.06	4.2350
22.4	292.55	0.003383	55.10	4.0092
23.6	296.75	0.003369	52.41	3.9591
24.8	297.95	0.003356	46.23	3.8336
26.5	299.65	0.003337	40.59	3.7063
28.1	301.25	0.003320	35.98	3.5831
30.2	303.35	0.003296	33.96	3.5252
32.8	305.95	0.003269	28.37	3.3453
33.8	306.95	0.003258	26.80	3.2884
35.9	309.05	0.003236	21.90	3.0865
38.2	311.35	0.003212	18.60	2.9232
39.5	312.65	0.003198	17.72	2.8747
43.5	316.65	0.003158	13.72	2.6187
45.9	319.05	0.003134	12.42	2.5196

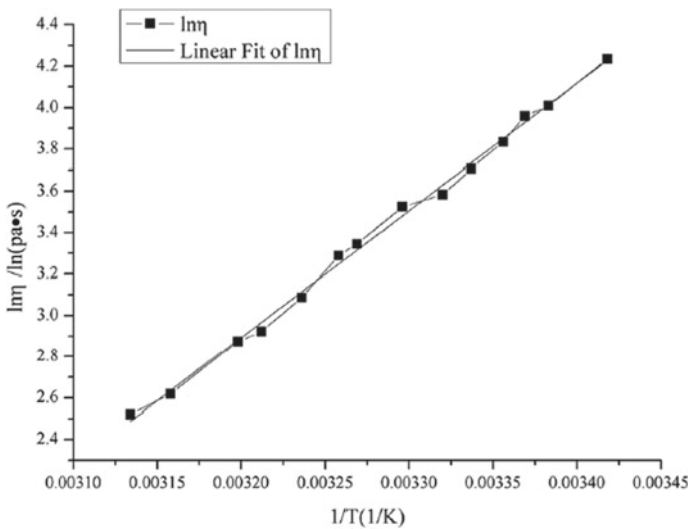


Fig. 4 Relationship between the natural logarithm of the ink viscosity and the reciprocal of thermodynamic temperature [49]

Table 6 Parameters after refitting; the model parameters are described in relations (5a) and (5b) [49]

$\ln A$ (ln(Pa s))	A (Pa s)	E_a/R (K)	E_a (KJ/mol)
-16.725	5.45×10^{-8}	6134.2	51

and Bingham model, the power law model was chosen to interpret the results. The power law model is simple, with only two variables, and is one of the most frequently used models in engineering applications. However, it significantly overestimates the viscosity (η_0) for zero shear strain rate. The Cross–Williamson model, with three parameters, also overestimates the zero shear rate viscosity, while it predicts smoother or longer transitions from the zero shear to the power law behavior. The Carreau model predicts η_0 relatively well but predicts a very sharp transition from the low shear plateau to the power law behavior. Finally, the Ellis model is described as a function of shear stress and predicts η_0 and a shear-thinning (power law model) behavior well at moderate shear strain rates. Figure 1 and Table 1 compare experimental results of offset yellow ink flows with the four model predictions. In Fig. 1, shear stress variation versus shear strain rate are shown, and in Table 2, the parameter values of the five models are listed, as well as the stability index R^2 between the model predictions and experimental data. The model predictions were performed by using the viscosity estimated with Eqs. (1) and (4). The index (n) included in the power law model indicates a Newtonian fluid ($n = 1$), shear-thinning behavior ($n < 1$), or shear thickening behaviors ($n > 1$). In Fig. 3, the predictions of the rheological models on the viscosity variations for shear strain rates for the five metal NP conductive inks, at varying concentrations, are shown. All the five ink flows exhibit shear-thinning behaviors as the viscosity reaches a maximum and begins to plateau at higher shear rates.

Finally, through the simulation and analysis of the metal NP conductive ink fluids, the variations of shear stress with respect to shear strain rate are shown in Figs. 1 and 2. The shear stress is calculated using Eq. (1), and the shear strain rate is obtained by power law model using Eq. (4). As shown in Eq. (4), the slopes of profiles in Figs. 1 and 2 correspond to the ink viscosity. Due to a higher Ag, Cu, Au, Al, and Ni content, the ink flows in Fig. 3 have a stronger nonlinearity in the profile. The ink viscosities, based on Ag and Au NPs, are much higher at similar concentrations compared to Cu, Al, and Ni NPs due to their higher molecular weight differences. Table 4 also compares the representative viscosities, shear rate and the ink concentrations estimated by the experiments and the model. The representative viscosities have been determined with the asymptote of the viscosity at large shear strain rates using the power law model.

Conclusion

In conclusion, rheological behavior of five different metal NP conductive inks were investigated using the power law model. These inks exhibit non-Newtonian characteristics and can be used in printed electronics utilizing inkjet printing technology. The proposed rheological model is suitable for metal nanoparticle conductive ink development with desirable rheological properties. We found that all the ink flows exhibit shear-thinning behaviors and that the non-Newtonian characteristics of the ink flows become stronger as the metal nanoparticle contents in the ink increases.

Among the five metal nanoparticles considered, inks with Ag and Au nanoparticles show higher viscosities at higher shear rate with Au NPs being the highest. Cu, Al, and Ni nanoparticles have much lower viscosities at varying concentrations. These differences in rheological properties are due to the differences in their molecular weights. Based on the results obtained, the power law model can be used to predict the rheological behavior of conductive inks for inkjet printing and printed electronics applications. A strong linear relationship between ink viscosities and inverse temperature, based on Arrhenius' law, has been established.

References

1. Krebs FC (2009) Fabrication and processing of polymer solar cells: a review of printing and coating techniques. *Sol Energy Mater Sol Cells* 93(4):394–412. <https://doi.org/10.1016/j.solmat.2008.10.004>
2. Ahn SH, Guo LJ (2008) High-speed roll-to-roll nanoimprint lithography on flexible plastic substrates. *Adv Mater* 20(11):2044–2049. <https://doi.org/10.1002/adma.200702650>
3. de Gans B-J, Duineveld PC, Schubert US (2004) Inkjet printing of polymers: state of the art and future developments. *Adv Mater* 16:203–213
4. Xu T, Jin J, Gregory C, Hickman JJ, Boland T (2005) Inkjet printing of viable mammalian cells. *Biomaterials* 26:93–99
5. Tekin E, Smith PJ, Hoepfner S, van den Berg AMJ, Susha AS, Rogach AL, Feldmann J, Schubert US (2007) Inkjet printing of luminescent CdTe nanocrystal–polymer composites. *Adv Funct Mater* 17:23–28
6. Lee HH, Chou KS, Huang KC (2005) Inkjet printing of nanosized silver colloids. *Nanotechnology* 16(10):2436–2441. <https://doi.org/10.1088/0957-4484/16/10/074>
7. Tseng WJ, Chen CN (2006) Dispersion and rheology of nickel nanoparticle inks. *J Mater Sci* 41(4):1213–1219. <https://doi.org/10.1007/s10853-005-3659-z>
8. Prasad P, Reddy AV, Rajesh PK, Ponnambalam P, Prakasan K (2006) Studies on rheology of ceramic inks and spread of ink droplets for direct ceramic ink jet printing. *J Mater Process Technol* 176(1–3):222–229. <https://doi.org/10.1016/j.jmatprotec.2006.04.001>
9. Izu N, Shen RH, Shin W, Itoh T, Nishibori M, Matsubara I (2009) Preparation of core-shell type cerium oxide/polymer hybrid nanoparticles for ink-jet printing. *J Ceram Soc Jpn* 117(1366):769–772
10. Roberts MT, Mohraz A, Christensen KT, Lewis JA (2007) Direct flow visualization of colloidal gels in microfluidic channels. *Langmuir* 23(17):8726–8731. <https://doi.org/10.1021/la700562m>
11. Curtin DM, Newport DT, Davies MR (2006) Utilising μ -PIV and pressure measurements to determine the viscosity of a DNA solution in a microchannel. *Exp Therm Fluid Sci* 30(8):843–852. <https://doi.org/10.1016/j.expthermflusci.2006.03.014>
12. Degre G, Joseph P, Tabeling P, Lerouge S, Cloitre M, Ajdari A (2006) Rheology of complex fluids by particle image velocimetry in microchannels. *Appl Phys Lett* 89(2):024104–0241043. <https://doi.org/10.1063/1.2221501>
13. Girardo S, Cingolani R, Pispignano D (2007) Microfluidic rheology of non-Newtonian liquids. *Anal Chem* 79:5856–5861. <https://doi.org/10.1021/ac062405t>
14. Mortazavi S (2017) Computational analysis of the flow of pseudoplastic power-law fluids in a microchannel plate. *Chin J Chem Eng* 25:1360–1368
15. Lavrov A (2014) Radial flow of non-Newtonian power-law fluid in a rough-walled fracture: effect of fluid rheology. *Transp Porous Media* 105:559–570
16. Han ZX (2014) Simulation analysis of temperature field of the offset inking system. Xi'an University of Technology, Xi'an

17. Yang C, Gu H, Lin W, Yuen MM, Wong CP, Xiong M, Gao B (2011) Silver nanowires: from scalable synthesis to recyclable foldable electronics. *Adv Mater* 23:3052
18. Kim J, Kim WS (2014) Stretching silver: printed metallic nano inks in stretchable conductor applications. *IEEE Nanotechnol Mag* 8:6
19. Chu T-Y, Zhang Z, Tao Y (2018) Printing silver conductive inks with high resolution and high aspect ratio. *Adv Mater Technol* 3:1700321
20. Shen W, Zhang X, Huang Q, Xu Q, Song W (2014) Preparation of solid silver nanoparticles for inkjet printed flexible electronics with high conductivity. *Nanoscale* 6:1622
21. Cui Z, Poblete FR, Cheng G, Yao S, Jiang X, Zhu Y (2015) Design and operation of silver nanowire based flexible and stretchable touch sensors. *J Mater Res* 30:79
22. Xu F, Zhu Y (2012) Highly conductive and stretchable silver nanowire conductors. *Adv Mater* 24:5117
23. Yao S, Cui J, Cui Z, Zhu Y (2017) Soft electrothermal actuators using silver nanowire heaters. *Nanoscale* 9:3797
24. Kamyshny A, Magdassi S (2014) Conductive nanomaterials for printed electronics. *Small* 10:3515
25. Torrisi F, Hasan T, Wu W, Sun Z, Lombardo A, Kulmala TS, Hsieh G-W, Jung S, Bonaccorso F, Paul PJ, Chu D, Ferrari AC (2012) Inkjet-printed graphene electronics. *ACS Nano* 6:2992
26. Yang W, Wang C (2016) Graphene and the related conductive inks for flexible electronics. *J Mater Chem C* 4:7193
27. Chen K, Gao W, Emaminejad S, Kiriya D, Ota H, Nyein HY, Takei K, Javey A (2016) Carbon nanotubes: printed carbon nanotube electronics and sensor systems. *Adv Mater* 28:4397
28. De Volder MF, Tawfick SH, Baughman RH, Hart AJ (2013) Carbon nanotubes: present and future commercial applications. *Science* 339:535
29. Secor EB, Gao TZ, Islam AE, Rao R, Wallace SG, Zhu J, Putz KW, Maruyama B, Hersam MC (2017) Enhanced conductivity, adhesion, and environmental stability of printed graphene inks with nitrocellulose. *Chem Mater* 29:2332
30. Xu F, Durham JW, Wiley BJ, Zhu Y (2011) Fabrication of functional nanowire devices on unconventional substrates using strain-release assembly. *ACS Nano* 5:1556
31. Xu F, Wang X, Zhu Y, Zhu Y (2012) Highly conductive and stretchable silver nanowire conductors. *Adv Funct Mater* 22:1279
32. Secor EB, Hersam MC (2015) Emerging carbon and post-carbon nanomaterial inks for printed electronics. *J Phys Chem Lett* 6:620
33. Kim D, Moon J (2005) Highly conductive ink jet printed films of nanosilver particles for printable electronics. *Electrochem Solid-State Lett* 8:J30–J33
34. Kim D, Jeong S, Park BK, Moon J (2006) Direct writing of silver conductive patterns: improvement of film morphology and conductance by controlling solvent compositions. *ApplPhys Lett* 89:264101
35. Cao L, Bai X, Lin Z, Zhang P, Deng S, Du X, Li W (2017) The preparation of Ag nanoparticle and ink used for inkjet printing of paper based conductive patterns. *Materials* 10:1004
36. Pan H, Ko SH, Grigoropoulos CP (2008) Thermal sintering of solution-deposited nanoparticle silver ink films characterized by spectroscopic ellipsometry. *ApplPhys Lett* 93:234104
37. Bieri N, Chung J, Hafner S, Poulikakos D, Grigoropoulos C (2003) Microstructuring by printing and laser curing of nanoparticle solutions. *ApplPhys Lett* 82:3529–3531
38. Szczech J, Megaridis C, Zhang J, Gamota D (2004) Ink jet processing of metallic nanoparticle suspensions for electronic circuitry fabrication. *Microscale ThermophysEng* 8:327–339
39. Wu Y, Li Y, Ong BS, Liu P, Gardner S, Chiang B (2005) High-performance organic thin-film transistors with solution-printed gold contacts. *Adv Mater* 17:184–187
40. Park BK, Kim D, Jeong S, Moon J, Kim JS (2007) Direct writing of copper conductive patterns by ink-jet printing. *Thin Solid Films* 515:7706–7711
41. Jeong S, Woo K, Kim D, Lim S, Kim JS, Shin H, Xia Y, Moon J (2008) Controlling the thickness of the thickness of the surface oxide layer on Cu nanoparticles for the fabrication of conductive structures by ink-jet printing. *AdvFunct Mater* 18:679–686

42. Lee YJ, Lee C, Lee HM (2018) Synthesis of oxide-free aluminum nanoparticles for application to conductive film. *Nanotechnology* 29:055602
43. Jo YH, Jung I, Choi CS, Kim I, Lee HM (2011) Synthesis and characterization of low temperature Sn nanoparticles for the fabrication of highly conductive ink. *Nanotechnology* 22:225701
44. Lee H-H, Chou K-S, Huang K-C (2005) Inkjet printing of nanosized silver colloids. *Nanotechnology* 16:2436–2441
45. Layani M, Gruchko M, Milo O, Balberg I, Azulay D, Magdassi S (2009) Transparent conductive coatings by printing coffee ring arrays obtained at room temperature. *ACS Nano* 3:3537–3542
46. Jung I, Jo YH, Kim I, Lee HM (2012) A simple process for synthesis of Ag nanoparticles and sintering of conductive ink for use in printed electronics. *J Electron Mater* 41:115–121
47. Magdassi S, Grouchko M, Toker D, Kamyshtny A, Balberg I, Millo O (2005) Ring stain effect at room temperature in silver nanoparticles yields high electrical conductivity. *Langmuir* 21:10264–10267
48. Shimoni A, Azoubel S, Magdassi S (2014) Inkjet printing of flexible high-performance carbon nanotube transparent conductive films by “coffee ring effect”. *Nanoscale* 6:11084–11089
49. Zhang SJ (2012) Synthesis of high-performance rosin modified phenolic resin and its vehicles’s rheological behaviors. Fujian Normal University, Fuzhou
50. Moreno E, Lares A, Cervera M (2016) Modelling of Bingham and Herschel-Bulkley flows with mixed P1/P1 finite elements stabilized with orthogonal subgrid scale. *J Non-Newton Fluid* 228:1–16
51. Chu H, Lin X, Cai L (2019) Analysis of temperature characteristics of ink fluid based on power law model in microchannel. *AdvMechEng* 11(3):1–15. <https://doi.org/10.1177/1687814019833585>
52. Haj-KacemRB, Ouerfelli N, Herráez JV et al (2014) Contribution to modeling the viscosity Arrhenius-type equation for some solvents by statistical correlations analysis. *Fluid Phase Equilib* 383: 11–20.
53. Liu P (2014) Study on technical methods of online measurement and control for printing quality in offset press. Northwestern Polytechnical University, Xi’an, pp 46–49
54. Liu FP (2007) Numerical calculation and experimentation of permeating depth of power-law printing ink in porous paper printing. *Chin J Process Eng* 7:216–222
55. Versteeg HK, Malalasekera W (1995) An introduction to computational fluid dynamics: the finite volume method. Wiley, Hoboken

Performance of Chromium Doped Zinc Selenide Nanocrystals: Morphological and Fluorescence Characteristics



N. B. Singh, Ching Hua Su, Bradley Arnold, Fow-Sen Choa, Brett Setera, David Sachs, Christopher E. Cooper, Lisa Kelly, and K. D. Mandal

Abstract Chromium doped ZnSe nanocrystals were grown at low temperature using zinc acetate and sodium selenite. A capping agent was used to avoid agglomeration of particles. It was observed that the addition of the capping agent before or after chemical synthesis of ZnSe played a very important role in controlling the size of nanoparticles and to avoid agglomeration. Size of nanoparticles of ZnSe was as small as 10 nm for both doped and undoped material. In a few cases, in spite of preventative measures, clustering of particles produced large agglomerates at room temperature. Cr-ZnSe nano particles showed fluorescence at different wavelengths compared to Cr-doped bulk crystals. Cr-doped nanocrystals showed higher bandgap than PVT grown bulk Cr-ZnSe crystals. The fluorescence intensity for Cr-ZnSe nanoparticles was significantly higher compared to undoped ZnSe nanoparticles.

Keywords ZnSe · Nanocrystals · Physical vapor transport · Crystal · Optical properties

Introduction

Zinc sulfide (ZnS), zinc selenide (ZnSe), and their solid solutions have shown multifunctionality for their wide scale applications in industrial devices and components. Pure zinc sulfide, zinc selenide, and their solid solution have been used for optical windows and coatings due to low absorption coefficient across a wide wavelength range allowing both a desirable degree of transparency and high laser damage

N. B. Singh (✉) · C. H. Su · B. Arnold · F.-S. Choa · B. Setera · D. Sachs · C. E. Cooper · L. Kelly · K. D. Mandal
University of Maryland Baltimore County, 100 Hilltop Circle, Baltimore, MD 21250, USA
e-mail: singna@umbc.edu

C. H. Su
EM31, NASA Marshall Space Flight Center, Huntsville, AL 35812, USA

K. D. Mandal
Indian Institute of Technology, Banaras Hindu University, Varanasi, UP, India

threshold. A large number of papers have been published [1–5] to evaluate their suitability as the laser host and lasing materials. Along with many laser host materials, ZnS and ZnSe have been used to dope with rare earth and transition-metal ions (Cr^{2+} , Co^{2+} , Ni^{2+} and Fe^{2+} ions) to activate for lasing in the mid-wave infrared (MWIR). Significant progress has been made on the growth and effect of vapor transport, fluid flow, and convection driven effects on the quality of ZnSe by physical vapor transport was further studied by Su et al. [5–8]. Doping of ZnSe with rare earth or transition-metal ion creates point and line defects in the matrix, which ultimately affects the electrical and optical characteristics. As transition-metal dopants have different sizes and oxidation states, these create voids, precipitates, and other types of defects in the bulk. We synthesized the nanoparticles of chromium doped ZnSe and evaluate properties to compare with bulk materials.

Experimental Methods

PVT Grown Bulk ZnSe Crystal

Cr-doped ZnSe bulk crystals were grown to compare the performance with Cr-doped nanocrystal. The details of bulk crystals by the physical vapor transport method and detailed parameters are published earlier [5–8]. Crystals were grown in an independently controlled three-zone furnace. The chromium was added in the source material as chromium selenide and amount was 0.2 wt. percentage of total ZnSe mass in the source material.

Synthesis of ZnSe Nanoparticles

Nanocrystals of zinc compounds have been grown and studied by variety of high temperature solution and microwave methods [9, 10]. We have used a low temperature reactive solution synthesis method [8] using zinc acetate and sodium selenite solution. We prepared and dissolved 0.1 M zinc acetate in 50.0 mL dimethylformamide under constant stirring for 15 min. After complete dissolution, 5 drops (~1 mL) of thioglycerol was added as a capping agent to prevent the clustering/aggregating of particles. This solution was then reacted with a prepared 0.45 M sodium selenite in water. 15 mL sodium selenite solution was mixed with zinc acetate solution. As soon as mixing began, the formation of a cloudy greyish orange precipitate was observed. After complete mixing, the solution turned cloudy and had a noticeable orange color. This solution was heated at 95 °C for a period of 1 h to complete the reaction. Solution was stirred continuously to avoid segregation during heating. The color of the hot solution slowly faded, and two visible layers were formed: a grey-green colored colloidal precipitate on the bottom while the top layer was clear.

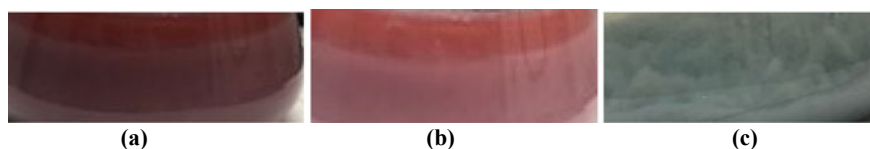


Fig. 1 Color transition in the Cr-doped ZnSe nanoparticles **a** at early stage of heating, **b** after 30 min of heating, and **c** final color of Cr-doped ZnSe. (Color figure online)

Synthesis of Cr-Doped ZnSe Nanoparticles

Cr-doped ZnSe was prepared similar to that of described in Section “[Synthesis of ZnSe Nanoparticles](#)” for pure ZnSe nanoparticles. In a solution of 0.1 M Zinc acetate prepared in 50.0 mL dimethylformamide was added and stirred for 15 min. For chromium doping, 0.09 g of chromium chloride hexahydrate was added and stirred into the solution. The temperature of the solution was raised to 95 °C and maintained for 1 h. During heating, the solution turned a dark magenta red color. After 30 min, the dark red magenta color started fading. After one hour, two layers were observed once more with a clear solution on the top. The colloidal/precipitate layer was a green-grey light color in the bottom portion. At this stage, we added 3–5 drops (~1 mL) of isopropanol to the solution while continuously stirring. Figure 1 shows the transition and colors observed at different stages of the synthesis.

Effect of Pre-capping Agent in the Solution

The early steps of synthesis were similar to Sections “[Synthesis of ZnSe Nanoparticles](#)” and “[Synthesis of Cr-Doped ZnSe Nanoparticles](#).” A solution of 0.1 M zinc acetate solution was prepared in 50.0 mL dimethylformamide, and solution was stirred for a period of 15 min to mix homogeneously. One mL of capping agent thioglycerol was mixed in to prevent the clustering/lumping of particles. A 0.4 M solution of sodium selenite was prepared in 15 mL water solvent. The sodium selenite solution was added drop wise to the zinc acetate solution for the synthesis of ZnSe nanoparticles.

We observed colloidal precipitate formation as soon as reaction started seen as a color change to cloudy white. Chromium chloride hexahydrate (0.1 g) was added as the dopant, and the solution was stirred and heated to 95 °C for a period of 1 h. Similar to case of post capping, the solution turned an orange red color during heating. The color faded gradually during heating until disappearing completely after approximately 30 min. The bottom precipitate layer was a green-grey color, and the solution layer was clear as seen in Fig. 1c. One mL of isopropanol was stirred into the solution, and the color change was noted. Color transition in the Cr-doped ZnSe nanoparticles, when pre-capping process was used, was different from the post capping tests. A light green color after 30 min of heating was observed which changed to a green precipitate.

Measurement of Size by Scattering Method

Particle size was determined by light scattering experiments using the dynamic light scattering apparatus Malvern Zetasizer Nano-ZS is shown in Fig. 2. Size distribution data supported by scattering studies indicated large number of particles smaller than 1 nm. Agglomerates were apparent in the ranges of 300–1000 and 3000–5000 nm. These agglomerates were expected since the solution was kept for a term of one month to evaluate the coarsening effect. This data corroborates the SEM morphology, which showed clusters and coarsened particles of different sizes, appearing as small needles or plates. The synthesized nanoparticles had polydispersity but stayed in the three described ranges.

Bulk and Micromorphology

As grown bulk, crystal was cut, and a 1 cm thick slab was polished on parallel surface for detailed characterization. The bulk matrix did not show discontinuity, precipitate or voids, and crystal slab was free from the gross defects. Scanning electron microscope (SEM) model NOVA NANOSEM 450 under a voltage of 5 and 10 kV determined the morphology of crystals similar to that described in Ref. [11].

Optical Characterization

We studied absorption, excitation, and emissive characteristics to measure the steady-state luminescence spectral properties in the near-infrared wavelength regions. Measurements performed using an Edinburg F920 fluorescence spectrometer with

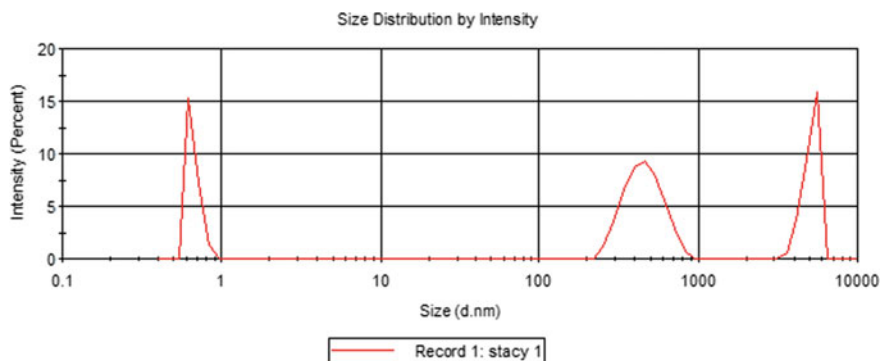


Fig. 2 Size distribution observed by scattering data taken by dynamic light scattering. (Color figure online)

xenon source and cadmium selenide detector for the emission and photoluminescence studies. The Acton SpectraPro 500i software was used for this study. A He-Ne (35 mW) laser was used as an excitation source. All studies were performed using 1-s acquisition time and one nm steps for 10 accumulations.

Results and Discussion

Bulk Transparency

We fabricated chromium doped ZnSe (Cr-ZnSe) boule into slabs by cutting and polishing parallel surfaces. Figure 3 shows the fabricated Cr-ZnSe disks used for detailed characterization. The thickness of the disks was >1.8 cm. We did not observe any gross defects such as inclusions, precipitates, and distortion in the polished crystals. As shown in the transparency results using wire mesh, there was no optical distortion in the crystal.

Micromorphology of Cr-ZnSe Crystal and Nanoparticles

Similar to that of ZnSe crystal, scanning electron microscope NOVA NANOSEM 450 system was used to determine micromorphology. Figure 4 shows morphology of Cr-ZnSe crystals at increasing magnifications.

Figure 5 showed regular patterns of grains oriented in a direction. We observed that facets of few micrometer sizes also grew in the same orientation. Morphology indicated that interface breakdown during growth had created multiple line defects. Morphology showed small crystallites on the facets of the crystals. Micromorphology did not indicate micro voids, micro bubbles, or discontinuity in the crystal. Large steps and grains indicated layered growth of facets and ridges.



Fig. 3 Fabricated Cr-ZnSe slab from the grown crystal. (Color figure online)

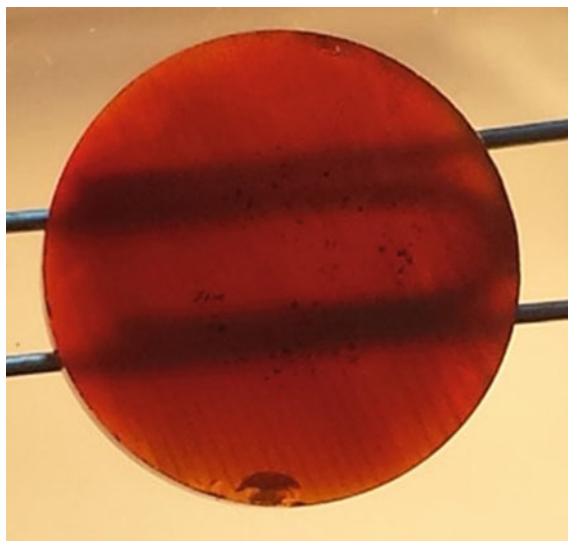


Fig. 4 Optical transparency of Cr-ZnSe bulk crystal with metal clip. (Color figure online)

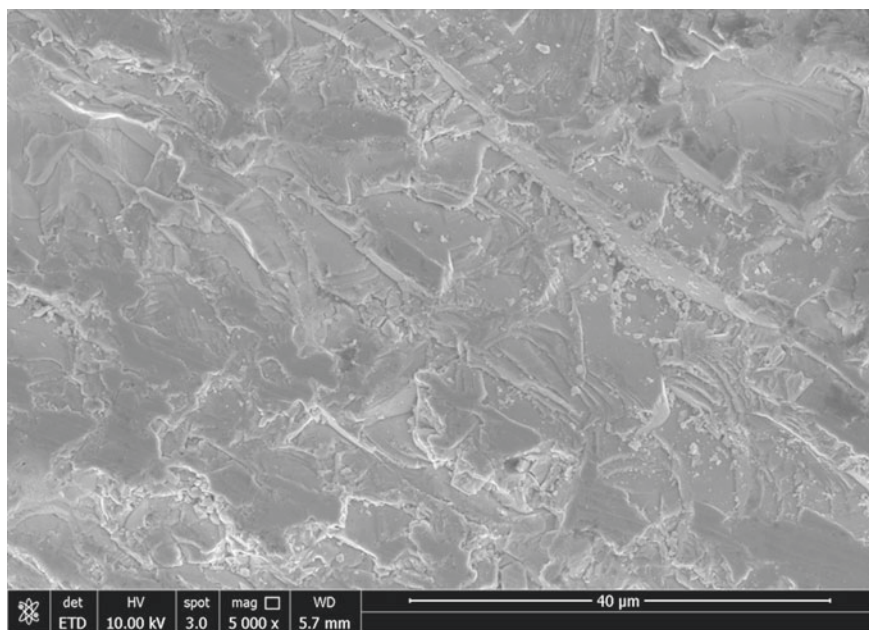


Fig. 5 Microstructure of Cr-ZnSe crystals showing faceted grains and boundaries

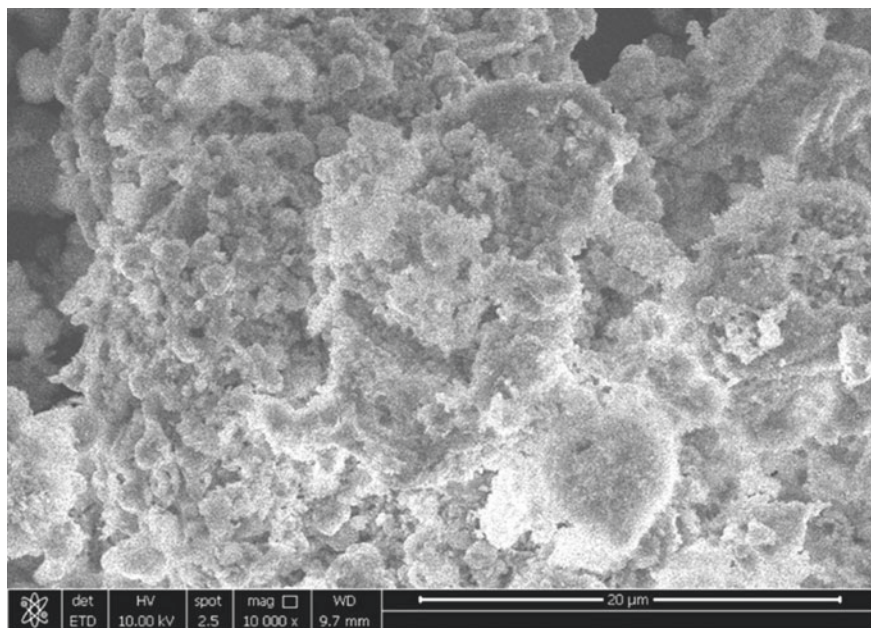


Fig. 6 Aged (one-month) material in solution at room temperature

The morphology of Cr-doped ZnSe nano particles is shown in Fig. 6. The morphology observed for the large portion of undoped ZnSe material was free from clustering. Figure shows the morphology of nanoparticles which were placed for a period of one months at room temperature to evaluate stability and segregation. It appears that large number of clusters were grouped together. This indicates that some type of coarsening is occurring at room temperature in the doped material as function of time.

Optical Characteristics of Cr⁺² Doped ZnSe Crystals

Optical characterization was performed by exposing the crystal surface using He-Ne laser to different laser wavelengths at room temperature. Figure 7 shows Raman scattering of Cr-doped bulk crystal sample. The observed transverse (TO) and longitudinal (LO) peaks at 233.1 and 279 cm^{-1} (small peak) for the x -axis (first order) polarization Raman peaks are slightly shifted relative to pure ZnSe peaks [2, 4]. Further studies using a longpass filter that can efficiently transmit lower than 160 cm^{-1} may provide more information on peaks close to the excitation wavelength.

Figure 8 shows the results of fluorescence spectroscopy of the Cr-ZnSe crystal. In some parts of the crystal, we observed slight shifts in the maximum peak. This shift may be due to the segregation effects causing variation in the solute (chromium)

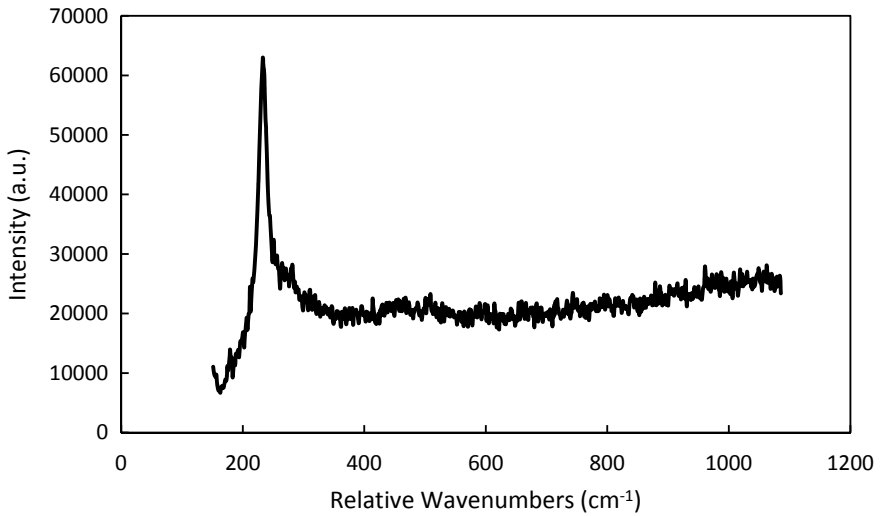


Fig. 7 Transverse and longitudinal TO and LO at 233.1 and 279 cm^{-1} for the *x*-axis (first order) polarization Raman peaks. The notch filter removed signal closer than 200 relative wavenumbers away from fundamental

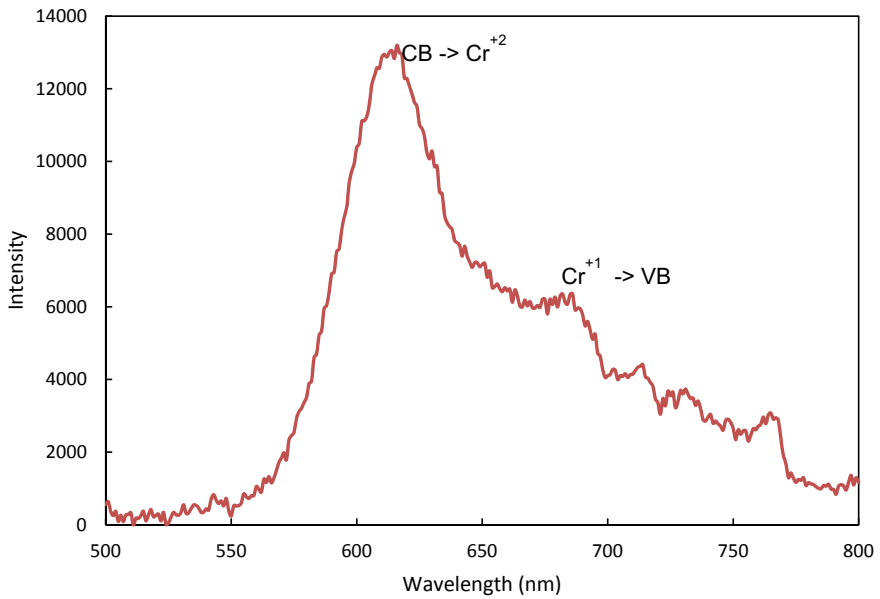


Fig. 8 Fluorescence spectrum of ZnSe-Cr^{+2} crystal showed different intensity (peaks at 618 nm peaks, weaker peaks at 687, 767 nm) using an excitation wavelength of 350 nm. (Color figure online)

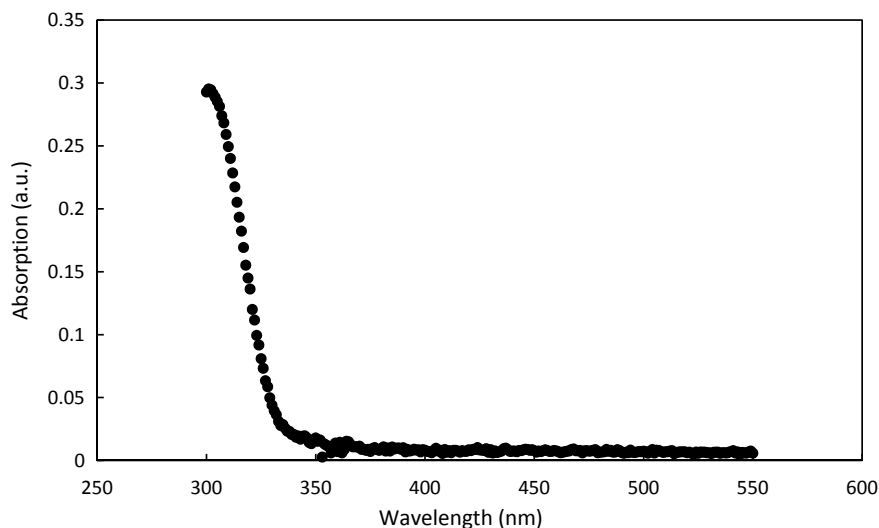


Fig. 9 Absorption characteristics of post capped Cr-ZnSe nanoparticles

concentration in the sample. Crystals showed emission around 618 nm, but different excitation showed change in intensity. We observed some weaker peaks at 687 and 767 nm wavelength also. Data on Cr-doped ZnSe were taken with excitation wavelengths at 850, 860, 870, and 880 nm with a 645 nm filter, and there were slight shifts in peaks [4] with different excitation wavelengths.

Spectral Characteristics

The absorption curve for the Cr-ZnSe nanoparticles is shown in Fig. 9. Although the direct bandgap of the bulk ZnSe was observed approximately 2.7 eV, the cutoff wavelength for Cr-ZnSe nanoparticle observed in Fig. 9 indicates a bandgap of 3.8 eV. This indicates that synthesized nanoparticles had a significantly large bandgap compared to the chromium doped or sulfur doped bulk ZnSe crystals. The fluorescence spectra of pure ZnSe and Cr-ZnSe reduced temperature synthesized nanoparticles were determined at room temperature. Fluorescence was induced for the nanoparticles in solution using 280 nm wavelength excitation source. Both doped and undoped samples showed high intensity peaks around 336 nm. This value is much higher than Cr-ZnSe bulk crystal [4], where scattering was at 233 and a weak peak at 279 nm. The positions of peaks in Figs. 10 and 11 are closer to 390 and 420 nm closed to that observed for the bulk Cr-ZnSe. A sharp scattering peak in the lower wavelength region (<350 nm) is indicative of scattering through monodispersed particle. Small splitting and peaks may indicate size dependent scattering. The shift of fluorescence peaks and absorption spectra may be due to Stokes shift. In addition, the small

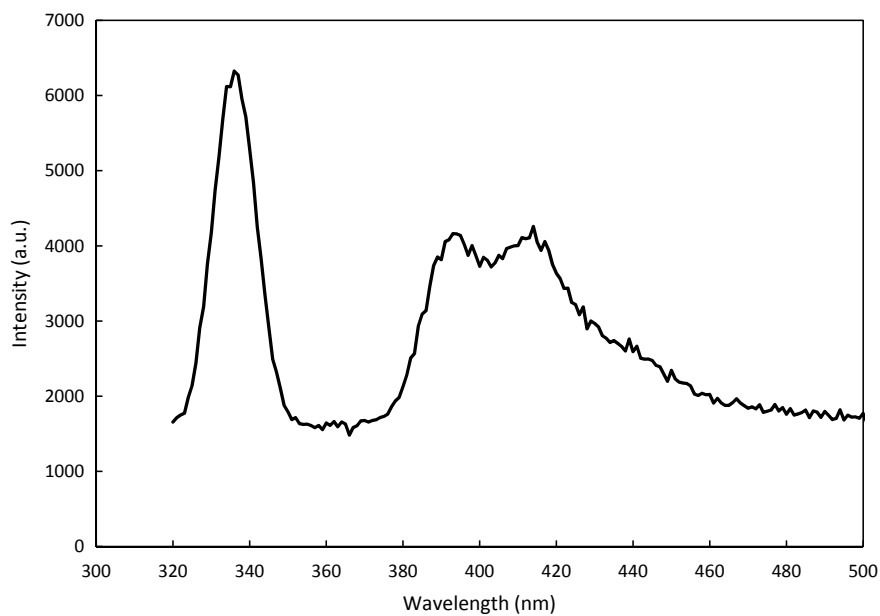


Fig. 10 Fluorescence spectrum of undoped ZnSe nanoparticles

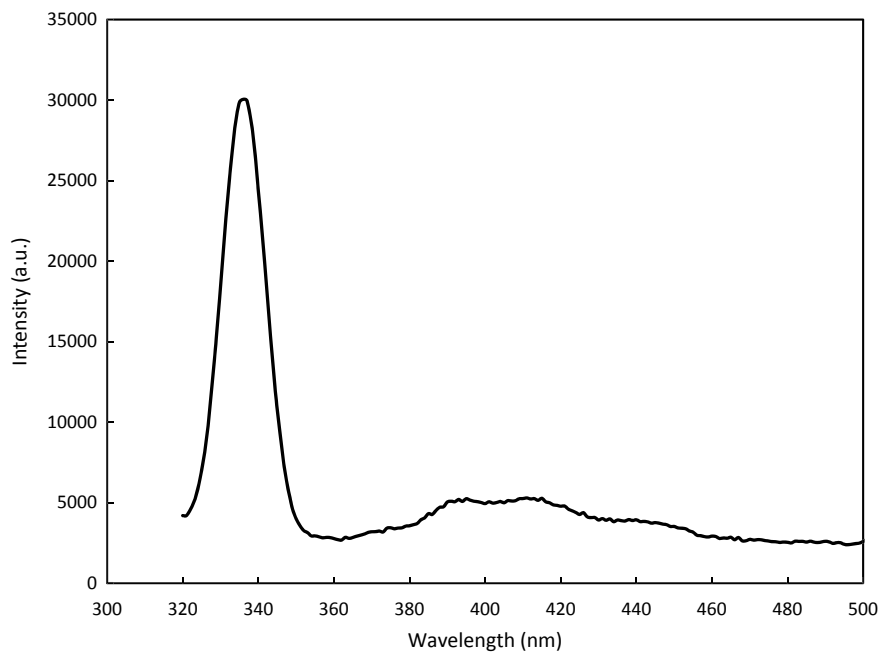


Fig. 11 Fluorescence spectrum of Cr-ZnSe nanoparticles

shoulder peaks observed in each case can be attributed to the size variation of sizes and different trap sites.

It appears that in case of nanoparticles in solvent, the solvation cage along with agglomeration may cause new set of bands to appear. The rearrangement energy for potentially broad structures changes with particle size and degree of solvation rearrangement difficulty may cause changes in electrical energies (bandgap) allowing different transitions and thus new bands.

In case of chromium, doped sample intensity at 380 nm was at least one order (X -axis scale is different) of magnitude higher. Although the mechanism of increased intensity is not clear, we expect the difference of one order of magnitude intensity may be due to the residual impurities in the solvent and source materials. Since CrCl_3 solution was used during the synthesis for doping, the residual HCl may have contained dissolved residual impurities and may be the reason for higher intensity.

Summary

Nanocrystals of chromium doped ZnSe were synthesized and characterized. The synthesis of nanoparticles of the pure and doped ZnSe was carried out using zinc acetate and sodium selenite. A capping agent was used to avoid agglomeration of particles. The pre-addition of capping agent before crystallization of ZnSe produced significantly lower clustering of nanoparticles and inhibited formation of needles and plates. Optical characterization including absorption, fluorescence, and morphology were determined to determine the effect of doping and size on the performance of material. Both pure and Cr-doped ZnSe nanoparticles showed a much higher bandgap compared to that of bulk ZnSe. The doped Cr-ZnSe nano particles showed order of magnitude higher emission intensity compared to pure ZnSe nanoparticles.

Acknowledgements The authors would like to acknowledge the support of Space Life and Physical Sciences Division, Human Exploration and Operations Mission Directorate, NASA Headquarter through NASA Marshall Space Flight Center. The authors are also grateful to the program and management team for technical discussion during this study.

References

1. Reddy RB, Scheppler K, Moore E, Hoelscher J, Vangala S, Clafin B, Singh NB, Evan J (2015) Surface characterization studies of orientation patterned ZnSe doped with Cr^{2+} . In: Konstantin L (ed) SPIE proceeding: nonlinear frequency generation and conversion: materials, devices, and applications XIV. Vodopyanov vol 9347: XIV, 93471–11
2. Singh NB, Su CH, Arnold B, Choa FS (2016) Optical and morphological characteristics of ZnS-ZnSe solid solution. *J Opt Mater* 60:474–480

3. Singh NB, Su CH, Arnold B, Choa FS, Cullum B, Sova S, Cooper C (2019) Morphological and optical characteristics of transition metal doped PVT grown zinc selenide single crystal. *J Cryst Res Technol* 180023:1–10
4. Steinbruegge KB, Henningsen T, Hopkins RH, Mazelsky R, Melamed NT, Riedel EP, Roland GW (1972) Laser properties of Nd(+3) and Ho(+3) doped crystals with the apatite structure. *Appl Opt* 11(5):999–1012
5. Su CH, Feth S, Wang LJ, Lehoczky SL (2001) Photoluminescence studies of ZnSe starting materials and vapor grown bulk crystals. *J Cryst Growth* 224:32–40
6. Su CH, Feth S, Zhu S, Lehoczky SL, Wang LJ (2000) Optical characterization of bulk ZnSeTe solid solutions. *J Appl Phys* 88:5148–5152
7. Su CH, Sha YG, Volz MP, Carpenter B, Lehoczky SL (2000) Vapor growth and characterization of ZnSeTe solid solutions. *J Cryst Growth* 216:104–112
8. Su CH, George MA, Palosz W, Feth S, Lehoczky SL (2000) Contactless growth of ZnSe single crystals by physical vapor transport. *J Cryst Growth* 213:267–275
9. Despande A, Singh SB, Kazemian AM, Pascricha R, Kulkarni SK (2008) Low temperature synthesis of ZnSe nanoparticle. *Mater Lett* 62:3803–3805
10. Sakir M, Kushwaha SK, Maurya KK, Bhagavannarayana G, Wahab MA (2009) Characterization of ZnSe nanoparticles synthesized by microwave heating process. *Solid State Commun* 149:2047–2049
11. Singh NB, Cooper C, Strobbia P, Prasad NP, Su CH, Arnold B, Choa FS (2017) Nanomorphology and performance of pure and doped lead selenide for infrared detector. *Opt Eng* 56(7):077106–077110

Part XXXIX
**Recycling and Sustainability for Emerging
Technologies and Strategic Materials**

Characterisation and Techno-Economics of a Process to Recover Value from E-waste Materials



Md Khairul Islam, Nawshad Haque, and Michael A. Somerville

Abstract Printed circuit boards, collected from Bangladesh, were melted to determine the proportion of metal, ceramic and volatile components. The concentration and amount of valuable elements in the e-waste were calculated from the analysis of the metal and ceramic phases. This information was used to design a simple three-stage process to recover the valuable components. The stages included smelting, electrorefining of a copper rich anode and melting of anode slimes and reduction of a tin rich slag. In this process, copper would be recovered as a high purity cathode, silver and gold recovered as a precious metal bullion from the processed anode slimes and tin recovered from the reduction of tin rich slag. A flowsheet simulation of this process was used to estimate the size of unit operations and process streams. Capital costs of the process situated in Bangladesh were estimated based on the equipment required and included capital on-costs. Operating costs were estimated from power, labour and consumables required as well as operating factors such as maintenance and administration. Cash inputs to the process were estimated from the value of product streams. The preliminary financial viability of the process was estimated, and net present value and internal rate of return are determined.

Keywords E-waste · Value recovery · Operating costs · Capital costs · Smelter

Introduction

The sustainable treatment of e-waste is a growing problem throughout the world. Ideally a commercially and technically viable process would remove hazardous materials from waste processing systems while at the same time extract the embedded

M. K. Islam · N. Haque (✉) · M. A. Somerville
CSIRO Mineral Resources, Private Bag 10, Clayton South, VIC 3169, Australia
e-mail: nawshad.haque@csiro.au

M. K. Islam
Bangladesh Council of Scientific and Industrial Research (BCSIR), IMMM, Joypurhat 5900,
Bangladesh

value in e-waste materials which could pay for the treatment and provide a financial return to the e-waste processor.

Although many e-waste treatment processes have been proposed or tested, possibly the only commercially successful route is through a primary metal smelter [1]. In this option, the valuable components can be recovered in conventional metallurgical circuits, the plastic components can be combusted and the heat used as a supplementary fuel and the inorganic components can be fixed in the primary smelting slag. However, in many parts of the world, this is not possible because a primary smelter is removed from large population centres or is not present in the country.

Bangladesh is a small country with a high population density but without a primary metal smelter. Bangladesh suffers from a growing problem of e-waste generation and disposal. A possible solution could be a small-scale smelting-based process to extract value from e-waste at the local level. Work at CSIRO has attempted to establish the commercial feasibility of such a process.

In this study, samples of mobile phone printed circuit boards (PCBs) from Bangladesh were collected. The work entailed three main stages including e-waste characterisation, flowsheet modelling of a process to extract value from the e-waste materials and a preliminary techno-economic study of the proposed treatment process.

E-waste Generation in Bangladesh and Characterisation

Bangladesh is a developing country with a population of around 170 million with a very high population density. Around 2.7 million tonnes of e-waste are generated every year in Bangladesh, including almost 2.2 million tonnes from ship breaking yards. The second highest e-waste generation comes from television sets (0.182 million tonnes) [2]. These are mostly from developed countries through transboundary transport. However, internal generation of e-waste is not small and is growing. Over the last 10 years, the Bangladesh IT sector generated around 35,000 metric tonnes of e-waste. More than 500,000 computers were in use in 2004 and this number has been growing at 11.4% annually [2]. The number of mobile phones disposed into the waste stream every year was estimated by a group of researchers. They followed the methodology of surveying metropolitan shopping centres, repair and selling shops, taking interviews, analysing reports of the regulatory authorities and analysing the data of six mobile phone operators [3]. Around 990 m³ or 1125 tonnes of mobile phone -based e-waste was added to the stream each year according to their report.

Experimental

In this work, end-of-use (EOU) PCBs of mobile phones were collected from local electronic repair shops in the Joypurhat district of northern Bangladesh. Most of the phones were an early button type variety, while some were touch screen type just before the emergence of more modern smartphones. The PCBs were categorised in three types depending on their models and brand. The PCBs were physically cleaned through air blowing before being manually cut into 2×3 cm pieces before being further reduced in size to less than 1.5 mm using a rotary cutter.

The shredded PCB samples were mixed thoroughly. Melting and then phase separation of the PCBs were performed in two stages. Firstly, to remove most of the organic material in the PCB, a weighed quantity of sample was placed in an alumina crucible and put into a kiln type furnace which is equipped with a fume extraction and scrubbing system. In this stage, the e-waste sample was heated to 600 °C at a rate of 5 °C/min, held at temperature for 2 h before being cooled to room temperature.

The calcined PCBs were mixed with 30% by weight of borax as a fluxing agent. An alumina crucible was filled with pre-treated e-waste sample, fluxing agent and charcoal. 10 wt% of fine charcoal powder, derived from eucalypt red gum, was added and the top of the crucible was covered by some small charcoal lumps. Charcoal was used to maintain a reducing environment to protect the metallic components from oxidation. The crucible was placed inside a muffle furnace for melting. The furnace was heated to 1200 °C at a heating rate of 180°C/h, held at temperature for 2 h and then cooled to room temperature in situ. The crucible was then taken out of the furnace, and the metal and slag phases were separated and weighed. Representative samples of each phase were collected for analysis. The proportion of metallic, inorganic and organic matter was calculated through the mass loss in the two-stage melting process.

During this process, the fume produced is likely to contain a high proportion of volatile inorganic components such as zinc and lead oxides. Fume was not collected for analysis.

The major and minor elemental components of the slag samples were determined by XRF analysis. Finely ground samples were fused with lithium metaborate/tetraborate flux and the resulting glass disks were analysed using a Bruker S8 Tiger WD-XRF system. Samples of the metal alloy were digested in a mixture of bromine, nitric, hydrofluoric and perchloric acids. The solutions were diluted and analysed using an ICP-OES apparatus. The analysis of trace elements in the slag and metal samples was determined using an Agilent 7700 ICP-MS apparatus.

Results and Discussion

Table 1 shows the calculated proportion of metals, inorganic and organic matters in the PCBs. The proportion of metal components was determined from the amount of alloy collected. The amount of organic matter was estimated from the mass loss

Table 1 Proportion of three major constituents in mobile phone PCBs

PCB type	Metal phase (wt%)	Inorganic (wt%)	Organic matter (wt%)
Button type-1	30.3	47.4	22.3
Button type-2	30.7	45.0	24.3
Touchscreen type	28.2	42.7	29.1

after the pyrolysis and melting procedures and the amount of inorganic components was calculated by difference. The results clearly show that the range of variation in the phases of the three types of PCBs is small. The average metal portion is around 30%, inorganic around 45% while the organic matter comprises 25% of the total PCB mass.

The results in Table 1 agree broadly with the results of Takanori et al. [4] who found approximately 30% metallic material (copper in circuitry; tin, iron and lead in the soldering and lead frames; gold, silver and palladium in the integrated circuits), approximately 40% organic resin materials, and about 30% glass materials used as resin reinforcing fibres in the e-waste).

The concentration of major components in the metal phase is shown in Table 2. Copper is the most abundant element, ranging from around 81 to 84%. Tin is the second highest constituent metal at about 6 wt%. Iron and nickel each constitute around 3%. The silver content was quite high, at greater than 0.3%, which may be significant in terms of monetary value. Other metals include zinc (0.21–0.57%) and lead (0.56–0.81%). The gold content varied between 28 and 40 ppm with an average of about 32 ppm.

The composition of the slag phase expressed in terms of oxides is shown in Table 3. It is seen that the slag composition for the three types of mobile phone PCBs are close except for some variation of B_2O_3 in case of button type-2 and in the sum

Table 2 Concentration of major components in the metal phase (wt%)

Element	Button type-1	Button type-2	Touchscreen type	Average in the metal phase	Average in PCBs
Ag	0.32	0.36	0.35	0.34	0.10
Cu	83.7	81.7	84.4	83.3	25.0
Fe	3.10	3.30	3.9	3.4	1.02
Ni	3.40	3.30	3.7	3.5	1.05
Pb	0.81	0.75	0.56	0.71	0.21
Sn	6.00	6.40	5.8	6.06	1.82
Zn	0.50	0.21	0.57	0.43	0.13
Au (ppm)	40.5	28.5	28.0	32.3	9.69
Others ^a	2.09	4.18	0.7	2.32	0.70

^aOther metals were calculated by difference

Table 3 Composition of major and minor components of the slag phase (wt%)

Oxides	Button type-1	Button type-2	Touchscreen type
B ₂ O ₃	21.7	28.5	20.0
SiO ₂	28.2	28.5	25.2
Al ₂ O ₃	15.5	15.0	9.68
CaO	9.74	9.67	8.51
CuO	2.96	3.01	4.01
Na ₂ O	8.65	8.54	7.99
TiO ₂	0.81	0.94	0.92
Fe ₂ O ₃	1.01	0.89	1.88
SnO ₂	0.38	0.38	0.62
Cr ₂ O ₃	0.40	0.64	0.50
PbO	0.127	0.131	0.130
NiO	0.077	0.081	0.191
ZnO	0.061	0.055	0.219
Others	10.30	3.66	20.15

of the others. Silica (SiO₂) and alumina (Al₂O₃) are the major inorganic components comprising around 28 and 15%. The main source of these species would be the ceramic components of the PCBs. Another source of SiO₂ could be the silicon used in the integrated circuit components of the PCBs. During the high temperature processing steps, the silicon would be oxidised to silica. Despite the reducing atmosphere inside the crucible, a small portion of copper and tin was oxidised and reported to the slag.

Process Simulation

Process modelling of the proposed e-waste value recovery process was performed using the flowsheet simulation module of HSC Chemistry (version 10). The process is illustrated schematically in Fig. 1. Four unit operations are shown. In the first operation (e-waste smelter), the shredded e-waste material is smelted to produce a slag, alloy and gas streams. The alloy stream is basically a copper alloy which is refined in the second operation (electrorefiner). Products from this operation are high purity cathode copper and anode slimes. In addition, an electrolyte stream is also produced. All the silver and gold in the alloy report to the anode slimes. The third operation is an anode slimes melter in which silver and gold alloy is produced. The residue, called tin slag, is reduced in the fourth operation to produce tin bullion and a reduced slag which is recycled to the e-waste smelter. The third and fourth operations could be performed in a single furnace using a two-stage batch operation, i.e. melting and tapping of the silver alloy followed by reduction of the remaining slag. Hence, the valuable products from this process are cathode copper, silver/gold

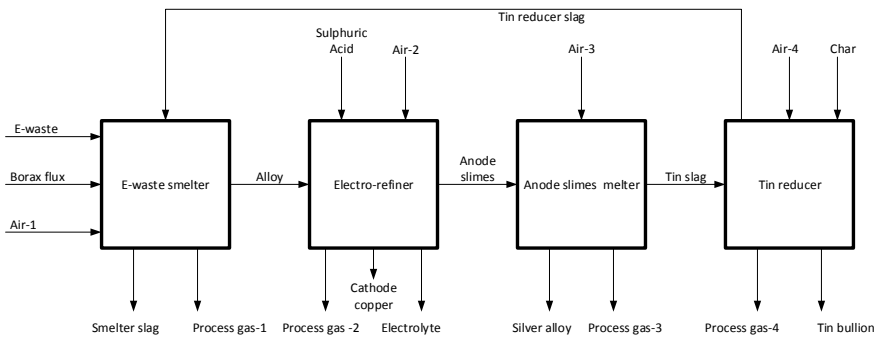


Fig. 1 Schematic diagram of the e-waste value recovery process

alloy and tin bullion. Other outputs include smelter slag and electrolyte which also may have some value. Each of the four operations also produce a process gas. Inputs to the process are e-waste, borax flux, sulphuric acid and char.

In modelling the e-waste value recovery process many assumptions on the department of elements were made.

E-waste Smelter

- The composition of the e-waste feed was calculated from the composition and amount of each component of the alloy and slag phases. These components were normalised to give the e-waste composition. The plastics composition was represented by carbon only for simplicity as any contained hydrogen would be lost in the volatiles when the e-waste was heated.
- Borax fluxing was 30% of feed on a dry basis.
- Air was added to the smelter to combust the carbon. The CO/CO₂ ratio in the exhaust gas was controlled by the smelter heat balance.
- The distribution of elements to the alloy and slag phases was determined based on the results of the experimental work.
- All the silica, alumina and lime in the e-waste reports to the slag stream.

Electro-refiner

- Air input was required to create the oxide or sulphate components of the anode slimes. The amount of air was calculated based on the exhaust gas containing zero oxygen.
- In the electrolyte, Pb forms PbSO₄, Sn forms SnO₂, Fe forms Fe₂O₃ and Cu forms CuSO₄.

- Sulphuric acid input is 98% H₂SO₄.
- The distribution of elements between slimes, cathode copper and electrolyte was assumed to be the same as in conventional copper electrorefining [5].
- Acid requirements are based on an electrolyte bleed rate of 0.1 m³/t of copper and an electrolyte containing 160 g/L H₂SO₄.

Slimes Melter

- An air input is required to allow for an output gas stream containing SO₂ and O₂ produced from the decomposition of sulphates in the slimes.
- All the silver and gold in the slimes report to the silver alloy along with 5% of the copper and tin and 1% of the lead, iron and nickel.

Tin Reducer

- Char addition was calculated at about 68% greater than stoichiometric requirements to reduce the SnO₂ to tin metal.
- Air input is controlled to combust the added char to give a CO to CO₂ ratio of 1.0 with zero oxygen in exhaust gas.
- 95% of input tin, 80% of copper and 10% of iron, nickel, zinc and lead report to the tin bullion.
- Char is 100% carbon.

The e-waste process simulation was based on a yearly treatment rate of 1000 tonnes. The size of the condensed streams in kg/h and gas streams in Nm³/h were calculated using the process simulation flowsheet module within the HSC Chemistry 10 package. The calculated flow of the various process streams, illustrated in Fig. 1, is contained in Tables 4, 5, 6 and 7.

Table 4 Mass and volume flow of the e-waste smelter

Inputs		Outputs	
E-waste	500 kg/h	Slag	311.1 kg/h
Borax flux	150 kg/h	Alloy	188.7 kg/h
Recycled tin slag	5.19 kg/h	Process gas	2503.9 Nm ³ /h
Air	2500 Nm ³ /h		

Table 5 Mass and volume flow of the electrorefiner

Inputs		Outputs	
Alloy	118.7 kg/h	Cathode copper	157.2 kg/h
Sulphuric acid	2.56 kg/h	Anode slimes	22.24 kg/k
Air	11.86 Nm ³ /h	Electrolyte	15.29 kg/h
		Process gas	9.37 Nm ³ /h

Table 6 Mass and volume flow of the slimes melter

Inputs		Outputs	
Anode slimes	22.38 kg/h	Silver alloy	0.65 kg/h
Air	1 m ³ /h	Tin slag	19.96 kg/h
		Process gas	1.74 Nm ³ /h

Table 7 Mass and volume flow of the tin reducer

Inputs		Outputs	
Tin slag	19.96 kg/h	Tin bullion	11.70 kg/h
Char	2 kg/h	Tin reducer slag	5.19 kg/h
Air	3.10 Nm ³ /h	Process gas	6.18 m ³ /h

Techno-Economic Assessment

The cost of processing 1000 t/y of e-waste in Bangladesh was calculated by estimating the capital and operating costs of the three unit operations in the flowsheet shown in Fig. 1. All costs are expressed in US dollars.

Capital costs were calculated from the size of principal equipment required for each stage and included indirect cost factors, EPCM (engineering, procurement, construction and management) factors and a 30% contingency. Operating costs were based on estimates of electricity, labour, reagents and industrial consumables for each operation. In addition, factors for maintenance and contingency were also included.

Table 8 summarises the capital and operating costs. The most expensive capital equipment costs were for the electrorefiner plant at \$330,700 followed by the e-waste smelter at \$226,000 and the slime smelter at \$196,800. Total capital costs including all associated installation factors into consideration would be \$3.9 M.

The operating costs have been expressed as \$/t of input material for the different operations. The most expensive plant to operate was the e-waste smelter at about \$200,000 per year. The electrorefiner and slimes melter plant were estimated to cost \$36,313 and \$34,953 per year, respectively. The total operating cost was \$272,065 per year which is equivalent to \$272/tonne of e-waste. Including end-of-mobile phone buy-back (\$654/t) this operating cost would be \$926/t. Including other fixed operating cost (e.g. contribution of capital on the operating cost), the total operating is estimated to be \$1784/t of e-waste processed.

Table 8 Summary of capital for the e-waste value recovery process

Capital cost items	Basis	Cost (AU\$M ex. GST)
E-waste smelter	Based on capacity	226,000
Electrorefiner	Based on capacity	330,700
Slimes smelter	Based on capacity	196,800
<i>Equipment purchase cost</i>	EPC (3 equipment)	754,000
Freight	10% of EPC	75,000
Direct equipment cost (DEC)	EPC + freight	829,000
Installation	45% of (DEC)	373,000
Instrumentation	25% of (DEC)	207,000
Minor piping	16% of (EPC)	121,000
Structural	15% of (EPC)	113,000
Electrical	25% of (DEC)	207,000
Buildings	25% of (EPC)	188,000
Yard improvements	15% of (EPC)	113,000
Service facilities	40% of (EPC)	301,000
HSE functions	10% of (EPC)	75,000
<i>Total indirect costs</i>		
Land	5% of (DEC)	41,000
Engineering supervision	50% of (DEC)	414,000
Legal expenses	4% of (DEC)	33,000
Construction expenses	40% of (DEC)	332,000
<i>Working capital</i>	15% of (direct plant cost + total indirect cost)	502,000
Total capital (ex. GST)		3,900,000

The detail itemised operating cost per tonne of e-waste processing is shown in Table 9.

Possible revenue from the recovery process includes the value of metal products cathode copper, tin bullion and the silver/gold alloy. There may also be some value attached to the smelter slag which contains rare earth metals and other minor elements such as tantalum and indium. The electrolyte bleed stream may also contain valuable chemicals which could be recovered. In the financial evaluation of the process, only the value contained in the copper, tin and silver/gold alloy was considered.

The cathode copper was assumed to be high purity with a value of \$5.95/kg [6]. Tin was assumed to be produced at a grade of 96% with the major impurity being lead (4%). The value of the tin was priced at \$19.1/kg which is an average of the metal price in 2018 [6]. Value calculations assumed that only 95% of the amount of copper and tin is paid due to refining and purchasing costs.

Selling silver and gold alloys to the Perth mint attracts a treatment charge of 35 cents/oz or about \$12.37/kg. In addition, only 99% of the silver and 99.9%

original material. Costs associated with the collection and transportation of the e-waste from different locations of the country to the plant were assumed at \$654 per tonne of feed. The total capital cost of the process is \$3,900,000 (USD) and the operating cost per tonne of e-waste feed is \$1784 (USD).

Possible revenue from ancillary equipment such as the mobile phone body, plastics, speaker, electronic chips mounted on the PCBs and other components has been omitted. In addition, the potential value embedded in the slag phase and electrorefining electrolyte has also been omitted from these calculations.

The net profit of the operation is given by Eq. (1). The minimum amount of PCBs which need to be processed to recover the capital costs is found by dividing the capital costs by the net profit (Eq. 2). The payback time is given by dividing the minimum processing amount by the plant processing rate (1000 t/y) (Eq. 3).

$$\text{Net profit (\$/t)} = \text{Revenue (\$/t)} - \text{operating costs (\$/t)} - \text{collection costs (\$/t)} \quad (1)$$

$$\text{Minimum processing amount (t)} = \frac{\text{capital costs (\$)}}{\text{net profit (\$/t)}} \quad (2)$$

$$\text{Payback time (y)} = \frac{\text{minimum processing amount (t)}}{\text{plant processing rate (t/y)}} \quad (3)$$

The net profit is \$1449/tonne (3233–1784), the minimum processing amount is 2692 tonnes (3,900,000 ÷ 1449) and the operating time required to simple payback of the capital cost is 2.7 years (2692 ÷ 1000). If it is assumed 95% value in the alloy is recoverable (e.g. \$3071), with a cash-flow analysis, it was found that the net present value (NPV) can be \$4.1 M, internal rate of return can be 23.3% and a discounted payback period is expected to be just over 5 years.

Conclusions

A simple process to treat and extract value from e-waste materials in Bangladesh was shown to be potentially feasible. A melting and analysis characterisation of collected PCB materials showed a metal phase could be produced which contained 83% copper, 6% tin, 0.34% silver and 32.2 ppm gold. A three-stage process was devised to extract cathode copper, a silver/gold alloy and tin bullion as valuable products. The capital costs of the process were estimated to be \$3.9 M and operating costs to be \$1784/t of e-waste. For a plant to process 500 kg/h of PCB, the possible revenue was \$3.2 M/year. Such a process could generate a net profit of \$1449/tonne and would take 2.7 years to pay back the capital using simple equation. However, using a discounted cashflow analysis, the estimated NPV is likely to be over \$4.1 M, with IRR of 23.3% and a payback of over 5 years. Further sensitivity assessment of the input variables is recommended.

Acknowledgements Authors would like to acknowledge the Department of Education and Training, the Australian Government for awarding an Endeavour Fellowship which allowed Mr. Md Khairul Islam to work at CSIRO Mineral Resources. Also, the authors are grateful to the management teams of BCSIR, Bangladesh and CSIRO, Australia for funding this research. The authors are grateful for the Material Characterisation team at CSIRO Mineral Resources for the careful analysis of materials generated in this work.

References

1. Hagelucken C (2006) Improving metal returns and eco-efficiency in electronics recycling—a holistic approach for interface optimisation between pre-processing and integrated metals smelting and refining. In: Proceedings of the 2006 IEEE international symposium on electronics and the environment, Scottsdale, 8–11 May 2006
2. Alam M, Bahauddin KM (2015) Electronic waste in Bangladesh: evaluating the situation, legislation and policy and way forward with strategy and approach. *Present Environ Sustain Dev* 9(1):81–101
3. San Q, Muntaha C, Hossain MM (2016) E-waste generation from mobile phone and its recovery potential in Bangladesh. *J Environ Sci Nat Resour* 9(1):91–94
4. Takanori H, Ryuichi A, Youichi M, Minoru N, Yasuhiro T, Takao A (2009) Techniques to separate metal from waste printed circuit boards from discarded personal computers. *J Mater Cycles Waste Manag* 11(1):42–54
5. Schlesinger ME, King MJ, Sole KC, Davenport WG (2011) *Extractive metallurgy of copper*, 5th edn. Elsevier
6. LME (2018) <https://lme.com/en-GB/Metals/Precious-metals/LMEprecious#tabindex=0>. Accessed 14 Sept 2018

Computational Modeling of Current Density Distribution and Secondary Resistances for Aluminum Electrorefining in Ionic Liquids



M. K. Nahian, Y. Peng, L. Nastac, and R. G. Reddy

Abstract A numerical model was developed to simulate the current density distribution and secondary resistances for the aluminum electrorefining process from the room temperature ionic liquid (RTIL) consisting of 1-butyl-3-methylimidazolium chloride and aluminum chloride with the molar ratio of 2:1 (AlCl_3 : BMIC). The materials and geometry were created based on the experimental parameters. The current density distribution was calculated via simulation. The effects of applied voltage, temperature, composition of the electrolyte, and the surface roughness of cathode on the secondary resistances were investigated in this research. It was found that the summation of contact and charge transfer resistance decreases with increasing the potential and the temperature as well as decreasing the surface roughness.

Keywords Process modeling and simulation · Ionic liquid · BMIC

Introduction

Industrial methods for producing aluminum require higher temperatures, which consume not only higher energy, but also are non-eco-friendly [1]. In recent years, room temperature ionic liquids (RTILs), which melt below 100°C are showing a great promise to electrodeposit aluminum in a greenway at low temperatures. A mixture of imidazolium chloride-based ionic liquid such as 1-butyl-3-methylimidazolium chloride (BMIC) and aluminum chloride exhibit adherent, dendrite free deposition with high purity during aluminum electrorefining and electrowinning [2–4]. Several modelings have been developed to simulate the various type of cell conditions. Zhang and Reddy developed a mathematical 3-D model to forecast the current distribution, electric field distribution, fluid flow, and concentration for near room-temperature aluminum electrowinning cell using Ansys (paired with FLOTTRAN and EMAG) and Ansys CFX programs [5, 6]. In this research, a model is developed to predict the

M. K. Nahian · Y. Peng · L. Nastac · R. G. Reddy (✉)

Department of Metallurgical and Materials Engineering, The University of Alabama, Tuscaloosa, AL 35487, USA

e-mail: reddy@eng.ua.edu

current density distribution and secondary resistances for Al electrodeposition by using Ansys Fluent program. The electrolyte was an eutectic mixture of 1-butyl-3-methylimidazolium chloride (BMIC) and aluminum chloride (AlCl_3) in 1:2 (BMIC: AlCl_3) molar ratio where the anode is aluminum and the cathode is copper. Experimental data was used to calculate the contact resistance and investigate the electric potential distribution. This CFD software offers superior quality meshing, essential models for species transfer, electric potentials, fluid flow, heat transfer, solution accuracy, computational speed (allowing for parallel computations via domain decomposition), facilitating the implementation of complex boundary conditions and source terms via user-defined functions (UDF). This modeling study has five targets: 1. Analyzing the geometry and mesh of the model; 2. Analyzing the parameters on the boundary conditions; 3. Determining the properties of electrolyte and electrodes, such as density, viscosity, and electrical conductivity; 4. Calculating the contact resistance using experimental current density data; 5. Simulating the potential distribution on the electrodes and electrolyte.

Current density distribution plays an important role in the morphology of the deposition. Due to the geometry of the system, conductivity of cell component activation overpotential, diffusion overpotential and hydrodynamics of electrolyte, current density deviates in the different points of the electrode [7]. An accurate current density profile is possible to predict by using Ansys's Fluent modeling, which can help to estimate the electrodeposition morphology. If we consider the electrochemical cell as a simple electric circuit, we may define the current and potential in this way,

$$I = \frac{U}{R_s + R_e + R_c + R_{ct}}$$

where U is the electric potential, R_s is the resistance of solution, R_e is the resistance of the electrode, R_c is contact resistance between electrode and electrolyte, and R_{ct} is reaction resistance or charge-transfer resistance. Normally, solution resistance R_s and electrode resistance R_e contribute much more total resistance. So here, we consider contact resistance R_c and charge-transfer resistance R_{ct} as secondary resistances. Resistance at the interface between electrode and electrolytes plays an important role in the current density. Although the studies on this contact resistance have been done on energy storage systems, contact resistance studies on the electrodeposition method is rarely found [8–10]. When an electron transfers from the electrode to the electrolyte (or vice versa), it has to overcome the charge-transfer resistance. Conductivities of the solution were investigated in a previous study [11], and resistances of electrode materials were chosen from the modeling software. However, R_c and R_{ct} are necessary to be defined in the present work. Also, R_c is attributed to contacting interface of electrode and electrolyte, and R_{ct} is related to reaction, temperature, potential, as well as the concentration of reacted species. Therefore, the effect of temperature, potential, the concentration of Al species, type of ionic liquid, and surface morphology on secondary resistances are studied in the present work.

Process Modeling

The geometry of the electrochemical cell was developed by using the experimental cell dimensions. The diameter and height of the cylinder were 4 and 3 cm, respectively. The dimensions of the cathode electrode (Cu) were $1.5 \times 1.5 \times 0.1$ cm, and the dimensions of the anode electrode (Al) were $1.5 \times 1.5 \times 0.15$ cm. The distance between the two electrodes is 2.3 cm. One small cylinder with 0.5 cm height and 1 cm diameter was created at the bottom as a stirrer. All the above parameters are corresponding to the practical experiment. Then, a mesh with a good aspect ratio and skewness was established. The domain was filled with 1:2 mol ratio of BMIC- AlCl_3 as an ionic liquid electrolyte. Figure 1 shows the geometry and mesh of the model.

The quality of the geometry and mesh are listed in Table 1.

We selected the “Electrical potential” model. The steady-state and incompressible flow was assumed. And, the methods and equations used in this model are listed in Eqs. (1–9). In general, the electric field E can be written as:

$$E = -\Delta\varphi - \frac{\partial A}{\partial t} \quad (1)$$

where φ and A are the scalar potential and vector potential.

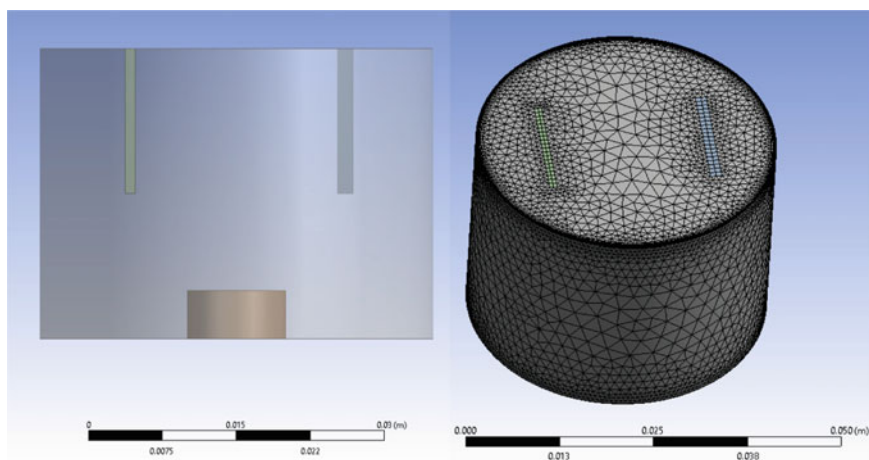


Fig. 1 Model geometry and mesh. (Color figure online)

Table 1 Geometry and mesh data

Geometry data	Mesh data
Cylinder: diameter 4 cm and height 3 cm	Cells: 157,286
Cathode (Cu): $1.5 \times 1.5 \times 0.1$ cm	Nodes: 48,943
Anode (Al): $1.5 \times 1.5 \times 0.15$ cm	

Ohm's law can be described as:

$$j = \sigma E \quad (2)$$

Here, j = current density, σ = electrical conductivity of media. If U = velocity field and B = magnetic field, it also can be written as:

$$j = \sigma(E + U \times B) \quad (3)$$

As in the steady-state,

$$\frac{\partial A}{\partial t} = 0 \quad (4)$$

Ohm's law can be written as:

$$j = \sigma(-\Delta\varphi + (U \times B)) \quad (5)$$

For sufficiently conducting media, the principle of conservation of electric charge gives:

$$\nabla \cdot j = 0 \quad (6)$$

Therefore,

$$\nabla^2\varphi = \nabla(U \times B) \quad (7)$$

The potential on the boundary can be defined as:

$$\frac{\partial\varphi}{\partial n} = (B \times U)_{\text{boundary}} \cdot n \quad (8)$$

where n = vector normal to the boundary, and

$$\varphi = \varphi_0 \quad (9)$$

φ_0 is a specific potential on the boundary.

Properties of the electrolyte were defined, which is from our previous experimental results [11]. Properties of the anode (Al) and the cathode (Cu) were built-in with the software.

After defining the properties of the electrolyte, thermal and potential conditions and values of those boundaries were set rational and compared to the real experiment. For the final calculation process, we chose solution methods, such as Gauss–Seidel or ILU methods, set reference and initialization values.

Results and Discussion

Current Density Distribution

The vector of the electric current density magnitude is shown in Figs. 2 and 3. In this case we considered, applied Voltage = 1.5 V, distance of electrodes = 2.3 cm, Stirring speed = 12.57 rad/s (120 rpm). Viscosity and electrical conductivity of the electrolyte at 100°C were used. Contact resistance at cathode and anode were both set as 0 ohm-m² for the first simulation.

As shown in Figs. 2 and 3, the current density is larger at the bottom and edge of the Cu electrode. That might be one of the reasons for the easy formation of Al dendrite at the bottom and the edge parts of the electrode [11]. Also, the backside of the Cu electrode, which is face to the beaker boundary, has a lower current density than the front side. That is why there is more deposition at the front side than the backside of the electrode in the experiment.

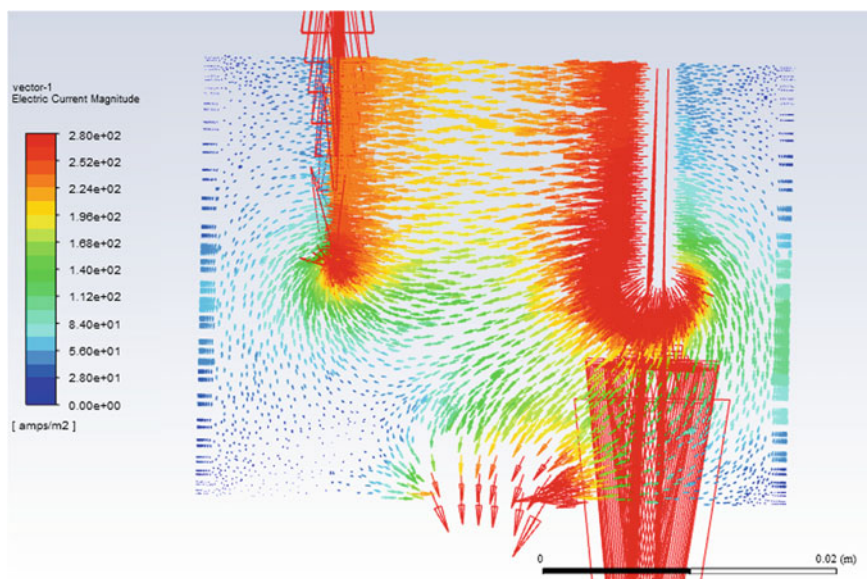


Fig. 2 Distribution of electric current density in the X-Z plane (left side is Cu cathode and right side is Al anode). (Color figure online)

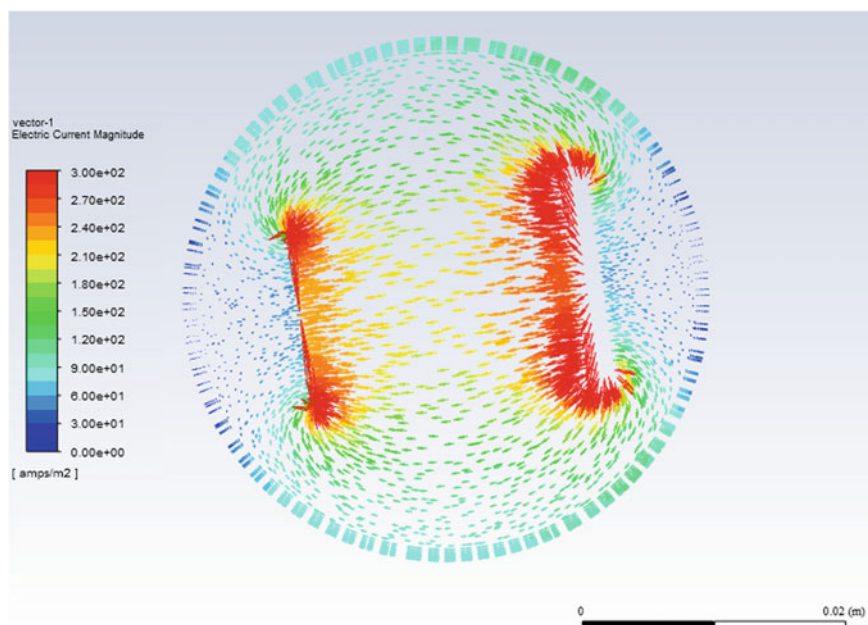


Fig. 3 Distribution of electric current density in the X - Y plane, 0.005 m from the top of the ionic liquid (left side is Cu cathode and the right side is Al anode). (Color figure online)

Calculation of Secondary Resistances ($R_c + R_{ct}$)

In this modeling approach, we calculated $R_c + R_{ct}$ based on the experimental current density as a function of applied potential, temperature, and surface roughness. In Table 2, the $R_c + R_{ct}$ was given for different applied potential values (Deposition temperature: 100°C; stirring rate: 120 rpm; deposition time: 2 h; surface roughness of Cu electrode: 543.1 ± 59.7 nm; electrode distance: 23 mm; electrolyte BMIC: AlCl_3 at a molar ratio of 1: 2).

The relationship between $R_c + R_{ct}$ and the temperature was also simulated. During the simulation, a variation of temperature has changed the conductivity and viscosity

Table 2 $R_c + R_{ct}$ as a function of the applied potential

Applied potential (V)	Experimental current density (A m^{-2}) [12]	$R_c + R_{ct}$ ($\text{ohm}\cdot\text{m}^2$)
1	160.1	0.0172
1.25	272.8	0.0138
1.5	357.6	0.0131
1.75	420.6	0.0128

Table 3 Secondary resistances as a function of temperature

Temperature (°C)	Conductivity (S m ⁻¹) [our previous work]	Viscosity (kg m ⁻¹ s ⁻¹) [13]	Experimental current density (A m ⁻²) [12]	$R_c + R_{ct}$ (ohm·m ²)
80	2.36	0.0078	167.5	0.023
90	2.73	0.0061	291.3	0.0155
100	3.11	0.00485	396.7	0.012
110	3.34	0.0045	481.7	0.0101

Table 4 $R_c + R_{ct}$ as a function of surface roughness

The arithmetical average surface roughness of Cu cathode: Ra (nm)	Experimental current density (A m ⁻²) [12]	$R_c + R_{ct}$ (ohm·m ²)
543.1 ± 59.7 (320 G)	396.7	0.012
126.7 ± 24.7 (600 G)	419.7	0.0115
78.6 ± 16.4 (800 G)	498.1	0.0101
46.2 ± 8.2 (1200 G)	534.8	0.0095
23.3 ± 4.8 (mirror polishing)	654.6	0.0081

of the ionic liquid. Thus, we set the different conductivities and viscosities of ionic liquid to simulate the secondary resistances at different temperatures.

The variables and results for the study of deposition temperature effect on $R_c + R_{ct}$ are given below (stirring rate: 120 rpm; applied potential 1.5 V; deposition time: 2 h; surface roughness of Cu electrode: 543.1 ± 59.7 nm; electrode distance: 23 mm) (Table 3).

The effect of cathode surface roughness as a function of $R_c + R_{ct}$ is given in Table 4 (deposition temperature: 100 °C; stirring rate: 120 rpm; applied potential 1.5 V; deposition time: 2 h; electrode distance: 23 mm).

In the last part of the study, the effect of electrolyte composition was investigated. The molar ratio of AlCl₃ was changed to 1.4, 1.6, 1.8, and 2 where the molar ratio of BMIMCl was fixed to 1. The $R_c + R_{ct}$ decreased with an increasing AlCl₃ molar ratio. With the increasing molar ratio of AlCl₃, the concentration of Al₂Cl₇⁻ ion increases [14]. Al₂Cl₇⁻ ion raises the electrical conductivity and reduces the viscosity [15–17]. Because of this, $R_c + R_{ct}$ decreases. The values of secondary resistances are listed in Table 5 (temperature: 100 °C; stirring rate: 120 rpm; applied potential 1.5 V; deposition time: 2 h; surface roughness of Cu electrode: 543.1 ± 59.7 nm; electrode distance: 23 mm).

The correlation between these parameters and surface roughness is given in Fig. 4.

As shown in Fig. 4, the $R_s + R_{ct}$ decreased as applied potential and temperature increased, while increased as surface roughness increased. On the other hand, the redox reaction of Al species is easier to take place at higher potential, temperature, and AlCl₃ molar ratio as well as lower surface roughness. So, the contact resistance response to change these variables is expected.

Table 5 $R_c + R_{ct}$ as a function of $AlCl_3$ molar ratio

Molar ratio of $AlCl_3$ (molar ratio of BMIMCl was fixed to 1)	Experimental current density ($A\ m^{-2}$) [12]	$R_c + R_{ct}$ ($ohm\cdot m^2$)
1.4	169.3	0.14
1.6	180.5	0.13
1.8	282.6	0.083
2	396.7	0.057

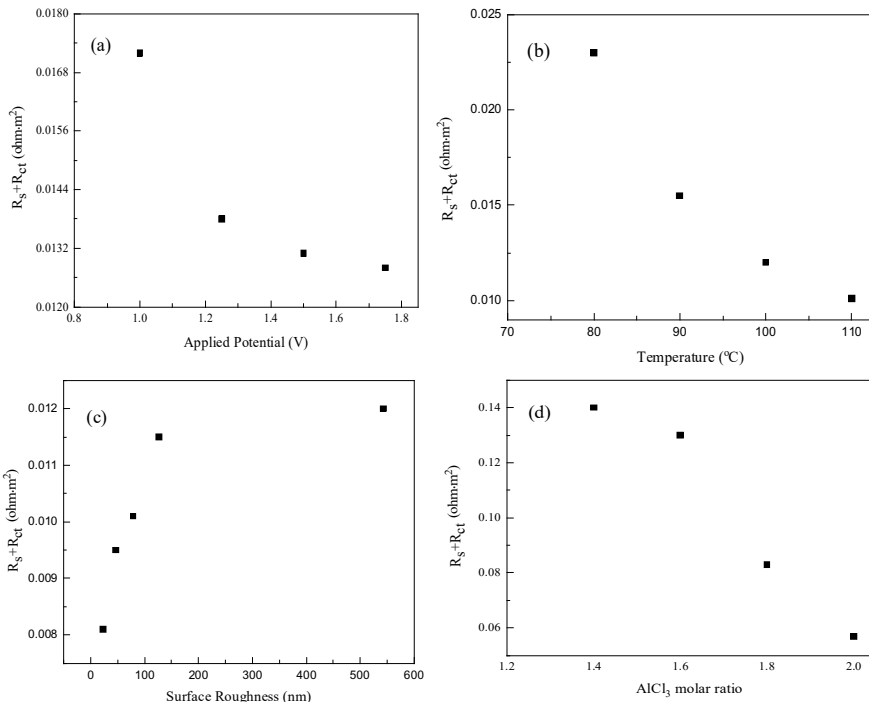


Fig. 4 Variation of secondary resistances in the cell with **a** applied potential, **b** temperature, **c** surface roughness, and **d** $AlCl_3$ molar ratio

Conclusions

A 3-D numerical model of aluminum electrodeposition from chloroaluminate-based electrolyte was developed in ANSYS Fluent. The potential distribution and contact resistance in the electrochemical cell were determined. The result showed that electrode potential is uniform in the electrodes. The contact resistance between the electrode and electrolyte decreased with increasing applied voltage, temperature, and $AlCl_3$ molar ratio. In contrast, increasing surface roughness increased the contact resistance.

Acknowledgements The authors acknowledge the financial support received from the Department of Energy (DOE) RAPID Manufacturing Institute and ACIPCO for this research project. Authors also thank the Department of Metallurgical and Materials Engineering, The University of Alabama for providing experimental and analytical facilities.

References

1. Zhang M, Kamavarum V, Reddy RG (2003) New electrolytes for aluminum production: ionic liquids. *JOM* 55(11):54–57. <https://doi.org/10.1007/s11837-003-0211-y>
2. Pradhan D, Reddy RG (2012) Dendrite-free aluminum electrodeposition from AlCl_3 -1-ethyl-3-methyl-imidazolium chloride ionic liquid electrolytes. *Metall Mater Trans B* 43(3):519–531. <https://doi.org/10.1007/s11663-011-9623-1>
3. Zhang M, Kamavaram V, Reddy RG (2005) Aluminum electrowinning in ionic liquids at low temperature. *Light Met* 2005:583–588
4. Wu B, Reddy RG, Rogers RD (2013) Aluminum reduction via near room temperature electrolysis in ionic liquids. In: *Essential readings in light metals*, pp 1100–1107. <https://doi.org/10.1002/9781118647851.ch161>
5. Zhang M, Reddy RG (2017) Modeling of aluminum electrowinning in ionic liquid electrolytes. In: *Applications of process engineering principles in materials processing, energy and environmental technologies*, pp 65–79. https://doi.org/10.1007/978-3-319-51091-0_6
6. Zhang M, Reddy RG (2006) Ionic liquids electrowinning of aluminum in batch mode cells. *Light Met* 2006:451–456
7. Popov KI, Djokić SS, Grgur BN (2010) The current distribution in electrochemical cells. In: *Fundamental aspects of electrometallurgy*. Springer, Boston, pp 101–143
8. Mirzaeian M, Fathinejad H, Mirzaeian M (2015) Effect of the electrode/electrolyte contact resistance on the energy storage capacity and cycleability of Li/O_2 batteries [Abstract]. *ECS Meet Abstr*. <https://doi.org/10.1149/ma2015-03/2/489>
9. Wang L, Liu D, Huang T, Geng Z, Yu A (2020) Reducing interfacial resistance of a $\text{Li}_{1.5}\text{Al}_{0.5}\text{Ge}_{1.5}(\text{PO}_4)_3$ solid electrolyte/electrode interface by polymer interlayer protection. *RSC Adv* 10(17):10038–10045. <https://doi.org/10.1039/d0ra00829j>
10. Mayer S, Geddes LA, Bourland JD, Ogborn L (1992) Faradic resistance of the electrode/electrolyte interface. *Med Biol Eng Comput* 30(5):538–542. <https://doi.org/10.1007/bf02457834>
11. Shinde P, Ahmed AN, Nahian MK, Peng Y, Reddy RG (2020) Conductivity of 1-ethyl-3-methylimidazolium chloride (EMIC) and aluminum chloride (AlCl_3) ionic liquids at different temperatures and AlCl_3 mole fractions. *ECS Trans* 98:129–139. <https://doi.org/10.1149/09810.0129ecst>
12. Wang Y (2020) Development of aluminum electrorefining in ionic liquids: the effect of experimental conditions on the deposition behavior and microstructure. MS thesis, The University of Alabama
13. Kamavaram V (2004) Novel electrochemical refining of aluminum based materials in low temperature ionic liquid electrolytes. Ph.D. thesis, The University of Alabama
14. Karpinski ZJ, Osteryoung RA (1984) Determination of equilibrium constants for the tetrachloroaluminate ion dissociation in ambient-temperature ionic liquids. *Inorg Chem* 23(10):1491–1494. <https://doi.org/10.1021/ic00178a039>
15. Kim K, Lang C, Kohl PA (2005) The role of additives in the electroreduction of sodium ions in chloroaluminate-based ionic liquids. *J Electrochem Soc* 152(1):E9–E13. <https://doi.org/10.1149/1.1834898>
16. Ferrara C, Dall'Asta V, Berbenni V, Quartarone E, Mustarelli P (2017) Physicochemical characterization of AlCl_3 -1-ethyl-3-methylimidazolium chloride ionic liquid electrolytes for

- aluminum rechargeable batteries. *J Phys Chem C* 121(48):26607–26614. <https://doi.org/10.1021/acs.jpcc.7b07562>
17. Jiang T, Brym MC, Dubé G, Lasia A, Brisard G (2006) Electrodeposition of aluminium from ionic liquids: part I—electrodeposition and surface morphology of aluminium from aluminium chloride (AlCl_3)–1-ethyl-3-methylimidazolium chloride ([EMIm]Cl) ionic liquids. *Surf Coat Technol* 201(1–2):1–9. <https://doi.org/10.1016/j.surfcoat.2005.10.046>

Conductivity of AlCl₃-BMIC Ionic Liquid Mixtures Containing TiCl₄ at Different Temperatures and Molar Ratios



M. K. Nahian, A. N. Ahmed, P. S. Shinde, and R. G. Reddy

Abstract The conductivity of the mixture of 1-butyl-3-methylimidazolium chloride (BMIC) ionic liquid with aluminum chloride (AlCl₃) and titanium chloride (TiCl₄) are systematically investigated over a range of temperature (70–110 °C) using the electrochemical impedance spectroscopy (EIS) method. The molar ratios of the components are changed to study the effect of molar ratio on the conductivity. The conductivity data are plotted against temperature to check whether it obeys the Arrhenius law. The activation energy and the density are calculated. The conductivity of the solution increases with increasing temperature for every composition. For varying molar ratio, conductivity increases with increasing TiCl₄ content up to a certain composition then starts to decrease for each temperature. At room temperature, density of the solution increases with increasing TiCl₄ content in the solution.

Keywords Conductivity · Ionic liquid · Titanium · Electrometallurgy

Introduction

Ionic liquids are gaining interest day by day due to their functional physical properties, for example, low vapor pressure, good electrical conductivity, exceptional thermal stability, and wide electrochemical window [1–4]. Apart from these properties, ionic liquids are eco-friendly, which makes them a potential candidate as an electrolyte in green electrodeposition and energy storage materials. The conductivity of the electrolyte plays a vital role in the deposition thickness, deposition morphology, and current efficiency during the electrodeposition process [5]. Conductivity also represents the existence and concentration of the conducting ions. Several research works have already been done on measuring the conductivity of various ionic liquid systems [6–10]. Though many experiments have been done on titanium

M. K. Nahian · A. N. Ahmed · P. S. Shinde · R. G. Reddy (✉)

Department of Metallurgical and Materials Engineering, The University of Alabama, Tuscaloosa, AL 35487, USA

e-mail: reddy@eng.ua.edu

© The Minerals, Metals & Materials Society 2021

TMS 2021 150th Annual Meeting & Exhibition Supplemental Proceedings,

The Minerals, Metals & Materials Series,

https://doi.org/10.1007/978-3-030-65261-6_90

1017

alloy electrodeposition using titanium tetrachloride (TiCl_4) and ionic liquid solutions, there is no report on the conductivity of these electrolyte systems. Electrochemical impedance spectroscopy (EIS) has been applied widely for characterizing corrosion, electroplating, and energy storage materials [11, 12]. A sinusoidal signal is passed through the system, and the resulting Nyquist plot (imaginary versus real impedance) is obtained. Resistance can be calculated from the following simple mathematical expression.

$$\rho = \frac{l}{RA}$$

A is the effective current collector area, R is the solution resistivity, which can be calculated from the Nyquist plot, l is the current carrier length, and ρ is the resistivity. Conductivity (κ) is the reciprocal of this resistivity value. EIS method has been used to measure the solid-state electrolyte [13, 14]. The conductivity of aluminum chloride (AlCl_3) and 1-butyl-3-methylimidazolium (BMIC) solution has been determined as well by using conductivity meter and EIS. The data from these two sources are comparable to each other. Lu et al. obtained the conductivity of 2.3 S/m for the AlCl_3 and BMIC solution at 2:1 molar ratio at 70 °C using a conductivity meter. Whereas, Shinde et al. applied the EIS method to quantify it as 2.36 S/m for the same temperature and molar ratio [10, 15]. The conductivity for other compositions of AlCl_3 and BMIC solution at different temperatures are also similarly reported.

Reddy et al. have studied the AlCl_3 -BMIC system extensively as an electrolyte [16, 17]. This electrolyte shows great prospects in metal deposition. However, Ti-Al alloys were obtained with relatively higher Ti content than other studies, an energy-efficient way of pure Ti electrodeposition is still out of reach. The addition of TiCl_4 in the AlCl_3 -BMIC system can be used for the electrowinning study of titanium. Characterization of the physical and chemical properties of electrolytes displays a wider view of the electrolysis system. This data can be used to not only resolve the existing problems, but also for numerical modeling. In this article, we studied the response of conductivity for variation in the temperature and molar ratio for BMIC with AlCl_3 and (TiCl_4) system. The TiCl_4 molar ratio in the solution was varied as 0.08, 0.12, 0.16, and 0.32, whereas the molar ratio of BMIC to AlCl_3 is fixed at 1:2. The temperature was varied from 70 to 110 °C at 10 °C intervals. The activation energy for each solution composition was measured by applying the Arrhenius equation. Physical properties such as density are the essential factors of the 3-D modeling of the electrolysis process as well as calculating the ion concentration. We also reported the relationship between the density and the molar ratio of the solution in this paper.

Experimental Procedure

Materials

The AlCl₃ (95%, HPLC), TiCl₄ (99%) and BMIC (98%, HPLC) salt were collected from Alfa Aesar, Beantown Chemical and Sigma-Aldrich respectively. The AlCl₃ and BMIC (which were in powder form) were taken into a 50 ml beaker and sealed with parafilm tape. After this, the solution was heated at a fixed temperature for 40 min. After 40 min, the required amount of liquid TiCl₄ was added quickly to the AlCl₃ and BMIC mixture under argon gas. Again, this solution was stirred at a set temperature by a magnetic stirrer for 20 min for homogenous mixing. In this way, solutions with different molar ratios were prepared. The molar ratios of the AlCl₃:BMIC:TiCl₄ was 2:1:0.08, 2:1:0.12, 2:1:0.16 and 2:1:0.32.

Electrical Conductivity Measurement

The electrical resistance of the solution was carried out using a VersaSTAT 3 (M-100) potentiostat. Two nickel electrodes of identical dimensions were used in this experiment. Here, the effective current collector surface area, which we considered in our calculation, is the area of the working electrode in contact with the electrolyte. Both the electrodes were polished with 600 grit silicon carbide abrasive paper, washed with water, and then air-dried just before every experiment. These electrodes were placed in a quartz cuvette. Electrodes were attached to the opposite wall of the cuvette. This cell was filled with the ionic liquid solution, and argon gas was purged to get rid of air from the top surface of the solution. Subsequently, the cell was sealed by Teflon tape. The whole system was put in an oil bath for uniform heating. The thermometer was inserted in the oil bath to record the temperature. The cell was connected to the potentiostat. The schematic representation of the experimental setup is shown in Fig. 1.

After reaching the desired temperature, the temperature was fine-tuned. The temperature of the ionic liquid was stabilized for at least 10–15 min. The applied DC potential and the area of the electrode were fixed at 0.2 V and 144 mm², respectively. The amplitude of the sinusoidal wave was 10 mA, where the start frequency was 100,000 Hz, and the end frequency was 1 Hz. The density of the solution was measured by a labeled bottle. The weight of the dry bottle was recorded, and then 1.5 ml of the solution was poured into the bottle. The weight of the solution and subsequently, the density of the solution was estimated at room temperature.

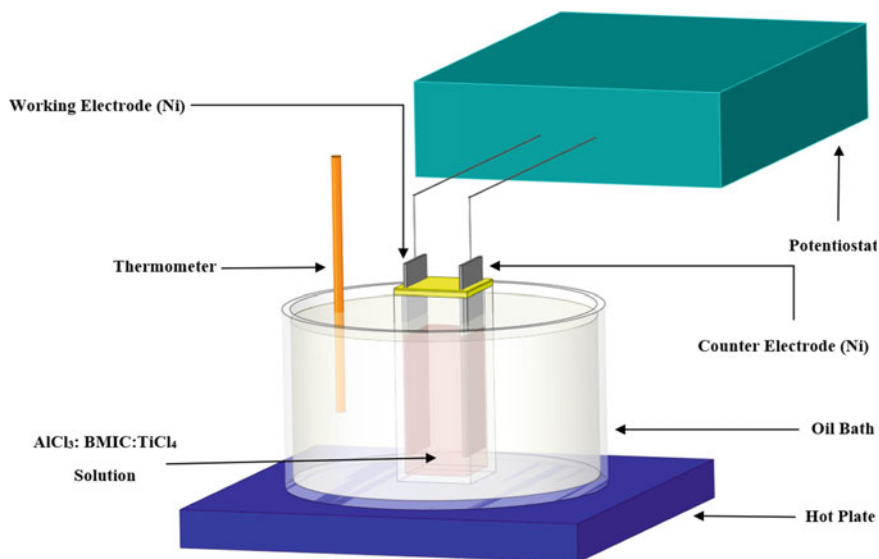


Fig. 1 A schematic of the electrical conductivity measurement setup. (Color figure online)

Results and Discussion

All the conductivity data mentioned in this paper were taken during the heating of the solution. The temperature of the solution was increased to 70 °C from room temperature and after measuring the impedance value, the temperature was raised to the next data point. Electrical conductivity data as a function of temperature (in Kelvin scale) for the different molar ratios of the solute is given in Table 1.

The variation of electrical conductivity versus temperature for the different molar ratios of AlCl_3 : BMIC: TiCl_4 solutions are presented in Fig. 2. For comparison, the conductivity data of AlCl_3 : BMIC (the molar ratio is 2:1) is also plotted from literature data [10].

Table 1 Electrical conductivity of AlCl_3 : BMIC: TiCl_4 ionic liquids for various temperatures and molar ratios

Temperature (K)	Conductivity (κ) for AlCl_3 : BMIC: TiCl_4 with different molar ratios				
	2:1:0.0 (S/m) [10]	2:1:0.08 (S/m)	2:1:0.12 (S/m)	2:1:0.16 (S/m)	2:1:0.32 (S/m)
343	1.96 ± 0.003	2.63 ± 0.002	2.75 ± 0.014	2.72 ± 0.019	2.49 ± 0.007
353	2.36 ± 0.006	2.99 ± 0.011	3.14 ± 0.002	3.01 ± 0.004	2.79 ± 0.011
363	2.73 ± 0.001	3.32 ± 0.007	3.49 ± 0.001	3.4 ± 0.009	3.18 ± 0.015
373	3.11 ± 0.013	3.61 ± 0.005	3.88 ± 0.033	3.76 ± 0.024	3.57 ± 0.083
383	3.34 ± 0.011	4.04 ± 0.012	4.15 ± 0.007	4.1 ± 0.043	3.74 ± 0.000

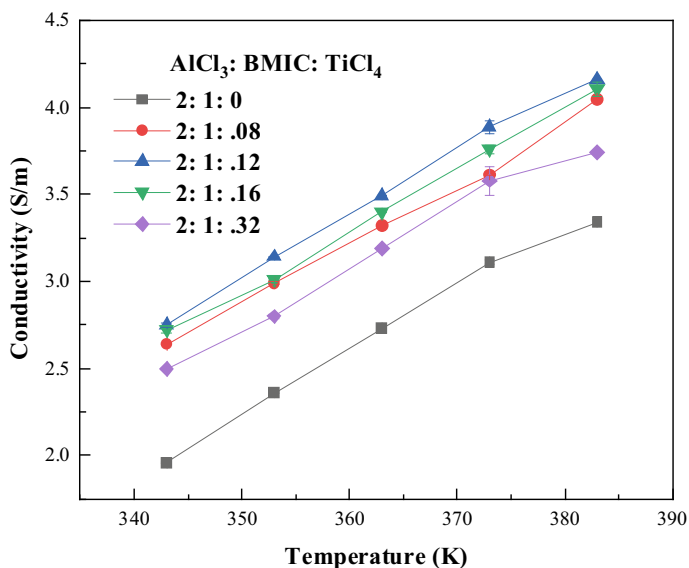


Fig. 2 Conductivity versus temperature with varying concentrations of TiCl₄ in AlCl₃: BMIC: TiCl₄ system. (Color figure online)

With increasing temperature, the charge transfer rate increases and the viscosity decreases. Viscosity has a direct effect on transport properties [18]. The mobility of the ions increases with temperature in the liquid solution. Apart from this, high temperature may be a probable cause of dissociation of molecules. Several reports also find this behavior [18–20].

The plot of electrical conductivity versus molar ratio of the TiCl₄ at different temperatures is shown in Fig. 3. Conductivity at zero molar ratio of TiCl₄ is taken from the conductivity data of AlCl₃: BMIC (2:1), which is equivalent to the AlCl₃: BMIC: TiCl₄ system which has the molar ratio of 2:1:0, respectively.

From Fig. 3, the conductivity value increases up to the composition of 2:1:0.12 (AlCl₃: BMIC: TiCl₄) and decreases as the molar ratio increases for all temperatures. This is likely due to the decrease in mobility of the ions causing significant decrement in the viscosity [21]. Because of this, conductivity goes to the maximum where the mobility of the charge carriers is maximum. After this threshold level, mobility decreases and thus conductivity decreases. Tong et al. found that the self-diffusion coefficient in lithium-ion-based ionic liquid solution increases up to a certain concentration of lithium-ion and then drops [22]. The Arrhenius plot of the conductivity is shown in Fig. 4.

The activation energy of each system was calculated from this plot, which is given in Table 2.

The activation energy is the lowest energy required to occur a reaction. For electronic conductivity, it indicates the needed energy to jump an ion to a hole [23]. From the table, it can be found that the activation energy of AlCl₃: BMIC: TiCl₄

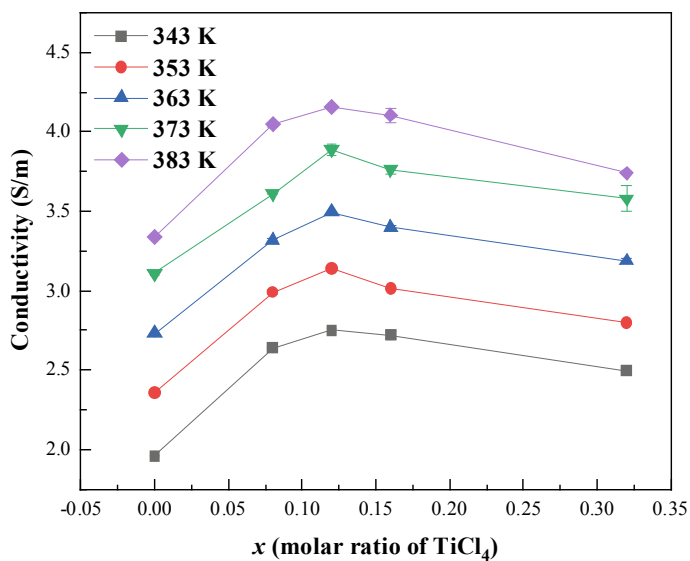


Fig. 3 Plot of conductivity versus the molar ratios of TiCl₄ (x) curves for AlCl₃: BMIC: TiCl₄ (2:1: x) at varying temperatures from 343 to 383 K. (Color figure online)

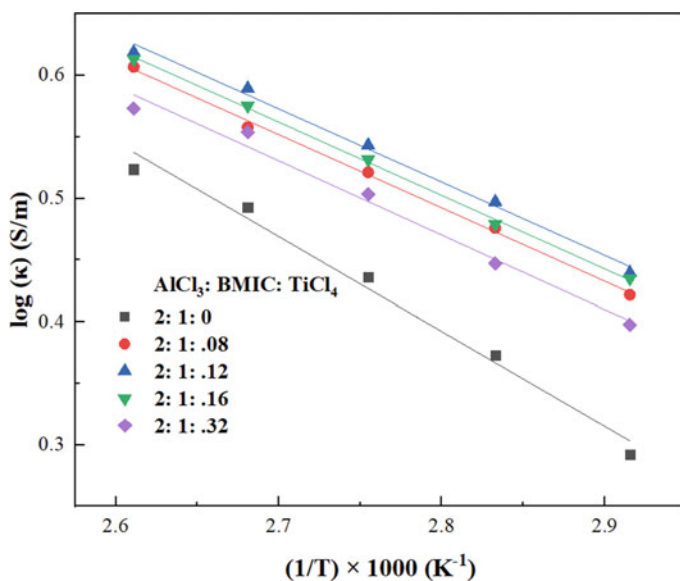
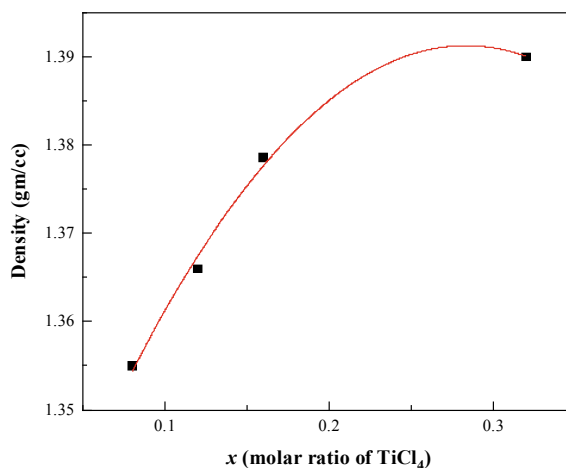


Fig. 4 Arrhenius plots of the conductivity for different AlCl₃: BMIC: TiCl₄ system. (Color figure online)

Table 2 Activation energy for different AlCl₃: BMIC: TiCl₄ systems

AlCl ₃ : BMIC: TiCl ₄ molar ratio	Slope	Activation energy (kJ/mol)
2:1:0	-769.0 ± 54.57	14.725 ± 1.044
2:1:0.08	-595.5 ± 17.15	11.402 ± 0.328
2:1:0.12	-595.2 ± 26.72	11.396 ± 0.511
2:1:0.16	-596.5 ± 12.84	11.421 ± 0.245
2:1:0.32	-606.4 ± 43.18	11.610 ± 0.826

Fig. 5 Plot of density versus the molar ratio of TiCl₄ (x), for BMIC: AlCl₃: TiCl₄ (1:2: x) system measured at room temperature. (Color figure online)

(2:1:0) solution is much higher than the other systems. As a result, the electrical conductivity of AlCl₃: BMIC: TiCl₄ (2:1:0) solution is relatively lower. In the other compositions, activations energies are very close and overlap with each other within the standard deviation range. The plot of density versus different TiCl₄ molar ratios of the solution is shown in Fig. 5.

The density of 2:1 molar ratio of AlCl₃: BMIC solution is 1.347 g/cc [24]. A density of AlCl₃:BMIC system increases with addition of TiCl₄, and is higher (1.387 g/cc) for TiCl₄ mole ratio of 0.32. So, with increasing the TiCl₄ molar ratio in the AlCl₃: BMIC: TiCl₄ solution, the density also increases, which agrees with our findings.

Conclusions

The conductivity response with varying temperature and molar ratio of AlCl₃: BMIC: TiCl₄ solution is reported. The effect of molar ratio on density is also presented. Conductivity for each molar composition of the solution increased with temperature

from 70 to 110 °C. However, the conductivity increased up to 2:1:0.12 molar ratio of AlCl_3 : BMIC: TiCl_4 solution. After this composition molar ratio, the conductivity decreases with each temperature. Effect of TiCl_4 on the electrical conductivity of the AlCl_3 : BMIC mixture is remarkably higher compared to the conductivity data of AlCl_3 : BMIC solution without TiCl_4 . There is a little difference between the activation energy for a different composition. Nevertheless, the addition of TiCl_4 reduces the activation energy for electrical conduction. The density of AlCl_3 : BMIC: TiCl_4 system increased with increasing TiCl_4 .

Acknowledgements The authors acknowledge the financial support from the National Science Foundation (NSF) and ACIPCO for this research project. The authors also thank the Department of Metallurgical and Materials Engineering, The University of Alabama, for providing the experimental and analytical facilities.

References

1. Galiński M, Lewandowski A, Stepniak I (2006) Ionic liquids as electrolytes. *Electrochim Acta* 51:5567–5580. <https://doi.org/10.1016/j.electacta.2006.03.016>
2. Huddleston JG, Visser AE, Reichert WM et al (2001) Characterization and comparison of hydrophilic and hydrophobic room temperature ionic liquids incorporating the imidazolium cation. *Green Chem* 3:156–164. <https://doi.org/10.1039/b103275p>
3. Sakaebe H, Matsumoto H, Tatsumi K (2007) Application of room temperature ionic liquids to Li batteries. *Electrochim Acta* 53:1048–1054. <https://doi.org/10.1016/j.electacta.2007.02.054>
4. Andriyko YO, Reischl W, Nauer GE (2009) Trialkyl-substituted imidazolium-based ionic liquids for electrochemical applications: basic physicochemical properties. *J Chem Eng Data* 54:855–860. <https://doi.org/10.1021/je800636k>
5. Mahapatro A, Suggu SK (2018) Modeling and simulation of electrodeposition: effect of electrolyte current density and conductivity on electroplating thickness. *Adv Mater Sci*. <https://doi.org/10.15761/ams.1000143>
6. Vila J, Ginés P, Rilo E et al (2006) Great increase of the electrical conductivity of ionic liquids in aqueous solutions. *Fluid Phase Equilib* 247:32–39. <https://doi.org/10.1016/j.fluid.2006.05.028>
7. Zhang Q-G, Sun S-S, Pitula S et al (2011) Electrical conductivity of solutions of ionic liquids with methanol, ethanol, acetonitrile, and propylene carbonate. *J Chem Eng Data* 56:4659–4664. <https://doi.org/10.1021/je200616t>
8. Wileńska D, Anusiewicz I, Freza S et al (2014) Predicting the viscosity and electrical conductivity of ionic liquids on the basis of theoretically calculated ionic volumes. *Mol Phys* 113:630–639. <https://doi.org/10.1080/00268976.2014.964344>
9. Leys J, Wübbenhorst M, Menon CP et al (2008) Temperature dependence of the electrical conductivity of imidazolium ionic liquids. *J Chem Phys* 128:064509. <https://doi.org/10.1063/1.2827462>
10. Shinde PS, Ahmed AN, Nahian MK, Peng Y, Reddy RG (2020) Conductivity of 1-Ethyl-3-Methylimidazolium Chloride (EMIC) and Aluminum Chloride (AlCl_3) Ionic Liquids at Different Temperatures and AlCl_3 Mole Fractions. *ECS Trans* 98:129–139. <https://doi.org/10.1149/09810.0129ecst>
11. Middlemiss LA, Rennie AJ, Sayers R, West AR (2020) Characterisation of batteries by electrochemical impedance spectroscopy. *Energy Rep* 6:232–241. <https://doi.org/10.1016/j.egy.2020.03.029>

12. Encinas-Sánchez V, Miguel MD, Lasanta M et al (2019) Electrochemical impedance spectroscopy (EIS): an efficient technique for monitoring corrosion processes in molten salt environments in CSP applications. *Sol Energy Mater Sol Cells* 191:157–163. <https://doi.org/10.1016/j.solmat.2018.11.007>
13. Uddin M-J, Cho S-J (2018) Reassessing the bulk ionic conductivity of solid-state electrolytes. *Sustain Energy Fuels* 2:1458–1462. <https://doi.org/10.1039/c8se00139a>
14. Wei Z, Ren Y, Wang M et al (2020) Improving the conductivity of solid polymer electrolyte by grain reforming. *Nanoscale Res Lett* 15:122. <https://doi.org/10.21203/rs.3.rs-17250/v1>
15. Lu J, Dreisinger D (2003) Electrochemistry: ionic liquid electroprocessing of reactive metals. *ACS Symp Ser* 495–508. <https://doi.org/10.1021/bk-2003-0856.ch039>
16. Shinde PS, Peng Y, Reddy RG (2020) Electrodeposition of titanium aluminide (TiAl) alloy from AlCl₃-BMIC ionic liquid at low temperature. In: TMS 2020 149th annual meeting & exhibition supplemental proceedings. The minerals, metals & materials series, pp 1659–1667. https://doi.org/10.1007/978-3-030-36296-6_153
17. Pradhan D, Reddy R, Lahiri A (2009) Low-temperature production of Ti-Al alloys using ionic liquid electrolytes: effect of process variables on current density, current efficiency, and deposit morphology. *Metall Mater Trans B* 40:114–122. <https://doi.org/10.1007/s11663-008-9214-y>
18. Yuan W-L, Yang X, He L et al (2018) Viscosity, conductivity, and electrochemical property of dicyanamide ionic liquids. *Front Chem*. <https://doi.org/10.3389/fchem.2018.00059>
19. Zheng Y, Dong K, Wang Q et al (2012) Density, viscosity, and conductivity of Lewis acidic 1-butyl- and 1-hydrogen-3-methylimidazolium chloroaluminate ionic liquids. *J Chem Eng Data* 58:32–42. <https://doi.org/10.1021/je3004904>
20. Ferrara C, Dall'Asta V, Berbenni V et al (2017) Physicochemical characterization of AlCl₃-1-ethyl-3-methylimidazolium chloride ionic liquid electrolytes for aluminum rechargeable batteries. *J Phys Chem C* 121:26607–26614. <https://doi.org/10.1021/acs.jpcc.7b07562>
21. Rosol ZP, German NJ, Gross SM (2009) Solubility, ionic conductivity and viscosity of lithium salts in room temperature ionic liquids. *Green Chem* 11:1453. <https://doi.org/10.1039/b818176d>
22. Tong J, Wu S, Solms NV et al (2020) The effect of concentration of lithium salt on the structural and transport properties of ionic liquid-based electrolytes. *Front Chem*. <https://doi.org/10.3389/fchem.2019.00945>
23. Vila J, Ginés P, Pico J et al (2006) Temperature dependence of the electrical conductivity in EMIM-based ionic liquids. *Fluid Phase Equilib* 242:141–146. <https://doi.org/10.1016/j.fluid.2006.01.022>
24. Kamavaram V (2004) Novel electrochemical refining of aluminum based materials in low temperature ionic liquid electrolytes. Ph.D. thesis, The University of Alabama

Determination of Physico-Chemical and Hardness Properties of Mullite Rich Tailings from Density Separated Copper Smelter Dust for Ceramic Application



D. O. Okanigbe, A. P. I. Popoola, and T. N. Makua

Abstract Aligning with the global goal of conserving mineral resources, it becomes necessary to evaluate the potential ceramic application of mullite rich tailings from density separated copper smelter dust (CSD). The aim was achieved by determining the physico-chemical analyses and mechanical property of mullite rich tailings for size fractions, chemical species, and hardness property, respectively. Screening test, XRF analysis, and Vickers hardness test of spark plasma sintered samples at 700 °C, 800 °C, and 900 °C were methods used. Results, showed 309.475 g of total mass (400.078 g) passed 53 μm sieve. Chemical analysis showed significant presence of silica (36.6 wt.%) and alumina (28.4 wt.%) in tailings. While, the micro-hardness results showed tailings sintered at 900 °C had the highest hardness value of 23.64 HV; presupposing increased sintering temperature will result in increased micro-hardness. In conclusion, results show copper tailings can be used for high temperature ceramic applications; thus, making the proposed density separation-hydrometallurgical-based approach for treatment of CSD, a sustainable technology, with high chances of zero waste production.

Keywords Copper smelter dust · Mullite rich tailings · Density separation · Spark plasma sintering · Ceramic application · Hardness test

Introduction

Based on reports in the open literature, ceramics are considered solid material encompassing inorganic compound of metal, non-metal or metalloid atoms, primarily held in ionic and covalent bonds [1]. According to Munz and Fett [2], ceramics have found use in refractories [3–6], spark plugs [7–9], dielectrics in capacitors [10, 11], sensors [12, 13], abrasives [14], and magnetic recording media [15]. They are also used as coatings to glass and metallic objects. They appear in nature as oxides [2, 16, 17].

D. O. Okanigbe (✉) · A. P. I. Popoola · T. N. Makua
Department of Chemical, Metallurgical and Materials Engineering, Tshwane University of Technology, Pretoria 0183, South Africa
e-mail: okanigbedo@tut.ac.za

mullite rich tailings can be used to produce quality type construction ceramic [18–22]. Utilizing this waste resource will not only improve environmental conditions but also results in a ceramic of high quality with improved strength and durability [23, 24]. mullite rich tailings can be blended with other raw materials to produce unglazed tiles [25–27]. Several studies have investigated the use of tailings waste in manufacturing of bricks of high quality fired at firing temperature of 950 °C [27–30].

The mullite rich tailings produced from the density separated copper smelter dust (CSD), a waste metal dust, obtained from the smelting factory of Palabora copper (PTY), Limpopo, in Phalaborwa, South Africa (PC), during copper smelting and refining processes, contains significant amount of aluminosilicates, as shown by chemical analysis results obtained using the X-Ray fluorescence (XRF). However, the need to investigate its suitability as a material for the production of high temperature ceramic products, in order to consolidate the goal of conserving natural resources and reduction of earth's excavation for natural resources.

This can be achieved by determining the suitability (i.e., Physico-Chemical and Hardness Properties) of this mullite rich tailings for ceramic application, owing to the significant amount of aluminosilicates, it contains as previously mentioned. According to Li et al. [31], mechanical properties are key in structural and building materials. In modern materials science, fracture mechanics is an essential tool in enhancing the mechanical performance of materials and components [32]. It adopts the physics of stress and strain, with particular reference to theories of elasticity and plasticity, in relation to microscopic crystallographic defects found in real materials with the intent of predicting macroscopic mechanical failure of bodies [32]. Fractography have been extensively used in area of fracture mechanics to better understand the causes of failures and also verify the theoretical failure predictions with real life failures. According to Barsoum and Barsoum [33], more often than not ceramic materials are usually ionic or covalently bonded materials, which can occur as crystalline or amorphous material ionically or covalently bonded which tend to fracture prior to plastic deformation, thus resulting in poor toughness in these materials. Additionally, these materials have a tendency of being porous, the pores and other microscopic imperfections presents challenges of stress concentrators, which consequently decreases the toughness further, thereby reducing the tensile strength. These combine to give catastrophic failures, as opposed to the more ductile failure modes of metals.

The absence of literature on the properties of the mullite rich tailings from density separated CSD, leaves a gap of knowledge that needs to be filled. Hence, this research seek to determine and present findings from study on the physico-chemical and hardness properties of mullite rich tailings from the density separated CSD from Palabora copper (PTY), Limpopo, South Africa.

Experimental Approach

Materials and Methods

Material

The starting material used for this study is the mullite rich tailings obtained from the density separation of CSD from Palabora copper (PTY), Limpopo, South Africa.

Methods

Ore Handling and Sample Preparation

- **Ore Handling**

The mullite rich tailings weighed 830 g after sampling. The 830 g of mullite rich tailings was divided into two fractions. The fraction that was used for this experiment weighed 400.078 g. This mass was homogenized and divided with the rotary splitter to produce representative samples that were used in the characterization of the mullite rich tailings.

- **Sample Preparation**

The rotary splitter is used to homogenize a material or sample. After the sieve test, the material was combined and fed to the rotary splitter in order to obtain an identical product of the material sample. For this study using the bulk density calculation and the number of samples required, a mass of 65 g was required and it was weight from the product sample of the rotary splitter. This mass will be sintered and analyzed for mechanical properties.

Characterization of DST

- **Particle Size Distribution (PSD)**

The individual sieves were prepared by first washing with tap water and drying in the hot rapid drying oven at a temperature of 300 °C for 20 min. The sieves used were as follows: 212, 150, 106, 75, 53 μ m, and pan. These sieves were weight as empty using the weighing balance before the test. They were stacked from large opening to small opening and the 400.078 g was poured on the 212 sieve which is the top sieve. The shaker was set to a frequency of five for a period of one hour upon completion it was further set to a frequency of ten for thirty minutes. The individual sieves were weight again to determine the amount of mass retained in each sieve and the material loss. The data obtained was recorded under the particle size distribution table and plotted on a graph, which will be later discussed.

• Chemical Composition

The chemical species present in density separated CSD tailing was analyzed with the XRF machine.

Spark Plasma Sintering

The sintering parameters used for study are as follows: temperature: 700 °C, 800 °C, and 900 °C; heating rate: 90 °C/min; pressure: 50 MPa and cooling time: 10 min.

Spark Plasma Sintering Graphs

• First Batch: Two Samples

The graph detail the spark plasma sintering trend of mullite rich tailings, sintered at an initial temperature of 250 °C to a maximum temperature of 700 °C. The samples were cooled for 10 min and maintaining a pressure of 50 MPa and heating rate of 90 °C/min (Fig. 1a, b).

• Second Batch: Two Samples

The samples were sintered at an initial temperature of 250 °C to a maximum temperature of 800 °C, maintain the pressure of 50 MPa and heating rate of 90 °C/min. The sintering trend is detailed in the graph (Fig. 2a, b).

• Third Batch: Two Samples

The initial sintering temperature was 250 °C to a maximum temperature of 900 °C, maintain a pressure of 50 MPa and heat rate 90 °C/min, the graph detailed the results and a trend obtained during sintering (Fig. 3a, b).

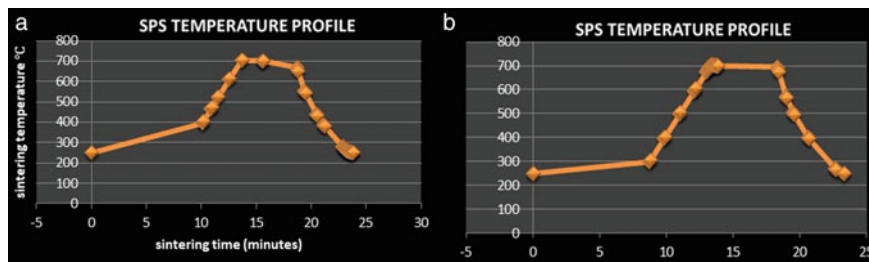


Fig. 1 a SPS curve at 700 °C for Sample 1, b SPS curve at 700 °C for Sample 2. (Color figure online)

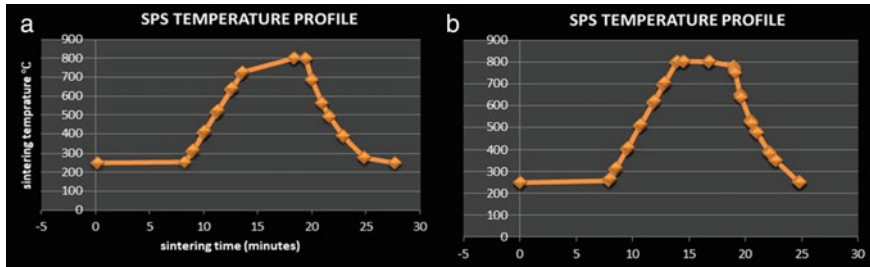


Fig. 2 a SPS curve at 800 °C for sample 3, b SPS curve at 800 °C for sample 4. (Color figure online)

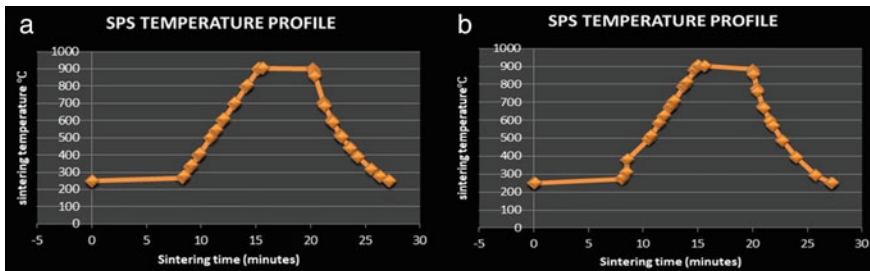


Fig. 3 SPS Curve at 900 °C for a Sample 5, b for Sample 6. (Color figure online)

Vickers' Hardness Test

The sintered samples (700 °C, 800 °C and 900 °C) were first prepared by cutting into smaller test samples (Fig. 4a–f), each sample was placed on the Vickers hardness test machine stand, clamped to prevent any movement during the test which can alter the hardness results by scratching the sample surface thereby giving wrong results. The machine was operated at a load of 25 g and dwell time of 15 s, with a pitch of 0.100 and a swing of 0.000. These parameters are programmed on the machine monitor before the test can proceed. The indentation is made and read off which is made visible by the microscope. The load was maintained at 25 g because the material is soft, a load of 100 g was first used, and it scratched the sample.

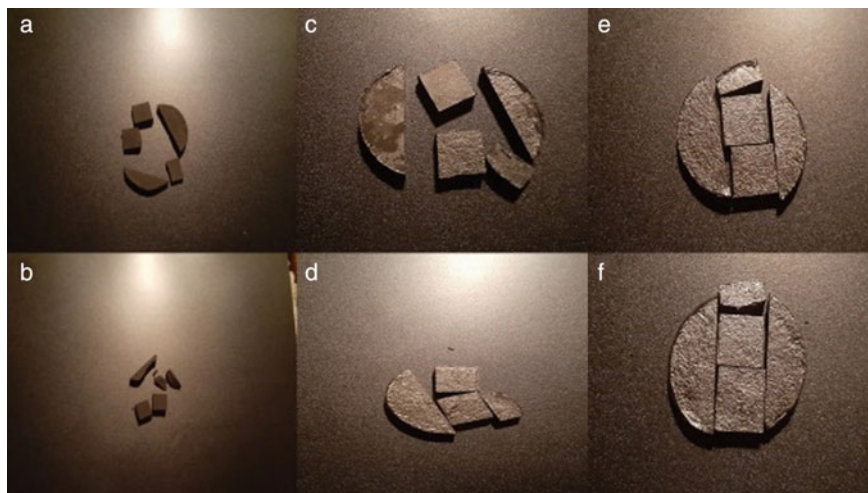


Fig. 4 Machined samples **a, b** 700 °C, **c, d** 800 °C, **e, f** 900 °C. (Color figure online)

Results and Discussion

Characterization

Particle Size Distribution

Table 1 outlines results from screening tests with the bulk of the material reporting to the 53 μm sieve. On the pan, the material that report as undersize was 309.475 g.

Table 1 Particle size analysis of density separated tailings

SN	SA	SM	SM + tailings	Tailings (g)	IR $f(x)$ %	CP $Q(x)$ %
1	212	280.3	281.706	1.403	0.352	99.648
2	150	260.94	263.08	2.139	0.537	99.111
3	106	258.1	260.991	2.896	0.727	98.384
4	75	257.82	273.051	15.235	3.824	94.560
5	53	243.1	310.35	67.249	16.880	77.680
6	0	419.68	729.15	309.475	77.680	0.000
Mass after sieving				398.397		
Initial mass				400.078		
Mass loss				1.681		
Percent mass loss				0.420		

Key SN = sieve number; SA = sieve aperture, SM = sieve mass, IR = individual retained, CP = cumulative passing

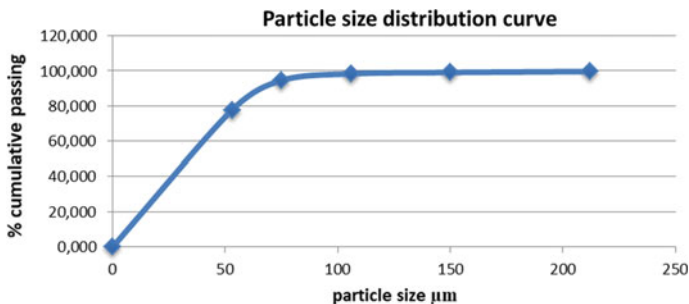


Fig. 5 Particle size distribution curve of CSD density separated tailings. (Color figure online)

After the test, there was a material loss of 1.881 g resulting in a percentage material loss of 0.420, this material was lost as dust. The particles that make up the copper tailings are such that about 0.352% is retained on the coarse sieve 212 μm , while 99.6648% passed through it. Similarly, about 0.889% of the dust constitutes the oversize on the 150 μm sieve, while 99.111% constitutes the undersize for it. It was further observed that about 77.680% of the materials passed through the 53 μm sieve unto the receiving pan. Qualitatively, most of the particles are very fine size below the 53 μm sieve aperture size falling within the range of 5–50 μm as reported in literature. Figure 5 outlines the PSD results showing cumulative passing against sieve aperture size.

Chemical Composition

The amount of chemical species present in mullite rich tailings is as compared to the parent material is shown in Table 2 (with emphasis on $\text{SiO}_2 = 36.61\%$ and $\text{Al}_2\text{O}_3 = 28.43\%$). The comparative analysis show that mullite content has been upgraded by 78% after one pass of the density separation. Mullite, a clay mineral, composed of aluminum oxide and silica oxide, is mainly used in ceramic application.

Table 2 X-ray fluorescence results of CTWR

Elements	CuO	Fe ₂ O ₃	S	ZnO	PbO	Bi ₂ O ₃	CaO	MgO	TiO	SiO ₂	Al ₂ O ₃	Others
CSD wt. (%)	18.02	13.36	3.44	0.27	0.12	0.002	3.52	2.86	1.11	33.06	22.19	1.95
Tailings wt. (%)	15.65	10.65	1.44	0.42	0.17	0.03	2.06	1.59	1.36	36.61	28.43	2.04

Table 3 Mechanical property of spark plasma sintered CSD density separated tailing

Sample number	Sintering temperature (°C)	Vickers' hardness (HV)		Dwell time (s)	Load
		Minimum	Maximum		
1	700	10.59	16.32	15	25
2	800	13.33	17.7	15	25
3	900	14.68	23.64	15	25

Mechanical Property

Hardness

Table 3 displays the results obtained after the micro-hardness test using the FM-800 Vickers hardness test, the results obtained show that as the sintering temperature increases the hardness value also increase. The sintering temperature of 900 °C has a hardness value of 23.64 HV while the sintering temperature of 700 °C and 800 °C has a hardness value of 16.32 and 17.7 HV respectively. The sample that was sintered at 900 °C has a higher hardness value than the one sintered at 800 and 700 °C, therefore an increase in sintering temperature results in an increase micro-hardness according to the results obtained above.

Conclusion

This study explored the possibility of utilizing mullite rich tailings for the production of ceramic profiles, and the deductions leading to this point are as follows:

1. 309.475 g of total mass (400.078 g) passed 53 μm sieve.
2. Chemical analysis showed significant presence of silica (36.6 wt.%) and alumina (28.4 wt.%) in tailings.
3. While, the micro-hardness results showed tailings sintered at 900 °C had the highest hardness value of 23.64 HV; presupposing increased sintering temperature will result in increased micro-hardness.

Hence, in conclusion, results show tailings can be used for high temperature ceramic applications, thus making the proposed density separation-hydrometallurgical-based for treatment of CSD, a sustainable technology, with high chances of zero waste production.

Acknowledgements The authors acknowledge the Department of Chemical, Metallurgical and Materials Engineering, Tshwane University of Technology for allowing access to facilities and providing material used for study.

References

1. Reed JS (1995) Principles of ceramics processing
2. Munz D, Fett T (2013) Ceramics: mechanical properties, failure behavior, materials selection, vol 36. Springer Science & Business Media
3. Kusiorowski R (2020) MgO-ZrO₂ refractory ceramics based on recycled magnesia-carbon bricks. *Constr Build Mater* 231:117084
4. Backman L, Gild J, Luo J, Opila EJ (2020) Part II: experimental verification of computationally predicted preferential oxidation of refractory high entropy ultra-high temperature ceramics. *Acta Mater* 197:81–90
5. Liu H, Jie C, Ma Y, Wang Z, Wang X (2020) Synthesis and processing effects on microstructure and mechanical properties of forsterite ceramics. *Trans Indian Ceram Soc* 79(2):83–87
6. Dai Y, Harmuth H, Jin S, Gruber D, Li Y (2020) R-curves determination of ordinary refractory ceramics assisted by digital image correlation method. *J Eur Ceram Soc*
7. Tsujii A, Kasashima T, Yamazaki M, Okimura Y (2020) Application of (K, Na) NbO₃-based lead-free piezoelectric ceramics to ultrasonic sensors. *J Ceram Soc Jpn* 128(8):464–468
8. Colombari P (2020) Chemical preparation routes and lowering the sintering temperature of ceramics. *Ceramics* 3(3):312–339
9. Yokoyama Y, Araki N, Tanaka K, Yoshida H, Uegaki H, Toshiki KON, Nomura Y, NGK Spark Plug Co Ltd (2020) Spark plug. U.S. Patent Application 16/574,170
10. Lu Z, Wang G, Bao W, Li J, Li L, Mostaed A, Yang H, Ji H, Li D, Feteira A, Xu F (2020) Superior energy density through tailored dopant strategies in multilayer ceramic capacitors. *Energy Environ Sci*
11. Li J, Shen Z, Chen X, Yang S, Zhou W, Wang M, Wang L, Kou Q, Liu Y, Li Q, Xu Z (2020) Grain-orientation-engineered multilayer ceramic capacitors for energy storage applications. *Nat Mater* 19(9):999–1005
12. Lei J, Zhang Q, Song Y, Tang J, Tong J, Peng F, Xiao H (2020) Laser-assisted embedding of all-glass optical fiber sensors into bulk ceramics for high-temperature applications. *Opt Laser Technol* 128:106223
13. Fan Z, Diao X, Hu K, Zhang Y, Huang Z, Kang Y, Yan H (2020) Structural health monitoring of metal-to-glass–ceramics penetration during thermal cycling aging using femto-laser inscribed FBG sensors. *Sci Rep* 10(1):1–13
14. Zhu D, Song S, Qu C, Lv Y, Wu C (2020) Numerical investigation of crack initiation, propagation and suppression in robot-assisted abrasive belt grinding of zirconia ceramics via an improved chip-thickness model. *Ceram Int*
15. Kumar A, Verma MK, Singh S, Das T, Singh L, Mandal KD (2020) Electrical, magnetic and dielectric properties of cobalt-doped barium hexaferrite BaFe_{12-x}Co_xO₁₉ (x = 0.0, 0.05, 0.1 and 0.2) ceramic prepared via a chemical route. *J Electron Mater* 1–12
16. Okanigbe DO, Popoola API, Adeleke, AA (2017a) Characterization of copper smelter dust for copper recovery. *J Procedia Manufacturing* 7:121–126
17. Okanigbe DO, Popoola API, Adeleke, AA (2017b). Hydrometallurgical processing of copper smelter dust for copper recovery as nano-particles: a review. In *Energy technology 2017*, Springer, Cham, pp 205–226
18. Ahmari S, Zhang L (2012) Production of eco-friendly bricks from copper mine tailings through geopolymerization. *Constr Build Mater* 29:323–331
19. Lemougna PN, Yliniemi J, Ismailov A, Levanen E, Tanskanen P, Kinnunen P, Roning J, Illikainen M (2019) Recycling lithium mine tailings in the production of low temperature (700–900 °C) ceramics: effect of ladle slag and sodium compounds on the processing and final properties. *Constr Build Mater* 221:332–344
20. Zadeh AJ, Sarrafi A, Izadpanah MR, Aminian F, Ghotbi E (2011) Production of ceramic tiles from the waste materials of copper extraction process
21. Lemougna PN, Yliniemi J, Adesanya E, Tanskanen P, Kinnunen P, Roning J, Illikainen M (2020) Reuse of copper slag in high-strength building ceramics containing spodumene tailings as fluxing agent. *Miner Eng* 155:106448

22. Suvorova OV, Selivanova EA, Mikhailova JA, Masloboev VA, Makarov DV (2020) Ceramic products from mining and metallurgical waste. *Appl Sci* 10(10):3515
23. Amin M, Tayeh BA (2020) Effect of using mineral admixtures and ceramic wastes as coarse aggregates on properties of ultrahigh-performance concrete. *J Clean Prod* 123073
24. Nwankwo CO, Bamigboye GO, Davies IE, Michaels TA (2020) High volume Portland cement replacement: a review. *Constr Build Mater* 260:120445
25. Mohaddes Khorassani S, Siligardi C, Mugoni C, Pini M, Cappucci GM, Ferrari AM (2020) Life cycle assessment of a ceramic glaze containing copper slags and its application on ceramic tile. *Int J Appl Ceram Technol* 17(1):42–54
26. Getem C (2020) Synthesis and characterization of β -wollastonite from limestone and rice husk as reinforcement for ceramic tile. Doctoral dissertation
27. Lemougna PN, Yliniemi J, Nguyen H, Adesanya E, Tanskanen P, Kinnunen P, Roning J, Illikainen M (2020) Utilisation of glass wool waste and mine tailings in high performance building ceramics. *J Build Eng* 101383
28. Sing SL, Yeong WY, Wiria FE, Tay BY, Zhao Z, Zhao L, Tian Z, Yang S (2017) Direct selective laser sintering and melting of ceramics: a review. *Rapid Prototyp J* 23(3):611–623
29. Rehman MU, Ahmad M, Rashid K (2020) Influence of fluxing oxides from waste on the production and physico-mechanical properties of fired clay brick: a review. *J Build Eng* 27:100965
30. dos Reis GS, Cazacliu BG, Cothenet A, Poullain P, Wilhelm M, Sampaio CH, Lima EC, Ambros W, Torrenti JM (2020) Fabrication, microstructure, and properties of fired clay bricks using construction and demolition waste sludge as the main additive. *J Clean Prod* 120733
31. Li HX, Li BW, Deng LB, Xu PF, Du YS, Ouyang SI (2018) Microwave assisted processing of graded structural tailings glass-ceramics. *J Eur Ceram Soc* 2632–2638
32. Hutchinson JW, Evans AG (2000) Mechanics of materials: top-down approaches to fracture. *Acta Mater* 48(1):125–135
33. Barsoum M, Barsoum MW (2002) Fundamentals of ceramics. CRC Press

Electrochemical Separation of Aluminum from Mixed Scrap Using Ionic Liquids



Aninda Nafis Ahmed and Ramana Reddy

Abstract Electrodeposition of aluminum was conducted on three types of ionic liquids (ILs); EMIC, BMIC and HMIC with AlCl_3 . The molar ratio of $\text{IL}:\text{AlCl}_3 = 1:2$ was determined to be optimum for all three ILs. Over 170 A/m^2 current density with more than 85% current efficiency was obtained for EMIC system. Similarly, for BMIC, over 300 A/m^2 current density was found with more than 85% current efficiency, and for HMIC, more than 250 A/m^2 of current density with over 85% current efficiency was obtained. Based on the lab-scale experimental findings, scale-up experiments were carried out for $\text{BMIC}:\text{AlCl}_3 = 1:2$ molar ratio. Significant increase in current density was observed when higher potentials were applied. More than 220 A/m^2 of current density was observed for the scale-up system. Additionally, shorter distance between anode and cathode ($\sim 1 \text{ cm}$) and higher stirring rate (120 rpm) produced higher current densities. The outcome of this work would facilitate the scale-up studies for the electrochemical separation of aluminum from mixed scrap.

Keywords Ionic liquids · Potential · Current density · Electrode distance · Stirring speed

Introduction

The commercial production of aluminum starts with the conversion of bauxite ore into alumina (Al_2O_3) followed by the electrolysis of alumina into aluminum metal, where alumina is dissolved in molten cryolite. The required process temperature in this case is $900\text{--}1000 \text{ }^\circ\text{C}$ high temperature process involves high-energy consumption and pollution as well. Apart from this, the other available commercial processes like carbothermic process, Alcoa's method also involve high temperatures. Since aluminum has a fast and expanding market, the demand can be fulfilled with effective primary production routes or by secondary recycling. However, minimizing the

A. N. Ahmed · R. Reddy (✉)

Department of Metallurgical and Materials Engineering, The University of Alabama, Tuscaloosa, AL 35487, USA

e-mail: reddy@eng.ua.edu

cost of production by ensuring low energy consumption and low pollution is also challenging. It has been found that, recycling of aluminum can save up to 70% energy in comparison with the primary production process [1]. Therefore, interest towards recycling has increased tremendously in recent years.

As aluminum has negative reduction potential, it cannot be used for electrochemical reduction in aqueous solution. As a result, an immersing route with ionic liquids can be promising for aluminum recycling due to their unique properties. Ionic liquids are salts having organic cation and organic/inorganic anion. Due to the nature of their bond, ionic liquids have much lower melting temperature ~ 100 °C than cryolite. They could provide much flexibility for aluminum synthesis in terms of wide liquidus temperature, high thermal stability, negligible vapor pressure, low melting point and wide electrochemical window [2]. Therefore, ionic liquid can significantly reduce the processing temperature of aluminum recycling to as low as 100 °C, which attracts researcher for exploring low temperature aluminum synthesis.

In recent years, researchers have studied different aspects of ionic liquids for aluminum electrorefining. For instance, some worked with constant potential approach [1–12]. While others studied with constant current approach [9, 13, 14]. Furthermore, studies have been conducted on different types of ionic liquids like EMIC, BMIC, HMIC, the major variables of the system are temperatures, potentials, types of electrodes, stirring speed, electrode distance etc.

Reddy and co-workers reported several works on several ionic liquid systems. For EMIC system, (EMIC:AlCl₃ = 1:2 molar ratio (MR)) more than 170 A/m² of current density was reported with a current efficiency more than 85% [1, 3]. They also reported works on BMIC system, (BMIC:AlCl₃ = 1:2 MR). Over 300 A/m² current density was found with more than 85% current efficiency [8]. For HMIC (MR 1:2), the current density was reported more than 250 A/m² [4]. Current efficiency was obtained more than 85% for the same system. All these works were conducted in 50 cc volume cells. However, limited scale-up experimental data are available, which is crucial to find the prospect of industrial use.

In this work, the electrorefining of aluminum was performed in a scale-up setup with 600 mL beaker cell, about ten times higher capacity than the lab-scale experiments. The 1-butyl-3-methylimidazolium chloride (BMIC) ionic liquid with AlCl₃ was used for the study. This paper includes the results obtained on the effect of applied potential, electrode distance, and stirring speed on current density and efficiency of electrochemical separation of aluminum from mixed scrap.

Experimental Procedure

The electrochemical separation of aluminum was carried out in 600 mL glass beaker cell fitted with teflon lid. The lid contained electrodes, thermometer and port for argon purging. Copper cathode was prepared by cutting 0.5 mm thick, 99.98% pure copper plate obtained from Sigma Aldrich® into ~ 75 mm \times 49 mm \times 0.5 mm size electrodes. Aluminum anodes were prepared from Al ingot, made from scrap metal,

into $\sim 70 \text{ mm} \times 40 \text{ mm} \times 3 \text{ mm}$ size electrodes. Both anode and cathode were polished with 240 SiC grit paper followed by 600 grit paper before using for electrolysis. The effective area of the electrodes was measured by measuring the actual area of the electrodes immersed into the electrolyte.

The ionic liquid was prepared by measuring 1-butyl-3-methylimidazolium chloride (BMIC) ($\geq 98.0\%$) from Sigma Aldrich[®] and anhydrous AlCl_3 (95%+) from Alfa Aesar[®] on electronic precision balance at 1:2 molar ratio and mixed in 600 ml beaker on a hot plate with 60 rpm magnetic stirring. After preparing the ionic liquid, the electrodes were inserted into the solution with argon purging at a rate of 60 cc/min throughout the experiments. Argon was continuously supplied at same rate to preserve the solution when experiments were not running.

Power source (Kepco[®] Programmable Power Supply) supplied the required voltage across anode and cathode, and current was measured by precision multimeter (Keithley[®] 2000 Multimeter). After maintaining a temperature of 100 °C, variable potentials were applied from power supply for different conditions. Solution was continuously stirred with magnetic stirrer with variable speed (60–120 rpm). Electrolysis was done for 4 h for each of the experiments, where anode–cathode distances were varied from 1 to 2 cm. Same solution was used for all the experiments since this was scale-up study. However, electrical conductivity of the solution was monitored from time to time in order to monitor the quality of the ionic liquid solution with (Corning[®] Pinnacle 541) conductivity meter. Temperature was continuously monitored by inserting thermometer into ionic liquid. Current density was calculated by dividing the current by active cathode area, and microstructure analysis was done by SEM (JEOL 7000).

Results and Discussion

Effect of Applied Potential on Current Density

Lab-scale experiments were optimized for 1:2 molar ratio with an applied potential of 1.5 V for EMIC, BMIC and HMIC where current density over 170, 300 and 250 A/m^2 was obtained, respectively [1, 3, 4, 8]. Therefore, initially scale-up experiments were designed for the BMIC: AlCl_3 (MR 1:2) system for which maximum current density was obtained in lab scale at 1.5 V. The following reactions take place during the electrolysis of aluminum in ionic liquids inside the cell:

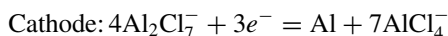
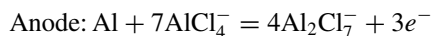


Figure 1 shows the current density with 1.5 V of applied potential across anode and cathode for scale-up experiment. The current density profile was found below

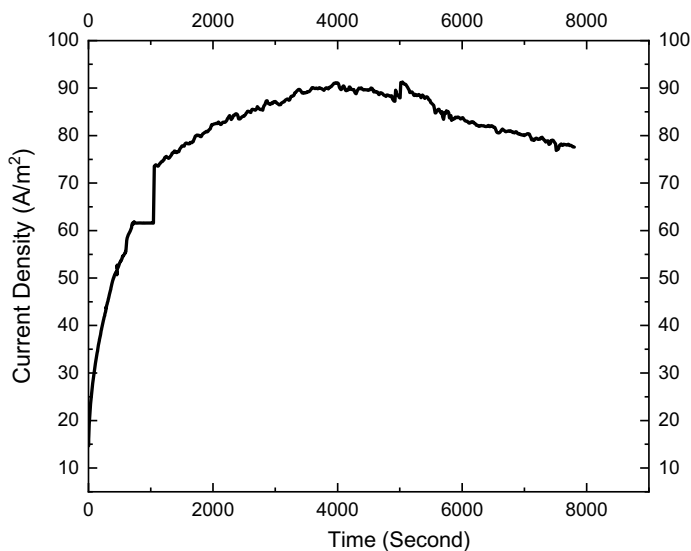


Fig. 1 Current density versus time for 1.5 V applied potential and, 2 cm electrode distance, 60 rpm stirring speed at 100 °C temperature

100 A/m², which is significantly lower than the lab-scale experiments as reported by Wang 307.5 A/m² [8]. Higher current density is always desired for higher deposition rates of the aluminum [8]. As a result, 1.5 V was not found enough for producing higher current density for scale-up system. Higher potential is needed for scale-up system in order to obtain higher current density.

Figure 2 illustrates the effect of applied potential on current density showing an increasing trend with applied voltage. The rate of reduction on cathode increases with higher potentials resulting in increased current density [6].

A significant rise in current density, is observed from 3 to 4 V compared to the applied potential from 2 to 3 V. Maximum current density of 146.7 A/m² for 3 V was found, while for similar lab-scale conditions at 140 °C and 105 °C, current densities of 310 A/m² and 235 A/m² were reported, respectively [5–7], which are higher than scale-up condition.

Furthermore, maximum current density of 257.98 A/m² was obtained for 4 V (Fig. 2), which is maximum for the applied range of potentials (1.5–4.0 V). However, researchers have reported higher current density (300 A/m²) for similar conditions at 3.4 V [5].

Therefore, it can be said that, scale-up experiments require higher potential for overcoming the system resistance, polarization and overpotentials.

The outcome of the 4 V encouraged the author to study the system with 4.5 V. However, fluctuating current density was observed in case of 4.5 V. The fluctuation is not desired for a stable production of aluminum. Therefore, 4 V was found optimum

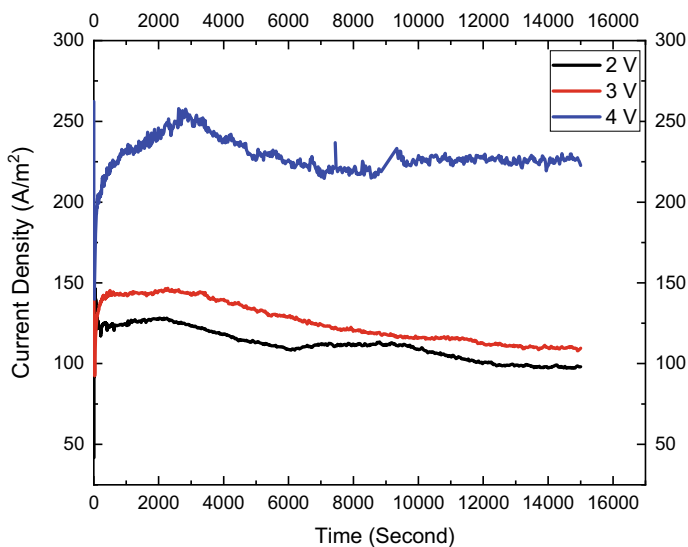


Fig. 2 Effect of applied potential on current density with 2 cm electrode distance, 60 rpm stirring speed and 100 °C temperature. (Color figure online)

for the scale-up system, and further studies were carried out at applied potential of 4 V to the cell.

Effect of Electrode Distance on Current Density

The effect of distance between anode and cathode on current density is shown in Fig. 3. With the decrease of electrode distance, current density increased. Reduction of electrode distance has stronger influence in lowering the internal resistance of the system, thus increasing current density of the system [15]. Moreover, in Fig. 2, the 4 V–2 cm distance data provided much higher current density than in Fig. 3. The drop can be attributed to the decrease of electrical conductivity with time. In Fig. 2, the electrical conductivity was found to be 2.43 S/m where as in Fig. 3 conductivity dropped to 1.88 S/m.

Effect of Stirring Speed on Current Density

Effect of stirring speed is shown in Fig. 4 where current density increased with increasing stirring speed. Though 90 rpm stirring produced higher current density in early stages but later in the stable region after 8000 s it followed the trend. Stirring

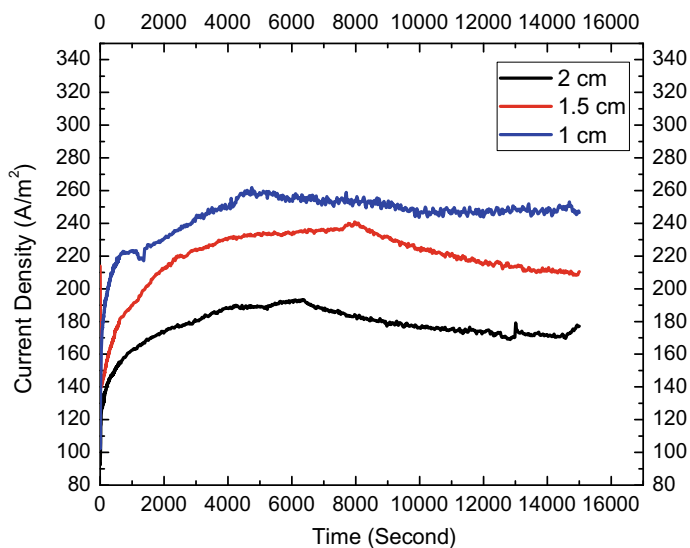


Fig. 3 Effect of electrode distance on current density with 4 V applied potential and 60 rpm stirring speed at temperature of 100 °C. (Color figure online)

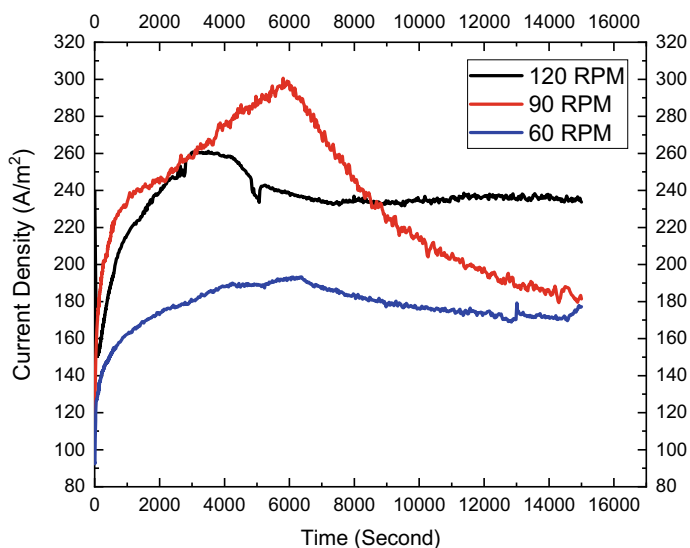


Fig. 4 Effect of stirring speed on current density with applied potential of 4 V, electrode distance of 2 cm and temperature of 100 °C. (Color figure online)

has significant effect in transporting the reducible ion (Al_2Cl_7^-) towards cathode essentially increasing the current density of the system [16]. More than 16% rise in current density was reported by Wang for lab-scale experiments from 60 to 120 rpm of stirring speed [8], whereas in this work, more than 37% rise was observed for the same conditions. However, higher stirring rate may produce some issues in scale-up experiments like spalling off metals from cathode, increasing ionic liquid in the deposited metals, which is important in the context of getting high purity and high yield during aluminum production.

Microstructure of Cathode Deposits

Figure 5 shows the SEM micrographs of the deposited aluminum collected from cathode, where it shows the granular morphology of the particles with different potential. The EDS study shows 96.8 at% Al for 2 V, 91.8 at% Al for 3 V and

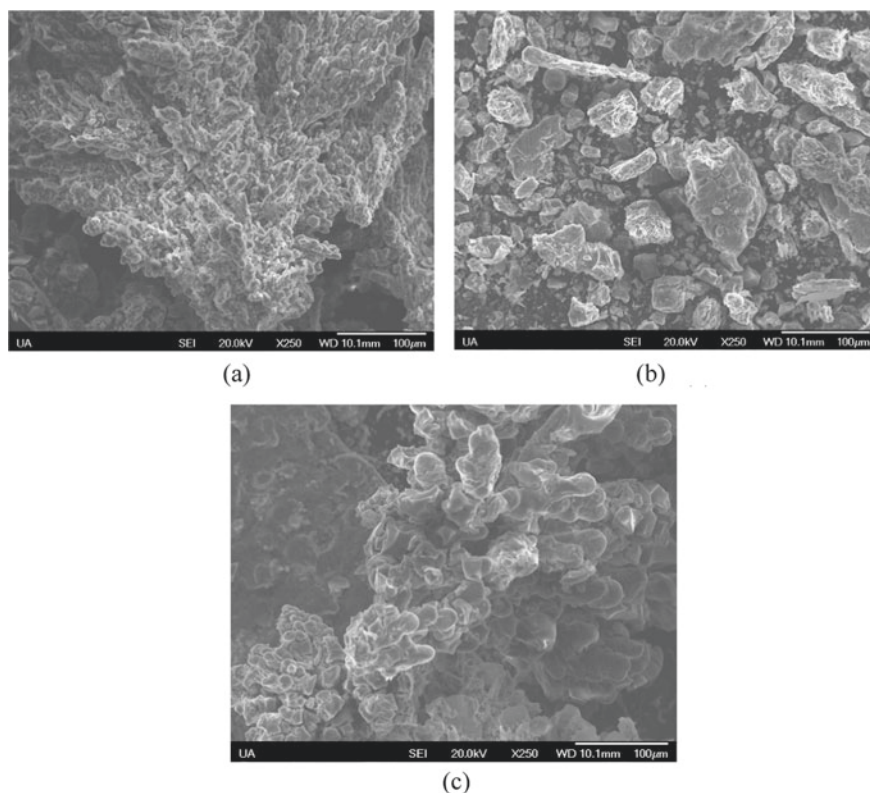


Fig. 5 SEM microstructures of deposited aluminum at varying potential **a** 2 V, **b** 3 V and **c** 4 V, with 60 rpm stirring speed and 2 cm electrode distance at 100 °C

88.6 at% Al for 4 V, respectively. Higher potential reduced the purity of the deposited aluminum on cathode. Moreover, copper, chlorine and manganese impurities were detected in EDS. Since Al anode is from scrap alloys like Al 2020, which contains copper and manganese [17], anode is the possible source of these elements. Chlorine may come from the ionic liquid, which contains chloride ions.

Conclusions

Electrolysis of aluminum in scale-up system was investigated on the basis of previously reported lab-scale data on BMIC:AlCl₃ = 1:2 molar ratio. Lab-scale voltage (1.5 V) was not enough for getting higher current density for scale-up system. Internal resistance and, polarization of the cell can be attributed to this phenomenon, and requires further study in the future. More than 220 A/m² current density was found for 4 V applied potential, which was optimum for the scale-up experiments. Additionally, lower electrode distance (~1 cm) and higher stirring speed (120 rpm) also facilitated the current density. However, lowering of electrical conductivity with time was found to be a significant factor for reduced current density for the same system. SEM analysis revealed the granular morphology of the deposited aluminum with 88–96% purity of aluminum with different voltages. On the basis of this work, future studies on internal resistance of system, polarization, diffusion mechanisms and energy requirement will be needed for efficient electrochemical separation of aluminum from mixed scrap scale-up applications.

Acknowledgements The authors acknowledge the financial support received from the Department of Energy (DOE) RAPID Manufacturing Institute and ACIPCO for this research project. Authors also thank the Department of Metallurgical and Materials Engineering, The University of Alabama for providing experimental and analytical facilities.

References

1. Pradhan D, Reddy RG (2012) Dendrite-free aluminum electrodeposition from AlCl₃-1-ethyl-3-methyl-imidazolium chloride ionic liquid electrolytes. *Metall Mater Trans B* 43(3):519–531
2. Pradhan D, Mantha D, Reddy RG (2009) The effect of electrode surface modification and cathode overpotential on deposit characteristics in aluminum electrorefining using EMIC–AlCl₃ ionic liquid electrolyte. *Electrochim Acta* 54(26):6661–6667
3. Pradhan D (2010) Fundamental studies on electrochemical production of dendrite-free aluminum and titanium-aluminum alloys (Order No. 3439836). Available from dissertations & theses @ University of Alabama; ProQuest dissertations & theses global (851877550). <https://search.proquest.com/docview/851877550>
4. Kamavaram V (2002) Electrorefining of aluminum in C₆mimCl + AlCl₃ ionic liquid at near room temperature. *ECS Proc Vol* 2002–19(1):840–846
5. Zhang M (2008) Modeling and experimental validation of aluminum electrowinning in chloroaluminate ionic liquids at low temperatures (Order No. 3371551). Available from dissertations &

- theses @ University of Alabama; ProQuest dissertations & theses global (304682633). <https://search.proquest.com/docview/304682633>
6. Kamavaram V, Mantha D, Reddy RG (2003) Electrorefining of aluminum alloy in ionic liquids at low temperatures. *J Min Metall Sect B Metall* 39(1–2):43–58
 7. Kamavaram V (2004) Novel electrochemical refining of aluminum based materials in low temperature ionic liquid electrolytes (Order No. 3163556). Available from dissertations & theses @ University of Alabama; ProQuest dissertations & theses global (305209849). <https://search.proquest.com/docview/305209849>
 8. Wang Y (2020) Development of aluminum electrorefining in ionic liquids: the effects of experimental conditions on the deposition behavior and microstructure. Masters thesis, The University of Alabama
 9. Jiang T, Chollier Brym MJ, Dubé G, Lasia A, Brisard GM (2006) Electrodeposition of aluminium from ionic liquids: part I-electrodeposition and surface morphology of aluminium from aluminium chloride (AlCl_3)-1-ethyl-3-methylimidazolium chloride ([EMIm]Cl) ionic liquids. *Surf Coat Technol* 201(1–2):1–9
 10. Ispas A, Bund A, Böttcher R, Mai S (2020) Aluminum deposition and dissolution in [EMIm]Cl-based ionic liquids—kinetics of charge—transfer and the rate—determining step. *J Electrochem Soc* 1
 11. Wang Q, Chen B, Zhang Q, Lu X, Zhang S (2015) Aluminum deposition from Lewis acidic 1-butyl-3-methylimidazolium chloroaluminate ionic liquid ([Bmim]Cl/ AlCl_3) modified with methyl nicotinate. *ChemElectroChem* 2(11):1794–1798
 12. Chang JK, Chen SY, Tsai WT, Deng MJ, Sun IW (2007) Electrodeposition of aluminum on magnesium alloy in aluminum chloride (AlCl_3)-1-ethyl-3-methylimidazolium chloride (EMIC) ionic liquid and its corrosion behavior. *Electrochem Commun* 9(7):1602–1606
 13. Al Farisi MS, Hertel S, Wiemer M, Otto T (2018) Aluminum patterned electroplating from AlCl_3 -[EMIm]Cl ionic liquid towards microsystems application. *Micromachines* 9(11)
 14. Guinea E, Salicio-Paz A, Iriarte A, Grande HJ, Medina E, García-Lecina E (2019) Robust aluminum electrodeposition from ionic liquid electrolytes containing light aromatic naphta as additive. *ChemistryOpen* 8(8):1094–1099
 15. Park JG, Lee B, Shi P, Kim Y, Jun HB (2017) Effects of electrode distance and mixing velocity on current density and methane production in an anaerobic digester equipped with a microbial methanogenesis cell. *Int J Hydrogen Energy* 42(45):27732–27740
 16. Pradhan D, Reddy RG (2014) Mechanistic study of Al electrodeposition from EMIC- AlCl_3 and BMIC- AlCl_3 electrolytes at low temperature. *Mater Chem Phys* 143(2):564–569
 17. Vasudévan AK, Bretz PE, Miller AC, Suresh S (1984) Fatigue crack growth behavior of aluminum alloy 2020 (AlCuLiMnCd). *Mater Sci Eng* 64(1):113–122

Iron Recovery from Nickel Slag by Aluminum Dross: A Static Model from Industrial Practice View



Guangzong Zhang, Nan Wang, Min Chen, Xiaobao Li, Hui Li, Ying Wang, and Yanqing Cheng

Abstract Nickel slag can be recycled as one of excellent secondary sources due to valuable iron resource. A static model of recycling nickel slag by aluminum dross was established based on material balance and non-isothermal thermodynamic calculations. Discussions had been carried out under different basicities of the modified slags and the reduction degree of 'FeO,' and the results showed that the dosage of nickel slag, aluminum dross, and modifier is 55.60%, 28.82%, and 15.58%, respectively, at the basicity of modified slag of 1.0. The non-isothermal thermodynamic model indicated that an increment of slag temperature from 114.3 to 430.2 K could be obtained with the reduction process, which not only signified the superiority of aluminothermy, but also laid a foundation for the industrial practice.

Keywords Nickel slag · Aluminum dross · Material balance calculation · Non-isothermal thermodynamic model

Introduction

Nickel slag can be recycled as one of excellent secondary sources due to valuable iron resource [1–3]. The iron content in quenched nickel slag from flash smelting can be as high as 50 wt%, which is the main reason why so many researchers have paid their attentions on its recycling in past years. Compared with stockpiling in heaps in the open air, iron exaction is no doubt an efficient way to reduce environmental pollution and resource waste.

Pyrometallurgical methods have the advantages in slag treatment, which can avoid the waste water produced by hydrometallurgy as well as make the full use of the considerable heat carried by molten slag [4–6]. Different from carbothermic reduction, aluminothermic reduction that is treated as a self-sustaining technique has been used in today's recovery, such as copper slag recycling [7–9]. However, aluminum dross from aluminum industries is used as the reductant in this work, and the higher Al

G. Zhang · N. Wang (✉) · M. Chen · X. Li · H. Li · Y. Wang · Y. Cheng
School of Metallurgy, Northeastern University, Liaoning 110819, China
e-mail: wangn@smm.neu.edu.cn

© The Minerals, Metals & Materials Society 2021
TMS 2021 150th Annual Meeting & Exhibition Supplemental Proceedings,
The Minerals, Metals & Materials Series,
https://doi.org/10.1007/978-3-030-65261-6_93

1045

content of ~35 wt% promotes a substitution of pure aluminum shots, where it should be mentioned that the contents of hazardous elemental N, Cl, and F in aluminum dross can meet the emission standard for harmless treatment after washing treatment and the high-temperature process [10]. Therefore, recycling nickel slag by aluminum dross can realize the full use of the metallurgical solid wastes as well as the environmental protection.

Thermal effect in waste treatment has always been a key issue for researchers, because the proper utilization of slag melt and application of exothermic property of aluminothermic reaction can both facilitate energy conservation. However, the thermodynamic foundations underlying the current recycling is still not clear, especially for the industrial practice, the dosage of reactants and the heat input that required has never been studied.

The objective of this work is to discuss the evolution of slag compositions and slag temperature based on the static model, which is established according to the calculations of material balance and non-isothermal thermodynamic model. Dependences of slag-composition variation on basicity of the modified slag and on the reduction degree of 'FeO' are analyzed to lay a foundation for the high-temperature experiment. Also, the heat energy underlying molten nickel slag with different discharge temperatures, the dependence of heat energy of slag system on reduction degree of 'FeO' and the slag temperature change under different basicities of the modified slag are successively discussed to evaluate the 'waste heat utilization' and the exothermic effect of aluminothermic reaction on slag treatment.

Experimental

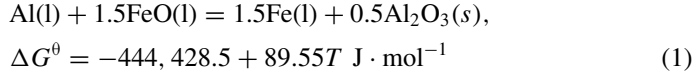
Nickel slag raw material was obtained during flash smelting and was supplied by a domestic nickel plant, the compositions of which is shown in in Table 1. It could be found that the mass fraction of 'FeO' is as high as 51.31 wt%, much higher than the average grade of iron ore in China (~27 wt%). Combined with nickel slag, the compositions of aluminum dross that was collected from an aluminum enterprise are also listed in Table 1. The content of metallic Al in aluminum dross is 33.14 wt%, and the lower contents of F, K, and Cl (~0.14%) can be ignored due to the process conditions without soluble-salt addition, which indicates that aluminum dross can be used as the reductant in slag treatment [11].

Table 1 Chemical compositions of nickel slag and aluminum dross (wt%)

Compositions	'FeO'	CaO	MgO	SiO ₂	Al ₂ O ₃	Al	AlN	Na ₂ O	Ni	Co	Cu	S
Nickel slag	51.31	3.58	8.41	31.60	–	–	–	–	0.16	0.08	0.22	1.20
Aluminum dross	–	2.04	6.97	10.12	40.83	33.14	4.85	2.05	–	–	–	–

Modeling Construction

When aluminum dross is added to the molten nickel slag, aluminothermic reaction as expressed in Eq. (1) will occur at the interface between aluminum and molten slag [12]. Based on mass conservation, the input and output of each element are analyzed, and the material calculation during the melting reduction can be realized.



Taking element Al as an example, the source contains Al, Al₂O₃, and AlN in aluminum dross and the output includes the left element Al in slag, the Al₂O₃ formed during reaction and the AlN that did not participate in the reaction. The balance equation is shown as follow:

$$\begin{aligned} m(\text{Al})_{\text{Aluminum dross}} + m(\text{Al}_2\text{O}_3)_{\text{Aluminum dross}} + m(\text{AlN})_{\text{Aluminum dross}} \\ = m(\text{Al})_{\text{Slag}} + m(\text{Al}_2\text{O}_3)_{\text{Slag}} + m(\text{AlN})_{\text{Slag}} \end{aligned} \quad (2)$$

Slag compositions during current reaction is dominated by oxides of CaO, SiO₂, 'FeO,' Al₂O₃, and MgO, and the mass fraction of each oxide can be calculated according to Eq. (3):

$$\begin{aligned} w(\text{MeO}, \text{Me} = \text{Ca}, \text{Si}, \text{Al}, \text{Fe}, \text{Mg}) \\ = \frac{\text{Mass of MeO in slag system after reaction}}{\text{Total mass of slag system after reaction}} \times 100\% \end{aligned} \quad (3)$$

Slag temperature during recycling will have an important influence on the kinetic conditions of the reduction and the separation of reduced product from slag in later period. From the perspective of thermodynamics, the aluminothermic reaction is a strongly exothermic process, a considerable heat energy will be released into slag pool, as shown in Eq. (1). However, the endothermic effect of the modifier and aluminum dross dissolutions should also be taken into account, which makes the heat-balance calculation more important.

Based on 100 kg of nickel slag, analysis of energy conservation is carried out upon established non-isothermal thermodynamic model, as shown in Eq. (4) [11].

$$\left\{ \begin{aligned} Q_{\text{input}} &= \sum \frac{m_i}{M_i} \Delta H_i \\ Q_{\text{output}} &= \sum \int_{T_0}^T C_{p,j} \cdot m_j + Q_{\text{heat loss}} \\ Q_{\text{input}} - Q_{\text{output}} &= \frac{dT}{dm} (m_{\text{Fe}} C_{p,\text{Fe}} + m_{\text{slag}} C_{p,\text{slag}}) \end{aligned} \right. \quad (4)$$

where Q_{input} and Q_{output} is the heat input and heat output per unit mass of the slag system, respectively, and Q_{input} includes the heat generated from aluminothermic reaction and the CaO modification, while Q_{output} includes the heat loss during recycling and the dissolution of aluminum dross and CaO (kJ kg^{-1}), m_i and m_j represent the masses of reactants (i refers to Al and the modifier CaO, j refers to the aluminum dross and the modifier CaO), and m_{Fe} and m_{slag} are the mass of the generated iron liquid and slag system, respectively (kg); M_i is the molar mass (g mol^{-1}), and ΔH_i is the enthalpy change of reaction (kJ mol^{-1}); T and T_0 is the slag and the room temperature (298 K), respectively (K); $C_{p,j}$, $C_{p,\text{Fe}}$, and $C_{p,\text{slag}}$ are the capacities of reactants, the generated iron liquid and the slag, respectively ($\text{kJ K}^{-1} \text{kg}^{-1}$), which can be obtained from Eq. (5) [13].

$$C_P = A_1 + A_2 \times 10^{-3}T + A_3 \times 10^5T^{-2} + A_4 \times 10^{-6}T^2 + A_5 \times 10^8T^{-3} \quad (5)$$

where A_1, A_2, A_3, A_4, A_5 are the coefficients relevant to the capacities and T is the temperature of the oxide, the iron or the slag (K).

Results and Discussion

Dependence of Slag-Composition Variation on Basicity of the Modified Slag

Table 2 shows the slag compositions and the dosage of reactants under different modification conditions. As basicity of the modified slag increases from 0.5 to 1.5, the mass fractions of SiO_2 , MgO , and 'FeO' in the modified slag gradually decrease, while the mass fractions of CaO gradually increase. In addition, combining the mass fraction of 'FeO' in the modified slag and Eq. (1), the dosage of aluminum dross under different basicities is calculated, which lays a foundation for the high-temperature experiments. It can be seen that the dosage of aluminum dross decreases from 31.59 to

Table 2 Chemical compositions of the modified slags and the percentages of reactants (mass fraction/%)

Basicity of modified slags	Slag compositions					Dosage of reactants		
	$w(\text{SiO}_2)$	$w(\text{Al}_2\text{O}_3)$	$w(\text{CaO})$	$w(\text{MgO})$	$w(\text{'FeO'})$	Nickel slag	Aluminum dross	CaO
0.5	29.50	0.00	14.76	7.85	47.89	60.96	31.59	7.45
0.75	27.48	0.00	20.61	7.31	44.60	58.15	30.14	11.71
1.0	25.71	0.00	25.71	6.84	41.74	55.60	28.82	15.58
1.25	24.16	0.00	30.20	6.43	39.22	53.26	27.60	19.14
1.5	22.78	0.00	34.17	6.06	36.98	51.11	26.49	22.40

26.49% with the increasing basicity of modified slag. Moreover, the dosage of nickel slag, aluminum dross, and modifier is 55.60%, 28.82%, and 15.58%, respectively, at the basicity of the modified slag of 1.0.

Dependence of Slag-Composition Variation on Reduction Degree of 'FeO'

Figure 1 shows the mass-fraction variation of oxides with the reduction degree of 'FeO,' where Fig. 1a shows the mass-fraction variation of all components under basicity of 1.0 and Fig. 1b shows the changes of 'FeO,' Al_2O_3 , and CaO under basicity of 0.75, 1.0 and 1.25, respectively. As shown in Fig. 1a, the mass fraction of 'FeO' in slag gradually decreases from 41.61% as the increasing reduction degree, yet the mass fraction of Al_2O_3 gradually increases, and it can reach up to 35.81% in secondary slag. Simultaneously, the contents of SiO_2 and MgO increase slightly, while the content of CaO remains unchanged. Based on the tendency of curves in Fig. 1b, CaO content in slags gradually increases with the increasing basicity at a fixed 'FeO' reduction degree. Taking the modified slag as an example, the mass fraction of CaO is 20.61%, 25.71%, and 30.20%, respectively, from the basicity of 0.75 to 1.25. In contrast, the contents of 'FeO' and Al_2O_3 in the slag decrease with the increasing basicity. The mass fractions of 'FeO' and the Al_2O_3 in modified and secondary slags are 44.60%, 41.74%, 39.22%, and 38.20%, 35.81%, 33.72%, respectively, under the three slag basicities.

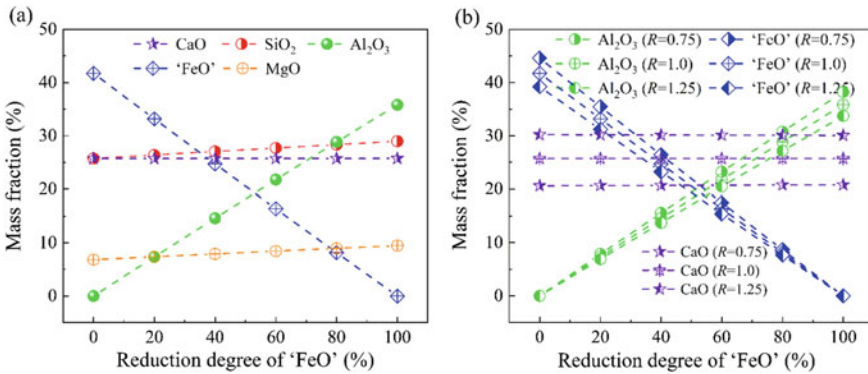


Fig. 1 Slag composition evolution of MeO (Me = Ca, Si, Al, Fe, Mg) with 'FeO' reduction degree. **a** $R = 1.0$; **b** $R = 0.75, 1.0$ and 1.25 . (Color figure online)

Heat Energy Underlying Molten Nickel Slag with Different Discharge Temperatures

According to Eq. (1), the relationship between the heat energy carried by 100 kg of molten nickel slag and its discharge temperature is calculated, as shown in Fig. 2. With temperature increasing from 1573 to 1633 K, the heat energy carried by the molten nickel slag gradually increases from 115.49×10^3 to 121.46×10^3 kJ. In addition, the ratio of the heat energy carried by initial molten nickel slag to the heat required for different reduction temperatures is also shown. Taking the reduction temperature of 1773 K as an example, the ratio varies in the range of 75.54–79.44%, which undoubtedly reflects the great value of ‘waste heat utilization’ during recycling metallurgical waste slags. As the reduction temperature increases from 1673 to 1873 K, the heat required to melt the nickel slag also increases, and the ratio under the same discharge temperature decreases as a consequence. For instance, the heat energy carried by molten nickel slag with discharge temperature of 1573 K accounts for 80.96%, 75.54%, and 70.79% under the three reduction temperatures, respectively.

Dependence of Heat Energy on Reduction Degree of ‘FeO’

Table 3 shows the heat-balance calculation results of slag system under basicity of the modified slag of 1.0, and Fig. 3 shows the proportions of heat input and heat output of the slag system accordingly. For the heat input of slag system, the exothermic heat of aluminothermic reaction gradually increases from 0.00 to 211.14×10^3 kJ with the increasing reduction degree of ‘FeO.’ As shown in Fig. 3a, the proportion occupies

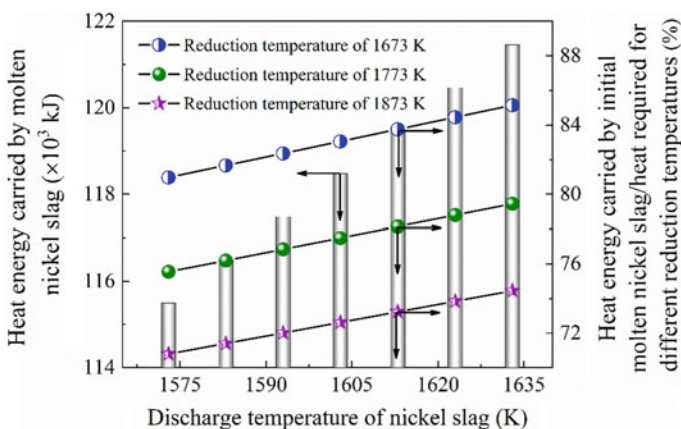


Fig. 2 Relationship of heat energy and the output temperature for 100 kg of nickel slag. (Color figure online)

Table 3 Calculation results of heat energy balance with modified basicity of 1.0

Reduction degree of 'FeO' (%)	Discharge temperature of nickel slag (K)	Heat input ($\times 10^3$ kJ)			Exothermic effect of modification	Heat output ($\times 10^3$ kJ)		ΔQ ($\times 10^3$ kJ)	Slag temperature (K)
		Heat energy carried by the molten nickel slag	Aluminothermic reaction			Endothermic heat of dissolution of the modifier and aluminum dross	Heat loss		
0	1573	115.49	0.00	70.47	36.66	14.93	18.88	1687.29	
20			42.22		58.61	16.96	37.12	1780.95	
40			84.44		82.06	18.84	54.02	1854.50	
60			126.70		106.61	20.61	69.96	1913.79	
80			168.92		131.94	22.30	85.16	1962.50	
100			211.14		157.87	23.92	99.82	2003.24	

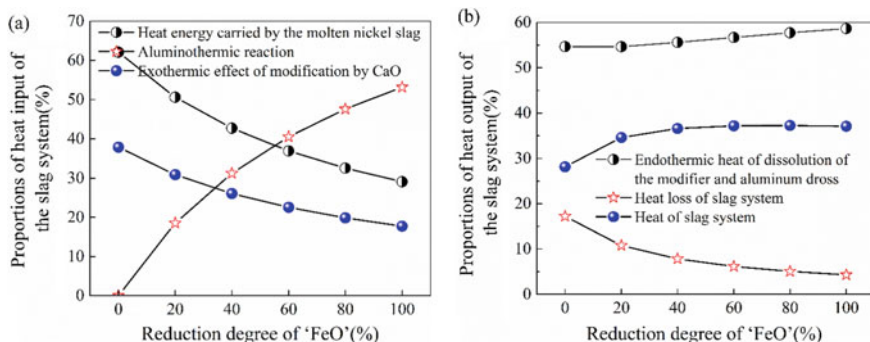


Fig. 3 Percentages of heat input and heat output of slag system with modified basicity of 1.0. (Color figure online)

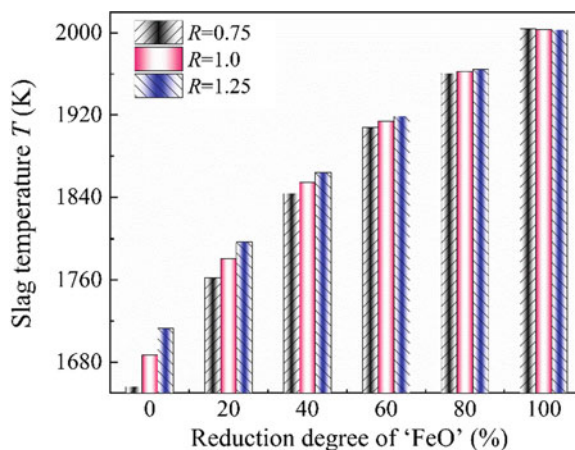
heat input of slag system from 0.00 to 53.17%. At the same time, the proportion of heat carried by molten nickel slag accounts for 62.10–29.08% of heat input, which plays dominant role before the reduction degree of 'FeO' of 55.33% and indicates the importance of 'waste heat utilization' in reducing energy consumption.

Combining Table 3 with Fig. 3b, the endothermic heat of dissolution of the modifier and aluminum dross varies from 36.66×10^3 to 157.87×10^3 kJ with the increase of the reduction degree of 'FeO,' which accounts for 54.65–58.63% of heat output of the system. Under the effect of heat input and output, the heat of slag system increases from 18.88×10^3 to 99.82×10^3 kJ, causing an increase in slag temperature from 1687.29 to 2003.24 K. Furthermore, the temperature increase of modified slag can be attributed to the exothermic effect of modification. Larger CaO addition under higher slag basicity induces a larger heat release and temperature increase.

Slag Temperature Change Under Different Basicities of Modified Slag

Figure 4 shows the slag temperature change with the reduction degree of 'FeO' under different basicities of modified slag of 0.75, 1.0, and 1.25, where the discharge temperature of nickel slag is set as 1573 K and the heat loss during the reaction is calculated as 10% of the physical heat of the whole slag system [11]. It can be seen that the slag temperature under the three basicities of modified slag gradually increases with the reduction degree of 'FeO.' Taking the basicity of 1.0 as an example, slag temperature changes from 1687.29 to 2003.24 K as mentioned above, 114.29–430.24 K higher than the discharge temperature of 1573 K. In addition, slag temperature increases in the range of 83.22–430.73 K and 140.16–429.80 K under basicities of 0.75 and 1.25, respectively. From the perspective of industrial practice,

Fig. 4 Slag temperature change under different basicities of modified slag. (Color figure online)



both the 'waste heat utilization' and the exothermic effect of aluminothermic reaction play a very important role in increasing the temperature of molten pool, laying a foundation for the high-valued utilization of metallurgical solid wastes.

Conclusions

Based on iron recovery from nickel slag by aluminum dross, the evolution of slag compositions and slag temperature based on the established static model have been discussed, and the following conclusions can be drawn:

- (1) Material balance calculations show that the dosage of nickel slag, aluminum dross, and modifier is 55.60%, 28.82%, and 15.58%, respectively, at the basicity of modified slag of 1.0. As the reduction degree of 'FeO' increases, the mass fraction of 'FeO' in slag gradually decreases from 41.61%, yet the mass fraction of Al_2O_3 gradually increases, which can reach up to 35.81% in secondary slag.
- (2) Calculation of non-isothermal thermodynamic model indicates that the heat energy carried by the 100 kg of molten nickel slag gradually increases from 115.49×10^3 to 121.46×10^3 kJ with discharge temperature increasing from 1573 to 1633 K. For reduction temperature of 1773 K, the ratio of the heat energy carried by initial molten nickel slag to the heat required for different reduction temperatures varies in the range of 75.54–79.44%, reflecting the great value of 'waste heat utilization' during recycling metallurgical waste slags.
- (3) The proportion of exothermic heat of aluminothermic reaction occupies the heat input of slag system from 0.00 to 53.17%. For 100 kg of molten nickel slag, the heat of slag system increases from 18.88×10^3 to 99.82×10^3 kJ under the effect of heat input and output, which causes an increment of slag temperature from 114.3 to 430.2 K with the reduction process.

Acknowledgements This work was supported by the National Natural Science Foundation of China (Grant numbers 51774072, 51774073 and 51974080) and the National Key R&D Program of China (Grant numbers 2017YFB0304201, 2017YFB0304203 and 2016YFB0300602).

References

1. Zhang GZ, Wang N, Chen M, Wang Y, Li H (2019) Iron recovery from nickel slag by aluminum dross: viscosity evolution in different periods. In: Gaustad G et al (eds) REWAS 2019: manufacturing the circular materials economy. The minerals, metals & materials series. Springer, Cham, pp 143–152
2. Ni W, Jia Y, Zheng F, Wang ZJ, Zheng MJ (2010) Comprehensive utilization of iron recovery from Jinchuan nickel residue. *J Univ Sci Technol B* 32:975–980
3. Ni W, Ma MS, Wang YL, Wang ZJ, Liu FM (2009) Thermodynamic and kinetic in recovery of iron from nickel residue. *J Univ Sci Technol B* 31:163–168
4. Roy S, Datta A, Rehani S (2015) Flotation of copper sulphide from copper smelter slag using multiple collectors and their mixtures. *Int J Miner Process* 143:43–49
5. Du CM, Shang C, Gong XJ, Wang T, Wei XG (2018) Plasma methods for metals recovery from metal-containing waste. *Waste Manage* 77:373–387
6. Zhang GZ, Wang N, Chen M, Cheng YQ (2020) Recycling nickel slag by aluminum dross: iron-extraction and secondary slag stabilization. *ISIJ Int* 60:602–609
7. Pan J, Zheng GL, Zhu DQ, Zhou XL (2013) Utilization of nickel slag using selective reduction followed by magnetic separation. *Trans Nonferrous Met Soc China* 23:3421–3427
8. Heo JH, Chung Y, Park JH (2016) Recovery of iron and removal of hazardous elements from waste copper slag via a novel aluminothermic smelting reduction (ASR) process. *J Clean Prod* 137:777–787
9. Sokolov VM, Babyuk VD, Zhydkov YA, Skok YY (2008) Aluminothermic studies of a liquid partial reduced ilmenite. *Miner Eng* 21:143–149
10. Zhou YM (2014) Research on the harmless treatment and comprehensive utilization of aluminum dross. Kunming University of Science and Technology, Kunming
11. Zhang GZ, Wang N, Chen M, Li H (2018) Viscosity and structure of CaO-SiO₂-FeO-Al₂O₃-MgO system during iron-extracting process from nickel slag by aluminum dross. Part 1: coupling effect of “FeO” and Al₂O₃. *Steel Res Int* 89:1800272
12. Chen JX (2010) Handbook of common figures, tables and data for steelmaking. Metallurgical Industry Press, Beijing, pp 646–666
13. Ye DL (2002) Handbook of practical inorganic thermodynamic data, 2nd edn. Beijing Industry Press, Beijing, pp 1–24

Resource Recovery of Cerium from Spent Catalytic Converter Using Aqueous Metallurgy



Sadia Ilyas, Hyunjung Kim, and Rajiv Ranjan Srivastava

Abstract Cerium recovery from a secondary waste stream generated after the extraction of Pt-group metals from spent catalytic converter has been investigated. Different mineral acids alone used as lixiviant could leach only 33% cerium; however, HF added acid mixture showed an increased leaching up to 96%. The determined value of activation energy 31.8 kJ/mol revealed that leaching progressed via diffusion-controlled mechanism. Subsequently, cerium from leach liquor was extracted using 4 tri-alkyl phosphine oxides in kerosene, which indicated the formation of extracted species to be $[\text{Ce}(\text{SO}_4)_2 \cdot 2\text{L} \cdot \text{HSO}_4^-]_{\text{org}}$. The loaded organic was quantitatively stripped back into the H_2SO_4 solution by adding an H_2O_2 dosage as a reducing agent. Thus, obtained Ce-bearing stripped solution was treated with oxalic acid to precipitate high-purity $\text{Ce}_2(\text{C}_2\text{O}_4)_3$. The process is simple and potentially dealt to recycle the critical metal values which remained less attractive until now.

Keywords Cerium · Rare earth metals · Spent automobile catalysts · HF leaching · Ce(IV) solvation · Ce(III) oxalate

S. Ilyas (✉) · H. Kim (✉)

Mineral Resources and Energy Engineering, Jeonbuk National University, Jeonju, Jeonbuk 54896, Republic of Korea

e-mail: sadailyas1@yahoo.co; ilyas.sadia24@gmail.com

H. Kim

e-mail: kshjkim@jbnu.ac.kr

H. Kim

Department of Environment and Energy, Jeonbuk National University, Jeonju, Jeonbuk 54896, Republic of Korea

R. R. Srivastava (✉)

Center for Advanced Chemistry, Institute of Research and Development, Duy Tan University, Da Nang 550000, Vietnam

e-mail: r2.srivastava@gmail.com

Faculty of Natural Sciences, Duy Tan University, Da Nang 550000, Vietnam

© The Minerals, Metals & Materials Society 2021

TMS 2021 150th Annual Meeting & Exhibition Supplemental Proceedings,

The Minerals, Metals & Materials Series,

https://doi.org/10.1007/978-3-030-65261-6_94

Introduction

Due to the stringent environmental regulation on automobiles' emissions, three-way catalytic converters became essential to modern automobiles for controlling the gaseous emissions [1, 2]. The catalytic converters usually consist of platinum group metals (PGMs) as the active components with wash-coated γ - Al_2O_3 on the cordierite support; however, CeO_2 acts as the structure stabilizer while promoting the catalytic activity [3, 4]. After being exhausted, the spent catalysts are usually sent to landfilling; however, certain parts are being recycled only for PGMs recovery [5]. Thus, the values of cerium are lost in residual landfilling, which is a non-sustainable practice and one of the key areas to pay the attention for recycling of this rare earth metal (REM). In contrast, cerium demands are continuously increasing in catalytic materials (including the fuel cells, auto-catalysts, and fluid-cracking catalysts), glass polishing, nuclear chemistry, semiconductor and ceramic industries, and low-energy fluorescence bulbs [6]. A compounded growth rate of cerium that is predicted to be 8% and the controlled trade of rare earths along with its reserves limited to certain geopolitical boundaries immensely pushes a need for the exploitation of alternative resources that could mitigate cerium's supply risks in the future [7, 8].

In recent times, the consumption of catalytic converters has increased proportionally with the soaring production of automobiles, therefore generating a large number of spent catalysts. The recovery of cerium from the spent catalysts can potentially contribute to the secondary supply route of this REM. Until now, numerous pyro- and hydro-metallurgical techniques have been studied for recycling of the exhausted catalytic converters [5, 9]; however, a few exist for resource recovery of cerium. Due to the refractory nature of CeO_2 , it is hard to leach in dilute acid solutions [10, 11], and hence, acid baking as a pre-treatment step has been suggested to yield 85% leaching efficiency [12]. HCl leaching in the presence of H_2O_2 followed by sulfate double-salt precipitation has also been reported by Steinlechner and Antrekowitsch [13]; however, the experimental details are missing. Due to the lacking study in this context, the present study accounts for a hydro-metallurgical route to cerium recovery from a secondary generated after the PGMs' leaching from spent auto-catalysts.

Notably, the leach residue generated via the bio-cyanidation leaching of PGMs has been used as the feed material for cerium recovery in this study. Acid leaching in the presence of hydrofluoric acid (HF) has been conducted for effective dissolution of cerium, while varying the parameters like HF addition, temperature, and time. Subsequently, the extraction of cerium from leach liquor has been conducted using an organophosphorus mixture as the extractant and the influential parameters are optimized. Finally, cerium stripped from the loaded organic in the presence of hydrogen peroxide has been recovered as the high-purity oxalate precipitate.

Experimental

The sample fed in this study was obtained through the bio-cyanidation of spent auto-catalyst that containing 26.4% Al, 4.3% Ce, 2.7% Mg, and 7.9% Si. The reagents like hydrochloric acid (30%, Merck), nitric acid (65%, Sigma-Aldrich), sulfuric acid (95%, Daejung), hydrofluoric acid (40%, Merck Millipore), hydrogen peroxide (30%, Merck), oxalic acid (90%, Junsei Chemical Co.), organophosphorus organic mixture (93%, Cytec Canada Inc.), and distilled kerosene (Junsei Chemical Co.) were used without further purification. 15 g sample and 150 mL acid solutions of pre-determined concentration was taken into 250 round-bottom flask under the stirring condition (provided agitation of 250 rpm). For heating and stirring purpose, a hot plate with a magnetic stirring facility was used. Until specified, leaching studies were conducted at 60 °C for 4 h duration. When required, HF was separately added into sulfuric acid by keeping the pulp density fixed at 10%. After completion of leaching, the slurry was filtered, and the filtrate was analyzed using an inductively coupled plasma optical emission spectrometer (ICP-OES, iCAP 7400 Duo, Thermo Scientific) for knowing the leaching efficiency. Subsequently, leach liquor containing 4.2 g/L cerium was contacted with an organic solvent of a pre-determined concentration at an O/A ratio of 1. For which, a 30-mL volume of each phase in a 100 mL separating funnel was contacted for 5 min at 25 ± 2 °C. The equilibrated solution was settled for 10 min; thereafter, the collected raffinate was analyzed for knowing the cerium content and determining the extraction efficacy. The back-extraction of cerium was conducted using a stripping solution of 1.0 mol/L H_2SO_4 with H_2O_2 . Further, the precipitation of cerium with a calculated oxalic acid was conducted using 50 mL stripped solution in 100 mL beaker, while maintaining temperature, $90(\pm 2)$ °C; agitation speed, 150 rpm; pH of the solution, $1.5(\pm 0.2)$, duration, 15 min; and settling time, 1 h. The slurry was filtered, and the filtrate was analyzed to determine the precipitation efficiency. On the other side, the precipitates were water-washed and overnight dried in a vacuum dryer for the characterization studies.

Results and Discussion

Acid Leaching

Leaching behavior of cerium in different acids was investigated at varying concentrations ranging from 1.0 to 6.0 mol/L acid. Experimental results are summarized in Fig. 1a, revealing the poor leachability for cerium (<33%) regardless of the acid media. This act can be ascribed to the acid resistance property of ceria [14]. Further, sulfuric acid was chosen due to low cost and less corrosive nature, and the change in leaching yield was investigated with the acid mixture prepared by mixing different concentrations of HF (0.25–2.0 mol/L) with 2.0 mol/L H_2SO_4 . Figure 1b depicts that cerium leaching was improved with increasing concentration of HF in the

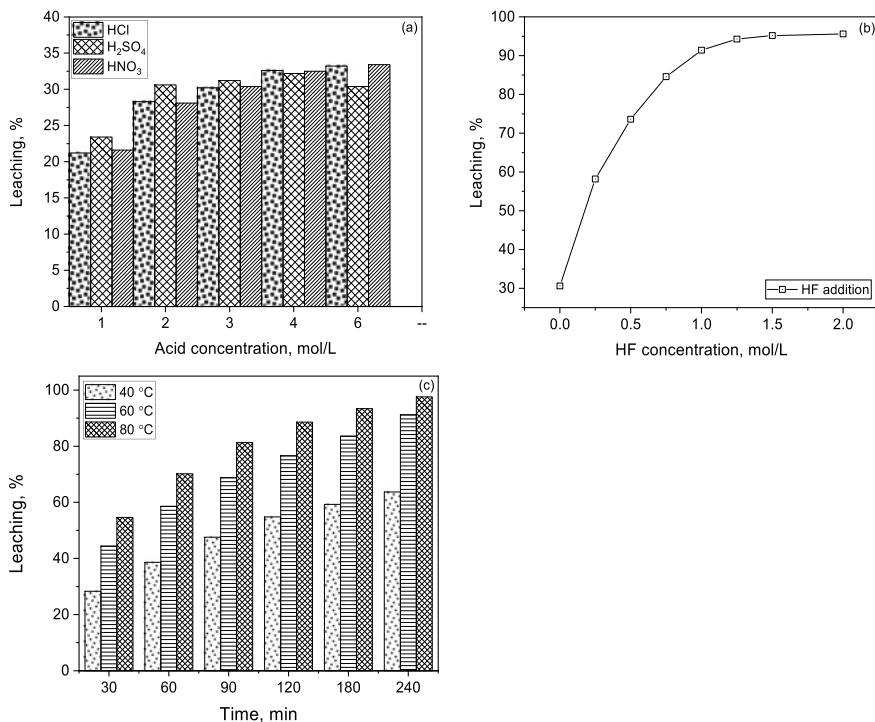


Fig. 1 Leaching behavior of cerium with different acids as a function of concentration (a); with acid mixture containing 2 mol/L H₂SO₄ and varied concentration of HF (b); and at different temperatures as a function of time (c)

acid mixture, indicating the influential act of fluoride ions. The leaching efficiency improved from 30.6 to 95.6% with respect to increasing concentration of HF up to 2.0 mol/L. However, not much improvement was observed above 1.0 mol/L HF in the acid mixture (increased from 91.4 to 95.6%), hence, the addition of 1.0 mol/L HF was optimized.

Further, the effect of temperature ranging from 40 to 80 °C with respect to time (up to 240 min) was investigated. Experimental results are shown in Fig. 1c depicted that at 40 °C, leaching efficiency was very low (~28% in 30 min) which could improve only to 63% in 240 min. At 60 °C, leaching was significantly improved (>90%) in 240 min which further increased up to 98% at 80 °C. To underpin the dissolution mechanism into the acid mixture, the following equation was employed to determine the apparent activation energy (E_a) [15]:

$$\ln\left(\frac{t_1}{t_2}\right) = \frac{E_a}{R} \left(\frac{1}{T_1} - \frac{1}{T_2}\right) \quad (1)$$

where the roasting at temperatures T_1 (40 °C) and T_2 (80 °C) for time t_1 (120 min) and t_2 (30 min) were considered (in which the leaching efficiency of cerium was approximately the same) to determine the E_a value. Thus, calculated E_a value (31.8 kJ/mol) indicated that the leaching process followed the diffusion-controlled mechanism [16].

Solvent Extraction with Organophosphorus Mixture

Cerium extraction from leach liquor was investigated with a commercially available organic mixture of 4 tri-alkyl phosphine oxides at different concentrations ranging from 2 to 20% (v/v). Experimental results are shown in Fig. 2a depicted that cerium extraction increased with increasing concentration of the organophosphorus compound, which can be corroborated to the shifting of distribution curve with more available extraction sites into the organic phase [17, 18]. The extraction improved from 14 to 90% with extractant concentration increased from 2 to 16%, and finally reached to ~93% using 20% extractant into the organic phase. The logarithmic plot for cerium distribution into both phases versus the extractant concentration yielding straight line with R^2 value 0.98 (not shown here) and slope value 1.99 could reveal that two moles of extractant are complexed with each mole of cerium extraction into the organic phase.

Further, the extraction behavior was examined as a function of acid concentration in the range of 0.25–2.0 mol/L H_2SO_4 using 20% (v/v) extractant in the organic phase. The results are shown in Fig. 2b depicted that the extraction decreased from 95 to <86% when H_2SO_4 concentration changed from 0.25 to 2.0 mol/L. This behavior can be a resultant of the competition between metal species and bisulfate ions [19, 20]. Additionally, a decline in cerium extraction with lower HF- H_2SO_4 ratio might be due to the presence of aluminum fluoride in the leach liquor which acts as a defluorinating agent to scrub the fluorinated species co-extracted into the organic phase. The logarithmic plot for cerium distribution versus H_2SO_4 concentration yielding straight line with R^2 value 0.976 (not shown here) and slope value 0.6 could reveal the requirement of one mole acid against each mole of cerium extraction. As sulfuric

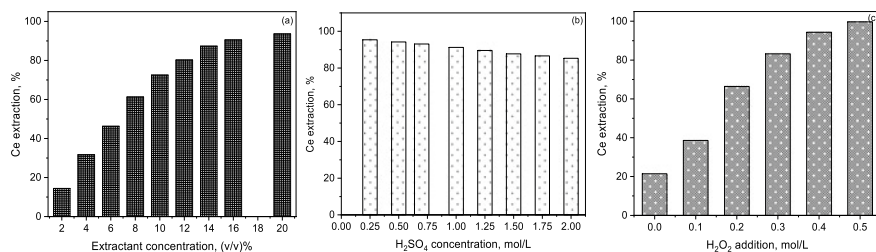
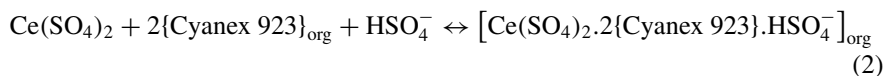


Fig. 2 Extraction behavior of cerium from leach liquor as a function of extractant concentration (a); acid concentration (b); and stripping behavior from the loaded organic as a function of H_2O_2 addition (c)

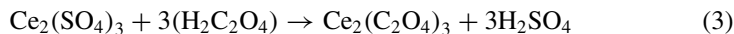
acid dissociates as bisulfate ions (pka value, 1.99), the stoichiometric reaction can be given as:



As per the phase ratio variations at different O/A between 1/4 and 4/1, the extraction could be increased from 30 to >99%. Using the experimental data, the McCabe–Thiele diagram was drawn, which showed that the quantitative extraction of cerium can be achieved in two-stages of counter-current extraction (CCE) at an O/A ratio of 1. A batch simulation under CCE yielded 4.1 g/L cerium extraction into the organic phase, which further underwent to stripping studies. Cerium stripping from the loaded organic was examined as a function of H₂O₂ addition in 1 mol/L H₂SO₄ solution. Results are shown in Fig. 2c revealed that the stripping efficiency increased with increasing addition of H₂O₂ and reached to about 98% using 0.5 mol/L H₂O₂.

Oxalate Precipitation

Cerium form insoluble compound in the presence of oxalate ions by following the reaction below:



The precipitation of cerium from stripped solution after maintaining the pH at ~1.5 was investigated as a function of oxalic acid addition in the variation range of Ce³⁺:H₂C₂O₄ = 1:0.5–1:5. The results are shown in Fig. 3a revealed that precipitation requires a high oxalic acid possibly due to the acceleration of nucleation

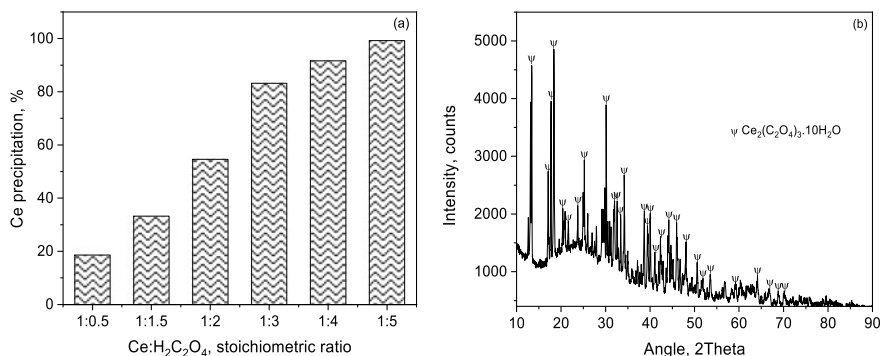


Fig. 3 Cerium precipitation from stripped liquor as a function of stoichiometric ratio with oxalic acid (a); and XRD patter of the oxalate precipitate (b)

growth in the presence of higher oxalate ions. The precipitation efficiency could be improved from 18.6 to 54% by changing addition from 1:0.5 to 1:2, which was further increased to achieve above 99% cerium recovery at 1:5. The vacuum-dried precipitate was characterized using the XRD technique, indicating the formation of $\text{Ce}_2(\text{C}_2\text{O}_4)_3 \cdot 10\text{H}_2\text{O}$ (Fig. 3b). Finally, the purity of the oxalate product was analyzed to be >99.6%.

Conclusions

The efficient recovery of cerium was conducted from the secondary waste of biocyanide processed auto-catalysts while using the advantages of aqueous metallurgy. Due to poor leaching of cerium (<34%) in strong mineral acids, HF was introduced with 2.0 mol/L H_2SO_4 solution that could improve efficiency up to 95%. The activation energy for leaching cerium into the acid mixture was determined to be 31.8 kJ/mol, which revealed that leaching followed the diffusion-controlled mechanism. Cerium from leach liquor was subsequently extracted using an organophosphorus mixture that forming $[\text{Ce}(\text{SO}_4)_2 \cdot 2\text{L} \cdot \text{HSO}_4^-]_{\text{org}}$ species into the organic phase. Further, the quantitatively extracted cerium into the organic phase was stripped back into the aqueous phase while contacting with 1.0 mol/L H_2SO_4 + 0.5 mol/L H_2O_2 . Finally, the high-purity $\text{Ce}_2(\text{C}_2\text{O}_4)_3 \cdot 10\text{H}_2\text{O}$ was recovered by precipitating cerium with oxalic acid at $\text{Ce}^{3+}:\text{H}_2\text{C}_2\text{O}_4$ mole ratio = 1:5.

Acknowledgements This work was supported by the Brain Pool Program through the National Research Foundation of Korea (NRF) funded by the Ministry of Science and ICT (Grant No. 2019H1D3A2A02101993) and Basic Science Research Program through the National Research Foundation of Korea (NRF) funded by the Ministry of Education (Project no. 2020R1H1A1A01074249).

Conflict of Interest The authors declare that they have no conflict of interest.

References

1. Heck MR, Farrauto RJ (2001) Automobile exhausted catalyst. *Appl Catal A* 221:443–457
2. Kašpar J, Fornasiero P, Hickey N (2003) Automotive catalytic converters: current status and some perspective. *Catal Today* 77:419–449
3. Lox ES (2008) Automotive exhaust treatment. In: Ertl G, Knözinger H, Schüth F, Weitkamp J (eds) *Handbook of heterogeneous catalysis*. WileyVCH Verlag GmbH & Co., KGaA, pp 2274–2344
4. Hickey N, Boscarato I, Kašpar J (2014) Air pollution from mobile sources: formation and effects and abatement strategies. In: Cao G, Orru R (eds) *Current environmental issues and challenges*. Springer, Dordrecht, pp 15–43
5. Dong H, Zhao J, Chen J, Wu J, Li B (2015) Recovery of platinum group metal from spent catalyst: a review. *Int J Miner Process* 145:108–113

6. Ilyas S, Kim H, Srivastava RR (2021) Extraction equilibria of cerium(IV) with Cyanex 923 followed by precipitation kinetics of cerium(III) oxalate from sulfate solution. *Sep Purif Technol* 254:117634
7. Hearty G (2019) Rare earths: next element in the trade war? Center for Strategic and International Studies. <https://www.csis.org/analysis/rare-earths-next-element-trade-war#:~:text=With%20the%20trade%20war%20having,next%20salvo%20in%20the%20conflict.&text=A1%3A%20Rare%20elements%20are,which%20possess%20similar%20chemical%20properties>. Accessed 14 Aug 2020
8. Cordier DJ (2009) Rare earths, metals and minerals. In: U.S. geological survey minerals yearbook
9. Ilyas S, Srivastava RR, Kim H, Cheema HA (2020) Hydrometallurgical recycling of palladium and platinum from exhausted diesel oxidation catalysts. *Sep Purif Technol* 248:117029
10. Lin S, Yang L, Yang X, Zhou R (2014) Redox behavior of active PdO_x species on (Ce, Zr)_xO₂-Al₂O₃ mixed oxides and its influence on the three-way catalytic performance. *Chem Eng J* 247(7):42–49
11. Morikawa A, Suzuki T, Kanazawa T, Kikuta K, Suda A, Shinjo H (2008) A new concept in high performance ceria–zirconia oxygen storage capacity material with Al₂O₃ as a diffusion barrier. *Appl Catal B* 78(3):210–221
12. Wu XF, Dong HG, Tong WF, Fan XX, Zhao JC, Lei Y (2015) Study on new technology for recovery of rare earth elements from used automobile catalysts. *Chin Rare Earths* 36(1):101–104
13. Steinlechner S, Antrekowitsch J (2015) Potential of a hydrometallurgical recycling process for catalysts to cover the demand for critical metals, like PGMs and cerium. *JOM* 67(2):406–411
14. Zhao Z, Qiu Z, Yang J, Ma B, Li Z, Lu S, Xu Y, Cao L, Zhang W (2019) Recovery of rare earth element cerium from spent automotive exhaust catalysts using a novel method. *Waste Biomass Valori* 11:4967–4976
15. Levenspiel O (1999) *Chemical reaction engineering*. Wiley, New York
16. Habashi F (1969) *Extractive metallurgy*. Gordon and Breach, Science Publishers, New York
17. Ritcey GM, Ashbrook AW (1984) *Solvent extraction part I*. Elsevier, Amsterdam
18. Srivastava RR, Ilyas S, Kim H, Tri NLM, Hassan N, Mudassar M, Talib N (2020) Liquid–liquid extraction and reductive stripping of chromium to valorize industrial effluent. *JOM* 72(2):839–846
19. Jun L, Zhenggui W, Deqian L, Gengxiang M, Zucheng J (1998) Recovery of Ce(IV) and Th(IV) from rare earths(III) with Cyanex 923. *Hydrometallurgy* 50:77–87
20. Liao W, Yu G, Li D (2001) Solvent extraction of cerium(IV) and fluorine(I) from sulphuric acid leaching of bastnasite by Cyanex 923. *Solvent Extr Ion Exch* 19:243–259

Transient Vortex Flow Characteristics in Three-Strand Bloom Tundish at the End of Casting



Mingtao Xuan, Min Chen, Kaizhu Zhang, and Xiaojie Hua

Abstract To increase the yield by decreasing the amount of residual molten steel in tundish, the vortex flow characteristics of the molten steel was investigated in a practical three-strand bloom tundish at the end of casting using physical and numerical simulation. The results showed that the vortex was strongly dependent to the asymmetric distribution of molten steel and the casting speed, so the vortex flow first occurred at strands 1 and 3, and the height of vortex formation was decreased by 25% while the casting speed was decreased from 0.65 to 0.48 m/min for the bloom with section size of 360 mm × 300 mm. Furthermore, the use of a square inhibiting baffle could disturb the upper fluid flow to decrease the height of vortex development by 23% at the casting speed of 0.48 m/min. Therefore, the installation of square inhibiting baffle is recommended, and the casting should be operated at lower casting speed.

Keywords Three-strand tundish · Vortex flow characteristics · Inhibiting baffle · Physical and numerical simulation

Introduction

Reducing inclusions and increasing alloy yield are an important issue to the alloy steel production. At the end of casting, vortexes can form above the submerged entry nozzle and entrap slag into the mold. The vortex slag entrainment can not only increase the inclusions in molten steel but also cause the oxidation of alloying elements. Moreover, some of the slag deposit in submerged entry nozzle internal surface and promote clogging. Although increasing the level height can inhibiting the vortex formation, but the alloy yield will decrease. Thus, the vortex flow characteristics in tundish at the end of casting are of crucial importance for the quality and cost of product.

M. Xuan · M. Chen (✉) · K. Zhang · X. Hua
School of Metallurgy, Northeastern University, Shenyang 110819, Liaoning, P. R. China
e-mail: chenm@smm.neu.edu.cn

Over recent years, free-surface vortex formation during liquid draining through a hole at the bottom of a vessel has been studied via physical and numerical simulation. Park and Sohn [1] investigated the air core in a circular tank by using experimental and computational methods. The critical height of vortex formation depended on the angular velocity of liquid. Li et al. [2, 3] used a mathematical model to analyze the mechanism and influencing factors of free-surface vortex formation during steel teeming process, and indicated that the initial tangential velocity and the position and diameter of nozzle had large effects on sink vortex formation. Although the phenomenon of free-surface vortex formation in the ladle is similar to that in the tundish, but the flow pattern in tundish is more complicated.

Solorio-Oiaz et al. and García-Hernández et al. [4, 5] studied a typical slab tundish by physical and numerical simulations, and indicated that even if the tundish was in normal operation, the unbalanced flow caused by the structure was still the source of the vortex formation. Meanwhile, the transient behavior of fluid flow was also an important reason for slag entrapment. Zhang et al. [6] studied the filling process in a practical tundish using VOF model and found that the unsteady flow pattern could cause slag entrapment and steel re-oxidation.

However, few works paid attention on the transient behavior of vortex flow at the end of casting. Ruan et al. [7] studied the free-surface formation and improved the unreasonable structure to prevent vortex flow in the slab tundish at the end of casting. Michalek et al. [8] developed a physical model to study the slag entrainment in a multi-strand billet tundish.

Despite researchers have studied the vortex formation and slag entrainment in the ladle and tundish by numerical and physical simulation, the vortex formation in bloom tundish was not well understood. The current work develops a mathematical model for investigating the transient behavior of vortex flow in a practical three-strand bloom tundish at the end of casting, and the control strategy was also discussed. The calculated results of this model were verified by water model experiments.

Model Descriptions

Physical Model

Based on the normal Froude similarity number [4], a 1:4 scaled physical model was established to study the characteristics and control strategy of vortex formation. Details of experiments could be found elsewhere. Table 1 gives the operating parameters and physical properties on the prototype and physical model.

Table 1 Operating parameters and physical properties in practical tundish and physical model

Parameter	Prototype	1/4 model
Casting speed (m ³ /h)	3110–4212	97–132
Mold width × thickness (mm ²)	360 × 300	90 × 75
Height of initial liquid level (mm)	850	212.5
Liquid density (kg/m ³)	7000	1000
Liquid viscosity (kg/(m·s))	0.0055	0.001
Gas density (kg/m ³)	1.2	0.56
Gas viscosity (kg/(m·s))	1.82 × 10 ⁻⁵	7.45 × 10 ⁻⁵

Mathematical Model

Mathematical Formulations

The assumptions applied in the present multiphase flow of tundish can be found elsewhere. In this study, the VOF model coupled with RNG *k-ε* turbulence model was developed to capture the characteristics of vortex formation at the end of casting. Among them, the RNG *k-ε* turbulence model provided the flow pattern in the computational domain, and the VOF model was used to track the phase interface between air and molten steel. The general form of one mass equation, three momentum equations, and two standard *k-ε* turbulence equations could be expressed as Eq. (1).

$$\frac{\partial(\rho u_i \phi)}{\partial x_i} = \frac{\partial}{\partial x_i} \left(\Gamma_\phi \frac{\partial \phi}{\partial x_i} \right) + S_\phi \tag{1}$$

$$\alpha_{\text{air}} + \alpha_{\text{steel}} = 1 \tag{2}$$

where ρ is the fluid density, kg/m³; u_i is the speed in i direction, m/s; ϕ is the variables including velocities at three directions, temperature, enthalpy, turbulent kinetic energy, and dissipation rate, x_i is the direction, Γ_ϕ is the coefficient of diffusion, and S_ϕ is the source term. The flow parameters of the mixed fluid were calculated by the weighted average of the volume fractions of the phases. Furthermore, the Coriolis force was added into the momentum equation as a source term [7].

Computational Details

To reduce the computational cost, the computational domain was half of the tundish, as shown in Fig. 1a. Additionally, the square inhibiting baffle was used to delay the vortex formation, and its structure was shown in Fig. 1b.

At the wall in the domain, the zero-slip boundary condition was used. The outlet velocity was calculated by the flow rate. The top surface was set as a pressure inlet condition. To guarantee computational efficiency, the pressure implicit with splitting

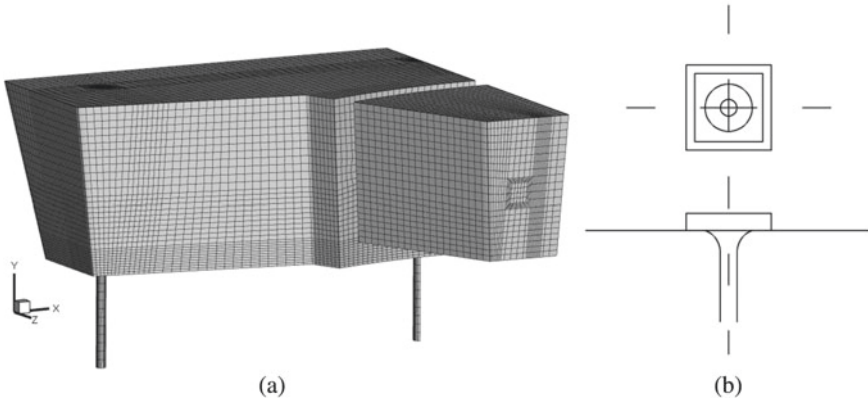


Fig. 1 Schematics of the simulation domain and square inhibiting baffle: **a** tundish model, **b** square inhibiting baffle

of operators (PISO) algorithm was chosen to solve the partial differential equation. A time step of 0.0005 s was used to ensure the stability of courant number in the transient process.

Results and Discussion

Vortex Formation Characteristics

To validate the developed mathematical model, a 1:4 scaled case was calculated to predict the free-surface vortex formation process and flow field in the water model of tundish at the casting speed of 0.48 m/min. Figure 2 shows the experimental and simulation results for the free-surface vortex formation at the strand 1. Compared with the figure in the physical model obtained by a camera, the phenomenon of free-surface vortex formation on the surface was captured well by numerical results. After the molten steel flows into the mold, the axial pressure gradient was increased in the

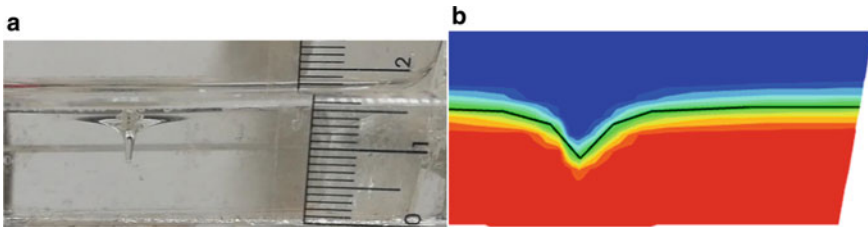
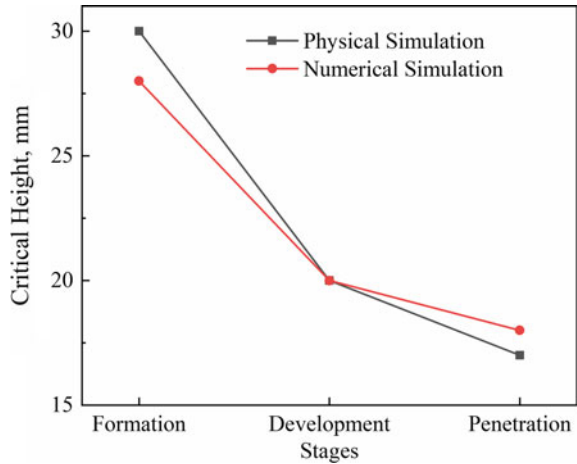


Fig. 2 Vortex formation obtained by **a** physical and **b** numerical simulation. (Color figure online)

Fig. 3 Volume fraction diagram at different stages of vortex. (Color figure online)



nozzle and forced the fluid into the nozzle. Therefore, the potential energy of molten steel was converted to kinetic energy, which was the source of vortex formation.

According to the experiments, the critical height of vortex formation at strand 2 was much smaller than that at strand 1, so this study only investigated the vortex formation at strand 1. Figure 3 shows the comparison of critical height between numerical simulation and physical modeling, in which three stages represented from the initial emergence to the final air-entrapment. All three stages were the formation, evolution, and penetration of vortex. In the formation stage, the vortex was formed in the tundish, and the free-surface was slightly deformed. With the process of casting, the angular momentum of molten steel near the nozzle gradually increased, which drove the upper liquid to rotate, causing the vortex to gradually develop. When the vortex extended to the nozzle, it was defined as the air-entrapment stage. In the same order as vortex development, the simulated critical heights was 28 mm, 20 mm, and 18 mm, respectively, which were in good agreement with the experimental results of 30, 20, and 17 mm.

Figure 4 shows the velocity distribution at different sections above the strand 1. At the free surface, which is 28 mm from the bottom of the tundish, the steel velocity was nearly 0.05 m/s, and the sink vortex was also formed. Several high velocity zones were found adjacent to the wall, and at the center of the tundish, and a clockwise vortex was formed by it. Figure 4b shows the velocity distribution 10 mm from the bottom. Compared with Fig. 4a, an increased flow velocity was detected, and the area of high velocity zones decreased. At the section 5 mm from the bottom, presented in Fig. 4c, the velocity distribution was centered on the nozzle, and the high velocity zones were narrowed further. In other words, the momentum of molten steel concentrated near the nozzle at the bottom and dissipated upward. This phenomenon indicated that amount of molten steel flowed from the walls to the nozzle and flowed from top to down, and this unbalance flow caused by asymmetric structures of tundish was the source of vortex formation.

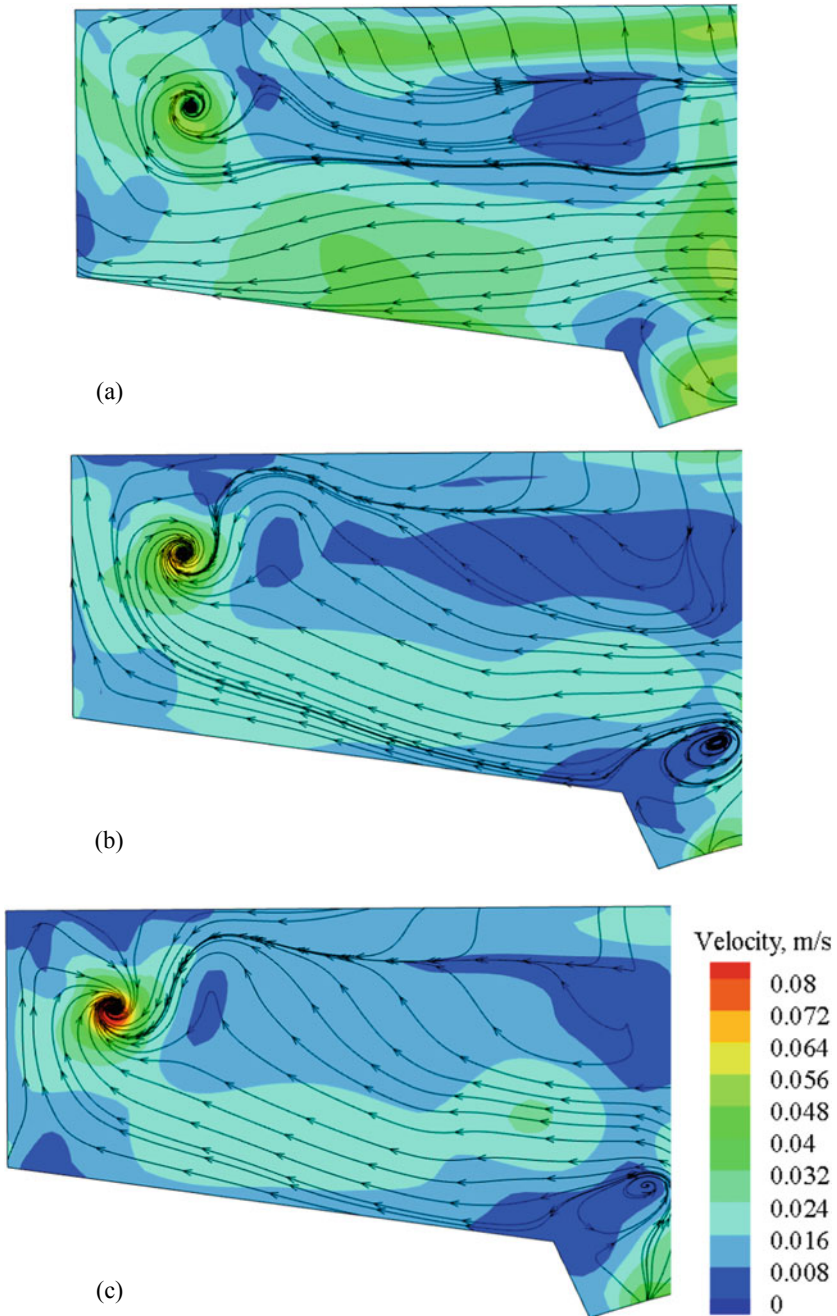


Fig. 4 Velocity distribution at different height from bottom: **a** free surface, **b** 10 mm, **c** 5 mm. (Color figure online)

Effect of Casting Speed

As mentioned previously in this study, the exit momentum at the end of continuous casting process had a significant effect on the flow pattern and promoted the vortex formation to the critical limits. Therefore, the effect of casting speed on vortex formation was studied in the practical tundish. For all cases, the simulation medium of molten steel and the similarity ratio of 1:1 were taken.

The velocity vector on the free surface 160 mm from the bottom of tundish are shown in Fig. 5. The simulation results correspond to two different casting speeds of 0.48 m/min and 0.65 m/min, respectively. At low casting speed (0.48 m/min), see Fig. 5a, the disturbance velocity was too low to form a distinct vortex, and the air-entrainment was not detect in this case. With the growing casting speed (0.65 m/min), as shown in Fig. 5b, a higher velocity developed on the interface, as well as a distinct vortex formed with air-entrainment. From the experimental results, when the casting speed increased to 0.65 m/min, the critical height of vortex formation was 40 mm, which was consistent with the numerical results.

Figure 6 shows the velocity distribution along the axis of the strand 1 nozzle corresponding to different casting speeds. For both the two cases, the velocity was very high in the nozzle, which meant the momentum dissipated less here. In the transition region, the velocity decreased rapidly with increasing the sectional area. Above the nozzle, the velocity continued to drop to near 0. Additionally, the results show that the velocity increased with casting speed; however, the velocity upon the nozzle was slightly increased, as shown in Fig. 5. This was because that most of the momentum was transferred to around rather than only above the nozzle. So the casting speed could be reduced, which was equivalent to reducing the momentum of molten steel in the tundish. The critical height of vortex formation could be decreased rapidly.

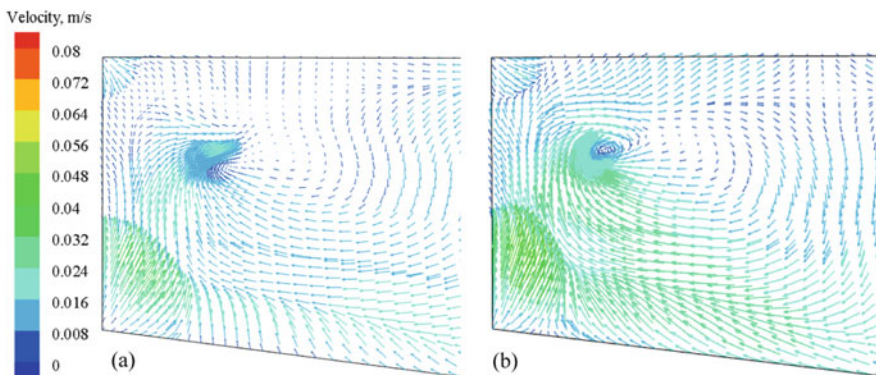
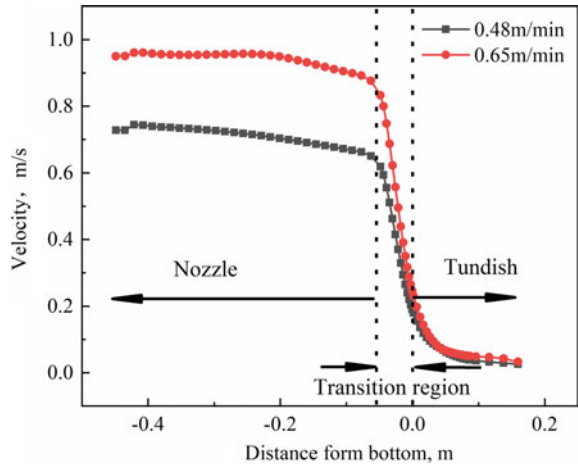


Fig. 5 Velocity vector diagram with liquid level of 160 mm at different casting speeds: **a** 0.48 m/min, **b** 0.65 m/min. (Color figure online)

Fig. 6 Velocity distribution along the axis of the nozzle. (Color figure online)



Control Strategy

According to the works ahead, the casting speed should be as small as possible to prevent the formation of vortex. However, due to the limitation of the heat energy and stable production, the casting speed should not be too low. Therefore, the casting speed of 0.48 m/min was taken in this section. The square inhibiting baffle was used to improve the flow pattern at the end of casting in the tundish and reduced the critical height of vortex formation. Figure 7 shows the simulation results of the square inhibiting baffle when the bath level is 90 mm.

Figure 7a shows that the free surface sank at this bath level which meant that the vortex was formed. For the original structure of tundish, the molten steel flowed directly into the nozzle. On the way to the nozzle, the molten steel flowed upward

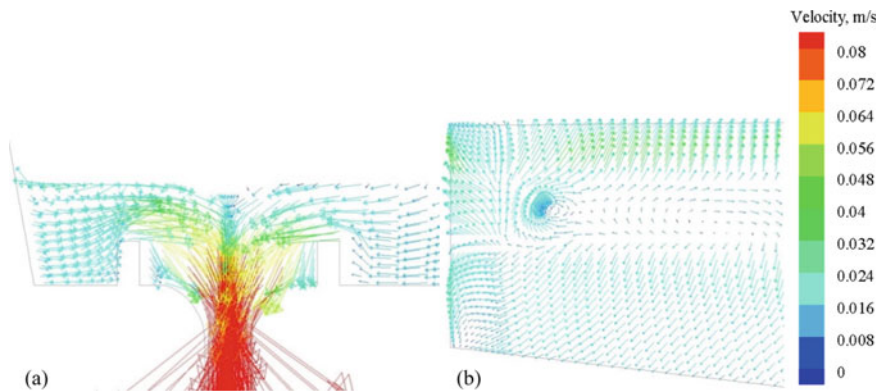


Fig. 7 Velocity vector diagram of vortex formation using square inhibiting baffle: **a** vertical section of nozzle center, **b** free surface. (Color figure online)

and passed through the square inhibiting baffle. This flow pattern increased the momentum loss and disturbed the upper fluid flow to the nozzle.

Figure 7b shows that the vortex was formed on the free surface. The square inhibiting baffle reduced the velocity and made it more even on the surface. Compared with the original tundish structure, the velocity difference on the surface was reduced, and the rotation speed upon the nozzle decreased. Therefore, the formation of vortex became more difficult, and the critical height reduced to 23 mm from experiments. Based on the experimental results and simulated results, the using of square inhibiting baffle could decrease the critical height of vortex formation significantly.

Conclusions

Based on the physical and numerical simulation, the transient vortex flow characteristics were investigated in a practical three-strand bloom tundish at the end of casting. Moreover, the control strategy was also discussed. The conclusions are as follows:

- (1) The momentum of molten steel near the nozzle gradually spread around in the process of upward propagation and high velocity zones were formed near the wall. The asymmetric distribution of high velocity regions on the free surface was the source of vortex formation.
- (2) The casting speed was a key parameter for the formation of vortex. As the casting speed increased, the critical height of vortex formation increased from 30 to 40 mm. So the casting speed should be as low as possible in this condition.
- (3) The square inhibiting baffle could force the molten steel at the bottom flow upward to disturb the upper fluid flow to the nozzle. When the casting speed was 0.48 m/min, the using of square inhibiting baffle could decrease the critical height of vortex formation to 23 mm.

Acknowledgements The authors gratefully acknowledge the National Key R&D Program of China (2017YFB0304203, 2017YFB0304201, 2016YFB0300602) and the National Natural Science Foundation of China (No. 51774072, 51774073, 51974080), which has made this research possible.

References

1. Park IS, Sohn CH (2011) Experimental and numerical study on air cores for cylindrical tank draining. *Int Commun Heat Mass Transfer* 38(8):1044–1049
2. Li HX, Wang Q, Lei H, Jiang JW, Guo ZC, He JC (2014) Mechanism analysis of free-surface vortex formation during steel teeming. *ISIJ Int* 54(7):1592–1600
3. Li HX, Wang Q, Lei H, Jiang JW, Guo ZC, He JC (2014) Analysis of factors affecting free surface vortex formation during steel teeming. *ISIJ Int* 56(1):94–102
4. Solorio-Oiaz G, Ramos-Banderas A, Barreto JJ, Morales RO (2007) Fluid dynamics of vortex formation in tundish operations: physical modelling. *Steel Res Int* 78(3):248–253

5. García-Hernández S, Solorio-Diaz G, Ramos-Banderas JA, Barreto JJ, Morales RD (2009) Fluid dynamics of vortex formation in tundish operations: mathematical modelling. *Steel Res Int* 80(4):256–263
6. Zhang H, Luo RH, Fang Q, Ni HW, Song X (2018) Numerical simulation of transient multiphase flow in a five-strand bloom tundish during ladle change. *Metals*. <https://doi.org/10.3390/met8020146>
7. Ruan YW, Yao Y, Shen SY, Wang B, Zhang JY, Huang JK (2020) Physical and mathematical simulation of surface-free vortex formation and vortex prevention design during the end of casting in tundish. *Steel Res Int*. <https://doi.org/10.1002/srin.201900616>
8. Michalek K, Gryc K, Socha L, Tkadleckova M, Saternus M, Pieprzyca J, Merder T, Pindor L (2016) Study of tundish slag entrapment using physical modelling. *Arch Metall Mater* 61(1):257–260

Part XL
Thermal Property Characterization,
Modeling, and Theory in Extreme
Environments

Energy Balance Investigation of Close-Coupled Optimized-Pressure Gas Atomization Pour-Tube Design Geometry to Prevent Melt Freeze-Off



F. Hernandez, E. Deaton, T. Prost, and I. E. Anderson

Abstract Metal additive manufacturing (AM) is an evolving technology, and the supply of quality feedstock material needs to follow suit. Closed-coupled optimized-pressure gas atomization (CCOPGA) promises narrow size distribution, spherical powder, and optimized use of gas. However, pour-tube melt solidification is an obstacle to enabling a wider alloy palette. Many solutions involve adding melt superheat, but do not account for all cooling influences. While the Joule-Thomson effect and forced convection promotes high cooling rates for the powder, excessive heat loss can lead to freeze-off. Therefore, optimizing the melt delivery geometry is needed to reduce freeze-off and down time. Analytical and numerical models are employed to study the heat transfer process between the pour tube and the surroundings for CCOPGA of both Ni and Ca melts. The effects of normalized length, radius, and thermal diffusivity are considered. Work supported by USDOE-EERE-AMO and USDOE-OE through Ames Laboratory Contract No. DE-AC02-07CH11358.

Introduction

Freeze-off in powder producing systems is of great concern because of the down time required to reactivate powder production, which can lead to significant costs. Two common solutions include: employing high-aspiration designs to increase melt

F. Hernandez (✉) · E. Deaton · T. Prost · I. E. Anderson
Ames Laboratory of US DOE, Ames, IA 50011-3020, USA
e-mail: fhernan@ameslab.gov

E. Deaton
e-mail: ericd1@ameslab.gov

T. Prost
e-mail: tprost@ameslab.gov

I. E. Anderson
e-mail: andersoi@ameslab.gov

flow rates, and increasing melt super heat. Therefore, the pour-tip design is of great significance from a transport perspective.

Unlike free-fall configurations, where the melt is mostly exposed to convective heat transfer and radiation, pour tubes in close-coupled systems also expose the melt to significant conductive heat transfer. Several freezing points have been observed in close-couple gas atomization which can be related to the principal contact regions between the melt and the system walls: the crucible, the melt delivery system, the base and tip of the pour tube, and the periphery of the truncated cone exposed to high-speed gas.

The metals in the crucible are typically heated above the liquidus or the highest melting-point temperature and this excess is known as super heat temperature (T_{sh}). Although freeze-off can be avoided for large T_{sh} , the maximum T_{sh} can be limited by several factors such as the boiling temperature of a given component, the melting point of the crucible, the maximum temperature achieved by the heating system, the activation energy of undesirable chemical reactions, among others. The melt delivery system is a pipe system that conveys the melt into the atomization chamber. This system is typically composed of straight tubes and nozzles. This region can reduce the melt temperature significantly, depending on the complexity of the design, leading to freeze-off. As the melt exits the pour tube, several breakup mechanisms and complex flows can lead to fragmentation and impingement on the pour-tube base. This flow can heat the base of the pour tube, but it can also lead to freeze-off. Another type of freeze-off occurs when the melt flows up the conical pour-tube sidewall region (lick back) and solidifies due to conduction with the pour tube and convection with the high-speed gas.

Optimal geometry (gas-die pour-tube system) implies reduced heat losses, lower operation costs and high yields. However, the design can depend on the thermo-physical and chemical properties of the materials involved, making the optimization process a case-by-case procedure. In this work, the effect of convective heat transfer, tip extension, tip radius and selected materials are studied to understand the parameters driving optimal systems. Radiation is not considered. Simplified mathematical and numerical models are employed to estimate the convective heat transfer and the temperature field. Steady-state and start-up conditions are considered.

Problem Formulation

The optimized-pressure close-coupled gas atomization process can be divided into three or more subsystems: the pressurized gas supply, the melt supply and the atomization region. Several close-coupled dies have been proposed in the literature. Here, we employ a traditional die with an annular slit to pour calcium or nickel from a stainless steel or zirconia (ZrO_2)/YSZ pour tube, respectively. A simplified domain of the problem is depicted in Figure 1 and the material properties are presented in Table 1. The thermal conductivity of calcium, κ , is obtained from the provisional values of resistivity, ρ_e , using the Wiedemann–Franz law, $k = LT/\rho_e$, where

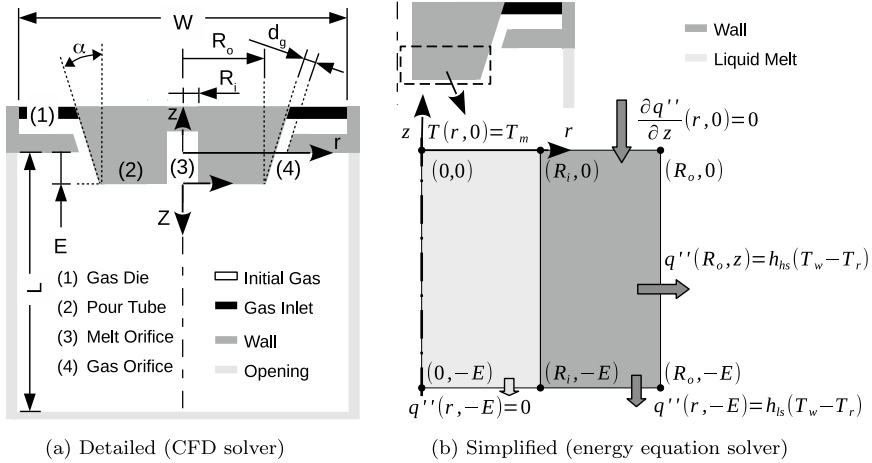


Fig. 1 Close-couple gas atomization geometry

Table 1 Material properties of the liquid (i.e. melting point) and the solid, available data (limited for Ca)

	Ar	Ca	Ni	Steel	Al ₂ O ₃	ZrO ₂ /YSZ
Density, ρ (kg/m ³)	Variable	1396.7	7810 [5]	8000 [7]	–	5680
Conductivity, k (W/m K)	0.024	82.5	54.2 [1]	21.4 [7] (1115 K)	12	3.0 [6]
Specific heat, C_p (J/kgK)	520.3	873.3 [2]	1176.8 [5]	665 [7]	–	420
Specific heat, C_v (J/kgK)	312.2	793.9 ($\gamma \sim 1.1$)	871.7 [5]	536 [5] (γ of Fe)	–	380
Melting point temperature, T_{mp} (°C)	–	842	1453	–	–	–

$L = 2.44 \times 10^{-8} \text{ W}\Omega\text{K}^{-2}$, $\rho_e = 33 \times 10^{-8} \Omega\text{m}$ and T is the liquid temperature[3]. This problem is analyzed in terms of the geometric parameters,

$$\mathcal{R} = \frac{R_o}{R_i}, \mathcal{D}_g = \frac{d_g}{E}, \mathcal{E} = \frac{E}{R_o} \tag{1}$$

where R_o is the base pour-tube radius, R_i is the melt orifice radius, d_g is the annular slit gap and E is the extension length of the pour tube.

Simplified Mathematical Model

The heat equation in cylindrical polar coordinates, $\mathbf{r} = (r, \theta, z)$, for a solid with constant conductivity can be used to understand the fundamental principles of the heat transfer problem,

$$\frac{\partial T}{\partial t} = \alpha_s \left[\frac{1}{r} \frac{\partial}{\partial r} \left(r \frac{\partial T}{\partial r} \right) + \frac{1}{r^2} \frac{\partial^2 T}{\partial \theta^2} + \frac{\partial^2 T}{\partial z^2} \right] \quad (2)$$

where α is the thermal diffusivity, $\alpha = \frac{k}{\rho C_v}$, ρ is density, C_v is the specific heat at constant volume, k is thermal conductivity and the subscript s stands for solid. Initially, the solid temperature is $T(0, r, z) = T_{w0}$, while the melt temperature is T_m . The simplest solution is the 1D steady-state problem without azimuthal heat transfer that is subject to a fixed temperature at the inner wall, $T(R_i) = T_m$, and convective heat transfer rate per unit area at the outer wall, $q_r(R_o) = h_g(T_w - T_r)$, where T_r is the adiabatic wall or recovery temperature associated with the convective heat transfer coefficient h_g , and $T_w = T(R_o)$. Solving Eq. (2) gives the steady-state temperature,

$$T_s(r) = T_m - \frac{Bi_s}{1 + Bi_s \ln \mathcal{R}} \ln \frac{r}{R_i} (T_m - T_r) \quad (3)$$

in terms of the radius ratio, $\mathcal{R} = \frac{R_o}{R_i}$, the solid Biot number, Bi_s , or the cylindrical Biot number, Bi_{cs} ,

$$Bi_s = \frac{h_g R_o}{k_s}, \quad Bi_{cs} = \frac{h_g R_o}{k_s} \ln \mathcal{R} \quad (4)$$

which evaluated at $r = R_o$ gives the minimum wall temperature,

$$T_w = \frac{T_m + Bi_s \ln \mathcal{R} T_r}{1 + Bi_s \ln \mathcal{R}}, \quad T_w \equiv \frac{T_w}{T_m} = \frac{1 + Bi_s \ln \mathcal{R} \frac{T_r}{T_m}}{1 + Bi_s \ln \mathcal{R}} \quad (5)$$

and the steady-state radial heat transfer rate for an extension length E ,

$$Q_r = \frac{2\pi R_o E h_g}{1 + Bi_s \ln \mathcal{R}} (T_m - T_r), \quad Q \equiv \frac{Q_r}{2\pi R_o E h_g (T_m - T_r)} = \frac{1}{1 + Bi_s \ln \mathcal{R}} \quad (6)$$

Equation (6) shows that reducing R_o and E while increasing \mathcal{R} can reduce reduce Q_r significantly, meanwhile increasing Bi_s while reducing h_g can reduce Q_r further. Typical values of Bi_s and Bi_{cs} are shown in Table 2, where $\mathcal{R} = 1$ occurs in co-flows, $\mathcal{R} \rightarrow \infty$ in free jets and the typical range for CCOPGA is $3 \lesssim \mathcal{R} \lesssim 8$. The solid can show more relevant temperature gradients, particularly for ZrO_2 since it is less conductive. The effect of material selection and temperature range operation is depicted in Figure 2 in terms of the normalized tip temperature, T_w , and the normalized heat conduction, Q . A case with $\mathcal{R} = 4$ and ZrO_2 could have $Q = 0.5$ or $Q = 0.35$ for relatively small or large R_o , respectively. A case with $\mathcal{R} = 2$ and

Table 2 Solid Biot numbers for different pour-tube materials considering $R_i = 1$ mm and $h_g = 500 \frac{W}{m^2K}$

\mathcal{R}	Bi_s			Bi_{cs}			Bi_s			Bi_{cs}				
	R_i (mm)	R_o (mm)	Steel	Al_2O_3	ZrO ₂	Steel	R_i (mm)	R_o (mm)	Steel	Al_2O_3	ZrO ₂	Steel	Al_2O_3	ZrO ₂
2	1	2	0.05	0.08	0.33	0.03	4	8	0.19	0.33	1.33	0.13	0.23	0.92
3	1	3	0.07	0.13	0.5	0.08	2.67	8	0.19	0.33	1.33	0.21	0.37	1.46
4	1	4	0.09	0.17	0.67	0.13	2	8	0.19	0.33	1.33	0.26	0.46	1.85
5	1	5	0.12	0.21	0.83	0.19	1.6	8	0.19	0.33	1.33	0.30	0.54	2.15
6	1	6	0.14	0.25	1.0	0.25	1.33	8	0.19	0.33	1.33	0.33	0.60	2.39
8	1	8	0.19	0.33	1.33	0.39	1	8	0.19	0.33	1.33	0.39	0.69	2.77

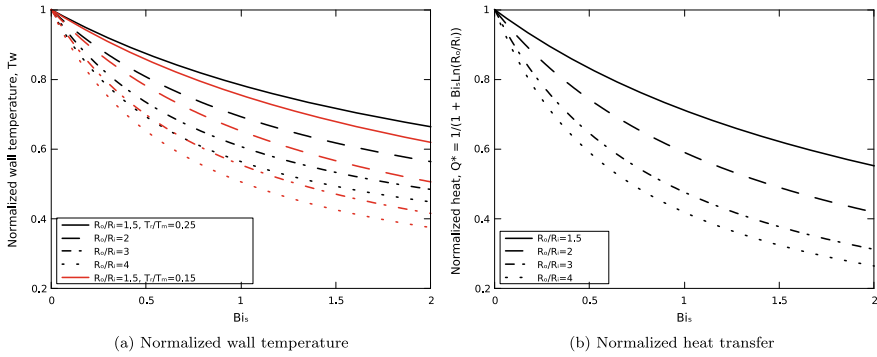


Fig. 2 Normalized wall temperature and heat transfer in terms of Bi_s . (Color figure online)

steel could have $Q = 0.96$ to $Q = 0.88$, for relatively small or large R_o , respectively. However, for a fixed Q , Q_r increases linearly with R_o .

Numerical Formulation

An immiscible multiphase model is employed, where the solid is considered quiescent, isobaric and incompressible, while the gas is compressible and the liquid metal is not considered. Mass, momentum and total energy are solved discretized using the finite volume method and Runge-Kutta-3. Details of the model can be found in [4]. The simplified 2D axisymmetric problem solves the thermal energy for the liquid and the solid only,

$$\frac{\partial \rho e}{\partial t} + \nabla \cdot [\rho \check{u} \mathbf{u}] = -\nabla \cdot \mathbf{q} \tag{7}$$

considering uniform velocity v_l entering the domain (thermal advection term). The discretion is based on Euler backward and finite volumes. Here, $e = \check{u} + \frac{1}{2} \mathbf{u} \cdot \mathbf{u}$ is the total energy per unit mass, \check{u} is the internal energy per unit mass and \mathbf{q} is the conduction heat flux given by the Fourier's law,

$$\mathbf{q} = -k \nabla T \tag{8}$$

Methodology

A fully 3D gas-solid flow solver is employed for estimating h_g and T_r . The solid temperature is initially uniform and set to $T_{w0} = 800$ K. The argon gas flow is suddenly started as in [4], where the gas total condition are p_0 and T_0 . From

Table 3 Geometric and flow conditions for the simulations

Flow		Geometric						
Property	Value	Case	R_i (mm)	R_o (mm)	E (mm)	\mathcal{E}	\mathcal{R}	\mathcal{D}_g
p_0 (psia)	100	0	1.5	7.25	2.9	0.4	4.8	0.44
T_0 (K)	286.5	1	1	7.25	4.2	0.58	7.3	–
p_∞ (atm)	1.1	2	1.5	7.25	4.2	0.58	4.8	–
T_∞ (K)	300	3	3	7.25	4.2	0.58	2.4	–
T_w (K)	800–1023	4	1.5	7.25	5.8	0.8	4.8	–
v_l (m/s)	2	5	2.0	4.0	4.0	1.0	2.0	–

the solution, $\frac{\partial T}{\partial r}$, mach number Ma and h_g are computed. The normal derivative is approximated to the radial derivative since the angle is relatively small. The convective heat transfer coefficient is estimated from the relation $h_g(z) = k_g \frac{dT}{dr_w} / (T_w - T_r)$, where T_r is grossly approximated to the flat plate solution $T_r \approx \left[1 + \sqrt{Pr^*} (\gamma - 1) / 2Ma_e^2 \right] T_\infty$. The Prandtl number, Pr^* , is computed at the reference temperature $T^* \approx (0.5 + 0.039Ma_e^2) T_\infty + 0.5T_w$ [8]. Then, the simplified 2D axisymmetric model is employed to calculate the liquid and solid temperature distribution. Several geometric conditions are studied, as summarized in Table 3.

Results and Discussion

The detailed gas flow over a close-coupled system (gas die and pour tube) is simulated for case 0. The convergence on mesh refinement is addressed. The temperature is extracted at time 0.16 ms, near the middle of the pour tube ($z/E \sim -0.5$) and along the radial coordinate. The convergence on local mesh refinement is presented in Figure 3. It can be observed that the difference in h_g and T reduces considerably between $\Delta r = 2.8 \mu\text{m}$ and $\Delta r = 5 \mu\text{m}$.

The convective heat transfer coefficients at the exterior and bottom walls are calculated for $T_{w0} = 800 \text{ K}$ and $\Delta r = 2.8 \mu\text{m}$. This is presented in Figure 4. As it can be observed, the temperature distribution varies considerably for different axial locations, which also affects h_g . For instance, h_g is larger at the start of the boundary layer, reduces diatonically until reaching a minimum at the flow detachment point (not shown) and then increases monotonically. The polynomial fit will be employed in the next section, scaled in terms of $\zeta = |z| / E$. Notice how the local T_∞ also varies. The recovery temperature variation is minimal ($\Delta T_r < 5 \text{ K}$). The proposed heat transfer rate per unit area is given by $q(\zeta) = h_{gr}(\zeta) (T_w - \bar{T}_r)$, where $h_{gr}(\zeta) = \sum_{i=0}^8 A_i \zeta^i$ (A_i is shown in Fig. 4) and $\bar{T}_r = 292 \text{ K}$.

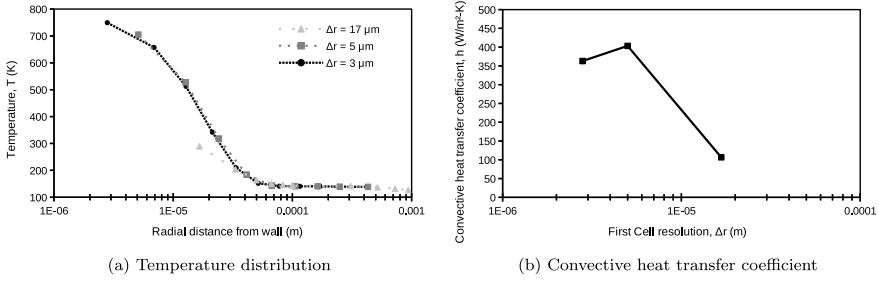


Fig. 3 Effect of mesh refinement at $t \sim 0.1$ ms and $z/E \sim -0.5$

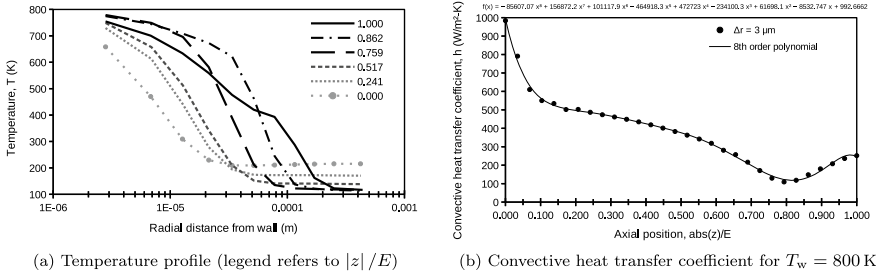


Fig. 4 Variation of properties at different locations ($|z|/E$) for the finest mesh $\Delta r = 3 \mu\text{m}$ and $t = 0.16$ ms

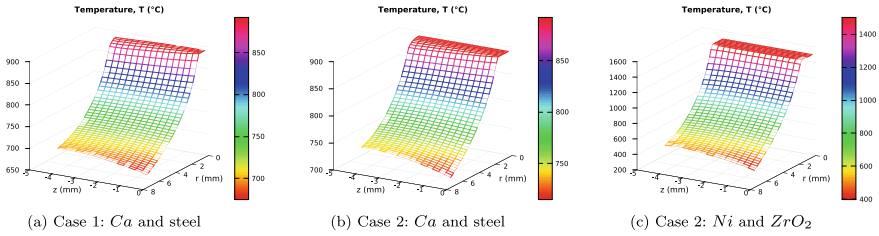


Fig. 5 Example of the pour-tube and melt temperature distribution. The liquid flows from right to left. (Color figure online)

Another important convective heat transfer coefficient is needed at the bottom of the pour-tube. For this initial study, gas-only flow conditions will be explored. Here, the subsonic heat transfer will consider $q(\zeta) = \bar{h}_{gb}(\zeta)(T_w - \bar{T}_\infty)$, where $\bar{h}_{gb} = 109 \text{ W/m}^2\text{-K}$ and $\bar{T}_\infty = 281 \text{ K}$.

Now, the 2D axisymmetric heat equation is solved and the steady-state solution is reported, considering superheat temperature of $T_{sh} = T_{mp} + 50 \text{ K}$, $T_{w0} = 750^\circ\text{C}$ and $\Delta r = 180 \mu\text{m}$. An example of the temperature profile is shown in Figure 5. The case with $\mathcal{R} = 4.8$ was observed to give sufficient insulation, as was predicted in Fig. 2 for $\mathcal{R} = 4$ ($Q = 0.79$). Notice how the Ni/ZrO_2 case achieves lower wall temperatures than the $Ca/Steel$ case.

Table 4 Steady-state minimum temperature (°C) and outflow heat transfer rate (W) of the pour tube

Case	Material	\mathcal{R}	\mathcal{E}	$T_{\text{melt min}}$	T_w	T_w 1D (Eq. (5))	Q_{radial}	$Q_{\text{radial 1D}}$ (Eq. (6))	Q_{bottom}	Q_{top}	Q_{net}
0	Ca/Steel	4.8	0.4	883	715	705	34.1	36.0	13.2	21.0	68.3
1	Ca/Steel	7.3	0.58	873	675	677	46.9	50.0	12.9	29.1	88.9
2	Ca/Steel	4.8	0.58	881	715	705	49.8	52.2	13.3	32.0	95.2
2	Ni/ZrO ₂	4.8	0.58	1501	396	612	30.8	43.9	12.6	13.1	56.5
3	Ca/Steel	2.4	0.58	887	782	760	54.6	56.3	12.8	32.4	99.7
4	Ca/Steel	4.8	0.8	879	715	705	69.4	72.0	13.5	40.7	123.6
5	Ca/Steel	2.0	1.0	888	843	803	30.8	31.5	3.7	9.0	43.5

Table 5 Minimum centerline temperature ($r = 0, z = -E$). Comparison against $T_{\text{mp}} = 842\text{ }^\circ\text{C}$

T_{w0} (°C)		750			600		500			300	
T_{sh} (°C)		892	942	992	892	942	892	942	992	1042	1092
\mathcal{R}	t (ms)	T_m (°C)			T_m (°C)		T_m (°C)			T_m (°C)	
9.0	2.2	853.8	890.4	926.9	813.5	850.0	786.6	823.1	859.7	842.4	879.0
7.3	2.3	868.2	909.9	951.5	843.1	884.8	826.4	868.0	909.7	917.8	859.5
4.8	2.7	888.9	937.8	986.8	885.7	934.6	883.5	932.4	981.3	1025.9	1074.8

The heat transfer rate and minimum temperature is presented in Table 4 for different cases. Notice how the minimum temperature does not reach T_{mp} for any of the selected cases. The most important heat exchange occurs radially, from the melt into the high-speed gas, follow by the top. From cases 1–3, lowering \mathcal{R} increases Q_{net} . Notice that case 4 has the largest Q_{net} primarily due to the large extension, E . Case 5 shows how reducing R_o for low \mathcal{R} and large \mathcal{E} lowers Q_{net} . Case 2 shows how using zirconia reduces T_w and Q_{net} for a liquid with large T_{mp} (Ni).

Now, the critical radius ratio and super heat for preventing calcium solidification at the central axis during start-up is investigated. Here, \mathcal{R} , T_{w0} and T_{sh} are varied for $\mathcal{E} = 0.58$ (constant R_0 and E) and radial mesh resolution $\Delta r = 73\text{ }\mu\text{m}$. The lowest centerline temperature of calcium is reported in Table 5. For $T_{w0} = 300\text{ }^\circ\text{C}$, using large \mathcal{R} requires superheat temperatures at least $200\text{ }^\circ\text{C}$ above the melting point, meanwhile only $50\text{ }^\circ\text{C}$ for $T_{w0} = 750\text{ }^\circ\text{C}$. For $\mathcal{R} \leq 4.8$, the effects of T_w and T_{sh} are relatively small or null ($\mathcal{R} < 2.4$, developing thermal boundary layer).

Conclusions

For a fixed pour-tube outer radius (constant Biot number), reducing the inner radius reduces radial heat transfer rates, predicted analytically and numerically, but can also reduce the melt core and minimum temperatures. Preheating reduces the required

superheat temperature, particularly for thick pour-tubes. The minimum liquid temperature reaches its lowest value during startup and increases with preheat temperature. Reducing the extension length, outer radius and selecting insulating materials such as YSZ are effective ways of reducing the cooling effect.

Acknowledgements Work supported by USDOE-EERE-AMO and USDOE-OE through Ames Laboratory Contract No. DE-AC02-07CH11358. Special thanks to Dustin Hickman for providing the estimation of calcium thermal conductivity.

References

1. Assael MJ, Chatzimichailidis A, Antoniadis KD, Wakeham WA, Huber ML, Fukuyama H (2017) Reference correlations for the thermal conductivity of liquid copper, gallium, indium, iron, lead, nickel and tin. *High Temperatures High Pressures* 46(6), 391–416. <https://pubmed.ncbi.nlm.nih.gov/29353915>
2. Chase M NIST-JANAF thermochemical tables, 4th edn, pp 1–1951. *J Phys Chem Ref Monograph* 9. American Institute of Physics (1998)
3. Chi TC (1979) Electrical resistivity of alkaline earth elements. *J Phys Chem Ref Data* 8(2):439–497. <https://doi.org/10.1063/1.555599>
4. Hernandez F, Riedemann T, Tiarks J, Kong B, Regele JD, Ward T, Anderson IE (2019) Numerical simulation and validation of gas and molten metal flows in close-coupled gas atomization. In: TMS 2019 148th annual meeting & exhibition supplemental proceedings. Springer International Publishing, Cham, pp 1507–1519
5. Nasch PM, Steinemann SG (1995) Density and thermal expansion of molten manganese, iron, nickel, copper, aluminum and tin by means of the gamma-ray attenuation technique. *Phys Chem Liquids* 29(1):43–58. <https://doi.org/10.1080/00319109508030263>
6. Schlichting KW, Padture NP, Klemens PG (2001) Thermal conductivity of dense and porous yttria-stabilized zirconia. *J Mater Sci* 36(12):3003–3010. <https://doi.org/10.1023/A:1017970924312>
7. Valencia J, Quested P (2008) Thermophysical properties. In: *Casting*. ASM international, vol 15. ASM International, pp 468–481. <https://doi.org/10.1361/asmhba0005240>. <http://hdl.handle.net/11115/166>
8. White FM (2006) *Viscous fluid flow*, Chap 7-3. McGraw Hill, pp 517–521

Author Index

A

Achakovsky, O. I., 657
Adam, Khaled, 565
Ahmed, Aninda Nafis, 1017, 1036
Ahmed, Farid, 131
Aifantis, E. C., 793
Algendy, A., 165
Ali, Usman, 131
Alvarez Montaña, Victor Emmanuel, 375
Anatoly, Popovich, 142
Anawati, John, 305
Anderson, I. E., 1075
Angiolini, M., 626
Antonelli, A., 626
Archambeau, Claude, 176
Arnold, Bradley, 247, 980
Avdeenkov, A. V., 615, 657
Avila, J., 189
Awd, M., 753
Azimi, Gisele, 305, 316

B

Barrera-Villatoro, E. F., 902
Barsoum, F., 879
Barz, Jakob, 230
Bassini, S., 626
Belgasam, Tarek, 565
Beygi, Mohamad, 777
Bieler, Thomas R., 207
Boot, Tim, 722
Bowen, Paul, 839
Brown, Francisco, 375
Brunstein-Ellenbogen, Tyler, 285

C

Campillo, B., 909
Cantarella, Giuseppe, 294
Cao, Yijun, 15
Cataldo, S., 626
Çelik, Osman Halil, 679
Chai, Wencui, 15
Chandrasekar, Srinivasan, 921
Chen, Chuantong, 701
Cheng, Yanqing, 1045
Chen, Min, 398, 1045, 1063
Chen, X. -G., 165
Choa, Fow-Sen, 247, 980
Chou, Kevin, 149
Chow, Tien See, 285
Cleary, William, 121
Conde, F., 189
Cooper, Christopher, 247
Cooper, Christopher E., 980
Costa, Júlio, 294

D

Dadfarnia, Mohsen, 853
Daroowalla, Rayan, 259
Deaton, E., 1075
Delp, A., 867
Deng, Xiang-yang, 891
Devanathan, Ram, 461
Dey, Poulumi, 730
Dhmi, Harish Singh, 921
Diao, Jiang, 765
Díaz-Villaseñor, P. G., 909
Dinda, Soumitra Kumar, 346
Ding, Rengen, 839
Di Piazza, I., 626

Dong, Aqi, 571
 Dong, Tony, 305
 Dong, Yingrui, 50
 Douin, Joël, 176
 Duan, Qianqian, 50
 Durán, Alejandro, 375
 Dvivedi, Akshay, 421
 Dzisah, Patrick, 964

E

Edge, Chelsea, 207
 Emadi, Rahmattollah, 359, 392
 Emile, Philippe, 176
 Engler-Pinto, Carlos, 75
 Engler-Pinto Jr., Carlos, 100
 Enoki, Manabu, 473
 Esmailizadeh, Reza, 131
 Evgenii, Borisov, 142

F

Fanciulli, Carlo, 527
 Fatemi, A., 753
 Feng, Chenyin, 777
 Ferroni, P., 626
 Fiore, A., 626
 Fisher, Zoe L., 121
 Fratello, Virginia San, 37
 Frewin, Christopher L., 777

G

Gallegos-Pérez, A. I., 902, 909
 Gao, Xiaoqiang, 514
 Garnica-González, P., 902
 Ghomashchi, R., 271
 Gokce, Oktay H., 219
 Gordon, Ali P., 110
 Gotawala, Nikhil, 669
 Graf, Thomas, 230
 Gu, J., 165
 Güner, Mehmet Buğra, 679
 Gu, Wen-Feng, 765

H

Haque, Nawshad, 995
 Harris, William, 553
 Hawk, Jeffrey, 461
 Heifetz, Alexander, 121
 Heinzl, Annette, 605
 Hemming, Daniel, 230
 Henn, Manuel, 230

Hernandez, F., 1075
 Hossain, Samiha, 219
 Hoyos, E., 189
 Hsieh, Ming-Chun, 701
 Hua, Xiaojie, 1063
 Huang, Shuheng, 331

I

Ickes, M. R., 626
 Ilyas, Sadia, 1055
 Inoue, Junya, 473
 Islam, Md Khairul, 995
 Isotta, Eleonora, 527
 Iwaki, Aya, 701

J

Jamshidi, Negar, 853
 Jamshidi, Nilofar, 853
 Jana, Swarup, 829
 Jardini, A. L., 189
 Jiang, Wenbo, 331
 Jiang, Yu, 92
 Jianu, Adrian, 605
 Jiao, Shuqiang, 92
 Jones, Katie, 553

K

Kabir, Nafees, 615
 Kaneshita, Takeshi, 473
 Kantyukov, Artem, 197
 Kelly, Lisa, 247, 980
 Kelly, Stephen, 553
 Keshavarzkermani, Ali, 131
 Khraishi, Tariq, 507
 Kikuchi, Tatsuya, 338
 Kim, Hyunjung, 1055
 Kirill, Starikov, 142
 Kitano, Masamichi, 473
 Kömmelt, Pascal, 730
 Konar, Murat, 679
 Kumar, Ashok, 777
 Kumar, N., 742
 Kumar, Pradeep, 421

L

Lai, Wei-Jen, 75, 100
 Lall, Amrita, 839
 Lamichhane, Aneer, 3
 Laudone, Giuliano, 553
 Lei, Jing, 765

Lepech, Michael, 711
 Liang, Jinglong, 409, 803, 935
 Liao, Yilong, 365
 Liewald, Mathias, 230
 Li, Hui, 409, 803, 935, 1045
 Li, Hui-cheng, 891
 Lim, Hojun, 507
 Li, Liang, 579
 Lin, Leqi, 259
 Li, Shao-xiang, 590
 Li, Song, 383
 Liu, Jinrui, 803
 Liu, K., 165
 Liu, Liang, 765
 Liu, Ping, 722
 Liu, Wei-dong, 579
 Li, Xiaobao, 1045
 Liu, Yang, 398
 Li, Yin, 943
 Li, Yuanhui, 365
 Li, Zhiye, 711
 Li, Ziang, 75
 Lopez-Castaño, Silvia, 176
 Luo, Chao, 409, 935
 Luo, Yiwa, 92
 Luo, Yongguang, 383
 Lu, Tengfei, 543

M

Ma, Aiyuan, 383
 Makua, T. N., 1026
 Malik, Monu, 316
 Ma, Mengyao, 15
 Mamun, Osman, 461
 Mandal, K. D., 980
 Mani, B. S., 285
 Mann, James B., 921
 Martelli, D., 626
 Marzbanrad, Ehsan, 131
 Ma, Zhen, 365
 McBrayer, I. M., 879
 Mehta, Vishal R., 955
 Meka, Venkatesh, 829
 Mishra, R. S., 742
 Mohanty, Debapriya Pinaki, 921
 Mukherjee, Binayak, 527
 Mukhopadhyay, Jyoti, 829
 Müller, Georg, 605
 Münzenrieder, Niko, 294

N

Nafisi, S., 271

Nagata, Kenji, 473
 Nahian, M. K., 1007, 1017
 Nastac, Laurentiu, 571, 1007
 Natsui, Shungo, 338
 Ng, Kok Long, 305, 316
 Nogami, Hiroshi, 338

O

Ojha, Avinesh, 75, 100
 Okanigbe, D. O., 1026
 Okuno, Katsuki, 473
 Okuno, Yoshishige, 473
 Oliveira, J. P., 189
 Orlov, A. I., 615, 657
 Özçelik, Gökem, 679

P

Padamata, Sai Krishna, 812
 Panda, Priti Ranjan, 921
 Parisis, K., 793
 Peng, Jun, 935
 Peng, Y., 1007
 Petti, Luisa, 294
 Pettinari-Sturmel, Florence, 176
 Piolle, N., 60
 Polozov, Igor, 197
 Polyakov, Peter, 812
 Popoola, A. P. I., 1026
 Popovich, Anatoly, 197
 Popovich, Vera, 197, 722, 730
 Prasad, Narasimha, 247
 Prost, T., 1075
 Pugno, Nicola M., 527

Q

Qiu, Guibao, 365, 543

R

Rabiei, Afsaneh, 839
 Rangaraju, Ritvik R., 259
 Rao, Rajashekar, 829
 Ravindra, Nuggehalli M., 3, 219, 259, 285, 955, 964
 Reddy, Ramana, 1036
 Reddy, R. G., 1007, 1071
 Reichardt, Gerd, 230
 Reichle, Paul, 230
 Reinton, Elise, 722
 Riedmüller, Kim, 230
 Riemslog, Ton, 722
 Rivera, Krystal, 110

Roccisano, A., 271
 Rodriguez, J., 189
 Rose, Kelly, 461
 Roy, Gour Gopal, 346
 Ruiz-Candelario, Isha, 110

S

Sachs, David, 247, 980
 Sadow, Stephen E., 777
 Sadeghzade, Sorour, 359, 392
 Sagar, Saurabh, 730
 Sanders, John W., 853
 Sarker, Dyuti, 131
 Sartorio, C., 626
 Scardi, Paolo, 527
 Scholz, R., 867
 Schroer, Carsten, 642
 Setera, Brett, 247, 980
 Sharma, Subhash, 375
 Shibuya, Ryota, 338
 Shinde, P. S., 1017
 Shrestha, Subin, 149
 Shribak, Dmitry, 121
 Shrivastava, Amber, 669
 Siddique, Abu Bakar, 507
 Siddique, S., 753
 Siddiqui, Sanna F., 110
 Singh, N. B., 247, 980
 Singh, Ramver, 421
 Somerville, Michael A., 995
 Sova, Stacey, 247
 Srirangam, Prakash, 346
 Srivastava, Rajiv Ranjan, 1055
 Stalheim, D., 271
 Stubbins, James, 853
 Su, Ching Hua, 980
 Su, Xuming, 75, 100
 Subramanian, Sankara, 853
 Suetake, Aiji, 701
 Suganuma, Katsuaki, 701
 Sun, Chengyu, 383
 Suzuki, Ryosuke O., 338

T

Takemoto, Shimpei, 473
 Tang, Hai-yan, 579, 590
 Tang, Ping, 331
 Tanjil, Md Rubayat-E, 777
 Tarantino, M., 626
 Tavangarian, Fariborz, 359, 392
 Tordoff, Benjamin, 553

Tovar, Günter E. M., 230
 Toyserkani, Ehsan, 131
 Tran, Anh, 447, 481, 495
 Tran, Hoang, 495
 Tu, Jiguo, 92

U

Udupa, Anirudh, 921
 Umlauf, Georg, 230

V

Vázquez-Gómez, O., 902, 909
 Vahlstrom, Logan, 691
 Varshney, P., 742
 Varyukhin, Dmitriy, 812
 Veater, Ben, 553
 Vera, Popovich, 142
 Vergara-Hernández, H. J., 902, 909
 Viswanathan, Koushik, 921
 Volkenandt, Tobias, 553

W

Walters, Carey L., 722
 Walther, F., 753, 867
 Wang, Cheng, 514
 Wang, Li, 943
 Wang, Michael Cai, 777
 Wang, Nan, 1045
 Wang, Pu, 579, 590
 Wang, Shan, 398
 Wang, Song-wei, 579
 Wang, Xu, 365
 Wang, Ying, 1045
 Wang, Yingtao, 25
 Wang, Yongzhou, 514
 Wang, Zhe, 331
 Weber, Rudolf, 230
 Weisenburger, Alfons, 605
 Wen, Guanghua, 331
 Wenzlick, Madison, 461
 White, Robin, 553
 Wildey, Tim, 447, 481

X

Xiao, Hong, 590
 Xie, Bing, 765
 Xie, You, 891
 Xuan, Mingtao, 1063
 Xu, Rui, 50
 Xu, Yanke, 409

Y

Yan, David P., [433](#), [691](#)
Yang, Ding, [543](#)
Yang, Xianglan, [398](#)
Yang, Yongbin, [50](#)
Yan, Hongyan, [409](#), [935](#)
Yao, Yaochun, [943](#)
Yasinskiy, Andrey, [812](#)
Yuan, Jing, [891](#)
Yuan, Meimei, [943](#)
Yuan, Zhichen, [50](#)

Z

Zhang, Guangzong, [1045](#)
Zhang, Jia-quan, [579](#), [590](#)
Zhang, Kaizhu, [1063](#)
Zhang, Keyu, [943](#)
Zhang, Shanshan, [149](#)
Zhang, Tianru, [605](#)
Zhang, Xian, [25](#)
Zhang, Zheng, [701](#)
Zhao, Da-tong, [579](#)
Zheng, Xuemei, [383](#)
Zheng, Zhong, [514](#)
Zhou, Hanghang, [543](#)
Zhu, Jun, [92](#)

Subject Index

A

Acid leaching, 1057
Acoustic emission, 880, 882, 883
Additive Manufacturing (AM), 37, 38, 41, 47, 48, 110, 121, 122, 131, 132, 134, 138, 139, 142, 176, 177, 189–193, 195, 197, 198
Advanced high strength steels, 731
Advantages of contactless transmission, 286
Advantages of lfw process, 64
Aerostructure, 66, 67, 72
Ag paste sinter-joining, 702, 707
Air quenching granulation, 765–767, 773
AlCl₃-urea, 316–318, 321–326
AlCl₃-urea ILAs, 318
Allocation, 514–516, 518–523
Al-Mg 5xxx alloys, 165
AlSi10Mg, 75, 77, 78, 86, 89, 100–104, 108, 109
Alumina–spinel castables, 398–401, 403, 407
Aluminum, 211–215, 680
Aluminum dross, 1045–1049, 1051–1053
Aluminum ion battery, 316, 326
A machine based process quality assurance, 64
Amorphous silicon carbide (a-SiC) supported PPF INI, 784
Analysis of element transfer, transport and re-precipitation, 644
Analysis of physical properties of zinc kiln slag, 936
Analysis of rheological properties of metal nps conductive ink, 969
Analytical techniques, 463
Anisotropy, 256

API X70, 271, 280
Applications on UHCSDB database, 499
Applications in aircraft engines, 65
Applications in aircraft structures, 66
Applications on aluminum parts, 71
Architecture, 37, 42, 43, 45, 48
Area-Selective ALD (AS-ALD), 220
A stochastic inverse problem for structure-property relationship in materials design, 452
Asynchronous parallel Bayesian optimization framework, 485
Atomic Layer Deposition (ALD), 219–226
Atomic Layer Etching (ALE), 219, 220

B

Background and boundary conditions”, 237
Basic assumptions and equations, 592
Basic characterization of used CO₂ as lubricant substitutes, 236
Bayesian learning for neural networks, 475
Bayesian optimization, 481, 482, 485, 486
Beam oscillation, 346, 349, 352–354
Bentonite, 50–58
Bio-ceramic, 392, 393
Biocompatibility of a-SiC, 784
Blisk, 60, 65, 66, 71, 72
BMG /Al interconnects, 691
Bond quality, 880
Boundary condition and solution modes, 581
Boundary conditions and solution methods, 594
Bulk and Micromorphology, 983
Bulk transparency, 984
Buy-to-Fly, 66, 68

C

Calculation of secondary resistances ($R_c R_{ct}$), 1012
 Capital costs, 995, 1002–1005
 Carbon-based nanomaterials, 777–779, 781
 Carbothermal reduction, 937
 Case design, 519
 Cavitation, 854
 Cellulose, 867, 868, 870, 873, 874
 Cement content, 398, 399, 404, 406, 407
 Center equiaxed crystal ratio, 579
 Ceramic application, 1026, 1027, 1032, 1033
 Cerium, 1055–1061
 Characterization and Electrochemical Testing of AlCl₃-TMAHCl IL, 308
 Characterization of DST, 1028
 Chardonnay, 46
 Chemical composition, 1029, 1032
 Chemical reactions with molten salt, 412
 Chemicals and materials, 318
 Circuits, 299
 Circularity, 351, 353, 354
 Clustering, 461, 463, 469–471
 Coal-based activated carbon, 15–17, 22
 Coating, 359–363, 421–426, 428
 Cobalt, 543–549
 Cogging operation, 831
 Coils, 288, 291, 292
 Colloidal metal, 339, 341
 Combination of lfw with other processes, 68
 Comparative study of coefficients of friction measured by SBTs using normal contact pressure, 243
 Comparison of the properties of HS binder and bentonite pellets, 57
 Comparison with the rotary friction welding, 65
 Compositional analysis of BMGs-to-Al joint interface, 697
 Computational details, 1066
 Conditioning, 294, 295, 298–301
 Conductive ink, 964–968, 970, 972–974, 976, 977
 Conductive wires, 957
 Conductivity, 1017–1024
 Constant voltage electrolysis, 803, 804, 808
 Construction improvement and application of material database, 898
 Constant voltage electrolysis, 803, 804, 808
 Contact angle, 247, 248, 254–256
 Contact angle measurements, 254
 Contactless torque transmission, 285

Contamination, 879–886
 Continuous heating dilatometry, 912
 Continuous tempering, 912
 Control strategy, 1070
 Convection, 1075, 1076
 Conventional semiconductors, 262
 Coolant, 615–620, 623
 Copper smelter dust, 1026–1029, 1032, 1033
 Copper tailings, 1026–1028, 1032
 Corrosion, 605, 606, 608, 611, 613–615, 618, 623, 642, 742, 744, 745, 747, 749
 Corrosion of materials in lead, 628
 Corrosion results, 629
 Cottonid, 867–877
 9% Cr alloy, 461, 462, 469, 471
 Cr₂AlC-Al₂O₃ (max-phase on Al₂O₃ substrate), 611
 Crack initiation, 873, 874
 Crash box, 679
 Creep, 853–856, 858–862
 Creep rupture test, 847
 Creep test microstructural observation, 848
 Criteria for quasi-equilibrium and crack-like void growth, 861
 Crystal, 980, 981, 983–988
 Crystal plasticity, 447
 Crystallographic textures – EBSD, 276
 Cs₂PbBr₄, 5–10
 CsPb₂Br₅, 5–10
 CsPbBr₃, 4–10
 Current density, 1036–1043
 Current intensity, 590, 591, 597, 599, 600
 Cutting temperature, 433, 435, 438, 439, 441, 442
 Cutting temperatures, 439
 Cyclic voltammetry, 730, 732, 733
 Cyclic voltammetry and full cell testing, 320

D

Damage, 711–720
 Damage mechanisms, 869
 Data analytics, 462
 Data collection, 462
 DC and AC performance, 296
 Deep drawing, 230–232, 240, 245
 Defects, 75–77, 79, 84–89
 DEFORM 3D, 829, 830
 Deformation processing, 923, 926, 927, 930, 931
 Dehydration, 383–385, 388–390
 Dehydration ratio analysis, 385

- Density functional theory, 730, 732
Density separation, 1026, 1028, 1032, 1033
Dependence of heat energy on reduction degree of 'FeO', 1050
Dependence of Seebeck coefficient on phase purity, 530
Dependence of slag-composition variation on basicity of the modified slag, 1048
Dependence of slag-composition variation on reduction degree of 'FeO', 1049
Deterioration, 712, 717
Determining data quality, 463
Device structure and fabrication, 295
Devices, 299
DFT results, 737
Die attach, 701–707
Dielectrics, 219–221, 224–226
Differential dilatometry, 911
Diffusion, 853–855, 857, 858, 862
Diffusion barriers, 219, 223, 224
Dilatometric Analysis, 904
Dilatometry, 909–912
Dipoles, 507–512
Directed Energy Deposition (DED), 176, 177, 181, 186
Disadvantages of contactless transmission, 287
Dislocation-based CPFEM, 450
Dislocations, 507–512
Dispersoids, 165–167, 172–174
Dissimilar joining, 691
Dissimilar material joining, 669, 670
Dissolution, 812–817, 819–821, 824
Dissolution of catalysts, 819
Dissolution rate, 816
Double hot thermocouple technique, 331, 332
3D printing, 37–41, 44, 48, 285, 287, 288, 956
3D printing and the role of rapid prototyping, 287
Dry forming, 231, 245
Drying apparatus and procedure, 384
Dynamic programming, 514, 516, 518, 521
Dynamic recrystallization, 669, 670, 672, 673, 677
- E**
E[⊙] and raw material ratio, 414
Effect of applied potential on current densities, 1038
Effect of ball-milling on raw materials, the, 368
Effect of casting speed, 1069
Effect of composition, 251
Effect of Coolant Supply on Microstructure Evolution in Hole Surface, 437
Effect of Cutting Speed on Precipitation of New α Phase in Hole Surface, 440
Effect of electrode distance on current density, 1041
Effect of high temperature annealing, 256
Effect of hydrogen on mechanical properties, 725
Effect of pre-capping agent in the solution, 982
Effect of reduction and strain rates, 834
Effect of sample mass on temperature increase characteristics, 387
Effect of stirring speed on current density, 1040
Effect of strengthening mixing HS type binder, 53
Effect of temperature gradient, 832
Effect of ultraviolet radiation, 253
Effect on microwave power on temperature increase characteristics, 385
Effect on the microstructure of material by adding FeV80 powder, 371
Effect on the pore structure and mechanical property of material by adding FeV80 powder, 372
Effects of electrolysis voltage on the product, 808
Efficiency, 259, 260, 262–264, 267
Electrical and mechanical performance, 296
Electrical conductivity, 1019
Electric Discharge Machining (EDM), 422–424, 426, 428
Electrochemical characterization, 945
Electrochemical performance, 15, 16, 18
Electrochemical performance analysis, 18
Electrochemical reduction, 803, 805, 806
Electrochemical stability, 316–318, 324
Electrochemical Testing and Measurements, 307
Electrode distance, 1037, 1040–1043
Electrode materials, 16, 19, 21
Electrode-oxygenation reaction, 410
Electrode processes at the LBE, 821
Electrode processes characterization, 818
Electrolysis, 812–816, 818, 822–824
Electrolysis temperature, 414
Electrolysis test, 818, 823
Electromagnet, 286

Electromagnetic field, 590, 591, 593, 594, 600
 Electron BackScatter Diffraction (EBSD), 273, 275, 277
 Electron beam welding, 346, 347, 349
 Electronic properties, 3, 5, 7, 10
 Electro-refiner, 1000
 Electrosorption experiments, 17
 Electrosorption performance, 23
 Elemental Mo, 609
 Energy density, 131–133, 136–139
 Energy Gap, 259–267
 Energy storage, 313
 Epoxy, 879, 880, 884–886
 Equiaxed grains for TWIP steels under uniaxial tension, case study, 454
 Estimation of Cell-level Energy and Power Density of Al/GCM Battery Employing Various AlCl₃-RCl ILs, 312
 Estimation of relative loss of iron in steel, 664
 Evolution of BMGs-to-Al joint interface, 697
 E-waste, 995–1005
 E-waste generation in Bangladesh and characterisation, 996
 E-waste smelter, 1000
 Experimental approach, 733

F

Fabrication of porous Ti-6Al-4V by SLM 3D-printing, 94
 Fatigue, 75–77, 79, 80, 82–89, 100, 101, 103–107, 109
 Fatigue test, 101
 Fe–Al alloys, 803–805, 807–810
 FeAl₂O₄ synthesis reaction, 940
 FeCrAl ODS alloy (MA 956), 631
 Fe-FeAl₂O₄ cermet, 935–937
 Fe-FeAl₂O₄ composite material, 409, 410
 Ferrovandium, 365, 367
 Fiber reinforced composites, 717, 718
 Films, 615–623
Finite element stress analysis, 103
 First batch: two samples, 1029
 Flexible active oxide electronics, 295
 Flexible electronics, 297
 Flow and meniscus behavior, 583
 Fluid flow, 590, 591, 600
 Force sensor, 957
 Formation of dispersoids during heat treatment, 171

Formation of intermetallics, 653
 Fractional gradient elasticity and dislocations, 794
 Fractional gradient interatomic potentials, 797
 Fractional Laplacian, 794–796
 Fractography, 725–727
 Friction investigations, 232, 237, 240, 241, 243, 245
 Friction welding, 65
 FTIR analysis, 21
 Full cell testing, 325
 Fundamental solution of the fractional Helmholtz equation, 796

G

Gas atomization, 1075–1077
 Gas sensors, 956
 Gaussian process regression, 451
 Gears, 286–288
 Global microstructure evolution, 182
 Gradient elasticity, 793, 794
 Grain boundary, 853–858, 860, 862
 Grain growth, 481, 482, 487, 488
 Grain size, 275
 Grain size and fraction, 566
 Graphene nanoplatelets, 316, 318, 319, 326
 Graphite, 553–555, 558, 559, 561, 562
 Grinding, 927–930

H

Hardening, 507, 508, 510, 512
 Hardness, 1033
 Hardness test, 1026, 1030, 1033
 Hardystonite, 359, 360, 362, 363
 Heat energy underlying molten nickel slag with different discharge temperatures, 1050
 Heat flux, 331–336
 Heat partition, 922–924, 926, 929, 930
 Heat partition problem, The, 923
 Heat transfer, 342
 Heat transfer and solidification behavior, 585
 Heat transfer operation, 830
 Heavy liquid metal coolant, 615
 Heterogeneity, 182
 Heterogeneous structures, 568, 569
 Heterostructures, 25, 26
 HF leaching, 1056, 1058, 1061
 High Cycle Fatigue (HCF) test, 80, 82
 High entropy alloy, 742

High flux simulation and calculation of experiment and materials, 893
High laser power, 143
High-performance, 305, 306, 313
High-speed digital microscopy, 339
High-speed drilling, 433, 435, 442
High-temperature mechanical properties, 402
High temperature test, 842
High throughput detection and characterization of experimental support, 896
High throughput experimental procedure, 893
High-Throughput (HT), 891–899
High throughput analysis of experimental data, 898
High throughput preparation of experimental samples, 895
Hot modulus of rupture, 402
Hour dwell loading, 850
Hsu-Nielsen, 879–881, 886
Hydrogen embrittlement, 722, 723
Hydrogen trapping, 734, 738, 739
Hydrophobicity, 247, 253, 257
Hydroxyapatite, 359, 360, 363

I
ICME, 447, 448, 450, 481–483
IGZO electronics in magnetic fields, 298
Image J, 354
Image inpainting, 497–503
Image processing, 350, 496
Image processing/analysis/visualization, 557
Implantable neural interface, 778, 787
Implementation and diagnostics, 452
Impurities, 615, 616, 657–660
 $\text{In}_{1+x}(\text{Ti}_{1/2}\text{Zn}_{1/2})_{1-x}\text{O}_3(\text{ZnO})_m$, 375, 376
Incremental forming, 927
Influence of dissolved oxygen, 652
Influence of electrolysis reaction, 413
Influence of HS binder dosage, 54
Inhibiting baffle, 1063, 1065, 1066, 1070, 1071
Inkjet printing, 965, 967, 976, 977
Inkjet printing processes, 967
In-situ heat treatment, 197, 198, 202
In-situ quantitative method, 331
In Situ Quasi-Static Tensile Tests in μCT , 874
In Situ Quasi-Static Tensile Tests in SEM, 873

In-situ SEM Characterization, 839
In situ testing, 723, 728, 867, 870
Integrated analog conditioning circuits, 298
Integration, 299
Interatomic potentials, 793, 794, 797–799
Intermetallic, 197, 198
Intermetallic phase, 654, 655
Interstitial-free steel, 599
Inverse problems, 448
Ionic conductivity, 316, 317, 319, 323, 326
Ionic conductivity and electrochemical stability of AlCl_3 -urea ILA, 323
Ionic liquid, 1007–1009, 1012, 1013, 1017, 1019–1021
Ionic Liquid Analogues (ILAs), 317
Ionic liquids, 1036–1038, 1042, 1043
Iron oxide reduction reaction, 937
Iron yield, 660–666
ITZO, 375, 377–381

J

Joint interface microstructure, 691

K

Kesterite (CZTS , $\text{Cu}_2\text{ZnSnS}_4$), 527, 528
KF- AlF_3 , 815, 816, 818–823
Kinetic Monte Carlo, 481, 487, 489
Kinetic Monte Carlo simulation, case study, 487
Kinetics, 902, 903, 905–907

L

Laser drilling, 230, 232, 233
Laser drilling of the microholes, 232
Laser Powder Bed Fusion (LPBF), 75, 100, 131–134, 136–139, 149–151, 159
Laser power effect on single-track formation, 153
Layered crystal structure, 375, 376
Lead, 616, 618, 620
Lead-bismuth, 618
Lead coolant, 660
Lead corrosion, 628
Level fluctuation, 579, 580, 585
LFR, 626, 627, 639, 641
Lfw application, 67
Lfw applications in aerospace industry, 65
Linear Friction Welding (LFW), 60–68, 70–72
Linear polarization and passive layer characterization, 744

- Linear sweep voltammetry and electrochemical impedance spectroscopy, 318
- Liquid metal, 642–645, 647–653, 655
- Liquid metal batteries, 605, 614
- Lithium ion batteries, 943
- Lithium iron phosphate, 943, 949
- Local evolution in the vicinity of the thermal bands, 183
- Lotus effect, 247, 248, 257
- M**
- Macro-segregation of Silicon, the, 573
- Macrostructure features, 179
- Magnetic Augmented Rotation System (MARS), 285–288, 292
- Magnetic flux density, 596
- Magnetic levitation, 286, 288, 289, 291
- Main concepts of motor, 288
- Maraging steel, 189, 190, 192, 195
- Market share, 961
- Martensite, 131, 132, 138, 139
- MASKA-LM code, 660
- Mass transfer, 617, 618, 620, 657–659, 666
- Material balance calculation, 1053
- Material processing route, 744
- Materials characterization by microstructure descriptors, 483
- Materials and methods, 755
- Materials Genome Initiative (MGI), 891
- Mathematical formulations, 1065
- Mathematical model, 1065
- Measures of differences between microstructures via microstructure descriptors, 484
- Mechanical strain, 297
- Mechanical properties, 64
- Mechanical properties and deformation mechanisms, 96
- Mechanical property, 92, 1033
- Mechanochemical synthesis, 393, 396
- Medium–Carbon Steel, 903–905, 907
- Mesoscopic surface formation, 150, 152
- Metal forming, 922
- Metallization, 222
- Metallization schemes, 222
- Metal materials, 891–894, 896, 898, 899
- Metal solution and selective leaching from alloys, 644
- Methods for GO synthesis, 782
- Methods for graphene growth, 781
- Micro and nanohardness, 912
- Microelectronics, 219, 222, 224
- Microfocus computer tomograph, 867, 869–871, 876
- Micro-friction stir spot welding, 692
- Micrograph, 497, 499
- Micromorphology of Cr-ZnSe Crystal and nanoparticles, 984
- Micro-scale x-ray Imaging, 556
- Microstructural characterization, 189
- Microstructural, electrochemical, and SCC characterization, 744
- Microstructural Evolution during tensile tests at various temperature, 845
- Microstructure, 134, 176–184, 186, 405, 571, 572, 576–578, 744, 869, 872
- Microstructure descriptors, 482–485, 487–489
- Microstructure generation, 449
- Microstructure reconstruction, 495–497, 499–503
- Microstructure and XRD Pattern of As-received Ti-5553, 436
- Microstructure evolution, 433, 435, 442, 576
- Microstructure evolution at Al 6061 and mild steel interface, 672
- Microstructure of cathode deposits, 1042
- Microstructures, 274
- Microstructure under as-deposited/as-cast and heat-treated conditions, 168
- Microwave drying, 384, 385, 388, 389
- Microwave drying experiment of zinc leaching residue, 388
- Misorientation angle versus $m'/\Delta b$, 210
- Misorientation angle versus the sum of the Schmid factors, 209, 214
- Misorientation angle vs. m' , 208, 212
- Misorientation angle vs. $m'/\Delta b$, 214
- Mo alloys, 631
- Model, 514, 515, 521
- Model assumption and governing equations, 581
- Model calculations for different steels, 660
- Model formulation, 767
- Model hypothesis, 766
- Modelling construction, 1047
- Modelling of viscosity-temperature relation, 969
- Model of shear stress-shear rate relation, 968
- Model of viscosity-shear rate relation, 968
- Models from the literature, 261
- Moisture, 711–717, 720
- Moisture transportation, 713
- Mold flux, 331–336
- Molten converter slag, 765–771, 773

Molten salt, 814, 816, 824
Molten salt deoxidation, 409
Molten salt electrolysis, 340
Molten salt system, 413
Monte Carlo Potts, 566, 567
Morphological characterizations, 20
Morphology, 248, 249, 251, 253, 256, 257
Multiphysics, 712, 713, 717
Multiphysics modeling of gfrps, 713
Multiple knapsack problem, 514
Multiscale, 553, 560–562
Multiscale modelling, 712
M' vs. residual Burgers vector (Δb), 209, 211

N

N₂ adsorption/desorption isotherms and pore structure, 22
Nanocomposites, 247, 254, 256
Nanocrystals, 980, 981, 990
Nanoindentation, 909, 910, 914, 915
Nano-powders, 393
Nano-scale x-ray imaging, 556
Near-dry, 421–424, 428
Ni-based alloys, 629
Nickel-based Alloy, 142
Nickel slag, 1045–1053
NIMONIC 115, 829–831
Nondestructive evaluation, 121
Non-isothermal thermodynamic model, 1045–1047, 1053
Normal contact pressure of radii using FE-methods, 241
Notch effect, 100, 106
Nozzle injection mode, 579, 580
Nuclear magnetic resonance analyses, 319
Numerical formulation, 1080
Numerical investigation of the fluid behaviour inside the microholes", 237
Numerical simulation, 766, 768
Numerical study, 158

O

Observed microstructure and its evolution, 182
Offline sensing, 960
Operating costs, 995, 1002–1005
Optical Characteristics of Cr₂ doped ZnSe crystals, 986
Optical characterization, 983
Optical properties, 3, 5, 9, 10

Order-disorder transition, 529, 530, 532–534, 536, 537
Order parameter, 529, 530, 534–537
Organic binder, 50, 51, 54, 55
Other oxide reduction reactions, 938
Oxalate precipitation, 1060
Oxidation, 642, 648, 652
Oxide semiconductors, 298
Oxide film, 657–666
Oxidized pellets, 50, 57
Oxygen control, 626, 627, 638–641
Oxygen Control activities in Pb alloys, 638
Oxygen regime, 657, 658, 660, 662, 665, 666

P

Parametric studies of apparent effusivity reconstruction with COMSOL computer simulations of heat transfer, 124
Particle Size Distribution (PSD), 1028, 1031
Partitioning Around Medoids/ K-Medoid Clustering, 469
Passive sensors, 955, 956, 960
Pelletizing, 53
Performance of Al/GNP Battery Employing AlCl₃-TMAHCl IL, 310
Permanent mold casting (PM), 165–174, 170, 172
Perovskites, 259, 260, 263–267
17-4 PH stainless steel, 131
Physical and numerical simulation, 1063, 1064, 1071
Physical model, 1064
Physical properties, 399, 401, 402, 407
Physical state, 320
Physical structures of the porous Ti-6Al-4V alloys, 95
Physical vapor transport, 981
Phytic acid, 943, 947
Pipeline steel, 722, 723, 728
Plant trial results, 587
Platform heating, 754, 755, 757, 760, 761
Platinum Group Metals (PGM), 812–815, 820, 824
Polymer, 359, 360, 363
Pore structure, 15, 16, 20, 22, 23
Porosity, 346–348, 351, 354, 355, 543, 547, 549, 553, 554, 558–562
Porosity distribution, 136
Post-joint profile and cross section configuration, 693
Potential, 1036–1043

Powder materials, 37, 48
 Powder metallurgy, 365, 544
 Power-law creep, 859
 Power law model, 964, 966–970, 973, 976, 977
 Power law model of conductive ink, 967
 Power law model (ostwald model), 969
 PPF electrode fabrication on a-SiC, 785
 Prediction of three properties, 479
 Prediction of two properties with a linear neural network, 476
 Pre-heating and roasting of HS binder pellets, 55
 Preheating roasting, 53, 58
 Preheating roasting experiment, 53
 Preliminary results of a-SiC/PPF device, 786
 Pre-melted samples preparation, 332
 Preparation of battery electrodes, 319
 Preparation of Electrolytes and GNP Electrodes, 307
 Preparation of Fe–Al alloy by molten salt electrolysis, 809
 Preparation of sample, 944
 Preprocessing, 517
 Pretreatment of raw materials, 368
 Primary creep effects, 860
 Principal component analysis, 463
 Principle of increasing property, the, 373
 Printable conductive nanomaterials, 966
 Printed electronics, 964–966, 976, 977
 Printing, 25–27, 29–32
 Priority confirmation in different scenarios, 517
 Probabilistic approach to fatigue strength prediction, 86
 Problem formulation, 483, 1076
 Problem configuration, 509
 Process-structure, 481–483, 487, 489
 Process modeling and simulation, 1009
 Process simulation, 999
 Proecess modelling, 1009
 Property, 365–367, 371–374
 PS/PMMA, 251
 PVT Grown bulk ZnSe crystal, 981
 Pyrolyzed-photoresist film, 777

Q
 Quality of slab with different process parameters, 599
 Quasi-static loading, 867
 Quasi static surface roughness, 156

R
 Rare Earth Metals (REM), 1056
 Rate of slag entrapment, 590, 599, 600
 Raw materials and composition, 399
 Reaction thermodynamics, 410
 Reduction mechanism, 804, 806, 810
 Reliability, 701, 702
 Remnant porosity, 754, 757, 758, 760, 761
 Residual stress, 92, 93, 95, 98, 99
 Response Surface Methodology (RSM), 566
 Retrieval of an order parameter from Seebeck curve, 533
 Rheological properties of conductive ink, 967
 Rotary Friction welding, 669–671
 Rupture, 853, 854, 860, 862

S
 Salt, 38
 Sample preparation, 101
 Sample preparation and testing, 400
 Saturation, 657, 660, 663–666
 Sb₃Sn₇ environment, 608, 609, 612
 SbBi₉ environment, 608, 611, 612
 Sb–Bi alloy, 613
 Sb–Sn alloy, 605, 613
 Scaffold, 359–363
 Scanning electron microscope, 867, 876
 SCC susceptibility, 279
 Secondary hardening, 909, 910, 914, 917
 Secondary phases, 527, 529–537
 Second batch: two samples, 1029
 Second well loading, 849
 Seebeck coefficient, 527–530, 532–537
 Seebeck coefficient as an effective method to observe and distinguish the effects of phase purity and degree of order, 536
 Segregation, 576
 Selective laser melting (SLM), 92, 93, 142, 143, 146, 147, 189, 190, 192, 197–200, 202, 203, 755
 Selective leaching, 642, 646, 649–655
 Self-cleaning process, 64
 SEM, 496
 Semiconductors, 259–264, 266, 267
 Sensor technology, 294, 295, 298–301
 Shear rate, 964, 967–970, 972–974, 976, 977
 Shear stress, 964, 966–970, 972, 976
 Shell thickness, 579, 586
 SiC, 782–784
 SiC Hexaloy, 636

- Signal consistency, 881
Simplified mathematical model, 1078
Simulation, 25–31, 33, 829–832, 834, 835, 1081
Simulation modelling, 830
Single crystal alloy, 143
Slimes melter, 1001
Slip transfer, 207–215
Slow Strain Rate Tensile Test (SSRT), 745
Smelter, 996, 999–1003
Softening, 507, 508, 510, 512
Soil, 41
Solar Cells, 259–264, 267
Solidification, 1075, 1083
Solidification and heat transfer, 765, 773
Solidification map, 578
Solid mechanics model at structural level, 715
Solid State Welding, 64
Solution, 642, 644–648, 650, 652, 653, 655
Solvent extraction with organophosphorus mixture, 1059
Solvothermal, 943, 944, 949
Spark plasma sintering, 1029
Spark plasma sintering graphs, 1029
Speciation, 316, 317, 321
Spent catalyst, 812–816, 820, 824
Spin casting on the glass and silicon surface, 250
Stainless-steel GP1, 110, 113, 116
Statistical microstructure descriptors as outputs, 487
Steel, 608
Stirring speed, 1037, 1039–1043
Stir zone temperature history relating to joint interface formation, 695
Strain based fatigue model, 715
Stress Corrosion Cracking (SCC), 271–273, 279–281, 742, 743
Stretch bending testing rig, 240
Structural properties, 3, 5, 10
Structural scale, 718, 720
Structure-property, 447–450, 452, 454, 456
Structure and stability, 6
Study on the preparation of pellets with added HS binder, 53
Sub-micron X-ray Radiography, 347, 350
Superheat dissipation, 580, 585, 587, 588
Surface grinding, 928
Surface integrity, 421, 423, 425
Surface roughness, 149, 150, 156
Sustainability, 38
Synthesis and modification of CAC, 17
Synthesis methods of CBN, 781
Synthesis of Cr-doped ZnSe nanoparticles, 982
Synthesis of Pyrolyzed Photoresist Films (PPF), 783
Synthesis of ZnSe nanoparticles, 981
- T**
Techno-economic assessment, 1002
Temperature, 259–267, 714, 964, 966–970, 972–975, 977
Temperature distribution, The, 769
Tempering, 902–907, 909–917
Tensile properties, 275, 843
Tensile property, 137
Tensile strength and fracture surface analysis, 674
Tensile test and hardness measurement, 79, 80
Test Setup for Microstructural In Situ Investigations, 870
Test specimens, 880
Test Strategy for Characterization of Damage Development on Surface and in Volume, 872
Texture, 271–273, 276–280
Theoretical approach, 733
Theory, 508
Thermal analysis, 923
Thermal cycling test, 701–704
Thermal resistance, 332–336, 701–703, 706, 707
Thermal shock resistance, 398, 399, 401, 404, 406, 407
Thermal tomography, 121, 122, 124, 125, 127
Thermal tomography principles, 122
Thermodynamic, 409, 410, 413, 941
Thermoelectric behavior of kesterite polymorphs, 530
Thermoelectric (TE) materials, 528
Thermo-Mechanical Control Processing (TMCP), 271, 272
Thermos-fluid modeling, 150, 159
Thin-film transistors, 294–296
Third batch: two samples, 1029
Three-dimensional geometrical model of M-EMS, 592
Three-strand tundish, 1063, 1064, 1071
Ti-5553, 433–438, 441, 442
Ti-6Al-4V, 61, 63, 64, 67, 92–99
Time-frequency, 879, 882

Time frequency analysis, 882
Tin reducer, 1001
Titanium, 207, 211–215, 543–548, 1017, 1018
Titanium alloys, 177
Titanium Nitride (TiN), 421, 423–426, 428
Titanium welding, 60, 61, 66, 71, 72
Tool and workpiece (2-body problem), 925
Tool, workpiece and chip (3-body problem), 925
Tool, workpiece and fluid (3-body problem), 926
Tool, workpiece, fluid and wear fragment (4-body problem), 926
Track repeatability, 152
Track surface morphology, 152
Tribological investigations, 240
Two-dimensional materials, 25–27, 29, 31–33

U

Ultrashort pulsed, 233
Uncertainty quantification, 447, 448
Unit interaction model, 923
Unplanned slab, 514–523
UV, 711, 712, 715–717, 720
UV radiation model, 714

V

Validity of developed model, 595
Value recovery, 999, 1000, 1003
Variable-amplitude fatigue, 110, 111, 114
Vickers' hardness test, 1030

Viscosity, 964–970, 972–977
Viscosity and temperature of conductive ink, 972
Void growth, 853–856, 858, 860–862
Vortex flow characteristics, 1063, 1071
Vortex formation characteristics, 1066

W

Waste heat recovery, 766
Wavelets, 879, 882–885
Weak Bonds, 879, 880
Willemite, 392–396
Wire + arc additive manufacturing (WAAM), 165–174

X

X-ray Radiography, 350
X-ray tomography, 553, 556

Y

Yield strength, 365, 371–373

Z

Zinc kiln slag, 935–941
Zinc leaching residue, 383–390
ZnSe, 980–982, 984, 986, 988–990
Zone 1, 179
Zone 2, 180
Zone 3, 181
2-zone furnace, 573
Zr alloys, 635